QA: QA

MDL-NBS-HS-000023 REV 01

May 2007

Simulation of Net Infiltration for Present-Day and Potential Future Climates

Prepared for:
U.S. Department of Energy
Office of Civilian Radioactive Waste Management
Office of Repository Development
1551 Hillshire Drive
Las Vegas, Nevada 89134-6321

Prepared by:
Sandia National Laboratories
OCRWM Lead Laboratory for Repository Systems
1180 Town Center Drive
Las Vegas, Nevada 89144

Under Contract Number:
DE-AC04-94AL85000

DISCLAIMER

This report was prepared as an account of work sponsored by an agency of the United States Government. Neither the United States Government nor any agency thereof, nor any of their employees, nor any of their contractors, subcontractors or their employees, makes any warranty, express or implied, or assumes any legal liability or responsibility for the accuracy, completeness, or any third party's use or the results of such use of any information, apparatus, product, or process disclosed, or represents that its use would not infringe privately owned rights. Reference herein to any specific commercial product, process, or service by trade name, trademark, manufacturer, or otherwise, does not necessarily constitute or imply its endorsement, recommendation, or favoring by the United States Government or any agency thereof or its contractors or subcontractors. The views and opinions of authors expressed herein do not necessarily state or reflect those of the United States Government or any agency thereof.

QA: QA

Simulation of Net Infiltration for Present-Day and Potential Future Climates

MDL-NBS-HS-000023 REV 01

May 2007

ACKNOWLEDGMENTS

This work relied on the expertise and hard work from a list of individuals too long to list here. The main technical contributors including their areas of responsibility are listed below:

Joshua Stein (SNL)	Lead author, project integrator, and team lead.
Al Reed (SNL)	Conceptual model development, MASSIF model developer, model validation (comparison to streamflow measurements)
Dan Levitt (LANL)	Conceptual model development and model validation (comparison to site-specific datasets)
John Stormont (UNM)	Conceptual model development
David Groeneveld (HydroBio)	Evapotranspiration model development and satellite measurement of vegetation
Bob Walsh (Apogen)	Stochastic precipitation model development, Parameter and model uncertainty
John Del Mar (Apogen)	Parameter and model uncertainty
Cedric Sallaberry (SNL)	Stochastic precipitation model development, uncertainty and sensitivity analysis
Rick Allen (UI)	Evapotranspiration model development (FAO-56 consultation and model development of solar radiation on slopes)
Kaylie Rasmuson (BSC)	Evapotranspiration model development (Site specific vegetation)
Elena Kalinina (GRAM)	Model validation (Lysimeter simulations and HYDRUS comparisons)
Joseph Kanney (SNL)	Model validation (comparison to regional net infiltration estimates)

INTENTIONALLY LEFT BLANK

Model Signature Page/Change History

Complete only applicable items.

1. Total Pages: ~~944~~ 942
CNH 5/24/07

2. Type of Mathematical Model

☒ Process Model ☐ Abstraction Model ☐ System Model

Describe Intended Use of Model

The purpose of the model documented in this report is to provide a spatial representation, including uncertainty, of the predicted average annual net infiltration at the Yucca Mountain site during three climates scenarios predicted for the next 10,000 years.

3. Title

Simulation of Net Infiltration for Present-Day and Potential Future Climates

4. DI (including Revision No. and Addendum No.):

MDL-NBS-HS-000023 REV 01

	Printed Name	Signature	Date
5. Originator	Joshua S. Stein	Joshua S. Stein	5/24/2007
6. Independent Technical Reviewer	Charles Haukwa		5/24/07
7. Checker	Earl Mattson	Earl D. Mattson	5/24/07
8. QCS/Lead Lab QA Reviewer	Brian Mitcheltree		5/24/07
9. Responsible Manager/Lead	Cliff Ho	Clifford K. Ho	5/24/2007
10. Responsible Manager	Stephanie Kuzio		5/24/2007

11. Remarks

Change History

12. Revision No. and Addendum No.	13. Description of Change
REV 00	Initial Issue This report is a revision of the report by the same title, Document Identifier ANL-NBS-HS-000032 (USGS 2003 [DIRS 166518]). In this new model report, changes were made in response to recommendations from the Regulatory Integration Team/Natural Systems Team. The entire model documentation was revised. Changes were too extensive to use Step 5.8f)1) per AP-SIII.10Q, REV 02, ICN 07.

REV 01	This report is an extensive rework of the previous revision. A new model, MASSIF (Mass Accounting System for Soil Infiltration and Flow) was developed. Changes were too extensive to use change bars. Upon completion of this report, the following 14 Condition Reports (CRs) are closed: CRs 2842, 3551, 5071, 5222, 5356, 5698, 5907, 6312, 6334, 6938, 7184, 7589, 7729, and 9227. There are no actions associated with this report for the following open CRs: 7626—is an opportunity for improvement. The reevaluation of input data for CR 7627 was considered exemplary and therefore a lessons-learned is required so the method used might be generally applied to other License Application documents. 7627—requires reevaluation of 68 DTNs that were shown as "Qualified" in the TDMS and were used as direct input to the previous version of this report. However, none are used as direct input to this revision. If appropriate, the qualification status of some DTNs will be changed, but that will not affect this revision. CR 9580—identifies preliminary output files from this document as containing errors; however, this revision shows these output files were rerun with errors corrected. A separate in-process data qualification report is qualifying the preliminary data for use as the errors were tolerably small. CR 10472—concerns a suspected error in streamflow measurements used to validate the MASSIF model. The model has been validated successfully with the existing streamflow data; if the resolution of the CR confirms this suspected error, it would provide further support to validation of the MASSIF model.

CONTENTS

Page

CONTENTS (Continued)

Page

CONTENTS (Continued)

Page

CONTENTS (Continued)

Page

CONTENTS (Continued)

Page

INTENTIONALLY LEFT BLANK

FIGURES

Page

FIGURES (Continued)

Page

FIGURES (Continued)

Page

FIGURES (Continued)

Page

FIGURES (Continued)

Page

FIGURES (Continued)

Page

FIGURES (Continued)

Page

FIGURES (Continued)

Page

FIGURES (Continued)

Page

FIGURES (Continued)

Page

FIGURES (Continued)

Page

INTENTIONALLY LEFT BLANK

TABLES

Page

TABLES (Continued)

Page

TABLES (Continued)

Page

TABLES (Continued)

Page

TABLES (Continued)

Page

TABLES (Continued)

Page

TABLES (Continued)

Page

TABLES (Continued)

Page

TABLES (Continued)

Page

INTENTIONALLY LEFT BLANK

ACRONYMS AND ABBREVIATIONS

B.P.	before present
BSC	Bechtel SAIC Company
CDF	cumulative distribution functions
cm	centimeter
CMB	chloride mass balance
COL	*Coleogyne* vegetation association
COTS	commercial-off-the-shelf
DEM	digital elevation model
DIRS	Document Input Reference System
DOE	U.S. Department of Energy
DOQQ	Digital Ortho-Quarterquad (from U.S. Geological Survey)
DOS	dark object subtraction
DOY	day of the year
DTN	data tracking number
E	amount of water evaporated from a unit cell
ENVI	Environment for Visualizing Images
EPA	U.S. Environmental Protection Agency
EROS	Earth Resources Observation and Science
ESF	Exploratory Studies Facility
ESP	ecological study plot
ESRI	Environmental Systems Research Institute
ET	evapotranspiration
ET_0	reference evapotranspiration
FACE	(Nevada) Free-Air CO_2 Enrichment Facility
FAO	Food and Agricultural Organization of the United Nations
FAO-56	Food and Agricultural Organization of the United Nations [FAO] Irrigation and Drainage Paper 56
fc	fraction covered
FC	field capacity
FEP	feature, event, or process
few	fraction exposed and wetted
GCP	ground control point
GFM	geologic framework model
GIS	geographic information system
GTC	Glacial Transition Climate
HC	holding capacity
HELP	Hydrologic Evaluation of Landfill Performance
IBP	International Biological Program

ACRONYMS AND ABBREVIATIONS (Continued)

IHU	infiltration hydrogeologic unit
IWCF	initial water content fraction
KTI	key technical issue
LA	*Larrea-Ambrosia* vegetation association
LAI	leaf area index
LG	*Lycium-Grayia* vegetation association
LHS	Latin Hypercube Sampling
LLG	*Larrea-Lycium-Grayia* vegetation association
LN m	lognormal mean
LSC	Lower Sheep Creek
LSCE	Lower Sheep Creek East
LSCW	Lower Sheep Creek West
LU	loguniform
m	meter
MAP	mean annual precipitation
MASSIF	Mass Accounting System for Soil Infiltration and Flow
MAT	mean annual temperature
MC	Monsoon Climate
MCMC	Markov Chain Monte Carlo
ME	Maxey-Eakin
mm	millimeter
MME	modified Maxey-Eakin
MPa	mega Pascal
MRC	moisture retention curve
MS	Microsoft
N	normal
NDVI	Normalized Difference Vegetation Index
NDVI'	NDVI corrected for the Yucca Mountain environment
NED	national elevation dataset
NIR	near infrared
NOAA	National Oceanic and Atmospheric Administration
NRC	U.S. Nuclear Regulatory Commission
NTS	Nevada Test Site
NWRC	Northwest Watershed Research Center
PC	personal computer
PET	potential evapotranspiration
PT	potential transpiration
PVR	potential vegetation response

ACRONYMS AND ABBREVIATIONS (Continued)

QA	Quality Assurance
RAW	readily available water
RCEW	Reynolds Creek Experimental Watershed
REW	readily evaporated water
RH	relative humidity
RMS	root mean square
ROI	region of interest
RWMS	Radioactive Waste Management Site
SRC	Standardized Regression Coefficients
SRRC	Standardized Rank Regression Coefficients
SRTM	Shuttle Radar Topography Mission
STN	software tracking number
SZ	saturated zone
TAW	total available water
TDMS	Technical Data Management System
TEW	total amount of water available for evaporation
TM	thematic mapper
TSPA	total system performance assessment
TWP	technical work plan
U	uniform
USDA	U.S. Department of Agriculture
USGS	United States Geological Survey
UTM	Universal Transverse Mercator
UZ	unsaturated zone
WB	water budget
WHC	water holding capacity
WY	water year
WYDOY	water year day of year
YM	Yucca Mountain
YMP	Yucca Mountain Project
YMRP	*Yucca Mountain Review Plan, Final Report*
ZFP	zero flux plane

INTENTIONALLY LEFT BLANK

1. PURPOSE

1.1 INTENDED USE

This model report documents the development and validation of a conceptual, mathematical, and numerical model for predicting net infiltration of water into the unsaturated zone. The model applies a simple water mass-balance approach to the near surface layer that is influenced by evapotranspiration. It uses a simplified representation of downward water flow whereby water moves from the top soil layer downward by sequentially filling each layer to "field capacity" before draining to the layer below. Water is removed from the "root zone" by evapotranspiration, which is represented using an empirical model based on reference evapotranspiration, transpiration coefficients, and moisture content in the root zone. Water is redistributed as surface runoff when the soil cannot accept all the available water at the surface. Precipitation is stochastically simulated on a daily timestep based on observed weather records.

This report also documents the use of the model for predicting the range and patterns of net infiltration at the Yucca Mountain site for the next 10,000 years. *Future Climate Analysis* (BSC 2004 [DIRS 170002], Section 7.1) forecasts three distinct climates during the next 10,000 years at Yucca Mountain. The present-day climate is predicted to persist for the next 400 to 600 years, followed by a warmer and much wetter monsoon climate lasting from 900 to 1,400 years. Following the monsoon climate, a cooler and wetter glacial-transition climate is expected. The work in this report provides an estimate of the net infiltration up to 10,000 years into the future for the Yucca Mountain Site.

Additional provisions in 10 CFR 63.341 [DIRS 176544] require the U.S. Department of Energy (DOE) to assess the peak dose that would occur after 10,000 years. The U.S. Nuclear Regulatory Commission (NRC) released proposed rules (70 FR 53313 [DIRS 178394]) that DOE represent the effects of climate change after 10,000 years by assuming that deep percolation rates vary between 13 to 64 mm/yr. Predictions of peak dose after 10,000 years are expected to utilize the deep percolation rates as proposed by the NRC.

The specific purpose of the model documented in this report is to provide a spatial representation, including epistemic and aleatory uncertainty, of the predicted mean annual net infiltration at the Yucca Mountain site during each climate. The resulting maps of mean annual net infiltration provide input directly to the updated versions of the following model reports:

- *UZ Flow Models and Submodels* (BSC 2004 [DIRS 169861])
- *Calibrated Properties Model* (BSC 2004 [DIRS 169857]).

Information from this model report indirectly feeds total system performance assessment (TSPA) through its connection with the identified downstream products. This model is not intended to be a direct input to TSPA.

Daily precipitation provides water for potential infiltration. The infiltration model simulates processes occurring in and on the soil, including return of water vapor to the atmosphere by evaporation and plant transpiration (evapotranspiration), flow along the ground surface (runoff/run-on), and infiltration into the bedrock below the soil.

This complete revision of the infiltration model report is developed in accordance with *Technical Work Plan for: Infiltration Model Assessment, Revision, and Analyses of Downstream Impacts* (BSC 2006 [DIRS 177492], Section 1.1.4). The purpose of the revision is to increase confidence in the results by improving the traceability, transparency, and reproducibility of the model development, the selection of inputs for calculations, and the determination of net infiltration maps and fluxes. To those ends, this revision includes the following changes:

- A Mathcad calculation, MASSIF (Mass Accounting System for Soil Infiltration and Flow), replaces the INFIL software (INFIL VV2.0, STN: 10307-2.0-00 [DIRS 139422]; INFIL VVA_2.a1. 2001, STN: 10253-A_2.a1-00 [DIRS 147608]) used in the previous revision of this report (BSC 2004 [DIRS 170007]), while the underlying conceptual models for MASSIF and INFIL remains similar. The reasons for replacing the INFIL software and completely revising the previous revision of this report are explained in a DOE report (DOE 2007 [DIRS 180680], Sections 5.2 and 5.3).

- This revision includes an uncertainty analysis, replacing and expanding work included in *Analysis of Infiltration Uncertainty* (BSC 2003 [DIRS 165991]).

- Instead of taking input directly from multi-decade precipitation records, those records provide the basis for the development of stochastic parameters. Precipitation inputs are selected from 1,000-year stochastic simulations, assuring that the full range of annual precipitation uncertainty is considered, including years with heavy precipitation. Ten representative years are selected from the 1,000-year simulations for each climate state.

- An evapotranspiration submodel, based on guidelines published by the Food and Agriculture Organization (FAO) of the United Nations in Irrigation and Drainage Paper 56 (FAO-56), replaces the submodel that was used in INFIL. The guidelines are based on a combination FAO Penman-Monteith model (Allen et al. 1998 [DIRS 157311], Preface).

- All previous inputs to the infiltration calculations have been revised or requalified.

1.2 LIMITATIONS

This section presents a list of limitations associated with the net infiltration model estimates presented in this report. These limitations arise from a number of sources, including limited knowledge of the system, simplifications invoked to represent the system, and general uncertainties.

The estimates of mean annual net infiltration at the soil–bedrock interface are made without consideration of how the properties of the rock at deeper locations vary with depth. Instead of net infiltration, some authors call this quantity “deep drainage” or “potential recharge.” *UZ Flow Models and Submodels* (BSC 2004 [DIRS 169861]) describes the method for calculating replenishment of the aquifer from the surface, “recharge,” taking into consideration the potential recharge as well as the complex, three-dimensional hydrogeologic structure and properties of the fractured bedrock and other considerations.

One consideration is the possibility that a significant fraction of the water that enters bedrock is lost to evaporation in the Tiva Canyon welded tuff (TCw). Such a water loss has been suggested by researchers looking at the stable oxygen isotopic chemistry of secondary calcite deposited in the TCw (Whelan et al. 2002 [DIRS 160442], pp. 743 to 744; Figure 8). This study suggests that evaporation losses from the unsaturated zone (UZ) may extend to the top of the Paintbrush nonwelded unit (PTn), which means that evaporative losses from the UZ may extend as deep as 100 m below the surface (Whelan et al. 2002 [DIRS 160442], Figure 8). The net infiltration model domain described in this report extends only from the surface to the soil–bedrock interface, and the net infiltration flux includes all water that moves downward across this interface. The current UZ flow model (BSC 2004 [DIRS 169861]) does not explicity allow water to evaporate from the UZ domain. Therefore, evaporation from the TCw is not explicitly captured by either of these models. However, the resulting UZ flow fields predicted by the UZ flow model (BSC 2004 [DIRS 169861]) are weighted by comparing UZ model results to thermal and chemical data observed in the UZ domain (deeper than the net infiltration modeling domain). These datasets generally indicate that percolation rates below the TCw are lower than the net infiltration predicted above the TCw. Thus, the UZ model assigns higher weights to the lower range of the net infiltration distribution and therefore may indirectly account for water loss in the TCw.

The model documented in this report is valid only for the Yucca Mountain site and for the climates specified in *Future Climate Analysis* (BSC 2004 [DIRS 170002], Section 7.1). For each climate, the model produces maps of average annual infiltration as a function of location, with no time dependence. These output maps cover the variability and range of uncertainty in average annual net infiltration over the modeling domain.

Infiltration predictions are limited by the uncertainty in future weather patterns. Although a substantial body of literature supports the use of stochastic precipitation models, there are no records to support extrapolation of historical weather records from the last few decades to 1,000 years. Each available and relatively complete precipitation record, whether from the Yucca Mountain site, from a nearby weather station, or from a site representative of a future climate, covers no more than about 60 years. The methods used to represent future climate conditions for this model are described in Section 6.5.1 and Appendix F.

Infiltration predictions are also limited by uncertainties in the hydrologic properties of the soil and upper zone of the fractured bedrock that covers the 125-km^2 infiltration modeling domain. These uncertainties arise primarily from several sources. The first is the use of a pedotransfer function to estimate soil hydrologic properties from measured grain size distributions. This work is documented and the resulting soil properties are qualified for use in *Data Analysis for Infiltration Modeling: Development of Soil Units and Associated Hydraulic Parameter Values* (BSC 2006 [DIRS 176335]). The pedotransfer approach introduces uncertainty due to the fact that the Hanford soil property database represents soils in a location and depositional environment that is different from Yucca Mountain (Hanford, WA). Another source of uncertainty is in the saturated conductivity of the bedrock at the soil–bedrock interface. This parameter set is based on work documented in *Data Analysis for Infiltration Modeling: Bedrock Saturated Hydraulic Conductivity Calculation* (BSC 2006 [DIRS 176355]). The saturated conductivity values and uncertainty are based on measurements of fracture apertures, fracture densities, saturated conductivities of bedrock matrix and fracture filling material, and a model of

conductivity based on the combination of these measurements. For each bedrock type, the lower end of the conductivity uncertainty range assumes completely filled fractures, and the upper end of the conductivity uncertainty range assumes a small open fracture component in each of the filled fractures. When multiple bedrock types are included in the uncertainty analysis, the extent of fracture filling can vary independantly between rock types (see Sections 6.5.2.5 and 6.5.2.6). However, a limitation of this approach is that heterogeneity within a bedrock type is not represented. Because this approach is based on indirect measurements of saturated conductivity, there is a potential for significant model uncertainty in the results of the conductivity estimates.

Uncertainty in the soil depth representing the zone of shallow soils is significant. The upscaled value of soil depth for the shallow soil depth class varies by a factor of 5 (see Section 6.5.2.4). Such variation is the result of the fact that very few qualified measurements of soil depth were available upon which to base a model of soil depth across the site. As shallow soil depth is shown to be the most significant physical parameter influencing mean net infiltration, the uncertainty in this parameter represents an important limitation on the accuracy of the mean net infiltration over the site.

Despite the intent of estimating the spatial distribution of mean annual net infiltration across the model domain, the accuracy of net infiltration estimates at any one location is limited by uncertainties in soil, bedrock, and vegetation properties at that location. As described briefly above, there are few direct measurements of soil and rock properties at Yucca Mountain. In order to run the model, it was necessary to define these properties for every 30 × 30-m grid cell in the infiltration modeling domain. The approach taken was to upscale and group the few available measurements and estimates for properties. This approach assumes that small scale variations in soil and rock properties are not as significant as variations that occur between different soil and rock types. This assumption is valid as long as small scale spatial variations in net infiltration are not important for downstream users. An example of this limitation is the answer to the question of whether net infiltration at Yucca Mountain is focused beneath stream channels. The results of the uncertainty analysis described in Section 6.5.7 indicate that little to no net infiltration occurs beneath stream channels where soil is especially thick. However, in Sections 7.1.3.1 and 7.1.3.2, it is shown that this particular result is very sensitive to the spatial distribution of soil conductivity. Since there is very little direct information about such a spatial distribution, there is considerable and significant uncertainty in the spatial distribution of net infiltration results. Furthermore, because soil and bedrock properties are represented as uniform over a spatial area assumed to define a given soil or rock type, the actual spatial variability of net infiltration is likely underestimated by the model. In addition, other processes that might effect the spatial distribution of net infiltration on a local scale (e.g., interflow) are assumed to be insignificant and are not included in the model (Section 5).

Finally, it should be stressed that the approach used to estimate water flow and storage within the rootzone is a simplification of the actual physical processes that control flow in this environment. The use of the "field capacity" concept acts as a flow switch allowing downward water flow at a rate equal to the saturated hydraulic conductivity when the average water content in a layer equals or exceeds "field capacity," and allowing no flow to occur when average water content in a layer is less than "field capacity." In reality, water will flow within the vadose zone in response to gradients in total soil-water potential, which is the sum of various components such

as elevation, matric, pressure, temperature, and osmotic potentials. This approximation is discussed more fully in Sections 5 and 6.4.

1.3 SCOPE OF THIS DOCUMENT

Sections 2 through 5 of this document address topics including quality assurance (QA), software, qualified inputs, and other prerequisites to a detailed discussion of model development and implementation, which is discussed in Section 6. Section 2 identifies the overall QA requirements and methods that were applied during model development and calculations. Section 3 identifies both qualified and exempt software used in the technical effort. Lists of qualified direct inputs are the primary content of Section 4. Section 5 documents assumptions used in the absence of direct confirming data or evidence.

The principal technical discussions are in Section 6. That discussion includes the conceptual model, the mathematical model, and the implementation as a Mathcad calculation (MASSIF), in Sections 6.1 through 6.4. Sections 6.5 through 6.7 discuss the development of site-specific climate inputs, a site-specific geospatial database, sensitivity studies, the treatment of uncertainty, and the results of calculations for the three climates.

Section 7 addresses validation of the model. The technical work plan (TWP) (BSC 2006 [DIRS 177492], Section 2.2.1) specifies the validation activities and validation criteria for this model.

The conclusions of this report appear in Section 8. They include a list of technical data items that are output from this product.

In order to improve the readability of this report, many technical details are included in appendices at the end of the report. More detailed technical information is available from the Technical Data Management System (TDMS), using data tracking numbers (DTNs) provided throughout this report.

Work documented in this report addresses the open Key Technical Issue (KTI): USFIC 3.01, *Monte Carlo approach for estimating net infiltration* (BSC 2004 [DIRS 180945], Appendix D). That KTI documented concerns that high net infiltration values in the statistical distribution of net infiltration estimates were not being adequately represented by the outputs of the previous analysis. The present model analysis is a complete revision to the previous estimates and does explicitly include representation of the upper end of the net infiltration uncertainty distribution. This work does not specifically evaluate impacts to closed KTIs supported by previous models of net infiltration.

1.4 DEVIATIONS FROM THE TECHNICAL WORK PLAN

One deviation from the TWP (BSC 2006 [DIRS 177492]) relates to the use of neutron logging data from 99 boreholes in the vicinity of Yucca Mountain. The TWP (BSC 2006 [DIRS 177492], Section 2.2.1.5) states the following:

> The neutron log data will be used for post-model validation by comparing the infiltration values (averaged over areas of similar infiltration characteristics such as similar soil type or thickness) to the area averaged values from MASSIF. The range of uncertainty of the infiltration values must overlap to allow validation to be accepted.

After examining the neutron data and reviewing the methods used to estimate net infiltration flux at each neutron borehole, this comparison was determined to be of limited use for the model development and validation and therefore was not used. See Section 7.2.1.1.3 for a discussion of the neutron logging data.

Another minor deviation from the TWP relates to the use of the soil lysimeter data from the Nevada Test Site (NTS). The TWP states that these data "are available in support of this post-model validation activity." In fact, the lysimeter data are used for confidence building during model development (Section 7.1.2.1) and not for post-model validation.

2. QUALITY ASSURANCE

Planning and preparation of this report was initiated under the Bechtel SAIC Company (BSC) Quality Assurance (QA) Program. Therefore, forms and associated documentation prepared prior to October 2, 2006, the date this work transitioned to the Lead Laboratory, were completed in accordance with BSC procedures as identified in Section 4.1 of the TWP (BSC 2006 [DIRS 177492]. Forms and associated documentation completed on or after October 2, 2006, were prepared in accordance with Lead Laboratory procedures.

Development of this model report and the supporting modeling activities are subject to the Yucca Mountain Project QA program, as indicated in the TWP (BSC 2006 [DIRS 177492], Section 8.1). Approved QA procedures (BSC 2006 [DIRS 177492], Section 4.1) have been used to conduct and document the activities described in this model report. The TWP also identifies the methods used to control the electronic management of data (BSC 2006 [DIRS 177492], Section 8.4). The modeling activities and associated calculations herein were conducted and documented following SCI-PRO-006, *Models*.

This model report provides simulation results for infiltration into the UZ under present and potential future climates. The UZ (including soil and rock above the water table) is part of natural barriers that are classified in *Q-List* (BSC 2005 [DIRS 175539]) as "Safety Category" because it is important to waste isolation. The report contributes to the process models used to support performance assessment; the conclusions do not directly impact engineered features important to preclosure safety.

INTENTIONALLY LEFT BLANK

3. USE OF SOFTWARE

A list of controlled and baselined software items used in this report is provided in Table 3-1. Each software item is used within the range for which it was qualified. All software used for the work documented in this report was selected because it was appropriate for the intended use. No limitations on the use of selected software or on the use of outputs from selected software were identified for this work. The use of the software items was consistent with its intended use and within the documented qualified validation ranges for the software. No software item was used prior to qualification to develop any qualified technical data outputs. Section 4 discusses the inputs used in this model for all software. Mathcad V. 13.1, Microsoft (MS) Excel 2003, Excel 2000, MS Access™ 2003, MS Internet Explorer v.6.0.2800, and Surfer 8 are commercial-off-the-shelf (COTS) software items that have been determined exempt in accordance with Section 2.0 of IM-PRO-003, *Software Management*. HYDRUS 1-D (Šimùnek et al. 2005 [DIRS 178140]) is unqualified software and was used solely for the purpose of model corroboration. The use of HYDRUS-1D for model corroboration is documented in Section 7.2.2 and Appendix K. This model corroboration activity provides indirect support for model validation, which is considered an unqualified activity. HYDRUS 2-D (Šimùnek 1999 [DIRS 178228]) is discussed in section 6.2.4.1, but is not used in the analysis. INFIL VVA_2.a1 [DIRS 147608] and INFIL VV2.0.2001 [DIRS 139422] are discussed in the report as historical references only and were not used in the analysis.

Table 3-1. Qualified Software Used in This Report

Software Name	Version	Software Tracking Number (STN)	Platform/Operating System	DIRS
LHS	2.51	10205-2.51-01	DEC AlphaServer ES45 Model 2/ Open VMS 8.2	178784
ArcGIS Desktop	9.1	11205-9.1-00	PC/Windows XP	176015
ENVI+IDL	4.2	11204-4.2-00	PC/Windows XP	178783
MVIEW	4.0	10072-4.0-00	PC/Windows 2000	173438

3.1 LHS V. 2.51

The Latin Hypercube Sampling (LHS) software, Version 2.51 (LHS V. 2.51 [DIRS 178784], STN: 10205-2.51-01), baselined October 03, 2006, uses the Open VMS 8.2 operating environment for quality-affecting work supporting the infiltration model. The LHS software: (1) performs Latin hypercube sampling; (2) generates the distribution for each parameter to be sampled: NORMAL, LOGNORMAL, UNIFORM, LOGUNIFORM, or USER-DEFINED distributions (cumulative, continuous, and discrete); (3) generates a correlation matrix; and (4) detects invalid input data sets.

3.2 ARCGIS DESKTOP V. 9.1

The ArcGIS Desktop software, Version 9.1 (ArcGIS Desktop V. 9.1 [DIRS 176015], STN: 11205-9.1-00), baselined in December 12, 2005, uses the Personal Computer (PC) MS Windows XP operating environment for quality-affecting work supporting the infiltration model. The ArcGIS Desktop software item integrates a collection of software files for developing a complete Geographic Information System (GIS) for the infiltration model. The

software item extends the shape file, geodatabase, and coverage model with support from advanced geometry (three-dimensional coordinates and true curves), complex networks and relationships among feature classes, planar topology, and other object-oriented features within the MS Windows XP operating environment.

3.3 ENVI+IDL V. 4.2

The ENVI+IDL software, Version 4.2 (ENVI+IDL V. 4.2 [DIRS 178783], STN: 11204-4.2-00), baselined December 5, 2005, uses the PC MS Windows XP operating environment for quality affecting work supporting the infiltration model. The ENVI+IDL software: (1) conducts Radiometric Corrections to the Region of Interest (ROI) data; (2) accepts image formats including but not limited to flat LANDSAT, QUICKBIRD and U.S. Geological Survey (USGS) digital elevation model maps; (3) conducts land cover characterization calculations based on data in the ROI; (4) conducts geometric corrections to the ROI data such that the precision of the calculated geographic locations are on the order of the precision of the input data pixels; and (5) accepts generic image formats including but not limited to ASCII, BMP, HDF and JPEG.

3.4 MVIEW V. 4.0

The MVIEW software, Version 4.0 (MVIEW V. 4.0 [DIRS173438], STN: 10072-4.0-00), baselined on July 1, 2005, for the PC MS Windows 2000 operating environment, is a stand-alone executable program that was used to perform sentivity analyses on net infiltration model outputs. Specifically, it was used for stepwise regression analysis and the calculation of partial correlation coefficients and standaradized regression coefficients. This work is described in Appendix H.

3.5 EXEMPT SOFTWARE ITEMS

The following COTS software is considered exempt under Section 2.0 of IM-PRO-003.

Standard spreadsheet and database software (MS Excel 2003 and MS Access 2003) were used for calculations supporting the development of the stochastic weather input files, generating visualization plots of data, and other miscellaneous standard calculations included this report. These software items are controlled as part of MS Office 2003 Professional SP-2 (STN: 610236-2003-00).

The plotting program Surfer 8.02 (STN: 610469-8.02-00) was used to generate visualization maps of net infiltration. The use of Surfer 8 is exempt from qualification under Section 2.0 of IM-PRO-003 because it is used solely for visual display or graphical representation of data. Maps of net infiltration results were generated using Surfer 8.02 and can be spot-checked by the reviewers. Grid cell results were imported into the Surfer 8.02 software and gridded using a Nearest-Neighbor algorithm, which employed the same grid-cell size of 30×30 m as the original data. The only data conversion performed by the software was to mask or blank out regions outside of the domain, since the gridding produces a domain that is a bounding box of the imported data. This was done using standard features of the Surfer 8 software.

Mathcad V. 13.1 (STN: 611161-13.1-00) is a COTS controlled software item determined to be exempt in accordance with Section 2.0 of IM-PRO-003. This exemption was reinforced by the conclusions of an Office of Quality Assurance surveillance (OQA-SI-06-015), which determined

that QARD Revision 18 had no impact on the exempt status of MASSIF as long as the procedural requirements of the modeling procedure were met (DOE 2006 [DIRS 179958]). Incremental checking of MASSIF documented in Output DTN: MO0703MASSIFIM.001 satisfied the checking verification requirement needed to meet these procedural requirements. The net infiltration model (MASSIF) was developed and implemented using standard functions included with Mathcad. MASSIF is a hydrologic mass-balance accounting calculation that accounts for the partitioning of water that falls as precipitation to runoff, evapotranspiration (ET), soil moisture storage, and net infiltration, through the automated solution of a series of standard equations which are amenable to verification by hand calculations.

Mathcad allows the infiltration model calculations to be automated, which allows that same set of calculations to be repeated as often as necessary to cover the domain of interest. The results of the MASSIF calculation are not dependent upon the software program used. The calculation was implemented in Mathcad because Mathcad calculational functions are easily recognizable and formatted consistent with their presentation in standard textbooks and hence, are innately traceable and transparent. The TWP (BSC 2006 [DIRS 177492]) describes how the net infiltration model, MASSIF, is verified by comparing each calculation against independent hand calculations performed by an independent checker/reviewer.

INTENTIONALLY LEFT BLANK.

4. INPUTS

4.1 DIRECT INPUT

All direct data inputs used in the development and application of the net infiltration model, MASSIF, to estimate net infiltration for Present Day and potential future climates are listed in Table 4-1. These data consist of topographic, geologic, vegetation, and climate parameters and properties that are appropriate to and required for the development and application of the water-balance approach to watershed modeling that is the basis for the net infiltration model. The data referenced in Table 4-1 contain information necessary to construct and implement the mathematical model as a Mathcad calculation. The data are fully appropriate for the site-scale infiltration model. All non-qualified direct inputs are qualified for their intended use in Appendix A.

Two direct input DTNs discussed below have been used for different purposes in Sections 6 (Model Discussion) and 7 (Model Validation). While the procedure SCI-PRO-006 Rev 02 indicates in Attachment 2 that data used to develop a model cannot be used to validate a model, it is argued here that the different uses of the same data are acceptable.

In the first case, weather observations from ten weather stations representing Present Day climate from DTN SN0608WEATHER1.005 [DIRS 177912] were used in Section 6 and Appendix F to develop stochastic model parameters used to simulate long-term weather for the site. These derived parameters were used as inputs to a stochastic precipitation simulation, which produced weather input files to the MASSIF model in Section 6. Note that the actual historical weather observations were not used as model input to MASSIF in Section 6, but rather to parameterize the general weather patterns and characteristics for a stochastic simulation that was used to generate a set of simulated weather years used as input to the calculations documented in Section 6.5. In contrast, in Section 7, certain local weather observations from specific stations were used as MASSIF model inputs to simulate net infiltration, evapotranspiration and runoff at specific locations and for specific historical periods in order to match measurements of net infiltration, evapotranspiration, and runoff made at these locations during those same periods. Because weather measurements are unique in time and space, it is unreasonable and impractical to separate their use in model development and model validation.

In the second case, a set of qualified borehole locations (DTN: MO9906GPS98410.000 [DIRS 109059]) were used in Section 6 and Appendix E to georeference satellite imagery so that the imagery could be used to characterize the vegetation response as a function of time and space. In contrast, in Section 7, neutron logging measurements made in the same boreholes were compared with the results of the MASSIF model. In order to identify the MASSIF model grid cells in which the boreholes lie, it was appropriate to use the set of qualified borehole locations for this identification.

Table 4-1. Direct Input Data

Input Data Type	Input Data Description	Location in This Model Report	Source
Conversion Factors	Conversion factor from watts to joules	Appendix D	IEEE/ASTM SI 10-1997 [DIRS 151762]
Shuttle radar topography	Surface elevation	Appendix B; Output DTNs: SN0608DRAINDYM.001, SN0608NDVIQBIM.001	DTN: SN0601SRTMDTED.001 [DIRS 177242]
LandSat images	Satellite imagery	Output DTNs: SN0608NDVIAUXD.001, SN0608NDVILSTM.001	DTN: SN0601ALANDSAT.001 [DIRS 177239]
Digital aerial orthorectified photographs	Aerial photography	Appendix E, Output DTN: SN0608NDVIAUXD.001	DTN: SN0601DOQQYM98.001 [DIRS 177240]
Quickbird images	Satellite imagery	Appendix E, Output DTN: SN0608NDVIQBIM.001	DTN: SN0601QBSAT802.001 [DIRS 177241]
Survey of field locations	Ground control point coordinates	Appendix E, Output DTN: SN0608NDVIAUXD.001	DTN: MO0512COV05112.000 [DIRS 177249]
	Borehole coordinates		DTN: MO9906GPS98410.000 [DIRS 109059]
	Ecological study plot coordinates	Appendix D; Section 6.5.3	DTN: MO9901ESPYMNYE.000 [DIRS 177247]
Soil maps	Soil depth class and type boundaries	Sections 6.5.2.2, 6.5.2.4, 6.5.2.5, Appendix B; Output DTNs: SN0606T0502206.011, SN0701SPALAYER.002	DTN: MO0608SPASDFIM.006 [DIRS 178082]
Bedrock map	Bedrock boundaries	Sections 6.5.2.2, 6.5.2.4, Appendix B; Output DTNs: SN0606T0502206.011, SN0701SPALAYER.002	DTN: MO0603SPAGRIDD.003 [DIRS 177121], file *lHU_map_file2.txt*
UZ model boundary and repository footprint	Identification of grid cells inside and outside boundaries	Appendix B; Output DTN: SN0612FTPRNUZB.002	DTN: LB0208HYDSTRAT.001 [DIRS 174491]
Soil properties	Permanent wilting point, moisture content, water holding capacity, saturated hydraulic conductivity	Section 6.5.2.3	DTN: MO0605SEPALTRN.000 [DIRS 178089]
	Terrain albedo	Table 6.5.4.1-4, Appendix A	Brutsaert 1982 [DIRS 176615], p. 136, Table 6.4
	Evaporation layer depth	Table 6.5.4.2-4, Appendix A	Allen et al. 2005 [DIRS 176009], p. 4
		Table 6.5.4.2-4	Allen et al. 1998 [DIRS 157311], p. 144
	Minimum transpiration coefficient	Table 6.5.4.2-2	Allen et al. 1998 [DIRS 157311], pp. 207 and 209
	Soil moisture depletion coefficient	Table 6.5.4.2-3	Allen et al. 1998 [DIRS 157311], p. 162
	Readily evaporable water	Table 6.5.4.2-5	Allen et al. 1998 [DIRS 157311], p. 144, Table 19
	Soil depth measurements	Section 6.5.2.4.1	DTN: GS011208312212.004 [DIRS 176317]

Table 4-1. Direct Input Data (Continued)

Input Data Type	Input Data Description	Location in This Model Report	Source
Bedrock saturated hydraulic conductivity	Saturated hydraulic conductivity	Section 6.5.2.5	DTN: MO0605SPABEDRK.005 [DIRS 177122]
Precipitation/climate	Atmospheric pressure, dew point, precipitation quantity, precipitation rate, relative humidity, solar flux, temperature, wind direction, wind speed, and/or wind vector magnitude	Appendix D, Section D3.2.4; Output DTNs: MO0602SPAWEATH.000, MO0602SPAPRECP.000	DTN: MO0206SEPQ1998.001 [DIRS 166731]
			DTN: MO0209SEPQ2000.001 [DIRS 166730]
			DTN: MO0305SEP01MET.002 [DIRS 166164]
			DTN: MO0305SEP02MET.002 [DIRS 166163]
			DTN: MO0312SEPQ1997.001 [DIRS 167116]
		Appendix D, Section D3.2.4; Output DTN: MO0607SEPTOTAL.003	DTN: MO0312SEPQ1993.001 [DIRS 176092] (Data was evaluated and determined to be appropriate prior to use)
			DTN: MO0606SEPRECIP.001 [DIRS 177136] (Data was evaluated and determined to be appropriate prior to use)
		Output DTN: SN0610T0502206.031	DTN: MO0605SEPHOURL.000 [DIRS 177237]
		Appendix D; Output DTN: MO0605SPADAYWA.000	DTN: MO0605SPASPOKA.000 [DIRS 177135]
		Appendix F; Output DTN: SN0609T0502206.023	DTN: SN0601PRECPTMP.002 [DIRS 176122]
		Appendix F; Output DTNs: SN0609T0502206.023, SN0608T0502206.019	DTN: SN0603DWEATHER.002 [DIRS 177917]
	Atmospheric pressure, dew point, precipitation quantity, relative humidity, temperature, and/or wind speed	Appendix F; Output DTNs: SN0609T0502206.023, SN0610T0502206.030, SN0608T0502206.019, SN0610T0502206.031	DTN: SN0608WEATHER1.005 [DIRS 177912]
	Stations representing future climate	Appendix F; Section 6.5.1.1, Table 6.5.1.1-1	DTN GS000308315121.003 [DIRS 151139]
	Psychrometric constant	Section 6.5.3.6.1	Allen et al 1998 [DIRS 157311], p. 214, Table 2.2
	Temperature lapse rate	Appendix F; Section 6.5.1	Maidment 1993 [DIRS 125317], p. 3.3
	Maximum daily precipitation amount	Appendix F; Section 6.5.1	Maidment 1993 [DIRS 125317], p. 3.36, Table 3.10.2
	Snowmelt coefficient	Section 6.5.1, Table 6.5.1.7-1, Appendix F	Maidment 1993 [DIRS 125317], p. 7.24
	Sublimation coefficient	Section 6.5.1, Table 6.5.1.7-1, Appendix A	Hood et al. 1999 [DIRS 177996], p. 1794
	Solar constant	Table 6.5.4.1-5	Allen et al. 1998 [DIRS 157311], p. 48
		Table 6.5.4.1-5, Appendix A	Dewitte et al. 2004 [DIRS 178528], p. 214

Table 4-1. Direct Input Data (Continued)

Input Data Type	Input Data Description	Location in This Model Report	Source
Precipitation/climate (continued)	Turbidity coefficient	Table 6.5.4.1-6, Appendix A	Allen et al. 2005 [DIRS 176207], Appendix D, p. D-8
	Dew point offset	Table 6.5.4.1-2, Appendix A	Allen et al. 2005 [DIRS 176207], Appendix D, p. D-29
			Temesgen et al. 1999 [DIRS 178312], pp. 29 to 30, Table 4
Vegetative coverage	Ground cover	Appendix D, Section D3.2.2, Tables D-6 through D-14; Output DTNs: MO0606SPAVEGAS.001, SN0608NDVIANAL.001	DTN: MO9907GCESPYMN.000 [DIRS 157659]
	Growth stage lengths	Appendices A, D, Section D3.2.1, Tables D-2 and/or D-3	Rundel and Gibson 1996 [DIRS 103614], Figure 4.13, p. 106
			Newman 1992 [DIRS 174673], p. 3
			Smith et al. 1995 [DIRS 103628], pp. 342, 349, Figure 2
			Hamerlynck et al. 2000 [DIRS 177022], p. 602, Figure 6
			Hamerlynck et al. 2002 [DIRS 177128], p. 103, Figure 7
			Hamerlynck et al. 2002 [DIRS 177046], p. 774
			Hulbert 1955 [DIRS 177129], p. 1
	Mean plant height, mean maximum plant height	Section 6.5.3.3, Table 6.5.3.3-1, Appendices A, D, Section D3.2.1, Table D-5	Hulbert 1955 [DIRS 177129], Table 6, p. 186
			Newman 1992 [DIRS 174673], p. 2
			Rundel and Gibson 1996 [DIRS 103614], Tables 4.1 and 4.2
	Stomatal resistance	Appendices A, D, Section D3.2.3, Table D-16	Huxman et al. 1999 [DIRS 177133], pp. 770 and 774
			Huxman and Smith 2001 [DIRS 177132], p. 197
			Hamerlynck et al. 2002 [DIRS 177128], p. 101
	Soil moisture depletion coefficient adjustment	Section 6.4.4.2	Allen et al. 1998 [DIRS 157311], p. 162
	Elevation of Crater Flat used to develop stomatal resistance inputs	Section D3.2.3	Smith et al. 1995 [DIRS 103628], p. 340
	Stomatal resistance	Appendices A, D, Section D3.2.3, Table D-16	Naumburg et al. 2003 [DIRS 177143], p. 280, Figure 3
			Hamerlynck et al. 2000 [DIRS 177130], p. 188
			Hamerlynck et al. 2004 [DIRS 176045], p. 213

Table 4-1. Direct Input Data (Continued)

Input Data Type	Input Data Description	Location in This Model Report	Source
Vegetative coverage (continued)	Stomatal resistance (continued)		Hamerlynck et al. 2000 [DIRS 177022], p. 602
			Pataki et al. 2000 [DIRS 177161], p. 893
			Smith et al. 1995 [DIRS 103628], pp. 343 and 344
	Atmospheric pressure	Appendices A, D, Table D-17	Allen et al. 1998 [DIRS 157311], pp. 213 to 214, Table 2.1
	Rooting depths	Section 6.5.3.2, Tables 6.5.3.2-1 and/or 6.5.3.2-2, Appendix A	Canadell et al. 1996 [DIRS 177626], pp. 583 to 595, Appendix 1
			Hansen and Ostler 2003 [DIRS 177619], p. 85, Table 7-1
			Jackson et al. 2002 [DIRS 177171], p. 624, Table 1
			Rundel and Gibson 1996 [DIRS 103614], p. 99, Figure 4-10
			Rundel and Nobel 1991 [DIRS 128001], pp. 355 to 357
			Schenk and Jackson 2002 [DIRS 177638], p. 491, Figure 9
			Yoder and Nowak 1999 [DIRS 177167], p. 91, Figure 6
			Harris 1967 [DIRS 177630], p.97, Figure 6
			Hulbert 1955 [DIRS 177129], p. 191
			Link et al. 1990 [DIRS 177142], p. 512
			Rickard 1985 [DIRS 177635], p.170
			Foxx et al. 1984 [DIRS 177628], p. 6, Table 3
			Richards and Caldwell 1987 [DIRS 177927], pp. 486 to 489
			Sturges and Trlica 1978 [DIRS 177928], pp. 1282 to1285
			Ryel et al. 2003 [DIRS 177632], p. 760
			Seyfried et al. 2005 [DIRS 178060], pp. 282 to 283
			Leffler et al. 2004 [DIRS 177926], p. 10, Figure 1
			Zlatnik 1999 [DIRS 177639], p. 7
			Anderson 2002 [DIRS 177625]

Table 4-1. Direct Input Data (Continued)

Input Data Type	Input Data Description	Location in This Model Report	Source
Vegetative coverage (continued)	Mean plant height	Section 6.5.3.3, Table 6.5.3.3-2, Appendix A	USDA 2002 [DIRS 178073]
			Schultz and McAdoo 2002 [DIRS 178065], p. 2
			Tirmenstein 1999 [DIRS 177641]
			Tirmenstein 1999 [DIRS 177642]
			Utah State University 2002 [DIRS 177646], p. 2
			Utah State University 2002 [DIRS 177644], p. 2
			Utah State University 2002 [DIRS 177647] , p. 1
			Utah State University 2002 [DIRS 177648], p. 2
			Utah State University 2002 [DIRS 177649], p. 2
			Utah State University 2002 [DIRS 177650], p. 2
			Utah State University 2004 [DIRS 177643], p. 1
			Weber et al. 1993 [DIRS 177931], pp. 355 to 357
			Zlatnik 1999 [DIRS 177639], p. 7
			Stewart and Hull 1949 [DIRS 177146], pp. 58 to 59

4.2 CRITERIA

The general requirements to be satisfied by the TSPA are stated in 10 CFR Part 63 [DIRS 176544]. The acceptance criteria that will be used by the NRC to determine whether the technical requirements have been met are identified in *Yucca Mountain Review Plan*, *Final Report* (YMRP) (NRC 2003 [DIRS 163274]).

The acceptance criteria identified in Section 2.2.1.3.5.3 of the YMRP (NRC 2003 [DIRS 163274]) that are applicable to this report are included below. How these components are addressed is summarized in Section 8.3 of this report.

A*cceptance Criteria from Section 2.2.1.3.5.3, Climate and Infiltration.*

Acceptance Criterion 1: ***System Description and Model Integration Are Adequate.***

(1) The total system performance assessment adequately incorporates, or bounds, important design features, physical phenomena, and couplings, and uses consistent and appropriate assumptions throughout the climate and net infiltration abstraction process.

(2) The aspects of geology, hydrology, geochemistry, physical phenomena, and couplings, that may affect climate and net infiltration, are adequately considered. Conditions and assumptions in the abstraction of climate and net infiltration are readily identified and consistent with the body of data presented in the description.

(3) The abstraction of climate and net infiltration uses assumptions, technical bases, data, and models that are appropriate and consistent with other related U.S. Department of Energy abstractions. For example, the assumptions used for climate and net infiltration are consistent with the abstractions of flow paths in the unsaturated zone (UZ) and flow paths in the saturated zone (SZ) (Sections 2.2.1.3.6 and 2.2.1.3.8 of the Yucca Mountain Review Plan, respectively). The descriptions and technical bases provide transparent and traceable support for the abstraction of climate and net infiltration.

(4) Sufficient data and technical bases to assess the degree to which FEPs have been included for this abstraction are provided.

(5) Adequate spatial and temporal variability of model parameters and boundary conditions are employed to model the different parts of the system.

(6) Average parameter estimates are used in process-level models over time and space scales that are appropriate for the model discretization.

(7) Projections of future climate change are based on evaluation of paleoclimate information over the past 500,000 years. For example, numerical climate models, if used for projection of future climate, are calibrated based on such paleoclimate data.

(8) Guidance in NUREG–1297 and NUREG–1298 (Altman et al. 1988 [DIRS 103597]; 1988 [DIRS 103750]), or other acceptable approaches for peer reviews and data qualification, is followed.

Acceptance Criterion 2: ***Data Are Sufficient for Model Justification.***

(1) Climatological and hydrological values used in the license application (e.g., time of onset of climate change, mean annual temperature, mean annual precipitation, mean annual net infiltration, etc.) are adequately justified. Adequate descriptions of how the data were used, interpreted, and appropriately synthesized into the parameters are provided.

(2) Estimates of present-day net infiltration using mathematical models at appropriate time and space scales are reasonably verified with site-specific climatic, surface, and subsurface information.

(3) The effects of fracture properties, fracture distributions, matrix properties, heterogeneities, time-varying boundary conditions, evapotranspiration, depth of soil cover, and surface-water run off and run-on are considered, such that net infiltration is not underestimated.

(4) Sensitivity or uncertainty analyses are performed to assess data sufficiency and determine the possible need for additional data.

(5) Accepted and well-documented procedures are used to construct and calibrate numerical models.

(6) Reasonably complete process-level conceptual and mathematical models are used in this model report. In particular: (a) mathematical models provided are consistent with conceptual models and site characteristics; and (b) the robustness of results from different mathematical models is compared.

(7) This Criterion was listed in the TWP, but is not included in present report because expert elicitation was not used to support model development.

Acceptance Criterion 3: ***Data Uncertainty Is Characterized and Propagated through the Model Abstraction.***

(1) Models use parameter values, assumed ranges, probability distributions, and bounding assumptions that are technically defensible, reasonably account for uncertainties and variabilities, and do not result in an under-representation of the risk estimate.

(2) The technical bases for the parameter values used in this abstraction are provided.

(3) Possible statistical correlations are established between parameters in this abstraction. An adequate technical basis or bounding argument is provided for neglected correlations.

(4) The hydrologic effects of future climate change that may alter the rates and patterns of present-day net infiltration into the UZ are addressed. Such effects may include changes in soil depths, fracture-fill material, and types of vegetation.

Acceptance Criterion 4*: Model Uncertainty Is Characterized and Propagated through the Model Abstraction.*

(1) Alternate modeling approaches of FEPs, consistent with available data and current scientific understanding, are investigated. The results and limitation are appropriately considered in the abstraction.

(2) The bounds of uncertainty created by process-level models are considered in this abstraction.

(3) Consideration of conceptual model uncertainty is consistent with available site characterization data, laboratory experiments, field measurements, natural analogue information and process-level modeling studies; and the treatment of conceptual model uncertainty does not result in an under-representation of the risk estimate.

Acceptance Criterion 5: ***Model Abstraction Output Is Supported by Objective Comparisons.***

(1) This Criterion was listed in the TWP, but is not included in present report because the output from this model is not a direct TSPA abstraction.

(2) Abstractions of process-level models may conservatively bound process-level predictions.

(3) Comparisons are provided of output of abstracted models of climate and net infiltration with output of sensitivity studies, detailed process-level models, natural analogs, and empirical observations, as appropriate.

Acceptance Criteria from Section 2.2.1.1.3

(3) Technical Basis for Barrier Capability is Adequately Presented.

4.3 CODES, STANDARDS, AND REGULATIONS

No codes, standards, or regulations, other than those identified above in Section 4.2, were used in this model report.

INTENTIONALLY LEFT BLANK

5. ASSUMPTIONS

In procedure SCI-PRO-006, an assumption is defined as:

> A statement or proposition that is taken to be true or representative in the absence of direct confirming data or evidence, or those estimations, approximations, limitations, simplifications, and/or decisions made during model development (such as when expanding the range of variables to achieve conservatism).

The assumptions included in this section are only those which are made in the absence of direct or confirming data. In Section 6, there are many "modeling decisions" that were made that might be thought of as assumptions. These are listed in Table 5-1 at the end of this section.

5.1 CERTAIN COMPONENTS OF THE WATER BALANCE MODEL CAN BE NEGLECTED FOR MODELING NET INFILTRATION AT YUCCA MOUNTAIN

The water balance equation used in this model of net infiltration includes the most important terms in the water balance and neglects terms that are reasonably assumed to be negligible. The model includes precipitation (rain and snow), evapotranspiration (ET), net infiltration, snowmelt, sublimation of snow, run-on, and runoff. The terms that are assumed to be negligible and are thus not represented in the model include: interception, interflow, storage of water on surface (either in puddles or in stream channels), subsurface vapor flow, and dew deposition.

- Interception is the process whereby a fraction of the total precipitation is stored on and eventually evaporated from the surface of plants without reaching the ground. In densely vegetated regions interception is a significant process; however, in arid regions with sparse vegetation, this process is assumed to be negligible.

- Interflow (sometimes called "storm seepage") is lateral flow of liquid water in the unsaturated zone that can occur during and following precipitation events. This flow is driven by a lateral head gradient component, which is typically the result of a sloping land surface. Such flows are neglected in the current model for the following reasons. First, most of the model domain is characterized by relatively low slopes. For example, the median slope for the model domain is approximately 10 degrees from horizontal and 90% of the domain has a slope less than 25 degrees. The lower the slope the less the lateral head gradient. Second, bulk bedrock conductivity values tend to be significantly higher than the conductivities in the overlying soil and, therefore, once water reaches the soil–bedrock interface, it would tend to enter bedrock instead of flowing laterally along the interface. Soil layering (anisotropic conductivity), if present, might increase the likelihood of interflow. However, steep slopes tend to be associated with shallow soils, where soil layering is unlikely to be important. Even if significant interflow does occur in certain areas, it is not likely to flow over several grid cells because of the shallow soils and high bedrock conductivity. Observations also support this assumption. For example, if significant interflow were occurring at the site, one would expect that stream flows would continue for several days following large precipitation events, seeps would form at the toes of slopes, and mass wasting would occur when thin soils on steep slopes became saturated. None of these indicators of significant interflow characterize the site.

- Storage of water on the surface can occur in the form of puddles and/or as stream channel storage. Small ephemeral puddles do form on areas of bare bedrock after precipitation events, but only about 0.3% of the domain consists of bare bedrock (431 cells out of 139,092 cells; see Table 6.5.2.4-1). Stream flows do not tend to persist significantly beyond the precipitation period as discussed in the validation section (Section 7.1.3). For these reasons, surface water storage is assumed negligible and is excluded from the water balance.

- Subsurface vapor flow is driven by a gradient in matric potential in the subsurface. Releatively significant gradients in matric potential have been measured in semiarid regions with deep soil profiles (Walvoord et al. 2002 [DIRS 178108]; Scanlon et al. 2003 [DIRS 178109]). The presence of these gradients indicates upward vapor flow (Walvoord 2002 [DIRS 178108]); however, the fluxes inferred are of very low magnitude compared with the fluxes associated with episodic liquid water infiltration events that characterize shallow soil regions. Results of the simplified water mass balance approach described in this report suggest that little to no net infiltration occurs beneath thick soils and, therefore, including subsurface vapor flow in deep soil areas would not significantly change these results. In contrast, most of the net infiltration occurs beneath shallow soils, and little is known about the relative magnitude of subsurface vapor flow in these regions. For this reason, this process is assumed to be negligible and is excluded from the water balance.

- Deposition of water as dew is not considered in the modeling. It is assumed that this deposition mechanism is small relative to precipitation and therefore any contribution to net infiltration will be negligible. Dew deposition may be an important source of water to native vegetation, especially during especially dry periods, but its effect on net infiltration is not considered to be important.

- The approach used to estimate water flow and storage within the root zone is a simplification of the actual physical processes that control flow in this environment. The use of the "field capacity" concept acts as a flow switch allowing downward water flow at a rate equal to the saturated hydraulic conductivity when the average water content in a layer equals or exceeds "field capacity" and allowing no flow to occur when average water content in a layer is less than field capacity. In reality, water will flow within the vadose zone in response to gradients in total soil-water potential, which is the sum of various components such as elevation, matric, pressure, temperature, and osmotic potentials. The approach used here assumes that these components can be adequately represented with a unit head gradient when field capacity is equaled or exceeded and with a head gradient of zero when water content is less than field capacity. For this application, the value of field capacity is defined as the water content range between values of suction pressure equal to −0.33 and −0.1 bars. As explained in Sections 6.2.2 and 6.5.2.3, this range of values is considered an approximation for the uncertainty in this property. Osmotic potential is usually a very minor contributor to the total potential unless pore-water concentration gradients are very high, which is not supported by observations at Yucca Mountain.

5.2 FAO-56 METHODS FOR DEVELOPING BASAL TRANSPIRATION COEFFICIENTS ARE APPROPRIATE FOR DESERT ENVIRONMENT

FAO-56 is an internationally recognized set of guidelines for estimating evapotranspiration. The guidelines were developed primarily for agricultural applications but also include guidance for applying the methods to natural, non-agricultural areas.

FAO-56 methods for developing basal transpiration coefficient (K_{cb}) profiles for natural vegetation (Allen et al. 1998 [DIRS 157311], pp. 187 to 193) are applicable to desert vegetation and appropriate and defensible for developing K_{cb} profiles for vegetation at Yucca Mountain (see Section 6.4.4 for description of FAO-56 methods and use of K_{cb}s in the MASSIF model).

This assumption is needed to support use of FAO-56 methods that were originally developed for agricultural crops. While methods for natural vegetation are included in FAO-56, they have not yet been widely used for desert vegetation. The FAO-56 methods for developing K_{cb}s (Allen et al. 1998 [DIRS 157311], pp. 187 to 193) are described, justified for use, and implemented in Appendix D.

Methods provided in FAO-56 for calculating K_{cb} (Allen et al. 1998 [DIRS 157311], pp. 187 to 193) from effective ground cover are appropriate for desert vegetation. The use of effective ground cover measured on reference area plots at Yucca Mountain (Section 6.5.3.6 and Appendix D) directly accounts for the sparse vegetation typical of the Yucca Mountain area. It also allows for weighting (by cover) of vegetation types (e.g., annuals and perennials) within associations. The FAO-56 methods provide for corrections in wind speed, minimum relative humidity, plant height, and stomatal resistance that differ between the FAO-56 standards for agricultural crops and the desert vegetation and climate of Yucca Mountain. Partitioning evaporation and transpiration and applying corrections for stomatal control in the FAO-56 methods are appropriate measures for the Yucca Mountain environment.

5.3 ASSUMPTIONS RELATED TO SIMULATING YUCCA MOUNTAIN VEGETATION USING LANDSAT TM DATA

In Yucca Mountain's arid climate, it is assumed that vegetation responds directly (and linearly) to the total annual precipitation and that the annual vegetation response is linearly related to the basal transpiration coefficient (K_{cb}) and, thus, evapotranspiration. This assumption is supported by correlations between precipitation and vegetation indices (NDVI) in semiarid environments (Scanlon et al. 2005 [DIRS 175977], pp. 6036 to 6037). It is also assumed that the vegetation response measured by NDVI over a single wet year (1998) can be scaled in magnitude to represent the vegetation response for other years (Section 6.5.3). This assumption implies that the timing and relative shape of the vegetation response with time can be represented by the response measured during a single year. The vegetation response for different years is simulated by multiplying the response for 1998 by a precipitation factor based on the difference in annual precipitation from the annual precipitation measured in 1998. This assumption is a necessary simplification because it would be a very significant undertaking to model the dynamic vegetation response to actual daily weather patterns, and such effort is not warranted for the intended purpose of the model. Data from two additional years (dry and moderate precipitation) were used to test the appropriateness of this assumption (Appendix E, Section E-7). The test

indicated that this assumption generally appears valid for predicting the vegetation during the wettest period of the year when net infiltration is most likely to occur. It is not as accurate in predicting the timing and magnitude of the tails of the vegetation response. However, the tails represent times when ET is not as important, and therefore the errors from year to year likely cancel each other out, depending on the weather patterns. It is possible that during the monsoon climate, this assumption may introduce a bias since the period of the year with significant precipitation moves later in the year (late summer). The current assumption will predict vegetation tailing off during this period rather than the vegetation responding to the late season precipitation. The net result of this bias is likely to be an overprediction of net infiltration for this climate, since transpiration may be underestimated during the period of maximum precipitation. Other implications of this assumption are that it ignores the potential effects to vegetation of fire, disease, pests, and other specific environmental factors that may change the vegetation response in the future.

5.4 PHYSICAL PROPERTIES ARE ASSUMED TO REMAIN CONSTANT

It is assumed in this model that the physical properties of the soil, bedrock, and water will remain constant over the time periods being considered in the model (1 day to 10,000 years).

- Over time periods significantly exceeding 10,000 years, it is likely that soil erosion and deposition processes will affect soil depth patterns over the site, but it is assumed that for the next 10,000 years soil depth will remain constant.

- It is assumed that soil formation processes that can significantly change soil properties (conductivity, porosity, field capacity, etc.) will not alter soil properties in the next 10,000 years.

- It is assumed that bedrock conductivity, which is controlled by the nature and properties of the material (caliche) that fills fractures near the soil bedrock interface, will not significantly change in the next 10,000 years.

It is assumed the fluid properties (viscosity and density) can adequately be represented as being constant. In reality, temperature variations result in variations in viscosity and density that contribute to variations in the hydraulic conductivity. For example, the increase in the viscosity of water from 30ºC to 10ºC is about 64% (CRC 2006 [DIRS 178081], p. 6-2), which results in a similar associated decrease in hydraulic conductivity. This temperature range was chosen as an example and is not representative of temperature changes expected within the root zone. The density of water also can influence the hydraulic conductivity. Water density changes as a function of temperature and dissolved concentrations of solutes. The density of water changes only slightly (<1%) in the temperature range between 30ºC and 10ºC (CRC 2006 [DIRS 178081] p. 6-2). The change in density due to dissolved constituents will also be very small since the total dissolved concentration of pore waters collected at the site is relatively low. These examples illustrate that water properties can affect hydraulic conductivity; however, the uncertainty in the hydraulic conductivity of the soil based on other factors is much larger than the potential influence of thermal changes to viscosity and density. Moreover, the sensitivity of net infiltration to soil conductivity has been shown to be low (Sections 6.7 and 7.1.4), and thus any thermal effect on conductivity can be neglected.

5.5 MISCELLANEOUS ASSUMPTIONS AND APPROXIMATIONS

This section lists an assortment of miscellaneous assumptions and approximations that were made using professional judgment in the process of developing the MASSIF model and applying it to Yucca Mountain (Table 5-1). The purpose of this list is to disclose explicitly all these assumptions in one place in the report and point interested readers to the relavant sections of the report where these assumptions are explained and justified. Many of the assumptions listed here were made because there was insufficient direct data with which to represent the process in question. In this case, a decision had to be made as to how to model the process. In these cases, professional judgement, informed by the YMRP acceptance criteria, guided the development of the assumption. There is the possibility that when additional field data is collected or reanalyzed, some of these assumptions may prove to be unsupported by data, which may result in a change to net infiltration predictions. The aim is that assumptions will not bias the net infiltration results, but in certain cases this was not possible. For example, the assumption that no water is removed from bedrock by evapotranspiration does bias the results towards overestimating net infiltration; however, reliable and quantitative information on how much water is removed from bedrock at the site was not available, and therefore a simplifying assumption was necessary given the explicit criteria stating that net infiltration not be underestimated (e.g., Criterion 2.3). Other items listed in Table 5-1 are considered approximations of the actual process. In these cases, it is not the intent of this report to argue that the approximation is what actually occurs in nature; rather, the intent is that the approximation is an adequate representation of the process considering the intended purpose of the model.

Table 5-1. Miscellaneous Assumptions and Their Locations in the Report

Misc. Assumption Number	Description of Assumption	Location in Report (Section)
1	Precipitation is assumed to occur at the same time in all parts of the domain. The frequency of precipitation is calculated for a reference elevation of 1,524 m and is applied to all cells of the domain. This assumption was necessary because there is insufficient data to predict the spatial distribution of precipitation for each event.	6.4.1.1, 6.5.1.3
2	Precipitation is assumed to fall as snow on days when the average daily temperature is below 0°C. Average daily temperature is assumed to be the arithmetic mean of the minimum and maximum daily temperature. This assumption is necessary because a daily time step is used in the modeling.	6.4.1.2
3	The duration during which snowmelt is available at the surface is assumed to be 12 hours on a day with no precipitation. If precipitation does occur, the duration that snowmelt is available at the surface is equal to the duration of the precipitation event on that day. The duration that run-on is available at the surface is assumed to be equal to the duration of the precipitation event.	6.4.2, 6.4.3
4	It is assumed that only one precipitation event can occur during a day. Observed multiple precipitation events during a day are combined into a single event that lasts for the sum of the duration of the multiple events and produces the combined precipitation. It is also assumed that precipitation events do not extend past midnight. For example, if it began to rain at noon on day 1 and continued to rain for 24 hours, this “event” would be represented in the model as two precipitation events (an 11-hour event on day 1 and a 13-hour event on day 2).	6.5.1.7, 6.4.3
5	Evaporation is assumed to cease when the water content of the soil reaches one half the wilting point for the soil.	6.4.4

Table 5-1. Miscellaneous Assumptions and their Locations in the Report (Continued)

Misc. Assumption Number	Description of Assumption	Location in Report
6	It is assumed that maximum rooting depth is uniform over the whole domain. Actual rooting depth is limited by the soil depth because it is also assumed that nearly all of the water that is evapotranspired comes from the soil layer in which active roots are present. This assumption means that it is valid to neglect any evapotranspiration from the bedrock immediately below the soil. It is recognized that roots do sometimes extend into bedrock along fractures; however, no locally relevant studies or data were identified which could be used to quantify the relative amount of water these roots might remove compared with roots in the soil.	6.5.3.2
7	Average daily wind speed is estimated from monthly mean wind speed data from weather stations located within the modeling domain. It is assumed that these daily wind speed estimates are adequate for representing wind speed during future climates over the next 10,000 years.	6.4.5.2
8	It is assumed that for the purpose of estimating incoming solar radiation that each grid cell has a uniform slope (flat surface) and that features that can shade parts of the surface are not important for estimating incoming solar radiation.	6.4.5.2
9	The Hargreaves adjustment coefficient calculated from weather data for years 1998, 2001, and 2002 is assumed to be representative of atmospheric conditions for the next 10,000 years.	6.4.5.2
10	It is assumed that the turbidity coefficient over the next 10,000 years will vary between 0.5 and 1.1. Conditions outside this range are not expected to occur.	6.5.4.1
11	Initial water content used for net infiltration calculation is set to a uniform and constant level for each soil type. It is assumed that this approach adequately represents the conditions in the soil at the beginning of the water year. Real saturations may differ spatially, but there is no basis upon which to set an appropriate initial condition for each grid cell separately.	6.5.4.2
12	For the purpose of using satellite imagery to estimate vegetation responses, it is necessary to assume that the air mass over the Yucca Mountain region is homogeneous everywhere in the satellite image.	E1.1
13	It is assumed that the timing of the vegetation response during the wet water year of 1998 is representative of the timing of the vegetation response during all other years. This assumption was tested for water year 2001 and shown to be generally valid. If the timing of the response in 1998 is close to the mean timing response for all years, then the assumption is still valid since the errors on any given year will tend to be canceled. However, if the timing of 1998 is biased in one direction, this assumption could result in a biased estimate of evapotranspiration. Given the uncertainties in parameters used to calculate evapotranspiration, the impact of such a bias is assumed to be relatively small.	E1.1
14	It is assumed that the linear relationship derived between NDVI and K_{cb} measurements for a few representative years is applicable for future climates expected over the next 10,000 years.	E1.1
15	It is assumed that the vegetation measured at environmental study plots during dry, moderate, and wet years is comparable and similar to vegetation in those same plots during different dry, moderate, and wet years. In order to make these comparisons, an effort was made to scale vegetation linearly with annual precipitation before comparing.	D2.2

Table 5-1. Miscellaneous Assumptions and their Locations in the Report (Continued)

Misc. Assumption Number	Description of Assumption	Location in Report
16	It is assumed that all subsurface flow can be represented by Darcy's Law and that all vertical flow in the soil and into the bedrock is driven by a unit gradient. It is also assumed that there is no conductivity limitation to water entering the surface (evaporation) layer. A conductivity limitation does exist for water flowing from the evaporation layer to the lower root zone. This assumption was made for the following reasons. The processes of interception and surface storage are not explicitly represented in the MASSIF model; however, these processes will act to store some initial amount of precipitation that is not available for runoff. In addition, the typically dry conditions in the surface layer of the soil will result in capillary suction that in effect reduces any limitation due to soil conductivity for this region and that draws in water faster than the saturated conductivity of the soil during the initial wetting period. Since the thickness of the evaporation layer is considered to be uncertain and is sampled in LHS, the effect of this assumption varies with the sampled thickness.	6.4.2
17	It is assumed that conditions affecting evaporation on east (E) and west (W) slopes represent an approximate average of the conditions that would exist on N and S slopes. Thus, vegetation on E and W slopes will be interpolated as a temporal average of N and S slopes.	E3.1
18	It is assumed that vegetation response on flat and gentle slopes (<5°) can be represented as averages between N and S slopes (and therefore, in this simple interpolation, equivalent to E and W slopes). Vegetation responses for all intermediate slopes and azimuths can be represented by weighted averaging between the endmember conditions for N and S slopes.	E3.1
19	It is assumed that any run-on generated in the northern part of Yucca Wash, which has been artificially cut off during watershed delineation, will not significantly affect estimates of net infiltration for that drainage.	6.5.2
20	It is assumed that the maximum daily precipitation possible at Yucca Mountain during the next 10,000 years is equal to or less than the largest observed rainfall in the USA during a 24-hour period over a 26-km^2 area (983 mm; Maidment 1993 [DIRS 125317], p. 3.36, Table 3.10.2).	6.5.1.7

INTENTIONALLY LEFT BLANK

6. MODEL DEVELOPMENT

Section 6 describes and discusses the model used to predict net infiltration at Yucca Mountain. Section 6.1 provides a listing of the features, events and processes (FEPs) addressed by the report.

Section 6.2 includes a description of the processes that are involved in and related to net infiltration. These processes are described in terms of the near-surface water (mass) balance, and include net precipitation, surface water run-on/runoff, change in water storage in the active zone, evaporation, and transpiration. A discussion related to modeling these processes is given, followed by a presentation of criteria for selecting models and model approaches for estimating net infiltration at Yucca Mountain. A brief discussion of existing models and why they were not used for this application is given.

In Section 6.3, the model developed to estimate net infiltration at Yucca Mountain is summarized, the rationale for its development is given, and some of its key features are described. This model, referred to as MASSIF (Mass Accounting System for Soil Infiltration and Flow) is based on a mass balance equation that is solved for each computational cell for each day of the simulation.

The mathematical basis for the MASSIF model is described in Section 6.4. The mathematical representations of the key water balance components are presented in this section, including those for precipitation (Section 6.4.1), water transport and storage (Section 6.4.2), surface runoff and run-on (Section 6.4.3), evapotranspiration (Section 6.4.4), and reference evapotranspiration (Section 6.4.5).

Analyses of Yucca Mountain net infiltration for three pre-10,000-year future climates using MASSIF are described in Section 6.5. Climatic inputs for anticipated climate episodes are described in Section 6.5.1 and include the amount of precipitation, the minimum and maximum temperatures, and the average wind speed. Geologic inputs such as spatial distributions for soil types, soil depth classes and bedrock types, and geologic data used to define watersheds and other site characteristics are given in Section 6.5.2. Vegetation parameters are presented in Section 6.5.3. This section includes a discussion of potential vegetation for different climates, rooting depth, plant height, transpiration coefficients, and vegetation coverages for different climates. A discussion of how Landsat images are used to estimate transpiration coefficients for future climates using predicted precipitation is included. Additional parameters related to describing vegetation are given in Section 6.5.4.

The criteria for considering parameter uncertainty in the calculation of net infiltration are given in Section 6.5.5. Section 6.5 also includes a discussion of the calculation procedures, including a description of the post-processing of results (Section 6.5.6). Finally, results of net infiltration calculations are provided in Section 6.5.7 for each of the three future climates considered.

Section 6.6 contains a discussion of the infiltration prediction uncertainties.

Sensitivity analyses of net infiltration at Yucca Mountain are given in Section 6.7. For each climate considered, a sensitivity study was conducted to identify those parameters whose uncertainty might significantly influence the uncertainty in average net infiltration. Parameters

considered included both generic model parameters and the input parameters that are specific to the Yucca Mountain site. Bases for exclusion of parameters from sensitivity studies are given.

This model is not intended to be a direct input to TSPA. Rather, it is intended to provide boundary conditions for the unsaturated zone (UZ) modeling, which in turn provides direct feeds to TSPA.

6.1 FEATURES, EVENTS, PROCESSES

Table 6.1-1 contains a list of 13 FEPs taken from the FEP List (DTN: MO0508SEPFEPLA.002 [DIRS 175064]). The selected FEPs are those that are associated with the subject matter discussed in the present report. The cross-reference for each FEP to the relevant section(s) of this report is also given in Table 6.1-1.

Table 6.1-1. FEPs Addressed in This Model Report

FEP Number	FEP Name	Relevant Sections
1.2.02.01.0A	Fractures	6.5.2
1.3.01.00.0A	Climate change	6.5.1, Appendix F
1.4.01.01.0A	Climate modification increases recharge	6.5.1, Appendix F
2.2.03.01.0A	Stratigraphy	6.5.2
2.2.03.02.0A	Rock properties of host rock and other units	6.5.2
2.2.07.01.0A	Locally saturated flow at bedrock/ alluvium contact	5, 6.2, 6.3, 6.4
2.2.07.02.0A	Unsaturated groundwater flow in the Geosphere	6.2, 6.3, 6.4
2.3.01.00.0A	Topography and morphology	6.5.2, Appendix B
2.3.11.01.0A	Precipitation	6.5.1, Appendix F
2.3.11.02.0A	Surface runoff and flooding	6.2, 6.3, 6.4
2.3.11.03.0A	Infiltration and recharge	Entire

6.2 INFILTRATION PROCESSES

This section includes a description of the processes that are involved in and related to net infiltration. These processes are described in terms of the near-surface water balance. Next a discussion related to modeling these processes is given, followed by a presentation of criteria for selecting models and model approaches for estimating mean annual net infiltration at Yucca Mountain. Finally, a brief discussion of existing models and why they were not used for this application is given.

6.2.1 Processes Controlling Net Infiltration

Near surface hydrologic processes are generally described in the context of the hydrologic cycle, which describes the pathways and reservoirs through which water moves near and on the surface of the earth. The hydrologic reservoirs consist of the atmosphere, biomass, soil, surface water (streams, lakes, puddles, etc.), snow, pore water in the bedrock overlying the water table, and

groundwater. Water moves between these reservoirs via a set of natural processes, including precipitation, infiltration, soil water movement and retention (e.g., drainage and interflow), evaporation, transpiration, run-off, and net infiltration (see Figure 6.2.1-1).

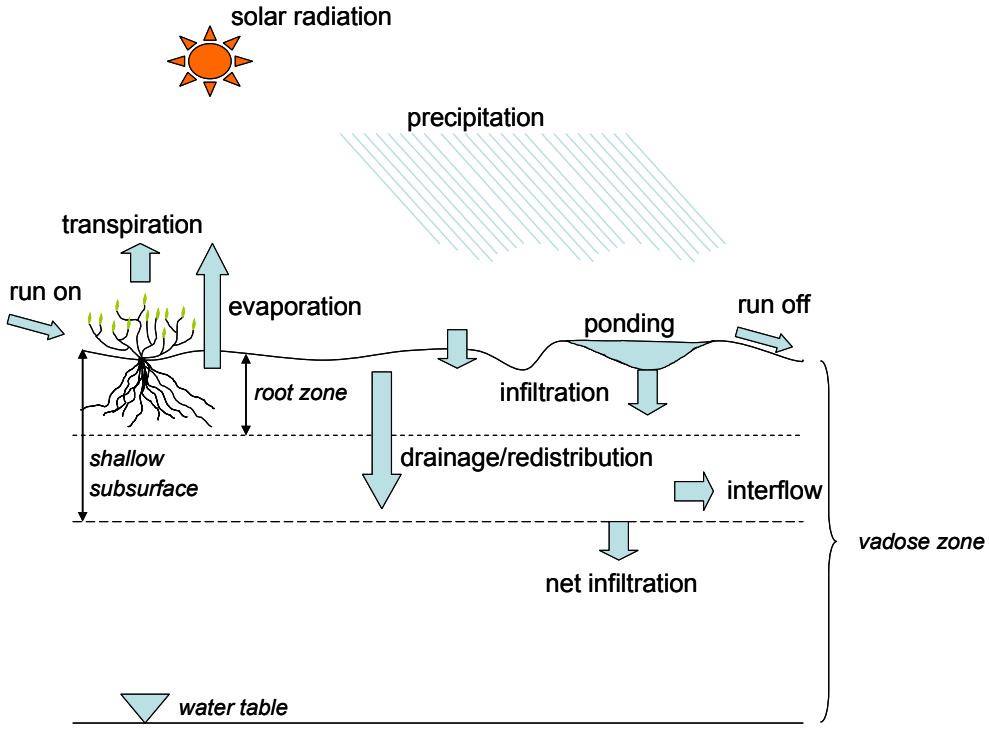

NOTE: Figure not to scale.

Figure 6.2.1-1. Processes Controlling Net Infiltration

The term "infiltration" refers to the volume flux of water through the soil–atmosphere interface, while the term "net infiltration" refers to the volume flux of water to below the shallow zone where most evaporation and transpiration occurs. In this report, "mean annual net infiltration" refers to the temporally averaged net infiltration at a given location, and "spatially averaged net infiltration" refers to the average of mean net infiltration over a specific area, such as the 125 km^2 infiltration modeling domain used for representing the region around Yucca Mountain.

The depth to which evaporation and transpiration are significant processes is often referred to as the active zone to reflect the dynamic nature of the processes in this zone. The active zone often coincides with the root zone or may extend beyond it. The amount of water in the active zone varies substantially over time; below this depth the water content changes are attenuated. In general, when thin soils predominate, the active zone is confined to the soil layer on top of the rock, and net infiltration is defined as the amount of water that moves from the surface layer of soil into the underlying rock. Others have used such terms as "recharge," "drainage," and "deep percolation" to describe net infiltration. These terms imply that water moving below the active zone will eventually recharge phreatic aquifers at depth. While this may occur in humid environments, in arid and semiarid environments with very deep vadose zones, all water moving below the active zone may not recharge the aquifer since lateral and upward flow within the deep vadose zone can occur (Scanlon et al. 1997 [DIRS 142228], p. 463).

In arid and semiarid regions such as the desert basins of the southwestern United States, the processes controlling net infiltration are highly variable in both time and space, and the dominant mechanisms may vary throughout the basin. Net recharge to underlying groundwater in desert basins is often considered to be the sum of several distinct dominant processes occurring in different regions of the basin. Important regions include mountain block, mountain front, and ephemeral stream channels and interdrainage areas of the basin floor.

Mountain block regions are characterized by very thin soils covering fractured bedrock. Areas with thin soils have less total water storage capacity and therefore have a greater potential for high net infiltration as compared with deeper soil regions. Precipitation tends to be higher here than in other regions but is highly variable in time and space. The source of precipitation (i.e., snow melt versus convective storms) can be important. Runoff may be very large in areas of high relief or other areas during storms. Evapotranspiration is often limited because vegetation is sparse. Difficulties in studying infiltration in this region (i.e., installing and maintaining gauging stations or other instrumentation) mean that very little quantitative information is available on mountain block net infiltration.

Soils in the mountain front region are typically thicker than that of mountain blocks, and relief is not as high. As with mountain block regions, the type of precipitation can be important. Runoff can also be important, and net infiltration in the mountain front region is very often focused beneath losing streams. Vegetation is also often focused around these streams, so evapotranspiration can be important.

Infiltration processes on basin floors have been studied more thoroughly than mountain block or mountain front regions. Basin floors typically receive less precipitation than surrounding mountains; however, they make up the majority of land surface and so may receive the majority of rain that falls within the basin. In contrast with mountain block and mountain front regions, basin floors are often characterized by deep vadose zones, although in the case of Yucca Mountain, the vadose zone is thinner under the basin floor than under the mountain. In general, limited infiltrability of soils, intense convective storms, and high evapotranspiration rates tend to limit net recharge in interdrainage areas of the basin floor. Ephemeral channels and surface water bodies, however, are often the locus of focused net infiltration.

A common approach for conceptualizing net infiltration (I) is by means of a near-surface water balance equation:

$$I = P + RO - \Delta W - E - T \qquad \text{(Eq. 6.2.1-1)}$$

where

P is net precipitation
RO is surface water run-on/runoff
ΔW is the change in water storage in the active zone
E is evaporation
T is transpiration.

Net precipitation is the supply of water to the soil surface in the form of rain and snowmelt, minus evaporation of liquid water stored on the surface and sublimation of snowpack. Infiltration across the soil atmosphere boundary is the sum of the net precipitation and run-on minus runoff.

Key processes of the near-surface water balance that affect net infiltration are described subsequently.

Net precipitation

In the general case, for net infiltration to occur at a location, water must be delivered to the ground surface as net precipitation and/or run-on (surface flow). Run-on is water that has moved on the surface from adjacent areas. Precipitation may be in the form of liquid water (rain) or a solid (snow), which later melts to supply liquid water to the soil surface. Precipitation can be described by the type (e.g., rain or snow), the amount (typically in depth units, e.g., mm) and duration of precipitation event. The intensity is the average precipitation rate (amount divided by duration). Snow has the added characteristic of water depth equivalent, averaging 10% water by volume. Some precipitation is temporarily stored on the surface and returned to the atmosphere before it infiltrates or runs off, including evaporation of water intercepted by vegetation and/or accumulated in surface depressions and sublimation of snowpack. Evaporation of surface water and sublimation of snowpack will depend principally upon climatic conditions.

Subsurface water movement and retention

Water movement in near-surface soil can be described by a flux law of the form:

$$\text{Flux} = \text{gradient} * \text{conductivity}$$

The applicable gradient for this flux law is that of the soil water potential. The soil water potential is most often comprises two principal terms: the gravitation potential and the pressure potential. For unsaturated systems, the pressure potential is a negative quantity and is often referred to as matric potential or by its positive-termed value, suction potential. The gradient attributable to gravity always acts downward, whereas the matric potential gradient can be in any direction. Consequently, the net soil water potential gradient and the resulting water movement can be in any direction (e.g., upward, downward, or laterally); the net soil water potential can also be zero corresponding to equilibrium conditions and no water movement. The hydraulic conductivity is the property that describes the ability of the soil to transmit liquid water and decreases nonlinearly with decreasing water content in an unsaturated soil, as capillary forces become relatively more important.

Infiltration

Water delivered to the soil surface from rain, snowmelt or run-on from adjacent areas will infiltrate the soil at a rate that depends on soil properties, transient soil water content, and water potential conditions. The infiltration rate is defined as the volume flux of water (mm^3/mm^2-yr) flowing into the soil profile per unit area of soil surface. The infiltration rate (or flux) resulting from water at atmospheric pressure being made freely available at the soil surface is referred to as the soil's infiltrability (Hillel 2004 [DIRS 178856], p. 260). Infiltrability varies with time and

is a function of the initial wetness and water potential, as well as soil texture, soil structure, and the layering of the soil profile. The rate of infiltration relative to the rate at which water is supplied to the surface will determine the amount that accumulates and/or runs off: water applied to the soil surface at a rate that exceeds the infiltrability of the soil will pond at the surface and/or run off; water applied to the soil surface at a rate less than the infiltrability will all infiltrate into the soil.

In general, infiltrability is highest in the early stages of infiltration and decreases with time, eventually approaching a constant rate. The decrease in infiltrability with time is usually due to the decrease in water potential gradients in the soil profile as infiltration proceeds. In some cases, however, the decreasing infiltrability may be caused by deterioration of the soil structure, formation of a surface crust, small particles migrating into and blocking soil pores, or entrapment of air bubbles.

Water movement after infiltration

When the natural processes that supply water to the soil surface (rain, snowmelt, run-on) stop operating and free water on the surface disappears, the infiltration process ceases. Depending on net soil water potential gradient, water in the soil can move downward, upward, remain stationary (retained), or move laterally (interflow).

Interflow can occur as a result of vertical heterogeneity in soil conductivity (e.g., vertical layering), conductivity differences along the soil–bedrock interface, and as a result of a lateral head gradient (e.g., from a sloping land surface).

Often after substantial infiltration, water will continue to move downward under unsaturated conditions, increasing the wetness of successively deeper layers. This type of flow is often referred to as redistribution. The relatively dry deeper soil draws water from the upper soil that has been wetted, redistributing water between the zones. The relative size of the two zones is a function of the initial wetting depth. Redistribution is a dynamic process that depends upon the relative dryness of the lower zone, the initial wetting depth, and the time-varying hydraulic properties of the conducting soil. The initial redistribution rate can be very high when driven by steep matric potential gradients (i.e., if the initial wetting depth is small and the underlying layer is very dry). When matric potential gradients are small (for example when the initial wetting depth is large and the lower zone is relatively wet), the initial redistribution rate is lower.

Whatever the initial rate, soil moisture redistribution will tend to decrease with time because the water potential gradient decreases and the hydraulic conductivity of the wetter layer decreases with decreasing moisture content. Often, water movement within a soil profile will slow sufficiently after an infiltration event to such an extent that the amount of water in the soil profile remains nearly constant, at least temporarily. Early observations of this tendency led to the concept of field capacity. It was noted that the rate of water content change during redistribution decreases with time and often becomes negligible after a few days. The water content at which internal drainage becomes negligible is taken as the definition of field capacity of a soil (Hillel 2004 [DIRS 178856], p. 310).

Upward soil water movement will occur when the net soil water potential gradient is upward. This situation can arise when the near-surface soil dries in response to evapotranspiration and the resulting upward matric potential gradient overcomes the gradient due to gravity. Upward soil water movement is limited to a large extent by the very low hydraulic conductivity of relatively dry soils. Some upward water movement may be in the form of water vapor movement.

Soil water retention

The amount of water in a soil layer or profile within the active zone will change with time in response to water that enters or leaves the system from downward or upward water movement and/or evapotranspiration. The amount of soil water retained is a function of its moisture characteristic curve, which is the relationship between the soil water potential and the water content. Moisture characteristic curves are different for soils of different characteristics (e.g., texture); two adjacent soil layers at equilibrium (i.e., same water potential) have different water contents if their moisture characteristic curves are different. Moisture characteristic curves are also hysteretic as the amount of soil water retained depends on whether the soil is being wetted or dried.

Surface Water Runoff

Whenever the water delivery rate (precipitation + run-on) exceeds the soil's infiltrability, water accumulates on the soil surface. This free water is often referred to as surface water excess. Some water can be stored on vegetation surfaces as well. Because the soil surface is not flat and smooth, the surface water excess collects in depressions, forming puddles (ponding). If ponding exceeds the surface water storage capacity of the depressions, surface runoff commences.

Runoff comprises a wide variety of flow patterns. At one extreme is thin, sheet-like runoff called overland flow. Overland flow is often the primary type of surface runoff from small natural areas or areas having little topographic relief. As runoff accelerates and gains in erosive power, it eventually forms channels. Further erosion can deepen these channels, and individual channels may eventually converge, forming dendritic networks characteristic of stream flow.

Evapotranspiration

Water within the soil profile can be removed from the soil profile by direct evaporation or through extraction and transpiration by plants. Direct evaporation is the dominant mechanism of water transfer from the soil to the atmosphere when the soil surface is bare, while transpiration may dominate for vegetated soil surfaces. However, since the processes of evaporation and transpiration are often difficult to discern separately, they are commonly lumped into a single process called evapotranspiration (ET). Evapotranspiration is dependent on a variety of biotic and abiotic factors including vegetation characteristics (e.g., root density), climatic conditions (e.g., solar radiation), and soil properties (e.g., hydraulic conductivity function).

Direct evaporation from the soil occurs when three conditions persist: (1) presence of a sustained supply of thermal energy to change water from liquid to gas phase (latent heat); (2) presence of a water vapor pressure gradient at the soil–atmosphere surface; and (3) presence of a continuous supply of water from or through the soil.

Transpiration, loss of water from the plant to the atmosphere, is largely a passive response to the atmospheric environment. Terrestrial plant growth requires CO_2 for photosynthesis, which diffuses through open stomata on plant leaf surfaces to intercellular spaces inside the leaf. Concurrently, water vapor diffuses out of the leaf, from wet cell membranes through stomatal pores to the much dryer atmosphere (transpiration). Some of the water extracted from the soil by plant roots is used in photosynthesis and other essential metabolic processes. However, 95% to 99% of the water that passes through a plant is lost to the atmosphere through transpiration (Nobel 1983 [DIRS 160500], p. 506). Transpiration requires energy to convert water within the vegetation to water vapor, and also requires a water vapor gradient between the vegetation and the atmosphere. The supply of water for transpiration is dependent on the water uptake from the soil and transport within the vegetation. As the adjacent soil dries, water uptake by the vegetation slows. As the rate of water uptake decreases, the vegetation becomes water stressed and eventually will be unable to extract any water from the soil. The amount of water in the soil at this point is referred to as the wilting point and depends on both soil and vegetation characteristics.

6.2.2 Modeling Processes Controlling Net Infiltration

A model to estimate net infiltration must account for the terms of the water balance described by Equation 6.2.1-1. Each of these terms is by itself a complex physical process that can be approximated with simplified representations or models. There are usually a number of models to choose from for each process, including empirical models and physical models of varying detail. In this section, the choices of modeling approaches will be introduced.

The physical processes involved in net infiltration are interdependent. Therefore, the estimate of one term affects the estimate of another and, consequently, affects the estimate of net infiltration. For example, runoff is often calculated as a function of the amount of water stored in the near-surface soil; the drier the soil, the less runoff occurs. As more water enters the soil surface, there is more opportunity for net infiltration.

Net infiltration models are most often implemented within computer programs that combine models of the relevant physical processes. There are many computer programs that can be used to calculate net infiltration along with other water balance components (e.g., Ravi and Williams 1998 [DIRS 178131]). These programs were often developed for specific applications (e.g., contaminant transport, agriculture) and with varying requirements for predictive accuracies. Consequently, existing computer programs can incorporate significantly different models and approaches for estimating water balance components.

Modeling the Components of the Near Surface Water Balance

This section examines various conceptual models used to represent the components of the water balance equation. These components include net precipitation, water movement in the soil profile, evapotranspiration, and runoff.

Net precipitation

A net infiltration model requires precipitation as an input, specifically, the amount, the type, and the duration of the precipitation. The precipitation input can be directly from records of meteorological data or can be derived from empirical models to represent a particular climate, including future climates. Most precipitation data and estimates provide daily total amounts. Daily amounts can be applied over a portion of a day to reproduce observations regarding precipitation intensity, which can vary as a function of season. Whether precipitation falls as rain or snow is a function of the temperature of the atmosphere through which it falls. Observations of snowfall and air temperature have shown that when air temperature is below 0°C, nearly 100% of precipitation falls as snow (Maidment 1993 [DIRS 125317], p. 7.2). Once snow has accumulated on the ground it can either sublimate or melt. Results of studies aimed at measuring sublimation in the field arrive at a wide range of values (1% to 80% of snow loss for the season), depending upon site location and methods used to measure sublimation (Hood et al. 1999 [DIRS 177996]). Snowmelt is commonly predicted from either an energy balance model or from an empirical temperature index approach. The energy balance approach requires extensive climatic data and parameters describing the snowpack characteristics. Snowmelt calculated from the temperature index method is calculated as proportional to the difference between the air temperature and the melting point of snow (0°C).

Soil water movement

The model for water movement within the near-surface soils is an important component of a net infiltration model. The amount and location of water within the soil profile as a function of time will be determined largely from the representation of this process. One common approach for modeling water movement and storage in unsaturated soil is based on the concept of "field capacity." Field capacity for a given soil layer is the amount of water that the soil can hold without significant gravity drainage occurring. Once the saturation of the soil layer exceeds the field capacity of the soil layer, excess water moves downward to the next soil layer. Field capacity is often described as the water content when gravity drainage from the soil becomes negligible. Because this definition is imprecise, field capacity is usually defined at a prescribed value of matric potential consistent with the hydraulic conductivity of the soil becoming very small. The most common value of matric potential associated with field capacity values is −1/3 bar, which is about −340 cm of matric potential head, although the water content at −0.1 bar is also considered representative, especially for coarse soils. Estimates of water movement within a soil profile can be made with the field capacity as the single material parameter for each layer or unit. The field capacity approach implies only gravity-driven (downward) advective water movement. Matric potential gradients, which will affect downward water movement and can result in upward water movement in some cases, are not accounted for with this approach.

A more physically based approach for estimating unsaturated water movement is by means of Richards' equation, which is a differential equation that describes transient flow in an unsaturated porous medium. Richards' equation must be solved numerically for essentially all realistic conditions. With this approach, water movement is driven by gradients in net soil water potential, so matric potential gradients as well as that from gravity are included. The rate of water movement is proportional to the hydraulic conductivity of a soil, which is a varying function of the amount of water in the soil. This approach utilizes the soil water characteristic

curve, which describes the amount of water a soil holds at all matric potentials, not just the single value assigned at "field capacity." This approach requires more parameters, such as the hydraulic conductivity function and the soil water characteristic curve of each soil layer or unit, than the field capacity approach.

Evapotranspiration

Evaporation and transpiration are processes by which water is removed from a soil. These processes are often combined together and referred to as evapotranspiration (ET), in part because it can be difficult to decouple water loss from these two processes. Estimates of ET are usually proportional to the climatic conditions that describe the atmosphere's demand for water (e.g., solar radiation, temperature, wind speed, relative humidity). Potential evapotranspiration (PET) and reference evapotranspiration (ET_0) are two terms that are commonly used to characterize the climatic conditions and usually represent an upper bound of the amount of ET that can occur. Often, actual ET is less than PET or ET_0, especially in drier climates, because soil moisture limits evaporation, transpiration, or both.

Evapotranspiration can be estimated as a combined term with no attempt to distinguish between evaporation and transpiration. However, because they are separate processes, many models estimate evaporation and transpiration separately. Evaporation can be estimated by different approaches. One common empirical approach is to estimate evaporation as a function of the near-surface water content of the soil, taking into account the observation that below some critical water content the evaporation rate decreases as the surface soil dries. This approach can also be implemented in terms of time by expressing the evaporation rate as a function of time after wetting. Alternatively, mechanistic models of evaporation can be implemented. Such a model often employs a boundary layer at the soil surface through which heat and moisture are exchanged with the atmosphere. Once the immediate soil surface layer dries, diffusive vapor movement occurs from within the soil profile. This type of model must be incorporated into a water movement model that allows for suction-driven flow in addition to water vapor diffusion.

Similar to evaporation, there are a wide range of models for estimating transpiration. There are models that incorporate elements of the plant physiology including water movement within individual roots. However, the most common transpiration models are largely empirical. One distinguishing characteristic of transpiration models is the location from which water is extracted from the soil profile. Lumped models extract moisture from the root zone uniformly with depth. Other models impose an assumed distribution of water extraction from the root zone, which can be proportional to a root density distribution that changes with depth. Some models employ root zones that change as vegetation matures.

Transpiration rates depend on the status of the vegetation with respect to its seasonal growth and development. A common modeling approach to capture this behavior is to use crop or transpiration coefficients, which describe the time-varying ability of the vegetation to extract moisture over the course of its growing season. A related approach is to estimate transpiration rates as a function of the amount of vegetation as measured or estimated from the fractional cover (fraction of soil surface covered by vegetation) or leaf area index (leaf surface area per unit soil surface beneath it).

Transpiration models often relate transpiration rate to the water content of the surrounding soils. Below some water content known as the wilting point, vegetation cannot extract sufficient moisture to sustain itself from the surrounding soils, and transpiration ceases. The wilting point is usually defined as water content at a value of suction head at which the vegetation will fail; thus, the value of suction depends on the vegetation and ranges from 15 bars for many common agricultural crops to greater than 60 bars for desert-adapted vegetation.

Another challenge for representing transpiration is defining the vegetation present at a study site as a function of location, time during the growing season, and under different annual conditions (e.g., drought). Depending on the scale of the site, either on-site vegetation characterization is performed or, if the site is large, satellite multispectral remote sensing (e.g., LANDSAT) data is typically used to measure the quantity and distribution of vegetation via the determination of a vegetation index (e.g., Normalized Difference Vegetation Index). When satellite data is used to characterize vegetation, it is typically calibrated with direct measurements made on the ground (e.g., Leaf Area Index).

Runoff

Runoff can be estimated a number of ways. One approach is to estimate runoff as the difference between precipitation and the surface infiltration. The infiltration into the surface soil in response to a specific precipitation event can be estimated using a model of subsurface water movement. A simple approach is to estimate runoff from a water balance of the near-surface soils; infiltration in excess of that required to fill the porosity of the near-surface soils will be runoff. Under some limited conditions, analytical infiltration models (e.g., the Green-Ampt model as discussed by Maidment 1993 [DIRS 125317], pp. 5.32 to 5.39) can also be used to estimate the surface infiltration and hence runoff.

A common alternative modeling approach is to estimate runoff as a function of surface condition and precipitation data. There are models of this type that estimate runoff in response to specific storms, daily precipitation, or on a seasonal or annual basis. Factors that can be used to describe the surface condition include the amount of moisture in the soil, the type of soil, and the extent to which the surface is vegetated and/or developed. Models of this type often utilize the "curve number" approach where runoff is estimated as a function of a single empirical term (the curve number) which is related to the soil and vegetative cover properties in the watershed that are tabulated in handbooks. Most runoff models include "abstraction," which is storage of precipitation in surface depressions and on vegetation.

6.2.3 Criteria for Selection of Net Infiltration Model Components

As described previously, there are a wide variety of models and model components that could be used for the net infiltration modeling, varying in terms of their conceptual basis and numerical implementation. Criteria for evaluating models and model components for net infiltration modeling at Yucca Mountain are given below.

1. The model and model components should be consistent with the overall project purpose.

The purpose of the net infiltration model is to produce estimates of annual net infiltration for the Yucca Mountain site over long periods of time subjected to different future climate scenarios. It

is not the purpose of the model to describe the detailed spatial and temporal character of water movement in the subsurface, describe the details of water consumption by plants or of transport of water vapor in the surface soils, or determine peak surface water flow rates and sediment transport during runoff events.

2. Model component complexity should be consistent with available input data.

The choice of a modeling approach should be consistent with the nature and quality of the data available. In general, as model complexity and detail increase, the requirements for input parameters increase as well. Because few direct and qualified measurements of soil properties exist for the Yucca Mountain site, it is appropriate to represent the ability of the soil to hold and transmit water with a simple model such as one based on the concept of field capacity rather than a more mechanistic model such as one based on Richards' equation. Since the modeling domain is so large and varied, the choice of a simple runoff model linked to the water balance model at each cell is justified over a more complicated runoff model. The availability of high quality satellite data which can be used to estimate the spatial and temporal variability of vegetation justifies the use of a more sophisticated model of evapotranspiration.

3. Model components must be consistent with other model components.

The model components of the water balance terms are interdependent both in a conceptual and computational sense and must be formulated and implemented in a consistent manner. For example, the amount of evapotranspiration is expected to depend on the subsurface water content. Downward water movement will depend on the amount of water removed from the soil by evapotranspiration. Thus, the water movement model and evapotranspiration must be integrated.

4. The model should be computationally efficient.

The computations will involve modeling a very large spatial extent over long periods of time. The model domain covers approximately 125 km^2, and estimates of net infiltration are required for many thousands of years. Further, numerous simulations will be required to assess parameter sensitivities and different climate scenarios. In order to perform all of the necessary computations in a reasonable amount of time, the model should be computationally efficient.

5. The model should be accessible and open.

To increase credibility and facilitate review of the calculations, the net infiltration model should be in as accessible a format as possible. Details of the calculations, including inputs, should be readily available to any interested party. In addition, the computations should be able to be independently reproduced.

6. The model and model components should demonstrate reasonable predictive capability.

The model and model components should be demonstrated to have the ability to reasonably predict or estimate the quantities of interest by comparing to measured data, results of other calculations, and/or other estimates.

6.2.4 Alternative Models Considered

There were a number of models that were considered to provide estimates of net infiltration at Yucca Mountain. The models can be grouped based on how they consider subsurface water movement, either with Richards' equation or with a water balance approach that uses field capacity. Within each of these groups are many specific models. One representative model is described below for each group in order to provide a representative description of the capabilities and limitations of existing models considered for estimating net infiltration at Yucca Mountain. These models are HYDRUS-1D and HELP, respectively.

6.2.4.1 Richards' Equation Approach: HYDRUS-1D Program

Summary of HYDRUS-1D

HYDRUS-1D (Šimůnek et al. 2005 [DIRS 178140]) is a software package for simulating water, heat, and solute movement in one-dimensional variably saturated media. There is also a HYDRUS-2D (Šimůnek et al. 1999 [DIRS 178228]) code, which is a two-dimensional version of the software.

The HYDRUS-1D program numerically solves the Richards' equation for variably saturated water flow and convection-dispersion type equations for heat and solute transport. The software has been used in many studies in support of agricultural projects, landfill design projects, and other studies where detailed predictions of soil moisture and storage, infiltration and evapotranspiration rates, and distribution of dissolved compounds and heat are required. It has also been used in near-surface water balance modeling to evaluate land–atmosphere interactions, deep drainage, and groundwater recharge.

HYDRUS-1D was compared to codes with similar capabilities. The benchmarking analyses presented by Chen et al. (2002 [DIRS 178132]) and Scanlon et al. (2002 [DIRS 177213]) suggested that all the codes considered provided similar results. HYDRUS-1D and HYDRUS-2D, along with the other four codes, were selected out of 248 fate and transport codes in an evaluation by MDH Engineered Solutions Corp. (2003 [DIRS 178204], Section 5.1, p. 20) and were considered as the best in their category.

HYDRUS-1D incorporates a modified Richards' equation in the following form:

$$\frac{\partial \theta}{\partial t} = \frac{\partial}{\partial x}\left[K\left(\frac{\partial h}{\partial x} + 1 \right) \right] - S \qquad \text{(Eq. 6.2.4.1-1)}$$

where

h is the water pressure head [L]
θ is the volumetric water content [L^3L^{-3}]
t is time [T]
x is the spatial coordinate [L] (positive upward)
S is the sink term [$L^3L^{-3}T^{-1}$]
K is the unsaturated hydraulic conductivity function [LT^{-1}] given by

$$K(h,x) = K_s(x)K_r(h,x) \quad \text{(Eq. 6.2.4.1-2)}$$

where K_r is the relative hydraulic conductivity [dimensionless] and K_s the saturated hydraulic conductivity [LT^{-1}]. The unsaturated soil hydraulic properties, $\theta(h)$ and $K(h)$, in Equation 6.2.4.1-1 are in general highly nonlinear functions of the pressure head. HYDRUS permits the use of five different analytical models for the hydraulic properties.

Equation 6.2.4.1-1 assumes that the air phase plays an insignificant role in the liquid flow process and that water flow due to thermal gradients can be neglected.

The equation incorporates a sink term to account for water uptake by plant roots. The sink term, S, is defined using the form proposed by Feddes et al. (1974 [DIRS 178173]):

$$S(h) = \alpha(h)S_p \quad \text{(Eq. 6.2.4.1-3)}$$

where the root-water uptake water stress response function $\alpha(h)$ is a prescribed dimensionless function of the soil water pressure head ($0 \le \alpha(h) \le 1$), and S_p the potential water uptake rate [T^{-1}].

When the potential water uptake rate is nonuniformly distributed over the root zone, S_p becomes

$$S_p = b(x)T_p \quad \text{(Eq. 6.2.4.1-4)}$$

where $b(x)$ is the normalized water uptake distribution [L^{-1}] and T_p is the potential transpiration [L/T]. This function describes the spatial variation of the potential extraction term, S_p, over the root zone and is obtained by normalizing any arbitrarily measured or prescribed root distribution function.

The flow region may be composed of nonuniform soils. The water flow part of the model can deal with prescribed head and flux boundaries and boundaries controlled by atmospheric conditions, as well as free drainage boundary conditions. The governing flow and transport equations are solved numerically using Galerkin-type linear finite element schemes.

Evaluation of HYDRUS for estimating infiltration at Yucca Mountain

There are several reasons that HYDRUS-1D was not used for estimating net infiltration at Yucca Mountain. The first is that HYDRUS-1D is a one-dimensional model and therefore unable to simulate water movement along the surface as runoff between cells. While this limitation could

have been overcome by either linking together adjacent models or examining other versions of the HYDRUS codes that include two- and three-dimensional implemtations, other models and methods were easier to implement. The second reason this code was not used was because the previous model used by the project was a mass-balance model and the available data sets describing soil properties were more compatible with a mass balance, field capacity approach. Appropriate properties could have been estimated and developed for a Richards' equation approach, but this was not pursued. Finally, the strength of a Richards' equation approach is that it can simulate the spatial and temporal details of unsaturated water movement in soil. This ability, however, requires substantial and detailed information about the soil structure and variability of properties such as moisture characteristic curves and hydraulic conductivity functions. At the Yucca Mountain site, the available soil property dataset was limited in the number of samples and the types of measurements made. For these reasons, it was decided to implement a mass balance modeling approach based on the field capacity concept instead of a more physically based approach using the Richards' equation.

6.2.4.2 Water Balance Model Incorporating Field Capacity Approach: Hydrologic Evaluation of Landfill Performance (HELP) Model Computer Program

Summary of HELP

Hydrologic Evaluation of Landfill Performance (HELP) (Schroeder et al. 1994 [DIRS 178136]) is the software package that incorporates a quasi-two-dimensional water balance model to simulate water movement in the unsaturated zone. The code was developed by the U.S. Army Engineer Waterways Experiment Station (WES) for the U.S. Environmental Protection Agency (EPA) Risk Reduction Engineering Laboratory. The primary purpose of the model was to assist in the comparison of landfill design alternatives as judged by their water balances.

The HELP program was tested extensively using both field and laboratory data (Schroeder et al. 1994 [DIRS 178136]). HELP simulation results were compared to field data for 20 landfill cells from seven sites (Schroeder and Peyton 1987 [DIRS 178857]). The lateral drainage component of HELP was tested against experimental results from two large-scale physical models of landfill liner/drain systems (Schroeder and Peyton 1987 [DIRS 178754]). The model is widely used in the USA and internationally (Dho et al. 2002 [DIRS 178133]).

The inputs to the HELP model are daily climatologic data, soil characteristics, and design specifications. The climatologic data include daily precipitation, mean daily temperature, and total global solar radiation and may be either provided by the user or generated stochastically. It also includes growing season, average annual wind speed, average quarterly relative humidity, normal mean monthly temperature, maximum leaf area index, evaporative zone depth and latitude.

The soil data include porosity, field capacity, wilting point, saturated hydraulic conductivity, and Soil Conservation Service runoff curve number for antecedent moisture condition II. The model contains default soil characteristics for 42 material types for use when measurements or site-specific estimates are not available. The layers in the landfill are typed by the hydraulic function that they perform. Four types of layers are available: vertical percolation layers, lateral drainage layers, barrier soil liners, and geomembrane liners.

HELP calculates water balance on a daily basis as follows. Snowfall and rainfall are added to the surface snow storage, if present, and then snowmelt plus excess storage of rainfall is computed. The total outflow from the snow cover is then treated as rainfall in the absence of a snow cover for the purpose of computing runoff. A rainfall-runoff relationship is used to determine the runoff. Surface evaporation is then computed. Surface evaporation is not allowed to exceed the sum of surface snow storage and intercepted rainfall. Interception is computed only for rainfall, not for outflow from the snow cover. The snowmelt and rainfall that does not run off or evaporate is assumed to infiltrate into the landfill. Computed infiltration in excess of the storage and drainage capacity of the soil is routed back to the surface and is added to the runoff or held as surface storage.

The rainfall-runoff process is modeled using the Soil Conservation Service curve-number method (Maidment 1993 [DIRS 125317], pp. 9.21 to 9.26). Potential evapotranspiration is modeled by an energy-based Penman method. The program uses an albedo of 0.23 for soils and vegetation and 0.60 for snow. The vegetation data is generated by a vegetative growth model. Vertical drainage is assumed to be driven by gravity alone and is limited only by the saturated hydraulic conductivity and available storage of lower segments. If unrestricted, the vertical drainage rate out of a segment is assumed to equal the unsaturated hydraulic conductivity of the segment corresponding to its moisture content, provided that moisture content is greater than the field capacity or the soil suction of the segment is less than the suction of the segment directly below.

Evaluation of HELP for estimating net infiltration at Yucca Mountain

HELP was not used to estimate net infiltration at the Yucca Mountain site primarily because it was developed for a different type of application, and consequently it is not consistent with the overall purpose of estimating net infiltration at Yucca Mountain for thousands of years under different climate conditions. To be used for this type of application, HELP would require substantial modifications.

Most water balance models that incorporate field capacity were developed for specific applications rather than as general purpose models. In the case of HELP, it was developed to evaluate landfill systems. Many of the features and capabilities of HELP, such as lateral flow in drainage layer and geomembrane layers, are not applicable for estimating net infiltration at Yucca Mountain. Other features, such as modeling entire slopes as a single element, are not consistent with the terrain of Yucca Mountain. Some of the features not explicitly included in HELP relevant to the Yucca Mountain site include: permitting run-on from adjacent locations; saturation of thin soil layers; ET that is a function of slope, azimuth, and elevation; and specifying bedrock as a lower boundary.

6.3 DESCRIPTION OF THE CONCEPTUAL MODEL – MASS ACCOUNTING SYSTEM FOR SOIL INFILTRATION AND FLOW (MASSIF)

The model developed to estimate net infiltration at Yucca Mountain is referred to as MASSIF (Mass Accounting System for Soil Infiltration and Flow). In this section, MASSIF is summarized, the rationale for its development is given, and some of its key features are summarized.

6.3.1 Summary of MASSIF

MASSIF estimates net infiltration at the Yucca Mountain site based on a daily water balance calculation of the near-surface soils. The MASSIF model defines net infiltration as the water that passes out of the soil layer into the underlying bedrock. The water balance includes net precipitation as input, water storage and movement within the soil including evapotranspiration, and water moving from the soil into the underlying bedrock.

The model domain is composed of a number of cells with equal surface area that extend from the surface to the contact with the underlying bedrock. The description of each cell includes the cell depth as defined by the soil layer depth; soil type and associated properties; cell elevation, azimuth and slope; and vegetation-related characteristics. Each cell is composed of one to three soil layers, depending on the soil depth. The topmost layer is relatively thin and is divided into two sections (nodes) representing the bare surface fraction and the fraction of the surface covered with vegetation (canopy fraction). The top layer is designated as the evaporation zone. The second layer extends from the bottom of the first layer to the bottom of the root zone or to the soil–bedrock interface in the case that the maximum rooting depth is greater than the soil depth. Layers 1 and 2 comprise the evapotranspiration zone. The third layer extends from the bottom of the root zone (Layer 2) to the soil–bedrock interface. When soil depth is less than maximum rooting depth, Layer 3 is not represented (thickness is set to zero).

Daily climatic data are input to the model, including precipitation and maximum and minimum air temperature. Precipitation and mean temperature are adjusted for cell elevation. Snow, snowmelt, and sublimation are included in the model.

Subsurface water movement within the model is one-dimensional; that is, there is no subsurface water movement between adjacent cells. The model allows rain and snowmelt to run off the top of one cell onto an adjacent cell that is at a lower elevation. Runoff can occur if the net precipitation exceeds the ability of the thin surface soil layer to store and transmit water to underlying soils. Runoff will also occur if the entire cell from the bedrock to the surface saturates. In the case of runoff, water is diverted to the surface of the next downstream cell.

Subsurface water movement is estimated by means of a daily water balance approach for each cell. Subsurface water movement within the model is one-dimensional; that is, there is no subsurface water movement between adjacent cells. Downward water movement from layer to layer within a cell is based on the field capacity concept. Field capacity of the soil represents the amount of water that is held by the layer after gravity drainage. Water in excess of the field capacity will be available to move downward to a lower layer. Water is removed from the root zone based on a daily calculation of evapotranspiration (ET) for each cell. The ET calculation is derived from the "dual crop" version of the FAO-56 method, which produces separate estimates of evaporation and transpiration depending upon the fraction of the surface covered by vegetation. ET is calculated proportional to a reference ET, which accounts for the atmospheric demand for water based on daily climatic conditions at each cell. The FAO-56 methods provide for corrections in wind speed, minimum relative humidity, plant height, and stomatal resistance that differ between the FAO-56 standards for agricultural crops and the desert vegetation and climate of Yucca Mountain. These adjustments were implemented in the model.

Water above field capacity in the bottom-most soil layer can enter the underlying bedrock layer, limited by the effective saturated hydraulic conductivity of the bedrock. Any water that moves into the bedrock layer is net infiltration for that cell and passes out of the bottom of the model.

6.3.2 Rationale for Key Components of MASSIF Model

The representations of subsurface water movement and evapotranspiration are key components of MASSIF. Subsubsurface water movement is modeled with a water balance that uses the field capacity approach and ET is calculated with the FAO-56 method that represents the root zone as a lumped entity.

The rationale for using these modeling approaches is discussed below in the context of the model component selection criteria given in Section 6.2.3.

1. Model components should be consistent with the overall project purpose.

The purpose of the net infiltration model is to produce estimates of annual net infiltration for the Yucca Mountain site over long periods of time. The net infiltration model is not being developed to describe the detailed spatial and temporal character of other water balance components, such as the details of water consumption by plants or of transport of water vapor in the surface soils. This purpose is reflected in the model components of MASSIF: a field capacity approach using estimates of the amount of water that drains from a soil layer but does not explicitly model water movement within the soil layer; and the FAO-56 method that estimates daily ET values over a lumped root zone but does not explicitly model ET details such as water uptake by individual roots or transport of water within the plant.

2. Model component complexity should be consistent with available input data.

The amount and type of available input data for the net infiltration model are necessarily limited due to the large spatial coverage of the model and the relatively few directly measured data. These limitations preclude the expectation of accurate predictions at specific locations. The need to estimate many of the inputs results in net infiltration values that are representative and consistent with the characteristics and properties of locations at Yucca Mountain rather than being considered site-specific predictions.

Data required as input to model subsurface water movement include soil thickness above bedrock, soil types and layering, and corresponding soil hydraulic properties. Most of these data are not measured directly for the vast majority of the Yucca Mountain domain and must be estimated from a few measurements, including soil thickness and soil properties. There are few available measurements of soil hydraulic properties, and very little information on subsurface soil characteristics such as layering. A significant advantage of using a field capacity approach is that it requires a very limited amount of input pertaining to hydraulic properties. Further, although not directly available for the Yucca Mountain soils, the field capacity values required as input can be reasonably estimated from other information that may be available, such as soil textural characteristics.

The lack of measured, site-specific input data indicates that there can be little merit in attempting to precisely model subsurface water movement at discrete locations within the domain and that an approach more complicated than one that uses field capacity is not warranted. With the limitations of the inputs, it is not apparent whether estimates of net infiltration would be more accurate with a model that implemented a water balance using the field capacity approach or a more complicated Richards' equation approach.

The detailed data required to explicitly model transpiration from vegetation associated with a particular cell are largely unknown. These unknowns include the number and distribution of specific plants and seasonally dependent plant surface characteristics such as leaf area index and height or root length and density. Further, extrapolating these data in response to future climate changes would be extremely difficult.

The FAO-56 method is consistent with the limited availability of detailed data regarding ET at Yucca Mountain. This method to estimate ET has been developed to allow for its use when there is limited direct information regarding vegetation characteristics. The FAO-56 method does not model individual plants but instead provides a typical response of vegetation types based on transpiration coefficients that involve day of the year, location, annual precipitation, and daily water status of the soil. Transpiration is assumed to remove water from the entire lumped root zone and does not specify a distribution of subsurface water extraction.

Despite the limitations on available field data, the methods incorporated into the MASSIF model provide an integrated tool that can be used to estimate net infiltration and evaluate uncertainty in net infiltration arising from parameter uncertainty. In addition, MASSIF is ideally suited for evaluating and ranking input parameter sensitivities. For these reasons the MASSIF conceptual model is considered adequate for its intended use.

3. Model components should be consistent with the complexity and uncertainties of other aspects of the net infiltration model.

Uncertainty in net infiltration estimates may come from sources other than the models for subsurface water movement and ET. An important example is the need for daily precipitation as a principal input for calculations of the daily water balance, subsequent runoff, soil water movement, and ET. The precipitation input relies on estimates of possible future climates that are by their nature associated with substantial uncertainty. For this reason, precipitation input is represented by a stochastically generated set of precipitation years that include rare and possibly important extremes.

4. Model components must be consistent with other model components.

Because they are both directly related to the water balance, the water movement model must be integrated with the model for ET. This is important with respect to net infiltration because a very large fraction of surface infiltration is expected to be consumed as ET. The FAO-56 method uses the field capacity concept to account for water in the near-surface and root zone, consistent with the use of the field capacity approach in the subsurface water movement model.

5. Model components should be computationally efficient.

Both the field capacity approach and the FAO-56 method are computationally straightforward and do not require iterative numerical solutions.

6. The model should be accessible and open.

MASSIF was developed using Mathcad, a widely available commercial software package that allows the combination of formatted text, figures, and mathematical calculations in the same document. The benefit of this approach over using compiled code is that the documentation of the calculation exists side-by-side with the actual calculation routines, inputs, and results. The use of Mathcad was practical largely because MASSIF utilizes a daily water balance using a field capacity approach, rather than another more involved approach to water movement that would require sophisticated and computationally intense numerical solution methods. All equations, inputs, assumed values, and constants are explicitly shown in the MASSIF Mathcad files, allowing independent verification and use of the model by those other than the model developers.

7. The model should demonstrate reasonable predictive capability.

The validation of MASSIF is discussed in Chapter 7.

6.3.3 Description of Key MASSIF Elements

Climatic input to model

Daily climatic data input to the model includes precipitation and minimum and maximum air temperature. These values are adjusted for the elevation of a particular cell. Precipitation is in the form of snow if the average air temperature is below 0°C. Snow is allowed to sublimate during snowfall rather than as part of the snowpack. When the average temperature is above 0°C, snowpack melts at a temperature-dependent rate. Rain and snowmelt are input to the top of each cell.

Initial runoff

The initial runoff from a cell is calculated based on the ability of the surface soil layer to store and transmit water to a lower layer. Net precipitation (rain, snowmelt, and run-on from an adjacent cell) are applied to the surface soil layer. If water content is in excess of the saturated water content of the soil after water redistribution (described below), this excess is diverted as runoff and is available to the next downstream grid cell.

Subsurface water movement

Subsurface water movement is modeled within each grid cell as a one-dimensional (vertical) water balance. The top boundary of each cell is the atmosphere/land surface contact and the bottom boundary is the underlying bedrock. The model of the soil between these boundaries depends on the soil depth at a cell location, the rooting depth of the vegetation, and the evaporation depth. The evaporation depth is the relatively shallow depth in which the soil is

dried directly by evaporation. The rooting depth is the assumed extent of the root system and defines the depth from which evapotranspiration will occur.

The soil is divided into one to three layers, depending on the soil depth for the cell (Figure 6.3.3-1):

The surface layer (Layer 1) is set to the evaporation depth unless the soil depth is less than this, in which case, the surface layer is set to the soil depth. The surface layer is divided into two nodes to differentiate between surface soil that is within the vegetation canopy and bare soil outside the canopy.

If the soil depth is greater than the evaporation depth, then a second soil layer is represented (Layer 2). If the soil depth is less than the rooting depth, the second layer extends from the surface layer to the bottom of the soil profile. If soil depth is greater than the maximum rooting depth, then the second layer extends to the maximum rooting depth.

If the soil depth is greater than the rooting depth, then a third soil layer is represented and extends from the maximum rooting depth to the bottom of the soil profile.

The bedrock interface is located beneath the bottom-most soil layer.

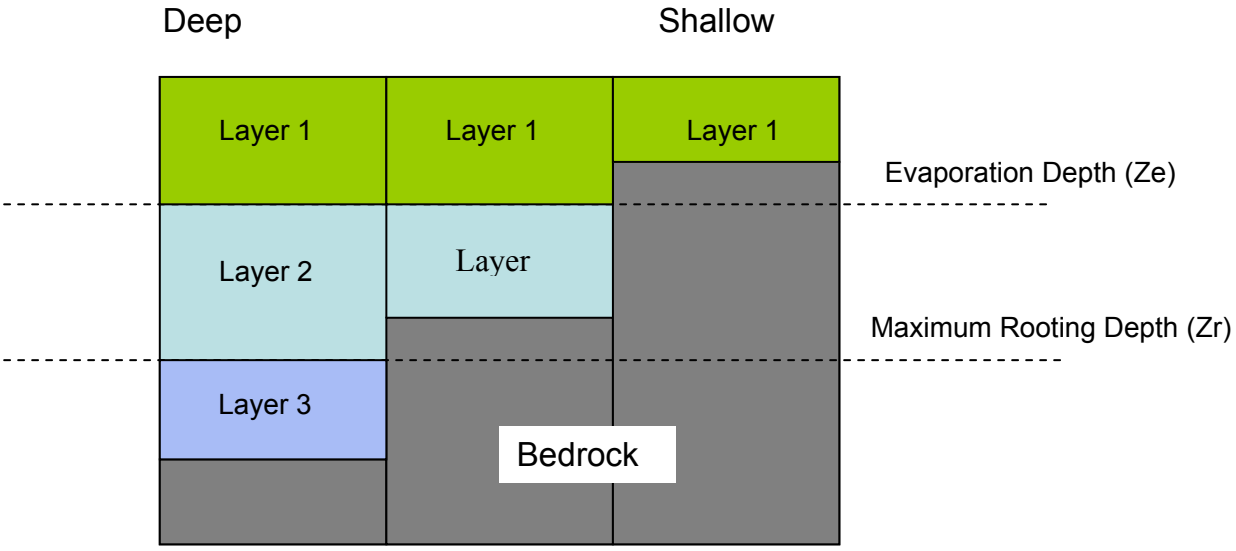

Figure 6.3.3-1. Schematic Figure Showing How Soil Layers Are Assigned for Different Soil Depth Scenarios

There are two principal computational steps that are calculated on a daily basis: water movement within the soil profile followed by water removal due to evapotranspiration.

a. Water movement

Surface infiltration is applied to the vegetated and bare soil nodes of the surface layer in proportion to their areal fraction. The total amount of water within each node is compared to the field capacity. Water in excess of the field capacity is allowed to move to the second layer,

which describes the balance of the root zone. The process is repeated, and water in excess of field capacity in the second layer is passed into the third soil layer which describes the region below the root zone. Finally, water in excess of field capacity in the third layer is passed into the underlying fractured rock, where it becomes net infiltration.

Flow limits are implemented between soil layers and between the soil and the rock. The amount of water that can pass between layers is calculated from Darcy's law assuming a unit gradient (gravity flow) and the effective saturated hydraulic conductivity value for the soil and for the bedrock. When one or more of these flow limits is reached, the overlying soil node can accumulate water in excess of field capacity and up to the soil saturated water content. When the soil saturated water content has been reached in the surface layer, excess water supplied to the soil is manifested as runoff.

The bare-soil and vegetated nodes that comprise the surface layer can have different water contents preceding a precipitation or run-on event. It is conceptually possible that one of them might reach the saturation limit while the other remains below. The physical distance between the bare-soil and canopy regions is on the order of the plant size, while the area of a "cell" is 30 m × 30 m. This means that excess water (runoff) from one of the surface nodes should first be supplied to the other surface node describing the surface layer before it is added to the runoff from the cell.

b. Evapotranspiration

Water is removed from the surface layer and Layer 2 based on a daily calculation of ET for each cell. The ET calculation is derived from the dual crop version of the FAO-56 method, which produces separate estimates of evaporation and transpiration. Evaporation is assumed to occur over the exposed and wetted fraction of the surface layer, which is the portion of the soil surface that is exposed to evaporative energy. Transpiration occurs from the "root zone," which comprises the surface layer and the underlying Layer 2.

The first step in estimating ET is to calculate the reference ET (ET_0), which is ET from a hypothetical crop of well-watered grass. ET_0 is the principal means by which the FAO-56 method accounts for the effect of daily climate on ET. For each cell, ET_0 is calculated based on the location of the cell with respect to the sun, cell elevation, daily temperatures and wind speed.

Total transpiration from the root zone is calculated by multiplying ET_0 times a transpiration coefficient for each cell. The transpiration coefficient accounts for the difference between the characteristics associated with a cell's specific vegetation to those assumed for the ET_0 calculation. The transpiration coefficient is a function of the day of the year to reflect the development stage of the vegetation. In the case where there is no vegetation or during dormant periods, the transpiration coefficient can be nonzero to allow for a relatively small amount of "diffuse evaporation" from Layer 2, which accounts for the slow process of water being drawn up from the second layer and evaporated.

A basal transpiration coefficient function, which reflects ideal climatic and soil water conditions, is first assigned to a cell based on the vegetation community anticipated for the year given the annual precipitation as well as the cell's azimuth and slope. The basal transpiration coefficient is

adjusted for daily climatic conditions and is reduced to account for soil water stress if the water content of the root zone is below a value that results in reduced transpiration for a particular vegetation type. When the root zone water content is reduced all the way down to the wilting point, plants are assumed to be unable to extract water from the soil and the transpiration coefficient is set to a minimal value. This minimum value represents conditions when evaporation and transpiration rates are at their minimum and water loss is primarily diffusive. This minimum value is a function of soil properties. The total transpiration is partitioned between the surface layer and Layer 2 based on the relative amounts of water in these layers.

Evaporation is assumed to occur only from the portion of the surface layer that is directly exposed to solar radiation, that is, the bare soil fraction. Evaporation is calculated by multiplying ET_0 times an evaporation coefficient for each cell. When the soil surface is wet, evaporation is limited by the energy available to the exposed surface, and the evaporation coefficient is determined from energy-related factors. As the soil surface dries below a critical water content, the evaporation coefficient is reduced, reflecting the influence of subsurface moisture diffusion (see Section 6.4 and Appendix G).

Surface water routing

The model first considers the highest elevation cell within a watershed, calculates the water balance for that cell, and then progresses to the cell with the next highest elevation. In this way, runoff from a cell can be included as run-on to an adjacent cell. All of the runoff is added to the neighboring adjacent cell with the lowest elevation.

6.4 MATHEMATICAL DESCRIPTION OF THE MODEL

This section of the report describes the mathematical foundations of the MASSIF model. It presents the equations used and introduces the input parameters required to run the model. The justification for parameter values and distributions for the calculation of net infiltration at Yucca Mountain are provided in later sections and appendices. As much as possible, only pointers to these sections of the report are provided in this section.

The objective of the MASSIF model is to calculate net infiltration for each cell of a grid representing a watershed bounded by surface water divides. The limitations and input requirements of the model are described in Appendix G along with a detailed description of the model algorithm. In this section, the mathematical basis for the model is discussed in terms of the applicable physics. The basis of the model is the following water (volume) balance equation for the soil that is solved for each computational cell for each day of the simulation:

$$R_{off} = P_{rain} + R_{on} + SM - \Delta\theta - ET - NI \qquad \text{(Eq. 6.4-1)}$$

where

R_{off} is runoff,
P_{rain} is precipitation as rain,
R_{on} is run-on,
SM is snowmelt,

$\Delta\theta$ is the change in water storage in the soil,
ET is evapotranspiration, and
NI is net infiltration.

Additionally, a water (volume) balance equation for the snowpack of each cell is solved for each day of the simulation:

$$\Delta SP = P_{snow} - SUB - SM \qquad \text{(Eq. 6.4-2)}$$

where

ΔSP is the change in the water storage of the snowpack
P_{snow} is precipitation as snow,
SUB is the sublimation,
SM is snowmelt.

Figure 6.4-1 illustrates that the soil and snowpack form the two water reservoirs represented in the water balance. Snowmelt (SM in Figure 6.4-1) is the only pathway for P_{snow} to reach the soil. Water movement in the model is considered to be vertical below the surface. The only water transport between cells is via runoff (R_{off}) from one cell, which is added to a downstream cell as run-on (R_{on}). In the sections below are descriptions of how each of these quantities is represented in the model.

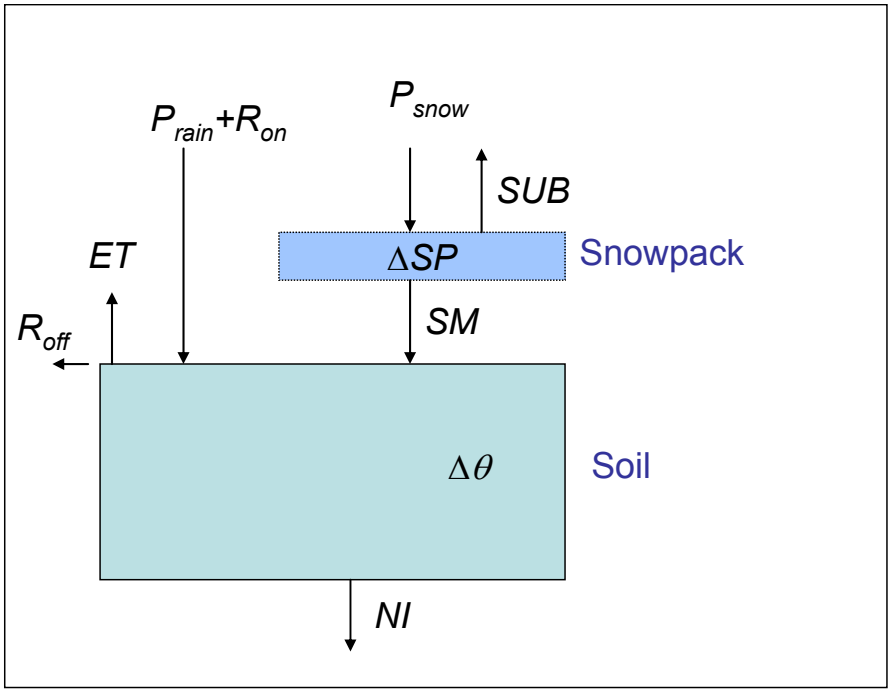

Figure 6.4-1. Schematic Showing the Water Reservoirs and Fluxes Included in the Water Balance

6.4.1 Precipitation (P)

6.4.1.1 Adjusting Precipitation for Elevation

Daily values of total precipitation ($P_{rain} + P_{snow}$) at a reference elevation are input to the model. Precipitation on a given day is either in the form of rain or snow depending on the air temperature where it falls. Studies of regional precipitation have shown that total annual precipitation for a given a site is typically correlated with elevation (e.g., Daly et al. 2002 [DIRS 177096], p. 102; Phillips et al. 1992 [DIRS 177091], p. 120). In addition, other factors such as local rain shadows caused by nearby mountains can also be important factors influencing the total amount of precipitation (Phillips et al. 1992 [DIRS 177091], p. 120). In the MASSIF model, elevation is the only factor considered for adjusting precipitation by location. Daily precipitation adjusted for elevation is given by:

$$P = P_{ref}\left(1 + (elev - elev_{ref})\, C_{Precipcor}\right) \qquad \text{(Eq. 6.4.1.1-1)}$$

where

P is the precipitation (mm) adjusted to an elevation, $elev$ (m),

P_{ref} is the precipitation (mm) at the reference elevation, $elev_{ref}$ (m), and

$C_{Precipcor}$ is the precipitation lapse rate (fractional change in precipitation at the reference elevation / m of elevation change).

The development of the precipitation lapse rate for the Yucca Mountain net infiltration calculation is discussed in detail in Appendix F, Section F2.1.

One limitation of this approach is that it is assumed that when precipitation occurs at the reference elevation, it occurs everywhere in the domain (Section 5). A more complicated model might allow precipitation to occur in parts of the domain while other parts of the domain remain dry. Such sophistication was deemed unnecessary for the current development.

6.4.1.2 Precipitation Type as a Function of Temperature

Precipitation is assumed to be snowfall (P_{snow}) whenever the average daily temperature at a cell location is equal to or less than 0°C. Inputs to the model are maximum and minimum daily air temperatures at the reference elevation. Average daily temperature at the reference elevation is calculated in the model as the mean of the minimum and maximum temperatures. These temperatures are then corrected for elevation from the reference elevation for each grid cell in the geospatial database. The elevation correction decreases temperature linearly with increasing elevation at a rate referred to as the temperature lapse rate. The temperature correction equation used in MASSIF is given in Section 6.4.5.3 and Appendix G. The development of the temperature lapse rate for the Yucca Mountain net infiltration calculation is discussed in detail in Section 6.5.1 and Appendix C.

6.4.1.3 Duration of Daily Precipitation Events

Precipitation can occur over a range of durations from brief and intense thunderstorms to prolonged storms that last the entire day. For the purposes of modeling the water transport in the soil, the period of time that water is available at the surface of the soil may be important. The MASSIF model requires as input an effective duration in hours for each day of precipitation (*duration*). The development of the precipitation durations for the Yucca Mountain net infiltration calculation is discussed in detail in Section 6.5.1 and Appendix F.

6.4.1.4 Fate of Snowpack

Snowpack will melt on days when the average air temperature at a cell location is above 0°C. The snow melts at a rate proportional to the average daily air temperature (T_{avg}) at a cell (Maidment 1993 [DIRS 125317], p. 7.24):

$$SM = C_{snowmelt} * T_{avg} \quad \text{(Eq. 6.4.1.4-1)}$$

where SM is the daily snow melt (mm of water) and $C_{snowmelt}$ is a constant (mm/°C). If it rains on a day when there is snowmelt, the rain and snowmelt are combined and applied as input to the top soil surface over the effective precipitation duration for that day. On days without precipitation, snowmelt is applied over a 12-hour duration. Rain is input to the top soil surface on the day of precipitation regardless of whether there is snow accumulated on the surface from prior snow events. These constraints simplify a complex process that is affected by the pattern of precipitation and temperature during the day. Such details are important for models designed for forcasting but are not considered important for the MASSIF model, which is aimed at making long-term predictions for large areas. Some portion of snow will sublimate; the total annual sublimation can be described as a percentage of the total annual amount of snow (Hood et al. 1999 [DIRS 177996]). In MASSIF, daily sublimation (SUB, mm) was calculated as a fixed percentage ($C_{sublime}$) of the precipitation (P_{snow}, mm) on days that it snows.

$$SUB = P_{snow} * (C_{sublime}) \quad \text{(Eq. 6.4.1.4-2)}$$

This approach ensures that the cumulative annual sublimation will be the desired percentage of the annual snow but does not necessarily accurately reproduce daily sublimation rates. However, this limitation is not considered to be important for the intended purpose of the MASSIF model, which is to estimate mean annual net infiltration as a function of location. The development of $C_{snowmelt}$ and $C_{sublime}$ for the Yucca Mountain net infiltration calculation is discussed in Section 6.5.1.

6.4.2 Mathematical Representation of Water Transport and Storage

As explained in Section 6.3, rather than employing a Richards' equation approach to solve for subsurface water movement, a simpler "field capacity" approach is adopted. In this approach the soil at a given location is divided into a series of layers and nodes (Figure 6.4.2-1). In this context, layers refer to vertical soil horizons and nodes refer to distinct volumes of soil considered in the water mass balance. The model accommodates up to three layers and four nodes. The top or surface layer is divided into two nodes and the bottom two layers are each

represented by a single node. A daily water balance is performed on each node in each cell of the watershed.

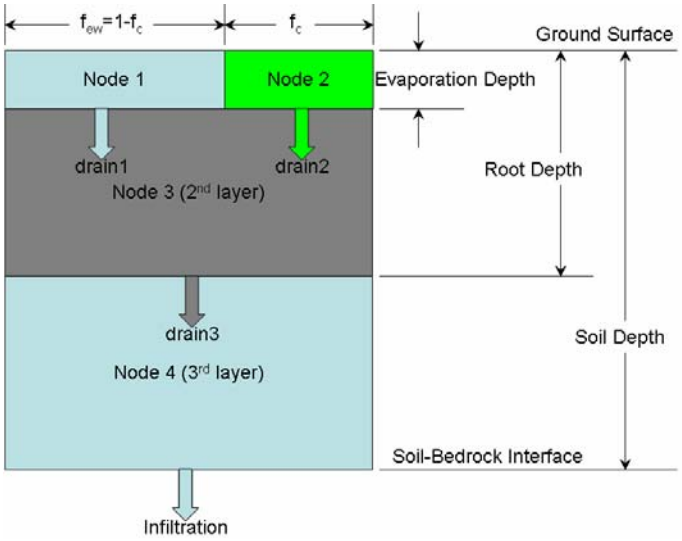

Source: Output DTN: SN0701T0502206.037.

NOTE: f_c is the fraction of the surface covered by the vegetation canopy and f_{ew} is the fraction of the surface that is exposed and wetted.

Figure 6.4.2-1. Schematic Showing the Vertical Soil Layers and Computational Nodes Present in a Single Model Cell

In each of the soil nodes, the amount of water is accounted for by the "*Water level*." *Water level* is the equivalent height of water in the layer per unit area and is measured in length units (e.g., cm). *Water level* is related to the average volumetric water content (θ) in a layer as:

$$Water\ level = \theta * node\ thickness \quad \text{(Eq. 6.4.2-1)}$$

Typically, the amount of water that can be stored in a layer is defined by the field capacity of the layer. The integrated field capacity (*FC,* mm) for a particular node is the product of the intrinsic field capacity (θ_{FC}, m^3/m^3) and the node thickness:

$$FC = \theta_{FC} * node\ thickness \quad \text{(Eq. 6.4.2-2)}$$

Drainage or downward daily water movement (*Drain*, mm) from a soil node to the next lower node is assumed to occur when the water level exceeds the field capacity for that node. Layers 2 and 3 (Nodes 3 and 4) can accept water at a maximum rate defined by the saturated hydraulic conductivity (K_{sat_soil}, mm/yr) and the precipitation duration. This rate, the soil conductivity infiltration limit ($Limit_{soil}$, mm), is given by:

$$Limit_{soil} = K_{sat\_soil} * duration \quad \text{(Eq. 6.4.2-3)}$$

The *duration* (hr) is the amount of time during the day during which precipitation occurs. If there is only snowmelt on a day, a 12-hour duration is assumed. The basis for this simplifying assumption is that snowmelt would be most likely to occur during the day when temperatures

tend to be higher and cease at night, when it is colder. K_{sat_soil} is the saturated conductivity of the soil. The amount of water that moves downward (*Drain*, mm) is:

$$Drain = MIN(Limit_{soil}, Water\ level - FC) \quad \text{(Eq. 6.4.2-4)}$$

The water level of the layer is reduced by this amount and the water level of the underlying layer is increased by this amount, thereby passing water to a lower layer. The development of θ_{FC} and K_{sat_soil} for the Yucca Mountain net infiltration calculation is discussed in Section 6.5.2.

The shading of the vegetative canopy retards evaporation under the canopy. As a result, the surface layer of soil under the canopy frequently has higher water content than the adjacent exposed soil. To reflect this, the surface layer is divided into two nodes. Node 1 (the "evaporation node") models the bare soil; Node 2 (the "canopy node") models the canopy region. The water levels in these two nodes are calculated separately.

During a precipitation event, one of the two surface nodes in a cell may exceed field capacity before the other. For instance, the canopy node (Node 2) may reach field capacity before the adjacent bare soil node (Node 1). The distance between the two nodes (Node 1 and Node 2) reflects the physical dimensions of the individual plant canopies and the inter-plant spacings. This distance is expected to be much smaller than the cell dimension (30 m). Therefore, in the MASSIF model, surplus water from Node 2 is supplied to Node 1 before it is supplied as runoff to the downstream cell. Conversely, surplus water from Node 1 is supplied to Node 2 before it is supplied as runoff to the downstream cell. Water will drain from the 1st to the 2nd layer only after the water levels of both Node 1 and Node 2 exceed field capacity.

It should be noted that there is no soil conductivity limitation imposed on the surface layer, which can accept all the water that it can hold regardless of the precipitation rate. The effect of this assumption is that a certain amount of water can be delivered to the surface before any runoff can result. As long as the thickness of the surface layer is relatively small, the effect of this assumption on infiltration will be small. See Section 5 for a more detailed discussion of this assumption. The development of a parameter representing the thickness of the surface layer (*Ze*) for the Yucca Mountain net infiltration calculation is discussed in Section 6.5.4.

Net infiltration or drainage from the bottom-most soil layer is calculated and is compared to the maximum amount of water the bedrock can accept. This maximum amount of water accepted by the rock ($Limit_{rock}$) is calculated from Darcy's law for saturated flow where a unit gradient is assumed (gravity flow).

$$Limit_{rock} = K_{sat\_rock} * duration \quad \text{(Eq. 6.4.2-5)}$$

K_{sat_rock} (mm/hr) is the saturated hydraulic conductivity of the rock. Thus, the amount of water that moves from Node 4 into the underlying bedrock (daily net infiltration, mm) is calculated as:

$$NetInfiltration = MIN(Limit_{rock}, Water\ level_4 - FC_4) \quad \text{(Eq. 6.4.2-6)}$$

The bedrock may not be able to accept all of the excess water from the bottom-most soil layer. In this case, the soil layer (Node 4) is permitted to exceed field capacity to accommodate the water that cannot move into the bedrock layer. If there is sufficient excess water to exceed the

porosity of the layer, then the excess water above full saturation is distributed to the next layer above (Layer 2, Node 3). If Layer 2 saturates, water is passed to Nodes 1 and 2 in proportion to the amount that was originally drained from them. The development of K_{sat_rock} for the Yucca Mountain net infiltration calculation is discussed in Section 6.5.2.

On days with precipitation events with durations less than 24 hours, the water redistribution calculation is conducted twice. First, the calculation is conducted for the duration equal to the precipitation event duration. It is during this calculation that water is added to the top of the cell. In the second calculation, if there is water in excess of field capacity in the bottom layer, it has the opportunity to enter the bedrock during the remainder of the day at a rate limited by the rock hydraulic conductivity. During this calculation, the duration is the difference between a full day and the precipitation event duration.

6.4.3 Surface Runoff and Run-on (Roff and Ron)

Runoff from a cell can result from the water redistribution calculation when either (1) the entire soil profile becomes saturated or, (2) the first layer becomes saturated due to the soil conductivity infiltration limit. In either case, the water in excess of saturation will produce runoff from the cell. This runoff is then added to the next downstream cell, which is identified in the input to the model (see Appendix B for an example). For this reason, the calculation for a watershed is conducted for cells in order of decreasing elevation. The run-on duration is assumed to be the precipitation duration (Section 5.6). The runoff events measured at the Yucca Mountain site (Section 7.1.3) rarely extend beyond days with precipitation. Furthermore, the runoff data is expressed as daily amounts and the duration of the events is not available and therefore this assumption was necessary.

6.4.4 Mathematical Representation of Evapotranspiration

The FAO-56 method (Allen et al. 1998 [DIRS 157311]) was adapted for use in calculating evapotranspiration (ET) (see Appendicies C, D, E, and Section 6.5.3). Water is removed from the root zone via ET as illustrated in Figure 6.4.4-1. There are five discrete components of ET in the model: (1) bare soil evaporation, which occurs only in the fraction exposed and wetted (f_{ew}) portion of surface layer; (2) transpiration from the f_{ew} portion of the surface layer; (3) transpiration from the canopy (f_c) portion of the surface layer; (4) transpiration from Layer 2; and (5) diffusive evaporation from Layer 2 (not shown on figure).

The “root-zone” thickness is considered to be constant over the entire domain. It represents the the depth to which water can be extracted by ET. Spatial variations in ET are determined by the amount of vegetation at a given location.

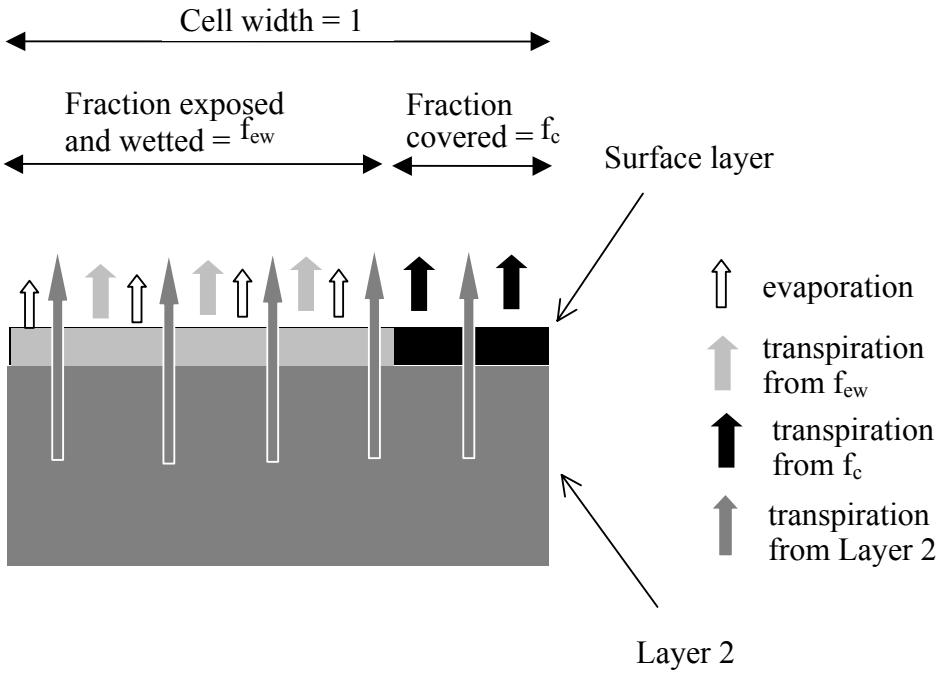

Source: Derived from conceptual model presented in Allen et al. 1998 [DIRS 157311], pp. 135 to 158.

NOTE: A diffusive evaporation component is part of the transpiration from Layer 2.

Figure 6.4.4-1. Evaporation and Transpiration from the f_{ew} and f_c Portions of the Root Zone

The ET calculations are made after the daily water redistribution calculation described above. The ET calculation follows the dual crop FAO-56 method, where *ET* (mm) is proportional to the reference ET (ET_0, mm), and explicitly accounts for soil evaporation and transpiration separately (Allen et al. 1998 [DIRS 157311], Equation 80).

$$ET = (K_e + K_s K_{cb}) * ET_0 \quad \text{(Eq. 6.4.4-1)}$$

where

K_e is the soil evaporation coefficient (dimensionless),
K_{cb} is the basal transpiration coefficient (dimensionless), and
K_s is a water stress coefficient (dimensionless).

The ET_0 calculation depends only on cell-specific, climatic conditions. The development of the parameters used in this calculation for the Yucca Mountain site is described in Appendix C and Section 6.5.4. The mathematical model for the calculation of ET_0 is described below in Section 6.4.5.

6.4.4.1 Basal Transpiration, Soil Evaporation Coefficients, and Canopy Coefficient

The basal transpiration coefficient (K_{cb}, dimensionless) depends on the amount and type of vegetation present within a cell and on the time of year. The value of K_{cb} is near zero when the plants are absent or dormant at the beginning and end of the growing season. K_{cb} reaches its peak near the middle of the growing season. For agricultural crops, FAO-56 provides look-up tables for determining K_{cb}. For native vegetation, FAO-56 provides methods for estimating K_{cb} based on specific plant characteristics (e.g., stomatal conductance) and fractional cover data, which can be either measured directly or estimated from satellite data. For the purpose of describing the mathematical foundation of the MASSIF model, K_{cb} is treated as an input to the calculation of ET. In the discussion below, it is assumed that values of K_{cb} for each day of the calculation are known in order to apply the MASSIF model. The development of K_{cb} values for the Yucca Mountain net infiltration calculation required developing a site-specific methodology, which is discussed as part of the analysis in Section 6.5.3, Appendix D, and Appendix E.

The basal transpiration coefficient is constrained to be between a minimum and maximum value. The maximum basal transpiration coefficient ($K_{c\,max}$) represents an upper limit of the evaporation and transpiration that can occur on a given day based on available energy. $K_{c\,max}$ (dimensionless) ranges between 1.05 and 1.30 and is calculated using Equation 72 from FAO-56 (Allen et al. 1998 [DIRS 157311]):

$$K_{c\max} = \max\left(\left\{1.2 + \left[0.04\left(u_2 - 2\right) - 0.004\left(RH_{\min} - 45\right)\right]\left(\frac{h_{plant}}{3}\right)^{0.3}\right\}, \left\{K_{cb} + 0.05\right\}\right) \quad \text{(Eq. 6.4.4.1-1)}$$

where u_2 (m/s) is the average daily wind speed at 2 m, RH_{min} is the minimum daily relative humidity, and h_{plant} is the characteristic plant height (m).

The minimum basal transpiration coefficient represents dry soil with no vegetation cover ($K_{c\,min}$, dimensionless). $K_{c\,min}$ may be greater than zero to account for evaporation occurring from Layer 2 (Node 3) and beneath the vegetation canopy (Node 2), as these evaporative losses are not explicitly included in the calculation of evaporation from the evaporative node (Node 1). The development of $K_{c\,min}$ for the Yucca Mountain net infiltration calculation is discussed in Section 6.5.4.

The soil evaporation coefficient (K_e) is found from Equation 71 of FAO-56 (Allen et al. 1998 [DIRS 157311]):

$$K_e = K_r * (K_{c\,max} - K_{cb}) <= f_{ew} * K_{c\,max} \quad \text{(Eq. 6.4.4.1-2)}$$

where K_r is a soil evaporation reduction coefficient described in the next section.

Vegetative cover varies seasonally. In the spring, the vegetative cover coefficient (f_c) increases as the plants grow. Later in the year, as the ground dries out and transpiration drops due to water stress, the vegetative cover coefficient declines. The correlation recommended in FAO-56 (Allen et al. 1998 [DIRS 157311], Equation 76) is used to model the time variation of the canopy coefficient:

$$f_c = \left(\frac{K_{cb} - K_{c\min}}{K_{c\max} - K_{c\min}} \right)^{\left(1+0.5h_{plant}\right)} \quad \text{(Eq. 6.4.4.1-3)}$$

To avoid numerical problems, f_c is constrained to be greater than 10^{-4} (Appendix G, Section G4.2.3.1, Step 9), which ensures that f_{ew} is always less than 1.

6.4.4.2 Depletions and Water Stress Coefficients

The amount of soil water in the root zone affects the daily ET. In the FAO-56 method, the amount of water in a soil layer is described in terms of depletion. *Depletion* (mm) is related to the *water level* parameter:

$$Depletion = FC - water\ level \quad \text{(Eq. 6.4.4.2-1)}$$

Depletions are calculated for the evaporation node of the surface layer, for the canopy node of the surface layer, and for the entire root zone. The approach used for these calculations is based on the approach outlined in the FAO-56 method, but is somewhat different in that depletions are calculated after the redistribution of water in the two surface nodes. The depletion for the evaporation and canopy nodes is calculated from the field capacities and water levels in these nodes. Depletion of the root zone is calculated from the field capacities and water levels in the surface layer and Layer 2 using area-weighted values for the evaporative (Node 1) and canopy (Node 2) nodes.

The total amount of water available for evaporation (*TEW*, mm) is calculated from Equation 73 of FAO-56 (Allen et al. 1998 [DIRS 157311]):

$$TEW = (\theta_{FC} - 0.5 * \theta_{WP}) * Z_e \quad \text{(Eq. 6.4.4.2-2)}$$

where θ_{WP} is the permanent wilting point (m^3/m^3), below which vegetation cannot extract moisture from the soil, and Z_e is the surface layer thickness (m). Z_e is dependent on soil texture and length of drying periods common to the model area. The equation for *TEW* implies that water will not be evaporated at water contents less than ½ θ_{WP}. This assumption is based on recommendations from FAO-56. The development of θ_{WP} and Z_e for the Yucca Mountain net infiltration calculation is discussed in Sections 6.5.2 and 6.5.4, respectively.

The evaporation rate depends on the amount of water in the evaporation node (Node 1). When the soil surface is wet, the maximum rate of evaporation is controlled by the amount of available energy at the soil surface (Allen et al. 1998 [DIRS 157311], p. 145). Readily evaporable water (*REW*) is the maximum depth of water that can be evaporated from the upper soil layer prior to the onset of hydraulic limitations that reduce the rate of water supply below that of energy

demands. When the depth of evaporation exceeds *REW*, there is a reduction of the evaporation rate. The development of *REW* for the Yucca Mountain net infiltration calculation is discussed in Section 6.5.4.

$$K_r = (TEW - D_e) / (TEW - REW) \quad \text{(Eq. 6.4.4.2-3)}$$

where D_e is the depletion of the evaporative node (Node 1). K_r is constrained to be between 0 and 1.

Depletion of the root zone is calculated from the field capacities and water levels in the surface layer and Layer 2, using area-weighted values for the evaporative and canopy nodes. Two additional parameters are used to describe the water status in the root zone, the total available water (*TAW*) and the readily available water (*RAW*). *TAW* (mm) is the amount of water available for ET in the root zone, and is calculated from Equation 82 of FAO-56 (Allen et al. 1998 [DIRS 157311]):

$$TAW = (\theta_{FC} - \theta_{WP}) * Z_r \quad \text{(Eq. 6.4.4.2-4)}$$

where Z_r is the root zone thickness (mm) (assumed to be greater than zero). The development of Z_r for the Yucca Mountain net infiltration calculation is discussed in Section 6.5.3. *RAW* (mm) is the limit of the water in the root zone below which the transpiration rate is affected. It is calculated as a function of *TAW* (Allen et al. 1998 [DIRS 157311], Equation 83):

$$RAW = p * TAW \quad \text{(Eq. 6.4.4.2-5)}$$

where p (dimensionless) is the fraction of *TAW* that vegetation can remove without suffering stress and is constrained to be between 0 and 1. Characteristics of the vegetation as well as the climate and soil type determine the value of p (Allen et al. 1998 [DIRS 157311], p. 162). The development of p for the Yucca Mountain net infiltration calculation is discussed in Section 6.5.4.

An adjustment of p as a function of daily ET is recommended in FAO-56 (Allen et al. 1998 [DIRS 157311], p. 162):

$$p_{adj} = \max(0.1,\min(p+0.04(5-ET),0.8)) \quad \text{(Eq. 6.4.4.2-6)}$$

In the MASSIF model the adjusted p (p_{adj}) is used in place of p in Equation 6.4.4.2-5.

The impact of water stress in the root zone on transpiration is reflected in the transpiration stress coefficient. The transpiration stress coefficient is calculated from Equation 84 of FAO-56 (Allen et al. 1998 [DIRS 157311]):

$$K_s = (TAW - D_r) / (TAW - RAW) \quad \text{(Eq. 6.4.4.2-7)}$$

where D_r (mm) is the root zone depletion. K_s is 1 when D_r is less than *RAW* and is 0 when D_r is greater than *TAW*.

Transpiration from the evaporation node (Node 1) is calculated as a portion of the total calculated transpiration and is based on the amount of water in the surface layer compared to the amount of water in the entire root zone. This fractional partitioning coefficient (K_{tie}) (Allen et al. 2005 [DIRS 176009], Equation 27) is:

$$K_{tie} = [(1 - D_e/TEW)/(1 - D_r/TAW)] * (Ze/Zr)^{0.6} \quad \text{(Eq. 6.4.4.2-8)}$$

Unlike the current model, the FAO-56 procedure does not explicitly keep track of the water content of the surface layer under the vegetation canopy (Node 2). Therefore, the fractional partitioning coefficient for the canopy region (K_{tic}) is calculated in a manner similar to K_{tie}:

$$K_{tic} = [(1 - D_c/TEW)/(1 - D_r/TAW)] * (Ze/Zr)^{0.6} \quad \text{(Eq. 6.4.4.2-9)}$$

where D_c (mm) is the depletion of the canopy node.

6.4.4.3 ET Calculation

The ET is calculated as the sum of the evaporative losses from the evaporative node portion of the surface layer and transpiration from the root zone. Daily evaporation (E, mm) is calculated as:

$$E = K_e * ET_0 \quad \text{(Eq. 6.4.4.3-1)}$$

The daily evaporation calculated by Equation 6.4.4.3-1 applies to the entire surface area of a cell. In reality, the evaporation only takes place in the bare soil portion of the cell (Node 1). Hence, the depth of water evaporated from the fraction of evaporative node is E / f_{ew}. E is constrained so that TEW is not exceeded.

Daily transpiration (T, mm) from the root zone is calculated as:

$$T = K_s * K_{cb} * ET_0 \quad \text{(Eq. 6.4.4.3-2)}$$

The total daily transpiration is partitioned between the surface layer nodes (Nodes 1 and 2) and Layer 2 (Node 3). The daily transpiration from the evaporative node (T_e) is:

$$T_e = K_{tie} * T \quad \text{(Eq. 6.4.4.3-3)}$$

For the canopy node, the daily transpiration (T_c) is:

$$T_c = K_{tic} * T \quad \text{(Eq. 6.4.4.3-4)}$$

The daily transpiration from Layer 2 (Node 3) is:

$$T2 = T - T_e * f_{ew} - T_c * f_c \quad \text{(Eq. 6.4.4.3-5)}$$

Transpiration is limited so that the water level of any of the nodes does not go below the wilting point.

After the ET calculation, the water levels in each node are updated. For the evaporative node (Node 1) and canopy node (Node 2), the changes in the water level due to ET is ($-E/f_{ew} - T_e$) and ($-T_c$), respectively. The change in the water level of Layer 2 is ($-T2$).

6.4.5 Mathematical Representation of Reference Evapotranspiration on Flat and Sloped Surfaces

The evapotranspiration rate from a reference surface, not short of water, is called the reference crop evapotranspiration or reference evapotranspiration and is denoted as ET_0 (Allen et al. 2005 [DIRS 176207], p. 2).

The concept of the reference evapotranspiration was introduced to study the evaporative demand of the atmosphere independent of vegetation type, phenological development, and management practices. As water is abundantly available at the reference evapotranspiring surface, soil factors do not affect ET. Relating ET to a specific surface provides a reference to which ET from other surfaces can be compared. This approach obviates the need to define a separate ET level for each type of vegetation and stage of growth. ET_0 values measured or calculated at different locations or in different seasons are comparable as they refer to the ET from the same reference surface.

For convenience and reproducibility, the reference surface has recently been standardized by the American Society of Civil Engineers (ASCE) as a hypothetical vegetated surface having specific characteristics (Allen et al. 2005 [DIRS 176207]). The reference evapotranspiration (ET_0) is defined as the ET rate from a uniform surface of dense, actively growing vegetation having an assumed height of 0.12 m and having a surface resistance of 70 s m^{-1} (for 24-hour calculation time-steps) and an albedo of 0.23, closely resembling the evaporation of an extensive surface of green, cool season grass of uniform height, not short of soil water (Allen et al. 1998 [DIRS 157311], p. 24).

The only factors affecting ET_0 are climatic parameters. Consequently, ET_0 is a climatic parameter and can be computed from weather data. ET_0 expresses the evaporating power of the atmosphere at a specific location and time of the year and does not consider the local vegetation characteristics, soil factors, or precipitation amounts. Even though there are many methods for calculating ET_0 cited in the literature, the FAO Penman-Monteith method is recommended as the standard method for determining ET_0 (Allen et al. 1998 [DIRS 157311], pp. 7 and 65; Irmak et al. 2005 [DIRS 176861] p. 1,064; Droogers and Allen 2002 [DIRS 176786], p. 33). The method has been selected because it closely approximates grass ET_0 at the location evaluated, is physically based, and explicitly incorporates both physiological and aerodynamic parameters (Allen et al. 1998 [DIRS 157311], p. 7). Moreover, procedures have been developed for estimating missing climatic parameters when the FAO Penman-Monteith equation is used.

The FAO Penman-Monteith method to estimate ET_0 was derived from the original Penman-Monteith equation (Jensen et al. 1990 [DIRS 160001], p. 93) and associated equations for aerodynamic and surface resistance for 24-hour calculation time-steps (Allen et al. 1998 [DIRS 157311], pp. 24 and 65):

$$ET_0 = \frac{0.408\Delta(R_n - G) + \gamma \frac{900}{T+273} u_2 (e_s - e_a)}{\Delta + \gamma(1 + 0.34 u_2)} \quad \text{(Eq. 6.4.5-1)}$$

where

ET_0 is the reference evapotranspiration [mm d^{-1}]
R_n is the net radiation at the crop surface [MJ m^{-2} d^{-1}]
G is the soil heat flux density [MJ m^{-2} d^{-1}]
T is the mean daily air temperature at 2 m height [°C]
u_2 is the wind speed at 2 m height [m s^{-1}]
e_s is the saturation vapor pressure [kPa]
e_a is the actual vapor pressure [kPa]
e_s-e_a is the saturation vapor pressure deficit [kPa]
Δ is the slope of the vapor pressure curve [kPa °C^{-1}]
γ is the psychrometric constant [kPa °C^{-1}].

The reference evapotranspiration, ET_0, provides a standard to which (1) evapotranspiration during different periods of the year or in other regions can be compared, and (2) evapotranspiration from specific vegetation types and surfaces can be related via some form of a 'crop coefficient.'

The FAO Penman-Monteith equation is a reasonable, simple representation of the physical and physiological factors governing the evapotranspiration process. By using the FAO Penman-Monteith definition for ET_0, one may calculate crop (or vegetation cover) coefficients (K_c) at research sites by relating the measured crop (or vegetation cover) evapotranspiration (ET) with the calculated ET_0, i.e., $K_c = ET/ET_0$. In the crop coefficient approach, differences in the vegetation canopy and aerodynamic resistance relative to the hypothetical reference crop are accounted for within the crop coefficient. Thus, the K_c factor serves as an aggregation of the physical and physiological differences between vegetation covers and surface wetness conditions and the reference definition (Allen et al. 1998 [DIRS 157311], p. 25). The net radiation in the ET_0 calculation (Equation 6.4.5-1) is defined for the reference (full cover clipped grass) surface. Differences in albedo, temperature, etc., that impact R_n for specific vegetation cover are incorporated into the K_c.

6.4.5.1 Data Required for Daily Calculation of ET0

Equation 6.4.5-1 is applied daily to compute reference evapotranspiration for each grid cell to account for influences of elevation, slope, and azimuth at each cell. Although calculation of ET_0 on an hourly time-step can provide a slightly more accurate calculation (Allen et al. 1998 [DIRS 157311], p. 74) provided high quality hourly weather data are available, calculation of ET_0 with the FAO Penman-Monteith equation using 24-hour time steps in most conditions can

provide accurate results (Allen et al. 1998 [DIRS 157311], p. 72; Allen et al. 2006 [DIRS 176785], pp. 2 to 3). The MASSIF model accepts data only in daily time-steps. The data for appropriate use of the FAO Penman Monteith equation consist of:

a) Meteorological data

- Air temperature: daily maximum (T_{max}) and minimum (T_{min}) air temperatures
- Air humidity: mean daily actual vapor pressure (e_a) derived from psychrometric, dew-point temperature or relative humidity data
- Wind speed: daily average over 24 hours for wind speed measured at or adjusted to 2-m height (u_2)
- Radiation: net radiation (R_n) measured or computed from solar and longwave radiation or from the recorded duration of sunshine.

To ensure the integrity of computations, the weather measurements should be made at 2 m (or translated to that height) above an extensive surface of green grass, fully shading the ground and not short of water (Allen et al. 1998 [DIRS 157311], p. 25).

b) Location information

- Altitude above sea level (m)
- Latitude (degrees north or south).

These data are used to adjust air temperature from the reference weather station for the average atmospheric pressure (function of site elevation) and to compute exoatmospheric radiation (R_a).

6.4.5.2 Use of the FAO Penman-Monteith Equation with a Limited Set of Weather Data

Modeling reference evapotranspiration over a study area requires an extensive dataset that reflects the anticipated variation in meteorological parameters over the range of grid cell elevation, slope, and exposure to the sun for all times of the year.

When a complete dataset of weather parameters is not available, the FAO Penman-Monteith equation can be applied using a minimum set of critical inputs. Daily maximum and minimum air temperature data are the minimum data requirements necessary to apply the FAO Penman-Monteith method (Allen et al. 1998 [DIRS 157311], p. 64; 2005 [DIRS 176207], p. E-1). The estimation of other weather variables can be based on minimum and maximum air temperature or on average values (for wind speed). Keying solar radiation and vapor pressure (via dew-point temperature) on daily air temperature extremes helps to preserve the strong correlation among these variables (Allen 1997 [DIRS 176568], p. 56; 1998 [DIRS 157311], p. 60; 2005 [DIRS 176207], pp. E-4 and E-5).

The use of an alternative ET_0 procedure requiring only limited meteorological parameters (for example, the Priestley-Taylor, Blaney-Criddle or Hargreaves ET equations) is not recommended by FAO-56 (Allen et al. 1998 [DIRS 157311], p. 58). The FAO Penman-Monteith method is

recommended as the sole standard method for the computation of ET_0 from meteorological data even for the cases when only a limited dataset is available (Allen et al. 1998 [DIRS 157311], p. 58; 2005 [DIRS 176207], p. E-1). Procedures used for estimating missing climatic data (solar radiation, vapor pressure, and wind speed) for the Yucca Mountain calculation of net infiltration are outlined in Appendix C. Differences between ET_0 estimated by the FAO Penman-Monteith equation with, on one hand, a limited data set and, on the other hand, a full data set, are expected to be small, especially when averaged over periods of 5 days or longer (Allen et al. 1998 [DIRS 157311], p. 60).

Next a discussion of the methods used to estimate weather parameters from air temperature is presented. These methods were used for the Yucca Mountain calculation of net infiltration and are described in Appendix C.

Solar Radiation Data Derived from Air Temperature Differences

The degree of cloud cover in a location is related to the difference between the daily maximum and minimum air temperature. Clear-sky conditions result in high temperatures during the day (T_{max}) because the atmosphere is transparent to the incoming solar radiation and in low temperatures during the night (T_{min}) because less outgoing long-wave radiation is absorbed by the atmosphere and retransmitted back to the surface. On the other hand, in overcast conditions, T_{max} is relatively lower because a significant part of incoming solar radiation never reaches the earth's surface and is instead absorbed or reflected to space by clouds. Similarly, $T_{\min}$ will be relatively higher, as cloud cover acts as a blanket and decreases the net outgoing long-wave radiation from the surface. Therefore, the difference between the maximum and minimum air temperature ($T_{max} - T_{min}$) is highly correlated with daily relative solar radiation and can be used as an indicator of the fraction of exoatmospheric radiation that reaches the earth's surface. This principle is the basis of the recommended FAO-56 equation when developing estimates of solar radiation using only air temperature data (Allen et al. 1998 [DIRS 157311], p. 60). The equation is the following:

$$R_s = K_{Rs}\ R_a \sqrt{(T_{\max} - T_{\min})} \qquad \text{(Eq. 6.4.5.2-1)}$$

where

R_a is the exoatmospheric solar radiation [MJ m^{-2} d^{-1}] (R_a is the solar radiation at the earth's surface if there were no atmosphere)
T_{max} is the maximum air temperature [°C]
T_{min} is the minimum air temperature [°C]
K_{Rs} is the Hargreaves adjustment coefficient [$°C^{-0.5}$] (Hargreaves and Allen 2003 [DIRS 176787], p. 55; Allen et al. 1998 [DIRS 157311], p. 60).

The development of K_{Rs} and related parameters for the Yucca Mountain net infiltration calculation is discussed in Appendix C and Section 6.5.4.

Solar radiation estimated from Equation 6.4.5.2-1 represents the solar radiation associated with T_{max} and T_{min} measured and assuming that the surface is horizontal. Additional computations are applied to consider the effect of slope and orientation, as well as differences in elevation.

Humidity Data

Where humidity data are lacking or are of questionable quality, an estimate of actual vapor pressure (e_a) can be made assuming that dew-point temperature (T_{dew}) is near the daily minimum air temperature (T_c). This estimation implicitly assumes that near sunrise, when the air temperature is near T_{min}, the air may be nearly saturated with water vapor and relative humidity may be nearly 100%. The relationship $T_{dew} \approx T_{min}$ holds for locations where the vegetation cover in the vicinity of the station is well watered. However, particularly for arid regions, the air might not saturate when its temperature is at its minimum due to dryness of the air mass. Hence, T_{min} will generally exceed T_{dew} by some amount. In these situations, T_{dew} is better approximated by subtracting a fixed temperature offset (K_o) from T_{min}, depending on the aridity of the region and local environment (Allen et al. 1998 [DIRS 157311], pp. 58 to 59; 2005 [DIRS 176207], p. E-2), so that:

$$T_{dew} = T_{\min} - K_o \qquad \text{(Eq. 6.4.5.2-2)}$$

where K_o is the average offset between T_{dew} and T_{min}. The development of K_o for the Yucca Mountain net infiltration calculation is discussed in Appendix C and Section 6.5.4.

Wind Speed

Daily wind speed is required as input for the calculation of ET_0. The development of daily wind speed estimates for the Yucca Mountain net infiltration calculation is discussed in Appendices C and F, and Section 6.5.1.

6.4.5.3 Effect of Surface Elevation, Orientation, and Slope on ET_0

Inclination and exposure of the surface to the sun impact several components of the surface energy balance and consequently ET_0 calculated by the FAO Penman-Monteith equation. In addition, substantial variation in surface elevation within a study area requires modification of some parameters. The next section provides a description of how input weather parameters for the FAO Penman-Monteith ET_0 equation are adjusted for elevation, slope, and orientation of a given grid cell.

Solar Radiation

The amount of solar radiation received by a given surface is controlled by the geometry of the surface, atmospheric transmittance, and the relative location of the sun. The local geometry is controlled by surface slope, azimuth, and elevation.

Most solar radiation (R_s) information is calculated at weather stations located in flat, nearly horizontal locations, so that estimation of R_s on sloped surfaces must be generally based on models. Equation 6.4.5.2-1 is applied to estimate solar radiation incident to a horizontal surface. For inclined surfaces, the total (global) radiation reaching the surface is modeled as a sum of three components: direct (beam) radiation, which is the solar radiation that is not absorbed or scattered by the atmosphere and that reaches the surface directly from the sun; diffuse radiation, which originates from the solar beam but is scattered toward the surface; and finally, a diffuse

radiation component incident on the subject surface due to reflection from ground surfaces in view of the subject surface.

Appendix C describes the procedure used for the MASSIF model to estimate solar radiation for an inclined surface based on solar radiation measured or estimated over a horizontal surface. The procedure for inclined surfaces assumes an extensive surface having uniform slope at each point of calculation, so that effects of protruding surrounding terrain on blocking the sun or reflecting radiation are not considered. This simplification of terrain substantially speeds computational time for application of the procedure to the relatively large study area composed of a large number of grid cells and allows the use of a purely analytical solution. The simplification of terrain form provides sufficiently accurate results and is congruent with the discretization of slopes and azimuths on the mountain, where slope is discretized into 6 general classes and azimuth into 12 general classes (Appendix C).

Elevation also affects the amount of radiation that reaches a surface due to atmospheric attenuation. In general, for a clear sky day, the solar radiation increases with altitude due to the smaller air mass.

Air Temperature

Atmospheric pressure decreases with increasing altitude. Consequently, rising parcels of air tend to cool by adiabatic expansion; similarly, falling parcels tend to warm up due to adiabatic compression. The net effect of this is a vertical decrease in temperature with increase in elevation following the adiabatic lapse rate. The rate at which air cools (or warms) depends on the moisture status of the air. If the air is unsaturated, the rate of temperature change is about 1°C/100 meters and is called the *dry adiabatic lapse rate* (Rosenberg et al. 1983 [DIRS 177526], p. 118). If the air is saturated, the rate of temperature change is smaller due to latent heat of vaporization of condensing water vapor and is called the *saturated adiabatic rate*. The saturated adiabatic lapse rate applies to rising air when the relative humidity has reached 100% and condensation of water vapor is taking place.

It is recognized that in addition to elevation, local topography can modify the relationship between elevation and temperature. These effects are governed largely by the relationship between slope orientation, received solar radiation, and surface heating. In the northern hemisphere, north-facing slopes receive less radiation than south-facing slopes and are typically cooler (Lookingbill and Urban 2003 [DIRS 176789], p. 142).

Additional topographic effects result from the influence of terrain on mountain winds and the generation of local airflows. As a result, mountain valleys, middle-hill slopes, and ridges can have different temperature regimes (Lookingbill and Urban 2003 [DIRS 176789], p. 142).

Because of uncertainties in estimating secondary topographic effects on temperature, the vertical lapse method is the most common approach for the estimation of air temperature changes based on mean elevation differences, particularly in areas with mountainous or complex terrain; this is the approach used in the MASSIF model. This method adjusts for the mean observed decrease in temperature with increase in elevation. Lapse models are most often applied to monthly averages or daily extremes (Bolstad et al. 1998 [DIRS 176784], p. 162). The lapse rate approach

ignores local effects associated with differences in aspect and relative slope position. A common approach to representing the lapse rate is by a linear equation such as:

$$T_{lapse} = T_{ref} - \frac{LR}{1{,}000}\left(z_{cell} - z_{ref}\right) \qquad \text{(Eq. 6.4.5.3-1)}$$

where

T_{lapse} is the elevation-adjusted daily air temperature for a given grid cell with elevation z_{cell} [°C]
z_{cell} is the elevation of the grid cell [m]
T_{ref} is the daily air temperature at the reference weather station [°C]
z_{ref} is the elevation of the reference weather station [m], and
LR is the temperature lapse rate in °C per 1,000 m.

This equation is used to represent the lapse rate in the MASSIF model. The development of the temperature lapse rate parameters (LR and z_{ref}) for the Yucca Mountain net infiltration calculation is discussed in Appendices C and F, and Section 6.5.1.

Vapor Pressure

The saturation vapor pressure decreases with a decreasing air temperature. Given a relatively constant amount of moisture in the air, represented by the actual vapor pressure, the ratio between actual and saturated vapor pressure (i.e., relative humidity) increases with any decrease in temperature. Because air temperature decreases with elevation, saturation vapor pressure will also decrease with elevation for a given air mass. Because actual vapor pressure is relatively constant for a given air mass over a region, the relative humidity of the air will increase with altitude up to a point where saturation is reached. At this point, actual vapor pressure will be limited to the mean saturation vapor pressure, with increasing condensation of part of the air moisture with any additional increase in attitude.

The actual vapor pressure (e_a) in the FAO Penman-Monteith equation (Equation 6.4.5-1) is computed from the daily lapse-corrected temperatures. The saturation limit to the vapor pressure is computed using the lapse-corrected estimated dew temperature (Equation 6.4.5.2-2). Details of the calculation of vapor pressure are given in Appendix C.

Wind Speed

Wind speed is affected by the topographical features of a given area, especially in mountainous terrain. However, simulation and modeling of wind speed as a function of surface topography is difficult for even highly instrumented terrain. Generally wind speed is extrapolated from area weather stations with adequate accuracy for estimating ET (Allen et al. 2005 [DIRS 176207], pp. E-6 to E-7). The MASSIF model does not adjust wind speed to account for elevation, slope, or aspect.

6.5 ANALYSIS OF YUCCA MOUNTAIN NET INFILTRATION

This section addresses the use of the model for the analysis of net infiltration at the Yucca Mountain site during anticipated future climates, beginning with descriptions of the methods used to prepare inputs. Sections 6.5.1, 6.5.2, 6.5.3, and 6.5.4, respectively, discuss the development of parameters representing the anticipated weather, the site geology, the anticipated vegetation, and miscellaneous parameters. Section 6.5.5 discusses parameter screening decisions for the uncertainty analysis. Sections 6.5.6 through 6.5.7 cover the calculation procedures and the results of the calculations.

It should be noted that in the development of uncertainty distributions for all input parameters to the model, there was a need to define "nominal" values for each of the parameters. Such nominal values are defined in each section along with their uncertainty distribution. The nominal values were chosen to be representative and a number of different approaches were taken depending on the underlying parameter distribution. For many parameters a mean or median value was selected; however, for others, other values were selected and are justified for use in the particular section of the report or appendix. Nominal values are used in the calculation of net infiltration uncertainty when the uncertainty of the given parameter was less than the threshold used to identify parameters to be varied in the uncertainty analysis.

6.5.1 Weather Parameters for Anticipated Climate Episodes

Calculation of net infiltration requires an input file containing precipitation, temperature extremes, and mean wind speed on a daily basis. The MASSIF model varies precipitation and temperature with elevation and accepts input for an elevation of 1,524 m (5,000 ft), corresponding to the top of Yucca Mountain. It also requires a linear fit to hours of precipitation as a function of total precipitation for the day.

Appendix F details the development of weather input files for calculation of net infiltration at Yucca Mountain. This section provides background information about anticipated climates at Yucca Mountain and summarizes Appendix F.

6.5.1.1 Climate Episodes

Future Climate Analysis (BSC 2004 [DIRS 170002) estimated climatic variables for the next 10,000 years by forecasting the timing and nature of climate change at Yucca Mountain. That analysis assumed that climate is cyclical, so past climates provide insight into potential future climates, and further assumed that a relation exists between the characteristics of past climates and the sequence of those climates in the 400,000-year earth-orbital cycle (BSC 2004 [DIRS 170002], Section 5). Each cycle, consisting of 400,000-year periods and four approximately 100,000-year subcycles, is a series of glacial and interglacial couplets. Radiometric and isotopic analyses of calcite deposits at Devils Hole corroborate that past climate is cyclical and linked to earth-orbital forcing functions (BSC 2004 [DIRS 170002], Sections 6.3 and 6.4). *Future Climate Analysis* uses the microfossil record from cores drilled at Owens Lake, California, to reconstruct a climate history for the last long orbital cycle, calibrated to an elevation equivalent to the top of Yucca Mountain (BSC 2004 [DIRS 170002], Section 6.5).

Based on these paleoclimate records and the cyclical nature of climate, *Future Climate Analysis* provides climate estimates for the next 10,000 years.

Nevertheless, forecasting long-term future climates is highly speculative and rarely attempted (BSC 2004 [DIRS 170002], Section 1). The uncertainty in such forecasts is aleatoric. That is, it arises from natural randomness and cannot be reduced through further testing and data collection; it can only be characterized. This analysis of net infiltration places emphasis on capturing the full range of the aleatoric uncertainty.

Future Climate Analysis (BSC 2004 [DIRS 170002], Section 6.6, Table 6-1) predicts three climate episodes during the next 10,000 years at Yucca Mountain. The Present-Day climate is part of the interglacial climatic interval, reflective of a warm and arid climatic condition. The Present-Day climate is predicted to persist for another 400 to 600 years. Following the Present-Day climate will be a warmer and wetter monsoonal climatic condition. The Monsoon climate will persist for approximately 900 to 1,400 years. Between the Monsoon climate and the next glacial climate interval is a transition period labeled the Glacial Transition climate. The Glacial Transition climate will be cooler and wetter than the relatively brief monsoonal period, persisting for the remainder of the 10,000-year regulatory period (BSC 2004 [DIRS 170002], Section 7).

There is variability within each climate state (Present-Day, Monsoon, and Glacial Transition) akin to the larger earth-orbital climatic cycle but of shorter frequency and smaller amplitudes. The seasonal cycles are related to the earth's orbit and the tropical and polar air masses. For all three future climates, temperature and precipitation variability in the western region of the conterminous United States is dominated by the interplay, expansion, and contraction of tropical and polar air masses, driven seasonally by the earth's solar orbit. The northern edge of the tropical air masses, the Subtropical Highs, are characterized by hot, dry, high-pressure and descending air. The southern edge of the polar air masses, called the Polar Lows, are typically low-pressure, consist of rising air that creates cool, wet, high precipitation and low evaporation climate (BSC 2004 [DIRS 170002], Section 6.2). A "mixing zone" exists between the tropical and polar air masses. This mixing zone in the northern hemisphere is called the westerlies. As the westerlies pass over large water bodies, moisture is picked up. When the moisture-laden westerlies cross over from water to land masses, moisture is released. In the western United States, the westerlies coming from the Pacific Ocean provide moisture to the western half of the United States. The Yucca Mountain region lies within a major rain shadow created and sustained by the Sierra Nevada Mountains and the Transverse Range. Consequently, as the westerlies move eastward from the Pacific Ocean inland, moisture-laden air is released west of the Yucca Mountain region. It is the interplay between these large air masses, which affect the expansion and contraction of the rain shadow, coupled with regional topology that dominates the annual cyclical weather in the Yucca Mountain region.

DTN: GS000308315121.003 [DIRS 151139] lists representative meteorological stations for each of the three anticipated climate episodes. These are reproduced in Table 6.5.1.1-1. Section 6.5.1.2 below explains how the precipitation and temperature record at a meteorological station is represented by a set of 24 parameters. For each of the three anticipated climate episodes, Sections 6.5.1.3 through 6.5.1.5 describe the development of nominal values and uncertainty ranges for the weather parameters, including twelve more parameters for wind speed. A MASSIF calculation requires an input weather file containing daily precipitation, temperature

extremes, and wind speed. Section 6.5.1.6 describes the development of the weather input file using specific values for each of the 36 precipitation, temperature, and wind speed parameters. Section 6.5.1.7 discusses additional weather parameters, those that are not included in the weather input file.

Table 6.5.1.1-1. Meteorological Stations Selected to Represent Future Climate States at Yucca Mountain

Climate State	Duration	Representative Meteorological Stations	Locations of Meteorological Stations	
Present-Day	400 to 600 years	Site and regional meteorological stations	Yucca Mountain region	
Monsoon	900 to 1,400 years	Average Upper Bound: Nogales, Arizona Hobbs, New Mexico	North Latitude 31° 21’ 32° 42’	West Longitude 110° 55’ 103° 08’
		Average Lower Bound: Site and regional meteorological stations	Yucca Mountain region	
Glacial Transition	8,000 to 8,700 years	Average Upper Bound: Spokane, Washington Rosalia, Washington St. John, Washington	North Latitude 47° 38’ 47° 14’ 47° 06’	West Longitude 117° 32’ 117° 22’ 117° 35’
		Average Lower Bound: Beowawe, Nevada Delta, Utah	North Latitude 40° 35’ 25” 39° 20’ 22”	West Longitude 116° 28’ 29” 112° 35’ 45”

Source: DTN: PGS000308315.003 [DIRS 151139].

6.5.1.2 Parameterization of Precipitation and Temperature Records

Existing weather records cover less than 100 years. Because the probability distribution for precipitation is very skewed, there is no *a priori* assurance that a sample of so few years for a given climate will adequately represent average infiltration over hundreds or thousands of years. In order to capture the full range of uncertainty, the performance assessment must assure that rare precipitation events have been considered. Therefore, rather than use the meteorological records directly as input, this analysis characterizes each record in terms of periodic functions and additional parameters. Periodic functions summarize the records of precipitation, temperature, and wind speed at a meteorological station. This approach assures that the climate inputs are appropriate and adequate for predicting average infiltration.

Two of the periodic functions represent the succession of wet and/or dry days as a first-order Markov process and are therefore stochastic (see Appendix F, Section F1.1.1). Two other stochastic, periodic functions represent the variation in daily precipitation as a lognormal distribution. Each function, either of the two for precipitation or either of the two Markov probabilities, varies with the day of the year. Specifically, the precipitation record is represented by the following four functions, each of which depends on the day of the year, *d*, for *d* between 1 and 365:

$p_{00}(d)$: the probability that day d is dry, given that day $d-1$ is dry

$p_{10}(d)$: the probability that day d is dry, given that day $d-1$ is wet

$\lambda(d)$: mean of the lognormal precipitation distribution, given that day *d* is wet

$m(d)$: mean of the natural logarithm of the amount of precipitation, given that day *d* is wet.

For each of the four stochastic precipitation functions, a two-term Fourier series represents its variation with *d*. For example:

$$p_{00}(d) = a_{00} + b_{00}\sin(\theta_{00} + 2\pi d / 365) \qquad \text{(Eq. 6.5.1.2-1)}$$

Therefore, there are twelve parameters that represent the precipitation record for a meteorological station: a_{00}, b_{00}, θ_{00}, a_{10}, b_{10}, θ_{10}, a_{λ}, b_{λ}, θ_{λ}, a_m, b_m, and θ_m. Appendix F describes the method used to calculate this set of precipitation parameters from a meteorological record and reports the results for each relevant meteorological station.

The value of a periodic precipitation function reaches its maximum when the sine function is 1.0. For example, the maximum value for $p_{00}(d)$ occurs when

$$d = d_{\max 00} = Mar1 + 365\left(\frac{1}{4} - \frac{\theta_{00}}{2\pi}\right) = May31 - 58\theta_{00} \qquad \text{(Eq. 6.5.1.2-2)}$$

The periodic functions that summarize the temperature record for a meteorological station are not stochastic. Rather, they represent the average minimum and maximum temperatures for each day of the year. Because wet days tend to have smaller differences between the minimum and maximum, wet days and dry days have separate representations, resulting in a total of four periodic temperature functions: $T_{md}(d)$, $T_{Md}(d)$, $T_{mw}(d)$, and $T_{Mw}(d)$. Each of these periodic temperature functions is also represented by a two-term Fourier series. For example,

$$T_{md}(d) = \gamma_{md} + \alpha_{md}\sin[2\pi(\beta_{md} + d)/365] \qquad \text{(Eq. 6.5.1.2-3)}$$

Therefore, there are twelve more parameters that represent the temperature record for a meteorological station: α_{md}, β_{md}, γ_{md}, α_{Md}, β_{Md}, γ_{Md}, α_{mw}, β_{mw}, γ_{mw}, α_{Mw}, β_{Mw}, and γ_{Mw}, where subscripts denote minimum (*m*) or maximum (*M*) temperature on wet (*w*) or dry (*d*) days. Appendix F describes the method used to calculate this set of temperature parameters from a meteorological record and reports the results for each relevant meteorological station.

6.5.1.3 Weather-File Parameters for the Remainder of the Present-Day Climate

The present-day-like climate interval is an interval of time when summers are warm to hot. Snowpack at high elevation is typically low to moderate because the polar front does not remain fixed at a southerly position during the winter and so does not set up a storm wave train that moves Pacific moisture over the Sierra Nevada Mountains. The wettest years, which represent the upper-bound moisture regimes during Present-Day climate, will typically be years when Pacific air flow focuses Pacific moisture toward southern Nevada, such as the El Nino climates that have been common during the last couple of decades. Dry years, which represent the lower-bound moisture regimes during Present-Day climate, will be those years with minimal winter precipitation, typically years when the polar front remains largely north of the region and summer precipitation is dominated by subtropical high activity but not to the degree necessary to a monsoon-type climate (BSC 2004 [DIRS 170002], pp. 6-46 to 6-47).

Tables F-1 and F-2 provide the results of parameterization of precipitation records for ten local and regional meteorological stations. These include five Yucca Mountain stations, four Nevada Test Site (NTS) stations, and one National Climatic Data Center (NCDC) station, Amargosa Farms.

The NCDC normal precipitation provides corroboration for the Fourier coefficients for Amargosa Farms (NOAA 2002 [DIRS 178676], pp. 3, 12). The NCDC normal precipitation for 1971 through 2000 is 100 mm, where missing data have been replaced using a weighting function derived from other station data and data from neighboring stations, and the peak precipitation months are February and March.

Table F-3 shows that the mean annual precipitation (MAP) calculated for Amargosa Springs from the zero-order Fourier coefficients (Equation F-42) is 119 mm, using the 26 years for which the records are complete, 1968, 1969, 1979-2000, 2002, and 2003. The phases of −1.17 radians and −2.61 radians for the Markov probabilities (Table F-4) correspond to maximum wet-day probabilities in February through April, using Equation 6.5.1.2-2. The phase of +2.34 radians for the precipitation amount (Table F-5) corresponds to peak storm size in January.

Tables F-7 and F-8 contain the results of parameterization of temperature records at four Yucca Mountain meteorological stations.

Appendix F also describes the use of temperature and precipitation lapse rates to adjust each station's parameters to an elevation equivalent to the top of Yucca Mountain (5,000 ft or 1,524 m). *Handbook of Hydrology* (Maidment 1993 [DIRS 125317], p. 3.3) provides a dry adiabatic temperature lapse rate of 0.01°C/m, with an implied uncertainty of ±0.005°C/m. In reality, a simple relationship does not exist to relate temperature and elevation at a given site. Rather, there are many complex factors which control local temperatures (e.g., ground conditions, wind patterns, slope and azimuth, etc.). It is assumed in this analysis that the use of the dry adiabatic temperature lapse rate is a reasonable approximation to the local terrestrial temperature lapse rate in areas such as Yucca Mountain, where terrain is not steep and conditions are generally windy enough to cause airflow over (rather than around) the terrain and dry enough that condensation is insignificant (Smith 2004 [DIRS 179904] pp. 193 to 222). It is shown in Section 7.1.4 that this assumption does not introduce a significant bias in estimates of net infiltration, and therefore this simplification is adequate for its intended use. This value has two applications:

1. In the development of Present-Day climate weather inputs, to adjust the zero-order temperature parameters to 1,524 m.

2. In the MASSIF model, for all climates, to adjust the input temperatures from an elevation of 1,524 m to the elevation of each cell, regardless of climate.

Appendix F uses the parameters for the ten stations to develop a lapse rate for each zero-order precipitation parameter of the Present-Day climate. These lapse rates provide the basis for adjustment of the zero-order parameters to 1,524 m. That is, both the frequencies of wet days and the wet-day precipitation amounts include adjustment for elevation.

Using an approximation (Equation F-42), the appendix estimates the MAP for each of the ten stations. These values lead to a lapse rate for MAP of 6.3 ± 0.7%/100 m (Table F-3). The MASSIF model uses this lapse rate to adjust input precipitation from an elevation of 1,524 m to the elevation of each cell. In effect, the model makes the assumption that the lower frequency of precipitation at lower elevations may be adequately represented by having the same wet days as at 1,524 m, but providing an extra reduction in the amount of precipitation.

For each selected station, Table F-6 lists the probability of a wet day and the MAP, calculated in accordance with the following formulas (Appendix F, Equations F-41 and F-42):

- Mean probability that a day is wet: $\frac{1-a_{00}}{1-a_{00}+a_{10}}$
- MAP: $365\frac{1-a_{00}}{1-a_{00}+a_{10}}a_{\lambda}$.

The adjusted values for MAP for each station range from 170 to 250 mm.

The potential range of MAP is corroborated by other data. For example, Thompson et al. (1999 [DIRS 109462]) interpolated Present-Day climate estimates to an elevation of 1,524 m. On the basis of U.S. Weather Service "normal" values, based on three decades of records, without detailed coverage near Yucca Mountain, the estimated MAP was 125 mm. However, a baseline derived from 10 years of NTS data yielded an estimated MAP of 189 mm (Thompson et al. 1999 [DIRS 109462], Table 4). Neither of these estimates used measurements taken at the Yucca Mountain site; however, both values are within the range of the combined parameter uncertainties.

Also, the National Oceanic and Atmospheric Administration (NOAA) provides historic climatic data by divisions, with Yucca Mountain located on the boundary between Nevada Division 3 to the north and Nevada Division 4 on the south. Thompson et al. (1999 [DIRS 109462]) found that one-year precipitation totals in Division 3, generally at higher elevation, ranged from about 75 mm to one value as high as 360 mm for the period of record (about 100 years). Division 4 areas, which are at lower elevation, had a range of one-year precipitation from less than 50 mm to one value as high as 325 mm for the period of record (Thompson et al. 1999 [DIRS 109462], p. 30, Figure 16). The range of MAP from the combined parameter uncertainties is well within the range of these one-year extremes.

The wind speed at two meters above ground is summarized for a meteorological station as an average for each month of the year. Therefore, there are twelve wind-speed parameters, $u_2(m)$, for m from 1 to 12. Appendix F, Section F3.1, describes the method used to calculate a monthly wind speed averaged over four Yucca Mountain meteorological stations.

Table F-22 lists the nominal value and uncertainty for each parameter of the weather input file for the Present-Day climate. The approximate uncertainty distribution for each zero-order precipitation parameter is a uniform distribution. The extremes of the distribution are the minimum and the maximum values among those obtained by analysis of the ten stations, extended by one standard error. These values also appear in Tables F-4 and F-5. The nominal value is the mid-point between these extremes.

For each of the eight first-order precipitation parameters, the nominal value is the mean of the values for the ten meteorological stations. The approximate uncertainty distribution is usually a normal distribution, established by the mean and standard deviation for the 10 stations. The one exception is $b_{10,1}$, which is only two standard deviations above zero, so that a uniform distribution, defined by the extreme values from the 10 stations, is a more representative distribution of this non-negative parameter. The values for the phase parameters are consistent with peak precipitation in the winter.

All of the temperature parameters have uncertainty distributions that are uniform, with a range determined by the minimum and maximum values for the four sites, as given in Tables F-8 through F-10. Each nominal value is at the center of its range. For determining temperature parameters, fewer weather stations were deemed necessary than for determining precipitation parameters because temperature is less directly related to net infiltration than precipitation and because the factors that effect temperature, such as ground conditions (color, vegetation) at sites far from Yucca Mountain may not be representative of conditions at Yucca Mountain. The wind speed averages have normal distributions, based on the mean and standard error calculated in Output DTN: SN0610T0502206.030.

The amount of runoff from a precipitation event is influenced by the intensity of the precipitation. The daily totals do not indicate the duration of an event within a day. Therefore, the duration of precipitation is one of the climate parameters required for simulating infiltration.

6.5.1.4 Weather-File Parameters for the Monsoon Climate

According to *Future Climate Analysis*, the monsoon climate is characterized in the Owens Lake record by species that imply a monsoon sufficient to generate diluting surface flow in the Owens River. An upper-bound value for the monsoon climate must have MAP higher than the values near Owens Lake (up to 270 mm) and mean annual temperature (MAT) as high or higher than Owens Lake today. *Future Climate Analysis* selected the stations at Hobbs, New Mexico, and Nogales, Arizona, with MAP levels of 418 mm and 414 mm, respectively, but noted that the MAP at these sites may not be high enough to generate the appropriate lake in the Owens Basin. An expansion of the summer rain regime to the Owens Basin region also would have expanded well north of Yucca Mountain. Because Yucca Mountain would be more centrally located within such a summer rain regime, it may experience upper-bound levels of MAP that are higher than those identified from the analogue meteorological stations (BSC 2004 [DIRS 170002], pp. 6-47 to 6-50).

Future Climate Analysis concludes that the conditions at Yucca Mountain today are representative of the dry lower bound for the monsoon climate. As for seasonal variation, climate during this period would vary from episodes of intense summer rain to present-day-like climates with relatively more winter and less summer precipitation (BSC 2004 [DIRS 170002], p. 6-50).

Tables F-12 and F-13 provide the results of parameterization of precipitation records for the Hobbs and Nogales meteorological stations. The NCDC precipitation normals provide corroboration for the Fourier coefficients for these stations. For each NCDC precipitation normal, missing data have been replaced using a weighting function derived from other station data and data from neighboring stations.

The NCDC normal precipitation for 1971-2000 at Hobbs is 461 mm, and the peak precipitation months are July and August (NOAA 2002 [DIRS 178675], pp. 3 and 15). The coefficients for Hobbs in Tables F-12 and F-13 are based on 38 years for which the records are complete, 1952, 1954, 1955, 1957, 1959 to 1967, 1969 to 1980, 1982, 1983, 1985 to 1990, 1992 to 1994, 1996, and 1998 (Output DTN: SN0609T0502206.023, *Monsoon/Precipitation Fourier Analyzer V2.3 Hobbs*, worksheet: "Input"). Applying Equation F-42 to the coefficients yields a MAP of 406 mm. The phases of +2.25 and +1.35 for the Markov probabilities (Table F-12) correspond to maximum wet-day probabilities in July through September. The phase of −1.09 for the precipitation amount (Table F-13) corresponds to peak storm size in July and August.

The NCDC normal precipitation for 1971 to 2000 at Nogales is 483 mm, and the peak precipitation months are July through September (NOAA 2002 [DIRS 178674], pp. 3 and 16). The coefficients for Nogales in Tables F-12 and F-13 are based on 29 years for which the records are complete, 1948, 1951, 1953 to 1958, 1960, 1962 to 1965, and 1967 to 1982 (Output DTN: SN0609T0502206.023, *Monsoon/Precipitation Fourier Analyzer V2.3 Nogales*, worksheet: "Input"). Applying Equation F-42 to the coefficients yields a MAP of 421 mm. The phases of +1.74 and +2.30 for the Markov probabilities (Table F-12) correspond to maximum wet-day probabilities in July and August. The phase of −2.01 for the precipitation amount (Table F-13) corresponds to peak storm size in September.

Equation F-42, which includes only the zero-order parameters, tends to underestimate MAP for stations experiencing a monsoon climate. That is because the first-order coefficients are relatively large and the seasonal variations in the Markov parameters are correlated with the seasonal variation in storm size.

The zero-order precipitation parameters in Tables F-12 and F-13 indicate that Hobbs has bigger storms, but Nogales has more storms. Combining the "wetter" value of each parameter would yield a MAP of 516 mm. This level of precipitation exceeds the NCDC normals and might have been enough to generate the appropriate lake in the Owens Basin during the previous cycle.

Tables F-14 and F-15 contain the results of parameterization of temperature records at the Hobbs and Nogales meteorological stations. Because Hobbs and Nogales were chosen for their values of MAP and their temperatures, without consideration of their elevation, they each represent conditions at the reference Yucca Mountain elevation of 5,000 ft (1,524 m) and need no adjustment for elevation.

It is assumed that the wind speed approximated for the Present-Day climate is an adequate approximation for the wind speed expected during the Monsoon climate.

Table F-23 lists the nominal value and uncertainty for each parameter. For the zero-order precipitation terms, the estimated uncertainty distribution is a uniform distribution. To assure that the extremes capture the full range of uncertainty, they are the minimum and maximum of all values from the analyses of Present-Day and upper-bound Monsoon sites.

As forecast in *Future Climate Analysis*, the monsoon climate is a climate where winter precipitation exists but does not dominate MAP. Climate during this period would vary from episodes of intense summer rain to present-day-like climates with relatively more winter and less summer precipitation (BSC 2004 [DIRS 170002], p. 6-50). Therefore, although the magnitude of the first-order precipitation term is uncertain, the phase of the first-order term must be that of the summer-precipitation upper-bound stations, not the winter-precipitation Yucca Mountain stations.

A monsoon climate has strong seasonal variation, which makes the first-order terms more important than for other climates. The amplitudes for the first-order terms differ greatly between the two upper-bound stations. Nogales has the greater seasonal variation in the probability that a day is wet. Hobbs has the greater variation in the average precipitation on wet days. Tables F-12 and F-13 show that some first-order magnitudes for the two stations differ by more than a factor of two, with standard deviations larger than the standard deviations in the corresponding zero-order terms.

Because *Future Climate Analysis* (BSC 2004 [DIRS 170002], p. 6-49) describes these stations as "the best choices available," it is not clear that the two values for a first-order amplitude, as different as they are, actually capture the full range of uncertainty. An alternate interpretation is that these stations are just two samples of potential upper-bound stations. In this interpretation, the potential upper-bound stations have a distribution for each parameter that may be approximated as a normal distribution, with the average and standard deviation for the two stations providing estimates for the mean and variance of the distribution. A range from one standard deviation below the lower value to one standard deviation above the upper value captures about 90% of this hypothetical distribution.

However, the magnitude of a first-order term is subject to constraints. The magnitude of a first-order term must be less than the magnitude of the zero-order term, because neither a Markov probability nor an average precipitation can be less than zero. Also, the first-order term may not cause a Markov probability to exceed 1.0. Therefore, an approximate uncertainty distribution for the magnitude of a first-order term for the upper-bound monsoon climate is a uniform distribution from one standard deviation below the lower value to one standard deviation above the upper value, subject to constraints.

The uncertainty distribution for the phase of each first-order precipitation term is a uniform distribution. The extreme values are the values for the two upper-bound stations.

Because the first-order terms for the lower-bound stations are completely out of phase with the upper-bound terms, they may be represented by negative values of the b parameters (b_{00}, b_{10}, b_{λ}, b_{m}). In Table F-23, the complete range for the amplitude of a first-order term may range from the largest value for the Present-Day climate, plus one standard deviation, but taken as negative, to the larger of the values from the upper-bound stations, plus one standard deviation, taken as positive.

All of the temperature parameters have uncertainty distributions that are uniform, with a range determined by the minimum and maximum values for the four sites, as given in Tables F-8 through F-10. Each nominal value is at the center of its range.

6.5.1.5 Weather-File Parameters for the Glacial Transition Climate

Judged from the Owens Lake record, the change to the glacial transition climate was large and fast, shifting from a strong monsoon system dominated by summer precipitation to a winter regime with sufficient effective moisture to sustain a fresh and spilling Owens Lake. Therefore, the polar front must be resident in the region during much of the winter, lowering the MAT. The genesis of greater snowpack with a resident polar mass must also lower temperature and increase MAP at Yucca Mountain, but the cooler climate never becomes very cold with high effective moisture as was true of the last two full-glacial periods. The climate during the glacial transition period was typically a cool, usually wet winter season with warm (but not hot) to cool summers that were usually dry relative to the present-day summers. The MAT should be no colder and preferably warmer than 8°C. The MAP should be higher than the 309 mm recorded near Owens Lake, because even the high historic discharge levels of that year would not be sufficient to fill and spill the lake as implied by the microfossil record. The three selected stations in eastern Washington—Rosalia, St. John, and Spokane—fit all of the criteria for the upper-bound glacial transition climate (BSC 2004 [DIRS 170002], pp. 6-50 to 6-52).

However, there are indications that there were also episodes during this climate period that were relatively warm and dry, thus demonstrating some degree of climate variability. The stations representing the lower bound should have a higher temperature, but lower than that for the Owens Lake Basin today. They may have MAP values that are similar to or even lower than present-day Owens Lake Basin, but dominated by winter precipitation. The set of meteorological data for Delta, Utah, fits all of these criteria. The site at Beowawe, Nevada, was added as a lower-bound station to avoid using a single site and because its data met most of the requirements (BSC 2004 [DIRS 170002], pp. 6-50 to 6-53).

The NCDC precipitation normal provides corroboration for the Fourier coefficients for these stations (NOAA 2002 [DIRS 178673] pp. 3 and 15; 2002 [DIRS 178677], pp. 3 and 15; and 2002 [DIRS 178676], pp. 3 and 15). For the NCDC precipitation normal, missing data have been replaced using a weighting function derived from other station data and data from neighboring stations. For each station, Table 6.5.1.5-1 provides the fraction of days that are wet and the MAP, calculated in accordance with Equations F-41 and F-42. Shown for corroboration are the normal MAPs and wettest months for these stations, as reported by the NCDC.

Table 6.5.1.5-1. Wet Day Fraction and Mean Annual Precipitation Implied by Adjusted Parameters

Meteorological Station	Wet Day Fraction	Implied MAP (mm)	Years Used for Fourier Analysis (Mar. 1 to Feb. 28)	NCDC Normal MAP for 1971 to 2000 (mm)	NCDC Wettest Month(s)
Beowawe	17%	241	10 years: 1983, 1986 to 1989, 1993 to 1995,1999,2001	225	May
Delta	18%	207	29 years: 1972, 1973. 1975, 1976, 1978 to 1981, 1983 to 2003	214	May, Oct.
Rosalia	30%	455	28 years: 1953, 1956, 1958 to 1960, 1963 to 1971, 1973, 1975 to 1978, 1980 to 1983, 1985 to 1988, 1993	467	Dec.
Spokane	31%	419	52 years: 1948 to 1952, 1954 to 1994, 1998 to 2003	423	Nov. to Dec.
St. John	27%	431	22 years: 1964 to 1969, 1972 to 1981, 1987, 1989 to 1991, 1994, 2001	436	Dec.

Source: Fourier analysis years from Output DTN: SN0609T0502206.023; 1971 to 2000 MAPs and wettest months from NOAA 2002 [DIRS 178673], p. 15; 2002 [DIRS 178677], p. 15; and 2002 [DIRS 178676], p. 12.

For the upper-bound stations, the phase parameters correspond to peak storm frequency in December through February, but peak storm magnitude in May through June. The lower-bound station parameters reflect peak frequency in the winter, but peak magnitude in June through August. The difference in wettest months arises because the upper-bound stations have larger seasonal variation in frequency, while the lower-bound stations have larger seasonal variation in magnitude.

Tables F-20 and F-21 contain the results of parameterization of temperature records at the five meteorological stations representing the glacial transition climate. Because these stations were chosen for their values of MAP and their temperatures, without consideration of their elevation, they each represent conditions at the reference Yucca Mountain elevation of 5,000 ft (1,524 m) and need no adjustment for elevation.

It is assumed that the wind speed approximated for the Present-Day climate is an adequate approximation for the wind speed expected during the Glacial Transition climate.

Table F-24 lists the nominal value and uncertainty for each parameter. Most of the uncertainty distributions for precipitation and temperature parameters are uniform with the ranges determined in Section F2.3 extended by one standard error where applicable, and the nominal values are the means of the distributions. The exceptions are the phase coefficients for precipitation. The table assigns a normal distribution to the phase coefficients for the Markov probabilities using the weighted average and standard deviation from Table F-18. In the case of the phase coefficients for the amount of precipitation of a wet day (Table F-19), however, the weighted standard deviations are so large that no nominal value seemed justified. These last two phase coefficients are considered as completely uncertain, so that any value is possible.

6.5.1.6 Generation of MASSIF Weather-File Input from Climate Parameters

One of the inputs to MASSIF is a weather file with data for each day. Each day's data set consists of the amount of precipitation, the minimum and maximum temperatures, and the average wind speed at two meters above the ground.

For a given set of weather parameters, a stochastic algorithm develops a 1,000-year sample of daily precipitation by sampling from a lognormal distribution. For wet days, the amount of precipitation, P, is determined from a random number $R \in (0,1)$ and the cumulative probability distribution; that is:

$$\int_0^{P(y,d)} \frac{e^{-[\ln x - m(d)]^2/2[s(d)]^2}}{xs(d)\sqrt{2\pi}} dx = R \qquad \text{(Eq. 6.5.1.6-1)}$$

where $s(d) = \sqrt{2[\ln \lambda(d) - m(d)]}$.

The domain for Yucca Mountain infiltration covers approximately 50 square miles. An infiltration calculation produces a map of daily infiltration through each of 143,000 pieces of land, averaged over a sample of years.

Therefore, it is not practical to calculate daily infiltration through each area for 1,000 years. This difficulty is addressed by taking a sample of the simulated years, including several years with high precipitation. Each sample year is weighted by its relative probability in calculating the map of average annual infiltration. This approach assures that the effects of extreme events are recognized, but given appropriate weight in the analysis.

Input to the infiltration model is a subsample of the 1,000-year sample. From the full sample sorted by total precipitation for the year, the subsample includes 1,000-year, 300-year, 100-year, 30-year, and 10-year events, with a few additional years to represent the drier portion of the probability distribution. Each year in the subsample carries a weight proportional to probability; for example, the 1,000-year event has a weight of 0.001. Appendix F contains the details of the procedures.

Daily temperature extremes and mean wind speeds are added to the weather input file as described in Appendix F.

6.5.1.7 Other Climate Parameters

Maximum Daily Precipitation

The lognormal fit to wet-day precipitation amount does not fit the probability of extreme events very well. Although the assigned probability for extremely heavy precipitation is very small, it appears to be higher than the data. Therefore, MASSIF accepts an input that limits the total precipitation for one day. The value chosen is the largest observed rainfall in the USA during a 24-hour period over a 26-km^2 area, 983 mm (Maidment 1993 [DIRS 125317], p. 3.36, Table 3.10.2).

Snowmelt Coefficient

MASSIF employs a temperature-index snowmelt equation from *Handbook of Hydrology* (Maidment 1993 [DIRS 125317], p. 7.24) for calculating daily snowmelt for days with snow accumulation. Table 7.3.7 in that source (Maidment 1993 [DIRS 125317], p. 7.24) provides temperature-index expressions for calculating daily snowmelt for various regions of North America. The closest site to Yucca Mountain is Sierra Nevada, California. This site has latitude similar to that of Yucca Mountain and is therefore the most appropriate site to use in this table. The general form of the temperature-index snowmelt equation is:

$$M = SM * T \qquad \text{(Eq. 6.5.1.7-1)}$$

where SM is the snowmelt coefficient in mm/day/°C (for days with mean daily air temperature greater than 0°C), M is snowmelt in mm/day and T is daily mean air temperature (°C). The snowmelt coefficients for the Sierra Nevada, California, are 1.78 and 1.92 for April and May, respectively (Maidment 1993 [DIRS 125317], p. 7.24).

There is large inherent uncertainty in this parameter. Maidment (1993 [DIRS 125317], Table 7.3.7, p. 7.24) reports values for the snowmelt coefficient (*SM*) ranging from 0.58 (for the Boreal forest) to 5.7 (for Southern Ontario). It appears that the greater the amount of forest cover, the lower the value of *SM*, which suggests that more snowmelt is slowed by the presence of tree shade. A mean value of 2 was selected for the MASSIF model, which is slightly higher than the Sierra Nevada values. A range of 1 to 3 (with a uniform distribution) is assumed to represent snowmelt conditions at Yucca Mountain during the Glacial Transition climate. This value was used for all climates because there is not significant snow during the Present-Day and Monsoon climates.

Sublimation Coefficient

Estimates of sublimation (or ablation) of snowpack vary widely. Hood et al. (1999 [DIRS 177996], p. 1,782) discuss a 1975 study in which sublimation was responsible for 80% of the ablation of fresh snow and 60% of the ablation of older snow during springtime conditions in the White Mountains of California. Hood et al. (1999 [DIRS 177996], p. 1,782) also discuss a 1959 study in which sublimation was only 2% to 3% of total ablation over the snow season at the Central Sierra Snow Laboratory in California.

Hood et al. (1999 [DIRS 177996], p. 1782) also discuss more recent studies (e.g., Kattelmann and Elder 1991 [DIRS 177998]) that estimated sublimation from snow to be 18% of total precipitation over two water years for Emerald Lake Basin in the Sierra Nevada, and Berg (1986 [DIRS 177995]), who reported sublimation losses from blowing show to be between 30% to 51% of precipitation for the two year period 1973 to 1975. Hood et al. (1999 [DIRS 177996], p. 1794) report sublimation from their own study to be 15%.

Based on the annual sublimation data reported by Hood et al. (1999 [DIRS 177996], p. 1794), a nominal value of 10% was selected for Yucca Mountain. This value is lower than those estimated for the Sierra Nevada; however, this is justified because the snow pack is expected to persist for shorter periods of time at Yucca Mountain in the future than it does in the Sierra

Nevada in the present climate. To incorporate uncertainty, a range of 0% to 20% (with a uniform distribution) is considered to represent annual snow sublimation amounts at Yucca Mountain during the Glacial Transition climate. This range is corroborated by the other studies discussed above. This value was used for all climates because there is not expected to be significant snow during the Present-Day and Monsoon climates.

The sublimation coefficient is multiplied by daily precipitation for days when the mean daily air temperature is less than 0°C, and that amount is removed from the precipitation total in the form of snow sublimation. The effect of this calculation is to partition 10% of daily precipitation on days when the mean daily temperature is less than 0°C into sublimation and thereby remove this water from the water balance.

Table 6.5.1.7.1 summarizes the snow parameters.

Table 6.5.1.7-1. Nominal Values and Uncertainties for Snow Parameters

Parameter Name	Parameter Symbol	Nominal Value	Uncertainty Range	Uncertainty Distribution
Snowmelt (SM)	$C_{snowmelt}$	2.0	1.0 to 3.0	Uniform
Sublimation (SUB)	$C_{sublime}$	0.1	0.0 to 0.2	Uniform

Source: Snowmelt coefficient estimates from Maidment 1993 [DIRS 125317], p. 7.24. Sublimation estimates from Hood et al. 1999 [DIRS 177996], p. 1794

Precipitation Duration

The precipitation duration is a highly variable parameter in the desert environments, so that the selection of the parameter values to be used in the MASSIF calculations needs a special justification. For each climate, this analysis develops a function that relates the precipitation duration to the amount of rain that falls on a given day. Because of limited data availability, only data from certain weather stations representing each climate were analyzed. Four sets of analyses were done to characterize precipitation duration parameters for each climate. Output DTN: SN0610T0502206.031 contains MathCAD applications in which the analyses are performed.

Table 6.5.1.7-2 lists the weather stations used for the four precipitation duration analyses.

Table 6.5.1.7-2. Weather Stations Used for Precipitation Duration Analyses

Precipitation Duration Analysis	Weather Stations	Source DTN
Present-Day	BSC Stations 1, 2, 3, 6	SN0608WEATHER1.005 [DIRS 177912]
Monsoon (upper)	Hobbs, NM, and Nogales, AZ	MO0605SEPHOURL.000 [DIRS 177237]
Glacial Transition (lower)	Delta, UT	MO0605SEPHOURL.000 [DIRS 177237]
Glacial Transition (upper)	Spokane, WA	MO0605SEPHOURL.000 [DIRS 177237]

For each analysis listed in Table 6.5.1.7-2, the daily precipitation **amount (*Amt*)** and the **number of hourly intervals (*Int*)** in which precipitation was measured at each of the weather stations were calculated for every day of the year. Days with zero precipitation (number of hourly

intervals equals zero) were filtered out. The remaining dataset was plotted (Figures 6.5.1.7-1 to 6.5.1.7-4) and fit to a linear model:

$$Int = a + b * Amt \qquad \text{(Eq. 6.5.1.7-2)}$$

where a is the y-intercept and b is the slope.

The standard error on b was estimated as:

$$SE_b = \frac{\sqrt{mean\left\{\left[\frac{Int_i - a}{Amt_i} - b\right]^2\right\}}}{\sqrt{n}} \qquad \text{(Eq. 6.5.1.7-3)}$$

where n is the number of data, and i is the data index from 1 to n.

For the MASSIF calculation, which uses a daily time step, an assumption is made that daily precipitation occurs as a single event rather than multiple shorter events separated by dry periods during the day. Given this assumption and for a given precipitation day, the number of hourly intervals is, on average, equal to one hour greater than the actual precipitation duration for that day. This is because for a given precipitation event the actual start and end times within the hourly intervals that bound these start and end times are equally likely to occur during the first half of the intervals as the last half of the interval. For example, given it rains for 0.5 hr, there is a 0.5 probability that the rain event occurred in one hourly interval and a 0.5 probability that it occurred in two hourly intervals. The mean number of intervals is 1.5, which is one hour more than the actual duration of the rainfall. This one hour offset can be shown to apply for any given duration event. Table 6.5.1.7-3 lists the results of the linear regressions as the slope and intercept-1. The intercept-1 represents the minimum precipitation duration considered in the model. Table 6.5.1.7-4 lists the nominal values and distributions for these parameters for each climate.

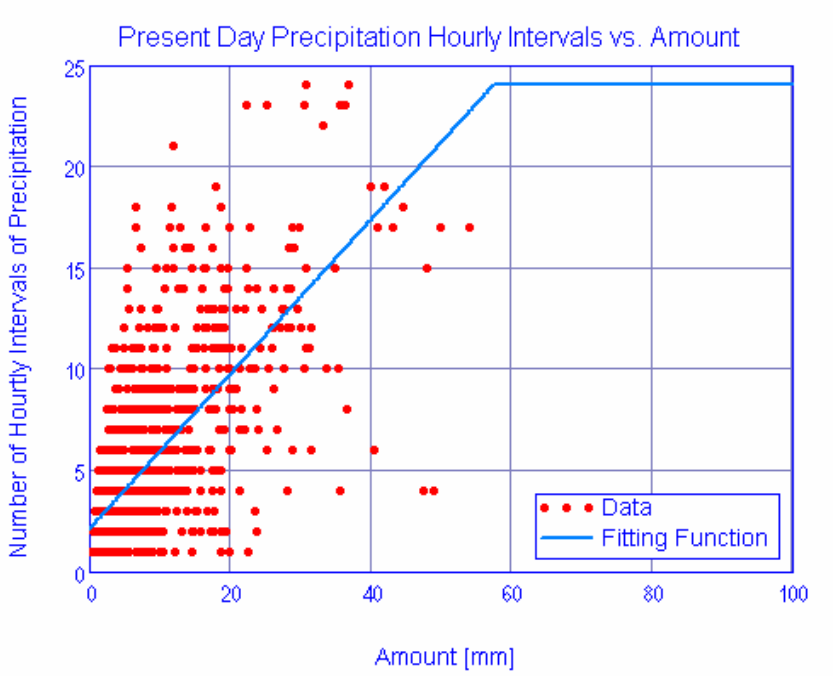

Source: Output DTN: SN0610T0502206.031.

Figure 6.5.1.7-1. Number of Hourly Intervals of Precipitation Plotted against the Daily Amount of Precipitation for the Present Weather Stations BSC1, BSC2, BSC3, and BSC6

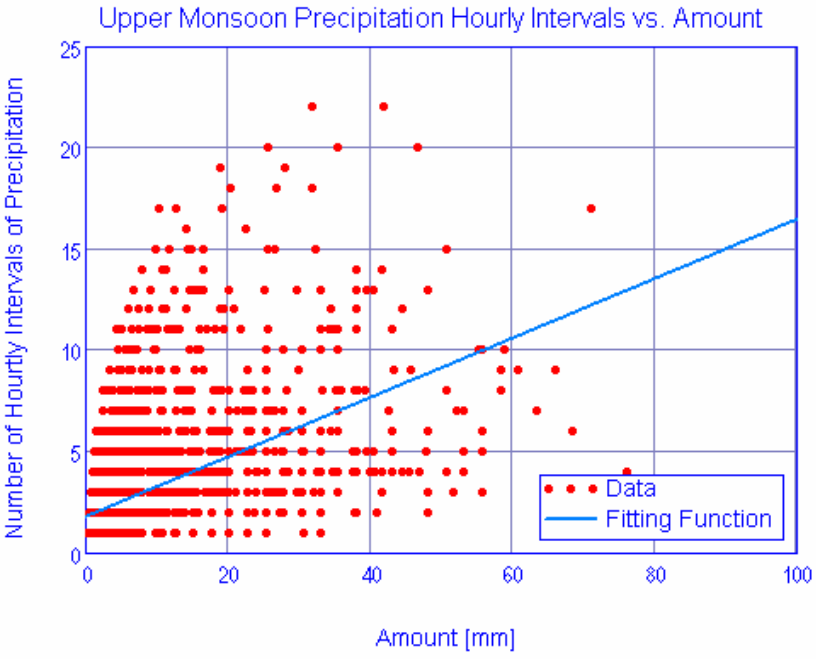

Source: Output DTN: SN0610T0502206.031.

Figure 6.5.1.7-2. Number of Hourly Intervals of Precipitation Plotted against the Daily Amount of Precipitation for the Upper Monsoon Weather Stations of Hobbs, NM, and Nogales, AZ

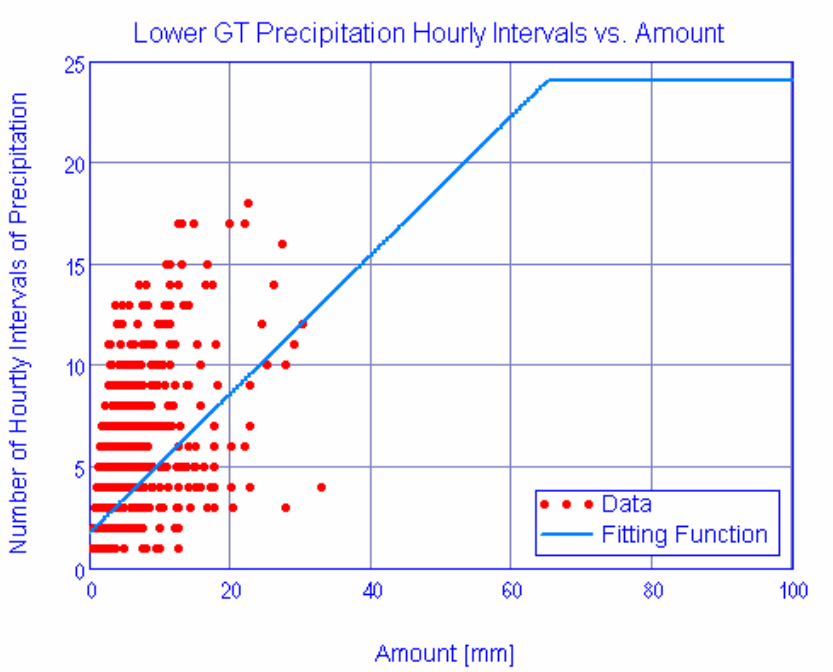

Source: Output DTN: SN0610T0502206.031.

Figure 6.5.1.7-3. Number of Hourly Intervals of Precipitation Plotted against the Daily Amount of Precipitation for the Lower Glacial Transition Weather Station of Delta, UT

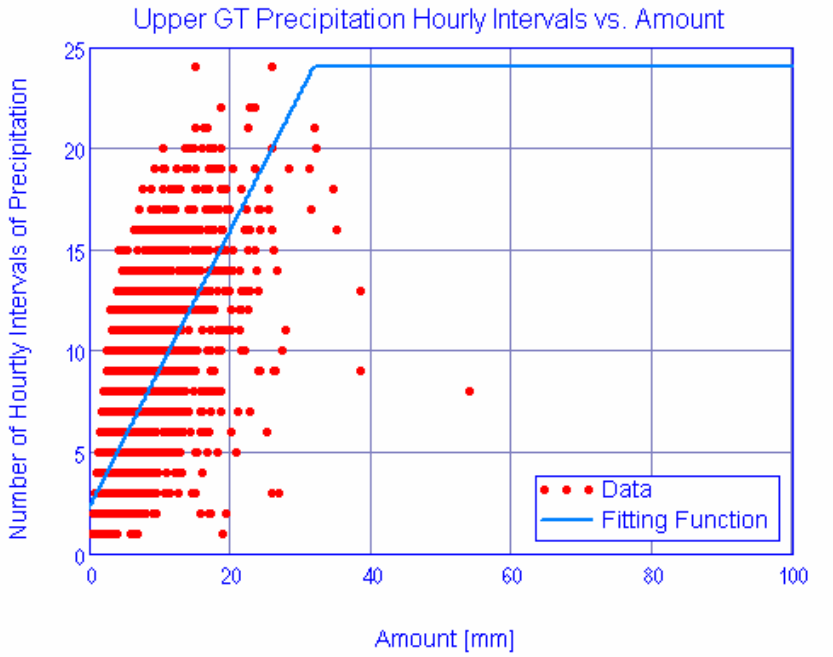

Source: Output DTN: SN0610T0502206.031.

Figure 6.5.1.7-4. Number of Hourly Intervals of Precipitation Plotted against the Daily Amount of Precipitation for the Upper Glacial Transition Weather Station of Spokane, WA

Table 6.5.1.7-3. Precipitation Duration Linear Regression Results

Precipitation Duration Analysis	Slope	Std Err on Slope	Minimum Precipitation Duration (Intercept-1)
Present-Day	0.38	0.05	1.07
Monsoon (upper)	0.15	0.01	0.76
Glacial Transition (lower)	0.34	0.02	0.70
Glacial Transition (upper)	0.68	0.03	1.22

Source: Output DTN: SN0610T0502206.031, *Precipitation Duration Parameter Values and Distributions.xls*.

Table 6.5.1.7-4. Precipitation Duration Parameter for Each Climate

Climate	Nominal Slope	Distribution (Slope)	Std Err on Slope	Minimum Precipitation Duration (Intercept-1)
Present-Day	0.38	Normal (mean = 0.38, SD = 0.05)	0.05	1.07
Monsoon	0.28 [a]	Uniform (0.14 – 0.43) [d]	0.08 [c]	0.91
Glacial Transition	0.52 [b]	Uniform (0.32 – 0.71) [d]	0.11 [c]	0.96

Source: Output DTN: SN0610T0502206.031, *Precipitation Duration Parameter Values and Distributions.xls.*

[a] Mean of Present-Day and Monsoon upper slope values (mean of values presented in Table 6.5.1.7-3 is 0.27 due to rounding in that table).

[b] Mean of Glacial Transition lower and upper slope values (mean of values presented in Table 6.5.1.7-3 is 0.51 due to rounding in that table).

[c] Standard deviation calculated using square root of Equation I-9.

[d] Upper and lower ends of uniform distribution are extended by one standard error.

6.5.2 Geologic and Geographic Inputs

Geologic inputs to MASSIF include parameters for Yucca Mountain soils and bedrock, and spatial distributions for soil types, soil depth classes, and bedrock types over the modeling domain. Geographic inputs include data used to define cell coordinates, elevations, slope, azimuth, watershed delineations, and other site characteristics. This section presents a summary of the methods used to determine each of the geologic and geographic inputs and presents the nominal values and uncertainty ranges for all the geospatial parameters. Geographic inputs are described in Section 6.5.2.1. Soil classification is presented in Section 6.5.2.2 followed by soil properties and soil depth in Sections 6.5.2.3 and 6.5.2.4, respectively. Bedrock classification and bedrock properties are presented in Sections 6.5.2.5 and 6.5.2.6, respectively.

The geologic and geographic parameters used by MASSIF were organized into a ‘geospatial’ database. Development of the geospatial database is presented in Appendix B. The database is used to identify spatially varying parameters for each cell within the modeling domain. The database includes the following:

- Cell ID
- UTM Easting (m)
- UTM Northing (m)
- Latitude (deg)

- Longitude (deg)
- Elevation (m)
- Downstream Cell ID – identifies the cell ID for the cell adjacent to and downstream of each cell, or specifies that there are no downstream cells
- Slope (deg)
- Azimuth (deg)
- Soil Depth Zone
- Soil Type
- Bedrock Type
- Potential Vegetative Response.

For the calculations described in this report, geospatial parameters are handled in two different ways. The values of some parameters are specified in the geospatial database such that they vary independently from cell to cell. Examples of parameters that very from cell to cell include elevation and potential vegetation response (PVR). For the remaining geospatial parameters, such as bedrock hydraulic conductivity or soil properties, the geospatial database contains an index that identifies groups of grid cells representing regions where particular properties are assigned uniform values. The value of the parameter is defined to be uniform over all locations with the same index. The following geospatial parameters are assigned to such grid cell groups or regions:

- Soil depth class (5 classes)
  - Soil depth
- Soil type (8 types)
  - Saturated hydraulic conductivity (K_{sat_soil})
  - Saturated water content (θ_s)
  - Field Capacity (θ_{FC})
  - Permanent Wilting Point (θ_{WP})
  - Water Holding Capacity (calculated from θ_{FC} and θ_{WP})
- Bedrock type (38 types)
  - Saturated hydraulic conductivity (K_{sat_rock}).

Geospatial parameters represent the effective properties of 30 × 30-m grid cells, or in the case of parameters assigned to grid cell groups, these parameters represent the effective properties of much larger regions of the modeling domain. For this reason, the probability distributions of the effective or "upscaled" values of geospatial parameters will vary from the underlying spatial distributions of these parameters, which are derived from individual measurements made on a smaller scale. The region boundaries for each of the parameters were established independently of the estimation of spatial distributions of properties. Therefore, the spatial distributions are interpreted as applying to the entire region within the given boundaries, regardless of the original rationale for setting the boundaries.

Uncertainty in geologic inputs is reported with the nominal values in Sections 6.5.2.2 through 6.5.2.6. For the purpose of this infiltration analysis, uncertainty in parameters is propagated through the calculation if the parameter of interest meets the criteria established for the uncertainty analysis described in Appendix I.

6.5.2.1 Geographic Inputs

Geographic inputs to MASSIF generally include data that describe the physical location and layout of each cell. Material properties associated with the soil, bedrock, or vegetation characteristics of each cell are treated separately in Sections 6.5.2.2 through 6.5.2.6 of this report. Geographic inputs include:

- UTM Easting (m)
- UTM Northing (m)
- Latitude (deg)
- Longitude (deg)
- Elevation (m)
- Downstream Cell ID – identifies the cell ID for the cell adjacent to and downstream of each cell, or specifies that there are no downstream cells
- Slope (deg)
- Azimuth (deg).

The geographic inputs were organized into a Geographic Information System (GIS) developed for the MASSIF model and described in Appendix B. The spatial inputs elevation, azimuth, and slope are used for calculations of runoff and temperature and precipitation adjustments for elevation, and are important for developing other parameters relating to evapotranspiration.

The Shuttle Radar Topography Mission (SRTM) data were selected as the best source for topography data for infiltration modeling based on criteria described in Appendix B. The SRTM data were obtained from the U.S. Geological Survey (USGS) Earth Resources Observation and Science (EROS) Data Center (DTN: SN0601SRTMDTED.001 [DIRS 177242]).

The MASSIF infiltration model domain includes the area that drains Yucca Mountain above the proposed repository waste emplacement area. Eleven separate drainages (or watersheds) were delineated; three larger basins drain the east face of the ridge and eight smaller basins drain the west face. The largest drainage in the north part of the domain (Yucca Wash) has been artificially cut off on its northern edge because of a lack of detailed information about soil and bedrock properties in this region. The implication of this cutoff is an assumption that any run-on from the parts of the drainage that are not included can be neglected for the purpose of estimating net infiltration inside this drainage. The delineation of watershed boundaries is presented in Appendix B.

The watersheds were delimited using elevation and slope to define surface water flow direction to a single outlet. The boundaries of the eleven watersheds also delineated the overall infiltration model boundary within the larger project boundary. Figure 6.5.2.1-1 shows the watershed boundaries, which lie within the larger project boundary area. The larger rectangular project boundary encompasses 226.34 km^2. The infiltration model boundary, composed of the combination of these eleven watersheds, encompasses 120.61 km^2. The eleven watersheds make up the individual model components that are used to calculate net infiltration. The individual watersheds are highlighted in Figure 6.5.2.1-2. The region identified as the "repository waste emplacement area" in Figure 6.5.2.1-2 (and Figure 6.5.2.1-1) refers to the area where infiltration results are expected to be passed on to downstream users of the infiltration data. This area is larger than the "repository footprint," which is also shown in Figure 6.5.2.1-1, and smaller than the entire infiltration modeling domain. The repository waste emplacement area is hereafter also referred to as the unsaturated zone (UZ) grid region or UZ model domain because it corresponds to the expected modeling boundaries to be used in the UZ model, downstream of this report (BSC 2004 [DIRS 169861]; BSC 2004 [DIRS 169857]). The UZ grid region is of particular interest in the present analysis because areas outside this region, though important to the infiltration model, are not expected to be used in downstream models (such as the UZ model). For this reason, grid cells within the UZ grid are given special consideration in terms of identifying which parameters to include in a model of net infiltration uncertainty for Yucca Mountain. The number of cells in each region is shown in Table 6.5.2.1-1.

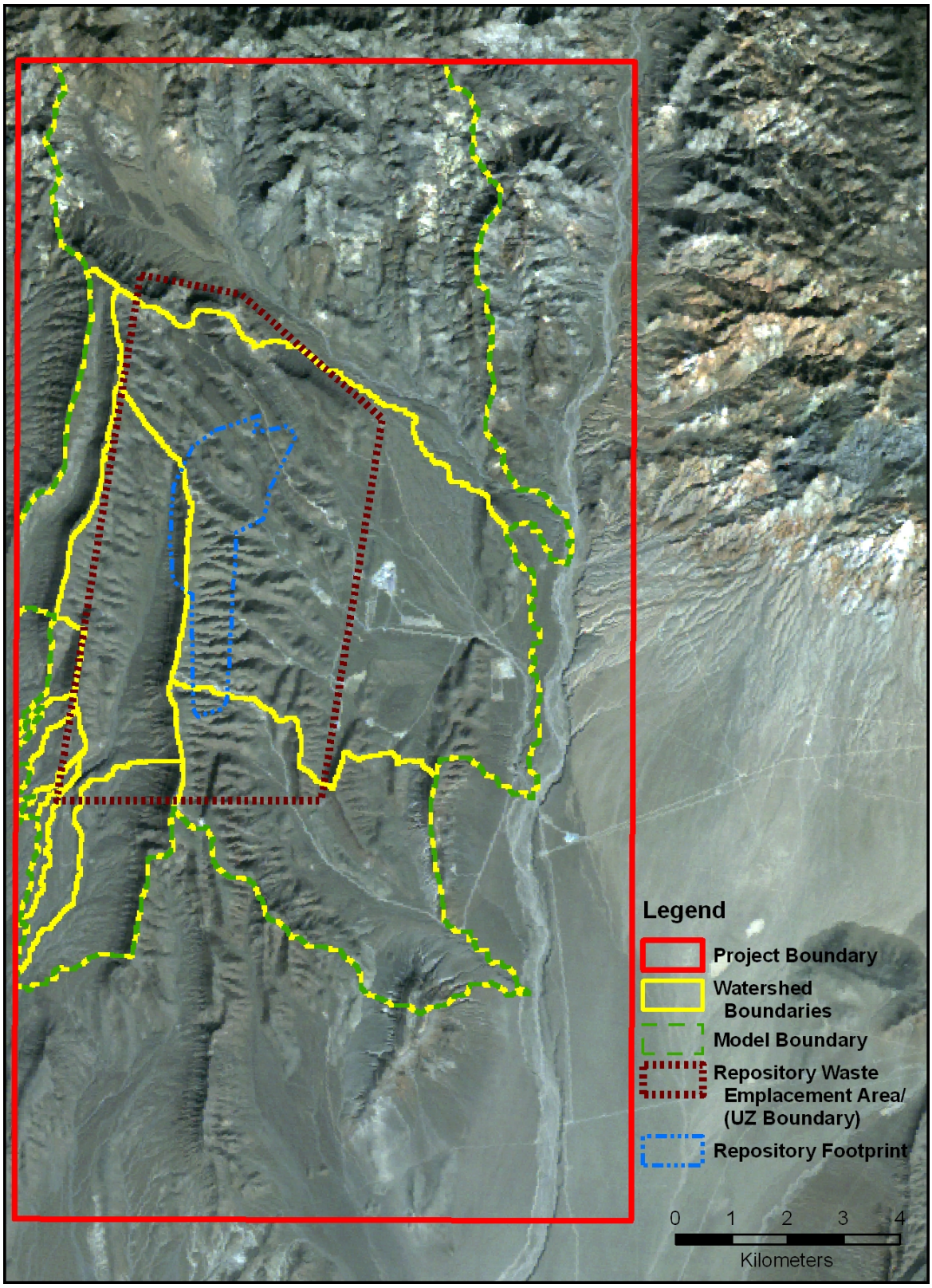

Source: Output DTNs: SN0608DRAINDYM.001, SN0612FTPRNUZB.002, and SN0608NDVILSTM.001.

Figure 6.5.2.1-1. Infiltration Modeling Boundaries

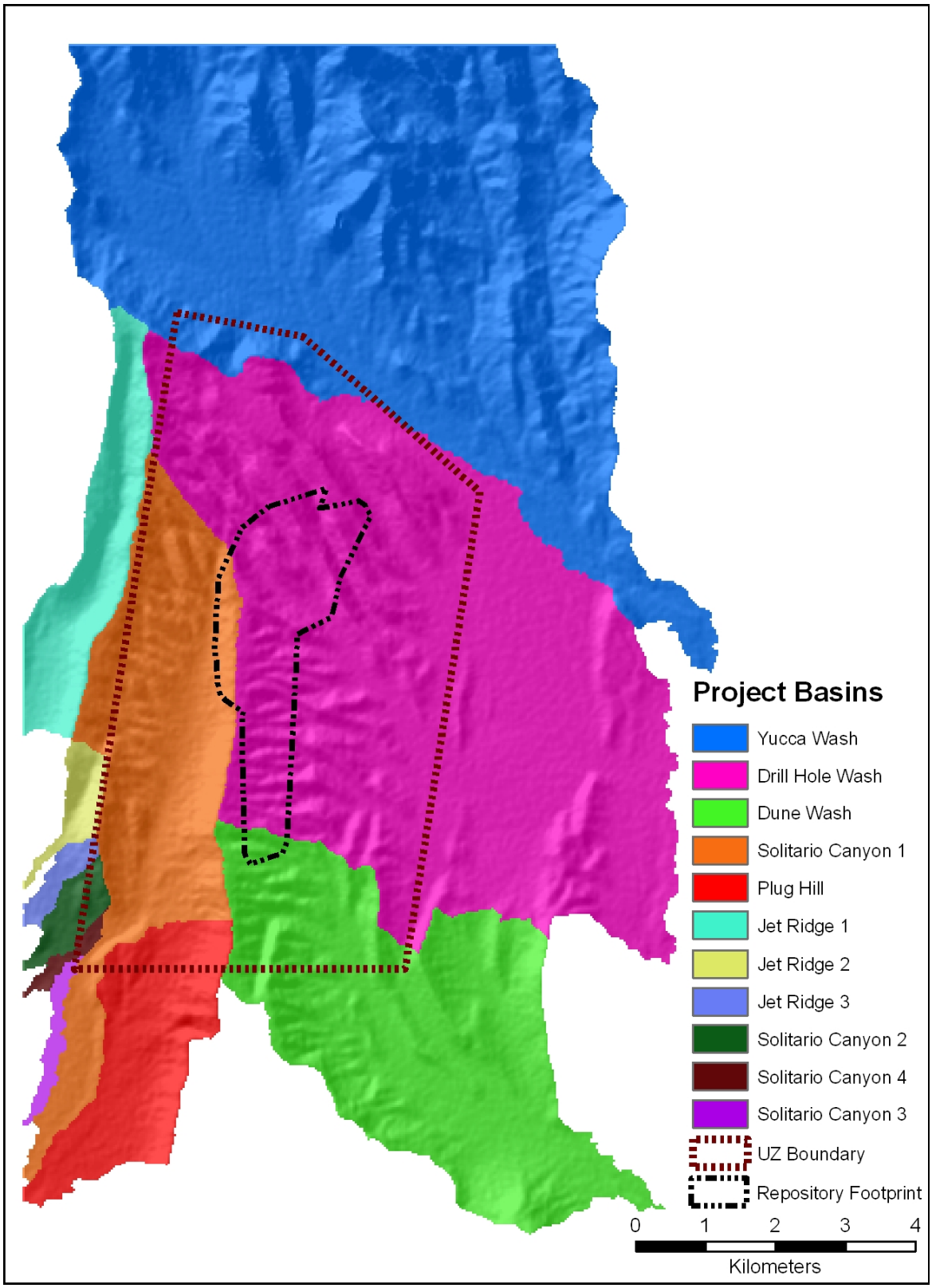

Source: Output DTNs: SN0701SPALAYER.002 and SN0612FTPRNUZB.002.

Figure 6.5.2.1-2. Yucca Mountain Watersheds (Basins)

Table 6.5.2.1-1. Number of Grid Cells within Various Boundaries in the Yucca Mountain Region

Boundary	Total Number of Cells
Project Boundary[a]	253,597
Infiltration Model Boundary (defined by eleven watersheds)[b]	139,092
Repository Waste Emplacement Area (UZ grid region)[c]	44,204
Repository Footprint [c]	6,322

[a] Output DTN SN0608ASSEMBLY.001.
[b] Output DTN SN0608DRAINDYM.001.
[c] LB0208HYDSTRAT.001 [DIRS 174491].

NOTE: Boundaries presented in this table correspond to the boundaries shown in Figure 6.5.2.1-1.

As described in Appendix B, a three-stage watershed delineation process was required to generate the fewest number of watersheds that would completely cover the Repository Waste Emplacement Area. Each watershed is a separate component of the MASSIF model, so fewer drainages result in fewer processing steps. However, the size of the drainages was dictated by two factors: the topography of the region and the UZ model domain. The surface area of each watershed varied widely, a result of the three nearly identical delineation stages needed to generate the eleven drainage basins that cover Yucca Mountain: three large, three moderate, and five small basins. During each stage, a specific threshold variable was set that would determine the size of the resulting drainages. Thus, each stage was responsible for generating either the large, medium, or small drainage basins. Variable basin sizes were necessary because the MASSIF model needed to trace potential infiltration from all locations directly over the UZ model domain down the mountain slopes to each basin pour point (the bottom-most part of the basin).

Elevation data from SRTM required processing for use in the geospatial database, as the SRTM cell size and map coordinate projections did not correspond to those needed for the infiltration model. Once cell size and projection were revised, the elevation data could then serve as the base data layer from which multiple derivative data layers could be created. These additional layers provided information, such as slope and aspect, which are required by the MASSIF infiltration model.

The raw form of the SRTM data layer was processed using Research Systems, Inc. (RSI) Environment for Visualizing Images (ENVI; ENVI + IDL, Version 4.2: STN: 11204-4.2-00) image processing software. The SRTM data were divided as a subset within the project boundary, converted to 30-m pixels and re-projected to accommodate the requirements of the MASSIF model. Elevations across the modeling domain are presented in Figure 6.5.2.1-3.

The elevation data were also used to create additional layers within the GIS including the slope and azimuth over the model area. The surface slope of each grid cell was calculated using the *slope* function in ArcGIS, which uses the elevations at eight neighboring cells. Slope was defined from 0° (horizontal) to 90° (vertical). Slopes over the infiltration modeling domain ranged between 0° and 49° (rounded to the nearest degree). A map of slopes over the modeling area is presented in Figure 6.5.2.1-4.

The azimuth layer was created using the *azimuth* function in ArcGIS, which estimates the compass direction of a vector normal to the surface of each grid cell. This parameter is used for

calculations involving the direction of incoming solar radiation. Azimuths were defined between 0° and 360° (rounded to the nearest degree). East is at 90°, South is at 180°, and West is at 270°. A map of azimuths over the modeling area is presented in Figure 6.5.2.1-5.

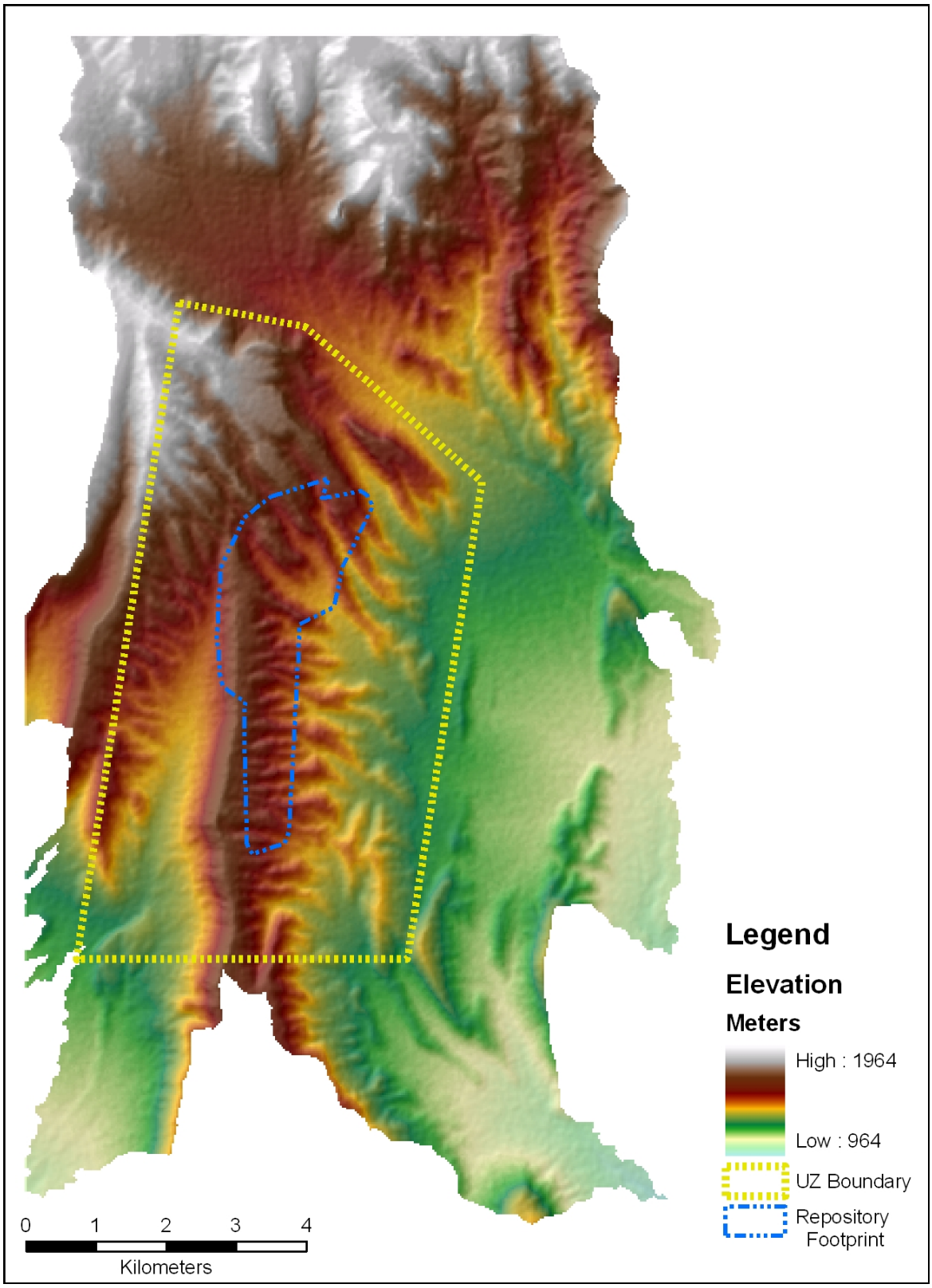

Source: Output DTNs: SN0701SPALAYER.002 and SN0612FTPRNUZB.002.

Figure 6.5.2.1-3. Elevation over the Model Area

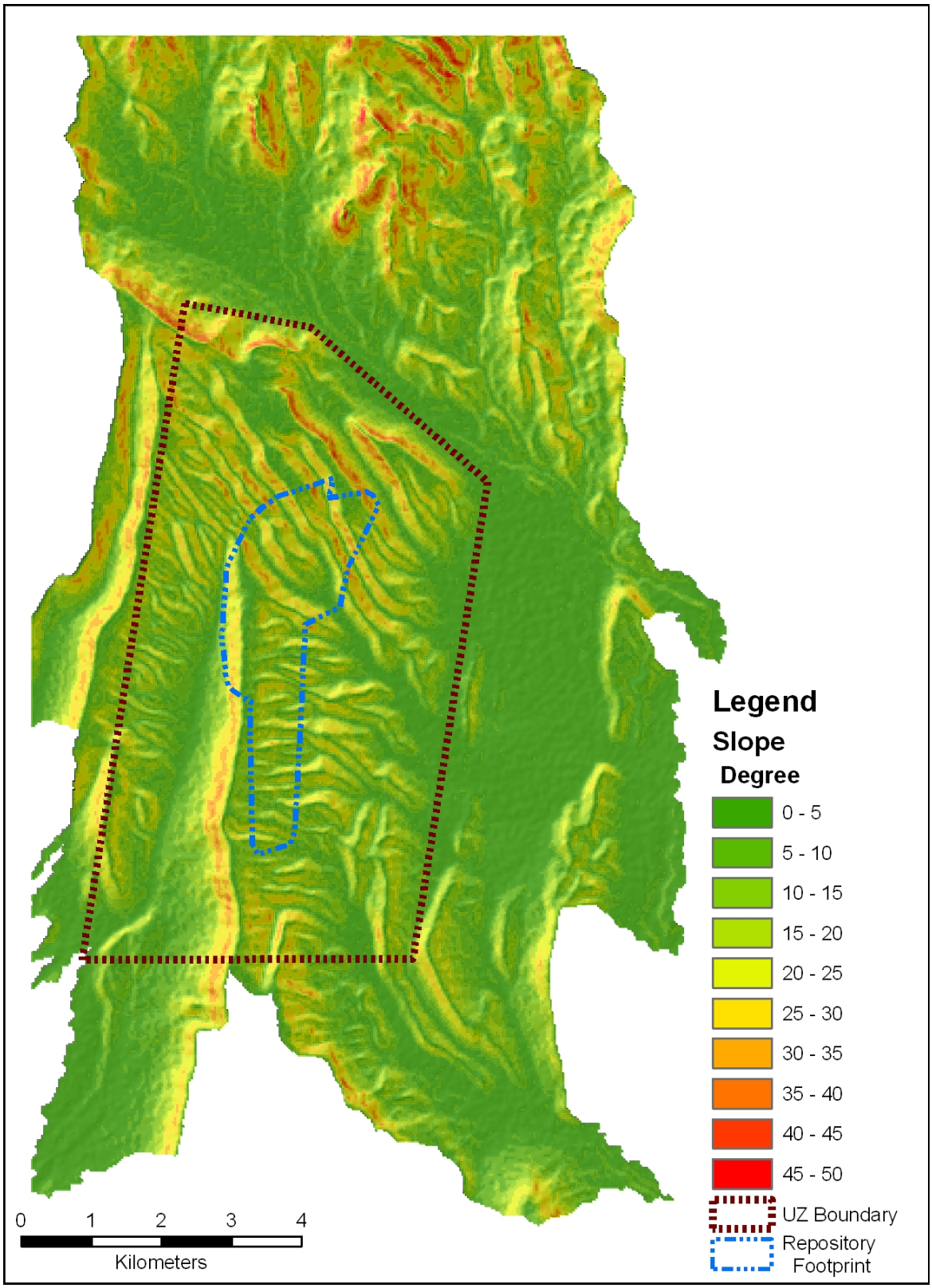

Source: Output DTNs: SN0701SPALAYER.002 and SN0612FTPRNUZB.002.

Figure 6.5.2.1-4. Slope over the Model Area

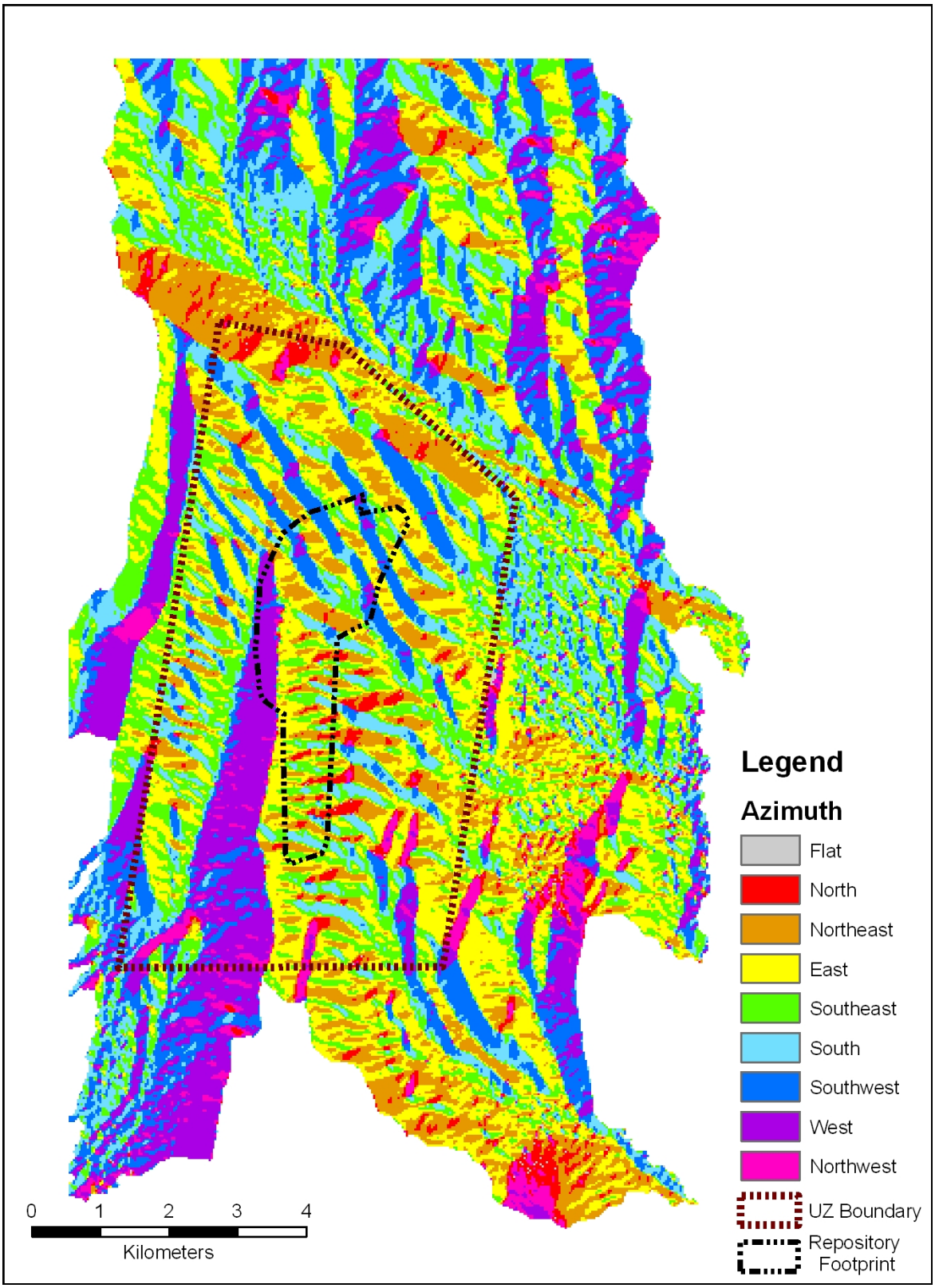

Source: Output DTNs: SN0701SPALAYER.002 and SN0612FTPRNUZB.002.

Figure 6.5.2.1-5. Azimuths for Model Area

Uncertainties in geographic inputs may arise from uncertainties in the underlying SRTM data, as well as processes used to calculate parameters from that data (i.e., slope and azimuth calculations, watershed delineation). To minimize errors caused by transforming grids between coordinate systems and projections, the grid cell locations and elevations for the infiltration modeling domain were based on the locations of the SRTM grid cells. Uncertainties in the SRTM data were analyzed by Rodriguez et al. (2005 [DIRS 177738]) and are discussed in Appendix B. The absolute geolocation error for SRTM data in North America is 12.6 m for a 90% confidence interval. The absolute elevation error for SRTM data in North America is 7 m for a 90% confidence interval.

6.5.2.2 Soil Classification

Yucca Mountain soil classifications and associated hydraulic properties are developed in *Data Analysis for Infiltration Modeling: Development of Soil Units and Associated Hydraulic Parameter Values* (BSC 2006 [DIRS 176335], Section 6.3). That report documents the development of site-specific soil units, hydraulic parameter values for soil units, and associated statistics and uncertainties for Yucca Mountain soils. Soil classifications and mapping based on analyses performed by the USGS in 1996 were evaluated for technical adequacy for use in infiltration modeling. The initial USGS soil classifications were developed from a map of surficial deposits that characterized soil types based primarily on extent of soil development, geomorphic character, and topographic position. These features provide relative ages of deposits (BSC 2006 [DIRS 176335], Section 6.2.1). The original 40 map units were combined into 10 soil units. The group of 10 soil units, referred to as the "base-case" units, is based on depositional character and relative age. The analysis (BSC 2006 [DIRS 176335], Section 6.2.3) concludes that the soil classifications developed by the USGS are appropriate for use in infiltration modeling.

The USGS classifications were also corroborated based on two other soil surveys that were completed for portions of the Yucca Mountain infiltration model area. In a 1989 soil survey, the distribution of four soil units was shown for Yucca Mountain (Resource Concepts 1989 [DIRS 103450], Figure 2). In 2004, a soil survey for the southwestern portion of Nye County was published (USDA 2004 [DIRS 173916]). The Busted Butte quadrangle of the 2004 survey (USDA 2004 [DIRS 173916]) covers the southwest portion of Yucca Mountain, which is administered by the Bureau of Land Management. The 2004 soil survey did not map the two-thirds of the Yucca Mountain infiltration model area that is administered by Nellis Air Force Base or the area that has been set aside for the Nevada Test Site. The mapping of soil units in the 1989 and 2004 soil surveys were compared with the USGS mapping of soil units (BSC 2006 [DIRS 176335], Section 6.2.4). The approach used by these two alternative soil surveys is equivalent to that used by the USGS in that the soils are identified by USDA taxonomic nomenclature and are subdivided by characteristics such as depth to bedrock, the presence or lack thereof of a duripan with depth, or observable pedogenic products. Overall, the 1989 soil survey (Resources Concepts 1989 [DIRS 103450]) and the 2004 soil survey (USDA 2004 [DIRS 173916]) corroborate the Yucca Mountain soil mapping used for input to an infiltration model with regard to approach and definition of units.

Table 6.5.2.2-1 shows the 10 soil classifications that represent the base case evaluated in *Data Analysis for Infiltration Modeling: Development of Soil Units and Associated Hydraulic Parameter Values* (BSC 2006 [DIRS 176335], Section 6.2). These soil types are described in detail that report (BSC 2006 [DIRS 176335], Section 6.2.3.2) based on their taxonomic classifications.

Table 6.5.2.2-1. Base Case Soil Units

Soil Unit	Type of Deposit [a]	Soil Taxonomic Name[a]	Number of 30 × 30-m Cells [b]	Map Area (%) [b]
1	Fluvial	Typic Argidurids	19,900	7.8
2	Fluvial	Typic Haplocalcids	44,065	17.4
3	Fluvial	Typic Haplocambids	33,115	13.1
4	Fluvial	Typic Torriorthents	4,630	1.8
5	Colluvium	Lithic Haplocambids	116,813	46.1
6	Eolian	Typic Torripsamments	12,205	4.8
7	Colluvium	Lithic Hapla	3,154	1.2
8	Bedrock	Rock	795	0.3
9	Colluvium	Typic Calciargids	16,441	6.5
10	Disturbed	Disturbed Ground	2,479	1.0

[a] BSC 2006 [DIRS 176335], Table 6-2.
[b] BSC 2006 [DIRS 176335], Table 6-3, based on a region surrounding the infiltration domain with 253,597 cells.

The distribution of soil types over the infiltration model domain is shown in Figure 6.5.2.2-1. It should be noted that Soil Unit 8 is used to describe regions of bare bedrock and thus does not have any soil properties associated with it. Similarly, Soil Unit 10, which represents only 1% of the map area, is used to identify regions of disturbed soil such as roads and parking areas. For the purpose of modeling infiltration, cells with Soil Unit 10 were replaced with the soil unit surrounding each of these grid cells. Soil Unit 10 is replaced throughout the domain because areas with disturbed soil are not expected to exist on Yucca Mountain over the time scale of interest in this analysis (10,000 years). Nearby soils best represent the soil characteristics of regions that have been disturbed.

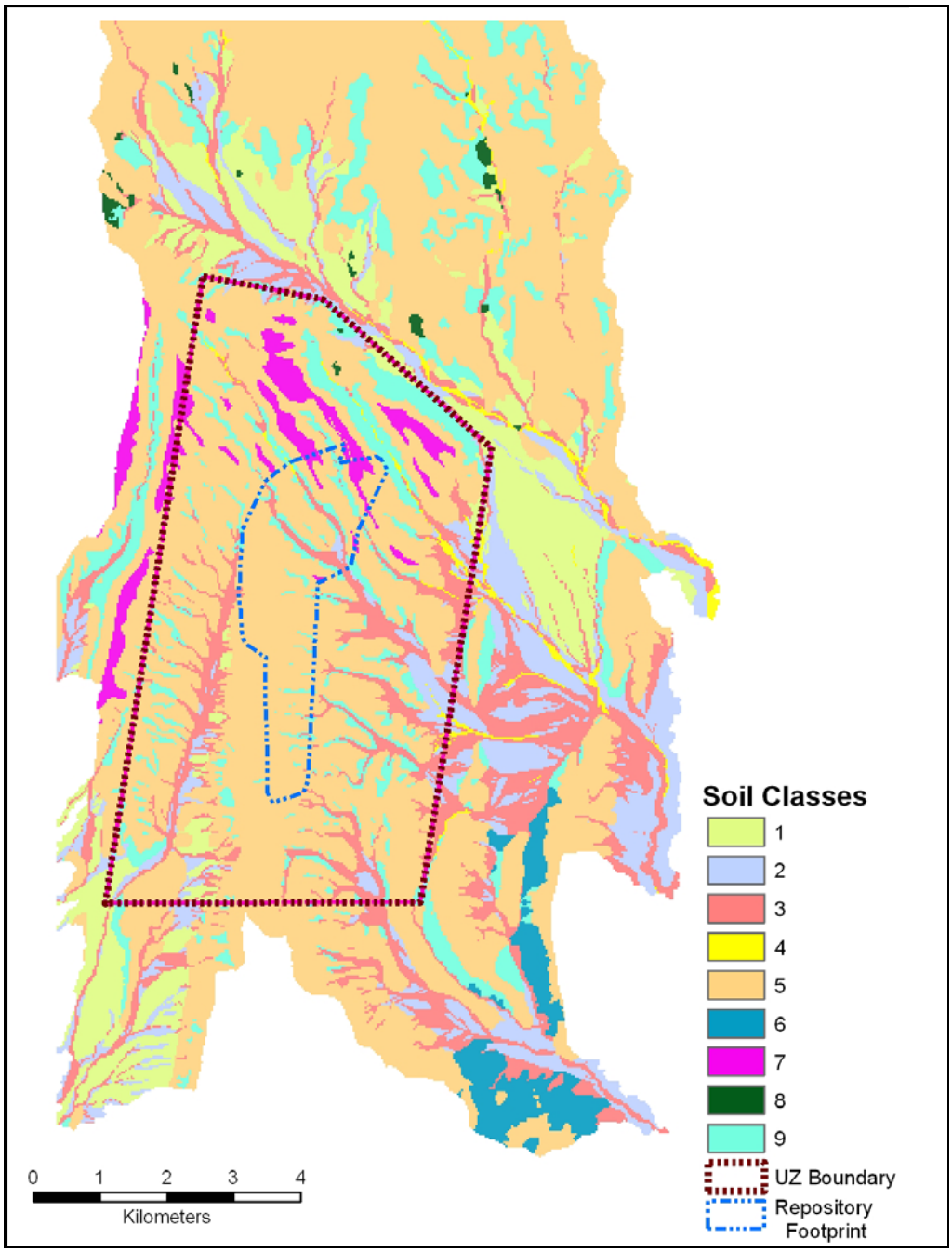

Source: Output DTNs: SN0701SPALAYER.002 and SN0612FTPRNUZB.002.

Figure 6.5.2.2-1. Map Showing Distribution of Soil Types Over the Infiltration Domain

An alternative soil classification system is presented in *Data Analysis for Infiltration Modeling: Development of Soil Units and Associated Hydraulic Parameter Values* (BSC (2006 [DIRS 176335], Section 6.2.5). The alternative soil grouping consists of four soil groups, which are combinations of the eight base case soil units. The four alternative soil groups are: Soil Group 1, Soil Group 2/6, Soil Group 3/4, and Soil Group 5/7/9. The alternative grouping was developed because several of the base case soil units had similar properties but a very limited

number of samples upon which to base the hydrologic properties for each unit. By combining soil units into fewer groups, based on depositional character (e.g., combining the 8 base case soil units into 4 groups), the sample size for each group was increased, thus providing a better basis for performing statistical analysis on the data sets without loss of relevant information or the characterization of uncertainty. Several of the base case soil units had such sparse data that it was not possible to characterize the spatial variability and uncertainty in the hydrologic properties. Figure 6.5.2.2-2 shows the distribution of the alternative soil groups over the infiltration modeling area.

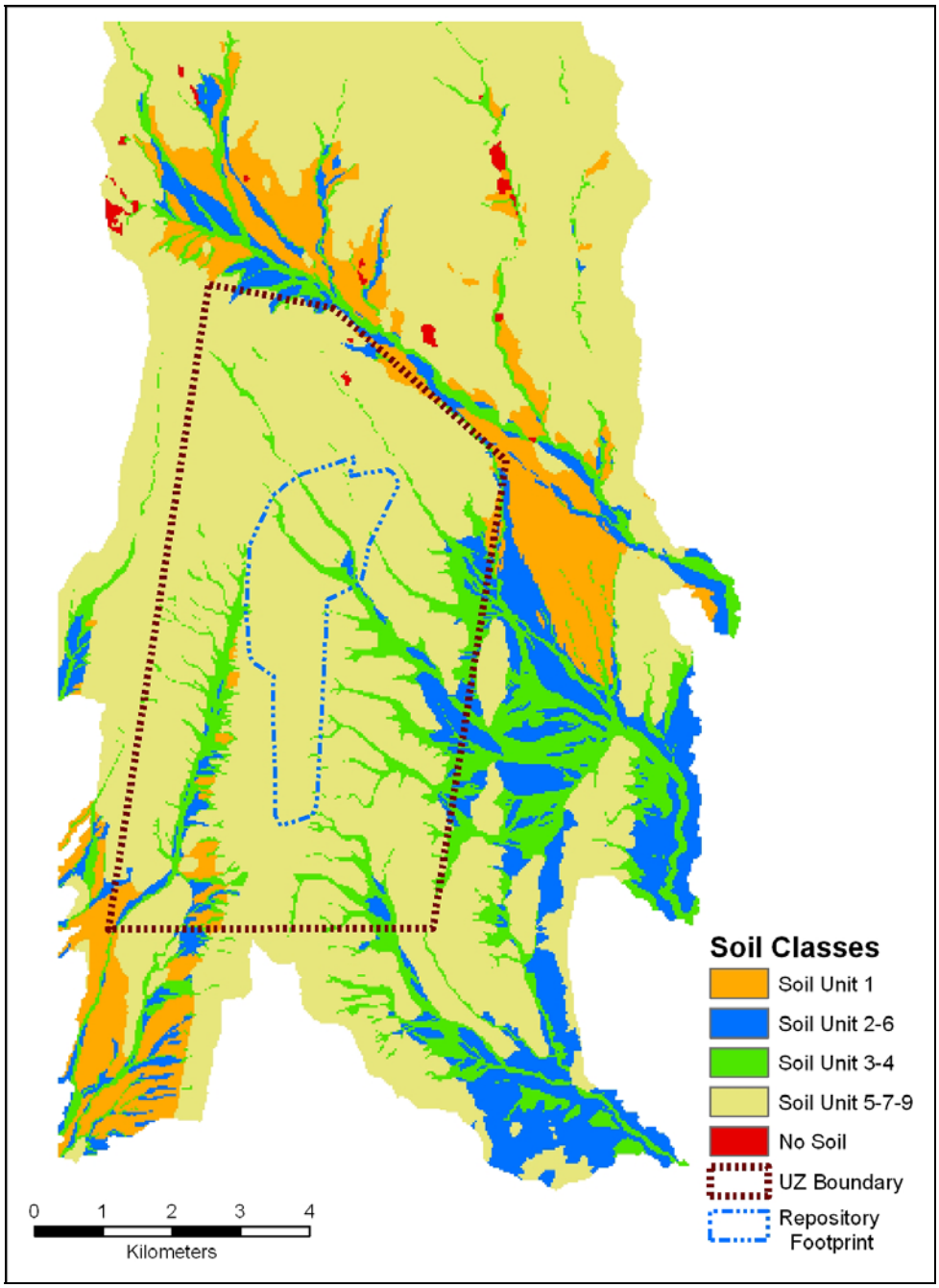

Source: Output DTNs: SN0701SPALAYER.002 and SN0612FTPRNUZB.002.

Figure 6.5.2.2-2. Map Showing Distribution of Alternative Soil Groupings over the Infiltration Domain

This infiltration analysis uses properties derived for the alternative soil grouping; however, the original base case soil unit identifiers are maintained. The base case soil units are the inputs provided in the geospatial database (see Appendix B). In order to use the properties derived for the alternative soil grouping, the appropriate properties are applied to the base case soil units (i.e., Soil Units 2 and 6 have the same properties). Table 6.5.2.2-2 shows how much of the UZ grid and total model domain each soil unit occupies.

Table 6.5.2.2-2. Soil Type Cell Counts for the UZ Grid and Infiltration Model Domain

Soil Unit	Total Cells (UZ Grid)	Percent (UZ Grid)	Total Cells	Percent (Total)
1	972	2	13,860	10
2	1,654	4	12,114	9
3	5,024	11	16,514	12
4	269	1	1,346	1
5	29,359	66	75,591	54
6	0	0	3,103	2
7	1,878	4	3,050	2
8	22	0	431	0
9	5,026	11	13,083	9
Total Cells	**44,204**		**139,092**	

Source: These values were obtained using database applications with input from DTNs: MO0608SPASDFIM.006 [DIRS 178082] (soil type and depth code for each cell) and MO0603SPAGRIDD.003 [DIRS 177121].

6.5.2.3 Soil Properties

Data Analysis for Infiltration Modeling: Development of Soil Units and Associated Hydraulic Parameter Values (BSC 2006 [DIRS 176335], Section 6.3) provides an analysis of soil properties using empirical data including grain-size distribution and fraction of rock fragments derived from laboratory analysis of soil samples collected from Yucca Mountain. Representative hydraulic parameter values of each of the soil units are developed by matching the texture of samples from Yucca Mountain soil units to similar soil textures in an analogous site (Hanford, WA) database (BSC 2006 [DIRS 176335], Section 6.1). The approach (BSC 2006 [DIRS 176335], Section 6.3) is nonparametric and is beneficial when the form of the relationship between the inputs and outputs is not known in advance, such as is the case with soil hydraulic properties.

Yucca Mountain soil samples were divided into 10 "base-case" units, and their respective hydraulic properties were determined based on a pedotransfer function approach. The soil samples were then further grouped into one of four groups that provided larger sample sizes for statistical analysis. The following hydraulic properties were determined for each of the soil groups:

- Saturated hydraulic conductivity (K_{sat_soil}).
- Field capacity (θ_{FC}), defined as the moisture content (m^3/m^3) at –0.33 bar and –0.10 bar. The range between the θ_{FC} at –0.33 bar and –0.10 bar, as well as the standard error, establishes the uncertainty range for this parameter as discussed below.
- Permanent wilting point (θ_{WP}), which is defined as the moisture content (m^3/m^3) at –60 bar.
- Saturated moisture content (θ_s) (m^3/m^3).

- Water holding capacity (θ_{HC}), which is defined as difference between the θ_{FC} and θ_{WP} (for alternative soil groups only) (m^3/m^3).

The parameters θ_{FC}, θ_{WP}, and θ_s were determined from the moisture retention curves (MRCs) provided in the analogous database from Hanford, WA. The MRCs were developed by fitting the van Genuchten soil-moisture retention model to the laboratory data, adjusted for gravel content if necessary. θ_{FC} and θ_{WP} are determined from these MRCs by scaling the appropriate moisture content from the MRC at selected matric potentials (BSC 2006 [DIRS 176335], Section 6.3).

Field capacity has been defined as the soil moisture content at which internal drainage ceases based on observations that the rate of flow and water-content changes decrease with time after a precipitation or irrigation event (Hillel 1980 [DIRS 100583], p. 67). This definition, however, was recognized as imprecise and not an intrinsic soil property independent of the way it is measured (Hillel 1980 [DIRS 100583], p. 68). This concept is most tenable on coarse-textured soils in which internal drainage is initially most rapid but soon slows down owing to the relatively steep decrease of hydraulic conductivity with increased matric potential (Hillel 1980 [DIRS 100583], p. 68). Although matric potentials of −0.33 bar or −0.10 bar have both been used to correlate measurements of soil moisture storage in the field, neither criterion applies universally to all soils and all conditions (BSC 2006 [DIRS 176335], Section 6.3). Therefore, both definitions of field capacity (−0.33 bar and −0.10 bar) have been used to estimate the range of uncertainty in this parameter as described below.

For the inputs to this infiltration model, the θ_{FC} values based on both matric potentials of –0.33 bar and –0.10 bar are used to capture the uncertainty inherent with the field capacity concept. This approach is based on using θ_{WP} and θ_{HC} as infiltration model inputs, from which θ_{FC} is calculated during model execution. The range of θ_{HC} samples incorporates both definitions of θ_{FC}. The minimum θ_{HC} value is the θ_{FC} at –0.33 bars minus the θ_{WP} minus the standard error in θ_{FC}; the upper θ_{HC} value is the θ_{FC} at –0.10 minus the θ_{WP} plus the standard error of θ_{FC}. This approach for determining the range of θ_{HC} values captures the uncertainty in the definition of θ_{FC} as well as the uncertainty in the data, as expressed by the standard error (BSC 2006 [DIRS 176335], Section 6.3). Figure 6.5.2.3-1 shows schematically the process of determining the uncertainty range in θ_{FC}. Once a range of uncertainty is established, a uniform distribution is used to select values over the range, with the nominal value taken as the midpoint of the range.

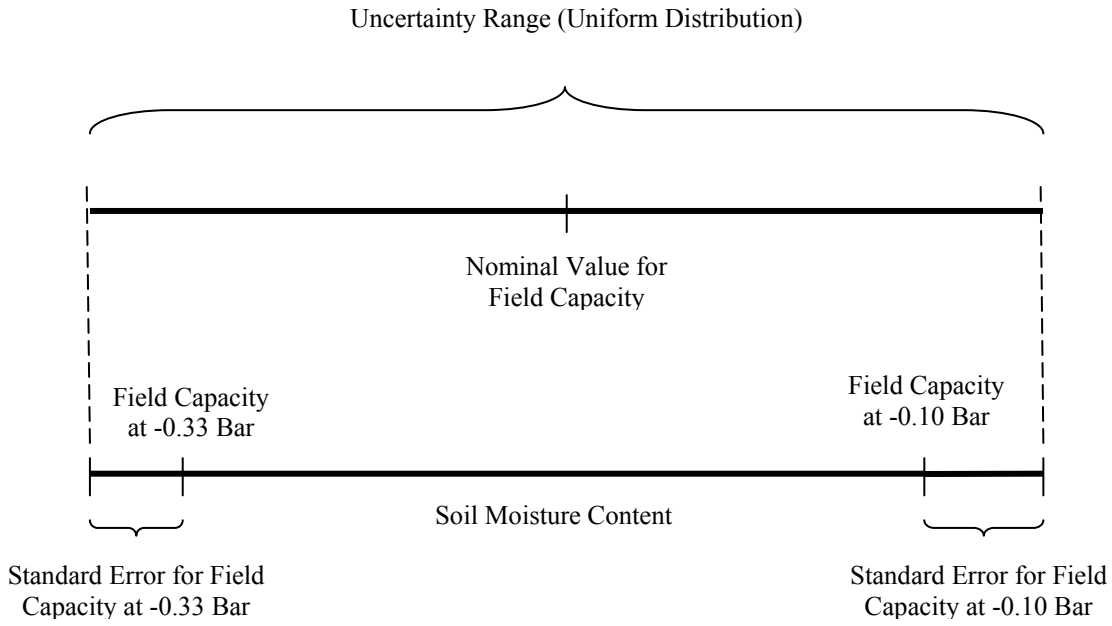

Source: Values defining the uncertainty distribution for each soil group are found in DTN: MO0605SEPALTRN.000 [DIRS 178089], *SoilUnit1FC1-10and1-3Bar_5-30-06.xls*, *SoilUnit2-6FC1-10and1-3Bar_5-30-06.xls*, *SoilUnit3-4FC1-10and1-3Bar_5-30-06.xls*, and *SoilUnit5-7-9 FC1-10and1-3Bar_5-30-06.xls*, worksheet: "HydraulicPropandStatistics."

Figure 6.5.2.3-1. Method for Determining Uncertainty Range in θ_{FC} (or θ_{HC})

The θ_{WP} is the soil moisture content below which plants are unable to withdraw soil moisture and is taken to correspond to −60 bar soil matric potential (BSC 2006 [DIRS 176335], Section 5.5). This matric potential is consistent with the lower limits of soil moisture extraction determined for several Mojave Desert shrubs that can survive soil water potentials as low −50 to −100 bars (BSC 2006 [DIRS 176335], Section 6.3). Like θ_{FC}, the definition of θ_{WP} is imprecise and therefore subject to additional variability and uncertainty as a result of the chosen definition or approach. However, because the permanent wilting point (θ_{WP}) represents the moisture content at the driest region of a soil's MRC, its values do not vary significantly from one definition to another, especially in dry desert soils. Because the θ_{HC} is defined as the difference between θ_{FC} and θ_{WP}, the uncertainty range established in the θ_{HC} captures the entire range of uncertainty of θ_{WP} as well.

Values for each of the soil parameters are given in Tables 6.5.2.3-1 and 6.5.2.3-2. Uncertainty ranges for K_{sat_soil}, θ_s, and θ_{WP} are based on a normal distribution defined with the mean and standard error as reported in DTN: MO0605SEPALTRN.000 [DIRS 178089]. Uncertainty ranges for θ_{FC} and θ_{HC} are based on the ranges described above (see Figure 6.5.2.3-1). The treatment of uncertainties, including the screening of parameters to be propagated in the uncertainty analysis for this report, is discussed in Appendix I.

Table 6.5.2.3-1. Nominal Values and Standard Error for K_{sat}, θ_s, and θ_{WP}

Saturated Hydraulic Conductivity (K_{sat_soil})				
Soil Group	**Mean Ln (K_{sat_soil}), (cm/sec)**	**Standard Error (Ln)**	**Nominal Value (cm/s)[a]**	**Nominal Value (m/s)**
1	−9.436	0.196	7.98×10^{-5}	7.98×10^{-7}
2/6	−9.105	0.175	1.11×10^{-4}	1.11×10^{-6}
3/4	−9.571	0.137	6.97×10^{-5}	6.97×10^{-7}
5/7/9	−9.593	0.079	6.82×10^{-5}	6.82×10^{-7}
Saturated Water Content (θ_s)				
Soil Group	**Mean θ_s (m^3/m^3)**	**Standard Error (m^3/m^3)**	**Nominal Value (m^3/m^3)[b]**	
1	0.23	1.31×10^{-2}	0.23	
2/6	0.21	1.18×10^{-2}	0.21	
3/4	0.16	6.69×10^{-3}	0.16	
5/7/9	0.23	7.61×10^{-3}	0.23	
Permanent Wilting Point (θ_{WP})				
Soil Group	**Mean θ_{WP} (m^3/m^3)**	**Standard Error (m^3/m^3)**	**Nominal Value (m^3/m^3) [b]**	
1	0.040	0.003	0.040	
2/6	0.037	0.003	0.037	
3/4	0.024	0.001	0.024	
5/7/9	0.039	0.002	0.039	

Source: DTN: MO0605SEPALTRN.000 [DIRS 178089], *SoilUnit1FC1-10and1-3Bar_5-30-06.xls,* S*oilUnit2-6FC1-10and1-3Bar_5-30-06.xls*, *SoilUnit3-4FC1-10and1-3Bar_5-30-06.xls*, and *SoilUnit5-7-9 FC1-10and1-3Bar_5-30-06.xls*, worksheet: "HydraulicPropandStatistics."

[a] Nominal values of saturated hydraulic conductivity are equal to exp(ln(K_{sat_soil})) for each soil group.
[b] Nominal values of θ_s and θ_{WP} are equal to mean values of θ_s and θ_{WP} for each soil group.

Table 6.5.2.3-2. Nominal Values and Standard Error for θ_{FC}, and θ_{HC}

Soil Field Capacity (θ_{FC})					
Soil Group	Mean θ_{FC} [a] (−0.10 bar) (m^3/m^3)	Standard Error (m^3/m^3)	Mean θ_{FC} [b] (−0.33 bar) (m^3/m^3)	Standard Error (m^3/m^3)	Nominal Value (m^3/m^3)
1	0.183	0.012	0.125	0.011	0.155
2/6	0.177	0.012	0.123	0.010	0.151
3/4	0.123	0.006	0.075	0.004	0.100
5/7/9	0.208	0.007	0.134	0.005	0.172
Soil Water Holding Capacity (θ_{HC})					
Soil Group	Mean θ_{HC} (−0.10 bar θ_{FC}) (m^3/m^3)	Standard Error (m^3/m^3)	Mean θ_{HC} (−0.33 bar θ_{FC}) (m^3/m^3)	Standard Error (m^3/m^3)	Nominal Value (m^3/m^3)
1	0.143	0.010	0.085	0.009	0.115
2/6	0.140	0.010	0.086	0.008	0.114
3/4	0.098	0.005	0.051	0.003	0.076
5/7/9	0.169	0.005	0.095	0.004	0.133

Source: DTN: MO0605SEPALTRN.000 [DIRS 178089], *SoilUnit1FC1-10and1-3Bar_5-30-06.xls*, *SoilUnit2-6FC1-10and1-3Bar_5-30-06.xls*, *SoilUnit3-4FC1-10and1-3Bar_5-30-06.xls*, and *SoilUnit5-7-9 FC1-10and1-3Bar_5-30-06.xls*, worksheet: "HydraulicPropandStatistics."

[a] Field capacity defined as moisture content at a pressure of −0.10 bar.
[b] Field capacity defined as moisture content at a pressure of −0.33 bar.

6.5.2.4 Soil Depth

Data Analysis for Infiltration Modeling: Technical Evaluation of Previous Soil Depth Estimation Methods and Development of Alternate Parameter Values (BSC 2006 [DIRS 178819], Section 6.2) evaluates soil depths at Yucca Mountain based on an approach that uses qualified data from boreholes, field surficial deposits mapping, and the geologic framework model (GFM) (BSC 2004 [DIRS 170029], Figure 6-10). The evaluation divides the infiltration model area into five soil depth classes. Each soil depth class region is associated with a spatial distribution of soil depth and recommendations on the treatment of soil depth for infiltration modeling. Due to the limited number of qualified measurements of soil depth within each soil depth class, it was decided that an upscaled, effective uniform value of soil depth would be used for each net infiltration realization.

A map of the soil depth classes over the infiltration model domain is given in Figure 6.5.2.4-1. The percentage of the infiltration domain as well as the percentage of the UZ model domain occupied by each soil depth class is given in Table 6.5.2.4-1.

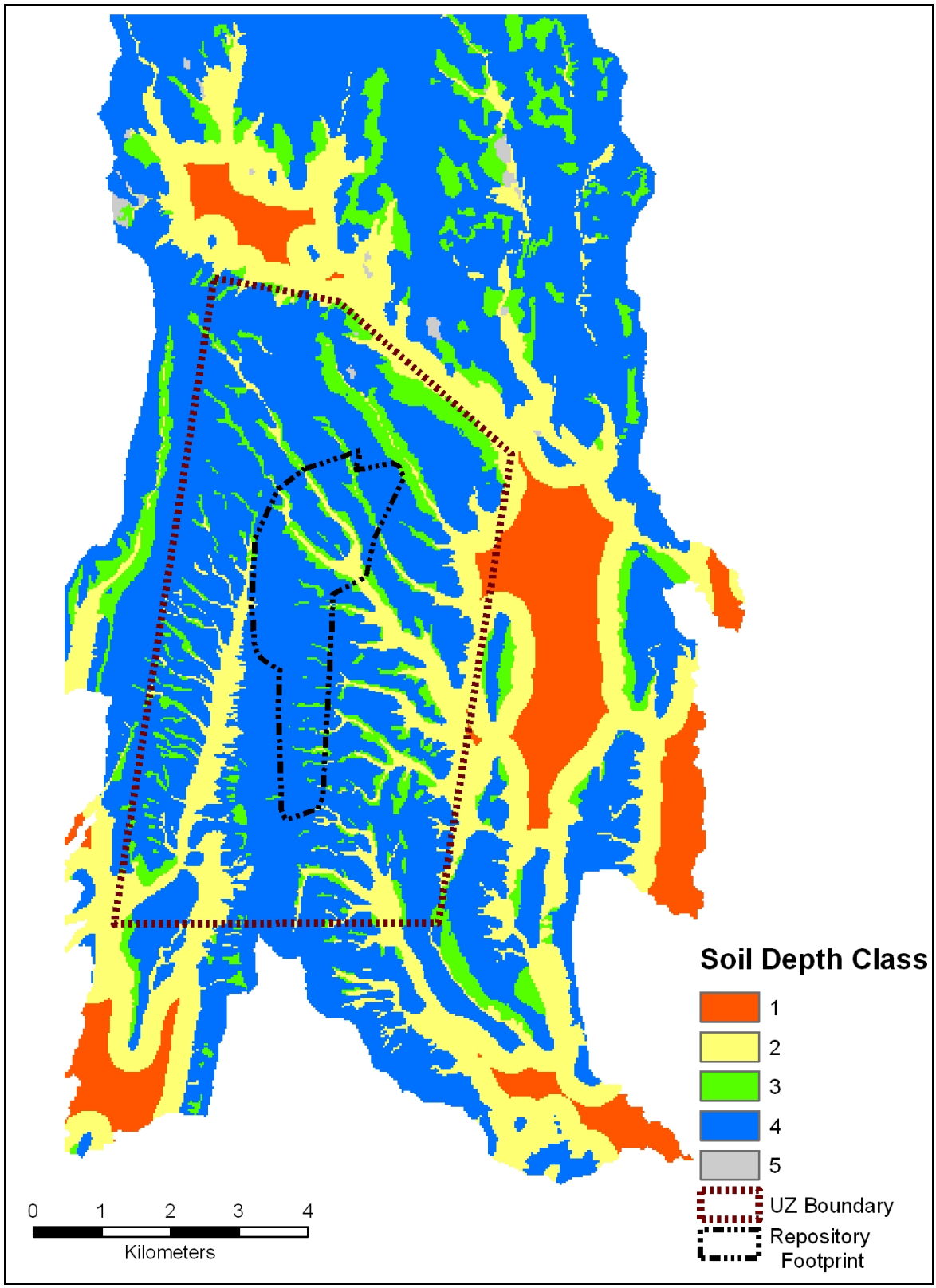

Source: Output DTNs: SN0701SPALAYER.002 and SN0612FTPRNUZB.002.

Figure 6.5.2.4-1. Map Showing Distribution of Soil Depth Classes over the Infiltration Domain

Table 6.5.2.4-1. Soil Depth Class Cell Counts for the UZ Grid and Infiltration Model Domain

Soil Depth Class	UZ Grid Total Cells	Percent (UZ Grid)	Total Cells	Percent (Total)
1	159	0	12,343	9
2	7,687	17	34,479	25
3	5,057	11	13,116	9
4	31,279	71	78,723	57
5	22	0	431	0
Total cells	**44,204**		**139,092**	

Source: These values were obtained using database applications with input from DTNS: MO0608SPASDFIM.006 [DIRS 178082] (soil type and depth code for each cell) and MO0603SPAGRIDD.003 [DIRS 177121].

Soil depth spatial distributions were developed in *Data Analysis for Infiltration Modeling: Technical Evaluation of Previous Soil Depth Estimation Methods and Development of Alternate Parameter Values* (BSC 2006 [DIRS 178819], Section 6.2.2). A discussion is presented in that report to provide recommendations on the spatial distribution of soil depth for each of the soil depth classes, and estimates of the population mean along with confidence intervals. A summary of the recommended soil depth spatial distributions for each depth class is presented in Table 6.5.2.4-2.

Table 6.5.2.4-2. Summary of Recommended Distributions for Soil Depth

Soil Depth Class Designator	1	2	3	4	5
Soil Depth Class	**Very Deep Soils**	**Moderately Deep Soils**	**Intermediate Depth Soils**	**Shallow Soils**	**Exposed Bedrock**
Sample Distribution Type	Uniform	Left-Truncated Normal (truncated at 0.5 m)	Lognormal	Lognormal	Single Value
Sample Mean	N/A	16.47 (m)	3.26 (m)	0.45 (m)	N/A
Sample Mean of the Natural Logarithm	N/A	N/A	0.61 (LN m) (1.84 m)	−1.29 (LN m) (0.27 m)	N/A
Sample Standard Deviation	N/A	14.61 (m)	4.71 (m)	0.67 (m)	N/A
Sample Standard Deviation of the Natural Logarithm	—	—	1.07 (LN m)	0.88 (LN m)	
Sample Standard Error	N/A	1.84	1.22	0.11	N/A
Sample Median (also Estimated Population Median)	95 m	12.19 (m)	2.07 (m)	0.25 (m)	N/A
Sample Minimum Value (m)	40 (m)	0.5	N/A	N/A	0
Sample Maximum Value (m)	150 (m)	64	N/A	N/A	0
Number of Data Points	4	63	15	35	N/A

Table 6.5.2.4-2. Summary of Recommended Distributions for Soil Depth (Continued)

Soil Depth Class Designator	1	2	3	4	5
Soil Depth Class	Very Deep Soils	Moderately Deep Soils	Intermediate Depth Soils	Shallow Soils	Exposed Bedrock
Estimated Population Mean	95 (m)	16.47 (m)	3.25 (m)	0.40 (m)	0
Confidence Interval for Population Mean at 80% Limit	—	14.09 to 18.86 (m)	2.21 to 5.73 (m)	0.33 to 0.52 (m)	N/A
Confidence Interval for Population Mean at 90% Limit	—	13.40 to 19.54 (m)	2.00 to 7.11 (m)	0.31 to 0.57 (m)	N/A
Confidence Interval for Population Median at 80% Limit	N/A	N/A	1.27 to 2.67 (m)	0.23 to 0.33 (m)	N/A
Confidence Interval for Population Median at 90% Limit	N/A	N/A	1.13 to 2.99 (m)	0.21 to 0.35 (m)	NA

Source: DTN: MO0608SPASDFIM.006 [DIRS 178082], *Summary of Recommended Distributions.doc*.

LN = natural logarithm; N/A = not applicable.

The soil depth class spatial distributions discussed in *Data Analysis for Infiltration Modeling: Technical Evaluation of Previous Soil Depth Estimation Methods and Development of Alternate Parameter Values* (BSC 2006 [DIRS 178819], Section 6.2) and displayed in Table 6.5.2.4-2 are subject to several types of uncertainty. Sources of uncertainty include (BSC 2006 [DIRS 178819], Section 6.2.2):

- Natural variability in soil depth that occurs at all scales in the infiltration modeling domain.
- Measurement errors made when determining soil depths at sampling localities.
- Uncertainty resulting from the difficulty in determining the soil–bedrock interface, especially in a borehole. This interface may be difficult to define when it is characterized by rubble or broken and fractured bedrock.
- Uncertainty in the statistical estimation of population parameters derived from a sample consisting of only a few observations from the population.

A summary of the characteristics of each depth class, including recommended distributions for the effective uniform soil depth to be used in the infiltration modeling, which are based on an analysis of the uncertainty in the parameters, is provided in *Data Analysis for Infiltration Modeling: Technical Evaluation of Previous Soil Depth Estimation Methods and Development of Alternate Parameter Values* (BSC 2006 [DIRS 178819], Section 6.2.3) and quoted below for all soil depth classes except Soil Depth Class 4, which is treated in more detail in the next section. The distributions used to represent the effective soil depth for these classes in this analysis are listed in Table 6.5.2.4-3.

Effective Soil Depth for Soil Depth Class 1 ($depth_{soil(1)}$)

This depth class represents very thick soils, described by a uniform distribution with lower and upper bound values of 40 and 150 m, respectively. Because this class represents depths much deeper than the rooting depth (below which water is not removed by the infiltration model), using a representative value equal to the mean for the class of 95 m is appropriate. Because soil depths in this class are large and infiltration is expected to be small, the specific value chosen within this range is unlikely to cause a significant change to predicted infiltration.

Effective Soil Depth for Soil Depth Class 2 ($depth_{soil(2)}$)

This depth class represents moderately deep soils that range in depth from 0.5 m to about 50 m. This class is intended to include the value where soil depth is sufficient to limit infiltration of water to the soil–bedrock contact, except in some channels, because the soils have sufficient storage capacity to retain precipitation in the root zone where it is subject to evapotranspiration. It is expected that infiltration in the Soil Depth Class 2 areas is most likely to occur where soil thickness is small. Consequently, the appropriate bulk parameter value will lie closer to the small soil thickness portion of the distribution, rather than near the large soil thickness values.

Effective Soil Depth for Soil Depth Class 3 ($depth_{soil(3)}$)

This depth class represents areas of thicker foot-slope soils that occur intermittently in the area. The data are represented by a lognormal distribution with an estimated population mean soil depth of 3.25 m and a sample median of 2.07 m, which is also the estimated population median; only one value is larger than 5.18 m (BSC 2006 [DIRS 178819], Figure 6-15 and Table 6-7). As seen in Figure 6.5.3.4-1, Depth Class 3 is most often found between soils of Depth Class 2 (moderately deep) and Depth Class 4 (shallow), acting as a transition from deeper to shallower soils. The depth in Soil Depth Class 3 will be small where it contacts Soil Depth Class 4 but increases where it contacts deeper depth classes, primarily Soil Depth Class 2. The majority of infiltration through Soil Depth Class 3 will occur where the depth is small. The appropriate effective uniform depth for Soil Depth Class 3 is a value that allows for the same total infiltration, through all of Soil Depth Class 3, as occurs through the spatially variable material that exists in nature. Estimating a uniform value for this depth class is especially challenging. There are very few measurements for this depth class (15 measurements, four of which indicate that there is no soil). Many of these measurements may represent disturbed regions where drilling pads were constructed and, thus, may not represent actual soil depth. Although it is common to choose the median of a lognormal distribution as a measure of central tendency, the potential underestimate previously noted suggests that the sample mean is a better measure of central tendency in this case. The 90% confidence interval about the mean ranges from 2 m to 7 m, where the lower bound of this range is approximately the median.

Effective Soil Depth for Soil Depth Class 5 ($depth_{soil(5)}$)

This class represents exposed bedrock in the area that does not have soil cover. Therefore, all cells in this class should be assigned a zero soil depth value.

Table 6.5.2.4-3 summarizes recommended distributions for all five soil depth classes.

Table 6.5.2.4-3. Summary of Recommended Distributions for Effective Soil Depths ($depth_{soil}$)

Soil Depth Class	Lower bound Soil Depth (m)	Upper Bound Soil Depth (m)	Nominal Value Soil Depth (m)	Distribution	Comments
1	N/A	N/A	95	Constant	Estimated population mean
2	N/A	N/A	16.47	Constant	Estimated population mean
3	N/A	N/A	3.26	Constant	Sample mean
4	0.1	0.5	0.25	Uniform	See Section 6.5.2.4.1
5	N/A	N/A	0	Constant	—

6.5.2.4.1 Effective Soil Depth Distribution for Soil Depth Class 4

Estimating the distribution of effective soil depth for this soil depth class is especially important because of the significant sensitivity of net infiltration to shallow soil depth and the large relative proportion of the modeling domain covered by this soil depth class. These two reasons prompted a more detailed analysis of shallow soil depth uncertainty than provided in *Data Analysis for Infiltration Modeling: Technical Evaluation of Previous Soil Depth Estimation Methods and Development of Alternate Parameter Values* (BSC 2006 [DIRS 178819], Section 6.2.2).

One upscaled value of soil depth is used to represent the spatial variability in Soil Depth Class 4 for each realization. The estimation of uncertainty in this upscaled depth is calculated from a two-steps process. The first step consists of determining a spatial distribution for Soil Depth Class 4. The second step is to determine which statistic in this distribution is an adequate upscaled soil depth (in the sense that it will lead to a reasonable estimate of spatially averaged infiltration).

Estimation of the Spatial Distribution of Soil Depth

In *Data Analysis for Infiltration Modeling: Technical Evaluation of Previous Soil Depth Estimation Methods and Development of Alternate Parameter Values* (BSC 2006 [DIRS 178819], Section 6.2.2), the spatial distribution of soil depth is represented by a lognormal distribution, estimated using probability plot fitting. This depth class is described by 35 individual measurements over an area of approximately 71 km^2. That report (BSC 2006 [DIRS 178819], Section 6.2.2) assigned each observation a distinct quantile value, even when duplicate values of soil depth were measured at different locations. Duplicate soil depth values should reflect the same quantile. Therefore, in this analysis the distribution fitting has been redone (although the probability plot fitting described below leads to nearly the same result). Two methods are applied for estimating parameters that define the lognormal distribution from the 35 observations: probability plotting and least-squares fitting. The updated fitting of these 35 observations is made in Output DTN: SN0612T0502206.039.

The first method of estimating the underlying lognormal distribution is based on a probability plot where the vertical axis represents the ordered values, while the horizontal axis represents the standard normal order distances (description of Normal Probability Plot can be found in NIST online statistical handbook at http://www.itl.nist.gov/div898/handbook/eda/section3/*normprpl.htm*). If the distribution is close to normal, then the points are linearly distributed on

the plot. The mean and standard deviation of the distribution corresponds to the Y-intercept and slope of a linear regression model, respectively.

The resulting probability plot is shown in Figure 6.5.2.4-2. The estimates for the mean and standard deviation are −1.295 and 0.93, respectively.

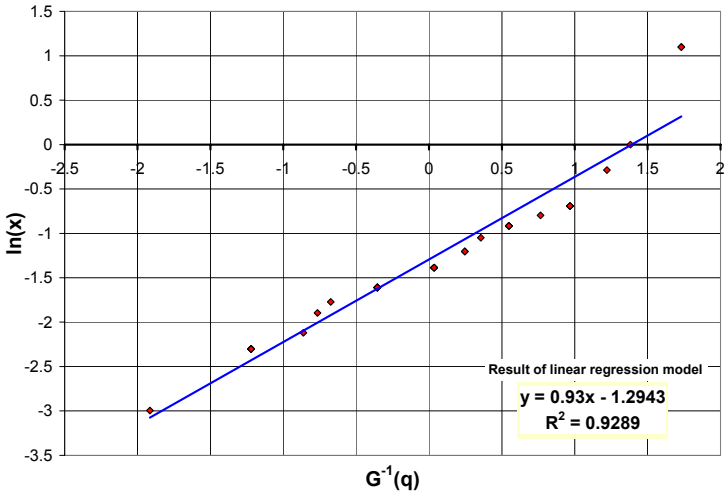

Source: Output DTN: SN0612T0502206.039, *LN_fitting_upper_bound_V2.0_12_2006.xls*. Data from DTN: GS011208312212.004 [DIRS 176317], Table S02086_001.

NOTE: Only 15 observations are displayed, as duplicates are assigned with an average quantile value.

Figure 6.5.2.4-2. Normal Probability Plot for 35 Observations of Soil Depth in Soil Depth Class 4 Region

The second method consists in fitting a lognormal distribution, such that the sum of the squared differences between the quantiles of the observed values and the quantiles of such values in the lognormal distribution is minimized.

The cumulative distribution functions (CDFs) of both lognormal fitted distributions compared with observed values are displayed in Figure 6.5.2.4-3, showing good agreement between the data and both fitting methods.

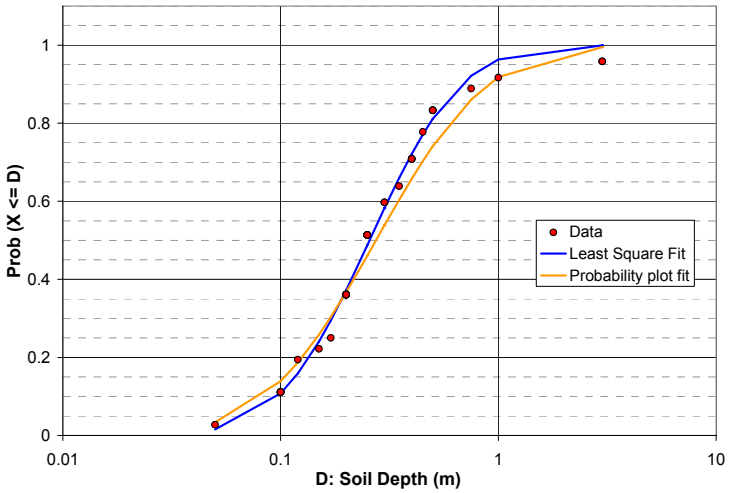

Source: Output DTN: SN0612T0502206.039, *LN_fitting_upper_bound_V2.0_12_2006.xls*. Data from DTN: GS011208312212.004 [DIRS 176317], Table S02086_001.

Figure 6.5.2.4-3. CDFs for 35 Observations (red plots), Least-square Fitted Lognormal Distribution (blue line), and Probability Plot Fitter Lognormal Distribution (orange line) in Log-scale for Soil Depth (X-axis)

However, it is unclear how well the 35 observations represent the actual spatial distribution of this soil depth class. There may be a bias toward deeper soils since none of the 35 observations include soil depth of 0 m, while observations of patches of bare rock have been made in the area covering Soil Depth Class 4 during field trips to the site. Moreover, the specific locations of observations are not documented, and it is likely that these locations were not randomly selected.

For this reason, a second source of information was used to create a second spatial distribution of shallow soil depth (Sanchez 2006 [DIRS 176569], pp. 62 to 68). This scientific notebook contains observations made by Alex Sanchez in several places at Yucca Mountain. The exact position of the observations is not known, although most of the observations are for shallow soil and should correspond to regions of Soil Depth Class 4. The observations from the scientific notebook are listed below:

Observations:

Page 62: (NRG-3 pad) Soil Depth from 0.3 to 0.5 m
Page 63: (Close up view NRG-3 pad) captured above – not considered
Page 64: (bleach bone ridge) half of the image is covered with rock (0 m) – the remaining part is with soil from 0.1 to 0.3 m
Page 65: (bleach bone ridge) same measurement as p. 3 – not considered
Page 66: (Above SD-9 pad) Soil Depth from 0 to 0.09 m
Page 67: (Yucca Crest) Soil range from 0 to 0.3 m
Page 67: (bleach bone ridge) consistent with p. 3 – not considered
Page 68: (tonsil ridge top) no soil – 0 m
Page 68: (tonsil ridge side-slope) thin soil 0.1 m
Page 68: (tonsil ridge foot-slope) up to 3 m – range from 0.1 to 3 m.

Out of these ten observations, three were not considered (as indicated above) as they concerned already included regions. One observation was split in two (p. 64) because two different patterns are seen in the photograph (one with soil and one with no soil). As a result, the new distribution was defined with eight ranges. Each range has been weighted equally (a weight of 1/8). The resulting ranges are listed in Table 6.5.2.4-4.

Table 6.5.2.4-4. Summary of Soil Depth Ranges Defined Based on Alex Sanchez Observations

Reference	Location Description	Minimum (m)	Maximum (m)	Weight	Page
A	NRG-3 pad	0.3	0.5	0.125	62
(not considered)	NRG-3 pad (closeup)	—	0.3	—	63
B	Bleach Bone Ridge (no soil)	0	—	0.125	64
C	Bleach Bone Ridge (soil)	0.1	0.3	0.125	64
(not considered)	Bleach Bone Ridge	0.1	0.3	—	65
D	SD-9 pad	0	0.09	0.125	66
E	Yucca Crest (natural)	0	0.3	0.125	67
(not considered)	Bleach Bone Ridge	0.2	0.2	—	67
F	Tonsil Ridge (Top)	0	0	0.125	68
G	Tonsil Ridge (Side)	0.1	0.1	0.125	68
H	Tonsil Ridge (Foot)	0.1	3	0.125	68

Source: Output DTN: SN0612T0502206.039, *Lower_Bound_distribution_V4.0_12_05_2006.xls*. Data from Sanchez 2006 [DIRS 176569].

All but one interval (Reference H in Table 6.5.2.4-4) were represented with a uniform distribution. The soil depth range for the Tonsil Ridge Foot (Reference H) is significantly larger than for the other observations. Therefore, it seems reasonable to increase the likelihood of values closer to the lower bound (i.e., 0.1 m), and a loguniform distribution was used instead of a uniform distribution. This approach is consistent with what was observed in the previous set of data (BSC 2006 [DIRS 178819]), for which two values are equal to 3.0 m, but no observations have been made between 1.0 and 3.0 m.

Two of the ranges included a component of bare rock (no soil) and result in lower bound values of zero (for which logarithm is not defined). In order to be able to work with log-transformed data, the distribution is defined starting with the 0.25 quantile (as a quarter of the distribution is equal to 0), and the remaining observations are associated with an equal weight of 1/6. This is consistent with the previously defined weight, as a weight of 1/6 for 3/4 of the distribution corresponds to a total weight of 1/8.

To represent the piecewise distribution, a series of two random numbers was generated; the first was used to randomly select one of the six predefined bins, and the second was used to sample a soil depth from within the selected bin. This bootstrapping approach was repeated 1,000 times to create a distribution. The resulting distribution is displayed in Figure 6.5.2.4-4.

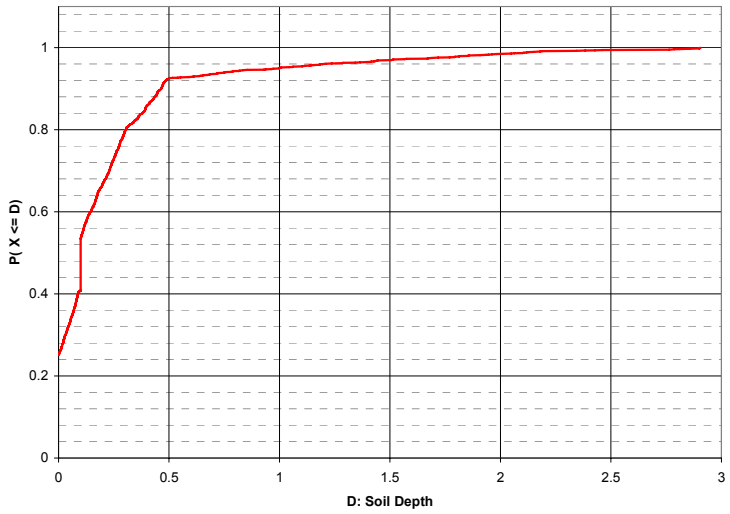

Source: Output DTN: SN0612T0502206.039, *Lower_Bound_distribution_V4.0_12_05_2006.xls*. Data from Sanchez 2006 [DIRS 176569].

Figure 6.5.2.4-4. CDF of Estimated Distribution Constructed with Eight Intervals Estimated from Alex Sanchez Notebook

The two fitting methods described above (probability plotting and least squares) were applied to the soil depth ranges obtained from the scientific notebook. However, because 25% of the distribution is equal to 0 m and a lognormal distribution is not defined for values of zero, each of these fitting methods had to be modified. Two approaches were considered for modifying the fitting methods:

- In the first approach, it is assumed that the information available is known only for values greater than zero and that nonzero values represent only 75% of the distribution. This assumption allows calculation of the arithmetic and geometric means of the fitted lognormal distributions directly, but it does not necessarily result in a good fit.

- In the second approach, it is assumed that the distribution is bimodal. Like the first approach, the fitting is done with nonzero values; however, they are considered to represent the whole distribution. The final estimates of the arithmetic and geometric means are corrected to include 25% of zero values. This approach leads to a better fit but makes the estimation of the geometric mean more difficult.

The normal probability plot is displayed in Figure 6.5.2.4-5, for both approaches. Not considering the first quarter of the distribution (first approach) leads to an asymmetry in the plot on the left (as the X-axis goes from about −0.6 to 3.2). The fit is linear except near the edges. If nonzero values are assumed to represent the whole distribution (second approach; right frame), the fit is better even near the edges.

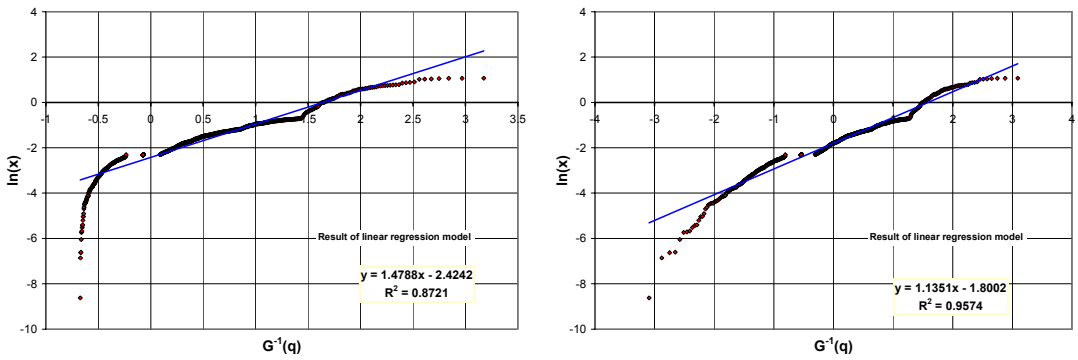

Source: Plots are produced in Output DTN: SN0612T0502206.039, *LN_fitting_lower_bound_V2.0_12_01_2006.xls*. The plot on the left is generated by setting the cell C2 on sheet "Calculations" to a value of 0.25. The plot on the right is generated when this cell is set to a value of zero. Data is from Sanchez 2006 [DIRS 176569].

NOTE: In the left frame, the non-zero values are considered to represent 3/4 of the distribution. In the right frame, the non-zero values represent the whole distribution.

Figure 6.5.2.4-5. Probability Plot for Estimated Distribution Based on Alex Sanchez Notebook

A least square fitting approach (based on quantile values) has been applied to generate a second distribution using both approaches (Figure 6.5.2.4-6).

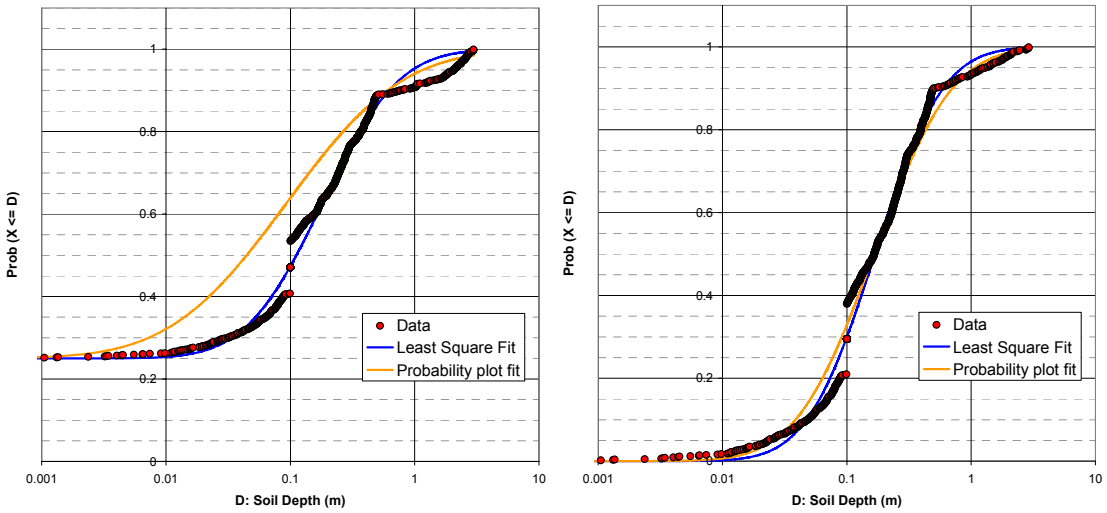

Source: Plots are produced in Output DTN: SN0612T0502206.039, *LN_fitting_lower_bound_V2.0_12_01_2006.xls*. The plot on the left is generated by setting the cell C2 on sheet "Calculations" to a value of 0.25. The plot on the right is generated when this cell is set to a value of zero. Data is from Sanchez 2006 [DIRS 176569].

NOTE: In the left frame, the non-zero values are considered to represent 3/4 of the distribution. In the right frame, the non-zero values represent the whole distribution.

Figure 6.5.2.4-6. CDFs for Estimated Distribution (red plots), Least-Square Fitted Lognormal Distribution (blue line), and Probability Plot Fitter Lognormal Distribution (orange line)

Regardless of the approach, the least-square fitting method results in a good fit for low values of soil depth (0 to 50 cm) but cannot capture the distribution behavior for deeper soils.

The probability plot fitting method does not fit the distribution for shallow soil using the first approach, but the fit for deeper soil is better. The second approach results in a reasonably good fit for shallow soil and better fit for deeper soil than the least square method.

Estimation of Upscaled Distribution of Soil Depth for Soil Depth Class 4

Because of nonlinearities between soil depth and average net infiltration, it is difficult to determine which statistic would best represent an effective uniform value of soil depth that would lead to an accurate estimate of spatially averaged net infiltration.

In hydrologic modeling, flow parameters such as permeability (typically represented with a lognormal spatial distribution) are generally upscaled to the geometric mean, and storage parameters such as porosity (typically represented with a normal spatial distribution) are typically upscaled to the arithmetic mean. Soil depth follows a lognormal spatial distribution but is a storage-type parameter. Therefore, it is hypothesized that the upscaled value should lie between the geometric and arithmetic means.

Both arithmetic and geometric means have been estimated for the fitted lognormal distributions as well as their standard errors (where standard error for geometric mean is based on the standard deviation of log-transformed data). A confidence interval has been estimated by adding or subtracting one standard error to the quantity of interest. The results are displayed below for geometric mean (Table 6.5.2.4-5) and arithmetic mean (Table 6.5.2.4-6). Confidence intervals are rounded to the first significant digit because an examination of the underlying observations seems to suggest that soil depths were generally measured or estimated to the nearest 5 cm, especially for deeper soils. Furthermore, because it can be difficult to identify the exact location of the soil–bedrock interface, it is assumed that the accuracy of the observations is only good to about 5 cm and certainly not to as little as 1 cm. For the first distribution (i.e., based on 35 observations) and for the second distribution using the first approach (i.e., considering non-zero values represents 75% of the distribution), the calculation of arithmetic and geometric means is straightforward. For the second approach on the second data set (scientific notebook), the estimate of both means has to be corrected to incorporate the second part of the bimodal distribution with values of zero soil depth.

Table 6.5.2.4-5. Estimation of Geometric Mean and Confidence Interval (by adding or subtracting one standard error)

	Estimation (log space)	Standard Error (log space)	Lower Bound (linear space)	Upper Bound (linear space)
First distribution a – Probability plot fitting	−1.2943189	0.157199	0.2	0.3
First distribution – Least Square fitting	−1.3625023	0.128382	0.2	0.3
Second distribution (1st approach) – Probability plot fitting	−2.3836264	0.053545	**0.1**	**0.1**
Second distribution (1st approach) – Least Square fitting	−1.7109852	0.035243	0.2	0.2
Second distribution – (2nd approach) – Probability plot fitting	−1.80019	0.035895	**0.1**[a]	**0.1**[a]
Second distribution – (2nd approach) – Least Square fitting	−1.78324	0.031237	**0.1**[a]	**0.1**[a]

[a] Lower and upper confidence bounds (CB) are first estimated in log scale using mean and standard deviation, and then corrected using the formula 0.75*CB+0.25*ln(0.01) – results are then calculated using an exponential function.

Table 6.5.2.4-6. Estimation of Arithmetic Mean and Confidence Bounds (by adding or subtracting one standard error)

	Estimation	Standard Error	Lower Bound	Upper Bound
First distribution – Probability plot fitting	0.4223722	0.08371	0.3	**0.5**
First distribution – Least Square fitting	0.3416151	0.051012	0.3	0.4
Second distribution (1st approach) – Probability plot fitting	0.3867008	0.0498	0.3	0.4
Second distribution (1st approach) – Least Square fitting	0.3362301	0.016686	0.3	0.4
Second distribution – (2nd approach) – Probability plot fitting	0.314756	0.016133	0.2[a]	0.2[a]
Second distribution – (2nd approach) – Least Square fitting	0.273798	0.011132	0.2[a]	0.2[a]

[a] Lower and upper confidence bounds (CB) are first estimated using mean and standard deviation and then corrected using the formula 0.75*CB+0.25*0.

The correction is applied directly on the lower and upper confidence bounds, as it is not possible to estimate directly the updated standard deviation.

The estimate of arithmetic mean is done by simply summing, for each bound, 75% of the previous value, to 25% of a value of 0.

The estimate of geometric mean is more difficult. Indeed, if any of the values of the distribution are equal to zero, the geometric mean is equal to zero. Thus, the inclusion of zero values will lead to a useless estimate. One solution to this problem is to associate a very small (constant) value to represent the fraction of the spatial distribution with zero soil depth. Of course, as the geometric mean is equivalent to an arithmetic mean calculated on log-transformed data, taking a value too small will lead again to a very low value of the geometric mean. Therefore, it was assumed that the presence of 1 cm of soil is essentially equivalent to there being no soil in regards to the resulting net infiltration. The geometric mean was then estimated using log-

transformed data, estimating the mean and its confidence bounds, summing 75% of these bounds with 25% of the logarithm of 0.01 m (approximately −4.6), and exponentiating the results to convert to a linear scale. Higher values of soil, from 2 to 9 cm, have been tested to represent the fraction of bare rock and to estimate the sensitivity of confidence bounds to the selected values. With a 10-cm accuracy, all values lead to the same confidence interval.

The minimum value estimate is equal to 0.1 m (bounds for geometric mean using probability plot fitting method on second data set using first approach and geometric mean on second data set using second approach). The maximum is equal to 0.5 m (upper bound of arithmetic mean using probability-plot fitting method on first dataset). Because there is no reason to favor any of these values (or any intermediate value), it has been decided to consider a uniform distribution between 0.1 m and 0.5 m to represent uncertainty in the upscaled quantity used to represent effective uniform value of Soil Depth Class 4.

6.5.2.5 Bedrock Classification

An infiltration hydrogeologic unit (IHU) system was developed consisting of bedrock types (IHUs) that have differing hydrogeologic properties with special emphasis on hydraulic conductivity (BSC 2006 [DIRS 176355], Section 6.2). The IHUs are defined on the basis of lithostratigraphic contacts in boreholes (BSC 2004 [DIRS 170029]). The correlation of lithostratigraphic units and IHUs enables the extrapolation of the IHUs to exposures at the ground surface where most of the correlated lithostratigraphic units have been documented on the following geologic maps:

- Preliminary Geologic Map of Yucca Mountain, Nye County, Nevada, with Geologic Sections (Scott and Bonk 1984 [DIRS 104181])

- Bedrock Geologic Map of the Central Block Area, Yucca Mountain, Nye County, Nevada (Day et al. 1998 [DIRS 101557])

- Digital Geologic Map of the Nevada Test Site and Vicinity, Nye, Lincoln and Clark Counties, Nevada, and Inyo County, California, Revision 4; Digital Aeromagnetic Map of the Nevada Test Site and Vicinity, Nye, Lincoln, and Clark Counties, Nevada, and Inyo County, California; and Digital Isostatic Gravity Map of the Nevada Test Site and Vicinity, Nye, Lincoln, and Clark Counties, Nevada, and Inyo County, California (Slate et al. 2000 [DIRS 150228]).

For map units that do not have any correlative IHUs, proxy IHUs have been proposed that are based on similarities in lithostratigraphic characteristics. These correlations of IHUs to lithostratigraphic units to map units are the basis for the new bedrock hydraulic conductivity map (Figure 6.5.2.5-1).

The infiltration model uses an input file containing 253,597 records of data with each record corresponding to a 30 × 30-m grid cell in the model area. The model area includes the entire Busted Butte 7.5 min quadrangle and the southern half of the Topopah Spring NW 7.5 min quadrangle. Because bedrock hydrologic properties are assigned on the basis of lithology, bedrock geologic units were assigned to each grid cell. This was accomplished with a digital

manipulation of existing geologic mapping data covering the area (BSC 2006 [DIRS 176355], Section 6.2.2).

In DTN: MO0603SPAGRIDD.003 [DIRS 177121] (*IHU_map_file2.txt*), each comma delimited record includes fields representing x- and y-coordinates for the center of the associated 30 × 30-m cell. The lithologic mapping unit corresponding to the center-cell coordinates was determined from the source polygon coverages using both ARCINFO and EarthVision (BSC 2006 [DIRS 176355], Section 6.2). The source files use a number code to designate stratigraphic units in the digital coverage files. The stratigraphic unit identified is shown at the point at the center of the cell in the "Geology" field of DTN: MO0603SPAGRIDD.003 [DIRS 177121].

The use of the center point of a grid cell to determine lithology can result in a generalization of the bedrock geology from that shown on the source maps. Cells that contain contacts between two or more units have been generalized to the unit found at the center of the cell. This means that thin units may occasionally be under- or over-represented in the file or that contacts may be displaced by up to 15 m. Given that the infiltration model contains over 250,000 cells, this level of generalization is considered acceptable for the purposes of the infiltration model when the natural variation within each lithologic unit and the uncertainties regarding the properties assigned to each unit are considered.

The three source maps (DTNs: GS971208314221.003 [DIRS 107128], *cb6k.ps*; MO0003COV00095.000 [DIRS 146848], *scotbons.e00*; and MO0603GSCGEOMP.000 [DIRS 176585], *ofr-99-0554-e00.tar*) each show significant areas covered by deep Quaternary alluvium (BSC 2006 [DIRS 176355], Figures 6-3, 6-4, and 6-5). Since the infiltration model needs the bedrock types underlying this alluvium to calculate infiltration into the bedrock from any water that percolates through the alluvium and reaches the bedrock contact, the GFM (DTN: MO0012MWDGFM02.002 [DIRS 153777]) was queried, and all cells within the GFM range that were classified as alluvial type were identified according to their underlying bedrock type (BSC 2006 [DIRS 176355], Section 6.2.2). Areas on the north, east, and south edges of the model area are not covered by the GFM and are still shown as alluvium (IHUs 490 and 491) in Figure 6.5.2.5-1. For infiltration modeling, the bedrock conductivity report (BSC 2006 [DIRS 176355], Section 7) recommends that the saturated hydraulic conductivity value for IHU 405 be used as the bedrock saturated hydraulic conductivity value for those areas mapped as IHUs 490 and 491 in DTN: MO0603SPAGRIDD.003 [DIRS 177121].

Table 6.5.2.5-1 shows the bedrock cell counts for each bedrock type in the UZ grid as well as the infiltration model domain. Note that the infiltration calculation model domain (containing 139,092 cells) is smaller than the region mention above (containing 253,597 cells) because the infiltration model uses watersheds within that domain as its boundaries. As can be seen in Table 6.5.2.5-1, bedrock types 405 and 406 are the most prominent in the UZ modeling domain, each occupying more than 15% of the total area.

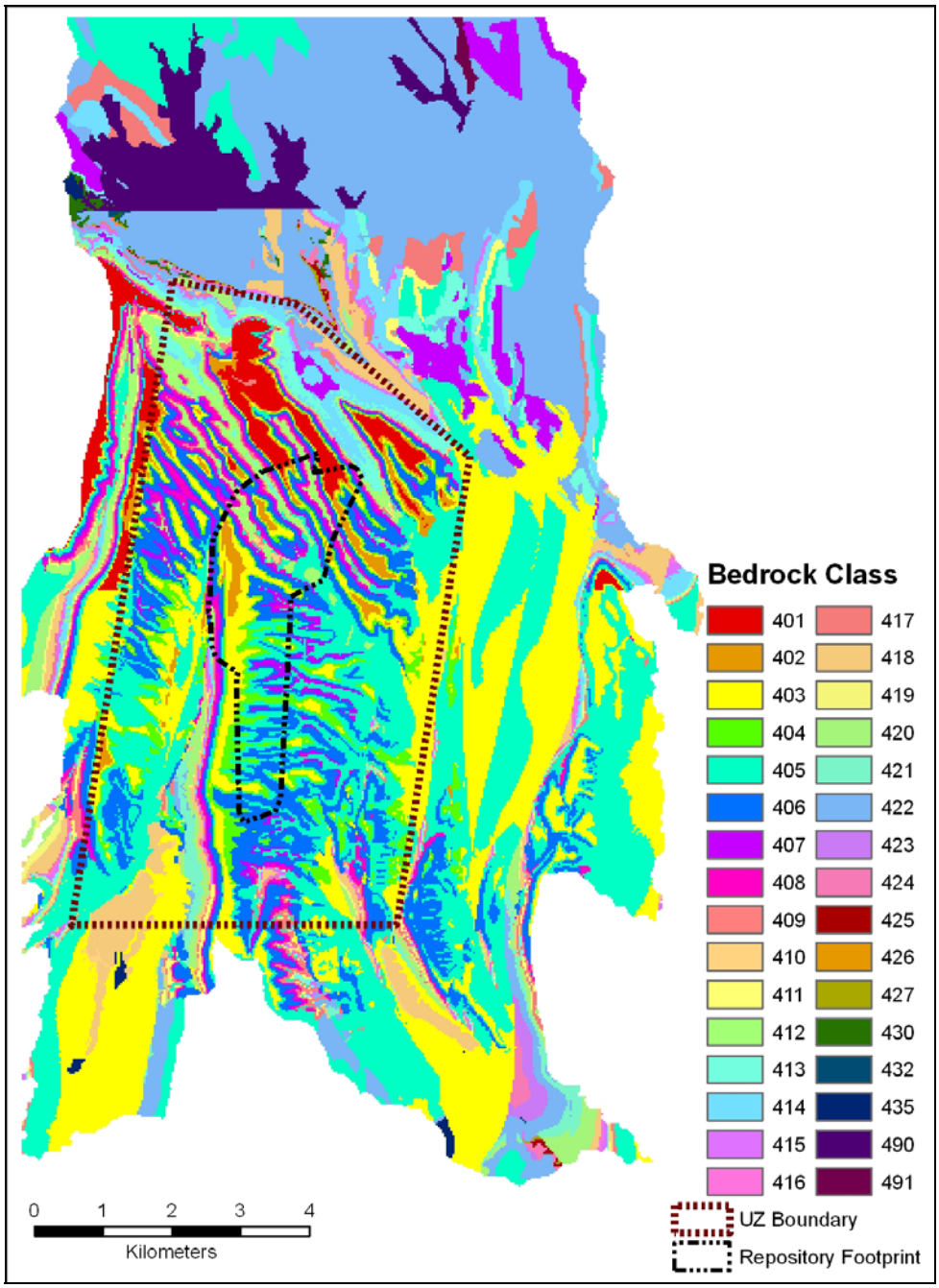

Source: DTN: MO0603SPAGRIDD.003 [DIRS 177121].

Output DTNs: SN0701SPALAYER.002 and SN0612FTPRNUZB.002.

Figure 6.5.2.5-1. Distribution of Infiltration Hydrogeologic Units across the Model Area

Table 6.5.2.5-1. Bedrock Cell Counts for the UZ Grid and Infiltration Model Domain

Bedrock IHU	UZ Grid Total Cells	Percent (UZ Grid)	Total Cells	Percent (Total)
401	1,757	4	2,974	2
402	1,482	3	1,651	1
403	6,317	14	24,672	18
404	3,589	8	3,921	3
405	9,980	23	30,953	22
406	8,617	19	11,819	8
407	2,658	6	5,701	4
408	1,607	4	2,562	2
409	771	2	1,827	1
410	149	0	483	0
411	147	0	1,058	1
412	1,765	4	2,620	2
413	1,037	2	2,608	2
414	1,304	3	3,974	3
415	289	1	1,106	1
416	47	0	373	0
417	174	0	2,222	2
418	1,256	3	4,702	3
419	41	0	296	0
420	454	1	1,742	1
421	379	1	1,044	1
422	362	1	24,427	18
423	11	0	483	0
424	11	0	432	0
425	0	0	124	0
426	0	0	20	0
427	0	0	85	0
428	0	0	0	0
429	0	0	0	0
430	0	0	234	0
431	0	0	0	0
432	0	0	30	0
433	0	0	0	0
434	0	0	0	0
435	0	0	257	0
436	0	0	0	0
437	0	0	0	0
438	0	0	0	0
490	0	0	4,513	3
491	0	0	179	0
Total cells	**44,204**		**139,092**	

Source: DTN: MO0603SPAGRIDD.003 [DIRS 177121].

6.5.2.6 Bedrock Saturated Conductivity

Saturated hydraulic conductivity (K_{sat}) data were developed for each of 38 rock types, or IHUs (Section 6.5.2.5) that form the bedrock at Yucca Mountain. Bulk hydraulic conductivity (K_{bulk}) is calculated for a composite porous medium consisting of matrix and fractures filled with permeable caliche.

In the conceptual model, bedrock hydraulic conductivity is the last resistance to flow before water enters the UZ model. As conceptualized, the bedrock has no thickness in the infiltration model; it only acts as a skin, limiting the portion of the flux reaching the bedrock that is allowed to infiltrate into the UZ model. The spatial distributions of the matrix and the filled-fracture K_{sat} are each described as lognormal, characterized by a median and standard deviation of the logarithm.

For each bedrock geologic unit, the approach used to calculate the mean and the variance of the bulk bedrock saturated hydraulic conductivity is as follows:

- The bedrock is modeled as consisting of matrix rock and fractures filled, at least at the soil–bedrock interface, with caliche
- Each of these materials is characterized by its median and standard deviation of $\log_{10} K_{sat}$ (BSC 2006 [DIRS 176355], Sections 6.4.3 and 6.4.4)
- The fraction of the soil–bedrock interface occupied by fractures, termed the fracture volume fraction, is characterized by a beta distribution (BSC 2006 [DIRS 176355], Section 6.3)
- The bedrock hydraulic conductivity is calculated by combining these data and by propagating the uncertainty (BSC 2006 [DIRS 176355], Section 6.4.5 and Appendix B). Uncertainties related to bedrock hydraulic conductivity are further discussed in Appendix I.

Conceptually, flow in the matrix and filled-fracture material is through parallel flow paths as represented by Equation 6.5.2.6-1. K_{bulk} for the composite porous medium of matrix and fractures filled with permeable caliche is, therefore, calculated as the arithmetic mean of the two K_{sat} values weighted by volume fraction (BSC 2006 [DIRS 176355], Equation 6-4):

$$K_{bulk} = f_{vf} K_{ff} + (1 - f_{vf}) K_m \qquad \text{(Eq. 6.5.2.6-1)}$$

where

f_{vf} is the fracture volume fraction,
K_{ff} is the K_{sat} of the fracture-filling material,
K_m is the K_{sat} of the matrix material, and
K_{bulk} is the K_{sat} of the composite bedrock.

K_{bulk} is the sum of two terms, of which the first is the product of a lognormal and a beta distribution. This multiplication does not lead to any classical distribution. Moreover, the addition of the two resulting distributions is difficult to estimate analytically because they are not independent, because of f_{vf}. Therefore, a Monte Carlo approach was used to estimate the shape of the resulting distribution: 30,000 values were sampled from the distribution of each input variable of f_{vf}, K_{ff}, and K_m, from which K_{bulk} is estimated (BSC 2006 [DIRS 176355], Section 6.4.5.1).

The resulting Monte Carlo distribution of K_{bulk} values, representing the spatial variability, is close to a lognormal distribution in shape for most of the 38 infiltration units. The distribution of bedrock saturated hydraulic conductivity over the infiltration model based on the consideration of filled fractures is shown in Figure 6.5.2.6-1, depicting the distribution of IHUs (Figure 6.5.2.5-1) with colors for various IHUs representing their respective saturated hydraulic conductivities. For most of the model area, bedrock saturated hydraulic conductivity based on the consideration of filled fractures is 2.4×10^{-7} m/s or less.

Field observations (Sanchez 2006 [DIRS 176569], pp. 26 to 61) indicate that caliche infilling of fractures and other voids is pervasive in many areas, but in others, particularly where soil cover is thin (because soil is the source of the caliche), it is spotty, does not completely fill fractures, or is absent. Also, additional field observations (Sweetkind et al. 1995 [DIRS 106959], p. 48, Figure 2, and Appendix 2; 1995 [DIRS 106958], pp. 12 and 34) show that in general at least some proportion of fractures are not completely filled (BSC 2006 [DIRS 176355], Section 6.4.5.4). Comparison of the infiltration rate measured in the Alcove 1 infiltration test with the mean bulk bedrock K_{sat} for IHU 404 (BSC 2006 [DIRS 176355], Section 6.4.5.3) also suggests that the fractures at that location are not completely filled. In view of these observations, the bulk bedrock saturated hydraulic conductivity calculated for filled fractures must be regarded as a lower bound of bulk bedrock saturated hydraulic conductivity. The upper bound of bulk bedrock saturated hydraulic conductivity must be set by some estimate of the percent of fractures containing an additional hydraulic aperture.

The relationship that was used to estimate the effect of open fractures on permeability is (Freeze and Cherry 1979 [DIRS 101173], Equation 2.87):

$$k = (Nb^3)/12 \qquad \text{(Eq. 6.5.2.6-2)}$$

where k is permeability, N is the fracture density, and b is the hydraulic aperture. The relationship between permeability and hydraulic conductivity (K_{sat}) is (Freeze and Cherry 1979 [DIRS 101173], Equation 2.28):

$$K_{sat} = kg\rho/\mu \qquad \text{(Eq. 6.5.2.6-3)}$$

where g is the acceleration due to gravity, and ρ and μ are the density and dynamic viscosity of water, respectively. Equations 6.5.2.6-1, 6.5.2.6-2, and 6.5.2.6-3 are used in calculations done in DTN: MO0605SPABEDRK.005 [DIRS 177122] (*Fracture_lengths2 v2.xls*). Resulting bulk K_{sat} values from some of these calculations are shown in Figure 6.5.2.6-2. Few data are available to quantify either the proportion of fractures that are unfilled or the hydraulic aperture to characterize them. Reasonable values may be inferred from the sources identified in *Data*

Analysis for Infiltration Modeling: Bedrock Saturated Hydraulic Conductivity Calculation (BSC 2006 [DIRS 176355], Section 6.4.5.4.2), including the Alcove 1 infiltration test (DTN: MO0605SPAFABRP.004 [DIRS 180539]), and analysis of fracture air-permeability data and fracture frequency data described in *Data Analysis for Infiltration Modeling: Bedrock Saturated Hydraulic Conductivity Calculation* (BSC 2006 [DIRS 176355]). Figure 6.5.2.6-2 shows a comparison of bedrock saturated hydraulic conductivities calculated using 100-µm and 200-µm aperture fractures for 10%, 50%, and 100% of fractures, and saturated hydraulic conductivities for completely filled fractures, and completely open fractures (data from air permeability measurements). Error bars are included for the plots of completely filled versus completely open fractures. In addition, the inferred saturated hydraulic conductivity from the Alcove 1 test (DTN: MO0605SPAFABRP.004 [DIRS 180539]) is included in this figure. Note that the Alcove 1 data point is approximately halfway between the filled fracture, and the 200-µm aperture fracture saturated hydraulic conductivities. Based on these values, the upper bound of bulk bedrock K_{sat} has been calculated based on the consideration of an additional 200-µm hydraulic aperture with all fractures. For the purpose of stochastic simulation, the distribution of bulk bedrock K_{sat} between these bounds is taken as loguniform. The upper and lower bounds, and the means and variances calculated from the bounds, are summarized in Table 6.5.2.6-1.

The range of K_{sat} values represented by the upper and lower bounds in Table 6.5.2.6-1 are used to establish uncertainty ranges for each of the bedrock types based on a loguniform distribution. The treatment of uncertainties, including the screening of parameters to be propagated in the uncertainty analysis for this report, is discussed in Appendix I.

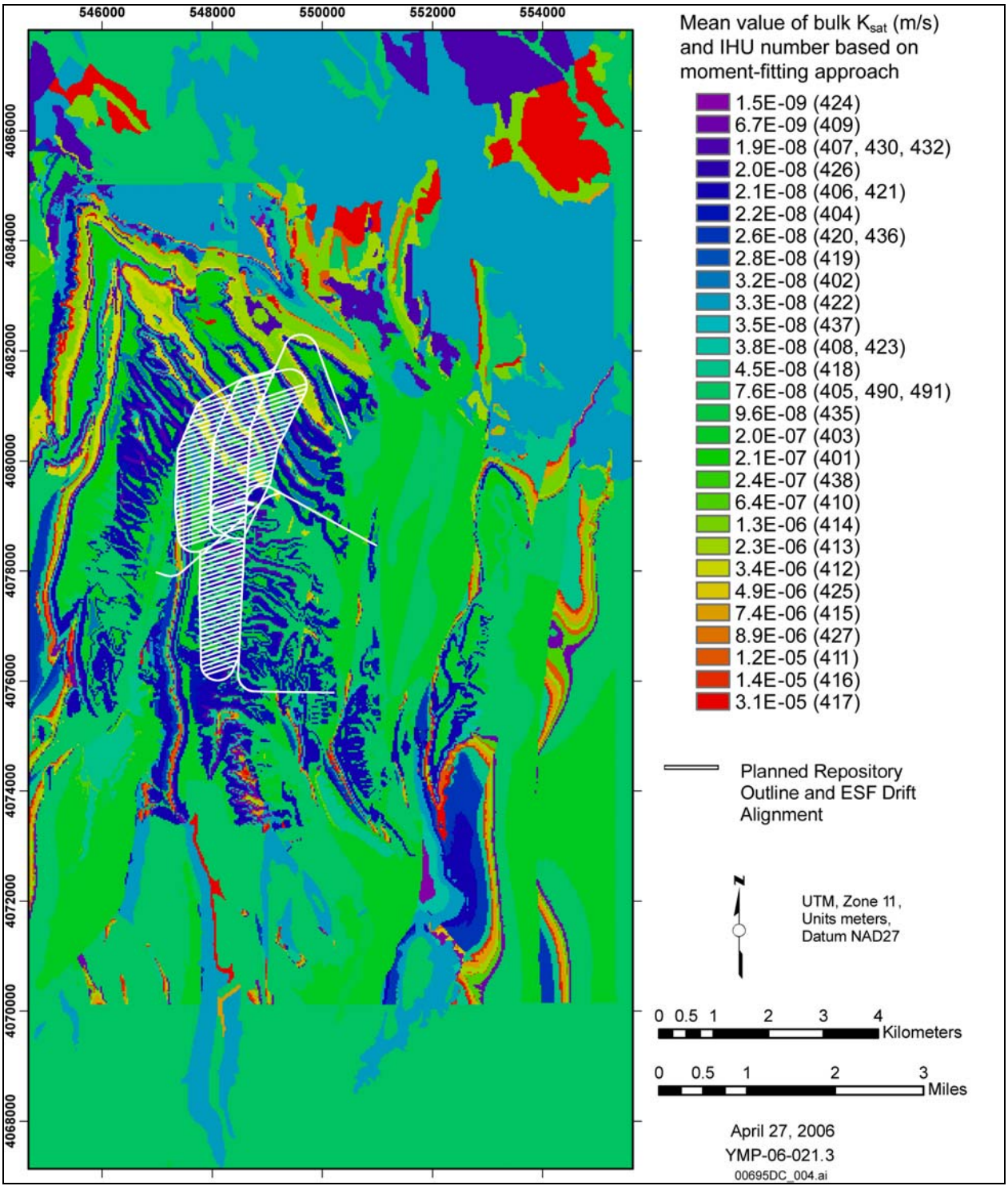

Source: BSC 2006 [DIRS 176355], Figure 6-11.

NOTE: Infiltration hydrogeologic unit (IHU) numbers are provided in parentheses in the map legend.

Figure 6.5.2.6-1. Distribution of Saturated Hydraulic Conductivity over the Model Area Based on the Consideration of Filled Fractures

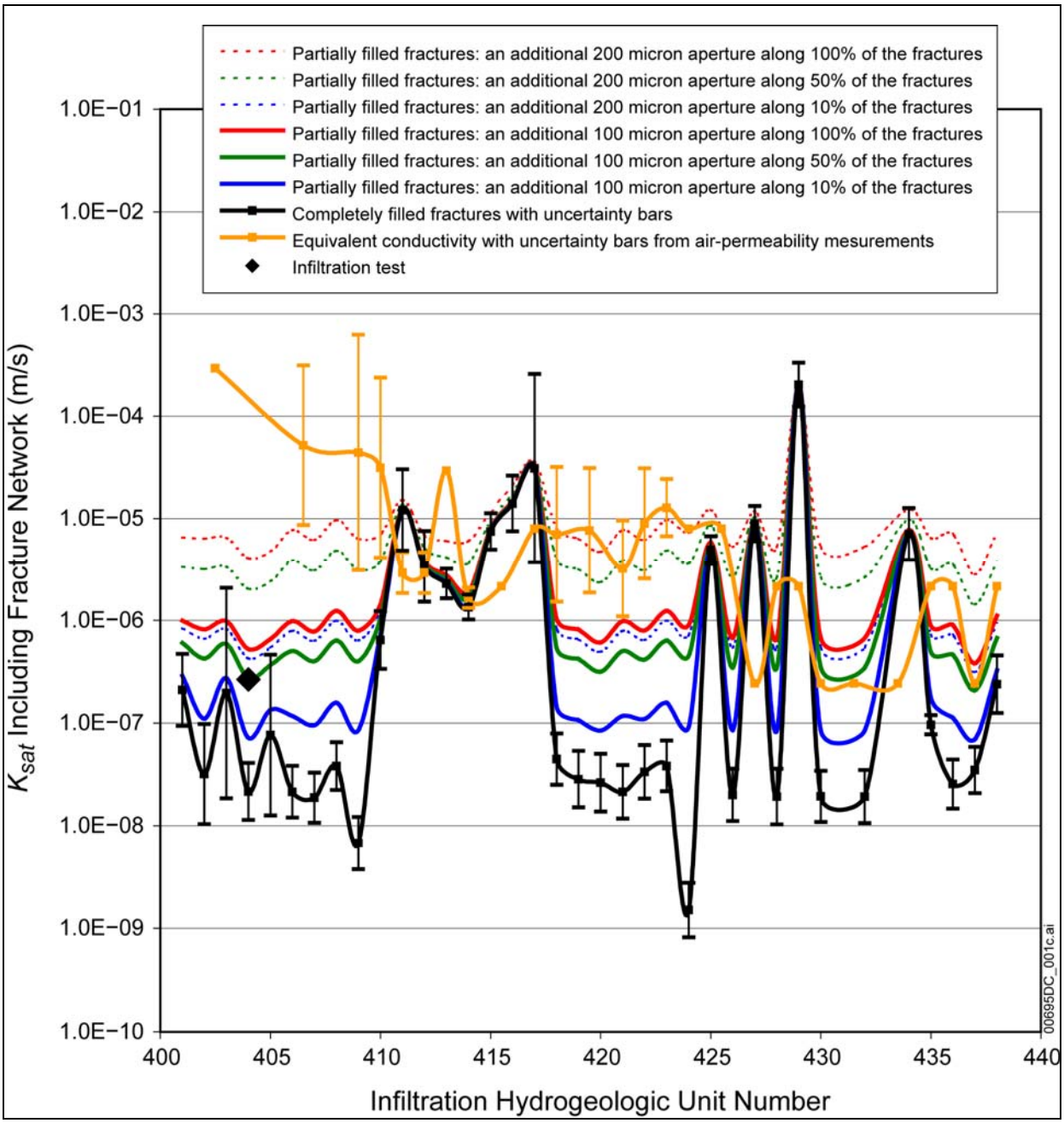

Source: DTN: MO0605SPABEDRK.005 [DIRS 177122], *Fracture_lengths2 v2.xls*, worksheet: "Comparison to Filled Fractures."

NOTES: While data are presented as continuous functions to improve visual depiction, the data are not continuous between IHUs. Filled-fracture data are the mean of K_{bulk} (DTN: MO0605SPABEDRK.005 [DIRS 177122]). For some IHUs, for example IHUs 411 through 417, the bedrock matrix material is sufficiently permeable without any unfilled fractures, so there is no significant increase in saturated hydraulic conductivity.

IHU = infiltration hydrogeologic unit.

Figure 6.5.2.6-2. Variation of Bulk Saturated Hydraulic Conductivity, K_{sat}, as a Function of Various Partially Filled Fracture Networks, with Comparison to the Alcove 1 Infiltration Test

Table 6.5.2.6-1. Bulk Bedrock K_{sat}

IHU		Upper Bound [a]	Lower Bound [b]	Mean [c]	Variance [c]
Number	Symbol	(m/s)	(m/s)	(m/s)	(m^2/s^2)
401	hcr4	6.5×10^{-6}	2.1×10^{-7}	1.8×10^{-6}	2.8×10^{-12}
402	hcr3	6.3×10^{-6}	3.2×10^{-8}	1.2×10^{-6}	2.4×10^{-12}
403	hcr2	6.5×10^{-6}	2.0×10^{-7}	1.8×10^{-6}	2.8×10^{-12}
404	hcr1	4.1×10^{-6}	2.2×10^{-8}	7.7×10^{-7}	9.9×10^{-13}
405	**hcul**	$\mathbf{4.8 \times 10^{-6}}$	$\mathbf{7.6 \times 10^{-8}}$	$\mathbf{1.1 \times 10^{-6}}$	$\mathbf{1.5} \times 10^{-12}$
406	**hcmn**	$\mathbf{7.7 \times 10^{-6}}$	$\mathbf{2.1 \times 10^{-8}}$	$\mathbf{1.3 \times 10^{-6}}$	$\mathbf{3.4 \times 10^{-12}}$
407	hcll	6.1×10^{-6}	1.9×10^{-8}	1.1×10^{-6}	2.1×10^{-12}
408	hcln	9.6×10^{-6}	3.8×10^{-8}	1.7×10^{-6}	5.4×10^{-12}
409	hcv2	6.3×10^{-6}	6.7×10^{-9}	9.2×10^{-7}	2.1×10^{-12}
410	hcv1	7.0×10^{-6}	6.4×10^{-7}	2.7×10^{-6}	3.0×10^{-12}
411	hbt4	1.5×10^{-5}	1.2×10^{-5}	1.4×10^{-5}	7.9×10^{-13}
412	hym	6.9×10^{-6}	3.4×10^{-6}	4.9×10^{-6}	1.0×10^{-12}
413	hbt3	6.0×10^{-6}	2.3×10^{-6}	3.9×10^{-6}	1.1×10^{-12}
414	hpc	6.0×10^{-6}	1.3×10^{-6}	3.1×10^{-6}	1.7×10^{-12}
415	hbt2	1.2×10^{-5}	7.4×10^{-6}	9.4×10^{-6}	1.4×10^{-12}
416	htrv3	2.1×10^{-5}	1.4×10^{-5}	1.7×10^{-5}	4.2×10^{-12}
417	htrv1	3.6×10^{-5}	3.1×10^{-5}	3.3×10^{-5}	2.1×10^{-12}
418	htrn	7.9×10^{-6}	4.5×10^{-8}	1.5×10^{-6}	3.8×10^{-12}
419	htrl	6.3×10^{-6}	2.8×10^{-8}	1.2×10^{-6}	2.3×10^{-12}
420	htul	4.7×10^{-6}	2.6×10^{-8}	9.0×10^{-7}	1.3×10^{-12}
421	htmn	7.7×10^{-6}	2.1×10^{-8}	1.3×10^{-6}	3.4×10^{-12}
422	htll	6.2×10^{-6}	3.3×10^{-8}	1.2×10^{-6}	2.3×10^{-12}
423	htln	9.6×10^{-6}	3.8×10^{-8}	1.7×10^{-6}	5.4×10^{-12}
424	htpv3	7.3×10^{-6}	1.5×10^{-9}	8.5×10^{-7}	2.4×10^{-12}
425	htv2v	1.2×10^{-5}	4.9×10^{-6}	8.0×10^{-6}	4.3×10^{-12}
426	htv2z	5.3×10^{-6}	2.0×10^{-8}	9.4×10^{-7}	1.6×10^{-12}
427	htv1v	1.2×10^{-5}	8.9×10^{-6}	1.0×10^{-5}	6.5×10^{-13}
428	htv1z	5.3×10^{-6}	1.9×10^{-8}	9.4×10^{-7}	1.6×10^{-12}
429	hacv	2.0×10^{-4}	2.0×10^{-4}	2.0×10^{-4}	5.2×10^{-13}
430	hacz	5.3×10^{-6}	1.9×10^{-8}	9.4×10^{-7}	1.6×10^{-12}
431	habtv	—	—	—	—
432	habtz	5.3×10^{-6}	1.9×10^{-8}	9.4×10^{-7}	1.6×10^{-12}
433	hpuvv	—	—	—	—
434	hpuvz	1.2×10^{-5}	7.0×10^{-6}	9.4×10^{-6}	2.3×10^{-12}
435	hpuc	6.4×10^{-6}	9.6×10^{-8}	1.5×10^{-6}	2.6×10^{-12}

Table 6.5.2.6-1. Bulk Bedrock K_{sat} (Continued)

IHU		Upper Bound [a]	Lower Bound [b]	Mean [c]	Variance [c]
Number	Symbol	(m/s)	(m/s)	(m/s)	(m^2/s^2)
436	hpmlc	7.0×10^{-6}	2.6×10^{-8}	1.2×10^{-6}	2.8×10^{-12}
437	hpbvz	2.8×10^{-6}	3.5×10^{-8}	6.4×10^{-7}	5.1×10^{-13}
438	hbucm	7.2×10^{-6}	2.4×10^{-7}	2.1×10^{-6}	3.5×10^{-12}

Source: DTN: MO0605SPABEDRK.005 [DIRS 177122], *Fracture_lengths2 v2.xls*, worksheet: "upper and lower bounds."

[a] Upper-bound K_{sat} is the sum of K_{sat} with all fractures filled and K_{sat} of 100% unfilled fractures with hydraulic aperture 200 μm.

[b] Lower-bound K_{sat} is the K_{sat} with all fractures filled (DTN: MO0605SPABEDRK.005 [DIRS 177122], moment-fitting mean value).

[c] Mean and variance are calculated based on the upper and lower bounds (BSC 2006 [DIRS 176355], Section 6.4.5.5, Equations 6-7 and 6-8).

NOTES: IHUs 405 and 406 (bolded) cover more than 15% of the UZ modeling domain and are included in the uncertainty analysis described in Sections 6.5.5 to 6.5.7.

IHUs 490 and 491 are assigned the same conductivity as IHU 405 as recommended in BSC 2006 [DIRS 176355], Section 7.

IHU = infiltration hydrogeologic unit.

6.5.3 Vegetation Parameters

This section describes the development of model input parameters used to describe the characteristics of the vegetation that is expected to be present at Yucca Mountain during the three future climates being considered. Parameters include maximum rooting depth (Z_r), plant height (h_{plant}), basal transpiration coefficients (K_{cb}), normalized difference vegetation index (NDVI) corrected for the Yucca Mountain environment (NDVI'), and the slope and intercept of the least squares regression between K_{cb} and NDVI'.

- Section 6.5.3.1 discusses the types of vegetation that are likely to be present during the Monsoon and Glacial Transition climates. Vegetation for the Present-Day climate is described in Section D2.2. This information is needed in order to estimate ranges for vegetation parameters.

- Section 6.5.3.2 describes the development of the parameter distributions for maximum rooting depth.

- Section 6.5.3.3 describes the development of the parameter distributions for plant height.

- Section 6.5.3.4 presents an overview of how estimates of transpiration coefficients are made in the model.

- Section 6.5.4.5 discusses inputs developed from satellite data that are used to estimate the effects of spatial and temporal factors on the vegetation response within the model domain.

- Section 6.5.3.6 discusses inputs developed from ground measurements of vegetation response at a set of ecological study plots at the Yucca Mountain site.

- Section 6.5.3.7 explains how satellite data and data collected on the ground are used together to determine transpiration coefficients.

6.5.3.1 Potential Vegetation for Monsoon and Glacial Transition Climates

To develop distributions for plant height and rooting depth for Monsoon and Glacial Transition climates it was necessary to consider what taxa might reasonably be expected to occur at Yucca Mountain. The species composition of future vegetation communities at Yucca Mountain is a complex issue. It is recognized that multiple possibilities for vegetation assemblages exist and outcomes are dependent on several factors including climate, disturbance, and species-specific ability to adapt or migrate. The potential for certain plant taxa to occur was evaluated by considering several factors including predicted future-climate rainfall and temperature patterns, natural vegetation associated with the climate at analogue meteorological station locations, historical vegetation change in response to climate change, species tolerance ranges and requirements, and current species composition of plant communities at Yucca Mountain. It is important to note that edaphic factors and topography at Yucca Mountain differ from those of natural vegetation stands associated with analogue meteorological station locations. Therefore, species were not selected as potential components of future vegetation simply on the basis that they are likely to occur in natural vegetation stands associated with the analogue meteorological stations.

6.5.3.1.1 Monsoon Climate and Vegetation at Analogue Sites

The Monsoon climate state is predicted to last around 900 to 1,400 years, with temperature and precipitation patterns in the lower bound similar to current conditions at Yucca Mountain (BSC 2004 [DIRS 170002], pp. 6-44 to 6-45, Table 6-1). Temperature and precipitation patterns during the upper bound Monsoon climate are predicted to be similar to those in Hobbs, New Mexico, and Nogales, Arizona (BSC 2004 [DIRS 170002], pp. 6-44 to 6-45, Table 6-1). The main difference between the Present-Day climate and upper-bound Monsoon climate that would affect species composition of plant communities at Yucca Mountain is a substantial increase in summer precipitation. Average monthly minimum and maximum air temperatures are predicted to be slightly lower for the upper-bound Monsoon climate state compared to the Present-Day climate (Table 6.5.3.1-1).

Table 6.5.3.1-1. Monthly Temperature and Precipitation for Upper-Bound Monsoon (Nogales, Arizona, and Hobbs, New Mexico) and Present-Day (Desert Rock) Climates

	Nogales, Arizona[a] (1971 to 2000)				Hobbs, New Mexico[b] (1914 to 2001)				Desert Rock, Nevada[b,c] (1984 to 2000)			
	Temperature[d] (°C)			Pcp[e] (mm)	Temperature[d] (°C)			Pcp[e] (mm)	Temperature[d] (°C)			Pcp[e] (mm)
Month	Mean	Max	Min		Mean[f]	Max	Min		Mean	Max	Min	
Jan.	7.5	17.7	−2.7	33.3	—	13.6	−2.3	11.4	6.6	12.7	0.4	23.6
Feb.	9.2	19.5	−1.2	27.7	—	16.6	0.0	11.2	9.1	15.5	2.7	22.1
March	11.5	21.8	1.1	25.4	—	20.5	2.9	13.0	12.1	19.1	5.1	15.0
April	14.7	25.7	3.6	12.4	—	25.3	7.8	20.3	16.3	23.8	8.7	8.9
May	18.7	30.1	7.3	8.1	—	29.7	12.9	52.8	20.8	28.5	13.2	7.1
June	23.9	35.4	12.4	13.7	—	33.7	17.4	48.0	25.9	34.1	17.8	1.8
July	26.1	34. 6	17.5	108.5	—	34.3	19.2	53.8	29.0	36.8	21.2	18.3
August	25.3	33.4	17.2	107.7	—	33.3	18.6	60.7	28.4	36.1	20.8	16.0
Sept.	22.8	32.3	13.2	42.7	—	29.9	15.2	66.8	23.9	31.8	16.1	8.4
Oct.	17.1	27.8	6.4	46.7	—	25.1	9.1	39.9	17.9	25.6	10.2	9.1
Nov.	11.2	22.0	0.3	19.8	—	18.4	2.6	14.7	10.1	16.9	3.2	11.2
Dec.	7.8	18.1	−2.4	37.3	—	14.4	−1.4	14.2	6.2	12.7	−0.2	14.2

[a] Western Regional Climate Center 2003 [DIRS 162307].
[b] Western Regional Climate Center 2002 [DIRS 165987].
[c] Desert Rock, located in Mercury, Nevada, is used here to represent climate at Yucca Mountain.
[d] Temperature was converted from °F to °C (°C = [°F−32]/1.8).
[e] Precipitation was converted from inches to millimeters (mm = inches × 20.54).
[f] Mean temperature was not available for Hobbs, New Mexico.

Using the monthly climate summaries for Nogales and Hobbs (Table 6.5.3.1-1), approximately 66% to 80% of total annual precipitation (average = 460 mm) falls between May and October when average monthly maximum temperatures range from 25°C to 34°C. Average minimum winter temperatures (November to February) range from −2.3°C to 2.8°C. These climate conditions support both high Sonoran (Nogales) and northern Chihuahuan (Hobbs) desert vegetation.

Much of the Sonoran Desert is subtropical and typically supports a diverse mix of trees, shrubs, and cacti represented by the genera *Cercidium* (paloverde), *Olneya* (desert ironweed), *Prosopis* (mesquite), *Larrea* (creosotebush), *Carnegiea* (saguaro), and *Lophocereus* (senita cactus), with distinct winter and summer floras (Smith et al. 1997 [DIRS 103636], p. 23). This diversity is due to a variety of factors including a mixture of soil types in the region, virtual absence of frost, and a bimodal pattern of yearly rainfall. However, low elevation bajadas and valley floors dominated by *Larrea – Ambrosia* desert scrub are typical of northern and western regions with vegetation similar to that found at Yucca Mountain. Nogales lies near the mid-eastern boundary of the Sonoran Desert.

Much of the Chihuahuan desert region has calcareous soils derived from limestone beds. Vegetation is often dominated by grasses and frost-tolerant plants such as yuccas and agaves. Grasslands generally dominate valley basins (Smith et al. 1997 [DIRS 103636], p. 24). Upper bajadas with deep soils are often dominated by desert scrub or arborescent woodland (Smith et al. 1997 [DIRS 103636], p. 24). Important perennial grass genera in the Chihuahuan Desert include *Bouteloua* (grama), *Erioneuron* (woollygrass), *Muhlenbergia* (muhly), *Scleropogon* (burrograss), *Pleuraphis* (galleta grass), and *Sporobolis* (dropseed). Desert scrub vegetation in northern reaches of the Chihuahuan Desert is dominated by *Larrea* and *Prosopis* with *Flourensia* (tarbush), *Ephedra* (jointfir), and *Yucca* as co-dominants. Hobbs, New Mexico, is near the northeastern boundaries of the Chihuahuan desert.

6.5.3.1.2 Glacial Transition Climate and Historical Vegetation Change

The Glacial Transition climate state is predicted to follow the Monsoon climate and last about 8,700 years. This climate state is characterized by cool wet winters and warm dry summers, with precipitation and temperature patterns similar to those in eastern Washington (BSC 2004 [DIRS 170002], pp. 6-44 to 6-45, Table 6-1). Data from analogue climate stations at St. John, Rosalia, and Spokane, Washington, indicate that total annual precipitation at Yucca Mountain during the Glacial Transition climate state will be about 460 mm, with about 60% falling between November and March (Table 6.5.3.1-2). Average minimum temperatures are below freezing during this time period. Cold desert shrub and shrub steppe vegetation typical of that found in the Great Basin extends into the eastern Washington area (Smith et al. 1997 [DIRS 103636], p. 6) where the analogue climate stations are located.

Table 6.5.3.1-2. Monthly Temperature and Precipitation for the Glacial Transition Climate

	Rosalia, Washington [a] (1948 to 2000)				Spokane, Washington [a] (1889 to 2000)			
	Temperature[b] (°C)			Pcp[c] (mm)	Temperature[b] (°C)			Pcp[c] (mm)
Month	Mean	Max	Min		Mean	Max	Min	
January	−2.1	1.3	−5.6	57.4	−2.7	0.5	−5.9	50.5
February	0.8	4.7	−3.1	41.4	0.1	3.9	−3.8	39.9
March	3.8	8.8	−1.1	40.1	4.1	9.0	−0.8	35.1
April	7.7	13.9	1.5	34.5	8.6	14.6	2.5	28.2
May	11.7	18.6	4.9	39.4	12.9	19.4	6.5	35.3
June	15.2	22.4	7.9	34.8	16.7	23.4	10.1	30.7
July	18.9	27.7	10.2	16.3	21.0	28.8	13.2	14.2
August	18.9	27.8	10.1	18.0	20.3	28.1	12.5	15.7
September	14.6	22.9	6.2	21.3	15.2	22.4	8.1	20.6
October	8.6	15.7	1.6	35.1	9.1	15.1	3.1	30.0
November	2.5	6.6	−1.7	56.6	2.4	6.0	−1.2	53.3
December	−1.2	2.1	−4.6	60.5	−1.4	1.5	−4.3	55.6

[a] Western Regional Climate Center 2002 [DIRS 165987].
[b] Temperature was converted from °F to °C (°C = [°F−32]/1.8).
[c] Precipitation was converted from inches to millimeters (mm = inches × 20.54).

Paleobotanical evidence from fossilized plant material preserved in packrat (*Neotoma* spp.) middens and fossil pollen preserved in lake and cave deposits have been used to reconstruct historical climate and floral composition of the four major deserts of western North America (Smith et al. 1997 [DIRS 103636], pp. 25 to 27). Packrat middens provide the primary source of evidence for historical vegetation in the Mojave Desert. The flora of the Mojave Desert during the late Wisconsin (21,000 to 11,000 years before present (B.P.)), early Holocene (11,000 to 8,000 years B.P.), and middle Holocene (8,000 to 4,000 years B.P.) are relevant to this analysis.

During the period 23,000 to 11,000 years B.P, juniper-dominated pygmy conifer woodlands (north of 36°N latitude) existed at lower elevations that are currently occupied by desert scrub vegetation (Smith et al. 1997 [DIRS 103636], p. 26). Desert taxa persisted in these woodlands as components of under-stories and south slopes. It was estimated that these woodlands were prevalent at elevations ranging from 600 m to 1,200 m below current distributions. Currently on the Nevada Test Site, open pygmy conifer woodlands occur at elevations above 1,830 m throughout the central and northwestern mountains and mesas (Wills and Ostler 2001 [DIRS 177624], p. 35). These woodlands are dominated by *Pinus monophylla* at higher elevations and *Juniperus osteosperma* at lower elevations (e.g., northwestern part of Pahute Mesa). *Artemisia* spp. are co-dominants in both woodlands (Wills and Ostler 2001 [DIRS 177624], p. 35). Thus, during this period, these woodlands would have existed at elevations starting at 630 to 1,230 m on the Nevada Test Site, well within the elevations of the infiltration model domain for Yucca Mountain.

During the terminal Wisconsin and early Holocene (12,000 to 8,000 years B.P.), summer precipitation increased in most of the Sonoran and Chihuahuan deserts due to monsoonal moisture patterns (Smith et al. 1997 [DIRS 103636], p. 27). However, this moisture did not reach the Mojave and western Sonoran Deserts, which had begun conversion to desert shrublands. During this time period coniferous woodlands still dominated most of the Sonoran and Chihuahuan deserts. *Larrea - Ambrosia* desert scrub of the Mojave and western Sonoran Deserts was in place by the middle Holocene (8,000 years B.P.). Elevational and geographic changes in species distributions have occurred over the past 8,000 years in response to climatic variation, but there has been little change in general floristic composition in the Mojave since the middle Holocene (Smith et al. 1997 [DIRS 103636], p. 28).

6.5.3.1.3 Potential Vegetation for Future Climate States at Yucca Mountain

During the Holocene, entire plant communities did not migrate intact to new ranges. Instead, different taxa responded individualistically to changes in climate, and plant communities were reshuffled based on differences in species' ability to reestablish themselves (Tausch et al. 1993 [DIRS 177620], pp. 442 to 443). Several factors affect migration and establishment of species into new areas not previously colonized, including:

(1) The ability to arrive in the new habitat. Long-haul dispersal mechanisms include dispersal by water, wind, birds, large mammals, and humans.

(2) The extent to which habitat conditions at the new site meet germination, establishment, growth, and reproduction requirements of the arriving species.

(3) The extent to which climatic change favors the new species over established species with respect to tolerance ranges and ability to compete for nutrients.

(4) The extent to which the new species tolerates or exploits disturbance patterns of the new site or affects changes in disturbance patterns (e.g., fire frequency).

Based on these requirements, several of the taxa that are common to the Sonoran and Chihuahuan Deserts would be unlikely candidates for colonization at Yucca Mountain during the Monsoon climate state. For example, assuming propagules arrived at Yucca Mountain either through migration or human introduction, establishment of taxa such as *Carnegiea* and *Lophocereus*, which are extremely susceptible to freezing temperatures, may be limited by average minimum air temperatures during winter months that are predicted for the Yucca Mountain Monsoon climate. Species such as *Flourensia cernua* grow in limestone or calcareous soils that are clay loams or gravelly clay, unlike those found at Yucca Mountain. *Cercidium* and *Prosopis* sp. are facultative riparian species in parts of their ranges but also occur in upland communities where precipitation is sufficient or where roots can tap into the water table. It is not likely that monsoon conditions predicted for Yucca Mountain would support establishment of *Cercidium*- or *Prosopis*-dominated communities.

Taxa that currently exist at Yucca Mountain and that are also found within the climatic regions of the analogue meteorological stations are likely to persist and in some cases perhaps expand their distributions. These include shrubs (e.g., *Larrea*, *Ambrosia*, and *Ephedra*), yuccas, cacti (e.g., *Echinocereus*), and grasses (e.g., *Muhlenbergia* and *Pleuraphis*). The Monsoon climate could support an increase in abundance of summer active grasses such as *Pleuraphis jamesii* and in species with relatively high temperature and moisture requirements for germination such as *L. tridentata*. While establishment of new species at Yucca Mountain during the Monsoon climate state cannot be ruled out, it is assumed instead that the abundance of grasses would increase, distinct winter/summer floras might develop with increases in abundance of existing winter/summer species, and shrub species such as *L. tridentata* and *A. dumosa* might increase in abundance. These changes would likely result in increased leaf area index over current climate values, proportional to the increase in precipitation, but overall physiognomy would be similar to current climate.

The predicted time period for the glacial transition climate state (8,700 years) is long enough that changes in vegetation at Yucca Mountain would be likely to occur. Changes in species composition, community types, and distribution ranges will likely be dynamic throughout the glacial transition period, influenced by disturbance type and frequency in addition to climate changes. Paleobotanical studies provide evidence to suggest that habitat conditions at elevations similar to those at Yucca Mountain likely supported open pygmy conifer woodlands during the last glacial transition state with pinyon dominant at higher elevations (> 1,800 m) and juniper at lower elevations. Pinyon-juniper woodlands exhibit widespread ecological amplitude and occupy steep mountain slope habitats to alluvial fans and steppes in the Great Basin. Recent range expansion into alluvial fan and steppe habitats has been attributed to fire suppression and overgrazing during the last 100 to 150 years (West 1999 [DIRS 178536], p. 21). This community type occurs across a wide range of surface soils from stony, cobbly, and gravelly sandy loams to clay loams with soil depths ranging from less than 0.5 m to greater than 1.5 m (Roundy and Vernon 1999 [DIRS 178534], p. 174), and average precipitation ranging from

280 mm per year (e.g., Pahute Mesa on the Nevada Test Site; Hansen and Ostler 2003 [DIRS 177619], p. 80) to around 400 mm (e.g., pinyon-juniper zone at the Spring Mountains, S. Nevada; Lei 1999 [DIRS 178535], p. 64). The soils at Yucca Mountain and predicted temperatures and precipitation for the glacial transition climate would support open juniper woodlands similar to those found on Pahute Mesa. Great Basin species that are currently present at Yucca Mountain that could increase in abundance under the glacial transition climate state include *Artemisia tridentata*, *Ephedra nevadensis*, *Krascheninnikovia lanata*, *Ericameria* spp., and *Chrysothamnus viscidiflorus*. Increased precipitation would support an increase in perennial grasses that are present at the mountain. These include *Achnatherum hymenoides*, *Poa* spp., *Achnatherum speciosum*, and *Elymus elymoides*. As with the Monsoon climate, these changes would likely result in increased leaf area index over current climate values, proportional to the increase in precipitation predicted for the glacial transition climate.

An alternative projection of vegetation under the glacial transition climate state is a system dominated by *Bromus tectorum*, an exotic annual grass (see Section D-5). Conversions of vast expanses of shrub steppe from communities dominated by perennial grasses and shrubs to communities dominated by *B. tectorum* have been documented throughout the Great Basin and Columbia Plateau, including the Spokane, Washington, area (e.g., Mack 1981 [DIRS 177164]). Shifts in dominance of native perennial shrubs to exotic annual grasses under glacial transition conditions have the potential to change net infiltration at Yucca Mountain. Increased net infiltration has been correlated with the presence of brome and other grass monocultures in Canada (van der Kamp et al. 2003 [DIRS 176050]). This correlation has been attributed to increases in macroporosity and permeability due to a high density of stalks and root holes that characterize grass monocultures (Bodhinayake and Si 2004 [DIRS 176211]). The shallow extent of brome grass roots may also allow excess water to infiltrate beyond the root zone and thus escape loss by evapotranspiration. Currently, two bromegrass species (*B. tectorum* and *B. madritensis* spp. *rubens*) are present at Yucca Mountain and dominate the annual flora (see Appendix D). Therefore, during the glacial transition climate, the possibility of a bromegrass monoculture at Yucca Mountain is considered for the infiltration model. Specifically, this possible future state is considered by including representative low values in the distribution range of maximum rooting depth for the glacial transition climate.

6.5.3.2 Maximum Rooting Depth

Mean maximum effective rooting depth (Z_r) is needed for water balance calculations for the root zone (Section 6.4). It is used in the calculation of water content in the root zone and root zone water depletion (Allen et al. 1998 [DIRS 157311], p. 170, Equation 85). It defines the depth to which water can be removed from the soil system, assuming that the soil depth equals or exceeds that depth. Mean maximum effective rooting depth distributions and nominal values for the different climate states are developed in this section. Based on potential composition of vegetation in future climates (Section 6.5.3.1), one distribution for Z_r was developed for the Present-Day and Monsoon climates, and a separate distribution was developed for the Glacial Transition climate.

Mean Maximum Effective Rooting Depth for Present-Day and Monsoon Climate States—The vegetation at Yucca Mountain consists mainly of deep-rooted perennial species (e.g., *Ericameria teretifolia, Larrea tridentata, Ephedra nevadensis*), shallow rooted perennials (e.g., Cactaceae and other families of CAM succulents), and shallow rooted winter/summer annuals (e.g., *Bromus madritensis* ssp. *rubens*). Great Basin desert species, such as *E. teretifolia,* tend to have deeper root systems and greater root-to-shoot ratios than Mojave Desert species such as *L. tridentata* (Smith et al. 1997 [DIRS 103636], p. 65). Root systems in general tend to exhibit a high degree of morphological plasticity and are influenced by both genetic and ecological determinants. Factors that can limit deep root growth in arid environments include decreasing nutrient concentration and microbial activity with depth, increasing soil compaction, lack of oxygen, presence of cemented hardpan, soil depth, and inter- or intra-specific competition for nutrients or space (Hansen and Ostler 2003 [DIRS 177619], pp. 22 to 28). Deep root growth is likely realized by plants at Yucca Mountain that are growing in areas where soil accumulates, such as washes, intermountain valleys, and lowlands. Also, roots can penetrate bedrock fractures where soil is present to extract stored water, but this process is assumed to be negligible compared with the amount of water that roots can extract from the soil layer, and therefore it is not included in the MASSIF model (see Section 5). A review of applicable literature was conducted to establish ranges of rooting depths for common plant species at Yucca Mountain. The information from the literature review was used to develop a nominal value and appropriate distribution of rooting depths for use in the MASSIF model.

Literature Review—Shallow rooted annual and perennial plant species are important contributors to total plant water use in the Yucca Mountain system. However, the MASSIF model, which is based on the FAO-56 method of modeling evapotranspiration, does not distinguish among depths for water extraction by roots. Therefore, the literature review focused primarily on deep-rooted perennial species in order to encompass the entire range of rooting depths. Most of the literature search focused on rooting depth studies that were conducted on the Nevada Test Site (NTS) or within the Mojave Desert. This was done to minimize uncertainty associated with generalizing findings from other areas that are based on different species, ecotypes, soils, or climate that might not be applicable to Yucca Mountain. Three studies conducted in arid to semi-arid habitats outside of the Mojave Desert were included to ensure that an appropriate range of variation was considered in development of mean maximum rooting depths. This was necessary because most of the studies that were conducted on the NTS and within the Mojave Desert limited evaluation of rooting depths to about 2 m and therefore did not provide information below that depth. The three studies conducted outside the Mojave Desert show potential for deeper rooting than 2 m and provide a measure of variation not accounted for in the Mojave Desert studies.

Brome grasses (*Bromus rubens* and *B. tectorum*) are generally the dominant annuals on Ecological Study Plots (ESPs) at Yucca Mountain (see Tables D-6 through D-14, and Section D5) and can form dense stands in wet years. These grasses generally have shallower root systems than most perennial shrub species. To account for the potential for brome monocultures to form at Yucca Mountain, rooting depths for these grasses were included in the literature search. No information was found for brome rooting depths in the Mojave Desert; therefore, studies from the Great Basin Desert were used for this grass.

Rooting depths and rooting morphologies for dominant plant species growing in Rock Valley on the NTS were described by Rundel and Gibson (1996 [DIRS 103614], pp. 98 to 99). Root systems were excavated from a wash area with relatively deep sediments. In general, shrub species had roots to depths of about 1 to 2 m. Scaled drawings of root systems showed roots for *L. tridentata*, *A. dumosa*, *E. nevadensis*, and *L. andersonii* to depths of about 1.5, 1.3, 1.5, and 2.0 m, respectively (Rundel and Gibson 1996 [DIRS 103614], p. 99, Figure 4-10). These four species are common at Yucca Mountain and are often dominant or primary species in vegetation associations in the area (Section D2.2). Rundel and Nobel (1991 [DIRS 128001], pp. 355 to 357) described the architecture of root systems for several desert plant species and provide community rooting profiles for shrub species in three Mojave Desert locations (California, Mid Hills, and Granite Mountains). The rooting profiles were determined from excavations of root systems and were provided for the following species that are important at Yucca Mountain: *Ericameria cooperi* (synonymous with *Haplopappus cooperi*), roots to 1.4 m; *Ericameria teretifolia* (synonymous with *Chrysothamnus teretifolius*), roots to 1.8 m; *Hymenoclea salsola*, roots to 2 m; *Eriogonum fasciculatum*, roots to 0.9 m; *Menodora spinescens*, roots to 1.2 m; and *Salazaria mexicana*, roots to 0.80 m.

Using measurements of soil water content beneath shrubs, Yoder and Nowak (1999 [DIRS 177167], p. 91, Figure 6) showed that deep roots of *L. tridentata*, *A. dumosa*, and *E. nevadensis* extracted soil water uniformly to depths of 1.2, 1.8, and 2.0 m, respectively (depths rounded to nearest tenth of a meter). The study was conducted over a three-year time period on eight study sites at the NTS. Volumetric soil water content was measured with a neutron probe at 0.2 m depth increments to the depth of the access tubes (about 2 m) (Yoder and Nowak 1999 [DIRS 177167], pp. 82 to 83). The authors suggested that the soil moisture extraction patterns indicated that even though rooting densities decrease significantly with depth, deep roots are important for soil water uptake and may contribute to long-term survival of desert plants (Yoder and Nowak 1999 [DIRS 177167], pp. 93 to 94).

Hansen and Ostler (2003 [DIRS 177619], pp. 49 to 65) estimated rooting depth for several native shrub species on the NTS. Rooting depth estimates were made using a conversion factor established from correlations between plant height and maximum root depth. The conversion factor was established in previous NTS studies (Hansen and Ostler 2003 [DIRS 177619], p. 43). Rooting depths were estimated as part of an effort to reduce uncertainties in performance assessment models that were developed for the Area 5 Radioactive Waste Management Site (RWMS) and the Area 3 RWMS. The vegetation in Area 5 and surrounding landscape was classified as a Larrea–Ambrosia association (Hansen and Ostler 2003 [DIRS 177619], p. 17). Because of the high amount of human-caused disturbance in Area 3 and the immediate vicinity, three plots at various distances were selected to represent vegetation (Hansen and Ostler 2003 [DIRS 177619], pp. 18 to 19). One of the plots was located in a Grayia–Lycium association, one in a Larrea–Grayia–Lycium association, and one in an Atriplex–Krascheninnikovia association. Vegetation characteristics were collected for *L. tridentata, Acamptopappus shockleyi, A. dumosa, H. salsola, Atriplex confertifolia, A. canescens, E. nevadensis, L. andersonii, Krascheninnikovia lanata, Grayia spinosa, Artemisia spinescens, Chrysothamnus viscidiflorus, Menedora spinescens,* and *Krameria erecta* (Hansen and Ostler 2003 [DIRS 177619], pp. 49, 52, 55, 58, 62, and 65). These species also commonly occur at Yucca Mountain. The ranges of estimated maximum rooting depths based on above-ground information collected for these species were

0.96 to 1.15 m for Area 5 and 0.72 to 1.8 m for Area 3 (Hansen and Ostler 2003 [DIRS 177619], p.85, Table 7-1).

In a review of maximum rooting depths of species found in eleven major terrestrial biomes, Canadell et al. (1996 [DIRS 177626]) compiled information from direct observations of roots in road cuts, mine shafts, open-cut mines, and trenches. For deserts, they included a rooting depth of 2.0 m for *C. viscidiflorus* growing at a study site in Idaho (Canadell et al. 1996 [DIRS 177626], p. 588, Appendix 1). Soils for this area were classified as aeolian sandy loam (Canadell et al. 1996 [DIRS 177626], p. 588, Appendix 1), similar to those in a subset of vegetation associations found at Yucca Mountain (CRWMS M&O 1998 [DIRS 104589], pp. 5, 9, and 10). While climatic conditions vary between the Idaho site and Yucca Mountain, both are considered arid to semi-arid environments, and genetic potential for reaching maximum rooting depths to 2 m was demonstrated for *C. viscidiflorus*.

Schenk and Jackson (2002 [DIRS 177638], p. 481 to 482) collected more than 1,300 records on rooting depths for individual plants from literature sources for a variety of arid to semi-arid ecosystems and for several vegetation growth forms. They found that maximum rooting depths of shrubs in xeric environments receiving 125 to 250 mm of precipitation were about 5 m (Schenk and Jackson 2002 [DIRS 177638], p. 491, Figure 9). In a study on woody plant invasions of grasslands, Jackson et al. (2002 [DIRS 177171], p. 624, Table 1) showed that desert plants at a study site in Jornada, New Mexico (mean annual precipitation = 230 mm) extracted nutrients from depths of at least 3 m.

Rooting depths for *B. tectorum* ranged from about 0.5 m to 2.0 m (Harris 1967 [DIRS 177630], p. 97, Figure 6; Hulbert 1955 [DIRS 177129], pp. 190 to 195; Link et al. 1990 [DIRS 177142], p. 512; Rickard 1985 [DIRS 177635], p. 170; Foxx et al. 1984 [DIRS 177628], p. 6, Table 3). Hulbert (1955 [DIRS 177129], pp. 190 to 195) studied root systems of bromegrasses using pit excavations, lithium chloride tracers, and soil moisture depletion. He found that the depth of *B. tectorum* roots ranged from about 0.75 to 2.0 m. Foxx et al. (1984 [DIRS 177628], p. 5, Table 3) reported a range of 0.3 to 1.10 m for *B. tectorum* rooting depths and Harris (1967 [DIRS 177630], p. 97, Figure 6) excavated roots of *B. tectorum* to depths of 1.1 m. In brome dominated communities in eastern Washington, Rickard (1985 [DIRS 177635], p. 170) reported that roots were inefficient at extracting soil moisture from below about 0.5 m. This result was similar to those reported by Link et al. (1990 [DIRS 177142], p. 512) with *B. tectorum* roots in natural stands to depths of 0.45 m.

Parameter Development—Based on the literature search, mean maximum rooting depths for desert shrubs was 1.6 m and ranged from 0.5 m to 5.0 m (Table 6.5.3.2-1). In general, root density decreases exponentially with depth. However, studies showed that Mojave desert shrubs used all the water available down to about 2 m (Yoder and Nowak 1999 [DIRS 177167], p. 91, Figure 6) and desert plants extracted nutrients from depths of 3 m (Jackson et al. 2002 [DIRS 177171], p. 624, Table 1), suggesting the potential importance of roots to deep water removal from the soil system at Yucca Mountain. In the MASSIF model, the depths of shallow soils on rocky slopes and the crest at Yucca Mountain control rooting depth (i.e., actual rooting depths are the lesser of maximum rooting depth and soil depth). However, soil depths for alluvium at Yucca Mountain (mean = 16.4 m for Soil Depth Class 2 and minimum = 40 m for Soil Depth Class 1; see Section 6.5.2, Table 6.5.2.4-4) exceed the genetic potential for rooting

depths of desert shrubs. The MASSIF model does not account for spatial variability in rooting depth. For each model run, one maximum rooting depth is selected for the entire model domain. Therefore, to avoid assignment of an extreme rooting depth to the entire model domain, the distribution ranges (for all climate states) were defined by means and standard deviations.

For Present-Day and Monsoon climate states, a nominal value of 1.6 m is used for maximum rooting depth (mean of values in Table 6.5.3.2-1). A uniform distribution with lower and upper bounds of 0.6 m and 2.6 m, respectively (the nominal value ±1 standard deviation, Table 6.5.3.2-1), is used for model uncertainty and sensitivity studies.

Table 6.5.3.2-1. Rooting Depths for Present-Day and Monsoon Climates

Reference	Vegetation and Associated Rooting Depths
Canadell et al. 1996 [DIRS 177626], p. 588, Appendix 1	*Chrysothamnus viscidiflorus* = 2.0 m
Hansen and Ostler 2003 [DIRS 177619], p. 85, Table 7-1	Area 5 RWMS[a] = 1.2 m Area 3 RWMS = 1.8 m
Jackson et al. 2002 [DIRS 177171], p. 624, Table 1	Desert shrubs = 3 m
Rundel and Gibson 1996 [DIRS 103614], p. 99, Figure 4-10	*Ambrosia dumosa* = 1.3 m *Ephedra nevadensis* = 1.5 m *Larrea tridentata* = 1.5 m *Lycium andersonii* = 2.0 m
Rundel and Nobel 1991 [DIRS 128001], pp. 355 to 357	*Ericameria cooperi* = 1.4 m *Ericameria teretifolia* = 1.8 m *Eriogonum fasciculatum* = 0.9 m *Hymenoclea salsola* = 2 m *Menodora spinescens* = 1.2 m *Salazaria mexicana* = 0. 80 m
Schenk and Jackson 2002 [DIRS 177638], p. 491, Figure 9	Maximum for xeric shrubs = 5.0 m
Yoder and Nowak 1999 [DIRS 177167], p. 91, Figure 6	*Larrea tridentata* = 1.2 m *Ambrosia dumosa* = 1.8 m *Ephedra nevadensis* = 2.0 m
Harris 1967 [DIRS 177630], p.97, Figure 6	*Bromus tectorum* (cheatgrass) = 1.1 m
Hulbert 1955 [DIRS 177129], p.191	*Bromus tectorum* = 2.0 m
Link et al. 1990 [DIRS 177142], p. 512	*Bromus tectorum* = 0.5 m
Rickard 1985 [DIRS 177635], p.170	*Bromus tectorum* = 0.5 m
Foxx et al. 1984 [DIRS 177628], p. 6, Table 3	*Bromus tectorum* = 1.1 m
	Mean = 1.6 m
	Standard Deviation = 0.95
	Range = 0.5 to 5.0 m
Recommended Distribution Parameters: Nominal Value = 1.6 m; Range = Uniform from 0.6 to 2.6 m	

[a] The maximum of the reported range was used.

Mean Maximum Rooting Depth for the Glacial Transition Climate State—Precipitation and temperatures predicted for the glacial transition climate state could support open juniper woodland/sagebrush vegetation assemblages (Section 6.5.3.1). This is based on historical biogeography of the Mojave Desert and tolerance ranges for common plants in Great Basin juniper woodland/sagebrush vegetation assemblages (see Section 6.5.3.1). Common Great Basin species that are currently present at Yucca Mountain, or within a reasonable migration distance,

were selected to represent future climate vegetation for establishing mean maximum rooting depth (Table 6.5.3.2-2).

Literature Review—Foxx et al. (1984 [DIRS 177628]) obtained means and ranges of rooting depths for several Great Basin species from an extensive bibliographic study that contained 1034 different rooting citations. Common Great Basin grasses that are currently present at Yucca Mountain and likely to occur under glacial transition climate conditions included *Achnatherum hymenoides* (previous nomenclature: *Oryzopsis hymenoides*), *Poa* spp., *Stipa comata,* and *Bromus tectorum* (Foxx et al. 1984 [DIRS 177628], p. 5, Table 3). (See the Present-Day and Monsoon climates section above for review of *B. tectorum* rooting depths.) *Achnatherum hymenoides*, *Poa* spp. and *S. comata* were reported to have relatively deep rooting depths with ranges of 0.45 to 1.22 m, 0.35 to 2.13 m, and 0.63 to 1.68 m, respectively (Table 6.5.3.2-2). The upper limit of these ranges, rounded to nearest tenth, was used to represent maximum rooting depths for these grasses (Table 6.5.3.2-2). Foxx et al. (1984 [DIRS 177628]) also included rooting depths for two common Great Basin shrubs (*Ericameria nauseosa* [previous nomenclature: *Crysothamnus nauseosus*] and *Artemesia tridentata*), and two trees (*Juniperus monosperma* and *Pinus edulis*) that are likely to occur in an open juniper woodland. Mean rooting depths reported for these species were used instead of the upper limit of the ranges. This was necessary because the reported upper limits were extremes that were much deeper than any other reports for these species and therefore not very likely to occur. The mean rooting depths for *E. nauseosa* and *A. tridentata* were 2.9 and 2.5 m, respectively (Table 6.5.3.2-2). The mean rooting depth for both *J. monosperma* and *P. edulis* was 6.4 m (Table 6.5.3.2-2). In a review of the botanical characteristics of *Juniperus osteosperma*, Zlatnik (1999 [DIRS 177639], p. 7) reported a rooting depth of 4.5 m (Table 6.5.3.2-2). In a review of the botanical characteristics of *P. edulis*, Anderson (2002 [DIRS 177625], p. 5) reported a rooting depth of 6.0 m (Table 6.5.3.2-2). The reviews by Zlatnik (1999 [DIRS 177639]) and Anderson (2002 [DIRS 177625]) were parts of the USDA Forest Service sponsored database: Fire Effects Information System (FEIS). The FEIS database contains comprehensive literature reviews of several hundred plant species that are thoroughly documented with complete bibliographies.

In a review of maximum rooting depths by Canadell et al. (1996 [DIRS 177626], p. 588, Appendix 1), which is described in the previous section, rooting depths were included for *A. tridentata* growing at study sites in Colorado and Idaho. The maximum rooting depths reported for this species were 1.8 and 2.3 m (Table 6.5.3.2-2). In a study on water transport between soil layers at a site in Utah, Richards and Caldwell (1987 [DIRS 177927], p. 488) determined that roots of *A. tridentata* occurred to depths of about 2 m. In another study of water transport through soils by roots of *A. tridentata*, Ryel et al. (2002 [DIRS 177632], p. 760) reported roots to 3.4 m. Sturges and Trlica (1978 [DIRS 177928]) excavated roots of *A. tridentata* from different positions on a north facing hillside at a study site in south central Wyoming. They found that *A. tridentata* roots at the lower and midslope sites extended into the 1.8 to 2.1 m sampling depth (Sturges and Trlica 1978 [DIRS 177928], p. 1,283). Roots tended to be shallower at the ridge location (1.2 to 1.5 m). The upper limits of the ranges for lower and midslope sites were used in this analysis (Table 6.5.3.2-2).

Parameter Development—A nominal value of 2.5 m is used for maximum rooting depth for the glacial transition climate state. This is the mean value of rooting depths in Table 6.5.3.2-2. A uniform distribution with a lower bound of 1.0 m and an upper bound of 4.0 m (mean ± one

standard deviation rounded to the nearest meter) is used for model uncertainty and sensitivity studies. The lower bound value of 1 m is equal to the mean of the rooting depths for the *Bromus tectorum* listed in Table 6.5.3.2-2, and therefore this distribution includes the possibility of a brome monoculture during the glacial transition climate period.

Table 6.5.3.2-2. Maximum Rooting Depth for the Glacial Transition Climate State

Reference	Plant Species	Reported Rooting Depth (m)	Rooting Depth Used in Distribution (m)[a]
Foxx et al. 1984 [DIRS 177628], p. 5, Table 3	*Achnatherum hymenoides*	0.45 to 1.22	1.2
Foxx et al. 1984 [DIRS 177628], p. 6, Table 3	*Artemisia tridentata* (big sagebrush)	2.5 [b]	2.5
Richards and Caldwell 1987 [DIRS 177927], p. 488	*Artemisia tridentata*	2.0	2.0
Sturges and Trlica 1978 DIRS 177928], p. 1,283	*Artemisia tridentata*	1.8 to 2.1	2.1
Canadell et al. 1996 [DIRS 177626], p. 588, Appendix 1	*Artemisia tridentata*	1.8 2.3	1.8 2.3
Ryel et al. 2003 [DIRS 177632], p.760	*Artemisia tridentata*	3.4	3.4
Seyfried et al. 2005 [DIRS 178060], pp. 282 to 283	*Artemisia tridentata*	1.7	1.7
Harris 1967 [DIRS 177630], p. 97, Figure 6	*Bromus tectorum* (cheatgrass)	1.1	1.1
Hulbert 1955 [DIRS 177129], p. 191	*Bromus tectorum*	1.0 to 2.0	2.0
Link et al. 1990 [DIRS 177142], p. 512	*Bromus tectorum*	0.45	0.5 (rounded)
Rickard 1985 [DIRS 177635], p. 170	*Bromus tectorum*	0.5	0.5
Foxx et al. 1984 [DIRS 177628], p. 5, Table 3	*Bromus tectorum*	0.30 to 1.10	1.1
Canadell et al. 1996 [DIRS 177626], p. 588 Appendix 1	*Chrysothamnus viscidiflorus* (green rabbitbrush)	2.0	2.0
Foxx et al. 1984 [DIRS 177628], p. 6, Table 3	*Ericameria nauseosa* [b]	2.9 [b]	2.9
Leffler et al. 2004 [DIRS 177926], p. 10, Figure 1	*Ericameria nauseosa* [b]	1.3	1.3
Foxx et al. 1984 [DIRS 177628], p. 6, Table 3, p. 18	*Juniperus monosperma* (utah juniper)	6.4 [b]	6.4
Zlatnik 1999 [DIRS 177639], p. 7	*Juniperus osteosperma*	4.5	4.5
Foxx et al. 1984 [DIRS 177628], p. 6, Table 3, p. 18	*Pinus edulis* (pinyon pine)	6.4	6.4
Anderson 2002 [DIRS 177625], p. 5	*Pinus edulis* (pinyon pine)	6.0	6.0
Foxx et al. 1984 [DIRS 177628], p. 5, Table 3	*Poa* spp.	0.35 to 2.13	2.1
Foxx et al. 1984 [DIRS 177628], p. 5, Table 3	*Stipa comata*	0.63 to 1.68	1.7
		Mean	2.5
		Standard Deviation	1.8
		Range	0.50 to 6.4
Recommended Distribution Parameters: **Nominal Value = 2.5 m; Distribution = Uniform from 0.7 to 4.3 m.**			

[a] Maximum of range.
[b] Mean rooting depth.

6.5.3.3 Plant Height

Mean plant height (h_{plant}) is used in Equation 76 from FAO-56 (Allen et al. 1998 [DIRS 157311], p. 149) to calculate the fraction of soil surface that is covered by vegetation (f_c). The f_c is one of the parameters used to calculate the evaporation component ($K_e \times ET_0$) in the soil water balance model (see Section 6.4). Mean plant height distributions and nominal values for the different climate states are developed in this section. Based on potential composition of vegetation in future climates (Section 6.5.3.1), one distribution for plant height was developed for the Present-Day and Monsoon climates, and a separate distribution was developed for the glacial transition climate.

Mean Plant Height for Present-Day and Monsoon Climate States—Several years of intensive ecological studies were conducted in Rock Valley and other areas of the Nevada Test Site under the International Biological Program (IBP) Desert Biome Program and were continued through research funded by the U.S. Department of Energy (DOE) and the University of California, Los Angeles. Rundel and Gibson (1996 [DIRS 103614]) describe these studies and the ecological communities and processes at Rock Valley and other locations on the NTS. Several characteristics of vegetation associations were studied including woody plant height.

Mean shrub heights for a variety of vegetation associations in Mojave, transition, and Great Basin desert locations reported by Rundel and Gibson (1996 [DIRS 103614], p. 89, Table 4.2) were used to develop mean plant heights for Present-Day and Monsoon climate states (Table 6.5.3.3-1). Shrub heights were collected from 68 permanent plots that were established on the NTS in 1963. Data reported from four of the associations (*Artemisia tridentata*-pinyon-juniper*, Artemisia nova,* and two *Artemisia nova*-pinyon-juniper) were not used in calculation of mean plant height because those associations do not occur on Yucca Mountain. This resulted in mean plant height values from 25 Mojave Desert sites, 24 transition desert sites, and six Great Basin Desert sites (Rundel and Gibson 1996 [DIRS 103614], p. 89, Table 4.2).

Table 6.5.3.3-1. Mean Plant Height for Present-Day and Monsoon Climates

Vegetation Association	Mean Plant Height (m)
Larrea–Ambrosia	0.34
Larrea–Lycium–Grayia	0.51
Larrea–Grayia–Lycium	0.47
Larrea–Atriplex	0.27
Larrea–Psorothamnus	0.41
Menodora–Ephedra	0.25
Larrea–Grayia–Lycium	0.47
Grayia–Lycium	0.38
Coleogyne	0.39
Coleogyne–Larrea–Grayia–Lycium	0.46
Coleogyne–Grayia–Lycium	0.39
Larrea–Atriplex–Coleogyne	0.35
Coleogyne–Grayia–Artemisia	0.47
Larrea–Lycium shockleyi–Atriplex	0.22
Lycium shockleyi–Atriplex	0.25

Table 6.5.3.3-1. Mean Plant Height for Present Day and Monsoon Climates (Continued)

Vegetation Association	Mean Plant Height (m)
Lycium pallidum–Grayia	0.59
Atriplex confertifolia	0.29
Atriplex–Kochia	0.21
Atriplex–Ceretoides	0.3
Atriplex canescens (lower elevation)	0.36
Atriplex canescens (higher elevation)	0.44
Artemisia tridentata	0.58
Mean	0.38
Standard Deviation	0.11
Range	0.21 to 0.59
Recommended Distribution Parameters: **Nominal Value = 0.40 m; Distribution = Uniform from 0.20 to 0.60 m**	

Source: Rundel and Gibson 1996 [DIRS 103614], p. 89, Table 4.2.

A nominal value of 0.4 m, based on the mean of values in Table 6.5.3.3-1 (rounded to the nearest tenth of meter), is recommended as the nominal value for average plant height for Present-Day and Monsoon climates. A uniform distribution with a lower bound of 0.2 m and an upper bound of 0.6 m is recommended for model sensitivity studies. The upper and lower bounds were determined from the range of average heights (rounded to the nearest tenth of a meter) in Table 6.5.3.3-1.

Mean Plant Height for the Glacial Transition Climate State—Precipitation and temperatures predicted for the glacial transition climate state could support open juniper woodland/sagebrush vegetation assemblages (Section 6.5.3.1). This is based on historical biogeography of the Mojave Desert and tolerance ranges for common plants in Great Basin juniper woodland/sagebrush vegetation assemblages (see Section 6.5.3.1). Common Great Basin species that are currently present at Yucca Mountain, or within a reasonable migration distance, were selected to represent future climate vegetation for establishing mean plant height (Table 6.5.3.2-2).

No single comprehensive source for plant height was available for common Great Basin Desert vegetation associations, and only one peer reviewed article reporting plant height was located in the literature search. Therefore, United States Department of Agriculture (USDA) divisions and university extensions that provided fact sheets on Great Basin plant species in Nevada and Utah were used (Table 6.5.3.3-2). Where a range of height values were reported for a species, the midpoint of the range was used to develop the nominal value and distribution limits (Table 6.5.3.3-2).

Junipers and/or pinyon pines rarely make up more than 10% to 15% cover in open woodlands. To account for this, a weighted mean and weighted range were calculated from the data in Table 6.5.3.3-2 using a weighting factor of 0.10 for juniper and pinyon heights, and 0.90 for the remaining vegetation. This resulted in a mean plant height of 1.3 m with a range of 0.64 to 1.8 m (Table 6.5.3.3-2). A uniform distribution with a nominal value of 1.3 m, a lower bound of 0.64 m, and an upper bound of 1.8 m is recommended for use in the MASSIF model.

Table 6.5.3.3-2. Plant Height for the Glacial Transition Climate State

Reference	Plant Species	Reported Height (m)	Height Used in Distribution (m)[a]
USDA 2002 [DIRS 178073], p. 2[b]	*Artemisia tridentata* (big sagebrush)	0.6 to 1.2	0.9
Schultz and McAdoo 2002 [DIRS 178065], p. 2	*Artemisia tridentata* (big sagebrush)	0.9 to 1.2	1.1
Tirmenstein 1999 [DIRS 177641], p. 1	*Artemisia tridentata* (big sagebrush)	0.9 to 3.0[c]	2.0
Tirmenstein 1999 [DIRS 177642], p.1	*Ericameria nauseosa* [d] (rubber rabbitbrush	0.3 to 2.3	1.3
Utah State University, Cooperative Extension 2002 [DIRS 177644], p. 2	*Ericameria nauseosa* (rubber rabbitbrush	0.3 to 2.3	1.3
Weber et al. 1993 [DIRS 177931], p. 1	*Ericameria nauseosa* (rubber rabbitbrush)	0.3 to 1.8	1.1
Zlatnik 1999 [DIRS 177639], p. 7	*Juniperus osteosperma* (Utah juniper)	3.0 to 8.0	5.5
Utah State University, Cooperative Extension 2004 [DIRS 177643], p. 1	*Juniperus osteosperma*	4.6	4.6
Utah State University, Cooperative Extension 2002 [DIRS 177646], p. 2	*Pinus monophylla* (singleleaf pinyon)	3.0 to 9.0	6.0
Stewart and Hull 1949 [DIRS 177146], pp. 58 to 59	*Bromus tectorum* (cheatgrass)	0.3 to 0.6	0.5
Utah State University, Cooperative Extension 2002 [DIRS 177647], p. 1	*Poa secunda* (Sandberg bluegrass)	0.3	0.3
Utah State University, Cooperative Extension 2002 [DIRS 177648], p. 2	*Stipa comata* (needle-and-thread grass)	0.1 to 0.3	0.2
Utah State University, Cooperative Extension 2002 [DIRS 177649], p. 2	*Achnatherum hymenoides* (Indian ricegrass)	0.3 to 0.8	0.6
Utah State University, Cooperative Extension 2002 [DIRS 177650], p. 2	*Elymus elymoides* (squirreltail)	0.2 to 0.5	0.4
Recommended Distribution Parameters: **Weighted Mean = 1.3[e]; Weighted Range = Uniform from 0.64 to 1.8 m[f]**			

[a] When ranges for heights were reported, the midpoint of the range was used to calculate distribution parameters.
[b] USDA = United States Department of Agriculture.
[c] Five m was reported as a maximum height for *A. tridentata*. However, this height is rarely reached and would not be supported by habitat conditions at Yucca Mountain. Therefore, the common range of 0.9 to 3.0 m that was reported was used here.
[d] Previous nomenclature: Chrysothamnus nauseosus.
[e] Weighted mean calculated as (0.1 × [5.5 +4.6+6.0 / 3]) + (0.9 × [0.9+1.1+2.0+1.3+1.3+1.1+0.5+0.3+0.2+0.6+0.4 / 11] = 1.3 m.
[f] Lower limit = (0.10 × 4.6) + (0.90 × 0.2) = 0.64, upper limit = (0.1 × 6.0) + (0.90 × 1.3) = 1.8.

6.5.3.4 Method for Estimating Basal Transpiration Coefficients for the Infiltration Modeling Domain

The MASSIF model requires a certain set of inputs in order to calculate basal transpiration coefficients (K_{cb} values), which are necessary for calculating evapotranspiration (ET) for the model domain. The purpose of this section is to describe the methodology used to estimate K_{cb} for each model grid cell as a function of location, day of the year, and annual precipitation. This calculation is done within the MASSIF model, but the description of the calculation is given here, rather than in Section 6.4.4, because the methodology is specific to the analysis of Yucca Mountain net infiltration rather than general to any area. All model inputs for this calculation are identified in this section and described in more detail in following sections and appendices referenced herein.

Basal transpiration coefficients estimated using FAO-56 methods and the normalized difference vegetation index (NDVI) based on satellite reflectance data are commonly used to estimate ET for agricultural crops (e.g., Kustas et al. 1994 [DIRS 176757]; Seevers and Ottman 1994 [DIRS 176764]; Szilagyi et al. 1998 [DIRS 176839]; Szilagyi 2002 [DIRS 176840]). They are used here to establish a K_{cb} estimation model based on NDVI derived from satellite data for the MASSIF model domain.

Multiple satellite images taken throughout the growing season of three representative years (wet, moderate, and dry) are used to estimate vegetation vigor represented by NDVI at each 30 × 30-m grid cell in the model domain. Using precipitation records, water year (WY) 1998 (wet), WY2001 (average), and WY2000 (dry) were identified for use (Section E1.5). WY1998 and WY2000 were selected because they represented record wet and dry years and were needed to establish timing of plant responses and a baseline of minimum plant activity for the Yucca Mountain area (Section E1.5). Vegetation expression during the record wet year (WY1998) was sufficiently robust for determining an "ideal" curve for annual vegetation response. WY2001 was chosen to represent an average precipitation year at Yucca Mountain.

Chlorophyll, responsible for the green color of plants, absorbs red light while leaf tissue reflects highly in near infrared (Buschmann and Nagel 1993 [DIRS 176736]). NDVI is determined from the differences of reflected light in the red (R) and near infrared (NIR) spectra, normalized over the sum of the two:

$$NDVI = (NIR - R) / (NIR + R) \qquad \text{(Eq. 6.5.3.4-1)}$$

NDVI is an indicator of vegetation vigor often used for measurement of environmental response to landscape-scale hydrology, including global climate change (e.g., Running and Nemani 1991 [DIRS 176819]), rainfall (e.g., Wang et al. 2003 [DIRS 176761]) and ET (e.g., Kustas et al. 1994 [DIRS 176757]; Seevers and Ottman 1994 [DIRS 176764]; Szilagyi et al. 1998 [DIRS 176839]; Szilagyi 2002 [DIRS 176840]). NDVI has been established as a competent surrogate for estimation of ET (Kustas et al. 1994 [DIRS 176757]; Seevers and Ottman 1994 [DIRS 176764]; Szilagyi et al. 1998 [DIRS 176839]; Szilagyi 2002 [DIRS 176840]). It is used here to characterize timing and magnitude of vegetation response to precipitation, and to capture spatial dynamics in ET related to slope, azimuth, elevation, and soil characteristics of each of the grid cells in the infiltration modeling domain. NDVI was determined for selected days during the

growing season using satellite imagery of the infiltration model domain (Section E2). The resulting values were corrected for differing atmospheric conditions between satellite overpasses and for specific ground conditions characterizing the Yucca Mountain environment, including the presence of desert varnish on rocks, which affects the NDVI signal (Sections 6.5.3.5 and E2).

The analysis of NDVI data for Yucca Mountain focused on two phenomena. The first is that the timing of the vegetation response in a mountainous region is affected by the slope and azimuth of the land. For example, plants on south facing slopes tend to begin their growing season before plants on north facing slopes due to warmer conditions earlier in the season. The second phenomenon is that the potential for vegetation varies by location. This variation is due to a number of factors including local soil and weather conditions. NDVI data is very useful for comparing the amount of vegetation present at each of the model grid cells, because it represents a "snapshot" of each cell at the same period in time. Observations can be compared through time by comparing different images.

6.5.3.4.1 NDVI Timing as a Function of Slope and Azimuth of the Ground Surface

NDVI varies with time reflecting the amount of green biomass present during the growing season. This temporal profile varies depending on the slope and azimuth of the land. To characterize this effect, NDVI from a representative wet year (1998) was extracted from two subregions that distinguished north-facing slopes from south-facing slopes in the uplands of Yucca Mountain (Section E3). Smooth functions were fit to NDVI versus time for these two subregions giving an NDVI value for each day of the water year (October 1 through September 30). Data from north and south facing slopes were used to estimate NDVI profiles for slope and azimuth bins between these orientations. These derived data are input to the K_{cb} calculation in the form of an NDVI look-up table (Output DTN: SN0606T0502206.012, *Daily_NDVI_Estimation.xls*) embedded in the MASSIF Mathcad model. The look-up table has 365 rows representing days of the water year and 25 columns representing different slope and azimuth bins. The development of this table is described in more detail in Sections 6.5.3.5 and E3.

6.5.3.4.2 Potential Vegetation Response (PVR) and Precipitation Adjustments

The NDVI dataset was also used to define a spatial parameter called potential vegetation response (PVR) that represents each grid cell's potential for vegetation cover given sufficient annual precipitation. Cells with high PVR values support conditions that lead to vigorous vegetation, such as sufficient soil, water, and nutrient availability. Cells with low PVR values do not support much vegetation due to the lack of necessary soil, water, or nutrients. The development of PVR values for the Yucca Mountain infiltration model domain is described in Sections 6.5.3.5 and E4. The values are listed in the geospatial input files (Output DTN: SN0606T0502206.011).

WY1998 was chosen for fitting all simulation parameters, including PVR, NDVI slope/azimuth response curves, and a precipitation ratio for scaling the magnitude of the vegetation response (Section E1.5 discusses the rationale for selecting this year). To simulate the strength of the vegetation response, the response curve is scaled using the total annual precipitation. This is

accomplished by using the ratio of the annual precipitation of the year in question to the annual total WY1998 precipitation (Sections E5 and 5).

6.5.3.4.3 Basal Transpiration Coefficient (K_{cb})

NDVI data is ideal for identifying vegetation patterns over large areas, especially when it would be impossible to make a similar number of observations on the ground. However, in order to use NDVI as an indicator of K_{cb} values, it is necessary to compare NDVI data with vegetation measurements made on the ground.

As discussed in Section 6.4.4, the MASSIF model uses a dual transpiration coefficient ($K_c = K_{cb} + K_e$) in conjunction with reference evapotranspiration (ET_0) to estimate actual evapotranspiration (ET) (Allen et al. 1998 [DIRS 157311], p. 135, Equation 69). This dual transpiration coefficient consists of a basal transpiration component (K_{cb}), representing plant transpiration under non-limiting water conditions, and an evaporation component (K_e; see Section 6.4.4). This approach can be applied to natural vegetation using measured values of leaf area index (LAI, a unitless measure of leaf area per ground area) or effective ground cover (percent of ground covered by vegetation) and adjustments for stomatal control (Allen et al. 1998 [DIRS 157311], pp. 187 to 193).

Measurements of vegetation cover that were made at a set of ecological study plots (ESPs) at Yucca Mountain during a period that included three representative water years (wet, average precipitation, and dry) were used to calculate K_{cb} values using FAO-56 methods (Allen et al. 1998 [DIRS 157311], pp. 187 to 193). The resulting K_{cb} profiles (or K_{cb} curves) are time-based and relate to ground conditions at the ESPs for the three representative years. The development of these profiles (Output DTN: MO0606SPABASAL.001) is described in Section 6.5.3.6 and Appendix D.

6.5.3.4.4 Estimating K_{cb} in the MASSIF Infiltration Model

A K_{cb} represents the amount of water that could be used by a stand of vegetation if water were not limiting (Allen et al. 1998 [DIRS 157311], p. 135). It is used in the MASSIF infiltration model with K_e and ET_0 to estimate actual evapotranspiration for each of the model grid cells for each daily time step according to the following equation (Allen et al. 1998 [DIRS 157311], p. 135, Equation 69):

$$ET_{cell} = ET_o \times \left(K_s K_{cb} + K_e\right) \qquad \text{(Eq. 6.5.3.4-1)}$$

where ET_{cell} is actual ET for a model grid cell on a given day and K_s is a stress coefficient (0 to 1) that reduces ET when soil water is limiting (Section 6.4.4). During dry periods or periods when plants are not actively transpiring, ET_{cell} is dominated by evaporation. When plants are physiologically active, transpiration becomes important.

The MASSIF infiltration model predicts K_{cb} from NDVI'[1] for each grid cell for each day of the year through the following steps:

1. A "base" NDVI' ($NDVI'_{base}$) is identified from the NDVI look-up table based on the day of year (row) and the cell's specific slope and azimuth values (column). This "base" NDVI' value accounts for the variation in the timing of the vegetation response due to the slope and azimuth of the cell (Sections 6.5.3.4.1, 6.5.3.5, and E3). This base value represents NDVI' in 1998 for a cell with PVR = 1, and the slope and azimuth in the same bin as the cell of interest.

2. The base NDVI' value is adjusted for PVR developed for each grid cell ($NDVI'_{base,pvr}$) (Sections 6.5.3.4.2, 6.5.3.5, and E4). This step accounts for spatial variability of vegetation.

$$NDVI'_{base,pvr} = NDVI'_{base} \times PVR_{cell} \qquad \text{(Eq. 6.5.3.4-2)}$$

3. The base NDVI' adjusted for PVR ($NDVI'_{base,pvr}$) is adjusted for precipitation to account for variations between yearly precipitation amounts ($NDVI'_{base,pvr,ppt}$) (Sections 6.5.3.5 and E5).

$$NDVI'_{base,pvr,ppt} = NDVI'_{base,pvr} \frac{PPT_{YR}}{PPT_{1998}} \qquad \text{(Eq. 6.5.3.4-3)}$$

where PPT_{YR} is the annual precipitation for the water year of interest, which is calculated within MASSIF from the weather input file (Appendix G), and PPT_{1998} is the annual precipitation for the water year 1998 (Output DTN: SN0606T0502206.012, *NDVI'_correct_to_90,91,93.xls*, sheet: "Precip_Ratios," cell: C22).

4. $NDVI'_{base,pvr,ppt}$ values are converted to cell values of K_{cb} (Kcb_{cell}) using a linear function derived in Section 6.5.3.7 as follows:

$$Kcb_{cell} = NDVI'_{base,pvr,ppt} \times C_{Kcb2} + C_{Kcb1} \qquad \text{(Eq. 6.5.3.4-4)}$$

C_{Kcb1} is the intercept and C_{Kcb2} is the slope of the linear function relating NDVI' and K_{cb} developed in Section 6.5.3.7.

6.5.3.5 NDVI' Look-up Table and PVR Parameter Development

This section summarizes the development of the NDVI' look-up table and the values of PVR for each cell in the model domain. The discussion is a summary of Appendix E, in which the details of this development are described.

[1] NDVI' is NDVI corrected for differing atmospheric conditions between satellite overpasses and for specific ground conditions characterizing the Yucca Mountain environment, including the presence of rock varnish. This correction is described in Sections 6.5.3.5 and E2.

6.5.3.5.1 Direct Inputs

Direct inputs used to develop the NDVI' look-up table and the values of PVR are:

- Landsat TM (thematic mapper) images of the infiltration model domain (DTN: SN0601ALANDSAT.001 [DIRS 177239])
- Precipitation for WYs 1990, 1991, 1993 (Output DTN: MO0607SEPTOTAL.003), 1998, 2000, and 2001 (Output DTN: MO0602SPAPRECP.000)
- Geospatial data including input to PVR, slope and azimuth of model grid cells, ESP location coordinates, etc.

Digital Ortho Quarter Quad (DOQQ)	DTN: SN0601DOQQYM98.001 [DIRS 177240]
Shuttle Radar Topography	DTN: SN0601SRTMDTED.001 [DIRS 177242]
Ground Control Points	DTN: MO0512COV05112.000 [DIRS 177249] DTN: MO9906GPS98410.000 [DIRS 109059]
ESP Location Coordinates	DTN: MO9901ESPYMNYE.000 [DIRS 177247]

6.5.3.5.2 Development of NDVI' Look-up Table

Selected scenes from a 20-year archive of Landsat TM were chosen as the basis for characterizing large-scale Yucca Mountain vegetation patterns. Table 6.5.3.5-1 lists the images chosen for three representative water years (dry [2002], moderate [2001], and wet [1998]).

Table 6.5.3.5-1. Landsat TM Data Used for Characterization of Yucca Mountain Vegetation

WY1998		WY2001		WY2002	
Filename	Sensor	Filename	Sensor	Filename	Sensor
t519971102	TM5	t520001009	TM5	t720011207	TM7
t519980121	TM5	t520010129	TM5	t720020124	TM7
t519980310	TM5	t520010318	TM5	t720020225	TM7
t519980411	TM5	t520010419	TM5	t720020329	TM7
t519980427	TM5	t520010505	TM5	t720020414	TM7
t519980529	TM5	t520010606	TM5	t720020430	TM7
t519980630	TM5	t520010724	TM5	t720020516	TM7
t519980716	TM5	t520011012	TM5	t720020601	TM7
t519980817	TM5	t720001220	TM7	t720020617	TM7
		t720010326	TM7	t720020719	TM7
		t720010630	TM7	t720020804	TM7
		t720010817	TM7		
		t720011004	TM7		

Source: DTN: SN0601ALANDSAT.001 [DIRS 177239].

NOTE: Filenames list satellite, year, month, and day.

Two Landsat satellites were available for the periods of interest, TM5 and TM7 (Section E2.1). The basic processing steps are summarized as follows:

1. Reflectance data from the scenes listed in Table 6.5.3.5-1 were used to calculate NDVI from Equation 6.5.3.4-1 for each pixel of each scene. Pixel size of TM data is approximately 28 × 28 m.

2. NDVI was then corrected for atmospheric differences between scenes and the images were geocorrected using a set of ground control points (DTN: MO0512COV05112.000 [DIRS 177249]) (Sections E2.2 and E2.3). Geocorrection ensures that pixels on each image overlie each other so that differences in pixels between scenes can be identified.

3. The NDVI values were scaled to calculate $NDVI_{offset}$, which is calculated as:

$$NDVI_{offset} = NDVI - NDVI_0 \qquad \text{(Eq. 6.5.3.5-1)}$$

   where NDVI is the atmospheric and geocorrected NDVI and $NDVI_0$ is the NDVI expected in areas with no vegetation (Section E2.4).

4. A positive NDVI signal arising from desert varnish that was present on many exposed rocks in the area was subtracted to get NDVI' for time steps throughout the growing season for the three water years. NDVI' represents a clean and coherent vegetation signal from the TM data To remove the effect of rock varnish, $NDVI_{offset}$ values from the lowest vegetation period of the driest year were subtracted from the other scenes (Section E2.6):

$$NDVI'_i = NDVI_{offset-i} - NDVI_{offset-min-i} \quad \text{(Eq. 6.5.3.5-2)}$$

where *i* refers to the i^{th} pixel and *min* refers to NDVI expression during a very dry year when vegetation response would be near zero.

The effects of slope and azimuth on NDVI' values over time for WY1998 were determined by extracting NDVI' from two subregions of pixels with either north- or south-facing slopes (Section E3.2). The NDVI' values from these subregions (Section E3.2) were fit with smooth curves and extended to other subregions of slope and azimuth by geometric interpolation (Figure 6.5.3.5-1). These curves represent NDVI' values for WY1998 and are referred to as "base" NDVI'.

Base NDVI' values for each day of the water year defined for 13 unique classes of slope and azimuth were organized into a table for use as direct input to the infiltration model (Section E3, Table E-4; Output DTN: SN0606T0502206.012, *Daily_NDVI_Estimation.xls*). Each of the model grid cells was assigned a slope-azimuth class (Section E3). Based on the slope-azimuth class, the model assigns the corresponding base NDVI' for the WYDOY from Table E-4 to each grid cell.

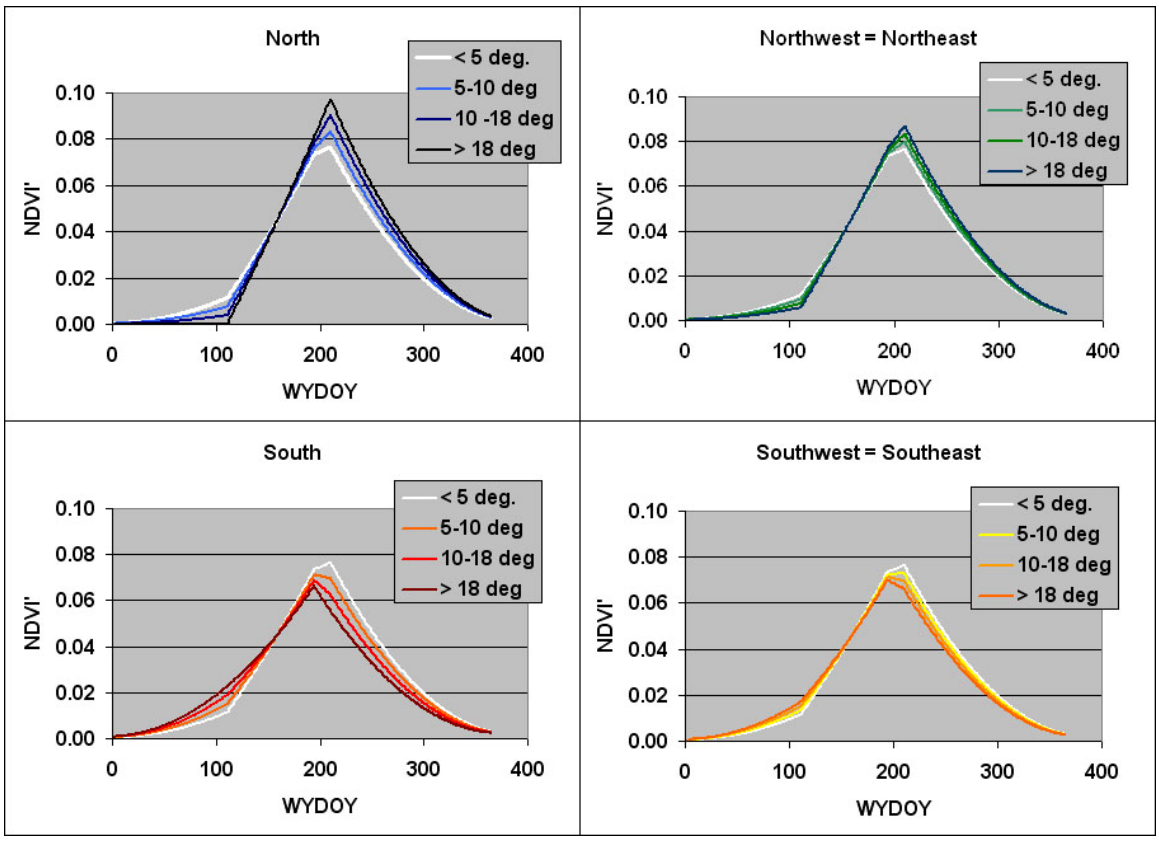

Source: Output DTN: SN0606T0502206.012, *Daily_NDVI_Estimation.xls*.

NOTE: There are 13 unique combinations of curves. The curve representing level ground (<5°) and E and W slopes is reproduced (white) in each graph.

Figure 6.5.3.5-1. Temporal Curves Developed by the Weighting Functions in Table E-4

6.5.3.5.3 Development of the Potential Vegetation Response for Each Grid Cell in the Model Domain

PVR was used to scale each model grid cell to the strength of the vegetation response for the actual conditions in that cell (Section E4) and was calculated as:

$$PVR_i = [(\text{average } NDVI_{offset})_{max} - (\text{average } NDVI_{offset})_{min}]_i / \text{average } NDVI_{1-i}$$

(Eq. 6.5.3.5-3)

where

$i = i^{th}$ model grid cell
max = wet year
min = dry year
average_{1-i} = average of grid cells, from the 1st to the i^{th}, within the area of interest.

The denominator of PVR, the average value of grid cells within the area of interest, normalized the results for a subset area overlying the proposed repository. This area was chosen as a rectangle of 12,702 grid cells (11.43 km^2) (Figure 6.5.3-2). Normalization provided scaling to permit better understanding of PVR distribution: a PVR of 1.0 represents the approximate average vegetation response overlying the repository. PVR varies from 0 (no vegetation response) to about 4 (see Section E4 for determination and verification of PVR). Figure 6.5.3.5-2 shows a map of PVR values for most of the infiltration modeling domain.

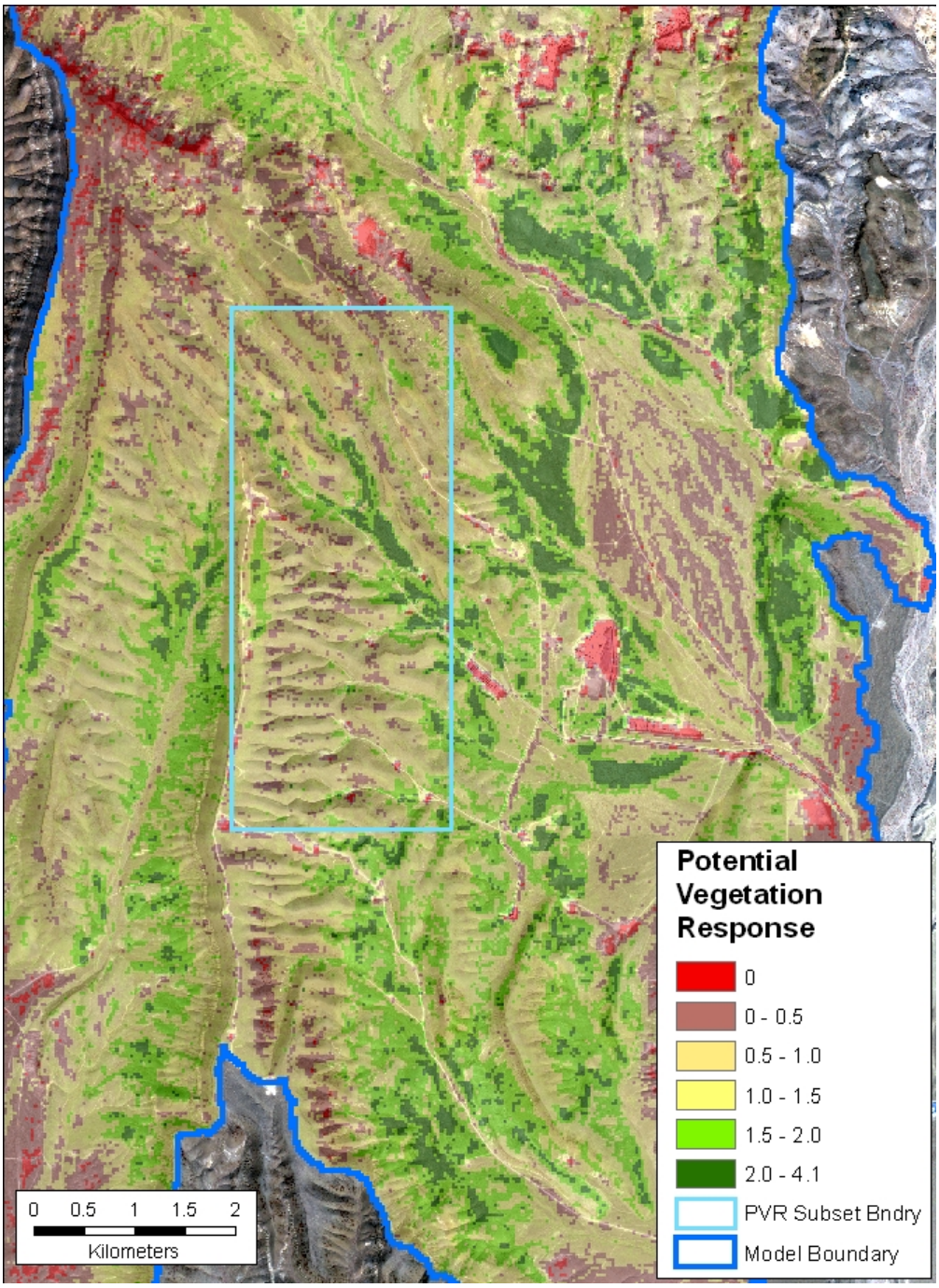

NOTE: The PVR data is one of the MASSIF Spatial Data inputs, Output DTN: SN0606T0502206.011. The other files are *PVR_subset_.evf* and *nad27_boundary_evf* in Output DTN: SN0608NDVIAUXD.001. Background is Quickbird DTN: SN0601QBSAT802.001 [DIRS 177241].

Figure 6.5.3.5-2. Map of Potential Vegetation Response for the Central Region of the Infiltration Modeling Domain

WY1998 was chosen for fitting all simulation parameters, including PVR, NDVI' look-up table, and a precipitation ratio for scaling the magnitude of the base NDVI' response. WY1998 is an ideal choice as the very high level of precipitation induced a maximal NDVI' response. This maximal response corresponds to a strong "signal" in an environment that generally has a weak vegetation signal, hence boosting the signal-to-noise ratio.

Methods are used in Appendix E to correct for non-systematic variation in NDVI parameters (Section E2.4). Analyses are performed in Appendix E to confirm the appropriateness of NDVI' processing parameters (Section E2.5) and the NDVI' algorithm (Section E7) to increase confidence in the values used in the MASSIF model. Additionally, uncertainties associated with calculation of NDVI' are addressed in Section E7.4.

6.5.3.6 Determination of K_{cb} from Ground Cover Measurements Made at Ecological Study Plots

This section provides a brief description of the calculation of K_{cb} values for a set of ecological study plots (ESPs), representing three vegetation associations, for three representative years (wet, moderate, and dry). These K_{cb} values are then used in Section 6.5.3.7 to determine appropriate parameter values to use to convert grid-cell values of NDVI' to K_{cb} values required for the calculation of evapotranspiration. Details of K_{cb} calculations and development of inputs are in Appendix D.

The FAO-56 K_{cb} profile for agricultural crops reflects transpiration under optimal growth and non-limiting water conditions. The generalized K_{cb} profile (Figure 6.5.3.6-1) includes four growth stages (Allen et al. 1998 [DIRS 157311], pp. 95 to 96): an initial growth stage (planting date to approximately 10% ground cover), a development stage (10% ground cover to effective full cover), a mid-season stage (effective full cover to start of maturity), and a late season stage (maturity to harvest or senescence). Effective full cover is defined as the time when soil shading is nearly complete (Allen et al. 1998 [DIRS 157311], p. 95). Transpiration coefficients are developed for the initial growth stage ($K_{cb\ ini}$), the mid-season stage ($K_{cb\ mid}$), and the end of the late season stage ($K_{cb\ end}$) (Figure 6.5.3.6-1). The curve is constructed by drawing straight line segments through each of the four growth stages (Figure 6.5.3.6-1).

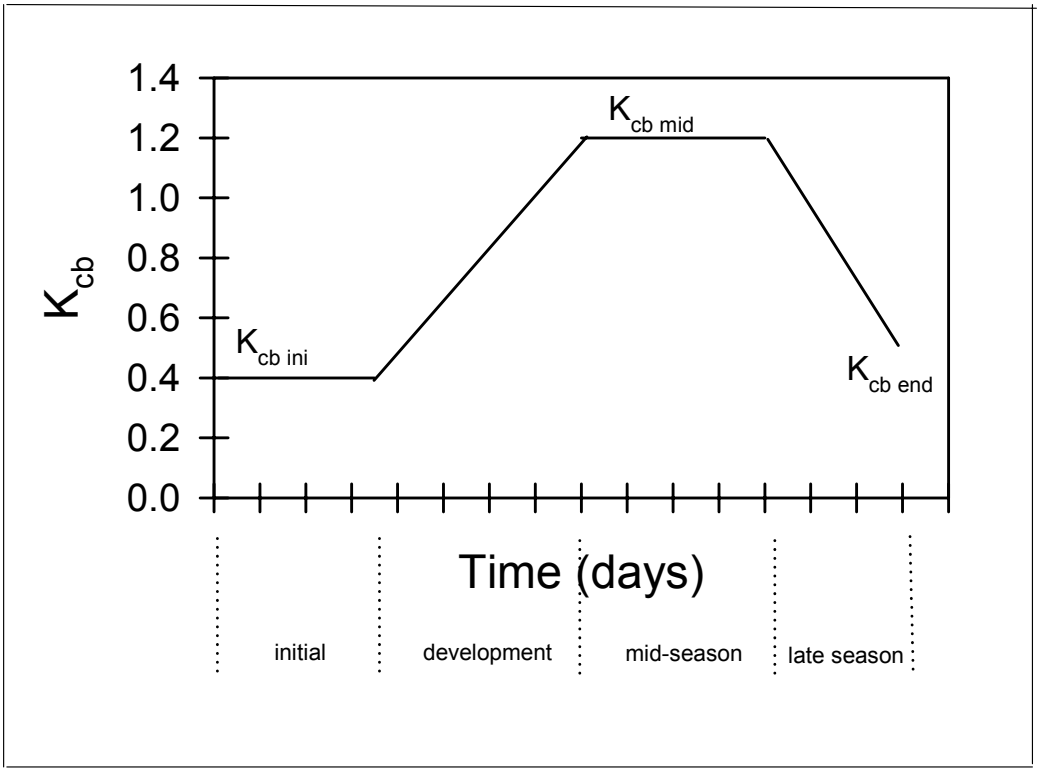

Source: Allen et al. 1998 [DIRS 157311], p. 100, Figure 26.

Figure 6.5.3.6-1. Generalized Crop Coefficient Curve

Characteristics of desert vegetation at Yucca Mountain differ from agricultural crops in several ways, including low effective ground cover that rarely exceeds 30% during peak growth periods (CRWMS M&O 1996 [DIRS 102235], p. 23), little morphological change in perennial vegetation across growth stages (e.g., little change in average maximum vegetation height and maintenance of a percentage of green canopy throughout the year), and greater degree of stomatal control resulting in lower rates of water loss compared to agricultural crops. Additionally, desert vegetation assemblages consist of a variety of plant species that have different growth stage lengths and contribute differently to total ground cover when compared to agricultural crops that are generally planted in monocultures. Climatic conditions at Yucca Mountain differ from standard FAO-56 conditions, with lower minimum relative humidity (RH_{min}) and higher wind speeds (u_2). To account for these differences, FAO-56 methods for calculating K_{cb} for natural vegetation using effective ground cover, adjustments for stomatal control over water loss, and adjustments for local RH_{min} and u_2 were used (Allen et al. 1998 [DIRS 157311], pp. 187 to 193; see Appendix D for details).

6.5.3.6.1 Vegetation Reference Areas

The flora and climate of Yucca Mountain have been described as characteristically Mojavean (Beatley 1975 [DIRS 103356]; 1976 [DIRS 102221]), with vegetation on the crest and upper slopes that is transitional to Great Basin Desert flora (Beatley 1976 [DIRS 102221]). Vegetation communities at Yucca Mountain have been characterized by a number of authors (e.g., Beatley 1976 [DIRS 102221]; O'Farrell and Collins 1984 [DIRS 102160]; CRWMS M&O 1996 [DIRS 102235]) and have often been described in terms of associations. Using a simple classification scheme, the vegetation at Yucca Mountain can generally be delineated into four associations named for dominant or co-dominant species: *Coleogyne* (COL), *Larrea-Ambrosia* (LA), *Lycium-Grayia* (LG), and *Larrea-Lycium-Grayia* (LLG) (CRWMS M&O 1996 [DIRS 102235], pp. 7 to 8, Table 2-1).

The LA, LG, and LLG vegetation associations are the most common in the infiltration model domain. The LG association is representative of the vegetation that overlies the proposed repository on the upper slopes and crest of Yucca Mountain (elevation = 1,300 to 1,600 m; DTN: MO9907SADESYYM.000 [DIRS 177169]). The LLG association is representative of the vegetation of mid-elevation intermountain valleys within the infiltration modeling domain (1,150 to 1,300 m; DTN: MO9907SADESYYM.000 [DIRS 177169]). The LA association is representative of low elevation vegetation within the infiltration modeling domain (940 to 1,150 m, DTN: MO9907SADESYYM.000 [DIRS 177169]). The LG association is considered critically important to the infiltration modeling effort because the vegetation is representative of that overlying the proposed repository where infiltration to interred waste casks could occur. Vegetation cover and plant species composition data from the LA, LG, and LLG vegetation associations were used to develop K_{cb} profiles over time using FAO-56 methods. K_{cb}s estimated for the LG association are used to develop the least-squares regression between K_{cb} and NDVI' as described in Section 6.5.3.7. K_{cb}s estimated for the LA, LLG, and LG associations are used to evaluate appropriateness of NDVI' (Sections E2 and E7) and to determine whether the magnitude of K_{cb}s is appropriate for desert vegetation (Section D7).

Parameter Inputs – Direct inputs to K_{cb} calculations were:

- Species-specific cover data and species composition from the ESPs collected in 1990, 1991, and 1993 (Output DTN: MO0606SPAVEGAS.001). Cover data (per species) were averaged over the 12 ESPs per association for each year. Total cover for annual, drought deciduous, and evergreen vegetation was determined for the LA, LG, and LLG associations and used as input to K_{cb} calculations. See Section D2.2 for description of annual, drought deciduous, and evergreen vegetation types.

- Growth stage lengths for annual, drought deciduous, and evergreen vegetation (Section D3.2.1).

- Plant height for LA, LG, and LLG associations (Section D3.2.1).

- Stomatal resistance for dominant species within annual, drought deciduous, and evergreen vegetation types (Section D3.2.3).

- Mean daily wind speed and air temperature, and minimum daily relative humidity from Yucca Mountain Meteorological Site 1 for WY1998, WY2000, and WY2001 (Output DTN: MO0602SPAWEATH.000). Minimum relative humidity (RH_{min}) and wind speed (u_2) adjustments to K_{cb}s were from the same water years as were used for NDVI' determinations. Adjustments in K_{cb}s invoked by RH_{min} and u_2 were small compared to variation in K_{cb}s among years, vegetation types, and associations (see Section D3.2.4).

- The psychrometric constant (γ) for the elevation of Yucca Mountain Meteorological Site 1 from Allen et al. (1998 [DIRS 157311], p. 214, Table 2.2).

These inputs are developed in Section D3.2.

Vegetation cover and species composition, needed for K_{cb} calculations, were measured on the ESPs during peak growth periods from 1989 to 1994 (Section D2.2). Vegetation cover at Yucca Mountain is largely dependent on precipitation; therefore, precipitation records for the ESPs from 1989 to 1994 were evaluated to determine wet, normal, and dry years that could be paired with the years that NDVI' were determined for (Section D2.2). Based on precipitation records, vegetation cover and species composition data were used from the following three years in K_{cb} calculations: WY1991 (average), an average precipitation year for the Yucca Mountain area (about 150 mm; CRWMS M&O 1996 [DIRS 102235], p. 21, Figure 4-3); WY1993 (wet), the highest precipitation year on record for the years that cover data were collected (about 240 mm; CRWMS M&O 1996 [DIRS 102235], p. 21, Figure 4-3); and WY1990 (dry), the lowest precipitation year on record for the years that cover data were collected (about 60 mm; CRWMS M&O 1996 [DIRS 102235], p. 21, Figure 4-3). For verification of NDVI processing parameters, wet, dry, and average precipitation years from the two data sets (NDVI' and K_{cb}) were paired by normalizing and scaling NDVI' using annual precipitation. For the K_{cb} − NDVI' regression, wet and average years from the two data sets were paired. The dry year was not used in the K_{cb} − NDVI' regression because the vegetation signal for 2002 was essentially zero throughout the year for the LG association (Section E7.1).

Profiles of K_{cb} versus day of year (Figure 6.5.3.6-2) were calculated from these direct inputs using equations from FAO-56 (Allen et al. 1998 [DIRS 157311], Chapter 9). These calculations are discussed in detail in Appendix D.

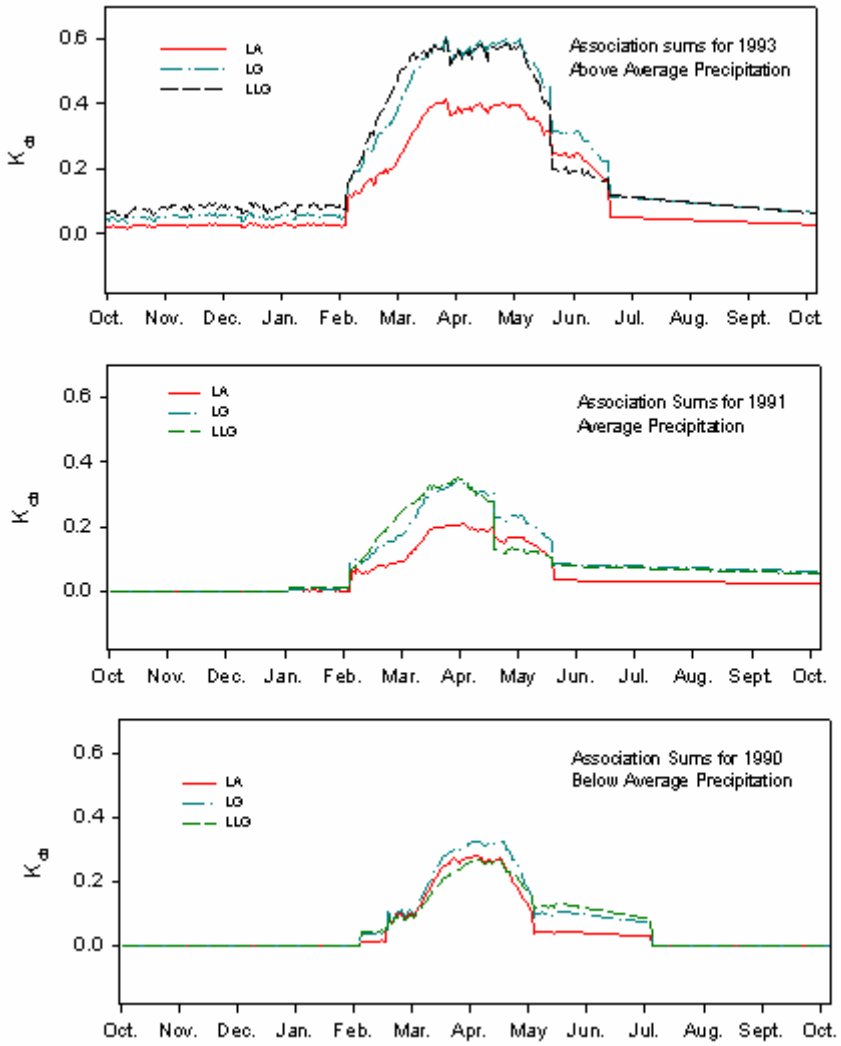

Source: Output DTN: MO0606SPABASAL.001.

Figure 6.5.3.6-2. Transpiration Coefficient (K_{cb}) Profiles for LA, LG, and LLG Vegetation Associations for Water Years 1993, 1991, and 1990

Use of separate K_{cb} − NDVI' regressions for each vegetation association would require that each model grid cell be assigned to one of the three associations. This was not feasible due to lack of detailed spatial data for vegetation associations and the potential for vegetation change through time. As an alternative to using separate K_{cb} − NDVI' regressions for each association, and for use in uncertainty analyses, upper and lower bounds for K_{cb}s were calculated for the LG association profiles for WY1991 and WY1993. Upper and lower bounds for daily K_{cb}s were determined for each profile by using high and low input values for vegetation cover, plant height, and stomatal resistance (Figure 6.5.3.6-3). The high and low values were taken from the input data sets. See Section D4 for selection of inputs and details of calculations. The uncertainty bounds for the LG association K_{cb} profiles encompassed the variation observed among associations (compare Figures 6.5.3.6-2 and 6.5.3.6-3). Therefore, the K_{cb}s with uncertainty bounds for WY1993 and WY1991 for the LG association (Figure 6.5.3.6-3) are recommended

for use in K_{cb} − NDVI regressions for the Yucca Mountain area. The upper and lower bounds of the profiles are used in Section 6.5.3.7 to calculate standard uncertainties for the LG association K_{cb} profiles.

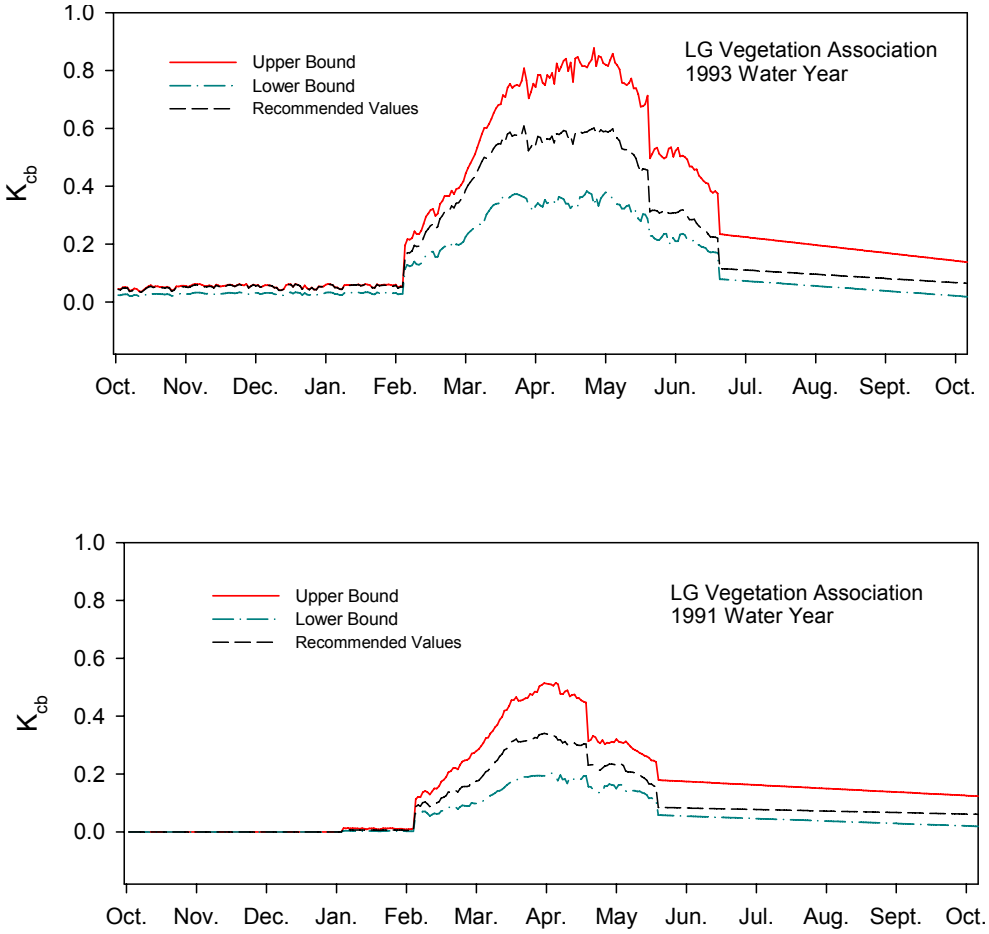

Source: Output DTN: MO0606SPABASAL.001.

NOTE: Recommended values are the same as those for the LG association for WY1993 and WY1991 in Figure 6.5.3.6-2.

Figure 6.5.3.6-3. Transpiration Coefficient Profiles for LG Vegetation Associations with Upper and Lower Bounds

6.5.3.7 Correlating K_{cb} Profiles with NDVI'

In order to implement the FAO-56 methodology for estimating evapotranspiration at Yucca Mountain, it was necessary to estimate values for basal transpiration coefficients (K_{cb}) as a function of NDVI corrected for the Yucca Mountain environment (NDVI'). NDVI is widely used by researchers to estimate green biomass, leaf area index (LAI), and patterns of productivity in both agricultural and natural ecosystems. Among other factors, transpiration coefficient values are dependent on LAI or cover of vegetation, both of which are dependent on precipitation. Several studies have demonstrated a strong linear relationship between transpiration coefficients and NDVI for agricultural crops (e.g., Duchemin et al. 2006

[DIRS 178498]; Tasumi et al. 2005 [DIRS 177653]; Bausch and Neale 1987 [DIRS 177652]; Ray and Dadhwal 2001 [DIRS 177336]). Verification analyses of the NDVI' algorithm (Sections E7.2 and E7.3) showed strong linear relationships between estimated K_{cb}s and simulated NDVI', and between average percent ground cover data collected during peak growth and simulated peak NDVI' for the ecological study plots (ESPs) at Yucca Mountain. Based on evidence that the K_{cb} − NDVI relationship is generally linear, a least-squares method was selected to fit a linear relationship to the K_{cb}s and NDVI' developed for Yucca Mountain.

The method of minimizing Chi squared (χ^2) as described by Bevington and Robinson (1992 [DIRS 147076], Chapter 6) was used to define a linear fit to the data in the form:

$$y(x) = a + bx \qquad \text{(Eq. 6.5.3.7-1)}$$

where

$y(x)$	=	estimated K_{cb}
a	=	y-intercept
b	=	slope of the regression line
x	=	NDVI' for a model grid cell

The slope and intercept parameters (a and b, respectively) are used as model input to the analysis of net infiltration. Their values and their associated uncertainties are developed in this section.

6.5.3.7.1 Use in the Infiltration Model

The slope and intercept parameters that define the linear fit between K_{cb} and NDVI' are used in the MASSIF model to predict K_{cb} from NDVI' for each model grid cell. The predicted K_{cb} is used in the calculation of evapotranspiration for each model grid cell. See Section 6.5.3.4.4 for a discussion of where and how these parameters are used in the calculation.

6.5.3.7.2 Parameter Development

Transpiration coefficient profiles (Appendix D) and NDVI' (Appendix E) developed for *Lycium-Grayia* (LG) ESPs were used in this analysis. As described in Section 6.5.3.6.1, the LG vegetation association was chosen because it best represents the type of vegetation that is present directly above the repository footprint.

Parameter Inputs—Direct inputs to the intercept and slope parameters were K_{cb}, NDVI', and water year precipitation data sets (Output DTNs: MO0606SPABASAL.001, MO0607SEPTOTAL.003, and MO0602SPAPRECP.000). Measured NDVI' data for 1998 (wet year) and 2001 (average precipitation year) were paired with the wet (1993) and average precipitation (1991) years for which K_{cb}s were estimated. The dry year (2002) was not included in the fitting analysis because the vegetation response measured by NDVI' was essentially zero throughout the year on the LG plots (Figure E-26). This minimal response was due to the exceptionally low amount of precipitation that fell that year (about 34 mm). Measured NDVI'

was scaled to 1993 and 1991 with a modified version of Equation E-8 that used the precipitation ratio for each of the two paired years:

$$NDVI'_{j1993} = NDVI'_{j1998} \times \frac{\sum WY\ 1993\ precip.}{\sum WY\ 1998\ precip.} \qquad \text{(Eq. 6.5.3.7-2)}$$

$$NDVI'_{j1991} = NDVI'_{j2001} \times \frac{\sum WY\ 1991\ precip.}{\sum WY\ 2001\ precip.} \qquad \text{(Eq. 6.5.3.7-3)}$$

where:

j = j^{th} day of the water year

Σ WY = sum of water year precipitation

Precipitation ratios were determined from the average water year precipitation for Yucca Mountain Meteorological Sites 2, 3, and 4 (Table 6.5.3.7-1). These sites were chosen because they represent a range of elevations at Yucca Mountain and variation in precipitation at those elevations.

Satellite images were chosen to establish vegetation responses throughout the water year (Section E2.1). For the LG sites, nine images were processed for 1998 and ten images were processed for 2001 (Section E2.1). The resulting NDVI' values were multiplied by the precipitation ratios to get the scaled NDVI' values used in the regression analysis (Table 6.5.3.7-2).

Table 6.5.3.7-1. Water Year Precipitation Totals, Means, and Ratios for Water Years 1991, 1993, 1998, and 2001

	Wet Years		Average Years	
Monitoring Site	1998 Pcp [a] (mm)	1993 Pcp (mm)	2001 Pcp (mm)	1991 Pcp (mm)
Site 2	369.32	261.87	186.18	91.56
Site 3	402.59	240.92	204.22	121.73
Site 4	360.93	248.67	192.28	99.05
Mean [b]	377.61	250.49	194.23	104.11
Ratio [c]	0.6633		0.5360	

Source: Output DTNs: MO0607SEPTOTAL.003 and MO0602SPAPRECP.000.

[a] Precipitation total for water year.
[b] Mean water year total for Sites 2, 3, and 4.
[c] Ratios of water year precipitation for wet years and average precipitation years.

Table 6.5.3.7-2. NDVI' Estimated for the LG Ecological Study Plots Scaled for Water Years 1993 and 1991

WY DOY[a]	Date of Satellite Image	NDVI' for WY 1998[b]	Scaled NDVI' for WY 1993[c]
33	11/2/97	0.0067	0.0044
113	1/21/98	0.0271	0.0180
161	3/10/98	0.0558	0.0370
193	4/11/98	0.0859	0.0570
209	4/27/98	0.0924	0.0613
241	5/29/98	0.0724	0.0480
273	6/30/98	0.0376	0.0249
289	7/16/98	0.0186	0.0123
321	8/17/98	0.0234	0.0155
WY DOY[a]	**Date of Satellite Image**	**NDVI' for WY 2001[b]**	**Scaled NDVI' for WY 1991[d]**
9	10/9/00	0.0168	0.0090
81	12/20/00	0.0237	0.1270
169	3/18/01	0.0472	0.0253
177	3/26/01	0.0539	0.0289
201	4/19/01	0.0773	0.0414
217	5/5/01	0.0490	0.0263
249	6/6/01	0.0277	0.0148
273	6/30/01	0.0218	0.0117
297	7/24/01	0.0202	0.0108
321	8/17/01	0.0166	0.0089

[a] WY DOY = Water year day of year.
[b] Output DTN: SN0606T0502206.012, *NDVI'_correct_to_90,91,93.xls*.
[c] NDVI' × precipitation ratio, where ratio = 0.6633 (from Table 6.5.3.7-1).
[d] NDVI' × precipitation ratio, where ratio = 0.5360 (from Table 6.5.3.7-1).

Figures 6.5.3.7-1 and 6.5.3.7-2 show the relationship between profiles of estimated K_{cb} and measured NDVI' as a function of time for the wet and average precipitation years. The uncertainties in these data are shown on the plots as upper and lower bounds for the K_{cb} profiles and as standard uncertainties (± one standard deviation) for the NDVI' values. See Appendices D and E for details about how uncertainty was estimated.

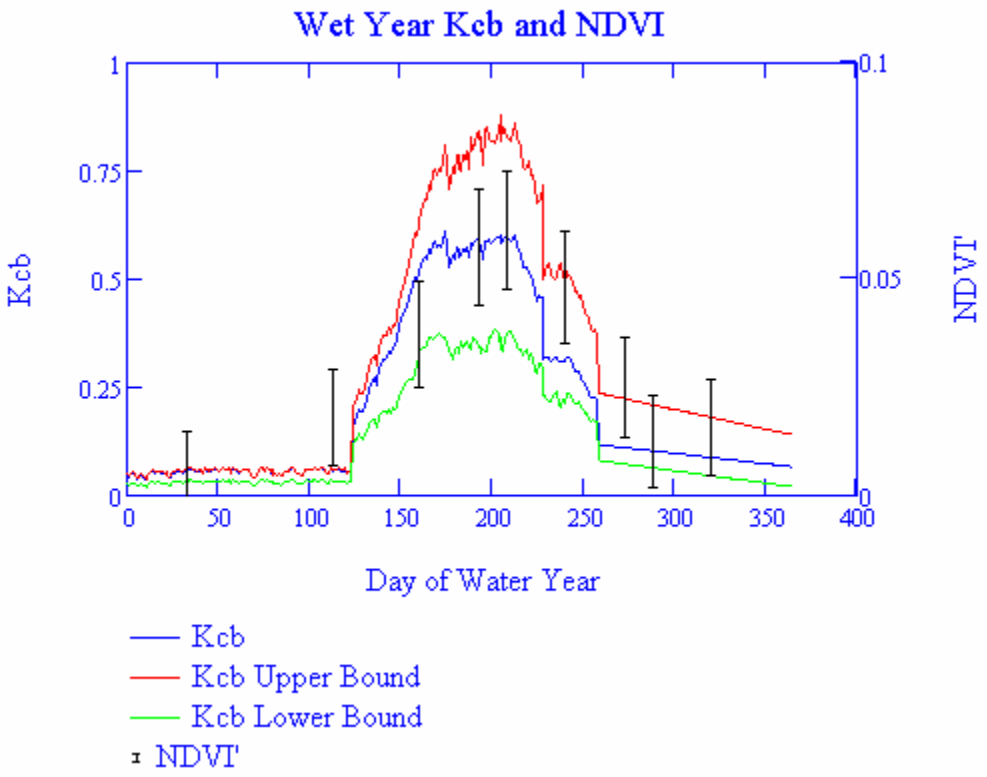

Source: Output DTNs: MO0606SPABASAL.001 and SN0606T0502206.012.

Figure 6.5.3.7-1. Comparison of Estimated K_{cb} and Precipitation-Scaled NDVI' for the LG Vegetation Association for a Wet Year

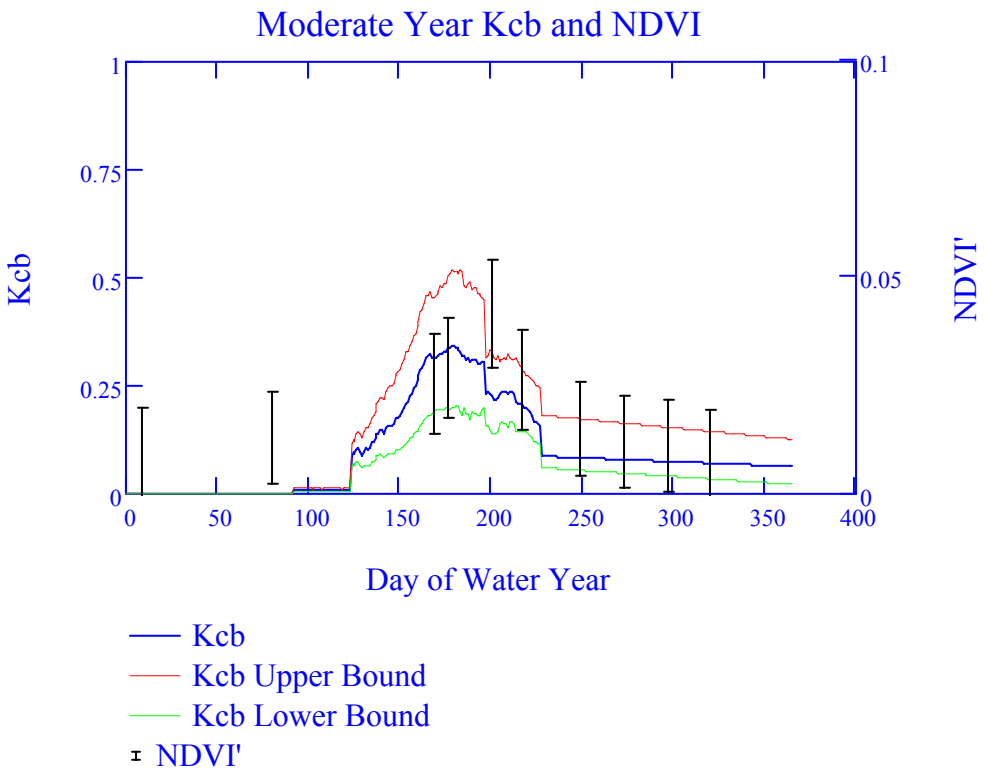

Source: Output DTNs: MO0606SPABASAL.001 and SN0606T0502206.012.

Figure 6.5.3.7-2. Comparison of Estimated K_{cb} and Precipitation Scaled NDVI' for the LG Vegetation Association for an Average Precipitation Year

Transpiration coefficients for the days that NDVI' was determined in the two water years were extracted from Output DTN: MO0606SPABASAL.001 (Table 6.5.3.7-3). These values and the corresponding NDVI' values were used in the regression analysis.

Table 6.5.3.7-3. Transpiration Coefficients (K_{cb}) with Standard Deviations for the LG Vegetation Association

WY 1993 DOY [a]	WY 1993 K_{cb}	Std Uncert [b]	WY 1991 DOY [a]	WY 1991 K_{cb}	Std Uncert [b]
33	0.0569	8.353×10^{-3}	9	0	1×10^{-3}[c]
113	0.0554	7.636×10^{-3}	81	0	1×10^{-2}[c]
161	0.5164	0.088	169	0.3112	0.077
193	0.5897	0.145	177	0.3363	0.089
209	0.5887	0.132	201	0.2238	0.055
241	0.3107	0.093	217	0.2057	0.042
273	0.1087	0.044	249	0.0811	0.034
289	0.1010	0.042	273	0.770	0.033
321	0.0855	0.039	297	0.0728	0.033
			321	0.0686	0.032

Source: Output DTN: MO0606SPABASAL.001.

[a] WY DOY = Water Year Day of Year.
[b] Standard Uncertainty for transpiration coefficients (K_{cb}).
[c] Calculated uncertainty was zero and therefore was set to 0.01 as described below and in source DTN.

Standard uncertainties for the individual K_{cb} values in Table 6.5.3.7-3 were based on a uniform distribution between the upper and lower bounds of the profile using the following equation:

$$\sigma(x) = \frac{A - B}{\sqrt{12}} \qquad \text{(Eq. 6.5.3.7-4)}$$

where:

σ = standard deviation
x = K_{cb}
A = upper bound for K_{cb}
B = lower bound for $K_{cb.}$

The derivation of Equation 6.5.3.7-4 is in Output DTN: MO0610SPALINEA.000. Under conditions when the calculated uncertainties were zero (e.g., early in the growing during the average precipitation year; Figure 6.5.3.7-2), the standard uncertainty was set to 0.01. This was done to avoid having to treat zero uncertainties as special cases in the slope and intercept formulas (Equations 6.5.3.7-6 and 6.5.3.7-7). The value of 0.01 was determined by decreasing the standard uncertainty until it had no effect on the final calculated slope value (Output DTN: MO0610SPALINEA.000).

Least Squares Regression Analysis—To determine the least squares fit between K_{cb} and NDVI' in the form of Equation 6.5.3.6-1, the method of minimizing χ^2 was used. In this case, χ^2 is defined as the sum of the weighted, squared deviations in the variable y_i (Bevington and Robinson 1992 [DIRS 147076], pp. 102 to 103, Equation 6.9):

$$\chi^2 = \sum \left[\frac{1}{\sigma_i} \left(y_i - a - b x_i \right) \right]^2 \qquad \text{(Eq. 6.5.3.7-5)}$$

where

σ_i = standard deviation of K_{cb} on the ith day
y_i = K_{cb} on the ith day
a = intercept of the least squares regression equation (Equation 6.5.3.6-5)
b = slope of the least squares regression equation (Equation 6.5.3.6-6)
x_i = NDVI' on the ith day

The following equations were used to determine values of a and b that minimize χ^2 (Bevington and Robinson 1992 [DIRS 147076], p. 104, Equation 6.12):

$$a = \frac{1}{\Delta} \left(\sum \frac{x_i^2}{\sigma_i^2} \sum \frac{y_i}{\sigma_i^2} - \sum \frac{x_i}{\sigma_i^2} \sum \frac{x^i y^i}{\sigma_i^2} \right) \qquad \text{(Eq. 6.5.3.7-6)}$$

$$b = \frac{1}{\Delta} \left(\sum \frac{1}{\sigma_i^2} \sum \frac{x_i y_i}{\sigma_i^2} - \sum \frac{x_i}{\sigma_i^2} \sum \frac{y_i}{\sigma_i^2} \right) \qquad \text{(Eq. 6.5.3.7-7)}$$

$$\Delta = \sum \frac{1}{\sigma_i^2} \sum \frac{x_i^2}{\sigma_i^2} - \left(\sum \frac{x_i}{\sigma_i^2} \right)^2 \qquad \text{(Eq. 6.5.3.7-8)}$$

where

a = intercept of the least squares regression equation
σ_i^2 = variance of K_{cb} on the ith day
y_i = K_{cb} on the ith day
b = slope of the least squares regression equation
x_i = NDVI' on the ith day.

These calculations were performed using Mathcad software and are available in Output DTN: MO0610SPALINEA.000. The resulting slope and intercept for the least squares regression equation were 9.7 and −0.05, respectively (Output DTN: MO0610SPALINEA.000). The K_{cb} and NDVI' data are plotted in Figure 6.5.3.7-3 with the fitted regression line and 95% confidence intervals. Methods for determining uncertainties in a and b are discussed below.

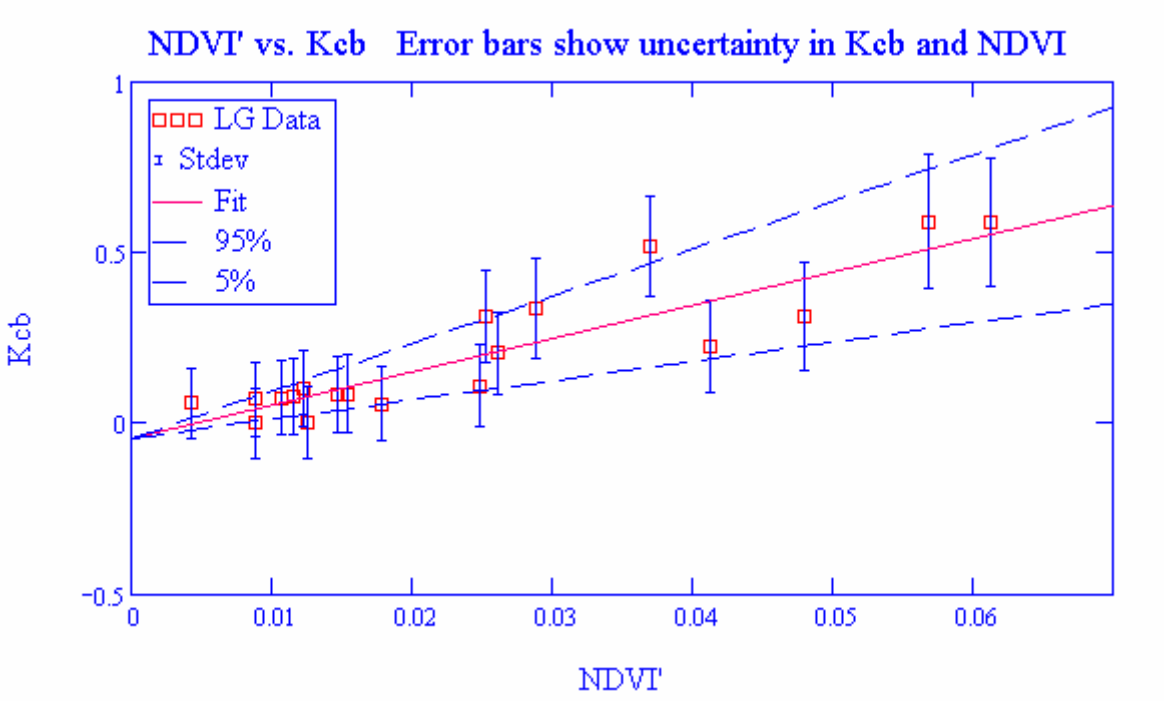

Source: Output DTN: MO0610SPALINEA.000.

Figure 6.5.3.7-3. Linear Relationship between Transpiration Coefficients (K_{cb}) and Normalized Difference Vegetation Indices Corrected for the Yucca Mountain Environment (NDVI')

Parameter Uncertainties and Distributions—Uncertainties in the intercept and slope were calculated as the variance in each parameter based on uncertainties associated with individual estimated points. The following equations were used from Bevington and Robinson (1992 [DIRS 147076], pp. 108 to 109, Equations 6.21 and 6.22):

$$\sigma_a^2 = \frac{1}{\Delta}\sum\frac{x_i^2}{\sigma_i^2} \qquad \text{(Eq. 6.5.3.7-9)}$$

$$\sigma_b^2 = \frac{1}{\Delta}\sum\frac{1}{\sigma_i^2} \qquad \text{(Eq. 6.5.3.7-10)}$$

where

σ_a^2 = variance of the intercept

σ_b^2 = variance of the slope.

The remaining variables are defined above.

Two sources of uncertainty were considered in the calculation of the variance in K_{cb}s used in Equations 6.5.3.7-6 through 6.5.3.7-10 These sources included a direct contribution due to uncertainties in K_{cb}s, and an indirect contribution from uncertainties in NDVI' to the total

uncertainty in predicted K_{cb}s. The following two functions were used from Bevington and Robinson (1992 [DIRS 147076], p. 100, Equations 6.2 and 6.3):

$$\sigma_{yI} = \sigma_x \frac{dy}{dx} \quad \text{(Eq. 6.5.3.7-11)}$$

$$\sigma_y^2 = \sigma_{yI}^2 + \sigma_{yD}^2 \quad \text{(Eq. 6.5.3.7-12)}$$

where

σ_{yI} = indirect uncertainty in K_{cb} due to uncertainties in NDVI'
σ_x = standard deviation of NDVI'
$\frac{dy}{dx}$ = slope of the function y = y(x)
σ_y^2 = combined variance of predicted K_{cb}
σ_{yD}^2 = direct uncertainty due to $K_{cb.}$

An iteration using Mathcad software was performed to determine the appropriate value of $\frac{dy}{dx}$ to use in Equation 6.5.3.7-11 (Output DTN: MO0610SPALINEA.000, *Kcb-NDVI_Regression.xmcd*). The resulting slope that was used in Equation 6.5.3.7-11 was 9.7 (Output DTN: MO0610SPALINEA.000; *Kcb-NDVI_Regression.xmcd*).

The standard deviations calculated for the slope and intercept were 2.1 and 0.05, respectively. These values were used to establish 90% confidence intervals for the least squares regression (Figure 6.5.3.7-3).

Table 6.5.3.7-4 summarizes the recommended values and distributions for the slope and intercept for the regression line for predicting K_{cb} from NDVI' in the MASSIF model. Because the magnitude of the intercept (C_{Kcb1}) is relatively small, it is appropriate to consider this parameter as a constant for the purposes of calculating net infiltration. The reasoning for this is that when K_{cb} is small, its value is controlled by the uncertainty in the value of $K_{c\ min}$ rather than C_{Kcb1}. When K_{cb} is large, its value is controlled by the value of C_{Kcb2}, which has a larger influence and uncertainty than C_{Kcb1}.

Table 6.5.3.7-4. Best-Fit Parameter Values Describing the Relationship between NDVI' and K_{cb}

Parameter Description	Symbol	Nominal Value (mean)	Standard Deviation	Distribution	Climate
Slope between NDVI' and K_{cb}	C_{Kcb2}	9.7	2.1	normal	all
Intercept for linear regression between NDVI' and K_{cb}	C_{Kcb1}	−0.05	0.05	normal	all

6.5.4 Additional Parameter Development

6.5.4.1 Input Parameters for Reference Evapotranspiration Calculations

Reference evapotranspiration (ET_0) is calculated for use in the infiltration model as a function of slope and azimuth using the standardized FAO-56 Penman-Montieth equation (Equation C-37). ET_0 is calculated for reference conditions that are defined for the grass reference crop as a vegetated, clipped, cool-season grass surface having uniform height (0.12 m), is actively growing, and completely shading the ground, with an adequate water supply (Allen et al. 1998 [DIRS 157311], p. 15). This ET_0 represents a near maximum evaporative index that occurs under conditions of high soil water availability to support ET and full vegetation cover (Allen et al. 1998 [DIRS 157311], pp. 7 and 23). The use of the ET_0 definition requires the input of weather data representing a well-watered environment. ET from native vegetation is calculated by multiplying ET_0 by a "crop" or "transpiration" coefficient. The upper limit on this coefficient is 1.2 (Allen et al. 1998 [DIRS 157311], pp. 110 (Table 12) and 189). Several input parameters that may vary with time or conditions are required for this calculation (Table 6.5.4.1-1). These input parameters are described in this section and nominal values and ranges of uncertainty are established.

Table 6.5.4.1-1. Input Parameters for Reference Evapotranspiration

Parameter	Description
$K_{0\,winter}$	Dew point offset from minimum temperature (T_{min}) for winter months
$K_{0\,rest}$	Dew point offset from T_{min} for spring, summer, and fall months
$K_{0\,winter\ start}$	Starting day of year for winter dew point
$K_{0\,winter\ end}$	Last day of year for winter dew point
K_{Rs}	Adjustment coefficient in Hargreaves' radiation formula
α_T	Terrain albedo
G_{sc}	Solar constant (MJ/m^2/min)
K_{cln}	Atmospheric turbidity coefficient

The methods in Appendix C assume that the only weather inputs to the FAO-56 Penman-Montieth equation are maximum and minimum air temperature, which are used to estimate all other needed weather parameters.

Dewpoint Offset (K_0)—Dewpoint temperature (T_{dew}) is used to calculate actual vapor pressure (e_a), which is used in Equation C-37 to calculate ET_0 (see Appendix C and Section 6.4.5.2). Allen et al. (1998 [DIRS 157311], p. 36 and Annex 6, pp. 257 to 262) recommended use of T_{dew} calculated from daily minimum temperature (T_{min}) when humidity data are not available, or when reference conditions are not met at the weather station location. Under humid, well-watered reference conditions, T_{min} is approximately equal to T_{dew} (Allen 1996 [DIRS 176485], pp. 103 to 104, Figure 7). This relationship is well established for reference ET conditions and occurs because condensation of vapor from the air and the corresponding release of latent heat prevent near-surface T_{min} from decreasing below T_{dew} (Allen 1996 [DIRS 176485], p. 103). However, under increasing aridity (i.e., in semiarid and arid climates), the difference between T_{min} and T_{dew} increases, even under reference conditions, due to dryness of the regional air mass and due to

reduced effects of evaporative cooling caused by lower ET (Allen 1996 [DIRS 176485], p. 104). Under non-reference (dry) conditions, the difference between T_{min} and T_{dew} increases even further. A dew point offset (K_o) is recommended for semiarid and arid climates to reflect the humidity levels anticipated under the standardized, well-watered reference ET conditions (Equation C-1; Allen et al. 1998 [DIRS 157311], Equation 6-6, p. 261).

The value for K_o in arid environments will vary seasonally with greater deviations between T_{min} and T_{dew} needed during warm dry months (Allen et al. 2005 [DIRS 176207], p. D-29). Evaluations of $T_{min} - T_{dew}$ have been performed for weather stations in a wide variety of locations (Jensen et al. 1997 [DIRS 177103], p. 398, Table 3; Temesgen et al. 1999 [DIRS 178312], pp. 29 to 30). Temesgen et al. (1999 [DIRS 178312], pp. 29 to 30, Table 4) reported values for $T_{min} - T_{dew}$ for six arid and three humid sites that ranged from 10°C to 18°C and 2°C to 6°C, respectively, for summer months, and from 4°C to 8°C and 1°C to 3°C, respectively, for winter months. However, the arid sites were non-reference (dry) stations with no irrigation to keep green vegetation growing in the vicinity of the weather station. The values reported for these stations are higher than those expected for a well-watered reference ET station in a desert environment. When local information on K_o is not available, a K_o range from 2°C to 4°C is suggested by Allen et al. (2005 [DIRS 176207], p. D-29).

It is important, in applying the $ET = K_c\ ET_0$ approach (where ET is actual ET and K_c is a transpiration or "crop" coefficient), that the ET_0 calculation represents the reference evapotranspiration that occurs from the standardized reference surface. This standardized reference surface, by definition, is an extensive surface of transpiring grass that conditions the atmospheric boundary layer by evaporative cooling and by the addition of water vapor. The conditioning of the boundary layer constitutes an important feedback process to the ET_0 rate and moderates it. The K_c coefficient, which represents the ratio of actual ET to ET_0, and the soil water stress reduction function, which reduces the ET value when soil water content is insufficient to support ET fully, are designed to function in concert with the standardized ET_0 value (Allen et al. 1998 [DIRS 157311], pp. 58, 91, and 161). The ET_0 calculation represents a near upper limit on ET that is experienced under full vegetation cover and adequate soil water supply. Under conditions of less than full vegetation cover or less than adequate soil water supply, the actual ET rate will be reduced below the standardized ET_0 rate, even though the actual air temperature may increase and humidity may decrease due to the reduced ET (Brutsaert 1982 [DIRS 176615], pp. 224 to 225 and Figure 10.5). Therefore, it is important that the ET_0 calculation be made using T_{dew} estimated using K_o values that represent the reference ET condition.

For the climate at Yucca Mountain, a nominal value for K_o of 2°C is used for winter months ($K_{o\ winter}$) when relative humidity levels are higher, and a nominal value of 4.5°C is used for spring through fall ($K_{o\ rest}$) (Table 6.5.4.1-2). These values are based on recommendations from Allen et al. (2005 [DIRS 176207], p. D-29). To account for uncertainty associated with both values, a range of 0°C to 10°C is used for uncertainty and sensitivity analyses (Table 6.5.4.1-2). The lower limit represents the potential for reference ET conditions to be met during humid times of the year or under future climate states (Allen et al. 2005 [DIRS 176207], p. D-29). The upper limit represents an extreme value for reference ET conditions under extremely arid climates and is based on work by Temesgen et al. (1999 [DIRS 178312], pp. 29 to 30).

Because the reference weather station is to reflect conditions for a well-watered setting, and because the Present-Day, Monsoon, and Glacial Transition climates and analogue stations all have lower annual precipitation than ET_0, these climates should all have similar relationships between T_{min} and T_{dew} under the reference setting. Therefore, the same nominal values and ranges were used for all climate states (Table 6.5.4.1-2).

Although the uncertainty range for this parameter is large (0°C to 10°C), it is shown in Section 7.1.4 that this parameter does not contribute significantly to uncertainty in net infiltration compared with other uncertain parameters.

Table 6.5.4.1-2. Nominal Values and Ranges for Dew Point Offset

Parameter	Climate States	Nominal Value	Range
$K_{o\ winter}$ [a]	All	2°C [b]	0°C to 10°C [c]
$K_{o\ rest}$ [d]	All	4.5°C	0°C to 10°C
$K_{o\ winter\ start}$ [e]	Present-Day and Monsoon	DOY 335 [f]	DOY 274 to 335
$K_{o\ winter\ end}$ [g]	Present-Day and Monsoon	DOY 90	DOY 90 to 151
$K_{o\ winter\ start}$	Glacial Transition	DOY 274	DOY 244 to 274
$K_{o\ winter\ end}$	Glacial Transition	DOY 120	DOY 120 to 151

[a] Dew point offset for winter period.
[b] Allen et al. 2005 [DIRS 176207], p. D-29.
[c] Lower limit from Allen et al. 2005 [DIRS 176207], p. D-29. Upper limit from Temesgen et al. 1999 [DIRS 178312], pp. 29 to 30, Table 4.
[d] Dew point offset for spring, summer, and fall period.
[e] Day of year that $K_{o\ winter}$ goes into effect.
[f] DOY = day of year.
[g] Day of year that $K_{o\ winter}$ ends.

Allen et al. (2005 [DIRS 176207], pp. D-29 and E-2) suggest application of $K_{o\ winter}$ during winter-like periods when relative humidity levels are higher than the rest of the year, and application of $K_{o\ rest}$ during spring, summer, and fall periods. At Yucca Mountain, higher relative humidity levels for winter months are likely to begin around the first of December and end in February or March (see temperatures in Table 6.5.3.1-1). Therefore, for Present-Day and Monsoon climates, it is recommended that use of the winter dew point begin on day of year 335 ($K_{o\ winter\ start}$) and end on day of year 90 ($K_{o\ winter\ end}$) (Table 6.5.4.1-2). To establish uncertainty ranges for $K_{o\ winter\ start}$ and $K_{o\ winter\ end}$, the winter period was extended by two months at each end. This resulted in a range for $K_{o\ winter\ start}$ from day of year 274 through 335 and for $K_{o\ winter\ end}$ from day of year 90 through 151 (Table 6.5.4.1-2).

Based on data from the Spokane and Rosalia analogue stations for the Glacial Transition climate, the winter period lasts (on average) from October to April (see temperatures in Table 6.5.3.1-2). During this time period, average minimum temperatures are near or below freezing; therefore, for the glacial transition climate, it is recommended that use of the winter dew point begin on day of year 274 (October 1) and end on day of year 120 (April 31) (Table 6.5.4.1-2). To establish uncertainty ranges for $K_{o\ winter\ start}$ and $K_{o\ winter\ end}$ the winter period was extended by one month at each end. This resulted in a range for $K_{o\ winter\ start}$ from day of year 244 through 274, and for $K_{o\ winter\ end}$ from day of year 120 through 151 (Table 6.5.4.1-2).

Adjustment Coefficient for Hargreaves' Radiation Formula (K_{Rs})—Net solar radiation is an input to the FAO-56 Penman-Monteith equation (Equation C-37). The Hargreaves radiation formula is used in Appendix C to estimate the incoming solar radiation on a horizontal surface from the difference in maximum and minimum temperatures (Equation C-13). The formula requires an empirical adjustment coefficient (K_{Rs} [$°C^{-0.5}$]). Allen (1997 [DIRS 176568]) demonstrated that four K_{Rs} values (0.16, 0.18, 0.19, and 0.20) were good estimators of solar radiation for different locations and elevation regimes in the western United States. These four K_{Rs} values were evaluated in Section C3 using solar radiation data measured near Yucca Mountain to determine which were most appropriate for estimating solar radiation for the Yucca Mountain area. The results of the analysis indicated that a K_{Rs} of 0.19 to 0.20 was the best estimator of solar radiation for Yucca Mountain (Output DTN: SN0602T0502206.005). Therefore, a nominal value for K_{Rs} of 0.19 is used in calculation of solar radiation (Table 6.5.4.1-3). Based on the analysis in Section C3, an uncertainty range of 0.15 to 0.22 is used (Table 6.5.4.1-3).

For the glacial transition climate, the range between maximum and minimum temperature could change some, with more humidity holding minimum temperatures at higher values. This could result in a slightly larger value for K_{Rs}. However, this increase would be small and probably would be compensated for by less R_s due to increased atmospheric attenuation under increased humidity and more general cloudiness. A general value of $K_{Rs} = 0.16$ is recommended by Allen et al. (2005 [DIRS 176207], pp. D-5 to D-6) for "interior regions" of the United States. This value is within the 0.15 to 0.22 uncertainty range. Because R_s for clear days should not be impacted by climate change by more than a few percent, the same nominal value and range for K_{Rs} are recommended for Present-Day, Monsoon, and Glacial Transition climates (Table 6.5.4.1-3).

Table 6.5.4.1-3. Nominal Value and Range for Hargreaves' Adjustment Coefficient

Parameter	Climate States	Nominal Value	Range
K_{Rs}[a]	All	$0.19°C^{-0.5}$	$0.15°C^{-0.5}$ to $0.22°C^{-0.5}$

Source: Output DTN: SN0602T0502206.005.

[a] Hargreaves' adjustment coefficient. Coefficient is developed in text based on analysis in Appendix C.

Terrain Albedo (α_T)—Terrain albedo is used to calculate reflected radiation from areas surrounding model grid cells (Equation C-24). Radiation reflected toward grid cells from surrounding surfaces can affect the energy balance of the grid cell and therefore impact ET_0. However, the value for α_T has only a small impact on the solar radiation estimate and ET_0 (Section C1.3).

The value of α_T is a function of soil color and moisture content, soil crusting and aging, and amount and characteristics of vegetation cover. The values suggested for α_T in areas with little vegetation range from 0.15 for dark soils to 0.35 for light soils (Brutsaert 1982 [DIRS 176615], p. 136, Table 6.4). Based on this range and the low cover of vegetation at Yucca Mountain, a nominal value of 0.22 is used for α_T (Table 6.5.4.1-4). Under the monsoon and glacial transition climates, terrain will be more vegetated and the value for albedo will tend toward 0.20 (Brutsaert 1982 [DIRS 176615], p. 136, Table 6.4). However, the estimation of solar radiation on slopes

(and subsequently ET_0) is relatively insensitive to terrain albedo (Section C1.3). Therefore, a nominal value of 0.22 is appropriate for all climate states. A uniform distribution between 0.15 to 0.35 is used for the three climate states for uncertainty and sensitivity analysis (Table 6.5.4.1-4). Values significantly higher than 0.35 (e.g., value of 0.90 represents snow covered ground (Brutsaert 1982 [DIRS 176615], p. 136, Table 6.4) is not justified because persistent snow cover is not expected in any of the future climate states.

Table 6.5.4.1-4. Nominal Value and Range for Terrain Albedo

Parameter	Climate States	Nominal Value	Range
α_T [a]	All	0.22 [b] (dimensionless)	0.15 to 0.35 [c]

[a] Terrain albedo.
[b] Brutsaert 1982 [DIRS 176615], p. 136, Table 6.4, low end of range for desert soils.
[c] Brutsaert 1982 [DIRS 176615], p. 136, Table 6.4, range for dark to light soils.

Solar Constant (G_{sc})—The solar constant (G_{sc} [MJ m^{-2} min^{-1}]) is used to calculate extraterrestrial radiation (R_a, Equation C-6). This constant has a small range. From approximately 1978 through 2004, the running yearly mean value of the solar constant (or total solar irradiance, TSI) ranged from 1,365.67 Wm^{-2} (0.0819 MJ m^{-2} min^{-1}) in 1987 to 1,367.42 Wm^{-2} (0.0820 MJ m^{-2} min^{-1}) in 2001 (Dewitte et al. 2004 [DIRS 178528], p. 214). The minimum and maximum of the readings (ignoring brief spikes of lower irradiance) appear to be 1,365 and 1,369 Wm^{-2} (0.0819 to 0.0821 MJ m^{-2} min^{-1}), respectively (Dewitte et al. 2004 [DIRS 178528], p. 212, Figure 2). Allen et al. (1998 [DIRS 157311], p. 47) recommended a value for G_{sc} of 0.0820 MJ m^{-2} min^{-1}. Therefore, a nominal value of 0.0820 MJ m^{-2} min^{-1} with an uncertainty range of 0.0819 to 0.0821 MJ m^{-2} min^{-1} is recommended for G_{sc} (Table 6.5.4.1-5). The nominal value and range are for all climate states.

Table 6.5.4.1-5. Nominal Value and Range for the Solar Constant

Parameter	Climate States	Nominal Value	Range
G_{sc} [a]	All	0.0820 (MJ m^{-2} min^{-1}) [b]	0.0819 to 0.0821 (MJ m^{-2} min^{-1}) [c]

[a] Solar constant.
[b] Allen et al. 1998 [DIRS 157311], p. 48.
[c] Dewitte et al. 2004 [DIRS 178528], p. 214. Values were converted from W m^{-2} to MJ m^{-2} min^{-1}.

Atmospheric Turbidity Coefficient (K_{cln})—The atmospheric turbidity coefficient (K_{cln} [dimensionless]) is used to calculate 24-hour transmissivity for beam radiation (Equation C-10). For clean sky conditions, K_{cln} should be set to 1.0 (Allen 1996 [DIRS 176485], pp. 97 and 99, and Allen et al. 2005 [DIRS 176207], p. D-8). For extremely turbid, dusty, or polluted air, K_{cln} should be $\leq$ 0.5 (Allen 1996 [DIRS 176485], pp. 97 and 99). Given that a K_{cln} of 0.5 is for extremely dirty air, and the air at Yucca Mountain is relatively clean, 0.5 is not likely to occur. Therefore, it is assumed that a value higher than 0.5 should be used for the lower limit of the K_{cln} distribution. As a reasonable alternative, a lower limit of 0.8 is used. Cleaner air in the future would cause the apparent value for K_{cln} to exceed 1.0. Therefore, a K_{cln} of 1.1 can be used to represent the impact of substantial reduction in aerosols in the atmosphere should this occur in the future (Liepert and Romanou 2005 [DIRS 178313], p. 623; Cohen et al. 2004 [DIRS 178314], p. 362).

A nominal value of 1.0 with an uncertainty range of 0.8 to 1.1 is used for K_{cln} (Table 6.5.4.1-6). A range of 0.8 to 1.1 is reasonable without going below what would be normally expected at Yucca Mountain. The nominal value and range apply to all climates.

Table 6.5.4.1-6. Nominal Value and Range for the Turbidity Coefficient

Parameter	Climate	Nominal Value	Range
K_{cln} [a]	All	1.0 [b]	0.8 to 1.1 [c]

[a] Turbidity coefficient.
[b] Allen et al. 2005 [DIRS 176207], p. D-8.
[c] Assumptions made in text.

6.5.4.2 Input Parameters for Soil Water Balance Calculations

The infiltration model contains a soil water balance component that considers water storage and movement within the soil column (Section 6.4.2). The water balance model is based on FAO-56 methods that require input parameters related to soil moisture evaporation and plant water use (Section 6.4.4). A subset of those parameters (Table 6.5.4.2-1) is described in this section and distributions and nominal values for use in the model are established. In addition, the initial water content used for each soil layer is discussed.

Table 6.5.4.2-1. Input Parameters for Soil Water Balance

Parameter	Description
K_{c_min}	*Minimum* transpiration coefficient (K_c) for dry surface soil (upper 0.10 to 0.15 m) with no vegetation cover
p	Soil moisture depletion coefficient. Average fraction of total available water for evapotranspiration (*TAW*) that can be depleted from the root zone before reduction in evapotranspiration (*ET*). Expressed as a fraction (0 to 1).
Z_e	Evaporation layer depth (m). Mean effective depth of soil experiencing drying by surface evaporation to near air dry water content.
REW	Readily evaporable water (mm). Depth of water that can be evaporated during Stage 1 drying before the drying rate declines below the potential evaporation rate.

Minimum Transpiration Coefficient ($K_{c\ min}$)—The minimum transpiration coefficient for a dry surface soil layer with no vegetation cover ($K_{c\ min}$, dimensionless) represents low-level, long-term diffuse evaporation when the soil surface layer is dry (at air dry). $K_{c\ min}$ is reduced to zero in the water balance calculations when the contributing soil profile is completely dry. K_{c_min} is also used during calculation of the fraction of soil surface that is covered by vegetation (f_c) in Equation 76 from Allen et al. (1998 [DIRS 157311], pp. 149 to 150). The f_c is used in the calculation of the evaporation component ($K_e \times ET_0$) in the soil water balance model. Under the arid conditions at Yucca Mountain, the upper soil layer often dries to low water content (air dry) during periods between precipitation events (CRWMS M&O 1999 [DIRS 105031], p. 14, Table 3). Under dry soil conditions and sparse rainfall, Allen et al. (1998 [DIRS 157311], pp. 207 and 209) recommended setting $K_{c\ min}$ to zero in order to provide for conditions when transpiration is equal to zero. For agricultural crops where residual soil water is common, a range for $K_{c\ min}$ of 0.15 to 0.20 was recommended by Allen et al. (1998 [DIRS 157311], pp. 149 to 150). Based on this information, a triangular distribution with 50% of the values equal to 0.0

and 50% of the values varying linearly between 0.0 and 0.2 is used. A nominal value of 0.0 is assumed (Table 6.5.4.2-2). However, a nominal value that is slightly higher than zero (perhaps the mean of the uncertainty distribution) would be appropriate for long periods with no precipitation. A value greater than zero allows for low-level diffusive evaporation from below the evaporation layer, a process consistent with observations that water content in a bare soil lysimeter near to the Yucca Mountain site continues to decrease even after long periods of no precipitation (Scanlon et al. 2005 [DIRS 175977]). The nominal value and distribution applies to all climates.

Table 6.5.4.2-2. Nominal Value and Range for the Minimum Transpiration Coefficient

Parameter	Climate	Nominal Value	Range
$K_{c\ min}$ [a]	All	0.0 [b]	0.0 to 0.2 [c]

[a] minimum transpiration coefficient for dry soil with no vegetation cover.
[b] Allen et al. 1998 [DIRS 157311], pp. 207 and 209. A slightly higher value is appropriate if long dry periods are to be simulated.
[c] Range from Allen et al. 1998 [DIRS 157311]. Lower bound from pp. 207 and 209, upper bound from pp. 149 to 150.

Soil Moisture Depletion Coefficient (p)—The soil moisture depletion coefficient (p, expressed as a fraction) is used to calculate readily available water (RAW) in the plant root zone (Section 6.4, Equation 6.4.4.2-5). It represents the average fraction of total available water (TAW) in the soil column that can be depleted from the root zone before reduction in actual ET occurs due to plant moisture stress (i.e., RAW is the depletion threshold at which water stress begins to occur). In the water balance model, p varies as a function of actual ET and is limited to ≤ 0.8 (Appendix G, Equation G-19).

For agricultural crops, p adjusted for actual ET rates is limited to $0.1 \leq p \leq 0.8$. Most crop species are relatively sensitive to water stress and have p values around 0.5 (Allen et al. 1998 [DIRS 157311], pp. 163 to 165, Table 22). Values for p that are less than 0.5 are for crops such as carrots and lettuce that have high water requirements and low stress thresholds. These crops require careful water management to give highest yields and quality. Desert plants are generally more tenacious than agricultural crops, and it is not likely that they exhibit stress thresholds as low as crops with high water requirements. Therefore, 0.5 should represent the lower limit of the range for p under Present-Day and future climates in this analysis (Table 6.5.4.2-3). Based on work by Allen et al. (1998 [DIRS 157311], p. 162), an upper limit for p of 0.8 is used. A nominal value of 0.65 (midpoint of range) is used (Table 6.5.4.2-3).

Table 6.5.4.2-3. Nominal Value and Range for the Soil Moisture Depletion Coefficient

Parameter	Climate State	Nominal Value	Range
p [a]	All	0.65[b]	0.5 to 0.8[c]

[a] Soil moisture depletion coefficient.
[b] Midpoint of range.
[c] Allen et al. 1998 [DIRS 157311], p. 162.

Evaporation Layer Depth (Z_e)—The mean effective depth of the surface soil layer that is subject to drying by evaporation to air dry (Z_e [m]) is used to calculate total evaporable water (TEW) using Equation 73 from Allen et al. (1998 [DIRS 157311], p. 144). The value is dependent on

soil texture and length of drying periods common to the model area, which implies that in reality it varies with location. However, in this analysis, a single effective value for this parameter is applied over the model domain. Allen et al. (1998 [DIRS 157311], p. 144; 2005 [DIRS 176009], pp. 10 to 12, Figure 9d, and Table 3) recommend a range between 0.10 to 0.15 m for Z_e. These references are primarily focused on agricultural soils. More generally, Allen et al. (2005 [DIRS 176009], p. 4) stated that a value for Z_e based on evaporation amounts observed over complete drying cycles for soils and conditions representative of the model area should be selected by the user. Coarse texture and long periods of drying that characterize most Yucca Mountain soils suggest it is reasonable to extend the evaporation layer depth somewhat beyond the upper bound (0.15 m) suggested by Allen et al. (1998 [DIRS 157311], p. 144). For this analysis it was decided to represent Z_e for the sandy-loam soils at Yucca Mountain with a uniform distribution between 0.1 and 0.2 m and a nominal value of 0.15 m (Table 6.5.4.2-4).

A number of studies from various locations corroborate this range. For instance, Rose (1968 [DIRS 178583]) found the soil water content in a sandy soil after four days to be near air-dry at the surface and increased to near field capacity at a depth of 0.12 to 0.15 m. Mutziger et al. (2005 [DIRS 178316]) found Z_e to range from 0.03 m for a clay loam soil to 0.16 m for a silt loam soil in comparisons against lysimeter measurements. Hunsaker et al. (2002 [DIRS 178529]) used Z_e = 0.15 m for a loam soil and Tolk and Howell (2001 [DIRS 178315]) and Howell et al. (2004 [DIRS 178317]) used Z_e = 0.10 for a fine sandy loam soil in Texas. Allen et al. (2005 [DIRS 178493], p. 21) found Z_e = 0.15 m for observed evaporation data from Imperial Valley, California, for silty clay and silty clay loam soils and Z_e = 0.35 m for Superstition sand. However, the authors argue that the high values of TEW (33 mm) and REW (20 mm) required to fit the Superstition sand data "do not seem realistic for a sand and may be some artifact of field data collection" (Allen et al. (2005 [DIRS 178493], p. 21). All these studies corroborate a range of 0.1 to 0.2 m.

Table 6.5.4.2-4. Nominal Value and Range for Evaporation Layer Depth

Parameter	Climate	Nominal Value	Range
Z_e [a]	All	0.15 m [b]	0.1 to 0.2 m [b]

[a] Evaporation layer depth.
[b] Range and nominal value are modified according to principles described by Allen et al. (2005 [DIRS 176009], p. 4), from a typical agricultural range also given by Allen et al. (1998 [DIRS 157311], p. 144).

Readily Evaporable Water (REW)—Readily evaporable water (*REW*, mm) is used to calculate the soil evaporation reduction coefficient (K_r) in Equation 74 from Allen et al. (1998 [DIRS 157311], p. 146). An energy limiting stage (Stage 1) and a falling rate stage (Stage 2) are considered in the evaporation process. In Stage 1, the soil surface is wet and the maximum rate of evaporation is controlled by the amount of available energy at the soil surface (Allen et al. 1998 [DIRS 157311], p. 145). Readily evaporable water is the maximum depth of water that can be evaporated from the upper soil layer during Stage 1, prior to the onset of hydraulic limitations that reduce the rate of water supply below that of energy demands. When the depth of evaporation exceeds *REW*, Stage 2 of the evaporation process begins (Allen et al. 1998 [DIRS 157311], p. 145).

The depth of *REW* is dependent on soil texture with values normally ranging from about 5 to 12 mm (Allen et al. 1998 [DIRS 157311], p. 145). Tolk and Howell (2001 [DIRS 178315]) and Howell et al. (2004 [DIRS 178317]) used *REW* = 10 mm for a clay loam soil and *REW* = 9 mm for a fine sandy loam soil near Amarillo, Texas, based on lysimeter observations. Mutziger et al. (2005 [DIRS 178316]) found best fit values for *REW* based on lysimeter observations to range from 2 mm for a clay loam to 13 mm for a silt loam soil. For sand to sandy loam soils such as those at Yucca Mountain, *REW* ranges from 2 to 10 mm (Allen et al. 1998 [DIRS 157311], p. 144, Table 19). Therefore, a uniform distribution with a range of 2 to 10 mm is used for *REW* (Table 6.5.4.2-5). A nominal value of 6.0 (midpoint of range) is used for *REW* (Table 6.5.4.2-5). Because *REW* is a function of soil properties, it is not expected to change under different climates. Therefore, the same distribution and nominal value are recommended for all climate states.

Table 6.5.4.2-5. Nominal Value and Range for Readily Evaporable Water

Parameter	Climate States	Nominal Value	Range
REW[a]	All	6 mm[b]	2 to 10 mm[c]

[a] Readily evaporable water.
[b] Midpoint of REW range reported by Allen et al. 1998 [DIRS 157311], p. 144, Table 19.
[c] From Allen et al. 1998 [DIRS 157311], p. 144, Table 19. Range of REW for sand, loamy sand, and sandy loam soils.

Initial Soil Water Content (IWCF)—The MASSIF calculation always starts at the beginning of the water year (October 1). At this time of year, the water content in the rooting zone (Layers 1 and 2) is expected, on average, to be closer to the wilting point than to the field capacity. Unaffected by evapotranspiration, soil below the rooting zone (Layer 3) is expected to be at field capacity.

If the soil is initially dry (i.e., near wilting point), part of the precipitation will result in a net increase in the soil water content over the course of the water year. If the soil is initially wet (i.e., near field capacity), the soil water content will likely decline over the water year. Generally, the net infiltration for a particular year will increase with increasing initial soil water content. The actual sensitivity is strongly dependent upon the timing and structure of the individual precipitation events.

When weather data is available, it is best to run MASSIF for the water year previous to the water year of interest. In so doing, the initial soil water contents for the water year of interest are a by-product of the calculation for the previous year. This, however, is not practical for the stochastically generated weather data used for predicting net infiltration for future climates at Yucca Mountain (Section 6.5.1 and Appendix F). The reason for this is that for each realization, 10 stochastically generated weather years are sampled from a set of 1,000 randomly generated years. Each of these sampled years is selected based on its annual precipitation and weighted for its probability of occurrence. Because many of the years are selected explicitly for their low probability and large annual precipitation, it is not appropriate to use soil water contents from these years as initial conditions for the analysis.

The statistical independence of the individual water years makes the initial soil water content, itself, stochastic. A net increase in soil water content is expected for some water years. Other

water years are expected to have a net decrease in soil water content. For a sufficiently large number of modeled water years for a particular climate, an appropriate value for initial water content should result in a net annual change in soil water content equal to zero, at the limit. However, to estimate an appropriate initial water content value with a high degree of accuracy would require running the model numerous times for each climate in order to adjust the initial water content until the net change approaches zero. Such effort was not considered necessary, because it can be shown that the resulting net infiltration is relatively insensitive to the value of the initial water content. Therefore, only two values of the initial water content were run as justification for an appropriate value to use.

The MASSIF calculation of mean infiltration for a particular climate involves modeling 400 water years (i.e., two replicates of 20 realizations, each containing 10 weighted water years). The weighted net change in soil water content for the 400 water years is calculated for each of two assumed initial water contents. One of the assumed initial contents results in a net increase in soil water content; the other results in a net decrease. Hence, the "correct" initial water content is bounded by the two assumed initial values. These assumed initial water contents (expressed as fractions) used in the estimating of net infiltration for the three climates considered are listed in Table 6.5.4.2-6. Comparison of the net infiltration rates calculated for each of the assumed initial values indicates the sensitivity of net infiltration to initial soil water content. The results of this comparison are included in Section 6.5.7.4. To convert initial water content fractions to actual water content (θ) apply the following:

$$\theta = IWCF(\theta_{FC} - \theta_{WP}) + \theta_{WP} \qquad \text{(Eq. 6.5.4-1)}$$

where *IWCF* is the initial water content fraction, θ_{FC} is the field capacity of the soil, and θ_{WP} is the permanent wilting point of the soil. Values for the field capacity and permanent wilting point for the Yucca Mountain soil groups are listed in Tables 6.5.2.3-2 and 6.5.2.3-1, respectively.

Table 6.5.4.2-6. Nominal Value and Range for Initial Water Content Fractions

Parameter	Climate States	Nominal Value	Upper Value
IWCF [a]	Present-Day and Glacial Transition	0[b]	0.1[c]
IWCF [a]	Monsoon	0.1[b]	0.2[c]

[a] Initial water content fraction expressed as the fractional value between wilting point and field capacity (0 = wilting point).
[b] Value used for estimating net infiltration.
[c] Value used to bound the "correct" initial water content.

6.5.5 Parameter Uncertainty Screening

This section describes the methodology used to determine which of all the uncertain input parameters listed in Appendix I and developed in the preceding sections are to be varied in the net infiltration uncertainty analysis performed for each climate state.

The first step in the uncertainty analysis is the elimination of parameters that do not have a large contribution to uncertainty in net infiltration. This step considers two properties associated with each parameter, its relative uncertainty, and its influence on the average net infiltration.

In several places, the MASSIF model uses a formula that is an approximation for a function. Such approximations have inherent uncertainties based on the form of the equation and the values of the coefficients. It is considered in this analysis that uncertainties in these approximations are small compared to uncertainties in other parameters. Therefore, the parameter uncertainty analysis does not vary any coefficients of function approximations. Appendix I, Section I1.1 identifies the coefficients that were not considered individually in the sensitivity studies but rather are included as part of model uncertainty.

Of the remaining parameters, some have different values for different climates. Others may have the same nominal values but different uncertainties. Parameters in either of these categories require a separate treatment for each climate.

Section I1.2 provides screening results for those parameters for which neither the nominal value nor its uncertainty varies appreciably for the three climates of interest. Subsequent sections of Appendix I summarize the screening for parameters specific to the Present-Day, Monsoon, and Glacial Transition climates, respectively.

The detailed analysis of parameter uncertainty excludes many parameters on the basis of low uncertainty. The criterion for low uncertainty is that the relative uncertainty is less than 15%. For most parameters, comparison with the nominal value of the parameter determines the relative uncertainty. The exceptions are:

- For the first-order term of a Fourier series for a Markov probability *a,* comparison with the smaller of *a* or 1-*a* determines the relative uncertainty
- For the first-order term of a Fourier series for a temperature minimum or maximum, comparison with the difference between the minimum and maximum determines the relative uncertainty
- The uncertainty of a second-order term of a Fourier series uses the same basis as the first-order term
- The uncertainty of a phase term in a Fourier series is relative to half of a year.

The analysis in Appendix I also excludes, on the basis of low influence, parameters that are not expected to influence more than 15% of the net infiltration. The most common exclusion arguments in such cases are:

- The parameter applies to less than 15% of the area of interest (e.g., geophysical properties)
- The parameter applies to less than 15% of the days in the analysis (e.g., monthly wind speed).

There remains the possibility of a systematic error that extends to a larger region of space or time. A systematic error in a group of parameters is an issue of model uncertainty rather than parameter uncertainty.

6.5.5.1 Sampled Parameter Values for Present-Day Climate

For the Present-Day climate, Table 6.5.5.1-1 summarizes the eleven parameters varied independently in the uncertainty analysis (the eight climate-independent parameters plus three additional parameters). Two plant parameters were varied (the mean plant height and the maximum effective rooting depth).

Table 6.5.5.1-1. Parameters Varied Independently in Uncertainty Analysis for Present-Day Climate

Parameter Symbol	Parameter Name and Description	Uncertainty Range	Uncertainty Distribution
a_m	Annual average of the natural logarithm of the amount of daily rainfall on days with precipitation (Section 6.5.1.2)	0.50 to 1.07 (ln mm)	uniform
h_{plant}	Plant height (Section 6.5.3.3)	0.2 m to 0.6 m	uniform
Z_r	Maximum rooting depth (Section 6.5.3.2)	0.6 m to 2.6 m	uniform
$depth_{soil}(4)$	Soil depth for soil depth class 4 (Section 6.5.2.4.1)	0.1 m to 0.5 m	uniform
$K_{sat\_rock}(405)$	Bulk saturated hydraulic conductivity of bedrock IHU 405 (Section 6.5.2.6)	7.6×10^{-8} m/s to 4.8×10^{-6} m/s	loguniform
$K_{sat\_rock}(406)$	Bulk saturated hydraulic conductivity of bedrock IHU 406 (Section 6.5.2.6)	2.1×10^{-8} m/s to 7.7×10^{-6} m/s	loguniform
$\theta_{HC}(5/7/9)$	Holding capacity of soil group 5/7/9 (Section 6.5.2.3)	0.09 to 0.17 (m^3/m^3)	uniform
REW	Readily evaporable water (Section 6.5.4.2)	2 to 10 mm	uniform
K_{c_min}	Minimum transpiration coefficient (K_c) (Section 6.5.4.2)	0.0 to 0.2 (unitless)	50% of values = 0.0, 50% of values vary linearly from 0.0 to 0.2 [pdf is $(0.2-K_{cmin})/0.04$]
Z_e	Evaporation layer depth (Section 6.5.4.2)	0.1 to 0.2 m	uniform
C_{Kcb2}	Slope of the NDVI' – K_{cb} function (Section 6.5.3.7)	9.7 ± 2.1 (unitless)	normal

NOTE: See Table I-2.

One weather parameter, a_m (Section 6.5.1.2), was also varied. Another weather parameter, a_λ, (Section 6.5.1.2) was not varied independently, but rather was correlated with a_m (Table 6.5.5.1-2). Although the relative uncertainty in a_λ is somewhat less than the arbitrary 15% criterion, it was included in the uncertainty analysis so that its value would remain consistent with the value of a_m.

Table 6.5.5.1-2. Parameters Correlated with Other Parameters That Varied Independently in Uncertainty Analysis for Present-Day Climate

Parameter Symbol	Parameter Name and Description	Uncertainty Range	Uncertainty Distribution
a_λ	Annual average of the mean amount of daily rainfall on days with precipitation (Section 6.5.1.2)	4.0 to 6.5 mm	uniform

NOTE: See Table I-3.

Tables 6.5.5.1-3 and 6.5.5.1-4 report two separate sets of sampled values for the parameters listed in Table 6.5.5.1-1. These are output from two separate LHS runs. Treating them as a single set risks the possibility that unintended correlations may go undetected.

Table 6.5.5.1-3. Sampled Parameter Values for Replicate 1 of Present-Day Net Infiltration Runs

Vector	a_m	h_plant	Z_r	Z_e	Sdepth4	lnRks_405	lnRks_406	HC_579	REW	Kc_min	CKcb2
unit	ln (mm/day)	m	m	m	m	ln (m/s)	ln(m/s)	m^3/m^3	n/a	mm	n/a
1	0.7581	0.4251	1.165	0.1472	0.2515	−13.47	−14.63	0.158	6.188	0	16.2
2	0.7418	0.2455	1.776	0.136	0.2883	−15.7	−12.8	0.09653	8.363	0.1755	10.21
3	0.5438	0.2623	0.872	0.159	0.2049	−14.75	−14.74	0.1276	6.934	0	12.89
4	0.5993	0.3259	1.261	0.1411	0.3894	−15.35	−16.36	0.1607	3.075	0	8.885
5	0.8359	0.5256	2.54	0.1676	0.1172	−12.67	−16.17	0.1035	5.974	0.05953	8.415
6	0.9782	0.3692	2.427	0.13	0.27	−16.26	−15.09	0.1153	3.539	0	8.19
7	0.9323	0.4083	0.6888	0.174	0.4557	−13.19	−13.53	0.1431	3.657	0.1076	6.045
8	0.8565	0.4926	2.116	0.1336	0.3451	−16.03	−12.51	0.152	6.671	0	6.331
9	1.029	0.3804	1.003	0.1078	0.1666	−15.4	−13.95	0.1487	4.581	0.0504	11.8
10	0.5624	0.5859	2.319	0.1927	0.4603	−14.28	−12.04	0.1389	5.383	0.00441	14.07
11	0.9179	0.4658	1.461	0.1876	0.4385	−14.35	−17.19	0.1202	2.773	0	9.318
12	0.8879	0.5693	0.982	0.1149	0.4161	−15.95	−16.7	0.1013	8.564	0.01971	11.46
13	0.7943	0.3504	2.07	0.1	0.328	−12.33	−13.57	0.1105	2.259	0.08441	12.36
14	1.053	0.2347	1.973	0.1833	0.2314	−12.95	−13	0.1693	9.479	0	10.43
15	1.011	0.2853	1.377	0.1989	0.3715	−13.86	−15.87	0.09083	7.343	0	10.96
16	0.6181	0.4443	1.68	0.1155	0.3051	−12.57	−15.37	0.1257	9.619	0	7.134
17	0.6674	0.3057	2.229	0.1218	0.493	−13.97	−16.82	0.1336	8.866	0.03784	7.366
18	0.6734	0.5428	1.506	0.1789	0.1434	−15.02	−17.46	0.1648	7.667	0.116	9.826
19	0.7188	0.5003	0.7734	0.1543	0.1359	−13.57	−12.36	0.1071	4.816	0	3.2
20	0.5131	0.2161	1.851	0.1609	0.1878	−14.66	−14.14	0.1357	4.275	0.02272	9.588

Source: Output DTN: SN0701T0502206.043, file: *LHS_PD_R1.OUT*.

Table 6.5.5.1-4. Sampled Parameter Values for Replicate 2 of Present-Day Net Infiltration Runs

Vector	a_m	h_plant	Z_r	Z_e	Sdepth4	lnRks_405	lnRks_406	HC_579	REW	Kc_min	CKcb2
unit	ln (mm/day)	m	m	m	m	ln (m/s)	ln(m/s)	m^3/m^3	n/a	mm	n/a
1	0.5654	0.5941	2.308	0.1237	0.381	−12.74	−15.78	0.1324	7.022	0	11.06
2	0.7297	0.4746	1.179	0.128	0.3764	−13.51	−11.85	0.1212	6.081	0.03304	9.318
3	0.7605	0.5753	2.278	0.1895	0.1741	−16.38	−13.96	0.1686	4.899	0.005494	5.31
4	0.6937	0.3278	1.662	0.1448	0.4845	−15.02	−13.5	0.1342	2.708	0.1917	8.319
5	0.5565	0.2071	1.897	0.1178	0.2575	−15.9	−14.42	0.1388	3.801	0	10.59
6	0.9578	0.5229	1.483	0.1006	0.4514	−16.16	−17.3	0.1272	8.884	0.04929	6.208
7	0.8666	0.429	0.9073	0.137	0.2097	−13.74	−14.72	0.1578	3.038	0.1424	13.54
8	0.8928	0.3409	0.8492	0.1978	0.4216	−14.36	−14.95	0.1599	8.476	0	8.862
9	0.6608	0.4175	1.989	0.1487	0.1102	−15.58	−16.95	0.09143	4.602	0.02741	11.22
10	0.6218	0.2798	1.302	0.1649	0.3126	−13.34	−15.6	0.1622	5.503	0	9.877
11	0.7144	0.3877	0.639	0.1075	0.2601	−14.9	−15.12	0.1454	7.854	0	12.42
12	0.9528	0.2539	1.01	0.1314	0.2339	−15.28	−12.43	0.1077	8.387	0	7.44
13	0.5894	0.3122	1.758	0.1575	0.1259	−12.62	−16.59	0.1149	9.991	0.07304	4.343
14	1.021	0.3608	2.447	0.113	0.2935	−12.36	−12.66	0.146	4.212	0	7.867
15	0.8056	0.5496	0.7667	0.1653	0.4018	−13.05	−17.39	0.1043	3.46	0	9.365
16	0.9094	0.4983	1.245	0.1768	0.1846	−13.98	−13.05	0.0943	2.379	0	6.962
17	0.5251	0.5132	1.502	0.1949	0.3357	−14.15	−12.16	0.1238	9.501	0.08352	12.87
18	0.8363	0.2251	2.542	0.1803	0.4721	−14.69	−16.34	0.1018	5.831	0.01402	10.18
19	1.048	0.4428	2.142	0.1729	0.3597	−15.42	−13.67	0.1118	7.234	0	15.47
20	0.9855	0.2889	2.046	0.1527	0.1593	−13.13	−15.99	0.1508	6.559	0.1059	11.67

Source: Output DTN: SN0701T0502206.043, file: *LHS_PD_R2.OUT*.

6.5.5.2 Sampled Parameter Values for Monsoon Net Infiltration Calculations

Tables 6.5.5.2-1 and 6.5.5.2-2 summarize the 19 parameters varied in the uncertainty analysis for the Monsoon climate, including the eight parameters that are climate independent. Two plant parameters were varied (the mean plant height and the maximum effective rooting depth). The slope of precipitation duration versus amount of precipitation was varied for this climate.

Four weather parameters were varied directly. Four additional weather parameters were not varied independently but rather were correlated with a_m and b_{m1} (Section 6.5.1.2). These seven weather parameters provided variation in the weather input files for model calculations.

Table 6.5.5.2-1. Parameters Varied Independently in Uncertainty Analysis for Monsoon Climate

Parameter Symbol	Parameter Name and Description	Uncertainty Range	Uncertainty Distribution
a_{00}	Annual average of the probability of no precipitation given that the previous day was dry (Section 6.5.1.2)	0.896 to 0.944 (unitless)	uniform
a_m	Annual average of the natural logarithm of the amount of daily rainfall on days with precipitation (Section 6.5.1.2)	0.5 to 1.3 (ln mm)	uniform
$b_{m,1}$	Amplitude of the annual variation in the median amount of daily rainfall on days with precipitation (Section 6.5.1.2)	−0.3 to +0.5 mm	uniform
γwet_{max}	Annual average maximum daily temperature on days with precipitation (Section 6.5.1.2)	14 C to 22 C	uniform
h_{plant}	Plant height (Section 6.5.3.3)	0.2 m to 0.6 m	uniform
Z_r	Maximum rooting depth (Section 6.5.3.2)	0.6 m to 2.6 m	uniform
Rate of duration increase with precipitation	Slope of the relationship between duration of daily precipitation and amount of daily rainfall (Section 6.5.1.7)	0.14 hr/mm to 0.43 hr/mm	uniform
$depth_{soil}(4)$	Soil depth for soil depth class 4 (Section 6.5.2.4.1)	0.1 m to 0.5 m	uniform
$K_{sat\_rock}(405)$	Bulk saturated hydraulic conductivity of bedrock IHU 405 (Section 6.5.2.6)	7.6×10^{-8} m/s to 4.8×10^{-6} m/s	loguniform
$K_{sat\_rock}(406)$	Bulk saturated hydraulic conductivity of bedrock IHU 406 (Section 6.5.2.6)	2.1×10^{-8} m/s to 7.7×10^{-6} m/s	loguniform
$\theta_{HC}(5/7/9)$	Holding capacity of soil group 5/7/9 (Section 6.5.2.3)	0.09 to 0.17 (m^3/m^3)	uniform
REW	Readily evaporable water (Section 6.5.4.2)	2 to 10 mm	uniform
K_{c_min}	Minimum transpiration coeficient (K_c) (Section 6.5.4.2)	0.0 to 0.2 (unitless)	50% of values = 0.0, 50% of values vary linearly from 0.0 to 0.2 [pdf is $(0.2-K_{cmin})/0.04$]

Table 6.5.5.2-1. Parameters Varied Independently in Uncertainty Analysis for Monsoon Climate (Continued)

Parameter Symbol	Parameter Name and Description	Uncertainty Range	Uncertainty Distribution
Z_e	Evaporation layer depth (Section 6.5.4.2)	0.1 to 0.2 m	uniform
C_{Kcb2}	Slope of the NDVI' – K_{cb} function (Section 6.5.3.7)	9.7 ± 2.1 (unitless)	normal

NOTE: See Table I-5.

The Monsoon climate is described in the future climate report (BSC 2004 [DIRS 170002]) as being something between the current desert climate (with most of the rain in winter) and a classical Monsoon climate (with most of the rain in summer). This uncertainty has been modeled by fixing the phase of the annual variation (all θ values) such that most of the rain falls in summer, and authorizing the amplitude (all b values) to vary between positive values (keeping most of the rain in summer) and negative values (switching the largest amount of rain to winter).

One of the amplitude values, b_m, is varied independently. All the other amplitudes are estimated using simple linear regression. Even though there is no correlation between annual average (a values) and amplitude (b values), the resulting weather parameters have to be checked in order to suppress any physical impossibilities:

- $b_{00,1}$ cannot be higher than $1-a_{00}$ (as it will create a probability of having a dry day larger than 1)
- b_λ cannot be higher than a_λ, as it will create a negative value for some daily amounts of rain
- (a_m-b_m) cannot be higher than $(b_\lambda-a_\lambda)$ as it will lead to a negative variance in the estimate of lognormal parameters
- a_m should not equal b_m, because this would lead to a probability of rain equaling zero one day of the year.

The first configuration is unlikely to happen. Therefore, in the event that sampling results in one vector that contains a physically impossible set of values, the entire set of sample vectors is discarded. The second configuration is more likely to happen. In order to reduce the likelihood, a very small positive correlation (0.2) has been induced between a_m and b_m in order to limit the high values of b_n associated with low values of a_m.

Tables 6.5.5.2-3 and 6.5.5.2-4 report two separate sets of sampled values for the parameters listed in Table 6.5.5.2-1. These are output from two separate LHS runs. Treating them as a single set risks the possibility that unintended correlations may go undetected.

Table 6.5.5.2-2. Parameters Correlated with Other Parameters that Varied Independently in Uncertainty Analysis for Monsoon Climate

Parameter Symbol	Parameter Name and Description	Uncertainty Range	Uncertainty Distribution
a_λ	Annual average of the mean amount of daily rainfall on days with precipitation (Section 6.5.1.2)	4.0 mm to 9.0 mm	uniform
$b_{00,1}$	Amplitude of the annual variation in the probability of no precipitation given that the previous day was dry (Section 6.5.1.2)	−0.03 to +0.07 (unitless)	uniform
$b_{10,1}$	Amplitude of the annual variation in the probability of no precipitation given that precipitation occurred during the previous day (Section 6.5.1.2)	−0.13 to +0.10 (unitless)	uniform
$b_{\lambda,1}$	Amplitude of the annual variation in the mean amount of daily rainfall on days with precipitation (Section 6.5.1.2)	−1.3 mm to +4.5 mm	uniform

NOTE: See Table I-6.

Table 6.5.5.2-3. LHS Sampled Parameter Values for Replicate 1 of Monsoon Net Infiltration Runs

Vector	a_00	a_m	b_m1	gTmaxwet	h_plant	Z_r	Z_e	Sdepth4	lnRks_405	lnRks_406	HC_579	REW	Kc_min	CKcb2	PDur_S
unit	n/a	ln(mm/day)	ln(mm/day)	C	m	m	m	m	ln (m/s)	ln(m/s)	m^3/m^3	n/a	mm	n/a	hr/mm
1	0.9067	1.125	0.4051	18.64	0.3054	1.824	0.1908	0.3113	−13.87	−13.3	0.1682	3.442	0.0843	7.826	0.3568
2	0.8965	0.5781	−0.2631	19.57	0.5387	1.114	0.1874	0.1264	−14.2	−16.79	0.1504	6.287	0	12.73	0.2712
3	0.9023	0.7363	0.3423	15.36	0.325	1.689	0.1118	0.4428	−14.56	−17.65	0.1429	8.985	0.1049	9.724	0.1696
4	0.9275	1.061	0.4207	21.44	0.4432	1.423	0.1602	0.1989	−16.23	−12.95	0.1306	9.243	0	8.984	0.3059
5	0.9213	0.7742	0.1524	21.94	0.2951	2.116	0.1666	0.3437	−13.92	−14.65	0.1055	9.615	0.01062	12.44	0.1886
6	0.933	0.9675	−0.03294	20.53	0.2452	2.29	0.1003	0.2006	−15.92	−14.12	0.1646	2.932	0	10.98	0.264
7	0.8996	0.9273	0.0448	17.79	0.3716	2.502	0.1415	0.1405	−13.14	−15.06	0.09422	4.91	0	6.884	0.3841
8	0.9252	1.002	0.2258	16.41	0.461	0.8874	0.171	0.1184	−15.08	−15.5	0.09803	4.457	0.006191	5.049	0.214
9	0.9229	1.178	−0.205	16.22	0.5855	2.499	0.1093	0.2328	−13.64	−13.15	0.1604	5.848	0.06511	9.505	0.1422
10	0.9156	0.6756	0.2745	21	0.3942	0.6282	0.1288	0.3785	−13.03	−15.96	0.1267	2.628	0	8.413	0.162
11	0.9102	0.581	0.2053	19.72	0.5406	1.288	0.1303	0.3815	−15.54	−11.85	0.1218	3.611	0.1635	10.18	0.4008
12	0.9391	0.8708	0.08648	17.28	0.2655	2.326	0.1975	0.3223	−12.53	−14.83	0.1108	4.374	0.03362	9.308	0.208
13	0.9118	1.225	−0.112	20.39	0.5031	1.903	0.1766	0.4864	−15.57	−17.26	0.1065	5.575	0	6.44	0.4055
14	0.9195	1.059	0.4613	14.58	0.4223	1.389	0.1588	0.2531	−13.35	−14.26	0.1226	8.454	0	11.79	0.3338
15	0.9315	0.8584	0.3102	14.88	0.4955	2.092	0.1529	0.2885	−15.18	−15.74	0.09032	2.114	0.02338	14.65	0.2873
16	0.9364	1.283	−0.1742	15.97	0.2213	0.7093	0.1351	0.1638	−14.86	−16.46	0.1403	6.561	0.1118	13.5	0.3274
17	0.913	0.6378	−0.2292	14.32	0.2024	1.564	0.1493	0.423	−16.16	−12.42	0.1351	7.142	0	5.214	0.2306
18	0.9411	0.8047	−0.06011	16.82	0.577	0.9239	0.1843	0.4775	−14.52	−13.73	0.1566	7.561	0	10.54	0.2441
19	0.9045	1.183	0.114	18.92	0.3409	1.04	0.1232	0.4081	−12.36	−12.35	0.1168	7.891	0	11.47	0.3638
20	0.9429	0.5327	0.0161	18.12	0.4199	1.746	0.1151	0.2717	−12.83	−16.91	0.1479	8.14	0.05213	7.808	0.4274

Source: Output DTN: SN0701T0502206.043, file: *LHS_MO_R1.OUT*.

Table 6.5.5.2-4. LHS Sampled Parameter Values for Replicate 2 of Monsoon Net Infiltration Runs

Vector	a_00	a_m	b_m1	gTmaxwet	h_plant	Z_r	Z_e	Sdepth4	lnRks_405	lnRks_406	HC_579	REW	Kc_min	CKcb2	PDur_S
Unit	n/a	ln(mm/day)	ln(mm/day)	C	m	m	m	m	ln (m/s)	ln(m/s)	m^3/m^3	n/a	mm	n/a	hr/mm
1	0.9227	1.273	0.01857	15.89	0.4409	1.859	0.1861	0.133	−14.78	−14.82	0.1498	6.326	0.07519	7.287	0.4036
2	0.9373	0.8946	0.4701	20.15	0.553	2.388	0.1388	0.4377	−12.74	−15.79	0.1354	4.975	0.1088	6.384	0.2138
3	0.9086	1.126	0.4439	14.19	0.2715	0.8323	0.1327	0.1795	−14.12	−17.46	0.1064	3.106	0.04746	13.31	0.1948
4	0.9346	0.5468	−0.1458	17.2	0.5617	0.7332	0.1411	0.2506	−12.53	−16.36	0.1214	4.784	0	7.781	0.3952
5	0.9031	0.8296	0.2223	18.9	0.3857	2.126	0.1736	0.4512	−13.4	−11.83	0.1103	8.644	0.1838	11.38	0.3509
6	0.9303	0.6374	0.05896	19.82	0.3568	1.233	0.1952	0.3069	−15.78	−17.32	0.1546	9.343	0.07028	9.864	0.1536
7	0.9037	1.044	0.1159	16.29	0.5336	2.272	0.1943	0.2997	−13.17	−13.68	0.1503	7.429	0	12.07	0.1989
8	0.9211	0.925	−0.1345	16.7	0.2395	2.055	0.1771	0.4068	−12.3	−15.24	0.1337	7.637	0	8.417	0.3154
9	0.9434	1.176	−0.2048	21	0.3732	1.36	0.1666	0.3408	−15.67	−12.36	0.1029	2.44	0.03615	12.71	0.2349
10	0.9397	0.5984	0.1465	17.89	0.25	0.9088	0.1451	0.2792	−13.82	−12.88	0.09914	8.287	0	11.03	0.2732
11	0.9186	1.084	−0.2737	18.42	0.4659	1.74	0.1175	0.4856	−13.66	−17.07	0.1439	7.048	0.0006832	11.79	0.2538
12	0.9166	1.008	0.3811	21.2	0.2165	1.674	0.1023	0.2064	−15.26	−15.34	0.1692	5.921	0	9.198	0.3094
13	0.9003	0.5226	−0.2312	17.51	0.3183	1.158	0.1243	0.1815	−13.96	−13.01	0.1605	4.333	0.1496	10.65	0.2949
14	0.9066	0.7207	−0.02292	14.95	0.2848	1.998	0.1522	0.3859	−16.21	−15.97	0.09321	6.706	0	4.349	0.3762
15	0.9105	0.795	0.0928	18.3	0.5842	1.454	0.1054	0.1563	−16.05	−14.28	0.1251	9.119	0	10.36	0.165
16	0.8981	1.207	0.3761	21.77	0.4923	0.6555	0.1804	0.3771	−14.35	−14.52	0.1149	3.852	0	8.936	0.3419
17	0.9324	1.26	0.3254	15.56	0.4199	1.079	0.1124	0.3267	−14.68	−13.27	0.1396	9.942	0.03252	9.452	0.3587
18	0.9271	0.6934	0.2956	20.66	0.5026	2.457	0.1615	0.2355	−14.95	−16.6	0.1291	5.459	0	16.2	0.4277
19	0.9146	0.9732	−0.06155	19.35	0.3301	2.587	0.1282	0.1006	−12.88	−13.86	0.09664	3.411	0.01259	5.306	0.1723
20	0.9293	0.7715	0.1949	14.52	0.426	1.53	0.1567	0.477	−15.4	−12.54	0.1641	2.068	0	7.876	0.2582

Source: Output DTN: SN0701T0502206.043, file: *LHS_MO_R2.OUT*.

6.5.5.3 Sampled Parameter Values for Glacial Transition Net Infiltration Calculations

A total of 17 parameters were varied for the Glacial Transition climate, as listed in Tables 6.5.5.3-1 and 6.5.5.3-2. Eight of these were climate independent. Two plant parameters were varied (the mean plant height and the maximum effective rooting depth). For this climate, the analyses varied both parameters of the precipitation duration model, but only one was varied independently, so that they could be correlated.

Table 6.5.5.3-1. Parameters Varied Independently in Uncertainty Analysis for Glacial Transition Climate

Parameter Symbol	Parameter Name and Description	Uncertainty Range	Uncertainty Distribution
a_{00}	Annual average of the probability of no precipitation given that the previous day was dry (Section 6.5.1.2)	0.78 to 0.89 (unitless)	uniform
a_m	Annual average of the natural logarithm of the amount of daily rainfall on days with precipitation (Section 6.5.1.2)	0.48 to 0.92 (ln mm)	uniform
$\theta_{\lambda,1}$	Phase of the annual variation of mean daily rainfall on days with precipitation (θ_λ in Section 6.5.1.2)	−π radians to + π radians	uniform
Rate of duration increase with precipitation	Slope of the relationship between duration of daily precipitation and amount of daily rainfall (Section 6.5.1.7)	0.32 to 0.71 hr/mm	uniform
h_{plant}	Plant height (Section 6.5.3.3)	0.6 to 1.8 m	uniform
Z_r	Maximum rooting depth (Section 6.5.3.2)	1.0 to 4.0 m	uniform
$depth_{soil}(4)$	Soil depth for soil depth class 4 (Section 6.5.2.4.1)	0.1 to 0.5 m	uniform
K_{sat_rock} *(405)*	Saturated hydraulic conductivity of bedrock IHU 405 (Section 6.5.2.6)	7.6×10^{-8} m/s to 4.8×10^{-6} m/s	loguniform
K_{sat_rock}*(406)*	Saturated hydraulic conductivity of bedrock IHU 406 (Section 6.5.2.6)	2.1×10^{-8} m/s to 7.7×10^{-6} m/s	loguniform
θ_{HC}*(5/7/9)*	Holding capacity of soil group 5/7/9 (Section 6.5.2.3)	0.09 to 0.17 (m^3/m^3)	uniform
REW	Readily evaporable water (Section 6.5.4.2)	2 to 10 mm	uniform
K_{c_min}	Minimum transpiration coefficient (K_c) (Section 6.5.4.2)	0.0 to 0.2 (unitless)	50% of values = 0.0, 50% of values vary linearly from 0.0 to 0.2 [pdf is $(0.2-K_{cmin})/0.04$]
Z_e	Evaporation layer depth (Section 6.5.4.2)	0.1 to 0.2 m	uniform
C_{Kcb2}	Slope of the NDVI' – K_{cb} function (Section 6.5.3.7)	9.7 ± 2.1 (unitless)	normal

NOTE: See Table I1.5-1.

Three weather parameters were varied directly. Two additional weather parameters were not varied independently but rather were correlated (Table 6.5.5.3-2). These five weather parameters provided variation in the weather input files for model calculations.

Tables 6.5.5.3-3 and 6.5.5.3-4 report two separate sets of sampled values for the parameters listed in Table 6.5.5.3-1. These are output from two separate LHS runs. Treating them as a single set risks the possibility that unintended correlations may go undetected.

Table 6.5.5.3-2. Parameters Correlated with Other Parameters That Varied Independently in Uncertainty Analysis for Glacial Transition Climate

Parameter Symbol	Parameter Name and Description	Uncertainty Range	Uncertainty Distribution
a_λ	*Constant term in Fourier series for λ(d)*	3.1 to 4.5 mm	uniform
$\Theta_{m,1}$	*Phase of first-order term in Fourier series for m(d)*	−π radians to + π radians	uniform
Intercept-1	Minimum precipitation duration	0.70 to 1.22 hr	uniform

NOTE: See Table I1.5-2.

Table 6.5.5.3-3. LHS Sampled Parameter Values for Replicate 1 of Glacial Transition Net Infiltration Runs

Vector unit	a_00 n/a	a_m nn(mm/day)	Theta_m Rad.	h_plant m	Z_r m	Z_e m	Sdepth4 m	lnRks_405 ln (m/s)	lnRks_406 ln(m/s)	HC_579 m^3/m^3	REW n/a	Kc_min mm	CKcb2 n/a	PDurS hr/mm
1	0.8747	0.7566	−1.623	0.8611	3.521	0.1932	0.2497	−16.38	−11.92	0.1148	4.581	0.0155	11.03	0.4411
2	0.8292	0.8827	2.278	1.42	2.554	0.1793	0.4767	−15.19	−12.55	0.1464	7.789	0.04158	8.484	0.4007
3	0.7971	0.6492	−2.833	1.487	1.419	0.1992	0.4258	−14.24	−17.22	0.1017	7.04	0.09898	8.721	0.5143
4	0.858	0.5297	−2.462	0.6196	2.869	0.1545	0.3851	−14.73	−15.18	0.1547	3.588	0	6.372	0.6802
5	0.8447	0.8589	−2.671	1.243	1.74	0.1477	0.1302	−12.86	−13.51	0.1392	3.619	0.1607	4.114	0.4314
6	0.8734	0.9179	−0.4545	1.569	3.333	0.1196	0.313	−13.96	−16	0.1111	6.643	0	9.093	0.3936
7	0.8808	0.4879	−0.7859	1.768	1.288	0.1326	0.275	−15.53	−13.79	0.1515	5.252	0	10.34	0.3647
8	0.7825	0.6082	2.97	1.199	2.999	0.1737	0.1163	−15.83	−16.42	0.1033	2.566	0	7.52	0.4645
9	0.7856	0.5563	0.263	1.043	3.683	0.123	0.4457	−13.55	−15.56	0.1642	2.859	0.06294	14.04	0.3385
10	0.8069	0.8465	−1.057	1.007	2.651	0.1137	0.1428	−13.84	−14.89	0.1245	5.005	0.02871	15.15	0.5591
11	0.864	0.5167	2.142	1.131	2.278	0.1407	0.2999	−13.37	−12.91	0.1095	7.229	0.1517	11.28	0.6545
12	0.8366	0.6785	1.592	1.702	3.814	0.1031	0.2148	−14.94	−15.73	0.1439	8.252	0.09082	5.406	0.6956
13	0.7944	0.7074	0.9706	1.549	1.105	0.1698	0.1803	−12.47	−12.28	0.1614	6.124	0	9.609	0.6191
14	0.8333	0.8214	−0.2879	0.9441	2.197	0.1556	0.222	−16.17	−17.01	0.1679	9.471	0.04516	11.98	0.6407
15	0.8088	0.724	−1.271	1.275	1.528	0.1265	0.4104	−15.68	−14.6	0.09311	5.98	0	12.25	0.598
16	0.8225	0.6255	−2.19	1.674	3.875	0.1885	0.3645	−13.21	−14.24	0.1366	8.821	0	10.45	0.5275
17	0.8894	0.7742	2.798	1.344	2.46	0.185	0.3535	−12.97	−17.45	0.1264	2.149	0	12.98	0.5525
18	0.8512	0.5774	0.3831	0.6971	1.833	0.1397	0.1702	−14.48	−16.53	0.119	9.614	0	7.98	0.3503
19	0.8131	0.8003	1.482	0.789	2.029	0.1092	0.4891	−14.96	−14.06	0.1317	4.113	0	6.983	0.5785
20	0.8525	0.6582	0.8224	0.7201	3.152	0.1629	0.3206	−12.43	−13.18	0.09419	8.679	0.002592	10.01	0.4816

Source: Output DTN: SN0701T0502206.043, file: *LHS_GT_R1.OUT*.

Table 6.5.5.3-4. LHS Sampled Parameter Values for Replicate 2 of Glacial Transition Net Infiltration Runs

Vector unit	a_00 n/a	a_m nn(mm/day)	Theta_m Rad.	h_plant m	Z_r m	Z_e m	Sdepth4 m	lnRks_405 ln (m/s)	lnRks_406 ln(m/s)	HC_579 m^3/m^3	REW n/a	Kc_min mm	CKcb2 n/a	PDurS hr/mm
1	0.8371	0.7218	−1.236	1.748	1.432	0.17	0.1171	−13.69	−12.99	0.1138	7.399	0.0509	6.478	0.6032
2	0.8595	0.8843	−2.887	0.7525	2.344	0.1115	0.2203	−15.28	−15.98	0.1386	8.307	0	12.84	0.6578
3	0.8681	0.8738	−0.8745	0.8444	2.795	0.1294	0.3214	−12.89	−12.16	0.1059	5.133	0	8.706	0.4326
4	0.7966	0.6956	0.5525	1.612	3.888	0.135	0.4615	−15.41	−11.83	0.1275	8.701	0	9.991	0.6206
5	0.8854	0.4926	1.872	1.478	3.283	0.1051	0.2466	−13.35	−13.67	0.1643	6.025	0.07518	10.88	0.5715
6	0.8161	0.5203	0.979	1.179	1.124	0.1239	0.4404	−14.42	−14.47	0.1475	3.193	0	12.01	0.6392
7	0.7927	0.7458	2.678	1.707	2.951	0.1618	0.2769	−12.62	−15.33	0.0938	6.829	0	11.42	0.5145
8	0.8225	0.7718	2.28	0.6145	3.153	0.1819	0.3755	−14.18	−12.51	0.143	3.413	0.008806	5.912	0.6903
9	0.7813	0.8071	−2.129	1.387	2.05	0.1158	0.4249	−13.97	−16.57	0.1611	4.725	0.06246	3.838	0.3543
10	0.8763	0.9106	3.06	1.109	1.519	0.1543	0.4049	−15.02	−15.74	0.1165	5.9	0.1032	9.484	0.4064
11	0.8643	0.5518	−1.415	1.039	2.437	0.1304	0.498	−12.75	−16.33	0.107	9.287	0	8.11	0.3792
12	0.8031	0.6281	−2.228	0.9849	1.774	0.1873	0.2066	−12.34	−15.1	0.1183	2.37	0.04421	12.26	0.4879
13	0.8309	0.5733	0.8117	0.9121	2.811	0.199	0.2801	−16.14	−14.05	0.1344	7.794	0	13.4	0.328
14	0.8281	0.6455	−0.2558	1.353	1.671	0.1917	0.3147	−14.89	−17.01	0.133	9.625	0.02813	10.56	0.6973
15	0.8504	0.8532	−2.696	1.674	2.516	0.1499	0.3976	−15.57	−12.9	0.1256	4.265	0.1277	14.82	0.4452
16	0.881	0.5436	−1.748	1.269	3.463	0.1762	0.3433	−15.83	−17.15	0.09403	2.694	0.0208	7.154	0.5809
17	0.8561	0.7389	−0.4868	1.209	1.233	0.1597	0.178	−14.6	−13.4	0.1549	6.542	0	7.402	0.3749
18	0.8429	0.82	2.177	1.532	3.783	0.1418	0.1952	−13.88	−17.52	0.1689	3.974	0	10.16	0.4602
19	0.7865	0.5986	1.491	0.8085	1.985	0.1003	0.1204	−16.2	−14.82	0.1011	5.334	0	9.013	0.5461
20	0.8078	0.6642	0.02717	0.6989	3.552	0.1652	0.148	−13.1	−14.37	0.1517	9.109	0.174	8.317	0.5152

Source: Output DTN: SN0701T0502206.043, file: *LHS_GT_R2.OUT*.

6.5.6 Calculation Procedure

6.5.6.1 Assembling Model Input

For each of the three future climates, two Latin Hypercube Sample (LHS) replicates were generated (Output DTN: SN0701T0502206.043). A LHS replicate is a complete structured set of Monte Carlo samples covering the entire probability range of all the sampled parameters (LHS User's Manual, STN 10205-2.51-01 [DIRS 178784]). Each replicate in this analysis consists of 20 realizations of input parameter values (Section 6.5.5). Two replicates were run to test the stability of the distribution of infiltration results. The comparison between these two replicates is discussed in Section 6.5.7.9. Tables in Section 6.5.5 list the parameters that were varied for each climate accompanied by the probability distributions from which the parameters were sampled. Some of the parameters that were varied included stochastic parameters describing precipitation that affect the generation of the weather input files (Appendix F). For each realization, a separate weather input file was generated, which used the sampled values of these parameters, representing epistemic uncertainty:

- Present-Day Weather files: Output DTN: SN0701T0502206.040
- Monsoon Weather files: Output DTN: SN0701T0502206.041
- Glacial Transition Weather files: Output DTN: SN0701T0502206.042.

In addition, each of these weather file realizations used a different set of random numbers, which resulted in differing patterns of precipitation and reflected aleatory uncertainty.

For each realization, the appropriate weather input file and parameter set was selected and the MASSIF net infiltration model was run for each of the 11 watersheds separately (Output DTN: SN0701T0502206.037).

6.5.6.2 Model Execution

MASSIF was run in a separate Mathcad file for each of the realizations. Names of these files were of the form *Present Day R1 V03.xmcd*. The first part of the name indicates the climate (Present-Day, Monsoon, Glacial Transition). The second part of the name (R1 or R2) indicates the replicate number. The third part of the name (V01 thru V20) indicates realization number. Within each of the 40 Mathcad files (20 realizations × 2 replicates), the MASSIF routine was executed for each of the 11 watersheds.

Results of each realization are stored in subdirectories named V01 thru V20, which are subdirectories of the directories "Replicate 1" and "Replicate 2." Each realization generated 55 separate ASCII output files. For each of the 11 watersheds, 5 types of files were generated:

1. File listing 10 annual values (columns 1 thru 10) and the weighted mean value (column 11) of precipitation for each cell [file name example: *Precip_WS01_PD_R1_V01.prn*]

2. File listing 10 annual values (columns 1 thru 10) and the weighted mean value (column 11) of net infiltration for each cell [file name example: *Infil_WS01_PD_R1_V01.prn*]

3. File listing 10 annual values (columns 1 thru 10) and the weighted mean value (column 11) of run-on for each cell [file name example: *Runon_WS01_PD_R1_V01.prn*]

4. File listing 10 annual values (columns 1 thru 10) and the weighted mean value (column 11) of runoff for each cell [file name example: *Runoff_WS01_PD_R1_V01.prn*]

5. File listing the annual integrated (spatially and temporally) values of (column 1) change in water storage, (column 2) change in snow level, (column 3) precipitation, (column 4) evapotranspiration, (column 5) net infiltration, (column 6) annual sublimation, and (column 7) runoff [file name example: *Watershed_WS01_PD_R1_V01.prn*].

The naming convention of the output files indicates the output variable stored and the source of the inputs. Hence, the output file name "Precip_WS01_PD_R1_V01" indicates that the file contains values of precipitation for watershed 1 (WS01) for the present day (PD) for replicate 1 (R1) and realization 1 (V01). The number of rows in each of the first 4 output types (Precip, Infil, Runon, and Runoff) is equal to the number of cells in the watershed. The cells are listed in the same sequence as in the corresponding geospatial file. The file containing integrated values (Watershed….) has 10 rows corresponding to the 10 precipitation years modeled.

The 40 Mathcad files (for each climate) in which each realization is computed were designed so that the calculation can be spot-checked at a later date by an independent reviewer. The reviewer is allowed to select a watershed (# 1 to 11) and a single precipitation year (1 to 10). MASSIF is then executed for the chosen combination. Results of the reviewer's calculation are automatically displayed along with the results that are stored in the appropriate results subdirectory. This process gives the independent reviewer the capability to verify the reproducibility of the stored results.

6.5.6.3 Post-Processing of Results

Post-processing of results for each climate consists of following a set of defined calculation steps, which are described in detail in Mathcad file *MASSIF Results Documentation.xmcd* in Output DTN: SN0701T0502206.037.

6.5.7 Results of Net Infiltration Calculations

The results of the net infiltration calculation performed for the 125 km^2 infiltration modeling domain around Yucca Mountain are presented in this section. The calculations described in this section are included in Output DTN: SN0701T0502206.037. *UZ Flow Models and Submodels* (BSC 2004 [DIRS 169861]) and *Calibrated Properties Model* (BSC 2004 [DIRS 169857]) are use preliminary set of results that were generated during the preparation of initial drafts of this report and are slightly different than the qualified output DTNs described in this section. These preliminary output DTNs are discussed in Appendix L. The output DTNs with net infiltration results for each climate that are considered qualified in this report include the following Output DTNs: SN0701T0502206.034 (Present-Day), SN0701T0502206.036 (Monsoon), and SN0701T0502206.035 (Glacial Transition).

As discussed in Sections 6.5.5 and 6.5.6, for each climate two LHS replicates of 20 realizations each were run in order to estimate the uncertainty and stability of model results. The differences between the two replicates for each climate are an indication of the additional uncertainty caused by the small sample size of 20 realizations. The results of both replicates are combined for the main uncertainty analysis.

This section is organized as follows: Sections 6.5.7.1 to 6.5.7.3 present an overview of precipitation and net infiltration results for each of the future climates considered (Present-Day, Monsoon, and Glacial Transition). These results include: (1) presentation of the precipitation variability between realizations, (2) comparisons of average values of net infiltration over various domains, and (3) a presentation of net infiltration maps representing the 10th, 30th, 50th, and 90th percentiles. Section 6.5.7.4 compares the magnitudes of the various water balance components for each climate and for runs made with an alternative set of initial soil moisture content initial conditions. Section 6.5.7.5 discusses factors that influence the temporal variability in net infiltration. Section 6.5.7.6 discusses factors that influence the spatial variability in net infiltration during the Present-Day climate. Section 6.5.7.7 illustrates daily conditions in a single grid cell in Pagany Wash in order to demonstrate some of the key features of the model. Section 6.5.7.8 summarizes the results of the uncertainty analysis.

Plots of daily precipitation and temperature used for each realization can be found in Output DTN: SN0701T0502206.037 in the individual Mathcad files in which the realizations are run.

6.5.7.1 Present-Day Simulation Results

6.5.7.1.1 Present-Day Precipitation Results

The mean annual precipitation (MAP) (at the reference elevation of 1,524 m) used for the 40 realizations representing Present-Day climate is summarized in Figure 6.5.7.1-1 and Table 6.5.7.1-1. The parameters used to represent Present-Day climate are described in Section 6.5.1 and Appendix F.

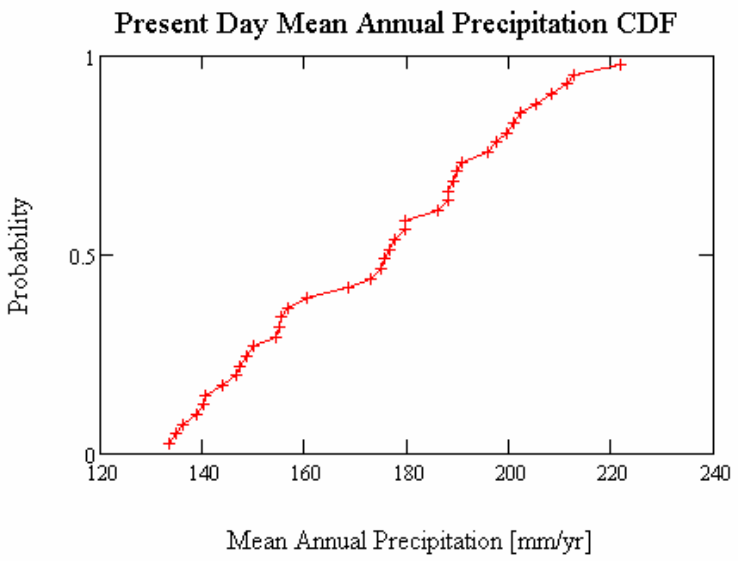

Source: Output DTN: SN0701T0502206.037, file: \Welcome to Massif\Massif\Present Day Uncertainty\Post Processing*PD_Combined_Replicates.xmcd*.

NOTE: A total of 40 realizations (2 LHS replicates) define the distribution. MAP values are for a reference elevation of 1,524 m above sea level.

Figure 6.5.7.1-1. Present-Day Mean Annual Precipitation CDF

Table 6.5.7.1-1. Mean Annual Precipitation Statistics for the 40 Realizations Used to Represent Present-Day Climate for Net Infiltration Calculations

Present-Day Precipitation	R1 (mm/yr)	R2 (mm/yr)	R1 and R2 (mm/yr)
Minimum [mm/yr]	134.9	133.6	133.6
Mean [mm/yr]	173.4	173.7	173.6
Median [mm/yr]	176.3	176.4	176.3
Maximum [mm/yr]	222.0	212.7	222.0
Standard Deviation [mm/yr]	26.2	25.3	25.4

Source: Output DTN: SN0701T0502206.037, file: \Welcome to Massif\Massif\Present Day Uncertainty\Post Processing*PD_Combined_Replicates.xmcd*.

6.5.7.1.2 Present-Day Net Infiltration Uncertainty Analysis Results

As described in Sections 6.5.5 and 6.5.6, two replicates (R1 and R2) of 20 realizations each were run for Present-Day climate mean annual net infiltration estimation. Table 6.5.7.1-2 compares mean annual net infiltration statistics for these realizations. Table 6.5.7.1-3 identifies the maps that represent the 10th, 30th, 50th, and 90th percentiles of mean annual net infiltration over the entire model domain. Figures 6.5.7.1-2 to 6.5.7.1-5 show maps of mean annual net infiltration for these four maps. Figure 6.5.7.1-6 presents a CDF of spatially averaged mean annual net infiltration over the full modeling domain for the Present-Day climate results.

Table 6.5.7.1-2. Spatially Averaged Mean Annual Net Infiltration [mm/yr] Statistics for Present-Day Simulations

Present-Day Climate	Domain	R1 (mm/yr)	R2 (mm/yr)	R1 and R2 (mm/yr)
Minimum [mm/yr]	Infiltration modeling domain (125 km^2)	2.0	3.1	2.0
	UZ modeling domain (39.8 km^2)	1.4	2.1	1.4
	Repository footprint (5.7 km^2)	1.5	1.9	1.5
Mean [mm/yr]	Infiltration modeling domain (125 km^2)	13.4	15.2	14.3
	UZ modeling domain (39.8 km^2)	14.2	16.0	15.1
	Repository footprint (5.7 km^2)	16.7	18.6	17.6
Median [mm/yr]	Infiltration modeling domain (125 km^2)	11.4	13.7	12.9
	UZ modeling domain (39.8 km^2)	12.2	12.8	12.4
	Repository footprint (5.7 km^2)	14.9	14.0	14.5
Maximum [mm/yr]	Infiltration modeling domain (125 km^2)	28.8	35.4	35.4
	UZ modeling domain (39.8 km^2)	32.6	40.9	40.9
	Repository footprint (5.7 km^2)	38.6	48.2	48.2
Standard Deviation [mm/yr]	Infiltration modeling domain (125 km^2)	8.3	9.5	8.8
	UZ modeling domain (39.8 km^2)	9.7	11.3	10.4
	Repository footprint (5.7 km^2)	11.5	13.6	12.5

Source: Output DTN: SN0701T0502206.037, file: \Welcome to Massif\Massif\Present Day Uncertainty\Post Processing*PD_Combined_Replicates.xmcd*.

Table 6.5.7.1-3. Realizations Identified for Selected Percentiles of Present-Day Spatially Averaged Mean Annual Net Infiltration

Percentile	Replicate	Realization	Net Infiltration (mm/yr)	Mean Annual Precipitation (mm/yr)
10th	R2	10	3.9	144.1
30th	R2	2	7.3	160.6
50th	R2	8	13.0	189.3
90th	R2	14	26.7	212.7

Source: Output DTN: SN0701T0502206.037, file: \Welcome to Massif\Massif\Present Day Uncertainty\Post Processing*PD_Combined_Replicates.xmcd*.

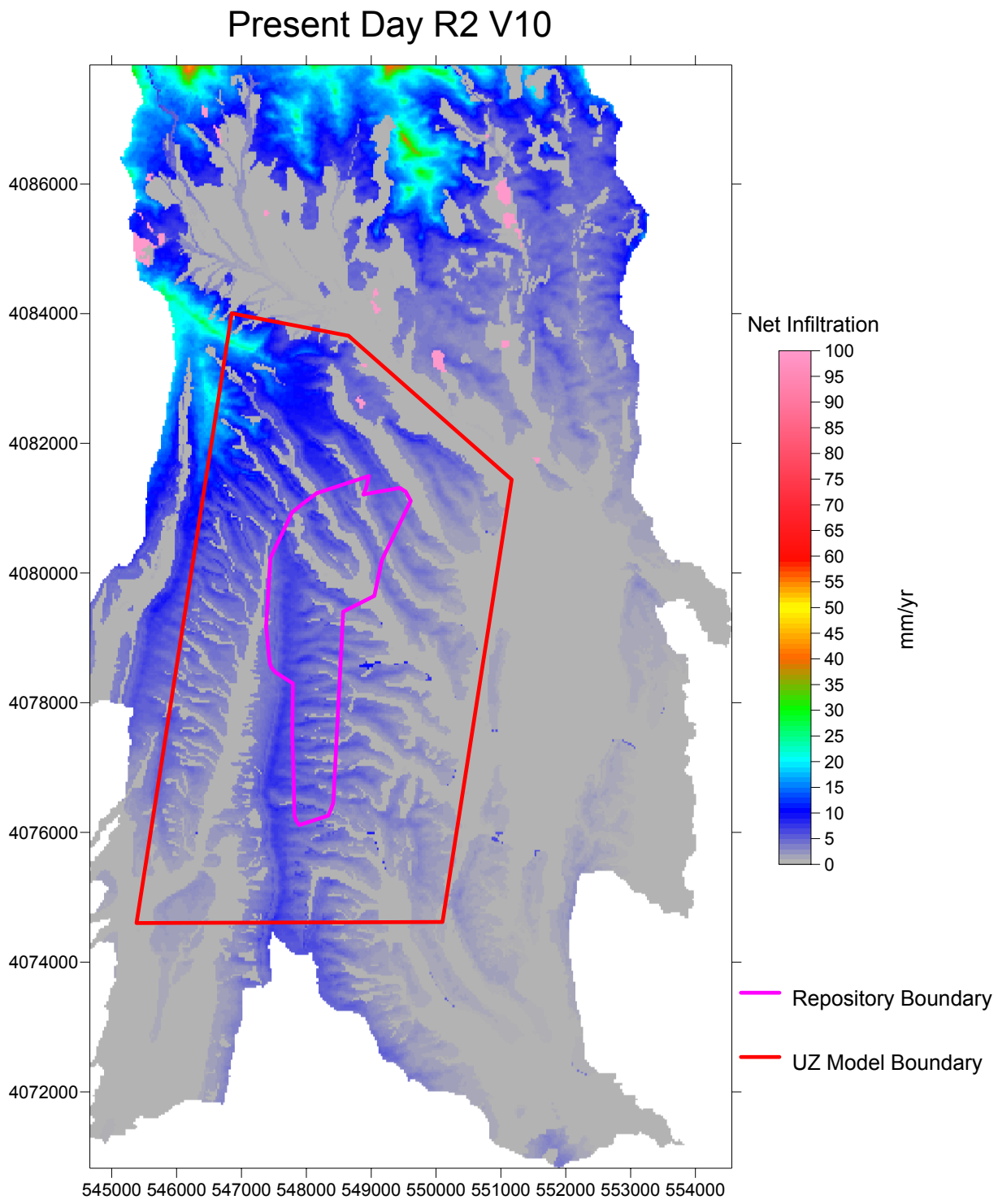

Coordinates are in meters; UTM NAD 27, Zone 11

Source: Output DTNs: SN0701T0502206.034 (Mean Annual Net Infiltration Results); SN0612FTPRNUZB.002 (UZ Model and Repository Boundaries).

Figure 6.5.7.1-2. Present-Day, 10th Percentile Mean Annual Net Infiltration Map (Replicate R2, Realization 10)

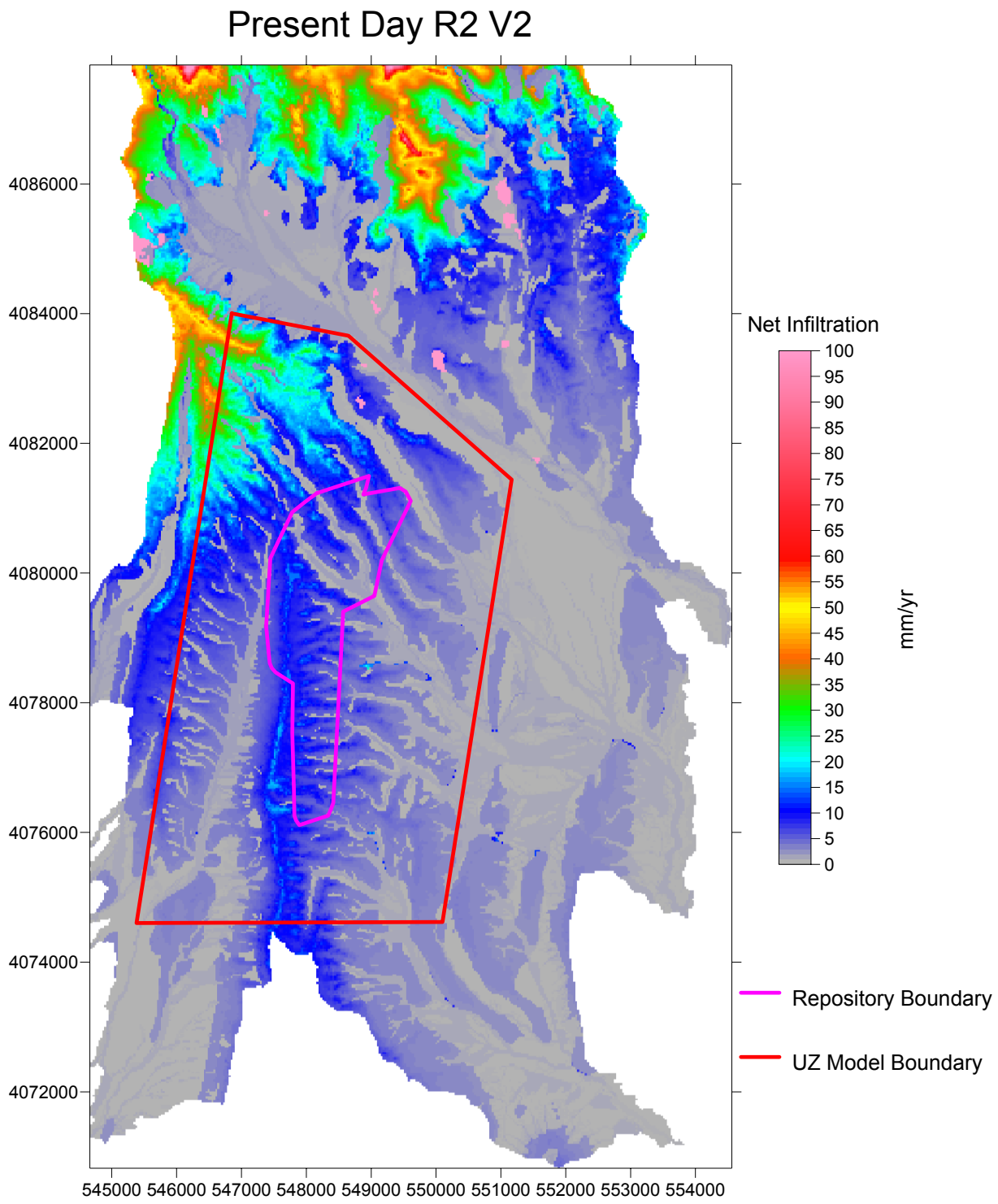

Coordinates are in meters; UTM NAD 27, Zone 11

Source: Output DTNs: SN0701T0502206.034 (Mean Annual Net Infiltration Results); SN0612FTPRNUZB.002 (UZ Model and Repository Boundaries).

Figure 6.5.7.1-3. Present-Day, 30th Percentile Mean Annual Net Infiltration Map (Replicate R2, Realization 2)

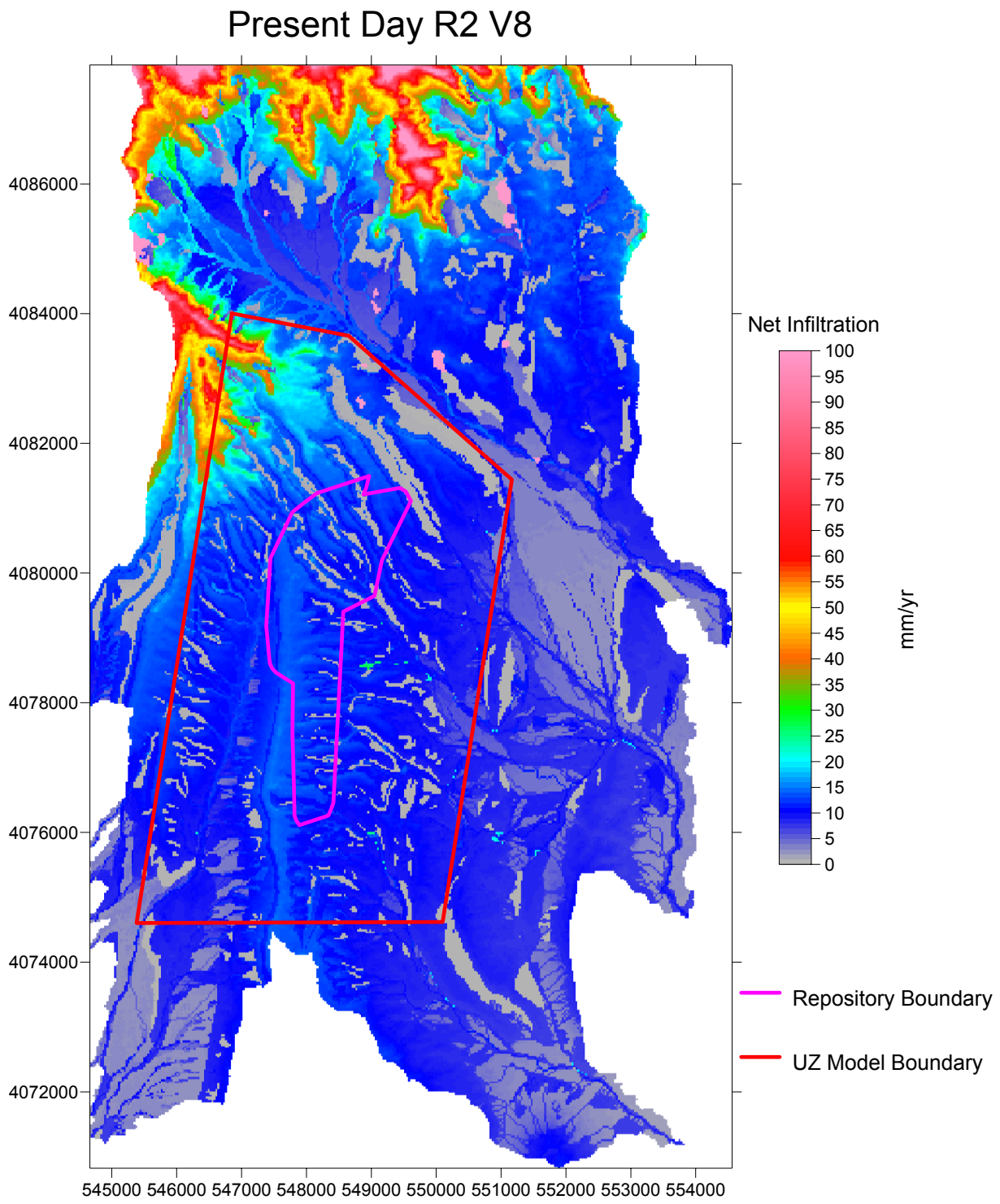

Coordinates are in meters; UTM NAD 27, Zone 11

Source: Output DTNs: SN0701T0502206.034 (Mean Annual Net Infiltration Results); SN0612FTPRNUZB.002 (UZ Model and Repository Boundaries).

Figure 6.5.7.1-4. Present-Day, 50th Percentile Mean Annual Net Infiltration Map (Replicate R2, Realization 8)

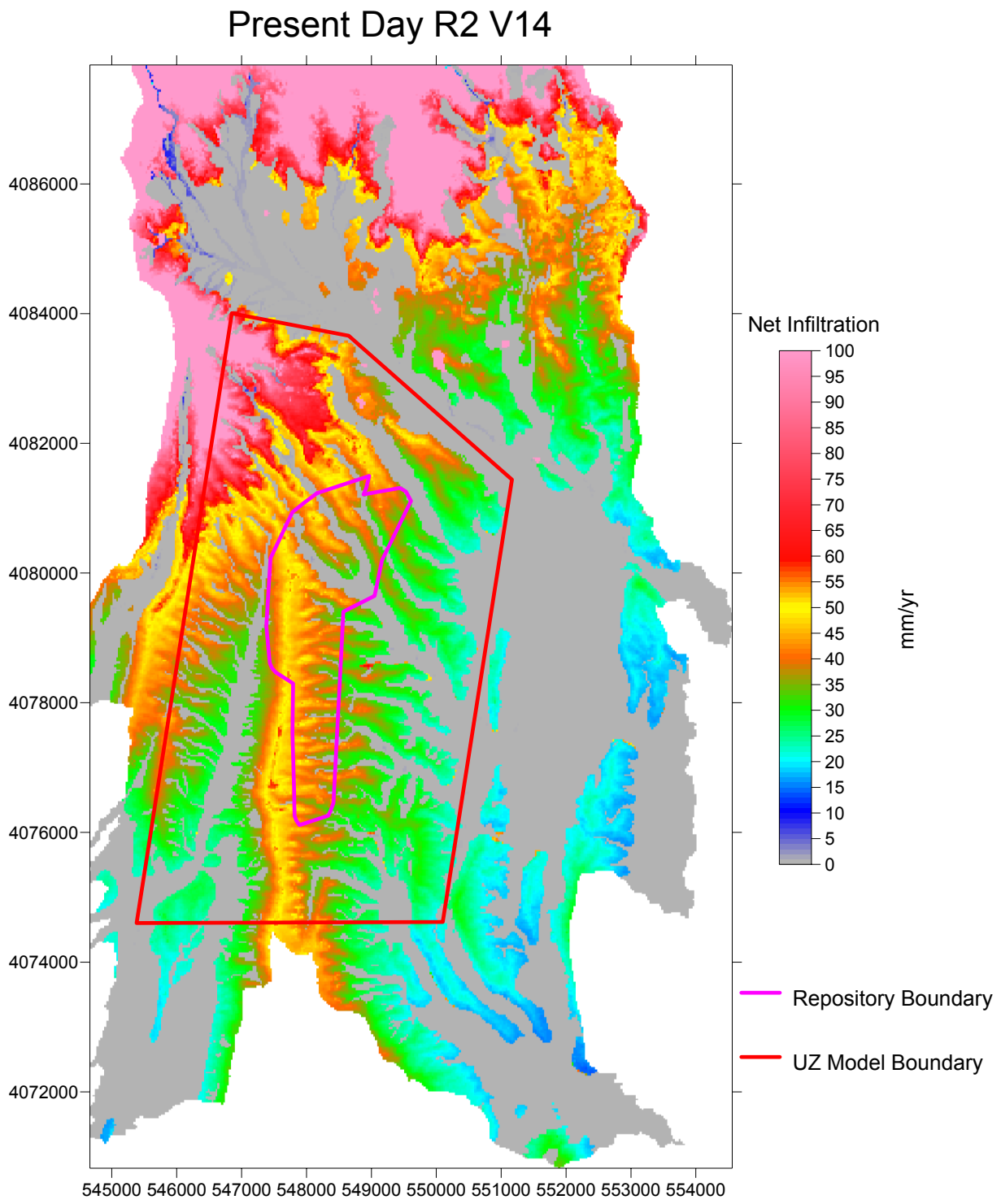

Coordinates are in meters; UTM NAD 27, Zone 11

Source: Output DTN: SN0701T0502206.034 (Mean Annual Net Infiltration Results); SN0612FTPRNUZB.002 (UZ Model and Repository Boundaries).

Figure 6.5.7.1-5. Present-Day, 90th Percentile Mean Annual Net Infiltration Map (Replicate R2, Realization 14)

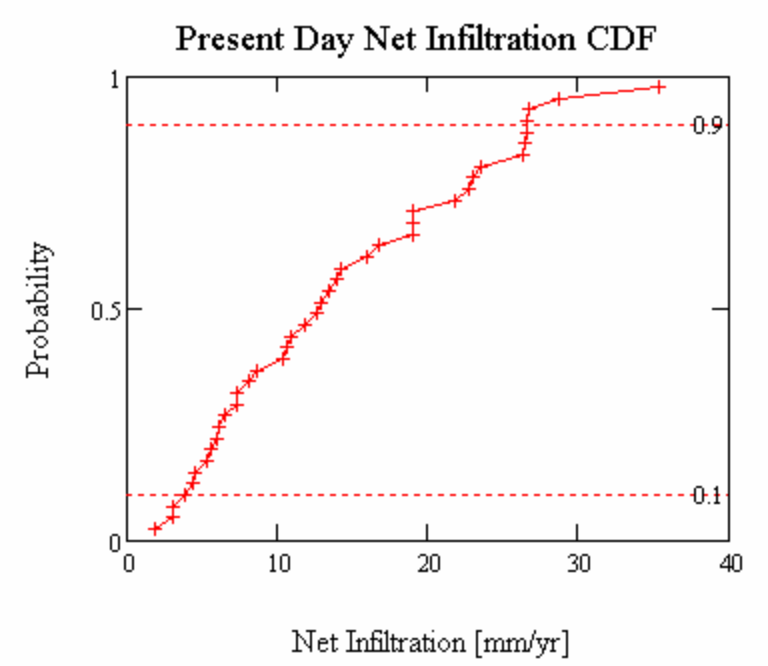

Source: Output DTN: SN0701T0502206.037, file: \Welcome to Massif\Massif\Present Day Uncertainty\Post Processing*PD_Combined_Replicates.xmcd*.

NOTE: A total of 40 realizations (2 LHS replicates) define the distribution.

Figure 6.5.7.1-6. Cumulative Distribution Function (CDF) of Present-Day Spatially Averaged Mean Annual Net Infiltration over the Infiltration Domain

6.5.7.2 Monsoon Simulation Results

6.5.7.2.1 Monsoon Precipitation Results

The mean annual precipitation (MAP) (at the reference elevation of 1,524 m) used for the 40 realizations representing Monsoon climate is summarized in Figure 6.5.7.2-1 and Table 6.5.7.2-1 below. The parameters used to represent Monsoon climate are described in Section 6.5.1 and Appendix F.

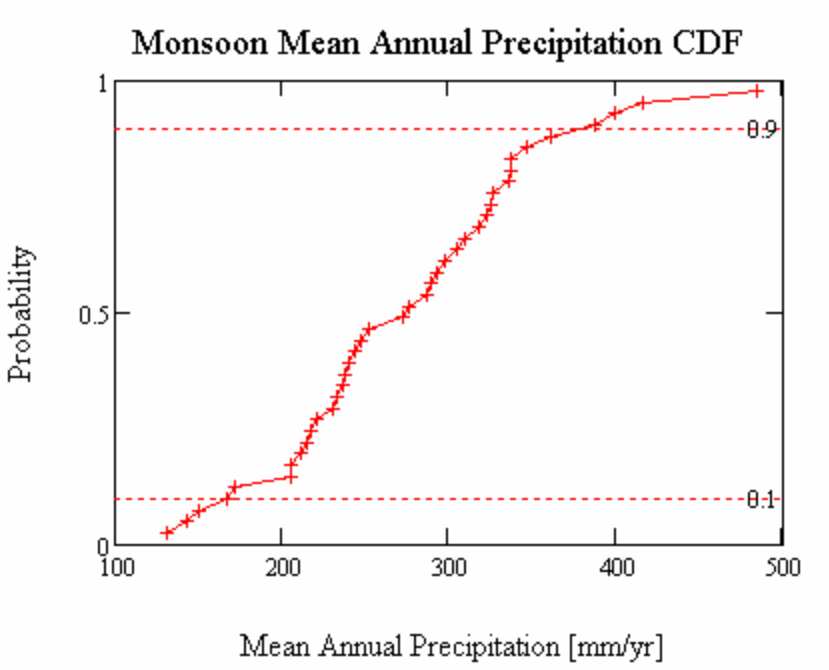

Source: Output DTN: SN0701T0502206.037, file: \Welcome to Massif\Massif\Monsoon Uncertainty\Post Processing*MO_Combined_Replicates.xmcd*.

NOTE: A total of 40 realizations (2 LHS replicates) define the distribution. MAP values are for a reference elevation of 1,524 m above sea level.

Figure 6.5.7.2-1. Monsoon Mean Annual Precipitation CDF

Table 6.5.7.2-1. Mean Annual Precipitation Statistics for the 40 Realizations used to Represent Monsoon Climate for Net Infiltration Calculations

Monsoon Precipitation	R1 (mm/yr)	R2 (mm/yr)	R1 and R2 (mm/yr)
Minimum [mm/yr]	132.1	144.0	132.1
Mean [mm/yr]	272.7	277.8	275.2
Median [mm/yr]	262.7	279.8	274.8
Maximum [mm/yr]	399.7	484.7	484.7
Standard Deviation [mm/yr]	71.9	85.5	78.0

Source: Output DTN: SN0701T0502206.037, file: \Welcome to Massif\Massif\Monsoon Uncertainty\Post Processing*MO_Combined_Replicates.xmcd*.

6.5.7.2.2 Monsoon Net Infiltration Uncertainty Analysis Results

As described in Sections 6.5.5 and 6.5.6, two replicates (R1 and R2) of 20 realizations each were run for the Monsoon climate net infiltration estimation. Table 6.5.7.2-2 compares spatially averaged mean annual net infiltration statistics for these realizations. Table 6.5.7.2-3 identifies the maps that represent the 10th, 30th, 50th, and 90th percentiles of spatially averaged mean annual net infiltration over the entire model domain. Figures 6.5.7.2-2 to 6.5.7.2-5 show maps of mean annual net infiltration for these four realizations. Figure 6.5.7.2-6 presents a CDF of spatially averaged mean annual net infiltration over the full domain for the Monsoon climate results.

Table 6.5.7.2-2. Spatially Averaged Mean Annual Net Infiltration [mm/yr] Statistics for Monsoon Simulations

Monsoon Climate	Domain	R1 (mm/yr)	R2 (mm/yr)	R1 and R2 (mm/yr)
Minimum [mm/yr]	Infiltration modeling domain (125 km^2)	3.0	2.4	2.4
	UZ modeling domain (39.8 km^2)	1.9	1.2	1.2
	Repository footprint (5.7 km^2)	2.0	1.2	1.2
Mean [mm/yr]	Infiltration modeling domain (125 km^2)	23.5	27.6	25.5
	UZ modeling domain (39.8 km^2)	25.8	30.1	28.0
	Repository footprint (5.7 km^2)	30.5	35.3	32.9
Median [mm/yr]	Infiltration modeling domain (125 km^2)	23.3	20.4	22.8
	UZ modeling domain (39.8 km^2)	25.0	22.7	24.2
	Repository footprint (5.7 km^2)	29.3	27.1	28.4
Maximum [mm/yr]	Infiltration modeling domain (125 km^2)	52.6	83.4	83.4
	UZ modeling domain (39.8 km^2)	62.2	86.2	86.2
	Repository footprint (5.7 km^2)	74.5	95.3	95.3
Standard Deviation [mm/yr]	Infiltration modeling domain (125 km^2)	14.9	21.1	18.2
	UZ modeling domain (39.8 km^2)	17.3	23.0	20.2
	Repository footprint (5.7 km^2)	20.4	26.2	23.3

Source: Output DTN: SN0701T0502206.037, file: \Welcome to Massif\Massif\Monsoon Uncertainty\Post Processing*MO_Combined_Replicates.xmcd*.

Table 6.5.7.2-3. Realizations Identified for Selected Percentiles of Monsoon Spatially Averaged Mean Annual Net Infiltration

Percentile	Replicate	Realization	Net Infiltration [mm/yr]	Mean Annual Precipitation [mm/yr]
10th	R1	17	6.3	206.5
30th	R2	10	14.4	150.7
50th	R1	2	22.9	240.8
90th	R1	7	52.6	310.2

Source: Output DTN: SN0701T0502206.037, file: \Welcome to Massif\Massif\Monsoon Uncertainty\Post Processing*MO_Combined_Replicates.xmcd*.

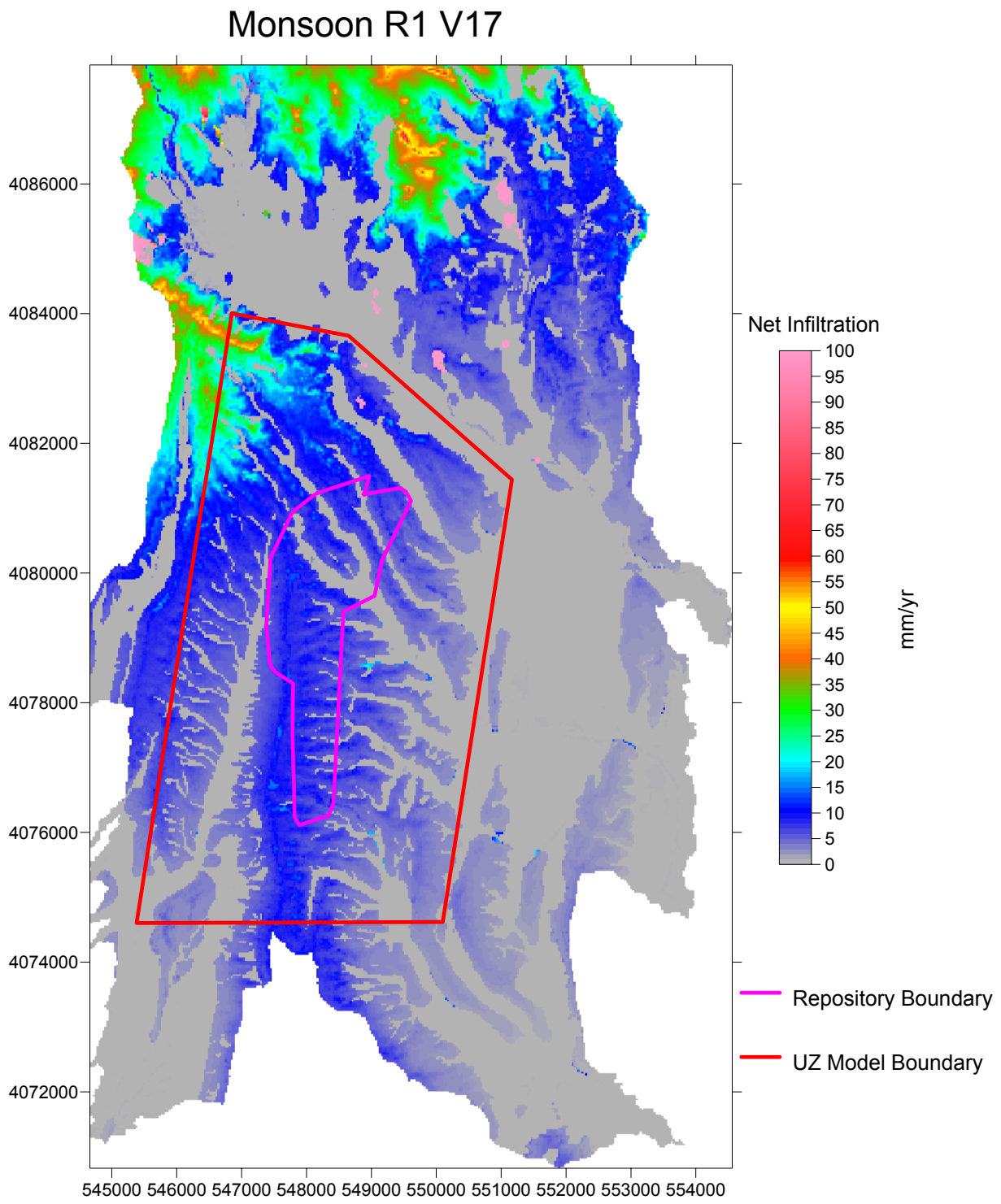

Coordinates are in meters; UTM NAD 27, Zone 11

Source: Output DTNs: SN0701T0502206.036 (Mean Annual Net Infiltration Results); SN0612FTPRNUZB.002 (UZ Model and Repository Boundaries).

Figure 6.5.7.2-2. Monsoon, 10th Percentile Mean Annual Net Infiltration Map (Replicate R1, Realization 17)

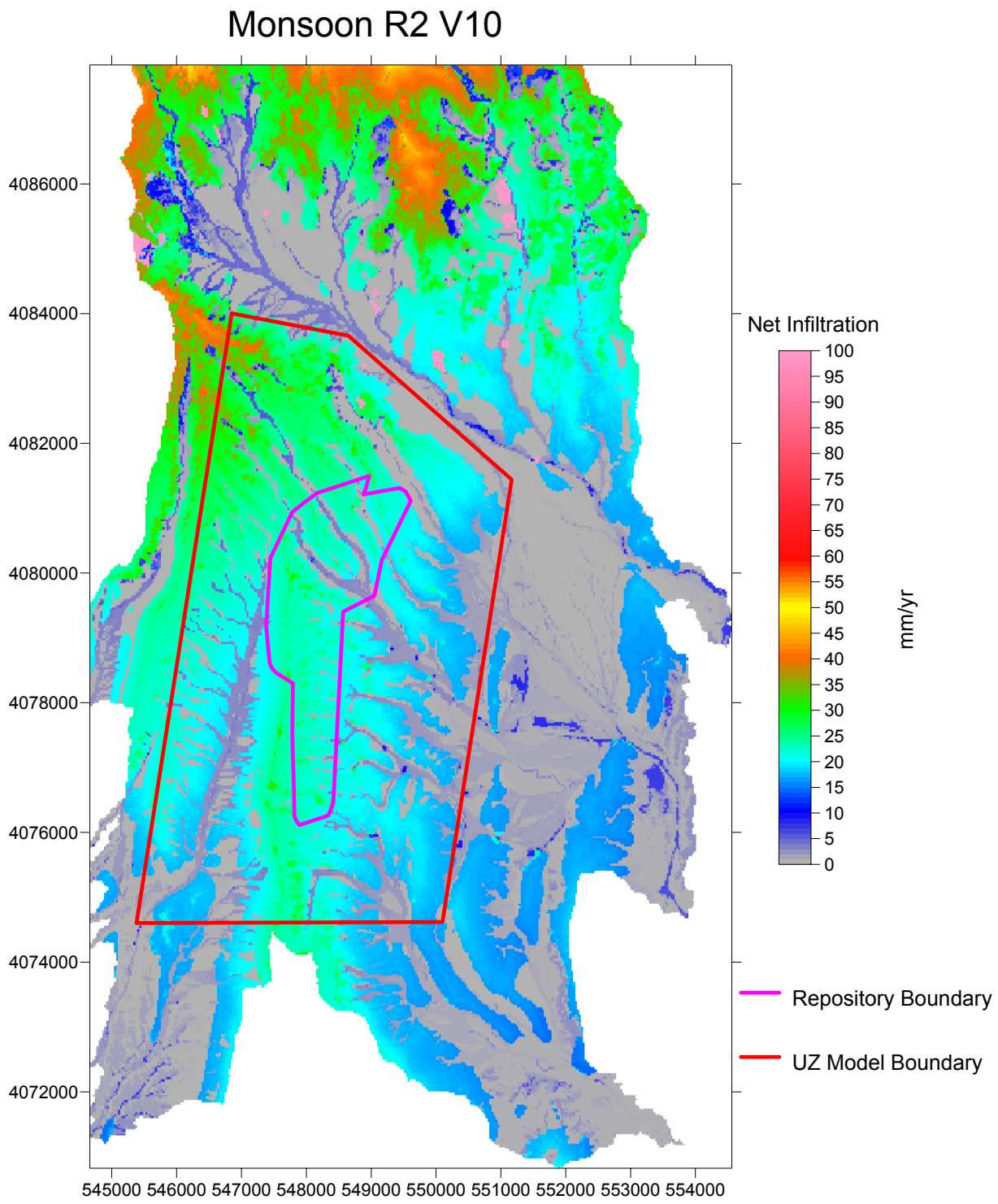

Coordinates are in meters; UTM NAD 27, Zone 11

Source: Output DTNs: SN0701T0502206.036 (Mean Annual Net Infiltration Results); SN0612FTPRNUZB.002 (UZ Model and Repository Boundaries).

Figure 6.5.7.2-3. Monsoon, 30th Percentile Mean Annual Net Infiltration Map (Replicate R2, Realization 10)

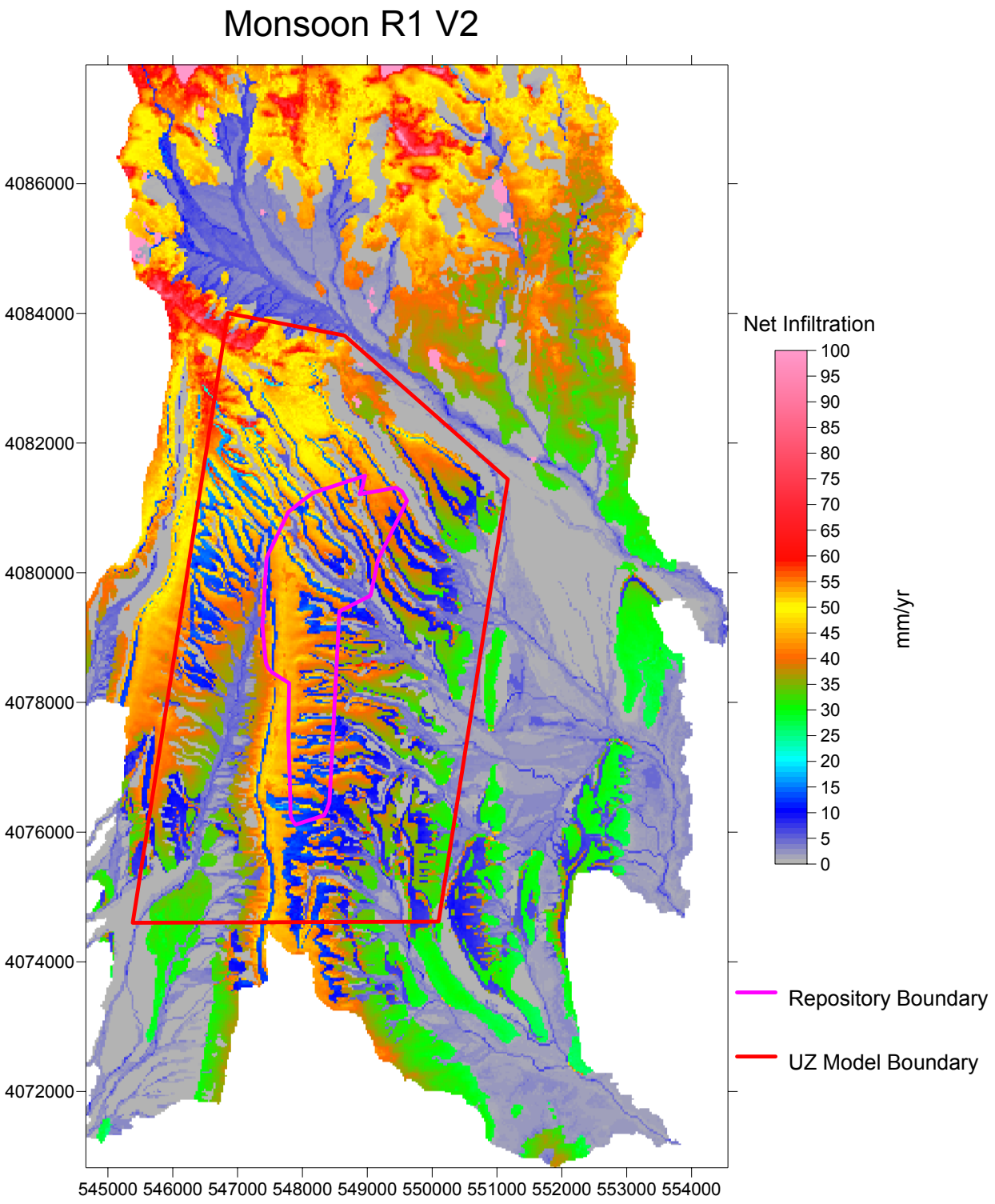

Coordinates are in meters; UTM NAD 27, Zone 11

Sourxe: Output DTNs: SN0701T0502206.036 (Net Infiltration Results); and SN0612FTPRNUZB.002 (UZ Model and Repository Boundaries).

Figure 6.5.7.2-4. Monsoon, 50th Percentile Net Infiltration Map (Replicate R1, Realization 2)

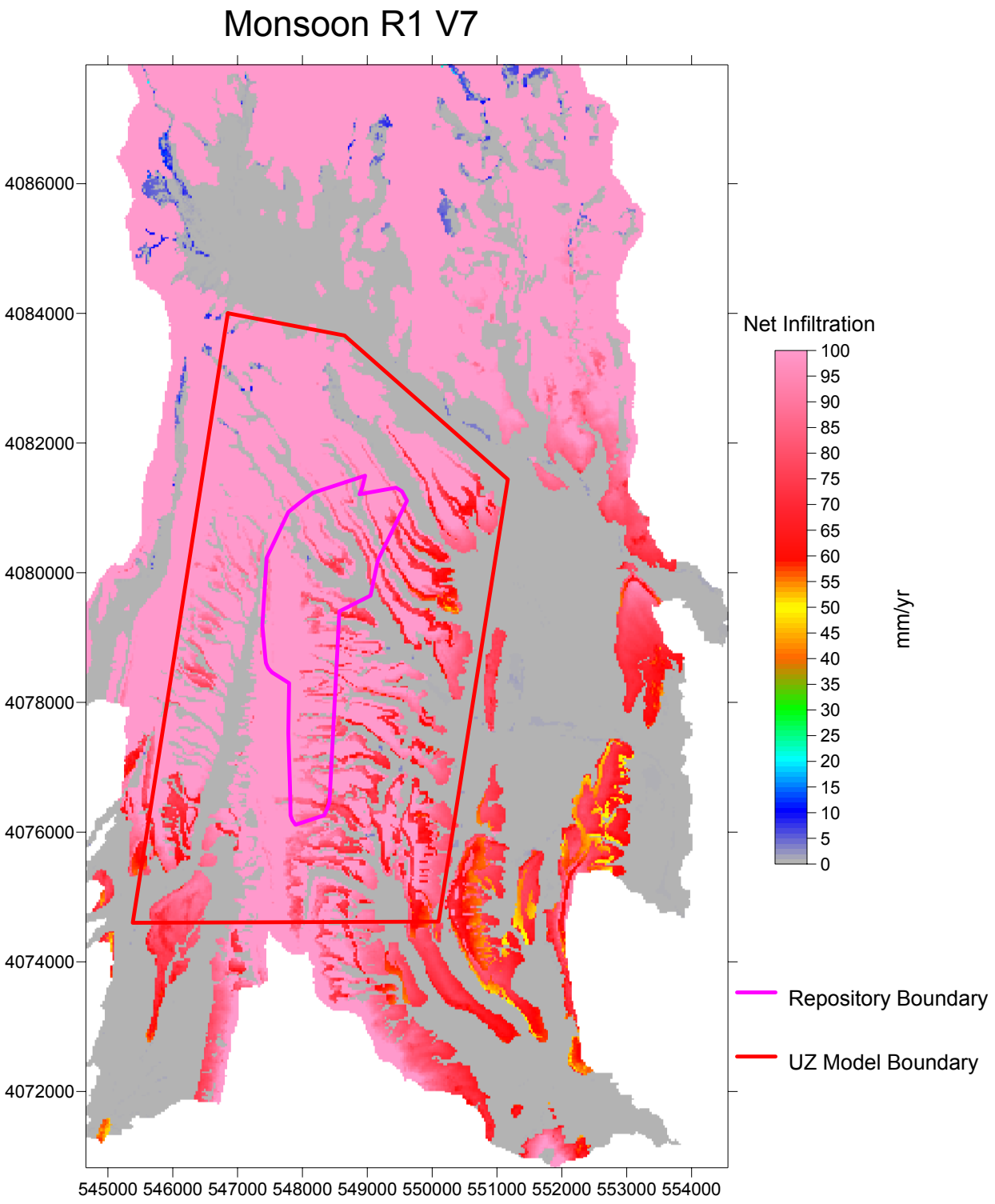

Coordinates are in meters; UTM NAD 27, Zone 11

Source: Output DTN: SN0701T0502206.036 (Net Infiltration Results); and SN0612FTPRNUZB.002 (UZ Model and Repository Boundaries).

Figure 6.5.7.2-5. Monsoon, 90th Percentile Net Infiltration Map (Replicate R1, Realization 7)

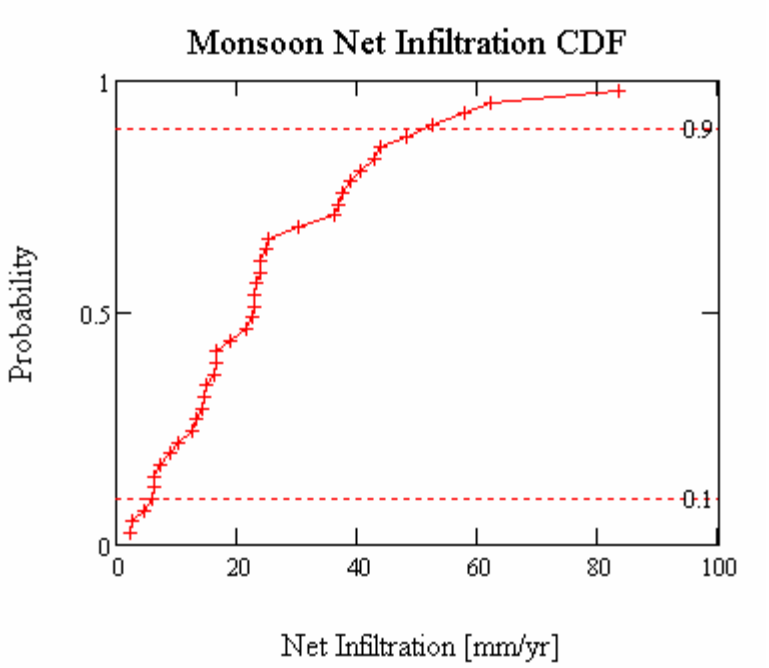

Source: Output DTN: SN0701T0502206.037, file: \Welcome to Massif\Massif\Monsoon Uncertainty\Post Processing*MO_Combined_Replicates.xmcd*.

NOTE: A total of 40 realizations (2 LHS replicates) define the distribution.

Figure 6.5.7.2-6. Cumulative Distribution Function (CDF) of Monsoon Net Infiltration Averaged over the Infiltration Domain

6.5.7.3 Glacial Transition Simulation Results

The mean annual precipitation (MAP) (at the reference elevation of 1,524 m) used for the 40 realizations representing Glacial Transition climate is summarized in Figure 6.5.7.3-1 and Table 6.5.7.3-1. The parameters used to represent Glacial Transition climate are described in Section 6.5.1 and Appendix F.

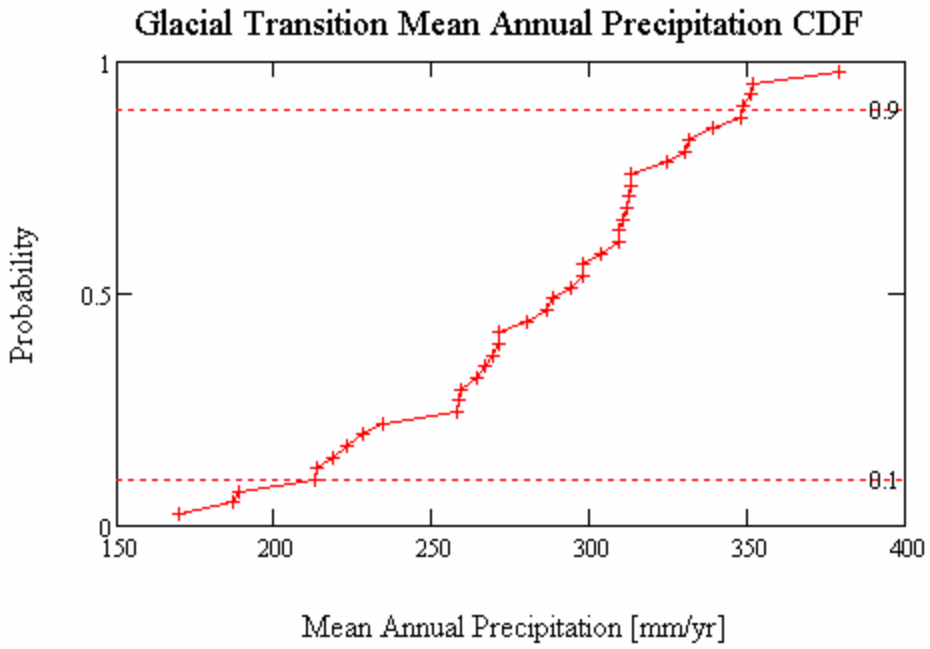

Source: Output DTN: SN0701T0502206.037, file: \Welcome to Massif\Massif\Glacial Uncertainty\Post Processing*GT_Combined_Replicates.xmcd*.

NOTE: A total of 40 realizations (2 LHS replicates) define the distribution. MAP values are for a reference elevation of 1,524 meters above sea level.

Figure 6.5.7.3-1. Glacial Transition Mean Annual Precipitation CDF

Table 6.5.7.3-1. Mean Annual Precipitation Statistics for the 40 Realizations Used to Represent Glacial Transition Climate for Net Infiltration Calculations

Glacial Transition Precipitation	R1 (mm/yr)	R2 (mm/yr)	R1 and R2 (mm/yr)
Minimum [mm/yr]	169.8	187.0	169.8
Mean [mm/yr]	282.2	284.6	283.4
Median [mm/yr]	296.5	290.3	291.5
Maximum [mm/yr]	351.9	379.3	379.3
Standard Deviation [mm/yr]	53.5	49.0	50.6

Source: Output DTN: SN0701T0502206.037, file: \Welcome to Massif\Massif\Glacial Uncertainty\Post Processing*MO_Combined_Replicates.xmcd*.

Two replicates (R1 and R2) of 20 realizations each were run for the Glacial Transition climate net infiltration estimation. Table 6.5.7.3-2 compares spatially averaged mean annual net infiltration statistics for these realizations. Table 6.5.7.3-3 identifies the maps that represent the 10th, 30th, 50th, and 90th, percentiles of spatially averaged mean annual net infiltration over the entire model domain. Figures 6.5.7.3-2 to 6.5.7.3-5 show maps of mean annual net infiltration for these percentiles. Figure 6.5.7.2-6 presents a CDF of spatially averaged mean annual net infiltration over the full domain for the Glacial Transition climate results.

Table 6.5.7.3-2. Spatially Averaged Mean Annual Net Infiltration Statistics for Glacial Transition Simulations

Glacial Transition Climate	Domain	R1 (mm/yr)	R2 (mm/yr)	R1 and R2 (mm/yr)
Minimum [mm/yr]	Infiltration modeling domain (125 km^2)	6.6	13.2	6.6
	UZ modeling domain (39.8 km^2)	4.3	8.2	4.3
	Repository footprint (5.7 km^2)	4.0	8.5	4.0
Mean [mm/yr]	Infiltration modeling domain (125 km^2)	30.8	29.2	30.0
	UZ modeling domain (39.8 km^2)	30.2	28.3	29.3
	Repository footprint (5.7 km^2)	39.9	37.5	38.7
Median [mm/yr]	Infiltration modeling domain (125 km^2)	28.5	28.1	28.5
	UZ modeling domain (39.8 km^2)	28.6	25.9	28.1
	Repository footprint (5.7 km^2)	38.6	35.9	38.6
Maximum [mm/yr]	Infiltration modeling domain (125 km^2)	64.7	56.2	64.7
	UZ modeling domain (39.8 km^2)	72.1	62.0	72.1
	Repository footprint (5.7 km^2)	97.3	81.7	97.3
Standard Deviation [mm/yr]	Infiltration modeling domain (125 km^2)	14.3	12.1	13.1
	UZ modeling domain (39.8 km^2)	16.8	14.4	15.5
	Repository footprint (5.7 km^2)	23.3	19.5	21.2

Source: Output DTN: SN0701T0502206.037, file: \Welcome to Massif\Massif\Glacial Uncertainty\Post Processing*GT_Combined_Replicates.xmcd*.

Table 6.5.7.3-3. Realizations Identified for Selected Percentiles of Glacial Transition Spatially Averaged Mean Annual Net Infiltration

Percentile	Replicate	Realization	Net Infiltration (mm/yr)	Mean Annual Precipitation (mm/yr)
10th	R2	6	13.2	271.7
30th	R2	10	22.8	264.8
50th	R1	18	28.6	223.1
90th	R2	1	47.0	286.6

Source: Output DTN: SN0701T0502206.037, file: \Welcome to Massif\Massif\Glacial Uncertainty\Post Processing*GT_Combined_Replicates.xmcd*.

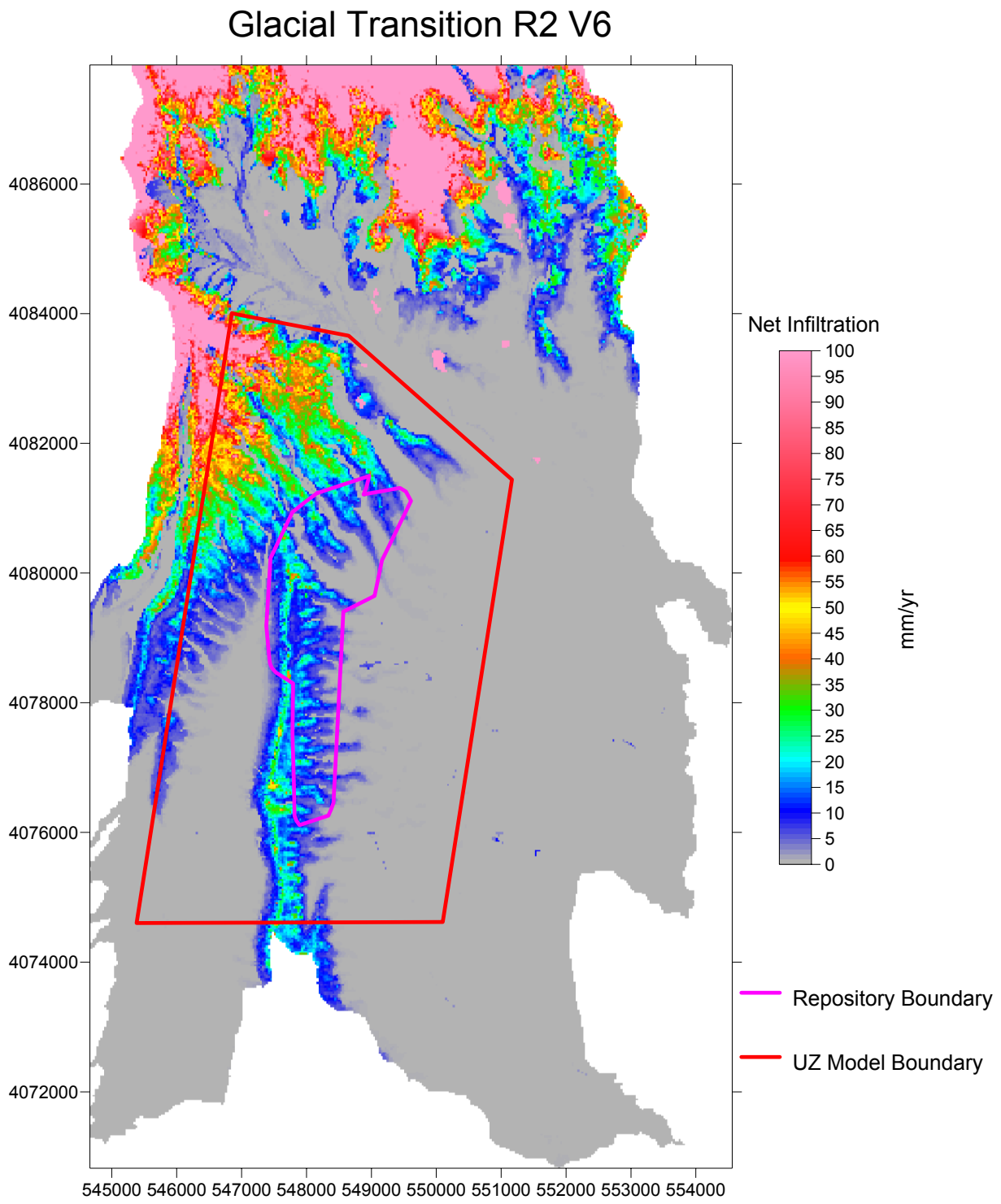

Coordinates are in meters; UTM NAD 27, Zone 11

Source: Output DTNs: SN0701T0502206.035 (Mean Annual Net Infiltration Results) and SN0612FTPRNUZB.002 UZ (Model and Repository Boundaries).

Figure 6.5.7.3-2. Glacial Transition, 10th Percentile Mean Annual Net Infiltration Map (Replicate R2, Realization 6)

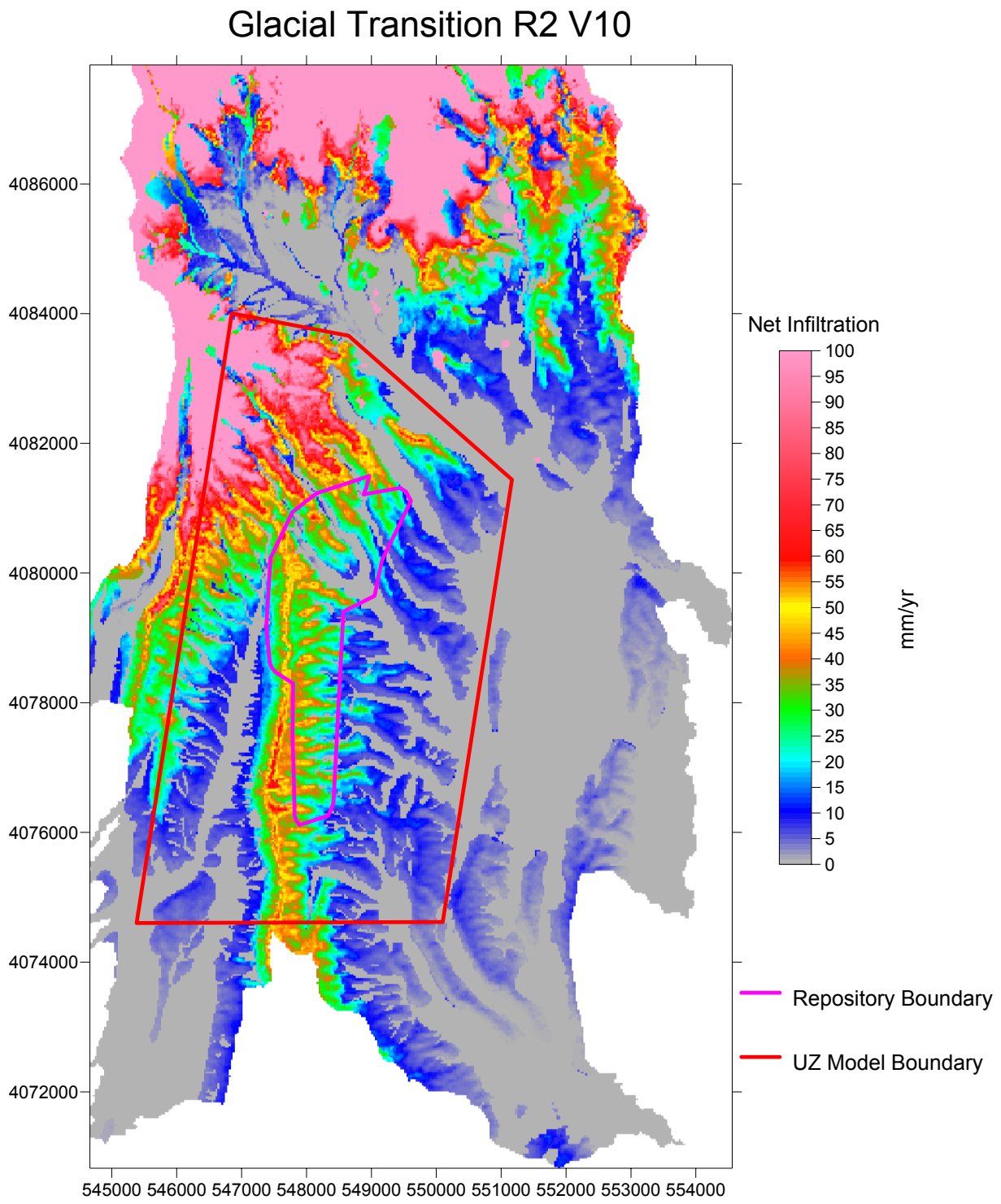

Coordinates are in meters; UTM NAD 27, Zone 11

Source: Output DTNs: SN0701T0502206.035 (Mean Annual Net Infiltration Results) and SN0612FTPRNUZB.002 UZ (Model and Repository Boundaries).

Figure 6.5.7.3-3. Glacial Transition, 30th Percentile Mean Annual Net Infiltration Map (Replicate R2, Realization 10)

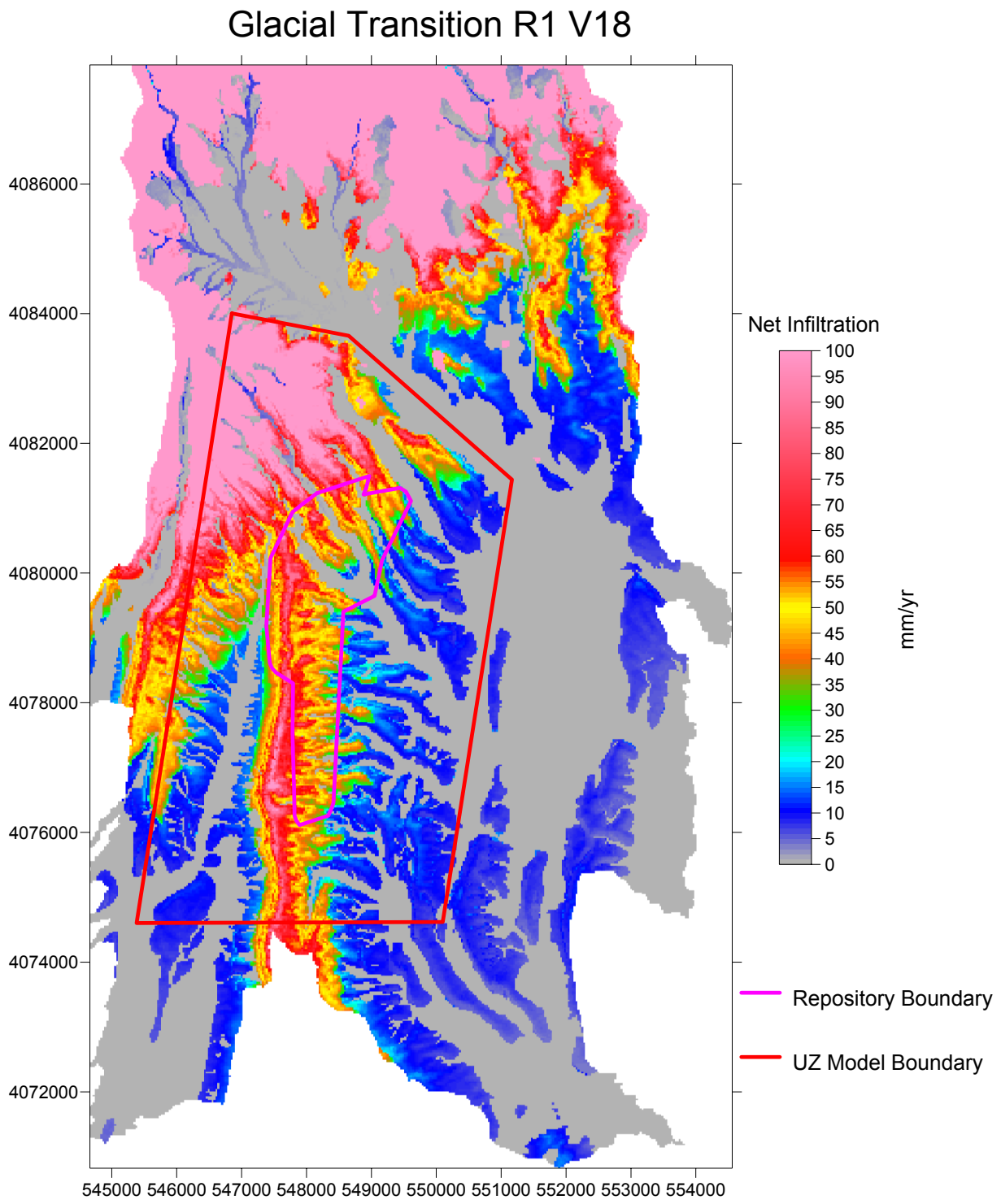

Coordinates are in meters; UTM NAD 27, Zone 11

Source: Output DTNs: SN0701T0502206.035 (Mean Annual Net Infiltration Results) and SN0612FTPRNUZB.002 UZ (Model and Repository Boundaries).

Figure 6.5.7.3-4. Glacial Transition, 50th Percentile Mean Annual Net Infiltration Map (Replicate R1, Realization 18)

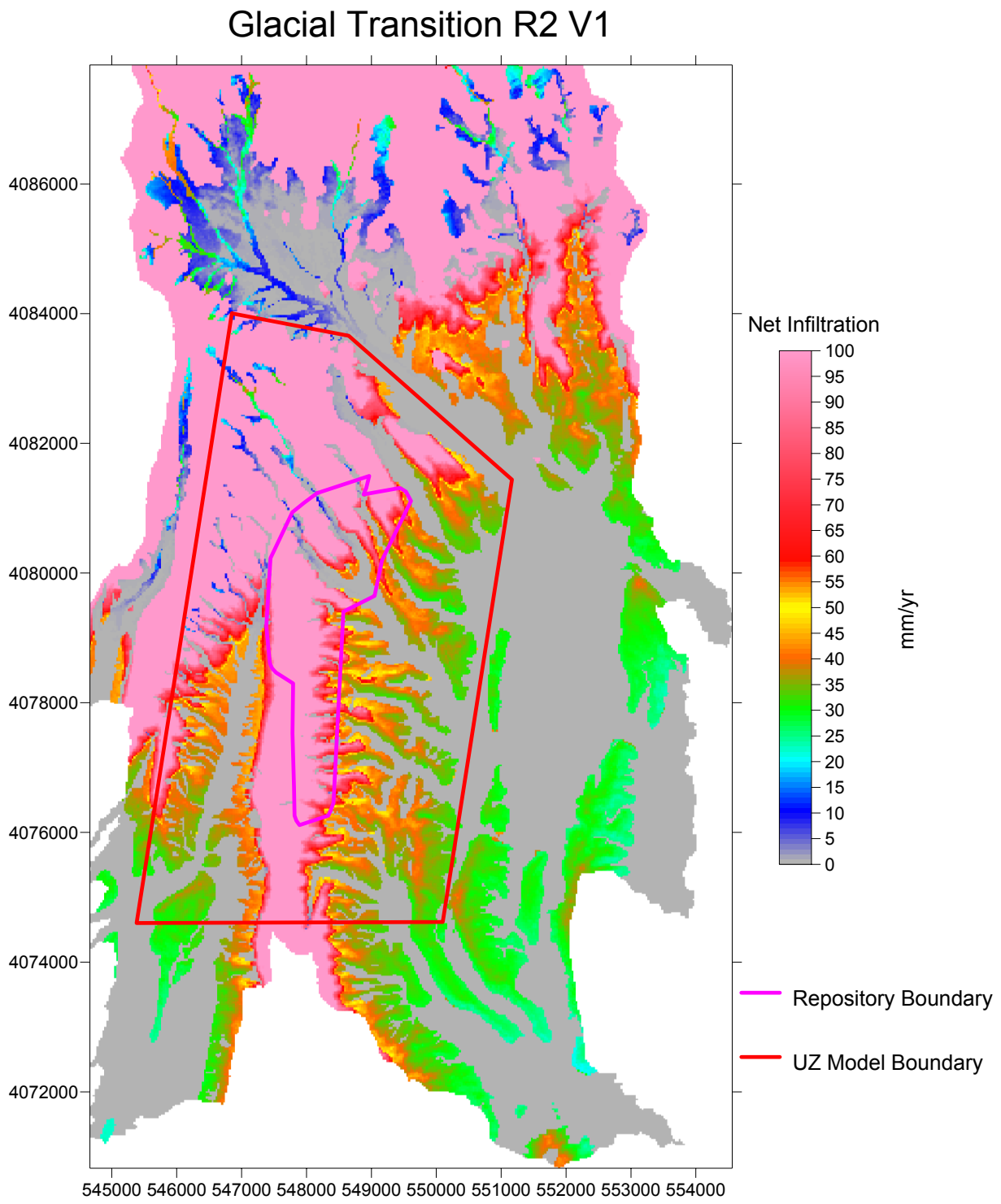

Coordinates are in meters; UTM NAD 27, Zone 11

Source: Output DTNs: SN0701T0502206.035 (Mean Annual Net Infiltration Results) and SN0612FTPRNUZB.002 UZ (Model and Repository Boundaries).

Figure 6.5.7.3-5. Glacial Transition, 90th Percentile Mean Annual Net Infiltration Map (Replicate R2, Realization 1)

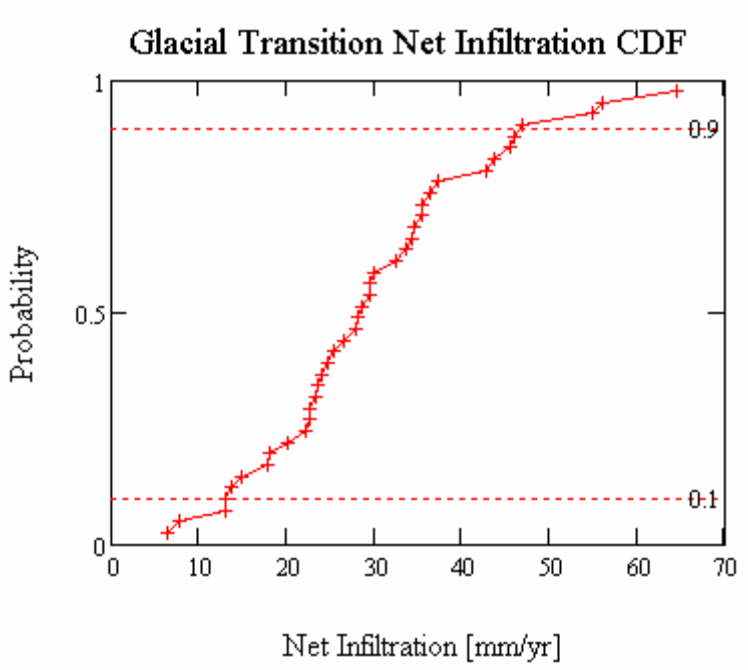

Source: Output DTN: SN0701T0502206.037, file: \Welcome to Massif\Massif\Glacial Uncertainty\Post Processing*GT_Combined_Replicates.xmcd*.

NOTE: A total of 40 realizations (2 LHS replicates) define the distribution.

Figure 6.5.7.3-6. Cumulative Distribution Function (CDF) of Glacial Transition Spatially Averaged Mean Annual Net Infiltration over the Infiltration Domain

6.5.7.4 Summary of Weighted Water Fluxes for Each Climate

For each realization, a calculation of the weighted (mean annual) amount of water that is accounted for by each of the water balance components is performed over the infiltration modeling domain for each climate (base case simulations). Because each realization consists of runs based on 10 representative years, the total water fluxes from each year are weighted by the probability of the year occurring. Thus, the weighted mean water flux represents a weighted mean water flux over the 10 representative years. All water enters the domain as precipitation and is partitioned into the various water balance components by the MASSIF model, including net infiltration (Infiltration), evapotranspiration (ET), runoff, sublimation, change in storage (Storage), and net snow pack (Snow). The mean and standard deviation of each of these weighted mean water fluxes are listed in Tables 6.5.7.4-1 to 6.5.7.4-3 for each of the three future climates, respectively. These climate means are expressed as both mm/yr and as a percentage of the mean annual precipitation. In addition, results from an alternative set of simulations (IC 1 runs) are presented in these tables. These IC1 simulations are identical to the base case simulations except that they were started with a higher soil moisture content initial condition. It is noted that the primary difference between these runs is that the IC 1 runs end up with a mean change in storage which is negative and a slightly higher net infiltration than the base case runs. This negative change in storage indicates that, on average, the IC1 runs are ending the year with lower soil moisture contents than were applied as initial conditions. The purpose of running the IC1 runs was to bracket the desired zero change in storage and demonstrate that the effect on net infiltration uncertainty is minor.

Table 6.5.7.4-1. Average and Standard Deviations of Weighted Mean Water Fluxes Fractions for the Present-Day Climate Simulations (fraction of precipitation)

Present-Day Climate	Mean (mm/yr)	SD (mm/yr)	Mean (% precip)	SD (% precip)	Mean IC1 (mm/yr)	SD IC1 (mm/yr)	Mean IC1 (% precip)	SD IC1 (% precip)
Precipitation	173.6	25.1	N/A	N/A	173.6	25.1	N/A	N/A
Infiltration	14.3	8.7	8.02%	4.50%	14.8	8.8	8.29%	4.50%
ET	151.6	20.1	87.68%	5.66%	158.9	20.5	92.02%	6.58%
Runoff	3.7	2.8	2.07%	1.56%	3.7	2.8	2.07%	1.56%
Sublimation	0.7	0.2	0.42%	0.11%	0.7	0.2	0.42%	0.11%
Storage	3.3	3.3	1.82%	1.77%	−4.6	3.9	−2.80%	2.42%
Snow	0.0	0.0	0.00%	0.00%	0.0	0.0	0.00%	0.00%

Source: Output DTN: SN0701T0502206.037, file: \Welcome to Massif\Massif\Post Processing*Flux Calculations All Climates.xls*.

Table 6.5.7.4-2. Average and Standard Deviation of Weighted Mean Water Fractions Fluxes for the Monsoon Climate Simulations

Monsoon Climate	Mean (mm/yr)	SD (mm/yr)	Mean (% precip)	SD (% precip)	Mean IC1 (mm/yr)	SD IC1 (mm/yr)	Mean IC1 (% precip)	SD IC1 (% precip)
Precipitation	275.2	77.0	N/A	N/A	275.2	77.0	N/A	N/A
Infiltration	25.5	17.9	8.69%	4.75%	26.1	18.0	8.89%	4.73%
ET	230.4	57.8	84.88%	8.18%	238.3	58.1	88.01%	8.93%
Runoff	15.6	12.1	5.35%	3.63%	15.6	12.1	5.36%	3.63%
Sublimation	0.1	0.2	0.04%	0.07%	0.1	0.2	0.04%	0.07%
Storage	3.6	8.6	1.04%	2.92%	−4.9	9.4	−2.29%	3.56%
Snow	0.0	0.0	0.00%	0.00%	0.0	0.0	0.00%	0.00%

Source: Output DTN: SN0701T0502206.037, file: \Welcome to Massif\Massif\Post Processing*Flux Calculations All Climates.xls*.

Table 6.5.7.4-3. Average and Standard Deviation of Weighted Mean Water Fractions Fluxes for the Glacial Transition Climate Simulations

Glacial Transition Climate	Mean (mm/yr)	SD (mm/yr)	Mean (% precip)	SD (% precip)	Mean IC1 (mm/yr)	SD IC1 (mm/yr)	Mean IC1 (% precip)	SD IC1 (% precip)
Precipitation	283.4	50.0	N/A	N/A	283.4	50.0	N/A	N/A
Infiltration	30.0	12.9	10.38	3.66	30.5	12.9	10.57	3.61
ET	243.7	41.7	86.16	3.90	254.6	42.2	90.15	4.46
Runoff	1.1	1.2	0.39	0.47	1.1	1.2	0.39	0.47
Sublimation	3.6	0.8	1.27	0.21	3.6	0.8	1.27	0.21
Storage	5.1	3.9	1.79	1.29	−6.4	4.7	−2.38	1.86
Snow	0.0	0.0	0.00	0.00	0.0	0.0	0.00	0.00

Source: Output DTN: SN0701T0502206.037, file: \Welcome to Massif\Massif\Post Processing*Flux Calculations All Climates.xls*.

6.5.7.5 Factors Influencing Temporal Variability in Net Infiltration

In the preceding sections, net infiltration results have been averaged over space and time for the purposes of comparing results within and between climates. A more representative model of net infiltration would include variations that occur over time. In fact, net infiltration is an episodic process. The results of these calculations shed light on the temporal nature of net infiltration at Yucca Mountain.

As described in Section 6.5.1, a long-term mean net infiltration is calculated as the weighted mean net infiltration for ten representative precipitation years, each with its associated probability of occurrence. Low probability years experience higher net infiltration but contribute only a small percentage to the long-term mean. Since the sum of the probabilities of occurrence equals 1 and the years were selected from a set of 1,000, it is possible to estimate a "recurrence interval" for each of the representative years based on its probability. The recurrence interval for a given representative year represents the average number of years that would pass before annual precipitation exceeded that predicted for the representative year. The recurrence interval is calculated as:

$$T_k = \frac{1}{1 - p_k} \qquad \text{(Eq. 6.5.7.5-1)}$$

where T_k is the recurrence interval (in years) of year k and p_k is the probability that annual precipitation on any one year will be less than the annual precipitation during year k (Maidment 1993 [DIRS 125317], p. 18.3). Thus the quantity $(1-p_k)$ represents the exceedance probability, which is the probability that annual precipitation during any one year will equal or exceed annual precipitation during year k. It is also possible to calculate the percent contribution to the long term mean net infiltration of each representative year. This is done by multiplying annual net infiltration for each year of each realization by the probability of occurrence for that year and then dividing by the long-term (weighted) mean net infiltration for each realization. Tables 6.5.7.5-1 to 6.5.7.5-3 list the exceedance probability, the mean annual net infiltration, the recurrence interval, and the fraction of contribution to long-term mean net infiltration for each of the 10 representative years (k = 1 to 10) for each of the three climates, respectively. Figures 6.5.7.5-1 to 6.5.7.5-3 plot the mean annual net infiltration and the cumulative percent contribution to the long-term mean against the recurrence interval for the three climates, respectively. The plots shows that as years with larger recurrence intervals are included, a greater percentage of the long-term mean can be estimated. The results suggest that about 80% of the long-term mean for Present-Day climate conditions is due to years with a recurrence interval of 10 years and less. The implication of these results is that net infiltration estimates based on relatively short historical weather records may tend to underestimate long-term net infiltration, however, not by more than 20%.

It is worth noting that the mean net infiltration for each representative year is not always higher for years with greater annual precipitation. For example, for the Present-Day climate, year number 1 has a lower mean net infiltration than year number 2. This occurs because factors other than total annual precipitation influence the magnitude of net infiltration. For example, annual precipitation may be very high because of an especially high amount of precipitation occurring on a single day. In such a case, runoff would tend to be higher and net infiltration

lower than if several days during the year experienced large amounts of precipitation, but the annual total was less.

Table 6.5.7.5-1. Comparison of the 10 Representative Years Used to Model Net Infiltration for the Present-Day Climate

Representative Year (k)	Probability That Precipitation Will Be Exceeded (1−p)	Mean Net Infiltration for Each Representative Year (mm/yr)	Recurrence Interval (yr)	Fraction of Contribution to Long-term Mean Infiltration
1	0.001	82.58	1,000.00	0.76
2	0.003	88.06	333.33	1.74
3	0.01	75.77	100.00	4.85
4	0.03	55.77	33.33	9.95
5	0.1	45.39	10.00	24.44
6	0.28	24.27	3.57	28.88
7	0.46	14.22	2.17	16.34
8	0.64	8.34	1.56	8.42
9	0.82	3.00	1.22	3.21
10	1	1.48	1.00	1.40

Source: Output DTN: SN0701T0502206.037, file: \Welcome to Massif\Massif\Present Day Uncertainty\Post Processing*PD_Combined_Replicates.xmcd*.

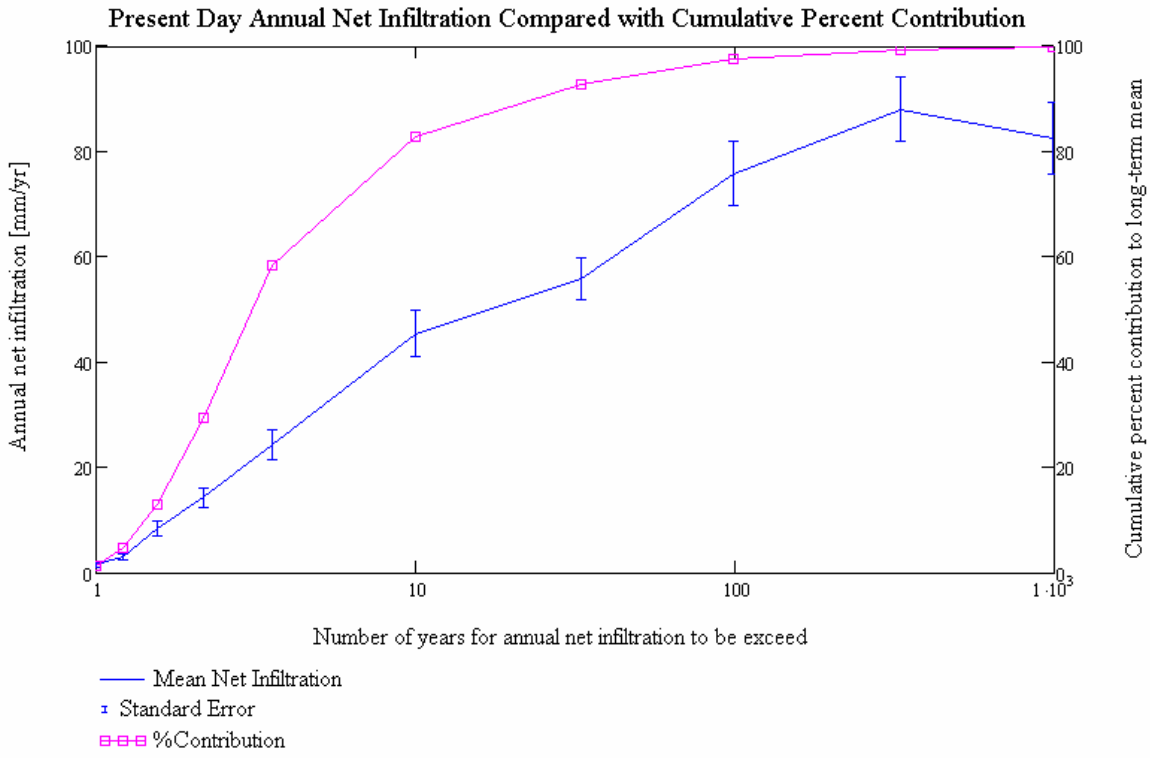

Source: Output DTN: SN0701T0502206.037, file: \Welcome to Massif\Massif\Present Day Uncertainty\Post Processing*PD_Combined_Replicates.xmcd*.

Figure 6.5.7.5-1. Annual Mean Net Infiltration and Cumulative Percent Contribution to Long-term Mean Net Infiltration as a Function of Recurrence Interval for the Present-Day Climate

Table 6.5.7.5-2. Comparison of the 10 Representative Years Used to Model Net Infiltration for the Monsoon Climate

Representative Year (k)	Probability That Precipitation Will Be Exceeded (1−p)	Mean Net Infiltration for Each Representative Year (mm/yr)	Recurrence Interval (yr)	Fraction of Contribution to Long-term Mean Infiltration
1	0.001	67.79	1,000.00	0.33
2	0.003	84.04	333.33	0.96
3	0.01	84.99	100.00	3.03
4	0.03	74.47	33.33	7.45
5	0.1	65.71	10.00	21.22
6	0.28	45.73	3.57	31.84
7	0.46	24.98	2.17	16.76
8	0.64	17.45	1.56	9.51
9	0.82	10.29	1.22	6.06
10	1	5.05	1.00	2.84

Source: Output DTN: SN0701T0502206.037, file: \Welcome to Massif\Massif\Monsoon Uncertainty\Post Processing*MOD_Combined_Replicates.xmcd*.

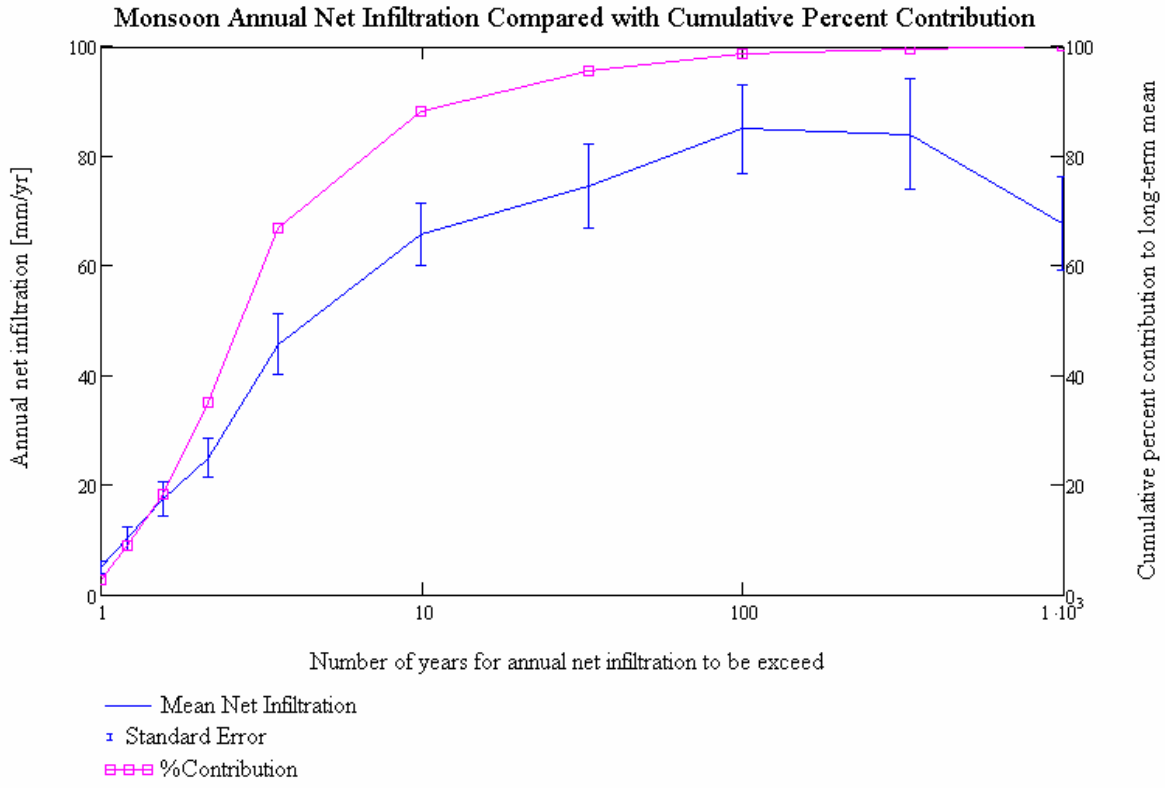

Source: Output DTN: SN0701T0502206.037, file: \Welcome to Massif\Massif\Monsoon Uncertainty\Post Processing*MO_Combined_Replicates.xmcd*.

Figure 6.5.7.5-2. Annual Mean Net Infiltration and Cumulative Percent Contribution to Long-term Mean Net Infiltration as a Function of Recurrence Interval for the Monsoon Climate

Table 6.5.7.5-3. Comparison of the 10 Representative Years Used to Model Net Infiltration for the Glacial Transition Climate

Representative Year (k)	Probability That Precipitation Will Be Exceeded (1−p)	Mean Net Infiltration for Each Representative Year (mm/yr)	Recurrence Interval (yr)	Fraction of Contribution to Long-term Mean Infiltration
1	0.001	96.45	1,000.00	0.37
2	0.003	94.04	333.33	0.69
3	0.01	78.96	100.00	2.07
4	0.03	64.75	33.33	4.76
5	0.1	53.44	10.00	12.56
6	0.28	40.90	3.57	24.85
7	0.46	32.01	2.17	19.38
8	0.64	27.07	1.56	15.45
9	0.82	20.50	1.22	11.75
10	1	13.33	1.00	8.13

Source: Output DTN: SN0701T0502206.037, file: \Welcome to Massif\Massif\Present Day Uncertainty\Post Processing*PD_Combined_Replicates.xmcd*.

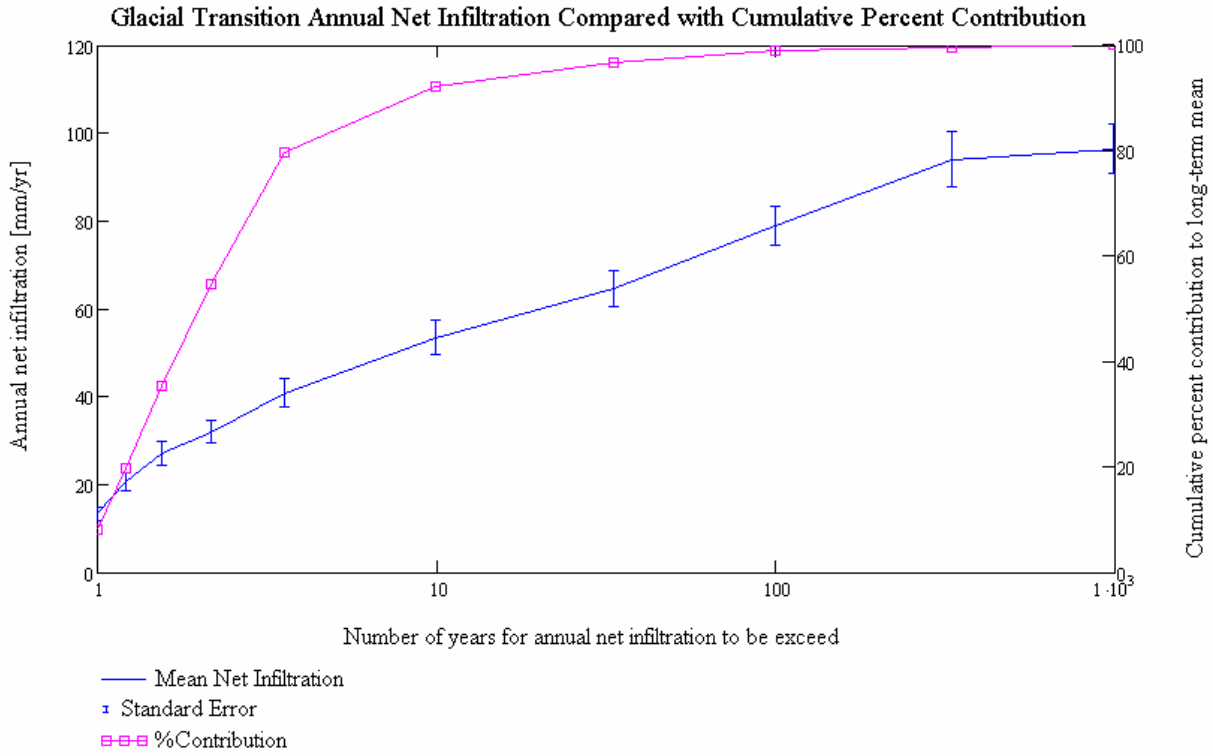

Source: Output DTN: SN0701T0502206.037, file: \Welcome to Massif\Massif\Glacial Uncertainty\Post Processing*GT_Combined_Replicates.xmcd*.

Figure 6.5.7.5-3. Annual Mean Net Infiltration and Cumulative Percent Contribution to Long-term Mean Net Infiltration as a Function of Recurrence Interval for the Glacial Transition Climate

6.5.7.6 Factors Influencing Spatial Variability in Net Infiltration

The spatial variability in net infiltration is controlled by spatial variations in the amount of precipitation, spatial heterogeneity in soil, bedrock, and vegetation properties, and lateral water distribution via runoff processes. In the MASSIF model, precipitation varies only as a function of elevation and is adjusted via a lapse correction (Section 6.4.1.1). The characterization of spatial heterogeneities of soil and bedrock properties is done by dividing the model domain into distinct soil groups, soil depth classes, and bedrock type regions inside which the given properties are assumed to be constant. The result of this approach is that the MASSIF model likely underestimates the actual spatial variability in net infiltration. The best that can be achieved with such a method is to generally characterize regional infiltration patterns. Given these limitations, the following sections illustrate which of the various property groups account for the most infiltration. The intent of this analysis is not to claim that particular property groups are necessarily significant contributors to infiltration uncertainty but rather to identify these property groups in case further study is deemed necessary. The analysis presented in this section is limited to the results of the Present-Day climate. However, since only runoff processes can divert water laterally in the model and since runoff fractions are relatively low for all climates, it is not expected that the spatial distribution of net infiltration for Monsoon and Glacial Transition climates would be all that different from that seen for the Present-Day climate.

6.5.7.6.1 Influence of Soil Depth

Soil depth is one of the most significant factors controlling local net infiltration (see Section 6.7 and Appendix H). Unfortunately, soil depth in each of the model grid cells is largely not known with any degree of accuracy (see BSC 2006 [DIRS 178819] for details). Instead, the domain has been divided into five soil depth classes where soil depth decreases with increasing class number (described in Section 6.5.2). Soil depth distributions are developed in Section 6.5.2.4 and the actual sampled soil depths for soil depth class 4 for each realization are listed in Section 6.5.5. Table 6.5.7.6-1 lists the percent of the total infiltration that occurs in each soil depth class regions for replicate R1 of the Present-Day climate net infiltration results. It is clear that areas with shallow soils (soil depth class 4) and areas with no soil (class 5) dominate the total predicted net infiltration over the full domain.

Table 6.5.7.6-1. Percent of Total Net Infiltration (and standard deviation) That Occurs in Each Soil Depth Class for Present-Day Climate Simulations (Entire Net Infiltration Modeling Domain)

Soil Depth Class	Percent of Total Infiltration [a]	Standard Deviation (%)	UZ Grid (%)	Total (%)
1	0.50	0.92	0	9
2	2.30	3.85	17	25
3	0.52	0.97	11	9
4	90.53	7.15	71	57
5	6.15	4.69	>1	>1

Source: Output DTN: SN0701T0502206.037, file: \Welcome to Massif\Massif\Present Day Uncertainty\Post Processing*PD_Combined_Replicates.xmcd*.

[a] Total infiltration is the average net infiltration over the entire 125-km^2 modeling domain over epistemic uncertainty

6.5.7.6.2 Influence of Soil Group

Soil properties also influence spatial variations in net infiltration. Table 6.5.7.6-2 lists the percent of the total infiltration that occurs in the regions a specific soil type group for the Present-Day climate simulations. Five soil type groups are used to represent spatial variations in soil properties (includes a group representing cells with bare bedrock). Soil group 5/7/9 covers approximately 65% of the infiltration domain but accounts for about 91% of the total infiltration. Areas with bare rock cover only 0.3% of the infiltration domain but account for more than 6% of the total infiltration.

Table 6.5.7.6-2. Percent of Total Net Infiltration (and standard deviation) That Occurs in Each Soil Group for Present-Day Climate Simulations (Entire Net Infiltration Modeling Domain)

Soil Group	Percent of Total Infiltration [a]	Standard Deviation (%)	UZ Grid (%)	Total (%)
1	0.48	0.94	2	10
2/6	0.66	1.27	4	11
3/4	1.78	2.65	12	13
5/7/9	90.93	6.68	81	65
Bare Rock	6.15	4.69	>1	>1

Source: Output DTN: SN0701T0502206.037, file: \Welcome to Massif\Massif\Present Day Uncertainty\Post Processing*PD_Combined_Replicates.xmcd*.

[a] Total infiltration is the average net infiltration over the entire 125-km^2 modeling domain over epistemic uncertainty.

6.5.7.6.3 Influence of Rock Type

The hydraulic conductivity of the underlying bedrock may influence the spatial variability of net infiltration. Table 6.5.7.6-3 lists the percent of the total infiltration that occurs in the regions underlain by a specific rock type for the Present-Day climate simulations. Nominal hydraulic conductivity values used for each rock type are explained in Section 6.5.2, and sampled values are listed in Section 6.5.5 for each climate-replicate combination. 30% of the total infiltration occurs in cells underlain by rock type 422, which accounts for 18% of the entire infiltration domain.

Table 6.5.7.6-3. Percent of Total Net Infiltration (and standard deviation) That Occurs in Each Rock Type for Present-Day Climate Simulations (Entire Net Infiltration Modeling Domain)

Rock Type	Percent of Total Infiltration [a]	Standard Deviation (%)	UZ Grid (%)	Total (%)
401	5.25	0.53	4	2
402	1.94	0.23	3	1
403	7.72	1.52	14	18
404	3.55	0.72	8	3
405	15.09	2.18	23	22
406	8.25	2.16	19	8
407	6.25	0.61	6	4
408	2.90	0.27	4	2
409	1.70	0.07	2	1
410	0.10	0.04	<1	<1
411	1.39	0.36	<1	1
412	2.09	0.20	4	2
413	1.40	0.08	2	2
414	2.88	0.10	3	3
415	0.55	0.07	1	1
416	0.08	0.04	<1	<1
417	2.43	0.17	<1	2
418	1.32	0.43	3	3
419	0.01	0.03	<1	<1
420	0.49	0.10	1	1
421	0.43	0.08	1	1
422	30.16	2.53	1	18
423	0.11	0.03	<1	<1
424	0.19	0.07	<1	<1
425	0.01	0.03	0	<1
426	0.01	0.03	0	<1
427	0.00	0.00	0	<1
430	1.81	1.13	0	<1
432	0.01	0.03	0	<1
435	0.20	0.02	0	<1
490	1.28	0.66	0	3
491	0.32	0.07	0	<1

Source: Output DTN: SN0701T0502206.037, file: \Welcome to Massif\Massif\Present Day Uncertainty\Post Processing*PD_Combined_Replicates.xmcd*.

[a] Total infiltration is the average net infiltration over the entire 125 km^2 modeling domain over epistemic uncertainty.

6.5.7.7 Illustration of Daily Water Balance Patterns

As an illustration of the daily behavior of the MASSIF model, a single grid cell, located in the upper part of Pagany Wash watershed, was selected for monitoring during a one-year simulation. The purpose of this illustration is to help provide a sense of the intricate calculations that are performed in the MASSIF model of net infiltration. In theory, such detailed data could be obtained for every grid cell for every simulated day. However, the number of grid cells in a watershed and computer memory resources limit the number of cells that can be monitored for a given run.

The parameter set selected was from the Present-Day Replicate 2, Realization V08, which is the 50th percentile net infiltration Present-Day simulation. The year chosen was Year 2 (probability of occurrence = 0.003) from the stochastically generated weather file for the realization. The sampled parameter values for this realization are shown in Table 6.5.5.1-4. The geospatial characteristics of this grid cell are listed in Table 6.5.7.7-1.

Table 6.5.7.7-1. Properties of the Grid Cell Selected for Illustration of Daily Water Balance Patterns

Parameter	Value
Easting [m]	548261
Northing [m]	4081803
Elevation [m]	1515
Slope [deg]	21
Azimuth [deg]	86
Soil Depth Class	4
Soil Type	5
Bedrock Type	403
PVR	0.5261

Source: Output DTN: SN0701T0502206, file: \Welcome to Massif\Massif\Present Day Uncertainty\Examples*Monitor Cell Characteristics.xls*.

There are a number of daily variables that can be monitored for a given grid cell. The figures below plot a selection of these variables for simulated year for the grid cell identified above. Figure 6.5.7.7-1 plots daily values of minimum and maximum temperatures and precipitation. The effect of precipitation on temperature in the model is evident in the plot as temperature depressions on days with rain. Such depressions result in reductions in the solar radiation and reference ET. Note that the temperature and precipitation values are lapse-corrected to the elevation of the monitored cell.

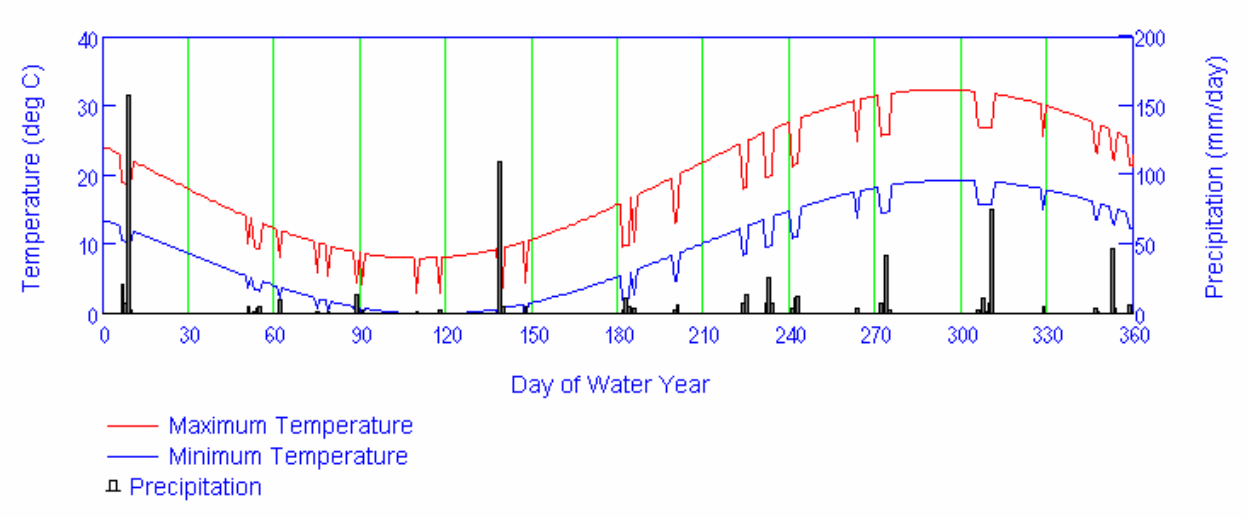

Source: Output DTN: SN0701T0502206, file: \Welcome to Massif\Massif\Present Day Uncertainty*Present Day R2 V08_example.xmcd*.

Figure 6.5.7.7-1. Daily Weather Inputs for the Simulated Year

Figure 6.5.7.7-2 shows how values of K_{cb} and the canopy coefficient (f_c) vary for this cell over the water year. These values are independent of the daily precipitation; however, the total annual precipitation for the water year, slope, azimuth, and PVR are used in the calculation of K_{cb} (see Section 6.5.3).

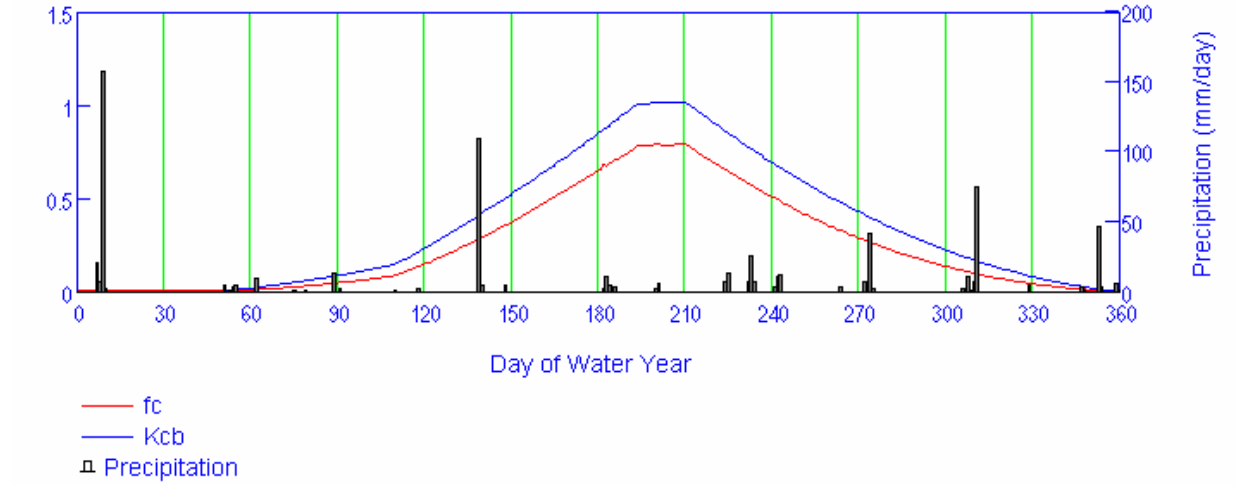

Source: Output DTN: SN0701T0502206, file: \Welcome to Massif\Massif\Present Day Uncertainty*Present Day R2 V08_example.xmcd.*

Figure 6.5.7.7-2. Daily Values of K_{cb} and Canopy Fraction (f_c) for the Simulated Year

Figure 6.5.7.7-3 shows the reference ET along with the daily water losses of evaporation and transpiration. Several features of the model are evident in these results. For example, both evaporation and transpiration are proportional to reference ET. In addition, transpiration is also proportional to K_{cb}.

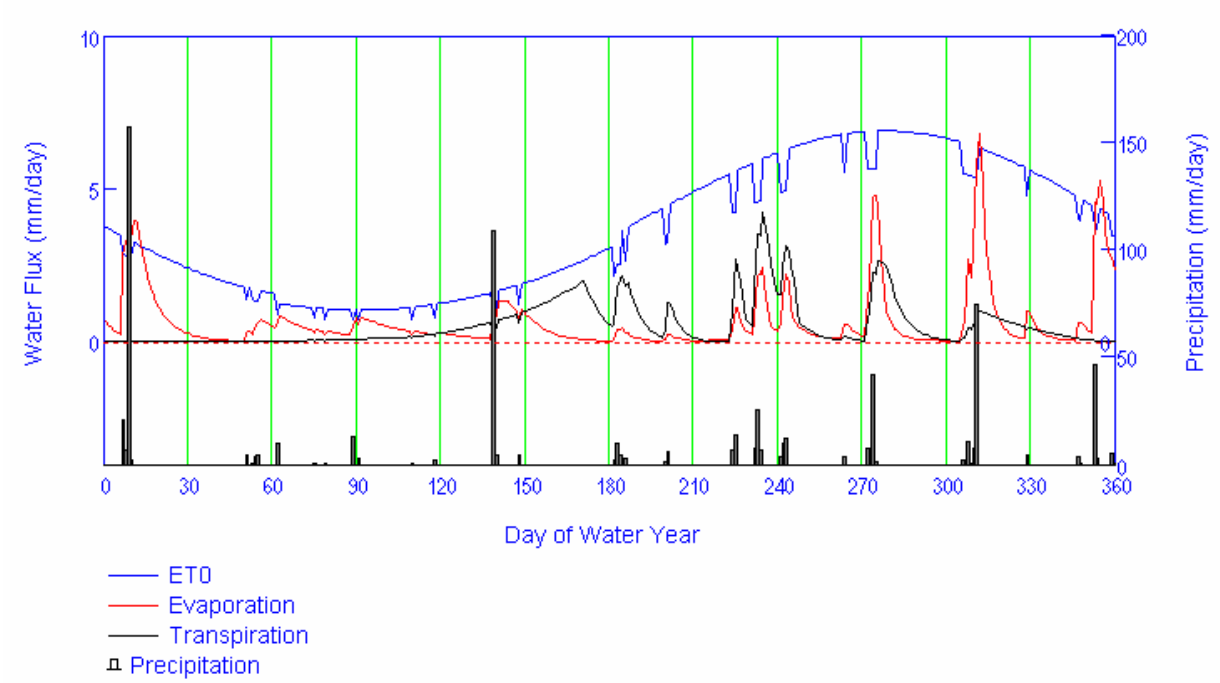

Source: Output DTN: SN0701T0502206, file: \Welcome to Massif\Massif\Present Day Uncertainty*Present Day R2 V08_example.xmcd*.

Figure 6.5.7.7-3. Daily Water Fluxes (Evaporation, Transpiration, and Reference ET) for the Simulated Year

Figure 6.5.7.7-3 shows the water levels in each of the four nodes in the water balance calculation. Water levels 1 and 2 are for the surface evaporation layer of thickness Z_e. Water level 3 is for layer 2 (layer below evaporation layer). In this case, layer 2 thickness is equal to soil depth minus Z_e. In this example, the thickness of node 4 is equal to zero, because soil depth is less than the maximum rooting depth. The plots illustrates that for small precipitation events, water levels can increase in the surface layer (nodes 1 and 2), while continuing to decrease in the underlying layer (for example see day 60). When precipitation is greater, enough water is added to the surface layer to exceed its field capacity and thus water levels increase in the next lower layer (for example, see day 135). Also note the difference in the rate of water level decrease between days 1 and 135 as opposed to the rate between days 135 and 200. The increased rate of water level decrease corresponds to periods of higher reference ET and vegetation vigor (K_{cb}).

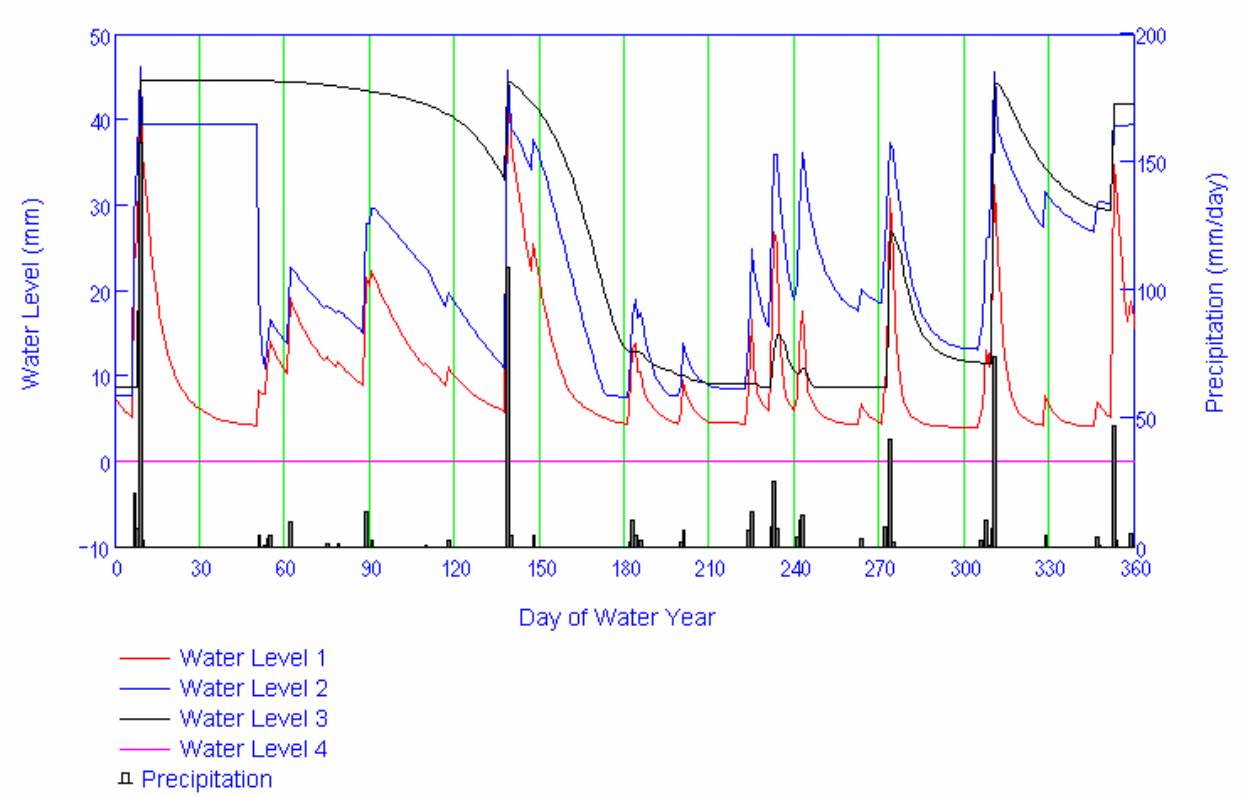

Source: Output DTN: SN0701T0502206, file: \Welcome to Massif\Massif\Present Day Uncertainty*Present Day R2 V08_example.xmcd*.

Figure 6.5.7.7-4. Daily Soil Water Levels for the Simulated Year

Figure 6.5.7.7-5 shows a plot of daily run-on flowing into the cell and daily runoff flowing out of the cell. In this example, such runoff events only occurred two times during the year, both during particularly large precipitation events.

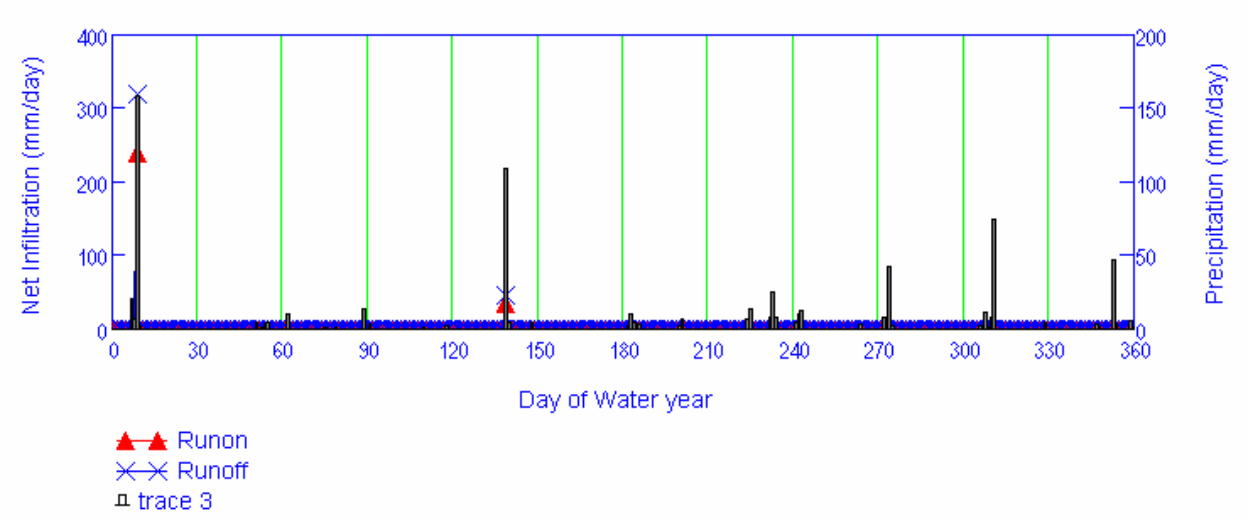

Source: Output DTN: SN0701T0502206, file: \Welcome to Massif\Massif\Present Day Uncertainty*Present Day R2 V08_example.xmcd*.

Figure 6.5.7.7-5. Daily Run-on and Runoff for the Simulated Year

Figure 6.5.7.7-6 shows daily net infiltration during the year. In this example, net infiltration occurred during three periods each lasting two days.

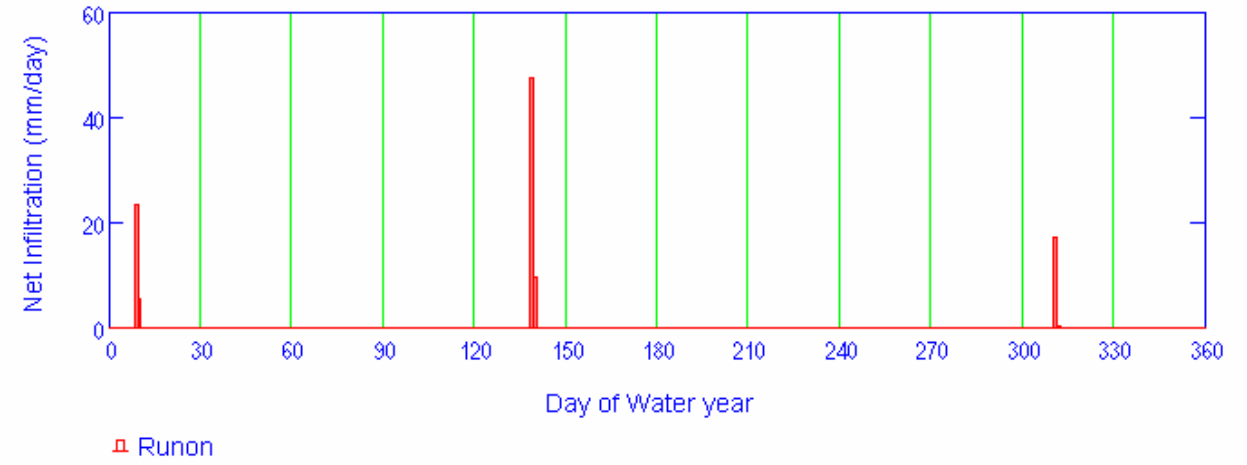

Source: Output DTN: SN0701T0502206, file: \Welcome to Massif\Massif\Present Day Uncertainty*Present Day R2 V08_example.xmcd*.

Figure 6.5.7.7-6. Daily Net Infiltration for the Simulated Year

6.5.7.8 Summary and Discussion of Net Infiltration Results for Present-Day and Future Climates

Table 6.5.7.8-1 summarizes the net infiltration statistics averaged over several spatial domains for all realizations and for all three climates. Predicted net infiltration generally is lowest for the Present-Day climate and increases in the Monsoon and Glacial Transition climates. However, net infiltration predictions for the Monsoon climate appear to be more uncertain (span a greater

range) than predictions for the Glacial Transition climate. This is the result of there being a greater amount of uncertainty in the expected precipitation in the Monsoon than for the Glacial Transition climate.

Table 6.5.7.8-1. Summary Net Infiltration Statistics for the Three Climates

	Domain	PD	MO	GT
Minimum [mm/yr]	Infiltration modeling domain (125 km^2)	2.0	2.4	6.6
	UZ modeling domain (39.8 km^2)	1.4	1.2	4.3
	Repository footprint (5.7 km^2)	1.5	1.2	4.0
Mean [mm/yr]	Infiltration modeling domain (125 km^2)	14.3	25.5	30.0
	UZ modeling domain (39.8 km^2)	15.1	28.0	29.3
	Repository footprint (5.7 km^2)	17.6	32.9	38.7
Median [mm/yr]	Infiltration modeling domain (125 km^2)	12.9	22.8	28.5
	UZ modeling domain (39.8 km^2)	12.4	24.2	28.1
	Repository footprint (5.7 km^2)	14.5	28.4	38.6
Maximum [mm/yr]	Infiltration modeling domain (125 km^2)	35.4	83.4	64.7
	UZ modeling domain (39.8 km^2)	40.9	86.2	72.1
	Repository footprint (5.7 km^2)	48.2	95.3	97.3
Standard Deviation [mm/yr]	Infiltration modeling domain (125 km^2)	8.8	18.2	13.1
	UZ modeling domain (39.8 km^2)	10.4	20.2	15.5
	Repository footprint (5.7 km^2)	12.5	23.3	21.2

Source: Output DTN: SN0701T0502206.037, file: \Welcome to Massif\Massif\Post Processing*Summary Net Infiltration All Climates.xls*.

PD = Present-Day, MO = Monsoon, GT = Glacial Transition.

One significant result of these simulations is the fact that most of the simulated net infiltration appears to occur in the regions with shallow soils rather than in the stream channels. This result raises some important questions about the predicted spatial distribution of net infiltration produced by the model. Section 7.1.3.2 presents some alternate simulations based on inferences made at Pagany Wash that result in significant infiltration in the stream channels. These alternate simulations allow soil conductivity to vary from the uncertainty distributions qualified in this report in Section 6.5.2, and therefore do not represent qualified net infiltration results. More field work would have to be performed in order to evaluate the accuracy of the spatial distribution of net infiltration in the current maps. There is greater confidence in the spatial averaged net infiltration values produced by this analysis.

6.5.7.9 Comparison of Results from Each LHS Replicate

An examination of Tables 6.5.7.1-2, 6.5.7.2-2, and 6.5.7.3-2 shows that the results from each of the two replicates run for each climate can vary considerably at the tails of the distribution but are more similar when comparing the mean and median. Because of random variation in any stochastic analysis, it is expected that there can be significant variation in the minimum and maximum values between the two replicate distributions. A more robust statistic to compare replicates is the first, second, and third quartiles (25th, 50th, 75th percentiles). The absolute differences between the two replicates for these quartiles in the infiltration modeling domain range from 0.0 (PD, 25%) to 4.8 mm (MO, 25%).

An estimate of the error on the mean net infiltration is given by the standard error on the mean (standard deviation divided by the square root of the number of samples). Standard deviations for each climate and spatial domain are listed in Tables 6.5.7.1-2, 6.5.7.2-2, and 6.5.7.3-2. The average standard errors on the mean for the infiltration modeling domain are listed in the last row of Table 6.5.7.9-1. It would not be surprising if the differences in the quartiles, closer to the tails of the distribution, were somewhat greater than the standard error on the mean. But, as is shown in Table 6.5.7.9-1, these differences are only 1.2, 0.8, and 1.3 mm greater, respectively, for the three climates (PD, MO, and GT).

The conclusion drawn from these comparisons is that there is an inherent uncertainty in the resulting net infiltration estimates made in this analysis, which is due to the small sample size. The uncertainty on the mean net infiltration over the infiltration modeling domain is estimated by the standard error on the mean, which varies from 2.0 to 4.0 mm/yr, depending on climate. This uncertainty is certainly similar to the difference between the two replicates compared at the 25th, 50th, and 75th percentiles. This result provides confidence that the results of the combined replicates are representative of the actual distribution given the uncertainty estimated by the standard error on the mean. This uncertainty would be reduced by running more LHS realizations; however, the accuracy of the model predictions will not be improved upon because this accuracy is also limited by other sources of uncertainty (e.g., model uncertainty).

Table 6.5.7.9-1. Differences in Net Infiltration Statistics between Replicates

ABS(R1-R2)	Domain	PD	MO	GT
25th Percentile [mm/yr]	Infiltration modeling domain (125 km^2)	***0.0***	***4.8***	***4.3***
	UZ modeling domain (39.8 km^2)	0.0	5.7	2.2
	Repository footprint (5.7 km^2)	0.4	6.9	1.9
50th Percentile [mm/yr]	Infiltration modeling domain (125 km^2)	***2.2***	***2.9***	***0.4***
	UZ modeling domain (39.8 km^2)	0.6	2.3	2.7
	Repository footprint (5.7 km^2)	0.9	2.2	2.7
75th Percentile [mm/yr]	Infiltration modeling domain (125 km^2)	***3.2***	***1.7***	***2.0***
	UZ modeling domain (39.8 km^2)	3.6	2.3	2.3
	Repository footprint (5.7 km^2)	4.4	2.4	3.1
Mean Standard Error on Mean	Infiltration modeling domain (125 km^2)	***2.0***	***4.0***	***3.0***

Source: Output DTN: SN0701T0502206.037, file: \Welcome to Massif\Massif\Post Processing*Summary Net Infiltration All Climates.xls*.

6.6 INFILTRATION PREDICTION UNCERTAINTIES

This section summarizes the results of the calculations reported in Section 6.5, including discussion of uncertainty. Section 6.6.1 analyzes the values of potential recharge (space-time averages of net infiltration) that are tabulated in Section 6.5.7. Section 6.6.2 is a discussion of the uncertainty in the calculated net infiltration at a particular location, averaged over time but not averaged over surface area. Section 6.6.3 discusses sources of model uncertainty.

Section 6.5.5 and Appendix I discuss the uncertainties in the input parameters and the screening of those uncertainties to select parameters to be varied for the uncertainty analysis. For each climate, a realization is a particular set of values for the selected parameters. Section 6.5.7 reports the results of the calculation for each realization.

A set of realizations for a particular climate provides an approximate uncertainty distribution for each calculated result. An uncertainty distribution developed from a set of realizations describes the contribution of parameter uncertainty to the uncertainty of the result. Model uncertainty also contributes to the overall uncertainty in the net infiltration estimates. Sources of model uncertainty are discussed and evaluated in Section 6.6.3.

6.6.1 Uncertainty in Potential Recharge Averaged over the UZ Model Grid

Section 6.5 reports the results of 120 calculations (2 replicates of 20 realizations for each of three climates). For each of the three climates, there are twenty calculations, called realizations, for which certain input parameters are varied in accordance with their uncertainty for that climate. This section develops summaries of the results.

Each of the sixty calculations reported in Section 6.5 provides three values for potential recharge, one for each of the following surface areas:

- Repository footprint
- Region planned for unsaturated-zone calculation (the UZ model grid)
- Entire surface treated by the MASSIF calculations.

Each value represents a space-time average over the area of interest and over the duration of the particular climate. A set of realizations for a particular climate provides three approximate uncertainty distributions, one for each of the space-time averages. This section models the uncertainty distributions of average potential recharge over the UZ model grid for each of the three climates. The UZ model grid represents the region expected to influence percolation of moisture from the surface to the vicinity of the repository.

Because the potential recharge must have positive values, a normal distribution cannot represent the uncertainty in potential recharge. Instead, this section models each uncertainty distribution as a lognormal distribution. The probability density for a lognormal distribution is (Gilbert 1987 [DIRS 163705], p. 152, Equation 12.1):

$$f(x) = \frac{1}{xS\sqrt{2\pi}} \exp\left[-\frac{1}{2S^2} (\ln x - M)^2 \right] \qquad \text{(Eq. 6.6.1-1)}$$

where M and S^2 are the true mean and variance of the random variable ln x, exp(M) is the median value of the random variable x, and M is the median value of the random variable ln x.

This section applies the W test to the logarithm of potential recharge over the UZ model grid. Testing the logarithm provides information about whether the uncertainty in potential recharge may be represented as a lognormal distribution.

This section combines both replicates for each climate and makes the approximation that the sample vectors represent random points in the parameter space. This permits the use of the W test for normality (Gilbert 1987 [DIRS 163705], Section 12.3.1). The null hypothesis for the W test is that the logarithms have a normal distribution. For a sample of size 40, the null hypothesis is rejected at the 0.02 significance level if W is less than 0.929 (Gilbert 1987 [DIRS 163705], Table A7). That is, the probability of W being less than 0.929 for a population of size 40 is less than 0.02.

If the hypothesis is not rejected, then:

- The experimental mean of ln x is an unbiased estimator of M (Gilbert 1987 [DIRS 163705], p. 27, Equation 4.3). The median value of x is exp(M).
- The experimental standard deviation of ln x is an unbiased estimator of S (ANSI/NCSL Z540-2-1997 [DIRS 157394], pp. 33, Section B.2.17, Note 1).
- The mean of x is exp(M+S^2/2) (Gilbert 1987 [DIRS 163705], p. 156, Table 12.1). (The mean of a lognormal distribution is always larger than the median.)

The following sections analyze the calculated amounts of potential recharge, averaged over the UZ model grid. To facilitate traceability, all values are rounded as shown in the tables before being used for subsequent calculations. The analyses show that the hypothesis of a lognormal distribution is not rejected for any of the three climates. Table 6.6.1-1 summarizes the parameters of the lognormal distributions. Because the uncertainty distribution is not symmetric, the table includes an uncertainty factor, defined to be exp(S). The uncertainty factor is (1) the ratio of the value "one sigma" above the median, exp(M+S), to the median and (2) the ratio of the median to the value one sigma below the median, exp(M−S).

The uncertainty in potential recharge over the UZ model grid is approximately a factor of two for the Present-Day climate or the Monsoon climate. For the Glacial Transition climate, the uncertainty factor is 1.8. Much of the uncertainty stems from uncertainty in parameters that are independent of climate. Section 6.7 discusses the relative contributions of the parameter uncertainties.

Table 6.6.1-1. Parameters of Lognormal Distributions Representing the Contributions of Parameter Uncertainty to Uncertainties in Potential Recharge, Averaged over the UZ Model Grid

Climate	M [(a)]	S [(b)]	Median (e^M) (mm/yr)	Uncertainty Factor (e^S)	Mean of Distribution exp(M+S^2/2) (mm/yr)
Present-Day	2.4	0.9	11	2	17
Monsoon	3.0	0.9	20	2	30
Glacial Transition	3.2	0.6	25	1.8	29

[(a)] Mean of ln(I_{avg}) from Tables 6.6.1.1-1, 6.6.1.2-1, and 6.6.1.3-1.
[(b)] Standard deviation of ln(I_{avg}) from Tables 6.6.1.1-1, 6.6.1.2-1, and 6.6.1.3-1.

6.6.1.1 Uncertainty in Potential Recharge over the UZ Model Grid during the Present-Day Climate

Table 6.6.1.1-1 presents the results of both replicates for the Present-Day climate, sorted by potential recharge over the UZ model grid. The table also shows the logarithms of the results, as well as the mean and standard deviation of each column.

Table 6.6.1.1-2 develops the W test for the logarithm of net infiltration. The value of W is 0.939, so that the hypothesis that the distribution is lognormal is not rejected at the 0.02 significance level. For the Present-Day climate, therefore, the uncertainty in potential recharge may be represented by a lognormal distribution. The parameters of the lognormal distribution are $M = 2.4$ and $S = 0.9$.

The median value of potential recharge is 11 mm/yr. The value of S is equivalent to an uncertainty of a factor of 2 in potential recharge over the UZ model grid. The mean value of the lognormal distribution is 17 mm/yr, close to the value of 15 mm/yr, which is the mean of the calculated values of potential recharge. The agreement between these two values corroborates that the lognormal distribution models the distribution of calculated results.

Table 6.6.1.1-1. Values of Potential Recharge over the UZ Model Grid as Calculated for the Present-Day Climate, Sorted

Replicate [a]	Vector [b]	I_{avg} (mm/yr) [c]	ln(I_{avg}) [d]		Replicate [a]	Vector [b]	I_{avg} (mm/yr) [c]	ln(I_{avg}) [d]
R1	4	1.4	0.34		R2	15	13.3	2.59
R2	4	2.1	0.74		R1	2	14.2	2.65
R1	10	2.4	0.88		R1	18	14.8	2.69
R2	10	3.4	1.22		R2	19	16.6	2.81
R2	18	3.4	1.22		R2	3	19.6	2.98
R1	7	3.7	1.31		R1	12	20.2	3.01
R2	17	3.9	1.36		R1	9	20.7	3.03
R2	1	5.4	1.69		R2	13	20.9	3.04
R1	1	5.5	1.70		R2	7	24.3	3.19
R1	17	5.5	1.70		R1	14	25.1	3.22
R1	11	5.9	1.77		R1	6	25.2	3.23
R2	2	6.0	1.79		R1	15	25.7	3.25
R1	8	6.8	1.92		R2	14	28.7	3.36
R1	20	8.3	2.12		R2	20	29.1	3.37
R2	5	8.6	2.15		R2	12	29.3	3.38
R2	6	10.3	2.33		R1	19	29.9	3.40
R2	8	10.9	2.39		R2	9	30.1	3.40
R1	3	11.4	2.43		R1	5	32.6	3.48

Table 6.6.1.1-1. Values of Potential Recharge over the UZ Model Grid as Calculated for the Present-Day Climate, Sorted (Continued)

Replicate[a]	Vector[b]	I_{avg} (mm/yr)[c]	ln(I_{avg})[d]		Replicate[a]	Vector[b]	I_{avg} (mm/yr)[c]	ln(I_{avg})[d]
R1	16	11.9	2.48		R2	16	40.9	3.71
R2	11	12.3	2.51			Mean[e]	15	2.4
R1	13	12.6	2.53		Standard Deviation[e]		10	0.9

Source: Output DTN: SN0701T0502206.037, files: \Welcome to Massif\Massif\Present Day Uncertainty\Post Processing\Intermediate Output Files*PD_Mean_Infiltration_R1.txt* and \Welcome to Massif\Massif\Present Day Uncertainty\Post Processing\Intermediate Output Files*PD_Mean_Infiltration_R2.txt*.

[a] Identifies source file in DTN.
[b] Identifies data line in source file.
[c] Rounded to nearest 0.1 mm before further calculation.
[d] Rounded to nearest 0.01.
[e] Standard deviation rounded to two significant digits if first digit is one, otherwise to one significant digit. Mean rounded consistent with standard deviation.

Table 6.6.1.1-2. W test for Lognormal Uncertainty Distribution for Potential Recharge over the UZ Model Grid during the Present-Day Climate

i [(a)]	$x_i = \ln(I_{avg})$ [(b)]	$x_i - x_{mean}$	a_i [(c)]	x_{41-i}	$a_i (x_{41-i} - x_i)$
1	0.34	−2.07	0.3964	3.71	1.336
2	0.74	−1.67	0.2737	3.48	0.750
3	0.88	−1.53	0.2368	3.40	0.597
4	1.22	−1.19	0.2098	3.40	0.457
5	1.22	−1.19	0.1878	3.38	0.406
6	1.31	−1.10	0.1691	3.37	0.348
7	1.36	−1.05	0.1526	3.36	0.305
8	1.69	−0.72	0.1376	3.25	0.215
9	1.70	−0.71	0.1237	3.23	0.189
10	1.70	−0.71	0.1108	3.22	0.168
11	1.77	−0.64	0.0986	3.19	0.140
12	1.79	−0.62	0.0870	3.04	0.109
13	1.92	−0.49	0.0759	3.03	0.084
14	2.12	−0.29	0.0651	3.01	0.058
15	2.15	−0.26	0.0546	2.98	0.045
16	2.33	−0.08	0.0444	2.81	0.021
17	2.39	−0.02	0.0343	2.69	0.010
18	2.43	0.02	0.0244	2.65	0.005
19	2.48	0.07	0.0146	2.59	0.002
20	2.51	0.10	0.0049	2.53	0.000
21	2.53	0.12		sum	5.245
22	2.59	0.18		$W=sum^2/d$	0.939
23	2.65	0.24			
24	2.69	0.28			
25	2.81	0.40			

Table 6.6.1.1-2. W test for Lognormal Uncertainty Distribution for Potential Recharge over the UZ Model Grid during the Present-Day Climate (Continued)

i [(a)]	$x_i = \ln(I_{avg})$ [(b)]	$x_i - x_{mean}$	a_i [(c)]	x_{41-i}	$a_i (x_{41-i} - x_i)$
26	2.98	0.57			
27	3.01	0.60			
28	3.03	0.62			
29	3.04	0.63			
30	3.19	0.78			
31	3.22	0.81			
32	3.23	0.82			
33	3.25	0.84			
34	3.36	0.95			
35	3.37	0.96			
36	3.38	0.97			
37	3.40	0.99			
38	3.40	0.99			
39	3.48	1.07			
40	3.71	1.30			
x_{mean}	2.41	29.3	$d=\text{sum}(x_i - x_{mean})^2$		

[(a)] Index number after sorting.
[(b)] From Table 6.6.1.1-1.
[(c)] Gilbert 1987 [DIRS 163705], Table A6.

6.6.1.2 Uncertainty in Potential Recharge over the UZ Model Grid during the Monsoon Climate

Table 6.6.1.2-1 presents the results of both replicates for the monsoon climate, sorted by potential recharge over the UZ model grid. The table also shows the logarithms of the results, as well as the mean and standard deviation of each column.

Table 6.6.1.2-2 develops the W test for the logarithm of net infiltration. The value of W is 0.930, so that the hypothesis that the distribution is lognormal is not rejected at the 0.02 significance level. For the monsoon climate, therefore, the uncertainty in potential recharge may be represented by a lognormal distribution. The parameters of the lognormal distribution are $M = 3.0$ and $S = 0.9$. The median value of potential recharge is 20 mm/yr. The value of S is equivalent to an uncertainty of a factor of 2 in potential recharge over the UZ model grid. The mean value of the lognormal distribution is 30 mm/yr, which is also the mean of the calculated values of potential recharge. The agreement between these two values corroborates that the lognormal distribution models the distribution of calculated results.

Table 6.6.1.2-1. Values of Potential Recharge over the UZ Model Grid as Calculated for the Monsoon Climate, Sorted

Replicate[a]	Vector[b]	I_{avg} (mm/yr)[c]	ln(I_{avg})[d]		Replicate[a]	Vector[b]	I_{avg} (mm/yr)[c]	ln(I_{avg})[d]
R2	20	1.2	0.18		R2	9	25.0	3.22
R1	18	1.9	0.64		R1	1	25.2	3.23
R1	20	4.6	1.53		R2	11	26.0	3.26
R1	17	5.4	1.69		R1	9	26.9	3.29
R1	3	6.5	1.87		R1	15	28.1	3.34
R2	6	6.9	1.93		R2	15	30.0	3.40
R2	4	7.6	2.03		R1	6	36.5	3.60
R1	10	9.2	2.22		R1	19	38.4	3.65
R1	11	10.6	2.36		R2	17	39.1	3.67
R1	5	13.9	2.63		R1	14	41.0	3.71
R2	14	14.6	2.68		R2	12	44.9	3.80
R2	5	15.1	2.71		R1	16	45.0	3.81
R2	10	16.0	2.77		R1	4	45.5	3.82
R1	12	17.1	2.84		R1	8	49.5	3.90
R2	18	18.1	2.90		R2	16	56.7	4.04
R2	8	18.2	2.90		R2	1	56.8	4.04
R2	13	19.3	2.96		R1	7	62.2	4.13
R2	2	22.0	3.09		R2	19	75.7	4.33
R1	13	23.3	3.15		R2	3	86.2	4.46
R2	7	23.5	3.16			Mean[e]	30	3.0
R1	2	24.9	3.21		Standard Deviation[e]		20	0.9

Source: Output DTN: SN0701T0502206.037, files: \Welcome to Massif\Massif\Monsoon Uncertainty\Post Processing\Intermediate Output Files*MO_Mean_Infiltration_R1.txt* and \Welcome to Massif\Massif\Monsoon Uncertainty\Post Processing\Intermediate Output Files*MO_Mean_Infiltration_R2.txt*.

[a] Identifies source file in DTN.
[b] Identifies data line in source file.
[c] Rounded to nearest 0.1 mm before further calculation.
[d] Rounded to nearest 0.01.
[e] Standard deviation rounded to two significant digits if first digit is one, otherwise to one significant digit. Mean rounded consistent with standard deviation.

Table 6.6.1.2-2. W Test for Lognormal Uncertainty Distribution for Potential Recharge over the UZ Model Grid during the Monsoon Climate

i [(a)]	$x_i = \ln(I_{avg})$ [(b)]	$x_i - x_{mean}$	a_i [(c)]	x_{41-i}	$a_i (x_{41-i} - x_i)$
1	0.18	−2.82	0.3964	4.46	1.697
2	0.64	−2.36	0.2737	4.33	1.010
3	1.53	−1.47	0.2368	4.13	0.616
4	1.69	−1.31	0.2098	4.04	0.493
5	1.87	−1.13	0.1878	4.04	0.408
6	1.93	−1.07	0.1691	3.90	0.333

Table 6.6.1.2-2. W Test for Lognormal Uncertainty Distribution for Potential Recharge over the UZ Model Grid during the Monsoon Climate (Continued)

i [(a)]	$x_i = \ln(I_{avg})$ [(b)]	$x_i - x_{mean}$	a_i [(c)]	x_{41-i}	$a_i (x_{41-i} - x_i)$
7	2.03	−0.97	0.1526	3.82	0.273
8	2.22	−0.78	0.1376	3.81	0.219
9	2.36	−0.64	0.1237	3.80	0.178
10	2.63	−0.37	0.1108	3.71	0.120
11	2.68	−0.32	0.0986	3.67	0.098
12	2.71	−0.29	0.0870	3.65	0.082
13	2.77	−0.23	0.0759	3.60	0.063
14	2.84	−0.16	0.0651	3.40	0.036
15	2.90	−0.10	0.0546	3.34	0.024
16	2.90	−0.10	0.0444	3.29	0.017
17	2.96	−0.04	0.0343	3.26	0.010
18	3.09	0.09	0.0244	3.23	0.003
19	3.15	0.15	0.0146	3.22	0.001
20	3.16	0.16	0.0049	3.21	0.000
21	3.21	0.21		sum	5.681
22	3.22	0.22		$W=sum^2/d$	0.930
23	3.23	0.23			
24	3.26	0.26			
25	3.29	0.29			
26	3.34	0.34			
27	3.40	0.40			
28	3.60	0.60			
29	3.65	0.65			
30	3.67	0.67			
31	3.71	0.71			
32	3.80	0.80			
33	3.81	0.81			
34	3.82	0.82			
35	3.90	0.90			
36	4.04	1.04			
37	4.04	1.04			
38	4.13	1.13			
39	4.33	1.33			
40	4.46	1.46			
x_{mean}	3.00	34.7	$d=sum(x_i - x_{mean})^2$		

(a) Index number after sorting.
(b) From Table 6.6.1.2-1.
(c) Gilbert 1987 [DIRS 163705], Table A6.

6.6.1.3 Potential Recharge over the UZ Model Grid during the Glacial Transition Climate

Table 6.6.1.3-1 presents the results of both replicates for the glacial transition climate, sorted by potential recharge over the UZ model grid. The table also shows the logarithms of the results, as well as the mean and standard deviation of each column.

Table 6.6.1.3-2 develops the W test for the logarithm of net infiltration. The value of W is 0.943, so that the hypothesis that the distribution is lognormal is not rejected at the 0.02 significance level. For the glacial transition climate, therefore, the uncertainty in potential recharge may be represented by a lognormal distribution. The parameters of the lognormal distribution are $M = 3.2$ and $S = 0.6$.

The median value of potential recharge is 25 mm/yr. The value of S is equivalent to an uncertainty of a factor of 1.8 in potential recharge over the UZ model grid. The mean value of the lognormal distribution is 29 mm/yr, which is the same as the mean of the calculated values of potential recharge. The agreement between these two values corroborates that the lognormal distribution models the distribution of calculated results.

Table 6.6.1.3-1. Values of Potential Recharge over the UZ Model Grid as Calculated for the Glacial Transition Climate, Sorted

Replicate [a]	Vector [b]	I_{avg} (mm/yr) [c]	$\ln(I_{avg})$ [d]		Replicate [a]	Vector [b]	I_{avg} (mm/yr) [c]	$\ln(I_{avg})$ [d]
R1	7	4.3	1.46		R1	1	28.6	3.35
R1	4	5.8	1.76		R2	12	29.1	3.37
R2	6	8.2	2.10		R1	18	29.4	3.38
R1	9	9.8	2.28		R1	10	33.1	3.50
R2	11	11.0	2.40		R2	18	33.5	3.51
R2	15	11.2	2.42		R2	20	33.5	3.51
R2	16	16.2	2.79		R1	19	33.7	3.52
R2	5	17.7	2.87		R2	8	33.7	3.52
R2	13	18.7	2.93		R2	3	34.2	3.53
R1	15	19.3	2.96		R1	14	35.3	3.56
R1	6	19.8	2.99		R1	2	37.2	3.62
R2	14	20.0	3.00		R2	2	43.8	3.78
R2	10	20.7	3.03		R1	12	46.5	3.84
R1	3	21.0	3.04		R2	7	47.2	3.85
R2	4	22.3	3.10		R1	5	49.7	3.91
R1	17	22.7	3.12		R2	1	51.8	3.95
R1	11	23.4	3.15		R1	13	57.7	4.06
R2	17	24.2	3.19		R2	19	62.0	4.13
R1	16	26.7	3.28		R1	8	72.1	4.28
R2	9	27.6	3.32			Mean [e]	29	3.2
R1	20	28.5	3.35			Standard Deviation [e]	15	0.6

Source: Output DTN: SN0701T0502206.037, files: \Welcome to Massif\Massif\Glacial Uncertainty\Post Processing\Intermediate Output Files*GT_Mean_Infiltration_R1.txt* and \Welcome to Massif\Massif\Glacial Uncertainty\Post Processing\Intermediate Output Files*GT_Mean_Infiltration_R2.txt*.

[a] Identifies source file in DTN.
[b] Identifies data line in source file.
[c] Rounded to nearest 0.1 mm before further calculation.
[d] Rounded to nearest 0.01.
[e] Standard deviation rounded to two significant digits if first digit is one, otherwise to one significant digit. Mean rounded consistent with standard deviation.

Table 6.6.1.3-2. W Test for Lognormal Uncertainty Distribution for Potential Recharge over the UZ Model Grid during the Glacial Transition Climate

i [(a)]	$x_i = \ln(I_{avg})$ [(b)]	$x_i - x_{mean}$	a_i [(c)]	x_{41-i}	$a_i (x_{41-i} - x_i)$
1	1.46	−1.76	0.3964	4.28	1.118
2	1.76	−1.46	0.2737	4.13	0.649
3	2.10	−1.12	0.2368	4.06	0.464
4	2.28	−0.94	0.2098	3.95	0.350
5	2.40	−0.82	0.1878	3.91	0.284
6	2.42	−0.80	0.1691	3.85	0.242
7	2.79	−0.43	0.1526	3.84	0.160
8	2.87	−0.35	0.1376	3.78	0.125
9	2.93	−0.29	0.1237	3.62	0.085
10	2.96	−0.26	0.1108	3.56	0.066
11	2.99	−0.23	0.0986	3.53	0.053
12	3.00	−0.22	0.0870	3.52	0.045
13	3.03	−0.19	0.0759	3.52	0.037
14	3.04	−0.18	0.0651	3.51	0.031
15	3.10	−0.12	0.0546	3.51	0.022
16	3.12	−0.10	0.0444	3.50	0.017
17	3.15	−0.07	0.0343	3.38	0.008
18	3.19	−0.03	0.0244	3.37	0.004
19	3.28	0.06	0.0146	3.35	0.001
20	3.32	0.10	0.0049	3.35	0.000
21	3.35	0.13		sum	3.761
22	3.35	0.13		$W=sum^2/d$	0.943
23	3.37	0.15			
24	3.38	0.16			
25	3.50	0.28			
26	3.51	0.29			
27	3.51	0.29			
28	3.52	0.30			
29	3.52	0.30			
30	3.53	0.31			
31	3.56	0.34			
32	3.62	0.40			
33	3.78	0.56			
34	3.84	0.62			
35	3.85	0.63			
36	3.91	0.69			
37	3.95	0.73			

Table 6.6.1.3-2. W Test for Lognormal Uncertainty Distribution for Potential Recharge over the UZ Model Grid during the Glacial Transition Climate

i [(a)]	$x_i = \ln(I_{avg})$ [(b)]	$x_i - x_{mean}$	a_i [(c)]	x_{41-i}	$a_i (x_{41-i} - x_i)$
38	4.06	0.84			
39	4.13	0.91			
40	4.28	1.06			
x_{mean}	3.22	15.0	$d=\text{sum}(x_i - x_{mean})^2$		

[(a)] Index number after sorting.
[(b)] From Table 6.6.1.1-1.
[(c)] Gilbert 1987 [DIRS 163705], Table A6.

6.6.2 Uncertainty in Local Net Infiltration

The maps resulting from the net infiltration calculations provide a value for each 30 × 30-m grid cell that represents the average over the duration of the climate. This report does not provide uncertainty estimates for each of these local values; however, at many locations the uncertainty in local conditions is much larger than the corresponding uncertainty in a spatial average.

This section provides a qualitative discussion of the uncertainty in local net infiltration. Numerical values are used, but because the analysis uses several equations that are only approximations, the results are only a rough guide to the extent of local uncertainty.

The calculations in Appendix H estimate the influence of uncertainty in input parameters on the uncertainty in a measure of infiltration. The measure of infiltration used is the average annual net infiltration over the infiltration modeling domain, as reported in Section 6.5.7. Sections H2.5, H3.6, and H4.6 conclude that the inputs whose uncertainty have the greatest impact on infiltration uncertainty are:

- Effective uniform soil depth assigned to the region defined as Soil Depth Class 4
- Precipitation parameters
- Effective uniform holding capacity assigned to Soil Group 7/8/9.

The uncertainty in precipitation is the same whether one is considering spatially averaged infiltration or local infiltration. However, the uncertainties in the other two parameters are less when taken over the entire infiltration modeling domain. This is because the averaging takes advantage of the law of large numbers: the uncertainty in the mean of an uncertainty distribution can be much less than the standard uncertainty of the distribution itself.

For example, the expected value of the throw of a single six-sided die, with sides numbered one through six, is 3.5. For a single throw, the standard uncertainty is 1.7. For the average of 100 throws, the standard uncertainty is 0.17.

This section provides a qualitative discussion of the uncertainty in calculated local net infiltration, taking Replicate 1 of the Present-Day climate as an example and considering only localities that are in Soil Depth Class 4. Further, this section considers only the effect of local uncertainty in soil depth. The analysis does not apply at any location where the soil depth is known and is approximately the same as the effective uniform depth for Soil Depth Class 4.

Let $\bar{I}_{PD}$ be the calculated annual potential recharge for the remainder of the Present-Day climate. That is, $\bar{I}_{PD}$ is the average over the infiltration modeling domain of the annual net infiltration at each location, $I_{PD}(lat, long)$, where *lat* and *long* are the latitude and longitude, respectively.

For consistency with Section 6.6.1, the analysis in this section focuses on uncertainty in the logarithm of net infiltration. The combined standard uncertainty in the logarithm of $\bar{I}_{PD}$, $u(\ln \bar{I}_{PD})$, is given by (ANSI/NCSL Z540-2-1997 [DIRS 157394], p. 19, Equation 10):

$$u^2(\ln \bar{I}_{PD}) = \sum_i \left[\frac{\partial \ln \bar{I}_{PD}}{\partial x_i} \right]^2 u^2(x_i) \qquad \text{(Eq. 6.6.2-1)}$$

where each $u(x_i)$ is the standard uncertainty of an input parameter. Equation 6.6.2-1 results from the following approximations (ANSI/NCSL Z540-2-1997 [DIRS 157394], p. 19):

- The input parameters are independent.
- The dependence of $\ln \bar{I}_{PD}$ on each input parameter, within that parameter's range of uncertainty, is linear. That is, the Taylor Series expansion about the nominal value of each parameter can be truncated after the linear term without changing the qualitative nature of the dependence.

From Section 6.6.1.1, $u(\ln \bar{I}_{PD})$ is the parameter *S* in the lognormal distribution and has a value of about 0.9, so that $u^2(\ln \bar{I}_{PD})$ is about 0.8. According to Table H-1, the regression coefficient for Soil Depth 4, R^2, is 0.33 for Replicate 1 of the Present-Day climate when aleatory uncertainty is varying. This is a low estimate; tables H-2 through H-4 provide larger coefficients for Replicate 2 or for aleatory uncertainty fixed. Therefore, the contribution from Soil Depth Class 4 is at least:

$$\left[\frac{\partial \ln \bar{I}_{PD}}{\partial x_{SD4}} \right]^2 u^2(x_{SD4}) \cong 0.33(0.9) \cong 0.3 \qquad \text{(Eq. 6.6.2-2)}$$

and the contribution to uncertainty from the other parameters is at most:

$$\sum_{i \neq SD4} \left[\frac{\partial \ln \bar{I}_{PD}}{\partial x_i} \right]^2 u^2(x_i) \cong 0.8 - 0.3 \cong 0.5\,, \qquad \text{(Eq. 6.6.2-3)}$$

where x_{SD4} is the effective uniform soil depth for Soil Depth Class 4.

The standard uncertainty in the effective uniform depth for Soil Depth Class 4, $u(x_{SD4})$, is about 0.12 m (Table I-2). To satisfy Equation 6.6.2-2, there must be:

$$\frac{\partial \ln \bar{I}_{PD}}{\partial x_{SD4}} \cong 5\ \mathrm{m}^{-1} \qquad \text{(Eq. 6.6.2-4)}$$

or more.

For the uncertainty in local net infiltration there is the following equation:

$$u^2(\ln I_{PD}(lat,long)) = \sum_i \left[\frac{\partial \ln I_{PD}(lat,long)}{\partial x_i}\right]^2 u^2(x_i) \qquad \text{(Eq. 6.6.2-5)}$$

Now the Taylor Series expansion is about the local value of each spatially varying parameter. Although the uncertainty distribution for a local parameter differs from the distribution for the effective uniform value, the nominal value is the same. Therefore, the Taylor Series expansion is taken about values similar to those in the previous expansion.

The approximation is made that the contribution to $u^2(\ln I_{PD}(lat,long))$ from each parameter other than Soil Depth Class 4 is the same as the contribution of that parameter to $u^2(\ln \bar{I}_{PD})$. This is clearly not true, especially for parameters that are clearly irrelevant, such as other Soil Depth classes. The justification for this approximation is that the contributions from such parameters are relatively small. Therefore,

$$u^2(\ln I_{PD}(lat,long)) \cong 0.5 + \left[\frac{\partial \ln I_{PD}(lat,long)}{\partial d(lat,long)}\right]^2 u^2(d(lat,long)), \qquad \text{(Eq. 6.6.2-6)}$$

where $d(lat,long)$ is the local soil depth.

To complete the estimation of $u^2(\ln I_{PD}(lat,long))$, this section first estimates $\frac{\partial \ln I_{PD}(lat,long)}{\partial d(lat,long)}$, then $u^2(d(lat,long))$. Note that, by definition,

$$\bar{I}_{PD} = \frac{1}{A}\iint_{lat,long} I_{PD}(lat,long)dA\,. \qquad \text{(Eq. 6.6.2-7)}$$

where A is surface area. Consequently,

$$\frac{\partial \bar{I}_{PD}}{\partial x_{SD4}} = \frac{1}{A}\iint_{lat,long} \frac{\partial I_{PD}(lat,long)}{\partial x_{SD4}}dA \qquad \text{(Eq. 6.6.2-8)}$$

$$\frac{\partial \ln \bar{I}_{PD}}{\partial x_{SD4}} = \frac{1}{A} \iint_{lat,long} \frac{I_{PD}(lat,long)}{\bar{I}_{PD}} \frac{\partial \ln I_{PD}(lat,long)}{\partial x_{SD4}} dA . \qquad \text{(Eq. 6.6.2-9)}$$

The integral on the right-hand side of Equation 6.6.2-9 involves integration over each soil depth class. Clearly, the partial derivative with respect to x_{SD4} will be much smaller within other soil depth classes than it is within Soil Depth Class 4. Also, Soil Depth Class 4 contributes over 90% of $\bar{I}_{PD}$ (Table 6.5.7.6-1), which suggests that

$$\frac{\partial \ln \bar{I}_{PD}}{\partial x_{SD4}} \cong \frac{1}{A} \iint_{(lat,long) \in SDC4} \frac{I_{PD}(lat,long)}{\bar{I}_{PD}} \frac{\partial \ln I_{PD}(lat,long)}{\partial x_{SD4}} dA . \qquad \text{(Eq. 6.6.2-10)}$$

Within Soil Depth Class 4, $I_{PD}(lat,long)$ must vary above and below $\bar{I}_{PD}$. Therefore, an intermediate estimate for $\frac{\partial \ln I_{PD}(lat,long)}{\partial x_{SD4}}$ is the value of $\frac{\partial \ln \bar{I}_{PD}}{\partial x_{SD4}}$, which is 5 m^{-1}.

Now, $\frac{\partial \ln I_{PD}(lat,long)}{\partial x_{SD4}}$ differs from $\frac{\partial \ln I_{PD}(lat,long)}{\partial d(lat,long)}$ in that the former is the change in local net infiltration as the soil depth increases in the entire region of Soil Depth Class 4, whereas the latter is the change in local net infiltration when only the local soil depth increases. The soil depth at other locations can only influence local net infiltration by adding run-on to the local precipitation at the site. However, because Table 6.5.4.7-1 indicates that runoff represents only about 2% of the precipitation, it is reasonable to estimate that, for a location within Soil Depth Class 4,

$$\frac{\partial \ln I_{PD}(lat,long)}{\partial d(lat,long)} \cong \frac{\partial \ln \bar{I}_{PD}}{\partial x_{SD4}} \cong 5 \ \text{m}^{-1}. \qquad \text{(Eq. 6.6.2-11)}$$

Table 6.5.2.4-2 indicates that the data for Soil Depth Class 4 have a standard deviation of about 0.7 m. This is an estimate of the uncertainty in local soil depth for locations within Soil Depth Class 4. Therefore, for locations within Soil Depth Class 4,

$$u^2(\ln I_{PD}(lat,long)) \cong 0.5 + [5]^2 0.7^2 \cong 13 \text{ or more,} \qquad \text{(Eq. 6.6.2-12)}$$

so that $u(\ln I_{PD}(lat,long))$ is about 4 or more, as compared with 0.9 for $u(\ln \bar{I}_{PD})$.

Recall that the standard uncertainty of 0.9 for $\ln \bar{I}_{PD}$ corresponds to an uncertainty of about a factor of two in $\bar{I}_{PD}$. The standard uncertainty of 4 for $\ln I_{PD}(lat,long)$ is equivalent to an uncertainty in $I_{PD}(lat,long)$ of a factor of fifty or more. Furthermore, the deviation of $I_{PD}(lat,long)$ from its expected value may not be in the same direction as the deviation of $\bar{I}_{PD}$ from its expected value. For example, it should not be surprising if the future measured value of $\bar{I}_{PD}$ is a factor of two higher than predicted, whereas at a particular location the measured value of $I_{PD}(lat,long)$ is a factor of twenty lower than predicted.

The preceding qualitative discussion is for the comparison of predicted and measured values of $I_{PD}(lat, long)$ for a point on the surface. In fact, MASSIF predictions of local net infiltration are not point values but averages over a 30 × 30-m grid. The effect of upscaling to 30 meters can depend strongly on the local topography. In some places, the soil depth may be nearly uniform on that distance scale and significantly different from the depth upscaled to the entire Soil Depth Class 4. In other places, the depth may vary substantially, even over this smaller distance.

If a downstream study takes as input the local net infiltration(s) from one or more calculations reported in Section 6.5, then the uncertainty analysis for that study should include an estimate of the uncertainty in local net infiltration.

6.6.3 Sources and Magnitude of Model Uncertainty

Model uncertainty represents a limitation of any model to accurately represent the physical processes being considered. Models are simplified representations of reality and, as such, introduce inherent errors in estimated quantities due to the simplifications and abstractions necessary for formulating the model. In addition to the limitations in model predictions due to model uncertainty, parameter uncertainty introduces additional uncertainty. Measurement theory provides a useful analogy to compare model and parameter uncertainties. Model uncertainty is similar to measurement accuracy, while parameter uncertainty is similar to measurement precision. Both sources of uncertainty contribute to the final uncertainty in a model prediction or measurement quantity.

In the analysis of net infiltration at Yucca Mountain, both sources of uncertainty are important and must be estimated. Most of the effort has been focused on evaluating and quantifying parameter uncertainty. As discussed in Section 6.6.1 and 6.6.2, parameter uncertainty represents approximately a factor of 2 uncertainty in the mean net infiltration averaged over the UZ model domain and a factor of approximately 6 in the uncertainty in local net infiltration predicted in areas with shallow soils. This parameter uncertainty conceivably could be reduced by additional geologic characterization work at the site (e.g., a more detailed soil depth map, a more detailed characterization of soil and rock properties).

Sources of model uncertainty in this study include: (1) the accuracy of the coupled NDVI/FAO-56 approach for estimating evapotranspiration at the site, (2) the accuracy of the layered field capacity approach for representing subsurface water flow, (3) the accuracy of the assumption that evapotranspiration from bedrock is negligible, and (4) the accuracy of the distributed runoff model used to represent surface water flow.

The uncertainty associated with the ET submodel is evaluated by comparing ET measurements using lysimeter data to simulated results using MASSIF (see Section 7.1.2). These comparisons indicate that the model performs well in the context of parameter uncertainty, especially for estimates of cumulative annual ET.

The present study was unable to explicitly test the accuracy of the field capacity approach for representing subsurface water flow against field data from the Yucca Mountain site. However, a comparison was made against HYDRUS 1-D (a comparable model that represents subsurface water flow using Richards' equation) in Section 7.2.2. This comparison demonstrates that while

the field capacity approach may not represent the transient nature of this flow accurately, it does an adequate job of representing the cumulative net infiltration over the year.

The assumption that ET from the bedrock is negligible is highly uncertain and is dependent upon knowledge of the bedrock properties and applicable physics of potential processes for water removal from bedrock overlain by soil. Certain neutron logs that extend into bedrock show that water removal does occur at certain locations (BSC 2004 [DIRS 170007], p. 6-16), however these results are not at all consistent when all the logs are examined. Therefore, the implication of this assumption is that it will tend to overestimate net infiltration model predictions, but it is not clear by how much and where these overestimates occur.

Finally, comparisons of runoff predictions with stream gauge observations (see Section 7.1.3) provide confidence that the model uncertainty related to the runoff submodel is not a significant source of uncertainty for mean net infiltration over the a large area (e.g., UZ model domain); however, this process may contribute significantly to uncertainty in local net infiltration (see Sections 7.1.3.1 and 7.1.3.2).

The challenge of estimating net infiltration model uncertainty is exacerbated by the difficulty of directly measuring net infiltration in this and similar environments. Instead, model uncertainty is usually inferred by comparing the results of the various submodels (e.g., ET, runoff, etc.) to available field data as described above. However, such comparisons do not directly evaluate the model uncertainty in net infiltration estimates. Another approach is to assume that the regional estimates of net infiltration presented in Section 7.2 are representative of net infiltration conditions expected for the UZ model domain at Yucca Mountain. If this assumption is valid, then model uncertainty could be estimated by comparing MASSIF model predictions with estimates of net infiltration and recharge from these other sites. The comparison presented in Figure 7.2.1.2-2 suggests that model uncertainty is comparable in magnitude to parameter uncertainty. However, it is not clear that the assumption that regional sites are comparable with the UZ model domain is entirely valid. The UZ model domain is characterized by uplands with very shallow soils and may host a different net infiltration regime than is more typical of the other hydrographic basins represented in Section 7.2. One indication that this assumption may not be valid is in the comparison of the net infiltration predictions with net infiltration inferred from an analysis of the 99 neutron boreholes at the Yucca Mountain site (Figure 7.2.1.1-2). This figure clearly shows that nearly all of the net infiltration estimates derived from the neutron logging analyses are higher than the values predicted by the MASSIF model. If the spatial distribution of neutron borehole locations is representative of the UZ modeling domain and the net infiltration estimates from the analysis of the neutron logs is representative of conditions away from the boreholes, this would suggest that the MASSIF model may underestimate actual net infiltration for this area by at least a factor of 2 (visually estimated from Figure 7.2.1.1-2). It is not clear, however, that either of these criteria is met, and therefore it is not clear how these data can help to estimate model uncertainty. Given these challenges, and the comparisons that have been made, it is difficult to quantify model uncertainty. Available comparisons suggest that model uncertainty may be of a comparable magnitude to parameter uncertainty. Given the complexity of modeling net infiltration over such a large and heterogeneous domain, such uncertainty is not unprecedented.

6.7 SENSITIVITY ANALYSIS

6.7.1 Introduction

A sensitivity analysis examines how uncertainty in input parameters affects the uncertainty in model results. In addition, a sensitivity analysis can identify which input parameters have the greatest influence on model predictions, so that characterization efforts and studies can be focused to reduce the uncertainty in those parameters, and thus most efficiently reduce uncertainty in the model outputs. A more detailed discussion of sensitivity analysis methods is included in Appendix H along with a detailed discussion of the results of this study for each climate.

In risk analysis, uncertainty is generally separated into two categories depending upon the source of the uncertainty. Epistemic uncertainty stems from a lack of knowledge about the system being considered. This type of uncertainty is characterized by assigning probability distributions to parameters that describe the properties of the system. Epistemic uncertainty can usually be reduced with more studies, experiments, and observations of the system. This uncertainty is also sometimes referred to as reducible or state-of-knowledge uncertainty. A second type of uncertainty is aleatory uncertainty, which refers to inherent and irreducible randomness, such as the uncertainty in weather and how much it will rain in the future. The distinguishing characteristic of aleatory uncertainty is that it is a property of the system and cannot be reduced by further study.

In the current analysis, any uncertainty associated with parameters describing the physical properties of the system is considered to be epistemic uncertainty. Moreover, the parameters characterizing mean annual precipitation (MAP) are also associated with epistemic uncertainty (there is a unique value for the average annual precipitation and associated parameters assuming analogue stations adequately represent future climates). In the modeling, the precipitation amount for a given day and the pattern of precipitation days over the year are considered as aleatory uncertainty. In order to represent the aleatory uncertainty, a Markov Chain Monte Carlo method has been used to generate a set of 1,000 possible years of daily precipitation (see Appendix F). From these 1,000 years, 10 representative years have been chosen based on annual precipitation and weighted according to their probability of occurrence. Because the parameters defining precipitation are changing in each LHS sample, so are the ten representative years. The distribution of daily precipitation within the year influences the annual infiltration. However, this influence cannot be easily quantified because it is not associated with any of the input parameters, but rather is controlled by inherent aleatory uncertainty in the system.

The sensitivity analysis summarized here includes the results of two related analyses. The first considers the results of the uncertainty analysis (see Section 6.5.7). This analysis mixes both epistemic and aleatory uncertainty. It is important to represent the effect of aleatory uncertainty, as this uncertainty is indeed present. An extension of this analysis combines the sampled precipitation parameter for each climate by only examining the effect of MAP on net infiltration for each realization. Including aleatory uncertainty in the sensitivity reduces the ability to define the influence of the physical parameters whose uncertainty can be reduced. Therefore, a second analysis was performed ("Fixed Aleatory") in which the MASSIF net infiltration model was run with LHS realizations in which only epistemic uncertainty was varied. In these fixed aleatory

analyses, for each replicate, each of the LHS realizations used the same set of ten representative years. Precipitation parameters were only changed between each climate and each replicate. Of course, in these conditions the influence of precipitation cannot be seen because it has a constant value for all realizations.

6.7.2 Summary of Results

Detailed results of the two replicates for each of the three climates are presented in Appendix H. These results are summarized here.

For all climates, the sensitivity analyses show that there are two general features that control the uncertainty in the average annual net infiltration over the modeling domain. These features include the mean annual precipitation (MAP) and the soil depth assigned to Soil Depth Class 4. These two features explain about 70% of the variance in simulated infiltration when both epistemic and aleatory uncertainty is included. MAP is not sampled directly but is the result of a stochastic simulation of representative precipitation years that relies on a set of sampled stochastic parameters, which is different for each climate.

For the Present-Day climate, a_m (annual average of the mean of the probability distribution for the natural logarithm of the amount precipitation on days with precipitation) is the only precipitation parameter that is included in the LHS sampling. For the Monsoon climate, MAP is a function of a_m, a_{00} (annual mean value of probability of a dry day given the previous day was dry), and b_m (annual amplitude of mean of the probability distribution for the natural logarithm of the amount precipitation on days with precipitation). During the Glacial Transition climate, the parameters influencing the MAP are a_m, a_{00}, and θ_m (phase of the annual variation of mean of the probability distribution for the natural logarithm of the amount precipitation on days with precipitation).

However, it is important to note that, for physical reasons, some of the precipitation parameters have been defined as linear functions of other parameters. These linear relationships are described in Appendix F.

When aleatory uncertainty is fixed, the results of the sensitivity analysis only reflect the influence of physical parameters, given a fixed precipitation record. The results of these fixed aleatory analyses are consistent for the three climates and indicate that the most important physical parameters are Soil Depth Class 4 and HC_579 (water holding capacity for soil group 5/7/9). Together the uncertainty in these parameters account for about 90% of the variance in mean net infiltration for the Present-Day and Glacial Transition climates, and about 75% of the variance for Monsoon climate. Both have a negative influence, which means that high values of these parameters leads to a reduction in net infiltration.

The influence of the other physical parameters is not clearly indicated by the analyses. Because of the small sample size of each replicate considered (20), it is probably inappropriate to draw conclusions about the influence of other physical parameters.

6.7.3 Conclusions

Mean net infiltration is primarily controlled by the uncertainty in three epistemic quantities: mean annual precipitation, soil depth of Soil Depth Class 4, and the water holding capacity of soil group 5/7/9 (HC_579).

The agreement between the two replicates for each climate and also between climates gives confidence that these results are robust.

6.8 NOMENCLATURE USED IN SECTION 6 EQUATIONS

Symbol	Description	Units	Where Used*
I	Net infiltration	L/T	Eq. 6.2.1-1
P	Net precipitation	L/T	Eq. 6.2.1-1
RO	Surface water run-on/runoff	L/T	Eq. 6.2.1-1
ΔW	Change in water storage in the active zone	L^3L^{-3}	Eq. 6.2.1-1
E	Evaporation	L/T	Eq. 6.2.1-1 (6.4.4.3-1)
T	Transpiration	L/T	Eq. 6.2.1-1 (6.4.4.3-2; 6.4.4.3-3; 6.4.4.3-4; 6.4.4.3-5)
h	Water head	L	Eq. 6.2.4.1-1
θ	Volumetric water content	L^3L^{-3}	Eq. 6.2.4.1; Eq. 6.4.2-1
t	Time	T	Eq. 6.2.4.1
x	Spatial coordinate (positive upward)	L	Eq. 6.2.4.1
S	Sink term	$L^3L^{-3}T^{-1}$	Eq. 6.2.4.1
K	Unsaturated hydraulic conductivity function	LT^{-1}	Eq. 6.2.4.1
K_r	Relative hydraulic conductivity	—	Eq. 6.2.4.1-2 (6.4.4.1-2; 6.4.4.2-3)
K_s	Saturated hydraulic conductivity	LT^{-1}	Eq. 6.2.4.1-2 (6.4.4.3-2)
α(h)	Root-water uptake water stress response function		Eq. 6.2.4.1-3
S_p	Potential water uptake rate	T−1	Eq. 6.2.4.1-3; Eq. 6.2.4.1-4
$b(x)$	Normalized water uptake distribution	L^{-1}	Eq. 6.2.4.1-4
R_{off}	Runoff	L/T	Eq. 6.4-1
P	Precipitation	L/T	Eq. 6.4-1
R_{on}	Run-on	L/T	Eq. 6.4-1
SM	Snowmelt	L/T	Eq. 6.4-1 (6.4.1.4-1)
SF	Snowfall	L/T	Eq. 6.4-1; Eq. 6.4.1.4-2
SUB	Sublimation	L/T	Eq. 6.4-1; Eq. 6.4.1.4-2)
$\Delta\theta$	Change in water storage in the soil	L^3L^{-3}	Eq. 6.4-1
ET	Evapotranspiration	L/T	Eq. 6.4-1 (6.4.4-1)
NI	Net infiltration	L/T	Eq. 6.4-1
P	Precipitation adjusted to an elevation, *elev*	L/T	Eq. 6.4.1.1-1
P_{ref}	Precipitation at the reference elevation, $elev_{ref}$	L/T	Eq. 6.4.1.1-1
$C_{Precipcor}$	Precipitation lapse rate	%change/100m	Eq. 6.4.1.1-1

Symbol	Description	Units	Where Used*
T_{avg}	Average daily air temperature	°C	Eq. 6.4.1.4-1
$C_{snowmelt}$	Snowmelt coefficient	(dimensionless)	Eq. 6.4.1.4-1
$C_{sublime}$	Sublimation coefficient	(dimensionless)	Eq. 6.4.1.4-2
Water level	Volume of water in the layer per unit area	L	Eq. 6.4.2-1 (6.4.2-4; 6.4.2-6; 6.4.4.2-1)
FC	Field capacity	L^3L^{-3}	Eq. 6.4.2-2 (6.4.2-4; 6.4.2-6; 6.4.4.21; 6.4.4.2-2; 6.4.4.2-4)
$Limit_{soil}$	Soil conductivity infiltration limit	L/T	Eq. 6.4.2-3 (6.4.2-4)
duration	Amount of time during the day during which precipitation occurs	T	Eq. 6.4.2-3 (6.4.2-5)
K_{sat_soil}	Saturated conductivity of the soil	L/T	Eq. 6.4.2-3
Drain	Amount of water that moves downward	L/T	Eq. 6.4.2-4
$Limit_{rock}$	Maximum amount of water accepted by the rock	L/T	Eq. 6.4.2-5 (6.4.2-6)
K_{sat_rock}	Saturated hydraulic conductivity of the rock	L/T	Eq. 6.4.2-5
Net infiltration	Amount of water that moves into the underlying bedrock	L/T	Eq. 6.4.2-6
K_e	Soil evaporation coefficient	(dimensionless)	Eq. 6.4.4-1 (6.4.4.1-3; 6.4.4.3-1; 6.5.3.4.1-1)
K_{cb}	Basal transpiration coefficient	(dimensionless)	Eq. 6.4.4-1 (6.4.4.1-1; 6.4.4.1-2; 6.4.4.1-3; 6.4.4.3-2; 6.5.3.4.1-1)
K_s	Water stress coefficient	(dimensionless)	Eq. 6.4.4-1 (6.4.4.2-7; 6.5.3.4.1-1)
ET_0	Reference evapotranspiration	L/T	Eq. 6.4.4-1 (6.4.4.3-1; 6.4.4.3-2; 6.4.5-1; 6.5.3.4.1-1)
u_2	Average daily wind speed at 2 m above ground	m/s	Eq. 6.4.4.1-1 (6.4.4.1-2, Eq. 6.4.5-1)
RH_{min}	Minimum daily relative humidity	(dimensionless)	Eq. 6.4.4.1-1 (6.4.4.1-2)
h_{plant}	Plant height	m	Eq. 6.4.4.1-1 (6.4.4.1-2; 6.4.4.1-3)
$K_{c\ max}$	Maximum basal transpiration coefficient	(dimensionless)	Eq. 6.4.4.1-1 (6.4.4.1-2; 6.4.4.1-3)
f_{ew}	Fraction of soil exposed and wetted	(dimensionless)	Eq. 6.4.4.1-2 (6.4.4.3-5)
f_c	Fraction of surface covered by vegetation	(dimensionless)	Eq. 6.4.4.1-3 (6.4.4.3-5)
K_{c_min}	Minimum basal transpiration coefficient	(dimensionless)	Eq. 6.4.4.1-3
TEW	Total amount of water available for evaporation	mm	Eq. 6.4.4.2-2 (6.4.4.2-3; 6.4.4.2-6; 6.4.4.2-8; 6.4.4.2-9)
θ_{FC}	Field capacity	L^3L^{-3}	Eq. 6.4.4.2-2 (6.4.4.2-4)
θ_{WP}	Wilting point below which vegetation cannot extract moisture from the soil	L^3L^{-3}	Eq. 6.4.4.2-2 (6.4.4.2-4)
Z_e	Surface layer thickness	m	Eq. 6.4.4.2-2
D_e	Depletion of the evaporative node at the end of the previous day	mm	Eq. 6.4.4.2-3 (6.4.4.2-6; 6.4.4.2-8)

Symbol	Description	Units	Where Used*
REW	Readily evaporable water = the maximum depth of water that can be evaporated from the upper soil layer prior to the onset of hydraulic limitations that reduce the rate of water supply below that of energy demands	mm	Eq. 6.4.4.2-3
TAW	Total available water = amount of water available for ET in the root zone	mm	Eq. 6.4.4.2-4 (6.4.4.2-5; 6.4.4.2-7; 6.4.4.2-8; 6.4.4.2-9)
Z_r	Root zone thickness	mm	Eq. 6.4.4.2-4
RAW	Readily available water = the limit of the water in the root zone below which the transpiration rate is affected	mm	Eq. 6.4.4.2-5 (6.4.4.2-7)
p	Fraction of *TAW* that vegetation can remove without suffering stress	(dimensionless)	Eq. 6.4.4.2-5
p_{adj}	Adjusted value of *p*	(dimensionless)	Eq. 6.4.4.2-6
D_r	Root zone depletion	mm	Eq. 6.4.4.2-7 (6.4.4.2-6; 6.4.4.2-8; 6.4.4.2-9)
K_{tie}	Fractional partitioning coefficient	(dimensionless)	Eq. 6.4.4.2-8 (6.4.4.3-3)
D_c	Depletion of the canopy node	mm	Eq. 6.4.4.2-9
K_{tic}	Fractional partitioning coefficient for the canopy region	(dimensionless)	Eq. 6.4.4.2-8 (6.4.4.3-4)
T_e	Daily transpiration from the evaporative node	L	Eq. 6.4.4.3-3 (6.4.4.3-5)
T_c	Daily transpiration from the canopy node	L	Eq. 6.4.4.3-4 (6.4.4.3-5)
$T2$	Transpiration from Layer 2	L	Eq. 6.4.4.3-5
R_n	Net radiation at the crop surface	MJ m^{-2} d^{-1}	Eq. 6.4.5-1
G	Soil heat flux density	MJ m^{-2} d^{-1}	Eq. 6.4.5-1
T	Mean daily air temperature at 2 m height	°C	Eq. 6.4.5-1 (6.5.1.7-1)
u_2	Wind speed at 2 m height	m s^{-1}	Eq. 6.4.5-1
e_s	Saturation vapor pressure	kPa	Eq. 6.4.5-1
e_a	Actual vapor pressure	kPa	Eq. 6.4.5-1
e_s-e_a	Saturation vapor pressure deficit	kPa	Eq. 6.4.5-1
Δ	Slope of the vapor pressure curve	kPa $°C^{-1}$	Eq. 6.4.5-1 (6.5.3.7-8)
γ	Psychrometric constant	kPa $°C^{-1}$	Eq. 6.4.5-1
R_s	Solar radiation on land surface	MJ m^{-2} $d^{-}1$	Eq. 6.4.5.2-1
R_a	Exoatmospheric solar radiation	MJ m^{-2} $d^{-}1$	Eq. 6.4.5.2-1
K_{Rs}	Hargreaves' adjustment coefficient	—	Eq. 6.4.5.2-1
T_{max}	Maximum air temperature	°C	Eq. 6.4.5.2-1
T_{min}	Minimum air temperature	°C	Eq. 6.4.5.2-1
T_{dew}	Dewpoint temperature	°C	Eq. 6.4.5.2-2
K_o	Average offset between T_{dew} and T_{min}	°C	Eq. 6.4.5.2-2
T_{lapse}	Elevation-adjusted daily air temperature for a given grid cell with elevation z_{cell}	°C	Eq. 6.4.5.3-1
z_{cell}	Elevation of the grid cell	m	Eq. 6.4.5.3-1
T_{ref}	Daily air temperature at the reference weather station	°C	Eq. 6.4.5.3-1
z_{ref}	Elevation of the reference weather station	m	Eq. 6.4.5.3-1
LR	Lapse rate	°C per 1,000 m	Eq. 6.4.5.3-1

Symbol	Description	Units	Where Used*
$p_{00}(d)$	Probability that day d is dry, given that day $d-1$ is dry	—	Eq. 6.5.1.2-1
a_{00}	Average annual value of $p_{00}(d)$	(dimensionless)	Eq. 6.5.1.2-1
b_{00}	Annual variability of $p_{00}(d)$	(dimensionless)	Eq. 6.5.1.2-1
θ_{00}	Phase of $p_{00}(d)$	(dimensionless)	Eq. 6.5.1.2-1
$p_{10}(d)$	Probability that day d is dry, given that day d-1 is wet	(dimensionless)	Section 6.5.1.2
$\lambda(d)$	Mean of the lognormal precipitation distribution, given that day d is wet	Ln(mm)	Section 6.5.1.2
$m(d)$	Median of the lognormal precipitation distribution, given that day d is wet	Ln(mm)	Section 6.5.1.2
$T_{md}(d)$	Temperature as a function of day of year	°C	Eq. 6.5.1.2-3
SM	Snowmelt coefficient	mm/day/°C	Eq. 6.5.1.7-1
M	Snowmelt	mm/day	Eq. 6.5.1.7-1
Int	Number of hourly intervals	(dimensionless)	Eq. 6.5.1.7-2 (6.5.1.7-3)
Amt	Amount	mm	Eq. 6.5.1.7-2 (6.5.1.7-3)
K_{bulk}	K_{sat} of the composite bedrock	m/s	Eq. 6.5.2.6-1
f_{vf}	Fracture volume fraction	(dimensionless)	Eq. 6.5.2.6-1
K_{ff}	K_{sat} of the fracture-filling material	m/s	Eq. 6.5.2.6-1
K_m	K_{sat} of the matrix material	m/s	Eq. 6.5.2.6-1
k	Permeability	m^2	Eq. 6.5.2.6-2; (6.5.2.6-3)
b	Hydraulic aperture	L	Eq. 6.5.2.6-2
K_{sat}	Saturated hydraulic conductivity	m/s	Eq. 6.5.2.6-3
ET_{cell}	Actual ET for a model grid cell on a given day	mm	Eq. 6.5.3.4.1-1
PVR	Potential vegetation response developed for each grid cell	(dimensionless)	Eq. 6.5.3.4.1-2
PPT_{YR}	Annual precipitation for the water year of interest	mm	Eq. 6.5.3.4.1-3
C_{Kcb1}	Intercept of the linear function relating NDVI' and K_{cb}	(dimensionless)	Eq. 6.5.3.4.1-4
C_{Kcb2}	Slope of the linear function relating NDVI' and K_{cb}	(dimensionless)	Eq. 6.5.3.4.1-4
T_k	Recurrence interval in years for the k^{th} representative year	yrs	Eq. 6.5.7.5-1
p_k	Probability of occurrence (weight) for year n	(dimensionless)	Eq. 6.5.7.5-1

* Defined in these equations. Equation numbers in parentheses show other equations where these terms are used but not redefined.

INTENTIONALLY LEFT BLANK

7. VALIDATION

Validation requirements for the infiltration model are specified in *Technical Work Plan for: Infiltration Model Assessment, Revision, and Analyses of Downstream Impacts* (BSC 2006 [DIRS 177492]) and SCI-PRO-006, *Models*. Planning and preparation of this report was initiated under the BSC QA Program. Therefore, forms and associated documentation prepared prior to October 2, 2006, the date this work transitioned to the Lead Laboratory, were completed in accordance with BSC procedures. Forms and associated documentation executed after October 2, 2006 were prepared in accordance with Lead Laboratory procedures.

A "Level I" validation is required for the infiltration model because the radiological dose calculated in a previous Total System Performance Assessment (TSPA) was only slightly sensitive to the net infiltration rate (BSC 2003 [DIRS 168796], Section 3.3.1). When net infiltration was increased to be more than an order of magnitude larger than in the net infiltration base case, there was little change to the mean annual dose in the nominal case, and less than a 0.01 mrem increase in the igneous-intrusion case. However, infiltration flux is important to the flow of water in the UZ above and below the repository, to seepage into the repository, and to radionuclide transport in the UZ below the repository. In recognition of this importance, a Level II validation was selected. Level II validation requires that Level I validation items 1 through 6 are satisfied, and requires documentation that demonstrates model predictions are reasonably corroborated by at least two postdevelopment model validation methods described in SCI-PRO-006, Step 6.3.2.

In accordance with the technical work plan (TWP) (BSC 2006 [DIRS 177492]), Section 7 is organized into two main sections: Section 7.1 describes validation activities associated with confidence building during model development; and Section 7.2 presents studies that address postdevelopment model validation. The model validation activities that are included in Section 7 include bullets 1, 2, and 3 from Step 6.3.2 of SCI-PRO-006. Bullet 2 is included to provide additional model corroboration and only indirectly supports model validation because the HYDRUS-1D software is unqualified and therefore cannot directly support model validation (Step 6.2.1 N of SCI-PRO-006). These validation activities are consistent with the TWP with exceptions that are documented in Section 1.4. These validation activities include:

1) *Corroboration of model results with data acquired from the laboratory, field experiments, analog studies, or other relevant observations, not previously used to develop or calibrate the model*. This activity is accomplished by comparing MASSIF results to lysimeter data from NTS and Reynolds Creek, ID; and to streamflow data and to some direct and indirect infiltration estimates from Yucca Mountain. This activity also includes the comparison of modeled precipitation to measured precipitation at Yucca Mountain and analog sites.

2) *Corroboration of model results with other model results obtained from the implementation of other independent mathematical models developed for similar or comparable intended use/purpose*. This activity is accomplished by comparing MASSIF results to HYDRUS-1D results using the same inputs and properties. This is also done in conjunction with the lysimeter data mentioned under validation activity 1.

Since HYDRUS-1D is unqualified software, this model corroboration activity only provides indirect input to model validation.

3) *Corroboration of model results with relevant information published in refereed journals or literature provided that data used to develop and calibrate a model shall not be used to validate a model*. This activity is accomplished by comparing MASSIF results to published results using other models for Nevada and other western states. Additional model corrboration activities were conducted that include an extended parameter sensitivity study, and comparison of MASSIF results to percolation flux predictions made by an expert elicitation panel on UZ flow (CRWMS M&O 1997 [DIRS 100335]).

Inputs to the model validation calculations described in this section are listed in Table 7-1. Inputs to model validation are not required to be qualified and are considered indirect inputs to this model report.

Table 7-1. Indirect Inputs to Model Validation Calculations

Input Data Description	Location in This Model Report	Source
Air temperature data from MEDA 5 for 1994-2004	Section 7.1.2.1	MO0607SEPMED94.000 [DIRS 178079]
Climate Data, Geospatial Information, and Soil Moisture and Property Data for Reynolds Creek Experimental Watershed (RCEW), Idaho	Section 7.1.2.2	SN0608T0502206.020 [DIRS 179875]
NTS lysimeter data	Section 7.1.2	Di Sanza 2006 [DIRS 178797]
RCEW lysimeter data	Section 7.1.2	Marks 2001 [DIRS 177512]
NTS lysimeter elevation, dimensions, soil properties	Section 7.1.2.1	Scanlon et al. 2005 [DIRS 175977]
Locations of the stream gauges near Yucca Mountain	Appendix B, Section 7.1.3	MO0601GSCSPINF.000 [DIRS 177236]
Surface water discharge data collected during water year 1998 from three sites near Yucca Mountain on the NTS	Section 7.1.3	MO0603SEPSTREA.000 [DIRS 179889]
Surface water discharge data collected during water year 1993 from two sites near Yucca Mountain on the NTS	Section 7.1.3	MO0605SEPSURFC.000 [DIRS 179890]
Surface water discharge data for the Yucca Mountain area, Southern Nevada, and Southern California for water year 1995	Section 7.1.3	GS960908312121.001 [DIRS 107375]
Surface water discharge data for the Yucca Mountain area, Southern Nevada, and Southern California for water year 1994	Section 7.1.3	GS941208312121.001 [DIRS 107374]
Locations of Neutron Logging Boreholes	Section 7.2.1.1.3	MO9906GPS98410.000 [DIRS109059]
Infiltration estimates made in Borehole UZ #4	Section 7.2.1.1.2	LeCain et al. 2002 [DIRS 158511]
Location of South Portal	Section 7.2.1.1.1	BSC 2003 [DIRS 165572], p. 15
Location of seepage in south ramp	Section 7.2.1.1.1	Finsterle and Seol 2006 [DIRS 177754], p. 1
Temperature data for 2003	Section 7.2.1.1.1	MO0503SEPMMD03.001 [DIRS 176097]

Table 7-1. Indirect Inputs to Model Validation Calculations (Continued)

Input Data Description	Location in This Model Report	Source
Wind speed data for 2003-2004, temperature data for 2004	Section 7.2.1.1.1	SN0607WEATHER1.005 [DIRS 177912]
Meteorological monitoring data for 2005	Section 7.2.1.1.1	MO0610METMND05.000 [DIRS 178328]
Meteorological Monitoring Data for 2004	Section 7.2.1.1.1	MO0607SEPMMD04.001 [DIRS 178311]
Storage Gauge Precipitation 2005	Section 7.2.1.1.1	MO0605SEPSGP05.000 [DIRS 178663]
Measured Soil Depth	Section 7.2.1.1	MO0004QGFMPICK.000 [DIRS 152554]
Measured Soil Depth	Section 7.2.1.1	MO0012MWDGFM02.002 [DIRS 153777]
Measured Soil Depth	Section 7.2.1.1	GS910808312212.001 [DIRS 175972]
Expert elicitation results	Section 7.2.3	CRWMS M&O 1997 [DIRS 100335], Table 3-2

The results or outputs of the model validation calculations are documented in a variety of ways. Model validation calculations using the MASSIF model are included in the folder: \Welcome to Massif\Massif\Validation Analyses, which is part of Output DTN: SN0701T0502206.037. Validation analyses related to the extended parameter sensitivity study (Section 7.1.4) is documented as part of Output DTN: SN0701T0502206.044. Other validation related analyses (e.g., analyses using HYDRUS-1D software, and comparison of precipitation records) are documented in unqualified data DTNs that are referred to as Validation Output DTNs. These DTNs are not considered to be Qualified upon completion of the AMR. In all cases, validation output DTNs are referenced in the text and figures that explain the validation calculations.

7.1 CONFIDENCE BUILDING DURING MODEL DEVELOPMENT

Confidence building during model development is described in this section for each of the primary components in the infiltration model. The primary components that contribute to the mass-balance calculation for infiltration in each cell of the model are depicted in Figure 7.1-1 and include precipitation, evapotranspiration (ET), storage, run-on, and runoff. The following sections detail the technical approach and basis for each of these components.

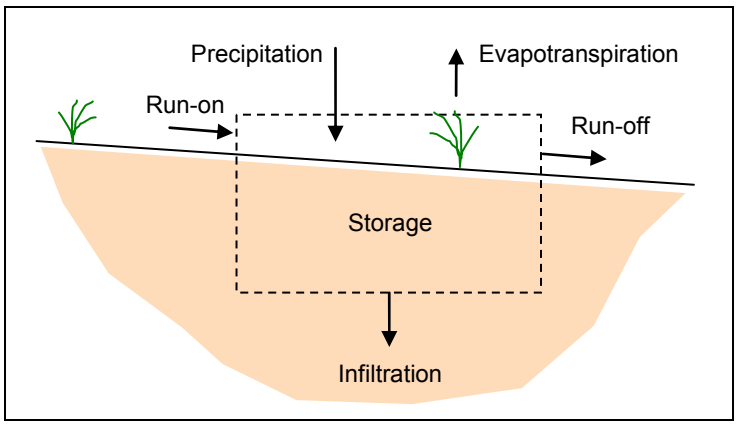

Figure 7.1-1. Control Volume for Mass-Balance Calculation of Infiltration

7.1.1 Precipitation

Existing weather records cover less than 100 years. There is no a priori assurance that a sample of so few years for a given climate will adequately represent average infiltration over hundreds or thousands of years. In order to capture the full range of uncertainty, the performance assessment must assure that rare events have been considered. Therefore, rather than use the meteorological records directly as input, this analysis used the records to characterize each record in terms of periodic functions and additional parameters. Periodic functions summarize the records of precipitation, temperature, and wind speed at a meteorological station.

Sections 7.1.1.1 and 7.1.1.2 describe the development of Fourier series parameters to simulate long-term precipitation. Sections 7.2.1.1.3, 7.2.1.1.4, and 7.2.1.1.5 compare actual precipitation data to the abstraction of precipitation data using Fourier series parameters for Present-Day, Monsoon, and Glacial Transition climates, respectively.

7.1.1.1 Comparison of Seasonal Precipitation Patterns

This section presents a comparison of monthly average precipitation measured at selected weather stations with monthly average precipitation from the 1,000-year stochastically-generated precipitation records for selected weather sites using the truncated Fourier series (one-harmonic). In addition, to provide a basis for comparison, the 1,000-year generated precipitation record for a two-harmonic truncated Fourier series is also presented. Adding another harmonic will always improve the fitting, however it also results in more parameters that need to be estimated. In addition, since each climate representation is based on weather records from several stations (rather than one) and these stations differ considerably in their precipitation seasonality, there is no meaningful way to combine parameters for the two-harmonic Fourier series such that they represent the suite of precipitation records from all stations. For this reason a single harmonic representation was used for representing precipitation patterns for each climate. Two sites for each of the three climate states predicted to occur at Yucca Mountain (Present-Day, Monsoon, and Glacial Transition climates) during the next 10,000 years are shown. The sites for the Present-Day climate are Yucca Mountain weather station Site 2 and NTS Station A12; for the Monsoon climate, Hobbs, NM and Nogales, AZ; and for the Glacial Transition climate, Spokane, WA and Delta, UT.

Figure 7.1.1.1-1(a) shows a comparison of recorded average monthly precipitation from the Yucca Mountain Site 2 weather station versus average monthly precipitation of 1,000-year generation using a one-harmonic truncated Fourier series. Figure 7.1.1.1-1(b) shows the same comparison using a two-harmonic truncated Fourier series. In this example, the two-harmonic estimate does little to improve the fit. This is because the annual precipitation pattern is characterized by a single wet and dry period rather than a two wet and dry periods during the year.

The comparison of NTS Station A12 average monthly precipitation record versus the 1,000-year generated precipitation using a one-harmonic truncated Fourier series is shown in Figure 7.1.1.1-2(a). The one-harmonic here captures the general trend of the precipitation but not as well as in the Site 2 case. The reason is that NTS Station A12 experiences a four-season trend variation that cannot be captured with only one harmonic. The two harmonic brings

significant improvement in allowing the capture of four seasons. As was the case for Site 2, the two-harmonic does a better job of more closely fitting the A12 data.

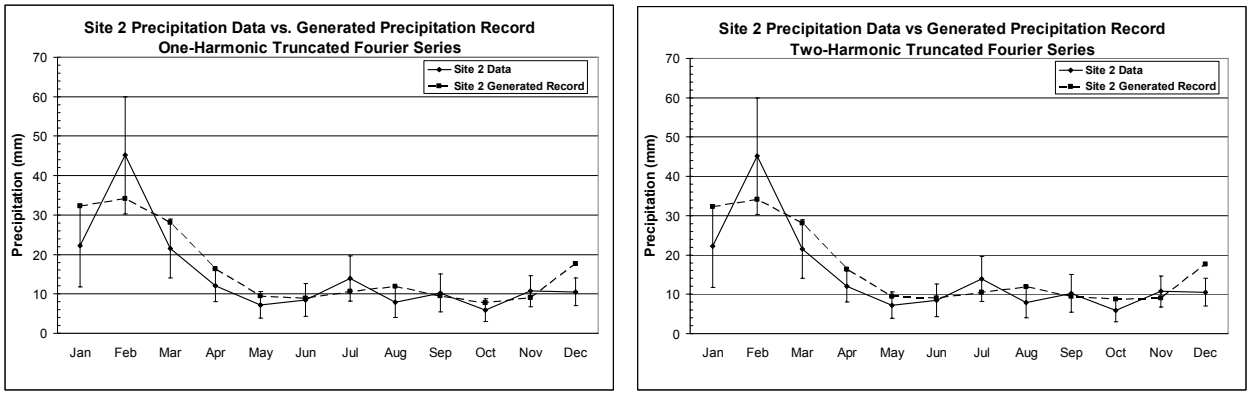

(a) (b)

Source: Validation Output DTN: SN0701T0502206.045.

Figure 7.1.1.1-1. Average Monthly Precipitation Comparison Between Observed Records and 1,000-Year Generation for Yucca Mountain Site 2: (a) Using Second Order (one-harmonic truncated) Fourier Series and (b) Using Third Order (one and two harmonics) Truncated Fourier Series

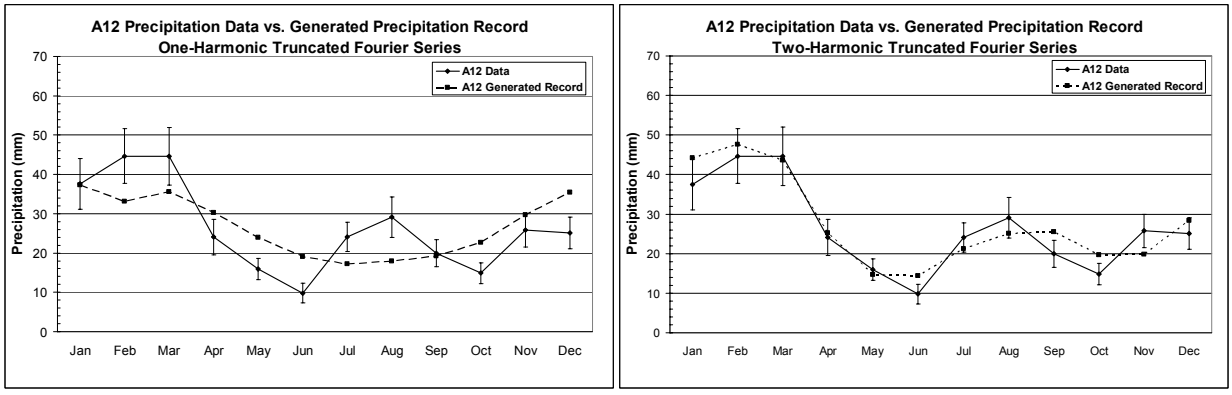

(a) (b)

Source: Validation Output DTN: SN0701T0502206.045.

Figure 7.1.1.1-2. Average Monthly Precipitation Comparison Between Observed Records and 1,000-Year Generation for Site A12: (a) Using Second Order (one-harmonic truncated) Fourier Series and (b) Using Third Order (one and two harmonics) Truncated Fourier Series

Monthly precipitation comparison for the upper-bound Monsoon analog site of Hobbs, NM is shown in Figure 7.1.1.1-3. In this case, recorded data shows a two-seasons behavior: a one-harmonic curve fits this behavior very well, as Figure 7.1.1.1-3(a) shows. Applying a two harmonic correction does not improve the fit significantly (Figure 7.1.1.1-3(b).

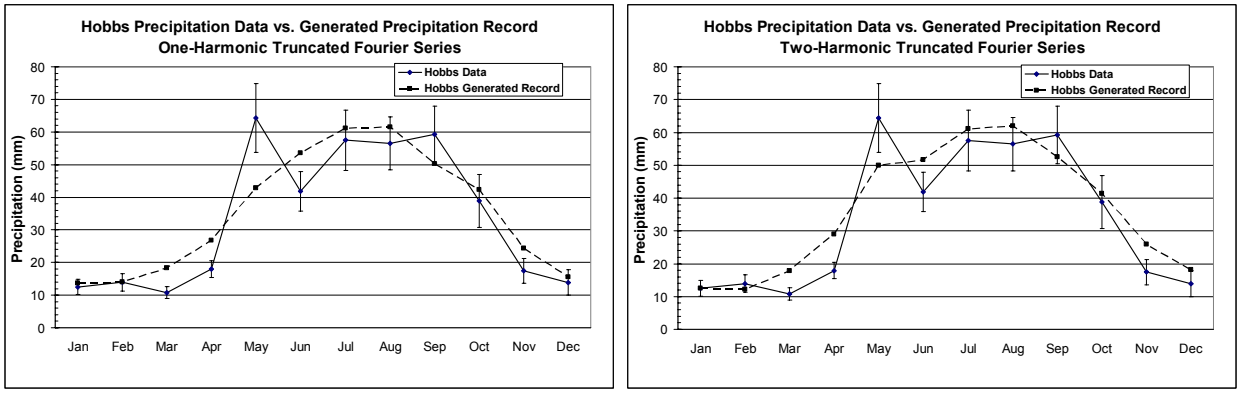

(a) (b)

Source: Validation Output DTN: SN0701T0502206.045.

Figure 7.1.1.1-3. Average Monthly Precipitation Comparison Between Observed Records and 1,000-Year Generation for Hobbs (NM): (a) Using Second Order (one-harmonic truncated) Fourier Series and (b) Using Third Order (one and two harmonics) Truncated Fourier Series

The data for the upper-bound Monsoon analog site of Nogales, AZ is shown in Figure 7.1.1.1-4. This Monsoon analog site has a more pronounced monsoon pattern that strongly spikes in July and August. The monthly average precipitation based on 1,000-year generated record using the one-harmonic truncated Fourier series does not provide a close match to the actual data. The limit is again due to the use of only one harmonic to represent a non-sinusoidal function. Adding a two-harmonic correction provides a significant improvement. It is important, however, to point out that Nogales site parameters are not directly used in our model but are first aggregated with the other representative site Hobbs, NM, which is matched quite well with a one-harmonic model.

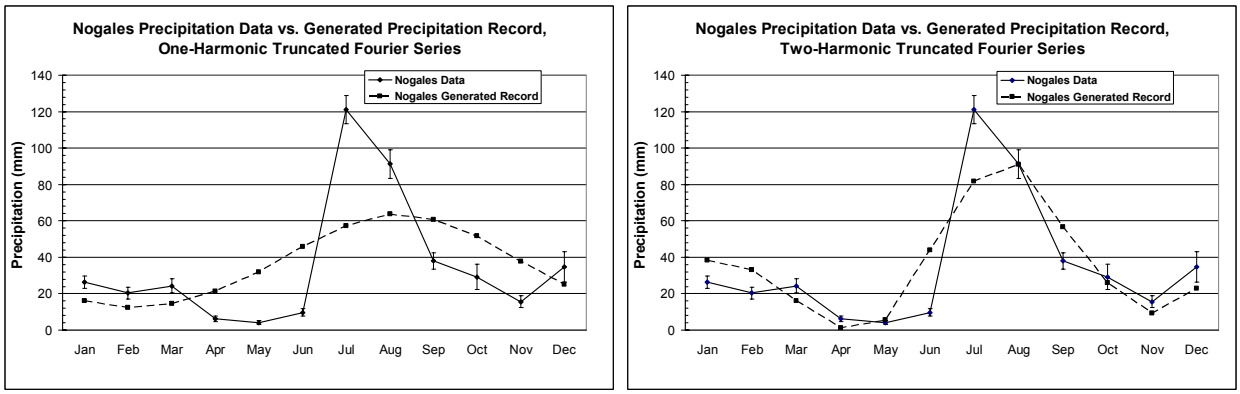

(a) (b)

Source: Validation Output DTN: SN0701T0502206.045.

Figure 7.1.1.1-4. Average Monthly Precipitation Comparison Between Observed Records and 1,000-Year Generation for Nogales (AZ): (a) Using Second Order (one-harmonic truncated) Fourier Series and (b) Using Third Order (one and two harmonics) Truncated Fourier Series

The comparison of site data for average monthly precipitation records at Spokane, WA (one of the upper-bound Glacial Transition analog site) versus the average monthly precipitation estimated from 1,000-year generated precipitation using one and two-harmonic truncated Fourier series is shown in Figure 7.1.1.1-5. The one-harmonic (a) fits the site data very well. The two-harmonic (b) correction provides a slightly improved fit.

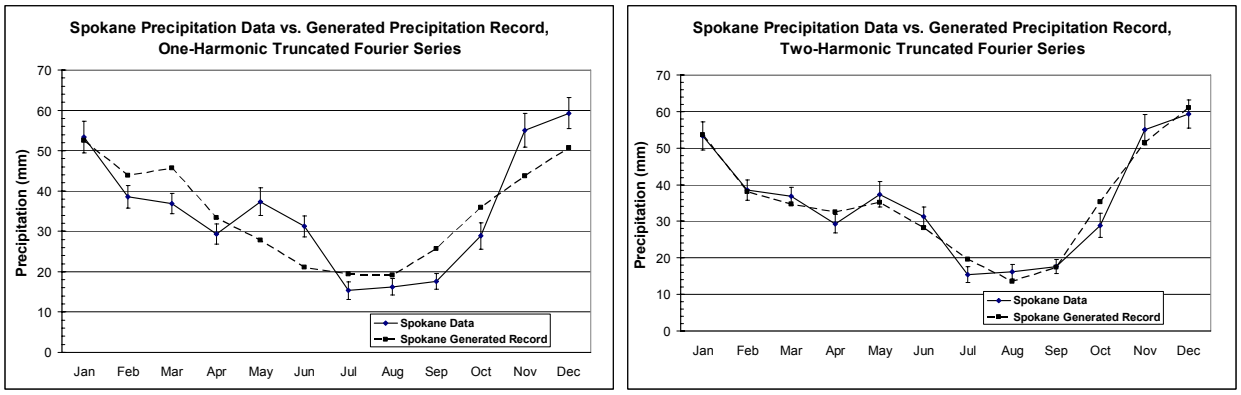

(a) (b)

Source: Validation Output DTN: SN0701T0502206.045.

Figure 7.1.1.1-5. Average Monthly Precipitation Comparison Between Observed Records and 1,000-Year Generation for Spokane (WA): (a) Using Second Order (one-harmonic truncated) Fourier Series and (b) Using Third Order (one and two harmonics) Truncated Fourier Series

The average monthly precipitation record at Delta, UT (lower-bound Glacial Transition analog site) is shown in Figure 7.1.1.1-6. Delta experiences a four-season variation with respect to precipitation, similar to the pattern at NTS Station A12 (see Figure 7.1.1.1-2). The monthly precipitation based on only one harmonic does not provide a good fit, and only a two-harmonic correction allows a good representation of monthly variation. As discussed for Nogales data, it is important to note that the parameters are aggregated with parameters fitted to other sites (e.g. Spokane), for which the one-harmonic fit is very good.

Adding another term to the Fourier series will always gives a better fit, as this additional term accounts for the residual between the Fourier series and the actual data. For half of the selected sites, precipitation records show a two-seasons variation over the year (on average), and a one-harmonic truncated Fourier series fits the data well. The second harmonic correction gives significant improvement when the selected site presents distinct four-season variations (see Figure 7.1.1.1-2 and Figure 7.1.1.1-6) or a strong gradient of differences for a period (see Figure 7.1.1.1-5).

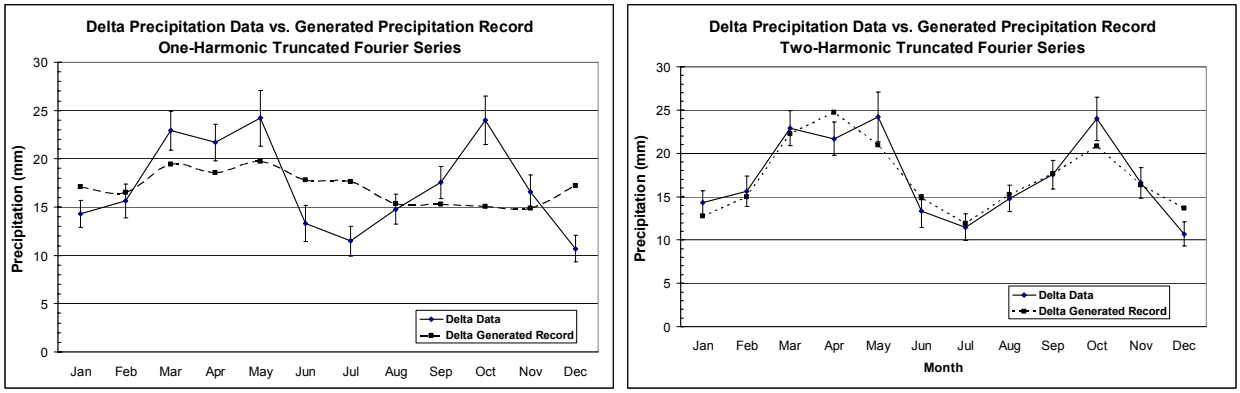

(a) (b)

Source: Validation Output DTN: SN0701T0502206.045.

Figure 7.1.1.1-6. Average Monthly Precipitation Comparison Between Observed Records and 1,000-Year Generation for Delta (UT): (a) Using Second Order (one-harmonic truncated) Fourier Series and (b) Using Third Order (one and two harmonics) Truncated Fourier Series

There is a cost of adding an additional harmonic in order to improve these fits. Four quantities are considered in our Markov Chain Monte Carlo (MCMC) model: p_{00} (probability that current day is dry knowing that previous day is dry), p_{10} (probability that current day is dry knowing that previous day is wet), λ (expected infiltration for a wet day) and m (median infiltration for a wet day). A new harmonic adds two parameters (an amplitude parameter b_i and a phase parameter θ_i) for each of the quantities, so eight new parameters are added. Several sites are used to represent the uncertainty on annual precipitation for each climate (10 for Present-Day climate, the same 10 plus 2 more for Monsoon climate, and 5 for Glacial Transition climate). The representation of uncertainty consists of aggregating each of these parameters. The value of attempting to aggregate the eight parameters representing the second harmonic is outweighed by the ambiguous and nonphysical meaning of the additional parameters. An attempt to add such complexity is considered to be unwarranted.

Moreover, each parameter has a physical meaning up to the first harmonic:

- a represents the average value of the quantity over the whole year (Appendix F, Section F1.1.2)
- b_1 represents the amplitude of (seasonal) variation of the quantity during the year
- θ_1 is the phase shift. In other words, it controls the date when the maximum value is obtained during the year.

The second harmonic parameters do not have a direct physical meaning because they represent a correction on the residual.

Therefore, it was decided to limit the representation of daily precipitation over the year with a 2nd order Fourier series (the average and one harmonic). The estimate reasonably represents the variation of daily precipitation over the year.

7.1.1.2 Comparison of Mean Annual Precipitation (MAP)

Section 7.1.1.3 to 7.1.1.5 present comparisons between the distribution of MAP measured at weather stations used to represent each climate state against distributions of MAP from the 1,000-year stochastic simulations for each climate.

Annual precipitation at Yucca Mountain for future climates is an uncertain quantity. In order to represent the possible future precipitation at the site, several representative sites have been selected for each climate. Each site has a different average annual precipitation record, representing the uncertainty.

In order to capture this uncertainty, each site has been first represented using 12 parameters. The variation of each parameter has been studied in order to determine whether this variation was significant (and should be taken into account) or not. Significant parameters were associated with a distribution and were sampled from this distribution using Latin Hypercube Sampling (a Monte Carlo technique).

Two (independent) samples of size 20 were created and used to estimate average annual precipitations. In order to verify that the distribution of average annual precipitation defined with the representative sites was captured correctly, they were compared with the distribution of average annual precipitation derived from these sites records.

Box-plots are a convenient way to represent distributions that allows easy comparison. They give a good summary of common statistics (mean, median, percentile) as well as distribution shape. The construction of a typical box-plot is shown in Figure 7.1.1.2-1.

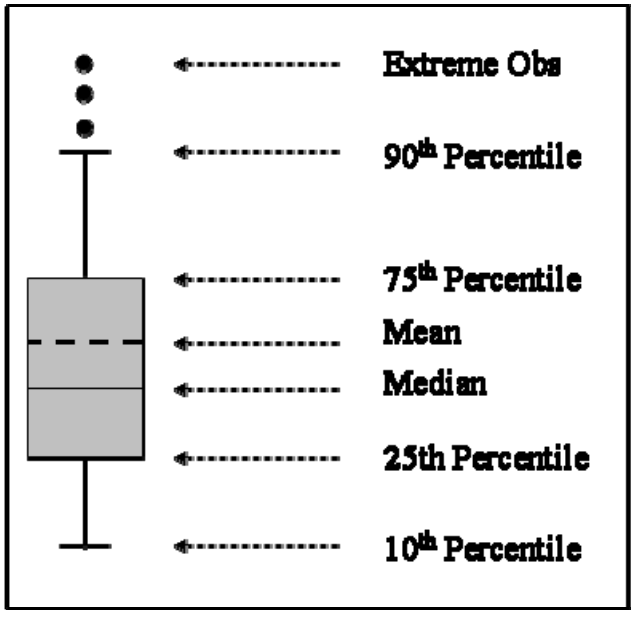

Figure 7.1.1.2-1. Theoretical Representation and Interpretation of a Box-Plot

7.1.1.3 Present-Day Precipitation Comparison

Sites used for representing Present-Day climate variations are located at different elevations. Elevation plays an important role in the amount of precipitation, and a direct comparison with raw data would not be appropriate (leftmost box-plot in Figure 7.1.1.3-1). The reference elevation applied to MASSIF is the top of Yucca Mountain (1,524 m). Parameters have first been adjusted to be more representative of average annual precipitation at the reference elevation (see second box-plot in Figure 7.1.1.3-1).

The third and fourth box-plots in Figure 7.1.1.3-1 provide a representation of annual precipitation distribution obtained with first and second set of replicate samples, respectively.

The last three box-plots of Figure 7.1.1.3-1 are similar enough to have good confidence that annual precipitation is correctly represented for Present-Day climate. Mean and median values are almost identical for all three boxes.

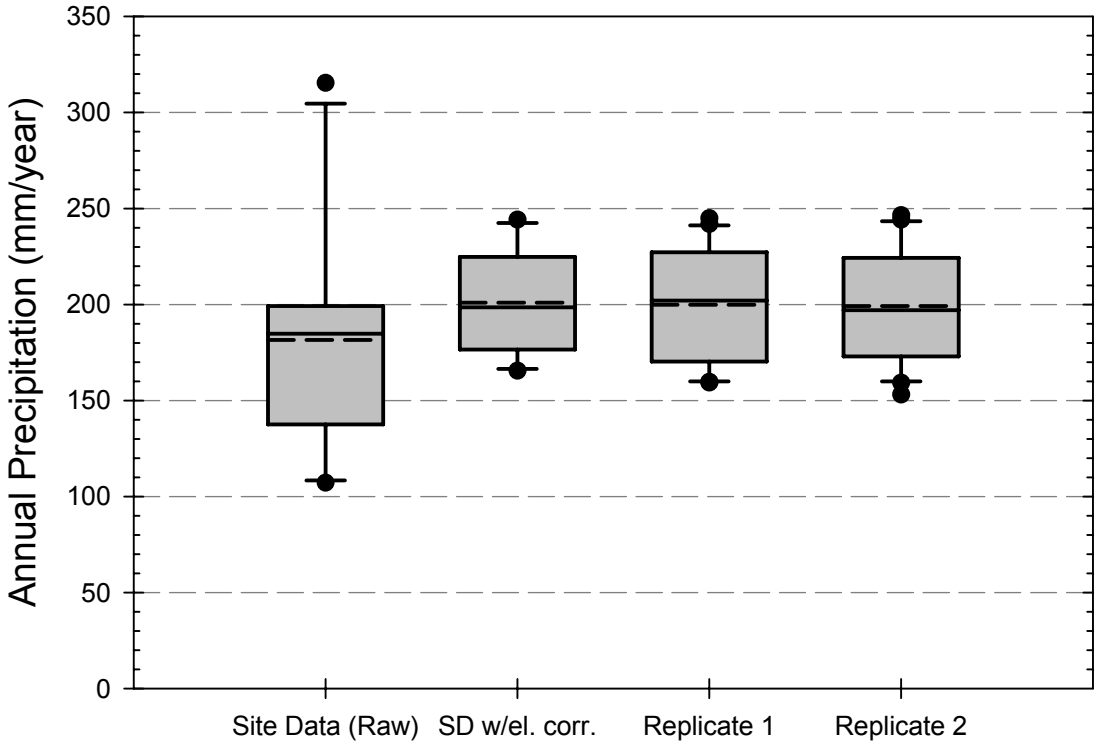

Source: Validation Output DTN: SN0701T0502206.045.

Figure 7.1.1.3-1. Box Plots Comparing Distribution of Observed Annual Precipitation from Representative Sites and Replicated Samples that Estimate Annual Precipitation for Present-Day Climate

7.1.1.4 Monsoon Precipitation Comparison

The Monsoon climate data includes the ten Present-Day climate sites as lower bounds and two sites (Hobbs, NM and Nogales, AZ) as upper bounds for annual precipitation representation. The two upper-bound sites are considered to be representative of the weather at the top of Yucca Mountain and therefore, do not need to be adjusted for elevation.

Even if their average annual precipitation is similar, the two upper-bound sites have different behavior over the year: Hobbs features a longer but less intense monsoonal period, while Nogales presents a shorter (2 months) but more intense monsoonal period (see Figures 7.1.1.1-3 and 7.1.1.1-4).

The aggregation of the two sites is thus a non-trivial issue. According to *Future Climate Analysis* (BSC 2004 [DIRS 170002]), the Hobbs and Nogales sites may underestimate annual precipitation for a monsoon climate identical to that of Owen's Lake (used as reference), so it was decided to consider the combination of parameters from Hobbs and Nogales giving the highest annual precipitation (a longer and more intense monsoonal period). This combination of parameters allows generating an average annual precipitation amount that is higher than either of the two upper bound sites.

Figure 7.1.1.4-1 presents the comparison of the range of uncertainty defined by Present-Day sites (first box) and upper-bound monsoon sites (Column 2) with the two samples of size 20 used to represent uncertainty in annual precipitation for the monsoon climate. About 75% of the data are within the range defined by the lower and upper bound of the monsoon climate representation shown in the last two boxes in Figure 7.1.1.4-1, with a mean and median around 300 mm/yr. Twenty-five percent of the data increases the range up to 580 mm/yr.

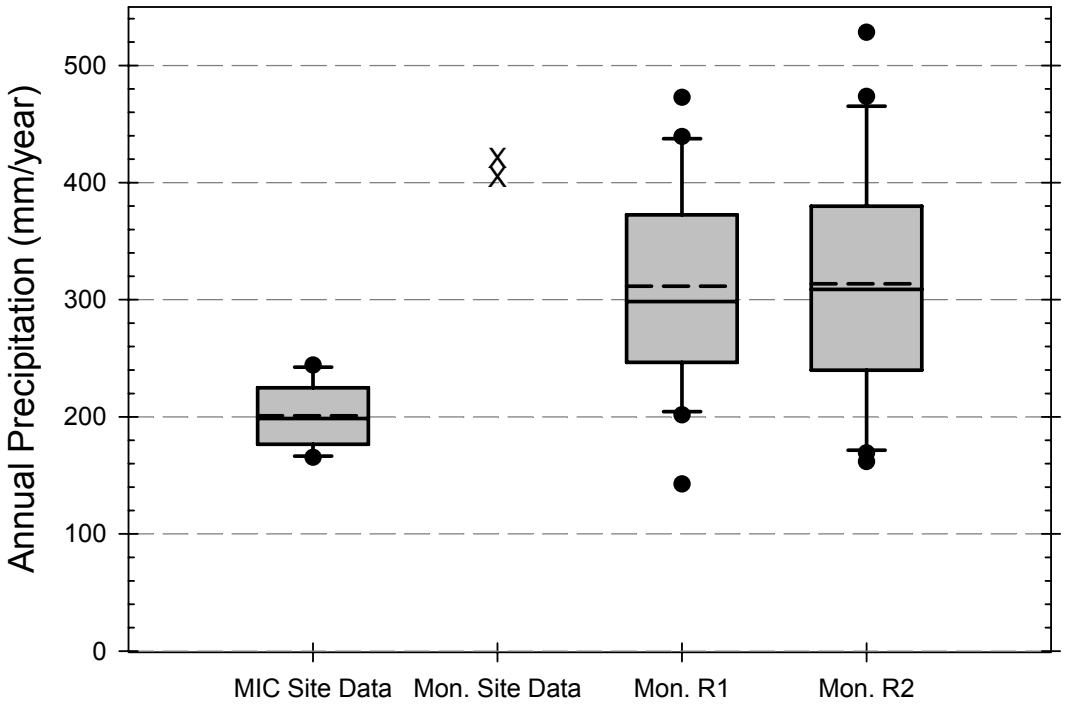

Source: Validation Output DTN: SN0701T0502206.045.

Figure 7.1.1.4-1. Box Plots Comparing Distribution of Observed Annual Precipitation from Representative Sites and Replicated Samples that Estimate Annual Precipitation for Monsoon Climate (MC). "MIC Site Data" Refers to Present-Day Climate Stations Adjusted for Elevation.

7.1.1.5 Glacial Transition Precipitation Comparison

The Glacial Transition climate data includes only two sites for lower-bound and three sites for upper-bound precipitation representations (see the five X's on the left part of Figure 7.1.1.5-1). Both sites are considered to be representative of future weather at the top of Yucca Mountain and therefore do not need to be adjusted for elevation. Distributions of mean annual precipitation based on the estimation of parameter uncertainty cover most of the range defined by the five bounding sites.

The average value for both replicates is almost identical and is close to the mid-point value of the average of the two low-bound sites annual precipitation and the three upper-bound sites annual precipitations. Therefore, this model gives a reasonable representation of uncertainty in annual precipitation for the Glacial Transition climate.

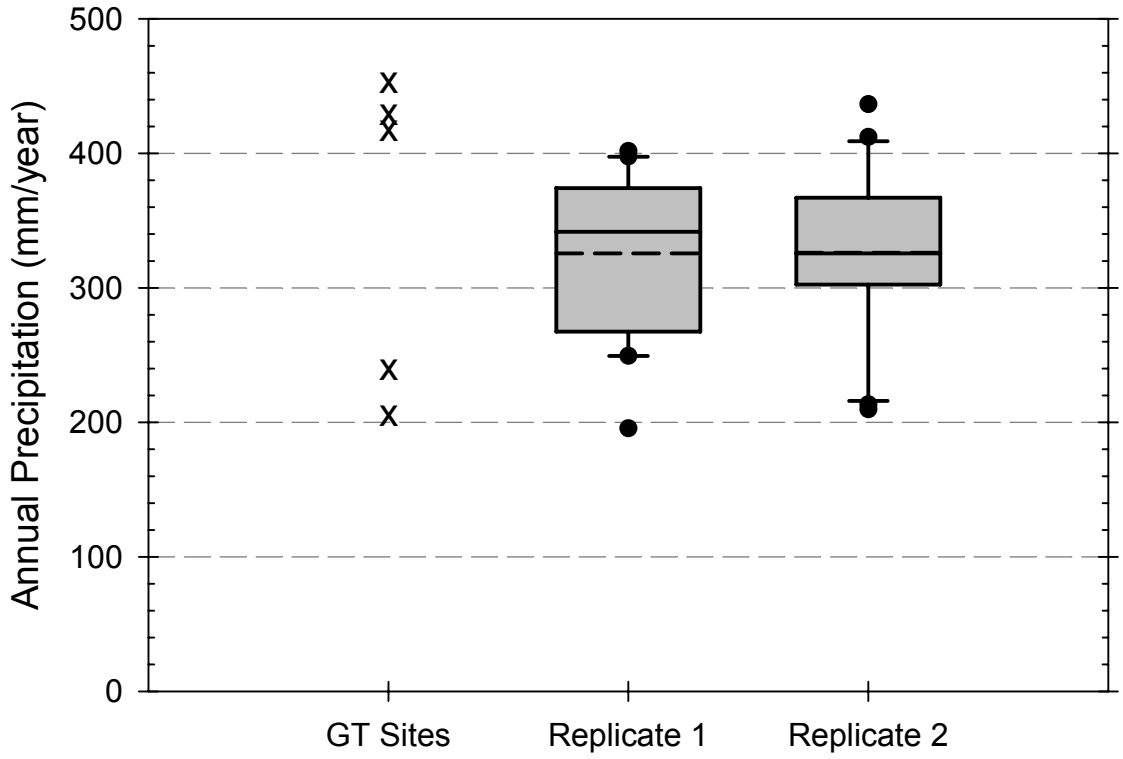

Source: Validation Output DTN: SN0701T0502206.045.

Figure 7.1.1.5-1. Plots Comparing Distribution of Observed Annual Precipitation from Representative Sites and Replicated Samples that Estimate Annual Precipitation for Glacial Transition Climate (GT).

7.1.2 Evapotranspiration and Storage

The ability of the MASSIF model to simulate daily actual ET and changes in daily soil water storage was evaluated by comparing MASSIF output to long-term observation data collected at lysimeter facilities at the NTS (Desotell et al. 2006 [DIRS 176858]), and at Reynolds Creek Experimental Watershed (RCEW) (Marks 2001 [DIRS 177512]). These lysimeter sites provide detailed water balance data that are especially valuable for evaluating model performance. The first lysimeter site is located near the Area 5 Radioactive Waste Management Site (RWMS) within the NTS and represents an analog to the present-day climate conditions at the Yucca Mountain. The second site is located within the RCEW in southwestern Idaho and represents a potential analog to the future glacial transition climate at Yucca Mountain. The climate at the RCEW is actually wetter and cooler than at Spokane, an analog site for the upper limit of the glacial transition conditions. RCEW was selected for this validation study because it represents significantly different conditions in terms of climate, soils, and vegetation from those at Yucca Mountain. Consequently, the model validation ranges can be extended as well.

The ability of MASSIF to simulate these data records provides additional model validation to establish confidence that the MASSIF mathematical model and its underlying conceptual model adequately represent with sufficient accuracy the phenomenon and processes in question as required by SCI-PRO-006. Validation includes corroboration of model results with data acquired from two analog sites, and corroboration of model results with other model results obtained from the implementation of mathematical models (the results from an alternative mathematical model incorporated using HYDRUS-1D code are discuss in Section 7.2.2). The summary of this validation activity is provided in this Section. Additional details are provided in Appendix J.

The primary purpose of weighing lysimeters is to estimate daily actual ET based on measured precipitation and observed changes in the lysimeter storage. The lysimeters are installed such that surface water run-on and runoff are removed from the water balance. Consequently, the daily water balance of such a lysimeter can be described using the following equation (Fetter 2001 [DIRS 156668], p. 31, Equation 2.1):

$$ET = P - \Delta S - D \qquad \text{(Eq. 7.1.2-1)}$$

where ET is daily actual ET, P is measured daily precipitation, ΔS is the observed daily change in the lysimeter storage (increase or decrease in storage with regard to the storage observed during the previous day), and D is the excess moisture drained from the soil. In cases when the lysimeter is sealed at the bottom, no drainage occurs, and D is equal to 0.

According to Equation 7.1.2-1, the ability to reproduce the observed changes in daily storage is equivalent to the ability to reproduce the actual daily ET in the absence of drainage. The longer the period of time over which the changes in storage are closely reproduced, the greater is the confidence in the ability of the model to adequately simulate the physical processes affecting actual ET.

The long-term observations required for good model evaluation and testing are available for both lysimeter sites. The description of the sites and the results of modeling are summarized below. The details of the modeling setup and simulations are presented in Appendix J. No drainage was observed from the NTS lysimeters. There was some small drainage from the RCEW lysimeters, but the timing and exact quantities of the drainage are not known. All files used for these simulations using MASSIF are located in \Welcome to Massif\Massif\Validation Analyses/Lysimeter within MASSIF (Output DTN: SN0701T0502206.037).

7.1.2.1 Lysimeter Simulations at the Nevada Test Site

Two weighing lysimeters were installed in Area 5 RWMS of the NTS in 1994 to conduct water balance studies. The lysimeters are located in northern Frenchman Flat (northern part of Mojave Desert). The lysimeter coordinates are: 36º 51' 9.13" (latitude) and 115º 56' 56.06" (longitude), and the lysimeter site elevation is 976 m (Scanlon et al. 2005 [DIRS 175977]).

There are a number of studies where the NTS lysimeter data were used for various water balance analyses, including calibration of flow models. The results of these studies are reported by Desotell et al. (2006 [DIRS 176858]), Scanlon et al. (2005 [DIRS 175977]), Levitt et al. (1999 [DIRS 177521]), and Levitt et al. (1996 [DIRS 163183]).

The long-term mean annual precipitation in this area reported by Desotell et al. (2006 [DIRS 176858]) is 125 mm. The mean annual precipitation calculated using the lysimeter data is 125.5 mm (Di Sanza 2006 [DIRS 178797], *NTSLysimeter.xls*), which is close to the long-term average. The mean annual temperature during the period of observation was 15.7ºC (DTN: MO0607SEPMED94.000 [DIRS 178079]). In only 1.3% of the observation time was the mean daily temperature below 0ºC. The average daily wind speed during the period of observation was 2.8 m/s (see Appendix J for details).

One lysimeter is vegetated with the creosote bush, four-wing salt bush, and annual grasses at the approximate density of the surrounding landscape (Desotell et al. 2006 [DIRS 176858]). Another lysimeter is maintained under the bare soil conditions. Each lysimeter is a 2-m by 4-m by 2-m deep steel tank filled with native alluvium at a bulk density of about 1.5 kg/m^3 (Scanlon et al. 2005 [DIRS 175977]). The alluvium was classified as a well- to poorly-graded sand with silt and gravel (Unified Soil Classification System) with approximately 70% sand, 20% gravel, and 10% fines. A schematic of one lysimeter is shown in Figure 7.1.2.1-1 (from Figure 7 in supporting information to Scanlon et al. 2005 [DIRS 175977]).

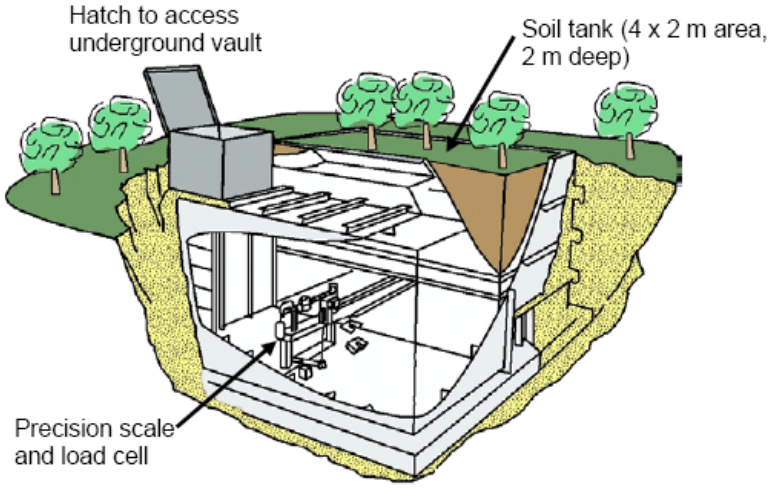

NOTE: Figure is reproduced from Figure 7 in supporting information to Scanlon et al. 2005 [DIRS 175977].

Figure 7.1.2.1-1. Schematic of one NTS Weighing Lysimeter

Eighteen core samples were collected throughout the lysimeter depth profile in 10-cm increments. The measured soil hydraulic properties are reported by Desotell et al. (2006 [DIRS 176858]) and include:

- Saturated hydraulic conductivity (geometric mean): 14 cm/hr
- Residual moisture content: 0.04 m^3/m^3
- Porosity: 0.357 m^3/m^3
- van Genuchten parameter alpha: 0.0328 cm^{-1}
- van Genuchten parameter n: 1.57.

Based on these parameters, the field capacity is 0.117 m^3/m^3 (calculated using pressure of -1/3 bar), and wilting point is 0.044 m^3/m^3 (calculated using pressure of -60 bars). Since a higher pressure may be more appropriate for the coarse grained textured soils (up to -1/10 bars) than the pressure of -1/3 bars (medium textured soils), the bare soil lysimeter storage data were analyzed during periods with heavy precipitation over a few or more consecutive days. The largest storage value was 277.3 mm. This corresponds to the moisture content of 0.139 m^3/m^3 and a pressure of -2/10 bars. This is consistent with the pressure range of -1/3 bars to -1/10 bars at which field capacity is calculated.

The lysimeter storage observations are available for the period of time from March 3, 1994 until December 31, 2004 from Di Sanza 2006 [DIRS 178797]. However, the vegetated lysimeter was irrigated for about 6 months to establish the vegetation cover and the irrigation rates are not available, and it took about 1.5 years for the transplanted vegetation to equilibrate with moisture conditions in the lysimeter box. Consequently, the period of observations for the vegetated lysimeter was considered from October 1, 1995 until December 31, 2004. The MASSIF model can be run only for a whole number of the water years. To satisfy this requirement, the bare soil lysimeter observations used began on October 1, 1994. Figure 7.1.2.1-2 shows the observation data and precipitation data for the NTS lysimeter site.

Analysis of precipitation data (see Appendix J for details) showed that 5% (bare soil lysimeter) to 10% (vegetated lysimeter) of observations have daily increases in storage that exceed daily precipitation. The maximum difference between the storage increase and precipitation was about 4 mm. Most of these observations are related to the high intensity precipitation events. Raingages are subject to under-measurement caused by (1) splash out of drops, (2) blow-by of drops due to venturi effects, and (3) evaporation of intercepted drops along the sides of the collector (Sevruk 1992 [DIRS 177480]). Consequently, some of the differences between precipitation data and lysimeter gains may have been caused by under-measurement by the precipitation gauge. The inaccuracy in precipitation measurements could be at least 4 mm. Since the ET is calculated as the difference between precipitation and storage, the 4-mm error in precipitation measurement will result in the corresponding error in the ET estimate.

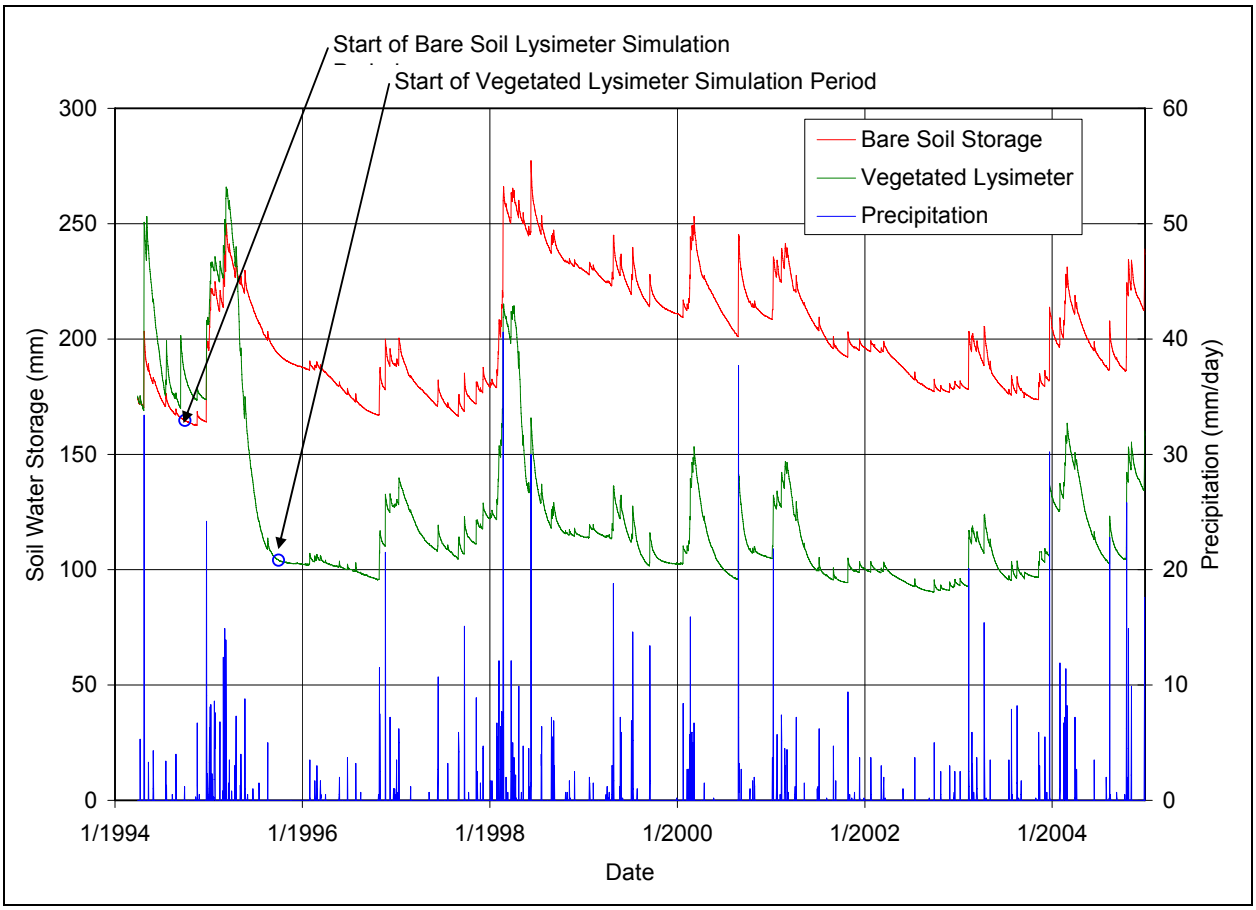

Source: Di Sanza 2006 [DIRS 178797]; compiled in Output DTN: SN0701T0502206.037, file: \Welcome to Massif\Massif\Validation Analyses\Lysimeter*NTSLysimeter.xls*.

Figure 7.1.2.1-2. Observed Daily Water Storage and Precipitation at the NTS Lysimeter Site

The MASSIF input parameters for the lysimeter simulations were defined in accordance with NTS site-specific information, when available. For certain parameters, NTS site-specific data were not available and parameter values were estimated using an inverse modeling approach described below and in Appendix J. The following MASSIF parameters cannot be specified based on the data available for the NTS lysimeter site:

- Diffusive evaporation parameter, K_{c_min}
- Canopy fraction, f_c
- C_{kcb} coefficient representing the slope of the NDVI-K_{cb} regression line (see Appendix E for details)

The values of these three parameters were estimated by minimizing the difference between the observed and calculated storages in both lysimeters. The following objective function $F1_{obj}$ was used in the conjugate gradient minimization procedure in MathCAD.

$$F1_{obj}(K_{c\_min}, f_c, C_{kcb}) = [\sum(BS^{obs}_i - BS^{cal}_i)^2 + \sum(V^{obs}_j - V^{cal}j)^2]/(N_{bs}+N_v) \quad \text{(Eq. 7.1.2.1-2)}$$

$$i=1, N_{bs} \text{ and } j=1, N_v$$

where BS^{obs}_i and BS^{cal}_i are observed and calculated bare soil lysimeter storage during the simulation day i; V^{obs}_j and $V^{cal}j$ are observed and calculated vegetated lysimeter storage during the simulation day j; N_{bs} is the number of days in the bare soil lysimeter data set; and N_v is the number of days in the vegetated lysimeter data set. As it was explained above, the bare soil lysimeter data set is from 10/01/1994 to 12/31/2004 (N_{bs}= 3745), and the vegetated lysimeter data set is from 10/01/1995 to 12/31/2004 (N_v= 3380).

In calculating bare soil lysimeter storage, the transpiration parameters p (depletion factor for computing readily available water), C_{kcb}, and f_c were set to zero to represent bare soil conditions. In calculating vegetated lysimeter storage, parameter p was set to 0.65 (see Section 6.3.3 and 6.3.4) and C_{kcb} and f_c were the objective function parameters as defined by Equation 7.1.2.1-2.

The results of the minimization are:

- $K_{c\_min} = 0.0135$
- $f_c = 0.26$
- $C_{kcb} = 2.4$
- $F1_{obj} = 137.92$ mm^2

Based on the obtained objective function value, the overall goodness of fit is 11.74 mm for both lysimeters. The estimated parameter values were used to calculate the root mean square errors for each lysimeter. The calculated mean root square errors are 11.63 mm and 11.87 mm (or about 9% of the mean annual precipitation) for the bare soil and vegetated lysimeters, respectively. Taking into account that the possible inaccuracy in storage measurements is at least 4 mm, the obtained goodness of fit is reasonable for both lysimeters. These root mean square errors are comparable to the ones reported by Desotell et al. (2006 [DIRS 176858]). The NTS lysimeters were modeled by Desotell et al. 2006 [DIRS 176858]) with UNSAT-H (Fayer 2000 [DIRS 177499]), which is a soil physics based code similar to HYDRUS-1D (see Sections 6.2.4.1, and 7.2.2) in its capability to model variably-saturated flow, except it allows for simulating vapor phase. Mean root square errors reported are 12 mm (bare soil) and 4 mm (vegetated). However, in order to obtain this fit, the potential evaporation was reduced by 50% during the winter time. No adjustment to reference ET was done in MASSIF calculations to improve the curve fitting.

The only interval with a noticeable difference between observed and calculated storages is during February through April of 1998. This corresponds to a series of large precipitation events that resulted in a significant increase in storage in both lysimeters (see Figure 7.1.2.1-2). The calculated increase in storages is about 40 mm smaller than was observed (Figure 7.1.2.1-3). The UNSAT-H curves (Desotell et al. 2006 DIRS 176858], Figures 3 and 4) also do not reproduce the observed increase.

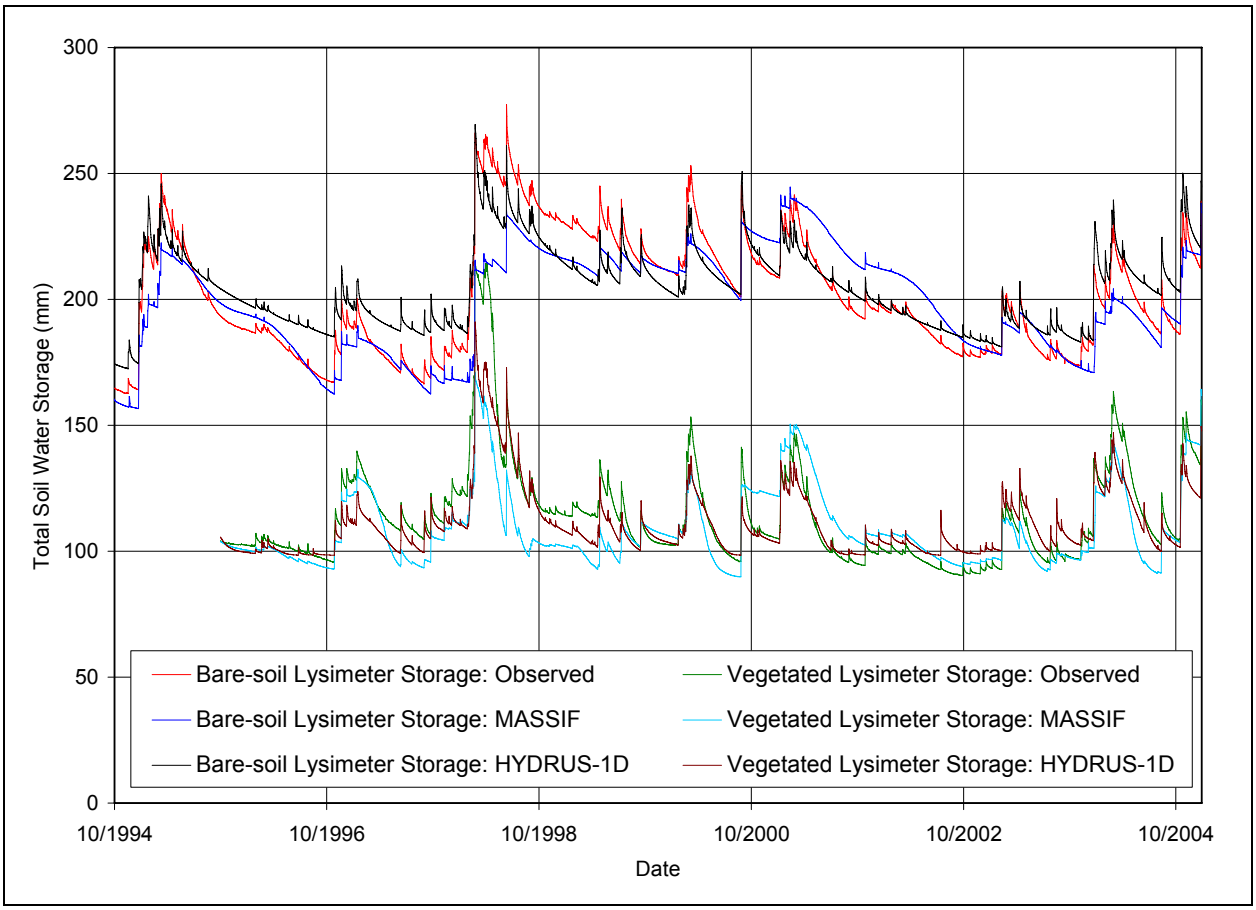

Source: Di Sanza 2006 [DIRS 178797] (lysimeter data); Validation Output DTN: SN0607T0502206.016 (Hydrus-1D data); Output DTN: SN0701T0502206.037, file: \Welcome to Massif\Massif\Validation Analyses\Lysimeter*NTSLysimeter.xls*.

Figure 7.1.2.1-3. Simulation of Soil Water Storage in the NTS Lysimeters

Some differences between the observed and calculated storages are also seen when soil water storage decreases during spring-fall periods of time. The observed storages tend to decrease more rapidly than the simulations. Desotell et al. (2006 DIRS 176858]), attributes this to the dynamic response of the plant growth that is not simulated by the model. However, the same tendency is observed in the bare soil lysimeter as well. Also, the difference between the decreasing portions of the storage curves are more pronounced in the case of the bare soil lysimeter. This may indicate evaporation at depth in the lysimeter that is a phenomenon of the lysimeter but not of the natural conditions. This can be caused by heat transfer along lysimeter walls from the surface and through lysimeter walls from the subterranean lysimeter chamber. This phenomenon is described by Howell et al. (1991 DIRS 177190]) in relation to the steel container weighing lysimeters. Other aspects of this phenomenon are given by Campbell et al. (1991 DIRS 177100]) and Kirkham et al. (1991 DIRS 177191]). However, the effects of this phenomenon cannot be bounded quantitatively in the absence of the soil profile temperature data. In contrast, it is possible that the lysimeter geometry is limiting rather than enhancing evaporation by preventing the slow upward evaporative flow of water from depths greater than the lysimeter depth.

The bare soil and vegetated lysimeter storages were also simulated with HYDRUS-1D. The same mean properties of the soil and climate data were used in the calculations (see Appendix J for details). The results of these simulations are shown in Figure 7.1.2.1-3. The mean root square errors obtained with HYDRUS-1D are 10.6 mm and 9.2 mm for bare soil and vegetated lysimeters, respectively. The same tendencies as described above in the differences between the calculated and observed storages can be noted. The mean root square errors between the storages calculated by HYDRUS-1D and MASSIF are 10.9 mm and 9.0 mm for the bare soil and vegetated lysimeters, respectively. This falls within the same range as the mean root square errors described above. The runoff and infiltration calculated by HYDRUS-1D were equal to zero (or negligibly small) during the entire period of observation in both lysimeters as well.

An important component of ET is transpiration. The transpiration in MASSIF is modeled using basal crop coefficient (K_{cb}) concept (Allen et al. 1998 [DIRS 157311]). As described in Sections 6.3.3 and 6.3.4 and Appendix E, the daily K_{cb} values are calculated from daily *NDVI'* values using the following formula (Equation 7.1.2.1-3):

$$K_{cb}=(C^{0}_{kcb}+C_{kcb} *NDVI')*P_i/P_{1998}*PVR \qquad \text{(Eq. 7.1.2.1-3)}$$

where C^{0}_{kcb} and C_{kcb} are intercept and slope of the regression line approximating the K_{cb} data plotted against the *NDVI'* data (see Appendix E); P_i is the total annual precipitation for the year in consideration; P_{1998} is the total annual precipitation in 1998 equal to 378 mm (representing the wet year); and *PVR* is the potential vegetation response. C^{0}_{kcb} and C_{kcb} were developed based on the K_{cb} and *NDVI'* values measured at the site. For the Present-Day climate nominal values for these parameters are -0.05 and 9.7, respectively (see Section 6.5.3.7). The daily *NDVI'* values used in MASSIF are tabulated for each day of the year and different combinations of the slopes and azimuths (see Appendix D for details). The base *NDVI'* values are used for the slopes less than 5º, and no azimuth correction is required for such slopes.

Regression coefficients C^{0}_{kcb} and C_{kcb} were set equal to 0 for the bare soil lysimeter. C_{kcb} was a parameter of the vegetated lysimeter in the optimization scheme described above. C^{0}_{kcb} is very small and was set to 0 for vegetated lysimeter as well. No information was available on the lysimeter site-specific *PVR* value, which is the MASSIF input parameter. The *PVR* was set equal to 1. Note that the optimization scheme estimates the value of the lumped transpiration parameter equal to C_{kcb} **PVR*. Thus, the actual values of *PVR* can be set to any arbitrary values without affecting the estimation of the lumped parameter. The estimation of this lumped parameter is achieved by adjusting $C_{kcb,}$ as a result of the manner in which the MASSIF calculation is implemented.

Shown in Figure 7.1.2.1-4 are daily K_{cb} and *NDVI'* values for the wet, average, and dry water years. These are the actual values measured at the Yucca Mountain site that include the water stress impacts caused by dry soil (see Appendix D for details on these data). The water stress impacts are maximal for the dry year and minimal for the wet year. The water years representing wet, average, and dry years are 1993, 1991, and 1990, respectively. The K_{cb} data used are for these 3 years. The *NDVI'* data (taken in 1998, 2001, and 2002) were corrected (see Appendix E) to represent the same years. The *NDVI'* data were scaled using a nominal regression slope of 9.7 (the details on how this slope was calculated are provided in Section 6.5.3.7), so they can be directly compared to the K_{cb} data.

The values based on the Yucca Mountain site-specific measurements are compared to the values calculated by MASSIF using Equation 7.1.2.1-3 above. The daily *NDVI'* values in this equation are base *NDVI'* values from the look-up table in MASSIF. P_{1998} is 378 mm. The precipitation (P_i) at the lysimeter site in 1998 (wet year), 2001 (average year), and 2002 (dry year) was 256 mm, 122 mm, and 31 mm, respectively. The *PVR* was set equal to 1, and C_{kcb} estimated from the optimization scheme is 2.4. The daily K_{cb} values calculated by MASSIF are shown in Figure 7.1.2.1-4 as "vegetated lysimeter K_{cb}" (the calculations are in the worksheet "NDVI" in *NTSLysimeter.xls* file located in folder \NTS in Validation Output DTN: SN0607T0502206.016. They are in good agreement with the *NDVI'* values measured for the LA plant association. This is the predominant association for the lower elevations and bajadas of the Yucca Mountain site (see Appendix D). LA association includes (see Appendix J) the following dominant species: *Ambrosia dumosa*, *Larrea tridentata* (creosotebush), *Menodora spinescens* (spiny menodora), and *Lycium pallidum*. The similar species are present at the vegetated lysimeter site (Scanlon et al. 2005 [DIRS 175977]).

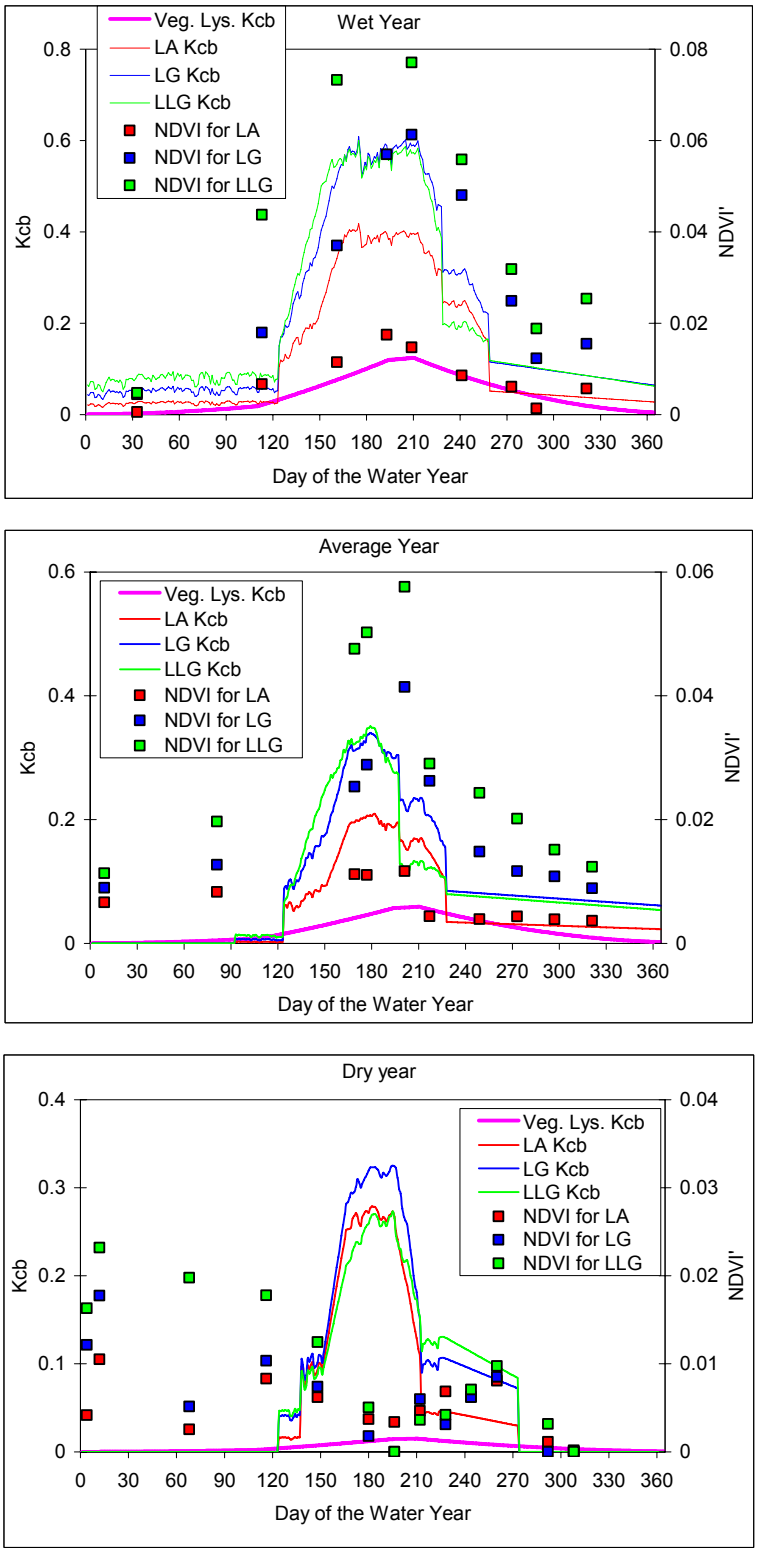

Source: Validation Output DTN: SN0607T0502206.016, file: NTS*NTSLysimeter.xls*.

Figure 7.1.2.1-4. Comparison Between the Measured K_{cb} and NDVI Values and Calculated Vegetated Lysimeter K_{cb} Values for the Different Water Years

Another parameter related to the vegetated lysimeter is the vegetation (canopy) fraction parameter f_c. It was assumed that f_c is constant for the entire period of simulation. As estimated in Appendix D, the vegetation fractions of LA association are 0.21, 0.11, and 0.15 for the wet, dry, and average years, respectively. The estimated f_c is 0.26 is close to the value for the wet year. Note that parameter K_{c_min} estimated value (0.0135) is within the ranges of K_{c_min} measured for LA association as described in Appendix D (0 for dry and average and 0.016 for the wet water years).

Summary of Lysimeter Simulations at NTS:

- The simplified water balance approach incorporated in MASSIF allows for adequate simulation of water storage and ET in both bare soil and vegetated NTS lysimeters.

- The ET parameters such as K_{cb}, K_{c_min}, and f_c estimated for the bare soil and vegetated lysimeters using MASSIF are in good agreement with the experimental data obtained for the plant association similar to the one present at the lysimeter site.

- The MASSIF results are comparable to the results obtained with physics-based models such as UNSAT-H (Desotell et al. 2006 [DIRS 176858]).

- MASSIF's ability to reproduce the lysimeter water storage over 10 years (bare soil) and 9 years (vegetated) confirms that the most important processes are represented correctly.

- The same tendencies in the differences between the observed storage and storage calculated with other models were also found using MASSIF. These tendencies are consistent with the ones described in the other studies related to the NTS lysimeters (e.g. Desotell et al. 2006 [DIRS 176858]). These differences may indicate evaporation at depth in the lysimeters that is a phenomenon of the lysimeter but not of the natural conditions.

7.1.2.2 Lysimeter Simulations at the Reynolds Creek Experimental Watershed

The RCEW data were collected by the US Department of Agriculture (USDA) Northwest Watershed Research Center (NWRC), in Boise, Idaho. The data are available from *ftp.nwrc.ars.usda.gov*. The data used in this analysis were obtained directly from USDA NWRC. The information included in the CD provided by the USDA NWRC can be found in DTN: SN0608T0502206.020 [DIRS 179875]. There are a series of articles published in the Water Resources Research Journal, vol. 37, No. 11 in November 2001 summarizing research goals and the data collection efforts at the RCEW. The series includes Seyfried et al. (2001 [DIRS 177515], 2001 [DIRS 177501], 2001 [DIRS 177505], 2001 [DIRS 177506]), Marks (2001 [DIRS 177512]), Marks et al. (2001 [DIRS 177504]), Slaughter et al. (2001 [DIRS 177354]), Pierson et al. (2001 [DIRS 177503]), Hanson et al. (2001 [DIRS 177509]), and Hanson (2001 [DIRS 177508]).

RCEW occupies 239 km^2 in the Owyhee Mountain region located in the southwestern Idaho, 80 km southwest of Boise (Hanson et al. 2001 [DIRS 177509]). Two sets of soil lysimeters were installed at RCEW. The lysimeter used in this analysis is located at the Lower Sheep Creek climate station, lysimeter LSCW. The details are presented in Appendix J.

The mean precipitation at the lysimeter site is 349 mm (Wight et al. 1986 [DIRS 177104]), and the mean annual temperature is 7.4ºC (Wight et al. 1990 [DIRS 177113]). About 21% of precipitation comes in the form of snow. These are wetter and cooler conditions than in Spokane (mean precipitation 325 mm and mean annual temperature 8.5ºC) an analog site representing the upper bound of the glacial transition climate.

The LSCW lysimeter is located at: 43º 08' 24.088" latitude, and 116º 43' 57.732" longitude, and the elevation is 1656 m (DTN: SN0608T0502206.020 [DIRS 179875]). The lysimeter diameter is 1.47 m and depth is 1.22 m. The lysimeter contains native undisturbed soil. The upper 0.1 m is loam. It is underlain by a 0.48-m-thick argillic horizon with up to 50% clay. The remaining cross section is sandy loam. The soil samples were taken at the neutron tubes 127707, 127807, and 127907 located within the lysimeter or next to it. Nine soil horizons were characterized down to the depth of 1.83 m. The soil layer is underlain by the basalt bedrock (Wight et al. 1986 [DIRS 177104]). The soil property average values weighted by the horizon thickness within the1.22 m lysimeter depth are as follows (see Appendix J for details):

- Porosity is 0.47 m^3/m^3
- Field capacity corresponds to a water content of 0.33 m^3/m^3 at the pressure of -1/3 bar
- Wilting point corresponds to a water content of 0.19 m^3/m^3 at the pressure of -15 bars (no measurements at -60 bars are available)

The vegetation at the lysimeter site is dominated by low sagebrush which grows to a height of about 0.3 m and is accompanied by perennial bunchgrasses and forbs (Seyfried et al. (2001 [DIRS 177515]). The lysimeter site contained a mature shrub along with the naturally associated plants with the slightly higher vegetation density than the surrounding landscape.

The climate data include precipitation and temperatures collected at the climate station 12 × 07 located next to the lysimeter site. The period of time from October 1, 1977 through September 30, 1984 was selected based on the availability of the soil storage data. The observation data used in this simulation are changes in water storage values during no snow season measured in the lysimeter from April 1978 through September 1984. The changes in storage were converted to the total soil water storage values using initial storage calculated for the point in time when the moisture within the profile was measured in the neutron tubes (see Appendix J for details). These data are shown in Figure 7.1.2.2-1.

The lysimeter calibration is described by Seyfried et al. (2001 [DIRS 177515]). As concluded in this publication, the lysimeter observations have the precision of $\pm$8 mm.

The MASSIF input parameters for the lysimeter simulations were defined in accordance with the site-specific information. The modeling set up is described in Appendix J. The following MASSIF parameters were estimated from the optimization scheme described below:

- Diffusive evaporation parameter, K_{c_min}
- Canopy fraction, f_c
- Coefficient representing the slope of the $NDVI'$-K_{cb} regression line, C_{kcb}
- Field capacity, θ_f.

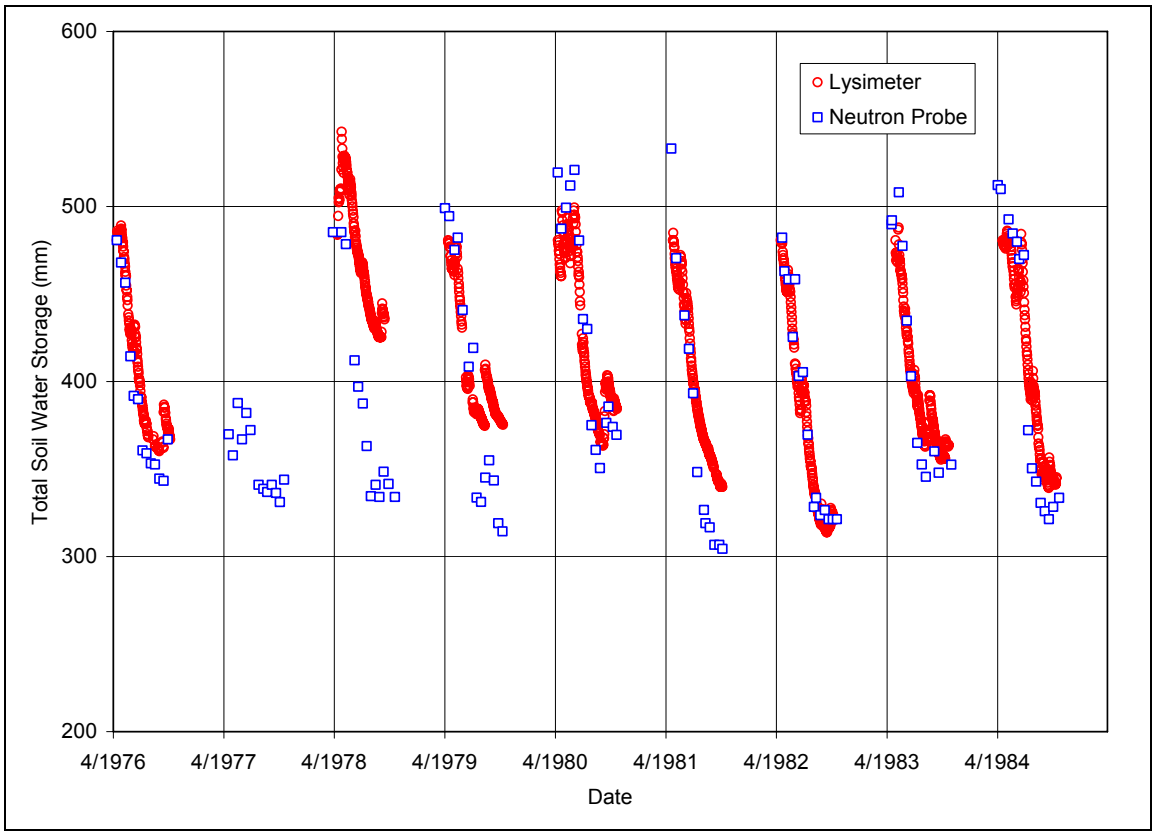

Source: Validation Output DTN: SN0607T0502206.016, *RCEWLysimeter.xls*.

Figure 7.1.2.2-1. Total Soil Water Storage Calculated Using Daily Change-in-storage from LSCW and Integrated Water Content from Neutron Probe Measurements

The values of these four parameters were estimated by minimizing the difference between the observed and calculated soil water storage. The following objective function $F3_{obj}$ was used in the conjugate gradient minimization procedure in MathCAD:

$$F3_{obj}(K_{c\_min}, f_c, C_{kcb}, \theta_f) = [\sum(S^{obs}_i - S^{cal}_i)^2]/N \qquad \text{(Eq. 7.1.2-4)}$$

where S^{obs}_i and S^{cal}_i are observed and calculated lysimeter storage during the simulation day i on which the observation data is available, and N is the number of observations (N=1179). Note that the lysimeter data were not recorded every day.

The results of the minimization and subsequent manual adjustment are:

- $K_{c\_min} = 0.0$
- $f_c = 0.7$
- $C_{kcb} = 13.685$
- $\theta_f = 0.415$
- $FI_{obj} = 1037.81$.

Based on the obtained objective function value, the overall goodness of fit is 32.22 mm (9.5 % of the mean annual precipitation). The goodness of fit is very similar to the one obtained for the NTS site, which is about 9% of the mean annual precipitation. Considering that the measurement precision is $\pm$8 mm, this is a reasonably good fit. The results of minimization are shown in Figure 7.1.2.2-2. The storage calculated based on the neutron probe measurements of moisture content within the soil profile is shown in Figure 7.1.2.2-2 in addition to the soil water storage measured in the lysimeter (see Appendix J for details). The storage calculated with MASSIF is well within the boundaries of the observed values.

The lysimeter site was designed to exclude run-on and runoff. The intent was also to exclude or minimize deep percolation. Very little drainage has probably occurred from the lysimeter bottom, but the timing of these small events is not known (Seyfried et al. 2001 [DIRS 177515]). Runoff and run-on calculated by MASSIF was zero. The mean annual infiltration calculated by MASSIF is 7 mm, which is 2% of the mean annual precipitation (349 mm). The actual site-specific infiltration is unknown. However, the infiltration for the rangeland in this area is considered to be around 4% (Wight et al. 1986 [DIRS 177104]). MASSIF-calculated infiltration is consistent with this estimate and the site conceptual model (little drainage). Since infiltration, if any, constitutes a very small portion of the overall water balance, it should not affect the estimates of the other water balance constituents, such as ET.

The RCEW lysimeter storage was also simulated with HYDRUS-1D. The same mean properties of the soil and climate data were used in the calculations (see Appendix J for details). The results of these simulations are shown in Figure 7.1.2.2-2. The mean root square error obtained with HYDRUS-1D is 42.3 mm (12% of the mean annual precipitation). The same tendencies as described above in the differences between the calculated and observed storages can be noted. The mean root square error between the storages calculated by HYDRUS-1D and MASSIF is 33.57 mm. The runoff calculated by HYDRUS-1D is zero during all period of observation. The mean annual infiltration is 3 mm (0.9% of precipitation), which is close to the value calculated by MASSIF.

The average monthly rates of the actual ET calculated by MASSIF for 1978 and 1979 were compared to the data presented by Wight et al. (1990 [DIRS 177113]). This is demonstrated in Figures 7.1.2.2-3 and 7.1.2.2-4. The calculated and measured ET values are in good agreement. The sum of the mean monthly ET for the six months in 1978 calculated by MASSIF and presented by Wight et al. (1990 [DIRS 177113]) are 10.05 mm and 9.84 mm, respectively. The sum of the mean monthly ET for the five months in 1979 calculated by MASSIF and presented by Wight et al. (1990 [DIRS 177113]) are 7.17 mm and 7.35 mm, respectively.

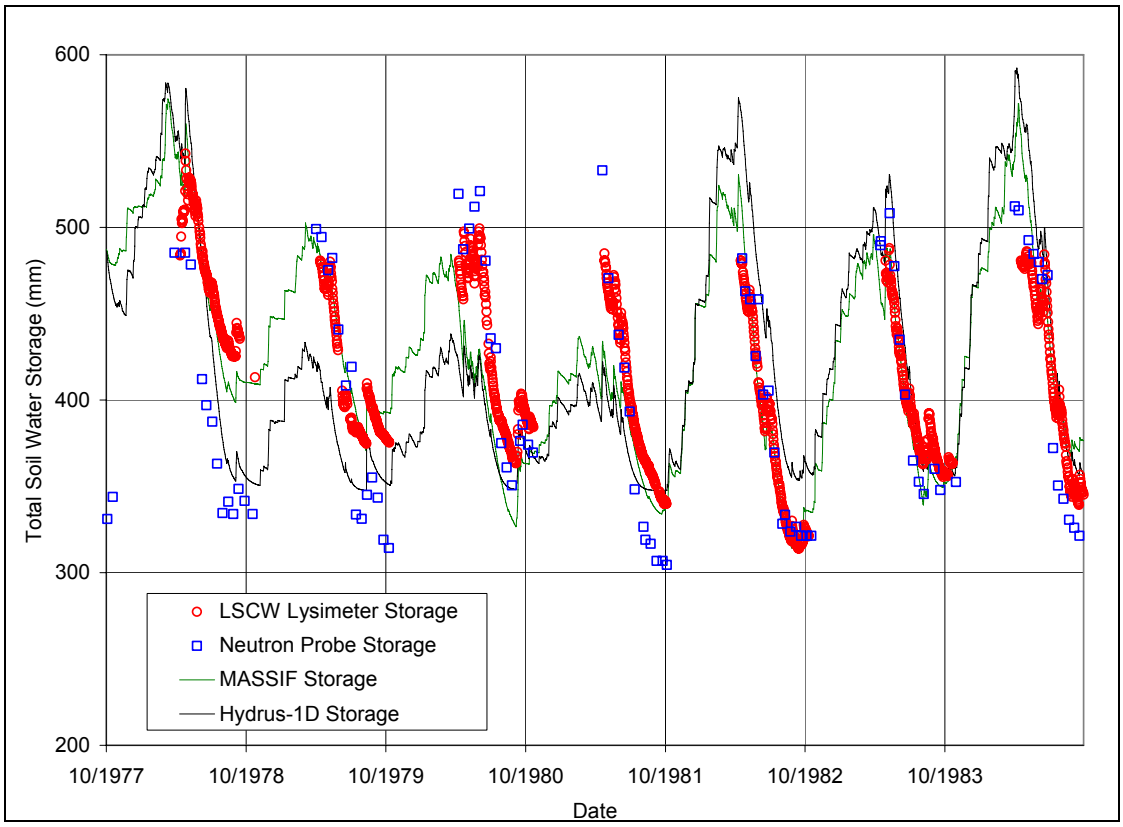

Source: DTN: SN0608T0502206.020 [DIRS 179875] (lysimeter and neutron probe data); Validation Output DTN: SN0607T0502206.016 (HYDRUS-1D data); Output DTN: SN0701T0502206.037, file: \Welcome to Massif\Massif\Validation Analyses\Lysimeter*RCEWLysimeter.xls*.

Figure 7.1.2.2-2. Simulation of Soil Water Storage in RCEW Lysimeter

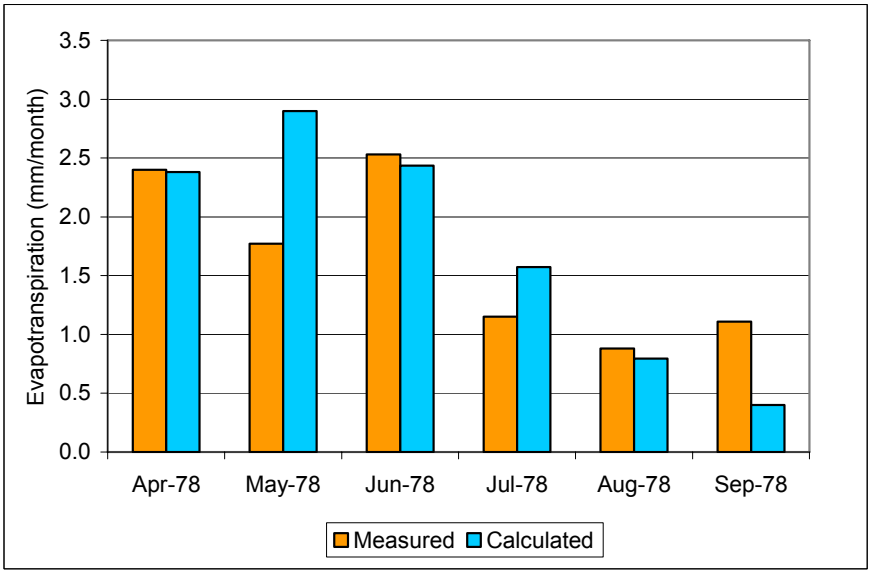

Source: Output DTN: SN0701T0502206.037.

Figure 7.1.2.2-3. 1978 Average Monthly Rates of Actual Evapotranspiration at RCEW

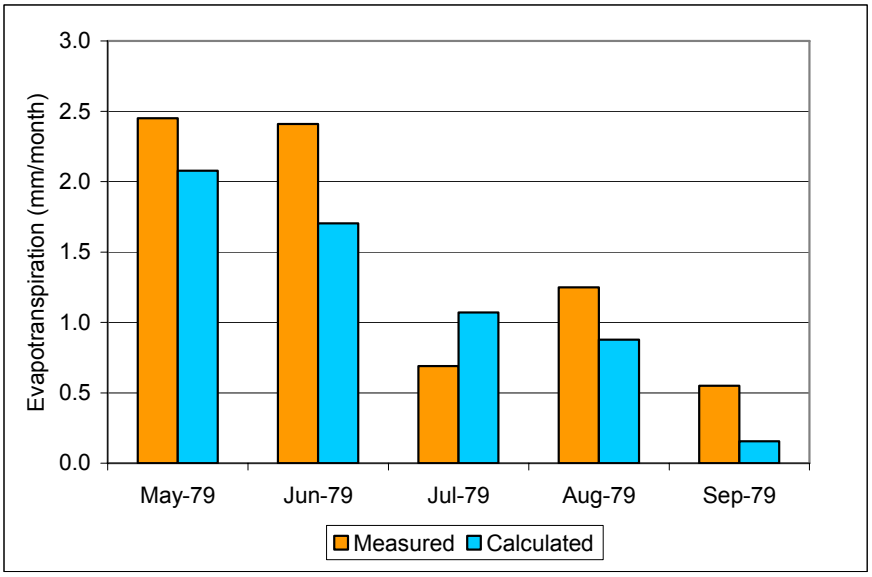

Source: Output DTN: SN0701T0502206.037.

Figure 7.1.2.2-4. 1979 Average Monthly Rates of Actual Evapotranspiration at RCEW

The field capacity estimated from the lysimeter modeling is 0.415. This falls into the range of the site-specific field capacity values of 0.28 to 0.42 obtained for the different soil horizons (see Appendix J). The maximum measured lysimeter storage was 542.7 mm. This corresponds to the field capacity of 0.44. Note that the actual soil profile is heterogeneous and the effective soil properties of the equivalent homogeneous profile are not known. The effective soil properties may be different from the weighted average values. In this case (effective field capacity is equal to the clay and clay loam field capacity), the amount of water that can be stored in the clay and clay loam layers controls the lysimeter storage.

The estimated K_{c_min} value is 0. This is consistent with the conceptual model of ET (see Section 6.3.3 and 6.3.4).

There are no daily K_{cb} data at the site. The mean K_{cb} value at the site for the growing season estimated for the site in Wight et al. (1990 [DIRS 177113]) is 0.85 (standard deviation is 0.06). The mean K_{cb} during the growing period over the seven years of observations (1978 through 1984) calculated using estimated C_{kcb} = 13.685 is 0.77. This is consistent with the estimate in Wight et al. (1990 [DIRS 177113]).

The vegetation cover f_c estimated for the site is 0.7. The estimate of the mean vegetation cover including live plants and litter at the site over the 11 years of observations provided in Wight et al. (1986 [DIRS 177104]) is 50% or 0.5.

Summary of Lysimeter Simulations at RCEW:

- The MASSIF water balance approach was capable of reproducing the changes in storage over the seven years of observations at the RCEW lysimeter site. This site is considerably different from the NTS site. The climate is wetter and cooler with 21% of

precipitation being snow, and the soils are finer with the smaller permeability and significantly higher field capacity and wilting point. The vegetation cover is twice as dense, and the plants species are different.

- The soil properties, ET parameters, and infiltration estimated using MASSIF for the RCEW lysimeter fall within the site specific ranges obtained from the literature.

- The MASSIF and HYDRUS-1D results are fairly consistent. The same tendencies in differences between the observed and calculated storages were obtained with MASSIF and HYDRUS-1D.

- The infiltration predicted by MASSIF is in good agreement with the infiltration predicted by HYDRUS-1D.

- The MASSIF ability to adequately model RCEW lysimeter site confirms that the physical processes incorporated in MASSIF are applicable to a wide range of condition. Both present-day and future climates can be thus accurately represented.

7.1.3 Run-on/Runoff

The hydrological processes of run-on and runoff are validated in the MASSIF model by comparison of measured streamflow data with MASSIF predictions of runoff (streamflow) at the discharge cells at the base of streamflow watersheds. Streamflow watersheds are sub-watersheds located within the primary eleven watersheds that encompass the Yucca Mountain infiltration model domain (see Table B-3). A streamflow watershed is defined by the location of its streamflow gauge. That is, a streamflow watershed includes all the upstream cells that can contribute runoff that eventually flows through a given streamflow gauge. Streamflow and runoff are terms that are often used interchangeably, but for this discussion, streamflow refers to the total amount of runoff within a streamflow watershed, while runoff can refer to total streamflow, or just the amount of runoff from one cell to another. Additional confidence building during model development is provided in this section by comparing streamflow data from the rare occasions during which streamflow has been recorded within the Yucca Mountain model domain, with MASSIF predictions of streamflow for those same streamflow events.

There are six streamflow gauges located within the Yucca Mountain infiltration model domain used in this analysis (see Section B5). These six gauges are part of the USGS streamflow monitoring network (Bauer et al. 1995 [DIRS 101486]). The Yucca Mountain infiltration model domain encompasses two Pagany Wash gauges, one Drill Hole Wash gauge, one Wren Wash gauge, and two Split Wash gauges.

Streamflow was recorded at some of these six gauges during storms in water years 1993, 1994, 1995, and 1998. Data collected during these four water years also include years with no streamflow, such as for water year 1994. The data record for water year 1994 is not complete for several gauges. Data with zero streamflow and incomplete records were not used, so streamflow data from water years 1995 and 1998 were used in this analysis. Streamflow data are reported as an average daily flow rate in units of cubic feet per second (cfs). These units are converted into cubic meters per day for this analysis. Table 7.1.3-1 summarizes all the available streamflow

data collected within the infiltration model domain. Total streamflow in m^3/yr are compiled in this table, and calculated by summing the average daily streamflow rate for a given water year, then converting from average daily streamflow into total annual streamflow.

The streamflow gauge locations can be found in DTN: MO0601GSCSPINF.000 [DIRS 177236]. Note that the UTM coordinates in this DTN are NAD83, while the figures in the report are NAD27. The locations of these six gauges and their associated streamflow watersheds are shown in Figure 7.1.3-1. This figure also includes the locations of all field data used for model validation (refer to Sections 7.2.1).

MASSIF calculations are performed for each of the watersheds for which runoff data was collected. Qualified runoff data exist for all of the streamflow gauges for water year 1995, and for some of the streamflow gauges for water years 1994 and 1998. All of the calculations are started at the beginning of water year 1994, and carried through to either water year 1995 or 1998, depending upon the existence of 1998 data for the particular watershed.

With the exception of soil saturated conductivity, all of the input values are the nominal values listed in Appendix I. Soil conductivities are varied by a single multiplicative factor between 0.1 and 1.2 in increments of 0.1. Hence, the first run multiplies all of the soil conductivities by 0.1, the next run multiplies all soil conductivities by 0.2, and so on. Weather data for the simulations are taken from qualified records for Yucca Mountain sites 1, 2, 3, and 6 (DTN: SN0608WEATHER1.005 [DIRS 177912]). Separate calculations are performed for each of the weather sets, and the results from the four calculations are compared. Although there are a total of seven weather stations located within the infiltration model domain (Sites 1, 2, 3, 4, 6, 7, and 8), only Sites 1, 2, 3, and 6 were used for these comparisons because they are located closest to the six streamflow watersheds.

The predicted cumulative runoff for water year 1995 at the Wren Wash streamflow gauge site is shown in Figure 7.1.3-2. The horizontal axis is the normalized soil saturated conductivity (i.e., the multiplying factor applied to the soil conductivities). Each of the colored curves is a prediction based upon a different weather station data set (YM Sites 1, 2, 3, and 6). The horizontal black line is the sum of the measured runoffs for water year 1995. The intersections of each of the prediction lines (colored lines with symbols) and the runoff measurement (solid black line) represents the best match between the MASSIF calculation and the data. For Wren Wash in water year 1995, the multipliers at the intersections are:

- YM Site 1: ~0.35
- YM site 2: ~0.36
- YM Site 3: ~0.59
- YM Site 6: ~0.60.

Table 7.1.3-1. Summary of Streamflow Gauge Data Used in this Report.

USGS Gaging Station Name	Gaging Station Name Used in this Report	USGS Station ID	Abbreviated Name	
Pagany Wash near the Prow	Upper Pagany Wash	102512531	PW8	
		Data Summary		
Water Year:	1993	1994	1995	1998
Total Streamflow (m^3/yr):	No Data	Incomplete Record	33,518	27,793
DTN:		GS941208312121.001 [DIRS 107374]	GS960908312121.001 [DIRS 107375]	MO0603SEPSTREA.000 [DIRS 179889]
Pagany Wash #1 near Well UZ-4	Lower Pagany Wash	102512533	PW9	
		Data Summary		
Water Year:	1993	1994	1995	1998
Total Streamflow (m^3/yr):	Zero	Zero	21,065	35,157
DTN:	MO0605SEPSURFC.000 [DIRS 179890]	GS941208312121.001 [DIRS 107374]	GS960908312121.001 [DIRS 107375]	MO0603SEPSTREA.000 [DIRS 179889]
Drillhole Wash above Well UZ-1	Drill Hole Wash	102512535	DW8	
		Data Summary		
Water Year:	1993	1994	1995	1998
Total Streamflow (m^3/yr):	No Data	Incomplete Record	12,233	No Data
DTN:		GS941208312121.001 [DIRS 107374]	GS960908312121.001 [DIRS 107375]	
Wren Wash	Wren Wash	1025125356	WW9	
		Data Summary		
Water Year:	1993	1994	1995	1998
Total Streamflow (m^3/yr):	No Data	Incomplete Record	10,325	No Data
DTN:		GS941208312121.001 [DIRS 107374]	GS960908312121.001 [DIRS 107375]	
Split Wash below Quac Canyon	Upper Split Wash	102512537	SW9	
		Data Summary		
Water Year:	1993	1994	1995	1998
Total Streamflow (m^3/yr):	Incomplete Record	Zero	11,254	15,413
DTN:	GS941208312121.001 [DIRS 107374]	GS941208312121.001 [DIRS 107374]	GS960908312121.001 [DIRS 107375]	MO0603SEPSTREA.000 [DIRS 179889]
Split Wash at Antler Ridge	Lower Split Wash	1025125372	SWAR	
		Data Summary		
Water Year:	1993	1994	1995	1998
Total Streamflow (m^3/yr):	Incomplete Record	Zero	Zero	No Data
DTN:	GS941208312121.001 [DIRS 107374]	GS941208312121.001 [DIRS 107374]	MO0605SEPSURFC.000 [DIRS 179890]	

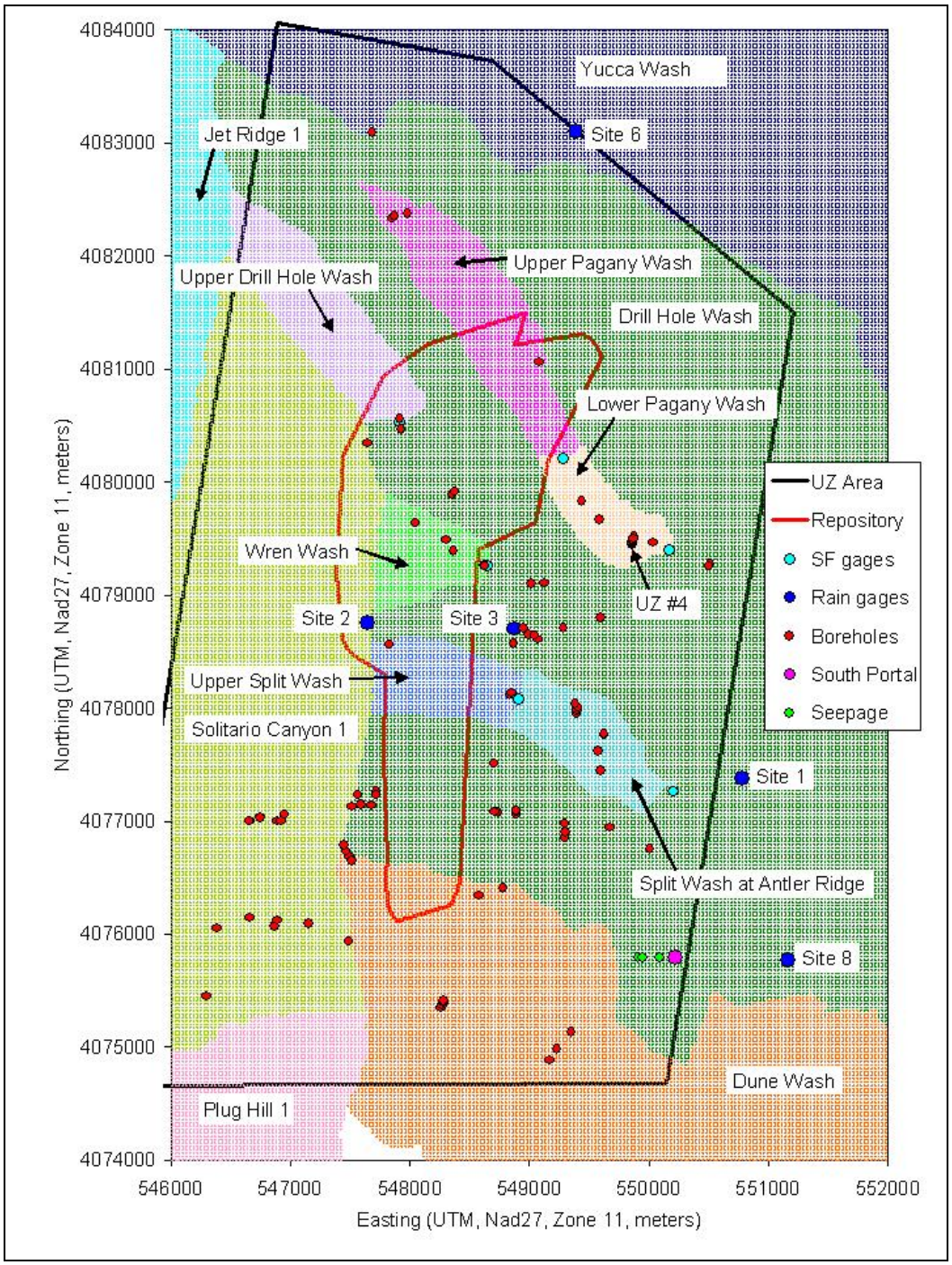

Sources: Output DTNs: SN0606T0502206.011 (Watersheds coordinates); SN0612FTPRNUZB.002 (UZ flow model and Repository areas); MO0601GSCSPINF.000 [DIRS 177236] (Locations of streamflow gauges); MO9906GPS98410.000 [DIRS 109059] (Locations of neutron logging boreholes); MO9906GPS98410.000 [DIRS 109059] (Location of UZ #4). Finsterle and Seol 2006 [DIRS 177754], p. 1 (Locations of seepage); CRWMS M&O 1997 [DIRS 100117], Table 2-1 (Locations of rain gauges); BSC 2003 [DIRS 165572], p. 15 (Location of south portal).

SF gauges = Streamflow gauges; UZ Area = UZ flow model area; Repository = Repository footprint.

Figure 7.1.3-1. Map View of Watersheds and Locations of Various Field Data

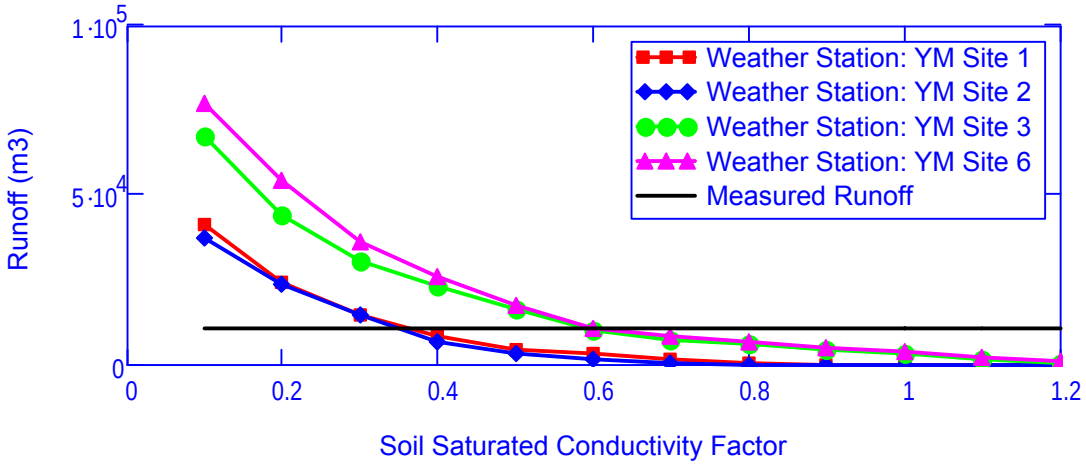

Source: Output DTN: SN0701T0502206.037, file: \Welcome to Massif\Massif\Validation Analyses\Stream Gauge Comparisons*Streamgage Plots.xmcd*.

Figure 7.1.3-2. Variation of Annual Cumulative Runoff with Soil Saturated Conductivity Factor (Wren Wash, Water Year: 1995)

While cumulative annual runoff, shown in Figure 7.1.3-2, is important, examination of the daily occurrence and amount of runoff is also important. Figure 7.1.3-3 shows calculations and measurements of daily runoff (reported as ft^3/s for a 24-hour day) for days 90 to 180 of the 1995 water year for Wren Wash. Runoff is neither calculated to occur nor measured outside of this range.

The recorded runoff is shown in the Figure 7.1.3-3 as a black arrow. Calculated runoffs are shown as vertical red and blue bars. The red and blue bars correspond to the lower and higher soil conductivity factors bounding the intercept of the measured runoff line in Figure 7.1.3-2. Hence, for weather station YM Site 1, the red bar corresponds to a soil conductivity factor of 0.3; the blue bar corresponds to a soil conductivity factor of 0.4. For YM Site 3, the red bar corresponds to a soil conductivity factor of 0.5; the blue bar corresponds to a soil conductivity factor of 0.6.

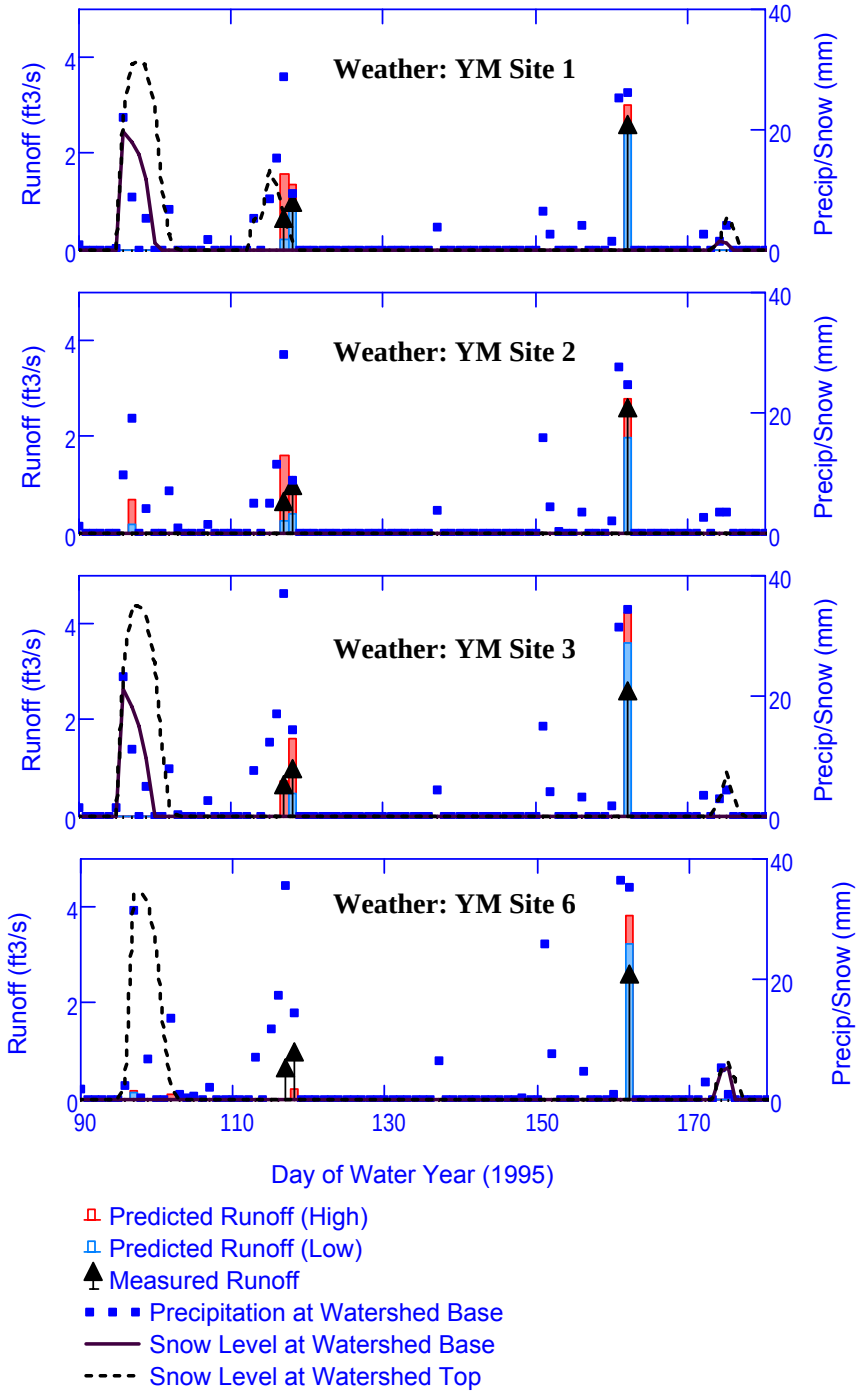

Source: Output DTN: SN0701T0502206.037, file: \Welcome to Massif\Massif\Validation Analyses\Stream Gauge Comparisons*Streamgage Plots.xmcd*.

NOTE: Daily precipitation at the base of the watershed is shown on the plots as blue squares. The amount of precipitation on any given day differs between weather stations. There are actually two reasons for this. The obvious reason is that precipitation amount varies with location. The less obvious reason is that each of the weather stations is located at a different elevation, and the recorded weather data must be lapse corrected to the elevation at the base of the watershed.

Figure 7.1.3-3. Predicted (Solid Bar) and Measured (Arrow) Runoff (Wren Wash, Water Year 1995)

Because the presence and/or melting of snow might affect runoff, the snow levels, in mm of water, are shown for the bottom (solid line) and top (dashed line) of the watershed. The predicted presence of snow varies with the weather data set. Use of Sites 1 and 3 produces snow at both the top and bottom of the watershed. Use of site 6 produces snow only at the top of the watershed. Use of Site 2 produces no snow at all.

This figure illustrates the fact that a comprehensive knowledge of precipitation and temperature does not exist even when measured data exists. Infiltration and runoff calculations require weather data for the entire domain. Weather station data exist for discrete locations. Geographic extrapolation of weather data has relative high levels of uncertainty. Comparison of the daily runoff plots based on each of the weather stations give some indication of the uncertainty of the runoff prediction due to uncertainty in weather data.

Given the uncertainty in soil conductivity and weather data, calculations of daily runoff are fairly good. Runoff occurs on the correct days and in roughly the "correct" amount. It is worth noting that no uncertainty estimates were recorded with the measured runoff data.

The balances of the streamflow gauge watersheds are listed below, along with the related figure numbers and figure titles. Comments on the results are inserted when characteristics of the plots deviate from the Wren Wash plots:

Upper Split Wash

Figure 7.1.3-4 Variation of Annual Cumulative Runoff with Soil Saturated Conductivity Factor (Upper Split Wash, Top: Water Year 1994, Middle: Water Year 1995, Bottom: Water Year 1998)

Figure 7.1.3-5 Predicted (Solid Bar) and Measured (Arrow) Runoff (Upper Split Wash, Water Year 1995)

Figure 7.1.3-6 Predicted (Solid Bar) and Measured (Arrow) Runoff (Upper Split Wash, Water Year 1998)

Comments: Measured runoff for water year 1994 was zero. All calculations produced zero runoff with the exception of YM Site 1 with a soil conductivity factor of 0.1

Lower Split Wash

Figure 7.1.3-7 Variation of Annual Cumulative Runoff with Normalized Saturated Conductivity of Soil (Lower Split Wash, Water Year: 1995)

Comments: Measured runoff for year 1995 was zero. Calculations using weather sites 1 and 2 produce zero or near-zero runoff for soil conductivity factors greater than or equal to 0.7. Calculations using weather sites 3 and 6 produce zero of near-zero runoff for soil conductivity factors greater than or equal to 1.1.

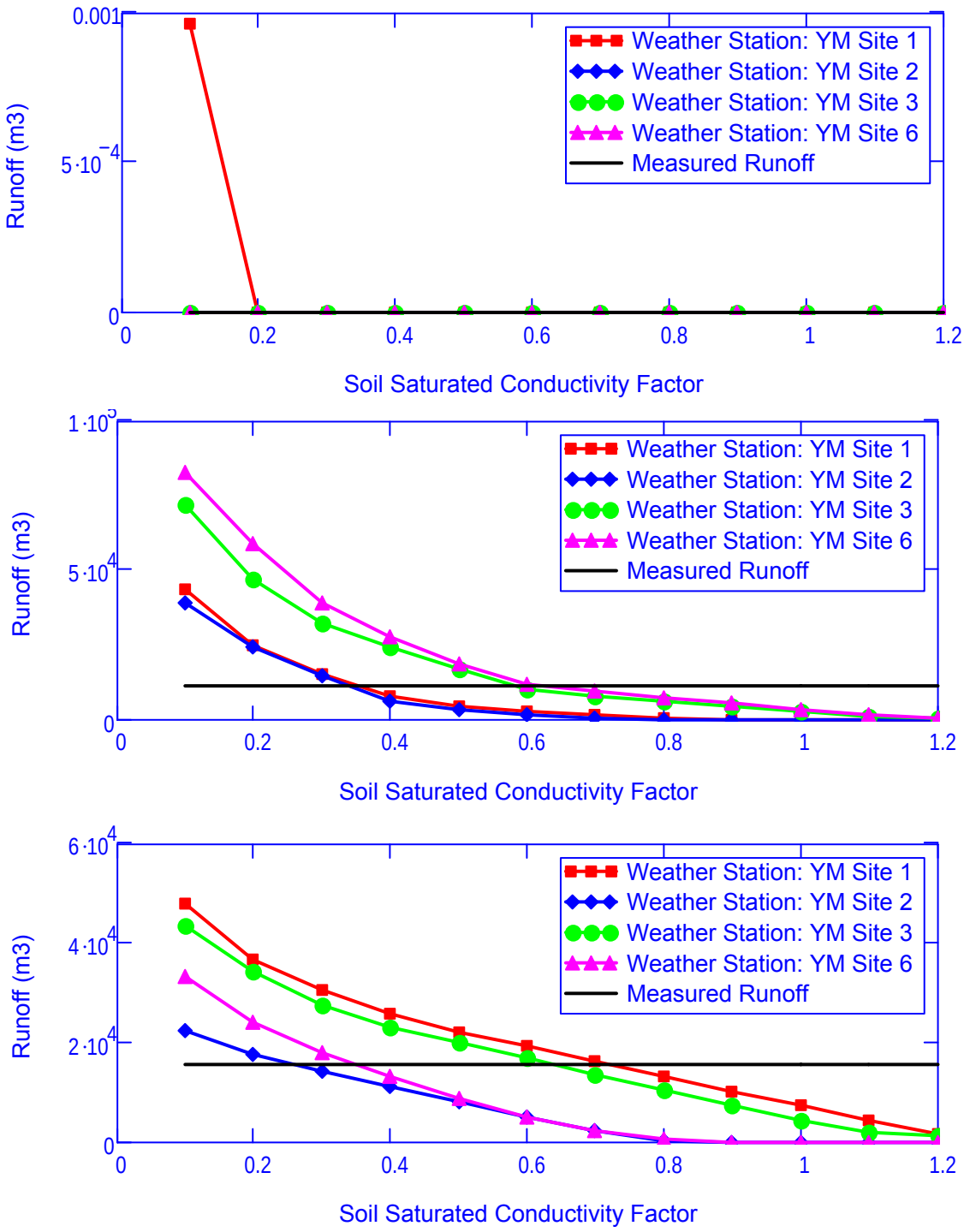

Source: Output DTN: SN0701T0502206.037, file: \Welcome to Massif\Massif\Validation Analyses\Stream Gauge Comparisons*Streamgage Plots.xmcd*.

NOTE: Upper Split Wash, Top: Water Year 1994, Middle: Water Year 1995, Bottom: Water Year 1998

Figure 7.1.3-4. Variation of Annual Cumulative Runoff with Soil Saturated Conductivity Factor

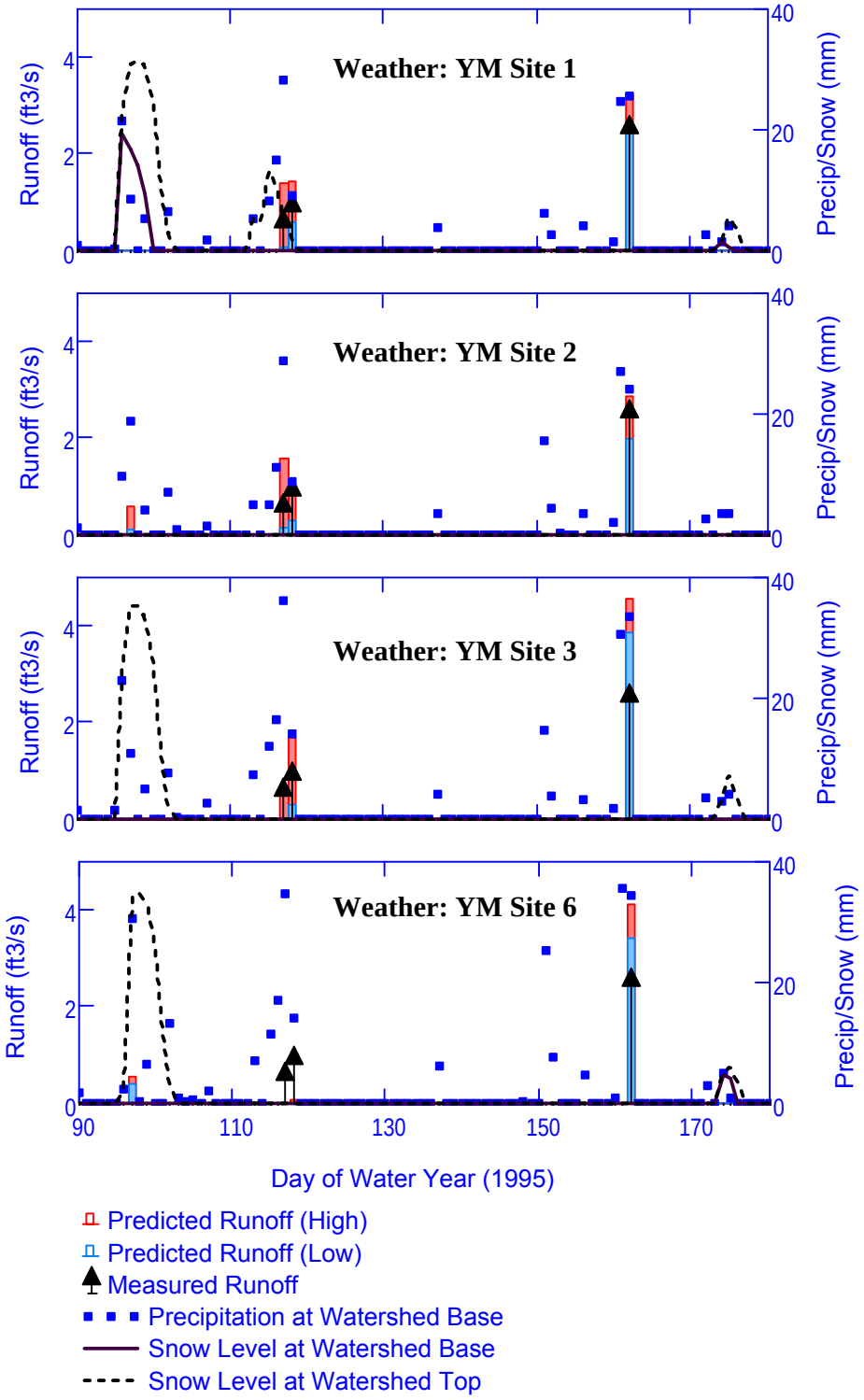

Source: Output DTN: SN0701T0502206.037, file: \Welcome to Massif\Massif\Validation Analyses\Stream Gauge Comparisons*Streamgage Plots.xmcd*.

Figure 7.1.3-5. Predicted (Solid Bar) and Measured (Arrow) Runoff (Upper Split Wash, Water Year 1995)

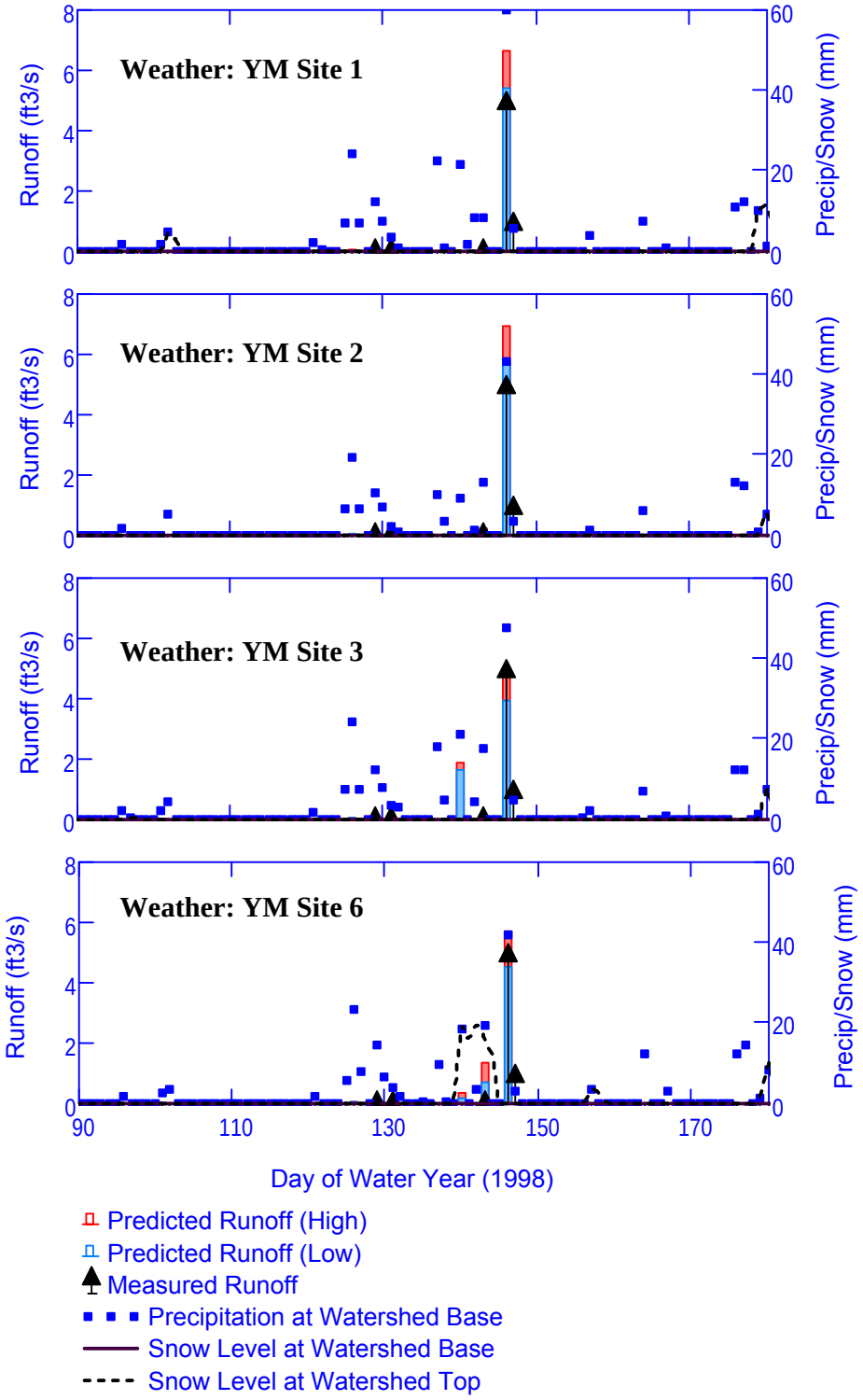

Source: Output DTN: SN0701T0502206.037, file: \Welcome to Massif\Massif\Validation Analyses\Stream Gauge Comparisons*Streamgage Plots.xmcd*.

Figure 7.1.3-6. Predicted (Solid Bar) and Measured (Arrow) Runoff (Upper Split Wash, Water Year 1998)

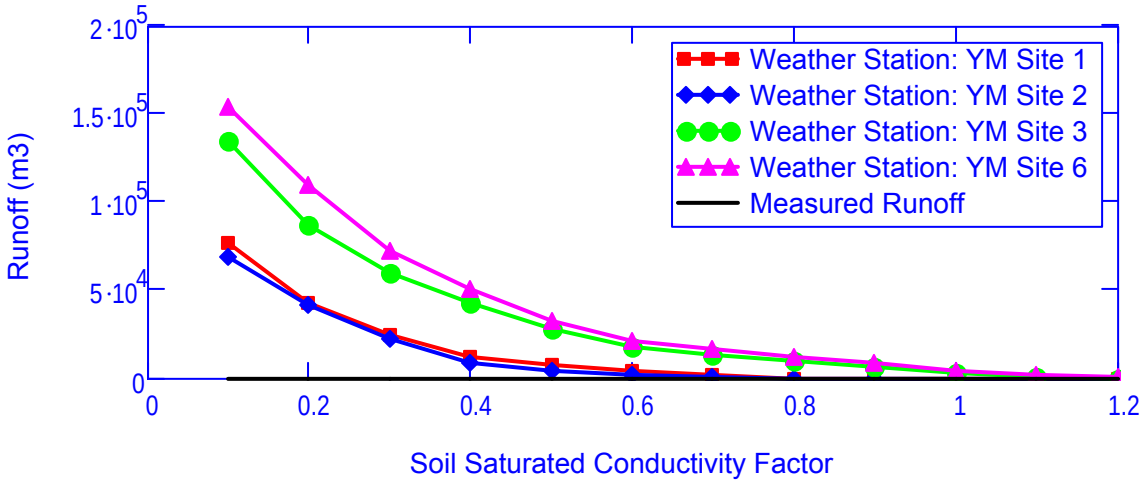

Source: Output DTN: SN0701T0502206.037, file: \Welcome to Massif\Massif\Validation Analyses\Stream Gauge Comparisons*Streamgage Plots.xmcd*.

Figure 7.1.3-7. Variation of Annual Cumulative Runoff with Normalized Saturated Conductivity of Soil (Lower Split Wash, Water Year: 1995)

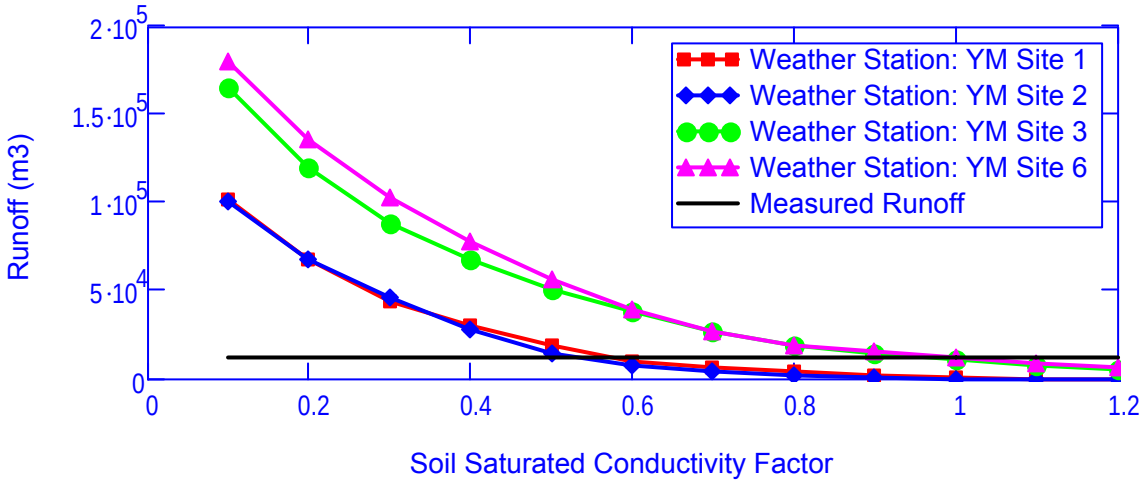

Source: Output DTN: SN0701T0502206.037, file: \Welcome to Massif\Massif\Validation Analyses\Stream Gauge Comparisons*Streamgage Plots.xmcd*.

Figure 7.1.3-8. Variation of Annual Cumulative Runoff with Soil Saturated Conductivity Factor (Drill Hole Wash, Water Year: 1995)

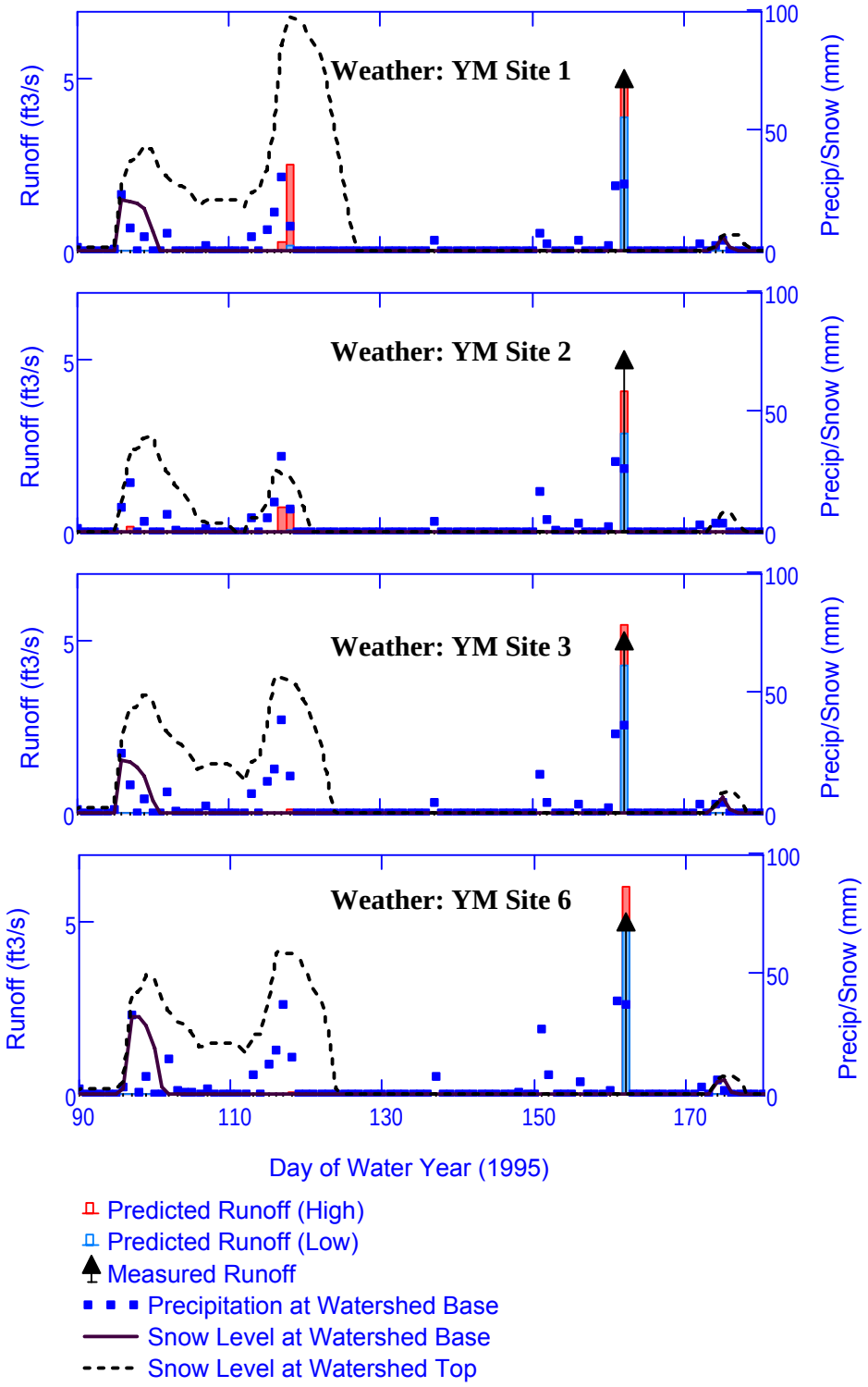

Source: Output DTN: SN0701T0502206.037, file: \Welcome to Massif\Massif\Validation Analyses\Stream Gauge Comparisons*Streamgage Plots.xmcd*.

Figure 7.1.3-9. Predicted (Solid Bar) and Measured (Arrow) Runoff (Drill Hole Wash, Water Year 1995)

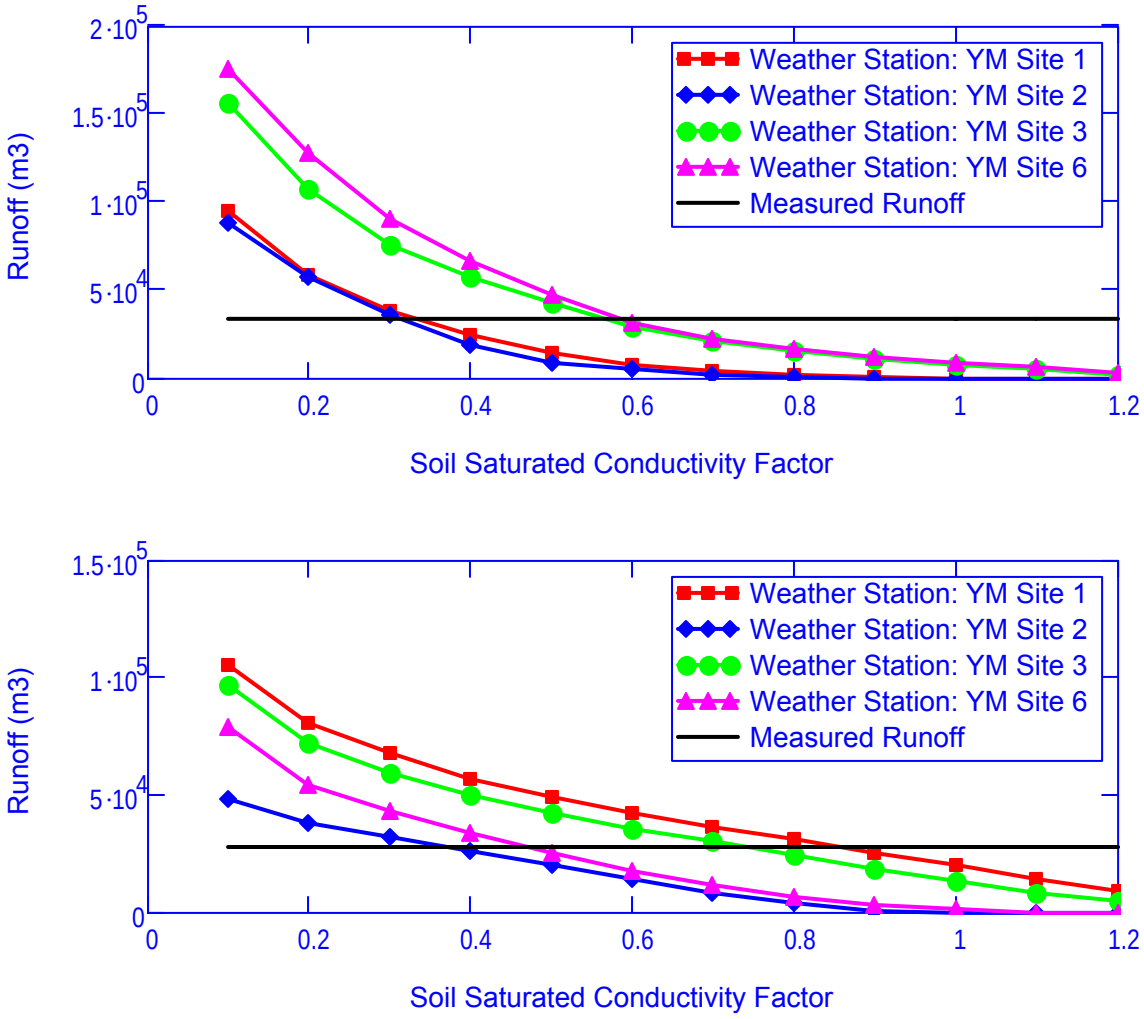

Source: Output DTN: SN0701T0502206.037, file: \Welcome to Massif\Massif\Validation Analyses\Stream Gauge Comparisons*Streamgage Plots.xmcd.*

Figure 7.1.3-10. Variation of Annual Cumulative Runoff with Soil Saturated Conductivity Factor (Upper Pagany Wash, Top: Water Year 1995, Bottom: Water Year 1998)

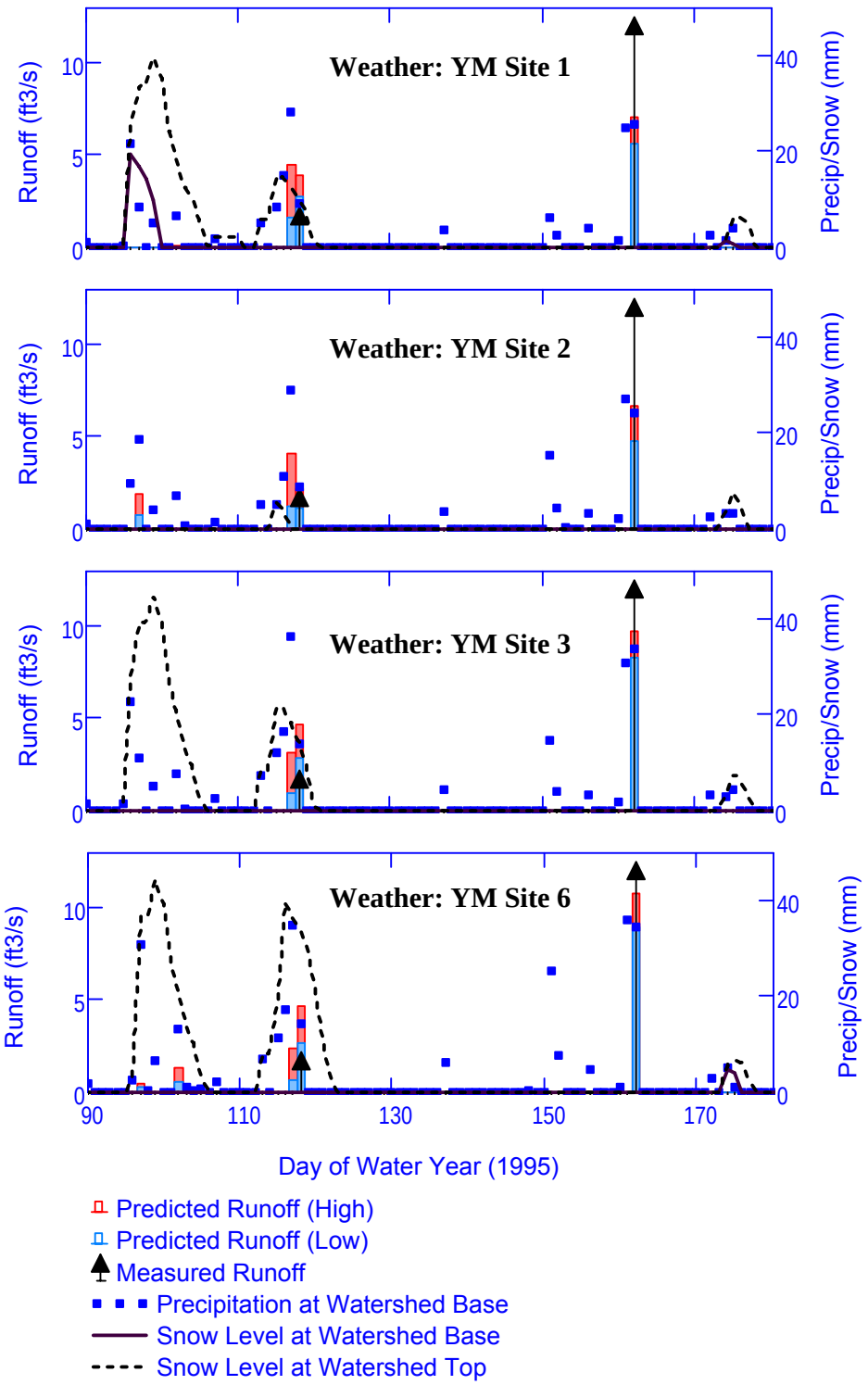

Source: Output DTN: SN0701T0502206.037, file: \Welcome to Massif\Massif\Validation Analyses\Stream Gauge Comparisons*Streamgage Plots.xmcd*.

Figure 7.1.3-11. Predicted (Solid Bar) and Measured (Arrow) Runoff (Upper Pagany Wash, Water Year 1995)

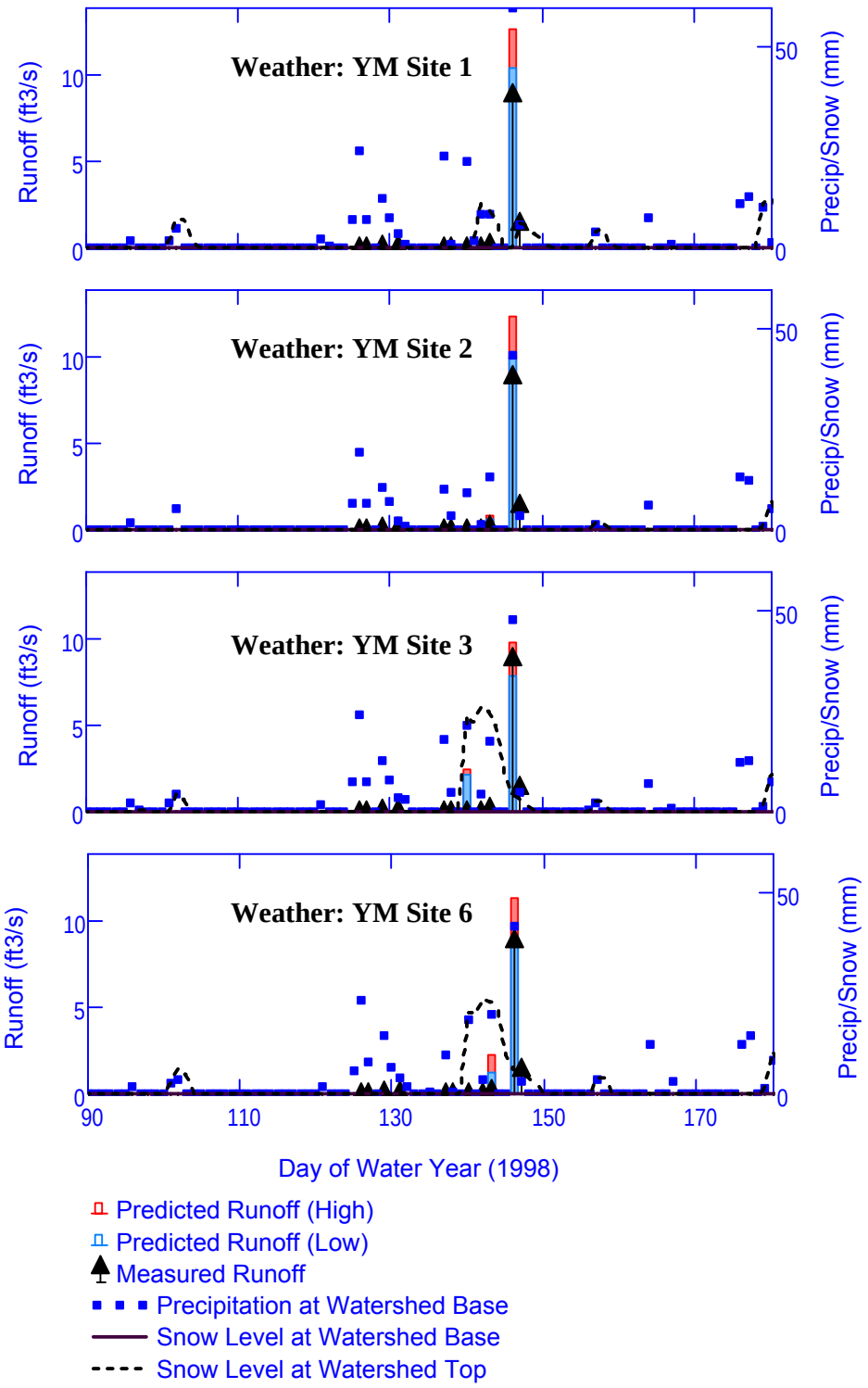

Source: Output DTN: SN0701T0502206.037, file: \Welcome to Massif\Massif\Validation Analyses\Stream Gauge Comparisons*Streamgage Plots.xmcd*.

Figure 7.1.3-12. Predicted (Solid Bar) and Measured (Arrow) Runoff (Upper Pagany Wash, Water Year 1998)

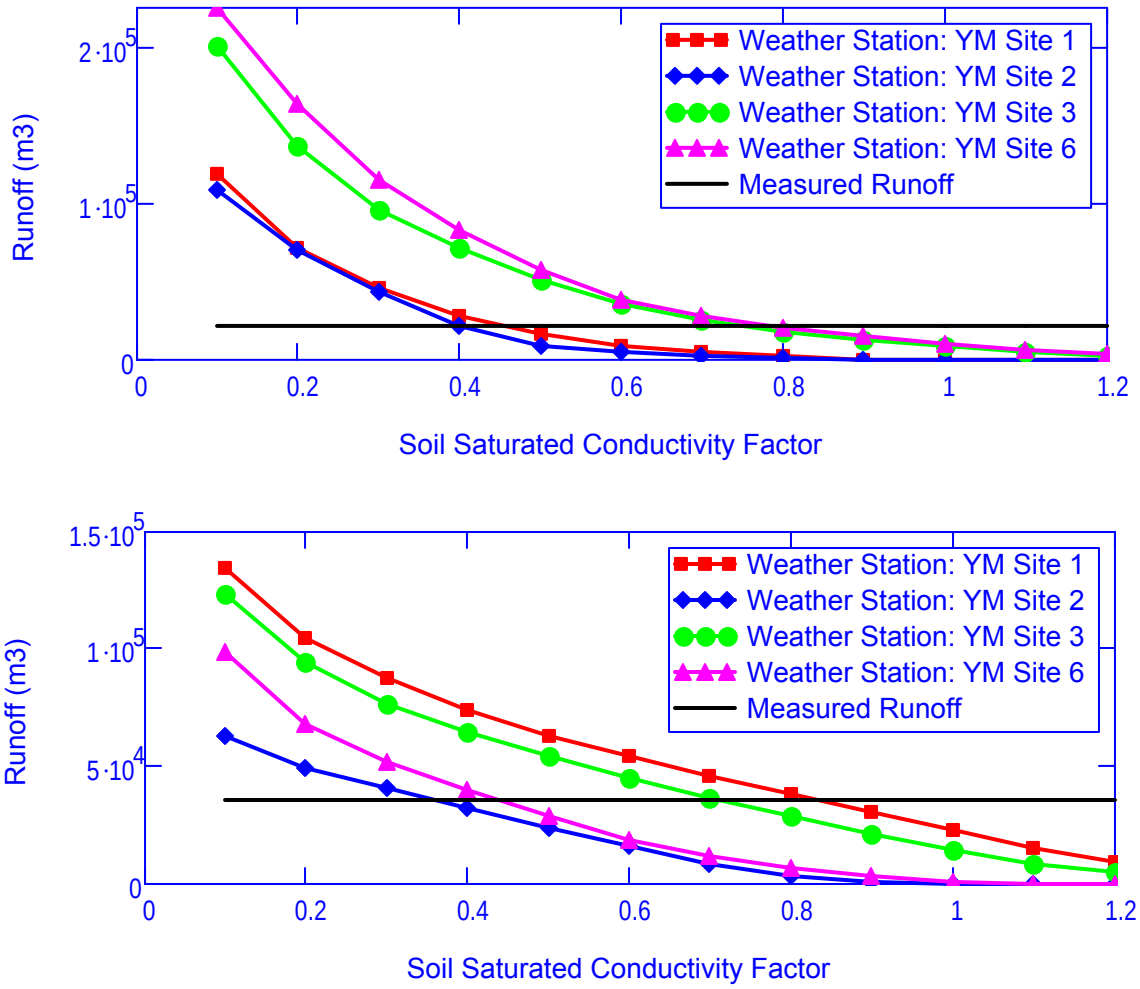

Source: Output DTN: SN0701T0502206.037, file: \Welcome to Massif\Massif\Validation Analyses\Stream Gauge Comparisons*Streamgage Plots.xmcd*.

Figure 7.1.3-13. Variation of Annual Cumulative Runoff with Soil Saturated Conductivity Factor (Lower Pagany Wash, Top: Water Year 1995, Bottom: Water Year 1998)

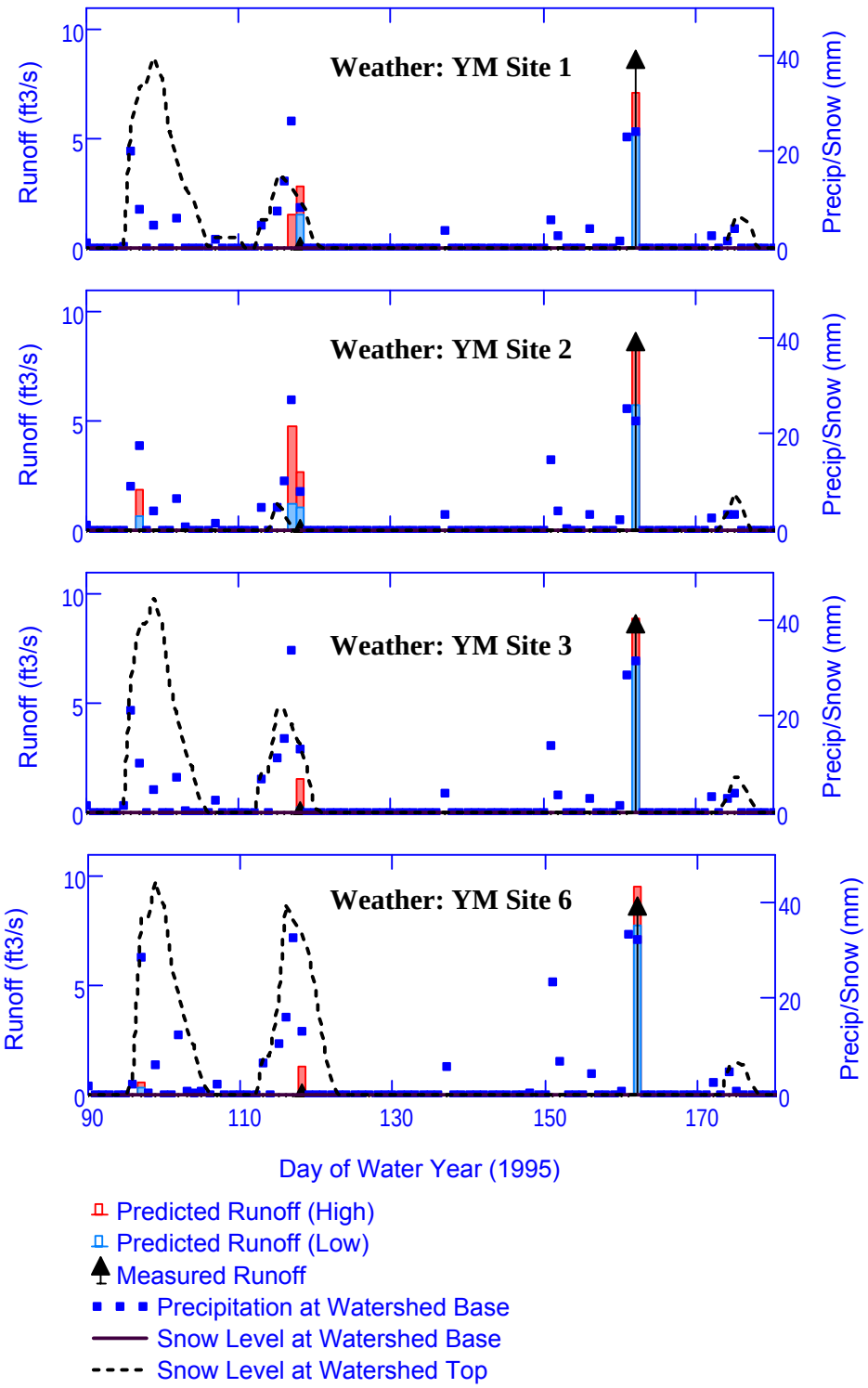

Source: Output DTN: SN0701T0502206.037, file: \Welcome to Massif\Massif\Validation Analyses\Stream Gauge Comparisons*Streamgage Plots.xmcd*.

Figure 7.1.3-14. Predicted (Solid Bar) and Measured (Arrow) Runoff (Lower Pagany Wash, Water Year 1995)

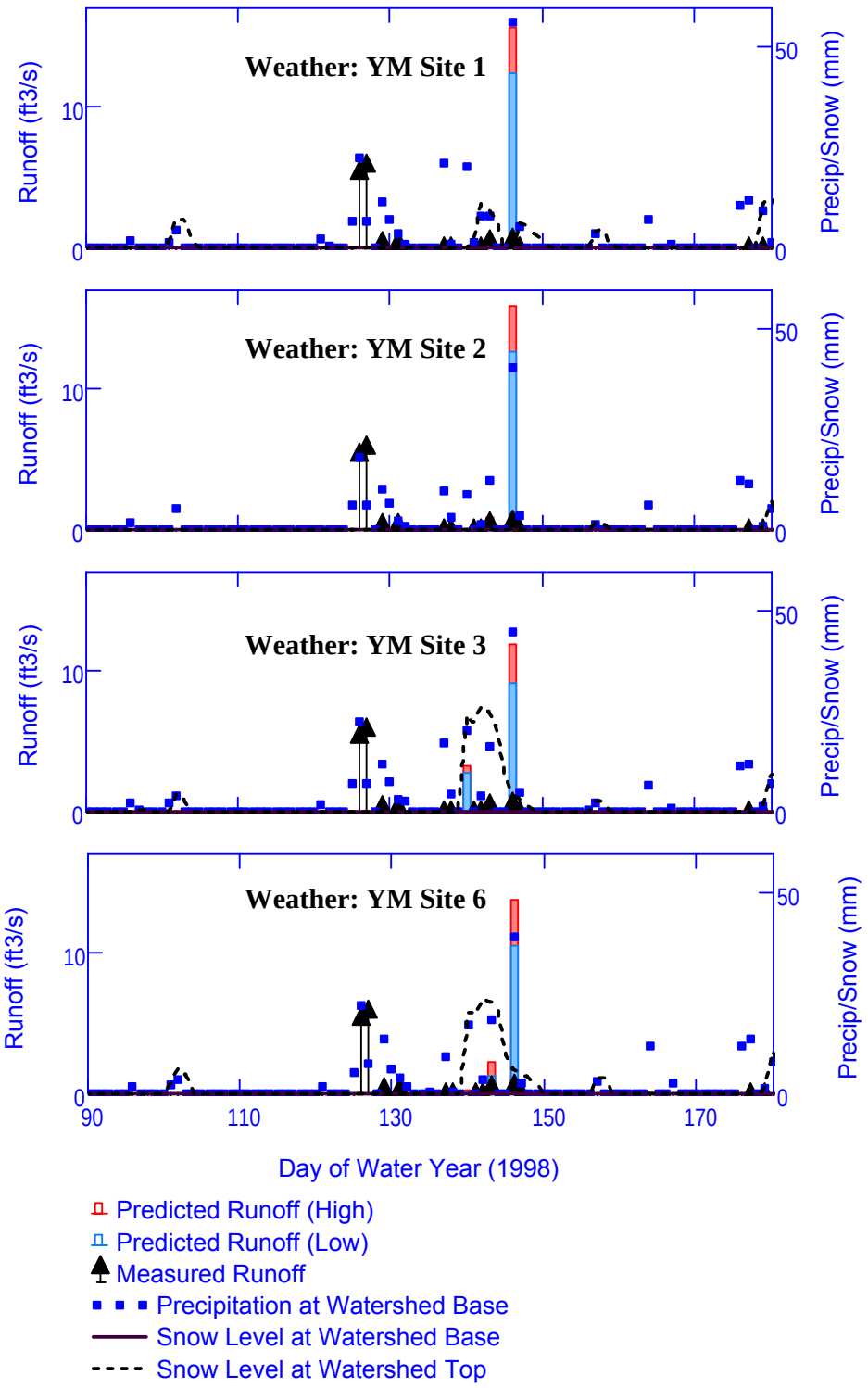

Source: Output DTN: SN0701T0502206.037, file: \Welcome to Massif\Massif\Validation Analyses\Stream Gauge Comparisons*Streamgage Plots.xmcd*.

Figure 7.1.3-15. Predicted (Solid Bar) and Measured (Arrow) Runoff (Lower Pagany Wash, Water Year 1998)

In general, MASSIF correctly predicts the timing and magnitude of runoff using the nominal parameter set with variations in the soil conductivity. Typically, the soil conductivities are reduced by multipliers of 0.3 to 0.7, which is within the range between the maximum and minimum soil conductivities for a given soil type from the Hanford soils data set (BSC 2006 [DIRS 176335], Table 6-7). Alternatively the conductivity reduction could be explained by soil structure, which can dominate water sorption in soils.

7.1.3.1 Runoff and Net Infiltration Comparison

When MASSIF is used to predict infiltration at the grid cell containing the UZ#4 borehole (LeCain et al. 2002 [DIRS 158511]) near the mouth of Lower Pagany Wash, the soil saturated conductivity must be increased by an order of magnitude to 7×10^{-6} m/s in order to match the measured infiltration (see Section 7.2.1.1.2). The rock conductivity was also increased to 10^{-3} m/s so that it had no influence on the infiltration. Soil Type 3 occupies the drainage channel in Lower Pagany Wash (Figure 7.1.3-16). Hofmann et al. (2000 [DIRS 153709]) measured the saturated hydraulic conductivity of the soil at two locations at Yucca Mountain. These locations included a measurement in Pagany Wash near borehole UE-25 UZN #14 and a measurement on a stable terrace adjacent to Fortymile Wash at borehole UE-25 UZN #85, both using a prototype-automated-infiltrometer. They found that the saturated hydraulic conductivity was 17.79 cm/hr (4.94×10^{-5} m/s) for the location in Pagany Wash and 1.78 cm/hr (4.94×10^{-6} m/s) for the terrace location (Hofmann et al. 2000 [DIRS 153709], Table 4). Both of these measurements are significantly higher than the soil conductivity used in this study. In addition, the value in Pagany Wash is an order of magnitude higher than the value on the stable terrace.

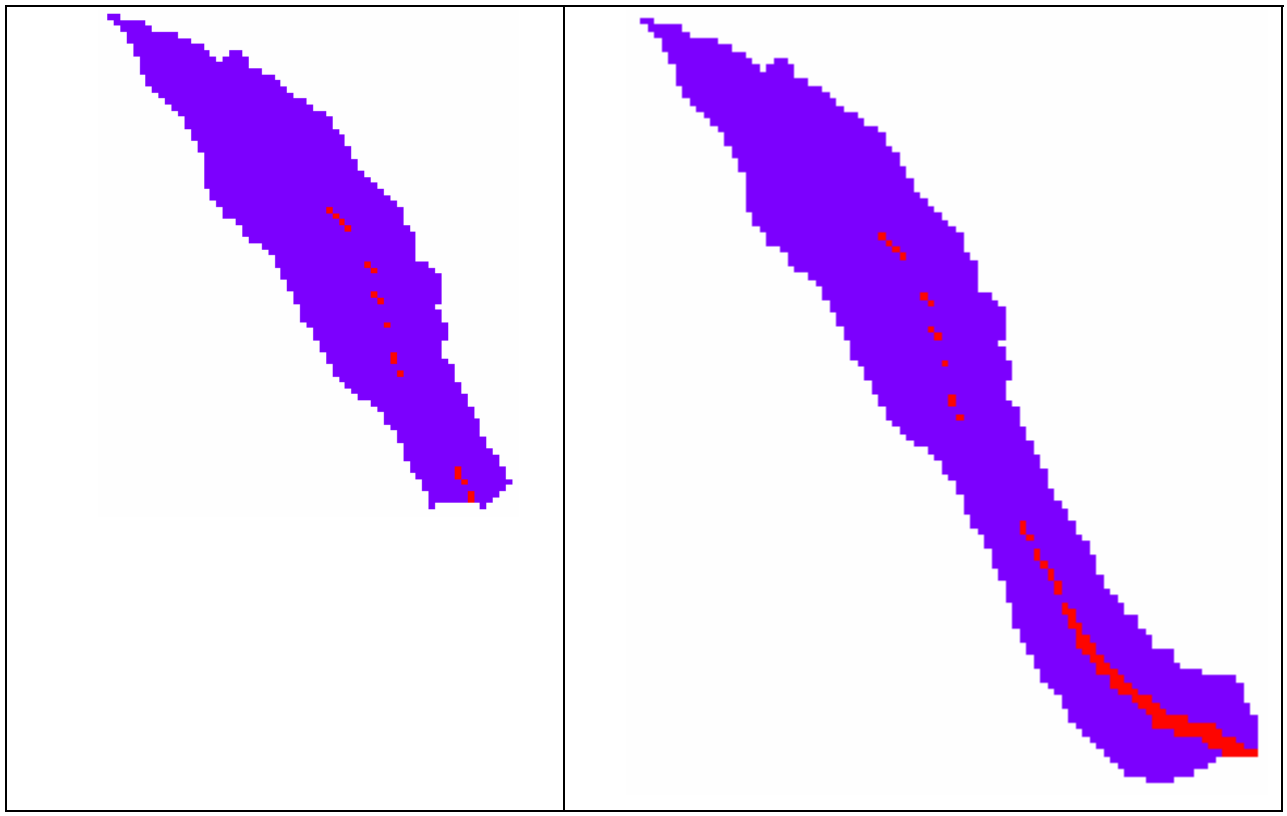

Source: Output DTNs: SN0606T0502206.011 and SN0701T0502206.037, file: \Welcome to Massif\Massif\Validation Analyses\Stream Gauge Comparisons*Streamgage Plots.xmcd*.

Figure 7.1.3-16. Locations of Soil Type 3 in Upper Pagany Wash watershed (left) and Lower Pagany Wash watershed (right) (Note: the Lower Pagany Wash watershed includes the Upper Pagany Wash watershed)

To test if this perturbation is consistent with the Pagany Wash streamflow gauge data, a variation scenario of the Pagany Wash calculations is performed with soil type 3 conductivity set to 7×10^{-6} m/s and the rock conductivities set to 1×10^{-3} m/s. The balance of the soil conductivities are varied as before using a soil saturated conductivity factor. The rest of the input parameters are set to their nominal values as in the base-case scenario described above.

For the Upper Pagany Wash, the calculated annual runoff as a function of soil conductivity factor does not change significantly for the variation scenario (compare Figure 7.1.3-17 to Figure 7.1.3-10). This is because soil type 3 occurs only sporadically in the Upper Pagany Wash (Figure 7.1.3-16). Daily runoff comparisons (Figures 7.1.3-18 and 7.1.3-19) are nearly the same as the base-case calculation (Figures 7.1.3-11 and 7.1.3-12).

For the Lower Pagany Wash, the change in the calculated annual runoff as a function of soil conductivity factor for the variation scenario (Figure 7.1.3-20) is more pronounced. The intercepts between the calculated runoffs (colored lines) and the measured runoff (solid black line) are shifted to the left when compared to the base-case calculation (Figure 7.1.3-13). This means that the conductivities of soils other than type 3 must be lower that in the base case in order to generate more run-on to the locations with soil type 3. In spite of this shift in the intercepts, the calculations of daily runoff (Figures 7.1.3-21 and 7.1.3-22) are comparable to

those for the base-case calculation of runoff (Figures 7.1.3-14 and 7.1.3-15). Both sets of soil saturated conductivities are consistent with the measured runoff data for Pagany Wash.

Despite the good agreement between the observed and predicted runoff in both of these scenarios, there is a pronounced difference in the spatial distribution of net infiltration for each of these scenarios even though the mean value of net infiltration is nearly identical between scenarios. Figures 7.1.3-23 and 7.1.3-25 show net infiltration maps for water year 1995 and 1998, respectively, for the base-case scenario (nominal soil conductivity values multiplied by the factor 0.75). Figures 7.1.3-24 and 7.1.3-26 show net infiltration maps for water year 1995 and 1998, respectively, for the variation scenario (soil type 3 conductivity set to 7×10^{-6} m/s, rock conductivities set to 10^{-3} m/s, and remaining soil conductivity values multiplied by the factor 0.55). The main difference between the scenarios is the location of the net infiltration. In the base-case scenario, net infiltration occurs primarily outside the central stream channel area and is highest in the higher portions of the watershed. In fact, there is little to no net infiltration in the upper reach of the channel and only a minor amount of infiltration in the lower reach. In the variation scenario, the net infiltration in the upper part of the basin is slightly reduced while the infiltration in the lower reach of the channel has increased greatly, especially in areas where soil type 3 is found.

This comparison between the base-case and variation simulations of Pagany Wash illustrates an important point about the inherent uncertainty in the spatial distribution of net infiltration. Soil conductivity values were not screened into the uncertainty analysis presented in Section 6.5 because the parameter uncertainty was either low or the fraction of the UZ model domain that was covered by a given soil type was below the 15% criterion (Section 6.5.2). Soil conductivity was included in the extended parameter sensitivity study (Section 7.1.4) and the uncertainty distributions for soil conductivity were even expanded in an effort to account for the need to adjust soil conductivity to match observed runoff data as described in this section. Nevertheless, soil conductivity did not result in being one of the most sensitive parameters for determining mean net infiltration. However, the present comparison suggests that there may be considerably more uncertainty as to where net infiltration is occurring than is represented by 40 realizations used to characterize infiltration uncertainty analysis in Section 6.5.7. In order to reduce this uncertainty for a given watershed more detailed information concerning the spatial distribution of soil types and properties would be required.

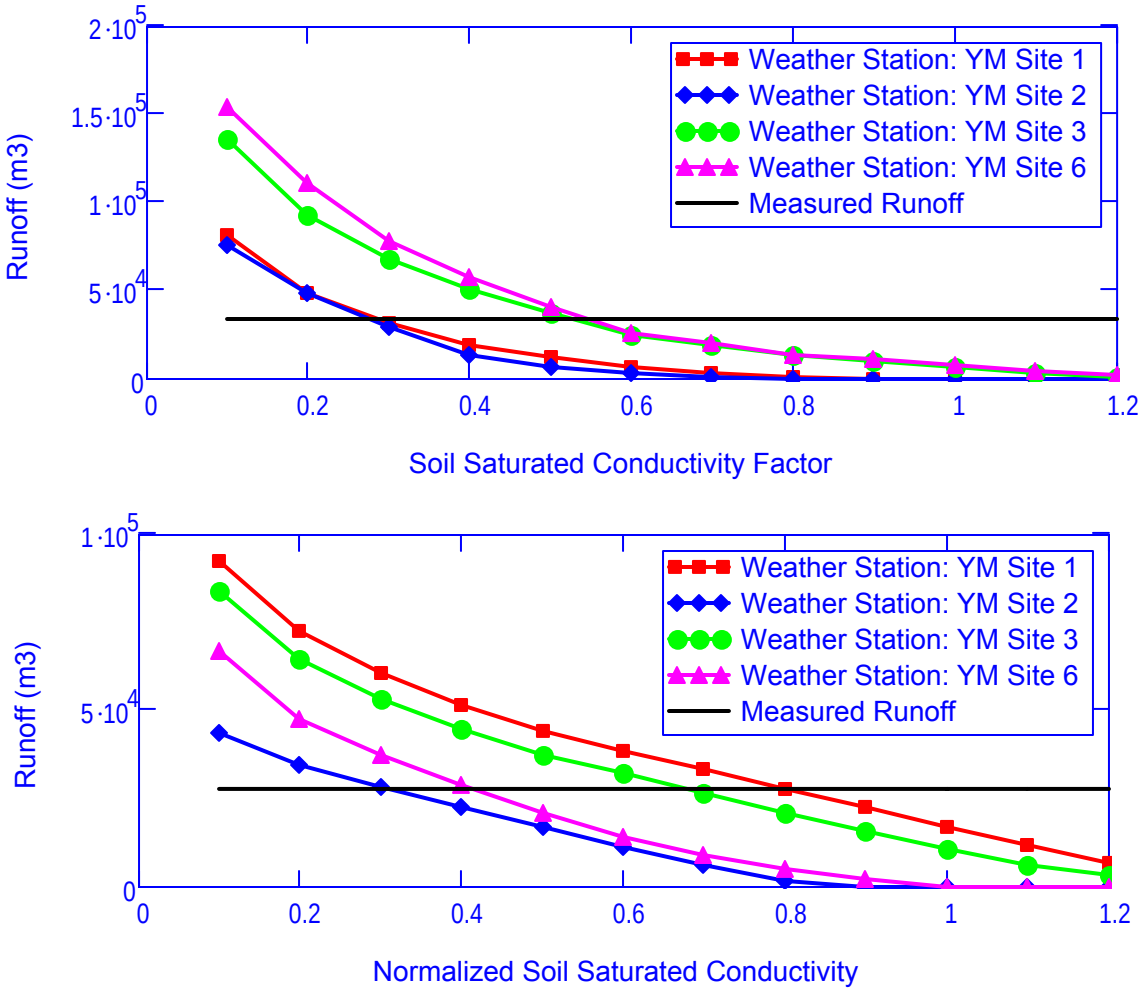

Source: Output DTN: SN0701T0502206.037, file: \Welcome to Massif\Massif\Validation Analyses\Stream Gauge Comparisons*Streamgage Plots.xmcd*.

Figure 7.1.3-17. Variation of Annual Cumulative Runoff with Soil Saturated Conductivity Factor: Soil Type 3 Conductivity Set to 7×10^{-6} m/s (Upper Pagany Wash, Top: Water Year 1995, Bottom: Water Year 1998)

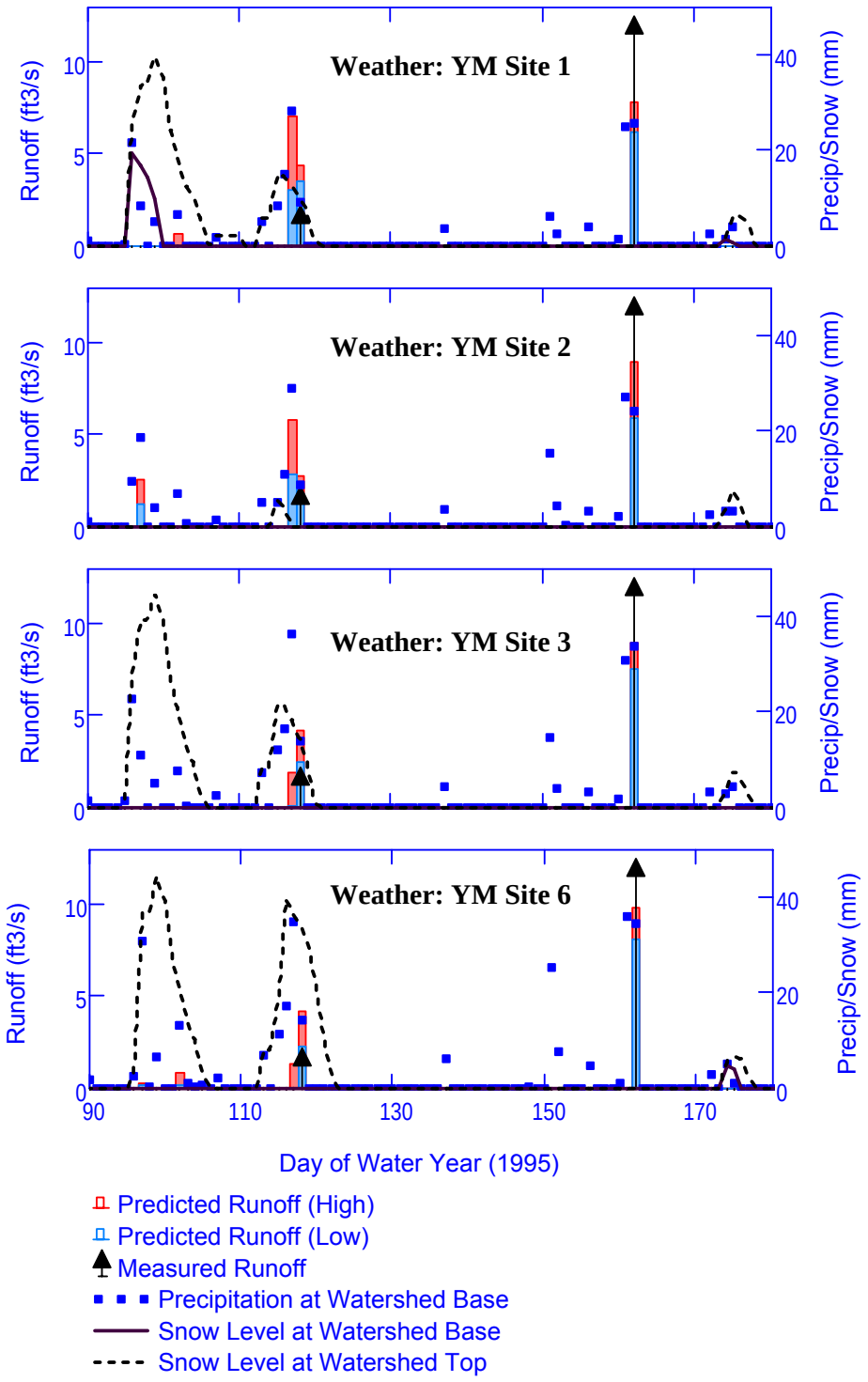

Source: Output DTN: SN0701T0502206.037, file: \Welcome to Massif\Massif\Validation Analyses\Stream Gauge Comparisons*Streamgage Plots.xmcd*.

Figure 7.1.3-18. Predicted (Solid Bar) and Measured (Arrow) Runoff: Soil Type 3 Conductivity Set to 7×10^{-6} m/s (Upper Pagany Wash, Water Year 1995)

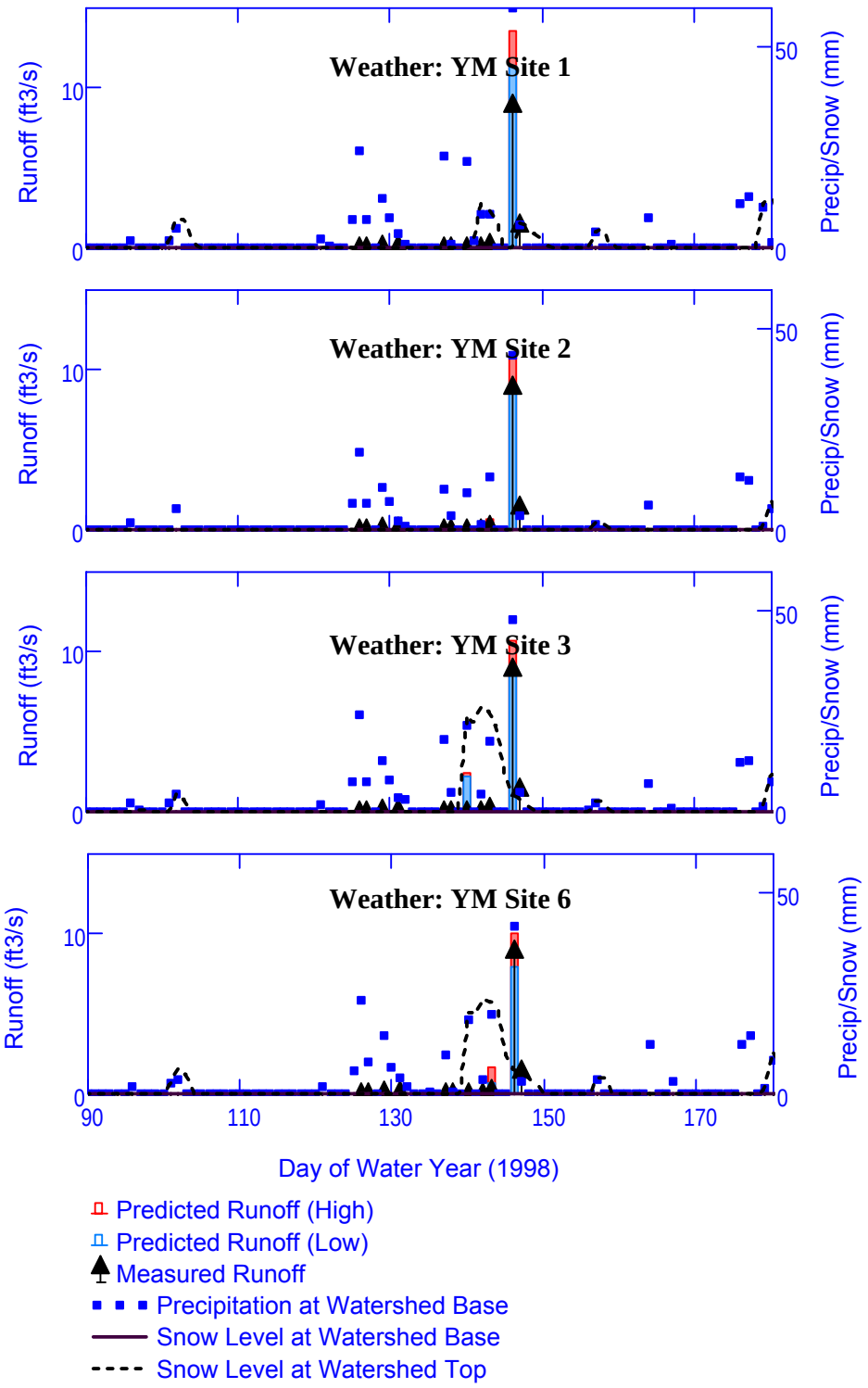

Source: Output DTN: SN0701T0502206.037, file: \Welcome to Massif\Massif\Validation Analyses\Stream Gauge Comparisons*Streamgage Plots.xmcd*.

Figure 7.1.3-19. Predicted (Solid Bar) and Measured (Arrow) Runoff: Soil Type 3 Conductivity set to 7×10^{-6} m/s (Upper Pagany Wash, Water Year 1998)

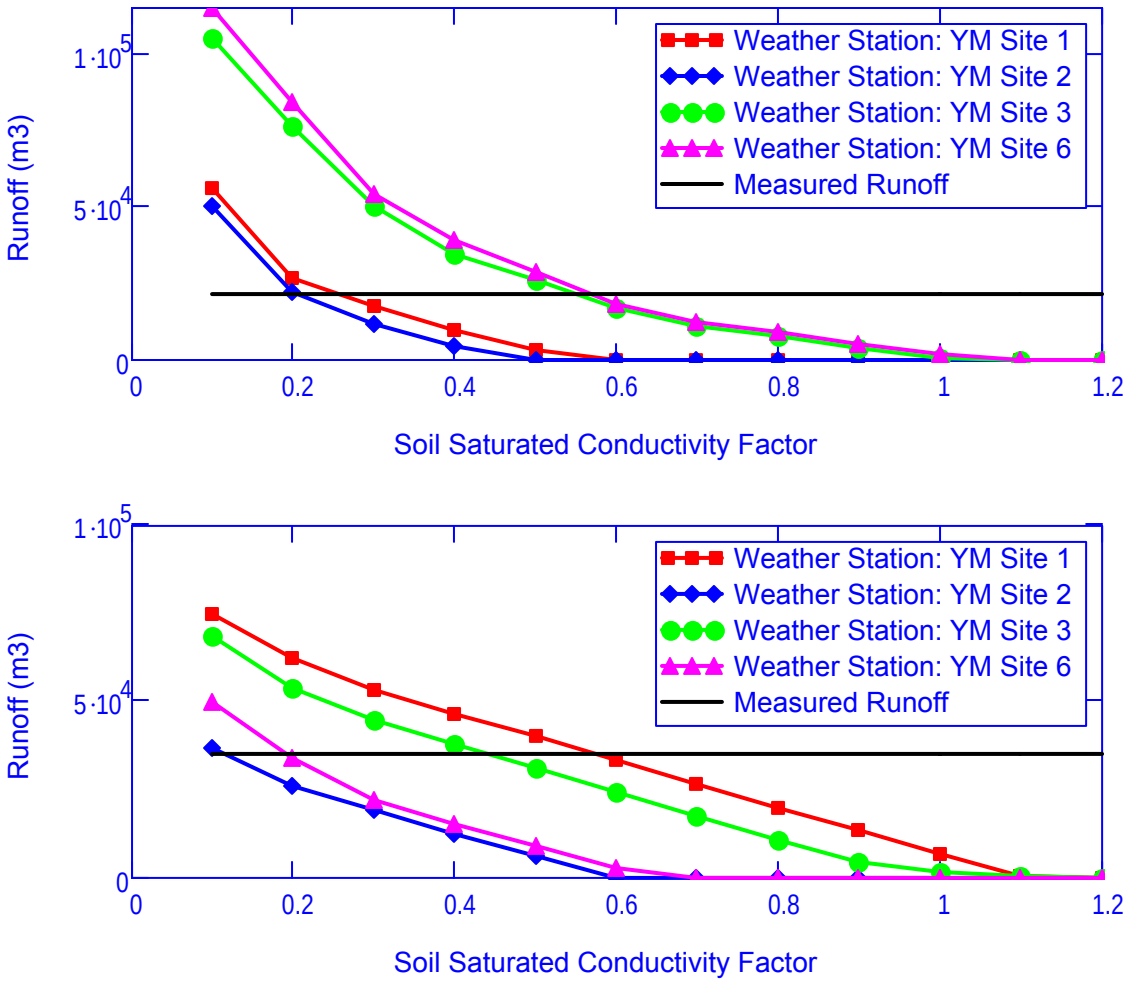

Source: Output DTN: SN0701T0502206.037, file: \Welcome to Massif\Massif\Validation Analyses\Stream Gauge Comparisons*Streamgage Plots.xmcd*.

Figure 7.1.3-20. Variation of Annual Cumulative Runoff with Soil Saturated Conductivity Factor: Soil Type 3 Conductivity Set to 7×10^{-6} m/s (Lower Pagany Wash, Top: Water Year 1995, Bottom: Water Year 1998)

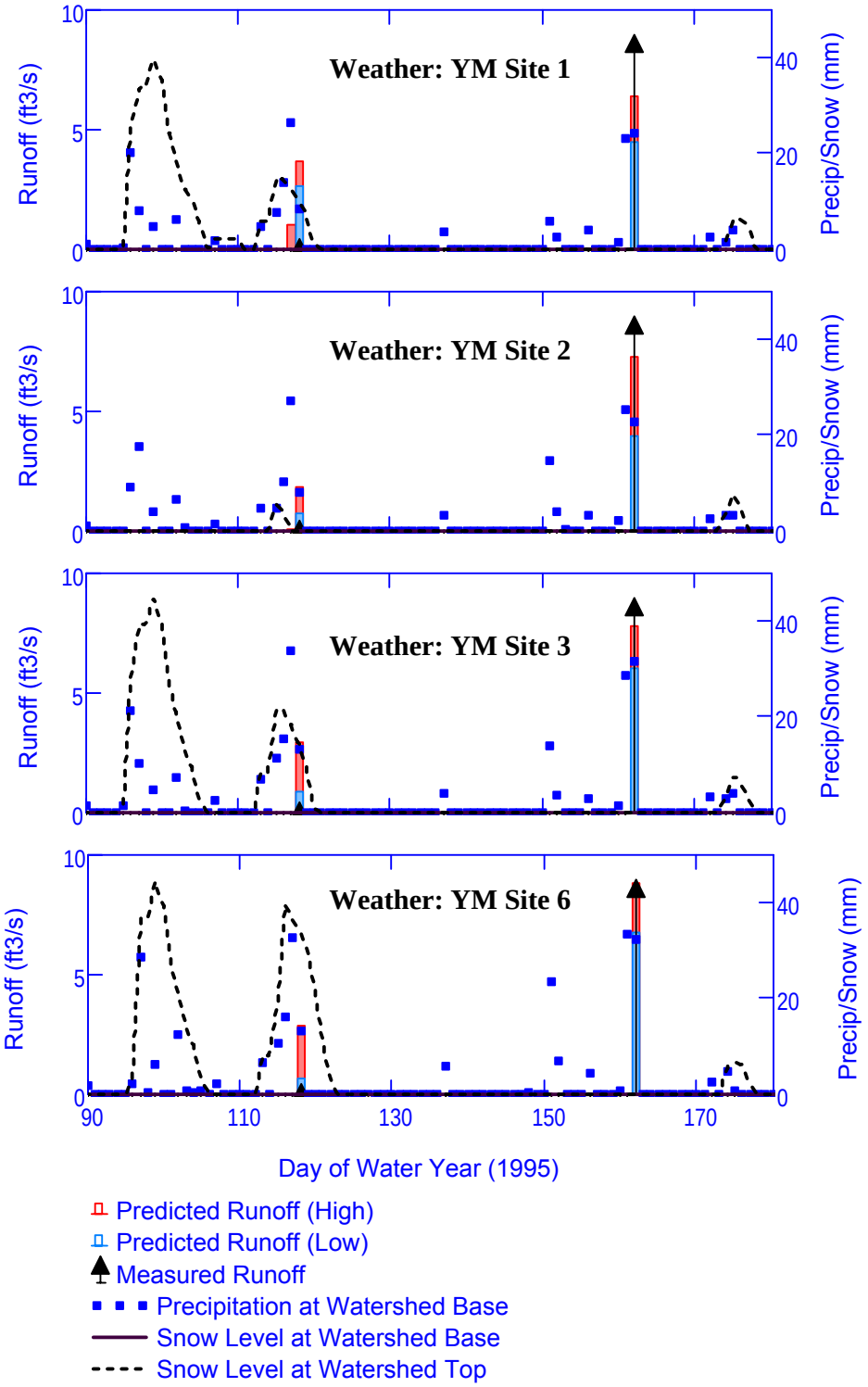

Source: Output DTN: SN0701T0502206.037, file: \Welcome to Massif\Massif\Validation Analyses\Stream Gauge Comparisons*Streamgage Plots.xmcd*.

Figure 7.1.3-21. Predicted (Solid Bar) and Measured (Arrow) Runoff: Soil Type 3 Conductivity Set to 7×10^{-6} m/s (Lower Pagany Wash, Water Year 1995)

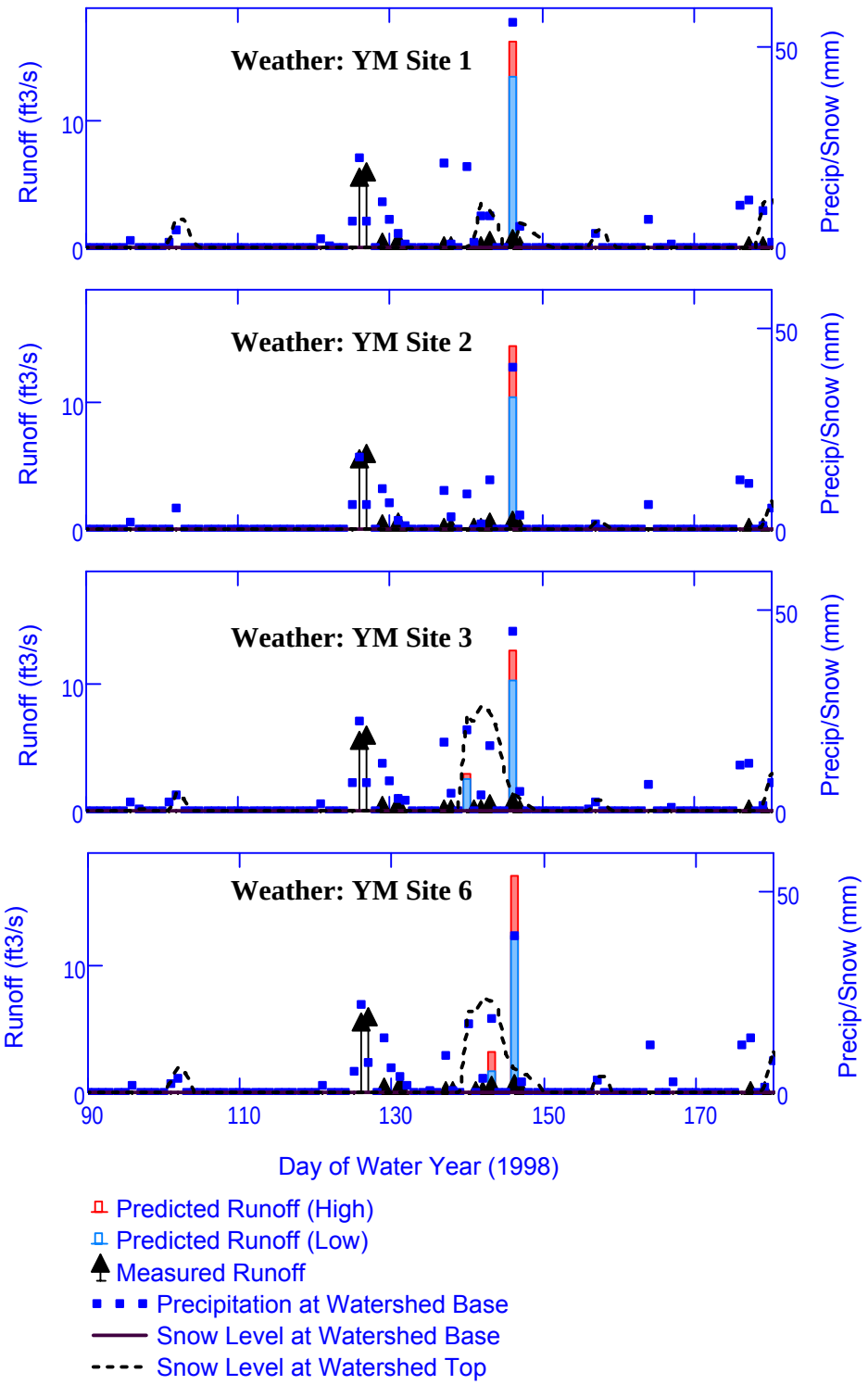

Source: Output DTN: SN0701T0502206.037, file: \Welcome to Massif\Massif\Validation Analyses\Stream Gauge Comparisons*Streamgage Plots.xmcd*.

Figure 7.1.3-22. Predicted (Solid Bar) and Measured (Arrow) Runoff: Soil Type 3 Conductivity set to 7×10^{-6} m/s (Lower Pagany Wash, Water Year 1998)

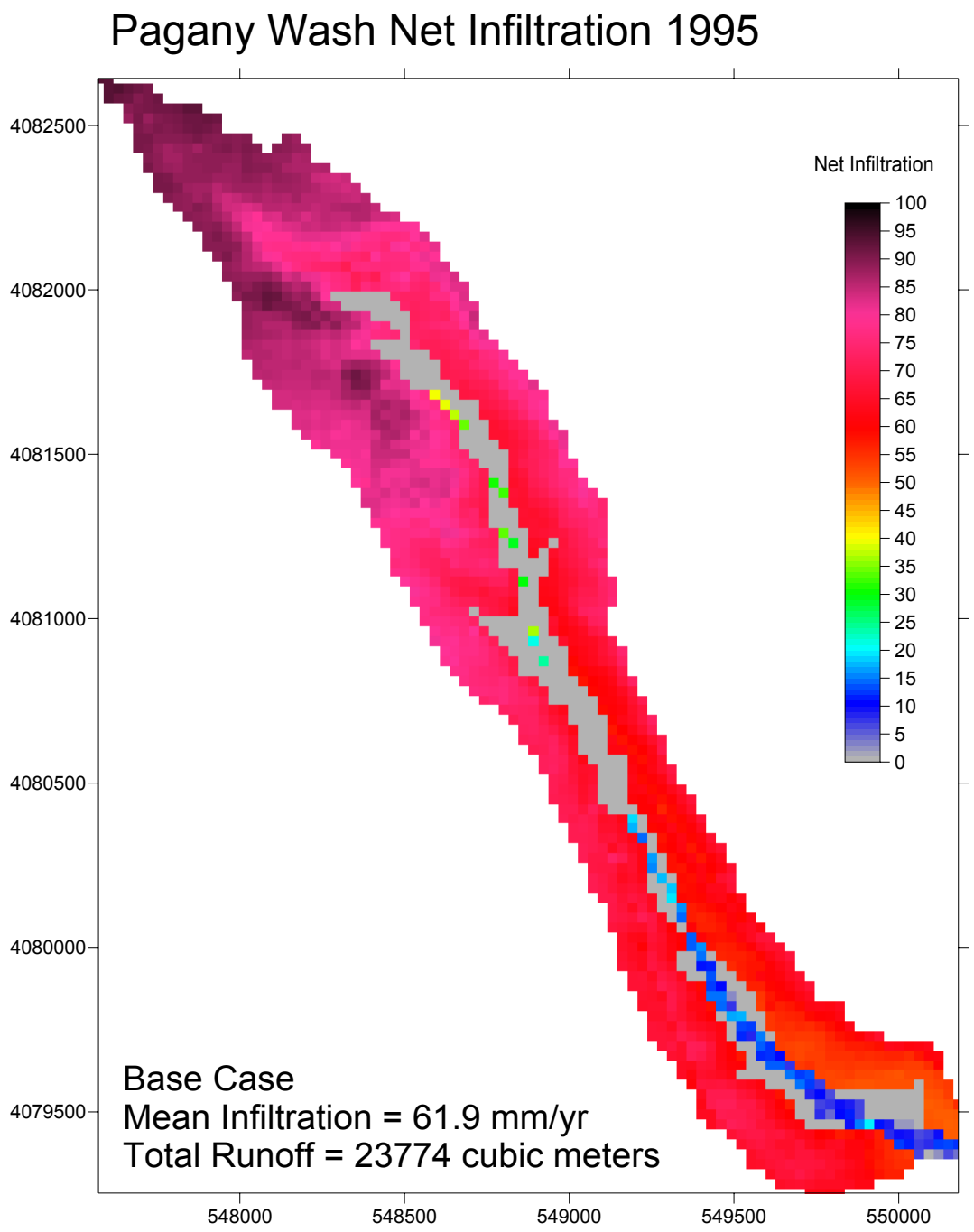

Coordinates are in meters; UTM NAD 27, Zone 11

Source: Output DTN: SN0701T0502206.037, file: \Welcome to Massif\Massif\Validation Analyses\Stream Gauge Comparisons*Infiltration Study Post Processing.xmcd*.

Figure 7.1.3-23. Net Infiltration Map for the Base-case Simulation at Pagany Wash for the Water Year 1995

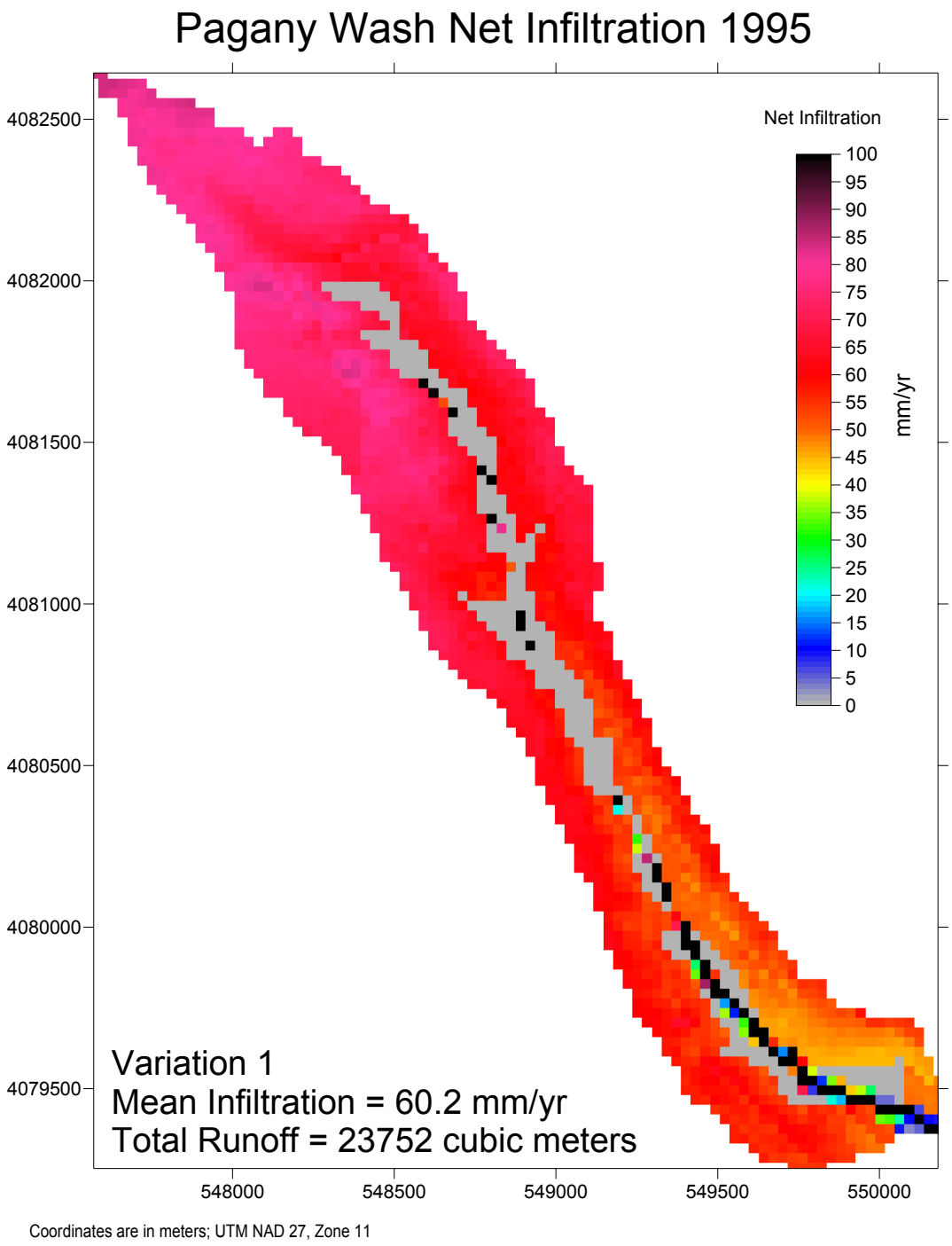

Source: Output DTN: SN0701T0502206.037, file: \Welcome to Massif\Massif\Validation Analyses\Stream Gauge Comparisons*Infiltration Study Post Processing.xmcd*.

NOTE: Upper end of the color scale is truncated such that cells that are colored black have infiltration greater than or equal to 100 mm/yr. Maximum net infiltration for this run is 463 mm/yr.

Figure 7.1.3-24. Net Infiltration Map for the Variation 1 Simulation at Pagany Wash for the Water Year1995

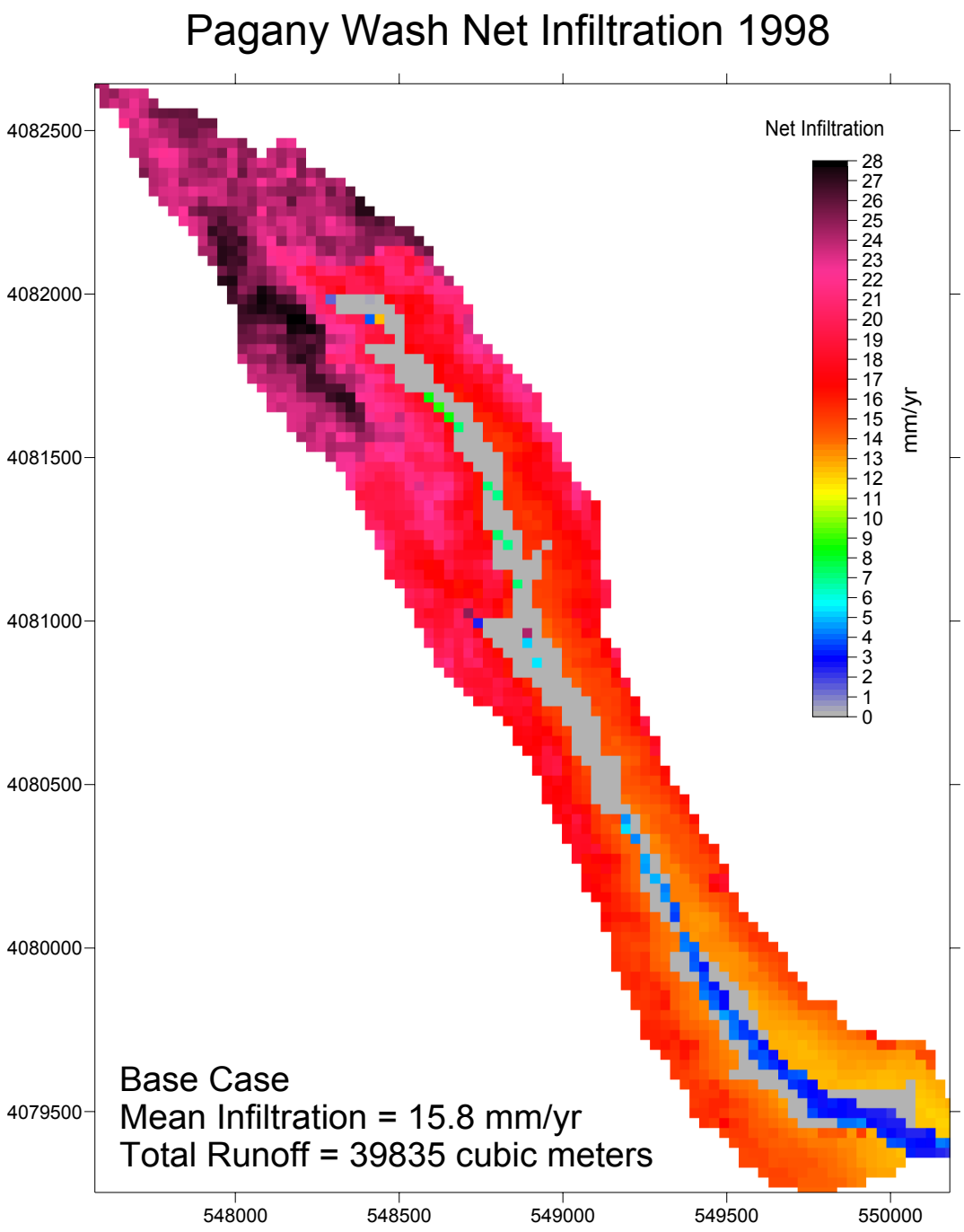

Source: Output DTN: SN0701T0502206.037, file: \Welcome to Massif\Massif\Validation Analyses\Stream Gauge Comparisons*Infiltration Study Post Processing.xmcd*.

Figure 7.1.3-25. Net Infiltration Map for the Base-case Simulation at Pagany Wash for the Water Year 1998

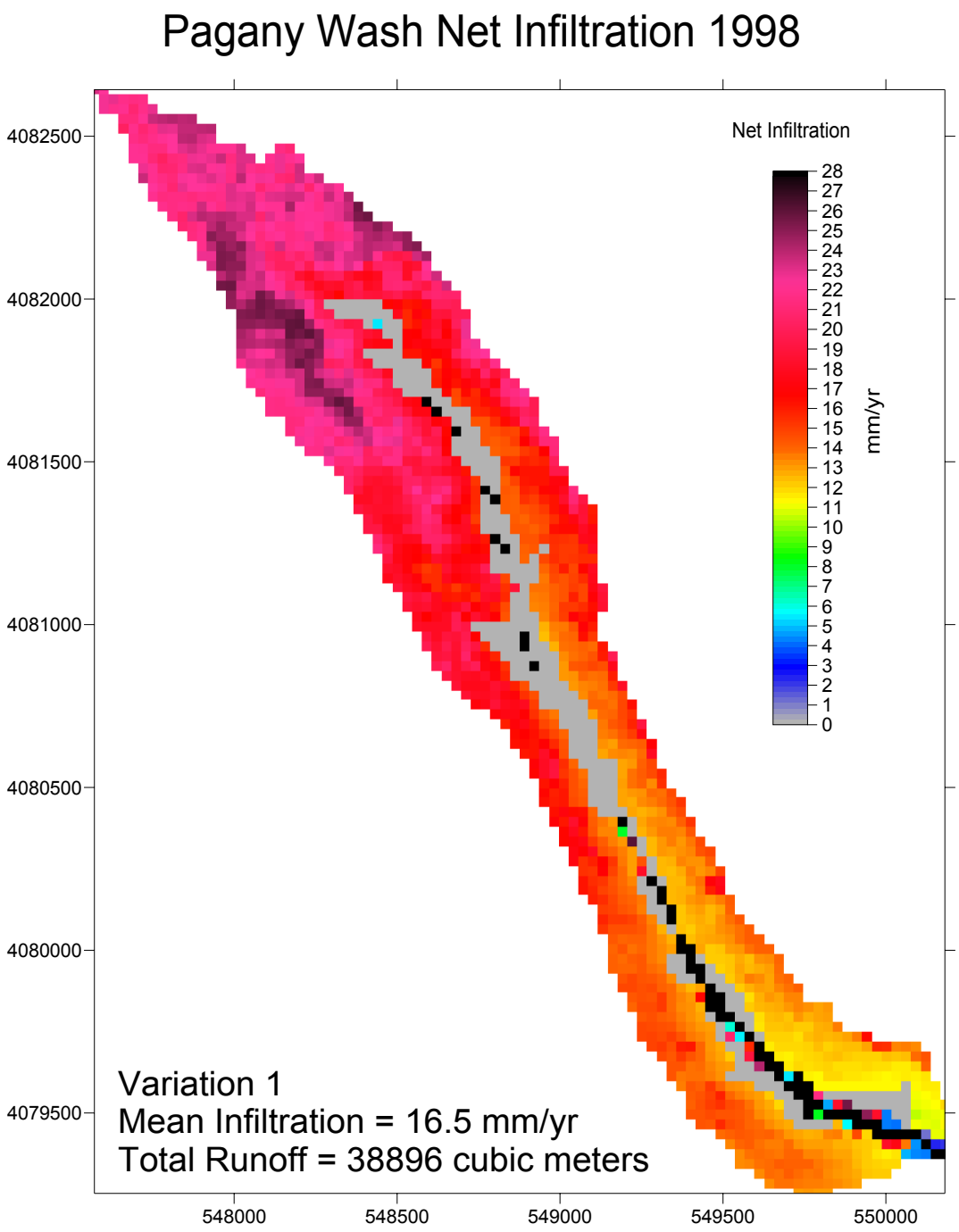

Coordinates are in meters; UTM NAD 27, Zone 11

Source: Output DTN: SN0701T0502206.037, file: \Welcome to Massif\Massif\Validation Analyses\Stream Gauge Comparisons*Infiltration Study Post Processing.xmcd*.

NOTE: Upper end of the color scale is truncated such that cells that are colored black have infiltration greater than or equal to 28 mm/yr. Maximum net infiltration for this run is 129 mm/yr.

Figure 7.1.3-26. Net Infiltration Map for the Variation 1 Simulation at Pagany Wash for the Water Year 998

7.1.3.2 Soil Conductivity Variation Illustration for Entire Net Infiltration Modeling Domain

When calculating runoff at monitored streamflow gauge sites (Section 7.1.3.2), a variation scenario was simulated for Pagany Wash watershed in which the soil conductivity of the dominant soil type representing stream channels (soil type 3) was increased by an order of magnitude while the conductivity of the other soil types was decreased by a constant factor. This scenario was investigated because of the LeCain borehole data on infiltration (Section 7.2.1.1.2). A conclusion of this scenario was to point out that the spatial distribution of soil conductivity plays an important role in determining the spatial distribution of net infiltration.

To explore the implications of the Pagany Wash study on the larger modeled domain, the four representative realizations (10th, 30th, 50th, and 90th) from the Present-Day simulations were run using an alternate soil conductivity assignment, as defined by the Pagany Wash example. Specifically, the four realizations identified in Table 6.5.7.1-3 were run with the following modifications: 1) the conductivity of soil types 3 and 4 were set to 7×10^{-6} m/s, 2) the rock conductivities were set uniformly to 10^{-3} m/s, and 3) the conductivity of the soil types other than 3 and 4 were reduced by a factor of 0.44. Soil types 3 and 4 were selected because, in general, these soil types are associated with the main stream channels (see Figure 6.5.2.2-2). These alternate runs are meant only as an example of how such differences could affect the final infiltration results. The choice of the specific soil conductivities is based on Pagany Wash simulations and data from a single high precipitation year, and this choice is probably not representative of the rest of the domain. Nevertheless, these results illustrate aspects of model sensitivity that are not explored in the sensitivity studies that look at spatial averages of net infiltration.

Figures 7.1.3.2-1 to 7.1.3.2-4 show net infiltration maps for the alternate soil conductivity realizations: 10th, 30th, 50th, 90th, respectively. These maps can be compared to Figures 6.5.7.1-2 to 6.5.7.1-5 to see how this change affects the patterns of net infiltration. One obvious difference is that the stream channels show up clearly on the infiltration maps representing the alternate soil conductivity scenario.

To quantitatively summarize these comparisons, two tables are presented below. Table 7.1.3.2-1 compares mean net infiltration over three different domains (net infiltration model domain, UZ model domain, and the repository footprint) for each realization. In addition, the runoff fraction is compared and the total weighted precipitation for each realization is listed. The tabulated results suggest that mean net infiltration over these regions and the total runoff leaving the domain are not significantly altered by this variation in soil conductivity.

Table 7.1.3.2-2 compares the percent of the total infiltration that occurs in each soil group. It is here that a significant difference can be seen from the original base-case results. In the base-case realizations, between 76% and 97% of the total net infiltration occurred in areas covered with soil types 5, 7, or 9. In the alternate soil conductivity (Variation) runs, this percentage range fell to 34% to 70%. The fraction of the total infiltration in soil types 3 and 4, increased from a range of 0.2% to 11% to a range of 20% to 55%. The lesson learned from these results is that it is impossible to determine from the available characterization data exactly where the bulk of the net infiltration occurs. Furthermore, the results suggest that the predicted mean net infiltration

over relatively large areas (e.g., UZ model domain and repository footprint) is fairly stable. It is the spatial distribution of net infiltration that is especially sensitive to the spatial distribution of soil properties.

Table 7.1.3.2-1. Comparison of Mean Net Infiltration Results of the Soil Conductivity Variation Simulations with Results of the Uncertainty Analysis

Present-Day Climate				
Percentile	10th	30th	50th	90th
Replicate	R2	R2	R2	R2
Realization	10	2	8	14
Entire Domain Infiltration (mm/yr)	3.9	7.3	13.0	26.7
Entire Domain Variation Infiltration (mm/yr)	4.1	7.7	15.9	27.2
UZ Infiltration (mm/yr)	3.4	6.0	10.9	28.7
UZ Variation Infiltration (mm/yr)	3.5	5.9	13.4	27.5
Repository Infiltration (mm/yr)	3.9	6.5	10.9	34.4
Repository Variation Infiltration (mm/yr)	3.9	4.9	9.5	28.3
Runoff Fraction (%)	0.9	1.8	3.8	1.3
Runoff Fraction Variation (%)	0.8	1.6	3.2	1.1
Mean Annual Precipitation (mm/yr)	144.1	160.6	189.3	212.7

Source: Output DTN: SN0701T0502206.037, file: \Welcome to Massif\Massif\Post Processing All Climates*PD Soil Conductivity Variation Study.xls*.

Table 7.1.3.2-2. Comparison of Percent of the Total Net Infiltration Occurring in Each Soil Group between the Soil Conductivity Variation Simulations and the Results of the Uncertainty Analysis

Present-Day Climate	Percent of Net Infiltration [%]			
Percentile	10th	30th	50th	90th
Replicate	R2	R2	R2	R2
Realization	10	2	8	14
Soil Group 1 (%)	0.2	0.7	3.5	0.0
Soil Group 1 Variation (%)	0.0	0.1	0.6	0.0
Soil Groups 2/6 (%)	0.4	1.0	5.2	0.0
Soil Groups 2/6 Variation (%)	0.0	0.1	0.7	0.0
Soil Groups 3/4 (%)	1.4	2.3	10.6	0.2
Soil Groups 3/4 Variation (%)	19.7	35.4	55.1	24.9
Soil Groups 5/7/9 (%)	85.7	88.6	76.0	97.1
Soil Groups 5/7/9 Variation (%)	66.6	54.6	34.4	69.9
Soil Group 8 (%)	12.3	7.3	4.7	2.7
Soil Group 8 Variation (%)	13.7	9.8	9.2	5.2

Source: Output DTN: SN0701T0502206.037, file: \Welcome to Massif\Massif\Post Processing All Climates*PD Soil Conductivity Variation Study.xls.*

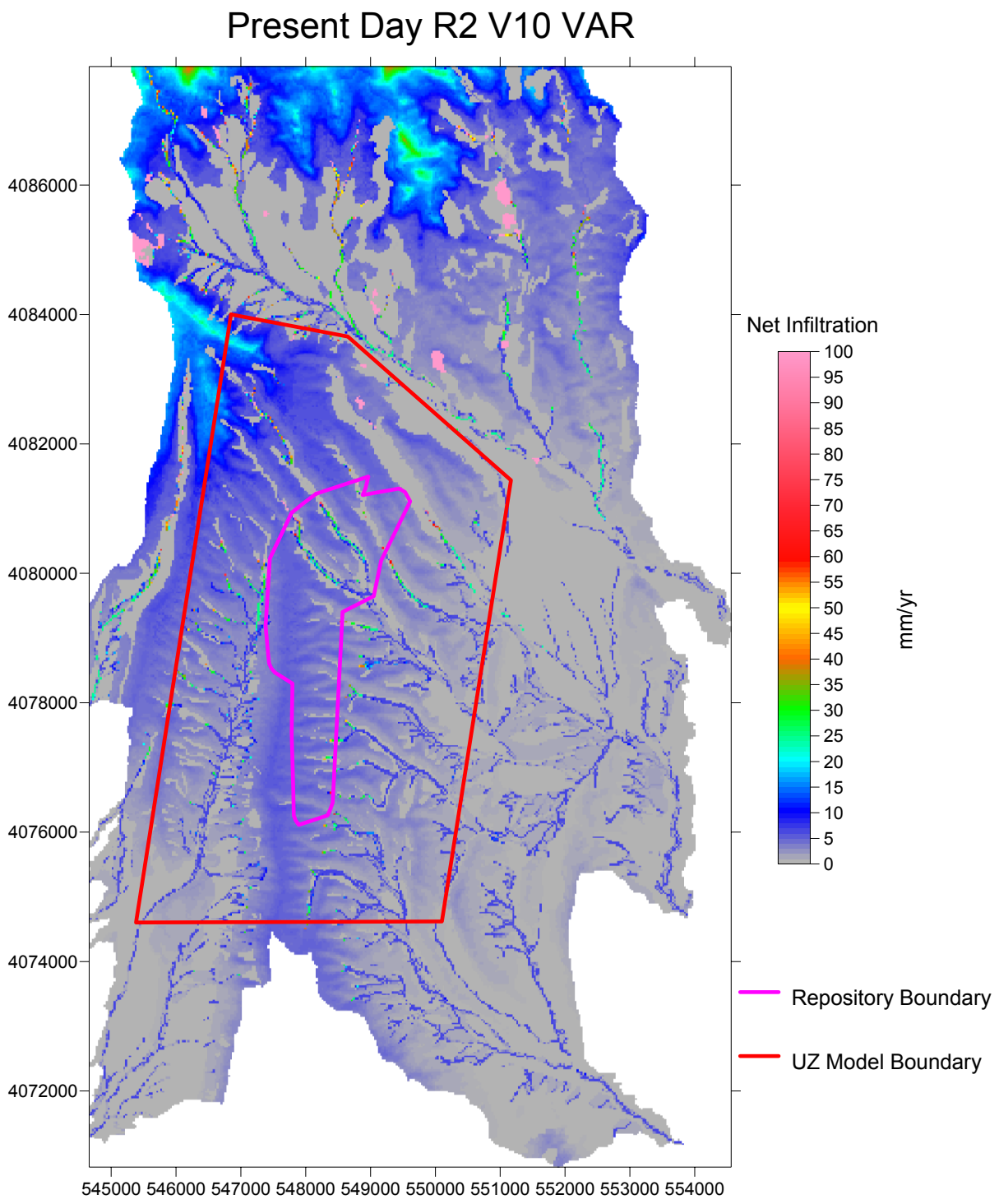

Coordinates are in meters; UTM NAD 27, Zone 11

Source: Output DTN: SN0701T0502206.037, file: \Welcome to Massif\Massif\Present Day Uncertainty\Infiltration Map Variations*Present Day R2 V10.xmcd* (net infiltration results from soil conductivity variation study); Output DTN: SN0612FTPRNUZB.002 (UZ model and repository boundaries).

Figure 7.1.3.2-1. Present-Day, 10th Percentile Net Infiltration Map (Soil Conductivity Variation) (Replicate R2, Realization 10)

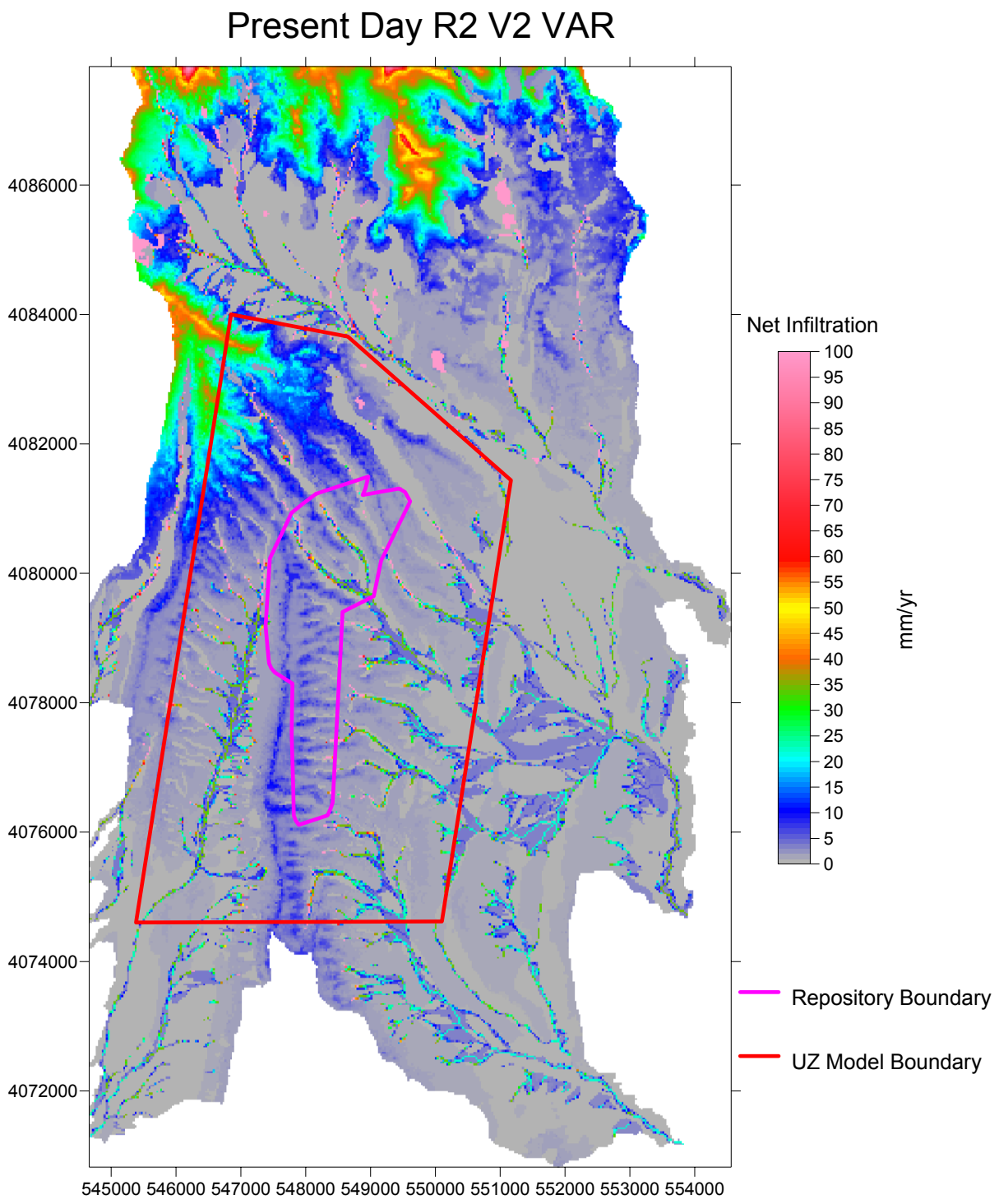

Coordinates are in meters; UTM NAD 27, Zone 11

Source: Output DTN: SN0701T0502206.037, file: \Welcome to Massif\Massif\Present Day Uncertainty\Infiltration Map Variations*Present Day R2 V02.xmcd* (net infiltration results from soil conductivity variation study); Output DTN: SN0612FTPRNUZB.002 (UZ model and repository boundaries).

Figure 7.1.3.2-2. Present-Day, 30th Percentile Net Infiltration Map (Soil Conductivity Variation) (Replicate R2, Realization 2)

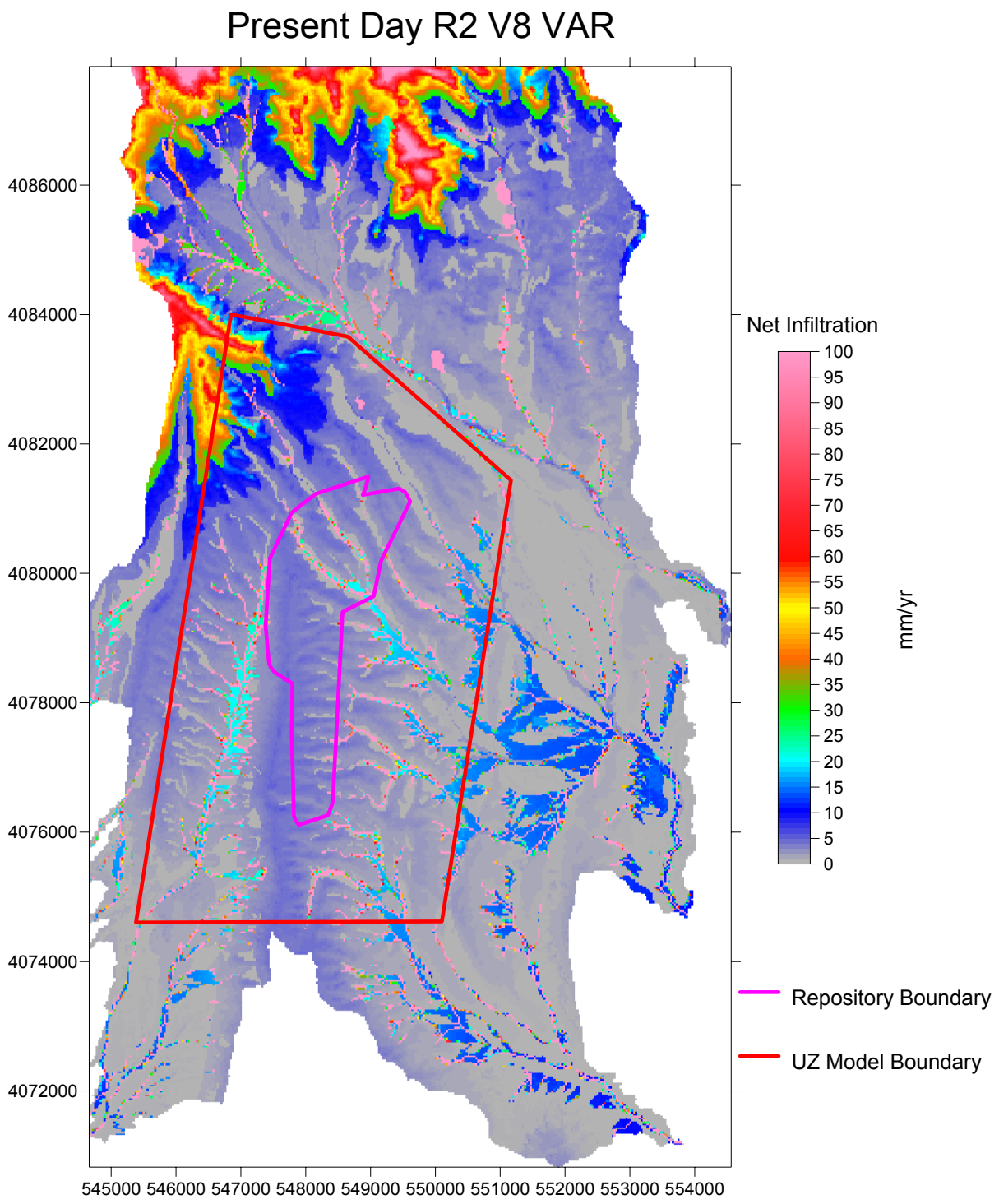

Coordinates are in meters; UTM NAD 27, Zone 11

Source: Output DTN: SN0701T0502206.037, file: \Welcome to Massif\Massif\Present Day Uncertainty\Infiltration Map Variations*Present Day R2 V08.xmcd* (net infiltration results from soil conductivity variation study); Output DTN: SN0612FTPRNUZB.002 (UZ model and repository boundaries).

Figure 7.1.3.2-3. Present-Day, 50th Percentile Net Infiltration Map (Soil Conductivity Variation) (Replicate R2, Realization 8)

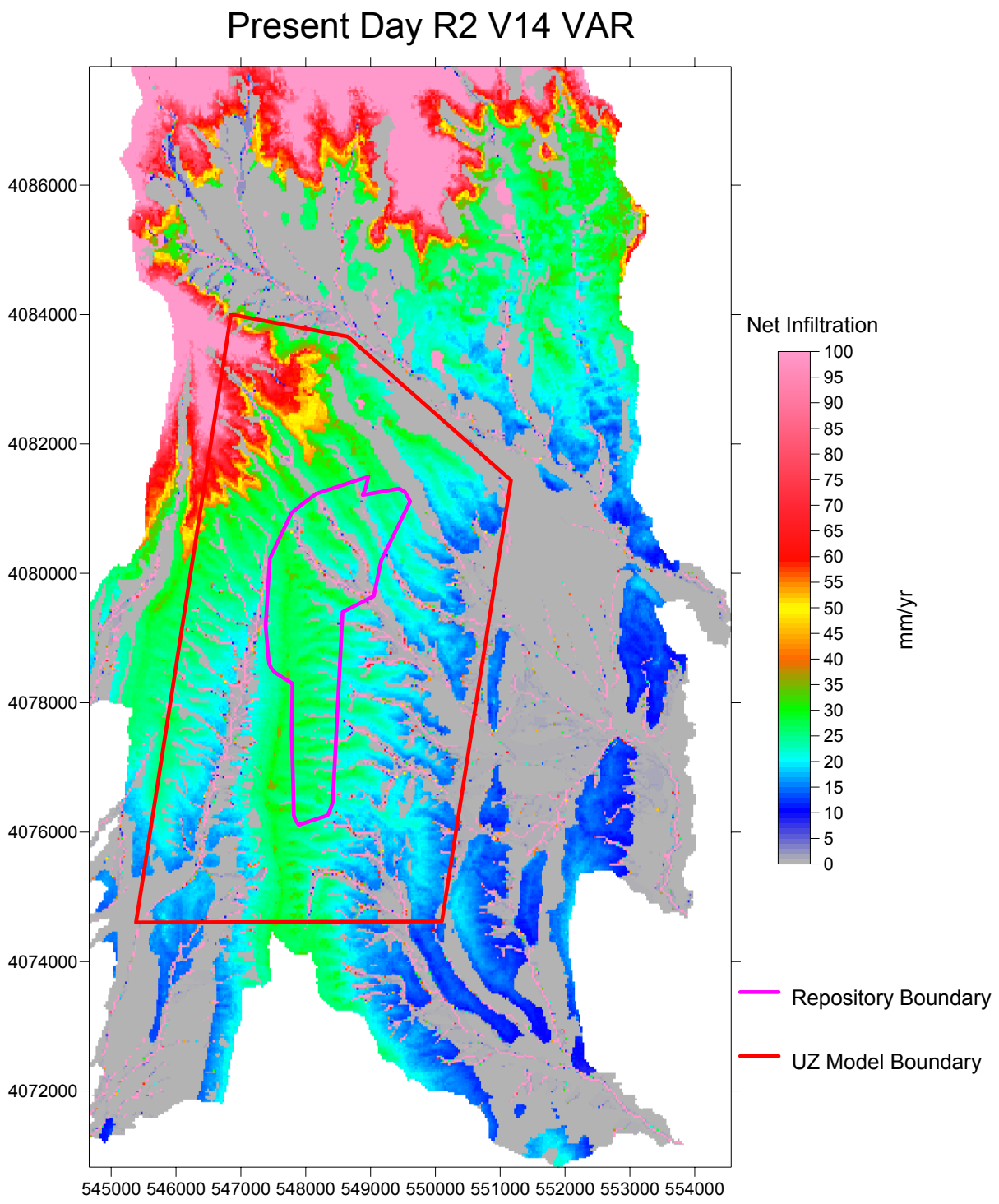

Coordinates are in meters; UTM NAD 27, Zone 11

Source: Output DTN: SN0701T0502206.037, file: \Welcome to Massif\Massif\Present Day Uncertainty\Infiltration Map Variations*Present Day R2 V14.xmcd* (net infiltration results from soil conductivity variation study); Output DTN: SN0612FTPRNUZB.002 (UZ model and repository boundaries).

Figure 7.1.3.2-4. Present-Day, 90th Percentile Net Infiltration Map (Soil Conductivity Variation) (Replicate R2, Realization 14)

7.1.4 Extended Parameter Sensitivity Study (Large LHS)

In an effort to confirm that the parameter screening criteria described in Section 6.5.5 and Appendix I did not inadvertently exclude a parameter that significantly influenced mean net infiltration, an extended parameter sensitivity study was performed. This extended study allowed 42 uncertain parameters to be varied in LHS (Output DTN: SN0701T0502206.043). A total of 200 realizations were run for the Drill Hole Wash watershed, which covers most of the repository footprint, using a single Present-Day weather input file (Output DTN: SN0701T0502206.037).

Table 7.1.4-1 lists the 42 parameter allowed to vary in this study along with their uncertainty distributions, units, and associated symbols (or descriptions) used in the report.

Table 7.1.4-1. Results of Stepwise Regression Analysis on Raw and Rank Data for Infiltration Estimate on Watershed

	LHS Name	Symbol or Description	Distribution	P1	P2	Units
1	lnRks_401	$K_{sat\_rock}(401)$	Loguniform	−15.38	−11.94	m/s
2	lnRks_402	$K_{sat\_rock}(402)$	Loguniform	−17.26	−11.97	m/s
3	lnRks_403	$K_{sat\_rock}(403)$	Loguniform	−15.42	−11.94	m/s
4	lnRks_404	$K_{sat\_rock}(404)$	Loguniform	−17.64	−12.4	m/s
5	lnRks_405	$K_{sat\_rock}(405)$	Loguniform	−16.39	−12.25	m/s
6	lnRks_406	$K_{sat\_rock}(406)$	Loguniform	−17.68	−11.77	m/s
7	lnRks_407	$K_{sat\_rock}(407)$	Loguniform	−17.78	−12.01	m/s
8	lnRks_408	$K_{sat\_rock}(408)$	Loguniform	−17.09	−11.55	m/s
9	lnRks_412	$K_{sat\_rock}(412)$	Loguniform	−12.59	−11.88	m/s
10	lnRks_414	$K_{sat\_rock}(414)$	Loguniform	−13.55	−12.02	m/s
11	lnRks_418	$K_{sat\_rock}(418)$	Loguniform	−16.92	−11.75	m/s
12	SDepth2	$depth_{soil}(2)$	Normal	10.9	22	m
13	SDepth3	$depth_{soil}(3)$	Uniform	2.1	3.2	m
14	SDepth4	$depth_{soil}(4)$	Uniform	0.1	0.5	m
15	Kc_min	K_{c_min}	Cumulative			none
16	Hc_579	$\theta_s(5/7/9)$	Uniform	9.00E-02	0.17	none
17	Hc_26	$\theta_s(2/6)$	Uniform	8.00E-02	0.15	none
18	Hc_34	$\theta_s(3/4)$	Uniform	5.00E-02	0.1	none
19	lnKs_579	$K_{sat\_soil}(5/7/9)$	Lognormal	−10.34	−8.85	cm/s
20	lnKs_26	$K_{sat\_soil}(2/6)$	Lognormal	−10.15	−8.06	cm/s
21	lnKs_34	$K_{sat\_soil}(3/4)$	Lognormal	−10.49	−8.65	cm/s
22	SWC_579	$\theta_s(5/7/9)$	Normal	0.21	0.25	none
23	SWC_26	$\theta_s(2/6)$	Normal	0.17	0.25	none
24	SWC_34	$\theta_s(3/5)$	Normal	0.14	0.18	none
25	p	p	Uniform	0.5	0.8	none
26	Z_r	Z_r	Uniform	0.6	2.6	m
27	h_plant	h_{plant}	Uniform	0.2	0.6	m
28	K0wint	$K_{o\ winter}$	Uniform	0	10	ºC

Table 7.1.4-1. Results of Stepwise Regression Analysis on Raw and Rank Data for Infiltration Estimate on Watershed (Continued)

	LHS Name	Symbol or Description	Distribution	P1	P2	Units
29	K0rest	$K_{o\ rest}$	Uniform	0	10	ºC
30	Sublim	$C_{sublime}$	Uniform	0	0.2	none
31	MAXPREC	Maximum daily precipitation	Uniform	496	983	mm
32	PREC_LR	$C_{Precipcor}$	Normal	4.1	8.5	%/100m
33	Smelt	$C_{snowmelt}$	Uniform	1	3	none
34	TEMP_LR	*LR*	Uniform	6.50E-03	1.00E-02	ºC/m
35	FDOY_DP	starting DOY for winter dew point	Uniform	274	335	none
36	LDOY_DP	ending DOY for winter dew point	Uniform	90	151	none
37	SLPRD	slope	Normal	0.23	0.53	
38	COEFHAR	K_{Rs}	Uniform	0.15	0.22	$ºC^{-0.5}$
39	Z_e	Z_e	Uniform	0.1	0.2	m
40	REW	*REW*	Uniform	2	10	mm
41	C_Kcb2	C_{Kcb2}	Normal	3.2	16.2	none
42	albedo	α_T	Uniform	0.15	0.9	none

Source: Output DTN: SN0701T0502206.043, file: *LHS_PD_SA.OUT*.

P1 and P2 represent minimum and maximum values for uniform distributions and 0.1% and 99.9% values for normal distributions. Values are natural log transformed for loguniform and lognormal distributions.

Stepwise regression analysis was performed on the mean net infiltration results considering both raw and rank transformed input parameters. The results of this analysis are shown in Table 7.1.4-2. The parameters are listed in order of decreasing influence.

Table 7.1.4-2. Results of Stepwise Regression Analysis on Raw and Rank Data for Infiltration Estimate on Watershed

	Stepwise Regression (linear)				Stepwise Regression (rank)			
Step	Variable	tot. R^2	inc. R^2	SRC	Variable	tot. R^2	inc. R^2	SRRC
1	SDepth4	0.61	0.61	−0.79	SDepth4	0.61	0.61	−0.79
2	Hc_579	0.78	0.17	−0.42	Hc_579	0.82	0.21	−0.46
3	K0wint	0.81	0.03	−0.17	K0wint	0.85	0.03	−0.18
4	Z_r	0.84	0.03	−0.18	Z_r	0.87	0.02	−0.15
5	Z_e	0.85	0.01	−0.11	lnKs_579	0.89	0.01	0.11
6	lnKs_579	0.86	0.01	0.10	Z_e	0.90	0.01	−0.10
7	PREC_LR	0.87	0.01	−0.08	Kc_min	0.90	0.00	−0.06
8	Kc_min	0.88	0.01	−0.07	lnRks_406	0.90	0.00	0.06
9	Sublim	0.88	0.00	−0.06				
10	lnRks_404	0.88	0.00	0.05				

Source: Output DTN: SN0701T0502206.044, file: \MIC 01_03_2007\BIG LHS\Stepwise\ *Stepwise_Analysis_Infiltration_01_08_2007.xls*.

The results of the extended parameter sensitivity study confirm that the initial parameter screening criteria used for the uncertainty analysis are valid. Approximately 80% of the variance in mean net infiltration in the set of 200 realizations can be accounted for by the uncertainty in the same two input parameters that describe most of the variability in the uncertainty analysis results (Soil depth of Soil Depth Class 4 and Holding Capacity of Soil Group 5/7/9). The other parameters explain less than 3% of the variance each and are therefore not considered to be as important for estimating mean net infiltration. It is worth noting that several of these other parameters were not screened into the uncertainty analysis (K0wint, lnKs_579, PREC_LR, Sublim, lnRks_404, and lnRks_406), however, none these other parameters account for more than 3% of the variance in net infiltration.

7.1.5 Summary of Confidence Building During Model Development

As discussed previously, a Level II validation requires that Level I validation items 1 through 6 from SCI-PRO-002 are satisfied. The validation activities described within this section satisfied all 6 items as follows:

1) *Evaluate and select input parameters and/or data that are adequate for the model's intended use* Input parameters and data selected to represent precipitation are described in Section 7.1.1. Input parameters and data selected to represent evapotranspiration are described in Section 7.1.2. Input parameters and data selected to represent run-on and runoff are described in Section 7.1.3. The results of an extended sensitivity study that allowed 42 uncertain parameters to be varied are described in Section 7.1.4. These sections describe the selection of parameters and data that demonstrate that they are adequate for the model's intended use.

2) *Formulate defensible assumptions and simplifications that are adequate for the model's intended use.* Defensible assumptions and simplifications described in Section 7.1 include: the simplification of precipitation patterns using Fourier series parameters; the simplification of vegetation properties into parameters K_{cb} and NDVI'; and the adjustments made to soil hydraulic conductivities in order to match model results to streamflow data. These assumptions and simplifications are defensible and have been shown to be adequate for the model's intended use.

3) *Ensure consistency with physical principles, such as conservation of mass, energy, and momentum, to an appropriate degree commensurate with the model's intended use.* MASSIF is a water balance model, and closure of the mass balance equation is ensured by the mass balance accounting processes built into the model. Eq. 6.4-1 in Section 6.4 describes the mass balance equation that is calculated for every grid cell and every day in each simulation. Runoff is calculated as the remainder of the mass balance equation. This approach ensures closure of the mass balance equation.

4) *Represent important future state (aleatoric), parameter (epistemic), and alternative model uncertainties to an appropriate degree commensurate with the model's intended use.* Both aleatoric and epistemic uncertainties are considered in the model and parameter development discussed in Sections 6.6 and 6.7.

5) *Ensure simulation conditions have been designed to span the range of intended use and avoid inconsistent outputs or that those inconsistencies can be adequately explained and demonstrated to have little impact on results.* Simulation conditions have been designed to span the range of intended use. Sensitive parameters have been determined in Sections 6.7 and 7.1.4, and parameter uncertainties have been captured in Section 6.6 to ensure that simulation conditions span the range of intended use.

6) *Ensure that model predictions (performance parameters) adequately represent the range of possible outcomes, consistent with important uncertainties and modeling assumptions, conceptualizations, and implementation.* The sensitivity studies described in Sections 6.7 and 7.1.4, and the results of the uncertainty simulations described in Section 6.6 ensure that model parameters adequately represent the range of possible outcomes.

7.2 POST MODEL-DEVELOPMENT VALIDATION

Post-development validation includes several methods listed in Paragraph 6.3.2) of SCI-PRO-006. The methods used to validate the infiltration model include (1) corroboration of model results with data (e.g., field data, analog studies) not previously used to develop or calibrate the model and (2) corroboration of model results with other alternative mathematical model results. In addition, post-development validation includes one method given in Paragraph 6.3.2b) of SCI-PRO-006, technical review by an external agency, and documented by the external agency. This review is the 1997 expert elicitation panel on unsaturated zone (UZ) flow model issues (CRWMS M&O 1997 [DIRS 100335]. Although this review was conducted 10 years ago, and the panel reviewed an entirely different infiltration model from that presented in this report, the conceptual models employed by the infiltration models are quite similar, and the conclusions of the expert elicitation project remain generally relevant in 2007.

Section 7.2.1 describes corroboration of the model results with data, Section 7.2.2 presents corroboration of the model results with alternative models, and Section 7.2.3 summarizes the conclusions and infiltration estimates from the 1997 expert elicitation panel on UZ flow model issues.

7.2.1 Corroboration of Model Results with Data and Relevant Observations

In Section 7.2.1, MASSIF predictions of infiltration are compared to limited field data collected, and relevant observations made at Yucca Mountain (Section 7.2.1.1), and compared to large-scale estimates of net infiltration or recharge for other locations in Nevada (Section 7.2.1.2.1), other locations in the southwestern United States (Section 7.2.1.2.2), and for other locations in the western United States (Section 7.2.1.2.3).

7.2.1.1 Corroboration of Model Results with Field Data

No measurements have ever been made at Yucca Mountain that directly quantify net infiltration under ambient conditions. Net infiltration, and recharge, are extremely difficult to directly measure in arid climates (Hogan et al. 2004 [DIRS 178487], page vii). Field data that were considered for comparison to MASSIF predictions in the report include 1) observations of seepage in the south ramp of the Exploratory Studies Facility (ESF) in the spring of 2005; 2)

estimates of net infiltration at borehole UZ#4 in Pagany Wash in the spring of 1998; and 3) estimates of net infiltration from neutron logging data. There are a variety of other field data that indirectly provide estimates of net infiltration below the root zone. Some of these datasets have been used for model validation of the 2000 net infiltration model (USGS 2001 [DIRS 160355]), and validation of the 2004 revision of the 2000 net infiltration model (BSC 2004 [DIRS 170007]) such as borehole temperature data, chloride mass balance data, calcite data, and perched water chemistry data.

However, in this report, data collected from depths greater than a few meters into the UZ were considered to be invalid for comparison to MASSIF predictions of net infiltration. The reason for this is that the validity of comparing point measurements from boreholes with model predictions with 30-m × 30-m grid cells are questionable for surface measurements due to extreme scale differences between borehole data and grid cell size. In addition, data collected from rock/water samples at greater than a few meters depth, especially at many tens of meters of depth additionally has been strongly influenced by its transit through the deep UZ. In addition, the validity of some of the UZ data and methods is questionable. For example, the 1997 expert elicitation panel did not embrace the use of temperature gradient and heat flux data to estimate percolation flux, and they viewed the chloride mass balance method as supportive of other methods but insufficient for obtaining independent estimates of percolation flux (CRWMS M&O 1997 [DIRS 100335], pp. 3-15 and 3-17). They also concluded that net infiltration is equivalent to percolation flux at the repository horizon, with some differences in spatial distribution, so their conclusions are relevant to validation of the net infiltration model (CRWMS M&O, 1997 [DIRS 100335], p. 3-5). Refer to Section 1.2 for additional discussion on the limitations of using data collected from the UZ for validation of the infiltration model.

The difficulty in comparing data from a point measurement to model predictions for a 30-m × 30-m grid cell is exacerbated by the paucity of soil depth data and soil hydraulic property data for the site. Without a good estimate of soil depth and soil hydraulic properties, comparison of point measurements to model grid cells is not reliable. Consider the comparison of model soil depth versus actual soil depth for 95 neutron logging boreholes located within the infiltration model domain. For this comparison, the grid cell IDs containing the 95 neutron logging boreholes were found using the Mathcad file *Infiltration at NL Boreholes (Preprocess).xmcd* located in Neutron Logging Boreholes folder in the Validation Analyses folder within the MASSIF calculation (Output DTN: SN0701T0502206.037). This file outputs the cell ID# for the 95 neutron logging boreholes. Borehole locations can be found in DTN: MO9906GPS98410.000 [DIRS 109059]. Soil depths can be found in three DTNs that include some qualified sources and some unqualified sources. These DTNs are listed below Figure 7.2.1.1-1. These data sources are compiled in an Excel file *Soil depth at NL boreholes.xls* located within the following path in the MASSIF calculation: (Output DTN: SN0701T0502206.037):

\\Welcome to Massif\Massif\Validation Analyses\Data\Borehole Locations\

Figure 7.2.1.1-1 shows the poor correlation between measured and modeled soil depth within each soil depth class region. This figure is included to demonstrate the difficulty in making comparisons between modeled infiltration data for a grid cell, compared to infiltration calculated from measured data collected at boreholes, particularly for the extreme case where measured soil

depths are close to zero, but modeled soil depth has a nominal value of 16.47 m (for Soil Depth Class 2). Note that none of the 95 boreholes are located in cells with Soil Depth Class 1 (95-m soil depth).

Notwithstanding the previous discussion, MASSIF was compared to measurements of net infiltration at Pagany Wash and to net infiltration calculated from neutron logging data. These comparisons do not generally provide conclusive validation of the infiltration model, but they are summarized in this report nonetheless. In addition, a discussion of some heat dissipation probe data that measure water potential (and can be converted into water content) is included below.

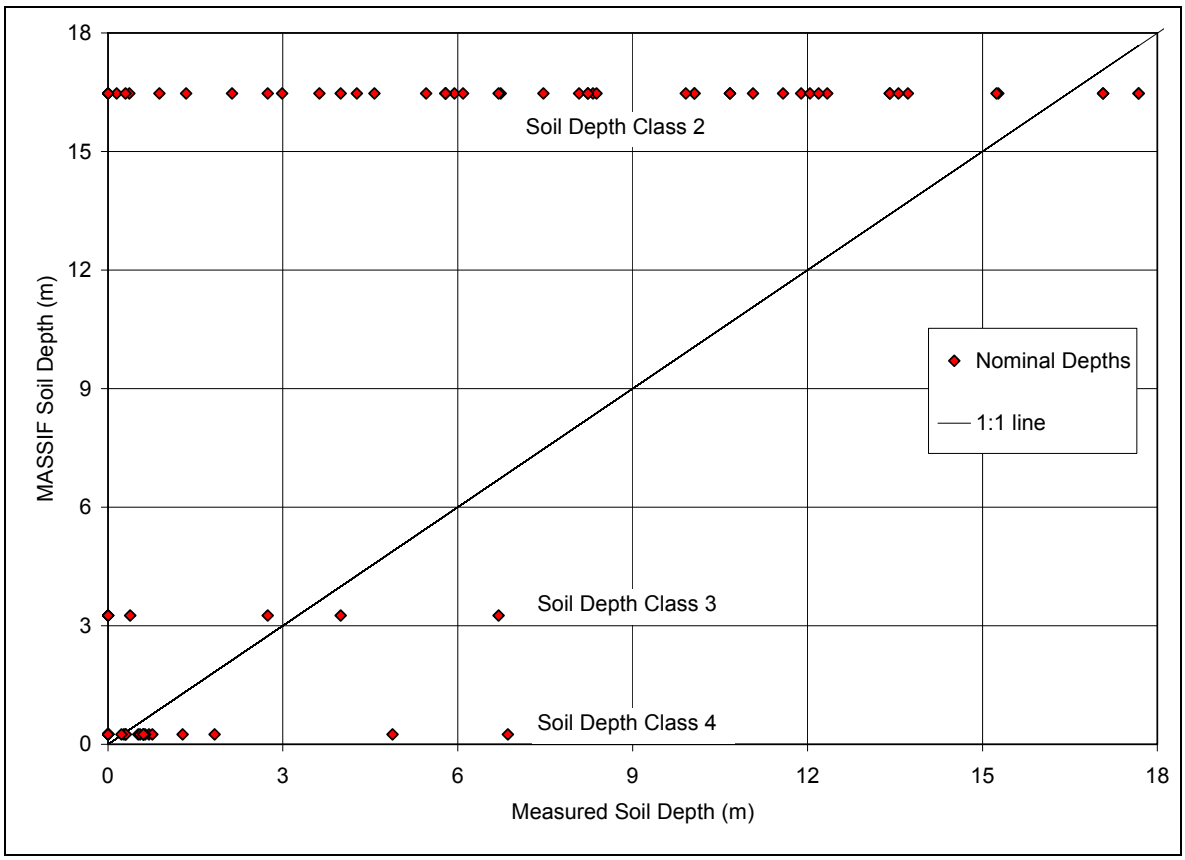

Source: Table 6.5.2.4-2 (modeled soil depths); Output DTN: SN0606T0502206.011 (soil depth class); DTNs: MO0004QGFMPICK.000 [DIRS 152554] (measured soil depth); MO0012MWDGFM02.002 [DIRS 153777]; and GS910808312212.001 [DIRS 175972].

Figure 7.2.1.1-1. Measured versus Modeled Soil Depth for 95 Neutron Logging Boreholes

7.2.1.1.1 Comparison of Model Predictions of Infiltration with Seepage Observations and Simulations above the South Ramp in 2005

During the 5-month period between October 2004 and February 2005, 324 mm (12.75 inches) of precipitation fell in the Yucca Mountain area. On February 28, 2005, YMP personnel working in the South Ramp of the ESF observed wet spots on the main drift's crown, ribs, and invert. This field observation is considered the first unambiguous evidence of seepage under ambient conditions. Based on several assumptions, it was estimated that 13% of a 5.1-m long drift section experienced seepage (Finsterle and Seol 2006 [DIRS 177754]).

Finsterle and Seol (2006 [DIRS 177754]) applied a Monte Carlo simulation using the *Seepage Model for PA Including Drift Collapse* (BSC 2004 [DIRS 167652]) in order to simulate the seepage fraction to resolve whether or not the observed seepage was an unexpected condition. Percolation flux was assumed to be equivalent to net infiltration flux, which was assumed to be on the order of 10% of precipitation, whose rate ranged from 393 mm/yr to 1309 mm/yr for November 2004, and February 2005, respectively. These precipitation rates are considerably higher than the long-term average value of 188.5 mm/yr reported by Finsterle and Seol (2006 [DIRS 177754], Table 1). Using probability distributions for fracture and capillary parameters and for net infiltration flux, it was estimated that seepage would occur along about 37% of the ESF South Ramp, compared with the observation that about 13% of the length exhibited wet spots. Therefore, these simulations confirm that the seepage observations in 2005 were not an unexpected condition, given the precipitation during this 5-month period (Finsterle and Seol 2006 [DIRS 177754], p. 17).

This section describes how MASSIF was used to corroborate the net infiltration fluxes assumed in Finsterle and Seol (2006 [DIRS 177754]). Although MASSIF results cannot be directly compared with quantitative field measurements of seepage, MASSIF infiltration can be compared to the ranges used by Finsterle and Seol (2006 [DIRS 177754]) in their seepage simulations. If MASSIF results are consistent with their infiltration ranges used to predict seepage, then this calculation provides additional model validation.

Monitor cells were identified at the ground surface directly above the areas identified as having seepage in the south ramp of the ESF. Precipitation and air temperature data for WY2004 and WY2005 were acquired for Site 8, located about 1.2 km east of the seepage observations. Since wind speed data were not collected at Site 8, wind speed data from Site 1 were used instead. Site 1 weather station has an elevation of only 12 m higher than the Site 8 station (CRWMS M&O 1997 [DIRS 100117], Table 2-1). MASSIF was used to calculate the average net infiltration for WY2005, with particular focus on monthly rates in November 2004 through February 2005.

MASSIF was run for WY 2004 and WY2005 (October 1, 2003 through September 2005). The sources for the weather data used in the simulation follows:

2003 weather data:

- Maximum and minimum air temperature and precipitation data from Site 8: DTN: MO0503SEPMMD03.001 [DIRS 176097].
- Wind speed data from Site 1: DTN: SN0608WEATHER1.005 [DIRS 177912].

2004 weather data:

- Maximum and minimum air temperature and precipitation data from Site 8: DTN: MO0607SEPMMD04.001 [DIRS 178311]
- Wind speed data from Site 1: DTN: SN0608WEATHER1.005 [DIRS 177912].

2005 weather data:

- Maximum and minimum air temperature and precipitation data from Site 8 and wind speed data from Site 1: DTN: MO0610METMND05.000 [DIRS 178328].

Note that the 2005 Site 8 precipitation dataset from DTN: MO0610METMND05.000 [DIRS 178328] is not complete. Missing data information was used for a storage gauge (DTN: MO0605SEPSGP05.000 [DIRS 178663]). The timing of the missing data is taken from Site 1: DTN: MO0610METMND05.000 [DIRS 178328]. See Excel file *Site 8 Pcp vs Site 1 Pcp.xls* in Output DTN: SN0701T0502206.037 for details on how Site 1 hourly data were scaled with a factor of 1.41 in order to replace Site 8 missing data.

Monitor cells were identified at the ground surface directly above the locations within the South Ramp of the ESF where seepage was observed in 2005. Three primary wet areas were identified in the ESF between stations 75+62 and 75+82, Stations 75+92 and 76+07, and Stations 77+48 to 77+53 (Finsterle and Seol 2006 [DIRS 177754], p. 1). These locations were converted into UTM coordinates using reference points and documented in the Excel file *seepage locations.xls* located in the South Ramp Infiltration folder within the MASSIF model Output DTN: SN0701T0502206.037. The Mathcad file *Locate cells above SR Seepage.xmcd* was used to locate the monitor cell IDs for these UTM coordinates. These three areas of observed seepage are directly beneath three monitor cells in the Drill Hole Wash watershed. Refer to Figure 7.1.3-1 for a map view of the infiltration watersheds, and the location of the South Portal and the grid cells below which seepage was observed. This figure also includes locations of other field data that are discussed later in Chapter 7.

MASSIF predicted net infiltration totals of 133 mm, 130 mm, and 113 mm for the three monitor cells for WY2005. This is equivalent to 31.4%, 30.7%, and 27.3% of precipitation for the three monitor cells. On a monthly basis, the infiltration/precipitation ratio ranged from 0.0 to 0.54. Refer to Table 7.2.1.1-1 for the results of the MASSIF simulations of infiltration above the South Ramp. These values are compared to the monthly values used in (Finsterle and Seol 2006 [DIRS 177754]).

Table 7.2.1.1-1. Summary of MASSIF Results for South Ramp Infiltration Simulations

Month	Year	Precipitation (mm/yr)			
		Finsterle & Seol 2006	MASSIF Cell1	MASSIF Cell2	MASSIF Cell3
October	2004	814.0	861.5	856.8	839.5
November	2004	393.0	419.2	416.9	408.5
December	2004	575.0	564.4	561.4	550.0
January	2005	865.0	894.5	889.6	871.7
February	2005	1309.0	1317.0	1309.8	1283.4

Table 7.2.1.1-1. Summary of MASSIF Results for South Ramp Infiltration Simulations (Continued)

Month	Year	Infiltration (mm/yr)			
		Finsterle & Seol 2006 LBNL	MASSIF Cell1	MASSIF Cell2	MASSIF Cell3
October	2004	81.4	143.3	136.0	107.9
November	2004	39.3	108.7	103.2	86.3
December	2004	57.5	242.7	238.9	210.4
January	2005	86.5	391.3	377.8	329.7
February	2005	130.9	714.7	698.4	619.9

Source: Output DTN: SN0701T0502206.037, file: \Welcome to Massif\Massif\Validation Analyses\South Ramp Seepage*South Ramp Results.xls*.

The results of this MASSIF calculation demonstrate that the estimate of net infiltration used as a boundary condition to predict seepage in the South Ramp by Finsterle and Seol (2006 [DIRS 177754]) was reasonable and in fact, considerably lower than the monthly infiltration predicted by MASSIF. Based on the assumption and conclusions in Finsterle and Seol (2006 [DIRS 177754]) and the MASSIF results in this section, observations of seepage in the South Ramp in 2005 were not unexpected.

However, the results of this MASSIF calculation beg the question of why wasn't more seepage observed in the south ramp if the seepage model predicted seepage along 37% of south ramp when about seepage along 13% of the south ramp was observed, and MASSIF predicts more infiltration than the boundary condition used by Finsterle and Seol (2006 [DIRS 177754]). One explanation is that Finsterle and Seol (2006 [DIRS 177754]) did not account for any delay of infiltration between the bottom of the root zone, and the ceiling of the south ramp, or for any change in storage or lateral flow in this zone that has a thickness ranging from 70 m to 40 m. This range in thickness is calculated in *Seepage Locations.xls* in the MASSIF calculation (Output DTN: SN0701T0502206.037). In addition, the seepage model did not account for evaporation effects in the ESF, which would have reduced their estimate of observed seepage in the ESF ceiling. These additional considerations would support the conclusion that the MASSIF results, the seepage model results, and the observed seepage in the ESF are not inconsistent.

7.2.1.1.2 Comparison of Model Predictions with Pagany Wash Infiltration Data from 1998

MASSIF was used to simulate infiltration at a monitor cell that contains the location of borehole UE-25 UZ #4 (also referred to as UZ #4). This is an instrumented borehole in Pagany Wash. The winter of 1997-1998 was an El Nino winter and therefore was considerably wetter than average winters. The total precipitation recorded at Site 3 for WY1998 was 402.6 mm (DTN: SN0608WEATHER1.005 [DIRS 177912]). In the spring of 1998, 183.4 mm of precipitation was recorded during 14 out of 23 days between February 2 and 24 (DTN: SN0608WEATHER1.005 [DIRS 177912]), and approximately 35,000 m^3 of runoff was recorded at the lower Pagany Wash streamflow gauge (see Table 7.1.3-1) during this 23-day period in February 1998 (DTN: GS960908312121.001 [DIRS 107375]). LeCain et al. (2002 [DIRS 158511]) describe infiltration data collected at this borehole during the spring of 1998. Borehole UZ #4 is located in the alluvial deposits of Pagany Wash, a stream-carved, dry channel. This borehole was instrumented with temperature, pressure, and water potential sensors in July

1995, in order to gain insight into infiltration through the alluvial deposits of the usually dry stream channels (LeCain et al. 2002 [DIRS 158511]). Refer to Figure 7.1.3-1 for a map view of the infiltration watersheds and the location of Pagany Wash and UZ #4.

LeCain et al. (2002 [DIRS 158511]) describe two methods for estimating infiltration in Pagany Wash based on data collected at UZ #4. The first is an analytical method in which the infiltration flux is calculated from soil saturated conductivity, porosity, and velocity of a wetting front observed to pass from a depth of 3.0 m to 6.1 m. The second method uses a numerical model to estimate infiltration flux given temperature data measured in UZ #4. The first method produced a percolation flux of 1.13 m while the second method produced a percolation flux of 1 to 2 m.

First, MASSIF was used with nominal input values to simulate infiltration at the monitor cell containing borehole UZ#4. Infiltration for WY1998 at UZ #4 was calculated to be 11.8 mm using precipitation data from the Site 6 station, and 28.3 mm using precipitation data from the Site 3 station. Second, soil and rock hydraulic conductivities (K_{sats}) for the grid cell containing borehole UZ #4 were adjusted to test the sensitivity of infiltration to K_{sat}, and to demonstrate that modeled infiltration can match the measured infiltration reported by LeCain et al. (2002 [DIRS 158511]) with adjustments to Ksats. Soil Ksat was increased by about one order of magnitude to a value of 7 m/s, and rock Ksat was increased to a value of 10^{-3} m/s so that it would not be a limiting factor on infiltration. The analytical method used by LeCain et al. (2002 [DIRS 158511]) to calculate infiltration flux from 3.0 to 6.1 m does not include rock hydraulic conductivity, so rock hydraulic conductivity should not be a limiting factor for a comparison with MASSIF. MASSIF calculated a total net infiltration for WY1998 at the grid cell containing UZ #4 of 414 mm and 375 mm for Site 3 and Site 6 stations, respectively. When soil Ksats were increased to 10^{-5} m/s, infiltration increased to 597 and 548 mm, for Site 3 and Site 6 precipitation, respectively. These MASSIF calculations can be found in the Pagany Wash Borehole folder in the Validation Analyses folder in the MASSIF calculation (Output DTN: SN0701T0502206.037, file: \Welcome to Massif\Massif\Validation Analyses\Pagany Wash Borehole*Pagany Wash Results.xls*.).

In the analytical method described by LeCain et al. (2002 [DIRS 158511]), if the value of soil porosity is changed from 0.31 to 0.157 m^3/m^3, which is the porosity assigned to the soil type in this grid cell, then the percolation flux would change from 1,130 to 573 mm (see file "PW infiltration analytical calculation.xmcd" in Output DTN: SN0701T0502206.037). This is very close to the net infiltration flux calculated by MASSIF when soil and rock Ksats are adjusted.

This comparison of percolation flux between MASSIF and an analytical method reported by LeCain et al. (2002 [DIRS 158511]) shows that MASSIF calculated approximately the same amount of infiltration at UZ #4, if soil Ksat for that grid cell is increased by ~1.5 orders of magnitude, and if rock hydraulic conductivity for that grid cell is increased so that it is not a limiting factor. Although this increase in soil Ksat is outside of the standard error range in soil Ksat for soil type 3 (Ksat range = 9.5 to 6.2×10^{-7} m/s) reported in *Data Analysis for Infiltration Modeling: Development of Soil Units and Associated Hydraulic Parameter Values* (BSC 2006 [DIRS 176335], Table 6-7), it is within the range of maximum and minimum values (1.7×10^{-7} to 1.7×10^{-5} m/s), and this adjusted soil Ksat may be more appropriate for the soil near the grid cell containing UZ #4 on Yucca Mountain. The soil Ksat values (BSC 2006 [DIRS 176335],

Table 6-7) are not directly measured, but are developed from Yucca Mountain textural data using pedotransfer functions (BSC 2006 [DIRS 176335], Section 6.4.5). Therefore, they are appropriate and defensible for large-scale assessments of infiltration at Yucca Mountain. However, they are likely to be inaccurate for comparison to borehole-scale infiltration estimates as we have seen in this validation calculation.

Although not referenced in *Data Analysis for Infiltration Modeling: Development of Soil Units and Associated Hydraulic Parameter Values* (BSC 2006 [DIRS 176335]), Hofmann et al. (2000 [DIRS 153709]) report measurements of soil saturated hydraulic conductivity at two locations at Yucca Mountain. These locations included a measurement in Pagany Wash near borehole UE-25 UZN #14 and a measurement on a stable terrace adjacent to Fortymile Wash at borehole UE-25 UZN #85, both using a prototype-automated-infiltrometer. They measured a saturated hydraulic conductivity of 17.79 cm/hr (4.94×10^{-5} m/s) for the location in Pagany Wash and 1.78 cm/hr (4.94×10^{-6} m/s) for the terrace location (Hofmann et al. 2000 [DIRS 153709], Table 4). The measurement in Pagany Wash corroborates the adjustments to soil conductivity that are required to match infiltration inferred at UZ #4.

7.2.1.1.3 Discussion of Water Content Data

Discussion of Neutron Logging Data

Neutron logging data were collected from mid-1989 through September 1995 at 99 boreholes. Ninety-five of the 99 boreholes are located within the current infiltration model domain. Refer to Figure 7.1.3-1 for a map view of the infiltration watersheds and the locations of the 95 neutron logging boreholes. All 95 boreholes are located within four watersheds; one borehole is located within Yucca Wash while the remaining 94 boreholes are located within Drill Hole Wash, Dune Wash, or Solitario Canyon 1 watersheds. Details of the neutron logging program and datasets can be found in *Technical Evaluation and Review of Results, Technical Procedures, and Methods Related to the Collection of Moisture Monitoring Data Using Neutron Probes in Shallow Boreholes* (BSC 2006 [DIRS 177083]), and by Flint and Flint (1995 [DIRS 100394]).

An uncertainty analysis of this dataset concluded that water content values from the neutron logging are accurate to approximately ±6% absolute water content within a 95% confidence interval (BSC 2006 [DIRS 177083], Section 5.3.2). Given a typical water content value of 20%, this uncertainty translates to a 30% relative error in the measured value. However, the precision of the measurement is higher (less than 2% relative difference), which suggests that estimates of changes in water content are more certain. This increased certainty is limited by the fact that precision errors associated with each log are additive when considering changes in water content over time.

The way neutron logging data has been used has changed over time on the Yucca Mountain Project. Neutron logging data were used to calibrate the 1996 USGS net infiltration model (Flint et al. 1996 [DIRS 100147]), however data-model comparisons are only shown for two of the 99 boreholes and the calibration method used and the results obtained are not adequately documented. Streamflow data (and no neutron logging data) were used to calibrate the 2000 USGS net infiltration model (USGS 2001 [DIRS 160355]). The 2004 revision of the 2000 USGS

net infiltration model (BSC 2004 [DIRS 170007]) only used neutron logging data for model validation.

This dataset was deemed to be of limited use for validation (or calibration) of the 2007 SNL net infiltration model for several reasons. First, the errors associated with water content derived from these measuements make direct comparison with simulated water contents problematic, especially since conditions at each borehole (such as soil depth and properties) are likely to differ from the average values assigned to the soil depth class and soil group assigned to the cell. Second, the field capacity modeling approach is a "lumped" approach and is therefore not intended to be used to match moisture profiles with depth in the soil. Third, flux estimates using the change in water content over an interval require an estimate of the root-zone depth, which is likely to vary for each location. Despite this limitation, fluxes were estimated assuming a constant root-zone depth and compared with net infiltration calculated over the same time interval (see below). The following comparisons between measured and modeled infiltration, and provides justification for its exclusion from model validation.

Neutron logging measures the number of reflected (thermalized) neutrons at depth intervals in a region surrounding a borehole. The count of neutrons is also affected by the integrated properties of the material (e.g., density, mineral composition, etc.) and in relatively homogeneous materials has successfully been used to estimate water content. Several researchers have estimated net infiltration fluxes from neutron logging data collected at time intervals during which water content profiles were changing (e.g., Looney and Falta (2000 [DIRS 154273], p. 457) and McElroy (1993 [DIRS 177910], p. 13)). However, many assumptions are required in order to estimate net infiltration flux from these measurements. Net infiltration flux can be estimated from the change in water content ($d\theta v$ in m^3/m^3), with time, multiplied by a given depth interval ($d\theta v*dz$), and then summing these changes, for depths below the root zone (Looney and Falta (2000 [DIRS 154273], p. 457) and McElroy (1993 [DIRS 177910], p. 13)). Net infiltration flux can also be calculated as the change in integrated water content below the root zone, between two time periods. This method was implemented with Mathcad in "Borehole Processing Nominal.xmcd" located in the "Neutron Logging Boreholes" folder in the "Validation Analyses" folder within the MASSIF calculation (Output DTN: SN0701T0502206.037), for the time period spanning the greatest increase in borehole water content between about January 1 and mid-March 1995. The root zone was assumed to be 2 m below the ground surface for soil depths of 2 m or greater, and the root zone was set equivalent to soil depth for soil depths less than 2 m.

The use of these methods for calculating flux from water content data has not been widely used, and limitations in the approach, as well as limitations within the dataset, should be acknowledged. For example, this approach assumes 1-D piston flow, with no lateral flow at the soil–bedrock interface. The MASSIF model assumes that lateral flow can be neglected for the purposes of estimating a water balance for a 30 × 30 m grid cell (Section 5). However, this assumption may not be appropriate for measurements occurring on the scale of a borehole, since the active fracture spacing in the bedrock is likely to be greater than the region measured by the neutron probe. In addition, single calibrations, independent of media, were developed for each neutron probe, and were applied to all the neutron measurements made in various media (e.g., soil, "rotten" tuff near the soil–bedrock interface, or intact tuff). Refer to *Technical Evaluation and Review of Results, Technical Procedures, and Methods Related to the Collection*

of Moisture Monitoring Data Using Neutron Probes in Shallow Boreholes (BSC 2006 [DIRS 177083]) for details of the neutron probe calibrations. Since calibrations provide the means of interpreting water contents, the consequence of using a single calibration for different media is that there may be systematic errors in water contents for media not used in the calibration. In addition, as a result of the drilling methods, preferential pathways for water flow along the annulus space between the borehole casing and the geologic media may have been inadvertently created, and formerly solid rock may have been extensively fractured.

Despite the limitations of the dataset, and the assumptions inherent in calculating infiltration from changes in water content, this six-year dataset represents the only YMP site-specific dataset that measured wetting front movement, depths of infiltration, and indirectly, net infiltration flux, over a large area of the infiltration model area, and over a period with wet years and dry years. Therefore, it is worthwhile to compare MASSIF predictions of infiltration at the grid cells containing the neutron logging boreholes, with the infiltration calculated from neutron logging data. Figure 7.2.1.1-2 shows such a comparison for a period of infiltration spanning the wet winter of 1995, using 3 precipitation stations with MASSIF. As the figure shows, the comparison is not good. Even the averaged infiltration for all boreholes was not good (67 mm for MASSIF using Site 6 precipitation versus 173 mm from neutron logging data). This figure is included to show that the borehole-scale neutron logging data do not match model predictions very well. This figure supports the argument given in Section 7.2.1.1 that MASSIF should not be expected to be able predict infiltration at the borehole-scale.

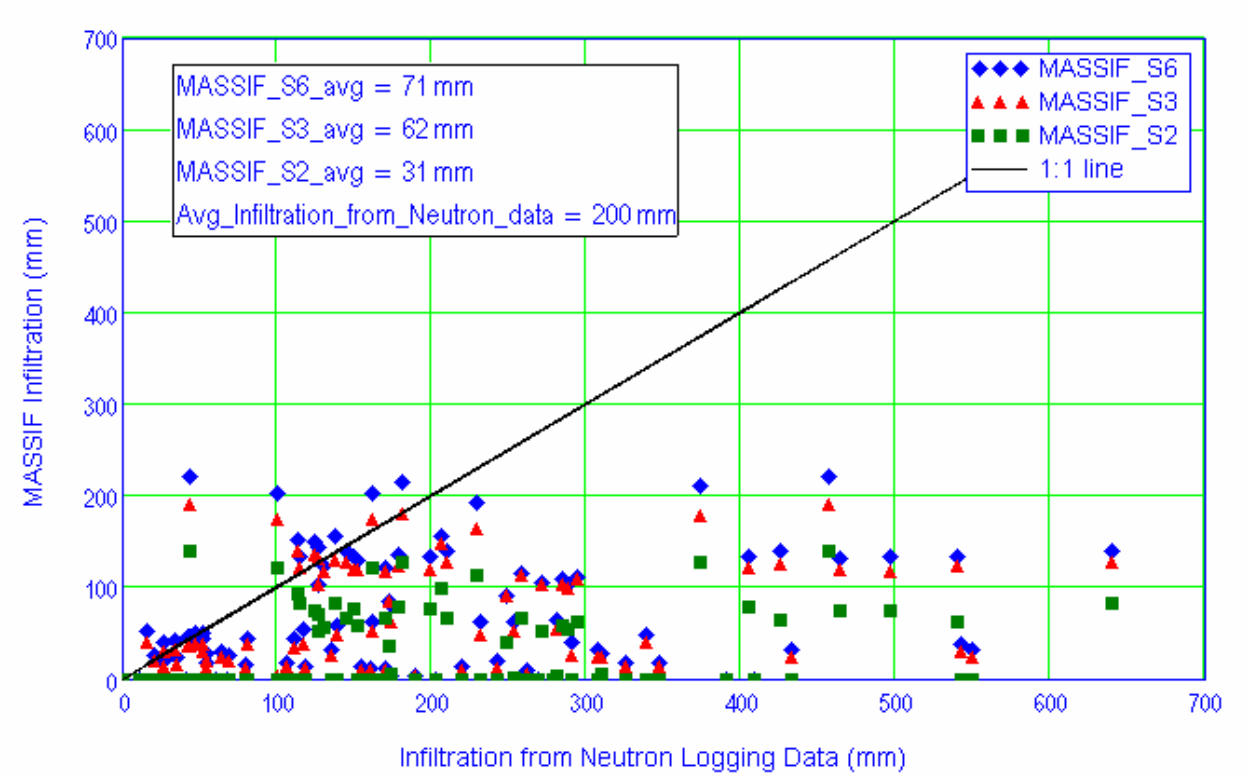

Source: Output DTN: SN0701T0502206.037, file: \Welcome to Massif\Massif\Validation Analyses\Neutron Logging Boreholes*Borehole_Processing_Nominal.xmcd*.

Figure 7.2.1.1-2. Comparison of Net Infiltration Calculated from Neutron Logging Data versus MASSIF Net Infiltration for Winter 1995

Discussion of Heat Dissipation Probe Data

Heat dissipation probe data, which measures water potential at different depths in the soil, are available for at least one location at Yucca Mountain (DTN: GS960908312211.004 [DIRS 146872]). Water potential data can be converted into water content data and then compared to model results using MASSIF, if the water retention properties of the soils are known. These data were not analyzed for additional model validation due to the problems with data traceability and the availability of site-specific soil property data needed to convert water potential to water content. However, if such soil property data could be found by additional soil sampling, then this dataset could be used for additional model validation in the future.

7.2.1.2 Comparison of Infiltration Estimates with Other Models and Data from Comparable Environments

In this section, MASSIF results for Present-Day, Monsoon, and Glacial Transition climates (Output DTNs: SN0701T0502206.034, SN0701T0502206.036, and SN0701T0502206.035, respectively) are compared to infiltration and/or recharge estimates from other models and data from comparable environments. These environments include other locations in Nevada (Section 7.2.1.2.1), the southwestern United States (Section 7.2.1.2.2), and the western United States (Section 7.2.1.2.3). Estimates from locations in the southwestern U.S. are approximately

analogous to the predicted recharge expected for the monsoon climate, based on the selection of analog climate sites in *Future Climate Analysis* (BSC 2004 [DIRS 170002], Table 6-1). And estimates from locations in the western are approximately analogous to the predicted recharge expected for the glacial-transition climate, based on the selection of analog climate sites in *Future Climate Analysis* (BSC 2004 [DIRS 170002], Table 6-1). Recharge and infiltration estimates for the Hanford site are briefly discussed in Section 7.2.1.2.3, although this site is quite dry and more analogous to Yucca Mountain under the present-day climate than the glacial-transition climate.

MASSIF results for Present-Day, Monsoon, and Glacial Transition climates (Output DTNs: SN0701T0502206.034, SN0701T0502206.036, and SN0701T0502206.035, respectively) are compared to several published models of infiltration and/or recharge versus precipitation and shown in Figure 7.2.1.2-1. The publication dates of these models span nearly 60 years and Figure 7.2.1.2-1 demonstrates the similarity of these models, despite the advances made in hydrologic sciences in the past 60 years. The step function of the Maxey-Eakin model (Maxey and Eakin 1950 [DIRS 100598], p. 40) is shown primarily for its historical significance as a well-recognized recharge model. A modified Maxey-Eakin model (Nichols 2000 [DIRS 178863], page C35), and a Maxey-Eakin model fit developed by Wilson and Guan (2004 [DIRS 172585], Equation 12) are also shown in this Figure. Figure 7.2.1.2-1 also shows MASSIF results compared to a model developed by Maurer and Berger (1997 [DIRS 177370], Equation 9) for west-central Nevada. The Maurer and Berger (1997 [DIRS 177370]) model predicts water yield based on precipitation in which water yield is defined as subsurface flow plus surface runoff, so it is not directly comparable to other models, but it is included for comparison purposes. Figure 7.2.1.2-1 also shows MASSIF results compared to a recent model developed by Faybishenko (2007 [DIRS 178766], Equation 16) for Yucca Mountain using analog meteorological data, and a fit to a dataset referred to as Davisson and Rose (Faybishenko (2007 [DIRS 178766], Figure 10). MASSIF results for three climate states are above the general trend of most of these models.

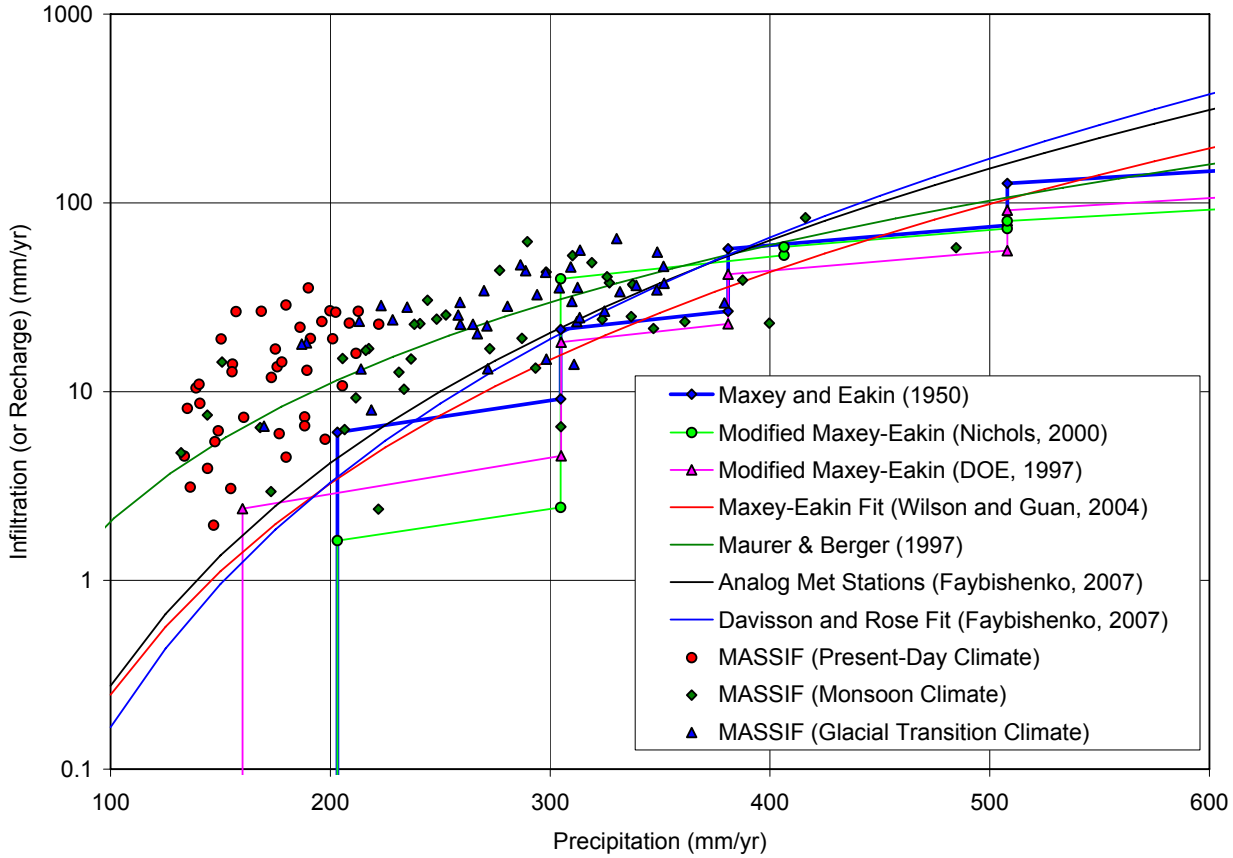

Source: Output DTNs: SN0701T0502206.034, SN0701T0502206.036, and SN0701T0502206.035; Validation Output DTN: SN0704T0502206.047.

NOTE: Vertical lines that extend to the horizontal axis associated with the Maxey-Eakin and Modified Maxey-Eakin models represent the precipitation amounts below which the models predict zero recharge.

Figure 7.2.1.2-1. Comparison of MASSIF Net Infiltration Results for Three Climates with Several Models

7.2.1.2.1 Infiltration Estimates for Other Locations in Nevada

The Nevada Division of Water Resources, Department of Conservation and Natural Resources and the U.S. Geological Survey have divided Nevada into 14 Hydrographic Regions or basins, which are used to compile information on water resources. These regions are further subdivided into 232 Hydrographic Areas (256 Hydrographic Areas and Sub-areas, combined) for more detailed study. A variety of technical publications have reported recharge estimates for Nevada Hydrographic Areas. Noteworthy examples include two series of publications by the Nevada Department of Conservation and Natural Resources: (1) the Groundwater Resources Reconnaissance Series; and (2) the Water-Resources Bulletins. In many cases, multiple recharge estimates using different methods, inputs and assumptions are available for the same area/subarea.

Thomas et al. (1989 [DIRS 177727], p. 15-16) estimated natural recharge for the Smith Creek Valley hydrographic area using both Maxey-Eakin and chloride mass balance methods and compared these results to a previous Maxey-Eakin estimate by another researcher (see Table 7.2.1.2-1). The two Maxey-Eakin estimates were approximately 15% and 45 % higher than the chloride mass balance estimate. The difference between the two Maxey-Eakin estimates was attributed to different altitude-precipitation relations and differences in delineation of recharge areas. The comparison illustrates that infiltration estimates can vary substantially between different methods or when the same method is applied by different researchers. However, when the results are expressed as recharge efficiency (recharge as a percentage of precipitation), all three the estimates compare fairly well.

Table 7.2.1.2-1. Recharge Estimates for Smith Creek Valley, Nevada [a]

Precipitation [b]		Recharge [b]		Efficiency	Method [c]
(acre-ft/yr)	(mm/yr)	(acre-ft/yr)	(mm/yr)	(%)	
92,000	75.3	9,600	7.9	10.4	ME
119,000	97.4	12,000	9.8	10.1	ME
92,000	75.3	8,300	6.8	9.0	CMB

[a] Thomas et al. 1989 [DIRS 177727], pp. 15-16.

[b] Precipitation and Recharge were reported in acre-ft/yr and converted to mm/yr using a basin area of 372,480 acres given in Horton 1998 [DIRS 174618], Appendix A-1.

[c] ME=Maxey-Eakin; CMB=chloride mass balance

Dettinger (1989 [DIRS 105384]) calculated chloride mass balance recharge estimates for a number of hydrographic areas/subareas in Nevada and compared them to Maxey-Eakin and water budget estimates obtained from Nevada Department of Conservation and Natural Resources Groundwater Resources Reconnaissance Reports and Water-Resources Bulletins (see Table 7.2.1.2-2). The basins were chosen to ensure a wide geographic coverage, a variety of areal extents and a variety of recharge efficiencies. Areal extents ranged from approximately 60,000 to 1,375,000 acres, with an average area of approximately 500,000 acres. Precipitation ranged from 29 mm/yr to 487 mm/yr. Recharge estimates from the three methods were generally in fair agreement. Estimated recharge efficiencies ranged from approximately 1% to 18%.

Avon and Durbin (1994 [DIRS 177200], Table 2) collected and evaluated basin-wide recharge estimates for a number of Nevada hydrographic areas/subareas. They developed comparisons between Maxey-Eakin estimates and water budget recharge estimates for 40 areas/subareas from studies published between 1946 and 1974 in the Nevada Department of Conservation and Natural Resources Groundwater Resources Reconnaissance Series and Water-Resources Bulletins (see Table 7.2.1.2-3). Estimates for five hydrographic areas/subareas (Duck Lake, Fish Lake, Penoyer, Southern Butte, and Northern Butte) were previously reported by Dettinger et al. (1989 [DIRS 105384]) and are not included in Table 7.2.1.2-3. The estimate for the eastern portion of the Honey Lake area was also excluded due to difficulty in determining an appropriate precipitation estimate. The basins studied covered a wide geographic area, a variety of areal extents, and a variety of recharge efficiencies. Areal extents ranged from approximately 6,000 to 1,240,000 acres, with an average area of approximately 320,000 acres. Precipitation ranged from 17 mm/yr to 476 mm/yr. Recharge estimates from the two methods were generally in fair agreement, with average differences of approximately 40% and a maximum difference of

approximately 200%. Estimated recharge efficiencies computed using the Maxey-Eakin method ranged from approximately 3% to 13%. Estimated recharge efficiencies computed from water budgets ranged from approximately 1% to 29%, with typical values below 12%.

Avon and Durbin (1994 [DIRS 177200], Table 3) also compared published Maxey-Eakin estimates and "model estimates" for 27 hydrographic areas/subareas. The "model estimates" were calculated using a variety of methods: (1) groundwater flow models; (2) a numerical infiltration model; (3) chloride mass balance; and (4) a deuterium-calibrated mixing-cell flow model. Table 7.2.1.2-4 lists the eight comparisons that do not overlap studies discussed above and for which precipitation estimates could be located. All eight comparisons include model estimates from the deuterium-calibrated mixing-cell flow model only. There is overlap between the studies used by Avon and Durban (1994 [DIRS 177200]) and those used in Dettinger (1989 [DIRS 105384]) and Thomas et al. (1989 [DIRS 177727], p. 15-16). In particular, all chloride mass balance estimates were obtained from Thomas et al (1989 [DIRS 177727], p. 15-16) and Dettinger (1989 [DIRS 105384]). The estimates are in fairly good agreement for each area. Recharge efficiencies for Maxey-Eakin estimates vary between approximately 3% and 7%, while the model estimated recharge efficiencies varied from approximately 2% to 14%.

Table 7.2.1.2-2. Recharge Estimates for Selected Nevada Hydrographic Areas/Subareas [a]

Number [b]	Name [b]	Size [b] (acres)	Precipitation [c]		Recharge [c] (mm/yr)			Efficiency (%)		
			(acre-ft/yr)	(mm/yr)	CMB	ME	WB	CMB	ME	WB
16	Duck Lake Valley	341,120	243,300	217	8.0	8.0	6.5	3.7	3.7	3.0
36	Independence Valley	220,800	251,410	347	13.4	22.4	16.8	3.9	6.5	4.8
56	Upper Reese River Valley	728,320	592,030	248	12.6	24.4	15.6	5.1	9.9	6.3
92	Lemmon Valley	59,520	30,818	158	8.3	8.3	8.3	5.3	5.3	5.3
117	Fish Lake Valley	451,840	251,410	170	18.1	22.4	18.1	10.6	13.2	10.6
122	Gabbs Valley	817,280	381,170	142	1.8	1.8	1.5	1.3	1.3	1.1
153	Diamond Valley	481,280	227,080	144	6.7	7.7	7.7	4.6	5.4	5.4
163	Mesquite Valley	151,040	30,007	61	3.3	3.3	4.9	5.4	5.4	8.1
170	Penoyer Valley	448,000	97,320	66	2.2	2.8	2.8	3.3	4.2	4.2
173A	Railroad Valley (Southern Part)	385,920	616,360	487	22.4	36.5	54.4	4.6	7.5	11.2
173B	Railroad Valley (Northern Part)	1,375,360	129,760	29	1.1	1.3	1.3	3.8	4.4	4.4
178A	Butte Valley (Northern Part)	173,440	48,660	86	4.3	7.1	15.7	5.0	8.3	18.3
178B	Butte Valley (Southern Part)	472,960	194,640	125	7.8	9.9	7.8	6.3	7.9	6.3
184	Spring Valley	1,063,040	786,670	226	17.7	21.6	21.2	7.8	9.6	9.4

[a] Dettinger 1989 [DIRS 105384], Table 2.
[b] Basin size given in Horton 1998 [DIRS 174618], Appendix A-1.
[c] Dettinger (1989 [DIRS 105384]) reported precipitation and recharge in cubic hectometers per year (hm^3/yr), which were converted to acre-ft/yr using a conversion factor of $1 hm^3/yr = 811$ acre-ft/yr given by Dettinger (1989 [DIRS 105384]). Precipitation and recharge converted to mm/yr using basin area.

Table 7.2.1.2-3. Maxey-Eakin and Water Budget Recharge Estimates for Selected Nevada Hydrographic Areas/Subareas [a]

Number [b]	Name [b]	Size [b] (acres)	Precipitation [c,d]		Recharge [d]				Efficiency	
					ME		WB		ME	WB
			(acre-ft/yr)	(mm/yr)	(acre-ft/yr)	(mm/yr)	(acre-ft/yr)	(mm/yr)	(%)	(%)
18	Painter Flat	19,840	31,000	476.3	1,300	20.0	1,200	6.3	3.6	2.8
21	Smoke Creek Desert	627,200	275,100	133.7	13,000	6.3	18,620	18.4	4.2	3.9
22	San Emidio Desert	195,200	47,900	74.8	2,100	3.3	3,200	9.0	4.7	6.8
24	Hualapai Flat	201,600	106,200	160.6	7,000	10.6	6,700	5.0	4.4	6.7
29	Pine Forest Valley	337,920	197,000	177.7	10,000	9.0	14,100	10.1	6.6	6.3
53	Pine Valley	641,280	654,000	310.8	45,500	21.6	24,000	12.7	5.1	7.2
55	Carico Lake Valley	240,640	86,600	109.7	4,300	5.4	4,500	11.4	7.0	3.7
71	Grass Valley	332,800	180,000	164.9	12,000	11.0	16,800	5.7	5.0	5.2
84	Warm Springs Valley	158,080	96,000	185.1	6,000	11.6	2,000	15.4	6.7	9.3
85	Spanish Springs Valley	48,640	16,000	100.3	600	3.8	1,000	3.9	6.3	2.1
86	Sun Valley	6,400	1,800	85.7	50	2.4	25	6.3	3.8	6.3
92	Lemmon Valley	59,520	43,400	222.3	1,800	9.2	900	1.2	2.8	1.4
95	Dry Valley	51,200	37,000	220.3	2,400	14.3	2,300	4.6	4.1	2.1
96	Newcomb Lake Valley	5,760	4,500	238.1	300	15.9	130	13.7	6.5	6.2
97	Honey Lake Valley	123,520	24,000	59.2	1,500	3.7	10,500	6.9	6.7	2.9
111A	Alkali Valley (Northern Part)	11,520	7027	185.9	400	10.6	300	7.9	5.7	4.3
113	Huntoon Valley	62,080	22,200	109.0	800	3.9	300	1.5	3.6	1.4
114	Teels Marsh Valley	206,720	38,400	56.6	1,300	1.9	1,400	2.1	3.4	3.6
118	Columbus Salt Marsh Valley	236,800	13,300	17.1	700	0.9	3,800	18.2	12.9	10.6
119	Rhodes Salt Marsh Valley	127,360	11,600	27.8	500	1.2	600	4.9	5.3	28.6
121	Soda Springs Valley/Eastern Part	240,640	19,600	24.8	700	0.9	430	1.4	4.3	5.2

Table 7.2.1.2-3. Maxey-Eakin and Water Budget Recharge Estimates for Selected Nevada Hydrographic Areas/Sub-Areas [a] (Continued)

Number [b]	Name [b]	Size [b] (acres)	Precipitation [c,d]		Recharge [d]				Efficiency	
					ME		WB		ME	WB
			(acre-ft/yr)	(mm/yr)	(acre-ft/yr)	(mm/yr)	(acre-ft/yr)	(mm/yr)	(%)	(%)
125-127	Stingaree Valley, Cowkick Valley, Eastgate Valley Area	236,160	94,100	121.5	6,000	7.7	6,000	0.5	3.6	2.2
128	Dixie Valley	833,920	116,200	42.5	6,000	2.2	9,200	7.7	6.4	6.4
132	Jersey Valley	90,880	16,970	56.9	800	2.7	800	3.4	5.2	7.9
133	Edwards Creek Valley	266,240	111,400	127.5	8,000	9.2	7,600	2.7	4.7	4.7
134	Smith Creek	372,480	92,000	75.3	9,600	7.9	7,000	8.7	7.2	6.8
136	Monte Cristo Valley	181,760	12,200	20.5	500	0.8	400	5.7	10.4	7.6
138	Grass Valley	380,800	211,000	168.9	13,000	10.4	13,000	0.7	4.1	3.3
150	Little Fish Lake Valley	277,760	181,000	198.6	11,000	12.1	10,000	10.4	6.2	6.2
153	Diamond Valley	481,280	319,000	202.0	21,000	13.3	21,000	11.0	6.1	5.5
156	Hot Creek	663,040	153,000	70.3	7,000	3.2	6,100	13.3	6.6	6.6
179	Steptoe Valley	1,242,880	810,000	198.6	85,000	20.8	70,000	2.8	4.6	4.0
183	Lake Valley	356,480	229,000	195.8	13,000	11.1	11,500	2.6	4.5	4.0
184	Spring Valley	1,063,040	791,000	226.8	75,000	21.5	74,000	9.8	7.9	8.6

[a] Avon and Durbin (1994 [DIRS 177200]), Table 2.
[b] Basin areas from Horton (1998 [DIRS 174618], Appendix A-1).
[c] Precipitation estimates from Lopes and Evetts (2004 [DIRS 175964], Appendix 1)
[d] Precipitation and recharge originally reported in acre-ft/yr were converted to mm/yr using basin areas reported by Horton (1998 [DIRS 174618], Appendix A-1).

Table 7.2.1.2-4. Maxey-Eakin and "Model" Recharge Estimates for Selected Nevada Hydrographic Areas/Sub-Areas [a]

Number [b]	Name [b]	Size [b] (acres)	Precipitation [c,d]		Recharge [d]				Efficiency (%)	
					ME [a]		Model Estimates [a]			
			(acre-ft/yr)	(mm/yr)	(acre-ft/yr)	(mm/yr)	(acre-ft/yr)	(mm/yr)	ME	Model
175	Long Valley	416,640	297,000	217.3	10,000	7.3	5,000	3.7	3.4	1.7
180	Cave Valley	231,680	206,000	271.0	14,000	18.4	12,000	15.8	6.8	5.8
181	Dry Lake Valley	564,480	118,000	63.7	5,000	2.7	6,700	3.6	4.2	5.7
182	Delamar Valley	245,120	34,000	42.3	1,000	1.2	1,800	2.2	2.9	5.3
206	Kane Springs Valley	149,760	10,000	20.4	500	1.0	1,000	2.0	5.0	10.0
208	Pahroc Valley	325,120	57,000	53.4	2,200	2.1	2,000	1.9	3.9	3.5
209	Pahranagat Valley	491,520	43,000	26.7	1,800	1.1	1,500	0.9	4.2	3.5
210	Coyote Springs Valley	420,480	39,000	28.3	2,100	1.5	5,300	3.8	5.4	13.6

[a] Avon and Durbin 1994 [DIRS 177200], Table 3.
[b] Basin areas from Horton 1998 [DIRS 174618], Appendix A-1.
[c] Precipitation estimates from Lopes and Evetts 2004 [DIRS 175964], Appendix 1.
[d] Precipitation and recharge originally reported in acre-ft/yr were converted to mm/yr using basin areas reported by Horton 1998 [DIRS 174618], Appendix A-1.

Lichty and McKinley (1995 [DIRS 100589], Tables 1 and 15) investigated groundwater recharge rates for 3-Springs and East Stewart basins, two small basins in central Nevada. Two independent modeling approaches were used at each site: water budget and chloride mass balance methods. Their results are presented in Table 7.2.1.2-5. The results for the East Stewart basin are included even though the precipitation in this basin is substantially higher than would be expected at Yucca Mountain, even for the glacial transition climate. One observes that for the 3-Springs basin, the chloride mass balance estimates are approximately three times higher than the water balance estimate. The recharge efficiency estimates vary from about 3% to 10%. The variation between the methods is much smaller for the East Stewart basin. The recharge efficiency for this basin is approximately 50%.

Table 7.2.1.2-5. Recharge to 3-Springs Basin, Central Nevada [a]

Basin	Area (km^2)	Precipitation (mm/yr)	Recharge (mm/yr)		Efficiency (%)	
			WB [b]	CMB [b]	WB [b]	CMB [b]
3-Springs	4.20	336.4	11.4	32.8	3.4	9.8
East Stewart	0.93	639.1	321.5	309.9	50.3	48.5

[a] Lichty and McKinley (1995 [DIRS 100589], Tables 1 and 15).
[b] WB= water balance; CMB = chloride mass balance.

Nichols (2000 [DIRS 178863]) estimated basin-scale recharge rates for 16 hydrographic basins in Nevada. These estimates, which used a modified Maxey-Eakin approach, are listed in Table 7.2.1.2-6. The basin areas used to calculate the annual precipitation in mm/yr are from Horton (1998 [DIRS 174618], Appendix A-1). These areas differ slightly from the areas reported by Nichols (2000 [DIRS 178863], Table C-19), however the differences are all less than 2%.

Table 7.2.1.2-6. Recharge Estimates for 16 Nevada Hydrographic Areas [a]

No. [b]	Name [b]	Area [b] (acres)	Precipitation [c]		Recharge [c]		Efficiency	Method [d]
			(acre-ft/yr)	(mm/yr)	(acre-ft/yr)	(mm/yr)	(%)	
150	Little Fish Lake Valley	276,482	236,430	261	9,628	10.6	4.1	MME
154	Newark Valley	509,282	515,470	309	49,092	29.4	9.5	MME
155	Little Smoky Valley	740,575	523,359	215	12,681	5.2	2.4	MME
156	Hot Creek Valley	658,501	424,067	196	5,756	2.7	1.4	MME
174	Jakes Valley	270,498	289,477	326	38,203	43.0	13.2	MME
175	Long Valley	419,844	452,368	328	47,740	34.7	10.6	MME
176	Ruby Valley	638,936	867,225	414	145,636	69.5	16.8	MME
177	Clover Valley	292,115	363,327	379	58,802	61.4	16.2	MME
178	Butte Valley	652,363	700,905	327	68,989	32.2	9.8	MME
179	Steptoe Valley	1,245,618	1,344,191	329	131,469	32.2	9.8	MME
184	Spring Valley	1,067,010	1,141,444	326	103,569	29.6	9.1	MME
185	Tippett Valley	221,574	211,904	291	12,389	17.0	5.8	MME
186	Antelope Valley	255,680	246,551	294	16,824	20.1	6.8	MME
187	Goshute Valley	612,169	592,875	295	40,911	20.4	6.9	MME

Table 7.2.1.2-6. Recharge Estimates for 16 Nevada Hydrographic Areas [a] (Continued)

No. [b]	Name [b]	Area [b] (acres)	Precipitation [c]		Recharge [c]		Efficiency	Method [d]
			(acre-ft/yr)	(mm/yr)	(acre-ft/yr)	(mm/yr)	(%)	
188	Independence Valley	360,670	394,415	333	50,065	42.3	12.7	MME
173B	Railroad Valley/Northern Part	1,369,671	1,089,249	242	61,083	13.6	5.6	MME

[a] Nichols 2000 [DIRS 178863], Chapter C.
[b] Basin area and number from Horton 1998 [DIRS 174618], Appendix A-1. The areas differ slightly from those listed in Nichols (2000 [DIRS 178863]). The differences are all less than 2% (see Output DTN SN0701T0502206.037, file: \Welcome to Massif\Massif\Validation Analyses\Excel Figures*Recharge_models_vs_MASSIF.xls*, sheet: "Nichols" for a comparison of this difference.
[c] Precipitation and recharge originally reported in acre-ft/yr by Nichols 2000 DIRS 178863], Table C-19, were converted to mm/yr using basin areas reported by Horton 1998 [DIRS 174618], Appendix A-1.
[d] MME = modified Maxey-Eakin.

The U.S. Geological Survey, in cooperation with the Nevada Division of Environmental Protection, has recently compiled estimates of natural recharge from published sources (Lopes and Evetts 2004 [DIRS 175964], Appendix 1). This report contains basin-wide estimates of average annual precipitation and recharge for basins in Nevada. These estimates of average annual precipitation and recharge for each basin are provided in Table 7.2.1.2-7. As with the report by Avon and Durbin (1994 [DIRS 177200]) there is some overlap between estimates reported by Lopes and Evetts (2004 [DIRS 175964], Appendix 1) and previous studies, so these estimates are excluded from the table. Also excluded are estimates for which no precipitation information was reported.

The recharge values reported in Table 7.2.1.2-7 are mainly Maxey-Eakin or modified Maxey-Eakin estimates, along with a much smaller number of water budget and chloride mass balance estimates. In many cases, Lopes and Evetts (2004 [DIRS 175964], Appendix 1) report multiple precipitation/recharge values for a single hydrographic area. Precipitation estimates for a single area can vary by a factor of 2 and as much as 4; recharge estimates for a single area can vary by as much as a factor of 5. Multiple methods and data sources were used to estimate these values, which is the primary reason for reporting multiple values and the source of the variability. However, irrespective of data source or estimation method, recharge values reported by Lopes and Evetts (2004 [DIRS 175964], Appendix 1) typically remain between 3% and 10% of precipitation. Estimates reported by Lopes and Evetts (2004 [DIRS 175964]) from Nichols (2000 [DIRS 178863]) are listed separately in Table 7.2.1.2-6.

Table 7.2.1.2-7. Recharge Estimates for Selected Nevada Hydrographic Areas/Subareas [a]

No. [b]	Name [b]	Area [b] (acres)	Precipitation [c]		Recharge [c]		Efficiency	Method [d]
			(acre-ft/yr)	(mm/yr)	(acre-ft/yr)	(mm/yr)	(%)	
1	Pueblo Valley	75,520	48,300	195	2,000	8.1	4.1	ME
2	Continental Lake Valley	136,960	254,200	566	11,000	24.5	4.3	ME
3	Gridley Lake Valley	124,800	97,900	239	4,500	11.0	4.6	ME
4	Virgin Valley	316,160	230,000	222	7,000	6.7	3.0	ME
6	Guano Valley	94,080	206,000	667	7,500	24.3	3.6	ME

Table 7.2.1.2-7. Recharge Estimates for Selected Nevada Hydrographic Areas/Subareas [a] (Continued)

No. [b]	Name [b]	Area [b] (acres)	Precipitation [c]		Recharge [c]		Efficiency	Method [d]
			(acre-ft/yr)	(mm/yr)	(acre-ft/yr)	(mm/yr)	(%)	
8	Massacre Lake Valley	112,640	88,200	239	3,500	9.5	4.0	ME
9	Long Valley	277,120	168,000	185	6,000	6.6	3.6	ME
11	Coleman Valley	32,640	28,000	261	1,000	9.3	3.6	ME
12	Mosquito Valley	20,480	14,300	213	700	10.4	4.9	ME
14	Surprise Valley	136,960	37,500	83	1,500	3.3	4.0	ME
15	Boulder Valley	56,320	50,400	273	2,000	10.8	4.0	ME
17	Pilgrim Flat	7,680	7,000	278	500	19.8	7.1	ME
19	Dry Valley	24,960	5,900	72	200	2.4	3.4	ME
20	Sano Valley	7,680	130	5	4	0.2	3.1	ME
23	Granite Basin	5,760	45,400	2,402	2,000	105.8	4.4	ME
24	Hualapai Flat	201,600	62,700	95	4,000	6.0	6.4	ME
25	High Rock Lake Valley	425,600	435,000	312	13,000	9.3	3.0	ME
26	Mud Meadow	316,800	130,600	126	8,000	7.7	6.1	ME
27	Summit Lake Valley	38,400	42,700	339	4,200	33.3	9.8	ME
28	Black Rock Desert	1,394,560	260,900	57	13,900	3.0	5.3	ME
30	Kings River Valley	264,320	260,000	300	15,000	17.3	5.8	ME
31	Desert Valley	673,280	100,000	45	5,000	2.3	5.0	ME
		673,280	110,000	50	7,000	3.2	6.4	ME
		673,280	110,000	50	3,300	1.5	3.0	CMB
32	Silver State Valley	200,320	35,000	53	1,400	2.1	4.0	ME
33	Quinn River Valley	783,360	880,000	342	62,000	24.1	7.0	ME
34	Little Owyhee River Area	458,240	357,000	237	2,700	1.8	0.8	ME
35	South Fork Owyhee River Area	838,400	1,004,000	365	28,000	10.2	2.8	ME
37	Owyhee River Area	341,120	458,000	409	17,000	15.2	3.7	ME
38	Bruneau River Area	328,960	497,000	460	26,000	24.1	5.2	ME
39	Jarbidge River Area	177,920	334,000	572	32,000	54.8	9.6	ME
40	Salmon Falls Creek Area	779,520	1,021,000	399	44,000	17.2	4.3	ME
41	Goose Creek Area	202,240	198,000	298	6,700	10.1	3.4	ME
46	South Fork Area	63,360	98,000	471	3,000	14.4	3.1	WB
47	Huntington Valley	503,680	554,000	335	14,000	8.5	2.5	WB
48	Dixie Creek-Tenmile Creek Area	250,880	235,000	286	13,000	15.8	5.5	WB
50	Susie Creek Area	142,720	147,000	314	9,700	20.7	6.6	ME
51	Maggie Creek Area	253,440	280,000	337	23,000	27.7	8.2	ME
52	Marys Creek Area	39,040	37,000	289	2,100	16.4	5.7	ME
53	Pine Valley	641,280	688,000	327	52,500	25.0	7.6	WB
		641,280	688,000	327	79,300	37.7	11.5	WB
		641,280	688,000	327	66,000	31.4	9.6	MME
54	Crescent Valley	481,280	200,000	127	14,000	8.9	7.0	Other
		481,280	446,000	282	25,200	16.0	5.7	WB
		481,280	446,000	282	26,200	16.6	5.9	WB

Table 7.2.1.2-7. Recharge Estimates for Selected Nevada Hydrographic Areas/Subareas [a] (Continued)

No. [b]	Name [b]	Area [b] (acres)	Precipitation [c]		Recharge [c]		Efficiency	Method [d]
			(acre-ft/yr)	(mm/yr)	(acre-ft/yr)	(mm/yr)	(%)	
		481,280	446,000	282	21,000	13.3	4.7	MME
55	Carico Lake Valley	240,640	239,000	303	18,700	23.7	7.8	WB
		240,640	239,000	303	20,400	25.8	8.5	WB
		240,640	239,000	303	18,000	22.8	7.5	MME
56	Upper Reese River Valley	728,320	803,000	336	71,400	29.9	8.9	WB
		728,320	803,000	336	110,000	46.0	13.7	WB
		728,320	803,000	336	93,000	38.9	11.6	MME
57	Antelope Valley	289,280	240,000	253	11,000	11.6	4.6	ME
		289,280	279,000	294	17,200	18.1	6.2	WB
		289,280	279,000	294	25,200	26.6	9.0	WB
		289,280	279,000	294	19,000	20.0	6.8	MME
58	Middle Reese River Valley	204,160	142,000	212	7,000	10.5	4.9	ME
		204,160	186,000	278	12,800	19.1	6.9	WB
		204,160	186,000	278	13,200	19.7	7.1	WB
		204,160	186,000	278	10,000	14.9	5.4	MME
59	Lower Reese River Valley	376,320	341,000	276	18,500	15.0	5.4	WB
		376320	341,000	276	19,000	15.4	5.6	WB
		376,320	341,000	276	13,000	10.5	3.8	MME
60	Whirlwind Valley	60,160	55,000	279	3,700	18.7	6.7	WB
		60,160	55,000	279	3,800	19.3	6.9	WB
		60,160	55,000	279	2,000	10.1	3.6	MME
61	Boulder Flat	348,160	291,000	255	14,000	12.3	4.8	ME
		348,160	308,000	270	19,100	16.7	6.2	WB
		348,160	308,000	270	19,300	16.9	6.3	WB
		348,160	308,000	270	11,000	9.6	3.6	MME
62	Rock Creek Valley	284,160	256,000	275	17,100	18.3	6.7	WB
		284,160	256,000	275	9,000	9.7	3.5	MME
		284,160	270,000	290	13,000	13.9	4.8	ME
63	Willow Creek Valley	259,200	279,000	328	20,000	23.5	7.2	ME
		259,200	280,000	329	27,500	32.3	9.8	WB
		259,200	280,000	329	28,000	32.9	10.0	MME
64	Clovers Area	460,800	401,000	265	17,900	11.8	4.5	WB
		460,800	401,000	265	18,400	12.2	4.6	WB
		460,800	401,000	265	13,000	8.6	3.2	MME
65	Pumpernickel Valley	191,360	169,000	269	8,800	14.0	5.2	WB
		191,360	169,000	269	9,000	14.3	5.3	WB
		191,360	169,000	269	7,500	11.9	4.4	MME
66	Kelly Creek Area	192,640	181,000	286	12,700	20.1	7.0	WB
		192,640	181,000	286	13,200	20.9	7.3	WB
		192,640	181,000	286	11,000	17.4	6.1	MME
67	Little Humboldt Valley	624,000	443,000	216	24,000	11.7	5.4	ME
68	Hardscrabble Area	106,880	115,000	328	9,000	25.7	7.8	ME

Table 7.2.1.2-7. Recharge Estimates for Selected Nevada Hydrographic Areas/Subareas [a] (Continued)

No. [b]	Name [b]	Area [b] (acres)	Precipitation [c]		Recharge [c]		Efficiency	Method [d]
			(acre-ft/yr)	(mm/yr)	(acre-ft/yr)	(mm/yr)	(%)	
69	Paradise Valley	384,000	121,000	96	10,000	7.9	8.3	ME
72	Imlay Area	493,440	82,000	51	4,000	2.5	4.9	ME
73	Lovelock Valley	406,400	60,000	45	3,200	2.4	5.3	ME
74	White Plains	104,960	100	0	3	0.0	3.0	ME
75	Bradys Hot Springs Area	113,920	4,800	13	160	0.4	3.3	ME
76	Fernley Area	76,800	13,000	52	600	2.4	4.6	ME
77	Fireball Valley	37,120	6,000	49	200	1.6	3.3	ME
78	Granite Springs Valley	618,880	97,600	48	3,500	1.7	3.6	ME
79	Kumiva Valley	213,120	28,000	40	1,000	1.4	3.6	ME
80	Winnemucca Lake Valley	237,440	61,000	78	2,900	3.7	4.8	ME
81	Pyramid Lake Valley	430,080	100,000	71	6,600	4.7	6.6	ME
82	Dodge Flat	58,880	21,000	109	1,400	7.2	6.7	ME
83	Tracy Segment	182,400	121,000	202	6,000	10.0	5.0	ME
85	Spanish Springs Valley	48,640	26,000	163	830	5.2	3.2	ME
		48,640	26,000	163	770	4.8	3.0	CMB
87	Truckee Meadows	129,920	161,000	378	27,000	63.3	16.8	ME
88	Pleasant Valley	24,960	46,000	562	10,000	122.1	21.7	ME
89	Washoe Valley	52,480	87,000	505	15,000	87.1	17.2	ME
91	Truckee CanyonSegment	53,760	110,000	624	27,000	153.1	24.5	ME
92	Lemmon Valley	59,520	44,000	225	1,500	7.7	3.4	ME
93	Antelope Valley	11,520	9,000	238	300	7.9	3.3	ME
94	Bedell Flat	33,920	27,000	243	1,100	9.9	4.1	ME
98	Skedaddle Creek Valley	27,520	17,680	196	600	6.6	3.4	ME
99	Red Rock Valley	37,120	7,700	63	900	7.4	11.7	ME
100	Cold Spring Valley	35,200	18,000	156	900	7.8	5.0	ME
101	Carson Desert	1,396,480	43,000	9	2,010	0.4	4.7	ME
102	Churchill Valley	307,200	32,000	32	1,300	1.3	4.1	ME
103	Dayton Valley	236,160	125,300	162	7,900	10.2	6.3	ME
		236,160	127,000	164	7,900	10.2	6.2	ME
		236,160	163,000	210	11,000	14.2	6.7	ME
		236,160	229,000	296	26,000	33.6	11.4	ME
104	Eagle Valley	44,160	58,000	400	8,700	60.0	15.0	ME
		44,160	67,000	462	8,000	55.2	11.9	WB
		44,160	67,000	462	10,000	69.0	14.9	WB
105	Carson Valley	268,160	254,000	289	25,000	28.4	9.8	ME
		268,160	350,000	398	49,000	55.7	14.0	ME
106	Antelope Valley	73,600	66,700	276	5,000	20.7	7.5	ME
107	Smith Valley	306,560	210,000	209	17,000	16.9	8.1	ME
108	Mason Valley	330,240	32,000	30	2,000	1.8	6.3	ME
109	East Walker Area	375,040	191,000	155	22,000	17.9	11.5	ME
110	Walker Lake Valley	864,000	101,000	36	6,500	2.3	6.4	ME
111	Alkali Valley	53,120	32,400	186	1,800	10.3	5.6	ME

Table 7.2.1.2-7. Recharge Estimates for Selected Nevada Hydrographic Areas/Subareas [a] (Continued)

No. [b]	Name [b]	Area [b] (acres)	Precipitation [c]		Recharge [c]		Efficiency	Method [d]
			(acre-ft/yr)	(mm/yr)	(acre-ft/yr)	(mm/yr)	(%)	
112	Mono Valley	17,280	16,000	282	700	12.3	4.4	ME
115	Adobe Valley	9,600	6,400	203	300	9.5	4.7	ME
116	Queen Valley	41,600	25,100	184	2,000	14.7	8.0	ME
120	Garfield Flat	58,880	9,400	49	300	1.6	3.2	ME
123	Rawhide Flats	145,280	5,000	10	150	0.3	3.0	ME
124	Fairview Valley	182,400	16,600	28	500	0.8	3.0	ME
		182,400	74,000	124	2,300	3.8	3.1	ME
125,6,7	Sum of HAs 125, 126, 127	236,160	171,000	221	6,700	8.6	3.9	ME
128	Dixie Valley	833,920	246,900	90	8,900	3.3	3.6	ME
130	Pleasant Valley	182,400	44,900	75	3,000	5.0	6.7	ME
		182,400	92,000	154	3,300	5.5	3.6	ME
132	Jersey Valley	90,880	41,000	138	1,400	4.7	3.4	ME
134	Smith Creek Valley	372,480	119,000	97	12,000	9.8	10.1	ME
135	Ione Valley	294,400	90,000	93	8,000	8.3	8.9	ME
137	Big Smoky Valley	1,872,640	741,000	121	77,000	12.5	10.4	ME
139	Kobeh Valley	555,520	110,000	60	11,000	6.0	10.0	ME
140	Monitor Valley	664,320	392,500	180	23,300	10.7	5.9	ME
141	Ralston Valley	621,440	340,000	167	16,000	7.8	4.7	ME
		621,440	115,000	56	5,000	2.5	4.3	ME
142	Alkali Spring Valley	200,320	2,800	4	100	0.2	3.6	ME
143	Clayton Valley	355,200	34,700	30	1,500	1.3	4.3	ME
144	Lida Valley	342,400	13,400	12	500	0.4	3.7	ME
145	Stonewall Flat	243,840	1,900	2	100	0.1	5.3	ME
146	Sarcobatus Flat	519,680	37,500	22	1,200	0.7	3.2	ME
147	Gold Flat	437,760	94,000	65	3,800	2.6	4.0	ME
148	Cactus Flat	257,920	15,000	18	600	0.7	4.0	ME
149	Stone Cabin Valley	630,400	362,000	175	16,000	7.7	4.4	ME
		630,400	103,000	50	5,000	2.4	4.9	ME
151	Antelope Valley	284,160	108,100	116	4,100	4.4	3.8	ME
152	Stevens Basin	10,880	8,500	238	200	5.6	2.4	ME
153	Diamond Valley	481,280	304,000	193	16,000	10.1	5.3	ME
154	Newark Valley	512,640	335,000	199	17,500	10.4	5.2	ME
155	Little Smoky Valley	741,120	140,000	58	5,400	2.2	3.9	ME
157	Kawich Valley	224,000	88,000	120	3,500	4.8	4.0	ME
158	Emigrant Valley	490,880	75,720	47	3,204	2.0	4.2	ME
159	Yucca Flat	195,200	19,300	30	700	1.1	3.6	ME
160	Frenchman Flat	296,320	3,200	3	100	0.1	3.1	ME
161	Indian Springs Valley	419,200	115,000	84	10,000	7.3	8.7	ME
163	Mesquite Valley	151,040	28,400	57	1,400	2.8	4.9	ME
164	Ivanpah Valley	208,640	13,350	20	700	1.0	5.2	ME
165	Jean Lake Valley	61,440	2,200	11	100	0.5	4.5	ME

Table 7.2.1.2-7. Recharge Estimates for Selected Nevada Hydrographic Areas/Subareas [a] (Continued)

No. [b]	Name [b]	Area [b] (acres)	Precipitation [c]		Recharge [c]		Efficiency	Method [d]
			(acre-ft/yr)	(mm/yr)	(acre-ft/yr)	(mm/yr)	(%)	
167	Eldorado Valley	339,200	37,000	33	1,100	1.0	3.0	ME
168	Three Lakes Valley	190,720	41,100	66	2,000	3.2	4.9	ME
169	Tikapoo Valley	638,720	115,000	55	6,000	2.9	5.2	ME
170	Penoyer Valley	448,000	97,300	66	13,500	9.2	13.9	ME
171	Coal Valley	294,400	62,000	64	2,000	2.1	3.2	ME
172	Garden Valley	315,520	137,000	132	10,000	9.7	7.3	ME
173	Railroad Valley	385,920	817,200	645	50,400	39.8	6.2	ME
175	Long Valley	416,640	297,000	217	10,000	7.3	3.4	ME
176	Ruby Valley	642,560	696,000	330	68,000	32.3	9.8	ME
177	Clover Valley	296,960	224,000	230	20,700	21.2	9.2	ME
180	Cave Valley	231,680	206,000	271	14,000	18.4	6.8	ME
181	Dry Lake Valley	564,480	118,000	64	5,000	2.7	4.2	ME
182	Delamar Valley	245,120	34,000	42	1,000	1.2	2.9	ME
185	Tippett Valley	220,800	114,000	157	6,900	9.5	6.1	ME
186	Antelope Valley	252,800	117,000	141	4,700	5.7	4.0	ME
188	Independence Valley	359,680	203,000	172	9,300	7.9	4.6	ME
189	Thousand Springs Valley	925,440	325,000	107	12,000	4.0	3.7	ME
190	Grouse Creek Valley	35,200	19,100	165	700	6.1	3.7	ME
191	Pilot Creek Valley	208,640	40,000	58	2,400	3.5	6.0	ME
192	Great Salt Lake Desert	324,480	77,600	73	4,800	4.5	6.2	ME
193	Deep Creek Valley	133,120	44,700	102	2,200	5.0	4.9	ME
197	Escalante Desert	67,840	76,000	341	2,300	10.3	3.0	ME
201	Spring Valley	183,680	177,000	294	10,000	16.6	5.6	ME
202	Patterson Valley	267,520	137,000	156	6,000	6.8	4.4	ME
206	Kane Springs Valley	149,760	10,000	20	500	1.0	5.0	ME
208	Pahroc Valley	325,120	57,000	53	2,200	2.1	3.9	ME
209	Pahranagat Valley	491,520	43,000	27	1,800	1.1	4.2	ME
210	Coyote Spring Valley	420,480	39,000	28	2,100	1.5	5.4	ME
211	Three Lakes Valley	199,040	56,000	86	6,000	9.2	10.7	ME
		199,040	56,000	86	7,300	11.2	13.0	MME
212	Las Vegas Valley	1,000,960	161,200	49	30,000	9.1	18.6	ME
		1,000,960	161,200	49	35,000	10.7	21.7	ME
		1,000,960	332,500	101	28,000	8.5	8.4	CMB
213	Colorado River Valley	360,320	5800	5	200	0.2	3.4	ME
214	Piute Valley	216,320	55,800	79	1,700	2.4	3.0	ME
215	Black Mountains Area	403,200	2,200	2	70	0.1	3.2	ME
216	Garnet Valley	99,840	11,000	34	400	1.2	3.6	ME
217	Hidden Valley	51,200	11,000	65	400	2.4	3.6	ME
218	California Wash	203,520	2,000	3	60	0.1	3.0	ME
220	Lower Moapa Valley	161,280	1,200	2	40	0.1	3.3	ME
221	Tule Desert	122,880	62,000	154	2,100	5.2	3.4	ME
222	Virgin River Valley	580,480	98,700	52	3,600	1.9	3.6	ME

Table 7.2.1.2-7. Recharge Estimates for Selected Nevada Hydrographic Areas/Subareas [a] (Continued)

No. [b]	Name [b]	Area [b] (acres)	Precipitation [c]		Recharge [c]		Efficiency	Method [d]
			(acre-ft/yr)	(mm/yr)	(acre-ft/yr)	(mm/yr)	(%)	
223	Gold Butte Area	341,120	27,600	25	1,000	0.9	3.6	ME
224	Greasewood Area	69,120	14,900	66	600	2.6	4.0	ME
225	Mercury Valley	70,400	5,200	23	250	1.1	4.8	ME
226	Rock Valley	52,480	900	5	30	0.2	3.3	ME
227	Fortymile Canyon	332,160	61,000	56	2,300	2.1	3.8	ME
228	Oasis Valley	294,400	33,500	35	1,000	1.0	3.0	ME
229	Crater Flat	116,480	6,700	18	220	0.6	3.3	ME
230	Amargosa Desert	573,440	90,000	48	1,500	0.8	1.7	ME
231	Grapevine Canyon	103,680	1,070	3	50	0.1	4.7	ME
232	Oriental Wash	116,480	8,500	22	300	0.8	3.5	ME

[a] Lopes and Evetts 2004 [DIRS 175964], Appendix 1.

[b] Basin areas from Horton 1998 [DIRS 174618], Appendix A-1.

[c] Precipitation and recharge originally reported in acre-ft/yr were converted to mm/yr using basin areas reported by Horton 1998 [DIRS 174618], Appendix A-1.

[d] CMB = chloride mass balance; ME=Maxey-Eakin; MME = modified Maxey-Eakin; WB = water budget.

Figure 7.2.1.2-2 summarizes the basin-scale, net infiltration estimates listed in Tables 7.2.1.2-1 through 7.2.1.2-7 and plots these data with the MASSIF net infiltration results for three climates. The Maxey-Eakin (1950 [DIRS 100598]) model (represented as a stepped line on the figure) is also shown for reference. Note that the Maxey-Eakin model line does not match the individual basin-scale Maxey-Eakin model net infiltration estimates, shown as black crosses on the figure. This is because each of these precipitation and recharge estimates is an area-weighted mean value derived from subareas of the basin in which precipitation is estimated locally. For each of these subareas an associated recharge amount is determined using the percent recharge values from Maxey-Eakin (1950 [DIRS 100598] p. 40). Thus the total precipitation and total recharge values are area-weighted mean values and vary depending on the precipitation patterns across the basin, which largely depend on the basin's topographic character. There is fairly good agreement among the methods for relatively low precipitation, but estimates tend to diverge as precipitation increases. The hydrographic areas closest to Yucca Mountain fall at the low end of the recharge scale (less than 10 mm/yr) and correspond well with the MASSIF net infiltration estimates for the Present-Day climate at Yucca Mountain. The MASSIF net infiltration estimates for the monsoon and glacial transition climates are generally within the range for the wetter Nevada basins.

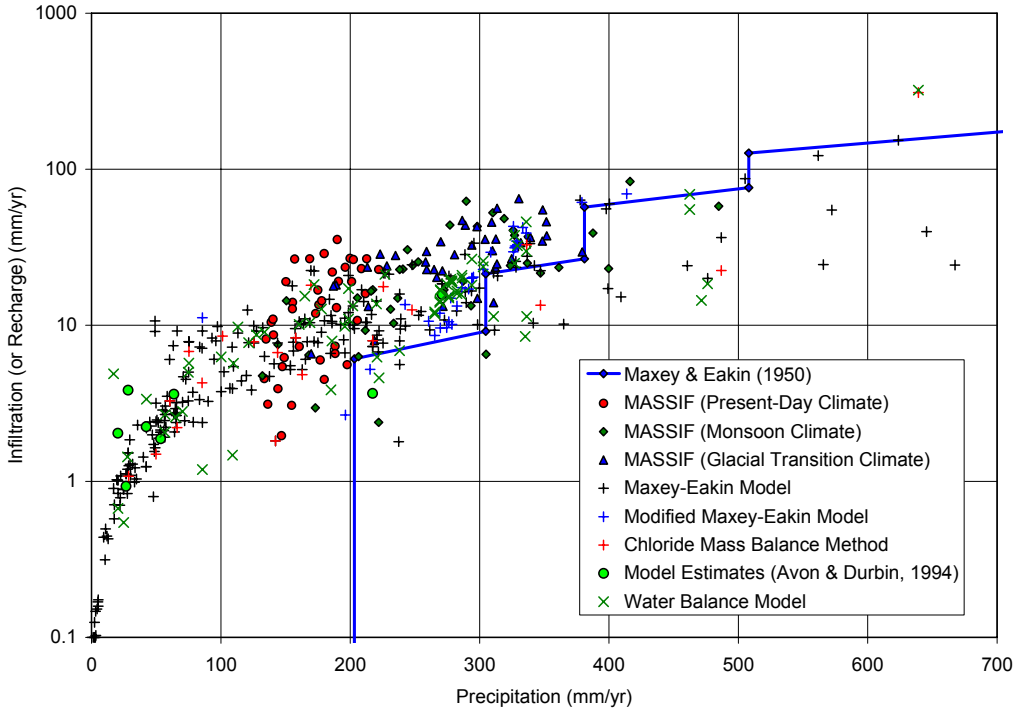

Source: Output DTNs: SN0701T0502206.034, SN0701T0502206.036, and SN0701T0502206.035, respectively (MASSIF results for Present-Day, Monsoon, and Glacial Transition climates). Data are from sources listed for Tables 7.2.1.2-1, 7.2.1.2-2, 7.2.1.2-3, 7.2.1.2-4, 7.2.1.2-5, and 7.2.1.2-6, which are also compiled in Validation Output DTN: SN0704T0502206.047.

NOTE: Vertical line that extends to the horizontal axis associated with the Maxey-Eakin model represents the precipitation amount below which the model predicts zero recharge.

Figure 7.2.1.2-2. Comparison of Recharge Estimates for Nevada Hydrographic Areas/Subareas with MASSIF Estimates of Net Infiltration at Yucca Mountain

7.2.1.2.2 Infiltration Estimates for Other Locations in the Southwestern United States

Infiltration data from the southwestern United States, including West Texas, New Mexico, and Arizona, are useful in assessing the model predictions for the monsoon climate. This region includes Hobbs, New Mexico and Nogales, Arizona (sites identified as average upper bound monsoon climate analogues in *Future Climate Analysis* (BSC 2004 [DIRS 170002], Table 6-1). Estimates for groundwater recharge in various locations in West Texas, New Mexico, and Arizona, and recharge estimates for other locations in the southwestern United States are shown in Table 7.2.1.2-8, which illustrates that recharge rates for the Southwestern United States, as a fraction of precipitation, remain consistent with Yucca Mountain and are typically between 0% and 10%. These data are compared with Yucca Mountain net infiltration rate predictions in Figure 7.2.1.2-3. A range of recharge rates for a site in northeastern Arizona, calculated using carbon-14 radiocarbon age dating combined with numerical modeling is also shown in Figure 7.2.1.2-3 even though this area is not a climate analog for Yucca Mountain under future climates (Zhu 2000 [DIRS 178539]).

Table 7.2.1.2-8. Recharge Estimates for West Texas, New Mexico, and Southeastern Arizona

Location	Precipitation (mm/yr)	Recharge (mm/yr)	Efficiency (%)	Method	Notes	Reference
Southeastern NM (Eddy County)	380	0.5	0.1	CMB	—	Shurbaji and Campbell 1997 [DIRS 178000]
	380	0.8	0.2			
	380	2.4	0.6			
Socorro, NM	200	7	3.5	Darcy's Law	pressure head data with harmonic mean conductivity	Stephens and Knowlton 1986 [DIRS 177281]
	200	36.6	18.3		pressure head data with geometric mean conductivity	
	200	37	18.5		Moisture content with unit hydraulic gradient	
Albuquerque, NM	510	23	4.5	regression of rainfall runoff data	Mountain block and mountain front recharge	Wilson and Guan 2004 [DIRS 172585], Table 2.
	510	66	12.9	regression of rainfall runoff data		
	510	31	6.1	CMB		
	510	132	25.9	basin model calibrated with inverse method		
	510	15	2.9	basin model calibrated with ^{14}C data		
Southern High Plains (Southeastern New Mexico and West Texas)	485	11	2.3	CMB	—	Wood and Sanford 1995 [DIRS 177304]
Heuco Bolson, West Texas (Chihuahuan Desert)	280	0.03	0.0	CMB	Range (.03 to .7) from 10 boreholes	Scanlon 1991 [DIRS 107233]
	280	0.7	0.3			

Table 7.2.1.2-8. Recharge Estimates for West Texas, New Mexico, and Southeastern Arizona (Continued)

Location	Precipitation (mm/yr)	Recharge (mm/yr)	Efficiency (%)	Method	Notes	Reference
Eagle Flat basin, West Texas (Chihuahuan desert)	320	0.03	0.0	CMB	Interdrainage (old eolian sheet)	Scanlon et al 1999 [DIRS 177852], Table 2.
	320	0.06	0.0		Interdrainage (young eolian sheet)	
	320	0.05	0.0		Interdrainage (young eolian sheet)	
	320	0.02	0.0		Interdrainage (alluvial fan)	
	320	0.03	0.0		Interdrainage (basin fill deposit)	
	320	0.02	0.0		Interdrainage (slope)	
	320	0.02	0.0		Interdrainage (10 m from fissure)	
Walnut Gulch Experimental Watershed, southeastern Arizona	124	7	5.6	Calibrated HYDRUS-1D simulations	(0.5 to 2m zone below surface), winter only	Scott et al. 2000 [DIRS 177853
	145	8	5.5			
	196	68	34.7			
	34	0	0.0			
	202	41	20.3			
	21	0	0.0			
	47	0	0.0			
	155	12	7.7			
	126	3	2.4			
	181	17	9.4			
	243	66	27.2			
	50	0	0.0			
	263	64	24.3			
	25	0	0.0			
	53	0	0.0			
	135	0	0.0			

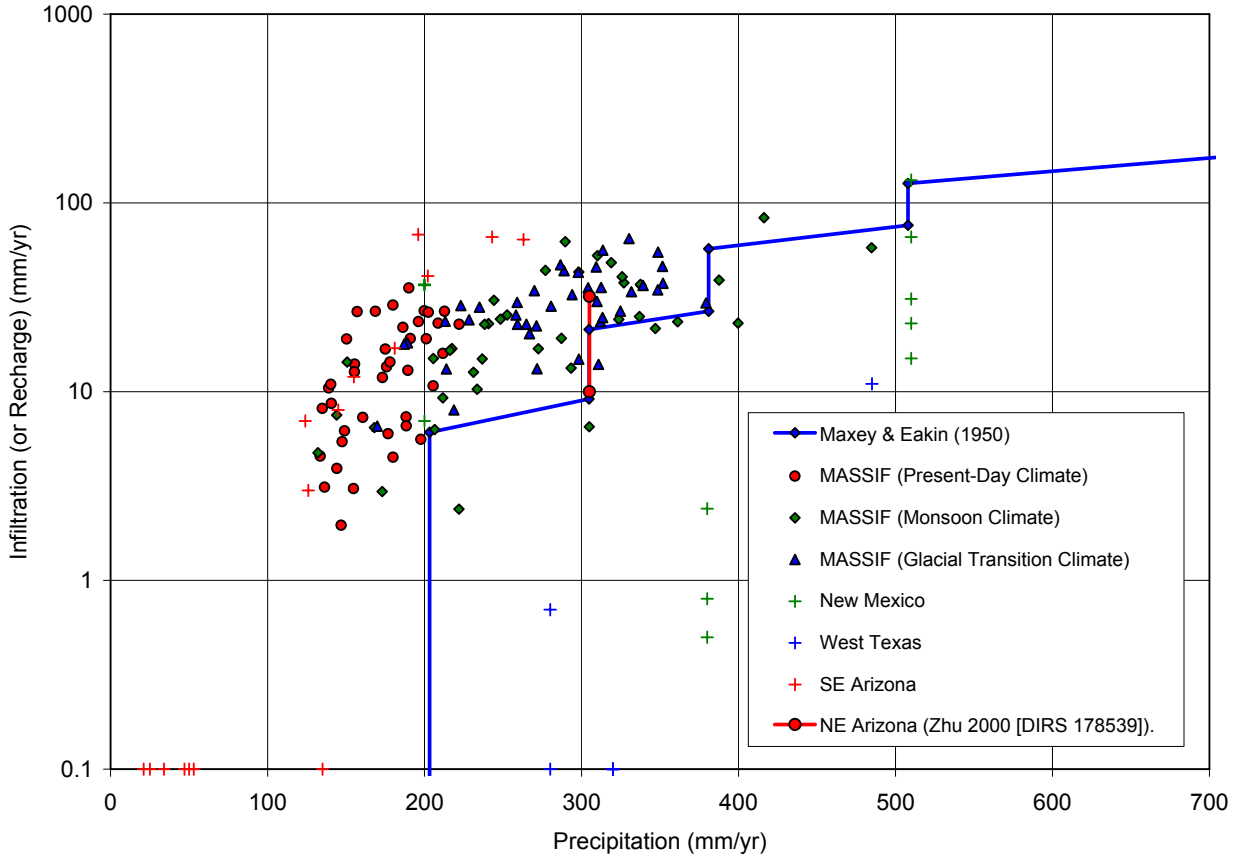

Source: Output DTNs: SN0701T0502206.034, SN0701T0502206.036, and SN0701T0502206.035, respectively (MASSIF results Present-Day, Monsoon, and Glacial Transition climates). Data points with <0.1 mm infiltration are plotted as 0.1 mm. All other data from Validation Output DTN: SN0704T0502206.047.

NOTE: Vertical line that extends to the horizontal axis associated with the Maxey-Eakin model represents the precipitation amount below which the model predicts zero recharge.

Figure 7.2.1.2-3. Comparison of Recharge Estimates for New Mexico, West Texas, and Arizona with MASSIF Estimates of Net Infiltration at Yucca Mountain.

7.2.1.2.3 Infiltration Estimates for Other Locations the Western United States

Future Climate Analysis (BSC 2004 [DIRS 170002], Table 6-1) identifies several sites on the Columbia Plateau in Eastern Washington (Spokane, Rosalia, and St. John) as average upper bound glacial transition climate analogs. Data from the Columbia Plateau in Washington State are therefore useful because they provide inferences into potential precipitation and recharge at Yucca Mountain during wetter climates. The Columbia Plateau's position in the rain shadow of the Cascade Mountains is also analogous to the Great Basin position behind the Sierra Nevada Mountains.

Model-derived estimates of average groundwater recharge to the Columbia Plateau regional aquifer system have been recently reported by Bauer and Vaccaro (1990 [DIRS 177726]). The deep-percolation model for estimating recharge used precipitation, temperature, streamflow, soils, land-use, and altitude data to calculate transpiration, soil evaporation, snow accumulation,

snowmelt, sublimation, and evaporation of intercepted moisture. Estimated annual average precipitation, and recharge rates for the various zones included in the Columbia Plateau study are shown in Table 7.2.1.2-9. The average annual precipitation for individual modeling zones ranges from approximately 168 to 410 mm/yr. Most precipitation values are clustered near the postulated range for the glacial transition lower bound mean annual precipitation (198 to 220 mm/yr). For these precipitation values, the recharge efficiency varies from about 0.1% to approximately 16%. The relatively fewer precipitation estimates that are near the postulated glacial transition upper bound exhibit the recharge efficiency varying from approximately 10% to 30%. Bauer and Vaccaro (1990 [DIRS 177726]) estimates are compared with predicted Yucca Mountain net infiltration rates in Figure 7.2.1.2-4. The Maxey-Eakin model is also shown in Figure 7.2.1.2-4 for reference.

Table 7.2.1.2-9. Recharge Estimates for Zones on the Columbia Plateau

Zone	Average Annual Precipitation (in/yr)	Average Annual Recharge (inch/yr)	Average Annual Precipitation (mm/yr)	Average Annual Recharge (mm/yr)	Efficiency (%)
1	7.29	0.43	185.2	10.9	5.9
2	8.91	1.25	226.3	31.8	14.0
3	9.34	1.37	237.2	34.8	14.7
4	6.61	0.38	167.9	9.7	5.7
5	8.77	1.18	222.8	30.0	13.5
6	8.64	0.66	219.5	16.8	7.6
7	8.26	1.31	209.8	33.3	15.9
8	6.95	0.3	176.5	7.6	4.3
9	7.64	0.43	194.1	10.9	5.6
10	7.93	0.45	201.4	11.4	5.7
11	7.76	0.44	197.1	11.2	5.7
12	7.41	0.15	188.2	3.8	2.0
13	8.19	0.47	208.0	11.9	5.7
14	7.95	0.23	201.9	5.8	2.9
15	6.98	0.13	177.3	3.3	1.9
16	8.31	0.39	211.1	9.9	4.7
17	8.09	0.26	205.5	6.6	3.2
18	12.05	1.3	306.1	33.0	10.8
19	10.09	0.83	256.3	21.1	8.2
20	9.19	0.87	233.4	22.1	9.5
21	17.27	5.39	438.7	136.9	31.2
22	22.75	10.52	577.9	267.2	46.2
23	22.32	6.01	566.9	152.7	26.9
24	9.64	0.57	244.9	14.5	5.9
25	10.33	1.36	262.4	34.5	13.2

Table 7.2.1.2-9. Recharge Estimates for Zones on the Columbia Plateau (Continued)

Zone	Average Annual Precipitation (in/yr)	Average Annual Recharge (inch/yr)	Average Annual Precipitation (mm/yr)	Average Annual Recharge (mm/yr)	Efficiency (%)
26	12.61	2.3	320.3	58.4	18.2
27	12.54	1.68	318.5	42.7	13.4
28	10.05	1.16	255.3	29.5	11.5
29	21.8	3.51	553.7	89.2	16.1
30	10.09	1.42	256.3	36.1	14.1
31	8.69	0.73	220.7	18.5	8.4
32	7.78	0.58	197.6	14.7	7.5
33	11.12	2.74	282.4	69.6	24.6
34	10.24	1.04	260.1	26.4	10.2
35	8.94	0.24	227.1	6.1	2.7
36	10.26	1.17	260.6	29.7	11.4
37	24.3	10.65	617.2	270.5	43.8
38	8.24	0.13	209.3	3.3	1.6
39	22.42	4.13	569.5	104.9	18.4
40	8.15	0.57	207.0	14.5	7.0
41	8.04	0.82	204.2	20.8	10.2
42	9.12	0.84	231.6	21.3	9.2
43	9.04	0.01	229.6	0.3	0.1
44	8.61	0.44	218.7	11.2	5.1
45	18.28	3.3	464.3	83.8	18.1
46	21.06	6.79	534.9	172.5	32.2
47	16.49	1.53	418.8	38.9	9.3
48	20.96	2.98	532.4	75.7	14.2
49	12.93	1.45	328.4	36.8	11.2
50	37.65	15.06	956.3	382.5	40.0
51	11.35	0.29	288.3	7.4	2.6
52	11.34	0.9	288.0	22.9	7.9
53	8.93	0.84	226.8	21.3	9.4

Source: Bauer and Vaccaro 1990 [DIRS 177726], Table 5.

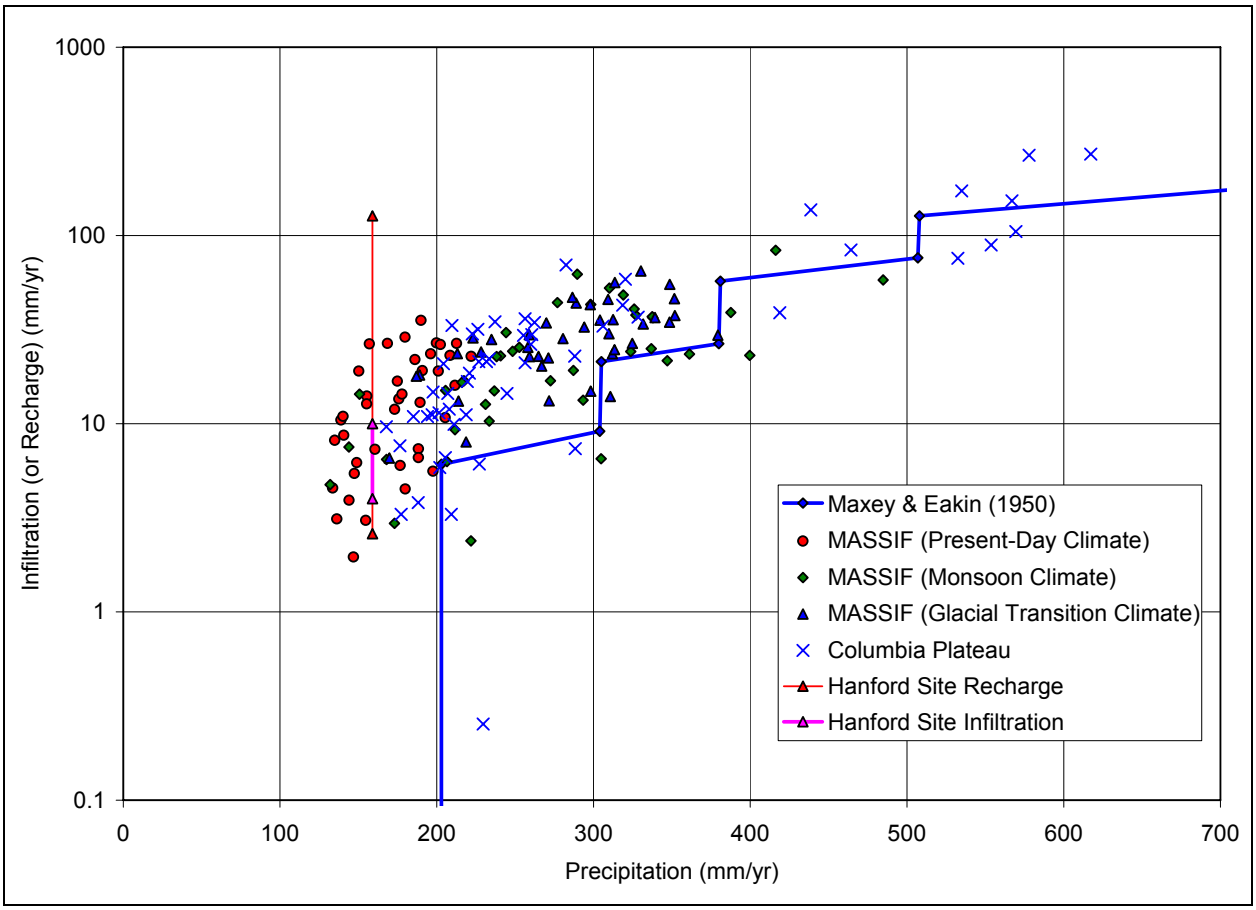

Source: Output DTNs SN0701T0502206.034, SN0701T0502206.036, and SN0701T0502206.035, respectively (MASSIF results for Present-Day, Monsoon, and Glacial Transition climates). All other data from Validation Output DTN: SN0704T0502206.047.

NOTE: Vertical line that extends to the horizontal axis associated with the Maxey-Eakin model represents the precipitation amount below which the model predicts zero recharge.

Figure 7.2.1.2-4. Comparison of Recharge Estimates for Columbia Plateau with MASSIF Estimates of Net Infiltration at Yucca Mountain

Fayer and Walters (1995 [DIRS 178191]) reported estimated recharge rates at the Hanford site in eastern Washington. They mapped soil type and vegetation/land use categories to measured or estimated recharge rates from a variety of sources (see Table 7.2.1.2-10). Estimation methods included lysimeter studies, chloride mass balance calculations, ^{36}Cl studies, and computer modeling. The long-term average recharge rates varied from 2.6 mm/yr for several soil and vegetation combinations to 127.1 mm/yr for basalt outcrop with no vegetation. The 30-year average annual precipitation value of 159 mm/yr for 1951 to 1980 is from the report by Fayer and Walters (1995 [DIRS 178191], Figure A.3). Maher et al. (2003 [DIRS 178540]) reported vadose zone infiltration rates of 4 to 10 mm/yr at the Hanford site. Their estimate was based on strontium isotope ratios measured in pore water, acid extracts, and sediments of a 70-m-thick vadose zone core.

Although average annual precipitation at the Hanford site is closer to the Yucca Mountain Present-Day climate than the Glacial Transition climate, the range in recharge rates from the report by Fayer and Walters (1995 [DIRS 178191], Table 4.1), and the range in infiltration rates from the report by Maher et al. (2003 [DIRS 178540]) are shown plotted in Figure 7.2.1.2-4 because the Hanford site is located in eastern Washington.

Table 7.2.1.2-10. Estimated Recharge Rates at the Hanford Site for Combinations of Soil Type and Vegetation/Land Use

Vegetation/Land Use		Recharge Rates (mm/yr)														
		Soil Types[a]														
Index	Description	Ri	Rp	He	Kf	Ba	E1	Ls	Eb	Ki	Wa	Sc	P	Qu	Rv	D
1	Shrub-steppe on slopes	3.4	8.6	2.6	2.6	2.6	2.6	3.4	2.6	3.4	3.4	3.4	3.4	3.4	8.6	8.6
2	Shrub-steppe on plain/uplands	3.4	8.6	2.6	2.6	2.6	2.6	3.4	2.6	3.4	3.4	3.4	3.4	3.4	8.6	8.6
3	Recovering shrub-steppe on plain/uplands	3.4	11.3	2.6	2.6	2.6	2.6	3.4	2.6	3.4	3.4	3.4	3.4	3.4	11.3	11.3
4	Bunchgrass on slopes	3.4	11.3	2.6	2.6	2.6	2.6	3.4	2.6	3.4	3.4	3.4	3.4	3.4	11.3	11.3
5	Hopsage/greasewood	3.4	8.6	2.6	2.6	2.6	2.6	3.4	2.6	3.4	3.4	3.4	3.4	3.4	8.6	8.6
6	Cheatgrass	4.8	25.4	3.4	3.4	2.6	4.9	4.8	4.9	4.8	4.8	4.8	4.8	4.8	25.4	25.4
7	Abandoned fields	4.8	25.4	3.4	3.4	2.6	4.9	4.8	4.9	4.8	4.8	4.8	4.8	4.8	25.4	25.4
10	Sand Dunes	55.4	55.4	55.4	55.4	55.4	55.4	55.4	55.4	55.4	55.4	55.4	55.4	55.4	55.4	55.4
11	Disturbed/Facilities	6.8	55.4	6.4	6.4	4.4	17.3	6.8	17.3	6.8	6.8	6.8	6.8	6.8	55.4	55.4
13	Basalt outcrops	86.7	86.7	86.7	86.7	86.7	86.7	127.1	86.7	86.7	86.7	86.7	86.7	86.7	86.7	86.7

Source: Table 4.1 in Fayer and Walters 1995 [DIRS 178191].

[a] Ri=Ritzville silt loam, Rp=Rupert sand, He=Hezel sand, Kf=Koehler sand, Ba=Burbank loamy sand, El=Ephrata sandy loam, Ls=Lickskillet silt loam, Eb=Ephrata stony loam, Ki=Kiona silt loam, Wa=Warden silt loam, Sc=Scootney stoney silt loam, P=Pasco silt loam, Qu=Esquatzel silt loam, Rv=Riverwash, D=Dune sand.

7.2.2 Corroboration of MASSIF Infiltration Model Using Alternative Model Approach

This section provides additional corroboration of the MASSIF infiltration model estimates. As discussed previously, there are no site-specific measurements of net infiltration that can be used for model validation. In this section, the model corroboration approach described in Step 6.2.1 of SCI-PRO-006 was used. The approach consists of corroborating model results with other model results obtained from the implementation of mathematical models. The alternative model considered is a one-dimensional unsaturated flow model based on Richards' equation. The computer code HYDRUS-1D (Simunek et al. 2005 [DIRS 178140]) was used to perform the simulations. Because HYDRUS-1D is unqualified software its use is limited (by SCI-PRO-006) to model corroboration and cannot be used to directly support model validation. The summary of this model corroboration activity is provided below. The details concerning modeling setup and supporting calculations are in Appendix K.

Four model scenarios were implemented with MASSIF and HYDRUS-1D in this coorboration analysis (see Figure 7.2.2-1). The four model scenarios represent one-dimensional homogeneous soil columns that are identical except for the depth of soil and roots in each column. The difference in the depths of the soil columns are as follows: Model 1 has a soil depth of 50 cm, Model 2 has a soil depth of 100 cm, Model 3 has a soil depth of 150 cm, and Model 4 has a soil depth of 200 cm. The plant rooting depth was assumed to be equal to the soil depth in each model scenario. The simulations were performed for one water year (365 days). These conceptual models were incorporated with MASSIF and HYDRUS-1D.

It was anticipated that significant infiltration would be generated in the case of Model 1 (thin soils) and negligible or zero infiltration would be generated in the case of the Model 4 (thick soils). This is consistent with the YMP site conceptual model according to which most infiltration occurs in the places where soils are thin or absent (bedrock outcrops). The corroboration can be considered successful if the cumulative infiltration estimates obtained with MASSIF and HYDRUS-1D are similar.

The same climate data were used as an atmospheric boundary condition in both MASSIF and HYDRUS-1D. The minimum and maximum daily temperatures, precipitation, and wind speed (wind speed is not used in HYDRUS-1D) for one water year were taken from *Weather Summary v2.1 for nominal of PD parameters.xls* located in *Present Day Precipitation* directory supplied with the MASSIF Package (Output DTN: SN0701T0502206.037). The climate data are for set 4 (representative year 952) with the probability of occurrence equal to 0.02. This set was selected because it has high total annual precipitation (471 mm) and consequently, may result in significant infiltration. This annual precipitation has 2% probability under the Present-Day climate at the YMP site.

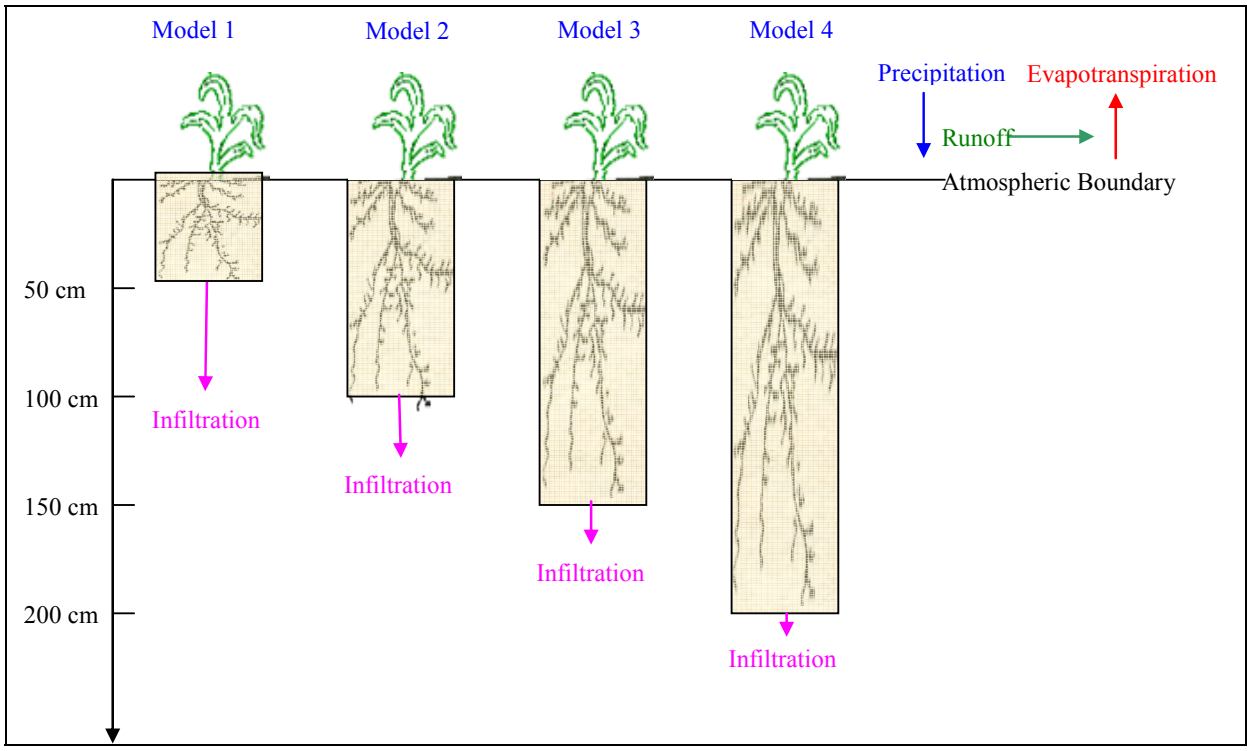

Figure 7.2.2-1. Conceptual Model Used in the Alternative Model Corroboration Analysis

Another input required at the atmospheric boundary is the limiting ET. Slightly different approaches are used in MASSIF and HYDRUS-1D to estimate the limiting ET. MASSIF uses the reference ET concept (Sections 6.3.3 and 6.4.4). Reference ET is calculated internally using the climate data. The default MASSIF parameters for the Present-Day climate (such as first and last day of winter) were used in calculating reference ET. HYDRUS-1D uses the concept of the potential ET. The potential ET is calculated externally using Hargreaves formula (Jensen et al. 1997 [DIRS 177103]). The details are presented in Appendix K. The potential evaporation and potential transpiration have to be specified separately to run HYDRUS-1D. The potential transpiration was calculated as the product of the potential ET and vegetation cover. The vegetation cover was assigned a value of 0.25 for both models. This is a reasonable assumption for the vegetation cover at the site (see Appendix D).

The atmospheric boundary conditions used in both codes are shown in Figure 7.2.2-2. As can be seen from this figure, the reference ET tends to be a little higher than the potential ET. This might be due to the fact that the reference ET accounts for the daily wind speed and the mean annual wind speed is higher than 2 m/s, and a value of 2 m/s characterizes the standard condition when the wind correction is not needed.

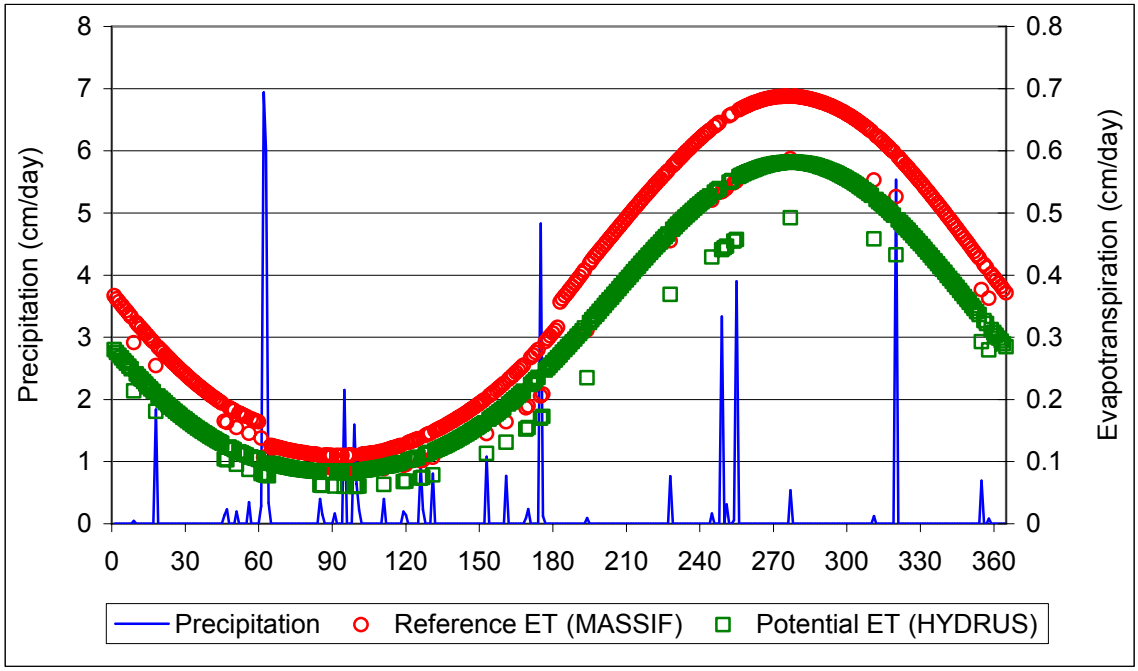

Source: Output DTN: SN0701T0502206.037; Validation Output DTN: SN0609T0502206.022 (HYDRUS 1D data).

Figure 7.2.2-2. Atmospheric Boundary Conditions Used in MASSIF and HYDRUS-1D

The lower boundary condition (the bottom of the soil profile) in MASSIF is incorporated through the bedrock layer. When the soil water holding capacity is exceeded, the bedrock drains the excess water at the rate equal to the bedrock saturated hydraulic conductivity. The lower boundary in HYDRUS-1D was defined as the seepage boundary. The seepage boundary condition assumes that a zero-flux boundary condition applies as long as the local pressure head at the bottom of the soil profile is negative. However, a zero pressure head will be used as soon as the bottom of the profile becomes saturated. This is conceptually close to, but not equivalent to the boundary condition in MASSIF. Note that this boundary condition does not require the presence of the lower soil or bedrock layer. Thus, the bedrock properties are not used in HYDRUS-1D modeling.

Different concepts are used in MASSIF and in HYDRUS-1D to calculate actual transpiration. MASSIF uses the K_{cb} function concept (Sections 6.3.3 and 6.3.4), and HYDRUS-1D uses the water stress function concept. The water stress function plays a role similar to K_{cb} function - it decreases the potential transpiration. The major difference is that water stress function reduces potential transpiration based on the pressure head (saturation) in the soil profile, and the K_{cb} function reduces potential transpiration based on the season of the year. Although the saturation is low during the dry season and high during the wet season, there is no direct translation from one function to another one.

The K_{cb} function is incorporated in MASSIF using two coefficients. The first coefficient (C_{kcb1}) represents the intercept and the second one (C_{kcb2}) represents the slope of the K_{cb} - *NDVI'* linear regression line (see Section 6.5.3). Both, C_{kcb1} and C_{kcb2} were set equal to MASSIF defaults for the Present-Day climate (-0.05 and 9.7, respectively).

The other transpiration and evaporation parameters in MASSIF were set equal to the defaults for the Present-Day climate as follow:

- Evaporation depth Z_e = 0.15 m
- Diffusive evaporation parameter K_{c_min} = 0
- Readily evaporable water parameter rew_1 = 6 mm
- Depletion factor parameter p = 0.65
- Plant height h_{plant} = 0.4 m.

There are no equivalents to these parameters in HYDRUS-1D. The actual ET in HYDRUS-1D is calculated based on the pressure and moisture within the soil profile.

The initial moisture conditions within the soil profile were set equal to 0.08 m^3/m^3 in both MASSIF and HYDRUS-1D.

The soil properties used in MASSIF are soil porosity, saturated hydraulic conductivity, field capacity, and wilting point. The additional parameter required is the bedrock saturated hydraulic conductivity. The most common soil grouping within the YMP site is soil group 5/7/9 with the saturated hydraulic conductivity of 6.82E-7 m/s. This group was selected for the analysis. The most common bedrock type selected for this analysis is bedrock type 405 with the saturated hydraulic conductivity of 1.1E-6 m/s. Minimum and maximum bedrock conductivities of 7.37E-7 m/s and 3.34E-6 m/s were used to see if the MASSIF estimates of infiltration would be affected by the type of the bedrock underlying the soil layer. Note that this range of conductivities for rock type 405 is different from the range of values reported in *Data Analysis for Infiltration Modeling: BedrockSaturated Hydraulic Conductivity Calculation* (BSC 2006 [DIRS 176355], Table 6-11) and used in the MASSIF net infiltration calculations.

The field capacity in MASSIF is considered to lie between the water contents at –1/3 bars and–1/10 bars (Section 6.5.2.3). The wilting point is defined as the water content at –60 bars. The water contents at –1/3 bars, –1/10 bars, and –60 bars were calculated using porosity, residual water content, and van Genuchten parameters *alpha* and *n* selected for HYDRUS-1D runs as described below. The details of these calculations are provided in Appendix K, but it should be noted that the resulting soil properties are not the same as defined for soil group 5/7/9 (Section 6.5.2.3) because the purpose of assigning parameter is to compare model results run with equivalent parameter inputs not to match Yucca Mountain soil data exactly. The resulting parameter values used in MASSIF are 0.173 m^3/m^3 (water content at –1/3 bars), 0.184 m^3/m^3 (water content at –1/10 bars), and 0.083 m^3/m^3 (water content at –60 bars). These parameters are close to the nominal properties of this soil group.

The soil parameters used in HYDRUS-1D are the parameters needed to define the moisture retention function and hydraulic conductivity–moisture relationship. The van Genuchten model in HYDRUS-1D was used to define these relationships. The input parameters are: residual water content, porosity, saturated hydraulic conductivity, and van Genuchten parameters *alpha* and *n*. The saturated hydraulic conductivity was set equal to the corresponding value in MASSIF. The van Genuchten parameter *alpha* and *n* were set equal to 0.002 cm^{-1} and 1.21. The residual water content and porosity were set equal to 0.022 and 0.19 m^3/m^3. Note that porosity is not used in MASSIF unless a significant runoff is generated (which should not be the case for the conceptual

models in consideration). As described above, these parameters result in the soil properties close to the nominal ones.

Four HYDRUS-1D models were developed using the initial and boundary conditions and modeling parameters described above. The inputs for these models are in Validation Output DTN: SN0609T0502206.021. The results of calculations are in Validation Output DTN: SN0609T0502206.022.

The MASSIF simulations were performed using an interface (*Alternative_Model.xmcd*) to MASSIF that was specifically designed for this purpose. This interface is provided as part of the MASSIF package (Output DTN: SN0701T0502206.037). The interface defines the MASSIF parameters described above, runs MASSIF calculations, and stores the results of the calculations. The interface calculates the soil water storage within the soil column, the daily cumulative infiltration, the total annual runoff, infiltration, and actual ET, and the change in storage. The interface reads the HYDRUS-1D results consisting of daily soil water storage and cumulative infiltration values. The interface displays the daily water storage and cumulative infiltration values calculated by MASSIF and HYDRUS-1D and calculates the mean root squared error between the MASSIF and HYDRUS-1D storage values to provide some basis for the comparison. The best match between the HYDRUS-1D and MASSIF results was obtained with the field capacity set equal to the water content at –1/10 bars (0.184 m^3/m^3).

The comparison between the water storage and cumulative infiltration calculated by MASSIF and HYDRUS-1D for the four models is presented in Figures 7.2.2-3 a through d).

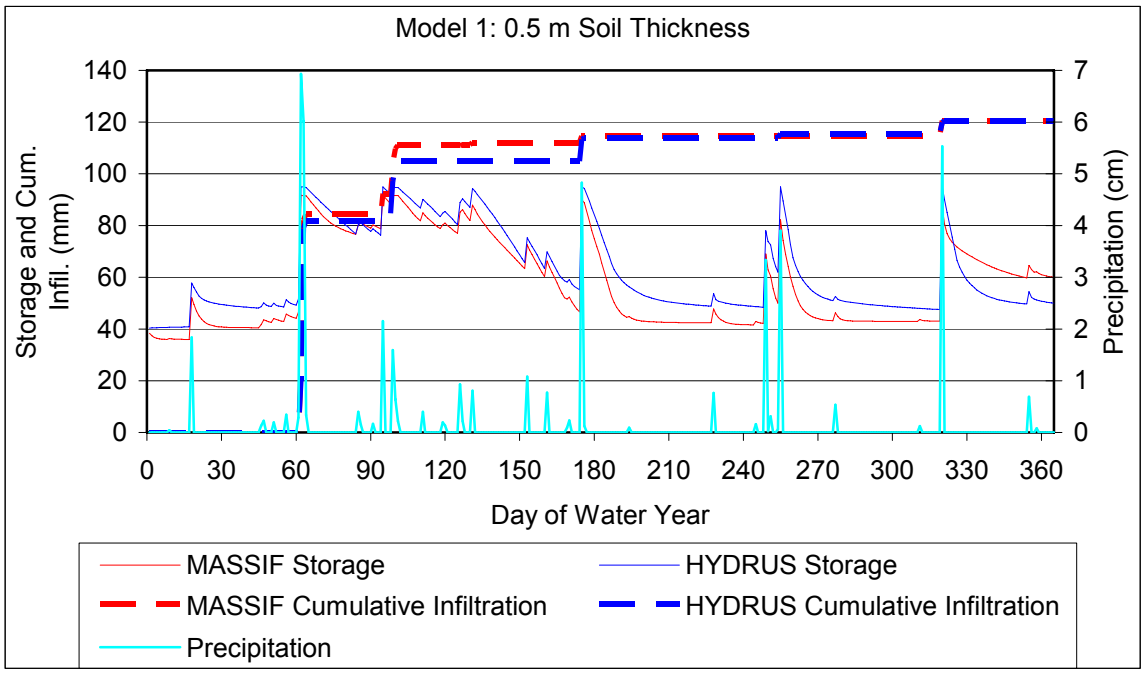

Source: Validation Output DTN: SN0609T0502206.022, *Alternative_Model_Outputs\Alternative_Model_Output.xls*.

Figure 7.2.2-3a. Soil Water Storage and Cumulative Infiltration for Model 1

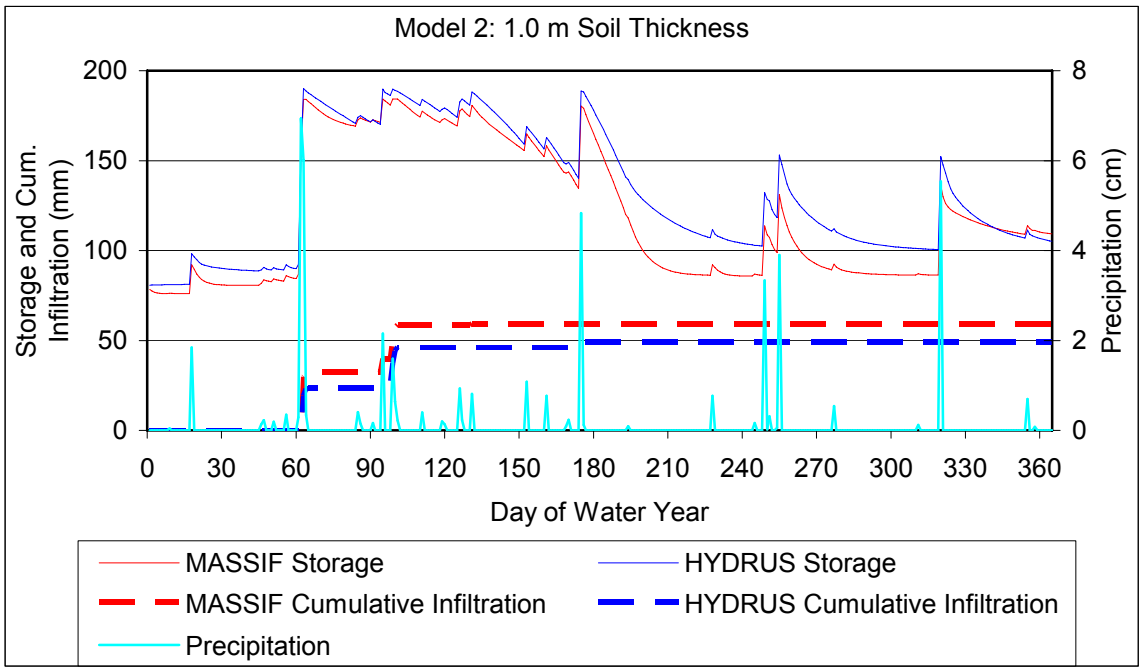

Source: Validation Output DTN: SN0609T0502206.022, *Alternative_Model_Outputs\Alternative_Model_Output.xls.*

Figure 7.2.2-3b. Soil Water Storage and Cumulative Infiltration for Model 2

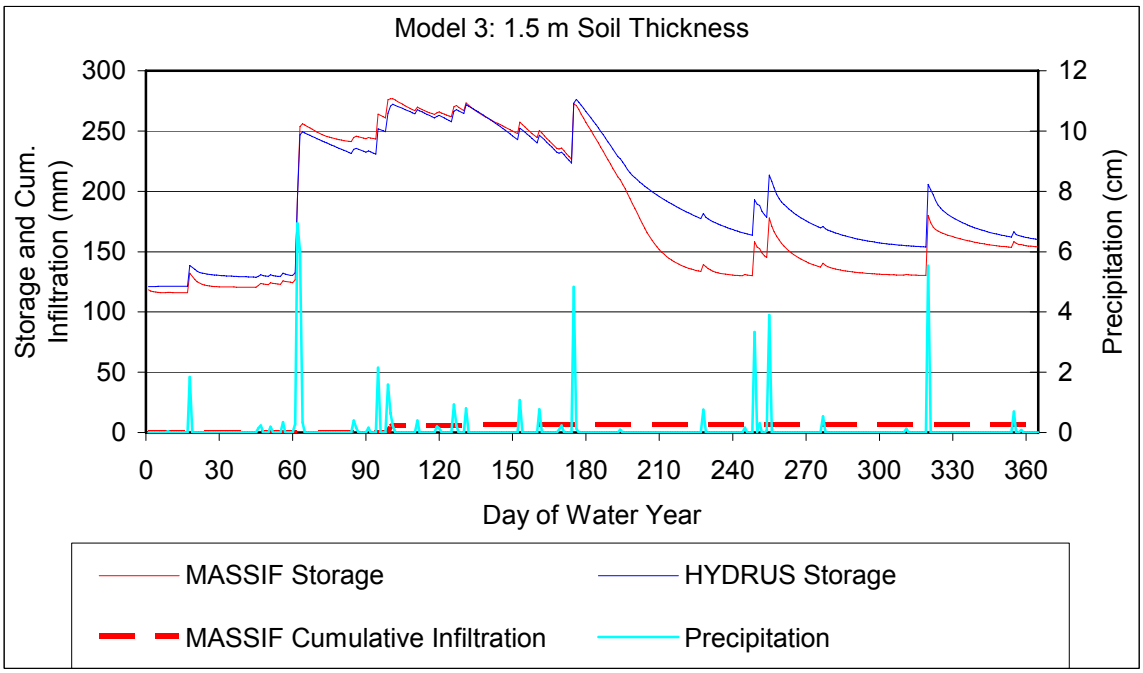

Source: Validation Output DTN: SN0609T0502206.022, *Alternative_Model_Outputs\Alternative_Model_Output.xls.*

Figure 7.2.2-3c. Soil Water Storage and Cumulative Infiltration for Model 3

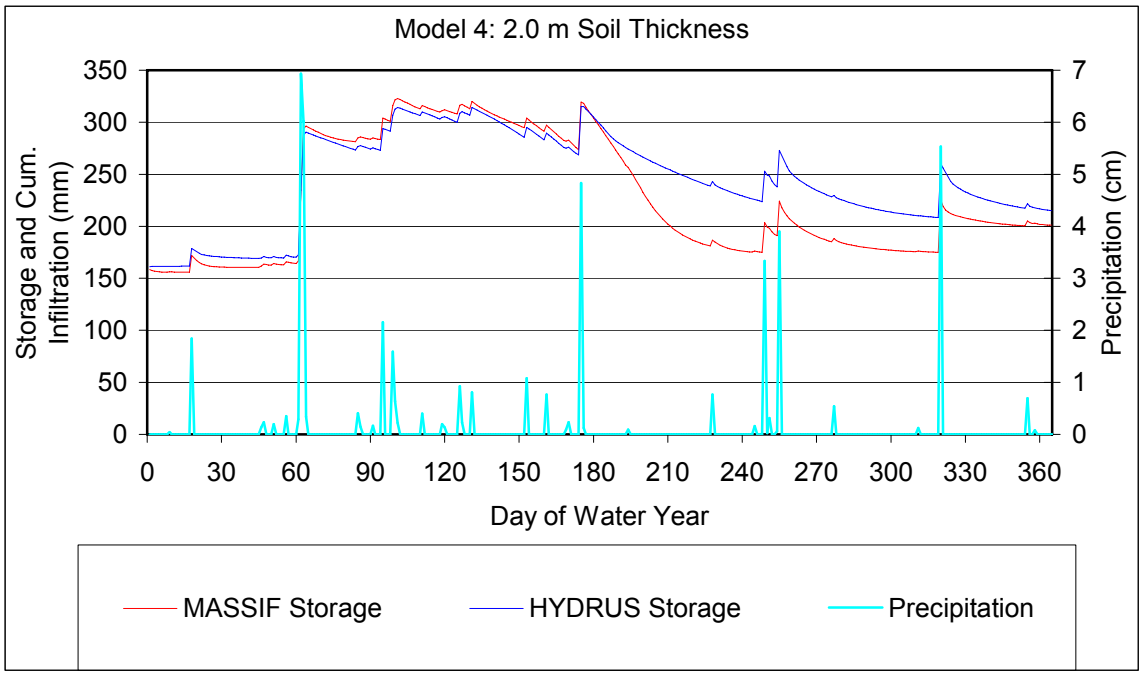

Source: Validation Output DTN: SN0609T0502206.022, *Alternative_Model_Outputs\Alternative_Model_Output.xls*.

Figure 7.2.2-3d. Soil Water Storage and Cumulative Infiltration for Model 4

The comparison between the annual values of the water balance components is presented in Figures 7.2.2-4 a through d. The summary of these results is in Table 7.2.2-1.

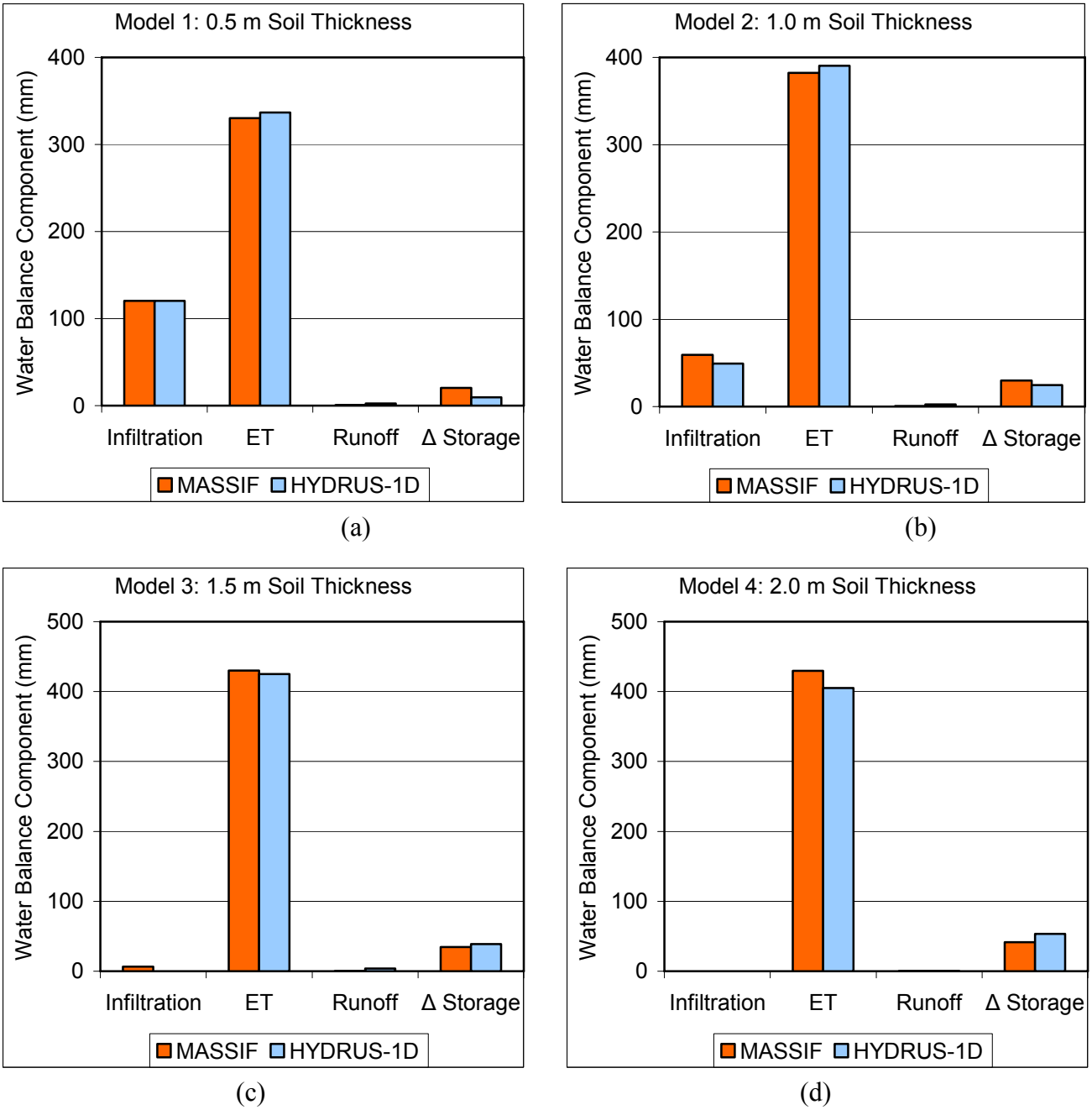

Source: Validation Output DTN: SN0609T0502206.022, *Alternative_Model_Outputs\Alternative_Model_Output.xls.*

Figure 7.2.2-4. Annual Water Balance Components for Alternative Model Comparison

Table 7.2.2-1. Summary of the Water Balance Results

Model	Code	Annual Water Balance Constituents				Mean Root Squared Error	
		Infiltration	Actual ET	Runoff	Change in Storage		
		mm	mm	mm	mm	mm	% Precipitation
Model 1	MASSIF	120.4	326.7	0.70	25.3	8.9	1.9
	HYDRUS-1D	120.5	336.8	2.5	9.6		
Model 2	MASSIF	63.9	377.8	0.70	30.8	17.1	3.6
	HYDRUS-1D	49.3	390.6	2.5	24.5		
Model 3	MASSIF	13.5	427.1	0.70	31.9	26.1	5.5
	HYDRUS-1D	0	425.1	3.7	39		
Model 4	MASSIF	0	437.5	0.70	35.0	33.4	7.1
	HYDRUS-1D	0	404.9	0.45	53.5		

Source: Validation Output DTN: SN0609T0502206.022, "*Alternative_Model_Outputs\Alternative_Model_Output.xls*.

As anticipated, Model 1 produced the highest infiltration. MASSIF and HYDRUS-1D calculated high total annual infiltration (120.4 mm from MASSIF and 120.5 mm from HYDRUS-1D), which constitutes 25% of the annual precipitation. As seen from Figure 7.2.2-3a, even the timing of the infiltration events is the same. The first infiltration event occurs at the time of the highest precipitation event. The soil moisture increases significantly and the following smaller precipitation events result in another infiltration event since the soil holding capacity is close to the maximum. A few following infiltration events coincide with the high precipitation events. The mean root squared difference between the MASSIF and HYDRUS-1D daily storage values is 8.9 mm (or 1.9% of the annual precipitation). The actual ET and runoff are in a close agreement as well (see Table 7.2.2-1).

The total annual infiltration calculated in Model 2 is 64 mm (MASSIF) and 49 mm (HYDRUS-1D). The timing of the infiltration events is the same. There are only two infiltration events in this case. The first infiltration event occurs at the time of the highest precipitation event. The second infiltration event occurs after a series of the smaller precipitation events during the period of time when the soil moisture content is high. The other high precipitation events do not result in infiltration as was in the case of Model 1 because the thicker soil was able to store all the moisture received. The mean root squared difference between the MASSIF and HYDRUS-1D daily storage values is 17.1 mm (or 3.6% of the annual precipitation). The actual ET and runoff are in a close agreement (see Table 7.2.2-1).

In the case of Model 3, MASSIF predicted one small infiltration event (13.75 mm) during the period of high moisture content that follows the highest precipitation event. The infiltration calculated by HYDRUS-1D is zero. The infiltration predicted by MASSIF in this case is a very small part (2.9%) of the annual precipitation. The mean root squared difference between the MASSIF and HYDRUS-1D daily storage values is 26.1 mm (or 5.5% of the annual precipitation). The actual ET and runoff are in a close agreement (see Table 7.2.2-1).

As anticipated, no infiltration occurs in the case of Model 4. Both, MASSIF and HYDRUS-1D predict zero infiltration. The mean root squared difference between the MASSIF and HYDRUS-1D daily storage values is 33.4 mm (or 7.1% of the annual precipitation). The actual ET and runoff are in a close agreement (see Table 7.2.2-1).

The difference between MASSIF and HYDRUS-1D results is slightly larger in the case when field capacity is defined at the water content at –1/3 bars. However, the agreement between these results is still good.

All four models were re-run with MASSIF, first using minimum and second using maximum values for the bedrock hydraulic conductivities. The estimates of all the balance constituents were identical to the cases when the hydraulic conductivity of the bedrock type 405 was used. This means that considering the seepage boundary condition in HYDRUS-1D (that does not require bedrock modeling) is appropriate. It also means that the conclusions made are not bedrock-specific.

Conclusions:

- The simplified water balance approach used in MASSIF produces annual infiltration estimates that are very close to the estimates obtained with physics based model such as HYDRUS-1D.

- MASSIF is capable of reproducing the same timing of the infiltration events as HYDRUS-1D. This means that the important physical processes resulting in infiltration are adequately represented in MASSIF.

- The other water balance components such as annual actual ET and annual runoff are in a good agreement with the HYDRUS-1D estimates as well.

- The mean root squared difference between the daily storage value calculated by MASSIF and HYDRUS-1D was in the range from 9 to 33 mm, which corresponds to 2% to 7% of the annual precipitation.

- Consequently, it can be concluded that corroboration of the MASSIF net infiltration model is successful. The corroboration criterion (close estimates of the cumulative infiltration calculated by MASSIF and HYDRUS-1D) was met.

7.2.3 Corroboration of Model Results with Infiltration and Percolation Estimates from 1997 Expert Elicitation Panel

In May 1997, an expert elicitation panel was convened in order to identify and assess the uncertainties associated with certain key components of the unsaturated zone flow system at Yucca Mountain. This assessment reviewed the data inputs, modeling approaches, and results of the unsaturated zone flow model and the infiltration model. In addition to data input and modeling issues, the assessment focused on percolation flux at the repository horizon. The seven panel members, who were experts from within and outside the Yucca Mountain project, represented a range of experience and expertise. The assessments and probability distributions

from this panel provide a reasonable aggregate representation of the knowledge and uncertainties about key issues regarding the unsaturated zone and the Yucca Mountain Site (CRWMS M&O 1997 [DIRS 100335], p. 1-1).

In order to provide a measure of the uncertainties associated with the estimates of net infiltration, the experts were asked to provide their judgments regarding the amount of net infiltration occurring at Yucca Mountain. Two of the 7 experts declined to give an assessment of net infiltration based on surface and near-surface data, citing inherent difficulties in attempting to model the area's highly complex and spatially variable surface and near-surface hydrologic system, as well as the paucity of data necessary to provide reliable estimates of episodic infiltration events (CRWMS M&O 1997 [DIRS 100335], p. 3-9).

For the five experts who provided an assessment of net infiltration, average infiltration rates in Table 3-1 ranged from 3.9 to 12.7 mm/yr, with an aggregate average of (7.4, 12.7, 8.4, 11.3, 3.9 mm/yr) = 8.7 mm/yr. Note that this range conflicts with the text of the report that cites a range of 3.9 to 11.3 mm/yr (CRWMS M&O 1997 [DIRS 100335], p. 3-10). All seven experts also provided a range for percolation flux at the repository horizon and noted that in most cases, net infiltration is equivalent to percolation flux at the repository horizon, although there may be perceived differences in their spatial distribution, and some experts used different methods to estimate the two quantities (CRWMS M&O 1997 [DIRS 100335], p. 3-5).

The experts predicted ranges of percolation fluxes at the repository horizon, and distribution types of those ranges. The combined average fluxes for all 7 experts yielded a mean value of 10.3 mm/yr, a median value of 7.2 mm/yr, and a 5th to 95th percentile range of 1.0 to 30 mm/yr (CRWMS M&O 1997 [DIRS 100335], Table 3-2). The cumulative distribution functions for the average of the experts' estimates, as well as the lower bound and upper bound CDFs are plotted on Figure 7.2.3-1. The CDF value corresponding to the experts' mean values were interpolated. MASSIF results for Present-Day climate for 40 LHS realizations are also plotted on this Figure. Note that with the exception of 3 of 40 data points, the MASSIF results fall between the experts' upper bound CDF and the experts' aggregate CDF. This comparison of results provides additional corroboration of the of the MASSIF results for the Present-Day climate.

Although the 1997 UZ expert elicitation panel convened nearly 10 years ago, their conclusions remain valid relative to the current infiltration model since it uses essentially the same conceptual model to that being developed in 1997. Therefore, it is relevant to highlight some of the panel's other conclusions with regard to infiltration and percolation flux, as follows.

Temporal Issues:

- The experts' general conclusion was that net infiltration is an episodic process linked to the occurrence of major storm events or sequences. The panel judged the average frequency of these episodic storm events to range from annual to approximately once every 20 years. Between these episodic infiltration events, there is little to no net infiltration.

- This conclusion is consistent with MASSIF predictions of net infiltration for Present-Day climate. Section 6.5.7.4 discusses the MASSIF predictions of net infiltration on a year-by-year basis and shows the small contribution of years with low to average precipitation to long-term mean net infiltration.

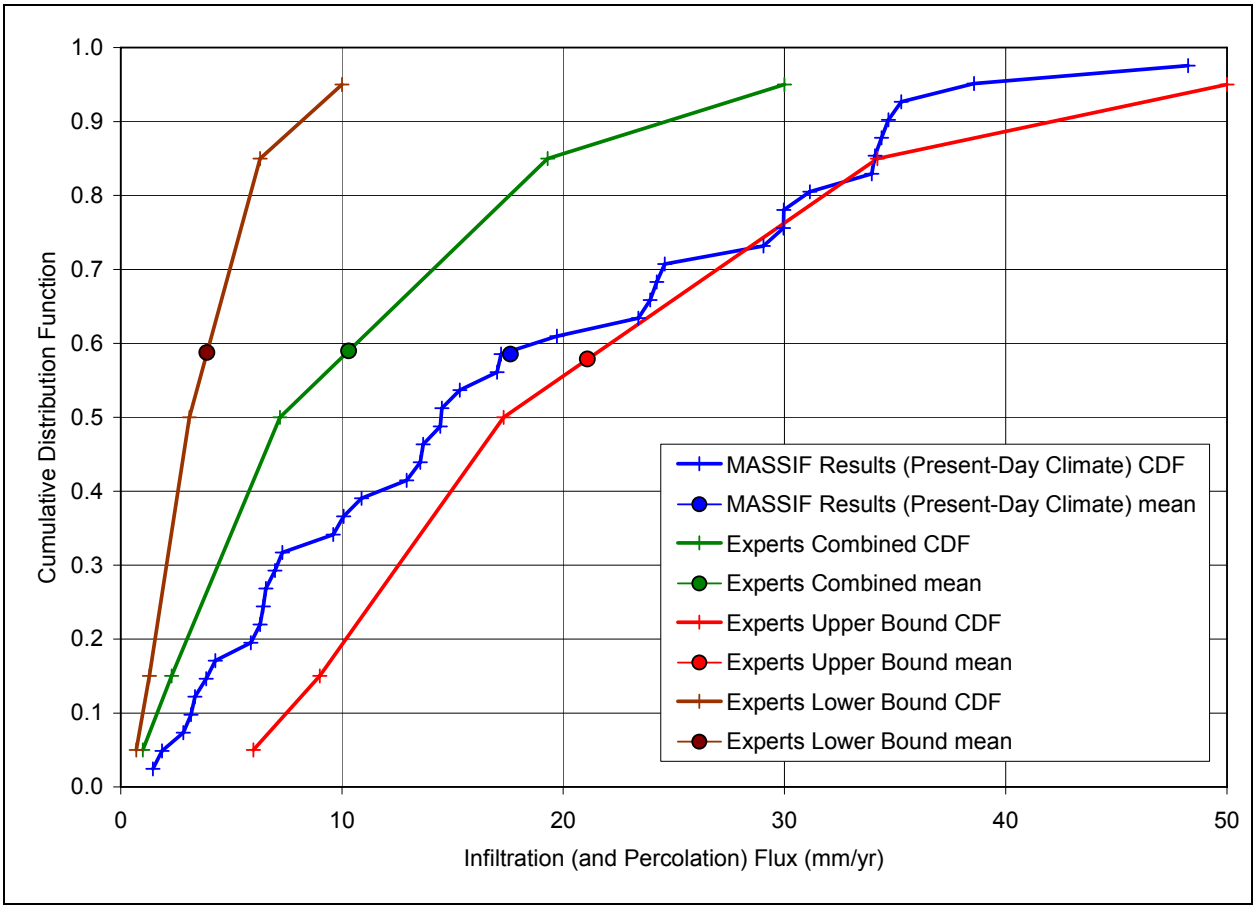

Source: Output DTN: SN0701T0502206.034 (MASSIF results for Present-Day climate); CRWMS M&O 1997 [DIRS 100335], Table 3-2 (Expert Elicitation Panel values).

NOTE: CDF values corresponding to mean values are interpolated.

Figure 7.2.3-1. MASSIF Net Infiltration Results for Present-Day Climate for the Repository Footprint Compared with Percolation Fluxes at the Repository Horizon from the 1997 Expert Elicitation Panel

Spatial Issues:

- All agreed that that the areas underlain by thick alluvial deposits likely experience the least infiltration because of the high storage capacity of the alluvium and the consequent opportunity for losses due to ET.

- This is consistent with MASSIF results.

- Some of the experts concluded that additional consideration of the potential for focused infiltration in washes and more explicit inclusion of surface runoff may lead to net infiltration estimates greater than those presented by USGS.

    - The conceptual model for surface water runoff in MASSIF is similar to the 2000 net infiltration model developed by the USGS, which was changed from the 1996 net infiltration model in response to this comment.

Modeling Issues:

- Some argued that the 1-D flow modeling is incapable of accounting for lateral flow at the soil–bedrock contact. However, another expert noted that the grid blocks used are too large to provide the spatial detail needed to take advantage of the additional information provided by a 2- or 3-D model.

    - Lateral flow is considered to be insignificant at the grid cell scale applied in MASSIF. Refer to the assumption on Interflow in Section 5.1.

- One expert placed low confidence in the "Bucket" model (field capacity model) used by the USGS (and implemented in MASSIF), concluding that it is inadequate for the level of detail considered in the analysis.

    - Given the lack of site-specific soil depth and soil hydraulic property data, the field capacity model is an appropriate model choice, rather than using a soil physics-based model that requires better soil depth and hydraulic property data.

7.3 VALIDATION AND CORROBORATION SUMMARY

Section 7.1 presented confidence building activities during model development. These activities included descriptions of MASSIF's abstraction of precipitation modeling using Fourier series parameters. MASSIF's ability to simulate ET and storage was demonstrated by comparing MASSIF output with lysimeter datasets from Area 5 at the Nevada Test Site, and Reynolds Creek, ID. These comparisons demonstrate that MASSIF can be applied to other sites to accurately predict water balance parameters such as ET. Section 7.1 also presented comparison of MASSIF predictions of streamflow with measured streamflow data. And Section 7.1 described the extended parameter sensitivity study (large LHS).

Section 7.2 presented post model development validation activities. These activities included comparison of MASSIF predictions of infiltration with seepage estimates observed in the South ramp of the ESF in the winter of 2005. MASSIF predictions of infiltration were qualitatively compared to borehole-scale estimates of infiltration, and this comparison was used to illustrate that MASSIF predictions of infiltration for a given grid cell cannot be accurately compared to borehole-scale estimates of infiltration due to the lack of site-specific Yucca Mountain soils data including soil depth data, and soil hydraulic property data.

Section 7.2 also compares MASSIF predictions of infiltration for Present-Day, Monsoon, and Glacial Transition climates for 40 realizations for each climate, with infiltration estimates from published models and data for the Yucca Mountain area, the southwestern United States, and the

western United States. The infiltration estimates from some southwestern sites is analogous to infiltration that could be expected during the monsoon climate state, and infiltration estimates from the Columbia River plateau sites is analogous to infiltration that could be expected during the glacial-transition climate state. These comparisons indicate that MASSIF predictions of infiltration for Present-Day, Monsoon, and Glacial Transition climates compare well to watershed-scale models and data for Nevada, and the southwestern and western United States.

Section 7.2 also describes an alternative model approach corroboration activity in which MASSIF results are compared to HYDRUS 1-D results for four different soil depths and using the same model inputs. These comparisons indicate that MASSIF and HYDRUS-1D give similar results. Finally, Section 7.2 summarizes some of the conclusions and infiltration and percolations estimates from the 1997 Expert Elicitation Panel on the UZ flow model. The MASSIF predictions of infiltration for Present-Day climate were almost entirely within the range between the mean and upper bounds of percolation flux predicted by the 1997 expert panel (who assumed that percolation flux was approximately equivalent to infiltration).

The results of calculations of net infiltration have been validated by applying acceptance criteria based on an evaluation of the model's relative importance to the potential performance of the repository system. Validation requirements defined in Technical Work Plan for: Infiltration Model Assessment, Revision, and Analyses of Downstream Impacts (BSC 2006 [DIRS 177492], Section 2.2.1) have been fulfilled (with the exceptions described in Section 1.4), including corroboration of model results with experimental data, and corroboration with alternative models. Activities requirements for confidence building during model development have also been satisfied. The model development activities and post-development validation activities described establish the scientific bases for the infiltration model. Based on this, the infiltration model used in this report is considered to be sufficiently accurate and adequate for the intended purpose.

Table 7.3-1 lists the Validation Output DTNs generated from model validation activities described in Section 7. These DTNs are not considered qualified product outputs.

Table 7.3-1. Validation Output Data Tracking Numbers

Title	Product Output DTN
Comparison of the calculated precipitation record with site data	SN0701T0502206.045
Analysis of soil water storage in Nevada Test Site (NTS) and Reynolds Creek Experimental Watershed (RCEW) lysimeters	SN0607T0502206.016
Recharge estimates used to validate the MASSIF model of net infiltration at Yucca Mountain	SN0704T0502206.047
Alternative infiltration model inputs	SN0609T0502206.021
Alternative infiltration modeling results	SN0609T0502206.022

INTENTIONALLY LEFT BLANK

8. CONCLUSIONS

8.1 SUMMARY AND FINDINGS

The purpose of the model documented in this report is to provide a spatial representation, including uncertainty, of the predicted average annual net infiltration at the Yucca Mountain site for three future climates predicted to occur at the site over the next 10,000 years. The resulting maps of average annual net infiltration provide input directly to the updated versions of the following model reports:

- *UZ Flow Models and Submodels* (BSC 2004 [DIRS 169861])
- *Calibrated Properties Model* (BSC 2004 [DIRS 169857])

The net infiltration model, MASSIF, presented in this report is a mass balance calculation of the surface and near surface water budget. Water enters the system as precipitation, which is simulated from a stochastic model of daily precipitation based on historical weather records from proxy climate sites identified in *Future Climate Analysis* (BSC 2004 [DIRS 170002]. The MASSIF infiltration model simulates processes occurring at the soil layer, including: flow through and storage of water in the soil layer, return of water vapor to the atmosphere by evaporation and plant transpiration (evapotranspiration), flow along the surface (runoff/run-on), and infiltration into the bedrock below the soil. Processes not included in the model are listed in Section 5.1.

The model documented in this report calculates net infiltration at the soil–bedrock interface without consideration of the properties of the rock at deeper locations. Instead of net infiltration, some authors call this parameter "deep drainage" or "potential recharge." *UZ Flow Models and Submodels* (BSC 2004 [DIRS 169861]) describes the method for calculating replenishment of the aquifer from the surface (i.e., recharge), taking into consideration the potential recharge and the make-up and orientation of the geologic strata, as well as other considerations.

The model documented in this report is valid only for the Yucca Mountain site for a 10,000-year period and for the climates specified in *Future Climate Analysis* (BSC 2004 [DIRS 170002], Section 7.1). For each climate, the model produces maps of average annual infiltration as a function of location, with no time dependence, although an examination of the nonaveraged results indicates that net infiltration in this environment is highly episodic (See Section 6.5.7). *UZ Flow Models and Submodels* (BSC 2004 [DIRS 169861]) provides the justification for characterizing net infiltration with non-episodic, time-averaged values. These output maps indicate the range of uncertainty in average annual steady-state net infiltration.

Infiltration predictions are limited by the uncertainty in future weather. Although a substantial body of literature supports the use of stochastic precipitation models, there are no records to validate our approach of extrapolation to 1000 years. Each available precipitation record, whether from the Yucca Mountain site, from a nearby weather station, or from a site representative of a future climate, covers periods of time much less than 100 years.

This model report documents the development and validation of a model for net infiltration of precipitation at the Yucca Mountain site and completely replaces the previous revision

(BSC 2004 [DIRS 170007] of this model report and model of net infiltration (BSC 2004 [DIRS 170007]). While the underlying conceptual model remains similar to the previous model, this revision increases confidence in the results by improving the traceability, transparency, and reproducibility of both the model development and the selection of inputs for calculations.

The results of this modeling work are the generation of 40 maps of net infiltration for each of the three future climates considered for the next 10,000 years (Output DTNs: SN0701T0502206.034, SN0701T0502206.036, and SN0701T0502206.035). For a given climate each of these 40 maps provides an equally probable outcome of net infiltration over the modeling domain. The range of net infiltration values within the set of 40 maps provides a reasonable estimate of the uncertainty in magnitude of net infiltration. This uncertainty is estimated using the structured Monte Carlo technique of Latin Hypercube sampling (see Sections 6.5.5 and 6.5.6). This method propagates uncertainty in a collection of input parameters to uncertainty in model outputs (net infiltration).

There are a number of ways that the results of this study could be used. First, for a given climate, the set of 40 maps could be ranked by net infiltration over some specified domain (e.g., full domain, UZ model domain, repository footprint) and predefined percentiles could be selected. Such a selection was done for the results in Section 6.5.7, where the 10th, 30th, 50th, and 90th percentiles are identified. A weight or probability of occurrence could be defined from the resulting empirical distribution. Second, the empirical distribution could be tested against a theoretical distribution (e.g., lognormal) and the representative maps could be defined from this "fitted" distribution. This was done in Section 6.6, where the results of each climate are compared and tested against lognormal distributions. Third, the results of this study can be used to estimate the nature and character of net infiltration at the site, including the timing and frequency of infiltration events and the relative importance of low-probability high precipitation years. Finally, the results of the sensitivity study can be used to define performance confirmation goals and identify sensitive parameters that could be the focus of possible future field studies at the site; however, this is not deemed necessary at this time.

The MASSIF model is validated using two of the methods available in SCI-PRO-006: (1) discussion of documented decisions and activities that are implemented during the model development process that build confidence and verify that a reasonable, credible, and technical approach using scientific and engineering principles was taken, and (2) postdevelopment model validation employing one of several methods described in Paragraph 6.3.2) of SCI-PRO-006. The first method is implemented by comparing certain model components (such as evapotranspiration, runoff, and precipitation) to field observations. The second method is to compare the results of the net infiltration calculations to independent regional measurements and estimates of net infiltration and recharge. Previous studies have used observations of steam flow measured at the site to calibrate models of net infiltration (BSC 2004 [DIRS 170007]). This methodology was considered invalid and not used in the present work. The reason for this lies in the fact that parameters that significantly influence surface run-off (e.g., soil hydraulic conductivity) in the model are not the same parameters that significantly influence net infiltration (e.g., soil depth and water holding capacity). As an alternative to model calibration, the MASSIF model was run with nominal input parameter values and compared to field observations of stream flow (Section 7.1.3), point estimates of net infiltration (Section 7.2.1), field observations from analogue sites (Sections 7.1.2 and 7.2.1), and infiltration model results from an alternative modeling approach (Section 7.2.2). Comparisons made in this model validation indicate that the

MASSIF model performs well, especially considering the uncertainty present in the input parameters.

The results of the uncertainty analysis for net infiltration are summarized in Section 8.2.

8.1.1 Data Tracking Numbers for Data Generated in This Report

The MASSIF model calculations of net infiltration are provided in Output DTN: SN0701T0502206.037. The results from the net infiltration model produced by these calculations are provided in the following output DTNs:

- SN0701T0502206.034 – present day net infiltration results (40 realizations)
- SN0701T0502206.036 – monsoon net infiltration results (40 realizations)
- SN0701T0502206.035 – glacial transition net infiltration results (40 realizations).

The complete list of developed output data generated in this report is listed by DTN in Table 8-1. In addition to the calculation and results DTNs, Table 8-1 includes developed data that provide input to the MASSIF net infiltration model and output resulting from the analysis of sensitivity and uncertainty. The flow of data associated with the net infiltration model, including both input data (from Table 4-1) and output data (from Table 8-1), is illustrated in Figure 8-1.

Appendix L discusses preliminary model outputs that are not considered the final technical product output of this report, but will be qualified in a separate data qualification report.

Table 8-1. Output Data Sets Generated in the Development and Application of the Net Infiltration Model

Description	Title	Product Output DTN
Results from the net infiltration model	Monsoon Net Infiltration Results, Rev 1	SN0701T0502206.036
	Present-Day Net Infiltration Results, Rev 1	SN0701T0502206.034
	Glacial Transition Net Infiltration Results, Rev 1	SN0701T0502206.035
Model calculation output	MASSIF Calculation of Net Infiltration at Yucca Mountain, Rev 1	SN0701T0502206.037
Developed input to the net infiltration model	Daily Precipitation for Water Years 1998, 2001, and 2002 – Sites 2, 3 & 4	MO0602SPAPRECP.000
	Daily Weather Data for Water Years 1998, 2001, 2002, Yucca Mountain Meteorological Site 1	MO0602SPAWEATH.000
	Reference Evapotranspiration (ET) for Yucca Mountain	MO0603SPAREFET.000
	Daily Weather Data for Spokane Washington	MO0605SPADAYWA.000
	Basal Transpiration Coefficients (K_{cb}) for Yucca Mountain Vegetation Associations (1993, 1991, and 1990 Water Years)	MO0606SPABASAL.001
	Transpiration Coefficients (K_{cb}) for a Bromus Tectorum Monoculture	MO0606SPATRANS.000

Table 8-1. Output Data Sets Generated in the Development and Application of the Net Infiltration Model (Continued)

Description	Title	Product Output DTN
Developed input to the net infiltration model (continued)	Cover Data for Vegetation Associations at Yucca Mountain (1990,1991, and 1993)	MO0606SPAVEGAS.001
	Total Annual Precipitation for Water Years 1990, 1991 and 1993 from Yucca Mountain Meteorological Sites 2, 3 and 4	MO0607SEPTOTAL.003
	Linear Regression Analysis for the MASSIF K_{cb} Versus NDVI Correlation	MO0610SPALINEA.000
	Solar Radiation and Reference Evapotranspiration (ET_0) on Inclined Surfaces	SN0602T0502206.003
	Calculated Daily Diffuse and Direct Solar Radiation from 2000 through 2004 and Measured at Desert Rock, Nevada	SN0602T0502206.004
	Evaluation of Hargreaves Solar Radiation Coefficient, K_{RS}, for Yucca Mountain	SN0602T0502206.005
	Evaluation of Published Diffuse and Total Solar Radiation Correlations for Yucca Mountain	SN0603T0502206.006
	Geospatial Inputs for Net Infiltration Model of Yucca Mountain	SN0606T0502206.011
	Daily Normalized Difference Vegetation Index (NDVI) Estimation for Selected Slopes/Azimuths at Yucca Mountain	SN0606T0502206.012
	Calculated Weather Summary for Present Day and Future Climates	SN0606T0502206.014
	Assembly Data for Geospatial Inputs to MASSIF Model of Yucca Mountain	SN0608ASSEMBLY.001
	Calibration Watersheds at Yucca Mountain Based on Pour Point Stream Gages	SN0608CWATSHED.001
	Drainage Delineation at Yucca Mountain	SN0608DRAINDYM.001
	Analysis Data Supporting Estimations of Normalized Difference Vegetation Index (NDVI) at Yucca Mountain, 1997–2002	SN0608NDVIANAL.001
	Auxiliary Data Used in Calculations of Daily Normalized Difference Vegetation Index (NDVI) Estimation for Selected Slopes/Azimuths at Yucca Mountain and Geospatial Inputs for Net Infiltration Model of Yucca Mountain	SN0608NDVIAUXD.001
	Normalized Difference Vegetation Index (NDVI) Derived from Calibrated and Geocorrected LANDSAT TM Data at Yucca Mountain, 1997–2002	SN0608NDVILSTM.001
	Normalized Difference Vegetation Index (NDVI) Imagery Derived from Calibrated and Georectified Quickbird Imagery of Yucca Mountain, August 31, 2002	SN0608NDVIQBIM.001
	Normalized Difference Vegetation Index (NDVI) on North and South Slopes and Supporting Data at Yucca Mountain, 1997–2002	SN0608NSSLOPES.001
	Potential Vegetation Response (PVR) at Yucca Mountain, 1997–2002	SN0608PVRATYMT.001
	Spatial Data Layers at Yucca Mountain	SN0701SPALAYER.002
	Temperature Model Fitting Parameters for Present-Day and Future Climate Proxy Sites	SN0608T0502206.019

Table 8-1. Output Data Sets Generated in the Development and Application of the Net Infiltration Model (Continued)

Description	Title	Product Output DTN
Developed input to the net infiltration model (continued)	Distribution of Slope on North-South Facing Terrain Slopes at Yucca Mountain	SN0609AZSLPHST.001
	Unsaturated Zone (UZ) Boundary and Repository Footprint	SN0612FTPRNUZB.002
	Thematic Mapper Processing Overview	SN0609LSTMPROC.001
	Precipitation Parameters Calculated using Fourier Analyses for Modern Interglacial and Future Climates	SN0609T0502206.023
	Calculated Weather Summary for Monsoon Climate, Rev 1	SN0701T0502206.041
	Calculated Weather Summary for Present Day Climate, Rev 1	SN0701T0502206.040
	Calculated Weather Summary for Glacial Transition Climate, Rev 1	SN0701T0502206.042
	Average Daily Wind Speed at 2 m Height above the Ground	SN0610T0502206.030
	Precipitation Duration Functions for the Present-Day, Monsoon, and Glacial Transition Climates for Infiltration Modeling at Yucca Mountain, NV	SN0610T0502206.031
LHS Files	Latin Hypercube Sample (LHS) Input and Output Files for MASSIF Calculation of Net Infiltration at Yucca Mountain, Rev 1	SN0701T0502206.043
Calculations supporting sensitivity analysis	Sensitivity Analysis of Average Net Infiltration for Three Climates	SN0701T0502206.044
Estimation of uncertainty for shallow soil depth	Estimation of Uncertainty on Upscaled Uniform Value for Soil Depth Class 4	SN0612T0502206.039
MASSIF verification	Independent Verification of MASSIF Infiltration Model	MO0703MASSIFIM.001

INTENTIONALLY LEFT BLANK

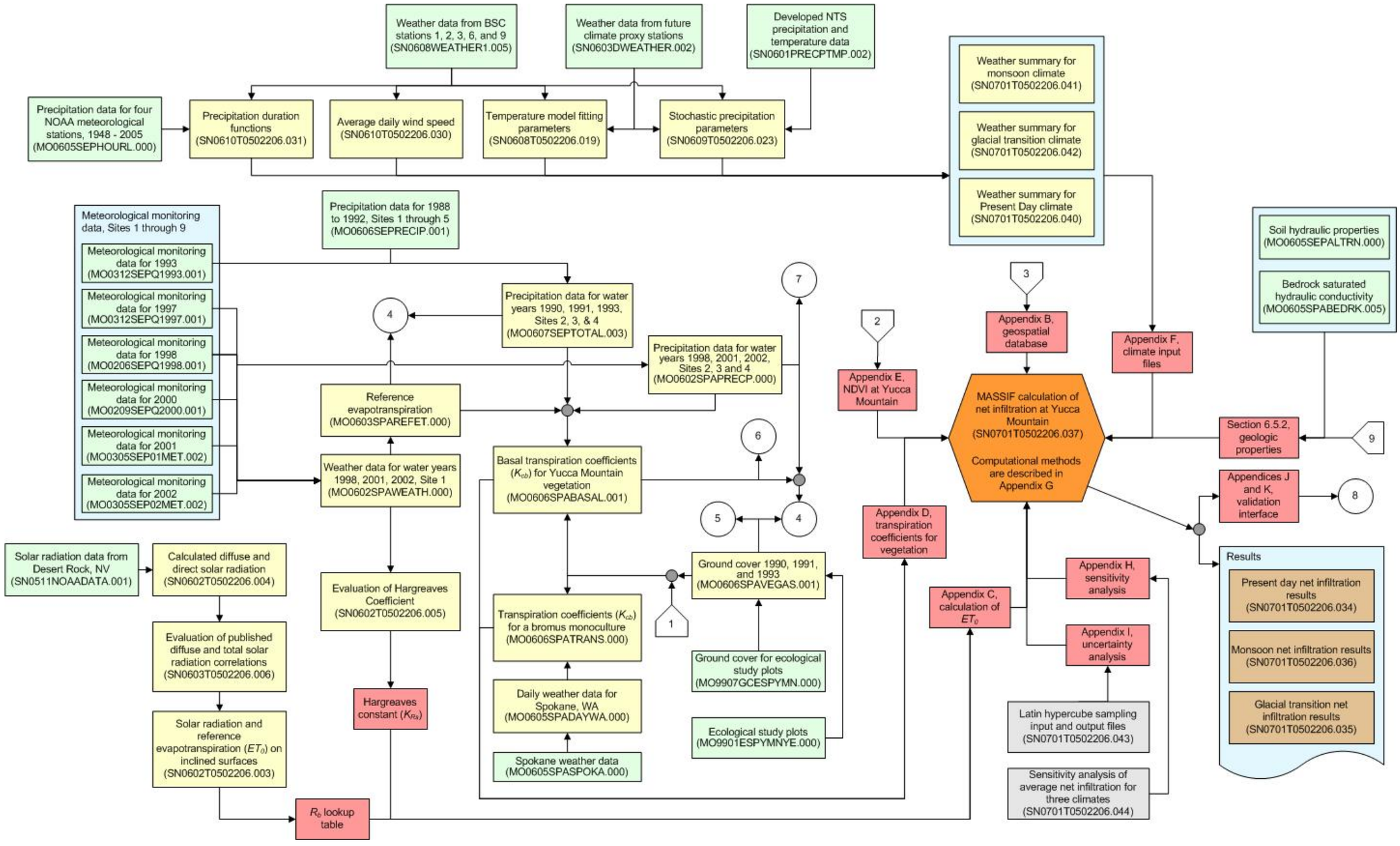

Figure 8-1. Data Flow for the MASSIF Net Infiltration Mode

INTENTIONALLY LEFT BLANK

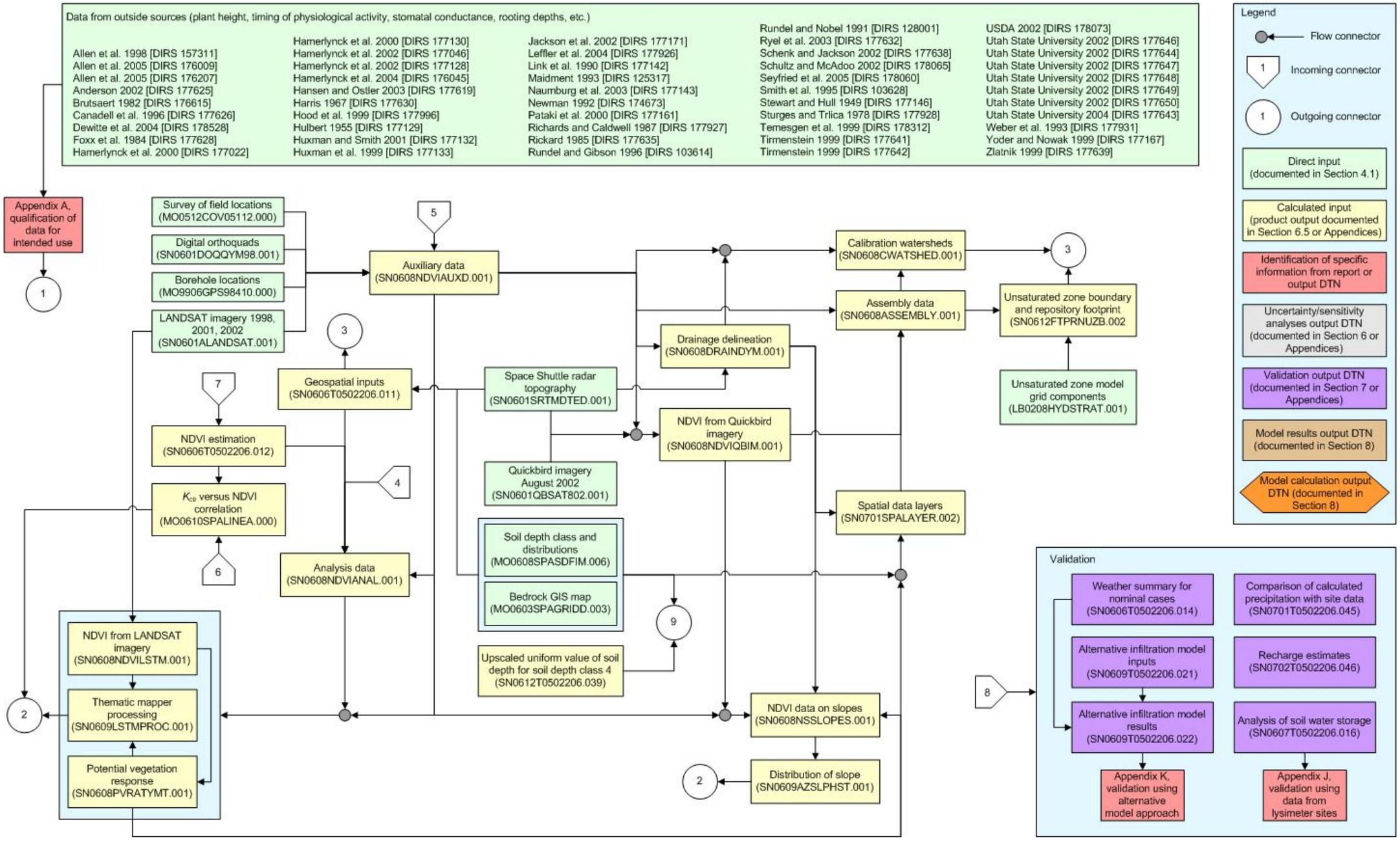

Figure 8-1. Data Flow for the MASSIF Net Infiltration Model (Continued)

INTENTIONALLY LEFT BLANK

8.2 MODEL UNCERTAINTY AND LIMITATIONS

The model documented in this report calculates net infiltration at the soil–bedrock interface without consideration of the properties of the bedrock at deeper locations. All water that enters the bedrock is assumed to be net infiltration. Instead of net infiltration, some authors call this parameter "deep drainage" or "potential recharge." Such terminology acknowledges that other mechanisms exist to move or remove water from the bedrock below the root zone. *UZ Flow Models and Submodels* (BSC 2004 [DIRS 169861]) describes the method used for simulating water flow from the bottom of the root zone through the unsaturated zone to the underlying aquifer (i.e., recharge), taking into consideration the potential recharge and the make-up and orientation of the geologic strata, as well as other considerations.

The model documented in this report is valid only for the Yucca Mountain site over a 10,000-year period and for the climates specified in *Future Climate Analysis* (BSC 2004 [DIRS 170002], Section 7.1). For each climate, the model produces maps of average annual infiltration as a function of location, with no time dependence. These output maps indicate the range of uncertainty in average annual net infiltration.

Infiltration predictions are limited by the uncertainty in future weather, and this uncertainty is accounted for in this model. Although a substantial body of literature supports the use of stochastic precipitation models, there are no records to support extrapolation to 1000 years. Each available precipitation record, whether from the Yucca Mountain site, from a nearby weather station, or from a site representative of a future climate, covers much less than 100 years.

Another significant uncertainty in the results of the net infiltration model is related to the spatial distribution of the net infiltration over the modeling domain. Sensitivity analyses presented in Sections 7.1.3 and 6.7 suggest that there may be insufficient characterization of soil properties (depth, holding capacity, and hydraulic conductivity) over the modeling domain to obtain accurate and detailed maps of net infiltration. Instead, results suggest that spatially averaged net infiltration estimates are more reliable than the resulting spatial distributions of net infiltration. This conclusion is supported by model validation comparisons of spatially averaged net infiltration model results with analogue site data from the region (Section 7.2).

8.3 YUCCA MOUNTAIN REVIEW PLAN CRITERIA ASSESSMENT

The general requirements to be satisfied by the TSPA are stated in 10 CFR 63 [DIRS 176544]. The acceptance criteria that will be used by the U.S. Nuclear Regulatory Commission to determine whether the technical requirements have been met are identified in *Yucca Mountain Review Plan*, *Final Report* (YMRP) (NRC 2003 [DIRS 163274]).

The acceptance criteria identified in Section 2.2.1.3.5.3 of the YMRP (NRC 2003 [DIRS 163274]) that are applicable to this report are included below along with a summary of where in this report each criterion is addressed.

Acceptance Criteria from Section 2.2.1.3.5.3, Climate and Infiltration.

Acceptance Criterion 1: *System Description and Model Integration Are Adequate.*

(1) The total system performance assessment adequately incorporates, or bounds, important design features, physical phenomena, and couplings, and uses consistent and appropriate assumptions throughout the climate and net infiltration abstraction process.

This model, which feeds the TSPA through the UZ flow model, explicitly includes the following natural features and physical phenomena and couplings that control the processes of net infiltration in the area above the planned Yucca Mountain repository: 1) terrain elevation and contours (Section 6.5.2 and Appendices B and C); 2) site specific estimates of vegetation as a function of mean annual precipitation (Section 6.5.3 and Appendix D); 3) change of climate through time using inputs from the future climates model report (Section 6.5.1); and 4) appropriate soil and bedrock permeability estimates as discussed in Section 6.5.2.

(2) The aspects of geology, hydrology, geochemistry, physical phenomena, and couplings, that may affect climate and net infiltration, are adequately considered. Conditions and assumptions in the abstraction of climate and net infiltration are readily identified and consistent with the body of data presented in the description.

This model includes the effects of geology by distinguishing soil and bedrock types present in the model domain (Sections 6.5.2.2 and 6.5.2.5) and assigning properties to these units consistent with available data (Sections 6.5.2.3 and 6.5.2.6). In addition, soil depth is represented as distinct soil depth class regions in the model domain (Section 6.5.2.4). The effects of local surface water hydrology (i.e., stream flow) are captured in the methods used to estimate surface runoff and run-on and watershed discharge (as summarized in Section 6.4.3) and controlled by the representation of elevation over the domain (Section 6.5.2.1 and Appendix B). Physical phenomena and couplings that are included in the modeling include: 1) elevation adjustments to precipitation and temperature (Sections 6.4.1 and 6.4.5.3); 2) adjustments to incoming daily solar radiation as a function of slope, azimuth, elevation, and day of year (Section 6.4.5.3); and 3) a detailed approach to estimating evapotranspiration as a function of reference evapotranspiration, site-specific vegetation characteristics, and soil water contents that all vary with time (Section 6.4.4)

(3) The abstraction of climate and net infiltration uses assumptions, technical bases, data, and models that are appropriate and consistent with other related U.S. Department of Energy abstractions. For example, the assumptions used for climate and net infiltration are consistent with the abstractions of flow paths in the unsaturated zone (UZ) and flow paths in the saturated zone (SZ) (Sections 2.2.1.3.6 and 2.2.1.3.8 of the Yucca Mountain Review Plan, respectively). The descriptions and technical bases provide transparent and traceable support for the abstraction of climate and net infiltration.

This model uses input data from the following DOE reports, all of which summarize YMP-relevant data:

1. ANL-NBS-GS-000008, *Future Climate Analysis* (BSC 2004 [DIRS 170002])

2. ANL-MGR-MD-000015, *Analysis for Infiltration Modeling: Extracted Weather Station Data Used to Represent Present Day and Potential Future Climate Conditions within the Vicinity of Yucca Mountain* (BSC 2006 [DIRS 177081])

3. TDR-NBS-HS-000019, *Technical Evaluation and Review of Results, Technical Procedures, and Methods Related to the Collection of Moisture Monitoring Data Using Neutron Probes in Shallow Boreholes* (BSC 2006 [DIRS 177083])

4. ANL-NBS-HS-000054, *Data Analysis for Infiltration Modeling: Bedrock Saturated Hydraulic Conductivity Calculation* (BSC 2006 [DIRS 176355])

5. ANL-NBS-HS-000077, *Data Analysis for Infiltration Modeling: Technical Evaluation of Previous Soil Depth Estimation Methods and Development of Alternate Parameter Values* (BSC 2006 [DIRS 178819])

6. ANL-NBS-HS-000055, *Data Analysis for Infiltration Modeling: Development of Soil Units and Associated Hydraulic Parameter Values* (BSC 2006 [DIRS 176335]).

The outputs (net infiltration maps) from this model are used as feeds to the UZ models to ensure continuity of repository system-wide modeling approach. Outputs from this model are indirectly coupled to the SZ through the coupling in the UZ. Output from this model is also indirectly coupled through the UZ flow fields (generated in the UZ models) to the predictions of in-drift temperature and humidity as described in *Multiscale Thermohydrologic Model* (BSC 2005 [DIRS 173944]).

(4) Sufficient data and technical bases to assess the degree to which FEPs have been included for this abstraction are provided;

This report addresses three FEPs included in *Features, Events, and Processes in UZ Flow and Transport* (BSC 2005 [DIRS 174191]).

- *Infiltration and Recharge* (2.3.11.03.0A) includes the effects of infiltration into the subsurface as a boundary condition for groundwater flow.

- *Precipitation* (2.3.11.01.0A) includes the effects of precipitation on the estimated net infiltration. Daily precipitation is explicitly included in the MASSIF modeling of net infiltration for Yucca Mountain.

- *Surface runoff and flooding* (2.3.11.02.0A) includes both the processes of surface runoff and evapotranspiration. These processes are explicitly included in the MASSIF modeling of net infiltration for Yucca Mountain.

(5) Adequate spatial and temporal variability of model parameters and boundary conditions are employed to model the different parts of the system.

Spatially varying parameters are listed in Section 6.5.2 and Appendix B. These parameters are distributed onto a grid comprised of 30 × 30-m grid cells. Spatial variations at a scale smaller than 30 × 30 m are not explicitly represented. Parameters associated with the terrain include elevation, slope, azimuth, and latitude for each 30 × 30-m grid cell. Elevation is used to divide the entire domain into 11 distinct watersheds (Appendix B). Each grid cell is assigned to a soil group, a bedrock type, and a soil depth group. The properties of these groups are represented with property sets that are uniform for all cells in the group. These properties include: bedrock hydraulic conductivity, soil depth, soil properties (conductivity, field capacity, wilting point, and saturated water content). Values and uncertainties for these parameters are described in Section 6.5.2. Potential vegetation response (PVR) is a spatially varying parameter that indicates the potential for vegetation at a given location given sufficient precipitation. This variable was developed from satellite measurements made at the site during a set of three representative years. This parameter is discussed in Section 6.5.3 and Appendix E. In addition, elevation adjustments are made to daily values of precipitation and temperature (Sections 6.4.1 and 6.4.5.3).

(6) Average parameter estimates are used in process-level models over time and space scales that are appropriate for the model discretization.

The MASSIF model is built on parameter estimates to enable infiltration estimates that are tailored to the site-specific conditions, including climate, vegetation type and coverage, soil types, properties, and depths and bedrock permeability. Net infiltration estimates are developed for Present-Day, as well as future climates predicted for the next 10,000 years. The modeling domain for Yucca Mountain Project infiltration covers approximately 125 km^2 and is comprised of 139,092 30 × 30-m grid cells. Each of these grid cells must be assigned parameters of elevation, slope, azimuth, potential vegetation response, soil depth, soil properties, and bedrock conductivity. The large expanse of the model domain required that these parameters be grouped into spatial zones, most often contiguously, and average properties over each of the zones were assigned based on available data. The delineations of the various parameters are displayed in Figures B-6 through B-11.

(7) Projections of future climate change are based on evaluation of paleoclimate information over the past 500,000 years. For example, numerical climate models, if used for projection of future climate, are calibrated based on such paleoclimate data.

Future climate predictions are based in part on *Future Climate Analysis* (BSC 2004 [DIRS 170002], Section 7.1), which forecasts three distinct climate states during the next 10,000 years at Yucca Mountain based on an examination of paleoclimate information over the past 500,000 years. The Present-Day climate is estimated to persist for the next 400 to 600 years, followed by a warmer and much wetter Monsoon climate spanning 900 to 1,400 years, and then

followed by a cooler and wetter Glacial Transition climate that is expected to last until and beyond the 10,000-year mark. Climate conditions expected beyond 10,000 years are not explicitly stated in *Future Climate Analysis* (BSC 2004 [DIRS 170002]). Proxy sites representing upper and lower bounds for each of these climates are specified, and data from these sites has been compiled and analyzed. Relevant weather parameters (e.g., mean annual temperature and precipitation) have been derived from these data, and the parameters have been used to generate stochastic simulations of weather for each of the three climates. Weather inputs are discussed in *Analysis for Infiltration Modeling: Extracted Weather Station Data Used to Represent Present Day and Potential Future Climate Conditions within the Vicinity of Yucca Mountain* (BSC 2006 [DIRS 177081]). Parameter extraction methods and applications to generate stochastic future weather inputs are described in Section 6.5.1 and Appendix F.

(8) Guidance in NUREG–1297 and NUREG–1298 (Altman et al. 1988a,b [DIRS 103597 and 103750]), or other acceptable approaches for peer reviews and data qualification, is followed.

No peer reviews were conducted in support of this report. A summary of findings from an Expert Elicitation Panel is discussed in Section 7.2.3. All direct input data used for estimates of net infiltration were qualified for use according to applicable procedures.

Acceptance Criterion 2: *Data Are Sufficient for Model Justification*.

(1) Climatological and hydrological values used in the license application (e.g., time of onset of climate change, mean annual temperature, mean annual precipitation, mean annual net infiltration, etc.) are adequately justified. Adequate descriptions of how the data were used, interpreted, and appropriately synthesized into the parameters are provided.

Future climates predictions are based in part on *Future Climate Analysis* which forecasts three distinct climates during the next 10,000 years at Yucca Mountain (BSC 2004 [DIRS 170002], Section 7.1). The Present-Day climate should persist for the next 400 to 600 years, followed by a warmer and much wetter Monsoon climate spanning 900 to 1,400 years, and then by a cooler and wetter Glacial Transition climate that is expected to last until and beyond the 10,000-year mark. Proxy sites representing upper and lower bounds for each of these climates are specified, and data from these sites has been compiled and analyzed. Relevant weather parameters (e.g., mean annual temperature and precipitation) have been derived from these data, and the parameters have been used to generate stochastic simulations of weather for each of the three climates. Weather inputs are discussed in *Analysis for Infiltration Modeling: Extracted Weather Station Data Used to Represent Present Day and Potential Future Climate Conditions within the Vicinity of Yucca Mountain* (BSC 2006 [DIRS 177081]). Parameter extraction methods and applications to generate stochastic future weather inputs are described in Section 6.5.1 and Appendix F.

(2) Estimates of present-day net infiltration using mathematical models at appropriate time and space scales are reasonably verified with site-specific climatic, surface, and subsurface information.

Present-Day net infiltration estimates have been reasonably verified, as discussed in Section 7. The evapotranspiration model has been shown to accurately predict evapotranspiration from weighing lysimeters at a location on the Nevada Test Site located approximately 40 miles from the YMP (Section 7.1.2). Runoff has been shown to be adequately predicted, as described in Section 7.1.3, where several runoff events were recorded at the YMP during two relatively wet years. The stochastic simulations of weather are shown to be a good representation of the weather observed at the proxy sites for each climate in Section 7.1.1.

(3) The effects of fracture properties, fracture distributions, matrix properties, heterogeneities, time-varying boundary conditions, evapotranspiration, depth of soil cover, and surface-water run off and run on are considered, such that net infiltration is not underestimated.

Bedrock fracture and matrix properties, distributions, and uncertainties are developed in *Data Analysis for Infiltration Modeling: Bedrock Saturated Hydraulic Conductivity Calculation* (BSC 2006 [DIRS 176355]), and inputs to the MASSIF model based on this report are summarized in Section 6.5.2. Uncertainty in bulk bedrock conductivity includes the possibility that some portion of the filled bedrock fractures contain open conduits, and therefore, the potential for net infiltration is not underestimated.

Parameter ranges and distributions used to develop evapotranspiration estimates are discussed in Sections 6.5.3 and 6.5.4, Appendix D, and Appendix E. Uncertainties in these parameters ensure that the full range of uncertainty in evapotranspiration is captured and not overestimated, and therefore, net infiltration is not underestimated.

Soil depth estimates, including uncertainty and spatial variability are developed in D*ata Analysis for Infiltration Modeling: Technical Evaluation of Previous Soil Depth Estimation Methods and Development of Alternate Parameter Values* (BSC 2006 [DIRS 178819]) and are further summarized for the MASSIF model in Section 6.6. Assumptions are made (in Section 5) that state that soil depth and properties can be considered to be constant for the next 10,000 years. The inclusion of uncertainties in soil depth provides confidence that net infiltration results and is not underestimated. This is because soil depth is one of the most important parameters controlling net infiltration over the modeling domain.

As part of model validation, comparisons are made between observations and model predictions of runoff. Within the uncertainty range of input variables, these comparisons are quite consistent (Section 7.1.3). Therefore, there is no reason to believe that net infiltration is underestimated.

All of the parameters that influence infiltration are briefly discussed in Appendix I where they are screened for inclusion in the uncertainty analysis. Appendix H describes sensitivity analyses and identifies parameters that have the greatest influence on net infiltration. The most influential parameters are included in the uncertainty analysis. The range of predicted net infiltration reasonably represents the uncertainty in a manner that precludes that net infiltration is underestimated.

(4) Sensitivity or uncertainty analyses are performed to assess data sufficiency and determine the possible need for additional data.

Sensitivity analyses have been conducted to determine the influence of various parameters over their expected ranges, which include uncertainty, and these analyses are developed in Section 6.7. Sufficient data exist to enable credible and bounding predictions of infiltration. These studies show that soil depth in Depth Class 4 (shallow soils) and water holding capacity of soil group 5/7/9 are the most important physical parameters in the MASSIF model. In addition, the uncertainty related to future precipitation patterns is another significant source of uncertainty. While further data are not needed to develop sufficiently accurate estimates of infiltration for the purposes of TSPA, such data would serve to reduce the uncertainty in predicted infiltration ranges.

(5) Accepted and well-documented procedures are used to construct and calibrate numerical models;

The fundamental conceptual model is based on a mass-balance calculation where water enters a grid cell through precipitation (rain or snowmelt) and/or run-on and water leaves a cell through evapotranspiration, sublimation, runoff, and/or net infiltration. Mass balance implies that the sum of these fluxes equals zero. The mass balance approach is generally accepted and well documented. The primary sub-components upon which MASSIF is built are described in Section 6 and include: 1) FAO-56 methods to estimate evapotranspiration, and 2) Darcy's Law in conjunction with the field capacity concept for estimating water movement and storage in the soil. Both of these procedures are well accepted and well documented approaches. The actual physics controlling run-on and runoff processes are not represented in the model. Instead, runoff is routed along flow networks through the model domain during the course of the day with the constraint of mass balance being enforced. The only calibration done is in the definition of the parameters used to convert satellite data quantifying vegetation (NDVI') to ground measurements of basal crop coefficients (K_{cb}) at ecological study plots. A linear regression accounting for measurement uncertainties was performed for this purpose. The methods used are accepted and well-documented. See Section 6.5.3 for details.

(6) Reasonably complete process-level conceptual and mathematical models are used in this model report. In particular: (a) mathematical models provided are consistent with conceptual models and site characteristics; and (b) the robustness of results from different mathematical models is compared.

The conceptual and mathematical models used in this report are complete in the sense that they represent the complete near surface hydrologic system at the YMP. Section 6 describes the conceptual model development process, the mathematical model, and the use of the model to estimate net infiltration at the YMP. The use of the FAO-56 procedures in conjunction with satellite and ground-based measurements of vegetation at the YMP site ensure that the ET component of the calculation is customized for the YMP site. The generation of stochastic precipitation records is also entirely based on weather data collected in the vicinity of the YMP site and at other locations that represent the predicted range of future climates.

An alternative mathematical model (HYDRUS 1-D) was run, and results were compared with similar runs of the MASSIF model for the purpose of model corroboration. These comparisons are described in Section 7.2.2. In addition, the MASSIF model was run with historical weather data for the purpose of comparing model results with observations of ET, runoff, and net

infiltration at various locations both on and off the YMP site (Section 7). In general these comparisons indicate that the MASSIF model is valid for its intended use.

Number 7 under Acceptance Criterion 2 was listed in the TWP, but it is not included in present report because expert elicitation was not used to support model development.

Acceptance Criterion 3: ***Data Uncertainty Is Characterized and Propagated through the Model Abstraction.***

(1) Models use parameter values, assumed ranges, probability distributions, and bounding assumptions that are technically defensible, reasonably account for uncertainties and variabilities, and do not result in an under-representation of the risk estimate.

Each of the parameters that potentially influence infiltration is briefly discussed in Appendix I where it is evaluated and screened for inclusion in the uncertainty analysis. Parameters are screened into the uncertainty analysis if their relative standard uncertainty (standard deviation) is above 15% or they represent the properties of materials that cover more than 15% of the UZ domain. Parameter uncertainty is propagated to net infiltration by way of a Monte Carlo analysis using Latin Hypercube Sampling (LHS) (see Sections 6.5.5 and 6.5.6). The range of net infiltration is demonstrated to reasonably bound the estimates of infiltration in a manner to preclude under-representation of the risk estimate.

(2) The technical bases for the parameter values used in this abstraction are provided.

Each of the parameters that serve as input to the infiltration analysis have been technically evaluated and selected based on their appropriateness for use in calculating infiltration. Bedrock fracture and matrix properties and distributions are developed in *Data Analysis for Infiltration Modeling: Bedrock Saturated Hydraulic Conductivity Calculation* (BSC 2006 [DIRS 176355]) and inputs to the MASSIF model are summarized in Section 6.5.2.6, *Bedrock Saturated Conductivity*. Parameter ranges and distributions used to develop evapotranspiration estimates are discussed in Sections 6.5.3 and 6.5.4 and Appendix D. Soil depth estimates, including uncertainty and spatial variability are developed in D*ata Analysis for Infiltration Modeling: Technical Evaluation of Previous Soil Depth Estimation Methods and Development of Alternate Parameter Values* (BSC 2006 [DIRS 178819]) and are further summarized for the MASSIF model in Section 6.5.2.4. Soil hydraulic properties and associated uncertainties are developed in *Data Analysis for Infiltration Modeling: Development of Soil Units and Associated Hydraulic Parameter Values* (BSC 2006 [DIRS 176335]) and are further summarized for the MASSIF model in Section 6.5.2.3. Geographic parameters such as elevation and slope are presented in Appendix B, and summarized in Section 6.5.2.1. All of the parameters that influence infiltration are briefly discussed in Appendix I, where they are screened for inclusion in the uncertainty analysis.

(3) Possible statistical correlations are established between parameters in this abstraction. An adequate technical basis or bounding argument is provided for neglected correlations;

Correlations between parameters have been considered in order to constrain the LHS sample of input parameters to physically realistic combinations. The sample size of each probabilistic analysis was limited to 20. Up to fifteen parameters were sampled to generate the inputs for each of the 20 realizations. For the physical parameters (parameter related to physical properties of materials), no technical basis justifying imposing correlations between parameters was identified. Therefore, no correlations were applied.

For some of the stochastic precipitation parameters, two strong correlations have been identified between parameters. The first one is an actual correlation between two parameters (e.g., the annual average of average daily precipitation amount and annual average of average daily log of precipitation amount). These parameters are strongly correlated, as they are estimated from the same data (records of daily precipitation). As the relation between the two parameters has been shown to be linear, correlation has been taken into account by sampling one of the two parameters and estimating the other with a linear regression model as discussed in Section 6.5.5 and Appendix I. The second correlation identified is associated with a set of assumptions present in *Future Climate Analysis* (BSC 2004 [DIRS 170002]). For instance, it is stated that Monsoon Climate will experience series of years either with small amounts of rain, mainly in winter, or with a larger amount of rain, mainly in summer (BSC 2004 [DIRS 170002]). Therefore, the annual variation of the precipitation parameters was adjusted to match either of the two cases. This weather pattern has been taken into account by sampling one of the parameters controlling seasonal variation and estimating the other parameters using linear regression models as discussed in Section 6.5.5 and Appendix I. The purpose of including these two correlations is to ensure that the parameter inputs represent a realistic combination of parameter values.

(4) The hydrologic effects of future climate change that may alter the rates and patterns of present-day net infiltration into the UZ are addressed. Such effects may include changes in soil depths, fracture-fill material, and types of vegetation.

The potential for future climates to affect various parameters is captured in inputs including stochastic weather parameters and vegetation parameters. The variation of stochastic weather parameters including temperature and stochastic precipitation parameters for future climates is discussed in Section 6.5.1 and Appendix F. The response in vegetation to the predicted climate change is provided in Section 6.5.3. The amount of vegetation is directly related to the annual precipitation which varies with climate. In addition, vegetation parameters (maximum rooting depth and plant height) are given climate specific and appropriate values and distributions. Field observations of bedrock fracture filling indicate that these fillings were stable during previous wet climate cycles, and therefore, these fillings are expected to remain stable for the regulatory period of the repository. Potential variation in soil depth as a result of future climate change is assumed to be negligible (Section 5.4).

Acceptance Criterion 4: ***Model Uncertainty Is Characterized and Propagated through the Model Abstraction.***

(1) Alternate modeling approaches of FEPs, consistent with available data and current scientific understanding, are investigated. The results and limitation are appropriately considered in the abstraction.

Net infiltration results of an alternative conceptual and numerical model (HYDRUS-1D) are compared with the results of the MASSIF model in Section 7.2.2 and Appendix K. HYDRUS-1D is a model based on the Richards' equation and thus solves a different set of equations than MASSIF. The comparison demonstrated that while the models exhibit different transient net infiltration behaviors the results are very similar when summed over the year. Thus, since the purpose of the net infiltration calculation is to calculate a steady-state, long term average flux, both MASSIF and HYDRUS-1D provide comparable results, which corroborates the MASSIF model.

(2) The bounds of uncertainty created by process-level models are considered in this abstraction.

It is assumed in this analysis (Section 5) that net infiltration uncertainty caused by the selection of the model is not as significant as the uncertainty caused by the epistemic parameter uncertainty.

(3) Consideration of conceptual model uncertainty is consistent with available site characterization data, laboratory experiments, field measurements, natural analogue information and process-level modeling studies; and the treatment of conceptual model uncertainty does not result in an under-representation of the risk estimate.

The model uncertainties have been estimated by comparing model predictions to field observations and predictions of an alternative model (HYDRUS-1D). These comparisons are described in the model validation sections of the report (Section 7.2.2 and Appendices J and K).

Acceptance Criterion 5: ***Model Abstraction Output Is Supported by Objective Comparisons***

Number 1 under Acceptance Criterion 5 was listed in the TWP, but it is not included in present report because the output from this model is not a direct TSPA abstraction.

(2) Abstractions of process-level models may conservatively bound process-level predictions.

Net infiltration estimates presented in this report include the quantification of uncertainty which bounds these estimates. While it was not the intent of this analysis to provide a "conservative" estimate of net infiltration, the results of the analysis may be conservative (over-estimate) due to the lack of certain site-specific data to constrain the results. For example, as identified in Section 1.2, it is assumed in this analysis that there is no significant water loss below the soil-rock interface. If, in fact, a significant amount of water is lost from within the rock, then the net infiltration estimates from this analysis provide an upper bound on net infiltration.

(3) Comparisons are provided of output of abstracted models of climate and net infiltration with output of sensitivity studies, detailed process-level models, natural analogs, and empirical observations, as appropriate.

Section 7 includes: (a) comparisons of model outputs of precipitation to observed patterns of precipitation at the Yucca Mountain site as well as at analog meteorological sites used to represent future climate conditions (Section 7.1.1), (b) comparisons of model predictions of evapotranspiration to lysimeter observations (Section 7.1.2), (c) comparisons of simulated runoff to observations at Yucca Mountain monitoring stations (Section 7.1.3), (d) results of an extended sensitivity study examining the influence of parameter uncertainty on net infiltration uncertainty (Section 7.1.4), (e) comparison of net infiltration predictions with field estimates of net infiltration from the region (Section 7.2.1), (f) comparisons of net infiltration estimates with estimates calculated using an alternative, more detailed and mechanistic model (HYDRUS-1D) (Section 7.2.2), and (g) comparisons of net infiltration model predictions with the estimates provided as part of an expert elicitation (Section 7.2.3).

Acceptance Criteria from Section 2.2.1.1.3

(3) Technical Basis for Barrier Capability is Adequately Presented

The near-surface hydrologic system is part of the natural barrier capability of the repository design. The net infiltration model contributes to the natural barrier system by simulating the precipitation of water to the land surface and calculating the fraction of that water that enters the unsaturated zone as deep percolation. The representation of precipitation processes is described in Section 6.5.1 and Appendix F. Evapotranspiration is discussed in Section 6.5.3, 6.5.4, and Appendices C, D, and E.

INTENTIONALLY LEFT BLANK

9. INPUTS AND REFERENCES

The following is a list of the references cited in this document. Column 1 lists the Document Input Reference System number (DIRS). Column 2 lists the bibliographic citation.

9.1 DOCUMENTS CITED

176485 Allen, R.G. 1996. "Assessing Integrity of Weather Data for Reference Evapotranspiration Estimation." *Journal of Irrigation and Drainage Engineering, 122,* (2), 97-106. New York, New York: American Society of Civil Engineers. TIC: 258098.

176568 Allen, R.G. 1997. "Self-Calibrating Method for Estimating Solar Radiation from Air Temperature." *Journal of Hydrologic Engineering, 2,* (2), 56-67. New York, New York: American Society of Civil Engineers. TIC: 258131.

157311 Allen, R.G.; Pereira, L.S.; Raes, D.; and Smith, M. 1998. *Crop Evapotranspiration, Guidelines for Computing Crop Water Requirements.* FAO Irrigation and Drainage Paper 56. Rome, Italy: Food and Agriculture Organization of the United Nations. TIC: 245062.

176009 Allen, R.G.; Pereira, L.S.; Smith, M.; Raes, D.; and Wright, J.L. 2005. "FAO-56 Dual Crop Coefficient Method for Estimating Evaporation from Soil and Application Extensions." *Journal of Irrigation and Drainage Engineering, 131,* (1), 2-13. Reston, Virginia: American Society of Civil Engineers. TIC: 257869.

178493 Allen, R.G.; Pruitt, W.O.; Raes, D.; Smith, M.; and Pereira, L.S. 2005. "Estimating Evaporation from Bare Soil and the Crop Coefficient for the Initial Period Using Common Soils Information." *Journal of Irrigation and Drainage Engineering, 131,* (1), 14-23. Reston, Virginia: American Society of Civil Engineers. TIC: 258906.

176785 Allen, R.G.; Pruitt, W.O.; Wright, J.L.; Howell, T.A.; Ventura, F.; Snyder, R.; Itenfisu, D.; Steduto, P.; Berengena, J.; Yrisarry, J.B.; Smith, M.; Pereira, L.S.; Raes, D.; Perrier, A.; Alves, I.; Walter, I.; and Elliott, R. 2006. "A Recommendation on Standardized Surface Resistance for Hourly Calculation of Reference ET_o by the FAO56 Penman-Monteith Method." *Agricultural Water Management, 81,* 1-22. New York, New York: Elsevier. TIC: 258241.

176207 Allen, R.G.; Walter, I.A.; Elliott, R.L.; Howell, T.; Itenfisu, D.; and Jensen, M. 2005. *The ASCE Standardized Reference Evapotranspiration Equation.* Reston, Virginia: American Society of Civil Engineers. TIC: 257138.

103750 Altman, W.D.; Donnelly, J.P.; and Kennedy, J.E. 1988. *Qualification of Existing Data for High-Level Nuclear Waste Repositories: Generic Technical Position.* NUREG-1298. Washington, D.C.: U.S. Nuclear Regulatory Commission. TIC: 200652.

103597 Altman, W.D.; Donnelly, J.P.; and Kennedy, J.E. 1988. *Peer Review for High-Level Nuclear Waste Repositories: Generic Technical Position.* NUREG-1297. Washington, D.C.: U.S. Nuclear Regulatory Commission. TIC: 200651.

177625 Anderson, M.D. 2002. "Pinus Eulis." Washington, D.C.: U.S. Department of Agriculture, Forest Service. Accessed September 5, 2006. ACC: MOL.20060907.0013. URL: http://www.fs.fed.us/database/feis/plants/tree/pinedu/all.htm

176754 Asrar, G.; Myneni, R.B.; and Choudhury, B.J. 1992. "Spatial Heterogeneity in Vegetation Canopies and Remote Sensing of Absorbed Photosynthetically Active Radiation: A Modeling Study." *Remote Sensing of Environment, 41,* 85-103. New York, New York: Elsevier. TIC: 258219.

177200 Avon, L. and Durbin, T.J. 1994. "Evaluation of the Maxey-Eakin Method for Estimating Recharge to Ground-Water Basins in Nevada." *Water Resources Bulletin, 30,* (1), 99-111. Herndon, Virginia: American Water Resources Association. TIC: 255352.

127394 Barbour, M.G.; Burk, J.H.; and Pitts, W.D. 1980. *Terrestrial Plant Ecology.* Menlo Park, California: Benjamin/Cummings Publishing Company. TIC: 243042.

101486 Bauer, D.J.; Foster, B.J.; Joyner, J.D.; and Swanson, R.A. 1996. *Water Resources Data for Nevada Water Year 1995.* Water-Data Report NV-95-1. Carson City, Nevada: U.S. Geological Survey. ACC: MOL.20010721.0049.

177726 Bauer, H.H. and Vaccaro, J.J. 1990. *Estimates of Ground-Water Recharge to the Columbia Plateau Regional Aquifer System, Washington, Oregon, and Idaho, for Predevelopment and Current Land-Use Conditions.* Water-Resources Investigations Report 88-4108. Denver, Colorado: U.S. Geological Survey. ACC: MOL.20061115.0001.

178678 Baugh, W.M. and Groeneveld, D.P. 2006. "Broadband Vegetation Index Performance Evaluated for a Low-Cover Environment." *International Journal of Remote Sensing, 27,* (21-22), 4715 - 4730. New York, New York: Taylor & Francis. TIC: 259019.

177652 Bausch, W.C. and Neale, C.M.U. 1987. "Crop Coefficients Derived from Reflected Canopy Radiation: A Concept." *Transactions of the ASAE, 30,* (3), 703-709. St. Joseph, Michigan: American Society of Agricultural Engineers. TIC: 258520.

103356 Beatley, J.C. 1975. "Climates and Vegetation Pattern Across the Mojave/Great Basin Desert Transition of Southern Nevada." *American Midland Naturalist, 93,* (1), 53-70. Notre Dame, Indiana: University of Notre Dame. TIC: 241488.

102221 Beatley, J.C. 1976. *Vascular Plants of the Nevada Test Site and Central-Southern Nevada: Ecologic and Geographic Distributions.* TID-26881. Oak Ridge, Tennessee: Energy Research and Development Administration. TIC: 204727.

177995 Berg, N.H. 1986. "Blowing Snow at a Colorado Alpine Site: Measurements and Implications." *Arctic and Alpine Research, 18,* (2), 147-161. Boulder, Colorado: University of Colorado, Institute of Arctic and Alpine Research. TIC: 258763.

147076 Bevington, P.R. and Robinson, D.K. 1992. *Data Reduction and Error Analysis for the Physical Sciences.* 2nd Edition. New York, New York: McGraw-Hill. TIC: 243514.

176211 Bodhinayake, W. and Si, B.C. 2004. "Near-Saturated Surface Soil Hydraulic Properties under Different Land Uses in the St. Denis National Wildlife Area, Saskatchewan, Canada." *Hydrological Processes, 18,* 2835-2850. New York, New York: John Wiley & Sons. TIC: 257866.

176784 Bolstad, P.V.; Swift, L.; Collins, F.; and Régnière, J. 1998. "Measured and Predicted Air Temperatures at Basin to Regional Scales in the Southern Appalachian Mountains." *Agricultural and Forest Meteorology, 91,* 161-176. New York, New York: Elsevier. TIC: 258239.

127406 Bonham, C.D. 1989. *Measurements for Terrestrial Vegetation.* New York, New York: John Wiley & Sons. TIC: 242274.

160019 Brady, N.C. and Weil, R.R. 1999. *The Nature and Properties of Soils.* 12th Edition. Upper Saddle River, New Jersey: Prentice-Hall. TIC: 242178.

176615 Brutsaert, W. 1982. *Evaporation into the Atmosphere, Theory, History, and Applications.* Environmental Fluid Mechanics. Csanady, G.T., ed. Boston, Massachusetts: D. Reidel Publishing Company. TIC: 239388.

165991 BSC (Bechtel SAIC Company) 2003. *Analysis of Infiltration Uncertainty.* ANL-NBS-HS-000027 REV 01. Las Vegas, Nevada: Bechtel SAIC Company. ACC: DOC.20031030.0003.

168796 BSC 2003. *Risk Information to Support Prioritization of Performance Assessment Models.* TDR-WIS-PA-000009 REV 01 ICN 01 [Errata 001]. Las Vegas, Nevada: Bechtel SAIC Company. ACC: MOL.20021017.0045; DOC.20031014.0003.

165572 BSC 2003. *Underground Layout Configuration.* 800-P0C-MGR0-00100-000-00E. Las Vegas, Nevada: Bechtel SAIC Company. ACC: ENG.20031002.0007; ENG.20050817.0005.

169857 BSC 2004. *Calibrated Properties Model.* MDL-NBS-HS-000003 REV 02. Las Vegas, Nevada: Bechtel SAIC Company. ACC: DOC.20041006.0004.

170002 BSC 2004. *Future Climate Analysis.* ANL-NBS-GS-000008 REV 01. Las Vegas, Nevada: Bechtel SAIC Company. ACC: DOC.20040908.0005.

170029 BSC 2004. *Geologic Framework Model (GFM2000).* MDL-NBS-GS-000002 REV 02. Las Vegas, Nevada: Bechtel SAIC Company. ACC: DOC.20040827.0008.

167652 BSC 2004. *Seepage Model for PA Including Drift Collapse.* MDL-NBS-HS-000002 REV 03. Las Vegas, Nevada: Bechtel SAIC Company. ACC: DOC.20040922.0008; DOC.20051205.0001.

170007 BSC 2004. *Simulation of Net Infiltration for Present-Day and Potential Future Climates.* MDL-NBS-HS-000023 REV 00. Las Vegas, Nevada: Bechtel SAIC Company. ACC: DOC.20041109.0004.

180945 BSC 2004. *Technical Basis Document No. 1: Climate and Infiltration.* Revision 1. Las Vegas, Nevada: Bechtel SAIC Company. ACC: MOL.20040804.0292.

169861 BSC 2004. *UZ Flow Models and Submodels.* MDL-NBS-HS-000006 REV 02. Las Vegas, Nevada: Bechtel SAIC Company. ACC: DOC.20041101.0004; DOC.20050629.0003.

174191 BSC 2005. *Features, Events, and Processes in UZ Flow and Transport.* ANL-NBS-MD-000001 REV 04. Las Vegas, Nevada: Bechtel SAIC Company. ACC: DOC.20050809.0002.

173944 BSC 2005. *Multiscale Thermohydrologic Model.* ANL-EBS-MD-000049 REV 03. Las Vegas, Nevada: Bechtel SAIC Company. ACC: DOC.20050711.0001.

175539 BSC 2005. *Q-List.* 000-30R-MGR0-00500-000-003. Las Vegas, Nevada: Bechtel SAIC Company. ACC: ENG.20050929.0008.

176335 BSC 2006. *Data Analysis for Infiltration Modeling: Development of Soil Units and Associated Hydraulic Parameter Values.* ANL-NBS-HS-000055 REV 00. Las Vegas, Nevada: Bechtel SAIC Company. ACC: DOC.20060912.0006.

178819 BSC 2006. *Data Analysis for Infiltration Modeling: Technical Evaluation of Previous Soil Depth Estimation Methods and Development of Alternate Parameter Values.* ANL-NBS-HS-000077 REV 01. Las Vegas, Nevada: Bechtel SAIC Company. ACC: DOC.20060918.0009.

176355 BSC 2006. *Data Analysis for Infiltration Modeling: Bedrock Saturated Hydraulic Conductivity Calculation.* ANL-NBS-HS-000054 REV 00. Las Vegas, Nevada: Bechtel SAIC Company. ACC: DOC.20060710.0001.

177083 BSC 2006. *Technical Evaluation and Review of Results, Technical Procedures, and Methods Related to the Collection of Moisture Monitoring Data Using Neutron Probes in Shallow Boreholes.* TDR-NBS-HS-000019 REV 00. Las Vegas, Nevada: Bechtel SAIC Company. ACC: DOC.20060425.0005.

177492 BSC 2006. *Technical Work Plan for: Infiltration Model Assessment, Revision, and Analyses of Downstream Impacts.* TWP-NBS-HS-000012 REV 02. Las Vegas, Nevada: Bechtel SAIC Company. ACC: DOC.20060831.0006.

176736 Buschmann, C. and Nagel, E. 1993. "In Vivo Spectroscopy and Internal Optics of Leaves as Basis for Remote Sensing of Vegetation." *International Journal of Remote Sensing, 14,* (4), 711-722. New York, New York: Taylor & Francis. TIC: 258202.

177100 Campbell, M.D.; Gee, G.W.; Kirkham, R.R.; Phillips, S.J.; and Wing, N.R. 1991. "Water Balance Lysimetry at a Nuclear Waste Site." *Lysimeters for Evapotranspiration and Environmental Measurements, Proceedings of the International Symposium on Lysimetry, Honolulu, Hawaii, July 23-25, 1991.* Allen, R.G.; Howell, T.A.; Pruitt, W.O.; Walter, I.A.; and Jensen, M.E., eds. Pages 125-132. New York, New York: American Society of Civil Engineers. TIC: 258304.

177626 Canadell, J.; Jackson, R.B.; Ehleringer, J.R.; Mooney, H.A.; Sala, O.E.; and Schulze, E.-D. 1996. "Maximum Rooting Depth of Vegetation Types at the Global Scale." *Oecologia, 108,* 583-595. Berlin, Germany: Springer-Verlag. TIC: 258180.

176748 Carlson, T.N. and Ripley, D.A. 1997. "On the Relation between NDVI, Fractional Vegetation Cover, and Leaf Area Index." *Remote Sensing of Environment, 62,* 241-252. New York, New York: Elsevier. TIC: 258215.

174674 Carpenter, A.T. and Murray, T.A. [n.d.]. *Element Stewardship Abstract for Bromus Tectorum L (Anisantha Tectorum (L.) Nevski).* Arlington, Virginia: The Nature Conservancy. TIC: 257692.

177572 Chander, G.; Helder, D.L.; Markham, B.L.; Dewald, J.D.; Kaita, E.; Thorne, K.J.; Micjevic, E.; and Ruggles, T.A. 2004. "Landsat-5 TM Reflective-Band Absolute Radiometric Calibration." *IEEE Transactions on Geoscience and Remote Sensing, 42,* (12), 2747-2760. New York, New York: Institute of Electrical and Electronics Engineers. TIC: 258551.

176788 Chavez, P.S., Jr. 1988. "An Improved Dark-Object Subtraction Technique for Atmospheric Scattering Correction of Multispectral Data." *Remote Sensing of Environment, 124,* 459-479. New York, New York: Elsevier. TIC: 258249.

178132 Chen, J-S.; Drake, R.; Lin, Z.; and Jewett, D.G. 2002. "A Benchmarking Analysis for Five Radionuclide Vadose Zone Models (CHAIN, MULTIMED_DP, FECTUZ, HYDRUS, AND CHAIN 2D) in Soil Screening Level Calculations." *HLW, LLW, Mixed, Hazardous Restoration -- Working Towards a Cleaner Environment, WM'02 Proceedings, Feb. 24-28, 2002, Tucson, Arizona.* 1-17. Tucson, Arizona: WM Symposia. TIC: 258782.

177127 Cline, J.F.; Uresk, D.W.; and Rickard, W.H. 1977. "Comparison of Soil Water Used by a Sagebrush-Bunchgrass and a Cheatgrass Community." *Journal of Range Management, 30,* (3), 199-201. Denver, Colorado: Society for Range Management. TIC: 243506.

178314 Cohen, S.; Liepert, B.; and Stanhill, G. 2004. "Global Dimming Comes of Age." *Eos, 85,* (38), 382-383. Washington, D.C.: American Geophysical Union. TIC: 258567.

176487 Collares-Pereira, M. and Rabl, A. 1979. "The Average Distribution of Solar Radiation—Correlations Between Diffuse and Hemispherical and Between Daily and Hourly Insolation Values." *Solar Energy, 22,* 155-164. New York, New York: Pergamon Press. TIC: 258100.

102235 CRWMS (Civilian Radioactive Waste Management System) M&O (Management and Operating Contractor) 1996. *The Vegetation of Yucca Mountain: Description and Ecology.* B00000000-01717-5705-00030 REV 00. Las Vegas, Nevada: CRWMS M&O. ACC: MOL.19970116.0055.

100117 CRWMS M&O 1997. *Engineering Design Climatology and Regional Meteorological Conditions Report.* B00000000-01717-5707-00066 REV 00. Las Vegas, Nevada: CRWMS M&O. ACC: MOL.19980304.0028.

103155 CRWMS M&O 1997. *Meteorological Monitoring Program 1996 Summary Report.* B00000000-01717-5705-00072 REV 00. Las Vegas, Nevada: CRWMS M&O. ACC: MOL.19980210.0202.

100335 CRWMS M&O 1997. *Unsaturated Zone Flow Model Expert Elicitation Project.* Las Vegas, Nevada: CRWMS M&O. ACC: MOL.19971009.0582.

104589 CRWMS M&O 1998. *Classification and Map of Vegetation at Yucca and Little Skull Mountains, Nevada.* B00000000-01717-5705-00083 REV 00. Las Vegas, Nevada: CRWMS M&O. ACC: MOL.19990615.0237.

105031 CRWMS M&O 1999. *Final Report: Plant and Soil Related Processes Along a Natural Thermal Gradient at Yucca Mountain, Nevada.* B00000000-01717-5705-00109 REV 00. Las Vegas, Nevada: CRWMS M&O. ACC: MOL.19990513.0037.

115672 CRWMS M&O 1999. *Meteorological Monitoring Program 1997 Summary Report.* B00000000-01717-5705-00107 REV 00. Las Vegas, Nevada: CRWMS M&O. ACC: MOL.19990804.0287.

177096 Daly, C.; Gibson, W.P.; Taylor, G.H.; Johnson, G.L.; and Pasteris, P. 2002. "A Knowledge-Based Approach to the Statistical Mapping of Climate." *Climate Research, 22,* (2), 99-113. Oldendorf/Luhe, Germany: Inter-Research. TIC: 258404.

101557 Day, W.C.; Potter, C.J.; Sweetkind, D.S.; Dickerson, R.P.; and San Juan, C.A. 1998. *Bedrock Geologic Map of the Central Block Area, Yucca Mountain, Nye County, Nevada.* Miscellaneous Investigations Series Map I-2601. Washington, D.C.: U.S. Geological Survey. ACC: MOL.19980611.0339.

176858 Desotell, L.T.; Hudson, D.B.; Yucel, V.; and Carilli, J.T. 2006. *Use of Long-Term Lysimeter Data in Support of Shallow Land Waste Disposal Cover Design.* DOE/NV11718--1148. Las Vegas, Nevada: U.S. Department of Energy, Nevada Site Office. ACC: MOL.20060413.0159.

105384 Dettinger, M.D. 1989. "Reconnaissance Estimates of Natural Recharge to Desert Basins in Nevada, U.S.A., by Using Chloride-Balance Calculations." *Journal of Hydrology, 106,* 55-78. Amsterdam, The Netherlands: Elsevier. TIC: 236967.

178528 Dewitte, S.; Crommelynck, D.; Mekaoui, S.; and Joukoff, A. 2004. "Measurement and Uncertainty of the Long-Term Total Solar Irradiance Trend." *Solar Physics, 224,* 209-216. Berlin, Germany: Springer. TIC: 258937.

178133 Dho, N.Y.; Koo, J.K.; and Lee, S.R. 2002. "Prediction of Leachate Level in Kimpo Metropolitan Landfill Site by Total Water Balance." *Environmental Monitoring and Assessment, 73,* 207-219. Amsterdam, The Netherlands: Kluwer Academic. TIC: 258769.

178797 Di Sanza, E.F. 2006. "Yucca Mountain Project (YMP) Request for Area 5 Weighing Lysimeter Data." Memorandum from E.F. Di Sanza (DOE/NVO) to E.T. Smistad (YMP), January 26, 2006, WMD:1671.JC, with attachments. ACC: MOL.20060510.0140.

147785 DOE (U.S. Department of Energy) 1995. *Meteorological Monitoring Program Environmental Field Programs, 1993 Annual Summary Report.* Las Vegas, Nevada: Yucca Mountain Site Characterization Office. ACC: MOL.19950721.0152.

179958 DOE 2006. *Report for Surveillance OQA-SI-06-015 of Infiltration Model at Bechtel, SAIC Company, LLC in Las Vegas, Nevada, September 20-29, 2006.* Surveillance Report OQA-SI-06-015. Las Vegas, Nevada: U.S. Department of Energy, Office of Civilian Radioactive Waste Management. ACC: MOL.20070103.0116.

176786 Droogers, P. and Allen, R.G. 2002. "Estimating Reference Evapotranspiration Under Inaccurate Data Conditions." *Irrigation and Drainage Systems, 16,* 33-45. Dordrecht, The Netherlands: Kluwer Academic Publishers. TIC: 258242.

178498 Duchemin, B.; Hadria, R.; Erraki, S.; Boulet, G.; Maisongrande, P.; Chehbouni, A.; Escadafal, R.; Ezzahar, J.; Hoedjes, J.C.B.; Kharrou, M.H.; Khabba, S.; Mougenot, B.; Olioso, A.; Rodriguez, J.-C.; and Simonneaux, V. 2006. "Monitoring Wheat Phenology and Irrigation in Central Morocco: On the Use of Relationships Between Evapotranspiration, Crops Coefficients, Leaf Area Index and Remotely-Sensed Vegetation Indices." *Agricultural Water Management, 79,* 1-27. New York, New York: Elsevier. TIC: 258870.

176264 Duffie, J.A. and Beckman, W.A. 1980. *Solar Engineering of Thermal Processes.* New York, New York: John Wiley & Sons. TIC: 258031.

176616 Duffie, J.A. and Beckman, W.A. 1991. *Solar Engineering of Thermal Processes.* 2nd Edition. New York, New York: John Wiley & Sons. TIC: 258123.

176486 Erbs, D.G.; Klein, S.A.; and Duffie, J.A. 1982. "Estimation of the Diffuse Radiation Fraction for Hourly, Daily and Monthly-Average Global Radiation." *Solar Energy, 28,* (4), 293-302. New York, New York: Pergamon Press. TIC: 258099.

178766 Faybishenko, B. 2007. "Climatic Forecasting of Net Infiltration at Yucca Mountain Using Analogue Meterorological Data." *Vadose Zone Journal, 6,* 77-92. Madison, Wisconsin: Soil Science Society of America. TIC: 259076.

177499 Fayer, M.J. 2000. *UNSAT-H Version 3.0: Unsaturated Soil Water and Heat Flow Model, Theory, User Manual, and Examples.* PNNL-13249. Richland, Washington: Pacific Northwest National Laboratory. ACC: MOL.20060712.0224.

178191 Fayer, M.J. and Walters, T.B. 1995. *Estimated Recharge Rates at the Hanford Site.* PNL-10285. Richland, Washington: Pacific Northwest Laboratory. ACC: MOL.20061026.0075.

178173 Feddes, R.A.; Bresler, E.; and Neuman, S.P. 1974. "Field Test of a Modified Numerical Model for Water Uptake by Root Systems." *Water Resources Research, 10,* (6), 1199-1206. Washington, D.C.: American Geophysical Union. TIC: 258772.

156668 Fetter, C.W. 2001. *Applied Hydrogeology.* 4th Edition. Upper Saddle River, New Jersey: Prentice Hall. TIC: 251142.

177754 Finsterle, S. and Seol, Y. 2006. *Preliminary Evaluation of Seepage Observations from the ESF South Ramp Using the Drift Seepage Abstraction Model.* Albuquerque, New Mexico: Sandia National Laboratories. ACC: MOL.20060510.0330.

100147 Flint, A.L.; Hevesi, J.A.; and Flint, L.E. 1996. *Conceptual and Numerical Model of Infiltration for the Yucca Mountain Area, Nevada.* Milestone 3GUI623M. Denver, Colorado: U.S. Geological Survey. ACC: MOL.19970409.0087.

100394 Flint, L.E. and Flint, A.L. 1995. *Shallow Infiltration Processes at Yucca Mountain, Nevada—Neutron Logging Data 1984-93.* Water-Resources Investigations Report 95-4035. Denver, Colorado: U.S. Geological Survey. ACC: MOL.19960924.0577.

177628 Foxx, T.S.; Tierney G.D.; and Williams, J.M. 1984. *Rooting Depths of Plants on Low-Level Waste Disposal Sites.* LA-10253-MS. Los Alamos, New Mexico: Los Alamos National Laboratory. TIC: 228561.

101173 Freeze, R.A. and Cherry, J.A. 1979. *Groundwater.* Englewood Cliffs, New Jersey: Prentice-Hall. TIC: 217571.

163705 Gilbert, R.O. 1987. *Statistical Methods for Environmental Pollution Monitoring.* New York, New York: John Wiley & Sons. TIC: 252619.

176763 Gillies, R.R.; Carlson, T.N.; Cui, J.; Kustas, W.P.; and Humes, K.S. 1997. "A Verification of the 'Triangle' Method for Obtaining Surface Soil Water Content and Energy Fluxes from Remote Measurements of the Normalized Difference Vegetation Index (NDVI) and Surface Radiant Temperature." *International Journal of Remote Sensing, 18,* (15), 3145-3166. New York, New York: Taylor & Francis. TIC: 258232.

177128 Hamerlynck, E.P.; Huxman, T.E.; Charlet, T.N.; and Smith, S.D. 2002. "Effects of Elevated CO_2 (FACE) on the Functional Ecology of the Drought-Deciduous Mojave Desert Shrub, Lycium Andersonii." *Environmental and Experimental Botany, 48,* (2), 93-106. New York, New York: Elsevier. TIC: 257779.

177130 Hamerlynck, E.P.; Huxman, T.E.; Loik, M.E.; and Smith, S.D. 2000. "Effects of Extreme High Temperature, Drought and Elevated CO_2 on Photosynthesis of the Mojave Desert Evergreen Shrub, Larrea Tridentata." *Plant Ecology, 148,* (2), 183-193. Dordrecht, The Netherlands: Kluwer Academic Publishers. TIC: 257773.

176045 Hamerlynck, E.P.; Huxman, T.E.; McAuliffe, J.R.; and Smith, S.D. 2004. "Carbon Isotope Discrimination and Foliar Nutrient Status of Larrea Tridentata (Creosote Bush) in Contrasting Mojave Desert Soils." *Oecologia, 138,* 210-215. New York, New York: Springer-Verlag. TIC: 257872.

177022 Hamerlynck, E.P.; McAuliffe, J.R.; and Smith, S.D. 2000. "Effects of Surface and Sub-Surface Soil Horizons on the Seasonal Performance of Larrea Tridentata (Creosotebush)." *Functional Ecology, 14,* 596-606. Malden, Massachusetts: Blackwell Publishing. TIC: 257772.

177046 Hamerlynck, E.P.; McAuliffe, J.R.; McDonald, E.V.; and Smith, S.D. 2002. "Ecological Responses of Two Mojave Desert Shrubs to Soil Horizon Development and Soil Water Dynamics." *Ecology, 83,* (3), 768-779. Washington, D.C.: Ecological Society of America. TIC: 258371.

177619 Hansen, D.J. and Ostler, W.K. 2003. *Rooting Characteristics of Vegetation Near Areas 3 and 5 Radioactive Waste Management Sites at the Nevada Test Site.* DOE/NV/11718-595. Las Vegas, Nevada: U.S. Department of Energy, National Nuclear Security Administration. ACC: MOL.20060712.0208.

177508 Hanson, C.L. 2001. "Long-Term Precipitation Database, Reynolds Creek Experimental Watershed, Idaho, United States." *Water Resources Research, 37,* (11), 2831-2834. Washington, D.C.: American Geophysical Union. ACC: MOL.20060712.0230.

177509 Hanson, C.L.; Marks, D.; and Van Vactor, S.S. 2001. "Long-Term Climate Database, Reynolds Creek Experimental Watershed, Idaho, United States." *Water Resources Research, 37,* (11), 2839-2841. Washington, D.C.: American Geophysical Union. ACC: MOL.20060712.0231.

176787 Hargreaves, G.H. and Allen, R.G. 2003. "History and Evaluation of Hargreaves Evapotranspiration Equation." *Journal of Irrigation and Drainage Engineering, 129,* (1), 53-63. Reston, Virginia: American Society of Civil Engineers. TIC: 258243.

177630 Harris, G.A. 1967. "Some Competitive Relationships Between Agropyron Spicatum and Bromus Tectorum." *Ecological Monographs, 37,* (2), 89-111. Ithaca, New York: Ecological Society of America. TIC: 258196.

176151 Hay, J.E. 1979. "Calculation of Monthly Mean Solar Radiation for Horizontal and Inclined Surfaces." *Solar Energy, 23,* 301-307. New York, New York: Pergamon Press. TIC: 258030.

176740 Helder, D.L. and Ruggles, T.A. 2004. "Landsat Thematic Mapper Reflective-Band Radiometric Artifacts." *IEEE Transactions on Geoscience and Remote Sensing, 42,* (12), 2704-2716. New York, New York: Institute of Electrical and Electronics Engineers. TIC: 258206.

100583 Hillel, D. 1980. *Applications of Soil Physics.* New York, New York: Academic Press. TIC: 217649.

178856 Hillel, D. 2004. *Introduction to Environmental Soil Physics.* New York, New York: Elsevier. TIC: 259102.

153709 Hofmann, L.L.; Guertal, W.R.; and Flint, A.L. 2000. *Development and Testing of Techniques to Obtain Infiltration Data for Unconsolidated Surficial Materials, Yucca Mountain Area, Nye County, Nevada.* Open-File Report 95-154. Denver, Colorado: U.S. Geological Survey. TIC: 249343.

178487 Hogan, J.F.; Phillips, F.M.; and Scanlon, B.R., eds. 2004. "Preface." In *Groundwater Recharge in a Desert Environment: The Southwestern United States,* Hogan, J.F.; Phillips, F.M.; and Scanlon, B.R., eds, *Water Science and Application 9.* Washington, D.C.: American Geophysical Union. TIC: 256760.

177996 Hood, E.; Williams, M.; and Cline, D. 1999. "Sublimation from a Seasonal Snowpack at a Continental, Mid-Latitude Alpine Site." *Hydrological Processes, 13,* 1781-1797. New York, New York: John Wiley & Sons. TIC: 258621.

174618 Horton, G.A. 1998. *Abbreviations and Acronyms, Appendices, and Selected References.* Part 2 of *Water Words Dictionary.* 8th Edition. Carson City, Nevada: Nevada Division of Water Planning. TIC: 241350.

180680 Howell, David M.and Runkle, Gene E. 2007. *Root Cause Analysis Report In Response to Condition Report 5223 Regarding Emails Suggesting Noncompliance with Quality Assurance Requirements.* Las Vegas, NV: U.S. DOE Office of Civilian Radioactive Waste Management. ACC: LLR.20070504.008.

178317 Howell, T.A.; Evett, S.R.; Tolk, J.A.; and Schneider, A.D. 2004. "Evapotranspiration of Full-, Deficit-Irrigated, and Dryland Cotton on the Northern Texas High Plains." *Journal of Irrigation and Drainage Engineering, 130,* (4), 277-285. Reston, Virginia: American Society of Civil Engineers. TIC: 258627.

177190 Howell, T.A.; Schneider, A.D.; and Jensen, M.E. 1991. "History of Lysimeter Design and Use for Evapotranspiration Measurements." *Lysimeters for Evapotranspiration and Environmental Measurements, Proceedings of the International Symposium on Lysimetry, Honolulu, Hawaii, July 23-25, 1991.* Allen, R.G.; Howell, T.A.; Pruitt, W.O.; Walter, I.A.; and Jensen, M.E., eds. Pages 1-9. New York, New York: American Society of Civil Engineers. TIC: 258304.

176738 Huete, A.R. and Liu, H.Q. 1994. "An Error and Sensitivity Analysis of the Atmospheric- and Soil-Correcting Variants of the NDVI for the MODIS-EOS." *IEEE Transactions on Geoscience and Remote Sensing, 32,* (4), 897-905. New York, New York: Institute of Electrical and Electronics Engineers. TIC: 258204.

177129 Hulbert, L.C. 1955. "Ecological Studies of Bromus Tectorum and Other Annual Bromegrasses." *Ecological Monographs, 25,* (2), 181-213. Washington, D.C.: Ecological Society of America. TIC: 258184.

176048 Hunsaker, D.J.; Pinter, Jr., P.J.; Barnes, E.M.; and Kimball, B.A. 2003. "Estimating Cotton Evapotranspiration Crop Coefficients with a Multispectral Vegetation Index." *Irrigation Science, 22,* 95-104. New York, New York: Springer-Verlag. TIC: 257868.

178529 Hunsaker, D.J.; Pinter, P.J., Jr.; and Cai, H. 2002. "Alfalfa Basal Crop Coefficients for FAO-56 Procedures in the Desert Regions of the Southwestern U.S.." *Transactions of the ASAE, 45,* (6), 1799-1815. St. Joseph, Michigan: American Society of Agricultural Engineers. TIC: 258938.

177302 Hunsaker, D.J.; Pinter, P.J., Jr.; and Kimball, B.A. 2005. "Wheat Basal Crop Coefficients Determined by Normalized Difference Vegetation Index." *Irrigation Science, 24,* 1-14. New York, New York: Springer-Verlag. TIC: 258499.

129944 Hunter, R. 1991. "Bromus Invasions on the Nevada Test Site: Present Status of B. Rubens and B. Tectorum with Notes on Their Relationship to Disturbance and Altitude." *Great Basin Naturalist, 51,* (2), 176-182. Provo, Utah: Brigham Young University. TIC: 245250.

177132 Huxman, T.E. and Smith, S.D. 2001. "Photosynthesis in an Invasive Grass and Native Forb at Elevated CO_2 During an El Niño Year in the Mojave Desert." *Oecologia, 128,* 193-201. Berlin, Germany: Springer-Verlag. TIC: 257774.

177133 Huxman, T.E.; Hamerlynck, E.P.; and Smith, S.D. 1999. "Reproductive Allocation and Seed Production in Bromus Madritensis Ssp. Rubens at Elevated Atmospheric CO_2." *Functional Ecology, 13,* 769-777. Malden, Massachusetts: Blackwell Publishing. TIC: 257771.

176861 Irmak, S.; Howell, T.A.; Allen, R.G.; Payero, J.O.; and Martin, D.L. 2005. "Standardized ASCE Penman-Monteith: Impact of Sum-of-Hourly vs. 24-Hour Timestep Computations at Reference Weather Station Sites." *Transactions of the ASAE, 48,* (3), 1063-1077. St. Joseph, Michigan: American Society of Agricultural Engineers. TIC: 258278.

177171 Jackson, R.B.; Banner, J.L.; Jobbagy, E.G.; Pockman, W.T.; and Wall, D.H. 2002. "Ecosystem Carbon Loss with Woody Plant Invasion of Grasslands." *Nature, 418,* (6898), 623-626. New York, New York: Nature Publishing Group. TIC: 258009.

177103 Jensen, D.T.; Hargreaves, G.H.; Temesgen, B.; and Allen, R.G. 1997. "Computation of ETo Under Nonideal Conditions." *Journal of Irrigation and Drainage Engineering, 123,* (5), 394-400. Reston, Virginia: American Society of Civil Engineers. TIC: 258407.

160001 Jensen, M.E.; Burman, R.D.; and Allen, R.G., eds. 1990. *Evapotranspiration and Irrigation Water Requirements.* ASCE Manuals and Reports on Engineering Practice No. 70. New York, New York: American Society of Civil Engineers. TIC: 246697.

176743 Ji, L. and Peters, A.J. 2003. "Assessing Vegetation Response to Drought in the Northern Great Plains Using Vegetation and Drought Indices." *Remote Sensing of Environment, 87,* 85-98. New York, New York: Elsevier. TIC: 258210.

176742 Justice, C.O.; Vermote, E.; Townshend, J.R.G.; Defries, R.; Roy, D.P.; Hall, D.K.; Salomonson, V.V.; Privette, J.L.; Riggs, G.; Strahler, A.; Wolfgang, L.; Myneni, R.B.; Knyazikhin, Y.; Running, S.W.; Nemani, R.R.; Wan, Z.; Huete, A.R.; van Leeuwen, W.; Wolfe, R.E.; Giglio, L.; Muller, J.-P.; Lewis, P.; and Barnsley, M.J. 1998. "The Moderate Resolution Imaging Spectroradiometer (MODIS): Land Remote Sensing for Global Change Research." *IEEE Transactions on Geoscience and Remote Sensing, 36,* (4), 1228-1249. New York, New York: Institute of Electrical and Electronics Engineers. TIC: 258208.

177998 Kattelmann, R. and Elder, K. 1991. "Hydrologic Characteristics and Water Balance of an Alpine Basin in the Sierra Nevada." *Water Resources Research, 27,* (7), 1553-1562. Washington, D.C.: American Geophysical Union. TIC: 258622.

176760 Kenea, N.H. 2001. "Influence of Desert Varnish on the Reflectance of Gossans in the Context of Landsat TM Data, Southern Red Sea Hills, Sudan." *International Journal of Remote Sensing, 22,* (10), 1879-1894. New York, New York: Taylor & Francis. TIC: 258230.

176823 Kerr, Y.H.; Imbernon, J.; Dedieu, G.; Hautecoeur, O.; Lagouarde, J.P.; and Seguin, B. 1989. "NOAA AVHRR and its Uses for Rainfall and Evapotranspiration Monitoring." *International Journal of Remote Sensing, 10,* (4 and 5), 847-854. Philadelphia, Pennsylvania: Taylor & Francis. TIC: 258269.

177191 Kirkham, R.R.; Rockhold, M.L.; Gee, G.W.; Fayer, M.J.; and Campbell, M.D. 1991. "Lysimeters: Data Acquisition and Analysis." *Lysimeters for Evapotranspiration and Environmental Measurements, Proceedings of the International Symposium on Lysimetry, Honolulu, Hawaii, July 23-25, 1991.* Allen, R.G.; Howell, T.A.; Pruitt, W.O.; Walter, I.A.; and Jensen, M.E., eds. Pages 362-370. New York, New York: American Society of Civil Engineers. TIC: 258304.

176152 Klein, S.A. 1977. "Calculation of Monthly Average Insolation on Tilted Surfaces." *Solar Energy, 19,* 325-329. New York, New York: Pergamon Press. TIC: 258029.

176484 Klein, S.A. and Theilacker, J.C. 1981. "An Algorithm for Calculating Monthly-Average Radiation on Inclined Surfaces." *Journal of Solar Energy Engineering, 103,* 29-33. New York, New York: American Society of Mechanical Engineers. TIC: 258097.

177134 Klemmedson, J.O. and Smith, J.G. 1964. "Cheatgrass (Bromus Tectorum L.)." *The Botanical Review, XXX,* 226-262. Bronx, New York: New York Botanical Garden. TIC: 258182.

176757 Kustas, W.P.; Perry, E.M.; Doraiswamy, P.C.; and Moran, M.S. 1994. "Using Satellite Remote Sensing to Extrapolate Evapotranspiration Estimates in Time and Space Over a Semiarid Rangeland Basin." *Remote Sensing of Environment, 49,* 275-286. New York, New York: Elsevier. TIC: 258221.

158511 LeCain, G.D.; Lu, N.; and Kurzmack, M. 2002. *Use of Temperature, Pressure, and Water Potential Data to Estimate Infiltration and Monitor Percolation in Pagany Wash Associated with the Winter of 1997–98 El Niño Precipitation, Yucca Mountain, Nevada.* Water Resources Investigations Report 02-4035. Denver, Colorado: U.S. Geological Survey. TIC: 252641.

177926 Leffler, J.A.; Ivans, C.Y.; Ryel, R.J.; and Caldwell, M.M. 2004. "Gas Exchange and Growth Responses of the Desert Shrubs Artemisia Tridentata and Chrysothamnus Nauseosus to Shallow- Vs. Deep-Soil Water in a Glasshouse Experiment." *Environmental and Experimental Botany, 51,* 9-19. New York, New York: Elsevier. TIC: 258768.

178535 Lei, S.A. 1999. "Gradient Analysis of Pinyon-Juniper Woodland in a Southern Nevada Mountain Range." *USDA Forest Service Proceedings, Odgen, Utah. RMRS-P-9,* 64-68. Washington, D.C.: U.S. Department of Agriculture, Forest Service. ACC: MOL.20061214.0118.

163183 Levitt, D.G.; Lohrstorfer, C.F.; Sully, M.J.; and Ginanni, J.M. 1996. "An Arid Zone Lysimeter Facility for Performance Assessment and Closure Investigations at the Nevada Test Site." *HLW, LLW, Mixed Wastes and Environmental Restoration — Working Towards a Cleaner Environment, WM '96, Proceedings, February 25-29, 1996, Tucson, Arizona.* Tucson, Arizona: Laser Options. TIC: 254421.

177521 Levitt, D.G.; Sully, M.J.; Dozier, B.L.; and Lohrstorfer, C.F. 1999. "Determining the Performance of an Arid Zone Radioactive Waste Site Through Site Characterization, Modeling and Monitoring." *HLW, LLW, Mixed Wastes and Environmental Restoration — Working Towards a Cleaner Environment, WM'99, Proceedings, February 28-March 4, 1999, Tucson, Arizona.* Tucson, Arizona: WM Symposia. TIC: 250888.

177166 Li-Cor 1989. *LI-1600 Steady State Porometer Instruction Manual, Revision 6.* Lincoln, Nebraska: Li-Cor. TIC: 258419.

100589 Lichty, R.W. and McKinley, P.W. 1995. *Estimates of Ground-Water Recharge Rates for Two Small Basins in Central Nevada.* Water-Resources Investigations Report 94-4104. Denver, Colorado: U.S. Geological Survey. ACC: MOL.19960924.0524.

178081 Lide, D.R., ed. 2006. *CRC Handbook of Chemistry and Physics.* 87th Edition. Boca Raton, Florida: CRC Press. TIC: 258634.

178313 Liepert, B.G. and Romanou, A. 2005. "Global Dimming and Brightening and the Water Cycle." *Bulletin of the American Meteorological Society, 86,* (5), 622-623. Boston, Massachusetts: American Meteorological Society. TIC: 258566.

177142 Link, S.O.; Gee, G.W.; and Downs, J.L. 1990. "The Effect of Water Stress on Phenological and Ecophysiological Characteristics of Cheatgrass and Sandberg's Bluegrass." *Journal of Range Management, 43,* (6), 506-513. Denver, Colorado: Society for Range Management. TIC: 258327.

176739 Liu, H.Q. and Huete, A. 1995. "A Feedback Based Modification of the NDVI to Minimize Canopy Background and Atmospheric Noise." *IEEE Transactions on Geoscience and Remote Sensing, 33,* (2), 457-465. New York, New York: Institute of Electrical and Electronics Engineers. TIC: 258205.

176821 Lo Seen Chong, D.; Mougin, E.; and Gastellu-Etchegorry, J.P. 1993. "Relating the Global Vegetation Index to Net Primary Productivity and Actual Evapotranspiration Over Africa." *International Journal of Remote Sensing, 14,* (8), 1517-1546. Bristol, Pennsylvania: Taylor & Francis. TIC: 258271.

176789 Lookingbill, T.R. and Urban, D.L. 2003. "Spatial Estimation of Air Temperature Differences for Landscape-Scale Studies in Montane Environments." *Agricultural and Forest Meteorology, 114,* 141-151. New York, New York: Elsevier. TIC: 258240.

154273 Looney, B.B. and Falta, R.W., eds. 2000. *Vadose Zone, Science and Technology Solutions.* Two volumes. Columbia, Ohio: Battelle Press. TIC: 249256.

175964 Lopes, T.J. and Evetts, D.M. 2004. *Ground-Water Pumpage and Artificial Recharge Estimates for Calendar Year 2000 and Average Annual Natural Recharge and Interbasin Flow by Hydrographic Area, Nevada.* Scientific Investigations Report 2004-5239. Carson City, Nevada: U.S. Geological Service. ACC: MOL.20060116.0023.

177164 Mack, R.N. 1981. "Invasion of Bromus Tectorum L. into Western North America: An Ecological Chronicle." *Agro-Ecosystems, 7,* 145-165. Amsterdam, The Netherlands: Elsevier. TIC: 258181.

177141 Mack, R.N. and Pyke, D.A. 1983. "The Demography of Bromus Tectorum: Variation in Time and Space." *Journal of Ecology, 71,* 69-93. London, England: British Ecological Society. TIC: 258422.

178540 Maher, K.; DePaolo, D.J.; Conrad, M.E.; and Serne, R.J. 2003. "Vadose Zone Infiltration Rate at Hanford, Washington, Inferred from Sr Isotope Measurements." *Water Resources Research, 39,* (8), SBH 3-1-SBH 3-14. Washington, D.C.: American Geophysical Union. TIC: 259095.

125317 Maidment, D.R., ed. 1993. *Handbook of Hydrology.* New York, New York: McGraw-Hill. TIC: 236568.

177362 Markham, B.L. and Barker, J.L. 1987. "Thematic Mapper Bandpass Solar Exoatmospheric Irradiances." *International Journal of Remote Sensing, 8,* (3), 517-523. Elmont, New York: Taylor & Francis. TIC: 258864.

177512 Marks, D. 2001. "Introduction to Special Section: Reynolds Creek Experimental Watershed." *Water Resources Research, 37,* (11), 2817. Washington, D.C.: American Geophysical Union. ACC: MOL.20060712.0232.

177504 Marks, D.; Cooley, K.R.; Robertson, D.C.; and Winstral, A. 2001. "Long-Term Snow Database, Reynolds Creek Experimental Watershed, Idaho, United States." *Water Resources Research, 37,* (11), 2835-2838. Washington, D.C: American Geophysical Union. ACC: MOL.20060712.0227.

178523 Mata-González, R.; McLendon, T.; and Martin, D.W. 2005. "The Inappropriate Use of Crop Transpiration Coefficient (K_c) to Estimate Evapotranspiration in Arid Ecosystems: A Review." *Arid Land Research and Management, 19,* 285-295. Philadelphia, Pennsylvania: Taylor & Francis. TIC: 258847.

177370 Maurer, D.K. and Berger, D.L. 1997. *Subsurface Flow and Water Yield from Watersheds Tributary to Eagle Valley Hydrographic Area, West-Central Nevada.* Water-Resources Investigations Report 97-4191. Carson City, Nevada: U.S. Geological Survey. ACC: MOL.20060808.0017.

100598 Maxey, G.B. and Eakin, T.E. 1950. *Ground Water in White River Valley, White Pine, Nye, and Lincoln Counties, Nevada.* Water Resources Bulletin No. 8. Carson City, Nevada: State of Nevada, Office of the State Engineer. TIC: 216819.

177910 McElroy, D.L. 1993. *Soil Moisture Monitoring Results at the Radioactive Waste Management Complex of the Idaho National Engineering Laboratory, FY-1993.* EGG-WM-11066. Idaho Falls, Idaho: EG&G Idaho, Idaho National Engineering Laboratory. ACC: MOL.20061016.0249.

178204 MDH Engineered Solutions 2003. *Evaluation of Computer Models for Predicting the Fate and Transport of Salt in Soil and Groundwater, Phase I Report.* Pub. No: T/403. Edmonton, Alberta, Canada: Alberta Environment, Science and Standards Branch. TIC: 258784.

176887 Moreno, J.M. and Oechel, W.C., eds. 1995. *Global Change and Mediterranean-Type Ecosystems.* Ecological Studies, Vol. 117, Analysis and Synthesis. Lange, O.L. and Mooney, H.A., eds. New York, New York: Springer. TIC: 258254.

178316 Mutziger, A.J.; Burt, C.M.; Howes, D.J.; and Allen, R.G. 2005. "Comparison of Measured and FAO-56 Modeled Evaporation from Bare Soil." *Journal of Irrigation and Drainage Engineering, 131,* (1), 59-72. Reston, Virginia: American Society of Civil Engineers. TIC: 258629.

177143 Naumburg, E.; Housman, D.C.; Huxman T.E.; Charlet, T.N.; Loik, M.E.; and Smith, S.D. 2003. "Photosynthetic Responses of Mojave Desert Shrubs to Free Air CO_2 Enrichment are Greatest During Wet Years." *Global Change Biology, 9,* 276-285. Malden, Massachusetts: Blackwell Science. TIC: 258423.

174673 Newman, D. 1992. *Element Stewardship Abstract for Bromus Rubens.* Arlington, Virginia: The Nature Conservancy. TIC: 257691.

178863 Nichols, W.D. 2000. *Regional Ground-Water Evapotranspiration and Ground-Water Budgets, Great Basin, Nevada.* U.S. Geological Survey Professional Paper 1628. Reston, Virginia: U.S. Geological Survey. ACC: LLR.20070213.0076.

178674 NOAA (National Oceanic and Atmospheric Administration) 2002. *Monthly Station Normals of Temperature, Precipitation, and Heating and Cooling Degree Days 1971-2000, 02 Arizona.* Climatography of the United States No. 81. Asheville, North Carolina: National Oceanic and Atomspheric Administration. ACC: MOL.20070125.0051.

178676 NOAA 2002. *Monthly Station Normals of Temperature, Precipitation, and Heating and Cooling Degree Days 1971-2000, 26 Nevada.* Climatography of the United States No. 81. Asheville, North Carolina: National Oceanic and Atmospheric Administration. ACC: MOL.20070125.0053.

178675 NOAA 2002. *Monthly Station Normals of Temperature, Precipitation, and Heating and Cooling Degree Days 1971-2000, 29 New Mexico.* Climatography of the United States No. 81. Asheville, North Carolina: National Oceanic and Atmospheric Administration. ACC: MOL.20070125.0052.

178677 NOAA 2002. *Monthly Station Normals of Temperature, Precipitation, and Heating and Cooling Degree Days 1971-2000, 42 Utah.* Climatography of the United States No. 81. Asheville, North Carolina: National Oceanic and Atmospheric Administration. ACC: MOL.20070125.0054.

178673 NOAA 2002. *Monthly Station Normals of Temperature, Precipitation, and Heating and Cooling Degree Days 1971-2000, 45 Washington.* Climatography of the United States No. 81. Asheville, North Carolina: National Oceanic and Atmospheric Administration. ACC: MOL.20070125.0050.

160500 Nobel, P.S. 1983. "Plants and Fluxes." *Biophysical Plant Physiology and Ecology*. Pages 461-523. New York, New York: W.H. Freeman and Company. TIC: 252952.

159953 Nobel, P.S. 1983. "Temperature—Energy Budgets." *Biophysical Plant Physiology and Ecology*. Pages 339-386. New York, New York: W.H. Freeman and Company. TIC: 253519.

163274 NRC (U.S. Nuclear Regulatory Commission) 2003. *Yucca Mountain Review Plan, Final Report.* NUREG-1804, Rev. 2. Washington, D.C.: U.S. Nuclear Regulatory Commission, Office of Nuclear Material Safety and Safeguards. TIC: 254568.

102160 O'Farrell, T.P. and Collins, E. 1984. *1983 Biotic Studies of Yucca Mountain, Nevada Test Site, Nye County, Nevada.* EGG 10282-2031 S-764-R. Goleta, California: EG&G Energy Measurements. ACC: HQS.19880517.1810.

176483 Orgill, J.F. and Hollands, K.G.T. 1977. "Correlation Equation for Hourly Diffuse Radiation on a Horizontal Surface." *Solar Energy, 19,* 357-359. New York, New York: Pergamon Press. TIC: 258101.

177161 Pataki, D.E.; Huxman, T.E.; Jordan, D.N.; Zitzer, S.F.; Coleman, J.S.; Smith, S.D.; Nowak, R.S.; and Seemann, J.R. 2000. "Water Use of Two Mojave Desert Shrubs Under Elevated CO_2." *Global Change Biology, 6,* 889-897. Malden, Massachusetts: Blackwell Science. TIC: 258767.

177091 Phillips, D.L.; Dolph, J.; and Marks, D. 1992. "A Comparison of Geostatistical Procedures for Spatial Analysis of Precipitation in Mountainous Terrain." *Agricultural and Forest Meteorology, 58,* 119-141. Amsterdam, The Netherlands: Elsevier. TIC: 258405.

177503 Pierson, F.B.; Slaughter, C.W.; and Cram, Z.K. 2001. "Long-Term Stream Discharge and Suspended-Sediment Database, Reynolds Creek Experimental Watershed, Idaho, United States." *Water Resources Research, 37,* (11), 2857-2861. Washington, D.C.: American Geophysical Union. ACC: MOL.20060712.0226.

178131 Ravi, V. and Williams, J.R. 1998. *Estimation of Infiltration Rate In the Vadose Zone: Compilation of Simple Mathematical Models.* EPA/600/R-97/128a. Volume 1. Cincinnati, Ohio: U.S. Environmental Protection Agency. ACC: MOL.20061030.0075.

177336 Ray, S.S. and Dadhwal, V.K. 2001. "Estimation of Crop Evapotranspiration of Irrigation Command Area Using Remote Sensing and GIS." *Agricultural Water Management, 49,* 239-249. New York, New York: Elsevier. TIC: 258486.

176480 Reindl, D.T.; Beckman, W.A.; and Duffie, J.A. 1990. "Evaluation of Hourly Tilted Surface Radiation Models." *Solar Energy, 45,* (1), 9-17. New York, New York: Pergamon Press. TIC: 258102.

103450 Resource Concepts 1989. *Soil Survey of Yucca Mountain Study Area, Nye County, Nevada.* NWPO EV 003-89. Carson City, Nevada: Resource Concepts. TIC: 206227.

176482 Revfeim, K.J.A. 1976. "Solar Radiation at a Site of Known Orientation on the Earth's Surface." *Journal of Applied Meteorology, 15,* 651-656. Boston, Massachusetts: American Meteorological Society. TIC: 258104.

177165 Rice, K.J.; Black, R.A.; Radamaker, G.; and Evans, R.D. 1992. "Photosynthesis, Growth, and Biomass Allocation in Habitat Ecotypes of Cheatgrass (Bromus Tectorum)." *Functional Ecology, 6,* 32-40. Malden, Massachusetts: Blackwell Publishing. TIC: 258322.

177927 Richards, J.H. and Caldwell, M.M. 1987. "Hydraulic Lift: Substantial Nocturnal Water Transport Between Soil Layers by Artemisia Tridentata Roots." *Oecologia, 73,* 486-489. Berlin, Germany: Springer-Verlag. TIC: 258563.

177635 Rickard, W.H. 1985. "Shoot Production and Mineral Nutrient Assimilation in Cheatgrass Communities." *Northwest Science, 59,* (3), 169-179. Pullman, Washington: Washington State University Press. TIC: 258186.

176758 Rivard, B.; Arvidson, R.E.; Duncan, I.J.; Sultan, M.; and El Kaliouby, B. 1992. "Varnish, Sediment, and Rock Controls on Spectral Reflectance of Outcrops in Arid Regions." *Geology, 20,* 295-298. Boulder, Colorado: Geological Society of America. TIC: 258227.

176741 Rivard, B.; Petroy, S.B.; and Miller, J.R. 1993. "Measured Effects of Desert Varnish on the Mid-Infrared Spectra of Weathered Rocks as an Aid to TIMS Imagery Interpretation." *IEEE Transactions on Geoscience and Remote Sensing, 31,* (1), 284-291. New York, New York: Institute of Electrical and Electronics Engineers. TIC: 258207.

177738 Rodríguez, E.; Morris, C.S.; Belz, J.E.; Chapin, E.C.; Martin, J.M.; Daffer, W.; and Hensley, S. 2005. *An Assessment of the SRTM Topographic Products.* D-31639. Pasadena, California: Jet Propulsion Laboratory. ACC: MOL.20061011.0062.

178583 Rose, C.W. 1968. "Evaporation from Bare Soil Under High Radiation Conditions." Chapter 7 of *Transactions.* Volume 1. Pages 57-66. New York, New York: Elsevier. TIC: 258919.

177526 Rosenberg, N.J.; Blad, B.L.; and Verma, S.B. 1983. *Microclimate, The Biological Environment.* 2nd Edition. New York, New York: John Wiley & Sons. TIC: 222878.

178534 Roundy, B.A. and Vernon, J.L. 1999. "Watershed Values and Conditions Associated with Pinyon-Juniper Communities." *USDA Forest Service Proceedings, Odgen, Utah. RMRS-P-9,* 172-187. Washington, D.C.: U.S. Department of Agriculture, Forest Service. ACC: MOL.20061214.0117.

177246 Rouse, J.W., Jr.; Haas, R.H.; Schell, J.A.; and Deering, D.W. 1974. "Monitoring Vegetation Systems in the Great Plains with ERTS." *Third Earth Resources Technology Satellite-1 Symposium, Volume I: Technical Presentations, Section A, Proceedings of a Symposium held by Goddard Space Flight Center, Washington, D.C., December 10-14, 1973.* Freden, S.C. and Mercanti, E.P., eds. Paper A 20. Pages 309-317. Washington, D.C.: National Aeronautics and Space Administration. ACC: MOL.20060501.0105.

103614 Rundel, P.W. and Gibson, A.C. 1996. *Ecological Communities and Processes in a Mojave Desert Ecosystem: Rock Valley, Nevada.* New York, New York: Cambridge University Press. TIC: 223005.

128001 Rundel, P.W. and Nobel, P.S. 1991. "Structure and Function in Desert Root Systems." *Plant Root Growth, An Ecological Perspective, Special Publication Number 10,* 349-378. London, England: Blackwell Scientific Publications. TIC: 242299.

176819 Running, S.W. and Nemani, R.R. 1991. "Regional Hydrologic and Carbon Balance Responses of Forests Resulting from Potential Climate Change." *Climatic Change, 19,* (4), 349-368. Dordrecht, The Netherlands: Kluwer Academic Publishers. TIC: 258228.

177632 Ryel, R.J.; Caldwell, M.M.; Leffler, A.J.; and Yoder, C.K. 2003. "Rapid Soil Moisture Recharge to Depth by Roots in a Stand of Artemisia Tridentata." *Ecology, 84,* (3), 757-764. Washington, D.C.: Ecological Society of America. TIC: 258010.

176569 Sanchez, A. 2006. Conducting Confirmatory Field Observations for Special Infiltration Project [partial submittal]. Scientific Notebook SN-M&O-SCI-053-V1. Pages 1-83. ACC: MOL.20060306.0186.

107233 Scanlon, B.R. 1991. "Evaluation of Moisture Flux from Chloride Data in Desert Soils." *Journal of Hydrology, 128,* 137-156. Amsterdam, The Netherlands: Elsevier. TIC: 224126.

177213 Scanlon, B.R.; Christman, M.; Reedy, R.C.; Porro, I.; Simunek, J.; and Flerchinger, G.N. 2002. "Intercode Comparisons for Simulating Water Balance of Surficial Sediments in Semiarid Regions." *Water Resources Research, 38,* (12), 59/1-59/16. Washington, D.C.: American Geophysical Union. TIC: 255363.

178109 Scanlon, B.R.; Keese, K.; Reedy, R.C.; Simunek, J.; and Andraski, B.J. 2003. "Variations in Flow and Transport in Thick Desert Vadose Zones in Response to Paleoclimate Forcing (0-90 kyr): Field Measurements, Modeling, and Uncertainties." *Water Resources Research, 39,* (7), 3/1-3/6. Washington, D.C.: American Geophysical Union. TIC: 258648.

177852 Scanlon, B.R.; Langford, R.P.; and Goldsmith, R.S. 1999. "Relationship Between Geomorphic Settings and Unsaturated Flow in an Arid Setting." *Water Resources Research, 35,* (4), 983-999. Washington, D.C.: American Geophysical Union. TIC: 252295.

175977 Scanlon, B.R.; Levitt, D.G.; Reedy, R.C.; Keese, K.E.; and Sully, M.J. 2005. "Ecological Controls on Water-Cycle Response to Climate Variability in Deserts." *Proceedings of the National Academy of Sciences of the United States of America, 102,* (17), 6033-6038. Washington, D.C.: National Academy of Sciences of the USA. TIC: 257888.

142228 Scanlon, B.R.; Tyler, S.W.; and Wierenga, P.J. 1997. "Hydrologic Issues in Arid, Unsaturated Systems and Implications for Contaminant Transport." *Reviews of Geophysics, 35,* (4), 461-490. Washington, D.C.: American Geophysical Union. TIC: 246881.

177638 Schenk, H.J. and Jackson, R.B. 2002. "Rooting Depths, Lateral Root Spreads and Below-Ground/Above-Ground Allometries of Plants in Water-Limited Ecosystems." *Journal of Ecology, 90,* 480-494. Oxford, England: Blackwell Publishing. TIC: 257985.

178754 Schroeder, P.R. and Peyton, R.L. 1987. *Verification of the Lateral Drainage Component of the HELP Model Using Physical Models.* EPA/600/2-87/049. Cincinnati, Ohio: U.S. Environmental Protection Agency, Hazardous Waste Engineering Research Laboratory. ACC: MOL.20070126.0113.

178857 Schroeder, P.R. and Peyton, R.L. 1988. *Verification of the Hydrologic Evaluation of Landfill Performance (HELP) Model Using Field Data.* EPA/600/S-2-87/050. Washington, D.C.: U.S. Government Printing Office. ACC: LLR.20070213.0075.

178136 Schroeder, P.R.; Lloyd, C.M.; Zappi, P.A.; and Aziz, N.M. 1994. *The Hydrologic Evaluation of Landfill Performance (HELP) Model, User's Guide for Version 3.* EPA/600/R-94/168a. Washington, D.C.: U.S. Environmental Protection Agency, Office of Research and Development. ACC: MOL.20060831.0163.

178065 Schultz, B. and McAdoo, K. 2002. *Common Sagebrush in Nevada.* Special Publication SP-02-02. Reno, Nevada: University of Nevada, Reno, Cooperative Extension. TIC: 258542.

104181 Scott, R.B. and Bonk, J. 1984. *Preliminary Geologic Map of Yucca Mountain, Nye County, Nevada, with Geologic Sections.* Open-File Report 84-494. Denver, Colorado: U.S. Geological Survey. ACC: HQS.19880517.1443.

177853 Scott, R.L.; Shuttleworth, W.J.; Keefer, T.O.; and Warrick, A.W. 2000. "Modeling Multiyear Observations of Soil Moisture Recharge in the Semiarid American Southwest." *Water Resource Research, 36,* (8), 2233-2247. Washington, D.C.: American Geophysical Union. TIC: 252313.

176764 Seevers, P.M. and Ottmann, R.W. 1994. "Evapotranspiration Estimation Using a Normalized Difference Vegetation Index Transformation of Satellite Data." *Hydrological Sciences Journal, 39,* (4), 333-345. Wallingford, Oxfordshire, England: International Association of Hydrological Sciences. TIC: 258233.

176824 Sellers, P.J.; Berry, J.A.; Collatz, G.J.; Field, C.B.; and Hall, F.G. 1992. "Canopy Reflectance, Photosynthesis, and Transpiration. III. A Reanalysis Using Improved Leaf Models and a New Canopy Integration Scheme." *Remote Sensing of Environment, 42,* (3), 187-216. New York, New York: Elsevier. TIC: 258268.

177480 Sevruk, B. 1982. *Methods of Correction for Systematic Error in Point Precipitation Measurement for Operational Use.* Operational Hydrology Report No. 21. WMO - No. 589. Geneva, Switzerland: World Meteorological Organization. TIC: 258537.

177501 Seyfried, M.; Harris, R.; Marks, D.; and Jacob, B. 2001. "Geographic Database, Reynolds Creek Experimental Watershed, Idaho, United States." *Water Resources Research, 37,* (11), 2825-2829. Washington, D.C.: American Geophysical Union. ACC: MOL.20060712.0225.

177505 Seyfried, M.S.; Flerchinger, G.N.; Murdock, M.D.; Hanson, C.L.; and Van Vactor, S. 2001. "Long-Term Soil Temperature Database, Reynolds Creek Experimental Watershed, Idaho, United States." *Water Resources Research, 37,* (11), 2843-2846. Washington, D.C.: American Geophysical Union. ACC: MOL.20060712.0228.

177515 Seyfried, M.S.; Hanson, C.L.; Murdock, M.D.; and Van Vactor, S. 2001. "Long-Term Lysimeter Database, Reynolds Creek Experimental Watershed, Idaho, United States." *Water Resources Research, 37,* (11), 2853-2856. Washington, D.C.: American Geophysical Union. ACC: MOL.20060821.0215.

177506 Seyfried, M.S.; Murdock, M.D.; Hanson, C.L.; Flerchinger, G.N.; and Van Vactor, S. 2001. "Long-Term Soil Water Content Database, Reynolds Creek Experimental Watershed, Idaho, United States." *Water Resources Research, 37,* (11), 2847-2851. Washington, D.C.: American Geophysical Union. ACC: MOL.20060712.0229.

178060 Seyfried, M.S.; Schwinning, S.; Walvoord, M.A.; Pockman, W.T.; Newman, B.D.; Jackson, R.B.; and Phillips, F.M. 2005. "Ecohydrological Control of Deep Drainage in Arid and Semiarid Regions." *Ecology, 86,* (2), 277-287. Washington, D.C.: Ecological Society of America. TIC: 258561.

178000 Shurbaji, A.-R. and Campbell, A.R. 1997. "Study of Evaporation and Recharge in Desert Soil Using Environmental Tracers, New Mexico, USA." *Environmental Geology, 29,* (3/4), 147-151. New York, New York: Springer-Verlag. TIC: 258630.

150228 Slate, J.L.; Berry, M.E.; Rowley, P.D.; Fridrich, C.J.; Morgan, K.S.; Workman, J.B.; Young, O.D.; Dixon, G.L.; Williams, V.S.; McKee, E.H.; Ponce, D.A.; Hildenbrand, T.G.; Swadley, W C; Lundstrom, S.C.; Ekren, E.B.; Warren, R.G.; Cole, J.C.; Fleck, R.J.; Lanphere, M.A.; Sawyer, D.A.; Minor, S.A.; Grunwald, D.J.; Laczniak, R.J.; Menges, C.M.; Yount, J.C.; Jayko, A.S.; Mankinen, E.A.; Davidson, J.G.; Morin, R.L.; and Blakely, R.J. 2000. *Digital Geologic Map of the Nevada Test Site and Vicinity, Nye, Lincoln and Clark Counties, Nevada, and Inyo County, California, Revision 4; Digital Aeromagnetic Map of the Nevada Test Site and Vicinity, Nye, Lincoln, and Clark Counties, Nevada, and Inyo County, California; and Digital Isostatic Gravity Map of the Nevada Test Site and Vicinity, Nye, Lincoln, and Clark Counties, Nevada, and Inyo County, California.* Open-File Report 99-554—A, —B, and —C. Denver, Colorado: U.S. Geological Survey. TIC: 248049; 251985; 251981.

177354 Slaughter, C.W.; Marks, D.; Flerchinger, G.N.; Van Vactor, S.S.; and Burgess, M. 2001. "Thirty-Five Years of Research Data Collection at the Reynolds Creek Experimental Watershed, Idaho, United States." *Water Resources Research, 37,* (11), 2819–2823. Washington, D.C.: American Geophysical Union. TIC: 258491.

177358 Smith, B. and Sandwell, D. 2003. "Accuracy and Resolution of Shuttle Radar Topography Mission Data." *Geophysical Research Letters, 30,* (9), 20-1-20-4. Washington, D.C.: American Geophysical Union. TIC: 258765.

179904 Smith, R.B. 2004. "Mountain Meteorology and Regional Climates." Chapter 9 of *Atmospheric Turbulence and Mesoscale Meteorology: Scientific Research Inspired by Doug Lilly.* Fedorovich, E.; Rotunno, R.; and Stevens, B., eds. Pages 193-222. New York, New York: Cambridge University Press. TIC: 259247.

103628 Smith, S.D.; Herr, C.A.; Leary, K.L.; and Piorkowski, J.M. 1995. "Soil-Plant Water Relations in a Mojave Desert Mixed Shrub Community: A Comparison of Three Geomorphic Surfaces." *Journal of Arid Environments, 29,* (3), 339-351. New York, New York: Academic Press. TIC: 240834.

103636 Smith, S.D.; Monson, R.K.; and Anderson, J.E. 1997. *Physiological Ecology of North American Desert Plants.* New York, New York: Springer-Verlag. TIC: 242260.

177081 SNL (Sandia National Laboratories) 2006. *Data Analysis for Infiltration Modeling: Extracted Weather Station Data Used to Represent Present-Day and Potential Future Climate Conditions in the Vicinity of Yucca Mountain.* ANL-MGR-MD-000015 REV 00. Las Vegas, Nevada: Sandia National Laboratories. ACC: DOC.20070109.0002.

176745 Song, C.; Woodcock, C.E.; Seto, K.C.; ax Lenney, M.; and Macomber, S.A. 2001. "Classification and Change Detection Using Landsat TM Data: When and How to Correct Atmospheric Effects?" *Remote Sensing of Environment, 75,* 230-244. New York, New York: Elsevier. TIC: 258212.

176751 Spatz, D.M. and Taranik, J.V. 1989. "Regional Analysis of Tertiary Volcanic Calderas (Western U.S.) Using Landsat Thematic Mapper Imagery." *Remote Sensing of Environment, 28,* 257-272. New York, New York: Elsevier. TIC: 258217.

177281 Stephens, D.B. and Knowlton, R., Jr. 1986. "Soil Water Movement and Recharge Through Sand at a Semiarid Site in New Mexico." *Water Resources Research, 22,* (6), 881-889. Washington, D.C.: American Geophysical Union. TIC: 258458.

177146 Stewart, G. and Hull, A.C. 1949. "Cheatgrass (Bromus Tectorum L.) - An Ecologic Intruder in Southern Idaho." *Ecology, 30,* (1), 58-74. Ogden, Utah: Ecological Society of America, Duke University Press. TIC: 258421.

176705 Stothoff, S.A.; Or, D.; Groeneveld, D.P.; and Jones, S.B. 1999. "The Effect of Vegetation on Infiltration in Shallow Soils Underlain by Fissured Bedrock." *Journal of Hydrology, 218,* 169-190. New York, New York: Elsevier. TIC: 257887.

177928 Sturges, D.L. and Trlica, M.J. 1978. "Root Weights and Carbohydrate Reserves of Big Sagebrush." *Ecology, 59,* (6), 1282-1285. Tempe, Arizona: Ecological Society of America. TIC: 258560.

106958 Sweetkind, D.S.; Verbeek, E.R.; Geslin, J.K.; and Moyer, T.C. 1995. *Fracture Character of the Paintbrush Tuff Nonwelded Hydrologic Unit, Yucca Mountain, Nevada.* Administrative Report. Denver, Colorado: U.S. Geological Survey. ACC: MOL.19960311.0125.

106959 Sweetkind, D.S.; Verbeek, E.R.; Singer, F.R.; Byers, F.M., Jr.; and Martin, L.G. 1995. *Surface Fracture Network at Pavement P2001, Fran Ridge, Near Yucca Mountain, Nye County, Nevada, Draft.* Administrative Report. Denver, Colorado: U.S. Geological Survey. ACC: MOL.19960603.0119.

176735 Szilagyi, J. 2000. "Can a Vegetation Index Derived from Remote Sensing be Indicative of Areal Transpiration?" *Ecological Modelling.* 127. 65-79. New York, New York: Elsevier. TIC: 258201.

176840 Szilagyi, J. 2002. "Vegetation Indices to Aid Areal Evapotranspiration Estimations." *Journal of Hydrologic Engineering, 7,* (5), 368-372. Reston, Virginia: American Society of Civil Engineers. TIC: 258267.

176839 Szilagyi, J.; Rundquist, D.C.; Gosselin, D.C.; and Parlange, M.B. 1998. "NDVI Relationship to Monthly Evaporation." *Geophysical Research Letters, 25,* (10), 1753-1756. Washington, D.C.: American Geophysical Union. TIC: 258266.

177653 Tasumi, M.; Allen, R.G.; Trezza, R.; and Wright, J.L. 2005. "Satellite-Based Energy Balance to Assess Within-Population Variance of Crop Coefficient Curves." *Journal of Irrigation and Drainage Engineering, 131,* (1), 94-109. Reston, Virginia: American Society of Civil Engineers. TIC: 258519.

177620 Tausch, R.J.; Wigand, P.E.; and Burkhardt, J.W. 1993. "Viewpoint: Plant Community Thresholds, Multiple Steady States, and Multiple Successional Pathways: Legacy of the Quaternary?." *Journal of Range Management, 46,* (5), 439-447. Wheat Ridge, Colorado: Society for Range Management. TIC: 258420.

178312 Temesgen, B.; Allen, R.G.; and Jensen, D.T. 1999. "Adjusting Temperature Parameters to Reflect Well-Watered Conditions." *Journal of Irrigation and Drainage Engineering, 125,* (1), 26-33. New York, New York: American Society of Civil Engineers. TIC: 258490.

177727 Thomas, J.M.; Carlton, S.M.; and Hines, L.B. 1989. *Ground-Water Hydrology and Simulated Effects of Development in Smith Creek Valley, a Hydrologically Closed Basin in Lander County, Nevada.* U.S. Geological Survey Professional Paper 1409-E. Denver, Colorado: U.S. Geological Survey. ACC: MOL.20061115.0002.

109462 Thompson, R.S.; Anderson, K.H.; and Bartlein, P.J. 1999. *Atlas of Relations Between Climatic Parameters and Distributions of Important Trees and Shrubs in North America - Introduction and Conifers.* Professional Paper 1650-A. Washington, D.C.: U.S. Geological Survey. TIC: 245909.

177641 Tirmenstein, D. 1999. "Artemisia Tridentata Spp. Tridentata." Washington, D.C.: U.S. Department of Agriculture, Forest Service. Accessed September 5, 2006. ACC: MOL.20060907.0010. URL: http://www.fs.fed.us/database/feis/plants/shrub/arttri/all.html

177642 Tirmenstein, D. 1999. "Chrysothamnus Nauseosus." Washington, D.C.: U.S. Department of Agriculture, Forest Service. Accessed September 5, 2006. ACC: MOL.20060907.0011. URL: http://www.fs.fed.us/database/feis/plants/shrub/chrnau/all.html

178315 Tolk, J.A. and Howell, T.A. 2001. "Measured and Simulated Evapotranspiration of Grain Sorghum Grown with Full and Limited Irrigation in Three High Plains Soils." *Transactions of the ASAE, 44,* (6), 1553-1558. St. Joseph, Michigan: American Society of Agricultural Engineers. TIC: 258632.

177149 Upadhyaya, M.K.; Turkington, R.; and McIlvride, D. 1986. "The Biology of Canadian Weeds. 75. Bromus Tectorum L." *Canadian Journal of Plant Science, 66,* 689-709. Ottawa (Ontario), Canada: Agricultural Institute of Canada. TIC: 258324.

178073 USDA (U.S. Department of Agriculture) 2002. "Big Sagebrush, Artemisia Tridentata Nutt." *Plant Fact Sheet.* Washington, D.C.: U.S. Department of Agriculture, Natural Resources Conservation Service. ACC: MOL.20060712.0207.

173916 USDA 2004. *Soil Survey of Nye County, Nevada, Southwest Part.* Two parts. Washington, D.C.: U.S. Department of Agriculture. ACC: MOL.20050614.0146.

160355 USGS (U.S. Geological Survey) 2001. *Simulation of Net Infiltration for Modern and Potential Future Climates.* ANL-NBS-HS-000032 REV 00 ICN 02. Denver, Colorado: U.S. Geological Survey. ACC: MOL.20011119.0334.

177649 Utah State University 2002. "Indian Ricegrass." *Range Plants of Utah.* Logan, Utah: Utah State University, Cooperative Extension. Accessed July 11, 2006. TIC: 258428. URL: http://extension.usu.edu/rangeplants/Grasses/indianricegrass.htm

177648 Utah State University 2002. "Needle-and-Thread." *Range Plants of Utah.* Logan, Utah: Utah State University, Cooperative Extension. Accessed July 11, 2006. TIC: 258429. URL: http://extension.usu.edu/rangeplants/Grasses/needleandthread.htm

177646 Utah State University 2002. "Pinyon Pine." *Range Plants of Utah.* Logan, Utah: Utah State University, Cooperative Extension. Accessed July 11, 2006. TIC: 258431. URL: http://extension.usu.edu/rangeplants/Woody/pinyonpine.htm

177644 Utah State University 2002. "Rubber Rabbitbrush." *Range Plants of Utah.* Logan, Utah: Utah State University, Cooperative Extension. Accessed July 11, 2006. TIC: 258432. URL: http://extension.usu.edu/rangeplants/Woody/rubberrabbitbrush.htm

177647 Utah State University 2002. "Sandberg Bluegrass." *Range Plants of Utah.* Logan, Utah: Utah State University, Cooperative Extension. Accessed July 11, 2006. TIC: 258430. URL: http://extension.usu.edu/rangeplants/Grasses/sandbergbluegrass.htm

177650 Utah State University 2002. "Squirreltail." *Range Plants of Utah.* Logan, Utah: Utah State University, Cooperative Extension. Accessed July 11 2006. TIC: 258427. URL: http://extension.usu.edu/rangeplants/Grasses/squirreltail.htm

177643 Utah State University 2004. "Utah Juniper, Juniperus Osteosperma, Cupressaceae or the Cypress Family." *Utah Trees and Forests.* Logan, Utah: Utah State University, Cooperative Extension. Accessed July 11, 2006. TIC: 258426. URL: http://extension.usu.edu/forestry/utahforests/treeid/juos.htm

176050 van der Kamp, G.; Hayashi, M.; and Gallen, D. 2003. "Comparing the Hydrology of Grassed and Cultivated Catchments in the Semi-Arid Canadian Prairies." *Hydrological Processes, 17,* 559-575. New York, New York: John Wiley & Sons. TIC: 257865.

176481 Vignola, F. and McDaniels, D.K. 1986. "Beam–Global Correlations in the Pacific Northwest." *Solar Energy, 36,* (5), 409-418. New York, New York: Pergamon Press. TIC: 258103.

176746 Vogelmann, J.E.; Helder, D.; Morfitt, R.; Choate, M.J.; Merchant, J.W.; and Bulley, H. 2001. "Effects of Landsat 5 Thematic Mapper and Landsat 7 Enhanced Thematic Mapper Plus Radiometric and Geometric Calibrations and Corrections on Landscape Characterization." *Remote Sensing of Environment, 78,* 55-70. New York, New York: Elsevier. TIC: 258213.

176752 Walter-Shea, E.A.; Privette, J.; Cornell, D.; Mesarch, M.A.; and Hays, C.J. 1997. "Relations Between Directional Spectral Vegetation Indices and Leaf Area and Absorbed Radiation in Alfalfa." *Remote Sensing of Environment, 61,* 162-177. New York, New York: Elsevier. TIC: 258218.

176737 Walthall, C.L.; Norman, J.M.; Welles, J.M.; Campbell, G.; and Blad, B.L. 1985. "Simple Equation to Approximate the Bidirectional Reflectance from Vegetative Canopies and Bare Soil Surfaces." *Applied Optics, 24,* (3), 383-387. Washington, D.C.: Optical Society of America. TIC: 258203.

178108 Walvoord, M.A.; Plummer, M.A.; Phillips, F.M.; and Wolfsberg, A.V. 2002. "Deep Arid System Hydrodynamics 1. Equilibrium States and Response Times in Thick Desert Vadose Zones." *Water Resources Research, 38,* (12), 44/1-44/15. Washington, D.C.: American Geophysical Union. TIC: 255212.

176761 Wang, J.; Rich, P.M.; and Price, K.P. 2003. "Temporal Responses of NDVI to Precipitation and Temperature in the Central Great Plains, USA." *International Journal of Remote Sensing, 24,* (11), 2345-2364. New York, New York: Taylor & Francis. TIC: 258231.

177931 Weber, D.J.; Hess, W.M.; Bhat, R.B.; and Huang, J. 1993. "Chrysothamnus: A Rubber-Producing Semi-Arid Shrub." *Proceeding of the Second National Symposium NEW CROPS-Exploration, Research, and Commercialization, Indianapolis, Indiana, October 6-9, 1991.* Janick, J. and Simon, J.E., eds. Pages 355-357. New York, New York: John Wiley & Sons. TIC: 258559.

178536 West, N.E. 1999. "Distribution, Composition, and Classification of Current Juniper-Pinyon Woodlands and Savannas Across Western North America." *USDA Forest Service Proceedings, Odgen, Utah. RMRS-P-9,* 20-23. Washington, D.C.: U.S. Department of Agriculture, Forest Service. ACC: MOL.20061214.0119.

160442 Whelan, J.F.; Paces, J.B.; and Peterman, Z.E. 2002. "Physical and Stable-Isotope Evidence for Formation of Secondary Calcite and Silica in the Unsaturated Zone, Yucca Mountain, Nevada." *Applied Geochemistry, 17,* (6), 735-750. New York, New York: Elsevier. TIC: 253462.

177113 Wight, J.R. and Hanson, C.L. 1990. "Crop Coefficients for Rangeland." *Journal of Range Management, 43,* (6), 482-485. Denver, Colorado: Society for Range Management. TIC: 258409.

177104 Wight, J.R.; Hanson, C.L.; and Cooley, K.R. 1986. "Modeling Evapotranspiration from Sagebrush-Grass Rangeland." *Journal of Range Management, 39,* (1), 81-85. Denver, Colorado: Society for Range Management. TIC: 258408.

177624 Wills, C.A. and Ostler, W.K. 2001. *Ecology of the Nevada Test Site: An Annotated Bibliography.* DOE/NV/11718–594. Las Vegas, Nevada: U.S. Department of Energy, National Nuclear Security Administration. ACC: MOL.20060712.0222.

172585 Wilson, J.L. and Guan, H. 2004. "Mountain-Block Hydrology and Mountain-Front Recharge." In *Groundwater Recharge in a Desert Environment: The Southwestern United States,* Hogan, J.F.; Phillips, F.M.; and Scanlon, B.R., eds, *Water Science and Application 9.* Pages 113-137. Washington, D.C.: American Geophysical Union. TIC: 256760.

177304 Wood, W.W. and Sanford, W.E. 1995. "Chemical and Isotopic Methods for Quantifying Ground-Water Recharge in a Regional, Semiarid Environment." *Ground Water, 33,* (3), 458-468. Dublin, Ohio: Ground Water Publishing. TIC: 258473.

176108 Woolhiser, D.A. and Pegram, G.G.S. 1979. "Maximum Likelihood Estimation of Fourier Coefficients to Describe Seasonal Variations of Parameters in Stochastic Daily Precipitation Models." *Journal of Applied Meteorology, 18,* 34-42. Boston, Massachusetts: American Meteorological Society. TIC: 257886.

165987 WRCC (Western Regional Climate Center) 2002. *Western U.S. Historical Summaries by State [Arizona, California, Idaho, Nevada, New Mexico, Oregon, Utah, and Washington]*. Reno, Nevada: Western Regional Climate Center, Desert Research Institute. TIC: 253357.

162307 WRCC 2003. "Nogales 6N, Arizona, NCDC 1971-2000 Monthly Normals." Reno, Nevada: Desert Research Institute, Western Regional Climate Center. Accessed March 4, 2003. TIC: 253915. http://www.wrcc.dri.edu/cgi-bin/cliNORMNCDC2000.pl?aznoga

152233 WRCC 1997. "Spokane, Washington: Normals, Means, and Extremes." Reno, Nevada: Desert Research Institute, Western Regional Climate Center. Accessed August 23, 2000. TIC: 248857. http://www.wrcc.dri.edu/cgi-bin/clilcd.pl?wa24157

177167 Yoder, C.K. and Nowak, R.S. 1999. "Soil Moisture Extraction by Evergreen and Drought-Deciduous Shrubs in the Mojave Desert During Wet and Dry Years." *Journal of Arid Environments, 42,* 81-96. San Diego, California: Academic Press. TIC: 258179.

178539 Zhu, C. 2000. "Estimate of Recharge from Radiocarbon Dating of Groundwater and Numerical Flow and Transport Modeling." *Water Resources Research, 36,* (9), 2607-2620. Washington, D.C.: American Geophysical Union. TIC: 252313.

177639 Zlatnik, E. 1999. "Juniperus Osteosperma." Washington, D.C.: U.S. Department of Agriculture, Forest Service. Accessed September 5, 2006. ACC: MOL.20060907.0012. URL: http://www.fs.fed.us/database/feis/plants/tree/junost/all.html

9.2 CODES, STANDARDS, REGULATIONS, AND PROCEDURES

176544 10 CFR 63. 2006. Energy: Disposal of High-Level Radioactive Wastes in a Geologic Repository at Yucca Mountain, Nevada. Internet Accessible.

178394 70 FR 53313. Implementation of a Dose Standard After 10,000 Years. Internet Accessible.

157394 ANSI/NCSL Z540-2-1997. 1997. *American National Standard for Calibration — U.S. Guide to the Expression of Uncertainty in Measurement.* Boulder, Colorado: NCSL International. TIC: 251472.

153195 ASME PTC 19.1-1998. *Test Uncertainty, Instruments and Apparatus.* New York, New York: American Society of Mechanical Engineers. TIC: 249327.

151762 IEEE/ASTM SI 10-1997. 1997. *Standard for Use of the International System of Units (SI): The Modern Metric System.* New York, New York: Institute of Electrical and Electronics Engineers. TIC: 240989.

IM-PRO-003, Rev. 02, ICN 0. *Software Management*. Washington, DC: U.S. Department of Energy, Office of Civilian Radioactive Waste Management. ACC: DOC.20070228.0002.

SCI-PRO-001, Rev. 02, ICN 0. *Qualification of Unqualified Data*. Washington, DC: U.S. Department of Energy, Office of Civilian Radioactive Waste Management. ACC: DOC.20070522.0016.

SCI-PRO-002, Rev. 02, ICN 0. *Planning for Science Activities*. Washington, DC: U.S. Department of Energy, Office of Civilian Radioactive Waste Management. ACC: DOC.20070320.0001.

SCI_PRO-006, Rev. 02, ICN 00. *Models.* Washington, DC: U.S. Department of Energy, Office of Civilian Radioactive Waste Management. ACC: DOC.20070420.0001.

9.3 SOURCE DATA, LISTED BY DATA TRACKING NUMBER

151139 GS000308315121.003. Meteorological Stations Selected to Represent Future Climate States at Yucca Mountain, Nevada. Submittal date: 03/14/2000.

176317 GS011208312212.004. SN-USGS-SCI-113 V1: Empirical Calculation of Soil Thickness Based on Field Measurements. Submittal date: 01/24/2002.

175972 GS910808312212.001. Geohydrologic Data Collected from Shallow Neutron-Access Boreholes and Resultant Preliminary Geohydrologic Evaluations, Yucca Mountain Area, Nye County, Nevada. Submittal date: 08/09/1991.

107374 GS941208312121.001. Surface-Water Discharge Data for the Yucca Mountain Area, Southern Nevada and Southern California, 1994 Water Year. Submittal date: 11/30/1994.

107375 GS960908312121.001. Surface-Water Discharge Data for the Yucca Mountain Area, Southern Nevada and Southern California, 1995 Water Year. Submittal date: 10/10/1996.

146872 GS960908312211.004. Heat Dissipation Probe Data: Bleach Bone Ridge 3/95 - 11/95. Submittal date: 09/19/1996.

107128 GS971208314221.003. Revised Bedrock Geologic Map of the Central Block Area, Yucca Mountain, Nevada. Submittal date: 12/30/1997.

174491 LB0208HYDSTRAT.001. 2002 UZ Model Grid Components. Submittal date: 08/26/2002.

146848 MO0003COV00095.000. Coverage: Scotbons. Submittal date: 03/01/2000.

152554 MO0004QGFMPICK.000. Lithostratigraphic Contacts from MO9811MWDGFM03.000 to be Qualified Under the Data Qualification Plan, TDP-NBS-GS-000001. Submittal date: 04/04/2000.

153777 MO0012MWDGFM02.002. Geologic Framework Model (GFM2000). Submittal date: 12/18/2000.

166731 MO0206SEPQ1998.001. Meteorological Monitoring Data for 1998. Submittal date: 06/26/2002.

166730 MO0209SEPQ2000.001. Meteorological Monitoring Data for 2000. Submittal date: 09/09/2002.

166164 MO0305SEP01MET.002. Meteorological Monitoring Data for 2001. Submittal date: 05/21/2003.

166163 MO0305SEP02MET.002. Meteorological Monitoring Data for 2002. Submittal date: 05/21/2003.

176092 MO0312SEPQ1993.001. Meteorological Monitoring Data for 1993. Submittal date: 12/24/2003.

167116 MO0312SEPQ1997.001. Meteorological Monitoring Data for 1997. Submittal date: 12/24/2003.

176097 MO0503SEPMMD03.001. Meteorological Monitoring Data for 2003. Submittal date: 03/03/2005.

175064 MO0508SEPFEPLA.002. LA FEP List and Screening. Submittal date: 08/22/2005.

177249 MO0512COV05112.000. Special Infiltration Project - Survey of Field Observation Locations. Submittal date: 12/12/2005.

177236 MO0601GSCSPINF.000. Special Infiltration Project Position of Field Observation Locations of Ecological Study Plot Corners and Streamflow Gauges. Submittal date: 01/30/2006.

176585 MO0603GSCGEOMP.000. Digital Geologic Map of Nevada Test Site and Vicinity, Nye, Lincoln, and Clark Counties, Nevada, and Inyo County, California. Submittal date: 03/09/2006.

179889 MO0603SEPSTREA.000. Surface Water Discharge Data Collected During Water Year 1998 from Streamflow Gauge Stations 102512531, 102512533 and 102512537. Submittal date: 03/22/2006.

177121 MO0603SPAGRIDD.003. Gridded Infiltration Model Input File Showing Infiltration Hydrogeologic Units. Submittal date: 03/06/2006.

178089 MO0605SEPALTRN.000. Alternative Soil Units, Hydraulic Parameters, and Associated Statistics for Infiltration Modeling at Yucca Mountain, NV. Submittal date: 05/31/2006.

177237 MO0605SEPHOURL.000. Hourly Precipitation Data for Four NOAA Meteorological Stations for the Years 1948 through 2005. Submittal date: 05/17/2006.

178663 MO0605SEPSGP05.000. Storage Gauge Precipitation 2005. Submittal date: 05/19/2006.

179890 MO0605SEPSURFC.000. Surface Water Discharge Data Collected During WY 1993 from Streamflow Gauge Station No. 102512533 (Pagany Wash No. 1), and During WY 1995 from Streamflow Gauge Station No. 1025125372 (Lower Split Wash). Submittal date: 05/15/2006.

177122 MO0605SPABEDRK.005. Bedrock Saturated Hydraulic Conductivity for Infiltration Hydrogeologic Units. Submittal date: 05/25/2006.

180539 MO0605SPAFABRP.004. Supporting Calculation Files for the Assessment of Bedrock Saturated Hydraulic Conductivity. Submittal date: 05/25/2006.

177135 MO0605SPASPOKA.000. Spokane Weather Data - Daily Values. Submittal date: 05/19/2006.

177136 MO0606SEPRECIP.001. Precipitation Data Collected at Yucca Mountain Meteorological Sites 1 through 5 for the Period January 1, 1988 through December 31, 1992. Submittal date: 06/01/2006.

178079 MO0607SEPMED94.000. Air Temperature Data from Meteorological Data Acquisition (MEDA) Station 05 for 1994 - 2004. Submittal date: 07/12/2006.

178311 MO0607SEPMMD04.001. Meteorological Monitoring Data for 2004. Submittal date: 07/18/2006.

178082 MO0608SPASDFIM.006. Soil Depth Input File for Use in Infiltration Modeling. Submittal date: 8/31/2006.

178328 MO0610METMND05.000. Meteorological Monitoring Data for 2005. Submittal date: 09/18/2006.

177247 MO9901ESPYMNYE.000. Ecological Study Plots at Yucca Mountain, Nye County, Nevada. Submittal date: 01/04/1999.

116056 MO9903CLIMATOL.001. Climatological Tables from 1986-1997 Meteorological Data from Site 1 through Site 9 EFPD Meteorological Sites. Submittal date: 03/23/1999.

150118 MO9905VMMDAJ90.000. Validated Meteorological Monitoring Data, April - June 1990. Submittal date: 05/21/1999.

150056 MO9905VMMDJM90.000. Validated Meteorological Monitoring Data, January - March 1990. Submittal date: 05/21/1999.

150119 MO9905VMMDJS90.000. Validated Meteorological Monitoring Data, July - September 1990. Submittal date: 05/21/1999.

150120 MO9905VMMDOD90.000. Validated Meteorological Monitoring Data, October - December 1990. Submittal date: 05/21/1999.

109059 MO9906GPS98410.000. Yucca Mountain Project (YMP) Borehole Locations. Submittal date: 06/23/1999.

157659 MO9907GCESPYMN.000. Ground Cover Data for Ecological Study Plots at Yucca Mountain, Nevada. Submittal date: 07/29/1999.

177169 MO9907SADESYYM.000. Soil Analysis Data for Ecological Study Plots at Yucca Mountain, Nevada. Submittal date: 07/28/1999.

177238 SN0511NOAADATA.001. NOAA and SORAD Meteorological and Solar Radiation Data Measured at Desert Rock, Nevada. Submittal date: 11/22/2005.

177239 SN0601ALANDSAT.001. Landsat Imagery of Yucca Mountain from January 1998 to August 2002. Submittal date: 02/07/2006.

177240 SN0601DOQQYM98.001. Digital Ortho Quarter Quad (DOQQ), Yucca Mountain 06/01/1998 - 08/18/1998. Submittal date: 01/24/2006.

176122 SN0601PRECPTMP.002. Developed Precipitation Data at NTS Sites from 1959-2004, and Precipitation and Temperature Data at Amargosa Farms-Garey from 1965-2005. Submittal date: 01/16/2006.

177241 SN0601QBSAT802.001. Quickbird (QB) Satellite Imagery, Yucca Mountain, 31 August 2002. Submittal date: 04/25/2006.

177242 SN0601SRTMDTED.001. Shuttle Radar Topography Mission (SRTM) Digital Terrain Elevation Data (DTED) of Yucca Mountain, February 2000. Submittal date: 01/23/2006.

177917 SN0603DWEATHER.002. Developed Weather Station Data for Beowawe, NV (1982-2004), Delta, UT (1968-2004), Hobbs, NM (1947-2004), Nogales, AZ (1948-1983), Rosalia, WA (1949-2004), St. John, WA (1963-2004), and Spokane, WA (1948-2004). Submittal date: 03/20/2006.

179875 SN0608T0502206.020. Climate Data, Geospatial Information, and Soil Moisture and Property Data for Reynolds Creek Experimental Watershed (RCEW), Idaho. Submittal date: 08/21/2006.

177912 SN0608WEATHER1.005. Temperature, Precipitation, Wind Speed, Relative Humidity, Dew Point Temperatures, and Barometric Pressure Data Collected from 1993-2004 Measured at Yucca Mountain Weather Stations 1,2,3,6, and 9. Submittal date: 08/23/2006.

9.4 DEVELOPED DATA, LISTED BY DATA TRACKING NUMBER

MO0602SPAPRECP.000. Daily Precipitation for Water Years 1998, 2001, and 2002 – Sites 2, 3 & 4. Submittal date: 02/16/2006.

MO0602SPAWEATH.000. Daily Weather Data for Water Years 1998, 2001, 2002, Yucca Mountain Meteorological Site 1. Submittal date: 02/16/2006.

MO0603SPAREFET.000. Reference Evapotranspiration (ET) for Yucca Mountain. Submittal date: 03/01/2006.

MO0605SPADAYWA.000. Daily Weather Data for Spokane Washington. Submittal date: 05/24/2006.

MO0606SPABASAL.001. Basal Transpiration Coefficients (K_{cb}) for Yucca Mountain Vegetation Associations (1993, 1991, and 1990 Water Years). Submittal date: 06/28/2006.

MO0606SPATRANS.000. Transpiration Coefficients (K_{cb}) for a Bromus Tectorum Monoculture. Submittal date: 06/05/2006.

MO0606SPAVEGAS.001. Cover Data for Vegetation Associations at Yucca Mountain (1990,1991, and 1993). Submittal date: 06/26/2006.

MO0607SEPTOTAL.003. Total Annual Precipitation for Water Years 1990, 1991 and 1993 from Yucca Mountain Meteorological Sites 2, 3 and 4. Submittal date: 07/13/2006.

MO0610SPALINEA.000. Linear Regression Analysis for the MASSIF K_{cb} Versus NDVI Correlation. Submittal date: 10/19/2006.

MO0703MASSIFIM.001. Independent Verification of MASSIF Infiltration Model. Submittal date: 03/05/2007.

SN0602T0502206.003. Solar Radiation and Reference Evapotranspiration (ET_0) on Inclined Surfaces. Submittal date: 02/20/2006.

SN0602T0502206.004. Calculated Daily Diffuse and Direct Solar Radiation from 2000 through 2004 and Measured at Desert Rock, Nevada. Submittal date: 03/13/2006.

SN0602T0502206.005. Evaluation of Hargreaves Solar Radiation Coefficient, K_{RS}, for Yucca Mountain. Submittal date: 02/28/2006.

SN0603T0502206.006. Evaluation of Published Diffuse and Total Solar Radiation Correlations for Yucca Mountain. Submittal date: 03/13/2006.

SN0606T0502206.011. Geospatial Inputs for Net Infiltration Model of Yucca Mountain. Submittal date: 05/31/2006.

SN0606T0502206.012. Daily Normalized Difference Vegetation Index (NDVI) Estimation for Selected Slopes/Azimuths at Yucca Mountain. Submittal date: 05/31/2006.

SN0606T0502206.014. Calculated Weather Summary for Present Day and Future Climates. Submittal date: 06/07/2006.

SN0607T0502206.016. Analysis of Soil Water Storage in Nevada Test Site (NTS) and Reynolds Creek Experimental Watershed (RCEW) Lysimeters. Submittal date: 08/24/2006.

SN0608ASSEMBLY.001. Assembly Data for Geospatial Inputs to MASSIF Model of Yucca Mountain. Submittal data: 08/15/2006.

SN0608CWATSHED.001. Calibration Watersheds at Yucca Mountain Based on Pour Point Stream Gages. Submittal date: 08/15/2006.

SN0608DRAINDYM.001. Drainage Delineation at Yucca Mountain. Submittal date: 08/15/2006.

SN0608NDVIANAL.001. Analysis Data Supporting Estimations of Normalized Difference Vegetation Index (NDVI) at Yucca Mountain, 1997–2002. Submittal date: 08/15/2006.

SN0608NDVIAUXD.001. Auxiliary Data Used in Calculations of Daily Normalized Difference Vegetation Index (NDVI) Estimation for Selected Slopes/Azimuths at Yucca Mountain and Geospatial Inputs for Net Infiltration Model of Yucca Mountain. Submittal date: 08/15/2006.

SN0608NDVILSTM.001. Normalized Difference Vegetation Index (NDVI) Derived from Calibrated and Geocorrected LANDSAT TM Data at Yucca Mountain, 1997–2002. Submittal date: 08/15/2006.

SN0608NDVIQBIM.001. Normalized Difference Vegetation Index (NDVI) Imagery Derived from Calibrated and Georectified Quickbird Imagery of Yucca Mountain, August 31, 2002. Submittal date: 08/15/2006.

SN0608NSSLOPES.001. Normalized Difference Vegetation Index (NDVI) on North and South Slopes and Supporting Data at Yucca Mountain, 1997–2002. Submittal date: 08/15/2006.

SN0608PVRATYMT.001. Potential Vegetation Response (PVR) at Yucca Mountain, 1997–2002. Submittal date: 08/15/2006.

SN0608T0502206.019. Temperature Model Fitting Parameters for Present-Day and Future Climate Proxy Sites. Submittal date: 08/16/2006.

SN0609AZSLPHST.001. Distribution of Slope on North-South Facing Terrain Slopes at Yucca Mountain. Submittal date: 09/18/2006.

SN0609LSTMPROC.001. Thematic Mapper Processing Overview. Submittal date: 09/21/2006.

SN0609T0502206.021. Alternative Infiltration Model Inputs. Submittal date: 09/18/2006.

SN0609T0502206.022. Alternative Infiltration Modeling Results. Submittal date: 09/18/2006.

SN0609T0502206.023. Precipitation Parameters Calculated using Fourier Analyses for Modern Interglacial and Future Climates. Submittal date: 09/07/2006.

SN0609T0502206.024. Monsoon Net Infiltration Results. Submittal date: 09/18/2006. [Preliminary]
SN0609T0502206.025. Calculated Weather Summary for Monsoon Climate. Submittal date: 09/21/2006. [Preliminary]

SN0609T0502206.026. Calculated Weather Summary for Present-Day Climate. Submittal date: 09/21/2006. [Preliminary]

SN0609T0502206.027. Calculated Weather Summary for Glacial Transition Climate. Submittal date: 09/21/2006. [Preliminary]

SN0609T0502206.028. Present-Day Net Infiltration Results. Submittal date: 09/22/2006. [Preliminary]
SN0609T0502206.029. Glacial Transition Net Infiltration Results. Submittal date: 09/28/2006. [Preliminary]
SN0610T0502206.030. Average Daily Wind Speed at 2 m Height above the Ground. Submittal date: 10/09/2006.

SN0610T0502206.031. Precipitation Duration Functions for the Present-Day, Monsoon, and Glacial Transition Climates for Infiltration Modeling at Yucca Mountain, NV. Submittal date: 10/09/2006.

SN0610T0502206.032. MASSIF Calculation of Net Infiltration at Yucca Mountain. Submittal date: 10/31/2006. [Preliminary]

SN0610T0502206.033. Latin Hypercube Sample (LHS) Input and Output Files for MASSIF Calculation of Net Infiltration at Yucca Mountain. Submittal date: 10/20/2006. [Preliminary]

SN0612FTPRNUZB.002. Unsaturated Zone (UZ) Boundary and Repository Footprint. Submittal date: 12/14/2006.

SN0612T0502206.039. Estimation of Uncertainty on Upscaled Uniform Value for Soil Depth Class 4. Submittal date: 12/06/2006.

SN0701SPALAYER.002. Spatial Data Layers at Yucca Mountain. Submittal date: 01/16/2007.

SN0701T0502206.034. Present-Day Net Infiltration Results, Rev 1. Submittal date: 01/11/2007.

SN0701T0502206.035. Glacial Transition Net Infiltration Results, Rev 1. Submittal date: 01/11/2007.

SN0701T0502206.036. Monsoon Net Infiltration Results, Rev 1. Submittal date: 01/11/2007.

SN0701T0502206.037. MASSIF Calculation of Net Infiltration at Yucca Mountain, Rev 1. Submittal date: 02/13/2007.

SN0701T0502206.040. Calculated Weather Summary for Present Day Climate, Rev 1. Submittal date: 01/10/2007.

SN0701T0502206.041. Calculated Weather Summary for Monsoon Climate, Rev 1. Submittal date: 01/10/2007.

SN0701T0502206.042. Calculated Weather Summary for Glacial Transition Climate Rev 1. Submittal date: 01/10/2007.

SN0701T0502206.043. Latin Hypercube Sample (LHS) Input and Output Files for MASSIF Calculation of Net Infiltration at Yucca Mountain. Submittal date: 01/11/2007.

SN0701T0502206.044. Sensitivity Analysis of Average Net Infiltration for Three Climates. Submittal date: 01/18/2007.

SN0701T0502206.045. Comparison of the Calculated Precipitation Record with Site Data. Submittal date: 01/23/2007.

SN0704T0502206.047. Recharge Estimates Used to Validate the Massif Model of Net Infiltration at Yucca Mountain. Submittal date: 04/19/2007

9.5 SOFTWARE CODES

176015 ArcGIS Desktop V. 9.1. 2005. WINDOWS XP. STN: 11205-9.1-00.

178783 ENVI+IDL V. 4.2. 2005. XP. STN: 11204-4.2-00.

139422 INFIL VV2.0. 2001. PC, Windows NT 4.0. 10307-2.0-00.

147608 Infil VVA_2.a1. 2001. DEC Alpha, VMS AXP V7.2-1. 10253-A_2.a1-00.

178784 LHS V. 2.51. 2006. OPENVMS 8.2. STN: 10205-2.51-01.

173438 MVIEW V. 4.0. 2005. WINDOWS 2000. STN: 10072-4.0-00.

178228 Šimùnek, J.; Šejna, M.; and van Genuchten, M.Th. 1999. *The HYDRUS-2D Software Package for Simulating the Two-Dimensional Movement of Water, Heat, and Multiple Solutes in Variably-Saturated Media.* Version 2.0. Riverside, California: U.S. Salinity Laboratory, U.S. Department of Agriculture. ACC: MOL.20061101.0023.

178140 Šimùnek, J.; van Genuchten, M.Th.; and Šejna, M. 2005. *The HYDRUS-1D Software Package for Simulating the One-Dimensional Movement of Water, Heat, and Multiple Solutes in Variably-Saturated Media.* Version 3.0. Riverside, California: University of California, Department of Environmental Sciences. ACC: MOL.20060828.0051.

APPENDIX A
OUTSIDE SOURCES QUALIFIED FOR INTENDED USE

A.1 QUALIFICATION OF VEGETATION PARAMETERS FOR USE AS DIRECT INPUT

This section documents the demonstration that data for vegetation parameters are suitable for their intended use as inputs for calculating net infiltration at Yucca Mountain. Appropriate data sources were identified through literature searches for each of vegetation parameter inputs. Because these data were not acquired or developed for the Yucca Mountain Project (YMP), they are qualified for use as input to this report in accordance with SCI-PRO-006, *Models* Section 6.2.1.K. The following vegetation parameter inputs are addressed:

- Plant height (Sections A1.1 to A1.3)
- Timing of phenological events (Section Al.1) and physiological activity (Section A1.2)
- Stomatal conductance (Section A1.4)
- Rooting depth (Sections A1.5 and A1.6).

The attributes of the data considered in the determination of suitability are the extent to which the data demonstrate properties of interest and the reliability of the data source.

A1.1 PLANT HEIGHT AND TIMING OF PHENOLOGICAL EVENTS

Plant heights were used in the calculation of transpiration coefficients (K_{cb}) (Section D.3.2.1), and in the calculation of the fraction of soil surface covered by vegetation (f_c) used in soil water balance calculations (Section 6.5.3.3). Plant heights for Present-Day and Monsoon climates are addressed in this section. Plant heights for the Glacial Transition climate are addressed in Section A1.3.

Timing of phenological events for dominant vegetation at Yucca Mountain was used in conjunction with timing of physiological activity (e.g., stomatal conductance, transpiration, and photosynthesis) to establish growth stages for use in development of K_{cb} profiles (Section D.3.2.1). Timing of phenological events is addressed in this section. Timing of physiological activity is addressed in Section A1.2.

Statistics describing shrub height for Mojave Desert vegetation associations reported by Rundel and Gibson (1996 [DIRS 103614], p. 88, Table 4.1 and p. 89, Table 4.2) were used in the calculation of K_{cb}s and f_c, respectively. Timing of phenological stages for drought-deciduous and evergreen species reported by Rundel and Gibson (1996 [DIRS 103614], Figure 4.13, p. 106) were used to establish the initial ranges for growth stages. Timing of phenological stages for *Bromus madritensis* ssp. *rubens* reported by Newman (1992 [DIRS 174673], p. 3) were used to develop growth stages for annual vegetation. Applicable plant height and timing data (i.e., months when stages were documented) from these publications are presented in Table 6.5.3.3-1, Table D-4, Section D3.2.1, and Table D-2.

The following information was used to evaluate whether the plant height and timing data reported by Rundel and Gibson (1996 [DIRS 103614], pp. 88 and p.89, Tables 4.1 and 4.2, respectively) and timing data reported by Newman (1992 [DIRS 174673], p. 3) were suitable for use in K_{cb} and f_c development.

- **Extent to Which the Data Demonstrate Properties of Interest**—Plant heights are most applicable to K_{cb} and f_c calculations if they are for vegetation associations that are common at Yucca Mountain and are based on data gathered from field studies conducted at the Nevada Test Site (NTS) or within the Mojave Desert region. As described in Sections D3.2.1 and 6.5.3.3, plant heights from Rundel and Gibson (1996 [DIRS 103614], pp. 88 and 89, Tables 4.1 and 4.2, respectively) were for several vegetation associations that occur at Yucca Mountain including those typical of Mojave (low to mid elevations at Yucca Mountain), transition (mid to upper elevations at Yucca Mountain), and Great Basin deserts (upper elevation north slopes). Plant heights in Rundel and Gibson (1996 [DIRS 103614], p. 88, Table 4.1 and p.89, Table 4.2) were based on data gathered during field studies conducted on the NTS.

  Timing of phenological stages for desert plants are most applicable to establishing growth stages for this analysis if they are for dominant plant species at Yucca Mountain and if they are based on data gathered from field studies conducted at the NTS or within the Mojave Desert region. As described in Section D3.2.1 the phenological stages from Rundel and Gibson (1996 [DIRS 103614], Figure 4.13, p. 106) were from studies conducted on the NTS for two evergreen species (*Ephedra nevadensis* and *Larrea tridentata*) and four drought deciduous species (*Ambrosia dumosa, Grayia spinosa, Lycium andersonni,* and *Lycium palladum*), all of which are dominant or co-dominant in Yucca Mountain vegetation associations (see Section D.2.2 for a description of Yucca Mountain vegetation). The phenological stages from Newman (1992 [DIRS 174673], p. 3) were for the dominant annual species in Yucca Mountain vegetation associations and were based on a literature review of *Bromus madritensis* ecology in the Mojave Desert.

- **Reliability of Data Sources**—The data reported by Rundel and Gibson (1996 [DIRS 103614]) were the results of several years of intensive ecological studies collected under prestigious research programs. The research programs were conducted by organizations such as the Desert Biome program of the International Biological Program (IBP) and the Laboratory of Biomedical and Environmental Sciences at the University of California, Los Angeles. The data reported by Newman (1992 [DIRS 174673], p. 3) were compiled by the Nature Conservancy to provide the Nature Conservancy's Stewardship staff and other land managers with current information on those species that are most important to protect or control. It was concluded that these data sources were reliable for use as input to this model.

- **Availability of Corroborating Data**—Plant heights reported by Rundel and Gibson (1996 [DIRS 103614], p. 88, Table 4.1 and p. 89, Table 4.2) reflect the short stature of plants in Mojave Desert vegetation associations and are corroborated by general descriptions of true desert vegetation which is dominated by shrubs and dwarf shrubs (Smith et al. 1997 [103636], p. 21). Phenological stages for desert plants are variable among species and across years of differing precipitation. Those reported by Rundel and Gibson (1996 [DIRS 103614], Figure 4.13, p. 106) reflected this variability and were generally corroborated by the physiological data used to help develop growth stages. The timing of phenological stages for *Bromus madritensis* reported by Newman (1992 [DIRS 174673], p. 3) was typical of that described for winter annuals. In general, winter

annuals are known to germinate in the fall, over winter they remain in a semi-dormant condition, resume rapid growth in late winter or early spring, and have seed set and senescence in late spring to early summer (Hulbert 1955 [DIRS 177129], p. 191).

Because the data considered here were for appropriate vegetation associations and dominant species found at Yucca Mountain, were from studies conducted on the NTS and Mojave Desert region, and were from reliable data sources, it was concluded that the data were suitable for the specific applications in this analysis. Confidence in the reliability of the data was increased by corroborative information. Thus, the data were considered qualified for the intended uses.

A1.2 TIMING OF PHYSIOLOGICAL ACTIVITY FOR MOJAVE DESERT VEGETATION

Measured periods of physiological activity (e.g., photosynthesis, stomatal conductance, and transpiration) for Mojave Desert shrub species reported by Hamerlynck et al. (2000 [DIRS 177022], p. 602, Figure 6), Hamerlynck et al. (2002 [DIRS 177128], Figure 7, p. 103) Hamerlynck et al. (2002 [DIRS 177046], p 774), and Smith et al. (1995 [DIRS 103628], Figure 2, pp. 342, 343, and 349) were used, along with the timing of phenological stages, to establish growth stages used in development of K_{cb} profiles (Section D.3.2.1). Applicable timing information (i.e., start/end and type of activity) from these publications are presented in Section D.3.2.1.

The following information was considered to evaluate whether the timing of physiological activity data in the listed publications were suitable for use in establishment of growth stages for K_{cb} development.

- **Extent to Which the Data Demonstrate Properties of Interest**—Timing of physiological activity for desert plants is most applicable to establishing growth stages for this analysis if they are for dominant plant species at Yucca Mountain and if they are based on data gathered from field studies conducted on the NTS or within the Mojave Desert region. As described in Section D3.2.1, physiological studies used in this analysis were conducted on two evergreen species (*L. tridentata* and *E. nevadensis*) and two drought deciduous species (*L. andersonii* and *A. dumosa*) that are dominant in Yucca Mountain vegetation associations. The studies were conducted on the NTS (Hamerlynck et al. 2000 [DIRS 177022], p. 602, Figure 6; Hamerlynck et al. 2002 [DIRS 177128], Figure 7, p. 103; Smith et al. 1995 [DIRS 103628], Figure 2, pp. 342 to 343) and on the East Mojave National Preserve (Hamerlynck et al. 2002 [DIRS 177046], p 774).

- **Reliability of Data Sources**—The data from Hamerlynck et al. (2000 [DIRS 177022], p. 602, Figure 6), Hamerlynck et al. (2002 [DIRS 177128], Figure 7, p. 103), Hamerlynck et al. (2002 [DIRS 177046], p. 774), and Smith et al. (1995 [DIRS 103628], Figure 2, pp. 342 to 343) came from peer-reviewed publications and were thus judged to be appropriate for publication by experts in the field of vegetation science specific to the Mojave Desert. In addition, the methods of data collection were described in sufficient detail to determine whether the data were applicable for determining growth stages. It was concluded that these data sources were reliable for use in this analysis.

Because the data considered here were for dominant species relevant to Yucca Mountain, were from studies conducted at the NTS and Mojave Desert region, and were from reliable data sources, it was concluded that the data are suitable for the specific application in this model. Thus, the data are considered qualified for the intended use.

A1.3 PLANT HEIGHT FOR THE GLACIAL TRANSITION CLIMATE

Plant heights from the sources in Table A-1 were used in Section 6.5.3.3 to develop the nominal value and distribution for plants heights used to calculate f_c for the Glacial Transition climate. Because the vegetation of the Glacial Transition climate will likely differ from that of the Present-Day and Monsoon climates, a different dataset was required to establish plant height. Plant heights from these sources are presented in Table 6.5.3.3-2.

Table A-1. Sources for Plant Heights for the Glacial Transition Climate

Source
Stewart and Hull 1949 [DIRS177146], pp. 58 to 59
Schultz and McAdoo 2002 [DIRS 178065], p. 2
Weber et al. 1993 [DIRS 177931], p. 1
Utah State University, Cooperative Extension 2004 [DIRS 177643], p. 1
Utah State University, Cooperative Extension 2002 [DIRS 177644], p. 2
Utah State University, Cooperative Extension 2002 [DIRS 177646], p. 2
Utah State University, Cooperative Extension 2002 [DIRS 177647], p. 1
Utah State University, Cooperative Extension 2002 [DIRS 177648], p. 2
Utah State University, Cooperative Extension 2002 [DIRS 177649], p. 2
Utah State University, Cooperative Extension 2002 [DIRS 177650], p. 2

- **Extent to Which the Data Demonstrate Properties of Interest**—Plant heights are most applicable to this model if they are for common plant species of the Great Basin desert that could occur at Yucca Mountain under Glacial Transition conditions (see Section 6.5.3.1 for analysis of potential future vegetation). Data should be collected from Great Basin desert environments. As described in Section 6.5.3.2, all plant heights in the listed sources were for common Great Basin plant species. All data from the listed sources were collected in the Great Basin desert in Nevada and Utah.

- **Reliability of Data Sources**—Stewart and Hull (1949 [DIRS 177146], pp. 58 to 59) and Weber et al. (1993 [DIRS 177931]) were peer-reviewed publications and were thus judged to be appropriate for publication by experts in the field of vegetation science.

Because of the paucity of peer-reviewed literature that actually reported plant height for Great Basin plants, the literature search was extended to include United States Department of Agriculture (USDA) divisions and University Cooperative extensions that provided fact sheets on Great Basin plant species in Nevada and Utah (Table 6.5.3.3-2).

The USDA Natural Resources Conservation Service (NRCS) PLANTS Database provides standardized information about vascular plants of the United States (U.S.). The database includes names, plant symbols, checklists, distributional data, species abstracts, characteristics

(including plant height), images, crop information, automated tools, onward Web links, and references. PLANTS is a collaborative effort of the USDA NRCS National Plant Data Center (NPDC), the USDA NRCS Information Technology Center (ITC), the USDA National Information Technology Center (NITC), and many other partners. This data is considered to be Established Fact.

The USDA Forest Service sponsors a Fire Effects Information System (FEIS) that is available online. The FEIS database contains literature reviews, taken from current English-language literature, for about 900 plant species, 7 lichen species, about 100 wildlife species and 10 research project summaries, and 16 Kuchler plant communities of North America. Background information on taxonomy, distribution, basic biology, and ecology of each species is included. Reviews are thoroughly documented, and each contains a complete bibliography. Managers from several land management agencies (United States Department of Agriculture, Forest Service and United States Department of Interior, Bureau of Indian Affairs, Bureau of Land Management, Fish and Wildlife Service, and National Park Service) identified the species to be included in the database. Those agencies funded the original work and continue to support maintenance and updating of the database. Data from these sources are considered to be Established Fact.

The Utah State University (USU) Cooperative Extension web page "Range Plants of Utah" was established through collaboration of range conservationists, botanists, and other experts from the USU Cooperative Extension. The University of Nevada Reno (UNR) Cooperative Extension sponsors publication of a variety of topics on natural resources including management and ecology of common sagebrush in Nevada. The sources listed in Table A-1 were prepared by professionals in the field of natural resources. Cooperative Extension Services are partnerships between state land-grant colleges and the U.S. Department of Agriculture Cooperative State Research, Education, and Extension Service. They serve as the outreach branches of state universities and the Department of Agriculture. The mission of the Cooperative Extension Services is to develop and disseminate information on agriculture, horticulture, health, environment, economics, and other topics of importance developed by the USDA and universities. Personnel working for Cooperative Extension Services are recognized experts in botany, range conservation, agriculture, and horticulture.

Because the plant height data considered here were for common species of the Great Basin desert of Nevada and Utah and were from reliable data sources, it was concluded that the data are suitable for the specific application in this analysis. Thus, the data are considered qualified for the intended use.

A1.4 STOMATAL CONDUCTANCE

Stomatal conductance values from published literature sources in Table A-2 were used in Section D3.2.3 to calculate stomatal resistance (r_l) for dominant plant species in Yucca Mountain vegetation associations. These data were needed to calculate the stomatal resistance correction factor (F_r) for use in development of K_{cb}s (Equation D-6). Applicable stomatal conductance information (i.e., rates, temperatures, plant species) from these publications are presented in Table D-17.

Table A-2. Sources of Published Measurements of Stomatal Conductance for Mojave Desert Vegetation

Sources
Hamerlynck et al. 2000 [DIRS 177130], p. 188
Hamerlynck et al. 2000 [DIRS 177022], p. 602
Hamerlynck et al. 2002 [DIRS 177128], p. 101
Hamerlynck et al. 2004 [DIRS 176045], p. 213
Huxman et al. 1999 [DIRS 177133], p. 774
Huxman and Smith 2001 [DIRS 177132], p. 197
Naumburg et al. 2003 [DIRS 177143], p. 280, Figure 3
Pataki et al. 2000 [DIRS 177161], p. 893
Smith et al. 1995 [DIRS 103628], pp. 343 and 344

The following information was considered to evaluate whether the stomatal conductance data in the listed publications were suitable for calculating stomatal resistance for use in K_{cb} calculations.

- **Extent to Which the Data Demonstrate Properties of Interest**—Rates of stomatal conductance are most applicable to calculating stomatal resistance for this analysis if they are for dominant plant species at Yucca Mountain, are measured during periods of peak activity for mid-season growth stages and during periods of reduced activity for initial and end-of-late season growth stages, and if they are based on data gathered from field studies conducted on the NTS or within the Mojave Desert region. As described in Section D3.2.3 and Table D-17, rates of stomatal conductance in the listed sources were measured for the dominant annual (*Bromus madritensis*), three dominant drought-deciduous species (*L. andersonii*, *A. dumosa,* and *Krameria erecta*), and three dominant evergreens (*L. tridentata, E. nevadensis*, and *Ericameria cooperi*) in Yucca Mountain vegetation associations. Conductances were measured under a variety of conditions during several time periods allowing identification of low and high physiological activity. All but two of the studies were conducted in the field on the NTS or within the Mojave Desert region. Two of the studies (Hamerlynck et al. (2000 [DIRS 177130], p. 188 and Huxman et al. (1999 [DIRS 177133], p. 774) were conducted in a glasshouse at the University of Nevada, Las Vegas. Treatments were evaluated and data from those that induced stress and resulted in low conductance were not used. Data from control treatments and treatments that created optimum growing conditions were compared to field measured values and deemed appropriate for initial/end and mid-season stages, respectively.

- **Reliability of Data Sources**—The data from the listed sources (Table A-2) came from peer-reviewed publications and were thus judged to be appropriate for publication by experts in the field of vegetation science specific to the Mojave Desert. In addition, the methods of data collection were described in sufficient detail to determine whether the data were applicable for calculating stomatal resistance. It was concluded that these data sources were reliable for use in this analysis.

Because the data considered here were for dominant species relevant to Yucca Mountain, were from studies conducted at the NTS, Mojave Desert region, or from appropriate glasshouse studies, and were from reliable data sources, it was concluded that the data were suitable for the specific application in this analysis. Additionally, study methods were described in sufficient detail to determine that the data were suitable for use as input to this model. Thus, the data were considered qualified for the intended use.

A1.5 ROOTING DEPTHS FOR PRESENT-DAY AND MONSOON CLIMATES

Rooting depths from published literature sources in Table A-3 were used in Section 6.5.3.2 to develop mean maximum effective rooting depth (Z_r) for present-day and monsoon climate states. Z_r is used in the MASSIF model to calculate water content in the root zone and root zone water depletion (Section 6.4). Rooting depths from these publications are presented in Table 6.5.3.2-1.

Table A-3. Sources of Published Measurements of Rooting Depths for Desert Plants

Sources
Canadell et al. 1996 [DIRS 177626], p. 588, Appendix 1
Hansen and Ostler 2003 [DIRS 177619], p. 85, Table 7-1
Jackson et al. 2002 [DIRS 177171], p. 624, Table 1
Rundel and Gibson 1996 [DIRS 103614], p. 99, Figure 4-10
Rundel and Nobel 1991 [DIRS 128001], p. 355 – 357
Schenk and Jackson 2002 [DIRS 177638], p. 491, Figure 9
Yoder and Nowak 1999 [DIRS 177167], p. 91, Figure 6
Harris 1967 [DIRS 177630], p.97, Figure 6
Hulbert (1955 [DIRS 177129] p.191
Link et al. 1990 [DIRS 177142], p. 512
Rickard 1985 [DIRS 177635], p.170
Foxx et al. 1984 [DIRS 177628], p. 5, Table 3

The following information was considered to evaluate whether rooting depths in the listed publications were suitable for use in development of Z_r for Present-Day and Monsoon climates.

- **Extent to Which the Data Demonstrate Properties of Interest**—Rooting depths are most applicable to this analysis if they are for common plant species at Yucca Mountain that have the potential for deep root growth. Study locations should be in desert environments and can be outside of the Mojave Desert in order to include maximum rooting depth potentials for xeric shrubs. As described in Section 6.5.3.2, all rooting depths in the listed publications were for common deep rooting species at Yucca Mountain, for shrubs in xeric environments in western and southwestern United States receiving the same range of precipitation as Yucca Mountain, or for a common exotic grass with the potential for forming monocultures. Sources with rooting depths for the exotic grass were included because of its presence at Yucca Mountain and its potential for forming monocultures at the expense of deeper-rooted shrubs. All of the studies were conducted in appropriate desert environments, including the NTS, Chihuahuan, and Great Basin deserts. For the reasons listed above, the data provided in these sources demonstrate the property of interest (maximum rooting depth).

- **Reliability of Data Sources –** The data from all but two of the listed sources (Table A-3) came from peer-reviewed publications and were thus judged to be appropriate for publication by experts in the field of plant root science specific to desert environments. In addition, the methods of data collection were described in sufficient detail to determine whether the data were applicable for calculating Z_r. The two, non peer-reviewed sources, Hansen and Ostler (2003 [DIRS 177619], p. 85, Table 7-1) and Foxx et al. (1984 [DIRS 177628]), p. 6, Table 3) were publications by Bechtel Nevada Ecological Services and Los Alamos National Laboratory, respectively. Hansen and Ostler (2003 [DIRS 177619]) included a comprehensive literature search and a limited field study on rooting depths for several plant species on the NTS. Both authors have advanced degrees in vegetation science fields and have several years of experience studying Mojave Desert plant ecology. Foxx et al. (1984 [DIRS 177628]) obtained means and ranges of rooting depths for several species (including several from the Great Basin and Mojave deserts) from an extensive bibliographic study that contained 1,034 different rooting citations. The authors are professionals employed by national laboratory. Based on these factors, it was concluded that these data sources were reliable for use in this analysis.

Because the data considered here were for xeric shrubs and an exotic grass relevant to Yucca Mountain, were from studies conducted at the NTS and other appropriate desert habitats, and were from reliable data sources, it was concluded that the data were suitable for the specific application in this analysis. Additionally, study methods were described in sufficient detail to determine whether the data were applicable for this analysis. Thus, the data were considered qualified for the intended use.

A1.6 ROOTING DEPTHS FOR THE GLACIAL TRANSITION CLIMATE

Rooting depths from sources in Table A-4 were used in Section 6.5.3.2 to develop mean maximum effective rooting depth (Z_r) for the Glacial Transition climate. Rooting depths from these sources are presented in Table 6.5.3.2-2.

Table A-4. Sources of Rooting Depths for Potential Glacial Transition Vegetation

Sources
Canadell et al. 1996 [DIRS 177626], p. 588, Appendix 1
Foxx et al. 1984 [DIRS 177628], p. 5 and 6, Table 3
Harris 1967 [DIRS 177630], p. 97, Figure 6
Hulbert 1955 [DIRS 177129], p. 191
Leffler et al. 2004 [DIRS 177926], p. 10, Figure 1
Link et al. 1990 [DIRS 177142], p. 512
Richards and Caldwell 1987 [DIRS 177927], p. 488
Rickard 1985 [DIRS 177635], p. 170
Ryel et al. 2003 [DIRS 177632], p. 760
Sturges and Trlica 1978 [DIRS 177928], pp. 1282 to 1285
Seyfried et al. 2005 [DIRS 178060], pp. 282 to 283

The following information was considered to evaluate whether rooting depths in the listed sources were suitable for use in development of Z_r for the Glacial Transition climate.

- **Extent to Which the Data Demonstrate Properties of Interest**—Rooting depths are most applicable to this analysis if they are for common plant species of the Great Basin desert that could occur at Yucca Mountain under Glacial Transition conditions (see Section 6.5.3.1 for analysis of potential future vegetation). The plant species considered should have the potential for deep root growth. Data should be collected from Great Basin desert environments. As described in Section 6.5.3.2, all rooting depths in the listed sources were for common Great Basin species. With one exception, all of the species had potential for growing roots deep into the soil profile. Sources with rooting depths for *Bromus tectorum,* an exotic annual grass, were included because of the potential for this species to form mononcultures at the expense of deeper rooting shrubs and grasses. All data from the listed sources were collected in the Great Basin desert.

- **Reliability of Data Sources—**The data from all but one of the listed sources (Table A-4) came from peer-reviewed publications and were thus judged to be appropriate for publication by experts in the field of plant root science specific to desert environments. The use of the source that is not peer reviewed, Foxx et al. 1984 [DIRS 177628] is justified in Section A1.5.

Because the data considered here were for common Great Basin plants, were from studies conducted in Great basin desert habitats, and were from reliable data sources, it was concluded that the data were suitable for the specific application in this analysis. Additionally, study methods were described in sufficient detail to determine whether the data were applicable for developing Z_r. Thus, the data were considered qualified for the intended use.

A2. QUALIFICATION OF EVAPOTRANSPIRATION DATA AND CALCULATION METHODS FOR USE AS DIRECT INPUT

This Section documents the demonstration that data and calculation methods are suitable for their intended use as inputs for calculating evapotranspiration at Yucca Mountain. Because these data were not acquired or developed for the Yucca Mountain Project (YMP), they are qualified for use as input to this report in accordance with SCI-PRO-006, *Models*, Section 6.2.1.K. The following inputs are addressed:

- Surface Albedo (Section A2.1)
- Solar Radiation on Inclined Surfaces (Section A2.2)
- Evaporation Layer Depth (Section A2.3)
- Solar Constant (Section A2.4)
- Dew point temperature offset (Section A2.5).

The attributes of the data considered in the determination of suitability are the extent to which the data demonstrate properties of interest and the reliability of the data source.

A2.1 SURFACE ALBEDO VALUES

The following information was used to evaluate whether the surface albedo values presented by Brutsaert (1982 [DIRS 176615], p 136, Table 6.4) were suitable for use in development of input parameters for simulating evapotranspiration.

Extent to Which the Data Demonstrate Properties of Interest—Terrain albedo is used to calculate reflected radiation from areas surrounding model grid cells, which affects the energy balance of these grid cells.

Reliability of Data Source—The referenced source by W. Brutsaert, *Evaporation into the Atmosphere*, was published in 1982 and has been in print ever since. The book, even though it is dated, is still current in its theory and is regarded as a foremost authority on evapotranspiration theory and boundary layer meteorology. The text is widely cited and the information contained therein is considered reliable and qualified for the intended use. The author W. Brutsaert is a professional and highly regarded expert in the technical field of environmental physics and engineering. Dr. W. Brutsaert, a professor at Cornell University since 1962, is a member of the national Academy of Engineering, and was awarded the 1999 Horton Medal by the American Geohysical Union for outstanding contributions to geophysical aspects of hydrology and the 2003 Jule G. Charney Award from the American Meteorological Society for research achievement in the atmospheric and hydrologic sciences. He has published extensively on the topic of environmental biophysics and has received many awards and honors. Therefore, the information from the source by W. Brutsaert is considered to be reliable and qualified for the intended use.

A2.2 SOLAR RADIATION ON INCLINED SURFACES

The following information was used to evaluate whether the values and equations in studies by Duffie and Beckman (1980 [DIRS 176264]; 1991 [DIRS 176616]) were suitable for use in calculation solar radiation on inclined surfaces.

Extent to Which the Data Demonstrate Properties of Interest—The equations and parameters taken from these sources are intended for, and are sufficient for, the calculation of available solar radiation on inclined surfaces. Therefore they are appropriate for calculation of potential evapotranspiration.

Reliability of Data Source—The referenced sources by Duffie and Beckman, *Solar Engineering of Thermal Processes,* were published in 1980 ([DIRS 176264], First Edition) and 1991 ([DIRS 176616], Second Edition). The third Edition of *Solar Engineering of Thermal Processes* was recently published in August, 2006; therefore, the information from this book is considered to be reliable and qualified for the intended use and has been in publication for approximately 26 years. The book provides a complete coverage on the basic theory of solar radiation and its calculation. The authors are recognized authorities on the topic of solar radiation and they hold several professional awards. John A. Duffie (deceased) was Professor Emeritus of Chemical Engineering and past Director of the Solar Energy Laboratory at the University of Wisconsin–Madison. William A. Beckman is the Ouweneel-Bascom Professor Emeritus of Mechanical Engineering and Director of the Solar Energy Laboratory at the University of

Wisconsin–Madison. Therefore, the equations for solar energy input to inclined surfaces are considered to be reliable and qualified for the intended use.

A2.3 EVAPORATION LAYER DEPTH

The following information was used to evaluate whether the recommendations on assigning evaporation layer depth presented by Allen et al. (2005 [DIRS 176009], p. 4) were suitable for use in developing net infiltration estimates for Yucca Mountain.

Extent to Which the Data Demonstrate Properties of Interest—Due to the differences between soil characteristics at Yucca Mountain and those more typical of agricultural areas, it was considered appropriate to expand the range in evaporation layer depth suggested by Allen et al. (1998 [DIRS 157311], p. 144). This paper provides guidance to consider the length of drying periods in the assignment of this parameter, which would tend to increase the evaporation layer thickness for a relatively dry site such as Yucca Mountain.

Reliability of Data Source—The referenced source by Allen et al., *FAO-56 Dual Crop Coefficient Method for Estimating Evaporation from Soil and Application Extensions*, was published in 2005 in the Journal of Irrigation and Drainage Engineering. The author, Dr. Richard G. Allen, is a professor of water resources engineering at the University of Idaho. Allen has published extensively on subject topics specifically relating to the calculation of reference evapotranspiration and holds many professional awards, including three best paper awards from ASCE Journals. Allen is regarded as an international authority on the calculation of evapotranspiration and supporting components. Allen is also the main author of *Crop evapotranspiration* (Allen et al. 1998 [DIRS 157311]) and a principal editor of *The ASCE Standardized Reference Evapotranspiration Equation* (Allen et al. 2005 [DIRS 176207]), two widely used publications on the subject of reference evapotranspiration considered here as Established Fact. Therefore, the guidance provided in this paper is considered to be reliable and qualified for its intended use.

A2.4 SOLAR CONSTANT

The following information was used to evaluate whether the data summary of measurements of the solar constant as a function of time presented by Dewitte et al. (2004 [DIRS 178528], p. 214) were suitable for use in developing net infiltration estimates for Yucca Mountain.

Extent to Which the Data Demonstrate Properties of Interest—Dewitte et al. (2004 [DIRS 178528]) presents a time history of available solar irradiance measurements and estimates the uncertainty in any long term estimates of this quantity. The solar constant is used as direct input to calculations of evapotranspiration and therefore a good understanding of possible changes in this value with time is potentially important.

Reliability of Data Source—The referenced source by Dewitte et al., *Measurement and Uncertainty of the Long Term Total Solar Irradiance Trend*, was published in 2004 in the journal Solar Physics. The first author, Steven Dewitte is a Professor in the department of Electronics and Information Processing at the Royal Meteorological Institute Belgium. The second author, Dominique Crommelynck is the honorary head of the Royal Meteorological Institute Belgium

and is a noted expert in the field of solar measurements. Therefore, the data and analysis provided in this paper is considered reliable and qualified for its intended use.

A2.5 DEW POINT TEMPERATURE OFFSET

The following information was used to evaluate whether the data obtained from a peer-reviewed journal article by Temesgen et al. (1999 [DIRS 178312], pp. 29 to 30) were suitable for use in developing net infiltration estimates for Yucca Mountain. The specific data used from this source is the upper bound on the dew point temperature offset used in the calculation of reference evapotranspiration in Section 6.5.4.1.

Extent to Which the Data Demonstrate Properties of Interest—Temesgen et al. (1999 [DIRS 178312], p. 29 to 30) paper presents a study that compared predicted and measured evapotranspiration at a number of international sites that differed in their atmospheric aridity. In relatively humid environments, the minimum daily temperature is typically very near the dew point temperature due to latent heating that occurs when water vapor condenses at or below the dew point temperature. However, in arid climates, minimum daily temperature frequently falls significantly lower than the dew point temperature because there is little water available to condense. Because the calculation of reference evapotranspiration requires that the meteorological data be collected over "an extensive surface of green grass, shading the ground and not short of water" (Allen et al. 1998 [DIRS 157311], p. 25), a dew point temperature offset is generally applied in the calculation of reference evapotranspiration in order to adjust temperature data collected over nonideal surfaces so it is more representative of these reference conditions (e.g., Allen et al. 1998 [DIRS 157311], pp. 58 to 59). Temesgen et al. (1999 [DIRS 178312], pp. 29 to 30, Table 4) lists a range of dew point temperature offsets for various arid and humid sites around the world. The highest dew point temperature offset (shown as "TD") value listed on Table 4 is 10°C for several of the arid locations for both summer and winter seasons. This value is used as direct input for the upper bound on the uncertainty distribution for the dew point offset parameter discussed in Section 6.5.4.1. The source contains the exact type of information needed to constrain this parameter and is appropriate for its intended use.

Reliability of Data Source—The referenced source by Temesgen et al., *Adjusting Temperature Parameters to Reflect Well-Watered Conditions*, was published in 1999 in the Journal of Irrigation and Drainage Engineering. The first author, B. Temesgen was a graduate student of Dr. Richard G. Allen, the second author and now a professor of water resources engineering at the University of Idaho. Allen has published extensively on subject topics specifically relating to the calculation of reference evapotranspiration and holds many professional awards, including three best paper awards from ASCE Journals. Allen is regarded as an international authority on the calculation of evapotranspiration and supporting components. Allen is also the main author of *Crop evapotranspiration* (Allen et al. 1998 [DIRS 157311]) and a principal editor of *The ASCE Standardized Reference Evapotranspiration Equation* (Allen et al. 2005 [DIRS 176207]), two widely used publications on the subject of reference evapotranspiration considered here as Established Fact. Finally, the third author, Dr. Donald T. Jensen is currently the Utah state climatologist. The qualifications of these authors and the reliability of the peer-reviewed journal both justify the qualification of this data for use in this report.

A3. QUALIFICATION OF SUBLIMATION COEFFICIENT FOR USE AS DIRECT INPUT

The following information was used to evaluate whether the measurements of fraction of snowpack lost to sublimation reported by Hood et al**.** (1999 [DIRS 177996]) were suitable for use in development of the sublimation parameter (SUB). This source is used as direct input in Section 6.5.1.7.

Extent to Which the Data Demonstrate Properties of Interest—Hood et al., (1999 [DIRS 177996]) report measured sublimation over a nine-month period and is therefore more reliable than previous studies which were based on data only from the snowmelt season.

Reliability of Data Source—The median value of 10% snow sublimation used in the infiltration model originates from studies cited by Hood et al. (1999 [DIRS 177996]). These studies include the author's own study in which they found snow sublimation to be about 15% of the total seasonal snow accumulation at Niwot Ridge in the Colorado Front Range. They also cite seasonal sublimation estimates of 18% and 20% for the Sierra Nevada, California, reported in two other studies. Seasonal snow sublimation is extremely difficult to measure, and there is large inherent uncertainty in this parameter. Hood et al. (1999 [DIRS 177996]) can be considered to be experts in the field given their organizations and publication records. Their organizations include the Institute of Arctic and Alpine Research (INSTAAR) at University of Colorado, Boulder, and the National Operational Hydrologic Remote Sensing Center, which provides comprehensive snow observations, analyses, data sets and map products for the Nation. Eran Hood, Mark Williams, and Don Cline have all published numerous articles related to snow. Therefore, the information from this journal article is considered to be reliable and qualified for the intended use.

A4. ESTABLISHED FACT INPUTS

A number of references cited as direct input are Established Fact as defined in SCI-PRO-004 Rev 2, p. 7 and Attachment 1. These are listed below with an explanation. These do not include DTNs designated as established fact.

1. Allen et al., 1998 [DIRS 157311] *FAO Irrigation and Drainage Paper No. 56 Crop Evapotranspiration*. This is a United Nations report that is a set of guidelines used by international scientists and engineers in their work practices.

2. Allen et al. 2005 [DIRS 176207] *The ASCE Standardized Reference Evapotranspiration Equation.* This is an ASCE publication that is considered the standard handbook and reference on calculating reference evapotranspiration.

3. Maidment 1993 [DIRS 125317] *Handbook of Hydrology*. This is a scientific handbook and a standard reference utilized by civil engineers and hydrologists.

4. IEEE/ASTM SI 10-1997 Standard for Use of the International System of Units (SI): The Modern Metric System. This is the standard by which all scientists apply units.

5. U.S. Department of Agriculture government publications including “fact sheets” by Anderson (2002 [DIRS 177625]), Tirmenstein (1999 [DIRS 177641]; 1999 [DIRS 177642]), USDA (2002 [DIRS 178073]), and Zlatnik (1999 [DIRS 177639]). The USDA intended these for scientists to use as sources of information regarding specific plant species.

APPENDIX B
GEOSPATIAL DATABASE

B1. INTRODUCTION

This appendix describes the technical processes within a Geographic Information System (GIS) to develop spatial inputs for the Mass Accounting System for Soil Infiltration and Flow (MASSIF) model. A GIS is the combined hardware and software used for storage, retrieval, mapping and analysis of geographic data. Using a GIS, data were collated from a range of sources, processed into a usable format, and combined into a single spatial database containing input values and their associated spatial coordinates for the MASSIF model. A complementary set of calibration data was produced in conjunction with the overall model inputs. These calibration files provided model inputs for areas with existing stream gage data to serve as a check of model accuracy.

A spatial database is a table with fields (columns) of variables that include real world coordinates. In a GIS, these coordinates can be used to visually display the tabular data as points, lines, or for the MASSIF model, rectangular map grids that form the individual model cells. Each record (row) in the table represents a single 30-m^2 grid cell within the MASSIF model. A spatial database is constructed by combining individual data layers based on shared coordinates or data within a field. A GIS also allows queries of the spatial relationship between the various data fields. For the purpose of the MASSIF model, for each record in the database, the GIS stores a unique grid cell number, universal transverse mercator (UTM) coordinates, latitude and longitude, elevation, a downstream grid cell identifier, slope, azimuth, soil depth, soil type, bedrock type, and a measure of vegetation called "potential vegetation response" (PVR; see Appendix E). The GIS can be queried to give data values at a given point or the full range of variables contained in an area. The visual display capability together with the measurement of spatial relationships makes GIS an ideal tool for preparing and examining data inputs for the MASSIF model.

Building the infiltration model spatial database was a multistage process involving importing some data layers and using the GIS to generate others within the spatial database. The database contains nine data layers supplying inputs to the MASSIF model and four spatial values that supply geographic coordinates within a 30- × 30-m grid framework. The project grid measures 367 columns by 691 rows resulting in 253,597 grid cells. The project area boundary is defined by UTM NAD 27 Zone 11 coordinates with a southwest corner at 544,646-m east/4,067,118-m north and a northwest corner at 555,656-m east/4,087,848-m north.

During the process of building the spatial database, several important tasks were completed. Defining the watershed subset boundaries within the larger project area boundary was the first task (Section B2). This delineation in turn defined the model boundary, a 139,092-grid-cell subset of the project area. The initial data layer, elevation, was selected and the processing steps developed (Section B2.1). Next, the elevation data needed to undergo a three-stage watershed characterization process that defined the actual watershed boundaries and created ancillary data layers required by the spatial database (Section B2.2). Then, these files required formatting to prepare them for the spatial database (Section B2.3).

Not all the necessary data were created during the watershed delineation process. Additional spatial database information consisted of bedrock and soil characteristics that required formatting and editing to prepare the layers for the spatial database (Section B3.1). The PVR was a data

layer calculated using Normalized Differentiated Vegetation Index (NDVI) measurements as detailed in Appendix E. The last required data layer was the field with the downstream cell identification number. This field was determined using a grid cell identification number and the direction of surface water flow leaving that grid cell (Section B3.2).

The assembly of the spatial database required conjoining the separate data layers into a single more comprehensive format (Section B4). The database covers the entire model area, but it was necessary to subdivide it into the individual watersheds delineated earlier (Section B4.1).

Concurrent with the modeled watersheds, a study using actual surface flow data required the delineation of six streamflow watersheds (Section B5). This process used imported stream gage locations (Section B5.1) to constrain the watershed delineation process. The streamflow watershed boundaries were used to divide the spatial database into small study areas that can be used to compare model results to real world observations (Section B5.2).

The final result from this process was a spatial database split into eleven project watersheds and subdivided into six, smaller representative drainages that sample select portions of the project area. These final files are formatted into comma-delimited text files that serve as direct input into the MASSIF model.

B2. GIS WATERSHED CHARACTERIZATION

The MASSIF infiltration model addresses the area that drains Yucca Mountain above the proposed repository waste emplacement area. Eleven separate drainages (or watersheds) were identified; three larger watersheds drain the east face of the ridge and eight smaller watersheds drain the west face. Each watershed formed a component of the MASSIF model.

The watersheds were delimited using elevation and slope to define surface water flow direction to a single outlet (pour point). Defining the eleven watersheds also delineated the overall infiltration model boundary within the larger project boundary. The larger rectangular project boundary encompassed 226.34 km^2. The mix of eleven larger (up to 41.16 km^2) and smaller (down to 0.11 km^2) watersheds made up the individual model components that were used to calculate net infiltration. The infiltration model boundary, comprised of the combination of these eleven watersheds, encompassed 125.18 km^2. Figure B-1 shows the relationship between these three sets of boundaries. The following discussion details the tools and source data used to create these watershed delineations.

B2.1 SOFTWARE AND DATA CONSIDERATIONS

In a GIS, spatial attributes are stored in conjunction with descriptive attributes allowing tabular data to be displayed in reference to their position on the earth. Data can consist of points, lines, and polygon shapes with multiple attributes connected to each of these features, allowing a layering of data values. With the layered features, spatial relationships can be measured and complex models can be constructed. The capacity to combine separate data layers and run a model to extract additional data layers from existing layers is extremely important for the infiltration model database; therefore, GIS is the perfect tool for the tasks required.

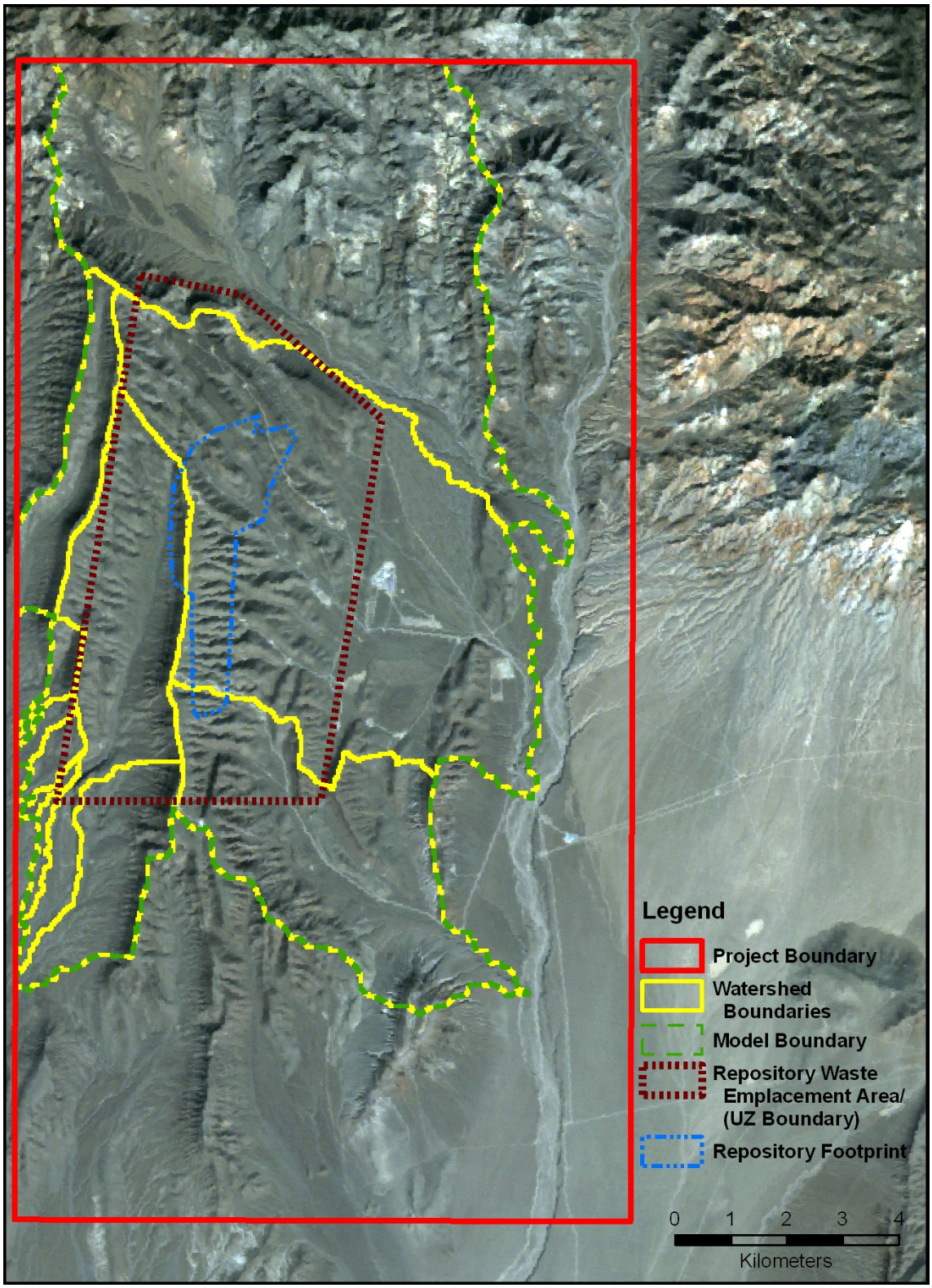

Source: Output DTNs: SN0608DRAINDYM.001, SN0612FTPRNUZB.002, and SN0608NDVILSTM.001.

Figure B-1. Boundaries within Project Area

The GIS used for these tasks is ArcGIS (ArcGIS Desktop Version 9.1 STN: 11205-9.1-00 [DIRS 76015]), from Environmental Systems Research Institute (ESRI), the market leader in off-the-shelf GIS software. In addition, the Spatial Analyst extension increases the flexibility of ArcGIS to work with raster-based data. Using the Model Builder functionality of the ArcGIS ArcToolbox, a fully automated routine was established where base data and parameters can be loaded into the model to then have a series of watershed characterization tasks applied iteratively to derive a final watershed catchment grid. In addition, nearly all the data processing functions required to prepare the spatial inputs for MASSIF were conducted within the GIS database. The spatial database format also allowed data queries to be conducted prior to running MASSIF.

The most accurate topographic data available were chosen from a field of three data sets. Spatial data supply the measures of elevation, azimuth, and slope that play important roles for accessing parameters, including vegetation cover, runoff, and evapotranspiration (ET) that are active in the calculation of net infiltration in each model grid. Therefore, spatial accuracy is crucial for model accuracy.

The three candidate data sets for topographic data were U.S. Geological Service (USGS) digital elevation model (DEM), the USGS National Elevation Dataset (NED) and the Shuttle Radar Topography Mission (SRTM) data. All elevation data sets are created through a sampling technique using different methods and resolution. A set of single elevation values can never truly represent all the variability found in all represented grid cells no matter the data resolution be it 10 m or 30 m. With this knowledge, there is an understanding that the data may need some modification to effectively model certain aspects of the landscape.

DEM, and as a result NED, data is created from using existing contour maps and augmented with aerial photography. Much of this data consists of passively collected data, so even though the resolution may be quite high (up to 10-m square) actual measurements used to create the data are limited and most data values were created through interpolation.

USGS DEM data often are used to supply the topological information necessary to run basic watershed characterization models. A DEM is constructed as a 10-m or 30-m grid where the centroid of each grid cell is assigned an elevation based on its corresponding location on a topographic map. Because they are digitized from maps that represent earlier interpretation of topography, these data incorporate inherent flaws, especially in areas that experience significant elevation change over a short distance.

NED was compiled by the USGS to assemble the best available topographic data into a continuous elevation model for the entire country. This dataset typically employs the USGS 10-m DEM data, when available, that is nine times more detailed than the coarser 30-m data. For the YMP, the NED metadata indicated that 10-m data were available and incorporated into the dataset; however, these data still contain inherent limitations of accuracy because they were formulated by extrapolating elevation data from topographic maps.

SRTM is a more recent dataset that was collected through an interferometric synthetic-aperture radar system carried aboard a U.S. space shuttle mission during February 2000. These data are highly accurate because the active sensor collected a data value for each 30-m target, meaning no extrapolation was necessary. The data will still be limited by having a single value in a 30-m^2

grid cell represent all the possible variation in that cell, but this is the case with all three of the data sets spacing. One drawback with SRTM datasets are occasional problematic gaps due to radar shadow at low angles of incidence or signal interference from numerous vertical surfaces (i.e., signal bounces between tall buildings or forest tree trunks). These influences are not problematic for the remote treeless Yucca Mountain region, and the dataset showed none of these characteristics.

The availability of three adequate data sets raised the issue of which would best serve the model's needs. The 30-m DEM was eliminated because, with its 10-m resolution, the NED superseded the coarser DEM; however, the question remained whether to use NED or SRTM data. A raster subtraction method was employed to observe the differences between these datasets. The resulting grid showed a misalignment between the two data sets. Smith and Sandwell (2003 [DIRS 177358]) faced this question on a project in the Amazon and devised a selection method that compared SRTM, NED, and high-resolution aerial laser datasets. Their results showed the NED possessed an 11.87-m longitudinal and 10.58-m latitudinal shift versus the spatially accurate, high-resolution laser imagery. The laser data were used as the benchmark because a Laser Imagining Detection and Range (LIDAR) system is an active sensor, typically flown from an aircraft that has very fine resolution and can easily incorporate ground control points for accuracy. A comparable shift was not detected with the SRTM. On the basis of the Smith and Sandwell (2003 [DIRS 177358]) results, SRTM data were selected as the superior choice for the infiltration model. In addition, the SRTM data has been subjected an independent assessment of accuracy that is detailed below (Rodriguez et al. 2005 [DIRS 177738]). A similar investigation for the NED data set is planned, but has not been completed and users have to compile the errors present in each contributing DEM to access overall accuracy.

The SRTM data were obtained from the USGS Earth Resources Observation and Science (EROS) Data Center (DTN: SN0601SRTMDTED.001 [DIRS 177242]).

Assessment of SRTM Accuracy

The NASA Shuttle Radar Topography Mission (SRTM) collected interferometric radar data that was used to generate a near global topography data product. This data underwent a ground-truth analysis to provide a detail measure of the different components of the error, their magnitudes, and spatial structure (Rodriguez et al. 2005 [DIRS 177738]).

The data was collected to meet the following performance requirements:

1. The linear vertical absolute height error shall be less than 16 m for 90% of the data
2. The linear vertical relative height error shall be less than 10 m for 90% of the data
3. The circular absolute geolocation error shall be less than 20 m for 90% of the data
4. The circular relative geolocation error shall be less than 15 m for 90% of the data.

The table shown below summarizes the SRTM performance observed by comparison against the available ground-truth data. The displayed measurements represent 90% errors in meters. It has been modified here to display just the North America results.

	N. America – Observed	Required
Absolute Geolocation Error	12.6	<16
Absolute Height Error	9.0	<10
Relative Height Error	7.0	<15

The study's authors found, "the analysis had shown that the SRTM error could be divided into very long wavelength (continental scale or larger) errors and short wavelength random errors. The ground-truth data were not appropriate for validating relative geolocation errors. It is expected that the main sources of geolocation errors are also long wavelength, so that the relative geolocation error will in general be smaller than the absolute geolocation error, since common errors will cancel. The absolute geolocation performance is better than that required for the relative geolocation, which provides indirect evidence that the relative geolocation requirement was also met" (Rodriguez et al. 2005 [DIRS 177738], page 9).

Smith and Sandwell (2003 [DIRS 177358]) further showed the small error involved in the geolocation measurements in the SRTM data. In all, the error falls within the breadth of a single model pixel. As to the height error, for this infiltration model a small flux in actual measured height could potentially interfere in the delineation of a watershed by creating a pixel surrounded with higher elevation values, creating a 'sink' with no access for flowing water to exit the cell. A GIS step of filling such sinks and thus removing the error impact is discussed in Section B2.2, Processing the Elevation Data.

B2.2 PROCESSING THE ELEVATION DATA

The raw form of the SRTM data required processing for use in the spatial database, as the SRTM file format and map coordinate projection do not correspond to those needed for the infiltration model. Once format and projection were revised, the elevation data could then serve as the base data layer from which multiple derivative data layers could be created. These additional layers provided information, such as slope direction and steepness that is required by the MASSIF infiltration model.

The raw form of the SRTM data layer was processed using Research Systems, Inc. (RSI) Environment for Visualizing Images (ENVI; ENVI + IDL, Version 4.2: STN: 11204-4.2-00) image processing software. ENVI offers more options in choosing how to process raster data than ArcGIS software. All the data processing represented in Sections B2.2 and B2.3 are archived in 'Drainage Delineation at Yucca Mountain' (Output DTN: SN0608DRAINDYM.001). The SRTM data were divided as a subset within the project boundary, set to 30-m pixels and reprojected to UTM NAD 83 Zone 11. This conflicted with the MASSIF model requirement of UTM NAD 27 Zone 11 but would be reprojected in Section B-4, *Assembling the Spatial Database*, after concurrent image processing tasks detailed in Appendix E were completed. With the data resized and reprojected, the elevation data were saved as an ESRI grid file ready for watershed delineation. Figure B-2 highlights the elevation range from 964 m to 1,964 m across the YMP area.

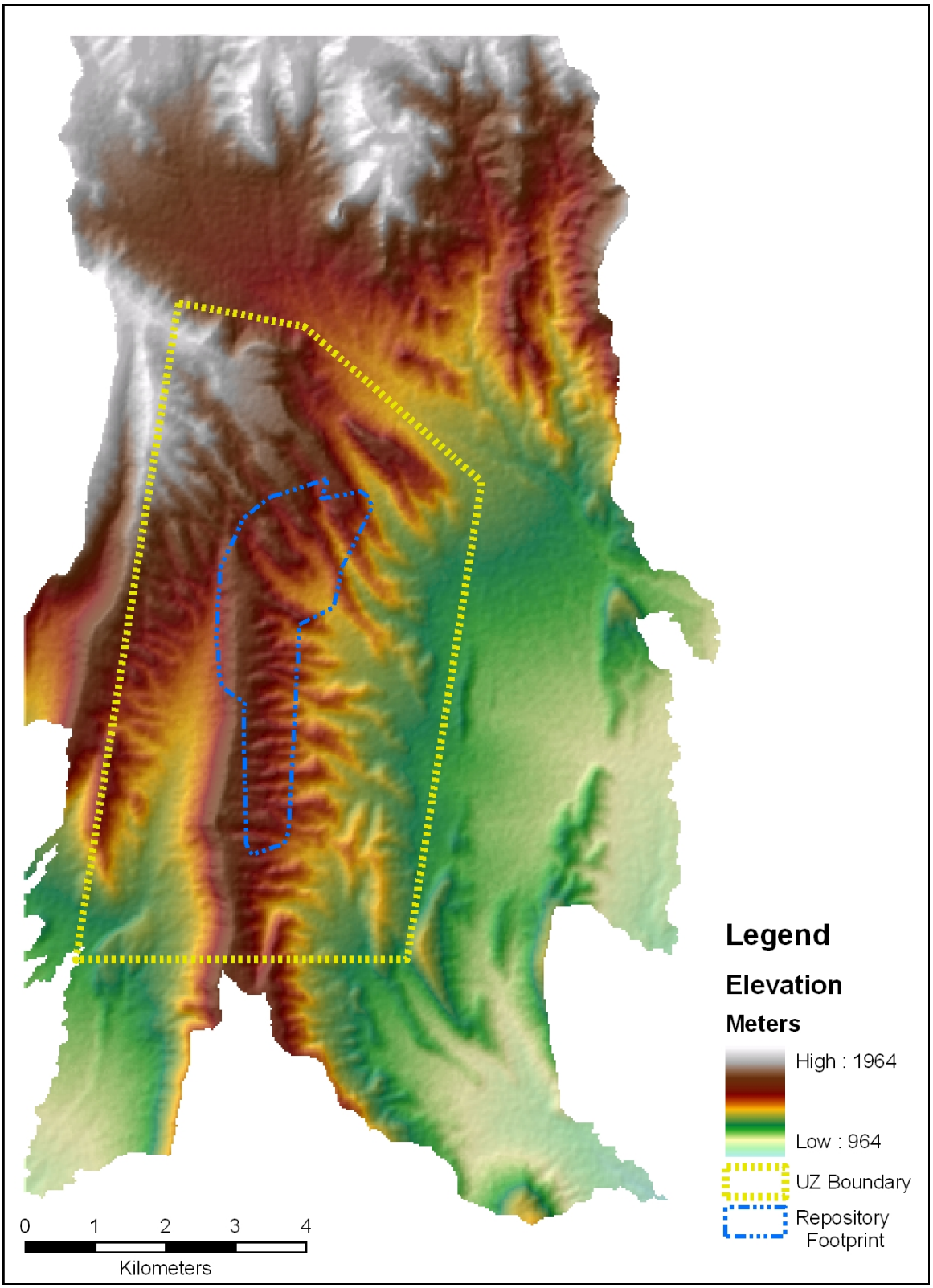

Source: Output DTNs: SN0701SPALAYER.002 and SN0612FTPRNUZB.002.

Figure B-2. Elevation across Project Area

A three-stage watershed delineation process was required to generate the fewest number of watersheds that would cover the Repository Waste Emplacement Area. Each stage set a different water flow accumulation value (15,000, 1,000, and 200) which controlled the size of the resulting model watersheds. The MASSIF model runs each watershed separately, so a fewer number of drainages results in fewer modeling steps. Moreover, all watersheds must drain to single points on the edge of the YMP area, otherwise intermediate runoff values would need to be passed between drainages during the computation. Therefore, the size of the drainages was dictated by two factors: the topography of the region and the placement of the YMP boundary. The surface area of each watershed varied widely, a result of the three nearly identical delineation stages needed to generate the eleven drainage basins that cover Yucca Mountain: three large, three moderate, and five small basins. During each stage, a specific threshold variable was set that would determine the size of the resulting drainages. Thus each stage was responsible for generating either the large, medium, or small drainage basins. Variable basin sizes were necessary because the MASSIF model needed to trace potential infiltration from all locations directly over the repository footprint down the mountain slopes to each basin's pour point (the bottom-most part of the basin). The further the drainage travels, the greater is the size of the watershed; i.e., the more distant a pour point is from the headwaters, more space is provided for numerous smaller drainages to combine together and form larger, wider basin delineations. The YMP boundary, as defined, allowed the less steep eastern slopes to be followed out to distant pour points resulting in three large watersheds, but the steeper western basins were truncated by the close proximity of the YMP boundary. This limited the distance the drainages traveled before a pour point was assigned. Thus several small- and medium-sized watersheds were generated, as opposed to a few larger units had the YMP boundary allowed the drainages to travel further downslope. The results would be the same no matter how many watersheds were defined, as long as each grid unit within the Repository Waste Emplacement Area was assigned to a watershed within MASSIF.

The required size of the watersheds in each stage also limited how much of the Repository Waste Emplacement Area was covered. The first stage created a few large watersheds but did not cover areas where only smaller drainages could fit. Stage two created many more watersheds, but only three added additional coverage in areas previously missed in stage one. Stage three created many, very small drainages, but only five were required to fill the remaining coverage gap over the Repository Waste Emplacement Area. The final step was the process of fitting the eleven watersheds from the three-stage delineation process back together to create a single file representing the MASSIF model project area. Below are the details that completed this process.

The full Terrain Processing toolbox that ArcGIS utilized was a series of nine separate computations. The accompanying schematic, recreated (for legibility) from a screen-captured image while using the 'Full Terrain Processing' ArcToolbox, graphically displays the steps detailed here (Figure B-3). The figure shows the GIS tasks used and output files created during watershed delineation. All the tasks contained in the Full Terrain Processing toolbox are available individually within the ArcGIS Spatial Analyst.

The *fill* function was the first process applied to the SRTM data. *Fill* located low points or 'sinks' in the data set where all the surrounding pixels were of higher values. These sinks were accurate elevation values at the center of a data collection grid. However, elevation variation within a specific 30-m grid cell might be high enough that the elevation at the center might not

represent an elevation suitable to allow a small potential drainage to pass through the grid cell from an upstream grid cell or into a downstream cell. These sinks are probably artifacts of the sampling technique used to create the elevation dataset, where 900 potential $1m^2$ elevation values are represented by a single value. Thus, these sinks are a consequence of simplifying the YMP area elevation to a specific set of grid-cell elevations, which neglect smaller scale features. There is really no geomorphic reason to expect significant sinks in the model domain because spillover from these sinks during heavy precipitation events would lead to erosion and the elimination of the sinks over time. Such features are more characteristic of karst terrain. If a pixel was identified as a sink, the *fill* function raised the elevation value in the pixel until a surrounding pixel is identified as having an equal or lower value, thus capable of accepting any potential accumulated surface flow that would have collected within the sink with no identified outlet cell in which to flow. The output 'filled SRTM' grid mirrored the original SRTM data with only small adjustments made to certain 'sink' pixels. Simple spatial subtraction between these two grids showed that most of the sinks occurred along drainage bottoms. Table B-1 shows how many pixels' elevation was modified by the *Fill* function over the YMP area, within the smaller delineated watersheds model area, and over the repository footprint, stressing just how slightly (1.06 %, 0.44%, and 0.11%) this vital step affected the data. *Fill* is a required process to convert the current elevation dataset into a usable form for hydrology modeling within ArcGIS, because an uninterrupted flow is critical as opposed to slightly modifying a representative grid cell elevation value.

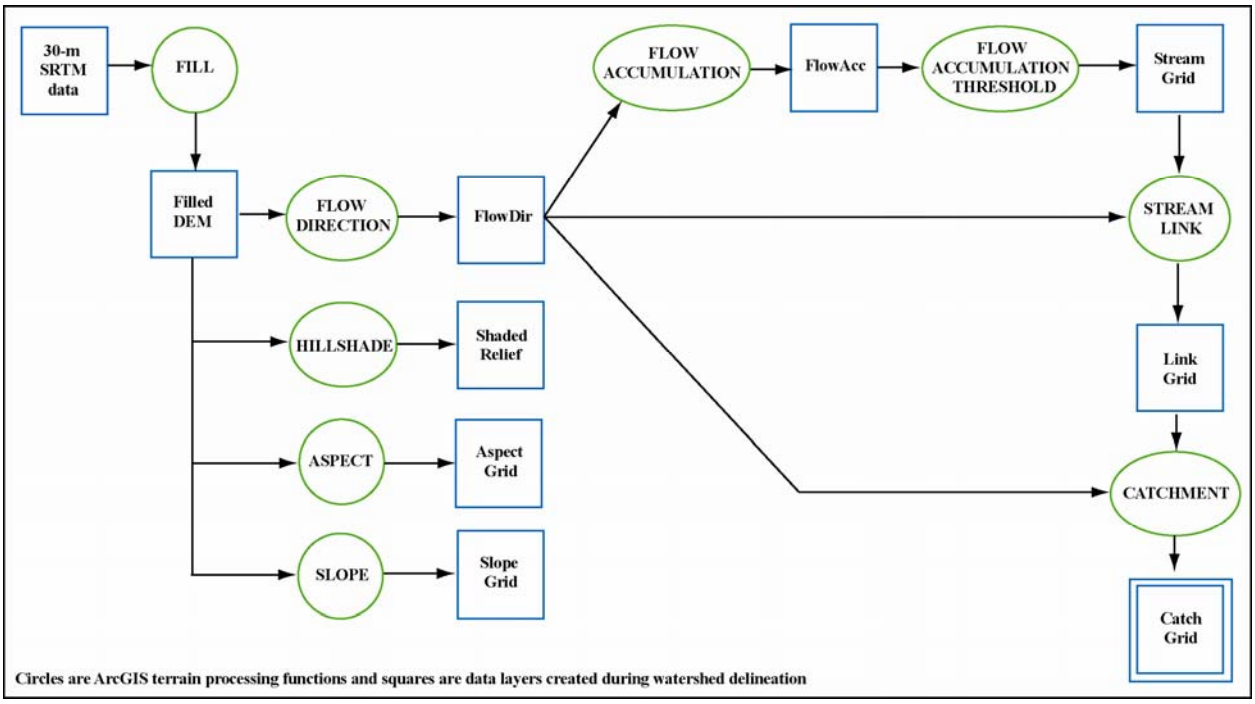

Figure B-3. Full Terrain Processing ArcToolbox Steps

Table B-1. Elevation Change Documented as a Result of the *Fill* Process

Elevation Change	Number of Pixels in Project Area	Percentage of Project Area	Number of Pixels in Model Area	Percentage of Model Area	Number of Pixels in Footprint Area	Percentage of Footprint Area
0	250,916	98.94	138,483	99.56	6,350	99.89
1	2,248	0.89	502	0.36	5	0.07
2	376	0.15	90	0.06	2	0.03
3	50	< 0.01	13	< 0.01	1	0.01
4	5	< 0.01	2	< 0.01	0	0
9	1	< 0.01	1	< 0.01	0	0
16	1	< 0.01	1	< 0.01	0	0

Source: DTN: SN0601SRTMDTED.001 [DIRS 177242]; Output DTN: SN0608DRAINDYM.001.

The resulting 'filled SRTM' layer provided the elevation data layer for the MASSIF model, but this layer was also used to create five additional datasets equally important to the model. Two of these extra layers, slope and azimuth, were stand-alone products; two more, catchment and flow accumulation, were used to organize the database but were not included in the final database; and the fifth, flow direction, required additional processing to convert it into a layer providing the downslope cell ID number. The filled elevation data, and all subsequent generated data layers used to create the MASSIF spatial database, are assembled together in Output DTN: SN0606T0502206.011.

The full suite of output created in the Full Terrain Processing ArcToolbox (Figure B-3) was as follows. The *hillshade* function created a raster layer that resembled a three-dimensional representation of the YMP area by calculating light and shadow effects based on topography and a default sun angle of 315° and a 45° incident angle. The hillshade layer was only a visual aid in presenting the data layers and did not provide a direct input to the MASSIF model.

The elevation data were also used to create additional layers within the GIS including the slope and azimuth over the model area. The surface slope of each grid cell was calculated using the *slope* function in ArcGIS, which uses the elevations at eight neighboring cells. Slope is defined from 0° (horizontal) to 90° (vertical). Slopes over the infiltration modeling domain ranged between 0° and 49° (rounded to the nearest degree). A map of slopes over the modeling area is presented in Figure B-4.

The azimuth layer was created using the *azimuth* function in ArcGIS, which estimates the compass direction of a vector normal to the surface of each grid cell. This parameter is used for calculations involving the direction of incoming solar radiation. Azimuths were defined between 0° and 360° (rounded to the nearest degree) and proceeding clockwise, with 90° representing east. A map of azimuths over the modeling area is presented in Figure B-5.

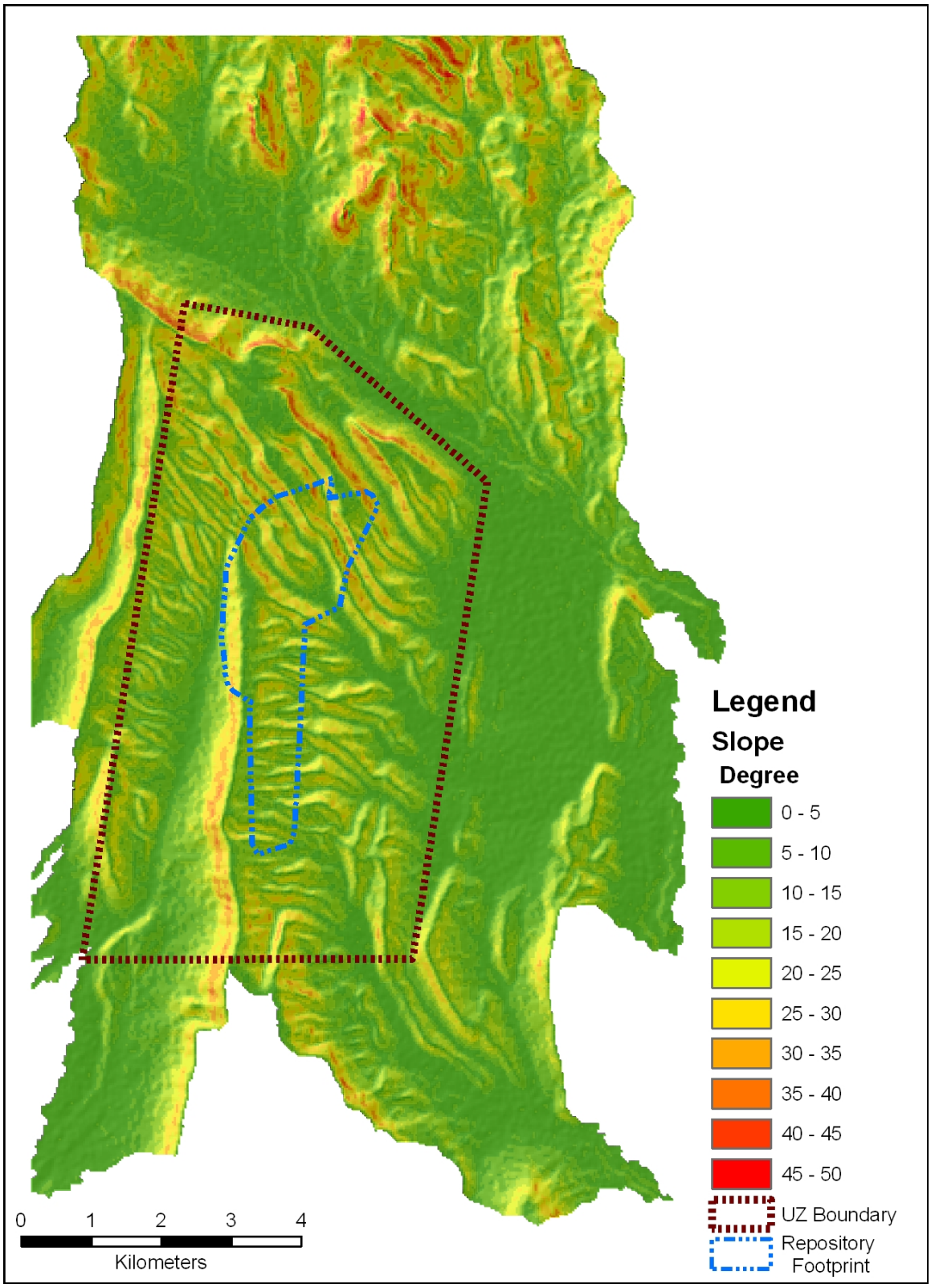

Source: Output DTNs: SN0701SPALAYER.002 and SN0612FTPRNUZB.002.

Figure B-4. Slope across Project Area

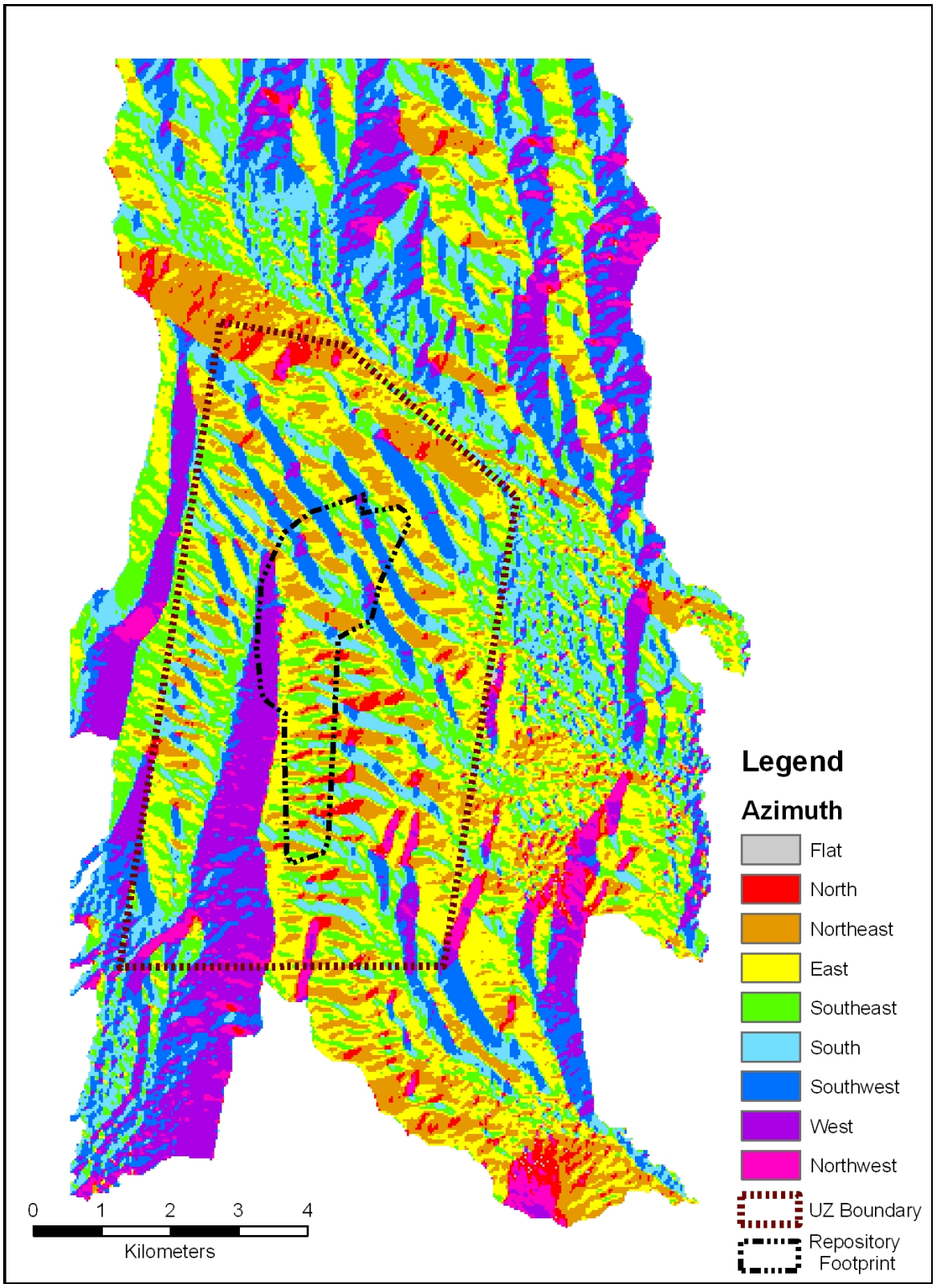

Source: Output DTNs: SN0701SPALAYER.002 and SN0612FTPRNUZB.002.

Figure B-5. Azimuth across Project Area

The *flow direction* function is similar to azimuth, but instead of a compass direction, the function created a numeric code for each cell that represented which neighboring cell water would flow into when leaving the current cell. The resulting layer had values 1, 2, 4, 8, 16, 32, 64, and 128 representing east, southeast, south, southwest, west, northwest, north, and northeast, respectively. This need to determine a direction of flow was why all 'sinks' in the SRTM data set needed to be filled in the previous step. The Full Terrain Processing ArcToolbox used the resultant 'flow direction' data layer to create three additional data sets.

By examination of the flow direction relationships, the *flow accumulation* function calculated the number of upstream pixels for every pixel. The 'flow direction' layer was employed to trace paths of flow with accumulation counts increasing with each new pixel entered or when joining two or more convergent flow paths. A *Flow Accumulation Threshold* was applied to this function to limit the number of drainages represented to only those representing significant accumulation, in this initial case 15,000 upstream grid cells. The resulting 'stream grid' highlighted just these larger streams that possessed a total accumulation of 15,000 upstream cells. The *Stream Link* function assigned unique identifiers to each stream identified as having overcome the flow accumulation threshold.

The last model layer prepared from the topographic data was 'catchment' delineation, the definition of each basin boundary. This delineation process used the concept of pour point, the lowest point along a drainage representing the downslope edge of a drainage basin before it joins another stream from an adjoining basin. Using these pour point locations and the 'flow direction' raster as input, the *Catchment* function mapped all basin boundaries. This function observed where flow direction diverged in opposing directions and assigned that as a basin boundary with all sub-basin boundaries dissolved within the larger basin defined by the pour point at the catchment's outlet.

The resulting catchment raster layer formed seven watersheds. Only three of these watersheds covered a portion of the Repository Waste Emplacement Area and were retained for use in the MASSIF model. This completed the first stage of the project area watershed delineation process. With the Flow Threshold set at 15,000, the resulting basin catchments were all large, but more of the Repository Waste Emplacement Area still fell outside these initial large watersheds. Therefore, the process had to be repeated to generate smaller watersheds to fit into gaps left by the large watersheds. The second and third stages followed the same delineation process using the Full Terrain Processing ArcToolbox, but the flow accumulation value was set to 1,000 and 200 to produce medium and small catchment basins, respectively. The end result of this delineation process was three nearly identical sets of output files, with only the size of the basins in the catchment layer the significant difference, as set by the flow accumulation threshold.

B2.3 FORMATTING THE TERRAIN DATA

During the drainage delineation process, several GIS layers were calculated from the SRTM data. These data files required additional processing to convert them to a format for import into the spatial database. All the GIS layers prepared to this point were raster files, square grid cells with single data values attached. To build a single output file, the data were converted into vector files, a series of rectilinear shapes bounding areas of equal value, whose data values could be combined into multiple-field tables. This process of data formatting is discussed below.

The catchment delineation process used three similar processing streams to produce the necessary outputs. Most of the steps in each delineation produced identical output, except for the catchment size layer, which was dependent on the flow accumulation setting. Therefore, elevation, slope, azimuth and other files were consistent throughout the processing and were not affected by the variable flow accumulation settings between the separate processing streams. With three sets of identical data, only one set needed to be prepared for inclusion in MASSIF. For consistency in description, unless otherwise specified, all terrain data extractions used data prepared during the processing run with flow accumulation set to 200 instead of the identical data sets from the 1,000 and 15,000 flow accumulation model runs.

Four of the raster layers, 'Filldem200', 'Azimuth200', 'Slope200' and 'Flowaccum200' comprised continuous data (floating point grids) that would not transfer into vector format without an additional process. To accomplish this, the decimal range of the values for each raster layer needed to be rounded up or down to create integer values.

The *Raster Calculator* ArcGIS Spatial Analyst performed this with the following formula that analyzes the portion of the continuous value fight of the decimal and rounds up or down accordingly:

```
Int(con([grid1] > 0,con(Abs([grid1] - Int([grid1])) >= 0.5,Ceil([grid1]), Floor([grid1])),con(Abs([grid1]
- Int([grid1])) >= 0.5,Floor([grid1]),Ceil([grid1]))))
```

The delineated catchment files required a different approach to prepare them for the spatial database. The goal of the watershed delineation was to generate as few watersheds as possible that intersect with the Repository Waste Emplacement Area. Experimentation with threshold settings came upon the combination of three settings that would effectively accomplish this goal. Each of the terrain processing stages created a unique catchment file based on the value of flow accumulation threshold (15,000; 1,000; and 200). Each file contained certain watersheds that needed to be included in the final model (those covering a portion of the Repository Waste Emplacement Area and not already covered by a larger watershed) while the others were discarded. The watersheds identified for inclusion were each given a unique sequential number and the remaining watersheds (those that fall completely outside of the Repository Waste Emplacement Area) were set as 'No Data' using the *Reclass* function on each file. The flow accumulation set at 15,000 produced seven basins, three of which were saved. The second stage with a 1,000 flow accumulation produced 105 watersheds. Five of the watersheds covered portions of the Repository Waste Emplacement Area not already covered by the 15,000 flow accumulation settings. Three of the watersheds drain to the same pour point on the edge of the project boundary, so they were combined. Therefore of the five saved watersheds, three were ready to be used in MASSIF. The final stage produced 600 watersheds with the flow accumulation value set at 200. Six of these watersheds covered the last unaccounted for parts of the Repository Waste Emplacement Area. Two of these basins shared a pour point and were combined into a single watershed, thus resulting in five final watersheds. The sets of three, three, and five basins were merged into a final collection of 11 project watersheds. Figure B-6 shows this three-stage process and the final 11 drainages. This file was converted to a vector file producing a set of shapes that outlined the project grid cell that belonged in each surface drainage.

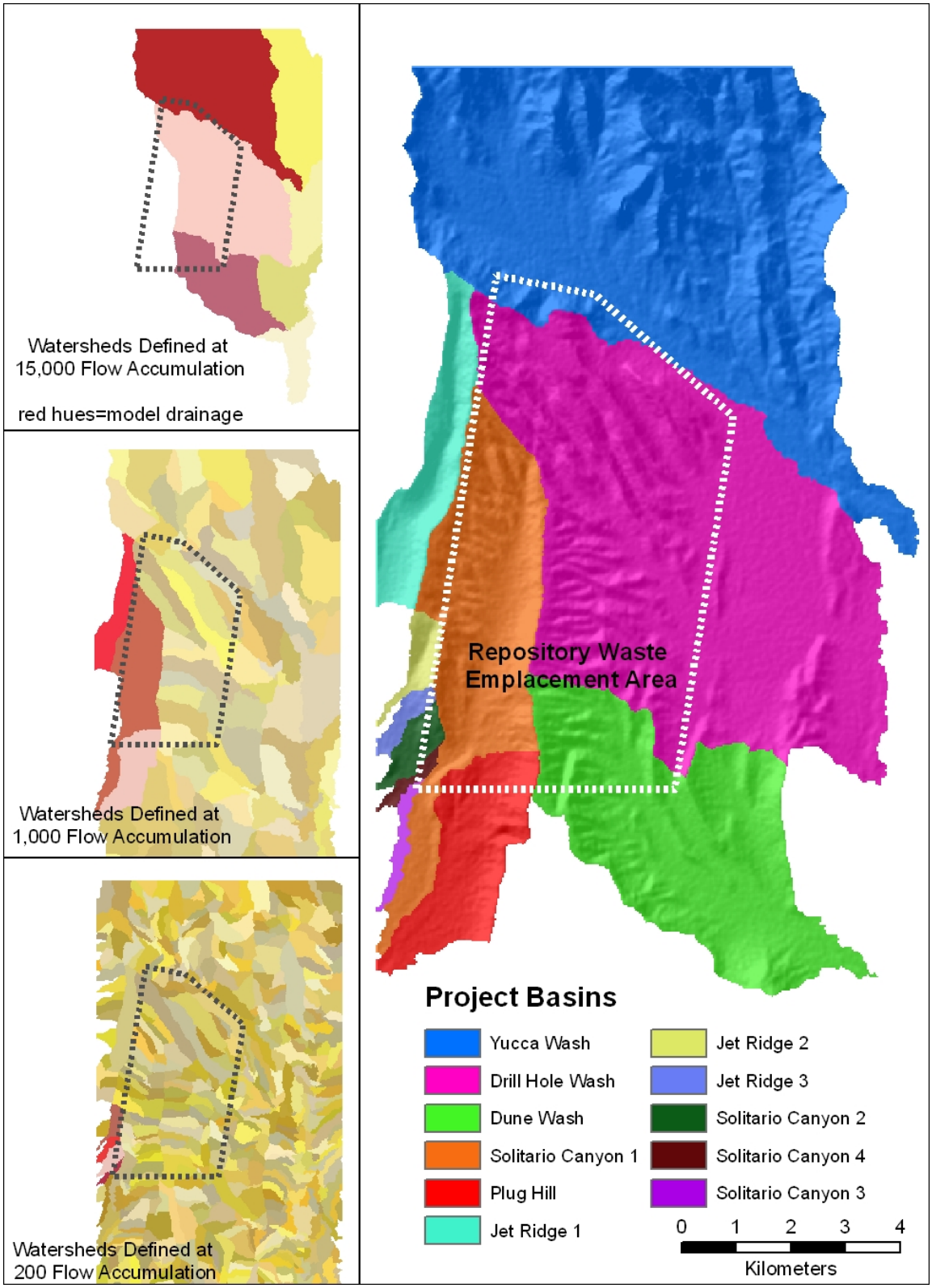

Source: Output DTNs: SN0701SPALAYER.002 and SN0612FTPRNUZB.002.

Figure B-6. Results of Three-Stage Watershed Delineation and Final Basin Combination

B3. ADDITIONAL SPATIAL DATABASE PREPARATION

The final form of the spatial database for the MASSIF infiltration model contained 13 data fields compiled from different data layers. Some layers were created in the steps detailed above and others had been prepared as stand alone data products. Three such products, soil type, soil depth, and bedrock geology, were prepared from geology and soil data outside of the current GIS and were provided in a spatial database for inclusion in MASSIF. The potential vegetative response (PVR) data were created concurrently with the spatial database and imported upon its completion. From the SRTM data and the watershed delineation process, elevation, downstream grid cell identification (ID), slope, azimuth, catchment, and flow accumulation were made available. Two other layers created during the delineation process, catchment and flow accumulation, did not actually go into the final version of the database but were necessary to divide and sort the final data. The grid cell identification number and the spatial coordinates in UTM and latitude and longitude are generic data layers based on the location and dimensions of the YMP area.

B3.1 IMPORTING PREPARED DATA LAYERS

Soil type, soil depth, and bedrock geology were model inputs independently prepared by project specialists. Each input layer was prepared from existing geologic and pedologic data for Yucca Mountain. It was necessary to update each of these three inputs to format them to MASSIF requirements. Details of their preparations and a discussion of the significances of individual classes are in Section 6.5.2. Their DTNs are MO0608SPASDFIM.006 [DIRS 178082] (containing soil type and soil depth) and MO0603SPAGRIDD.003 [DIRS 177121] (containing Bedrock geology), respectively. These data were large ASCII files supplied as tables detailing the data values for each 30-m cell in the MASSIF project boundary. The tables also included latitude, longitude, and UTM coordinates to allow the data to be displayed in a spatial database. All data processing tasks represented in Sections B3.1 and B3.2 are archived in 'Spatial Data Layers at Yucca Mountain' (Output DTN: SN0701SPALAYER.002).

The range of bedrock values and soil depth across the project area from these files are displayed in Figures B-7 and B-8, respectively. During the course of the project, questions arose about the third downloaded data sets, soil type. A decision, documented in Section 6.5.2.1, was made to edit these data prior to entering them into MASSIF due to an unusable data field.

Soil type data required changes from its downloaded form (DTN: MO0608SPASDFIM.006 [DIRS 178082]). The following change was conducted in ArcGIS, and the edited version is preserved in the spatial database (Output DTN: SN0606T0502206.011). Ten values were represented in this layer, but two of the values did not represent an actual soil class. Soil class '8' represented exposed bedrock, and everywhere it is present, it is paired with the accompanying soil depth class '5,' that represents no soil depth. Soil Class '10' had a similar problem as it was originally assigned to areas that had been disturbed by dirt roads or ground clearing. This designation was not consistent across the project area, as most grid cells containing a road were not designated as such. This designation also represented the surface condition and not the actual soil properties, so the accompanying data tables possessed no soil characteristic information for grid cells with this '10' value. Therefore, each '10' value was subjected to a nearest neighbor correction. Cell values of '10' were on-screen edited to the soil

value most prevalent of those surrounding it while taking topographic factors (slope breaks and drainages) into consideration. Figure B-9 displays the inconsistent road classification and the 'fix' that was applied. In this figure, seventeen red pixels are overlaying roads and bladed surfaces in the left-hand frame, but are replaced with the model soil classes in the right-hand frame. Nine classes were now present in the final soil class input layer instead of the original ten. This edit occurred in grid cells with surface disturbances across the entire project area and is displayed in Figure B-10.

After completing these changes, the soil and bedrock datasets were imported into the spatial database. The soil type layer contained fields for grid cell ID and UTM coordinates, and latitude/longitude coordinates, providing a means of adding this information to the model.

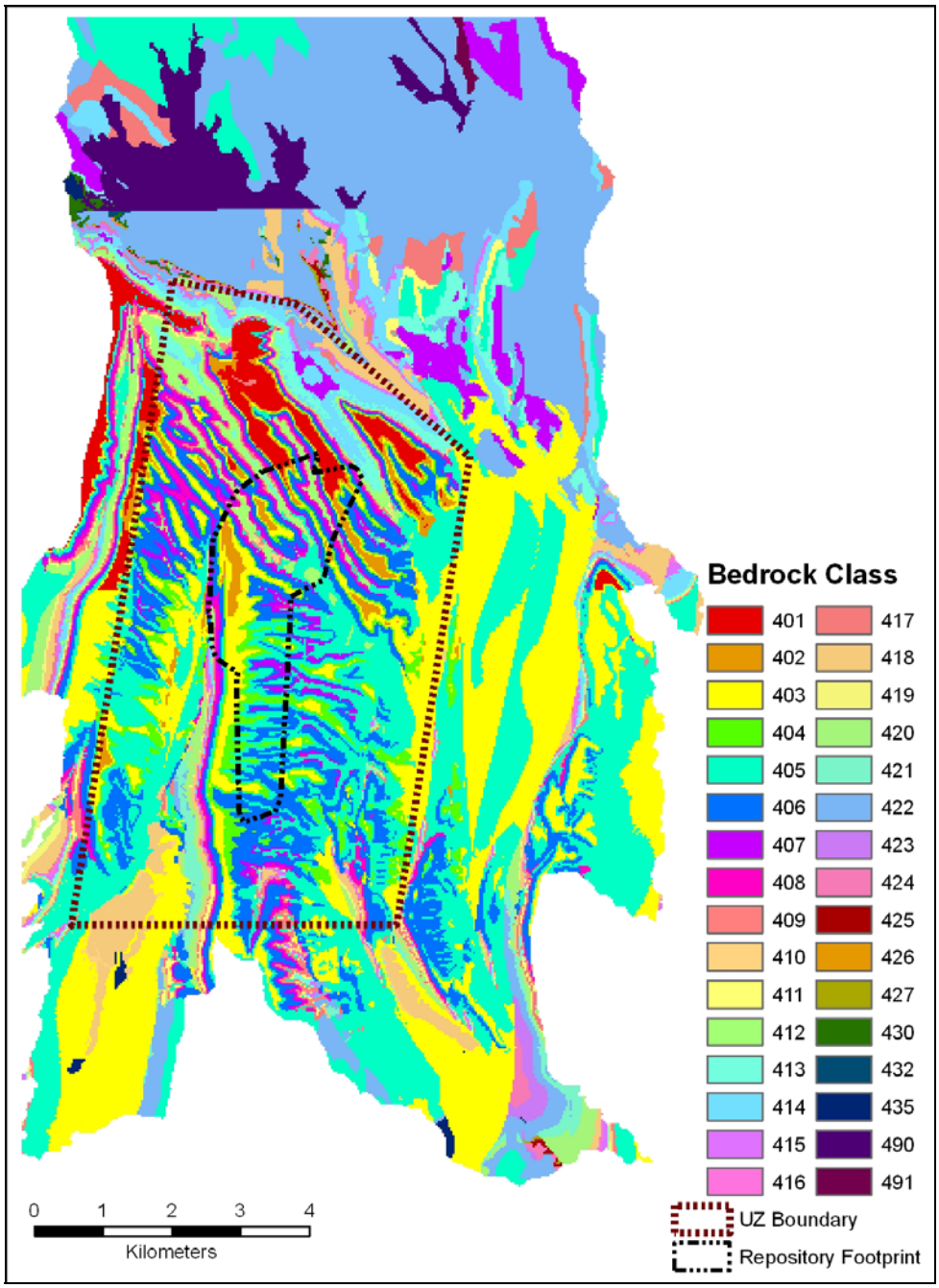

Source: Output DTNs: SN0701SPALAYER.002 and SN0612FTPRNUZB.002. DTN: MO0603SPAGRIDD.003 [DIRS 177121].

Figure B-7. Bedrock Zones across Project Area as described in Section 6.5.2

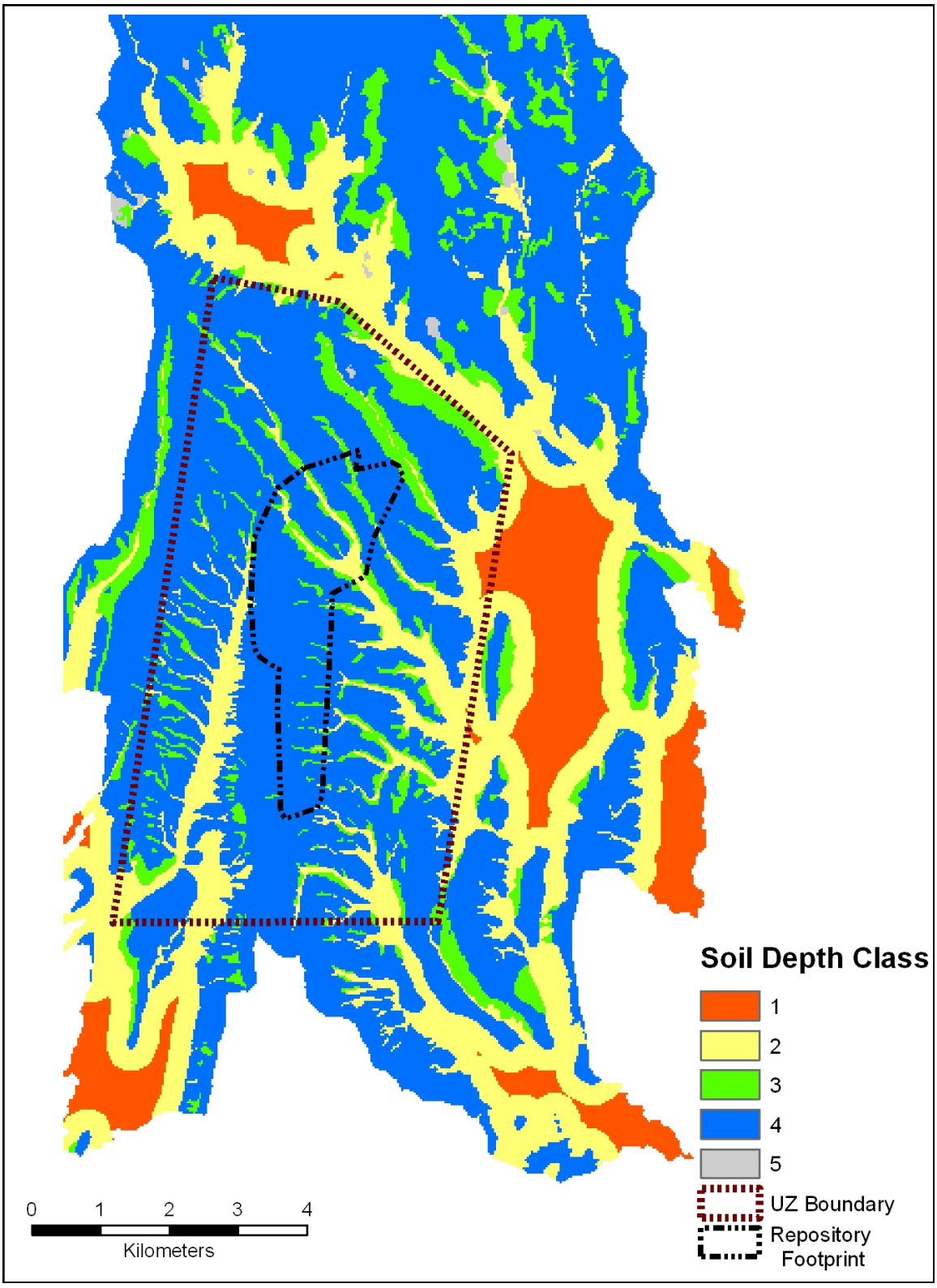

Source: Output DTNs: SN0701SPALAYER.002 and SN0612FTPRNUZB.002.

Figure B-8. Soil Depth Zones across Project Area as described in Section 6.5.2

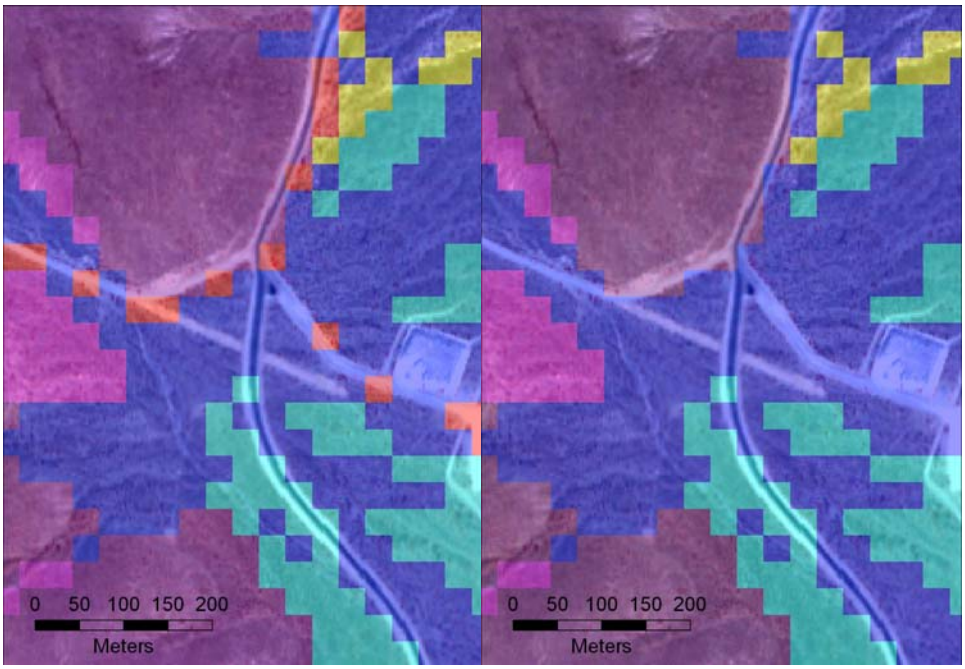

Source: Output DTN: SN0701SPALAYER.002.

Figure B-9. Road Soil Class (Red pixels in left frame) Removed within Project Area and Replaced with Appropriate Soil Class (right frame)

One other data layer was imported from outside the GIS, the PVR, prepared concurrently from Normalized Difference Vegetation Index (NDVI) calculations conducted in ENVI 4.2. Construction of the PVR layer is performed in Output DTN: SN0608PVRATYMT.001 and described in Appendix E with the final result displayed in Figure B-11. The PVR data layer comes out of the image processing ready for inclusion into the spatial database and no further processing was required.

B3.2 DOWNSTREAM CELL CALCULATIONS

The MASSIF model required each model grid cell to know which model cell its surface water flows into. This was important to model correctly the overland flow within the model. ArcGIS did not have a direct means for calculating this value, so additional steps were required to create this data layer. To generate the downstream cell number from each cell, the Flow Direction grid from the Flow200 processing was required. As detailed earlier, Flow Direction provides a grid of eight numbers (1, 2, 4, 8, 16, 32, 64, 132) that represent the downslope direction into the eight surrounding grid cells. Using this information, together with the width of the model boundary grid (367 cells), it was possible to reclassify the flow direction grid into a template for use in Spatial Analyst's Raster Calculator. The Figure B-12 diagram below details the spatial relationships involved during the reclassification.

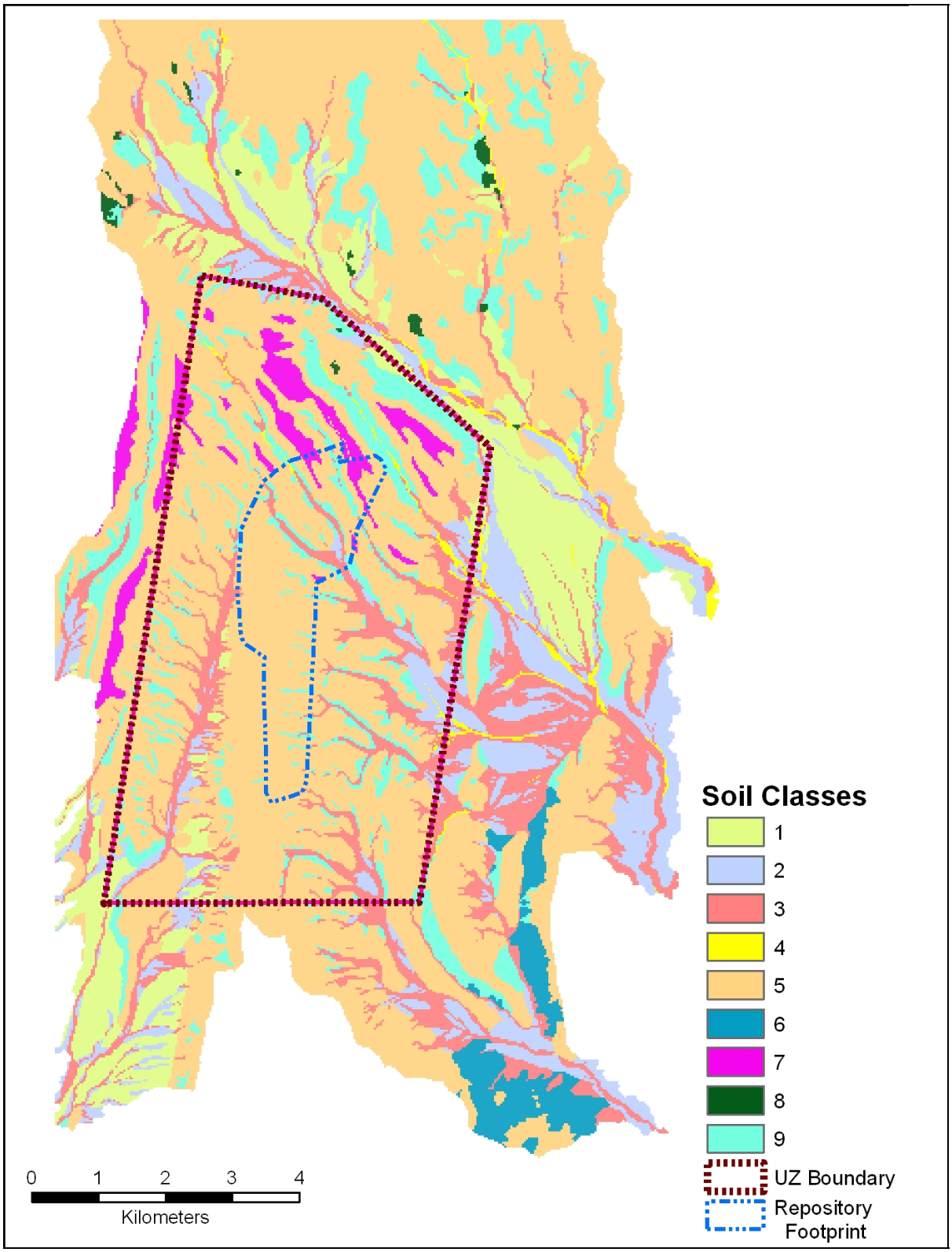

Source: Output DTNs: SN0701SPALAYER.002 and SN0612FTPRNUZB.002.

Figure B-10. Soil Type Zones across Project Area as described in Section 6.5.2

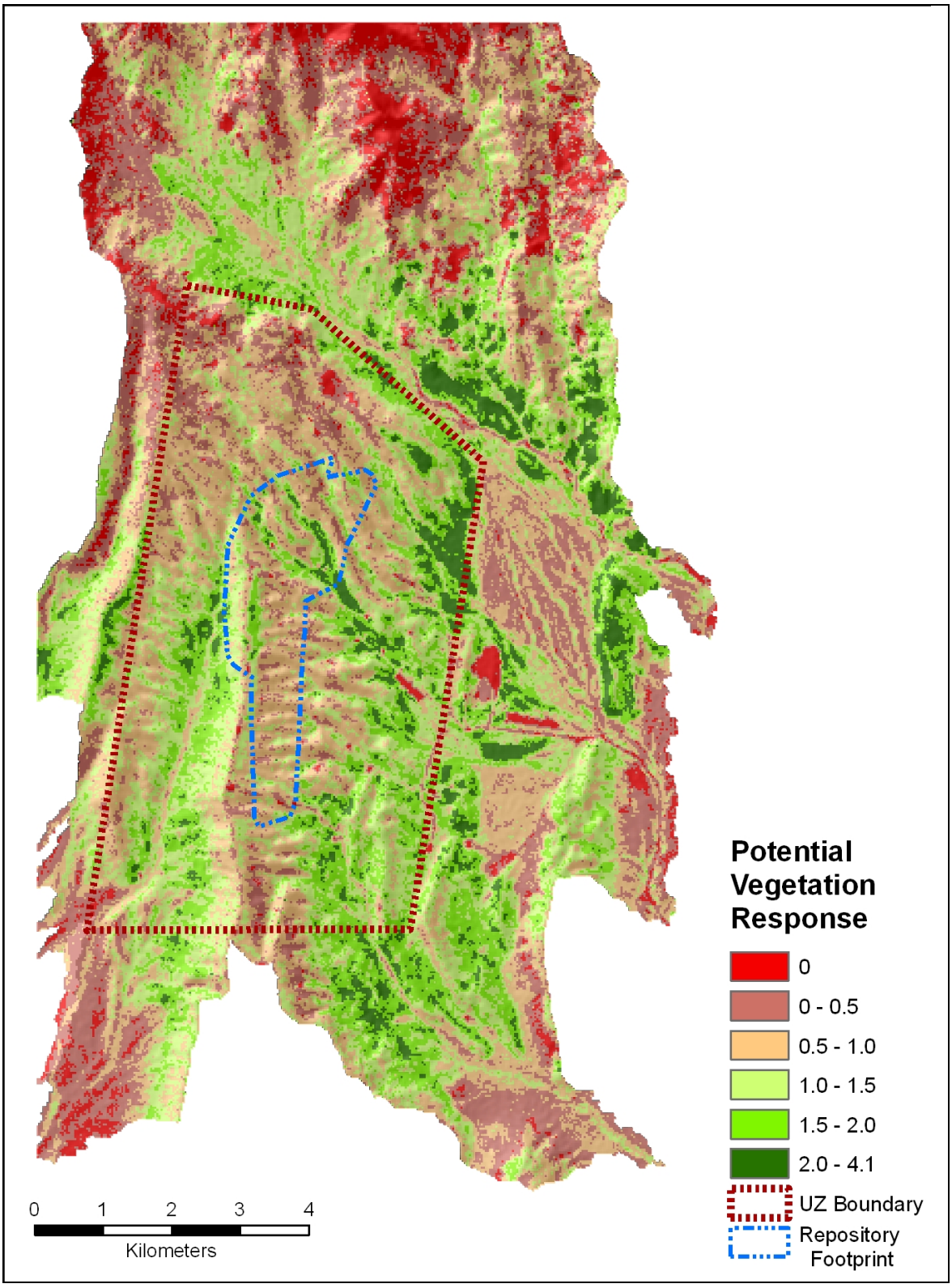

Source: Output DTNs: SN0701SPALAYER.002 and SN0612FTPRNUZB.002.

Figure B-11. PVR Values across Project Area as described in Appendix E

Each cell's ID number was added to the downslope reclassified layer (right grid in Figure B-12) to provide the cell ID of the downslope cell. For an example, if the overland flow from cell ID number 1,000 moved into the cell to the southeast, its downslope ID number would be 1,368 (1,000 + 368). The output of this calculation served as the final input layer. With the exception of the downloaded data, all the remaining data layers were extracted from data projected in UTM NAD 83. ArcGIS 9 can integrate data that are in different reference projections, but as a service for future users without this version of ESRI GIS software, each data layer was reprojected to UTM NAD 27 as the last step. All the necessary data now resided in the spatial database, but the spatial relationships among these layers still needed to be developed.

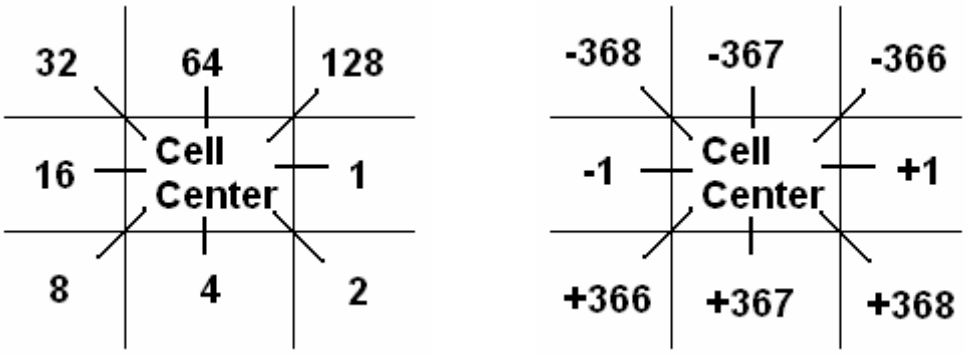

Figure B-12. Downstream Cell ID Adjustment Values

B4. ASSEMBLING THE SPATIAL DATABASE

To assemble the files into a single output, a series of tabular joins were performed on the previously prepared layers (soil type, soil depth, and bedrock) using the cell ID number as the field shared between layers. A tabular join combines two data sets that share a common field of unique values in their attribute tables. These joins brought the data fields, Cell ID, UTM coordinates, Lat/Long, Soil Depth, Soil Type, and Bedrock Type together in a single file projected to UTM NAD 27 Zone 11. All data processing tasks represented in Sections B4 and B4.1 are archived in Output DTN: SN0608ASSEMBLY.001, 'Assembly data for geospatial inputs to MASSIF Model of Yucca Mountain.'

The terrain data layers (elevation, slope, and azimuth) were spatially joined due to their lack of the model cell ID field. A spatial join is a method of combining data layers that share an identical location, in this case a grid cell location. The spatial join started by examining terrain layers that were grids of polygons, each of which covered the center of one or more model grid cell centers. The grid cells in the joined file gained the table attributes of the data layers polygons that overlaid its center. The intersect tool was used in ArcMap to perform these spatial joins. Since the intersect tool was limited to working with two files at a time, a series of intermediate files were created and further combined to create a final file that brought together model inputs Elevation, Slope, Azimuth, and PVR along with accessory files Downslope Adjustment, Catchment, and Flow Accumulation, all projected to UTM 83 Zone 11. Before continuing, this combined file was reprojected to UTM NAD 27 Zone 11 to bring it into agreement with the other earlier joined file of soil and bedrock information.

A final spatial join brought these two files together in a single database. Since the Cell ID and Downslope Adjustment fields were together in the same table, it was possible to perform a calculation that created the last required model input, Downslope Cell ID. The Downslope Adjustment column was created to factor the difference between a current Cell ID and the Cell ID of its downslope neighbor. Within the attribute table, a new column was created, named Downstream, and its values were calculated as Cell ID + Downslope Adjustment.

As a result of the tabular and spatial joins, all necessary data were assembled into a single file. The required data fields were present, but duplicate information was joined as well. It was therefore necessary to delete unneeded or repeated fields until only those fields shown in Table B-2 were present. Some of these fields (FID, Catchment, FlowAcc) were not needed for the MASSIF model but were necessary for the organization of the final spatial database preparation, as detailed below. This shapefile was preserved as Output DTN: SN0606T0502206.011, to better review the individual layers prior to the watershed division in the next step.

Table B-2. Preliminary Spatial Database Attributes

Field	Name	Description
1	FID	Feature ID, an ArcGIS identifier
2	Shape	A field placeholder for the feature polygon geometry
3	Cellid	Unique grid cell ID number for the MASSIF model
4	Utm_E	UTM NAD 27 Zone 11 easting coordinate in meters
5	Utm-N	UTM NAD 27 Zone 11 northing coordinate in meters
6	Lat	Latitude coordinate in decimal degrees
7	Long	Longitude coordinate in decimal degrees
8	Elevation	Grid cell elevation in meters
9	Downstream	Unique grid cell ID number of downstream grid cell
10	Catchment	ID number of one of eleven project watersheds
11	Slope	Grid cell slope in degrees
12	Azimuth	Grid cell slope orientation in compass bearing degrees
13	SoildepthC	Grid cell soil depth class
14	Soil_type	Grid cell soil type class
15	IHU	Grid cell bedrock type class
16	PVR	Grid cell potential vegetation response
17	FlowAcc	Grid cell total flow accumulation count

Source: Output DTN: SN0606T0502206.011.

B4.1 WATERSHED BASIN SUBDIVISION

The data now resided in one data file representing every 30-m pixel in the project area with a set of geographic data attached to each in an attribute table. Combined, the data from these pixels represented all surface water flow across the project area toward eleven separate catchment outlets. The MASSIF model could not process these different flow patterns concurrently; therefore, it was necessary to divide the model into separate drainages, each processed in turn. Total net infiltration across the model area was the combined sum from each of eleven basins.

The subdivision of the spatial database was accomplished using the 'catchment' field in the data table. The catchment column represented spatial boundaries defined during the watershed delineation. The catchment layer contains a number from one to eleven for each grid cell that represents the basin where the grid cell was located. Each set of cells, defined by a unique catchment number, was saved separately and named for their representative drainage. Table B-3 shows the eleven values representing the drainages in the project area.

Table B-3. Project Area Watershed Catchments

Catchment ID	Catchment Name
1	yucca_wash
2	drill_hole_wash
3	dune_wash
4	solitario_canyon1
5	plug_hill
6	jet_ridge1
7	jet_ridge2
8	jet_ridge3
9	solitario_canyon2
10	solitario_canyon4
11	solitario_canyon3

Source: Output DTN: SN0701SPALAYER.002.

The result of the database subdivision was eleven spatial database files comprising ArcGIS shapefiles each consisting of a set of files that detailed the graphic representation, the map coordinate system and a Dbase 4 spreadsheet (*.dbf*) containing the associated tabular attribute information. The MASSIF model required that the data be entered in a particular order. The data needed to have the columns in a particular order, labeled consistently, and the records needed to be sorted in order from highest elevation to lowest. This generic .dbf spreadsheet was opened in Microsoft Excel 2003 where the columns and records were sorted.

Elevation was the primary column (Table B-2) that constrained the data sort, but it was possible for more than one cell (in each drainage) to share an elevation value. Excel could not know which value was actually upstream and would default to the first listed in the file, which might not actually be upstream, especially on a slight north facing slope where upstream cell ID numbers are greater than their corresponding downstream neighboring cells. For this very reason, the flow accumulation layer was prepared. Using the 'flow accumulation' column as the secondary sort constraint, the computer differentiated downslope cells by knowing a greater water accumulation value would occur in downstream cells that shared the same elevation on a gentle slope. Each of the eleven files was subjected to the same process of sorting with 'elevation' descending and 'flow accumulation' ascending.

A few last edits rendered each file ready for input into the MASSIF model. The last record in each file represented the pour point, the basin outlet, or the model cell where all the accumulated water exited the drainage. Since the downstream cell from this grid cell resided in a different drainage, the MASSIF model needed to know that this record represented the last cell in the respective drainage. For the model's purposes, a '−3' was entered as the downstream cell

identifier to signify that this value represented the final record. In addition, all extraneous columns were eliminated, specifically, Catchment, Flow Accumulation, Shape, and FID (Table B-2) as these data values were not required for the infiltration model. The remaining data in the following order formed the spatial inputs for the MASSIF model, as shown in Table B-4. New column headings were added to each table to format each to MASSIF specifications. As a last step, each drainage was saved as a comma-separated value (*.csv*) text file, a format easily imported into the MASSIF model. For the purpose of simplicity within MASSIF, the drainage output files were renumbered into a sequential order based on the grid cell count within each drainage as shown in Table B-5 (Output DTN: SN0606T0502206.011).

Table B-4. Final Spatial Database Specifications

Field #	Database Name	MASSIF Name
1	Cellid	Cell_ID
2	Utm_E	UTM_E(m)
3	Utm-N	UTM_N(m)
4	Lat	Latitude(deg)
5	Long	Longitude(deg)
6	Elevation	Elevation(m)
7	Downstream	Dnstream_ID
8	Slope	Slope(deg)
9	Azimuth	Azimuth(deg)
10	SoildepthC	Soil_Depth_Zone
11	Soil_type	Soil_Type_Zone
12	IHU	Bedrock_Type_Zone
13	PVR	PVR

Source: Output DTN: SN0606T0502206.011.

Table B-5. Final Spatial Database Filenames

Catchment #	Final File Name	Order Change	Grid Count
1	*01_yucca_wash.csv*		45,981
2	*02_drill_hole_wash.csv*		45,103
3	*03_dune_wash.csv*		19,423
4	*04_solitario_canyon1.csv*		13,944
5	*05_plug_hill.csv*		6,272
6	*06_jet_ridge1.csv*		5,074
9	*07_solitaro_canyon2.csv*	×	943
7	*08_jet_ridge2.csv*	×	917
8	*09_jet_ridge3.csv*	×	567
11	*10_solitaro_canyon3.csv*	×	545
10	*11_solitaro_canyon4.csv*	×	334

Source: Output DTN: SN0606T0502206.011.

B5. DELINEATING GAUGED WATERSHEDS

In addition to the eleven drainage basins that make up the model area, a subset of six drainages were needed to calculate model results that could be compared directly against actual runoff values collected at six surface stream gages located in the project area. This comparison was

used to validate the model. Principles similar to those used to create the project area catchments were used to create these gauged watersheds. Previously during the watershed delineation (Section B2.2), the amount of flow accumulation was used to define the project area drainages. In the case of the gauged watersheds, specific locations (stream gages) defined the lower end of each drainage (pour points). All data processing tasks represented in Sections B5.1 and B5.2 are archived in Output DTN: SN0608ASSEMBLY.001, 'Assembly data for geospatial inputs to MASSIF Model of Yucca Mountain.'

B5.1 IMPORTING THE GAUGE LOCATIONS

The stream gage locations were provided as sets of coordinates DTN: MO0601GSCSPINF.000 [DIRS 177236]. These spatial tabular data were input into the GIS to incorporate them into the spatial database. The gage locations were compared to the created elevation model of the project area.

Due to slight variations in the original elevation data set and the subsequent *Filled* data layer, the model stream network did not always follow actual stream channels. The differences between the two did not overly affect the delineation process, as all that was needed was a slight lateral shift in the pour point location, while the upstream dimensions (number of model grid cells) remained the same (Figure B-13).

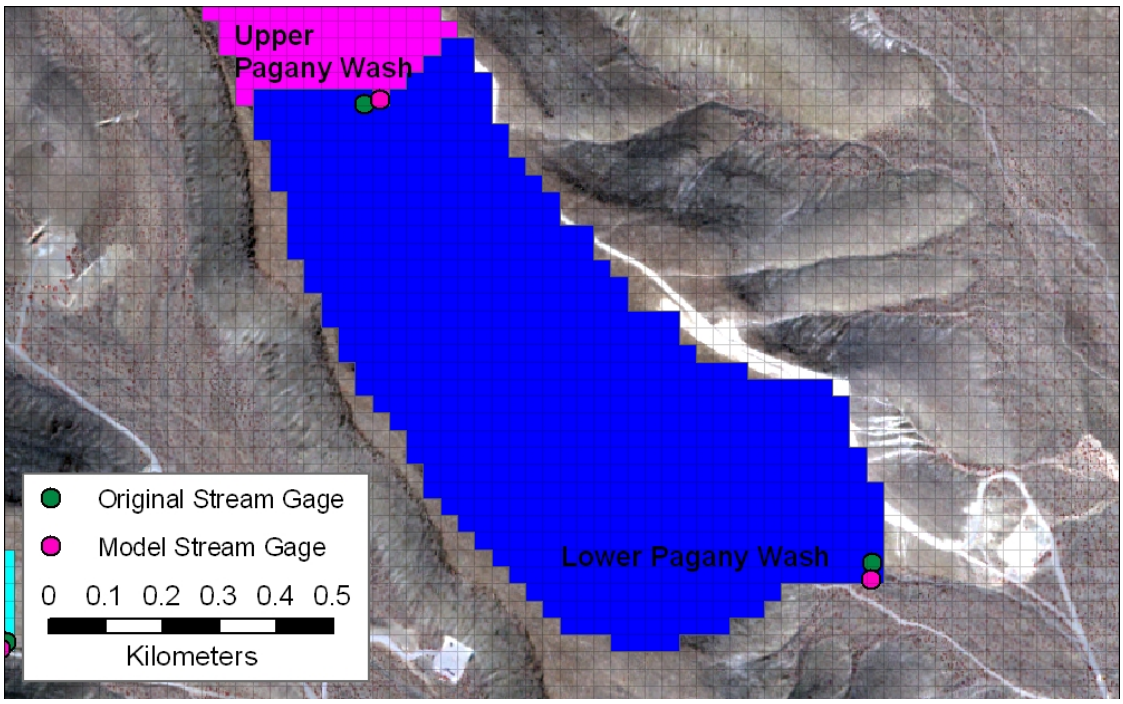

Source: Output DTN: SN0608CWATSHED.001.

Figure B-13. Stream Gages: Original and Spatial Database Locations

This is a common situation when hydrologic modeling uses cell based elevation data. The elevation data is represented by a sample value that does not always reflect the lowest potential

elevation in that cell, which is required for watershed delineation. For the MASSIF model, a single elevation value was being used to represent all variations within a 30-m by 30-m square grid cell, so often a small, narrow drainage was not captured as the dominate trait of that grid cell. However, the general trend of the landscape was incorporated, and the drainage was defined to follow this trend. In steep narrow valleys the model easily follows the natural terrain, but in wide flat valleys with little relief, the model might struggle to follow a small braided stream. In these cases, the model would instead create a representative drainage that followed the general slope and azimuth trend with the understanding that this was the highest probability for the drainage location. The model would follow this slope/azimuth trend until a difference in elevation would once again create a break in the slope to help redefine where the drainage actually has to run.

The *Snap Pour Point* function in ArcGIS hydrology tools was developed to compensate for this drainage discrepancy. *Snap Pour Point* takes point features, such as gages, and assigns it an exact location on the modeled drainage system so that it can be used for direct future output from the model. The *Snap Pour Point* function is an automated task that is most helpful in manipulating large datasets. For the small number of gages in this model, the same function was replicated manually with on-screen digitizing with a higher degree of accuracy, as pour point/gage could be snapped to the drainage to ensure the shift is minimized to as small a lateral shift as possible in order to maintain the watershed dimension.

As a result of this process, the watershed surface area upstream from a particular model pour point was a close match to actual upstream dimensions from stream gage. Two of the actual stream gages fell within a cell designated as a model stream. In three of the six examples, the necessary shift was only into the adjacent cell. Only one example needed a two-pixel shift due to low elevation variability and filled DEM characteristics associated with the drainage passing through a culvert under an elevated road. The shifts are not that important in construction of the gauged watersheds, as the size of any watershed is based on the topography of the land to provide width and the overall distance of the drainage to provide length. Shifting the pour point perpendicular to the drainage does not change the length of the watershed and has minimal effect on the resulting grid cell count (surface area).

B5.2 DELINEATION AND GAUGED AREA CLIP

This delineation process used the two original and four adjusted gage locations to generate the gauged watersheds. This step used the same filled DEM generated during project area watershed delineation processing with flow accumulation set to 200. The delineation was performed by the GIS identifying all upstream grid cells from each gage location based on flow direction and slope characteristics. The output was six small watersheds, two of which were located immediately below their upstream neighbors (Figure B-14). These files were used to create the boundary file that will clip the previous project area data file. Using the same spatial database for the project area that was assembled previously (Output DTN: SN0606T0502206.011) and instead of splitting it into the eleven project drainages, it was divided into the six much smaller gauged basins. This clip confined the input cells to just those that feed the streams that pass each gage. This allows a direct comparison between actual stream gage measurements and the modeled expected results.

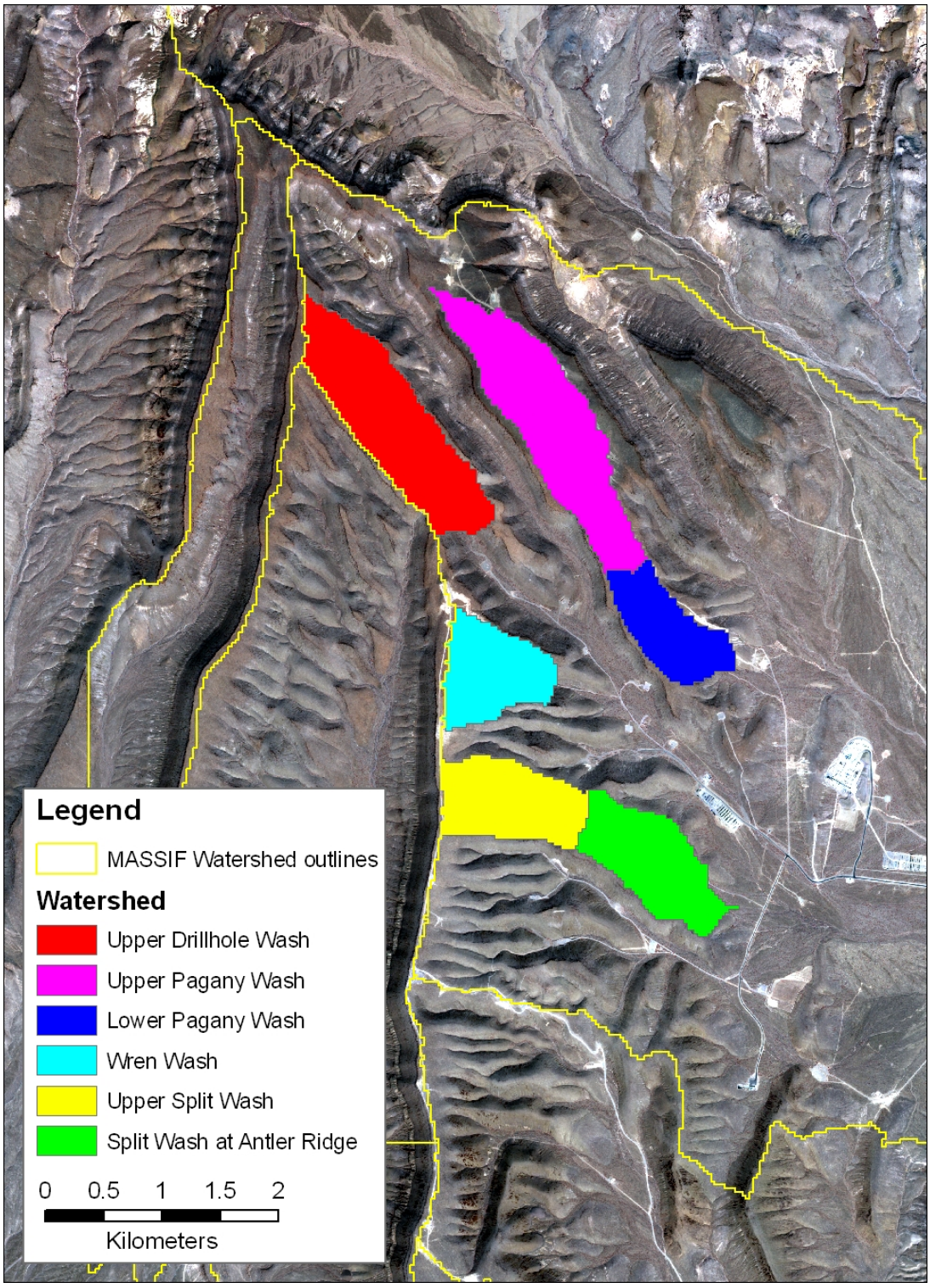

Source: DTN: MO0601GSCSPINF.000 [DIRS 177236]; Output DTN: SN0608CWATSHED.001.

Figure B-14. Gauged Watersheds within the Drill Hole Wash Watershed

As was the case with the other input files prepared, the MASSIF model required that the data be entered in a particular order. The data needed to have the columns in a particular order and the records needed to be sorted in order from highest elevation to lowest and the secondary sort variable set as flow accumulation. Again, the final record in each file needed a '−3' entered as the downstream cell value. In the two cases where there were adjacent upper and lower delineated drainages, the lower drainages output table was a combination of both the upper and lower catchments representing the total surface flow passing the lower pour point.

These six files supplied all the spatial information needed to run the MASSIF infiltration model on just these six gauged watersheds. The required resorted and relabeled columns resembled the details earlier provided in Table B-4.

B6. ADDING BOUNDARY IDENTIFIERS TO THE SPATIAL DATA

After the completion of the spatial database for the MASSIF model (Output DTN: SN0606T052206.011), an ancillary database was created that would include model cell identifiers keyed to the location of the repository footprint and the larger area of impact, the Repository Waste Emplacement Area, also referred to as the unsaturated zone (UZ) area. The knowledge of whether a model grid cell was located within the UZ or repository footprint boundaries was not required to run the MASSIF model properly, but it was useful for explanatory purposes when examining MASSIF results. The file was structured to be easily incorporated into MASSIF model calculations when desired. All data processing tasks represented in Sections B6.1 and B6.2 are archived in 'Assembly data for geospatial inputs to MASSIF Model of Yucca Mountain' (Output DTN: SN0608ASSEMBLY.001).

B6.1 ANCILLARY BOUNDARY FILES CREATION

Boundary coordinates for the repository footprint and the UZ area were both imported from DTN: LB0208HYDSTRAT.001 [DIRS 174491]. *Repository02_Table.xls* contained the 30 vertices of the irregular-shaped footprint. These coordinates were provided in the form of State Plane 27 meters. This was converted to State Plane 27 feet (the traditional unit of measurement for State Plane projections) and saved as *repository_footprint.txt*. This text file was opened in ArcView where the coordinates were displayed as points and saved as an ESRI shapefile. This point shapefile was converted to UTM NAD 27 Zone 11 and saved once again. Using these points as guides, a polygon shapefile was constructed using each vertex in order. This resulted in *Repository_Footprint_update.shp*.

The same steps were used for the UZ boundary coordinates as found *UZ02_Model_Domain.txt*. It was also in the form of State Plane meters, and converted to State Plane feet in *UZ_boundary2.txt*. Once entered into ArcView, the coordinates were displayed as points, saved, and reprojected to UTM NAD 27 Zone 11. This resulting file was saved as *UZ_Boundary_UTM_NAD27.shp*. Figure B-15 displays these two boundaries and their relationship to the MASSIF model watersheds.

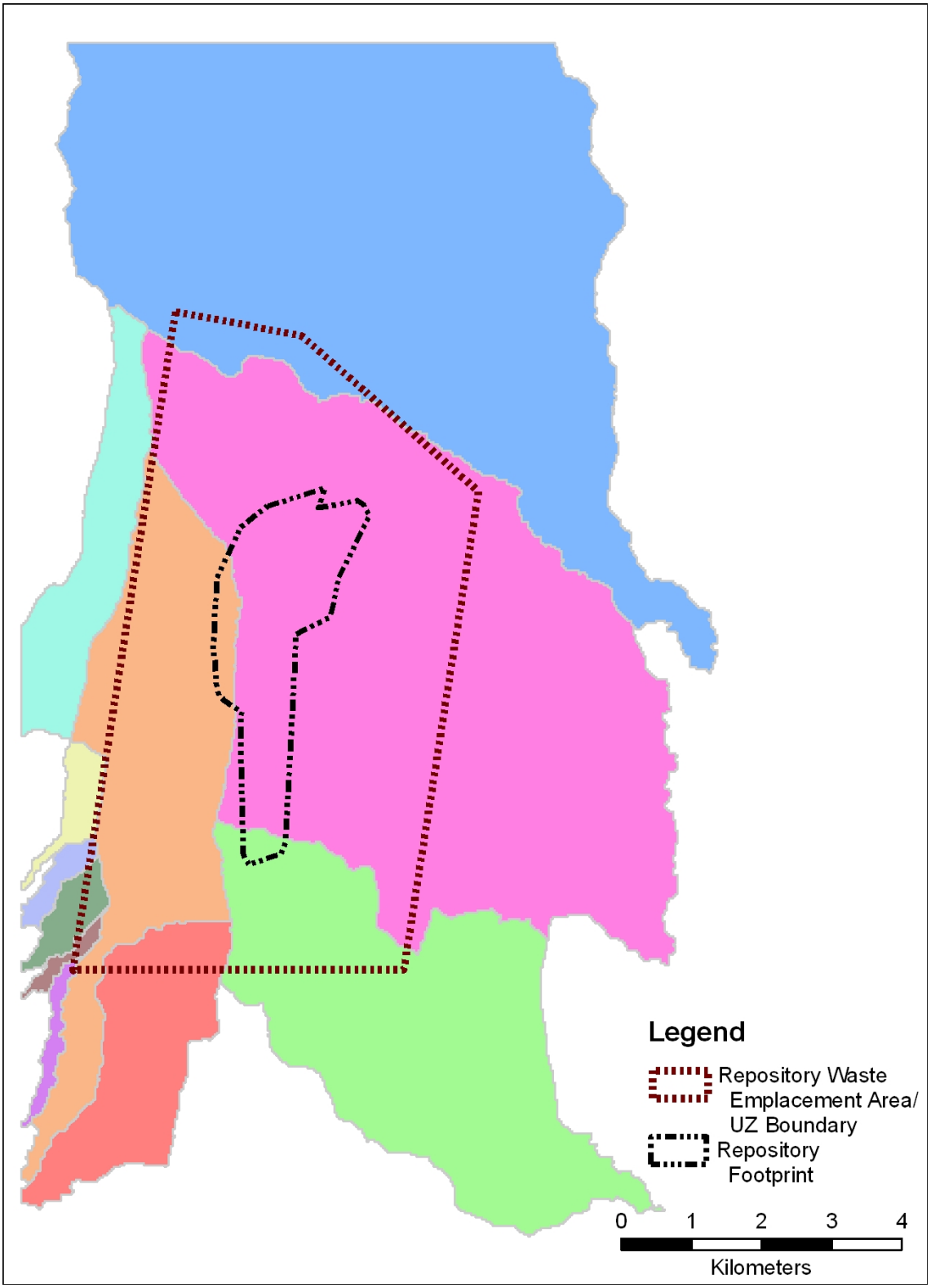

Source: Output DTNs: SN0608DRAINDYM.001 and SN0612FTPRNUZB.002.

Figure B-15. Repository Waste Emplacement Area/UZ Boundary and the Repository Footprint

In order to make these data compatible to the existing spatial database, it was necessary to modify one of the interim data files that led to the creation of the final spatial database. *All_Layers_Joined_nad27.shp* points file from folder *E2_All_Join* in Output DTN: SN0608ASSEMBLY.001. This file is a point shapefile for the entire project area where each point contains all the MASSIF inputs for a specific model grid cell and is the version of the spatial database prior to the final step of subdivision in the eleven model drainages. Two fields were added to the shapefile's attribute table, one titled 'footprint' and another labeled 'UZ'. A subset of points within *All_Layers_Joined_nad27.shp* was then selected using the UZ boundary file as the selection criterion. All points selected were assigned a '1' value in the attribute table, leaving the unselected points as '0' under the UZ heading. The selection was cleared and second selection of points was conducted using the repository footprint shapefile. These selected points were assigned a '1', leaving the remainder as '0' in the footprint column. The final was saved as *All_Layers_plus_footprint_and_UZ.shp*.

B6.2 BOUNDARY FILES SUBDIVISION

The following preparation methods were nearly identical to the steps taken in Section B4.1 except only three data columns were required and the output was condensed into a single output file, *All_Layers_plus_footprint_and_UZ.shp*. It was then saved into eleven separate shapefiles, once again based on using catchment in the selection process, but this time incorporating the file renaming scheme by size in a single step.

As was the case with the other input files prepared, the MASSIF model required that the data be entered in a particular order. The data needed to be sorted in order from highest elevation to lowest. The renumbering of the final elevation record in each file to a '−3' was not necessary at this step since this column will not be part of the final output.

A few last edits rendered each file ready for input as an ancillary input into the MASSIF model. All columns were deleted with the exception of Cell_ID, Footprint, and UZ and saved as .csv files. The contents in each file were combined into a single file based on order of watershed size that is evident in each file name (order shown in Table B-6). This final combined file is saved as *Updated_UZ_and_Footprint_with MASSIF_ID_Number.csv* and is made available to the MASSIF model as Output DTN: SN0612FTPRNUZB.002.

Table B-6. Boundary Files Watershed Catchments

Catchment ID	Catchment Name
1	01_yucca_wash
2	02_drill_hole_wash
3	03_dune_wash
4	04_solitario_canyon1
5	05_plug_hill
6	06_jet_ridge1
7	08_jet_ridge2
8	09_jet_ridge3
9	07_solitario_canyon2
10	11_solitario_canyon4
11	10_solitario_canyon3

Source: Output DTN: SN0612FTPRNUZB.002.

APPENDIX C
CALCULATION OF ET_0 (REFERENCE EVAPOTRANSPIRATION) AS A FUNCTION OF SLOPE AND AZIMUTH

C1. CALCULATIONS

This appendix contains step-by-step procedures for calculating grass reference evapotranspiration (ET_0) for surfaces having a variety of combinations of slope and aspect. Procedures include the calculation of solar radiation (R_S) for sloping surfaces by translating measurements or estimates of solar radiation made on a horizontal plane. The translation procedures follow those used by Reindl et al. (1990 [DIRS 176480]) and by Duffie and Beckman (1980 [DIRS 176264] and 1991 [DIRS 176616]). The procedure assumes that each surface has an extensive uniform slope at each point of calculation (grid cell). Effects of protruding surrounding terrain that cast shadows on the grid cell are not considered (see Section 5). This simplification of terrain provides the ability to utilize daily integrations, of direct and diffuse solar radiation over the mountain, that have an analytical basis. The calculated solar radiation is used to compute ET_0 and is applied to discrete classes of azimuth and slope for infiltration modeling. The procedure applies to present-day climatic conditions and to future expected climates.

The ET_0 calculations follow the standardized FAO-56 Penman-Monteith method (Allen et al. 1998 [DIRS 157311]). The ET_0 procedure by Allen et al. (1998 [DIRS 157311]) uses weather inputs of daily maximum and minimum air temperature from a representative reference weather station. Weather parameters of solar radiation, humidity, and wind speed, commonly used in calculating ET_0, are estimated using air temperature as input or, in the case of wind speed, as a general value that varies with the time of year. The techniques for estimating solar radiation, humidity, and wind speed are described in this section.

The base estimated solar radiation on the horizontal surface, and its translation to solar radiation for each grid cell, uses a single value for latitude representing the study area associated with a particular reference weather station. A single value for latitude is used because solar calculations change less than 2% on any given day over the range in latitude of the study area, which is less than 40 km in length in a north-south direction. The small change in solar radiation was determined by comparing theoretical daily extraterrestrial radiation listed in Allen et al. (1998 [DIRS 157311], Table 2.6), over the latitude range of the study area.

C1.1 INITIAL CALCULATIONS

Steps 1 through 18 are calculations required in solar radiation computations or in ET_0 computations. These calculations are general to all grid cells on Yucca Mountain.

INPUTS: Daily maximum and minimum air temperature, $T_{max\ reference}$ and $T_{min\ reference}$ respectively, associated with the reference weather station along with the latitude and elevation of the weather station.

Step 1. Estimate mean daily dew-point temperature, $T_{dew\ general}$ using $T_{min\ reference}$ measured at or simulated for the reference weather station, as described by Allen et al. (2005 [DIRS 176207], Equation E.1):

$$T_{dew\ general} = T_{min\ reference} - K_o \qquad \text{(Eq. C-1)}$$

where

K_o is an empirically derived offset. For the southern Nevada climate present-day conditions, K_o was set to 4.5°C, which is an average of 4°C to 5°C recommended in Allen et al.(2005 [DIRS 176207], p. D-29) for spring, summer, and fall periods when the climate is arid to semiarid. K_o was set to 2°C for winter when the climate is somewhat more humid. The values used for K_o will create dew-point temperature–humidity data sets that reflect weather conditions over an ET reference setting of well-watered clipped grass cover that is part of the standard ET_0 calculation definition. It is important, in applying the $ET = K_c ET_0$ approach (where ET is actual ET and K_c is a transpiration or 'crop' coefficient and ET_0 is the reference ET), that the ET_0 calculation represents the reference evapotranspiration that occurs from the standardized reference ET surface. This standardized reference surface, by definition, is an extensive surface of transpiring grass that conditions the atmospheric boundary layer by evaporative cooling and by the addition of water vapor. The conditioning of the boundary layer constitutes an important feedback process to the ET_0 rate and moderates it. The K_c coefficient, which represents the ratio of actual ET to ET_0, and the soil water stress reduction function, which reduces the ET value when soil water content is insufficient to support ET fully, are designed to function in concert with the standardized ET_0 value (Allen et al. 1998 [DIRS 157311], pp. 58, 91, and 161). The ET_0 calculation represents a near upper limit on ET that is experienced under full vegetation cover and adequate soil moisture supply. Under conditions of less than full vegetation cover or less than adequate soil moisture supply, the actual ET rate will be reduced below the standardized ET_0 rate, even though the actual air temperature may increase and humidity may decrease due to the reduced ET (Brutsaert 1982 [DIRS 176615], pp. 224, 225 and Figure 10.5). Therefore, even though the ambient potential ET rate computed from ambient temperature and humidity conditions for the dry environment increases under these conditions, by definition, the standardized ET_0 rate remains constant, as it should, due to the adherence to humidity (i.e., dew-point temperature) conditions defined for the reference ET condition. Therefore, it is important that the ET_0 calculation be made using $T_{dew\ general}$ estimated using K_o values that represent the reference ET condition.

The value simulated for $T_{dew\ general}$ will change daily as the value for $T_{min\ reference}$ changes. The $T_{dew\ general}$ from Equation C-1 is applied for a single reference weather location, or locations within the study area, with the value derived for $T_{dew\ general}$ used to represent T_{dew} and humidity conditions at all locations within the study area. Section 6.5.4.1 discusses exactly what values of K_o were used and when they were applied for the Mass Accounting System for Soil Infiltration and Flow (MASSIF) analysis of net infiltration. The value K_o = 4.5°C recommended by Allen et al. (2005 [DIRS 176207], p. D-29) for use in a range of climates spanning arid and semiarid is expected to hold for future climate regimes.

Step 2. Calculate actual vapor pressure e_a for use in the FAO Penman-Monteith equation and for estimating precipitable water (W) over the study area (Allen et al. 1998 [DIRS 157311], Equation 14):

$$e_{a\ general} = e^o\left(T_{dew\ general}\right) = 0.6108\ exp\left[\frac{17.27\ T_{dew\ general}}{T_{dew\ general} + 237.3}\right] \quad \text{(Eq. C-2)}$$

where

$e_{a\ general}$ = actual vapor pressure (kPa)
$T_{dew\ general}$ = dew point temperature (°C), from Step 1.

The entire air mass that passes across Yucca Mountain is assumed to have actual vapor pressure as represented by $e_{a\ general}$.

Step 3. Calculate the inverse square relative distance between earth and sun, d_r, for use in the extraterrestrial radiation (R_a) calculation (Allen et al. 1998 [DIRS 157311], Equation 23):

$$d_r = 1 + 0.033\cos\left(\frac{2\ \pi}{365}\ J\right) \quad \text{(Eq. C-3)}$$

where

J = number of the day in the year between 1 (1 January) and 365 or 366 (31 December).

Step 4. Calculate declination of the earth, δ (Allen et al. 1998 [DIRS 157311], Equation 24):

$$\delta = 0.409\ \sin\left(\frac{2\ \pi}{365}\ J - 1.39\right) \quad \text{(Eq. C-4)}$$

Steps 5 through 18 can be computed outside of the grid cell calculation loop when all grid cells are assumed to have the same latitude. This is a valid assumption provided that the entire study area is less than about 40 mi north to south, because extraterrestrial radiation, R_a, varies only slightly with small changes in latitude.

Step 5. Calculate the sunset hour angle, ωs, for a horizontal surface (Allen et al. 1998 [DIRS 157311], Equation 25):

$$\omega_s = \arccos\left[-\tan\left(\varphi_{reference}\right)\tan\left(\delta\right)\right] \quad \text{(Eq. C-5)}$$

where

ω_s = sunset hour angle (rad)
$\varphi_{reference}$ = latitude of the reference weather station (rad) (input)
δ = solar declination, from Step 4.

Step 6. Calculate extraterrestrial radiation on a horizontal surface for one 24-hr period, $R_{a\ hor}$ (Allen et al. 1998 [DIRS 157311], Equation 21):

$$R_{a\ hor} = \frac{24(60)}{\pi} G_{sc}\, d_r \left[\omega_s \sin(\varphi_{reference}) \sin(\delta) + \cos(\varphi_{reference}) \cos(\delta) \sin(\omega_s)\right] \quad \text{(Eq. C-6)}$$

where

$R_{a\ hor}$ = 24-hr extraterrestrial radiation for a horizontal surface (MJ m^{-2} d^{-1})
G_{sc} = solar constant (0.0820 MJ m^{-2} min^{-1})
d_r = squared inverse relative distance factor for the earth-sun, dimensionless, from Step 3
ω_s = sunset hour angle (radians), from Step 5
$\varphi_{reference}$ = latitude of the reference weather station (rad) (input)
δ = solar declination (radians), from Step 4.

Step 7. Calculate sine of mean solar elevation over 24-hr period, $sin\beta_{24}$, weighted by extraterrestrial radiation (Allen et al. 2005 [DIRS 176207], Equation D.5):

$$sin\beta_{24} = sin\left[0.85 + 0.3\,\varphi_{reference}\, sin\left(\frac{2\pi}{365} J - 1.39\right) - 0.42\left(\varphi_{reference}\right)^2\right] \quad \text{(Eq. C-7)}$$

where

$sin\beta_{24}$ = sine of the average β (radians) during the daylight period, weighted according to R_a
$\varphi_{reference}$ = latitude of the reference weather station (rad) (input)
J = day of the year.

Values for $sin\beta_{24}$ from Equation C-7 should be limited to greater than or equal to 0.01 for numerical stability in Step 10 (Allen et al. 2005 [DIRS 176207], p. D-9).

Step 8. Calculate mean atmospheric pressure for the reference weather station, $P_{reference}$ using the elevation of the reference weather station (Allen et al. 1998 [DIRS 157311], Equation 7):

$$P_{reference} = 101.3\left(\frac{293 - 0.0065\, z_{reference}}{293}\right)^{5.26} \quad \text{(Eq. C-8)}$$

where

$P_{reference}$ = atmospheric pressure at the reference weather station (kPa)
$z_{reference}$ = elevation of reference weather station, relative to mean sea level (m).

The 293 parameter in Eq. C-8 results from the defintion of the standard atmosphere for reference ET_0 calculation where standard air temperature equals 20°C (Allen et al. 1998 [DIRS 157311], p. 31).

Step 9. Calculate precipitable water, W, at the reference weather station (Allen et al. 2005 [DIRS 176207], Equation D.3):

$$W = 0.14\, e_{a\ general}\, P_{reference} + 2.1 \qquad \text{(Eq. C-9)}$$

where

W = precipitable water in the atmosphere passing over the study area (mm)

$P_{reference}$ = atmospheric pressure at reference weather station (kPa), from Step 8

$e_{a\ general}$ = general, actual vapor pressure of the air, at approximately 2 m (kPa), from Step 2.

Step 10. Calculate 24-hr transmissivity for beam radiation, $K_{Bo\ hor}$ (Allen et al. 2005 [DIRS 176207], Equation D.2):

$$K_{Bo\,hor} = 0.98\, exp\left[\frac{-0.00146\ P_{reference}}{K_{cln}\ sin\beta_{24}} - 0.075\left(\frac{W}{sin\beta_{24}}\right)^{0.4}\right] \qquad \text{(Eq. C-10)}$$

where

$K_{Bo\ hor}$ = 24-hr transmissivity for clear-sky beam radiation (dimensionless)

K_{cln} = atmospheric cleaness–turbidity coefficient (dimensionless), $0 < K_{cln} \leq 1.0$ where K_{cln} = 1.0 for clean air and $K_{cln} \leq 0.5$ for extremely turbid, dusty or polluted air. K_{cln} = 1.0 was used for Yucca Mountain for present day conditions, because the air in the area is unpolluted. The K_{cln} = 1.0 was used in determing K_{Rs} in Eq. C-13 for estimating $R_{sm\ hor}$ from daily maximum and minimum air temperature and is therefore set to 1.0 here to be congruent with the $R_{sm\ hor}$ estimate.

$P_{reference}$ = atmospheric pressure at reference weather station (kPa), from Step 8

W = precipitable water in the atmosphere (mm), from Step 9

$sin\beta 24$ = sine of average β during the daylight period (radians), from Step 7. Values for $sin\beta 24$ must be limited to greater than or equal to 0.01 for numerical stability (Allen et al. 2005 [DIRS 176207], p. D-8).

Equation C-10 was developed by Allen et al. (2005 [DIRS 176207], Equation D.2) for specific application to clear sky conditions.

Step 11. Calculate 24-hr transmissivity for diffuse radiation, $K_{Do\ hor}$ using the ASCE EWRI function (Allen et al. 2005 [DIRS 176207], Equation D.4):

$$K_{Do\,hor} = 0.35 - 0.36\,K_{Bo\,hor} \quad for\ K_{Bo\,hor} \geq 0.15$$
$$K_{Do\,hor} = 0.18 + 0.82\,K_{Bo\,hor} \quad for\ K_{Bo\,hor} < 0.15 \qquad \text{(Eq. C-11)}$$

where

$K_{Do\ hor}$ = 24-hr transmissivity for clear-sky diffuse radiation (dimensionless)

$K_{Bo\ hor}$ = 24-hr transmissivity for direct radiation (dimensionless), from Step 10.

Step 12. Calculate clear sky solar radiation over the 24-hr period, $R_{so\ hor}$ (Allen et al. 2005 [DIRS 176207], Equation D.1):

$$R_{so\,hor} = (K_{Bo\ hor} + K_{Do\,hor})\,R_{a\,hor} \qquad \text{(Eq. C-12)}$$

where

$R_{so\ hor}$ = clear sky solar radiation over the 24-hr period (MJ m^{-2} d^{-1})

$K_{Do\ hor}$ = transmissivity for clear-sky diffuse radiation (dimensionless), from Step 11

$K_{Bo\ hor}$ = transmissivity for direct radiation (dimensionless), from Step 10

$R_{a\ hor}$ = extraterrestrial radiation, horizontal surface (MJ m^{-2} d^{-1}), from Step 6.

The $R_{so\ hor}$ is calculated using humidity data from the reference station. It applies, however, to the entire study area, because $R_{so\ hor}$ is only weakly sensitive to elevation, changing less than 1% to 2% over the range in elevations experienced in the study area (Appendix C3).

Step 13. Estimate solar radiation on a horizontal surface, $R_{sm\,hor}$, using T_{max} and T_{min} at reference weather station (Allen et al. 1998 [DIRS 157311], Equation 50; Allen 1997 [DIRS 176568], Equation 1):

$$R_{sm\,hor} = K_{Rs} \sqrt{(T_{\max reference} - T_{\min reference})}\, R_{a\,hor} \qquad \text{(Eq. C-13)}$$

where

$R_{sm\,hor}$ = estimated solar radiation for horizontal surface (MJ m^{-2} d^{-1})

$R_{a\,hor}$ = extraterrestrial radiation for horizontal surface (MJ m^{-2} d^{-1}), from Step 6

$T_{max\,reference}$ = maximum air temperature measured at the reference weather station (°C)

$T_{min\,reference}$ = minimum air temperature measured at the reference weather station (°C)

K_{Rs} = adjustment coefficient ($°C^{-0.5}$).

The $R_{sm\,hor}$ from Equation C-13 must be limited to less than or equal to $R_{so\,hor}$ from Equation C-12, since it is theoretically impossible for R_s on a horizontal surface (i.e., the estimate from Eq. C-13) to exceed R_s for a horizontal surface under cloud-free conditions (i.e., the estimate from Eq. C-12).

The R_{smhor} is calculated for use at all grid cells, provided, a single latitude is used to represent the mountain for purposes of computing extraterrestrial radiation on a horizontal surface in Step 6. For present-day (and future climate) conditions, K_{Rs} = 0.19 is used for Yucca Mountain, rather than the general value of 0.16 recommended in FAO-56 (Allen et al. 2005 [DIRS 176207]), based on an analysis of diffuse solar radiation measurements from Yucca Mountain (Appendix C3) and on findings by Allen (1997 [DIRS 176568]) for high elevation locations. $R_{sm\,hor}$ is applied to the entire Yucca Mountain study area because clear sky solar radiation, $R_{so\,hor}$, and consequently $R_{sm\,hor}$, is only weakly sensitive to elevation, changing less than 1% to 2% over the range in elevations experienced in the study area, based on a sensitivity analysis conducted in Appendix C3.

C1.2 SETUP FOR TRANSLATION OF HORIZONTAL SOLAR RADIATION TO ANY SLOPE AS REPRESENTED BY FIXED COMBINATIONS OF SLOPE AND ASPECT

These calculations are general to all grid cells associated with the reference weather station. The horizontal solar radiation is calculated for the reference weather station using a single latitude and reference elevation for the study area. This value is then modified at each grid cell to account for effects of slope and azimuth.

Step 14. Calculate total short-wave transmissivity, $\tau_{sw\,hor}$, also referred to in literature as a 'clearness index, K_t', associated with the measured R_s value (Duffie and Beckman 1991 [DIRS 176616], Equation 2.9.2):

$$\tau_{sw\,hor} = \frac{R_{sm\,hor}}{R_{a\,hor}} \qquad \text{(Eq. C-14)}$$

where

$\tau_{sw\,hor}$ = total short-wave transmissivity (dimensionless)

$R_{sm\,hor}$ = solar radiation for horizontal surface (MJ m^{-2} d^{-1}), from Step 13,

$R_{a\,hor}$ = extraterrestrial radiation for horizontal surface (MJ m^{-2} d^{-1}), from Step 6.

Because $R_{sm\,hor}$ is estimated using Eq. C-13, Eq. C-14 reduces to $\tau_{sw\,hor} = K_{Rs}$ $(T_{max\ reference} - T_{min\ reference})^{0.5}$, which defines $\tau_{sw\,hor}$ as a function of the difference between daily extremes in air temperature.

Step 15. Partition the atmospheric transmissivity from Step 14 into its diffusive and direct beam components. Calculate apparent $K_{B\,hor}$ associated with the actual total short-wave transmissivity using the procedure by Vignola and McDaniels (1986 [DIRS 176481]). The partitioning of atmospheric transmissivity is applied to all days, including those having cloud cover. Therefore, the clear sky-oriented equations of Equations C-10 and C-11 (Allen et al. 2005 [DIRS 176207]) do not apply here. A form of the equation by Vignola and McDaniels (1986 [DIRS 176481], p. 411) from Equation C-51 is used:

$$K_{D\,hor} = 0.984\,\tau_{sw\,hor} \quad for\ \tau_{sw\,hor_r} < 0.175$$
$$K_{D\,hor} = -0.022 + 1.280\,\tau_{sw\,hor} - 0.828(\tau_{sw\,hor})^2 - 0.765(\tau_{sw\,hor})^3 \quad for\ 0.175 \le \tau_{sw\,hor} \le 0.8$$
$$K_{D\,hor} = 0.08 \quad for\ \tau_{sw\,hor} > 0.8 \qquad \text{(Eq. C-15)}$$

where

$K_{D\,hor}$ = 24-hour transmissivity for diffuse radiation (dimensionless)
$\tau_{sw\,hor}$ = total short-wave transmissivity (dimensionless), from Step 14.

Equation C-15 has been rearranged from the equation by Vignola and McDaniels (1986 [DIRS 176481], p. 411), so that the left-hand side of the equation contains only $K_{D\,hor}$, rather than $K_{B\,hor}$. Equation C-15 has been found to agree closely with diffuse versus transmissivity data collected near Yucca Mountain (Section C4). The last line of Equation C-15 is required to limit the original polynomial expression by Vignola and McDaniels (1986 [DIRS 176481], p. 411) to the domain of their regression data set ($\tau_{sw\,hor} \le 0.8$) where $K_{D\,hor}$ is set to 0.08.

Equation C-15 is used to adjust $R_{sm\ hor}$ to all slopes, and it describes the atmospheric transmissivity component representing diffuse radiation well under both clear and cloudy conditions as compared to Equation C-11 (Allen et al. 2005 [DIRS 176207]), which is intended primarily for clear sky conditions only. Equations C-10 and C-11 are used in calculating $R_{so\ hor}$, because they explicitly consider the effects of humidity and elevation. Appendix C4 includes the analysis performed to develop Equation C-15.

Step 16. Calculate actual direct beam transmissivity or index, $K_{B\ hor}$, as the difference between total transmissivity and diffuse transmissivity (Allen 1996 [DIRS 176485], Equation 7):

$$K_{B\ hor} = \tau_{sw\ hor} - K_{D\ hor} \quad \text{(Eq. C-16)}$$

where

$K_{B\ hor}$ = 24-hr transmissivity for direct radiation (dimensionless)

$K_{D\ hor}$ = 24-hr transmissivity for diffuse radiation (dimensionless), from Step 15

$\tau_{sw\ hor}$ = total short-wave transmissivity (dimensionless), from Step 14.

Step 17. Calculate direct beam radiation on the horizontal surface, $I_{b\ hor}$, based on the measured $R_{sm\ hor}$:

$$I_{b\ hor} = K_{B\ hor} * R_{a\ hor} \quad \text{(Eq. C-17)}$$

where

$I_{b\ hor}$ = direct beam radiation on the horizontal surface (MJ m^{-2} d^{-1})

$R_{a\ hor}$ = extraterrestrial radiation for horizontal surface (MJ m^{-2} d^{-1}), from Step 6

$K_{B\ hor}$ = 24-hr transmissivity for direct radiation (dimensionless), from Step 16.

Step 18. Calculate the diffuse component, $I_{d\ hor}$, of $R_{sm\ hor}$ for a horizontal surface:

$$I_{d\ hor} = K_{D\ hor} * R_{a\ hor} \quad \text{(Eq. C-18)}$$

where

$I_{d\ hor}$ = diffuse radiation on the horizontal surface (MJ m^{-2} d^{-1})

$K_{D\,hor}$ = 24-hr transmissivity for diffuse radiation (dimensionless), from Step 15

$R_{a\,hor}$ = extraterrestrial radiation for horizontal surface (MJ m^{-2} d^{-1}), from Step 6.

C1.3 CELL-SPECIFIC CALCULATIONS

The following steps are unique to each grid cell because of the requirement of specific values for slope or aspect (azimuth) affecting solar radiation and elevation affecting air temperature and ET_0.

Step 19. Define terrain albedo α_T for the valley areas adjacent to the study area. A value α = 0.15 (Brutsaert 1982 [DIRS 176615], p. 136, Table 6.4) is recommended for darker soils or significant vegetation and α = 0.35 for light soils having little vegetation.

$$\alpha_T = [\text{Input Value}] \text{ (dimensionless)} \quad \text{(Eq. C-19)}$$

The terrain albedo is used in Step 24 for calculating reflected radiation from areas below a sloped grid cell that reaches the specified grid cell. Therefore, the terrain albedo does not represent the albedo of the grid cell itself; it represents a spatially averaged value of the albedo of the surrounding valley areas that can reflect solar radiation toward grid cells. This value can be affected by seasonality and climatic regimes that can also affect ground cover of surrounding areas. The value for terrain albedo has only a small effect on the solar radiation estimate and ET_0, changing ET_0 by less than 0.3 mm d^{-1} for all slope–aspect combinations in the study area when terrain albedo is varied from 0.1 to 0.4. The 0.3 mm d^{-1} value is less than the 1.0 mm d^{-1} uncertainty noted for ET using precision weighing lysimeters by Allen et al. (2005 [DIRS 176009], p. 12). Therefore, a single value α_T = 0.22 is used for the study area.

The following steps must be computed for each specific grid cell using the R_b adjustment factor from the R_b look-up table that is created in Appendix C2. This R_b look-up table is not printed here; it is read into the MASSIF infiltration model.

Step 20. Calculate I_b, the direct beam on the inclined surface having a specific slope–aspect combination, using the R_b adjustment factor determined from the look-up table, computed in Step 44 (Duffie and Beckman 1980 [DIRS 176264], Equations 2.15.2):

$$I_b = I_{b\,hor} * R_b \quad \text{(Eq. C-20)}$$

where

I_b = direct beam radiation on the inclined surface (MJ m^{-2} d^{-1})
$I_{b\,hor}$ = direct beam radiation on the horizontal surface (MJ m^{-2} d^{-1}), from Step 17

R_b = direct radiation ratio (dimensionless), from R_b look-up table, Output DTN: SN0602T0502206.003 (Appendix C2).

R_b is defined as the ratio of beam radiation on an incline to the beam radiation on a horizontal plane. R_b is a function of latitude, slope, azimuth, and day of year. The R_b look-up table (Appendix C2) includes values for R_b for specific values of slope and azimuth for every day of the year.

The following calculations in Steps 21 to 27 are based on the anisotropic diffuse model by Reindl et al. (1990 [DIRS 176480], Equation 5).

Step 21. By definition, the anisotropic index A_t for simulating circumsolar brightening is (Reindl et al. 1990 [DIRS 176480], p. 11; Duffie and Beckman (1991 [DIRS 176616], Equation 2.16.3):

$$A_t = K_{B\,hor} \qquad \text{(Eq. C-21)}$$

where

A_t = anisotropic index (dimensionless)

$K_{B\,hor}$ = 24-hr transmissivity for direct radiation (dimensionless), from Step 16.

Step 22. Calculate the modulating function (f) for horizontal brightness (Reindl et al. 1990 [DIRS 176480], p. 11; Duffie and Beckman 1991 [DIRS 176616], Equation 2.16.6):

$$f = \sqrt{\frac{I_{b\,hor}}{R_{sm\,hor}}} \qquad \text{(Eq. C-22)}$$

where

f = modulating function for diffuse brightening near the horizon (dimensionless)

$I_{b\,hor}$ = direct beam radiation on the inclined surface (MJ m^{-2} d^{-1}), from Step 17

$R_{sm\,hor}$ = solar radiation for horizontal surface (MJ m^{-2} d^{-1}), from Step 13.

Step 23. Calculate the diffuse component for the inclined surface (Reindl et al. 1990 [DIRS 176480], Equation 5; Duffie and Beckman 1991 [DIRS 176616], Equation 2.16.5):

$$I_d = I_{d\,hor}\left[(1-A_t)\left(\frac{1+Cos(s)}{2}\right)\left(1+f*\sin^3(s/2)\right)+A_t R_b\right] \qquad \text{(Eq. C-23)}$$

where

I_d = diffuse radiation on the inclined surface (MJ m^{-2} d^{-1})

$I_{d\,hor}$ = diffuse radiation on the horizontal surface (MJ m^{-2} d^{-1}), from Step 18

A_t = anisotropic index for circumsolar brightening (dimensionless), from Step 21

f = modulating function for diffuse brightening near the horizon (dimensionless), from Step 22

R_b = direct radiation ratio (dimensionless), from the look-up table (Output DTN: SN0602T0502206.003) (Appendix C2)

s = slope (radians).

Step 24. Calculate the reflected radiation from lower lying terrain to the inclined surface (Reindl et al. 1990 [DIRS 176480], Equation 1):

$$I_r = R_{sm\,hor} * \alpha_T * \left(\frac{1 - Cos(s)}{2} \right) \quad \text{(Eq. C-24)}$$

where

I_r = reflected radiation that reach the inclined surface (MJ m^{-2} d^{-1})

$R_{sm\,hor}$ = solar radiation for horizontal surface (MJ m^{-2} d^{-1}), from Step 13

s = cell slope (radians)

α_T = albedo of the surrounding terrain (dimensionless), from Step 19.

Step 25. Calculate the total radiation received by the inclined surface (Hay 1979 [DIRS 176151], Equation 21):

$$R_{sm\,inc} = I_b + I_d + I_r \quad \text{(Eq. C-25)}$$

where

$R_{sm\,inc}$ = solar radiation for the inclined surface (MJ m^{-2} d^{-1})

I_b = direct beam radiation on the inclined surface (MJ m^{-2} d^{-1}), from Step 20

I_d = diffuse radiation on the inclined surface (MJ m^{-2} d^{-1}), from Step 23

I_r = reflected radiation that reaches the inclined surface (MJ m^{-2} d^{-1}), from Step 24.

The I_r is reflected radiation from lower lying terrain. This equation is used implicitly by Reindl et al. (1990 [DIRS 176480]) and Duffie and Beckman (1980 [DIRS 176264]; 1991 [DIRS 176616]), but is used in equation form by Hay (1979 [DIRS 176151]). Equation C-25 is equivalent to the equation by Duffie and Beckman (1991 [DIRS 76616], Equation 2.16.7) when all equation substitutions are made for I_b, I_d and I_r, as in Equations C-20, C-23, and C-24.

Step 26. Reproject $R_{sm\ inc}$ to a horizontal projection (equivalent):

$$R_{s(equiv)hor} = \frac{R_{sm\ inc}}{\cos(s)} \quad \text{(Eq. C-26)}$$

where

$R_{s\ (equiv)\ hor}$ = solar radiation for the inclined surface, reprojected to a horizontal plane (MJ m^{-2} d^{-1})

$R_{sm\ inc}$ = solar radiation for the inclined surface (MJ m^{-2} d^{-1}), from Step 25

s = cell slope (radians).

The $R_{s\ (equiv)\ hor}$ is the R_s that occurs on the inclined slope, but it is expressed in terms of energy per horizontal grid area to be consistent with precipitation and other water balance terms.

C1.4. ET_0 CALCULATION

Step 27. Using $T_{max\ reference}$ and $T_{min\ reference}$ from the reference weather station, calculate $T_{max\ lapse}$ and $T_{min\ lapse}$ for each cell in the grid using a terrestrial temperature lapse rate. The terrestrial temperature lapse rate is set equal to the standard dry, adiabatic lapse rate of 10°C per 1,000 m (Maidment 1993 [DIRS 125317], p. 3.3). This adiabatic lapse rate is a reasonable approximation to the terrestrial lapse rate in areas, like Yucca Mountain, where the terrain is not steep and conditions are generally windy enough to cause airflow over (rather than around) the terrain and dry enough that condensation is insignificant. Under conditions of condensation, a saturated adiabatic lapse rate can be used, where that rate ranges from 6.9°C per 1,000 m at 0°C to 3.6°C per 1,000 m at 30°C at sea level (Rosenberg et al. 1983 [DIRS 177526], p. 120). The rate averages 5.4°C per 1,000 m at 0°C at 50 kPa air pressure (Rosenberg et al. 1983 [DIRS 177526], p. 120), which corresponds to about 5,700 m elevation. For the elevation range of the study area (approximately 970 to 1,970 m), the saturated adiabatic lapse rate would be expected to range from

approximately 6.4°C per 1,000 m at 0°C to approximately 3.3°C per 1,000 m at 30°C. However, because conditions of water vapor condensation occur only during precipitation events, which are relatively rare to the study area, the terrestrial lapse rate will follow the adiabatic lapse rate a majority of the time. The sensitivity of infiltration to the value for the lapse rate has been shown to be small (Section 71.4). Therefore, the dry adiabatic lapse rate has been used as the environmental lapse rate for all conditions. The correction to air temperature for lapse is made as:

$$T_{max} = T_{max\ reference} - \frac{LR}{1000}\left(z_{cell} - z_{reference}\right) \quad \text{(Eq. C-27a)}$$

$$T_{min} = T_{min\ reference} - \frac{LR}{1000}\left(z_{cell} - z_{reference}\right) \quad \text{(Eq. C-27b)}$$

where

T_{max} = maximum temperature during the 24-hr period corrected for elevation (°C)

T_{min} = minimum temperature during the 24-hr period corrected for elevation (°C)

$T_{max\ reference}$ = maximum air temperature measured at the reference weather station (°C)

$T_{min\ reference}$ = minimum air temperature measured at the reference weather station (°C) LR = environmental lapse rate (°C per 1,000 m)

z_{cell} = elevation of the grid cell (m)

$z_{reference}$ = elevation of the reference weather station (m).

The corrected T_{max} and T_{min} are used in the ET_0 calculations.

Step 28. Wind speed at 2-m height. For the study area application, daily wind speed has been approximated by linearly interpolating between mean monthly values for wind speed developed from measured data (Output DTN: SN0610T0502206.030). This approach accounts for seasonal differences. The monthly wind speed set was used for the total study area and for future climates (assumption in Section 5). Wind speed parameter development is discussed in Section 6.5.1, Appendix F, and in detail in Output DTN: SN0610T0502206.030 and follows the following form:

$$u_2(day) = u_2(month_i) + \frac{u_2(month_i) - u_2(month_{i+1})}{midday(month_i) - midday(month_{i+1})} * (day - midday(month_i)) \quad \text{(Eq. C-28)}$$

where

$u_2(day)$ = wind speed at 2-m height (m s^{-1}) on Julian day = *day*
$u_2(month_i)$ = mean monthly wind speed for month, *i*
$midday(month_i)$ = Julian day that is the middle of month, *i*

In this calculation, the months bounding the each day of the linear interpolation are determined manually in Output DTN: SN0610T0502206.030.

Step 29. Calculate daily mean saturation vapor pressure, e_s, associated with the daily extreme temperatures corrected for elevation (Allen et al. 1998 [DIRS 157311], Equation 12):

$$e_s = \frac{e^o(T_{max}) + e^o(T_{min})}{2} \quad \text{(Eq. C-29a)}$$

where

$$e^o(T_{max}) = 0.6108\ exp\left[\frac{17.27\ T_{max}}{T_{max} + 237.3}\right] \quad \text{(Eq. C-29b)}$$

$$e^o(T_{min}) = 0.6108\ exp\left[\frac{17.27\ T_{min}}{T_{min} + 237.3}\right] \quad \text{(Eq. C-29c)}$$

and

e_s = daily mean saturation vapor pressure (kPa)

T_{max} = maximum temperature during the 24-hr period (°C) corrected for elevation, from Step 27

T_{min} = minimum temperature during the 24-hr period (°C) corrected for elevation, from Step 27.

$e°(T)$ = saturation vapor pressure function calculated at temperature *T*.

Step 30. Calculate mean air temperature corrected for elevation (Allen et al. 1998 [DIRS 157311], Equation 9):

$$T = \frac{T_{max} + T_{min}}{2} \quad \text{(Eq. C-30)}$$

where

T = mean air temperature, °C, corrected for elevation

T_{max} = maximum temperature during the 24-hr period (°C), from Step 27, corrected for elevation

T_{min} = minimum temperature during the 24-hr period (°C), from Step 27, corrected for elevation

Step 31. Limit actual vapor pressure, e_a, of the grid cell to less than or equal to e_s to keep the vapor pressure deficit ($e_s - e_a$) in the ET_0 equation (Step 37), nonnegative:

$$e_a = min\left[e_{a\ general}, e_s\right] \quad \text{(Eq. C-31)}$$

where

e_a = actual vapor pressure at the grid cell (kPa)

$e_{a\ general}$ = general actual vapor pressure of the general air mass (kPa), from Step 2

e_s = saturation vapor pressure (kPa), from Step 29.

The occurrence of $e_s = e_a$ indicates that air is saturated at the mean condition for the day and the potential for cloud formation exists. In these situations, the amount of solar radiation estimated by Equation C-13 will generally produce $R_{sm\ hor}$ less than or equal to $R_{so\ hor}$ due to relatively small difference between T_{max} and T_{min} responsible for producting this condition ($e_s = e_a$) as compared to clear sky conditions when T_{max} and T_{min} tend to be larger. Under clear sky conditions, e_s will tend to exceed e_a and C-31 will not be implemented. Implementation of Equation C-31 will therefore tend to be synchronized with estimated cloudy condtions implicit to the $R_{sm\ hor}$ estimate.

Step 32. Calculate slope of saturation vapor pressure curve at air temperature T (Δ) (Allen et al. 1998 [DIRS 157311], Equation 13):

$$\Delta = \frac{4098\left[0.6108\exp\left(\frac{17.27\ T}{T + 237.3}\right)\right]}{\left(T + 237.3\right)^2} \quad \text{(Eq. C-32)}$$

where

Δ = slope of saturation vapor pressure curve (kPa °C^{-1})
T = lapsed air temperature (°C), from Step 30.

Step 33a. Calculate atmospheric pressure, P, at each grid cell for calculating the psychrometric constant. Use the elevation of each grid cell (Allen et al. 1998 [DIRS 157311], Equation 7):

$$P_{cell} = 101.3\left(\frac{293 - 0.0065\, z_{cell}}{293}\right)^{5.26} \quad \text{(Eq. C-33a)}$$

where

P_{cell} = atmospheric pressure at the grid cell (kPa)
z_{cell} = elevation of grid cell above sea level (m).

The calculation of P_{cell} changes with cell elevation.

Step 33b. Calculate psychrometric constant Gamma (Allen et al. 1998 [DIRS 157311], Equation 8):

$$\gamma_c = \frac{c_p\ P_{cell}}{\varepsilon\ \lambda} = 0.665\, x\, 10^{-3}\ P_{cell} \quad \text{(Eq. C-33b)}$$

where

γ_c = psychrometric constant (kPa °C^{-1})
P_{cell} = atmospheric pressure (kPa), from Step 33a
λ = latent heat of vaporization = 2.45 (MJ kg^{-1})
c_p = specific heat at constant pressure, 1.013 × 10^{-3} (MJ kg^{-1} °C^{-1})
ε = ratio molecular weight of water vapor/dry air = 0.622.

Step 34. Calculate the horizontal equivalent for net short wave radiation on the incline R_{ns} (Allen et al. 1998 [DIRS 157311], Equation 38):

$$R_{ns} = (1-\alpha) R_{s\,(equiv)\,hor} \quad \text{(Eq. C-34)}$$

where

R_{ns} = net solar or shortwave radiation (MJ m^{-2} day^{-1})

α = albedo of the standard grass reference, which is 0.23 (dimensionless)

$R_{s(equiv)\ hor}$ = incoming solar radiation on the incline, reprojected to a horizontal equivalent (MJ m^{-2} day^{-1}), from Step 26.

Step 35. Calculate the net outgoing long wave radiation (Allen et al. 1998 [DIRS 157311], Equation 39):

$$R_{nl} = \sigma\left[\frac{T_{max,K}^{\ 4} + T_{min,K}^{\ 4}}{2}\right]\left(0.34 - 0.14\sqrt{e_a}\right)\left(1.35\frac{R_{sm\,hor}}{R_{so\,hor}} - 0.35\right) \qquad \text{(Eq. C-35)}$$

where

R_{nl} = net outgoing longwave radiation (MJ m^{-2} day^{-1}) (on a horizontal equivalent projection)

σ = Stefan-Boltzmann constant, 4.903×10^{-9} (MJ K^{-4} m^{-2} day^{-1})

$T_{max,K}$ = daily maximum absolute temperature, K = °C + 273.16, from Step 27

$T_{min,K}$ = daily minimum absolute temperature, K = °C + 273.16, from Step 27

e_a = actual vapor pressure for the grid cell (kPa), from Step 31

$R_{sm\,hor}$ = calculated solar radiation on horizontal surface (MJ m^{-2} day^{-1}), from Step 13

$R_{so\,hor}$ = calculated clear-sky radiation on a horizontal surface (MJ m^{-2} day^{-1}), from Step 12.

The $R_{sm\ hor}/R_{so\ hor}$ is an indicator of overall cloudiness for the area and must be limited to less than or equal to 1.0. The value represents conditions at the reference weather station and is applied to all grid cells.

Step 36. Calculate net radiation on the inclined surface, R_n (Allen et al. 1998 [DIRS 157311], Equation 40), projected to a horizontal projection:

$$R_n = R_{ns} - R_{nl} \qquad \text{(Eq. C-36)}$$

where

R_n = net radiation (MJ m^{-2} day^{-1}) (on a horizontal equivalent projection)
R_{ns} = net solar or shortwave radiation (MJ m^{-2} day^{-1}), from Step 34
R_{nl} = net outgoing long-wave radiation (MJ m^{-2} day^{-1}), from Step 35.

Step 37. Calculate ET_0 using Penman-Monteith equation (Allen et al. 1998 [DIRS 157311], Equation 6):

$$ET_0 = \frac{0.408\,\Delta(R_n - G) + \gamma_c \frac{900}{T+273} u_2 (e_s - e_a)}{\Delta + \gamma_c (1 + 0.34 u_2)} \qquad \text{(Eq. C-37)}$$

where

ET_0 = reference evapotranspiration (mm day^{-1})

R_n = net radiation on the inclined slope (but with horizontal reprojection) (MJ m^{-2} day^{-1}), from Step 36

G = soil heat flux density (MJ m^{-2} day^{-1}), use G=0 for daily time step (Allen et al. 1998 [DIRS 157311], Equation 42)

T = lapsed mean daily air temperature at 2- m height (°C), from Step 30

u_2 = wind speed at 2-m height (m s^{-1}), from Step 28

e_s = saturation vapor pressure (kPa), from Step 29

e_a = actual vapor pressure (kPa), from Step 31

e_s-e_a = saturation vapor pressure deficit (kPa), ($e_s - e_a \geq 0$)

Δ = slope vapor pressure curve (kPa $°C^{-1}$), from Step 32

γ_c = psychrometric constant (kPa $°C^{-1}$), from Step 33.

The ET_0 from Step 37 represents the reference ET in mm d^{-1} for an inclined surface but is expressed on a horizontal basis.

C2. CREATION OF LOOK-UP TABLE (LUT) FOR PARAMETER R_b

The R_b is defined as the ratio of beam radiation on an incline to the beam radiation on a horizontal plane. The R_b parameter is used by Duffie and Beckman (1980 [DIRS 176264], Equation 2.15.2) to translate direct beam radiation from horizontal to tilted surfaces. The R_b parameter is used in Step 20 of the ET_0 calculation procedure. The Duffie and Beckman (1980 [DIRS 176264]) equation in Step 44 stems from work by Klein (1977 [DIRS 176152]).

The product of Steps 38 to 44 is the R_b look-up table that includes values for R_b that are unique for each slope–aspect day-of-year combination associated with a reference latitude. It is produced by applying Steps 38 to 44 for a series of specific slope–aspect day-of-year combinations.

Steps 38 to 44 (Duffie and Beckman 1980 [DIRS 176264] and 1991 [DIRS 176616]; Klein 1977 [DIRS 176152]; Revfeim 1976 [DIRS 176482]) are used to compute integration limits for beam radiation during the 24-hr period. These equations are generally valid for all slope–aspect combinations except those where the sun may appear twice during the day. Twice-per-day solar appearance may occur for steep north facing slopes whenever the slope is greater than the solar angle above the horizon at solar noon; that is, when:

$$sin\, s > sin\varphi \cos\delta + \cos\varphi \sin\delta$$

where s is the slope in radians, φ = latitude (radians), and δ = solar declination (radians), from Step 4. This condition does not occur within the defined latitude, slope, and azimuth classifications utilized in the MASSIF infiltration model.

Nomenclature of slope and aspect used in all steps:

s is surface slope where, by definition here and by Duffie and Beckman (1980 [DIRS 176264] and 1991 [DIRS 176616]):

s = 0 for horizontal, and

s = $\pi/2$ radians for vertical slope (s is always positive and represents the slope in any direction).

γ is the surface aspect angle where, as defined by Duffie and Beckman (1980 [DIRS 176264] and 1991 [DIRS 176616]):

γ = 0 for slopes oriented due south
γ = $-\pi/2$ radians for slopes oriented due east
γ = $+\pi/2$ radians for slopes oriented due west
γ = $\pm\pi$ radians for slopes oriented due north.

Step 38. Calculate the effective latitude (φ_{eff}) for a given slope and aspect as described by Revfeim (1976 [DIRS 176482], Equation 2):

$$\varphi_{\text{eff}} = \arcsin\left[\cos(s) * \sin(\varphi) - \sin(s) * \cos(\varphi) * \cos(\gamma)\right] \qquad \text{(Eq. C-38)}$$

where

s = slope (radians)
φ = latitude (radians)
γ = surface aspect angle (radians).

The φ_{eff} is used in subsequent calculation steps to determine limits for beginning and ending of beam (direct) radiation during a day. The φ_{eff} is effective latitude that incorporates the effect of slope and aspect angle on the solar angle relative to the slope.

Step 39. Check whether the inclined surface receives any direct beam radiation during the day:

a. Calculate φ_{eff} - δ, where φ_{eff} is from Step 38, and δ is the declination from Step 4.

b. If φ_{eff} - $\delta \geq \pi/2$, then the surface does not receive any direct beam radiation during the day, so that $R_b = 0$. Therefore, if this conditional is true, no additional calculations are made for R_b.

In equation form:

$$if \quad \varphi_{eff} - \delta \geq \pi / 2 \quad then \;\; R_b = 0 \qquad \text{(Eq. C-39)}$$

and Steps 40 to 44 are skipped.

Otherwise, if $\varphi_{eff} - \delta < \pi/2$:

Step 40. Set up for the solution of daily integration limits for beam (direct) radiation using Duffie and Beckman (1991 [DIRS 176616]). Calculate parameter A for each slope-aspect combination (Duffie and Beckman 1991 [DIRS 176616], Equation 2.20.5g):

$$A = \cos(s) + \tan(\varphi)\cos(\gamma)\sin(s) \qquad \text{(Eq. C-40)}$$

where

s = slope (radians)
φ = latitude (radians)
γ = surface aspect angle (radians).

Step 41. Calculate parameter B for each slope-aspect combination and day of the year (Duffie and Beckman 1991 [DIRS 176616], Equation 2.20.5h):

$$B = \cos(\omega_s)\cos(s) + \tan(\delta)\sin(s)\cos(\gamma) \qquad \text{(Eq. C-41)}$$

where

s = slope (radians)
δ = solar declination (radians), from Step 4
γ = surface aspect angle (radians)
ω_s = sunset hour angle (radians), from Step 5.

Step 42. Calculate parameter C for each slope–aspect combination (Duffie and Beckman 1991 [DIRS 176616], Equation 2.20.5i):

$$C = \frac{sin(s)sin(\gamma)}{cos(\varphi)} \quad \text{(Eq. C-42)}$$

where

s = slope (radians)
γ = surface aspect angle (radians)
φ = latitude (radians).

Step 43. Calculate the 24-hr integration limits ω_{sr} (sunrise hour angle for inclined surface) and ω_{ss} (sunset hour angle for inclined surface) (Duffie and Beckman 1991 [DIRS 176616], Equations 2.20.5e and 2.20.5f) for the R_b equation. The required steps are presented in sequential order of computation.

Steps 43.1, 43.2a, 43.3a, and 43.4 are not listed by Duffie and Beckman (1991 [DIRS 176616]) but are necessary to eliminate numerical errors caused by taking the square root of a nonpositive number (Step 43.1), or taking the arccosine of a value outside the –1 to 1 domain (Steps 43.2a, 43.2b, 43.3a, and 43.3b). The steps also eliminate negative values calculated for R_b. If any of the conditionals of Steps 43.1, 43.2a, or 43.3a are true, then the parameter listed as the second listed item of the "min" function of Equation 43.2b (sunrise) and/or Equation 43.3b (sunset) is disqualified, and the min function defaults to the first item (ω_{sr} and/or ω_{ss}). This conditional check is carried out in Step 43.1.

Step 43.1. Check for negative values in the square root argument used in Steps 43.3a and 43.3b.

According to Klein and Theilacker (1981 [DIRS 176484]), the quantity within the square root (Steps 43.2b and 43.3b) will be negative if the surface orientation is such that the solar incidence angle is less or greater than 90 degrees at all times; ω_{sr} and ω_{ss} should be set to $-\omega_s$ and ω_s, respectively, under these circumstances (Klein and Theilacker 1981 [DIRS 176484, p.31]).

Therefore,

$$if \quad \left(A^2 - B^2 + C^2 < 0 \right) \; then \; \omega_{sr} = -\omega_s \quad and \quad \omega_{ss} = \omega_s \quad \text{(Eq. C-43.1)}$$

where $\omega_{sr} = -\omega_s$ and $\omega_{ss} = \omega_s$ are the normal sunrise and sunset angles on horizontal slopes; proceed to Step 44.

Otherwise:

Step 43.2a. Check for out-of-domain values in the arccosine function in Step 43.2b:

$$if \left(\frac{AB + C\sqrt{A^2 - B^2 + C^2}}{A^2 + C^2} < -1 \right) or \left(\frac{AB + C\sqrt{A^2 - B^2 + C^2}}{A^2 + C^2} > 1 \right) then \ \omega_{sr} = -\omega_s \quad \text{(Eq. C-43.2a)}$$

where $\omega_{sr} = -\omega_s$ is the normal sunrise angle on horizontal slopes; proceed to Step 43.3a.

Otherwise:

Step 43.2b. Apply the equation by Duffie and Beckman (1991 [DIRS 176616], Equation 2.20.5e):

$$|\omega_{sr}| = min\left[\omega_s , arcos\left(\frac{AB + C\sqrt{A^2 - B^2 + C^2}}{A^2 + C^2} \right) \right] \quad \text{(Eq. C-43.2b)}$$

and

$$\omega_{sr} = \begin{cases} -|\omega_{sr}| & if \ (A > 0 \ and \ B > 0) \ or \ (A \geq B) \\ |\omega_{sr}| & otherwise \end{cases} \quad \text{(Eq. C-43.2c)}$$

where $\omega_{sr} = -|\omega_{sr}|$ is the normal limit.

Step 43.3a. Check for out-of-domain values for the arccosine function in Step 43.3b.

$$if \left(\frac{AB - C\sqrt{A^2 - B^2 + C^2}}{A^2 + C^2} < -1 \right) or \left(\frac{AB - C\sqrt{A^2 - B^2 + C^2}}{A^2 + C^2} > 1 \right) then \ \omega_{ss} = \omega_s \quad \text{(Eq. C-43.3a)}$$

where $\omega_{ss} = \omega_s$ is the normal sunset angle on horizontal slopes; proceed to Step 44.

Otherwise:

Step 43.3b. Apply the equation by Duffie and Beckman (1991 [DIRS 176616], Equation 2.205f):

$$|\omega_{ss}| = min\left[\omega_s , arcos\left(\frac{AB - C\sqrt{A^2 - B^2 + C^2}}{A^2 + C^2} \right) \right] \quad \text{(Eq. C-43.3b)}$$

and

$$\omega_{ss} = \begin{cases} |\omega_{ss}| \ \ if \ \ (A > 0 \ \ and \ \ B > 0) \ or \ (A \geq B) \\ -|\omega_{ss}| \ \ otherwise \end{cases} \qquad \text{(Eq. C-43.3c)}$$

where $\omega_{ss} = |\omega_{ss}|$ is the normal limit.

Step 43.4. Prevent negative values for R_b. As a last step, prior to calculation of R_b, a check should be performed to prevent negative values for R_b from being calculated in Step 44. Negative values for R_b may occur under conditions of very low sun angles during all of the day; for example, during winter on northerly facing slopes. This is prevented by reversing the signs computed for the integration limits.

$$if \ \ (A < B) \ \ and \ \gamma > 0 \ \ then \ \ \omega_{sr} = -\omega_{sr} \qquad \text{(Eq. C-43.4a)}$$

$$if \ \ (A < B) \ \ and \ \gamma < 0 \ \ then \ \ \omega_{ss} = -\omega_{ss} \qquad \text{(Eq. C-43.4b)}$$

Step 44. Calculate the beam adjustment ratio R_b (Duffie and Beckman 1980 [DIRS 176264], Equation 2.16.5; Klein 1977 [DIRS 176152], Equation 11):

$$R_b = \frac{\begin{array}{l} \cos(s)\sin(\delta)\sin(\varphi)(\omega_{ss} - \omega_{sr}) \\ -\sin(\delta)\cos(\varphi)\sin(s)\cos(\gamma)(\omega_{ss} - \omega_{sr}) \\ +\cos(\varphi)\cos(\delta)\cos(s)(\sin(\omega_{ss}) - \sin(\omega_{sr})) \\ +\cos(\delta)\cos(\gamma)\sin(\varphi)\sin(s)(\sin(\omega_{ss}) - \sin(\omega_{sr})) \\ -\cos(\delta)\sin(s)\sin(\gamma)(\cos(\omega_{ss}) - \cos(\omega_{sr})) \end{array}}{2(\cos(\varphi)\cos(\delta)\sin(\omega_s) + \omega_s \sin(\varphi)\sin(\delta))} \qquad \text{(Eq. C-44)}$$

Variable 's' (slope) in the equation for R_b is expressed as 'β' by Duffie and Beckman (1980 [DIRS 176264]). All angles are in radians. Parameter ω_s in the denominator of Equation 44 is from Step 5 and is not the same as the parameter ω_{ss} that appears in the numerator.

As described by Duffie and Beckman (1980 [DIRS 176264], p. 95): "This equation is not valid for surfaces that receive beam radiation more than once during the day; that is, for surfaces on which the sun sets and then rises between normal sunrise and sunset." No such surfaces exist within the Yucca Mountain net infiltration modeling domain.

Definition of Classes for the R_b Look-up Table

A look-up table of R_b values was developed based on latitude, slope, and azimuth classes defined in Table C-1. A total of 78 classes were specified with each class representing a unique slope and azimuth combination. The specified azimuth values were 0 degrees (surface facing north), 30, 60, 90 (east), 120, 150, 180 (south), 210, 240, 270 (west), 300, 330, and 360 (north). The

specified slope values were 0 degrees (horizontal surface), 2.5, 7.5, 15, 25, and 40 degrees. Steps 38 to 44 were applied to each of these 78 classes and for each day of the year resulting in 28,548 R_b values in the look-up table (Output DTN: SN0602T0502206.003, *Rb_Ver1.2.03.xls*).

In Table C-1, north azimuth is represented by both 0 and 360 to facilitate the use of the look-up table. For the same reason, there is a zero slope combination for each azimuth class, despite the fact that azimuth is undefined for a horizontal (zero slope) surface and R_b is unity (1).

Table C-1. Azimuth and Slope Combinations for Each Class Used to Construct the R_b Look-up Table

Class	Azimuth (deg)	Slope (deg)	Class	Azimuth (deg)	Slope (deg)	Class	Azimuth (deg)	Slope (deg)
1	0	0.0	31	150	0.0	61	300	0.0
2	0	2.5	32	150	2.5	62	300	2.5
3	0	7.5	33	150	7.5	63	300	7.5
4	0	15.0	34	150	15.0	64	300	15.0
5	0	25.0	35	150	25.0	65	300	25.0
6	0	40.0	36	150	40.0	66	300	40.0
7	30	0.0	37	180	0.0	67	330	0.0
8	30	2.5	37	180	2.5	68	330	2.5
9	30	7.5	39	180	7.5	69	330	7.5
10	30	15.0	40	180	15.0	70	330	15.0
11	30	25.0	41	180	25.0	71	330	25.0
12	30	40.0	42	210	40.0	72	330	40.0
13	60	0.0	43	210	0.0	73	360	0.0
14	60	2.5	44	210	2.5	74	360	2.5
15	60	7.5	45	210	7.5	75	360	7.5
16	60	15.0	46	210	15.0	76	360	15.0
17	60	25.0	47	210	25.0	77	360	25.0
18	60	40.0	48	210	40.0	78	360	40.0
19	90	0.0	49	240	0.0	—	—	—
20	90	2.5	50	240	2.5	—	—	—
21	90	7.5	51	240	7.5	—	—	—
22	90	15.0	52	240	15.0	—	—	—
23	90	25.0	53	240	25.0	—	—	—
24	90	40.0	54	240	40.0	—	—	—
25	120	0.0	55	270	0.0	—	—	—
26	120	2.5	56	270	2.5	—	—	—
27	120	7.5	57	270	7.5	—	—	—
28	120	15.0	58	270	15.0	—	—	—
29	120	25.0	59	270	25.0	—	—	—
30	120	40.0	60	270	40.0	—	—	—

Source: Output DTN: SN0602T0502206.003, *Rb_Ver1.2.03.xls.*

C3. PARAMETERIZATION OF SOLAR RADIATION EQUATIONS FOR YUCCA MOUNTAIN

Calibration of the solar radiation estimation procedure was performed using data collected at the Yucca Mountain meteorological monitoring site (Output DTN: MO0602SPAWEATH.000). The analysis consisted of the following:

- Analysis of measured daily solar radiation (R_s) data to evaluate the appropriate coefficient K_{Rs} (Step 13) to be used for the estimation of solar radiation from daily maximum and minimum air temperature (T_{max} and T_{min}) at the Yucca Mountain site.

- Analysis of the variation in estimated clear sky solar radiation over the elevation range of the Yucca Mountain study area.

Three years of daily R_s and T_{max} and T_{min} measurements from the Yucca Mountain meteorological monitoring site (Output DTN: MO0602SPAWEATH.000) were evaluated to determine the appropriate value of K_{Rs} in Equation C-13 and the estimation consistency from year to year. The three years evaluated, 1998, 2001 and 2002, were the same years used in the transpiration coefficient section (Appendix D), and represent relatively wet, average and dry years.

The analysis was performed in an Excel® worksheet named *Hargreaves_KRS_YM_xls*, included in Output DTN: SN0602T0602206.005.

C3.1 INTEGRITY ASSESSMENT OF SOLAR RADIATION DATA

Solar radiation data were visually examined by plotting 24-hr measurements of global solar radiation overlaid by clear sky (R_{so}) curves versus day of year (Allen et al. 2005 [DIRS 176207], p. D-5; Allen 1996 [DIRS 176485], p. 97). Figure C-1 shows R_{so} envelopes and measured values of daily global solar radiation R_s for the three years.

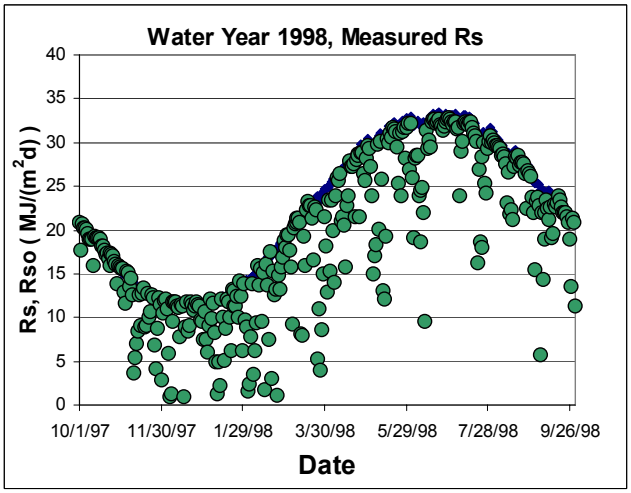

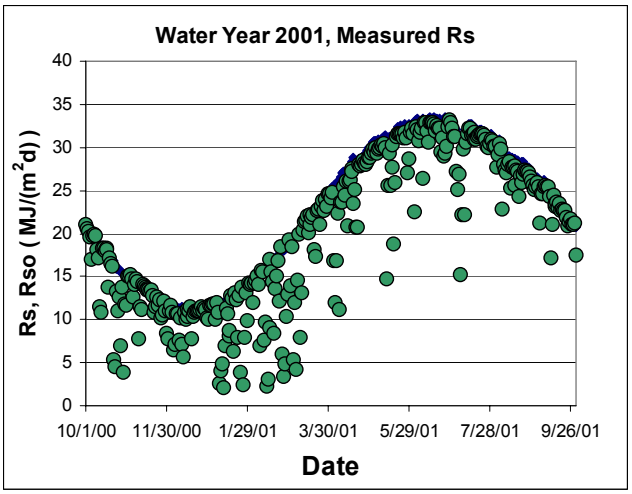

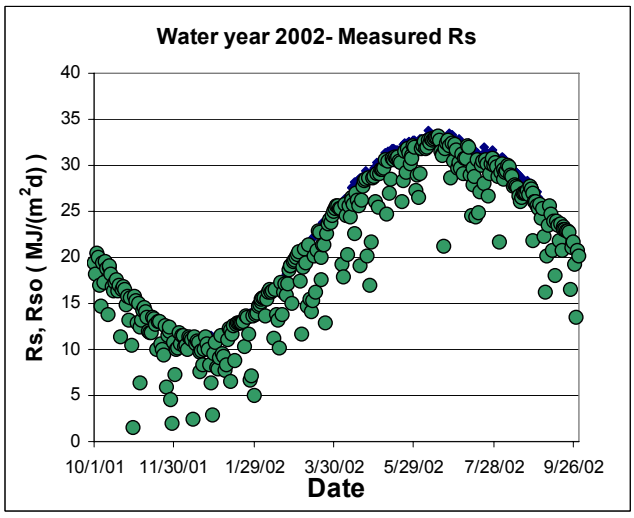

Source: Output DTN: SN0602T0502206.005.

Figure C-1. Comparison of Measured Total Solar Radiation (R_s) (points) with a Theoretical Clear Sky (R_{so}) Curve (solid line) for Yucca Mountain for Water Years 1998, 2001, and 2002

In general, upper values for R_s that typically occur on cloudless days were in close agreement with the estimated R_{so}, indicating good calibration of the sensor and good management of the sensor operation and data collection. The R_{so} curve was calculated using Equation C-12 with $K_{Bo\ hor}$ based on Equation C-10, and using W based on e_a from Equation C-46 of the following section, rather than using T_{dew} from Equation C-1. The e_a based on Equation C-46 used measured daily minimum relative humidity data, which is preferable during the assessment of data quality, rather than using the T_{dew} from Equation C-1, which is an estimated value.

C3.2 EVALUATION OF THE K_{Rs} COEFFICIENT OF HARGREAVES SOLAR RADIATION EQUATION

The Hargreaves equation (C-13) was used to estimate solar radiation from maximum and minimum daily air temperature (Allen et al. 1998 [DIRS 157311], Equation 50). Equation C-13 is repeated here as Equation C-45:

$$R_s = K_{Rs}\sqrt{(T_{max} - T_{min})}\ R_a \qquad \text{(Eq. C-45)}$$

where

R_a = extraterrestrial solar radiation (MJ m^{-2} d^{-1})
T_{max} = maximum air temperature (°C)
T_{min} = minimum air temperature (°C)
K_{Rs} = Hargreaves adjustment coefficient ($°C^{-0.5}$).

Equation C-45 is the same equation as Equation C-13.

Four values for the K_{Rs} coefficient were evaluated: 0.16, 0.18, 0.19, and 0.20. These values were found by Allen (1997 [DIRS 176568]) to be representative of locations in the western United States.

C3.3 CALCULATION OF ACTUAL VAPOR PRESSURE

The measurement parameter in the reviewed weather data set that represented humidity was minimum relative humidity. This parameter was used in calculations of W, the amount of precipitable water in the atmosphere. Actual vapor pressure was calculated from RH_{min} using the following equation (Allen et al. 2005 [DIRS 176207], Equation 13):

$$e_a = e^o(T_{max})\frac{RH_{min}}{100} \qquad \text{(Eq. C-46)}$$

where

e_a = actual vapor pressure (kPa)
T_{max} = maximum air temperature (°C)
RH_{min} = minimum relative humidity (%)
$e°(T_{max})$ = saturation vapor pressure corresponding to T_{max} (kPa).

The $e°(T_{max})$ is calculated as (Allen et al. 2005 [DIRS 176207], Equation 7):

$$e^o(T_{\max}) = 0.6108 \exp\left[\frac{17.27\, T_{\max}}{T_{\max} + 237.3}\right] \quad \text{(Eq. C-47)}$$

Precipitable water (W) used in the R_{so} equation was calculated from e_a using Equation C-9.

C3.4 RESULTS

Comparisons between measured and estimated solar radiation are shown in Figures C-2, C-4, and C-6 for the three water years evaluated. In all three years, solar radiation estimates were consistent with measurements and relatively little scatter was observed. A value for K_{Rs} between 0.19 $°C^{-0.5}$ and 0.20 $°C^{-0.5}$ tended to best estimate the daily R_s, based on the ratio of summed estimated R_s over each year to observed R_s equal to 1.0 and based on minimization of the root mean square error (RMSE).

Figures C-3, C-5 and C-7 show estimated values of R_s using Equation C-45 (Hargreaves equation) with specific values for K_{Rs} and clear-sky solar radiation envelopes for the water years 1998, 2001, and 2002. In these graphs and in the statistical analyses, estimated values for R_s were constrained to less than or equal to R_{so} because R_{so} represents a physical upper limit on R_s.

Table C-2 shows ratios between the sum of measured daily solar radiation and the sum of estimated daily solar radiation for four candidate values of K_{Rs}. A ratio = 1 means that the sum of measured daily solar radiation for the water year is equal to the sum of estimated solar radiation; a ratio < 1 means that total estimated solar radiation is less than total measured solar radiation (underestimation). Table C-3 summarizes RMSE for the three years and candidate values for K_{Rs}.

In general, the use of the standard value K_{Rs} = 0.16 $°C^{-0.5}$ from FAO-56 (Allen et al. 1998 [DIRS 157311], Equation 50) produced a significant underestimation of total solar radiation of around 15%. For year 1998, the best result, a ratio = 0.995, was obtained using K_{Rs} = 0.19 $°C^{-0.5}$and the RMSE was minimized with this value. For water years 2001 and 2002, an annual ratio of 1.0 was obtained for a value for K_{Rs} between 0.19 $°C^{-0.5}$ and 0.20 $°C^{-0.5}$. RMSE was lowest in 2001 for K_{Rs} = 0.19 $°C^{-0.5}$ and in 2002 for K_{Rs} = 0.20 $°C^{-0.5}$. The value for K_{Rs} = 0.192 $°C^{-0.5}$ over the three year period to obtain a mean annual ratio of 1.0. This value was rounded to 0.19 $°C^{-0.5}$ and was used to estimate daily solar radiation in the model.

C3.5 CONCLUSIONS

Based on the three year record, a value of K_{Rs} = 0.19 $°C^{-0.5}$ was determined to be the most appropriate value for estimating R_s from daily maximum and minimum air temperature for the Yucca Mountain site for Present-Day conditions. It is assumed that this value is adequate to use for future climate conditions at Yucca Mountain (Section 5.6, #9).

Table C-2. Ratio Between the Yearly Sum of Estimated Daily Solar Radiation (using Hargreaves Equation) and Yearly Sum of Measured Daily Solar Radiation for Water Years 1998, 2001, and 2002, Yucca Mountain Site

Water Year	K_{Rs}	Annual Ratio [a]
1998	0.16	0.839
	0.18	0.943
	0.19	0.995
	0.20	1.043
2001	0.16	0.832
	0.18	0.936
	0.19	0.987
	0.20	1.031
2002	0.16	0.825
	0.18	0.928
	0.19	0.979
	0.20	1.023

Source: Output DTN: SN0602T0502206.005.

[a] The annual ratio was calculated as:

$$Ratio = \frac{\sum_{i}^{n} R_{s\,(Hargreaves)}}{\sum_{i}^{n} R_{s\,(measured)}}$$

In this equation, the subscripts "i" and "n" represent the first and last days of the water year.

Table C-3. Root Mean Square Error (RMSE) for Daily Solar Radiation Estimated Using the Hargreaves Equation and Measured Daily Solar Radiation for Water Years 1998, 2001, and 2002, Yucca Mountain Site, for Four Values for Parameter K_{Rs}

Water Year	K_{Rs}	n	RMSE [a] MJ $m^{-2}d^{-1}$	RMSE % of Annual Daily Mean
1998	0.16	365	4.53	23.5
	0.18	365	3.24	16.8
	0.19	365	3.00	15.5
	0.20	365	3.10	16.1
2001	0.16	366	4.47	22.2
	0.18	366	2.92	14.5
	0.19	366	2.58	12.8
	0.20	366	2.62	13.0

Table C-3. Root Mean Square Error (RMSE) for Daily Solar Radiation Estimated Using the Hargreaves Equation and Measured Daily Solar Radiation for Water Years 1998, 2001, and 2002, Yucca Mountain Site, for Four Values for Parameter K_{Rs} (Continued)

Water Year	K_{Rs}	n	RMSE [a] MJ $m^{-2}d^{-1}$	RMSE % of Annual Daily Mean
2002	0.16	365	4.39	21.2
	0.18	365	2.66	12.9
	0.19	365	2.20	10.6
	0.20	365	2.19	10.6

[a] The RMSE was calculated as:

$$RMSE = \left[\frac{\sum_{i}^{n} \left(R_{s\,(Hargreaves)} - R_{s\,(measured)} \right)^2}{n} \right]^{0.5}$$

In this equation, the subscripts “i” and “n” represent the first and last days of the water year.

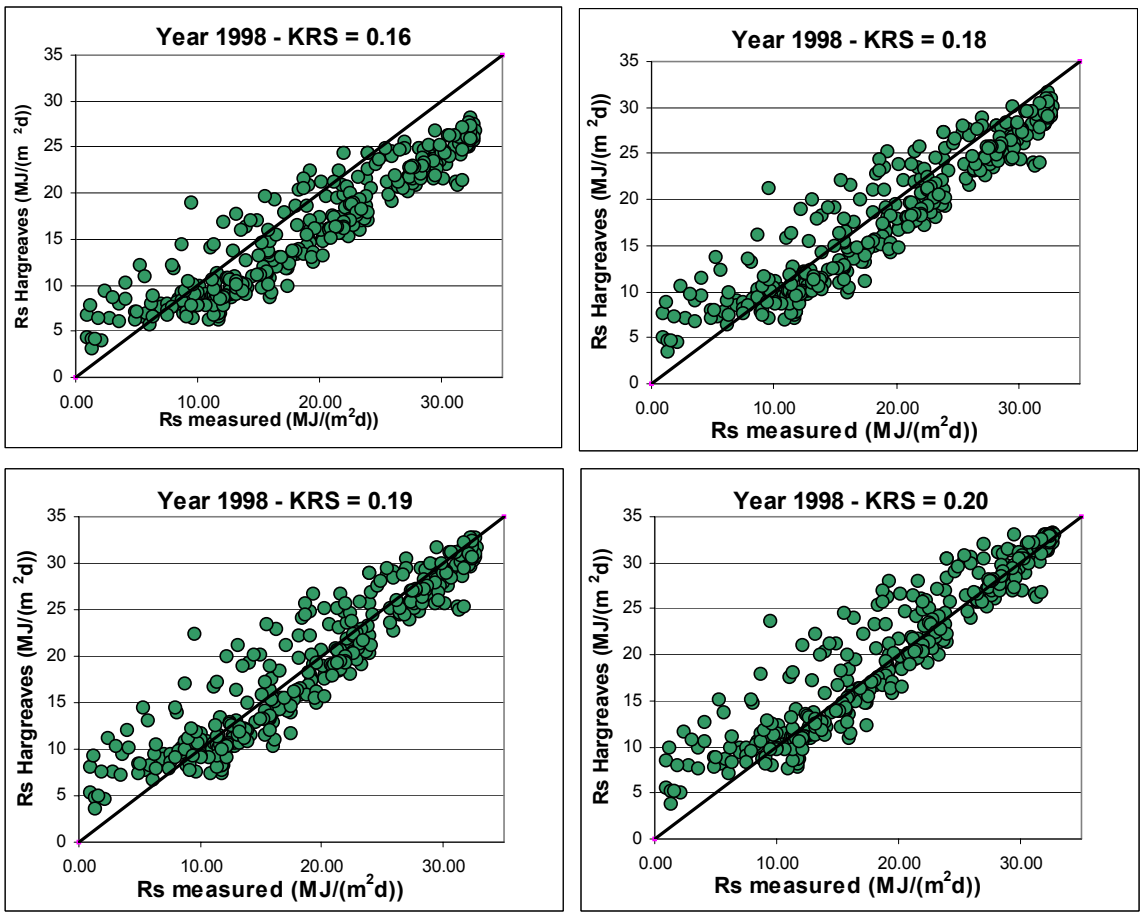

Source: Output DTN: SN0602T0502206.005.

Figure C-2. R_s Estimated Using the Hargreaves Equation with Four Values for K_{Rs} versus R_s Measured for Water Year 1998, Yucca Mountain Monitoring Site

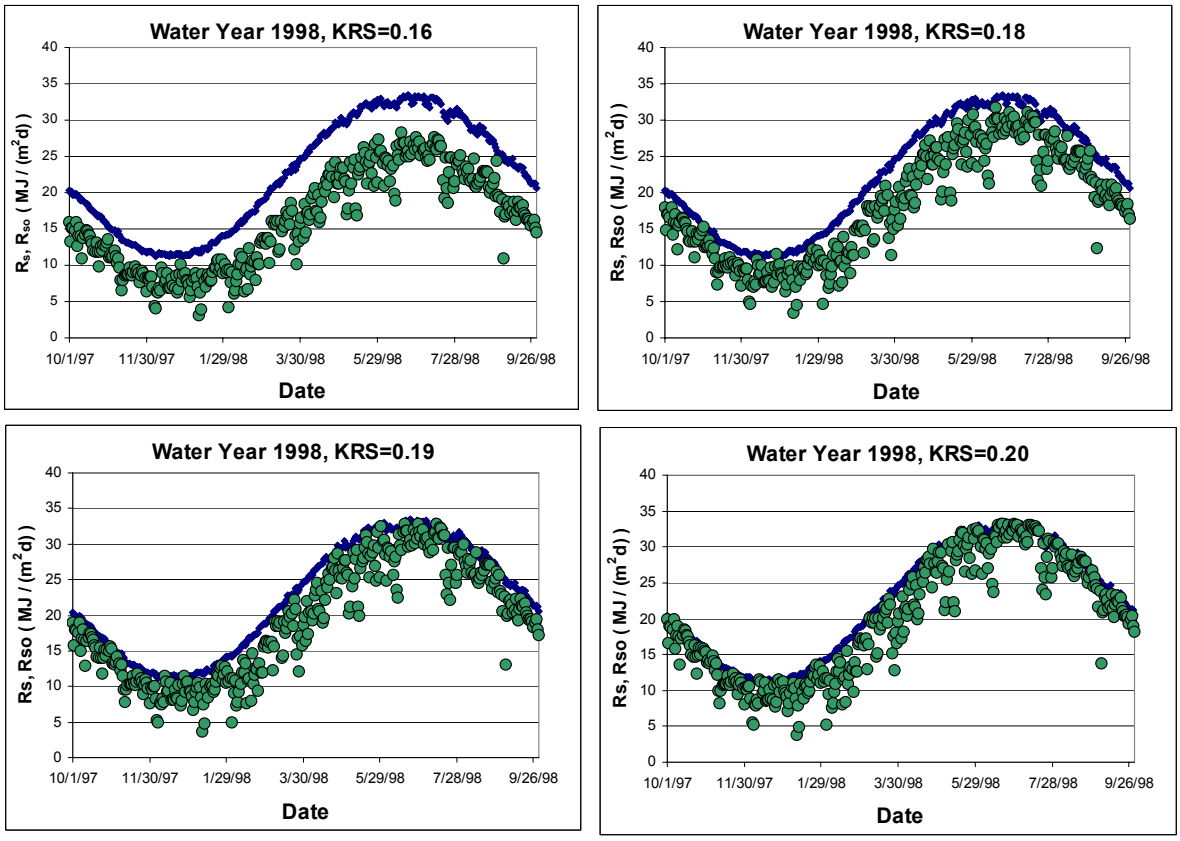

Source: Output DTN: SN0602T0502206.005.

Figure C-3. R_s Estimated Using the Hargreaves Equation with Four Values for K_{Rs} and Clear-sky Solar Radiation Envelopes for Water Year 1998, Yucca Mountain Monitoring Site

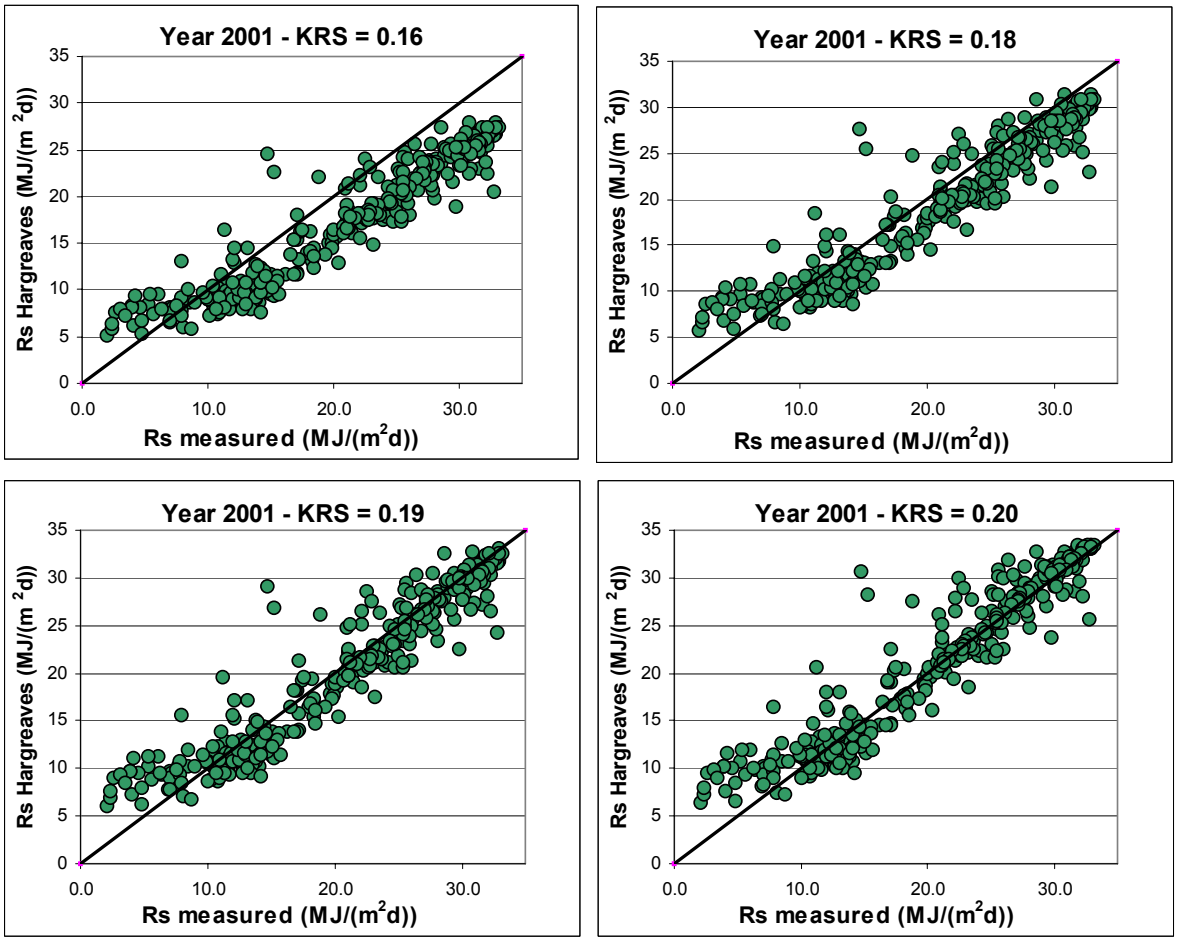

Source: Output DTN: SN0602T0502206.005.

Figure C-4. R_s Estimated Using the Hargreaves Equation with Four Values for K_{Rs} versus R_s Measured for Water Year 2001, Yucca Mountain Monitoring Site

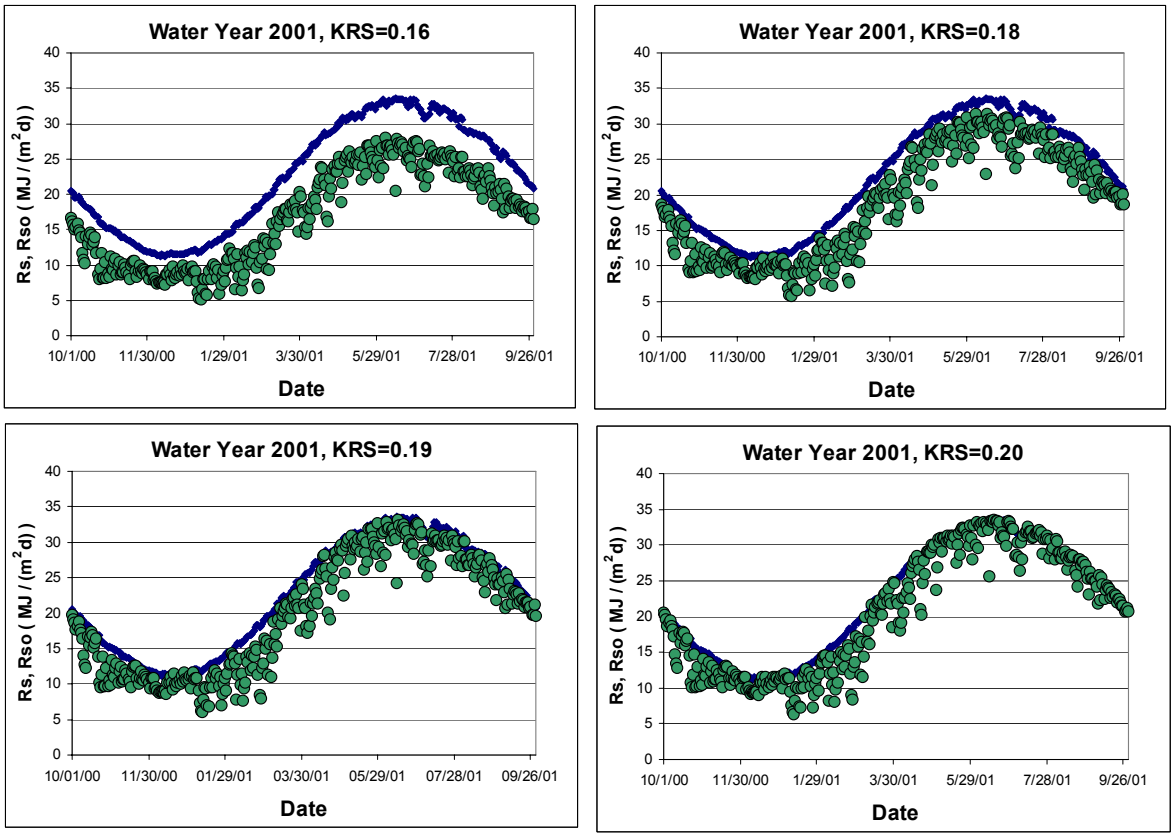

Source: Output DTN: SN0602T0502206.005.

Figure C-5. R_s Estimated Using the Hargreaves Equation with 4 Values for K_{Rs} and Clear-sky Solar Radiation Envelopes for Water Year 2001, Yucca Mountain Monitoring Site

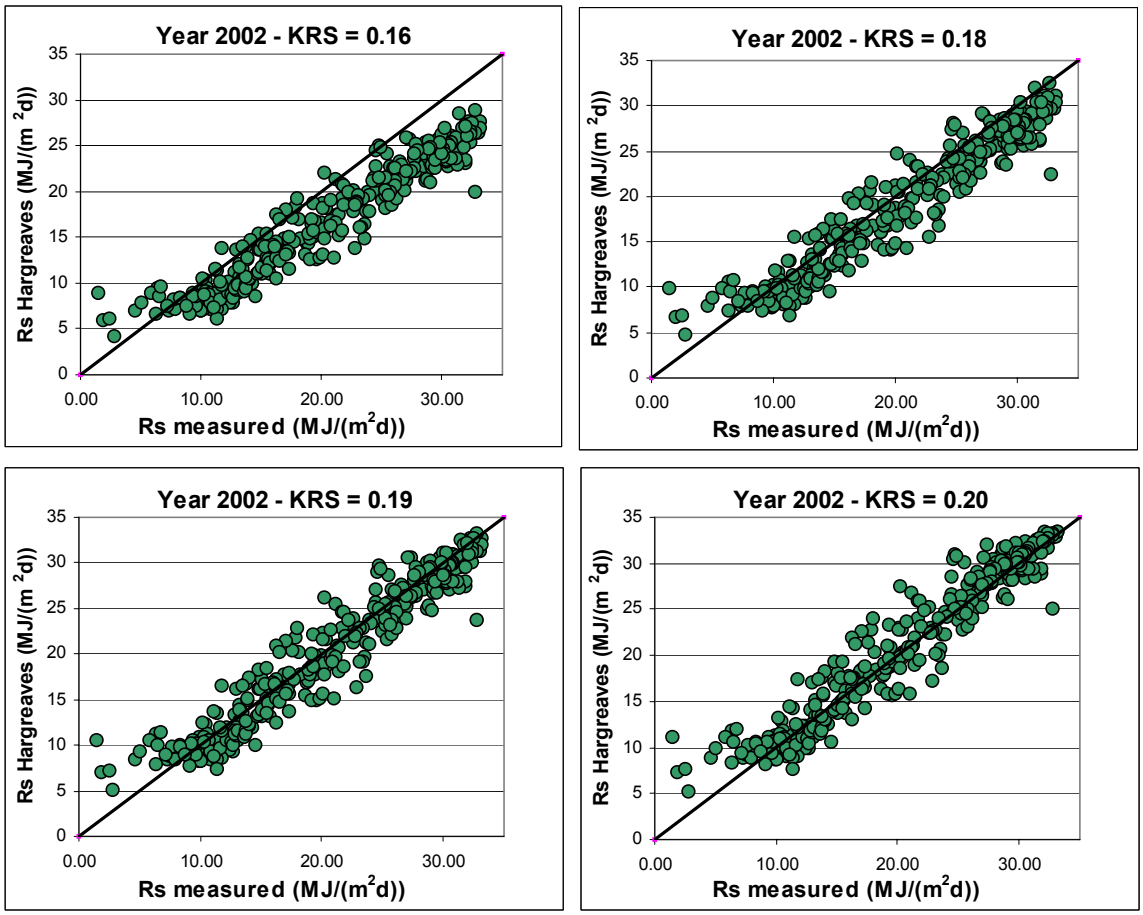

Source: Output DTN: SN0602T0502206.005.

Figure C-6. R_s Estimated Using the Hargreaves Equation with Four Values for K_{Rs} versus R_s Measured for Water Year 2002, Yucca Mountain Monitoring Site

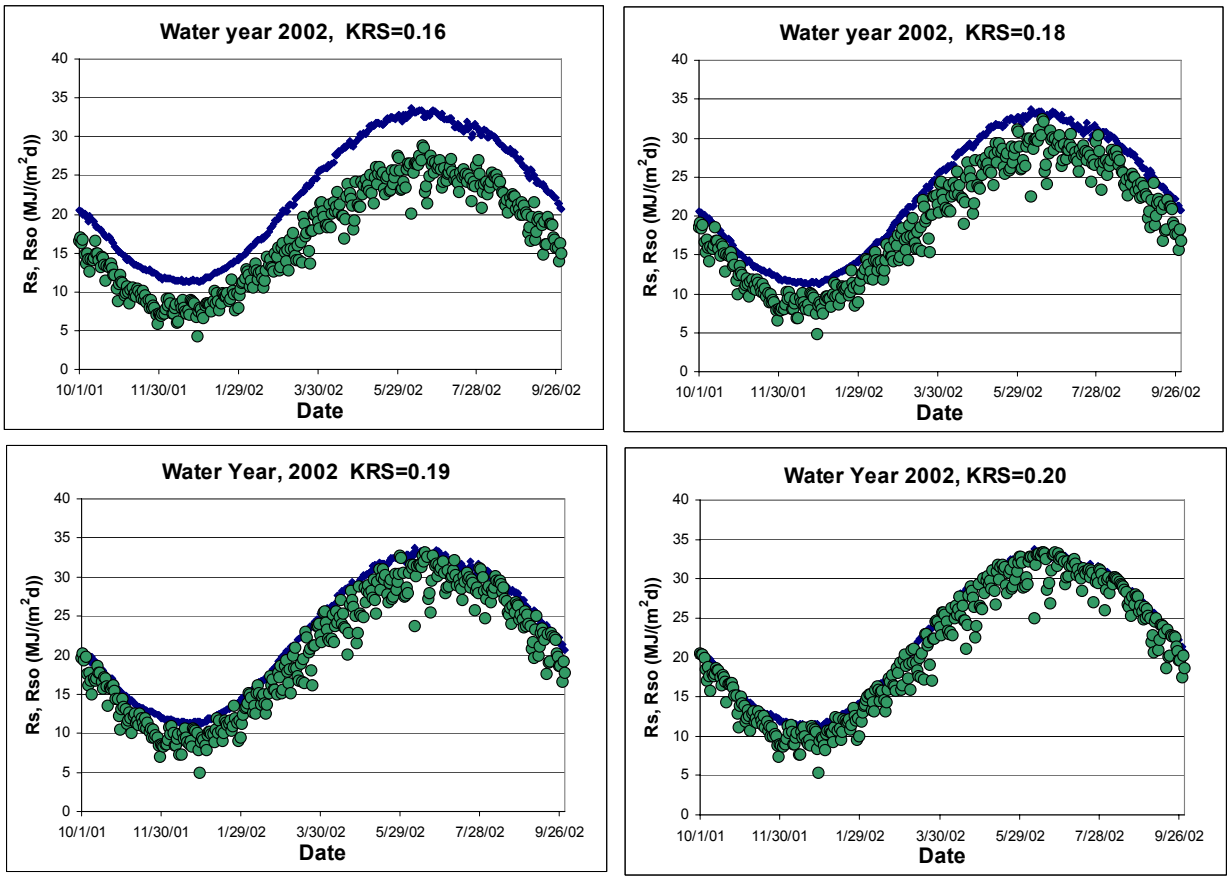

Source: Output DTN: SN0602T0502206.005.

Figure C-7. R_s Estimated Using the Hargreaves Equation with Four Values for K_{Rs} and Clear-sky Solar Radiation Envelopes for Water Year 2002, Yucca Mountain Monitoring Site

C3.6 ANALYSIS OF THE VARIATION OF CLEAR-SKY SOLAR RADIATION WITH ALTITUDE AT THE YUCCA MOUNTAIN SITE

The intensity of clear sky solar radiation increases with elevation due to smaller optical depth of the overlying atmosphere. An analysis was performed to determine the sensitivity of the estimation of $R_{so\ hor}$ and R_s from Equation C-45 over the elevation range for Yucca Mountain. The elevation range evaluated was from 967 to 1,971 m. This range included the elevation of the reference weather station used to determine K_{Rs} (1,143 m).

Figure C-8 shows the variation of the ratio between $R_{so\ hor}$ calculated at the two extreme altitudes and $R_{so\ hor}$ calculated at the elevation of the reference weather station based on measured relative humidity data (Output DTN: MO0602SPAWEATH.000) for water year 1998. $R_{so\ hor}$ was calculated using Equation C-12. The results were nearly identical for years 2001 and 2002. The ratio between $R_{so\ hor}$ calculated at 967 m over $R_{so\ hor}$ calculated at 1,143 m varied from 0.996 to 0.998 during each of the three water years 1998, 2001 and 2002 (data shown for year 1998 in Figure C-8); therefore, expected maximum variation in estimated R_{so} and R_s is about 0.4% between these elevations. The ratio of $R_{so\ hor}$ calculated at 1,971 m over $R_{so\ hor}$ calculated at 1,143 m ranged from 1.010 to 1.018 for all three water years; therefore, the maximum variation

in estimated R_{so} and R_s is less than 1.8% between these elevations. These differences are much smaller than the mean estimation error in daily $R_{so\ hor}$, which averaged about 13% over the annual periods. Therefore, the use of constant elevation during computation of R_{so} and estimation of R_s from temperature data is justified over the elevation range of the study area.

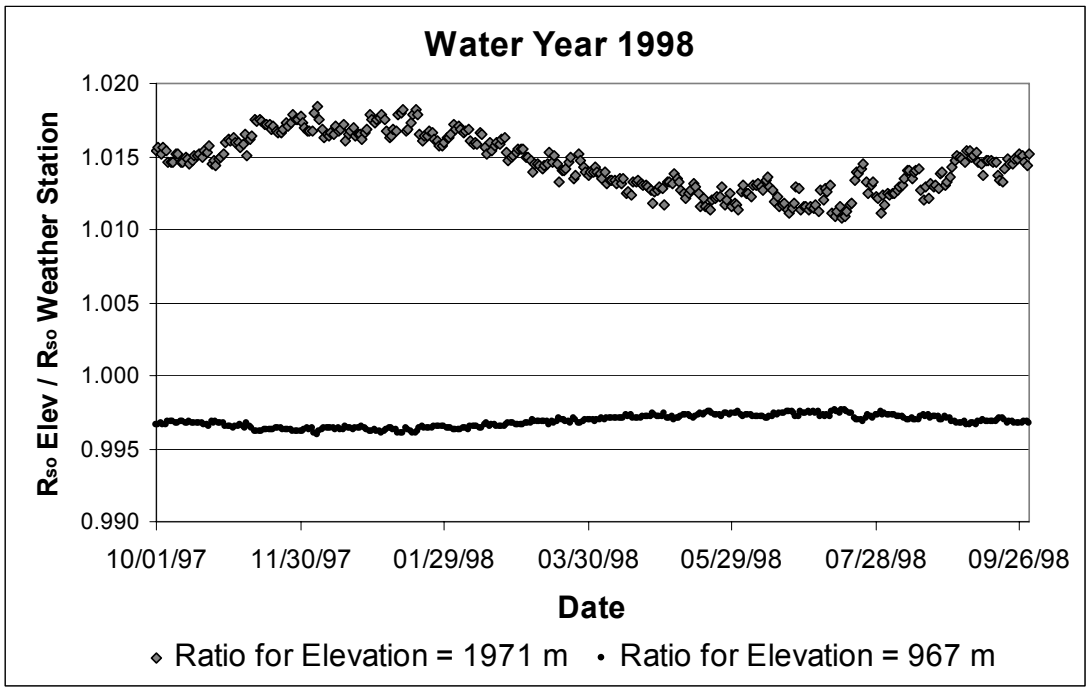

Source: Output DTN: SN0602T0502206.005.

Figure C-8. Variation of the Ratio between $R_{so\ hor}$ Calculated at Two Extreme Elevations (967 m and 1,971 m) near or on Yucca Mountain over $R_{so\ hor}$ Calculated at a Reference Weather Station (elevation = 1,143 m) during Water Year 1998

C4. EVALUATION OF DIFFUSE AND TOTAL RADIATION MEASUREMENTS FROM NEAR YUCCA MOUNTAIN

C4.1 INTRODUCTION

The following summarizes an analysis of diffuse radiation data collected near Yucca Mountain, Nevada, by the National Oceanic and Atmospheric Administration (NOAA) SURFRAD network. The purpose of the analysis was to demonstrate the ability for published equations, including those by Vignola and McDaniels (1986 [DIRS 176481]), to estimate diffuse solar radiation for the study area with relatively high accuracy. Daily totals of diffuse and direct solar radiation measured at the Desert Rock weather station in Nevada (DTN: SN0511NOAADATA.001 [DIRS 177238]) were used in the analysis (Output DTN: SN0602T0502206.004).

A station latitude of 36.6° and an elevation of 1,007 m for the Desert Rock station were used in calculations reported herein. The elevation parameter was used to estimate theoretical clear sky solar radiation, and latitude was used to determine sun angles.

Quality control of the data has been performed routinely by NOAA. The NOAA quality control process flagged records that were suspected to contain errors. Flagged records were not included in this analysis.

C4.2 COMPARISON OF DIFFUSE COMPONENT TO SIMPLE MODELS FOR AVERAGE DIFFUSE INDICES

Total shortwave transmissivity is the sum of direct and diffuse transmissivity (Allen 1996 [DIRS 176485], Equation 7):

$$\tau_{sw\,hor} = K_{B\,hor} + K_{D\,hor} \quad \text{(Eq. C-48)}$$

where

$K_{B\,hor}$ = 24-hr transmissivity for direct radiation (dimensionless)
$K_{D\,hor}$ = 24-hr transmissivity for diffuse radiation (dimensionless), from Step 15
$\tau_{sw\,hor}$ = total short-wave transmissivity (dimensionless), from Step 14.

The $K_{D\,hor}$ value is solved by rearranging Equation C-48 for $K_{D\,hor}$. The value for $\tau_{sw\,hor}$ was determined from the ratio of measured daily solar radiation (R_s) to estimated clear sky solar radiation (R_{so}) using Equation C-14.

Several models, as follows, were evaluated for estimating the diffuse solar component, based on the Desert Rock solar radiation data:

1. The ASCE-EWRI function (Allen et al. 2005 [DIRS 176207]) previously described for Equation C-11 is also used for Equation C-49 to estimate diffuse transmissivity for any sky conditions:

$$\begin{aligned} K_{D\,hor} &= 0.35 - 0.36\,K_{B\,hor} \quad for\ K_{B\,hor} \geq 0.15 \\ K_{D\,hor} &= 0.18 + 0.82\,K_{B\,hor} \quad for\ K_{B\,hor} < 0.15 \end{aligned} \quad \text{(Eq. C-49)}$$

where

$K_{D\,hor}$ = 24-hr transmissivity for diffuse radiation (dimensionless)
$K_{B\,hor}$ = 24-hr transmissivity for direct radiation (dimensionless).

2. Vignola and McDaniels (1986 [DIRS 176481], p. 411):

$$\begin{aligned} K_{B_{hor}} &= 0.016\,\tau_{sw_{hor}} \quad for\ \tau_{sw_{hor}} < 0.175 \\ K_{B_{hor}} &= 0.022 - 0.280\,\tau_{sw_{hor}} + 0.828(\tau_{sw_{hor}})^2 + 0.765(\tau_{sw_{hor}})^3 \quad for\ \tau_{sw_{hor}} \geq 0.175 \end{aligned} \quad \text{(Eq. C-50)}$$

where

$K_{Bo\,hor}$ = 24-hr transmissivity for diffuse radiation (dimensionless)
$\tau_{sw\,hor}$ = total short-wave transmissivity (dimensionless).

Equation C-50 was transformed to estimate $K_{D\,hor}$ by rearranging Equation C-48, $K_{B\,hor} = \tau_{sw\,hor} - K_{D\,hor}$, and limits were provided to the polynomial equation when beyond its development range of $\tau_{sw\,hor} \leq 0.8$.

$$K_{D\,hor} = 0.984\,\tau_{sw\,hor} \quad \text{for } \tau_{sw\,hor_r} < 0.175$$
$$K_{D\,hor} = -0.022 + 1.280\,\tau_{sw\,hor} - 0.828(\tau_{sw\,hor})^2 - 0.765(\tau_{sw\,hor})^3 \text{ for } 0.175 \leq \tau_{sw\,hor} \leq 0.8 \quad \text{(Eq. C-51)}$$
$$K_{D\,hor} = 0.08 \quad \text{for } \tau_{sw\,hor} > 0.8$$

3. Collares (Collares-Pereira and Rabl 1979 [DIRS 176487]; Duffie and Beckman 1980 [DIRS 176264], Equation 2.11.1):

$$K_{D\,hor}/\tau_{sw\,hor} = 0.99 \quad for\ \tau_{sw\,hor} \leq 0.17$$
$$K_{D\,hor}/\tau_{sw\,hor} = -0.54\,\tau_{sw\,hor} + 0.632 \quad for\ 0.75 < \tau_{sw\,hor} < 0.80$$
$$K_{D\,hor}/\tau_{sw\,hor} = 1.188 - 2.272\,\tau_{sw\,hor} + 9.473(\tau_{sw\,hor})^2 - 21.865(\tau_{sw\,hor})^3 + 14.648(\tau_{sw\,hor})^4 \quad for\ 0.17 < \tau_{sw\,hor} < 0.75 \quad \text{(Eq. C-52)}$$
$$K_{D\,hor}/\tau_{sw\,hor} = 0.2 \quad for\ \tau_{sw\,hor} \geq 0.8$$

4. Erbs (Erbs et al. 1982 [DIRS 176486]; Duffie and Beckman (1991) [DIRS 176151], Equation 2.10.1):

$$K_{D\,hor}/\tau_{sw\,hor} = 1.0 - 0.09\,\tau_{sw\,hor} \quad for\ \tau_{sw\,hor} \leq 0.22$$
$$K_{D\,hor}/\tau_{sw\,hor} = 0.9511 - 0.1604\,\tau_{sw\,hor} + 4.388(\tau_{sw\,hor})^2 - 16.638(\tau_{sw\,hor})^3 + 12.336(\tau_{sw\,hor})^4 \quad for \quad 0.22 < \tau_{sw\,hor} \leq 0.80 \quad \text{(Eq. C-53)}$$
$$K_{D\,hor}/\tau_{sw\,hor} = 0.165 \quad for\ \tau_{sw\,hor} > 0.8$$

5. Orgill and Hollands (1977 [DIRS 176483]; Duffie and Beckman 1980 [DIRS 176264], Equation 2.10.1):

$$K_{D\,hor}/\tau_{sw\,hor} = 1.0 - 0.249\,\tau_{sw\,hor} \quad for\ \tau_{sw\,hor} < 0.35$$
$$K_{D\,hor}/\tau_{sw\,hor} = 1.557 - 1.84\,\tau_{sw\,hor} \quad for\ 0.35 < \tau_{sw\,hor} < 0.75 \quad \text{(Eq. C-54)}$$
$$K_{D\,hor}/\tau_{sw\,hor} = 0.177 \quad for\ \tau_{sw\,hor} > 0.75$$

Figure C-9 shows plots of the measured diffusive component of daily solar radiation (I_d) divided by the total measured radiation (R_s) versus R_s divided by extraterrestrial radiation (R_a). The I_d was calculated as $K_{D\,hor}$ times R_a. Data from years 2000-2004 are plotted in the same figure along with estimated ratios from five different diffuse–transmissivity functions. The ASCE-EWRI function (Allen et al. 2005 [DIRS 176207]) models the relationship between

diffuse and direct beam radiation (Equation C-11), which is intended primarily for clear sky conditions. The function by Vignola and McDaniels (1986 [DIRS 176481]) is in the form of a relationship between beam radiation coefficients; the regression coefficients of Vignola and McDaniels, representing the average calibration over all sites in the Pacific Northwest study, were applied (Equation C-51). The Collares function is by Collares-Pereira and Rabl (1979 [DIRS 176487]) (Equation C-52), and the Erbs function is by Erbs et al. (1982 [DIRS 176486]) (Equation C-53). The Orgill and Hollands (1977 [DIRS 176483]) function is a close linearized approximation of the curvilinear Erbs function (Erbs et al. 1982 [DIRS 176486]) (Equation C-54).

The ASCE-EWRI function (Allen et al. 2005 [DIRS 176207]) fits the $K_{D\ hor}/\tau_{D\ hor}$ data relatively well in the $\tau_{D\ hor} > 0.5$ domain ($\tau_{D\ hor} = R_{s\ hor}/R_{a\ hor}$ where $R_{s\ hor}$ is 'total' radiation) (Figure C-9). This domain is where the ASCE-EWRI function has greatest focus; it was created primarily for predicting behavior under clear sky conditions. The Collares (Collares-Pereira and Rabl 1979 [DIRS 176487]), Orgill and Hollands (1977 [DIRS 176483]), and Erbs (Erbs et al. 1982 [DIRS 176486]) functions all represent the measured data set relatively well. All three of these methods, however, suffer from the establishment of too high a lower limit for estimated $K_{D\ hor}/\tau_{sw\ hor}$ (ranging from 0.165 to 0.2) at high values for $\tau_{sw\ hor}$. The relatively high elevation of Yucca Mountain coupled with its relatively clean air apparently reduce the ratio of diffuse to total radiation under clear sky conditions and produces higher values for $\tau_{sw\ hor}$ under the clear sky conditions.

The Vignola-McDaniels (1986 [DIRS 176481]) curve lies within the domain of the measured data and agrees well with the other published functions just discussed. The Vignola-McDaniels (1986 [DIRS 176481]) curve extends toward $K_{D\ hor} = 0.08$ in the domain of clear sky conditions.

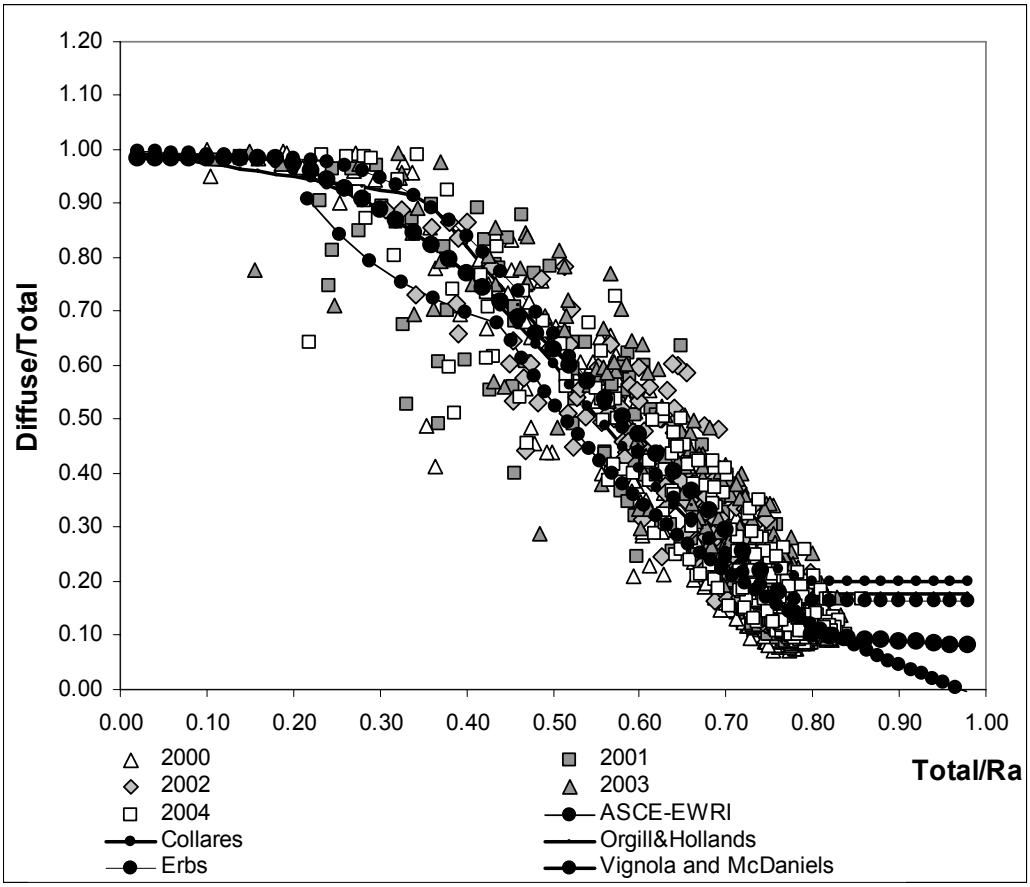

Source: Output DTN: SN0603T0502206.006.

Figure C-9. Comparison of Measured Diffusive Component of Daily Solar Radiation (I_d) Divided by the Total Measured Radiation (R_s) versus R_s Divided by Extraterrestrial Radiation (R_a) for Daily Measurements near Yucca Mountain with Some Established Functions for Estimating the Mean Relationship

C4.3 SELECTION AND ESTABLISHMENT OF A METHOD TO ESTIMATE THE DIFFUSE INDEX

Based on its simple shape, the relatively large scatter in the $K_{D\,hor}/\tau_{sw\,hor}$ data, its close agreement with data by Collares-Pereira and Rabl (1979 [DIRS 176487]), and its relatively good approximation of the mean behavior of the data, the Vignola and McDaniels (1986 [DIRS 176481]) curve was used to translate solar radiation from the horizontal surface to inclined surfaces on Yucca Mountain. Figure C-10 shows a plot of measured data versus estimated data using the Vignola and McDaniels (1986 [DIRS 176481]) function.

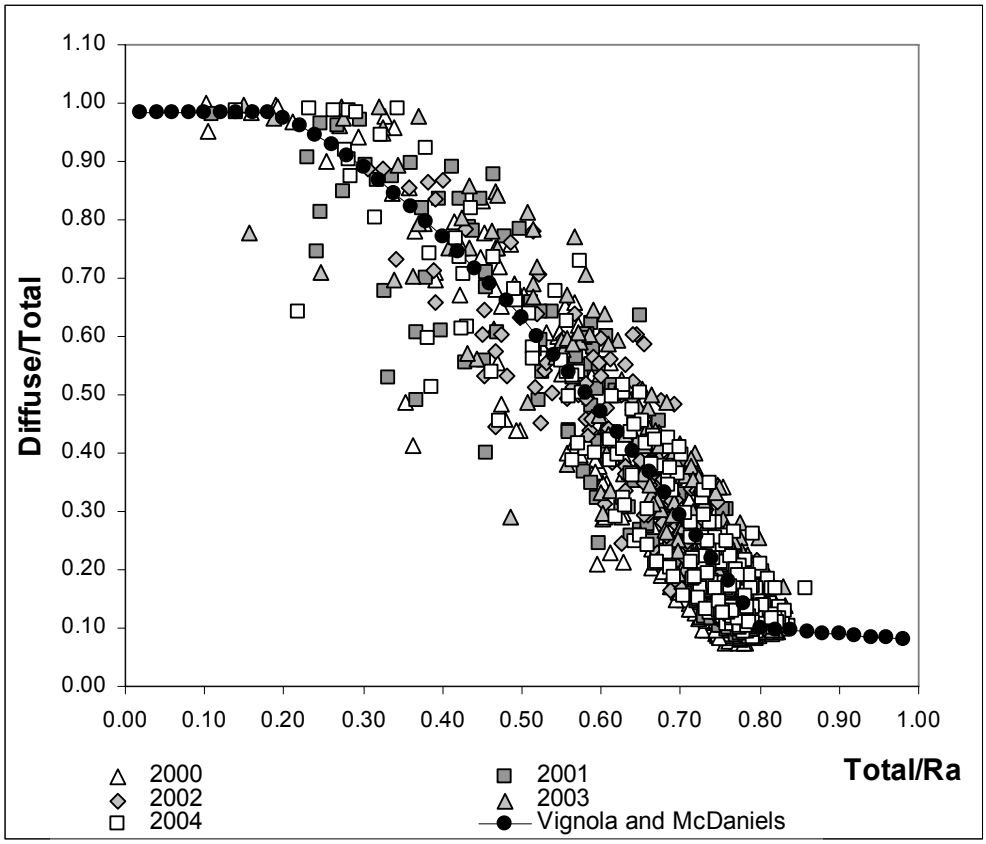

Source: Vignola and McDaniels 1986 [DIRS 176481]; Output DTN: SN0603T0502206.006.

Figure C-10. Comparison of Measured Diffusive Component of Daily Solar Radiation (I_d) Divided by the Total Measured Radiation (R_s) versus R_s Divided by Extraterrestrial Radiation (R_a) for Daily Measurements near Yucca Mountain with the Vignola and McDaniels Function

Table C-4. List of Symbols and Descriptions

Symbol	Description	Units
A	Duffie and Beckman 1991 parameter	(unitless)
A_t	anisotropic index	(unitless)
B	Duffie and Beckman 1991 parameter	(unitless)
C	Duffie and Beckman 1991 parameter	(unitless)
DOY	day of the year (1 – 365 or 366) J = 1 = January 1	(unitless)
ET_0	reference crop evapotranspiration	mm day^{-1}
G_{day}	daily soil heat flux density	MJ m^{-2} d^{-1}
HR_{min}	minimum relative humidity	%
$I_{b\ hor}$	direct beam radiation on the horizontal surface	MJ m^{-2} d^{-1}
I_b	direct beam radiation on the inclined surface	MJ m^{-2} d^{-1}
$I_{d\ hor}$	diffuse radiation on the horizontal surface	MJ m^{-2} d^{-1}
I_d	diffuse radiation on the inclined surface	MJ m^{-2} d^{-1}

Table C-4. List of Symbols and Descriptions (Continued)

Symbol	Description	Units
I_r	reflected radiation received by the inclined surface	MJ m^{-2} d^{-1}
J	day of the year (1 – 365 or 366) J = 1 = January 1	(unitless)
K_B	the clearness index for direct beam radiation (dimensionless)	(unitless)
$K_{Bo\ hor}$	the transmissivity index for clear-sky direct beam radiation, horizontal surface (dimensionless)	(unitless)
$K_{B\ hor}$	the transmissivity index for direct beam radiation, horizontal surface (dimensionless)	(unitless)
K_D	the transmissivity index for diffuse radiation (dimensionless)	(unitless)
$K_{Do\ hor}$	the transmissivity index for clear-sky diffuse radiation, horizontal surface (dimensionless)	(unitless)
$K_{D\ hor}$	the transmissivity index for diffuse radiation, horizontal surface (dimensionless)	(unitless)
K_{cln}	atmospheric turbidity coefficient (dimensionless)	(unitless)
K_o	average difference between T_{min} and mean daily T_{dew}	°C
K_{Rs}	adjustment coefficient for predicting R_s from air temperature	$°C^{-0.5}$
LR	adiabatic lapse rate	°C/1000 m
$P_{reference}$	atmospheric pressure at the reference weather station	kPa
P_{cell}	atmospheric pressure at grid cell	kPa
$R_{a\ hor}$	extraterrestrial radiation, horizontal surface	MJ m^{-2} d^{-1}
R_b	ratio between inclined and horizontal direct beam solar radiation	(unitless)
R_n	net radiation at the surface	MJ m^{-2} d^{-1}
R_{ns}	net short-wave radiation, defined as being positive downwards and negative upwards	MJ m^{-2} d^{-1}
R_s	measured or calculated solar radiation	MJ m^{-2} d^{-1}
$R_{sm\ hor}$	measured or calculated solar radiation, horizontal surface	MJ m^{-2} d^{-1}
$R_{sm\ inc}$	calculated solar radiation, inclined surface	MJ m^{-2} d^{-1}
$R_{sequiv\ hor}$	horizontally projected solar radiation for inclined surface	MJ m^{-2} d^{-1}
$R_{so\ hor}$	clear-sky radiation for horizontal surface	MJ m^{-2} d^{-1}
s	surface slope	radians
T	mean daily air temperature at 1.5-m to 2.5-m height	°C
$T_{dew\ general}$	dew point temperature representative of the air mass that passes across the *application area*	°C
$T_{max\ reference}$	daily maximum air temperature measured at reference weather station	°C
$T_{max\ lapse}$	lapse corrected daily maximum air temperature	°C
$T_{max\ lapse,K}$	lapse corrected daily maximum air temperature	K
$T_{min\ reference}$	daily minimum air temperature measured at reference weather station	°C
$T_{min\ lapse}$	lapse corrected daily minimum air temperature	°C
$T_{min\ lapse,K}$	lapse corrected daily minimum air temperature	K
W	precipitable water in the atmosphere	mm

Table C-4. List of Symbols and Descriptions (Continued)

Symbol	Description	Units
d_r	inverse relative distance earth-sun (dimensionless)	(unitless)
f	modulating function	(unitless)
e_a	mean actual vapor pressure at 1.5-m to 2.5-m height	kPa
$e_{a\ general}$	mean actual vapor pressure at 1.5-m to 2.5-m height kPa representative of the air mass that passes across the application area derived from a reference location	kPa
$e°T$	saturation vapor pressure function	kPa
e_s	saturation vapor pressure at 1.5-m to 2.5-m height	kPa
u_2	mean daily or hourly wind speed at 2-m height	m s^{-1}
z	site elevation above mean sea level	m
$z_{reference}$	elevation of the reference weather station above sea level	m
z_{cell}	elevation of cell above sea level	m
α_T	”alpha” = albedo or canopy reflection coefficient for a given grid cell (dimensionless)	(unitless)
β	“beta” = angle of the sun above the horizon	radians
γ	“gamma” = grid cell aspect	(unitless)
γ_c	“gamma” = psychrometric constant	kPa $°C^{-1}$
Δ	“delta” = slope of the saturation vapor pressure-temperature curve	kPa $°C^{-1}$
δ	“delta” = solar declination	radians
φ_{eff}	“phi” = effective latitude for a given cell slope and aspect	radians
$\varphi_{reference}$	“phi” = latitude of the reference weather station	radians
σ	“sigma” = Stefan-Boltzmann constant	4.901 10^{-9} MJ K^{-4} m^{-2} d^{-1-1}
$\tau_{sw\ hor}$	total shortwave transmissivity, associated with $R_{sm\ hor}$	(unitless)
ω	“omega” solar time angle, solar noon = 0	radians
ω_s	sunset hour angle for horizontal surface	radians
ω_{ss}	sunset hour angle for inclined surface	radians
ω_{sr}	sunrise hour angle for inclined surface	radians

INTENTIONALLY LEFT BLANK

APPENDIX D
METHODS FOR DERIVING TRANSPIRATION COEFFICIENTS FOR VEGETATION AT YUCCA MOUNTAIN

D1. INTRODUCTION

Plant water use is an important component of the water balance for vegetated natural systems and is the primary mechanism controlling water loss from the soil during periods when plants are active (i.e., during the growing season when soil moisture is available). Because of the inevitable loss of water through stomates during the acquisition of carbon for photosynthesis, 95% to 99% of the water that passes through a plant is lost through transpiration (Nobel 1983 [DIRS 160500], p. 506). Thus, transpiration is an accurate estimate of water uptake by plant roots (Nobel 1983 [DIRS 160500], p. 506). Estimates of evapotranspiration (*ET*) from vegetated surfaces are commonly used to evaluate water loss through the combined processes of evaporation and transpiration.

The arid climate at Yucca Mountain is characterized by low and unpredictable rainfall, extreme temperatures, and high evaporative demand. Vegetation cover in the Yucca Mountain area is limited by both timing and amount of precipitation that is received over the course of a water year (WY [October 1 through September 30]). Characterizing the timing and magnitude of vegetation response to precipitation and converting that response to values that can be used in the MASSIF model are crucial for representation of infiltration at the Yucca Mountain site.

Two methods of characterizing vegetation at Yucca Mountain were used, normalized difference vegetation index (NDVI) derived from satellite imagery (Appendix E) and basal transpiration coefficients (K_{cb}) derived from ground measurements of vegetation characteristics. The linear relationship between K_{cb} and NDVI makes it possible to estimate K_{cb} from NDVI (Bausch and Neale 1987 [DIRS 177652]; Duchemin et al. 2005 [DIRS 178498). This linear relationship is described for the vegetation at Yucca Mountain in Section 6.5.3.7 and used in the MASSIF model to estimate K_{cb} from NDVI for each grid cell in the infiltration model domain (Sections 6.5.3.4 through 6.5.3.7).

Normalized difference vegetation index is an indicator of vegetation vigor often used for measurement of environmental response to landscape-scale hydrology, including global climate change (e.g., Justice et al. 1998 [DIRS 176742]; Stow 1995 [DIRS 176887]; Running and Nemani 1991 [DIRS 176819]), rainfall (e.g., Wang et al. 2003 [DIRS 176761]; Ji and Peters 2003 [DIRS 176743]), and *ET* (e.g., Kerr et al. 1989 [DIRS 176823]; Chong et al. 1993 [DIRS 176821]; Kustas et al. 1994 [DIRS 176757]; Seevers and Ottman 1994 [DIRS 176764]; Szilagyi et al. 1998 [DIRS 176839]; Szilagyi 2000 [DIRS 176735]; Szilagyi 2002 [DIRS 176840]). It is used in the MASSIF model to characterize timing and magnitude of vegetation response to precipitation and to capture spatial dynamics in *ET* related to slope, elevation, soil characteristics, and aspect for each of the grid cells in the model domain (Appendix E).

Transpiration coefficients (K_c) are widely used in conjunction with reference evapotranspiration (ET_0) to estimate actual crop evapotranspiration (ET_c) in agricultural systems. The methods for estimating crop water use were standardized in the Food and Agricultural Organization of the United Nations [FAO] Irrigation and Drainage Paper 56 (Allen et al. 1998 [DIRS 157311]). The FAO-56 methods were extended to natural vegetation using measured values of leaf area index ([LAI] a unitless measure of leaf area per ground area) or effective ground cover (percent of ground covered by vegetation) and adjustments for stomatal control (Allen et al. 1998

[DIRS 157311], pp. 187 to 193). To account for the effects of soil evaporation, the FAO-56 methods included a dual transpiration coefficient ($K_c = K_{cb} + K_e$), which was selected for use in the MASSIF model (Section 6.4.4). This dual coefficient consists of a basal transpiration component (K_{cb}), representing plant transpiration under nonlimiting water conditions, and an evaporation component (K_e). K_{cb} profiles (or curves) are time based and are calculated in this appendix for the growing seasons of three representative wet, dry, and average precipitation years. The K_{cb} profiles are used to:

- Evaluate NDVI processing methods and algorithms in Sections E2.5, E3.3, and E7
- Confirm a linear relationship between K_{cb}s and NDVI developed for desert vegetation at Yucca Mountain (Section E7.2)
- Develop a least squares regression between K_{cb} and NDVI for use in the MASSIF model to predict K_{cb} from NDVI for each grid cell in the model domain (Section 6.5.3.7).

This appendix describes the development of K_{cb} profiles using FAO-56 methods and development of the K_{cb} input parameters that describe the characteristics of the vegetation that is expected to be present at Yucca Mountain. The input parameters include vegetation growth stages, vegetation height, vegetation cover and species composition, stomatal resistance, and weather parameters (e.g., wind speed and relative humidity). The output of these calculations is included in Output DTN: MO0606SPABASAL.001.

- Section D2 includes a brief discussion on plant water use, followed by a description of the vegetation at Yucca Mountain and how vegetation types and associations are used in the development of K_{cb}s.
- Section D3.1 describes equations from FAO-56 and how those equations are used to calculate K_{cb}s for desert vegetation.
- Section D3.2 describes the development of input parameters for K_{cb} calculations.
- Section D4 includes example calculations and K_{cb} profiles. Development of uncertainty for K_{cb} profiles is also described.
- Section D5 describes development of a potential Glacial Transition K_{cb} profile defined by an invasive annual grass.
- Section D6 describes development of ET_0 for a generic area at Yucca Mountain. This ET_0 is used with K_{cb}s to estimate potential transpiration (PT). The resulting PTs are used to evaluate the appropriateness of the magnitude of K_{cb}s for desert vegetation. Criticisms of the use of K_{cb}s to predict ET for desert vegetation are also addressed in this section.

D2. BACKGROUND INFORMATION

D2.1 PLANT WATER USE

A discussion of the processes that result in transpiration is included here to show how transpiration can be used as a reliable measure of plant water use. Photosynthesis is the process by which light energy is used to drive the synthesis of organic compounds in plants. The photosynthetic process requires atmospheric carbon dioxide (CO_2). To gain CO_2 for photosynthesis, plants must lose water to the atmosphere. Carbon dioxide diffuses through small pores in the leaf surface (stomata) to intercellular spaces of the leaf and photosynthetic cells (Figure D-1). Concurrently, water moves in the opposite direction, from wet cell membranes inside the leaf through open stomata to the atmosphere, a process called transpiration (Figure D-1). Because water and CO_2 share the same diffusional pathway through the stomata, there is an inevitable cost of water for CO_2 gain.

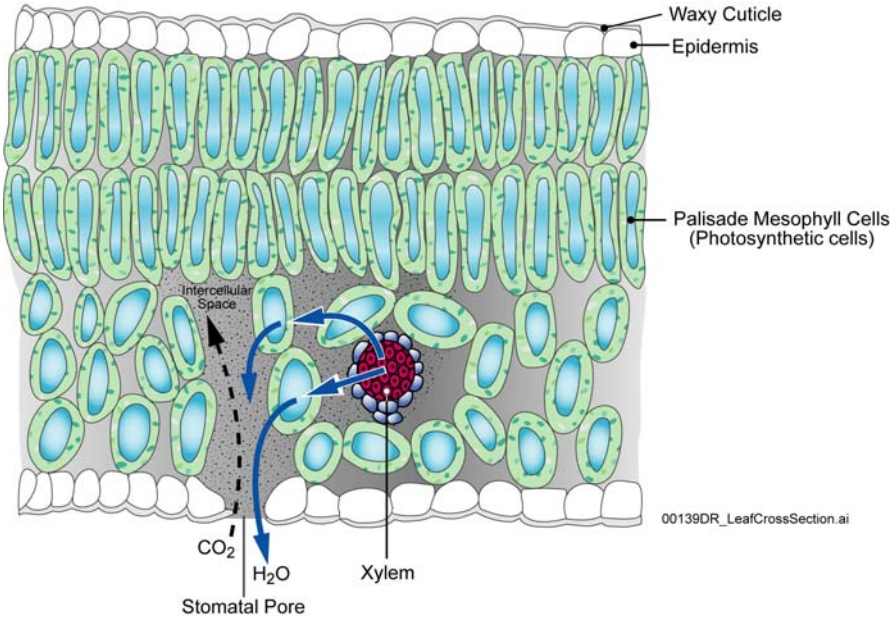

Figure D-1. Leaf Cross Section Showing Diffusional Pathway for Carbon Dioxide (CO_2) and Water (H_2O)

Water moves from the soil, through the plant, to the atmosphere down an increasingly negative water potential gradient (Figure D-2). Water potential is a thermodynamic parameter that describes the energy status of water in the soil−plant−atmosphere system (Brady and Weil 1999 [DIRS 160019], pp. 178 and 179). The soil acts as a water reservoir, with texture (percent of sand, silt, and clay) determining the water holding capacity. Soils with high clay and silt content hold water more tightly than sandy soils. Water enters the plant through the roots and moves in a column of high tensile water through specialized cells, called xylem, and into the atmosphere through open stomata. Water flow through the soil−plant−atmosphere system represents important processes in the overall hydrologic cycle.

When soil moisture is limiting, plants can reduce water loss through stomatal closure. However, stomatal closure also results in reducing the supply of CO_2, which ultimately reduces plant productivity. In arid regions, approximately 400 to 700 units of water are lost for every unit of dry matter produced by a plant (Brady and Weil 1999 [DIRS 160019], pp. 227 and 228). This is because the diffusion gradient for water from inside the leaf to the atmosphere is orders of magnitude steeper than that for CO_2 diffusion into the leaf. Water is required for photosynthesis and other metabolic processes; however, 95% to 99% of the water that passes through a plant is lost through transpiration (Nobel 1983 [DIRS 160500], p. 506). Thus, transpiration is an accurate estimate of water uptake by plant roots (Nobel 1983 [DIRS 160500], p. 506). Water is also lost from the soil and other surfaces (plant litter) through the process of direct evaporation. Direct evaporation from the soil generally occurs in the upper 0.15 m of the soil profile (Allen et al. 1998 [DIRS 157311], p. 144). Evapotranspiration (*ET*) is the combined water loss through plant transpiration and direct evaporation.

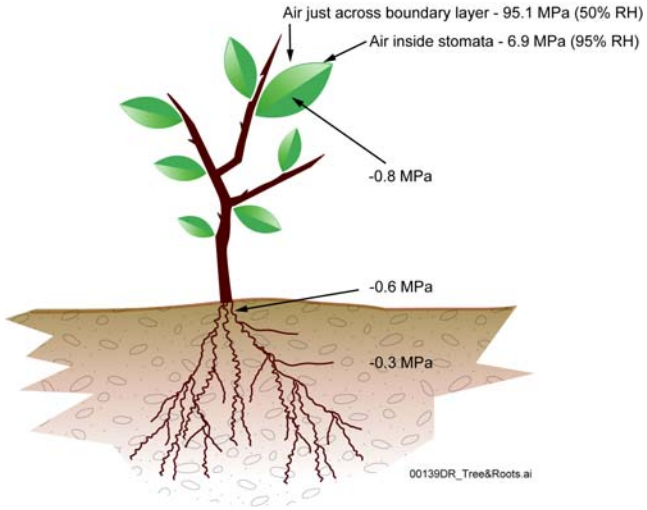

NOTE: Water moves through the system along a gradient of increasingly negative water potentials.

Figure D-2. Water Potential (MPa) in Various Components of the Soil−Plant−Atmosphere System

D2.2 YUCCA MOUNTAIN VEGETATION

The flora and climate of Yucca Mountain have been described as characteristically Mojavean (Beatley 1975 [DIRS 103356] and 1976 [DIRS 102221]), with vegetation on the crest and upper slopes that is transitional to Great Basin Desert flora (Beatley 1976 [DIRS 102221]). Lower elevations and midslopes up to about 1,300 m are dominated by Mojave Desert shrub species including *Larrea tridentata, Ambrosia dumosa, Grayia spinosa, Lycium andersonii, Lycium pallidum, Krameria erecta,* and *Ephedra nevadensis*. Dominance of these species and plant community composition is dependent on a variety of environmental factors including slope, aspect, soils, and elevation. The transition between the two deserts occurs above ~1,300 m at Yucca Mountain in a zone that varies between *Artemisia*-dominated shrub communities of the Great Basin (steep hill slopes facing northeast to northwest) and *Larrea*-dominated communities of the Mojave (lower elevations). Other important species at Yucca Mountain that inter-grade

into both desert types include *Coleogyne ramosissima, Atriplex confertifolia, Eriogonum fasciculatum, Lycium* spp., *Ephedra* spp., and *Ericameria* spp.

Vegetation communities at Yucca Mountain have been characterized by a number of authors (e.g., Beatley 1976 [DIRS 102221]; O'Farrell and Collins 1984 [DIRS 102160]; CRWMS M&O 1996 [DIRS 102235]) and have often been described in terms of associations. A vegetation association is defined as an assemblage of species with distinctive physiognomy and dominance hierarchy (Barbour et al. 1980 [DIRS 127394], p. 5). However, discrepancies among authors exist with respect to classification of vegetation associations at Yucca Mountain (e.g., classifications by Beatley 1976 [DIRS 102221]), and it is recognized that not all vegetation can be unambiguously classified. This is largely due to the complexity and variability of vegetation assemblages across the landscape, with plant species distributed according to individual tolerance limits and competitive ability. Regardless of such discrepancies, the concept can be useful for identifying dominant species and vegetation types for different areas of the infiltration model domain.

Based on Beatley (1976 [DIRS 102221]) and O'Farrell and Collins (1984 [DIRS 102160]), four vegetation associations were identified for use in ecological studies that were initiated in the late 1980s to address specific questions about the effects of the site characterization process on biological resources at Yucca Mountain (CRWMS M&O 1996 [DIRS 102235]). The four associations (*Coleogyne* [COL], *Larrea−Ambrosia* [LA], *Lycium−Grayia* [LG], and *Larrea−Lycium−Grayia* [LLG]) were described after the dominant plant species (Table D-1).

Table D-1. Classification of Vegetation Associations Sampled at Yucca Mountain

Vegetation Association[1]				
	Coleogyne	*Larrea−Ambrosia*	*Lycium−Grayia*	*Larrea−Lycium−Grayia*
Abbreviation	COL	LA	LG	LLG
Desert	Transition	Mojave	Transition	Mojave
Soil and Topography	Shallow, gravelly soils of upper bajadas and ridge tops with flat to gradually sloping terrain	Deep, loose sandy soil lacking surface pavement on low elevation bajadas and basins	Sandy soil, from volcanic parent material on bajadas and ridges; higher elevations	Sandy loam soil of volcanic origin on bajadas and valleys; mid elevations
Physiognomy	*Coleogyne* dominant	*Larrea* and *Ambrosia* dominant	No dominant	*Larrea* dominant
Dominant Species[2]	*Coleogyne ramosissima* (blackbrush), *Ambrosia dumosa* (burrobush), *Ephedra nevadensis* (Nevada jointfir), *Lycium pallidum* (pale wolfberry)	*Ambrosia dumosa, Larrea tridentata* (creosotebush), *Menodora spinescens* (spiny menodora), *Lycium pallidum*	*Ephedra nevadensis, Grayia spinosa* (spiny hopsage), *Eriogonum fasciculatum* (Eastern Mojave buckwheat), *Lycium andersonii* (Anderson's wolfberry)	*Larrea tridentata, Ephedra nevadensis, Ambrosia dumosa, Krameria erecta* (littleleaf ratany)

[1] Classification is based on Beatley 1976 [DIRS 102221] and O'Farrell and Collins 1984 [DIRS 102160].

[2] Dominant species are the perennials with the greatest mean cover. The common name is included in parentheses following the first use of the scientific name.

In 1989, twelve Ecological Study Plots (ESPs) were established in each of the four vegetation associations (total of 48 plots) at various locations in the Yucca Mountain area. The ESPs were 4 ha (200 × 200 m) in size and randomly located within each association (CRWMS M&O 1996

[DIRS 102235], p. 10, Figure 3-1; and DTN: MO9901ESPYMNYE.000 [DIRS 177247], for ESP locations). The ESPs were established to describe the vegetation and ecology of Yucca Mountain and to study the effects of site characterization on the Yucca Mountain environment. Biotic (e.g., vegetation cover, species composition, and primary production) and abiotic measurements (e.g., precipitation and soil characteristics) were made on the ESPs from 1989 through 1994.

Percent ground cover per plant species was measured on ESPs each spring following peak growth from 1989 through 1994 (CRWMS M&O 1996 [DIRS 102235] for complete description of data collection methods and results). Over the years of study, the COL association generally had intermediate cover of vegetation or cover equal to one or more of the remaining three associations (CRWMS M&O 1996 [DIRS 102235], p. 31, Figure 4-10). One of the main input parameters that distinguish K_{cb}s among vegetation associations is percent vegetation cover. Because vegetation cover for the COL association was similar to that of the LG and LLG associations, the K_{cb} profile would also be similar. Therefore, COL was not used as a separate association for K_{cb} calculations.

The LA, LG, and LLG vegetation associations are the most common in the infiltration model domain and K_{cb} calculations were based on cover data for these three associations. The LA association is representative of low elevation vegetation (940 to 1,150 m, DTN: MO9907SADESYYM.000 [DIRS 177169]). The low elevations of LA associations make them unimportant to infiltration that might occur above the proposed repository but were included because they occur within the infiltration modeling domain. The LG association is representative of the vegetation that overlies the proposed repository on the upper slopes and crest of Yucca Mountain (elevation = 1,300 to 1,600 m, DTN: MO9907SADESYYM.000 [DIRS 177169]). The LG association is considered critically important to the infiltration modeling effort because the vegetation is representative of that overlying the proposed repository. The LLG association is representative of the vegetation of midelevation (1,150 to 1,266 m, DTN: MO9907SADESYYM.000 [DIRS 177169]) intermountain valleys within the infiltration modeling domain. The K_{cb}s calculated for the LG association are used to develop the K_{cb}−NDVI'[1] relationship for desert vegetation at Yucca Mountain as described in Section 6.5.3.7. The slope and intercept of this relationship are used in the MASSIF model to estimate K_{cb} from NDVI' for each grid cell for each day of the year as described in Sections 6.5.3.4 through 6.5.3.7. The K_{cb}s estimated for the LA, LLG, and LG associations are used to evaluate the appropriateness of NDVI and associated processing parameters (Sections E2 and E7), potential contribution of vegetation types to association water use (Section D5), and whether use of FAO-56 methods results in K_{cb}s that are of an appropriate magnitude for desert vegetation (Section D6).

NDVI' was determined for WY1998 (wet), WY2001 (average), and WY2000 (dry), with precipitation totals of 358 mm, 186 mm, and 38 mm, respectiviely (Table D-2).

[1] NDVI' is NDVI corrected for differing atmospheric conditions between satellite overpasses and for specific ground conditions characterizing the Yucca Mountain environment, including the presence of rock varnish. This correction is described in Section 6.5.3.5 and Appendix E, Section E2.

Table D-2. Paired Wet, Average, and Dry Water Years used for NDVI' and K_{cb} Estimations

NDVI' Precipitation Totals[a]		K_{cb} Precipitation Totals[b]		Difference in WY Totals
Water Year	PCP (mm)	Water Year	PCP (mm)	PCP (mm)
1998 (wet)	358	1993 (wet)	240	118
2001 (average)	186	1991 (average)	150	36
2002 (dry)	38	1990 (dry)	60	22

[a] Output DTN: MO0602SPAWEATH.000.
[b] Approximate average annual precipitation for the different vegetation associations from CRWMS M&O 1996 [DIRS 102235], p. 21, Figure 4-3.

WY1998 and WY2000 were selected because they represented very wet and dry years and were needed to establish timing of plant responses and a baseline of minimum plant activity for the Yucca Mountain area (Section E1.4). Satellite images of the model domain (which included the ESPs) were obtained for selected days during the growing season for these three years for development of NDVI' (Section E1.4). Vegetation cover and species composition, needed for K_{cb} calculations, were measured on the ESPs during peak growth periods from 1989 to 1994. Vegetation cover at Yucca Mountain is largely dependent on precipitation, therefore, precipitation records for the ESPs from 1989 to 1994 were evaluated to determine wet, normal, and dry years that could be paired with the years that NDVI' were determined for. Based on precipitation records, vegetation cover data were used from the following three years in K_{cb} calculations:

- WY1991 (average), an average precipitation year for the Yucca Mountain area (about 150 mm [Table D-2])
- WY1993 (wet), the highest precipitation year on record for the years that cover data were collected (about 240 mm [Table D-2])
- WY1990 (dry), the lowest precipitation year on record for the years that cover data were collected (about 60 mm [Table D-2]).

To evaluate NDVI' processing parameters, the wet, dry, and average precipitation years (Table Dx) from the two data sets (NDVI' and K_{cb}) were paired by normalizing and scaling NDVI' using annual precipitation (Appendix E). For the K_{cb} – NDVI' regression, wet and average years (Table D-2) from the two data sets were paired. The dry year was not used in the K_{cb} – NDVI' regression because the vegetation signal for 2002 was essentially zero throughout the year for the LG association (Section E7.1).

The differences in precipitation between the paired dry years (1990 and 2002) and the paired average precipitation years (1991 and 2001) were small: 22 mm for the dry years and 36 mm for the average years (Table D-2). The differences were within the range of variation in precipitation observed within years among vegetation associations at Yucca Mountain (CRWMS M&O 1996 [DIRS 102235], p. 21, Figure 4-3). Therefore, it is reasonable to assume that vegetation cover would be similar for the two below average and the two average precipitation years. The difference in precipitation of 118 mm between the paired wet years (1993 and 1998, Table D-2) could have translated into differences in vegetation cover. However, there are limits

to the amount of vegetation that can be supported by the Yucca Mountain system that are imposed by factors other than total precipitation that is received during a water year. These factors include nutrient availability, inter- and intra-specific competition among plants, timing of precipitation, and precipitation runoff. To account for potential differences in cover that might have occurred between the paired water years, NDVI' was adjusted to account for differences in precipitation totals (and therefore potential vegetation) between cover data and satellite data collection years (Section 6.5.3.7 and Appendix E). The ratios of water year precipitation for paired wet years and paired average years were used to adjust NDVI' (Section 6.5.3.7 and Appendix E).

Plant species were divided into three types for K_{cb} calculations: annuals, drought deciduous shrubs, and evergreen to semi-evergreen shrubs. Annual plants complete their life cycle (germination, through flowering and seed production, through senescence) within a single growing season. Common annuals at Yucca Mountain include grasses such as *Bromus madritensis* ssp. *rubens* and *vulpia octoflora,* and forbs such as *Amsinckia tridentate, Cryptantha* spp., and *Chaenactis* spp. Drought deciduous shrubs shed their leaves in the summer, when soil moisture becomes limiting, and initiate leaf growth when temperature and soil moisture are favorable. Common drought deciduous shrubs at Yucca Mountain include *Ambrosia dumosa*, *Lycium* spp., and *Grayia spinosa*. Because perennial grasses (e.g., *Achnatherum hymenoides*) and forbs (e.g., *Sphaeralcea ambigua*) made up a small percentage of total cover on ESPs (Tables D-7 to D-15), and the length and timing of their development are similar to that of drought deciduous species, these growth forms were included in the drought deciduous vegetation type for the analysis. Evergreen to semi-evergreen shrubs are drought resistant plants that maintain a canopy throughout the year. These include leafless shrubs with green stems (i.e., *Ephedra* spp.), green stemmed shrubs with ephemeral leaves (i.e., *Ericameria* spp.), and shrubs that maintain leaves throughout the year (i.e., *Larrea tridentate*). For simplicity, the evergreen to semi-evergreen shrub type will be referred to as evergreen through the rest of this analysis.

Basal transpiration coefficient profiles for the LA, LG, and LLG vegetation associations were developed by calculating separate profiles for the three vegetation types (annuals, drought deciduous, and evergreen species), then summing those K_{cb}s to get one profile for each association. See Section D3.1 for further discussion on summing vegetation type profiles.

D3. METHODS

D3.1 BASAL TRANSPIRATION COEFFICIENT EQUATIONS

The equations used to develop K_{cb} profiles for desert vegetation are presented in this section.

The FAO-56 K_{cb} profile for agricultural crops reflects transpiration under optimal growth and nonlimiting water conditions. The generalized K_{cb} profile (Figure D-3) includes four growth stages (Allen et al. 1998 [DIRS 157311], pp. 95 and 96): an initial growth stage (planting date to approximately 10% ground cover), a development stage (10% ground cover to effective full cover), a midseason stage (effective full cover to start of maturity), and a late season stage (maturity to harvest or senescence). Effective full cover for agricultural crops is defined as the

time when soil shading is nearly complete or 100% covered (Allen et al. 1998 [DIRS 157311], p. 95).

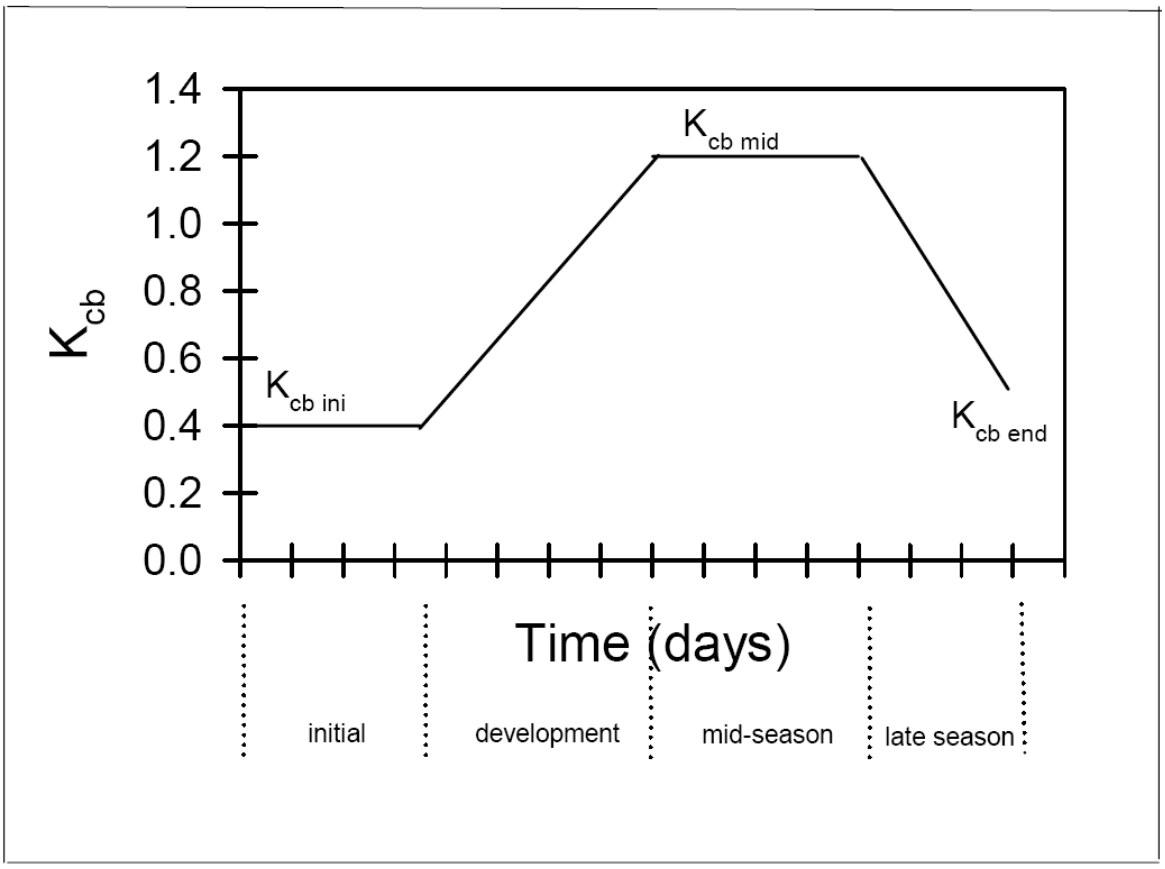

Source: Allen et al. 1998 [DIRS 157311], p. 100, Figure 26.

Figure D-3. Generalized Crop Coefficient Curve

Characteristics of desert vegetation at Yucca Mountain differ from agricultural crops in several ways, including low effective ground cover that rarely exceeds 30% during peak growth periods, little morphological change in mature perennial vegetation across growth stages compared to agricultural crops (e.g., little change in vegetation height and maintenance of a percentage of green canopy throughout the year), and greater degree of stomatal control resulting in lower rates of water loss compared to agricultural crops. Additionally, climatic conditions at Yucca Mountain differ from standard FAO-56 conditions with lower minimum relative humidity (RH_{min}) and higher wind speeds (u_2). To account for these differences, FAO-56 methods for calculating K_{cb} for natural vegetation using effective ground cover, adjustments for stomatal control over water loss, and adjustments for local RH_{min} and u_2 were used Allen et al. (1998 [DIRS 157311], pp. 187 to 193).

Transpiration coefficients for initial ($K_{cb\ ini}$), midseason ($K_{cb\ mid}$), and end of the late season ($K_{cb\ end}$) growth stages were calculated for vegetation types using Equation D-1 (Allen et al. 1998 [DIRS 157311], p. 187, Equation 98):

$$K_{cb} = K_{c\min} + (K_{cb\ full} - K_{c\min})\left(\min\left(1,\ 2f_c, (f_{c\ eff})^{\left(\frac{1}{1+h}\right)}\right)\right) \qquad \text{(Eq. D-1)}$$

where

K_{cb} = basal K_{cb} when plant density and/or leaf areas are lower than for full cover conditions
$K_{c\ min}$ = minimum K_c for bare soil in the presence of vegetation ($K_{c\ min} \approx 0$)
$K_{cb\ full}$ = estimated basal K_{cb} during the midseason, at peak plant size or height, and full ground cover (Equation D-4)
f_c = observed fraction of soil surface that is covered by vegetation type (0.01 to 1)
$f_{c\ eff}$ = effective fraction of soil surface covered or shaded by vegetation type (0.01 to 1)
h = plant height (m).

Equation D-1 was recommended for calculating $K_{cb\ mid}$ and $K_{cb\ end}$ (Allen et al. 1998 [DIRS 157311], pp. 187 to 193). Methods for calculating $K_{cb\ ini}$ under standard FAO-56 conditions were suggested for natural, nontypical vegetation (Allen et al. 1998 [DIRS 157311], p. 183). However, those methods were specifically suggested for newly planted annual crops with the magnitude of $K_{cb\ ini}$ primarily determined by soil wetting frequency during irrigation and natural precipitation events. Established perennial vegetation at Yucca Mountain maintains height and some percentage of leaf area during the initial growth stage. Therefore, to account for effects of perennial plant height and cover during the initial growth stage, Equation D-1 was used with plant height and reduced cover (compared to that measured at peak growth; Sections D3.2.1 and D3.2.2) to calculate $K_{cb\ ini}$. Because height of annual vegetation varies over the course of the growing season with shorter vegetation during the initial growth stage, both height and cover were reduced (from peak values) to calculated $K_{cb\ ini}$ for annuals using Equation D-1. Daily K_{cb} values for the initial, mid, and end of late season stages were estimated by using daily weather data inputs to calculate $K_{cb\ full}$ (Equation D-6) and the stomatal resistance correction factor (F_r, Equation D-7). According to Allen et al. (2005 [DIRS 176009], p. 4), the equation for $K_{cb\ full}$ can be used for daily estimates when daily measurements of u_2 and RH_{min} are available. To be consistent and to keep the equations on a daily time step, daily weather data inputs were also used for F_r calculations (Equation D-7).

The FAO-56 equation for area- and height-weighting where different fractions of ground are covered by different crops (Allen et al. 2005 [DIRS 176009], p. 199, Equation 104) was not used because of differences in growing season length and stomatal resistance for vegetation types (Section D.3.2). Using Equation 98 to calculate separate profiles for vegetation types and then summing to get one profile for each association (and water year) accounts for this variation, which is important with respect to seasonal *ET*. The vegetation types are independent of one another, with growth stage lengths, cover, and height developed for each type. Because each profile is essentially weighted by cover for the vegetation type, the relative importance of each type is accounted for in the summed profile for each association. Summing the vegetation type profiles resulted in use of total cover that was measured for each association. Setting Kcmin to

zero in Equation D-1 (as recommended for deserts [see below]) eliminates overestimation of residual evaporation from bare soil in the summed profiles.

Under arid conditions at Yucca Mountain, the upper soil layer dries to very low water content during periods between precipitation events (CRWMS M&O 1999 [DIRS 105031], p. 14, Table 3). Under dry soil conditions and sparse rainfall, Allen et al. (1998 [DIRS 157311], pp. 207 and 209) recommended setting $K_{c\ min}$ to zero to provide for conditions when transpiration is equal to zero. Under these conditions, the soil water balance is controlled by the evaporation term (K_e) of the dual transpiration coefficient. Evaporation following precipitation events is accounted for in the infiltration model by K_e.

In Equation D-1, the last term designates use of the minimum of 1, $2f_c$, and $(f_{c\ eff})^{(1/1+h)}$. Cover measurements showed that the total $2f_c$ summed across vegetation types for an association never exceeded a value of 1. Values for $f_{c\ eff}$ were determined for round or spherical shaped canopies using cover data from Yucca Mountain vegetation associations according to Equation D-2 (Allen et al. 1998 [DIRS 157311], p. 188):

$$f_{c\,eff} = \frac{f_c}{\sin(\eta)} \quad \leq 1 \qquad \text{(Eq. D-2)}$$

where $\sin(\eta)$ is the sine of the mean angle of the sun, η, above the horizon during midday hours when maximum evapotranspiration is likely to occur. Allen et al. (1998 [DIRS 157311], p. 188) suggest calculating $f_{c\ eff}$ for solar noon using Equation D-3 to calculate $\sin(\eta)$:

$$\sin(\eta) = \sin(\psi)\sin(\delta) + \cos(\psi)\cos(\delta) \qquad \text{(Eq. D-3)}$$

where

ψ = latitude (radians),
δ = solar declination (radians).

Solar declination (δ) is calculated daily (Allen et al. 1998 [DIRS 157311], p. 46, Equation 24):

$$\delta = 0.409 \sin\left(\frac{2\pi}{365} J - 1.39\right) \qquad \text{(Eq. D-4)}$$

where

J = day of year

To help minimize water loss in arid environments, desert plants are capable of a higher degree of stomatal control than agricultural species (Allen et al. 1998 [DIRS 157311], p. 191). Therefore, it was necessary to apply a stomatal resistance correction factor (F_r, Equation D-7) to Equation D-1 when stomatal resistance was estimated to be greater than 100 s m^{-1} (Allen et al. 1998 [DIRS 157311], p. 191). The F_r accounts for increases in stomatal resistance during periods of low physiological activity (i.e., initiating or senescing leaves). The F_r does not account for effects of water stress on stomatal resistance. The impact of water stress is

implemented by the stress factor (K_s) of the FAO-56 procedure that is used in the daily soil water balance model (Section 6.4).

Transpiration coefficients for development and late growth stages were calculated by linear interpolation between $K_{cb\ ini}$ and $K_{cb\ mid}$ and between $K_{cb\ mid}$ and $K_{cb\ end}$, respectively (Allen et al. 1998 [DIRS 157311], p. 132, Equation 66):

$$K_{cb\,i} = K_{cb\ prev} + \left(\frac{i - \sum L_{prev}}{L_{stage}} \right) \left(K_{cb\,next} - K_{c\,prev} \right) \qquad \text{(Eq. D-5)}$$

where

i = day number within the growing season (1…length of the growing season),

$K_{cb,\,i}$ = transpiration coefficient on day i,

$K_{cb\ prev}$ = K_{cb} at the end of the previous stage,

$K_{cb\ next}$ = K_{cb} at the beginning of the next stage,

L_{stage} = length of the stage under consideration (days),

ΣL_{prev} = sum of the length of all previous stages (days).

The following six steps were used to calculate daily K_{cb}s using Equation D-1 and adjusting for stomatal control:

1. Calculate adjustment for the influence of vegetation height for K_{cb} for full cover condition under standard climate ($K_{cb,h}$) (Allen et al. 1998 [DIRS 157311], p. 189, Equation 101):

$$K_{cb,h} = 1.0 + 0.1h \qquad \text{(Eq. D-6)}$$

$K_{cb,h}$ is limited to 1.2 for when h >2 (Allen et al. 1998 [DIRS 157311], p. 189).

2. Calculate $K_{cb\,full}$ (Allen et al. 1998 [DIRS 157311], p. 189, Equation 100):

$$K_{cb\,full} = K_{cb,h} + \left[0.04\left(u_2 - 2\right) - 0.004\left(RH_{\min} - 45\right) \right] \left(\frac{h}{3} \right)^{0.3} \qquad \text{(Eq. D-7)}$$

where

$K_{cb,\,h}$ = K_{cb} for full cover vegetation under a standard climate (Eq. D-6),
u_2 = mean wind speed at 2-m height (m s^{-1}),
RH_{min} = minimum daily relative humidity (%),
h = mean maximum plant height (m).

Equation D-7 adjusts for regional climatic differences from the standard climate of FAO-56 ($u_2 = 2$ m s^{-1} and RH_{min} = 45%). This equation can be used for daily estimates when daily measurements of u_2 and RH_{min} are available (Allen et al. 2005 [DIRS 176009], p. 4).

3. Calculate adjustment for stomatal control (Allen et al. 1998 [DIRS 157311], p. 191, Equation 102):

$$F_r \approx \frac{\Delta + \gamma(1 + 0.34u_2)}{\Delta + \gamma\left(1 + 0.34u_2 \frac{r_l}{100}\right)} \quad \text{(Eq. D-8)}$$

where

F_r = stomatal resistance correction factor,
Δ = slope of the saturation vapor pressure curve (kPa $°C^{-1}$),
γ = Psychrometric constant (kPa $°C^{-1}$),
r_l = mean leaf resistance for the vegetation in question (s m^{-1}).

4. Determine the minimum of (1, $2f_c$, and $f_{c\,eff}^{(1/1+h)}$).

5. Use values from Steps 1 through 4 in Equation D-1 to calculate daily K_{cb}s for each vegetation type per association and water year.

6. Adjust daily K_{cb}s (from Step 5) for stomatal control:

$$(K_{cb} \times F_r) \quad \text{(Eq. D-9)}$$

The final step in generating the K_{cb} profiles was to calculate K_{cb} for development and late stages using Equation D-5.

Example calculations using Equations D-1 through D-9 and K_{cb} profiles are in Section D4.

D3.2 INPUT DATA

Inputs required to develop K_{cb} profiles are developed in this section. Inputs include growth stage lengths, vegetation height (h), vegetation cover (f_c), stomatal resistance (r_l), minimum relative humidity (RH_{min}), wind speed (u_2), slope of the saturation vapor pressure curve (Δ), and the psychrometric constant (γ).

D3.2.1 Growth Stages and Vegetation Height

Growth stages for the three vegetation types and vegetation height for the three associations were developed from data collected from Rock Valley and the Nevada Test Site (NTS) under several research programs, including the Desert Biome program of the International Biological Program (IBP). Several years of intensive ecological studies were conducted under the IBP and were continued through research funded by the U.S. Department of Energy (DOE) and the University of California, Los Angeles. These studies and the ecological communities and processes at Rock

Valley and other locations on the NTS are described by Rundel and Gibson (1996 [DIRS 103614]).

For agricultural species, Allen et al. (1998 [DIRS 157311], pp. 103 to 108) divided vegetation development into four growth stages (initial, development, midseason, and late season) that are related to leaf area index (ground area covered by plant canopy) and developmental stages. The initial stage begins at the planting date, for annuals, or at the onset of leaf growth, for perennials, and ends when the vegetation has reached approximately 10% ground cover. The development stage runs from 10% cover to effective full cover, which for many agricultural species occurs when flowering is initiated. The midseason stage begins when effective full cover is reached and ends at the start of maturity. The late season stage runs from maturity to harvest or senescence. The stages are crop specific and the stage lengths are affected by local climatic factors.

For desert vegetation, the length of the growing season is constrained by species-specific developmental processes, adaptations to desert conditions, and local climatic factors. Significant variation in timing and period of phenological stages occurs in response to monthly and yearly climatic conditions. For Yucca Mountain, growth stages were developed for annual, drought deciduous, and evergreen vegetation types based on information for dominant species within each type. The timing of initiation of leaf buds, leaves, flowers, fruits, leaf fall, and dormancy reported for Mojave Desert shrubs in Rundel and Gibson (1996 [DIRS 103614], Figure 4.13, p. 106) was used to define initial, development, mid- and late season growth stages for drought deciduous and evergreen vegetation (Table D-3).

Table D-3. Phenological Stages for Drought Deciduous and Evergreen Species

Species[a]	Bud Initiation[a]	Leaf Initiation[a]	Flower Initiation[a]	Fruit Initiation[a]	Leaf Fall[a]	Dormancy[a]
Ephedra nevadensis	February to April	March to April	May	May to June	—	—
Larrea tridentata	April to May	March to July	May	June	July to March	—
Ambrosia dumosa	February to April	March to May	May	June	May to August	July to February
Grayia spinosa	February to March	March to May	April	April to May	May to July	July to February
Lycium andersonii	February to March	March to May	April	April to June	May to July	July to February
Lycium pallidum	February to April	March to May	April	May to June	May to August	July to February

[a] Dates are from Rundel and Gibson 1996 [DIRS 103614], Figure 4.13, p. 106; ranges were established from the 1969 and 1970 data.

The bud initiation period was considered for the initial growth stage (period of low physiological activity or leaf area index), the early period of leaf initiation was considered for the development stage (period of increasing physiological activity or leaf area index), the remaining period of leaf initiation through flower initiation and the beginning of fruit initiation was considered for the midstage (period of highest seasonal physiological activity or leaf area index), and fruit initiation through leaf fall was considered for the late stage (period of declining physiological activity or leaf area index) (Table D-3).

When available, measured periods of physiological activity (i.e., photosynthesis, stomatal conductance, or transpiration) for dominant shrub species were used along with the timing of phenological stages in Rundel and Gibson (1996 [DIRS 103614], p. 106, Figure 4.13) to develop growth stages. For annual vegetation, reported growing season lengths and timing of phenological stages for *Bromus madritensis* were used to develop growth stages.

Stage lengths were developed for average precipitation years. Appropriate stage lengths were reduced to represent below average precipitation years and were increased to represent above average precipitation years.

For evergreen species, *Ephedra nevadensis* exhibited bud initiation February through April, while *L. tridentata* initiated bud growth later in April and May (Table D-3). However, positive stomatal conductance was measured on evergreen leaves of *L. tridentata* as early as January (Hamerlynck et al. 2000 [DIRS 177022], p. 602, Figure 6), indicating physiological activity and transpiration. Leaf initiation occurred March through April for *E. nevadensis* and March through July for *L. tridentata*, with flower initiation in May for both species (Table D-3). Stomatal conductance measurements were shown to be relatively high in March and April for *E. nevadensis* plants growing in Crater Flat (13 km north–west of Yucca Mountain) and increased in May at two of three sites studied by Smith et al. (1995 [DIRS 103628], Figure 2, p. 343), indicating increased transpiration in May. Fruit initiation occurred from May to June for *E. nevadensis* and in June for *L. tridentata*, with leaf fall starting in July for *L. tridentata*. Low but positive stomatal conductance rates were reported for *E. nevadensis* and *L. tridentata* through the end of September and first of October, respectively (Smith et al. 1995 [DIRS 103628], Figure 2, p. 343; Hamerlynck et al. 2000 [DIRS 177022], p. 602, Figure 6).

Based on this information, February 1 through 28, March 1 through 31, April 1 through May 15, and May 16 through September 30 were assigned to the initial, development, mid, and late growth stages, respectively, for evergreen species (Table D-4). Summer rainfall is uncommon in the northern Mojave Desert with approximately 70% falling between November and March (Rundel and Gibson 1996 [DIRS 103614], p. 53). Once soil dries down from winter recharge, it generally stays dry (Rundel and Gibson 1996 [DIRS 103614], p. 53). This is especially true of drought years. Because of the slow growth habit and moderate water use efficiency of evergreen vegetation, it was assumed that, on average, the length of the late season growth stage would be most affected by drought. Additionally, for some evergreen species, leaf emergence may be triggered by photoperiod rather than precipitation (Smith et al. 1997 [DIRS 103636], p. 61). With high temperatures and little precipitation after March or April, it is reasonable to suggest that physiological activity of evergreen vegetation would slow, and stomata would close to prevent water loss around June or July in a drought year. This is supported by observations of leaf fall for *L. tridentata* in July and subsequent summer months (Table D-3), and low precipitation during summer months in the drought year of 2002 (Figure E-4). Therefore, to represent dry years for evergreen species, the late stage period was changed to May 16 through June 30 (Table D-4). During above average precipitation years, growth by evergreen vegetation can be maintained over longer time periods when water is available (Smith et al. 1997 [DIRS 103636], pp. 59 and 60). For evergreen vegetation it was assumed that the length of the mid stage would be most affected due to favorable temperatures and moisture availability later in the spring during an above average precipitation year. In 1998, precipitation that fell through April, May, and June (Figure E-4) may have been sufficient to prolong growth expected of evergreens during

the mid stage. Therefore, to represent above average precipitation years, the length of the mid stage for evergreen vegetation was increased by 30 days to April 1 through June 15 (Table D-4). The length of the late stage was changed to June 16 through September 30. The length of the late stage was not extended into October because it is likely that air temperature and depleted soil moisture would limit physiological activity in the fall and winter months (Smith et al. 1995 [DIRS 103628], pp. 342 and 349).

Drought deciduous species *A. dumosa, G. spinosa, L. andersonii,* and *L. pallidum* exhibited bud initiation from February through April, leaf initiation from March through July, and flower initiation in April or May (Table D-3). Leaves were present on *L. andersonii* in March at the onset of a study on the NTS by Hamerlynck et al. (2002 [DIRS 177128], Figure 7, p. 103) indicating that leaf initiation had occurred prior to March. Leaf area of *L. andersonii* increased and peaked between April 27 and May 11. Both leaf area and leaf number decreased substantially between May 11 and May 25 (Hamerlynck et al. 2002 [DIRS 177128], Figure 7, p. 103). Additionally, net photosynthesis in *A. dumosa* declined to the photosynthetic compensation point by May 4 in a study at the East Mojave National Preserve (Hamerlynck et al. 2002 [DIRS 177046], p 774).

Table D-4. Growth Stage Lengths for Three Vegetation Types at Yucca Mountain

Below-Average Precipitation Year			
Growth Stage	**Annual**	**Drought Deciduous**	**Evergreen**
Initial	N/A	Feb. 15 to 28 DOY 46 to 59	Feb. 1 to 28 DOY 32 to 59
Development	N/A	Mar. 1 to 15 DOY 60 to 74	Mar. 1 to 31 DOY 60 to 90
Mid	N/A	Mar. 16 to Apr. 15 DOY 75 to 105	Apr. 1 to May 15 DOY 91 to 135
Late	N/A	Apr. 16 to 30 DOY 106 to 120	May 16 to Jun. 30 DOY 136 to 181
Average Precipitation Year			
Growth Stage	**Annual[1]**	**Drought Deciduous[2]**	**Evergreen[3]**
Initial	Jan. 1 to 31 DOY 1 to 31	Feb. 1 to 28 DOY 32 to 59	Feb. 1 to 28 DOY 32 to 59
Development	Feb. 1 to 28 DOY 32 to 59	Mar. 1 to 15 DOY 60 to 74	Mar. 1 to 31 DOY 60 to 90
Mid	Mar. 1 to 31 DOY 60 to 90	Mar. 16 to Apr. 30 DOY 75 to 120	Apr. 1 to May 15 DOY 91 to 135
Late	Apr. 1 to 15 DOY 91 to 105	May 1 to 15 DOY 121 to 135	May 16 to Sept. 30 DOY 136 to 273

Table D-4. Growth Stage Lengths for Three Vegetation Types at Yucca Mountain (Continued)

Above-Average Precipitation Year (Continued)			
Growth Stage	**Annual**	**Drought Deciduous**	**Evergreen**
Initial	Oct. 1 to Jan. 31 DOY 274 to 31	Feb. 1 to 28 DOY 32 to 59	Feb. 1 to 28 DOY 32 to 59
Development	Feb. 1 to 28 DOY 32 to 59	Mar. 1 to 15 DOY 60 to 74	Mar. 1 to 31 DOY 60 to 90
Mid	Mar. 1 to May 1 DOY 60 to 121	Mar. 16 to May 31 DOY 75 to 151	Apr. 1 to Jun. 15 DOY 91 to 166
Late	May 2 to 16 DOY 122 to 136	Jun. 1 to Jun. 15 DOY 152 to 166	Jun. 16 to Sept. 30 DOY 167 to 273

Source: Newman 1992 [DIRS 174673], p. 3; Hulbert 1955 [DIRS 177129], p. 1.
Rundel and Gibson 1996 [DIRS 103614], Figure 4.13, p. 106; Hamerlynck et al. 2002 [DIRS 177128], Figure 7, p. 103; Hamerlynck et al. 2002 [DIRS 177046], p. 774.
Rundel and Gibson 1996 [DIRS 103614], Figure 4.13, p. 106; Hamerlynck et al. 2000 [DIRS 177022], p. 602, Figure 6; Smith et al. 1995 [DIRS 103628], pp. 342 to 343, Figure 2, and 349.

Thus, for the drought deciduous species during an average precipitation year, February 1 through 28, March 1 through 15, March 16 through April 30, and May 1 through 15 were assigned to the initial, development, mid, and late growth stages, respectively (Table D-4). Timing of precipitation for drought years is variable and unpredictable (CRWMS M&O 1996 [DIRS 102235], p. 3) and likely has a greater effect on lengths of different growth stages for drought deciduous than for evergreen vegetation. This is because timing of phenological events for drought deciduous vegetation, such as leaf or flower initiation, are dependent on precipitation (Smith et al. 1997 [DIRS 103636], p. 61). Additionally, drought deciduous vegetation is more sensitive to the onset of dry soil conditions than evergreen vegetation (e.g., leaf drop occurs more readily). It was assumed that, on average, during a drought year the phenological stages that would be most affected would be bud and leaf initiation, and flower development. Based on Rundel and Gibson (1996 [DIRS 103614], Table 4.14, p. 109), first dates of leafing for four drought deciduous species (*A. dumosa, G. spinosa, L. andersonii,* and *L. pallidum*) varied on average by about 15 days from one consecutive year to the next over nine years. Based on this, the initial, mid, and late growth stages were reduced by 15 days for a below-average precipitation year. This resulted in growth stage lengths of February 15 through 28, March 1 through 15, March 16 through April 15, and April 16 through 30 for the initial, development, mid, and late growth stages, respectively (Table D-4). As with evergreen vegetation, it was assumed that the length of the mid stage would be most affected by above-average precipitation years through extension of the time period of favorable temperatures and soil moisture for growth. Therefore, the length of the mid stage was increased by 15 days to March 16 through May 31 (Table D-4). This moved the late season stage to June 1 through June 15. The length of the late season stage was not increased because high temperatures and evaporative demands that are common in June generally result in rapid dry down of soils and subsequent leaf fall for drought deciduous species.

Bromus madritensis spp. *rubens* was the dominant annual species on vegetation associations and, in most cases, was the only annual species that exhibited significant cover (Tables D-7 through D-15). *Bromus madritensis* spp. *rubens* is an invasive winter annual grass that germinates in the fall (September through December) and remains a vegetative rosette or tuft until growth resumes in late winter or early spring (Newman 1992 [DIRS 174673], p. 3; Hulbert

1955 [DIRS 177129], p. 1). This grass grows quickly when temperatures allow, then generally sets seed and senesces in late spring to early summer months (Hulbert 1955 [DIRS 177129], p. 1; Newman 1992 [DIRS 174673], p. 3). Based on this information, the time periods of January 1 through 31, February 1 through 28, March 1 through 31, and April 1 through 15 were assigned to the initial, development, mid, and late stages, respectively (Table D-4). No annual cover was recorded for the representative dry year (Tables D-8, D-9, and D-10); therefore, growth stages were not developed. In above average precipitation years, fall rains could result in germination of *Bromus madritensis*, followed by slow growth to semi dormant conditions under cool winter temperatures (Newman 1992 [DIRS 174673], p. 3). Additionally, if moisture is available, *Bromus madritensis* can germinate in winter and spring months (Newman 1992 [DIRS 174673], p. 3). To account for fall germination in above-average precipitation years, the initial stage was changed to October 1 through January 31 (Table D-4). The midstage was extended by 30 days (March 1 through May 1) to account for growth of spring germinating cohorts and extension of the time period of available moisture with above average precipitation. This resulted in moving the late season to May 2 through May 16 (Table D-4). The length of the late season stage was not increased for the same reasons discussed for drought deciduous species.

Rundel and Gibson (1996 [DIRS 103614], pp. 87 to 89) describe vegetation characteristics for Great Basin, transition, and Mojave Desert associations that were based on 10 years of data. The range of mean vegetation heights for the *Larrea–Ambrosia* association (0.27 to 0.32 m) (Table D-5), *Larrea–Grayia–Lycium* association (0.34 to 0.48 m) (Table D-5), and *Grayia–Lycium* association (0.38 m) (Table D-5) were most appropriate for use in this analysis because the association descriptions based on Beatley's work (Rundel and Gibson 1996 [DIRS 103614], pp. 87 to 89) correspond to the LA, LLG, and LG associations for Yucca Mountain. Ranges for vegetation heights were reported for four additional associations (Table D-5) but were not selected for the following reasons:

1. Cover data for this analysis (Tables D-8, D-10, D-11, D-13, D-14, and D-16) show that for the LA and LLG vegetation associations, *L. tridentata*, a shrub that can grow to relatively large stature, is either codominant with shorter shrubs, such as *E. nevadensis,* or comprises much less cover than shorter shrubs, such as *A. dumosa*, making the reported maximum height of the range (0.82 m) for *Larrea–Ambrosia–Grayia–Lycium* too high.

2. *Coleogyne ramosissima* was not dominant in the vegetation associations that were chosen for this analysis. Therefore, associations with *C. ramosissima* as a dominant species were not selected.

Table D-5. Mean Vegetation Heights for Seven Vegetation Associations

Vegetation Association[a]	Corresponding Yucca Mountain Vegetation Association	Mean Height of Vegetation (m)
Larrea–Ambrosia	LA	0.27 to 0.32
Larrea–Ambrosia–Grayia–Lycium	NA [b]	0.41 to 0.82
Larrea–Grayia–Lycium	LLG	0.34 to 0.48
Grayia–Lycium [c]	LG	0.38
Coleogyne–Larrea–Grayia–Lycium	NA	0.42 to 0.51
Coleogyne–Grayia–Lycium	NA	0.31 to 0.39
Coleogyne	COL	0.37 to 0.41

Source: [a] Rundel and Gibson 1996 [DIRS 103614], Table 4.1, p. 88.
[b] Not applicable.
[c] Rundel and Gibson 1996 [DIRS 103614], Table 4.2, p. 89.

According to Equation D-4, mean maximum plant height is recommended for K_{cb} calculations; therefore, the maximum values for the range of heights in Table D-5 were selected for drought deciduous and evergreen species (Table D-6). Because established perennial vegetation was considered for K_{cb} calculations, one height value was used for all growth stages for drought deciduous and evergreen species.

Mean maximum plant height for annual vegetation was based on published literature values for *Bromus madritensis* and on vegetation heights from Table D-5. Plant height reported for *Bromus madritensis* ranged from 0.20 to 0.50 m (Newman 1992 [DIRS 174673], p. 2). Based on mean heights for perennial shrubs (Table D-5), it is not likely that the dry conditions at Yucca Mountain would normally support annuals with a mean maximum height of 0.50 m. Height ranges for perennial vegetation were lower for the LA association than for the LG and LLG associations, indicating a lower value for annuals would also be appropriate. Therefore, for the LA association, 0.27 m was selected as the mean maximum height for annuals, which is at the low end of the height range for the LA association (Table D-5). For the LG and LLG associations, 0.34 m was selected as the mean maximum height for annuals, which is at the low end of the height range for the LLG association (Table D-5).

Annual species germinate, grow, and complete their life cycle within a year, and so differences in height between the initial and midseason growth stages were considered. *Bromus madritensis* is a winter annual and generally germinates in late fall or winter, rapidly establishes a root system, then overwinters as a small basal rosette ranging from 0.01 to 0.05 m in height (height measured for *Bromus tectorum* in February; Hulbert 1955 [DIRS 177129], Table 6, p. 186). Ten percent of the midseason stage height (about 0.03 m) was about midrange of the height values in Hulbert (1955 [DIRS 177129], Table 6, p. 186). Therefore, 10% of the midseason stage height (about 0.03 m) was used for the initial growth stage for annual vegetation (Table D-6).

Vegetation height was not varied for low-, average, and high-precipitation years. Stress imposed by dryer years was accounted for with measured cover data and growing season length.

Table D-6. Mean Maximum Vegetation Heights

Vegetation Association	Mean Maximum Plant Height (m)		
	Annuals[a]	Drought Deciduous[b]	Evergreen[c]
LA	Initial growth stage = 0.027; midseason growth stage = 0.27	0.32	0.32
LG	Initial growth stage = 0.034; midseason growth stage = 0.34	0.38[3]	0.38[3]
LLG	Initial growth stage = 0.034; midseason growth stage = 0.34	0.48	0.48

Sources: [a] Newman 1992 [DIRS 174673], p. 2; Hulbert 1955 [DIRS 177129], Table 6, p. 186; Rundel and Gibson 1996 [DIRS 103614], Table 4.1, p. 88, and Table 4.2, p. 89.
[b] Rundel and Gibson 1996 [DIRS 103614], Table 4.1, p. 88.
[c] Rundel and Gibson 1996 [DIRS 103614], Table 4.2, p. 89.

D3.2.2 Vegetation Cover Data

Cover data collected during below average (1990), average (1991), and above average (1993) precipitation years from 11 to 12 plots (depending on the year) in the LA, LG, and LLG vegetation associations at Yucca Mountain were used to calculate cover means per species and vegetation type for each association (Tables D-7 through D-15). This was done by extracting the ESP cover data for the LA, LG, and LLG associations from the source file (DTN: MO9907GCESPYMN.000 [DIRS 157659]) for 1990, 1991, and 1993. The data were placed in an Excel® file (Output DTN: MO0606SPAVEGAS.001). Data were sorted by species and ground cover classification (bare ground, litter, gravel, rock, and cobble) within ESPs. For each ESP mean cover per species and ground cover classification was calculated by summing cover per species (or ground cover classification) and dividing the sum by the number of transects that were sampled (8 to 12 transects depending on the site). Association means per species were calculated from the ESP means by summing cover per species and dividing by the number of ESPs measured within an association (Tables D-7 through D-15). Total mean cover per vegetation type and association was determined by summing mean cover per species within a vegetation type and then summing mean cover for the three vegetation types to get the association total (Tables D-7 through D-15). Calculations were done in Excel® spreadsheets using the SUM and AVERAGE commands (Output DTN: MO0606SPAVEGAS.001).

Cover data means were sorted to identify dominant and important species within associations for each year. Species comprising 70% to 90% of the cover data means were considered dominant. Cover data means per species, vegetation type, and association are in Tables D-7 through D-15.

Vegetation cover is not static throughout the year. It changes with phenological stages and in response to environmental conditions. Evergreens such as *A. tridentata* and *L. tridentata* develop ephemeral leaves that are shed as soil moisture becomes limiting (Smith et al. 1997 [DIRS 103636], pp. 79 and 108), and drought deciduous shrubs experience complete defoliation during extended dry periods. Vegetation cover data were collected during peak growth periods for the three years used in this study and represent maximum cover for an average, above average, and below average water year. During the initial growth stage cover is lower than that measured at peak growth. During the initial stage, annuals are emerging and drought deciduous and evergreen species are initiating new leaf growth. However, there were no vegetation cover

data available from Yucca Mountain or in the literature to develop a percent reduction of cover from peak growth to use for the initial growth stage. Therefore, to avoid overestimation of plant water use during the initial stage, it was assumed that drought deciduous and evergreen vegetation cover was 50% of that measured at peak growth. Fifty percent was selected because drought deciduous vegetation puts on leaf area rapidly when soil moisture becomes available (Smith et al. 1997 [DIRS 103636], p. 62), and evergreen vegetation maintains a percentage of leaf area throughout the year (Smith et al. 1997 [DIRS 103636], p. 73). It was assumed for annual vegetation that cover was 10% of that measured at peak growth for normal precipitation years and 30% of that measured at peak growth for above average precipitation years. Ten percent of full cover was selected for normal precipitation years because of the small stature of annual seedlings. Thirty percent of full cover was selected for above average precipitation years because of the potential for initial crowding of *Bromus madritensis* seedlings in response to favorable germination conditions (Newman 1992 [DIRS 174673], p. 3).

Table D-7. Mean Cover from LA Vegetation Associations at Yucca Mountain for a Dry Year (1990)

LA 1990					
Vegetation Type/Species	**Life Form[1]**	**Cover (%)**	**Vegetation Type/Species**	**Life Form[1]**	**Cover (%)**
Annuals		0.00	**Evergreen**		
No annuals recorded			*Larrea tridentata*	S	1.02
Drought Deciduous			*Ephedra nevadensis*	S	0.70
Ambrosia dumosa	S	5.82	*Ericameria cooperi*[6]	*S*	0.45
Acamptopappus shockleyi	S	2.03	*Coleogyne ramosissima*	S	0.23
Menodora spinescens	S	1.74	*Hymenoclea salsola*	S	0.05
Krameria erecta[2]	S	0.90		**Total**	2.45
Lycium pallidum	S	0.53	**Association Total**		**14.55**
Atriplex confertifolia	S	0.35			
Grayia spinosa	S	0.23			
Achnatherum hymenoides[3]	G	0.15			
Krascheninnikovia lanata[4]	S	0.14			
Lycium andersonii	S	0.10			
Salazaria mexicana	S	0.03			
Machaeranthera tortifolia	F	0.03			
Psorothamnus fremontii	S	0.02			
Eriogonum fasciculatum	S	0.02			
Achnatherum speciosum[5]	G	0.01			
	Total	12.10			

Source: Output DTN: MO0606SPAVEGAS.001.

NOTE: Means are based on data collected from twelve 200 × 200 m plots in 1990. Species are arranged in order of dominance within a vegetation type.

[1] G = grass, F = forb, S = shrub.
[2] Previous nomenclature: *Krameria parvifolia*.
[3] Previous nomenclature: *Oryzopsis hymenoides*.
[4] Previous nomenclature: *Ceretoides lanata*.
[5] Previous nomenclature: *Stipa speciosa*.
[6] Previous nomenclature: *Happlopapus cooperi*.

Table D-8. Mean Cover from LG Vegetation Associations at Yucca Mountain for a Dry Year (1990)

LG 1990					
Vegetation Type/Species	**Life Form[1]**	**Cover (%)**	**Vegetation Type/Species**	**Life Form[1]**	**Cover (%)**
Annuals			**Evergreen**		
No annuals recorded		0.00	*Ephedra nevadensis*	S	2.13
Drought Deciduous			*Ericameria cooperi*[6]	S	1.28
Eriogonum fasciculatum	S	2.11	*Hymenoclea salsola*	S	0.67
Lycium andersonii	S	2.05	*Ericameria teretifolia*[7]	S	0.58
Grayia spinosa	S	1.82	*Chrysothamnus viscidiflorus*	S	0.32
Achnatherum speciosum[2]	G	0.85	*Gutierrezia sarothrae*	S	0.23
Atriplex confertifolia	S	0.78	*Ephedra viridis*	S	0.22
Pleuraphis jamesii[3]	G	0.50	*Artemisia tridentata*	S	0.18
Ambrosia dumosa	S	0.38	*Ericameria linearifolia*[8]	S	0.12
Krascheninnikovia lanata[4]	S	0.29	*Larrea tridentata*	S	0.09
Menodora spinescens	S	0.24	*Ericameria nauseosa*[9]	S	0.08
Salazaria mexicana	S	0.23		**Total**	5.90
Lycium pallidum	S	0.08	**Association**	**Total**	**15.62**
Atriplex canescens	S	0.07			
Tetradymia axillaris	S	0.07			
Elymus elymoides[5]	G	0.06			
Others		0.19			
	Total	9.72			

Source: Output DTN: MO0606SPAVEGAS.001.

NOTE: Means are based on data collected from twelve 200 × 200 m plots in 1990. Species are arranged in order of dominance within a vegetation type.

[1] G = grass, F = forb, S = shrub.
[2] Previous nomenclature: *Stipa speciosa*.
[3] Previous nomenclature: *Hilaria jamesii*.
[4] Previous nomenclature: *Ceretoides lanata*.
[5] Previous nomenclature: *Sitanion histere*.
[6] Previous nomenclature: *Happlopapus cooperi*.
[7] Previous nomenclature: *Chrysothamnus teretifolius*.
[8] Previous nomenclature: *Happlopapus linearifolius*.
[9] Previous nomenclature: *Crysothamnus nauseosus*.

Table D-9. Mean Cover from LLG Vegetation Associations at Yucca Mountain for a Dry Year (1990)

LLG 1990					
Vegetation Type/Species	**Life Form[1]**	**Cover (%)**	**Vegetation Type/Species**	**Life Form[1]**	**Cover (%)**
Annuals			**Evergreen**		
No annuals recorded		0.00	*Larrea tridentata*	S	2.79
Drought Deciduous			*Ephedra nevadensis*	S	2.69
Krameria erecta[2]	S	2.00	*Ericameria cooperi*[5]	S	0.69
Ambrosia dumosa	S	1.56	*Hymenoclea salsola*	S	0.52
Lycium andersonii	S	0.96	*Coleogyne ramosissima*	S	0.04
Grayia spinosa	S	0.70	*Ephedra viridis*	S	0.02
Salazaria mexicana	S	0.36		**Total**	6.75
Menodora spinescens	S	0.28	**Association Total**		**13.56**
Eriogonum fasciculatum	S	0.23			
Krascheninnikovia lanata[3]	S	0.20			
Achnatherum speciosum[4]	G	0.19			
Lycium pallidum	S	0.16			
Atriplex confertifolia	S	0.04			
Others		0.13			
	Total	6.81			

Source: Output DTN: MO0606SPAVEGAS.001.

NOTE: Means are based on data collected from eleven 200 × 200 m plots in 1990. Species are arranged in order of dominance within a vegetation type.

[1] G = grass, F = forb, S = shrub.
[2] Previous nomenclature: *Krameria parvifolia*.
[3] Previous nomenclature: *Ceretoides lanata*.
[4] Previous nomenclature: *Stipa speciosa*.
[5] Previous nomenclature: *Happlopapus cooperi*.

Table D-10. Mean Cover from LA Vegetation Associations at Yucca Mountain for an Average Precipitation Year (1991)

LA 1991					
Vegetation Type/Species	**Life Form[1]**	**Cover (%)**	**Vegetation Type/Species**	**Life Form[1]**	**Cover (%)**
Annuals			**Drought Deciduous**		
Chaenactis stevioides	F	0.66	*Ambrosia dumosa*	S	3.38
Vulpia octoflora	G	0.56	*Menodora spinescens*	S	1.25
Sisymbrium altissimum	F	0.14	*Lycium pallidum*	S	0.60
Unknown	G	0.11	*Acamptopappus shockleyi*	S	0.57
Bromus madritensis ssp. rubens	F	0.09	*Krameria erecta*[2]	S	0.40
Pectocarya platycarpa	F	0.08	*Atriplex confertifolia*	S	0.15
Eriogonum maculatum	F	0.05	*Lycium andersonii*	S	0.11
Mentzelia obscura	F	0.05	*Psorothamnus fremontii*	S	0.05
Others		0.32	Others		0.13
	Total	2.06		**Total**	6.64
			Evergreen		
			Larrea tridentata	S	1.06
			Ephedra nevadensis	S	0.46
			Coleogyne ramosissima	S	0.27
			Ericameria cooperi[3]	S	0.03
				Total	1.82
				Association Total	**10.52**

Source: Output DTN: MO0606SPAVEGAS.001.

NOTE: Means are based on data collected from twelve 200 × 200 m plots in 1991. Species are arranged in order of dominance within a vegetation type.

[1] G = grass, F = forb, S = shrub.
[2] Previous nomenclature: *Krameria parviflora*.
[3] Previous nomenclature: *Happlopapus cooperi*.

Table D-11. Mean Cover from LG Vegetation Associations at Yucca Mountain for an Average Precipitation Year (1991)

LG 1991					
Vegetation Type/Species	**Life Form[1]**	**Cover (%)**	**Vegetation Type/Species**	**Life Form[1]**	**Cover (%)**
Annuals			**Drought Deciduous**		
Bromus madritensis ssp. rubens	G	3.24	*Lycium andersonii*	S	1.16
Unknown	F	0.45	*Grayia spinosa*	S	1.04
Amsinckia tessellata	F	0.38	*Eriogonum fasciculatum*	S	1.04
Salsola iberica[2]	F	0.23	*Atriplex confertifolia*	S	0.69
Sisymbrium altissimum	F	0.13	*Ambrosia dumosa*	S	0.53
Mentzelia obscura	F	0.09	*Pleuraphis jamesii*[3]	S	0.41
Oxytheca perfoliata	F	0.09	*Achnatherum speciosum*[4]	S	0.40
Descurainia pinnata	F	0.07	*Krascheninnikovia lanata*[5]	S	0.27
Linanthus demissus	F	0.06	*Menodora spinescens*	S	0.27
Cryptantha nevadensis	F	0.05	*Lycium pallidum*	S	0.24
Cryptantha micrantha	F	0.05	*Salazaria mexicana*	S	0.18
Others		0.22	*Sphaeralcea ambigua*	S	0.12
	Total	5.06	*Atriplex canescens*	S	0.08
			Erioneuron pulchellum	G	0.06
			Encelia virginensis	S	0.05
			Eriastrum eremicum	F	0.05
			Others		0.18
				Total	6.77
			Evergreen		
			Ephedra nevadensis	S	2.00
			Ericameria cooperi[6]	S	0.79
			Hymenoclea salsola	S	0.55
			Ericameria teretifolia[7]	S	0.38
			Gutierrezia sarothrae	S	0.38
			Ephedra viridis	S	0.18
			Chrysothamnus viscidiflorus	S	0.13
			Artemisia tridentata	S	0.11
			Ericameria nauseosa[8]	S	0.09
			Ericameria linearifolia[9]	S	0.08
			Larrea tridentata	S	0.08
			Coleogyne ramosissima	S	0.01
				Total	4.78
				Association Total	**16.61**

Source: Output DTN: MO0606SPAVEGAS.001.

NOTE: Means are based on data collected from twelve 200 m × 200 m plots in 1991. Species are arranged in order of dominance within a vegetation type.

[1] G = grass, F = forb, S = shrub.
[2] Previous nomenclature: *Salsola kali*.
[3] Previous nomenclature: *Hilaria jamesii*.
[4] Previous nomenclature: *Stipa speciosa*.
[5] Previous nomenclature: *Ceratoides lanata*.
[6] Previous nomenclature: *Happlopapus cooperi*.
[7] Previous nomenclature: *Chrysothamnus teretifoliu*.
[8] Previous nomenclature: *Chrysothamnus nauseosus*.
[9] Previous nomenclature: *Haplopappus linearifolius*.

Table D-12. Mean Cover from LLG Vegetation Associations at Yucca Mountain for an Average Precipitation Year (1991)

LLG 1991					
Vegetation Type/Species	**Life Form[1]**	**Cover (%)**	**Vegetation Type/Species**	**Life Form[1]**	**Cover (%)**
Annuals			**Drought Deciduous**		
Bromus madritensis ssp. rubens	G	4.55	*Krameria erecta*[2]	S	0.96
Amsinckia tessellata	F	1.89	*Ambrosia dumosa*	S	0.49
Mentzelia obscura	F	0.88	*Lycium andersonii*	S	0.31
Descurainia pinnata	F	0.85	*Menodora spinescens*	S	0.21
Lotus humistratus	F	0.32	*Lycium pallidum*	S	0.18
Linanthus demissus	F	0.31	Grayia spinosa	S	0.09
Unknown	F	0.27	*Salazaria mexicana*	S	0.08
Chorizanthe brevicornu	F	0.18	*Eriogonum inflatum*	F	0.07
Sisymbrium altissimum	F	0.14	*Eriastrum eremicum*	F	0.06
Chaenactis stevioides	F	0.12	Others		0.16
Eschescholzia minutiflora	F	0.11		**Total**	2.61
Phacelia fremontii	F	0.06	**Evergreen**		
Oxytheca perfoliata	F	0.05	*Larrea tridentata*	S	1.92
Malacothrix glabrata	F	0.05	*Ephedra nevadensis*	S	1.78
Cryptantha nevadensis	F	0.05	*Hymenoclea salsola*	S	0.26
Others		0.26	*Coleogyne ramosissima*	S	0.11
	Total	10.09	*Ericameria cooperi*[3]	S	0.08
			Chrysothamnus viscidiflorus	S	0.01
				Total	4.16
				Association Total	**16.86**

Source: Output DTN: MO0606SPAVEGAS.001.

NOTE: Means are based on data collected from twelve 200 × 200 m plots in 1991. Species are arranged in order of dominance within a vegetation type.

[1] G = grass, F = forb, S = shrub.
[2] Previous nomenclature: *Krameria parvifolia*.
[3] Previous nomenclature: *Happlopapus cooperi*.

Table D-13. Mean Cover from LA Vegetation Associations at Yucca Mountain for a Wet Year (1993)

LA 1993					
Vegetation Type/Species	**Life Form[1]**	**Cover (%)**	**Vegetation Type/Species**	**Life Form[1]**	**Cover (%)**
Annuals			**Drought Deciduous**		
Chaenactis stevioides	F	1.90	*Ambrosia dumosa*	S	6.03
Bromus madritensis ssp rubens	G	1.89	*Menodora spinescens*	S	1.61
Pectocarya platycarpa	F	0.69	*Lycium pallidum*	S	1.36
Vulpia octoflora	G	0.48	*Acamptopappus shockleyi*	S	1.06
Cryptantha pterocarya	F	0.41	*Krascheninnikovia lanata*[2]	S	0.19
Unknown		0.34	*Lycium andersonii*	S	0.16
Eriophyllum pringlei	F	0.24	*Atriplex confertifolia*	S	0.15
Cryptantha spp	F	0.21	*Achnatherum hymenoides*[3]	G	0.14
Cryptantha micrantha	F	0.14	*Krameria erecta*[4]	S	0.11
Cryptantha circumscissa	F	0.10	*Grayia spinosa*	S	0.10
Cryptantha nevadensis	F	0.09	*Psorothamnus fremontii*	S	0.07
Malacothrix glabrata	F	0.07	Others		0.14
Amsinckia tessellata	F	0.06		**Total**	11.12
Rafinesquia neomexicana	F	0.05	**Evergreen**		
Others		0.37	*Larrea tridentata*	S	1.86
	Total	7.04	*Ephedra nevadensis*	S	0.50
			Coleogyne ramosissima	S	0.30
			Ericameria cooperi[5]	S	0.03
				Total	2.69
				Association Total	**20.85**

Source: Output DTN: MO0606SPAVEGAS.001.

NOTE: Means are based on data collected from twelve 200 × 200 m plots in 1993. Species are arranged in order of dominance within a vegetation type.

[1] G = grass, F = forb, S = shrub.
[2] Previous nomenclature: *Ceretoides lanata*.
[3] Previous nomenclature: *Oryzopsis hymenoides*.
[4] Previous nomenclature: *Krameria parvifolia*.
[5] Previous nomenclature: *Happlopapus cooperi*.

Table D-14. Mean Cover from LG Vegetation Associations at Yucca Mountain for a Wet Year (1993)

LG 1993					
Vegetation Type/Species	**Life Form[1]**	**Cover (%)**	**Vegetation Type/Species**	**Life Form[1]**	**Cover (%)**
Annuals			**Drought Deciduous**		
Bromus madritensis ssp rubens	G	11.13	*Lycium andersonii*	S	2.07
Cryptantha pterocarya	F	0.69	*Grayia spinosa*	S	1.90
Unknown		0.50	*Eriogonum fasciculatum*	S	1.34
Cryptantha spp	F	0.48	*Ambrosia dumosa*	S	0.82
Amsinckia tessellata	F	0.35	*Atriplex confertifolia*	S	0.56
Lotus humistratus	F	0.15	*Pleuraphis jamesii*[2]	G	0.42
Syntrichopappus fremontii	F	0.11	*Salazaria mexicana*	S	0.41
Cryptantha nevadensis	F	0.11	*Krascheninnikovia lanata*[3]	S	0.40
Cryptantha circumscissa	F	0.09	*Menodora spinescens*	S	0.32
Phacelia fremontii	F	0.08	*Eriogonum inflatum*	F	0.19
Pectocarya platycarpa	F	0.07	*Sphaeralcea ambigua*	F	0.18
Pectocarya setosa	F	0.07	*Achnatherum speciosum*[4]	G	0.17
Lupinus flavoculatus	F	0.06	*Encelia virginensis*	S	0.12
Bromus tectorum	G	0.05	*Stephanomeria pauciflora*	F	0.11
Chaenactis stevioides	F	0.05	*Atriplex canescens*	S	0.11
Others		0.26	*Lycium pallidum*	S	0.07
	Total	14.25	*Mirabilis bigelovii*	F	0.06
			Chamaesyce albomarginata[5]	F	0.05
			Others		0.22
				Total	9.52
			Evergreen		
			Ephedra nevadensis	S	2.61
			Ericameria cooperi[6]	S	1.22
			Hymenoclea salsola	S	0.99
			Ericameria teretifolia[7]	S	0.39
			Ephedra viridis	S	0.30
			Gutierrezia sarothrae	S	0.23
			Ericameria linearifolia[8]	S	0.19
			Chrysothamnus viscidiflorus	S	0.14
			Artemisia tridentata	S	0.12
			Ericameria nauseosa[9]	S	0.11
			Larrea tridentata	S	0.10
			Coleogyne ramosissima	S	0.04
				Total	6.44
				Association Total	**30.21**

Source: Output DTN: MO0606SPAVEGAS.001.

NOTE: Means are based on data collected from twelve 200 × 200 m plots in 1993. Species are arranged in order of dominance within a vegetation type.

[1] G = grass, F = forb, S = shrub.
[2] Previous nomenclature: *Hilaria jamesii*.
[3] Previous nomenclature: *Ceretoides lanata*.
[4] Previous nomenclature: *Stipa speciosa*.
[5] Previous nomenclature: *Euphorbia albomarginata*.
[6] Previous nomenclature: *Happlopapus cooperi*.
[7] Previous nomenclature: *Chrysothamnus teretifolius*.
[8] Previous nomenclature: *Happlopapus linearifolius*.
[9] Previous nomenclature: *Chrysothamnus nauseosus*.

Table D-15. Mean Cover from LLG Vegetation Associations at Yucca Mountain for a Wet Year (1993)

LLG 1993					
Vegetation Type/Species	**Life Form[1]**	**Cover (%)**	**Vegetation Type/Species**	**Life Form[1]**	**Cover (%)**
Annuals			**Drought Deciduous**		
Bromus madritensis ssp rubens	G	16.17	*Ambrosia dumosa*	S	1.23
Amsinckia tessellata	F	3.59	*Lycium andersonii*	S	0.53
Lotus humistratus	F	0.53	*Krameria erecta*[2]	S	0.47
Cryptantha pterocarya	F	0.44	*Lycium pallidum*	S	0.44
Vulpia octoflora	G	0.24	*Menodora spinescens*	S	0.31
Unknown		0.11	*Salazaria mexicana*	S	0.27
Pectocarya platycarpa	F	0.10	*Eriogonum inflatum*	F	0.16
Chaenactis stevioides	F	0.09	*Chamaesyce albomarginata*[3]	F	0.11
Cryptantha spp	F	0.07	*Grayia spinosa*	S	0.10
Erodium cicutarium	F	0.05	*Krascheninnikovia lanata*[4]	S	0.08
Pectocarya setosa	F	0.05	*Eriogonum fasciculatum*	S	0.05
Phacelia fremontii	F	0.04	*Encelia virginensis*	S	0.05
Others		0.26	*Achnatherum speciosum*[5]	G	0.05
	Total	21.74	Others		0.24
				Total	4.09
			Evergreen		
			Larrea tridentata	S	3.05
			Ephedra nevadensis	S	2.17
			Hymenoclea salsola	S	0.66
			Coleogyne ramosissima	S	0.14
			Ericameria cooperi[6]	S	0.14
				Total	6.16
			Association	**Total**	**31.99**

Source: Output DTN: MO0606SPAVEGAS.001.

NOTE: Means are based on data collected from twelve 200 × 200 m plots in 1993. Species are arranged in order of dominance within a vegetation type.

[1] G = grass, F = forb, S = shrub.
[2] Previous nomenclature: *Krameria parvifolia*.
[3] Previous nomenclature: *Euphorbia albomarginata*.
[4] Previous nomenclature: *Ceretoides lanata*.
[5] Previous nomenclature: *Stipa speciosa*.
[6] Previous nomenclature: *Happlopapus cooperi*.

To assess variability among ESPs within each association, and for the NDVI' analysis in Appendix E, association means, standard deviations, standard errors, 90% confidence intervals, and sample size requirements for percent cover were calculated (Table D-16). Total mean cover for the ESPs was placed in a separate Excel® worksheet in Output DTN: MO0606SPAVEGAS.001. Association means and standard deviations (Table D-16) were calculated using the AVERAGE and STDEV commands. Standard errors (Table D-16) were calculated according to Bohnam (1989 [DIRS 127406], p. 64, Equation 3.30) as the standard deviation divided by the square root of n (n = number of ESPs included in the mean calculation). Ninety percent confidence intervals (Table D-16) were calculated according to the following equation (Bohnam 1989 [DIRS 127406], p. 64, Equation 3.33):

$$CI = \frac{t\ s_c}{\sqrt{n}} \quad \text{(Eq. D-10)}$$

where

CI	=	Confidence interval
t	=	t-table value for single tailed test, with α = 0.10, and n−1 degrees of freedom
s_c	=	Standard deviation of cover data
n	=	Number of ESPs in mean calculation.

The following equation was used to determine if an adequate number of ESPs had been sampled to represent cover for the associations at Yucca Mountain (Bonham 1989 [DIRS 127406], p. 67, Equation 3.43):

$$n_c = \frac{t^2 s_c^2}{(d\bar{x}_c)^2} \quad \text{(Eq. D-11)}$$

where

n_c	=	Number of ESPs required to sample cover of an association to within 10% of the true population mean,
t	=	t-table value for single tailed test, with α = 0.10, and n−1 degrees of freedom,
s_c	=	Standard deviation of cover data for ESPs,
d	=	Precision that the true difference of the sample mean occurs from the population (= 0.10),
x_c	=	Mean of cover data for ESPs.

Twelve ESPs were adequate to sample within 10% of the true cover mean for the three vegetation associations (Table D-16). In all cases, more ESPs were sampled than required to meet the designated precision (Table D-16).

Table D-16. Vegetation Cover for Ecological Study Plots Representing the LA, LG, and LLG Vegetation Associations

Cover (%) for LA ESPs				Cover (%) for LG ESPs				Cover (%) for LLG ESPs			
ESP[1]	1990	1991	1993	ESP[2]	1990	1991	1993	ESP[3]	1990	1991	1993
LA2C	12.38	12.50	21.12	LG1C	13.12	15.50	30.87	LLG3C	16.75	16.12	31.72
LA3C	15.25	11.25	22.28	LG2C	15.62	16.88	31.87	LLG4C	12.62	15.50	30.38
LA4C	14.62	14.50	19.12	LG3C	17.38	20.38	36.76	LLG5C	12.87	19.94	32.54
LA5C	15.00	8.75	15.00	LG4C	15.25	14.38	30.38	LLG7C	13.50	16.88	28.88
LA6C	16.25	10.63	23.28	LG5C	13.88	17.62	23.15	LLG8C	14.75	17.12	39.25
LA7C	18.75	13.88	15.75	LG6C	17.38	13.37	25.12	LLG9C	14.25	17.39	25.38
LA1T	12.70	8.12	17.98	LG2T	20.10	22.80	37.00	LLG1T	13.30	19.30	36.76
LA2T	15.80	7.50	18.42	LG3T	14.30	20.40	31.00	LLG2T	8.40	16.90	38.67
LA3T	10.50	8.31	27.20	LG4T	16.60	15.00	28.51	LLG4T	17.40	18.20	29.83
LA4T	13.90	7.50	23.20	LG5T	13.90	11.89	24.09	LLG5T	12.60	18.00	35.62
LA5T	13.60	9.79	22.49	LG6T	14.60	16.80	34.23	LLG6T	12.70	14.67	27.17
LA7T	16.00	13.68	24.28	LG7T	16.00	15.00	29.46	LLG7T	n.d.[4]	12.70	27.42
Mean	14.56	10.53	20.84		15.68	16.67	30.20		13.56	16.89	31.97
SD[5]	2.15	2.60	3.64		1.97	3.19	4.53		2.38	1.99	4.66
SE[6]	0.62	0.75	1.05		0.57	0.92	1.31		0.72	0.57	1.34
90% CI[7]	0.85	1.02	1.43		0.77	1.26	1.78		0.98	0.78	1.83
Samples required[8]	4	11	6		3	7	4		6	3	4

Source: Output DTN: MO0606SPAVEGAS.001.

[1] Name of individual ecological study plots (ESP) representing the *Larrea–Ambrosia* (LA) vegetation association.
[2] Name of individual ESPs representing the *Lycium–Grayia* (LG) vegetation association.
[3] Name of individual ESPs representing the *Larrea –Lycium–Grayia* (LLG) vegetation association.
[4] No data collected from LLG7T in 1990.
[5] Standard deviation.
[6] Standard error.
[7] Confidence interval for vegetation cover mean calculated using Equation D-10.
[8] Number of ESPs required to adequately represent cover of vegetation associations. Samples required were calculated using Equation D-11.

D3.2.3 Stomatal Resistance

Several studies were identified for Mojave Desert plant species that included measurements of stomatal conductance (Table D-17). Only studies that were conducted in the vicinity of Yucca Mountain or nearby Mojave Desert regions were considered. Many of the studies reviewed were conducted at the Nevada Desert Free-Air CO_2 Enrichment (FACE) Facility located on the NTS (Naumburg et al. 2003 [DIRS 177143], p. 277 for description of site). These studies included conductance measurements made under elevated and ambient CO_2 conditions (e.g., Naumburg et al. 2003 [DIRS 177143]). Only plants in these studies that were measured under ambient CO_2 conditions were considered for this analysis. Conductance values measured under a variety of Mojave Desert conditions during several time periods were selected for dominant species in the three vegetation types so that representative mean values could be calculated for periods of low (initial growth stage and end of the late growth stage) and high (midseason) physiological activity. Relatively lower conductance values reported in the literature were used to represent

leaves at initiation of growth (initial growth stage) and old leaves near senescence (end of late growth stage). Higher conductance values were used to represent young fully expanded leaves expected during the midseason growth stage. Low conductance values indicating stomatal closure or dormancy (equal to or less than 0.01 mol m^{-2} s^{-1}) that were reported in some of the studies were not used in this analysis or reported in Table D-17. These low values were ignored because they reflect conditions when the plants were not active (nongrowing season or under other stress) and are thus not representative for estimating stomatal resistance.

Table D-17. Stomatal Conductance References and Values for Mojave Desert Plant Species

Reference	Species	Stomatal Conductance	Temperature	Comments
Huxman et al. 1999 [DIRS 177133], p. 770 [ambient temperature] and 774 [stomatal conductance]	*Bromus madritensis ssp rubens*	750 (mmol m^{-2} s^{-1})	Approximate average of ambient air temperature during the measurement period = 25.0°C	Prereproductive measurement. Glasshouse at UNLV[1]. Ambient outdoor conditions were tracked inside glasshouse.
		500 (mmol m^{-2} s^{-1})	25.0°C	Measurement made during seed fill.
Huxman and Smith 2001 [DIRS 177132], p. 197	*Bromus madritensis ssp rubens*	180 (mmol m^{-2} s^{-1})	Leaf temperature = 15.0°C	Measurements made in the field at the FACE[2] site. Measurements were midday maximum values and were made over course of growing season (DOY 69 to 103).
		300 (mmol m^{-2} s^{-1})	18.0°C	
		100 (mmol m^{-2} s^{-1})	21.0°C	
		200 (mmol m^{-2} s^{-1})	24.0°C	
		100 (mmol m^{-2} s^{-1})	27.0°C	
Hamerlynck et al. 2002 [DIRS 177128], p. 101	*Lycium andersonii*	0.225 (mol m^{-2} s^{-1})	Average high air temperature during study period = 20.8°C	Measurements made in the field at the FACE site over course of growing season (DOY 90 to 146). Conductances are the average midday maximum values of long shoots and short shoots measured during the same time period.
		0.39 (mol m^{-2} s^{-1})	20.8°C	
		0.25 (mol m^{-2} s^{-1})	20.8°C	
		0.525 (mol m^{-2} s^{-1})	20.8°C	
		0.375 (mol m^{-2} s^{-1})	20.8°C	
Naumburg et al. 2003 [DIRS 177143], p. 280, Figure 3	*Ambrosia dumosa*	300 (mmol m^{-2} s^{-1})	Mean air temperature = 19.0°C	Daily average stomatal conductance measurements made in the field at the FACE site during various months. Due to paucity of data for drought deciduous species, high conductance values measured in October and November (beyond the late season growth stage) were used.
		200 (mmol m^{-2} s^{-1})	19.0°C	
		50 (mmol m^{-2} s^{-1})	28.5°C	
		50 (mmol m^{-2} s^{-1})	28.5°C	
		200 (mmol m^{-2} s^{-1})	28.5°C	
		90 (mmol m^{-2} s^{-1})	28.5°C	
		50 (mmol m^{-2} s^{-1})	28.5°C	
Naumburg et al. 2003 [DIRS 177143], p. 280	*Krameria erecta*	100 (mmol m^{-2} s^{-1})	Mean chamber air temperature = 28.5°C	Average daily stomatal conductance measurements made in the field at the FACE site during various months. Three low values indicating stomatal closure were omitted.
		90 (mmol m^{-2} s^{-1})	28.5°C	
		90 (mmol m^{-2} s^{-1})	28.5°C	
		140 (mmol m^{-2} s^{-1})	19.0°C	
		50 (mmol m^{-2} s^{-1})	28.5°C	

Table D−17. Stomatal Conductance References and Values for Mojave Desert Plant Species (Continued)

Reference	Species	Stomatal Conductance	Temperature	Comments
		30 (mmol m^{-2} s^{-1})	28.5°C	
		75 (mmol m^{-2} s^{-1})	28.5°C	
		75 (mmol m^{-2} s^{-1})	28.5°C	
		50 (mmol m^{-2} s^{-1})	28.5°C	
		50 (mmol m^{-2} s^{-1})	28.5°C	
		75 (mmol m^{-2} s^{-1})	28.5°C	
		40 (mmol m^{-2} s^{-1})	28.5°C	
Hamerlynck et al. 2000 [DIRS 177130], p. 188	Larrea tridentata	400 (mmol m^{-2} s^{-1})	Chamber air temperature = 30.0°C	Glasshouse study at UNLV[2]. Pre− and post-heat treatments under well watered and drought conditions. Measurements made during high heat treatment were not used. Measurements made under drought conditions were used to represent low values expected of older leaves near senescence.
		500 (mmol m^{-2} s^{-1})	30.0°C	
		750 (mmol m^{-2} s^{-1})	30.0°C	
		200 (mmol m^{-2} s^{-1})	30.0°C	
		150 (mmol m^{-2} s^{-1})	30.0°C	
		25 (mmol m^{-2} s^{-1})	30.0°C	
		100 (mmol m^{-2} s^{-1})	30.0°C	
		25 (mmol m^{-2} s^{-1})	30.0°C	
Hamerlynck et al. 2004 [DIRS 176045], p. 213	*Larrea tridentata*	120 (mmol m^{-2} s^{-1})	Air temperature = 27.0°C	Measurements made in field in the Mojave National Preserve, CA, during peak growth and dry period. Plants grown on dune soils.
		85 (mmol m^{-2} s^{-1})	35.0°C	Measurement made during dry period used to represent low values expected of older leaves near senescence.
Hamerlynck et al. 2000 [DIRS 177022], p. 602	*Larrea tridentata*	110 (mmol m^{-2} s^{-1})	Chamber temperature = 20.0°C	Measurements made in field in the Mojave National Preserve, CA, at various times throughout growing season. Plants grown on dune soils. Measurements made during dry periods were used to represent low values expected of older leaves near senescence.
		70 (mmol m^{-2} s^{-1})	12.0°C	
		120 (mmol m^{-2} s^{-1})	25.0°C	
		85 (mmol m^{-2} s^{-1})	35.0°C	
		80 (mmol m^{-2} s^{-1})	40.0°C	
		80 (mmol m^{-2} s^{-1})	30.0°C	
		65 (mmol m^{-2} s^{-1})	40.0°C	
		65 (mmol m^{-2} s^{-1})	40.0°C	
		70 (mmol m^{-2} s^{-1})	30.0°C	
Naumburg et al. 2003 [DIRS 177143], p. 280, Figure 3)	*Larrea tridentata*	125 (mmol m^{-2} s^{-1})	Mean prevailing air temperature during measurements = 28.5°C	Measurements made in field at FACE facility over the course of four years. One value measured in December was omitted. Five low values indicating stomatal closure were omitted.
		50 (mmol m^{-2} s^{-1})	28.5°C	
		125 (mmol m^{-2} s^{-1})	28.5°C	
		100 (mmol m^{-2} s^{-1})	28.5°C	
		50 (mmol m^{-2} s^{-1})	28.5°C	
		30 (mmol m^{-2} s^{-1})	28.5°C	
		125 (mmol m^{-2} s^{-1})	19.0°C	
		30 (mmol m^{-2} s^{-1})	28.5°C	
		40 (mmol m^{-2} s^{-1})	28.5°C	

Table D−17. Stomatal Conductance References and Values for Mojave Desert Plant Species (Continued)

Reference	Species	Stomatal Conductance	Temperature	Comments
		100 (mmol m^{-2} s^{-1})	28.5°C	
		50 (mmol m^{-2} s^{-1})	28.5°C	
		40 (mmol m^{-2} s^{-1})	28.5°C	
		30 (mmol m^{-2} s^{-1})	28.5°C	
		30 (mmol m^{-2} s^{-1})	28.5°C	
Pataki et al. (2000 [DIRS 177161], p. 893)	*Larrea tridentata*	90 (mmol m^{-2} s^{-1})	Average air temperature during measurement period = 24.0°C	Measurements made in field at FACE facility midJune through midJuly.
		90 (mmol m^{-2} s^{-1})	24.0°C	
		80 (mmol m^{-2} s^{-1})	24.0°C	
		80 (mmol m^{-2} s^{-1})	24.0°C	
		80 (mmol m^{-2} s^{-1})	24.0°C	
		80 (mmol m^{-2} s^{-1})	24.0°C	
		90 (mmol m^{-2} s^{-1})	24.0°C	
		90 (mmol m^{-2} s^{-1})	24.0°C	
		90 (mmol m^{-2} s^{-1})	24.0°C	
		90 (mmol m^{-2} s^{-1})	24.0°C	
		90 (mmol m^{-2} s^{-1})	24.0°C	
		70 (mmol m^{-2} s^{-1})	24.0°C	
		80 (mmol m^{-2} s^{-1})	24.0°C	
		70 (mmol m^{-2} s^{-1})	24.0°C	
		80 (mmol m^{-2} s^{-1})	24.0°C	
		70 (mmol m^{-2} s^{-1})	24.0°C	
		70 (mmol m^{-2} s^{-1})	24.0°C	
		70 (mmol m^{-2} s^{-1})	24.0°C	
		70 (mmol m^{-2} s^{-1})	24.0°C	
		70 (mmol m^{-2} s^{-1})	24.0°C	
		70 (mmol m^{-2} s^{-1})	24.0°C	
		60 (mmol m^{-2} s^{-1})	24.0°C	
		60 (mmol m^{-2} s^{-1})	24.0°C	
		60 (mmol m^{-2} s^{-1})	24.0°C	
		60 (mmol m^{-2} s^{-1})	24.0°C	
		50 (mmol m^{-2} s^{-1})	24.0°C	
		60 (mmol m^{-2} s^{-1})	24.0°C	
		50 (mmol m^{-2} s^{-1})	24.0°C	
		50 (mmol m^{-2} s^{-1})	24.0°C	
		50 (mmol m^{-2} s^{-1})	24.0°C	
		50 (mmol m^{-2} s^{-1})	24.0°C	
		50 (mmol m^{-2} s^{-1})	24.0°C	
		90 (mmol m^{-2} s^{-1})	24.0°C	
		60 (mmol m^{-2} s^{-1})	24.0°C	
		160 (mmol m^{-2} s^{-1})	24.0°C	Maximum diurnal value

Table D−17. Stomatal Conductance References and Values for Mojave Desert Plant Species (Continued)

Reference	Species	Stomatal Conductance	Temperature	Comments
		160 (mmol m^{-2} s^{-1})	24.0°C	Maximum diurnal value
		100 (mmol m^{-2} s^{-1})	24.0°C	Maximum diurnal value
Pataki et al. (2000 [DIRS 177161], p. 893)	*Ephedra nevadensis*	190 (mmol m^{-2} s^{-1})	Average air temperature during measurement period = 24.0°C	Measurements made in field at FACE site mid-June through mid-July
		190 (mmol m^{-2} s^{-1})	24.0°C	
		170 (mmol m^{-2} s^{-1})	24.0°C	
		170 (mmol m^{-2} s^{-1})	24.0°C	
		160 (mmol m^{-2} s^{-1})	24.0°C	
		150 (mmol m^{-2} s^{-1})	24.0°C	
		170 (mmol m^{-2} s^{-1})	24.0°C	
		160 (mmol m^{-2} s^{-1})	24.0°C	
		150 (mmol m^{-2} s^{-1})	24.0°C	
		160 (mmol m^{-2} s^{-1})	24.0°C	
		160 (mmol m^{-2} s^{-1})	24.0°C	
		120 (mmol m^{-2} s^{-1})	24.0°C	
		130 (mmol m^{-2} s^{-1})	24.0°C	
		130 (mmol m^{-2} s^{-1})	24.0°C	
		130 (mmol m^{-2} s^{-1})	24.0°C	
		120 (mmol m^{-2} s^{-1})	24.0°C	
		130 (mmol m^{-2} s^{-1})	24.0°C	
		130 (mmol m^{-2} s^{-1})	24.0°C	
		130 (mmol m^{-2} s^{-1})	24.0°C	
		120 (mmol m^{-2} s^{-1})	24.0°C	
		130 (mmol m^{-2} s^{-1})	24.0°C	
		120 (mmol m^{-2} s^{-1})	24.0°C	
		120 (mmol m^{-2} s^{-1})	24.0°C	
		120 (mmol m^{-2} s^{-1})	24.0°C	
		110 (mmol m^{-2} s^{-1})	24.0°C	
		90 (mmol m^{-2} s^{-1})	24.0°C	
		110 (mmol m^{-2} s^{-1})	24.0°C	
		110 (mmol m^{-2} s^{-1})	24.0°C	
		70 (mmol m^{-2} s^{-1})	24.0°C	
		60 (mmol m^{-2} s^{-1})	24.0°C	
		60 (mmol m^{-2} s^{-1})	24.0°C	
		50 (mmol m^{-2} s^{-1})	24.0°C	
		80 (mmol m^{-2} s^{-1})	24.0°C	
		60 (mmol m^{-2} s^{-1})	24.0°C	
Smith et al. (1995 [DIRS 103628], p. 343)	*Ephedra nevadensis*	0.078 (mol m^{-2} s^{-1})	Temperature = 25°C	Maximum daily stomatal conductance measurements made at field sites in Crater Flat March through September. Conductance values are means for three locations (slope, bench, and wash). Two
		0.075 (mol m^{-2} s^{-1})	25°C	
		0.093 (mol m^{-2} s^{-1})	25°C	
		0.060 (mol m^{-2} s^{-1})	25°C	
		0.033 (mol m^{-2} s^{-1})	25°C	

Table D−17. Stomatal Conductance References and Values for Mojave Desert Plant Species (Continued)

Reference	Species	Stomatal Conductance	Temperature	Comments
		0.015 (mol m^{-2} s^{-1})	25°C	measurements made in mid-October and mid-December were omitted. Temperature was not reported in study.
		0.025 (mol m^{-2} s^{-1})	25°C	
Smith et al. (1995 [DIRS 103628], p. 344)	*Ericameria cooperi*[3]	0.18 (mol m^{-2} s^{-1})	Temperature = 25°C	Maximum daily stomatal conductance measurements made at field sites in Crater Flat March through September. Values are means for two locations (slope and bench). Two measurements made in mid-October and mid-December were omitted. One low measurement in August indicating stomatal closure was omitted.
		0.15 (mol m^{-2} s^{-1})	25°C	
		0.2 (mol m^{-2} s^{-1})	25°C	
		0.085 (mol m^{-2} s^{-1})	25°C	
		0.09 (mol m^{-2} s^{-1})	25°C	
		0.04 (mol m^{-2} s^{-1})	25°C	

[1] University of Nevada Las Vegas.
[2] Nevada Desert Free-Air CO_2 Enrichment (FACE) facility.
[3] Reported in Smith et al. 1995 [DIRS 103628] as *Happlopapus cooperi*.

Equation D-6 requires stomatal resistance (r_l, the inverse of stomatal conductance) to diffusion of water vapor in units of s m^{-1}. Therefore, published stomatal conductance values were converted from units of mol m^{-2} s^{-1} to velocity units in m s^{-1} according to the following conversion factor (LI-COR 1989 [DIRS 177166], p. 3-5):

$$g_v = \frac{\left(g_m \times R \times T_l\right)}{P} \qquad \text{(Eq. D-12)}$$

where

g_v = stomatal conductance in velocity units (m s^{-1}),
g_m = stomatal conductance in molar units (mol m^{-2} s^{-1}),
R = universal gas constant (8.314 Pa m^3 mol^{-1} K^{-1}),
T_l = leaf temperature (K),
P = atmospheric pressure (Pa).

Atmospheric pressure is dependent on elevation. The FACE facility, where most of the conductance data were measured, is at an elevation of 970 m (Naumburg et al. 2003 [DIRS 177143], p. 277), and the study in Crater Flat by Smith et al. (1995 [DIRS 103628], p. 340) was conducted at 1,300 m. To generate resistance values that would be representative of dominant vegetation types at Yucca Mountain, atmospheric pressure was determined for the elevations at which most of the conductance measurements were made and for two additional elevations at Yucca Mountain. Atmospheric pressure for the four elevations were determined from Allen et al. (1998 [DIRS 157311], Table 2.1, pp. 213 and 214). The mean of these pressures (Table D-18) was used in the conductance conversion calculations for all species except *L. tridentata*. Because *L. tridentata* is generally absent above 1,350 m (Rundel and Gibson 1996 [DIRS 103614], p. 84), mean atmospheric pressures for 970 m and 1,300 m were used in the conversion calculations for this species (Table D-18).

Table D-18. Elevation and Atmospheric Pressure

Elevation (m)	Atmospheric Pressure[a] (Pa)	Mean Atmospheric Pressure (Pa)
970[b]	90,300	*L. tridentata* = 88,550
1,300[c]	86,800	
1,400	85,800	86,925
1,500	84,800	

Sources: [a] From Allen et al. 1998 [DIRS 157311], Table 2.1, pp. 213 and 214.
[b] Naumburg et al. 2003 [DIRS 177143], p. 277.
[c] Smith et al. (1995 [DIRS 103628], p. 340.

The leaf temperature at which conductance measurements were made was reported for some of the studies (Table D-17). In cases where leaf temperature was not reported, the ambient air temperature at which the study was conducted was used. Smith et al. (1995 [DIRS 103628]) did not report leaf or air temperatures at which conductance measurements were made. In this case, a temperature of 25°C was used to represent the temperature at which plants generally operate at full stomatal opening.

Temperatures were converted from °C to K:

$$K = °C + 273.15 \quad \text{(Eq. D-13)}$$

Conversions of stomatal conductance from molar units to velocity units and temperature from Celsius to kelvin are in Table D-19. Prior to conversions (Table D-19, column 3), conductance data were sorted for each species and assigned to initial, mid, and end of late season stages. Maximum stomatal conductance rates are species specific and vary across vegetation types. In general, annual species exhibit higher conductances, followed by drought deciduous, then evergreen species. To determine high and low values, conductances were examined for each species within a vegetation type. High values measured on nonstressed plants were assigned to the midseason stage for each species. Low conductance values, generally 0.10 mol m^{-2} s^{-1} or less and 0.08 mol m^{-2} s^{-1} or less (depending on the species), were assigned to the initial stage and end of late stages, respectively, to represent the lower values expected of emerging or senescesing leaves. In cases where only one low conductance value was available (e.g., Bromus madritensis), it was used for both the initial and end of late season stages. For some species (e.g., *L. andersonii*) only high values appropriate for the midseason stage were reported in the reviewed literature.

Table D-19. Stomatal Conductance Values Converted From Molar Units to Velocity Units

Species	Growth Stage	g^1 (mol m^{-2} s^{-1})	T^2 (°C)	T^3 (K)	g^4 (m s^{-1})
Annual Species					
Bromus madritensis ssp. *rubens*	Initial/End	0.1	21	294.15	0.0028
		0.1	27	300.15	0.0029
	Mid	0.75	25	298.15	0.0214
		0.50	25	298.15	0.0143
		0.18	15	288.15	0.0050

Table D−19. Stomatal Conductance Values Converted From Molar Units to Velocity Units (Continued)

Species	Growth Stage	g[1] (mol m^{-2} s^{-1})	T[2] (°C)	T[3] (K)	g[4] (m s^{-1})
Bromus madritensis ssp. *rubens*	Mid	0.3	18	291.15	0.0084
		0.2	24	297.15	0.0057
Drought Deciduous Species					
Ambrosia dumosa	Initial	0.09	28.5	301.65	0.0026
	Mid	0.3	19	292.15	0.0084
		0.2	19	292.15	0.0056
		0.2	28.5	301.65	0.0058
	End	0.05	28.5	301.65	0.0014
		0.05	28.5	301.65	0.0014
		0.05	28.5	292.15	0.0014
Krameria erecta	Initial	0.1	28.5	301.65	0.0029
		0.09	28.5	301.65	0.0026
		0.09	28.5	301.65	0.0026
		0.075	28.5	301.65	0.0022
		0.075	28.5	301.65	0.0022
		0.075	28.5	301.65	0.0022
	Mid	0.14	19	292.15	0.0039
	End	0.05	28.5	301.65	0.0014
		0.05	28.5	301.65	0.0014
		0.04	28.5	301.65	0.0012
		0.03	28.5	301.65	0.0009
		0.05	28.5	301.65	0.0014
Lycium andersonii	Mid	0.225	20.8	293.95	0.0063
		0.39	20.8	293.95	0.0110
		0.25	20.8	293.95	0.0070
		0.525	20.8	293.95	0.0148
		0.375	20.8	293.95	0.0105
Evergreen Species					
Ephedra nevadensis	Initial	0.1100	24	297.15	0.0031
		0.1100	24	297.15	0.0031
		0.1100	24	297.15	0.0031
		0.0933	25	298.15	0.0027
		0.0900	24	297.15	0.0026
	Mid	0.1900	24	297.15	0.0054
		0.1900	24	297.15	0.0054
		0.1700	24	297.15	0.0048
		0.1700	24	297.15	0.0048
		0.1700	24	297.15	0.0048
		0.1600	24	297.15	0.0045
		0.1600	24	297.15	0.0045
		0.1500	24	297.15	0.0043
		0.1600	24	297.15	0.0045
		0.1600	24	297.15	0.0045
		0.1500	24	297.15	0.0043

Table D−19. Stomatal Conductance Values Converted From Molar Units to Velocity Units (Continued)

Species	Growth Stage	g[1] (mol m^{-2} s^{-1})	T[2] (°C)	T[3] (K)	g[4] (m s^{-1})
Ephedra nevadensis	Mid	0.1300	24	297.15	0.0037
		0.1300	24	297.15	0.0037
		0.1300	24	297.15	0.0037
		0.1300	24	297.15	0.0037
		0.1300	24	297.15	0.0037
		0.1300	24	297.15	0.0037
		0.1300	24	297.15	0.0037
		0.1200	24	297.15	0.0034
		0.1200	24	297.15	0.0034
		0.1200	24	297.15	0.0034
		0.1200	24	297.15	0.0034
		0.1200	24	297.15	0.0034
		0.1200	24	297.15	0.0034
	End	0.0800	24	297.15	0.0023
		0.0783	25	298.15	0.0022
		0.0750	25	298.15	0.0021
		0.0700	24	297.15	0.0020
		0.0600	25	298.15	0.0017
		0.0600	24	297.15	0.0017
		0.0600	24	297.15	0.0017
		0.0600	24	297.15	0.0017
		0.0500	24	297.15	0.0014
		0.0330	25	298.15	0.0009
		0.0250	25	298.15	0.0007
		0.0150	25	298.15	0.0004
Ericameria cooperi[1]	Initial	0.0900	25	298.15	0.0026
	Mid	0.0850	25	298.15	0.0024
		0.2000	25	298.15	0.0057
		0.1800	25	298.15	0.0051
		0.1500	25	298.15	0.0043
		0.0400	25	298.15	0.0011
Larrea tridentata	Initial	0.090	24	297.15	0.0025
		0.090	24	297.15	0.0025
		0.090	24	297.15	0.0025
		0.090	24	297.15	0.0025
		0.090	24	297.15	0.0025
		0.090	24	297.15	0.0025
		0.090	24	297.15	0.0025
		0.090	24	297.15	0.0025
		0.085	35	308.15	0.0025
	Mid	0.750	30	303.15	0.0213
		0.500	30	303.15	0.0142
		0.400	30	303.15	0.0114
		0.200	30	303.15	0.0057

Table D−19. Stomatal Conductance Values Converted From Molar Units to Velocity Units (Continued)

Species	Growth Stage	g^1 (mol m^{-2} s^{-1})	T^2 (°C)	T^3 (K)	g^4 (m s^{-1})
Larrea tridentata	Mid	0.160	24	297.15	0.0045
		0.160	24	297.15	0.0045
		0.150	30	303.15	0.0043
		0.125	28.5	301.65	0.0035
		0.125	28.5	301.65	0.0035
		0.125	19	292.15	0.0034
		0.120	27	300.15	0.0034
		0.120	25	298.15	0.0034
		0.110	20	293.15	0.0030
		0.100	30	303.15	0.0028
		0.100	28.5	301.65	0.0028
		0.100	28.5	301.65	0.0028
		0.100	24	297.15	0.0028
	End	0.085	35	308.15	0.0025
		0.080	40	313.15	0.0024
		0.080	30	303.15	0.0023
		0.080	24	297.15	0.0022
		0.080	24	297.15	0.0022
		0.080	24	297.15	0.0022
		0.080	24	297.15	0.0022
		0.080	24	297.15	0.0022
		0.080	24	297.15	0.0022
		0.070	30	303.15	0.0020
		0.070	24	297.15	0.0020
		0.070	24	297.15	0.0020
		0.070	24	297.15	0.0020
		0.070	24	297.15	0.0020
		0.070	24	297.15	0.0020
		0.070	24	297.15	0.0020
		0.070	24	297.15	0.0020
		0.070	24	297.15	0.0020
		0.065	40	313.15	0.0019
		0.065	40	313.15	0.0019
		0.070	12	285.15	0.0019
		0.060	24	297.15	0.0017
		0.060	24	297.15	0.0017
		0.060	24	297.15	0.0017
		0.060	24	297.15	0.0017
		0.060	24	297.15	0.0017
		0.060	24	297.15	0.0017
		0.050	28.5	301.65	0.0014
		0.050	28.5	301.65	0.0014
		0.050	28.5	301.65	0.0014
		0.050	24	297.15	0.0014

Table D−19. Stomatal Conductance Values Converted From Molar Units to Velocity Units (Continued)

Species	Growth Stage	g^1 (mol m^{-2} s^{-1})	T^2 (°C)	T^3 (K)	g^4 (m s^{-1})
Larrea tridentata	End	0.050	24	297.15	0.0014
		0.050	24	297.15	0.0014
		0.050	24	297.15	0.0014
		0.050	24	297.15	0.0014
		0.050	24	297.15	0.0014
		0.040	28.5	301.65	0.0011
		0.040	28.5	301.65	0.0011
		0.030	28.5	301.65	0.0008
		0.030	28.5	301.65	0.0008
		0.030	28.5	301.65	0.0008
		0.030	28.5	301.65	0.0008
		0.025	30	303.15	0.0007
		0.025	30	303.15	0.0007

[1] Stomatal conductance in molar units. Sources are listed in Table D-17.
[2] Air or leaf temperature for stomatal conductance measurements. Sources are listed in Table D-17.
[3] Air or leaf temperature for stomatal conductance measurements converted from Celsius to kelvin (Equation D-13).
[4] Stomatal conductance converted from molar units to velocity units (Equation D-12).

Weighted mean g_v for growth stages for the drought deciduous and evergreen vegetation within each association, and for the three years under consideration, were determined. Means were weighted according to relative cover values for each species included in the calculation of mean conductance. Relative cover was determined from Tables D-7 through D-15 by dividing cover per species by the total cover for species that were included in the calculation of mean conductance. Weighting factors and weighted mean conductances are in Table D-20. Because *Bromus madritensis* was the only species used for annual vegetation, it was not necessary to weight those means.

Table D-20. Weighting Factors and Weighted Conductance Means

Vegetation Type/Species	Growth Stage	Weighting Factor[1]			Weighted Mean g^2 (m/s)		
		1990	1991	1993	1990	1991	1993
LA Vegetation Association							
Drought Deciduous							
Ambrosia dumosa	Initial	0.866	0.894	0.982	0.0026	0.0026	0.0026
Krameria erecta	Initial	0.134	0.106	0.018			
Ambrosia dumosa	Mid	0.853	0.869	0.957	0.0063	0.0064	0.0067
Krameria erecta	Mid	0.132	0.103	0.018			
Lycium andersonii	Mid	0.015	0.028	0.025			
Ambrosia dumosa	End	0.866	0.894	0.982	0.0014	0.0014	0.0014
Krameria erecta	End	0.134	0.106	0.018			

Table D-20. Weighting Factors and Weighted Conductance Means (Continued)

Vegetation Type/Species	Growth Stage	Weighting Factor[1]			Weighted Mean g^2 (m/s)		
		1990	1991	1993	1990	1991	1993
Evergreen							
Ephedra nevadensis	Initial	0.323	0.297	0.209	0.0026	0.0026	0.0026
Ericameria cooperi	Initial	0.207	0.019	0.013			
Larrea tridentata	Initial	0.470	0.684	0.778			
Ephedra nevadensis	Mid	0.323	0.297	0.209	0.0048	0.0052	0.0054
Ericameria cooperi	Mid	0.207	0.019	0.013			
Larrea tridentata	Mid	0.470	0.684	0.778			
Ephedra nevadensis	End	0.407	0.303	0.212	0.0016	0.0016	0.0017
Larrea tridentata	End	0.593	0.697	0.788			
LG Vegetation Association							
Drought Deciduous							
Ambrosia dumosa	Initial	1.0	1.0	1.0	0.0026	0.0026	0.0026
Krameria erecta	Initial	0	0	0			
Ambrosia dumosa	Mid	0.156	0.314	0.284	0.0094	0.0089	0.0090
Krameria erecta	Mid	0	0	0			
Lycium andersonii	Mid	0.844	0.686	0.716			
Ambrosia dumosa	End	1	1	1	0.0014	0.0014	0.0014
Krameria erecta	End	0	0	0			
Evergreen							
Ephedra nevadensis	Initial	0.609	0.697	0.664	0.0028	0.0028	0.0028
Ericameria cooperi	Initial	0.366	0.275	0.310			
Larrea tridentata	Initial	0.026	0.028	0.025			
Ephedra nevadensis	Mid	0.609	0.697	0.664	0.0041	0.0041	0.0041
Ericameria cooperi	Mid	0.366	0.275	0.310			
Larrea tridentata	Mid	0.026	0.028	0.025			
Ephedra nevadensis	End	0.960	0.962	0.963	0.0016	0.0016	0.0016
Larrea tridentata	End	0.041	0.039	0.037			
LLG Vegetation Association							
Drought Deciduous							
Ambrosia dumosa	Initial	0.438	0.338	0.724	0.0025	0.0025	0.0026
Krameria erecta	Initial	0.562	0.662	0.276			
Ambrosia dumosa	Mid	0.345	0.278	0.552	0.0061	0.0057	0.0068
Krameria erecta	Mid	0.442	0.546	0.211			
Lycium andersonii	Mid	0.212	0.176	0.238			
Ambrosia dumosa	End	0.438	0.338	0.724	0.0013	0.0013	0.0014
Krameria erecta	End	0.562	0.662	0.276			

Table D-20. Weighting Factors and Weighted Conductance Means (Continued)

Vegetation Type/Species	Growth Stage	Weighting Factor[1]			Weighted Mean g[2] (m/s)		
		1990	1991	1993	1990	1991	1993
Evergreen							
Ephedra nevadensis	Initial	0.436	0.471	0.405	0.0027	0.0027	0.0027
Ericameria cooperi	Initial	0.112	0.021	0.026			
Larrea tridentata	Initial	0.452	0.508	0.569			
Ephedra nevadensis	Mid	0.436	0.471	0.405	0.0048	0.0049	0.0050
Ericameria cooperi	Mid	0.112	0.021	0.026			
Larrea tridentata	Mid	0.452	0.508	0.569			
Ephedra nevadensis	End	0.491	0.481	0.416	0.0016	0.0016	0.0016
Larrea tridentata	End	0.509	0.519	0.584			

[1] Weighting factor was determined from cover per species divided by the sum of cover for all species included in the mean stomatal conductance calculation. Cover values used to calculate weighting factors are in Tables D-7 through D-15.

[2] Mean stomatal conductance per vegetation type for growth stages. Mean conductance per species were calculated from Table D-18. The mean conductances were multiplied by species specific weighting factors then summed to get an average per vegetation type for each vegetation association.

The weighted mean conductances were converted to r_l according to Equation D-14 (Table D-21).

$$r_l = \frac{1}{g_v} \qquad \text{(Eq. D-14)}$$

where: r_l = stomatal resistance (s m^{-1})

Mean r_l values for growth stages and vegetation types (Table D-21) were used in Equation D-6 to calculate F_r (see Section D4 for example calculation).

Table D-21. Mean Stomatal Resistance Values Used in Transpiration Coefficient Calculations

Vegetation Association	Vegetation Type	Growth Stage	Mean rl (s/m)[1]		
All Associations[2]	Annual	Initial/End	345		
		Mid	91		
			1990	1991	1993
LA	Drought Deciduous	Initial	385	385	385
		Mid	159	156	149
		End	714	714	714
	Evergreen	Initial	385	385	385
		Mid	208	192	185
		End	625	625	588
LG	Drought Deciduous	Initial	385	385	385
		Mid	106	112	111
		End	714	714	714
	Evergreen	Initial	357	357	357
		Mid	244	244	244
		End	625	625	625

Table D−21. Mean Stomatal Resistance Values Used in Transpiration Coefficient Calculations (Continued)

Vegetation Association	Vegetation Type	Growth Stage	Mean rl (s/m)[1]		
LLG	Drought Deciduous	Initial	400	400	385
		Mid	164	175	147
		End	769	769	714
	Evergreen	Initial	370	370	370
		Mid	208	204	200
		End	625	625	625

[1] Mean stomatal resistance (r_l) of plant species in each vegetation type. Inputs are weighted mean stomatal conductances from Table D-20. Stomatal resistance was calculated using Equation D-14. Resistance values were rounded to the nearest whole number.

[2] Annuals were represented by *Bromus madritensis* in all associations.

D3.2.4 Meteorological Parameters

Precipitation data used in Appendices E and F, and meteorological parameters required to calculate K_{cb} and generic ET_0, are developed in this section. Meteorological parameters were either measured directly or derived from measured values (e.g., solar radiation).

Atmospheric humidity is an important driver of transpiration from plant leaves and affects stomatal behavior. The air in the intercellular spaces of a leaf is nearly saturated with water vapor (Section D2.1). As the air outside the leaf dries, the leaf-to-air water vapor gradient increases, increasing the rate of water loss through the stomata (Section D2.1). With increasing evaporative demands the plant will begin to close stomata to prevent water loss. However, stomatal closure also results in reduced concentrations of CO_2 for use in photosynthesis. Similarly, when atmospheric humidity is high, the leaf-to-air water vapor gradient decreases. This results in lower evaporative demand, allowing stomates to remain open without high rates of water loss. One humidity parameter (minimum daily relative humidity [RH_{min}]) was required for the calculation of $K_{cb\ full}$, and two (slope of the saturation vapor pressure curve [Δ] and the psychrometric constant [γ]) were required for the calculation of F_r (Equations D-4 and D-6, respectively). Mean daily air temperature (T) and wind speed at a height of 2 m (u_2) were also required for K_{cb} calculations. In addition to these parameters, the calculation of ET_0 (Section D5) required minimum and maximum daily air temperature and solar radiation (R_s). Precipitation data for the 1990, 1991, 1993, 1998, 2001, and 2002 water years were required for analyses in Appendices E and F.

Data from Yucca Mountain Meteorological Monitoring Sites—The Yucca Mountain Project has been collecting meteorological data from a network of nine sites since 1985. Meteorological data for calculations of K_{cb} and ET_0 for a generic location were taken from Yucca Mountain Meteorological Sites 1 and 4. Site 1 is the main meteorological tower located in western Midway Valley at an elevation of 1,143 m. Midway Valley is bounded on the west by Yucca Mountain. Site 4 is located on Alice Hill in the northeastern portion of Midway Valley at an elevation of 1,234 m (CRWMS M&O 1999 [DIRS 115672], pp. 1-1 to 1-6). Site 4 was selected because it was closest in elevation to Site 1 and it was used mainly for data substitutions when Site 1 data were missing.

Weather data collected at the Yucca Mountain monitoring sites during the years that vegetation cover was measured on ESPs (1990, 1991, and 1993) may be less reliable than data collected in later years. With the exception of precipitation, the weather data for 1990 and 1991 were not qualified for use at the time of this analysis, and possible errors were identified in 1993 precipitation data for Site 1. As described in Section D2.2, the years for cover data use were selected to correspond with the average, above average, and below average precipitation years that were selected for NDVI' analysis. For the NDVI' analysis, 2001 (average precipitation), 1998 (above average preciptiation), and 2002 (below average precipitation) were used. The RH_{min} and u_2 corrections to K_{cb}s used in Equation D-4 represent regional differences in arid climates compared to the representative subhumid climate with calm wind conditions in FAO-56 methods (Allen et al. 1998 [DIRS 157311]). While it is important to capture regional differences in RH_{min} and u_2 to increase the accuracy of K_{cb}s for arid climates, variation between years with similar precipitation within an arid climate have little effect on K_{cb}s (see below). Therefore, it was determined that use of weather data from 1998, 2001, and 2002 paired with cover data from 1993, 1991, and 1990, respectively, would be adequate for calculating K_{cb}s for above average, average, and below average precipitation years and would avoid use of unqualified weather data.

Hourly wind speed measured at a height of 10 m (u_{10}), T, and R_s data for 1997, 1998, 2000, 2001, and 2002 were taken from Site 1, which provided the most data for those years. Hourly relative humidity data for 1997 and 1998 were not collected at Site 1, and so data from Site 4 were used. Hourly relative humidity (RH) data for 2000, 2001, and 2002 were taken from Site 1. Source data were taken from DTNs: MO0312SEPQ1997.001 [DIRS 167116], MO0206SEPQ1998.001 [DIRS 166731], MO0209SEPQ2000.001 [DIRS 166730], MO0305SEP01MET.002 [DIRS 166164], and MO0305SEP02MET.002 [DIRS 166163].

Precipitation data were taken from Sites 1, 2 (located on the Yucca Mountain crest at an elevation of 1,478 m), 3 (located in Coyote Wash at an elevation of 1,279 m), and 4. This was done to evaluate precipitation at different elevations on the mountain in Appendix E (1997 to 2002) and to scale NDVI' by precipitation that fell during water years that cover data were collected for (1989 to 1993). The source data for 1997, 1998, 2000, 2001, and 2002 were from DTNs: MO0312SEPQ1997.001 [DIRS 167116], MO0206SEPQ1998.001 [DIRS 166731], MO0209SEPQ2000.001 [DIRS 166730], MO0305SEP01MET.002 [DIRS 166164], and MO0305SEP02MET.002 [DIRS 166163], respectively. The source data for 1989 to 1992 were from DTN: MO0606SEPRECIP.001 [DIRS 177136][2]. The source data for 1993 were from DTN: MO0312SEPQ1993.001 [DIRS 176092].

For 1997 to 2002, hourly temperature, wind speed, relative humidity, precipitation and solar radiation data were extracted from the source files and placed in Excel® files (Output DTN: MO0602SPAWEATH.000, “metadata” files for each year). Data that were not needed for this analysis were omitted from the files, resulting in spreadsheets with hourly wind speed, air temperature, relative humidity, precipitation and solar radiation for Site 1 (Output DTN: MO0602SPAWEATH.000), and precipitation for Sites 2, 3, and 4 (Output

[2]When the calculations were done, the source data was obtained from DTN: MO0604SEPRECIP.000, which was later superseded by the above DTN. The source data used from the original DTN was not altered in the superseding DTNs as determined by a comparison check.

DTN: MO0602SPAPRECP.000). The new files were sorted according to Julian Day and time of day and formatted into water years (October 1 to September 30).

Missing data in the source files were identified in cells by 9999. These values were located in the Excel® files and removed using the Find/Replace command. For Site 1, missing temperature, wind speed, relative humidity, and precipitation data were omitted if only 1 or 2 hours out of a day were affected. If more than 2 hours were affected, the data were replaced with data from YMP meteorological monitoring Site 4. All missing solar radiation data were replaced with data from YMP meteorological monitoring Site 4. A record of data replacement was created and placed in a worksheet titled data corrections in each of the Excel® files (Output DTN: MO0602SPAWEATH.000, "metadata" files for each year). Missing precipitation data for Sites 2, 3, and 4 (water years 1998, 2001, and 2002) were identified in a notes column in the Excel® file (Output DTN: MO0602SPAPRECP.000). With one exception, all missing precipitation data for water years 1998, 2001, and 2002 occurred during time periods when no precipitation occurred at the site, and so were not replaced. For water year 1998, day 54, at monitoring Site 3, two hours of data were missing when precipitation might have occurred. However, because of the short time period, the missing data were not replaced.

Hourly precipitation data for 1989 to 1993 (Sites 2, 3, and 4) were extracted from the source files and placed in an Excel® file with separate worksheets for each year (Output DTN: MO0605SEPTOTAL.002). The data were formatted into water years 1990, 1991, and 1993. Missing data in the source files were identified by 9999. Missing data were replaced in the Excel files with data from remaining stations. This was necessary because the gauge for Site 4 was not installed until February 5, 1990, resulting in six missed precipitation events for the water year, and several additional storms were missed at Sites 2, 3, and 4 over the course of the three water years due to gauge malfunctions. For data replacement, the inverse-distance-squared method of interpolating between sites using the following equation was considered for use:

Weighting Factor$_i$ = $(1/(d_i^2))/S_i(1/(d_i^2))$ where d_i is the distance of station *i* from the indicated coordinates.

However, because the three sites are situated in close proximity and only two were used at any one time to average, this method produced negligible differences compared to taking a simple average of the two sites. Therefore, the mean of two sites was used when a value was missing at one site during a precipitation event. If precipitation was recorded at only one site, and gauges malfunctioned at the other two, the recorded amount was used to replace the missing data at the two malfunctioning sites.

To develop daily totals for solar radiation from hourly values, negative values and values less than one that were recorded for night-time hours were deleted from the dataset (Output DTN: MO0602SPAWEATH.000, "metadata" files). The hourly data were then summed for each day and converted from watts per square meter to megajoules per square meter per day by multiplying the daily sums by the conversion factor 0.0036 (IEEE/ASTM 1997 [DIRS 151762]). These calculations and results are contained in the Excel® files in Output DTN: MO0602SPAWEATH.000.

Daily average wind speed and air temperature were determined from the hourly data using the Excel® command AVERAGE (Output DTN: MO0602SPAWEATH.000, "metadata" files). Daily minimum relative humidity (RH_{min}), minimum air temperature, and maximum air temperature were determined from the hourly data using the Excel® commands MINIMUM and MAXIMUM (Output DTN: MO0602SPAWEATH.000, "metadata" files). Daily precipitation totals for the 1998, 2000, and 2001 water years were determined from the hourly data, and yearly totals were determined from the daily totals using the Excel® command SUM (Output DTN: MO0602SPAPRECP.000). Yearly precipitation totals for the 1990, 1991, and 1993 water years were determined from hourly data using the Excel® command SUM (Output DTN: MO0605SEPTOTAL.002). These calculations and results are contained in the Excel® files in Output DTNs: MO0602SPAWEATH.000, MO0602SPAPRECP.000, and MO0605SEPTOTAL.002.

FAO-56 methodology (Allen et al. 1998 [DIRS 157311]) requires wind speed measurements at 2 m above the ground. This is the standard anemometer height required in agrometeorology (Allen et al. 1998 [DIRS 157311], p. 55). Anemometer height at the weather station used in this analysis was 10 m. Because wind speed increases with height above the soil surface, a logarithmic wind profile function is required to adjust wind speeds placed at heights other than the standard 2 m. Therefore, the following correction was made for wind speed (Allen et al. 1998 [DIRS 157311], Equation 47, p. 56):

$$u_2 = u_z \frac{4.87}{\ln(67.8z - 5.24)} \qquad \text{(Eq. D-15)}$$

where

u_z = wind speed measured at z m aboveground surface (m s^{-1}),

z = height of measurement aboveground surface (m).

Example: On day 60 of 1998, u_{10} = 2.3 m s^{-1} (Output DTN: MO0602SPAWEATH.000).

$$u_2 = 2.3\frac{4.87}{\ln(67.8*10 - 5.42)} = 1.7 \text{ m s}^{-1} \qquad \text{(from Eq. D-15)}$$

Mean daily u_2 calculations and values are in Output DTN: MO0603SPAREFET.000.

To assess potential impacts of using cover data and weather data from paired average, above average, and below average precipitation years, monthly mean RH_{min} and u_2 calculated for growing season months (January to September) of representative years were substituted into K_{cb} calculations. Water years 1998 and 1993 were selected as representative wet years. Water years 2002 and 1990 were selected as representative dry years. For 1998 and 2002, monthly mean RH_{min} and u_2 were calculated from data in Output DTN: MO0602SPAWEATH.000 by summing daily values for each month and dividing by the number of days in the month (Table D-22). For 1993, monthly averages were taken from DOE (1995 [DIRS 147785], p. B-2, Table B-1 [u_2] and p. B-9, Table B-8 [RH_{min}]). For 1990, monthly mean RH_{min} and u_2 were calculated from data in DTNs: MO9905VMMDJM90.000 [DIRS 150056], MO9905VMMDAJ90.000 [DIRS 150118],

MO9905VMMDJS90.000 [DIRS 150119], and MO9905VMMDOD90.000 [DIRS 150120] by combining the quarterly data files, then summing daily values for each month and dividing by the number of days in the month (Table D-22). For 1998 and 2002, data were taken from Site 1. Relative humidity was not measured at Site 1 in 1993, and errors were identified in precipitation measurements; therefore, RH_{min} and precipitation were taken from Site 8, which is close to Site 1 and at a similar elevation and exposure (CRWMS M&O 1997 [DIRS 103155], pp. 1-4 and 1-5). For 1990, data were taken from Site 4.

Table D-22. Mean Monthly Wind Speed and Minimum Relative Humidity for Representative Wet and Dry Years

	RH_{min} (%)					Wind Speed (m/s)			
	Below Average Precipitation		Above Average Precipitation			Below Average Precipitation		Above Average Precipitation	
	1990[1]	2002[2]	1993[3]	1998[2]		1990[1]	2002[2]	1993[4]	1998[2]
January	NA[5]	20.0	53.1	37.0		NA[5]	3.1	3.1	2.6
February	25.4	13.4	47.3	51.4		5.1	3.3	2.9	3.4
March	18.9	12.7	30.8	34.5		4.6	4.1	2.9	3.4
April	20.9	12.6	15.9	27.6		4.9	4.5	4.3	3.6
May	19.6	8.4	14.5	21.7		5.4	4.1	4.1	4.4
June	16.4	6.6	13.2	17.6		4.4	4.0	3.7	3.4
July	21.2	10.1	9.2	10.3		4.1	3.7	3.7	3.4
August	21.6	6.4	9.9	11.6		4.1	3.8	3.7	3.4
September	26.0	11.3	9.4	22.4		4.1	3.8	3.1	3.1

Source: [1] DTNs: MO9905VMMDJM90.000 [DIRS 150056], MO9905VMMDAJ90.000 [DIRS 150118], MO9905VMMDJS90.000 [DIRS 150119], and MO9905VMMDOD90.000. [DIRS 150120].
[2] Output DTN: MO0602SPAWEATH.000.
[3] DOE 1995 [DIRS 147785], Table B-8.
[4] DOE 1995 [DIRS 147785], Table B-1.
[5] No date were available for January 1990.

Slope of Saturation Vapor Pressure Curve (Δ)

The Δ is the slope of the relationship between the saturation vapor pressure of the air and air temperature. Vapor pressure is the component of total atmospheric pressure exerted by the motion of water vapor molecules. Saturation vapor pressure is the vapor pressure the air would have if it were saturated with water vapor molecules at a given temperature. As temperature increases, the saturation vapor pressure also increases. Δ is calculated from mean daily air temperature (°C) according to the following equation (Allen et al. 1998 [DIRS 157311], Equation 13, p. 37):

$$\Delta = 4098\left[\frac{0.6108\exp\left(\frac{17.27T}{T+237.3}\right)}{(T+237.3)^2}\right] \quad \text{(Eq. D-16)}$$

where

exp(x) = 2.7183 (base of natural logarithm) raised to the power (x),

T = mean daily air temperature (°C).

Example:

On day 60, 1998, T = 7.8°C (Output DTN: MO0602SPAWEATH.000).

$$\Delta = 4098\left[\frac{0.6108\exp\left(\frac{17.27\times 7.8}{7.8+237.3}\right)}{(7.8+237.3)^2}\right] = 4098\left[\frac{0.6108\times 1.7326}{60{,}074}\right] = 0.072 \text{ kPa } °C^{-1} \text{ (from Eq. D-16)}$$

Daily Δ values were used in Eq. D-6 to calculate daily F_r. Daily Δ values for the 1998, 2001, and 2002 water years are in Output DTN: MO0603SPAREFET.000.

Psychrometric Constant (γ)

The psychrometric constant represents a balance between the heat required to evaporate water into an air stream from the wick of a wet bulb thermometer (wet wick with thermometer beneath it) and the air's potential to absorb the water and carry it away. The constant is dependent on atmospheric pressure, latent heat of vaporization (energy required for evaporation), the specific heat of air at a constant pressure (quantity of energy required to raise the temperature of a given amount of air by one degree at constant pressure), and the ratio of molecular weight of water vapor to dry air. Values for γ at different altitudes are provided by Allen et al. (1998 [DIRS 157311], Table 2.2, p. 214). The weather station altitude of 1,143 m for the Yucca Mountain meteorological monitoring Site 1 corresponds to a table value for γ of 0.059 kPa $°C^{-1}$. This value was used in Equation D-6 to calculate F_r.

D4. EXAMPLE CALCULATIONS AND K_{CB} PROFILES

Transpiration coefficients were calculated daily for the initial, mid, and end of late season growth stages for annuals, drought deciduous, and evergreen species for each of the vegetation associations using Equations D-1 through D-8. The output of these calculations is included in Output DTN: MO0606SPABASAL.001. The following example is for drought deciduous vegetation on the first day of the midseason stage in an LG association using 1993 water year data (Table D-23).

Table D-23. Parameter Values for Example K_{cb} Calculations Using Annual Vegetation from an LG Vegetation Association

Parameter	Value	Source
First day of midseason stage	March 16, Julian Day 75	Table D-4
Cover for midseason stage	9.52% = 0.0952	Table D-14
Plant height	0.38 m	Table D-6
r_l	111 s m^{-1}	Table D-20
u_2	1.84 m s^{-1}	Output DTN: MO0603SPAREFET.000
RH_{min}	37.16%	Output DTN: MO0602SPAWEATH.000
Δ	0.093 kPa °C^{-1}	Output DTN: MO0603SPAREFET.000
γ	0.059 kPa °C^{-1}	Section D3.2.4

Step 1. Calculate $K_{cb,\,h}$ using Equation D-5:

$$K_{cb,h} = 1.0 + 0.1 \times 0.38 = 1.038$$

Step 2. Calculate $K_{cb\,full}$ using Equation D-4:

$$K_{cb\,full} = 1.038 + \left[0.04\left(1.84 - 2\right) - 0.004\left(37.16 - 45\right)\right]\left(\frac{0.38}{3}\right)^{0.3} = 1.05$$

Step 3. Calculate F_r using Equation D-6:

$$F_r \approx \frac{0.093 + 0.059\left(1 + 0.34 \times 1.84\right)}{0.093 + 0.059\left(1 + 0.34 \times 1.8 \times \frac{111}{100}\right)} = 0.983$$

Step 4. Determine the minimum of (1, $2f_c$, and $f_{c\,eff}^{(1/1+h)}$):

$$2f_c = 2 \times 0.0952 = 0.1904$$

$$f_{c\,eff}^{\left(\frac{1}{1+h}\right)} = \left(\frac{0.0952}{0.7773}\right)^{(0.7246)} = 0.2184$$

The minimum of (1, 2fc, and fc eff(1/1+h)) is 2fc = 0.1904

Step 5. Calculate K_{cb} using Equation D-1:

$$K_{cb} = 1.05 \times 0.1904 = 0.200$$

Step 6. Adjust K_{cb} with the stomatal resistance correction factor ($K_{cb} \times F_r$):

$$0.200 \times 0.983 = 0.197$$

Step 7. Calculate K_{cb} for development and late stages using Equation D-8. For the development stage, $K_{cb\ prev}$ was the K_{cb} for the last day of the initial stage, and $K_{cb\ next}$ was the K_{cb} for the first day of the mid stage. For the late stage, $K_{cb\ prev}$ was the K_{cb} for the last day of the mid stage, and $K_{cb\ next}$ was the value for $K_{cb\ end}$ (K_{cb} on the last day of the late stage).

The following example is for drought deciduous vegetation in an LG association on the first through third days of the late season stage, using data for the 1993 water year (Table D-24).

Table D-24. Parameter Values for Example Calculations of K_{cb} for the Late Season Stage

Parameter	Value	Source
$K_{cb\ prev}$	0.205	DTN: MO0606SPABASAL.001
$K_{cb\ next}$	0.108	DTN: MO0606SPABASAL.001
ΣL_{prev}	120 days	Table D-4
L_{stage}	15 days	Table D-4
First through third day of late season stage	121 to 123	Table D-4

Day 91: $K_{cb\,121} = 0.205 + \left(\frac{121-120}{15}\right)(0.108 - 0.205) = 0.198$

Day 92: $K_{cb122} = 0.205 + \left(\frac{122-120}{15}\right)(0.108 - 0.205) = 0.192$

Day 93: $K_{cb\,123} = 0.208 + \left(\frac{123-120}{15}\right)(0.108 - 0.205) = 0.185$

All K_{cb} calculations and results are available in Excel® spreadsheets in Output DTN: MO0606SPABASAL.001.

Daily K_{cb} values were set to zero outside the growing season for the three vegetation types (annuals, drought deciduous, and evergreen species) to represent the period of time when plants have completed their life cycle (annual species), are dormant (drought deciduous species), or physiologically inactive (evergreen species). The evaporation term (K_e) of the dual transpiration coefficient controls the soil water balance under conditions when plants are not actively transpiring.

The impact of the RH_{min} and u_2 corrections on K_{cb}s were assessed for representative above (1993 and 1998) and below (1990 and 2002) average precipitation years using data from the LG vegetation association. The monthly mean RH_{min} and u_2 for the growing season (January through September; Table D-21) were substituted into the K_{cb} calculations for annuals, drought deciduous, and evergreen vegetation for Julian days 91 to 99. This time period corresponded to a subset of the midseason growth stage during which all three vegetation types were considered active in the K_{cb} calculations. No other input parameters were varied. The resulting K_{cb}s for those nine days are in Table D-25.

Comparisons of K_{cb}s in above average precipitation years showed that differences in RH_{min} and u_2 translated into differences in K_{cb}s of 3% or less (Table D-25). For below average precipitation years, differences in RH_{min} and u_2 translated into differences in K_{cb}s of 2.6% or less (Table D-25). Additionally, variation in K_{cb}s that were averaged across wet and dry years was low, ranging from less than 1% to 4% (Table D-25, CV). Allen et al. (1998 [DIRS 157311], p. 124) suggest that only approximations of RH_{min} and u_2 are needed for the midseason growth stage because Equation 62, which has the same correction term as Equation D-1, is not sensitive to these values. The same argument applies to the initial and end of late season stages in this analysis, as Equation D-1 was used to calculate K_{cb}s for those stages. Thus, Equation D-1 is fairly insensitive to RH_{min} and u_2, and use of RH_{min} and u_2 from different years had negligable impact on K_{cb}s.

Table D-25. Comparison of K_{cb}s Calculated with Mean Monthly Wind Speed and Minimum Relative Humidity from Representative Wet and Dry Years

K_{cb}[1] 1998	K_{cb}[1] 1993	Percent Difference[2]	K_{cb}[1] 2002	K_{cb}[1] 1990	Percent Difference[3]	Mean[4]	SD[5]	CV[6]
0.572	0.555	−3.0	0.593	NA[7]	NA[7]	0.576	0.017	2.88
0.557	0.563	1.0	0.602	0.598	−0.7	0.580	0.023	4.01
0.579	0.582	0.4	0.607	0.602	−0.7	0.593	0.014	2.37
0.585	0.602	2.7	0.606	0.599	−1.2	0.598	0.009	1.53
0.595	0.602	1.1	0.608	0.603	−0.8	0.602	0.005	0.89
0.593	0.599	1.0	0.608	0.599	−1.5	0.600	0.006	1.03
0.603	0.605	0.4	0.604	0.593	−1.8	0.601	0.006	0.92
0.601	0.604	0.5	0.609	0.593	−2.6	0.602	0.007	1.11
0.589	0.604	2.4	0.604	0.589	−2.6	0.597	0.009	1.45

[1] Transpiration coefficients (K_{cb}) calculated using mean monthly minimum relative humidity (Rh_{min}) and wind speed (u_2) from two representative wet (1998 and 1993) and two representative dry (2002 and 1996) years. Relative humidity and wind speed data used in the calculation are from Table D-22.

[2] Percent difference between K_{cb}s calculated using RH_{min} and u_2 from 1998 and 1993 (two above average precipitation years).

[3] Percent difference between K_{cb}s calculated using RH_{min} and u_2 from 1996 and 2002 (two below average precipitation years).

[4] Mean K_{cb} of 1998, 1993, 2002, and 1996.

[5] Standard deviation of mean K_{cb}.

[6] Coefficient of Variation = (SD/mean) × 100.

[7] No data were available for January 1990.

K_{cb} profiles for the three vegetation types in the LA, LG, and LLG associations were generated for each water year (Figures D-4, D-5, and D-6, source data Output DTN: MO0606SPABASAL.001). The profiles showed that the magnitude of K_{cb}s for vegetation types was dependent on water year and vegetation association. Annuals were more important in the LLG association compared to LA and LG, and in the wet year compared to the average year for all associations. No annuals were recorded on plots during the dry year. These patterns reflect the relative importance of annuals in each of the associations with respect to water use. Cover was consistently greater for annuals on the LLG ESPs from 1991 to 1994, and consistently lower on the LA ESPs compared to the other associations over the same time period

(CRWMS M&O 1996 [DIRS 102235], p. 31, Figure 4-10). Drought deciduous vegetation was more important (higher K_{cb}s) than evergreen vegetation during the midseason growth stage for LG and LA associations across water years, but the two vegetation types were similar for the LLG association across water years. While shorter growing seasons were developed for the drought year (Table D-4), making potential seasonal water use by plants low, mid stage K_{cb}s for drought deciduous vegetation were higher than in the average precipitation year (1991) for the three associations. The absence of annuals in the drought year may have resulted in more available water early in the season for drought deciduous species, which could have caused the higher mid stage cover values (Tables D-7 through D-9 and D-13 through D-15). Alternatively, higher cover values in the drought year could have been due to a time lag of the effects of the 1990 drought on the 1991 response of drought deciduous vegetation.

Because the three vegetation types were independent of each other (i.e., each contained unique information relevant to the association) and were important with respect to water use, it was appropriate to sum the annual, drought deciduous, and evergreen K_{cb}s to get one profile for each association (Figure D-7). This resulted in K_{cb} profiles for each water year and association that accounted for major sources of variation due to differences in growing season length, growth characteristics, physiological activity, and ground cover among vegetation types.

Regardless of the differences in potential water use among the vegetation types across associations, when K_{cb}s were summed to produce association totals, the values were very similar for LG and LLG over most of the profiles for 1998 and 2001 (Figure D-7). This was due to similarities in total vegetation cover on LG and LLG reference plots (Tables D-11, D-12, D-14, and D-15). The similarity of the association profiles indicates that regardless of species composition, potential water use is similar for the two associations during average and above average precipitation years.

Transpiration coefficients for the LA association were generally lower for the wet and average years than those calculated for the LG and LLG associations, reflecting the tendency toward lower cover of vegetation in the low elevation LA association (Figure D-6). K_{cb} profiles for the three associations tended to converge in the dry year (Figure D-6), reflecting water limitation to vegetation growth across associations.

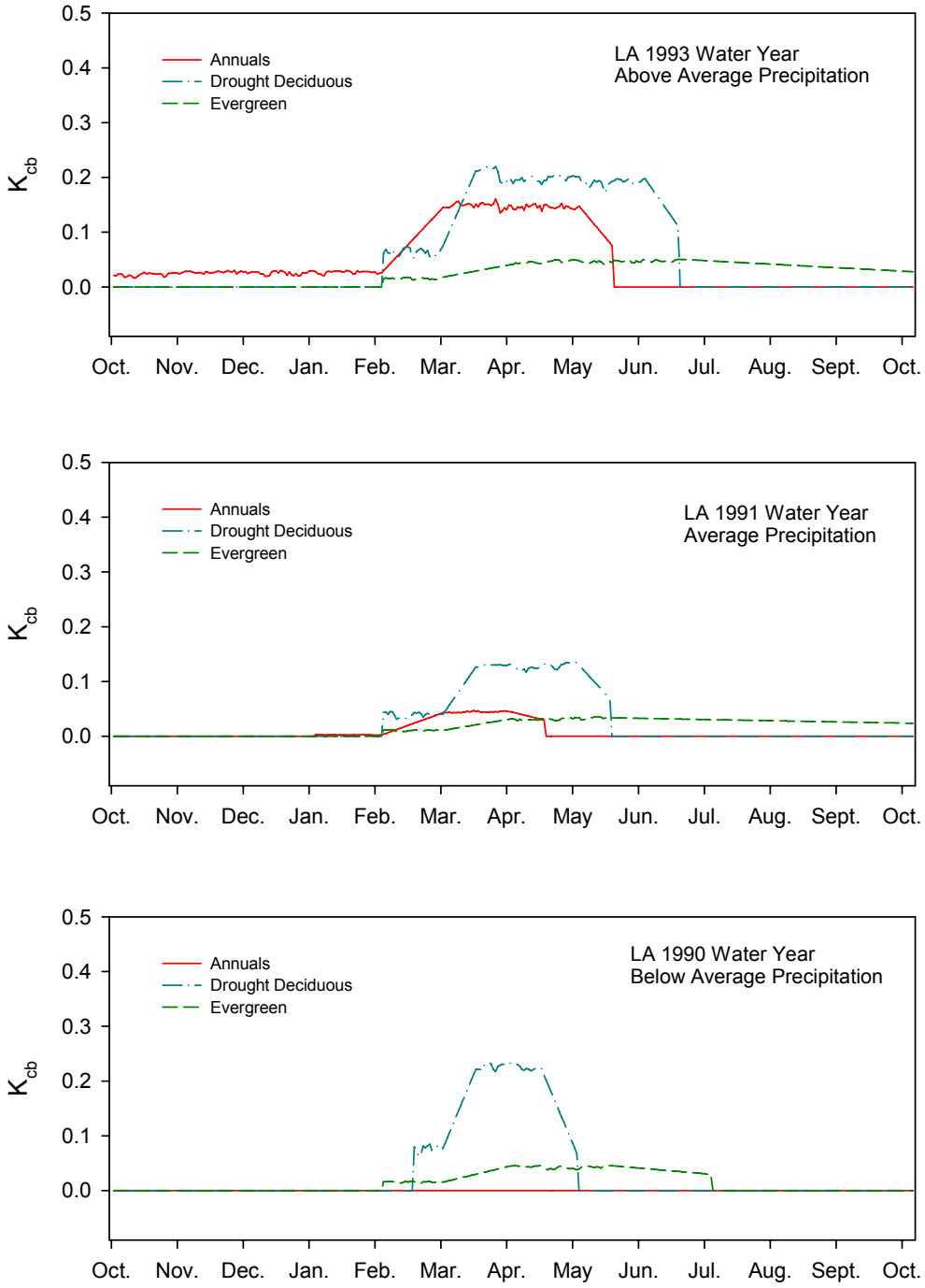

Source: Output DTN: MO0606SPABASAL.001.

Figure D-4. Transpiration Coefficient (K_{cb}) Profiles for Three Vegetation Types (Annuals, Drought Deciduous, and Evergreen) for the *Larrea−Ambrosia* Vegetation Association

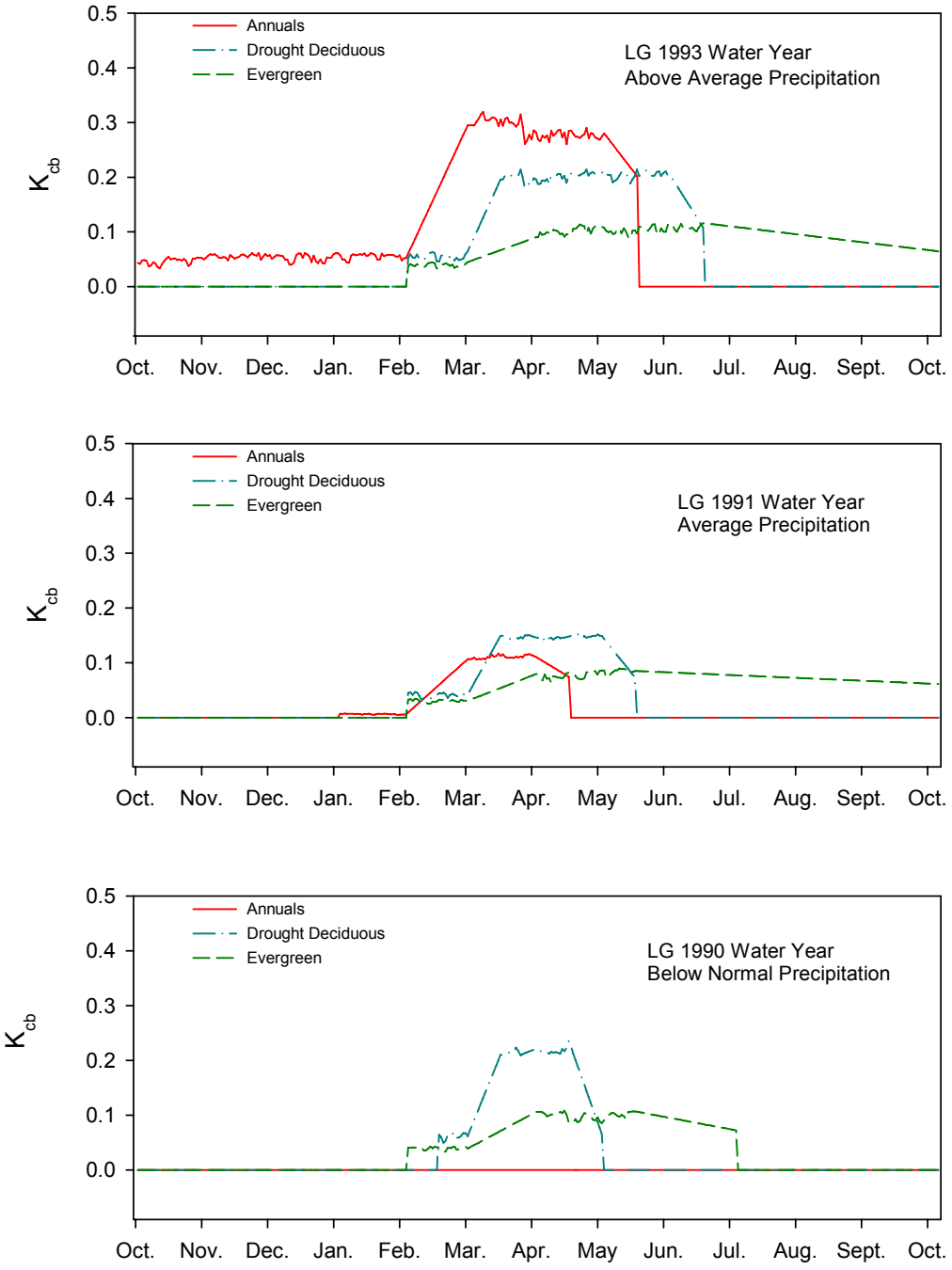

Source: Output DTN: MO0606SPABASAL.001.

Figure D-5. Transpiration Coefficient (K_{cb}) Profiles for Three Vegetation Types (Annuals, Drought Deciduous, and Evergreen) for the *Lycium−Grayia* (LG) Vegetation Association

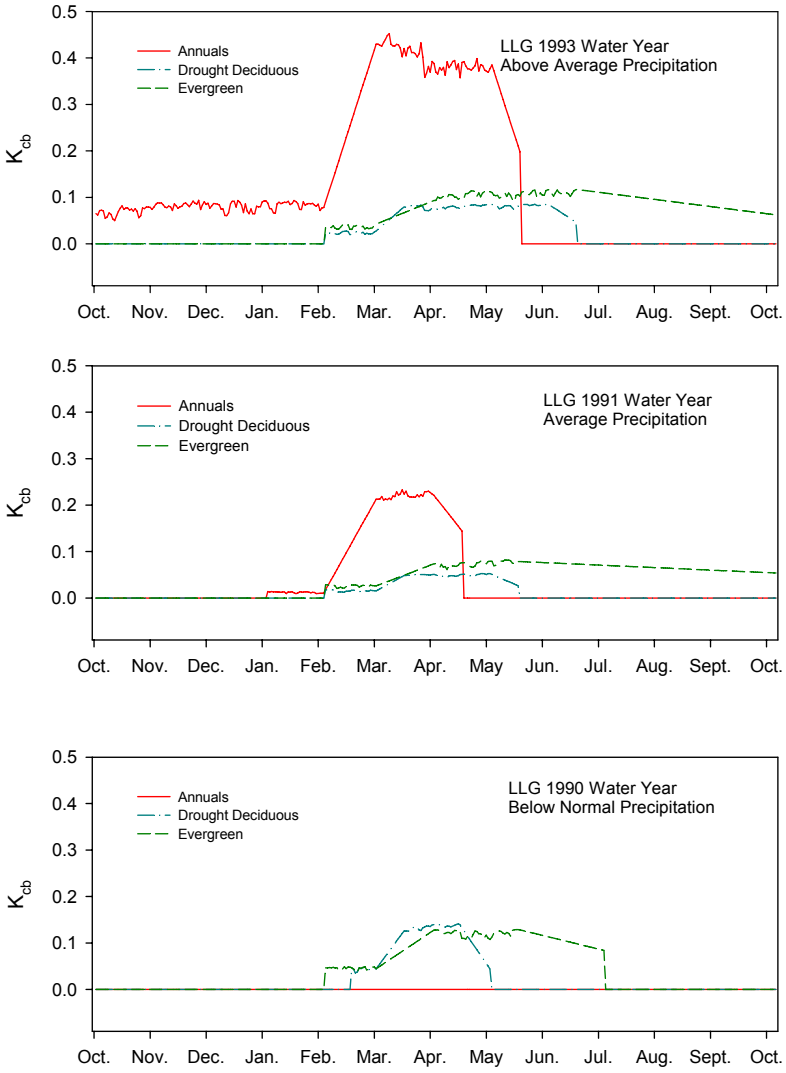

Source: Output DTN: MO0606SPABASAL.001.

Figure D-6. Transpiration Coefficient (K_{cb}) Profiles for Three Vegetation Types (Annuals, Drought Deciduous, and Evergreen) for the *Larrea−Lycium−Grayia* (LLG) Vegetation Association

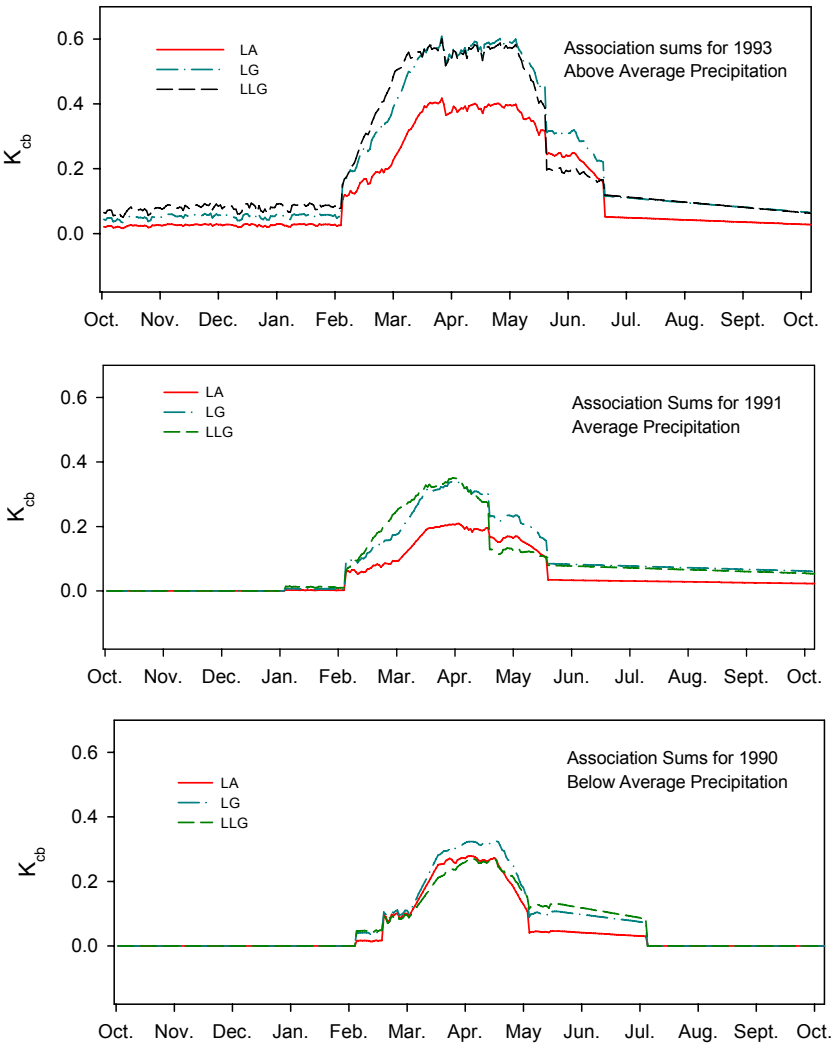

Source: Output DTN: MO0606SPABASAL.001.

Figure D-7. Transpiration Coefficient (K_{cb}) Profiles Summed Across Three Vegetation Types (Annuals, Drought Deciduous, and Evergreen) for Three Vegetation Associations (LA, LG, and LLG)

Use of separate K_{cb}−NDVI' correlations for each vegetation association would require that each model cell be assigned to one of the three associations. This was not feasible due to lack of spatial data for vegetation associations and potential for vegetation change through time. As an alternative to using three separate K_{cb} profiles for the K_{cb}−NDVI' correlations, and for use in uncertainty analyses (Appendix I), upper and lower bounds for K_{cb}s were calculated for the LG association. This association was selected because it is representative of the vegetation directly above the proposed repository and is therefore most important with respect to the potential for water to infiltrate and reach interred waste containers. Upper and lower bounds were determined by using high and low input values for vegetation cover, plant height, and stomatal resistance for calculating daily K_{cb}s and generating the yearly profiles of uncertainty for the 1993 and 1991 water years. Inputs are described below. It was determined that the 1990 water year would not be used in the K_{cb}−NDVI' correlations, and so upper and lower bounds were not calculated for

that year (Appendix E). The same methods outlined above for calculating K_{cb}s were used to generate the uncertainty bounds.

Cover data from 1993 (wet year) and 1991 (average precipitation year) were evaluated to determine which ESPs from those years had the highest and lowest cover values. Ecological Study Plots LG3C and LG5C had the highest and lowest recorded cover, respectively, for 1993 (Table D-16). Ecological Study Plots LG2T and LG5T had the highest and lowest recorded cover, respectively, for 1991 (Table D-16). Source data for these plots were extracted from DTN: MO9907GCESPYMN.000 [DIRS 157659] and placed in Excel® spreadsheets (Output DTN: MO0606SPAVEGAS.001). The data were sorted per species and vegetation type. Mean percent cover per species was determined by summing the cover data per species and dividing by the number of transects sampled on the ESP. Cover per vegetation type was determined by summing the species specific data for each type. Cover data used to calculate the K_{cb} bounds for LG are in Tables D-26 through D-29.

Table D-26. Mean Cover from Ecological Study Plot LG3C

LG3C 1993						
Vegetation Type/Species	**Life Form[1]**	**Cover (%)**		**Vegetation Type/Species**	**Life Form[1]**	**Cover (%)**
Annuals				**Drought Deciduous**		
Bromus madritensis ssp. *rubens*	G	10.76		*Lycium andersonii*	S	3.49
Unknown		0.75		*Menodora spinescens*	S	3.25
Lotus humistratus	F	0.63		*Grayia spinosa*	S	1.37
Cryptantha pterocarya	F	0.38		*Ambrosia dumosa*	S	1.00
Cryptantha spp.	F	0.38		*Eriogonum fasciculatum*	S	0.88
Cryptantha circumscissa	F	0.25		*Pleuraphis jamesii*[2]	G	0.38
Cryptantha nevadensis	F	0.25		*Atriplex confertifolia*	S	0.38
Phacelia fremontii	F	0.25		*Stephanomeria pauciflora*	F	0.37
Pectocarya platycarpa	F	0.13		*Sphaeralcea ambigua*	F	0.25
Chaenactis stevioides	F	0.13		*Krascheninnikovia lanata*[3]	S	0.13
Chorizanthe thurberi	F	0.13		*Calochortus flexuosus*	F	0.13
Eriogonum deflexum	F	0.13		*Delphinium parishii*	F	0.13
Lupinus flavoculatus	F	0.13			Total	11.74
Syntrichopappus fremontii	F	0.13				
Vulpia octoflora	G	0.13				
	Total	14.51		**Evergreen**		

Table D-26. Mean Cover from Ecological Study Plot LG3C (Continued)

LG3C 1993						
Vegetation Type/Species	**Life Form[1]**	**Cover (%)**		**Vegetation Type/Species**	**Life Form**	**Cover (%)**
Annuals				**Drought Deciduous**		
				Ephedra nevadensis	S	6.00
				Ericameri cooperi[4]	S	2.88
				Hymenoclea salsola	S	1.25
				Ericameria teretifolia[5]	S	0.37
					Total	10.50
				Plot Total		36.75

Source: Output DTN: MO0606SPAVEGAS.001.

NOTE: Means are based on data collected from 8 transects on LG3C. Species are arranged in order of dominance within a vegetation type.

[1] G = grass, F = forb, S = shrub.
[2] Previous nomenclature: *Hilaria jamesii*.
[3] Previous nomenclature: *Ceretoides lanata*.
[4] Previous nomenclature: *Happlopapus cooperi*.
[5] Previous nomenclature: *Chrysothamnus teretifolius*.

Table D-27. Mean Cover from Ecological Study Plot LG5C

LG5C 1993						
Vegetation Type/Species	**Life Form[1]**	**Cover (%)**		**Vegetation Type/Species**	**Life Form[1]**	**Cover (%)**
Annuals				**Drought Deciduous**		
Bromus madritensis ssp. rubens	G	6.26		*Eriogonum fasciculatum*	S	2.61
Cryptantha spp.	F	1.00		*Grayia spinosa*	S	2.26
Cryptantha pterocarya	F	0.50		*Ambrosia dumosa*	S	1.38
Syntrichopappus fremontii	F	0.13		*Lycium andersonii*	S	1.25
Stephanomeria exigua	F	0.12		*Atriplex confertifolia*	S	1.00
	Total	8.01		*Eriogonum inflatum*	F	0.50
				Achnatherum speciosum[2]	G	0.25
				Sphaeralcea ambigua	F	0.25
				Mirabilis bigelovii	F	0.13
				Stephanomeria pauciflora	F	0.13
					Total	9.76
				Evergreen		
				Ephedra nevadensis	S	2.63
				Hymenoclea salsola	S	1.63
				Ericameria teretifolia[3]	S	0.50

Table D-27. Mean Cover from Ecological Study Plot LG5C (Continued)

LG5C 1993						
Vegetation Type/Species	**Life Form[1]**	**Cover (%)**		**Vegetation Type/Species**	**Life Form**	**Cover (%)**
Annuals				**Drought Deciduous**		
				Ericameria nauseosa[4]	S	0.25
				Ericameria linearifolia[5]	S	0.25
				Larrea tridentata	S	0.13
					Total	5.39
					Plot Total	23.15

Source: Output DTN: MO0606SPAVEGAS.001.

NOTE: Means are based on data collected from 8 transects on LG5C. Species are arranged in order of dominance within a vegetation type.

[1] G = grass, F = forb, S = shrub.
[2] Previous nomenclature: *Stipa speciosa*.
[3] Previous nomenclature: *Chrysothamnus teretifolius*.
[4] Previous nomenclature: *Chrysothamnus nauseosus*.
[5] Previous nomenclature: *Happlopapus linearifolius*.

Table D-28. Mean Cover from Ecological Study Plot LG2T

LG2T 1991						
Vegetation Type/Species	**Life Form[1]**	**Cover (%)**		**Vegetation Type/Species**	**Life Form[1]**	**Cover (%)**
Annuals				**Drought Deciduous**		
Bromus madritensis ssp. rubens	G	4.50		*Eriogonum fasciculatum*	S	1.40
Salsola iberica	F	1.60		*Grayia spinosa*	S	0.90
Amsinckia tessellata	F	1.50		*Salazaria mexicana*	S	0.90
Sisymbrium altissimum	F	0.70		*Lycium andersonii*	S	0.80
Descurainia pinnata	F	0.20		*Achnatherum speciosum*[2]	G	0.70
Mentzelia obscura	F	0.20		*Atriplex canescens*	S	0.40
Phacelia fremontii	F	0.20		*Atriplex confertifolia*	S	0.20
Camissonia brevipes	F	0.10		*Eriogonum inflatum*	F	0.10
Lotus humistratus	F	0.10		*Krascheninnikovia lanata*[3]	S	0.10
Unknown	F	0.10		*Encelia virginensis*	S	0.10
	Total	9.20		*Eriastrum eremicum*	S	0.10
				Eriogonum microthecum	S	0.10
					Total	5.80
				Evergreen		
				Ephedra nevadensis	S	2.70
				Gutierrezia sarothrae	S	1.20
				Artemisia tridentata	S	1.10
				Ericameria teretifolia[4]	S	0.70
				Ephedra viridis	S	0.60

Table D-28. Mean Cover from Ecological Study Plot LG2T (Continued)

LG2T 1991						
Vegetation Type/Species	**Life Form[1]**	**Cover (%)**		**Vegetation Type/Species**	**Life Form**	**Cover (%)**
Annuals				**Drought Deciduous**		
				Ericameria cooperi[5]	S	0.60
				Hymenoclea salsola	S	0.40
				Ericameria nauseosa[6]	S	0.30
				Ericameria linearifolia[7]	S	0.20
					Total	7.80
				Plot Total		22.80

Source: Output DTN: MO0606SPAVEGAS.001.

NOTE: Means are based on data collected from 12 transects on LG2T. Species are arranged in order of dominance within a vegetation type.

[1] G = grass, F = forb, S = shrub.
[2] Previous nomenclature: *Stipa speciosa*.
[3] Previous nomenclature: *Ceretoides lanata*.
[4] Previous nomenclature: *Chrysothamnus teretifolius*.
[5] Previous nomenclature: *Happlopapus cooperi*.
[6] Previous nomenclature: *Chrysothamnus nauseosus*.
[7] Previous nomenclature: *Happlopapus linearifolius*.

Table D-29. Mean Cover from Ecological Study Plot LG5T

LG5T 1991						
Vegetation Type/Species	**Life Form[1]**	**Cover (%)**		**Vegetation Type/Species**	**Life Form**	**Cover (%)**
Annuals				**Drought Deciduous**		
Bromus madritensis ssp. rubens	G	1.00		*Ambrosia dumosa*	S	2.30
Amsinckia tessellata	F	0.30		*Atriplex confertifolia*	S	1.40
Salsola iberica	F	0.30		*Lycium andersonii*	S	0.30
Linanthus demissus	F	0.20		*Achnatherum speciosum*[2]	G	0.30
Sisymbrium altissimum	F	0.20		*Krascheninnikovia lanata*[3]	S	0.20
Unknown	F	0.20		*Eriogonum fasciculatum*	S	0.20
Lotus humistratus	F	0.20		*Grayia spinosa*	S	0.20
Cryptantha nevadensis	F	0.10		*Salazaria mexicana*	S	0.20
Chorizanthe thurberi	F	0.10		*Lycium pallidum*	S	0.20
	Total	2.60		*Eriogonum inflatum*	F	0.10
					Total	5.40
				Evergreen		
				Ephedra nevadensis	S	2.10
				Larrea tridentata	S	0.90
				Hymenoclea salsola	S	0.40

Table D-29. Mean Cover from Ecological Study Plot LG5T (Continued)

LG5T 1991						
Vegetation Type/Species	**Life Form[1]**	**Cover (%)**		**Vegetation Type/Species**	**Life Form**	**Cover (%)**
Annuals				**Drought Deciduous**		
				Ericameria nauseosa[4]	S	0.20
				Ericameria teretifolia[5]	S	0.20
				Ericameria cooperi[6]	S	0.10
					Total	3.90
				Plot Total		11.90

Source: Output DTN: MO0606SPAVEGAS.001.

NOTE: Means are based on data collected from 10 transects on LG5T. Species are arranged in order of dominance within a vegetation type.

[1]G = grass, F = forb, S = shrub
[2]Previous nomenclature: *Stipa speciosa*
[3]Previous nomenclature: *Ceretoides lanata*
[4]Previous nomenclature: *Chrysothamnus nauseosus*
[5]Previous nomenclature: *Chrysothamnus teretifolius*
[6]Previous nomenclature: *Happlopapus cooperi*

Minimum and maximum values for stomatal resistance were determined from conductance values in Table D-18 for vegetation types and growth stages and used in upper and lower bound K_{cb} calculations (Table D-30). Because the bounds were calculated for the LG association and *Krameria erecta* was not recorded on ESPs sampled for LG, conductance values for this species were not considered for drought deciduous vegetation. One low conductance value for *Ericameria cooperi* (0.0011 m/s) was not considered for the midseason stage for evergreen vegetation because it would have made an unrealistic resistance value (909 s/m) for that time period.

Table D-30. Minimum and Maximum Stomatal Resistance for Vegetation Types

Vegetation Type	Growth Stage	Minimum r_l (s/m)[1]	Maximum r_l (s/m)[2]
Annual	Initial/End	345	357
	Mid	47	200
Drought Deciduous	Initial	385	385
	Mid	68	179
	End	714	714
Evergreen	Initial	323	417
	Mid	47	357
	End	400	2,500

[1] Minimum stomatal resistance for each vegetation type from Table D-19 used in upper bound calculation for transpiration coefficients.

[2] Maximum stomatal resistance for each vegetation type from Table D-19 used in lower bound calculation for transpiration coefficients.

Minimum and maximum plant heights were determined from Table D-5 and used for all vegetation types. The minimum height recorded in Table D-5 was 0.27 m (used in lower bound calculations). The maximum height was 0.51 m. Maximum height was rounded to 0.5 for calculations (used in upper bound calculations).

The upper and lower bounds for K_{cb}s for the 1998 and 2001 water years are in Figure D-8. The calculations and profile values are in Output DTN: MO0606SPABASAL.001. The uncertainty bounds for the LG association K_{cb} profiles encompassed the variation observed among association profiles. The LG K_{cb} profiles with uncertainty bounds were recommended and used in the NDVI'−K_{cb} correlations in Section 6.5.3.4.

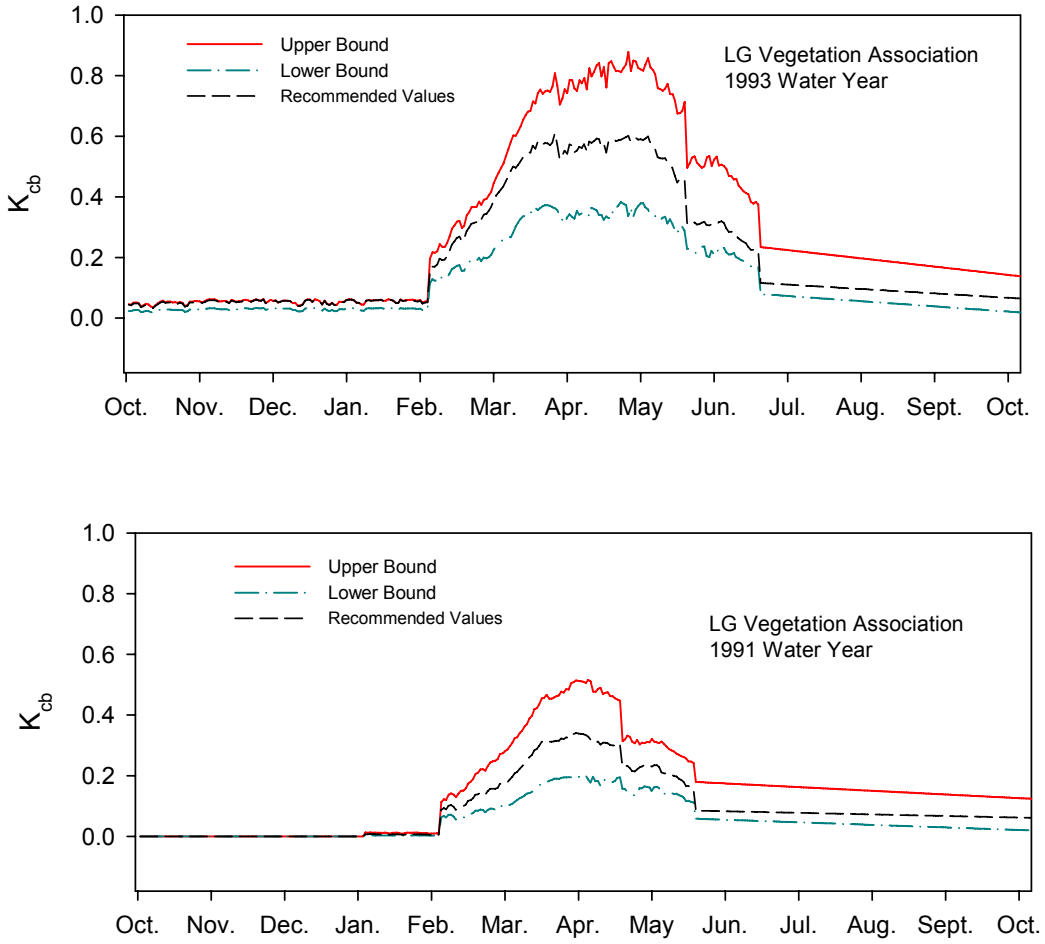

Source: Output DTN: MO0606SPABASAL.001.

Figure D-8. Transpiration Coefficient Profiles for LG Vegetation Associations with Upper and Lower Uncertainty Bounds for Wet (1993) and Average Precipitation (1991) Years

D5. FUTURE CLIMATE TRANSPIRATION COEFFICIENTS BASED ON AN EXOTIC GRASS MONOCULTURE

The Glacial Transition climate is expected to be colder and wetter than the modern interglacial climate at Yucca Mountain. Exotic grasses have invaded the current sagebrush steppes of the Great Basin and Columbia Plateau which have similar climate to that predicted for the Glacial Transition. Future climate K_{cb}s were calculated using *Bromus tectorum*. *Bromus madritensis* spp. *rubens* and *Bromus tectorum* are exotic annual grass species that were introduced to the western United States from Eurasia in the 1800s (Hunter 1991 [DIRS 129944], p. 176; Mack 1981 [DIRS 177164], pp. 145 and 146). Since their introduction, both species have become prominent invaders in cold deserts of the Great Basin and Columbia Plateau (*Bromus tectorum* (Mack 1981 [DIRS 177164], p. 157])) and across areas of the northern Mojave Desert (*Bromus madritensis* (Hunter 1991 [DIRS 129944], pp. 179 and 180])). The success of these two introduced grasses has been largely attributed to phenotypic plasticity, prolific seed production, early use of soil resources, and rapid establishment of root systems (Smith et al. 1997 [DIRS 103636], p. 202). Displacement of native perennial species by *Bromus tectorum* and *Bromus madritensis* is largely a consequence of opportunistic response to fire and their highly competitive nature once established (Smith et al. 1997 [DIRS 103636], p. 215). Both species mature early in the growing season and become extremely flammable, resulting in early season fires that are deleterious to metabolically active and fire intolerant species. Dense stands of *Bromus tectorum* have increased fire frequency in sagebrush steppe communities resulting in elimination of perennial shrubs in many of these habitats (Klemmedson and Smith 1964 [DIRS 177134], pp. 239 through 241). Conversion of sagebrush steppe to annual plant communities appears to be essentially irreversible.

Bromus tectorum and *Bromus madritensis* are present at Yucca Mountain in disturbed and undisturbed areas. *Bromus tectorum* occurs at higher elevations and can survive freezing temperatures, while *Bromus madritensis* is less tolerant of cold and killed by winter freeze. Studies have shown that densities of *Bromus madritensis* have increased over time on the NTS (e.g., Hunter 1991 [DIRS 129944]), and it has been the dominant annual species on ESPs during years of average and above average precipitation (Tables D-10 through D-15). Shifts in dominance of native perennial shrubs to exotic annual grasses have the potential to change net infiltration at Yucca Mountain. Maximum rooting depths of native shrub species in the Mojave Desert average about 2 m (Section 6.5.3.2), and studies have shown that native shrubs can extract water and nutrients to depths of two to three meters (Yoder and Nowak 1999 [DIRS 177167], p. 91, Figure 6; Jackson et al. 2002 [DIRS 177171], p. 624, Table 1). Mean maximum rooting depth for *Bromus tectorum* is about 1.0 m (Section 6.5.3.2), and studies have shown that water remains in the soil profile below about 0.5 to 0.6 m at the end of the growing season in brome dominated communities (Cline et al. 1977 [DIRS 177127], p. 200, Figure 3). The combination of shorter growing seasons and shallower root systems for *Bromus* spp. could result in increased net infiltration at Yucca Mountain should it become a brome dominated system.

Thus, with mechanisms that cause conversion from perennial shrub dominated communities to exotic annual communities already in place at Yucca Mountain and the potentially irreversible nature of these changes, a future climate scenario with a brome monoculture in place was considered for the infiltration model. Because the future climate is predicted to be colder and

wetter than the current climate, characteristics (timing of phenological events, rooting depths, and cover) of *Bromus tectorum* were used to calculate K_{cb}s. Additionally, increased fire frequencies and suppression of native perennial flora associated with *Bromus tectorum* invasions have been documented in southeastern Washington and areas around Spokane Washington (Mack 1981 [DIRS 177164], p. 151, Figure 1f; pp. 155 and 156), which is one of the future climate anlogues (BSC 2004 [DIRS 170002], pp. 6-44 and 6-45, Table 6-1).

The equations and methods documented in the previous sections for calculating K_{cb}s were used to calculate K_{cb}s for the brome monoculture and therefore will not be repeated here. Inputs to K_{cb} calculations for the brome monoculture and the resulting K_{cb} profile are described below.

D5.1. GROWTH STAGES AND VEGETATION HEIGHT

Growth stages for *Bromus tectorum* were developed from three sources: published values for timing of phenological stages; temperature requirements for growth established in Upadhyaya et al. (1986 [DIRS 177149], p. 695); and monthly mean temperatures from the future climate anlogue weather station in Spokane, Washington.

Generally *Bromus tectorum* germinates in the fall and rapidly establishes a root system (Stewart and Hull 1949 [DIRS 177146], p. 58; Smith et al. 1997 [DIRS 103636], p. 210). It over-winters as a small basal rosette in a dormant to semi-dormant condition and initiates growth again in the spring as soon as temperatures allow (Klemmedson and Smith 1964 [DIRS 177134], p. 231). Stewart and Hull (1949 [DIRS 177146], p. 58) observed germination and leaf growth in Idaho from late September through October (Table D-31). Mack and Pyke (1983 [DIRS 177141], p. 89) observed emergence of *Bromus tectorum* in late August to early September when early rains occurred at sites in eastern Washington. However, early rains were commonly followed by dry periods and these cohorts usually died. Cohorts emerging in October were more likely to survive (Mack and Pyke 1983 [DIRS 177141], p. 89). When snow cover occurred at these sites, it lasted from the end of October through midFebruary (Mack and Pyke 1983 [DIRS 177141], p. 75, Figure 2). Link et al. (1990 [DIRS 177142], p. 511, Figure 6) observed initiation of spring growth in midFebruary to midMarch, flowering in mid to late April, and senescence in late May (Table D-31). Hulbert (1955 [DIRS 177129], p. 190, Figure 4) observed flowering at the end of April at Idaho sites and senescence was observed from early to late June (Table D-31).

Table D-31. Timing of Phenological Stages for *Bromus tectorum*

Reference	Germination and Leaf Growth	Winter Semi-Dormant Stage	Initiation of Spring Growth	Flowering Stage	Senescence
Hulbert 1955 [DIRS 177129] p. 190, Figure 4				End of April	By June 22
Link et al. 1990 [DIRS 177142], p. 511, Figure 6			Mid February to Mid March	Mid to late April	Late May
Stewart and Hull 1949 [DIRS 177146], p. 58	Late September to October				June 5 to 30
Mack and Pyke 1983 [DIRS 177141], pp. 83 and 75, Figure 2	Late August to October	October 31 to February 15			

Upadhyaya et al. (1986 [DIRS 177149], p. 695) described three seasonal growth phases for *Bromus tectorum* related to soil temperature (Table D-32).

Table D-32. Growth Phases for *Bromus tectorum*[1]

Growth Phase	Soil Temperature	Growth Description
Limited	1.9°C to 3.5°C	Growth is initiated
Unaffected	3.5°C to 15°C	Optimum growth
Inhibited	> 15°C	Retarded growth
Senescence	≈ 27°C	Growth ceases

[1] Growth phases are from Upadhyaya et al. 1986 [DIRS 177149], p. 695.

Using mean monthly air temperature from the Glacial Transition climate anlogue station in Spokane (Table D-33) as a surrogate for soil temperature, the growth phases reported by Upadhyaya et al. (1986 [DIRS 177149], p. 695) correspond to following months:

- Limited phase − November and March
- Unaffected phase − April to May
- Inhibited phase − June to August.

Mean maximum air temperatures for the Glacial Transition climate anlogue station reach 24°C in June and remain high July through September (Western Regional Climate Center 1997 [DIRS 152233]), which suggests that soil temperatures during this time period correspond to the senescence phase. Mean monthly air temperatures for December through February (Table D-33) are too cold for growth and suggest that *Bromus tectorum* would be quiescent during those months.

Table D-33. Average Monthly Weather Data for Glacial Transition Climate

Month	Temperature[1] (°C)	Month	Temperature (°C)
January	−2.7	July	20.4
February	0.7	August	20.2
March	3.7	September	14.9
April	7.7	October	8.5
May	12.2	November	1.7
June	16.7	December	−2.3

Source: Western Regional Climate Center (1997 [DIRS 152233]).

[1]Temperature was converted from °F to °C (°C = [°F-32]/1.8).

Based on the timing of phenological stages (Table D-31) and the comparison of growth phases to average monthly temperatures for the Glacial Transition climate, October 1 through 31, November 1 to February 28, March 1 to 31, April 1 to 30, May 1 to 15, and May 16 to May 30 were assigned to the initial, quiescent, initial, development, mid-, and late-growth stages, respectively, for *Bromus tectorum* (Table D-34).

Table D-34. Growth Stages for *Bromus tectorum*

Growth Stage	Annual
Initial	Oct. 1 to 31 DOY 274 to 304
Quiescent	Nov. 1 to Feb. 28 DOY 305 to 59
Initial	Mar. 1 to 31 DOY 60 to 90
Development	Apr. 1 to 30 DOY 91 to 120
Mid	May 1 to May 15 DOY 121 to 135
Late	May 16 to 31 DOY 136 to 151

Vegetation Height—In comprehensive reviews of *Bromus tectorum* ecology, Carpenter and Murray ([n.d.] [DIRS 174674], p. 7) reported fall growth of 2 to 4 cm (0.02 to 0.04 m) prior to the onset of winter dormancy, and Stewart and Hull (1949 [DIRS 177146], pp. 58 and 59) reported ordinary heights of mature plants of 12 to 20 inches (0.30 to 0.50 m), with 24 (0.60 m) or more inches under favorable conditions. For this analysis, a height of 0.03 m (the mean of values reported for fall growth) was selected for the initial growth stage and 0.46 m (the mean of values reported for mature plants rounded down to the nearest tenth of a meter) was selected for the mid season growth stage.

D5.2. COVER DATA

To get estimates of potential ground cover for a brome monoculture scenario at Yucca Mountain, it was assumed that the grass would invade most areas that were not covered by gravel, cobble, or rock surfaces that would prevent or limit its ability to establish. Cover data collected from ESPs in 1990, 1991, and 1993 included measurement of percent of ground covered by gravel, cobble, and rock which were classified according to the following clast sizes:

- Gravel > 0.5 cm and ≤ 8 cm
- Cobble > 8 cm and ≤ 25 cm
- Rock > 25 cm.

Considering the range of particle size for gravel, it is unlikely that all gravel cover would omit brome establishment. However, there are other unmeasured factors that would exclude brome establishment including thin soils, rock outcrops, and soil surface crusts that form physical barriers. Therefore, gravel cover was included partly as a surrogate for these unmeasured factors.

Mean percent cover of gravel, cobble, and rock cover for ESPs representing the LA, LG, and LLG vegetation associations for 1990, 1991, and 1993 was determined using the same methods described for vegetation cover in Section D3.2.2. For each association, the means of gravel, cobble, and rock cover were summed to get a total cover for each year (Table D-35). Means and standard deviations based on the three years of data collection were calculated for each

association (Table D-35). The resulting mean values were subtracted from 100% to get the estimated potential cover of brome for each association for use in K_{cb} calculations (Table D-35).

Table D-35. Mean Cover of Gravel, Cobble, and Rock, and Potential Brome Cover

Vegetation Association	Mean Gravel Cover (%)	Mean Cobble Cover (%)	Mean Rock Cover (%)	Sum[1]	Mean of Years[2]	SD of Years[3]	Potential Brome Cover[4] (%)
LA 1990	38.13	1.11	0.84	40.08	33.91	5.423	66.09
LA 1991	28.03	1.33	0.54	29.9			
LA 1993	29.02	1.67	1.06	31.75			
LG 1990	27.69	9.06	15.43	52.18	48.413	5.713	51.59
LG 1991	25.67	9.29	16.26	51.22			
LG 1993	17.89	7.5	16.45	41.84			
LLG 1990	33.86	4.81	5.79	44.46	39.89	6.499	60.11
LLG 1991	32.41	5.06	5.29	42.76			
LLG 1993	20.94	5.12	6.39	32.45			

Source: Output DTN: MO0606SPAVEGAS.001.

[1] Sum of mean gravel, cobble, and rock cover for each year.
[2] Average of sums for 1990, 1991, and 1993.
[3] Standard deviation of sums for 1990, 1991, and 1993.
[4] Mean of years subtracted from 100.

D5.3. STOMATAL RESISTANCE

Two sources that measured stomatal conductance in velocity units were used to estimate r_l for *Bromus tectorum* (Table D-36). Link et al. (1990 [DIRS 177142]) measured stomatal conductance of bromus plants grown at a field site in southeastern Washington. Mean maximal stomatal conductance measured on April 11 and 18 were used in the estimate for the midseason growth stage, and mean maximal stomatal conductance measured on May 1 was used in the estimate for initial and end of late season growth stages (Table D-36). Rice et al. (1992 [DIRS 177165]) measured stomatal conductance of bromus plants grown from seed sources collected in southeastern Washington and northern Idaho. Plants were grown in a glass house under controlled conditions. The ten highest values for conductance that were measured prior to the onset of water stress were selected to estimate r_l for the midseason growth stage (Rice et al. 1992 [DIRS 177165], p. 36, Figure 4). Seven lower values were selected to estimate r_l for the initial and end of late season growth stages (0.25 to 0.60 cm/s, Table D-36). Mean r_l was calculated according to Equation D-14 (Table D-36). Mean r_l for the initial and end of late season growth stages was used in Equation D-6 to correct K_{cb}s for stomatal resistance that was higher than that of agricultural species (Allen et al. 1998 [DIRS 157311], p. 191). Mean r_l for the mid season growth stage was less than 100 stomatal resistance; therefore, the resistance correction factor was not required (Allen et al. 1998 [DIRS 157311], p. 191).

Table D-36. Stomatal Conductance and Resistance for *Bromus tectorum*

Reference	Comments	g[1] (cm/s)	g (m/s)	mean g (m/s)	mean r_l[2] (s/m)
Initial and Late Season Growth Stages					
Link et al. 1990 [DIRS 177142], p. 508, Table 2	Measured May 1	0.62	0.0062	0.0048	208
Rice et al. 1992 [DIRS 177165], p. 36, Figure 4	Values from low end of graph (0.25 to 0.60). Value below 0.25 not used.	0.60	0.006		
		0.60	0.006		
		0.60	0.006		
		0.60	0.006		
		0.30	0.003		
		0.25	0.0025		
		0.25	0.0025		
MidSeason Growth Stage					
Link et al. 1990 [DIRS 177142], p. 508, Table 2	Mean Maximal g measured Apr. 11 and 18; predawn water potentials indicate no stress.	0.78	0.0078	0.0140	71
		0.68	0.0068		
Rice et al. 1992 [DIRS 177165], p. 36, Figure 4	Values from upper end of graph where no stress is indicated (1.48 to 1.75).	1.75	0.0175		
		1.6	0.016		
		1.6	0.016		
		1.5	0.015		
		1.5	0.015		
		1.49	0.0149		
		1.49	0.0149		
		1.48	0.0148		
		1.48	0.0148		
		1.48	0.0148		

[1] g = stomatal conductance.
[2] r_l = stomatal resistance (Equation D-14).

D5.4 METEOROLOGICAL PARAMETERS

The upper bound Glacial Transition climate is semi-arid and characterized by cool, wet winters, and warm to cool dry summers relative to current conditions (BSC 2004 [DIRS 170002], Section 6.6.2). Recommended anlogue weather stations for the upper bound Glacial Transition climate are Spokane, St. John, and Rosalia, Washington (BSC 2004 [DIRS 170002], Table 6-1 and Section 6.6.2). Daily temperature data from the Spokane weather station (DTN: MO0605SPASPOKA.000 [DIRS 177135]) were used as source data to calculate RH_{min} and Δ for corrections to K_{cb}s. Daily data were averages of 10 to 13 years of data (DTN: MO0605SPASPOKA.000 [DIRS 177135]). Daily wind speed data from Yucca Mountain Meteorogical Site 1 for water year 1998 were used in the K_{cb} calculation. As described in Section D3.2.4, wind speed data were corrected for a height of 2 m according to Equation D-15 (Output DTN: MO0603SPAREFET.000).

Average daily maximum temperatures (T_{max}), average daily minimum air temperatures (T_{min}), and average daily precipitation were extracted from the source file (DTN: MO0605SPASPOKA.000 [DIRS 177135]) and placed in an Excel® file (Output DTN: MO0605SPADAYWA.000 [DIRS 177135]). Temperature was converted from Fahrenheit to Celsius (˚C = 5/9 × [˚F-32]) and precipitation from inches to mm (1 inch = 25.4 mm). Minimum relative humidity was calculated according to the following equations (Allen et al. 1998 [DIRS 157311], p. 124, Equation 64, and p. 36, Equation 11):

$$RH_{\min} = \frac{e^{\circ}(T_{dew})}{e^{\circ}(T_{\max})} \times 100 \qquad \text{(Eq. D-17)}$$

and

$$e^{o}(T) = 0.6108 \exp\left[\frac{17.27T}{T + 237.3}\right] \qquad \text{(Eq. D-18)}$$

where

$e^{\circ}(T)$ = Saturation vapor pressure at temperature T (kPa),
T_{dew} = Minimum daily air temperature minus 2 degrees (°C),
T_{max} = Maximum daily air temperature,
exp(x) = 2.7183 (base of natural logarithm) raised to the power (x).

Average daily temperature was calculated from the mean of T_{max} and T_{min} (Output DTN: MO0605SPADAYWA.000) and used to calculate Δ for use in the stomatal correction factor. As described in Section D3.2.4, Δ was calculated according to Equation D-16 (Output DTN: MO0605SPADAYWA.000).

An average profile of the three associations (Figure D-9) was calculated in the Excel® spreadsheet in Output DTN: MO0606SPATRANS.000. This calculation was done using the Excel® AVERAGE command. Daily K_{cb}s and supporting calculations are in Output DTN: MO0606SPATRANS.000.

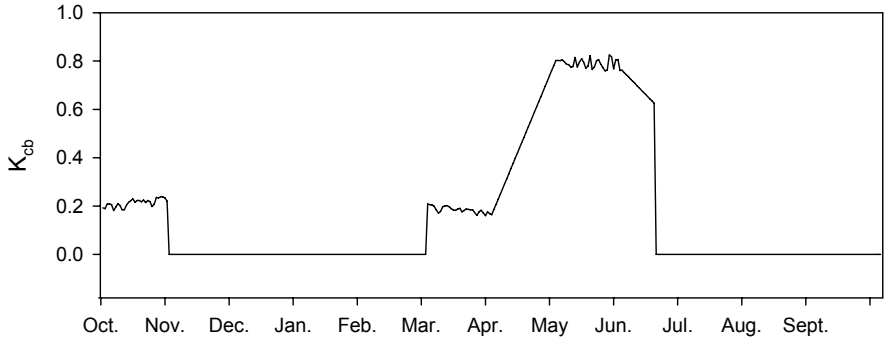

Source: Output DTN: MO0606SPATRANS.000.

Figure D-9. Transpiration Coefficients (K_{cb}) for a *Bromus* Monoculture at Yucca Mountain

D6. METHODS FOR CALCULATING REFERENCE EVAPOTRANSPIRATION FOR A GENERIC AREA AT YUCCA MOUNTAIN

To determine if reasonable values for plant water use in a desert environment were generated by the K_{cb} profiles, ET_0 was needed for a generic area at Yucca Mountain to estimate potential transpiration ($PT = ET_0 \times K_{cb}$ [Section 6.5.3.4]). Reference evapotranspiration was calculated as a function of slope and azimuth using the standardized FAO-56 Penman-Montieth equation in Appendix C for use in the infiltration model (Equation C-37). The ET_0 values calculated in Appendix C are direct input to specific model grid cells. The results of this calculation show that the K_{cb} values estimated for the Yucca Mountain site result in a reasonable estimate of potential transpiration, which is consistent with comparable field data.

Reference evapotranspiration for a generic area at Yucca Mountain was also calculated according to methods described in Allen et al. (1998 [DIRS 157311]) using the FAO Penman−Monteith equation (Allen et al. 1998 [DIRS 157311], Equation 6, p. 24):

$$ET_o = \frac{0.408\Delta(R_n - G) + \gamma \dfrac{900}{T + 273} u_2 (e_s - e_a)}{\Delta + \gamma(1 + 0.34u_2)} \qquad \text{(Eq. D-19)}$$

where

ET_0 = Reference evapotranspiration (mm/day),
R_n = Net radiation at the crop surface (MJ m^{-2} day^{-1}),
G = Soil heat flux density (MJ m^{-2} day^{-1}),
T = Mean daily air temperature at 2 m height (°C),
u_2 = Wind speed at 2 m height (m s^{-1}),
e_s = Saturation vapor pressure (kPa),
e_a = Actual vapor pressure (kPa),
$e_s - e_a$ = Saturation vapor pressure deficit (kPa),

Δ = Slope vapor pressure curve (kPa °C^{-1}),
γ = Psychrometric constant (kPa °C^{-1}).

Equation D-19 is the same as Equation C-37 used in Appendix C.

D6.1 CALCULATION OF REFERENCE EVAPOTRANSPIRATION FOR A GENERIC AREA AT YUCCA MOUNTAIN

Meteorological factors that drive evapotranspiration include solar radiation, air temperature, air humidity, and wind speed. Climatological and physical parameters required to derive daily ET_0 were either measured directly or derived from measured data. Daily ET_0 was calculated using weather data from water years 1998, 2001, and 2002 to represent above average, average, and below average precipitation years, respectively. Reference *ET* was used with NDVI' in Appendix E, and with K_{cb}s calculated in this appendix to estimate potential water use by desert vegetation for representative above average, average, and below average precipitation years. Weather data was used from Yucca Mountain Meteorological Site 1. The step-by-step methods to calculate ET_0 are described and example calculations are provided below.

D6.2 STEP-BY-STEP DESCRIPTION OF CALCULATIONS

Three atmospheric parameters were generated from meteorological data and used directly in the calculation of ET_0. These include the slope of the saturation vapor pressure curve (Δ), psychrometric constant (γ), and vapor pressure deficit ($e_s - e_a$). The slope of the saturation vapor pressure curve and γ were developed in Section D3.2.4. Values for Δ for the 1998, 2001, and 2002 water years are in Output DTN: MO0603SPAREFET.000. A value of 0.059, which corresponds to the elevation of meteorological monitoring Site 1, was selected for γ (Section D3.2.4). Vapor pressure deficits are developed below.

D6.2.1 Vapor Pressure

Vapor Pressure Deficit ($e_s - e_a$)—The vapor pressure deficit ($e_s - e_a$) is the difference between the saturation vapor pressure (e_s) and the actual vapor pressure (e_a) of the air. Essentially, it represents the evaporative power of the air. The air becomes dryer as the vapor pressure deficit increases.

Mean e_s is the average of the saturation vapor pressures calculated at the daily maximum (T_{max}) and minimum (T_{min}) air temperatures (Output DTN: MO0602SPAWEATH.000). The relationship of e_s to temperature is given by the following equations (Allen et al. 1998 [DIRS 157311], Equations 11 and 12, p. 36):

$$e^o(T) = 0.6108 \exp\left[\frac{17.27T}{T + 237.3}\right] \qquad \text{(from Eq. D-18)}$$

where

e°(T) = Saturation vapor pressure at temperature T (kPa),

T = Air temperature (°C),

exp(x) = 2.7183 (base of natural logarithm) raised to the power (x).

and

$$e_s = \frac{e^o(T_{\max}) + e^o(T_{\min})}{2} \qquad \text{(Eq. D-20)}$$

Example: For March 1, 1998 (day of year 60), T_{max} = 13.9°C and T_{min} = 2.3°C (Output DTN: MO0602SPAWEATH.000).

$$e^o(T_{\max}) = 0.6108 \exp\left[\frac{17.27(13.9)}{13.9 + 237.3}\right] = 0.6108 \text{ exp } 0.956 = 1.588 \text{ kPa} \qquad \text{(from Eq. D-18)}$$

$$e^o(T_{\min}) = 0.6108 \exp\left[\frac{17.27(2.3)}{2.3 + 237.3}\right] = 0.6108 \text{ exp } 0.166 = 0.721 \text{ kPa}$$

$$e_s = \frac{1.588 + 0.721}{2} = 1.154 \text{ kPa}$$

Daily $e°(T_{max})$, $e°(T_{min})$, and e_s for the 1998, 2001, and 2002 water years are in Output DTN: MO0603SPAREFET.000.

Actual vapor pressure (e_a) can be calculated from relative humidity (RH), the dewpoint temperature (T_{dew}), or psychrometric data. Monthly mean maximum and minimum RH values were available from meteorological monitoring Site 1. However, examination of RH values indicated they were not always representative of the expected conditions of the reference area defined for ET_0 in FAO-56 methods (Allen et al. 1998 [DIRS 157311]). Under reference area conditions, RH_{max} is expected to approach 90% to 100% (Allen et al. 1998 [DIRS 157311], Annex 6, pp. 257 to 262). At monitoring Site 1, daily RH_{max} was less than 70% for up to 80% of the time, depending on the year (Output DTN: MO0602SPAWEATH.000). Use of such low RH values would result in overestimation of ET_0. Allen et al. (1998 [DIRS 157311], p. 36, and Annex 6, pp. 257 to 262) recommended use of T_{dew} calculated from daily minimum temperature rather than using unreliable or unrepresentative RH values or when no humidity data are available. Therefore, instead of using RH_{max} to calculate e_a, T_{dew} was estimated from T_{min} (Allen et al. 1998 [DIRS 157311], Equation 6-6, p. 261):

$$T_{dew} = T_{\min} - K_o \qquad \text{(Eq. D-21)}$$

where K_o is a correction factor = 2°C for arid climates (Allen et al. 1998 [DIRS 157311], p. 261).

Use of Equation D-21 reflects the higher humidity anticipated under reference conditions. Dewpoint temperatures calculated with Equation D-21 are in Output DTN: MO0603SPAREFET.000.

The adjusted T_{dew} was used in the following equation to calculate daily values of e_a for the 1998, 2001, and 2002 water years (Allen et al. 1998 [DIRS 157311], Equation 14, p. 37):

$$e_a = e^o(T_{dew}) = 0.6108 \exp\left[\frac{17.27 T_{dew}}{T_{dew} + 237.3}\right] \quad \text{(Eq. D-22)}$$

Example: For March 1, 1998 (day of year 60), T_{min} = 2.3°C (Output DTN: MO0602SPAWEATH.000) and T_{dew} = 0.3°C (Output DTN: MO0603SPAREFET.000).

$$e_a = 0.6108 \exp\left[\frac{17.27 \times 0.3}{0.3 + 237.3}\right] = 0.6108 \exp(0.022) = 0.624\ kPa \quad \text{(from Eq. D-22)}$$

Daily e_a values for 1998, 2001, and 2002 water years are in Output DTN: MO0603SPAREFET.000.

Using e_s and e_a calculated for March 1, 1998, the vapor pressure deficit is:

$$(e_s - e_a) = 1.154 - 0.580 = 0.574\ kPa \quad \text{(Eq. D-23)}$$

Average daily (e_s and e_a) values for the 1998, 2001, and 2002 water years are in Output DTN: MO0603SPAREFET.000.

D6.2.2 Radiation

Net radiant energy is one of the main factors controlling the energy balance of a vegetated soil surface. Heat energy for *ET* is principally supplied by solar radiation, which can reach the plant canopy as direct sunlight or sunlight scattered by molecules and particles in the atmosphere. Both direct and scattered sunlight can be reflected by surroundings to the plant canopy. Net radiation (R_n) represents the balance between energy absorbed, reflected, and emitted by the earth's surface and is used directly in the calculation of ET_0. Extraterrestrial radiation (R_a), solar radiation (R_s), clear sky radiation (R_{so}), net shortwave radiation (R_{ns}), and net longwave radiation (R_{nl}) are required either directly or indirectly to calculate R_n.

Extraterrestrial Radiation (R_a)—Extraterrestrial radiation is the solar radiation received at the top of the earth's atmosphere on a horizontal surface. It is a function of latitude, date, and time of day. Daily R_a was calculated according to the following equations (Allen et al. (1998 [DIRS 157311], Equations 21 to 25, p. 46):

$$R_a = \frac{24(60)}{\pi} G_{sc}\ d_r \left[\omega_s \sin(\varphi)\sin(\delta) + \cos(\varphi)\cos(\delta)\sin(\omega_s)\right] \quad \text{(Eq. D-24)}$$

where

R_a = Extraterrestrial radiation (MJ m^{-2} day^{-1}),
G_{sc} = Solar constant = 0.0820 (MJ m^{-2} min^{-1}),
d_r = Inverse relative distance Earth−Sun (Equation D-26),
φ = Latitude (rad) (Equation D-25),
ω_s = Sunset hour angle (rad) (Equation D-28),
δ = Solar declination (rad) (Equation D-27).

$$\varphi\left(radians\right)=\frac{\pi}{180}\left[latitude\ \ in\ \ decimal\ \ \deg rees\right] \quad \text{(Eq. D-25)}$$

$$d_r=1+0.033\cos\left(\frac{2\pi}{365}J\right) \quad \text{(Eq. D-26)}$$

$$\delta=0.409\sin\left(\frac{2\pi}{365}J-1.39\right) \quad \text{(Eq. D-27)}$$

where J is the day of year.

$$\omega_s=\arccos\left[-\tan\left(\varphi\right)\tan\left(\delta\right)\right] \quad \text{(Eq. D-28)}$$

Example: Using meteorological monitoring Site 1 (latitude = 36° 51') and March 1 (day of year 60), convert latitude from degrees and minutes to decimal degrees, then to radians.

$$36+\frac{51}{60}=36.85\ (decimal\ \deg rees)$$

$$\varphi\left[Radians\right]=\frac{\pi}{180}36.85=0.64 \quad \text{(from Eq. D-25)}$$

Calculate d_r and δ.

$$d_r=1+0.033\cos\left(\frac{2\pi}{365}60\right)=1.017 \quad \text{(from Eq. D-26)}$$

$$\delta=0.409\sin\left(\frac{2\pi}{365}60-1.39\right)=-0.143 \quad \text{(from Eq. D-27)}$$

Calculate ω_s.

$$\omega_s=\arccos\left[-\tan\left(0.64\right)\tan\left(-0.143\right)\right]=1.463 \quad \text{(from Eq. D-28)}$$

Calculate R_a.

$$R_a = \frac{24(60)}{\pi} 0.082 \times 1.017 \left[1.463 \sin(0.64) \sin(-0.143) + \cos(0.64) \cos(-0.143) \sin(1.463)\right]$$
$$= 25.4 \text{ MJ m}^{-2} \text{ day}^{-1} \quad \text{(from Eq. D-24)}$$

Daily R_a values for the 1998, 2001, and 2002 water years are in Output DTN: MO0603SPAREFET.000.

Solar Radiation (R_s)—Solar radiation (R_s) measured at meteorological monitoring Site 1 for the 1998, 2001, and 2002 water years was used in ET_0 calculations. See Section D3.2.4 for description and development of solar radiation data. Solar radiation data for the 1998, 2001, and 2002 water years are in Output DTN: MO0602SPAWEATH.000.

Clear Sky Radiation (R_{so})—Clear sky radiation (R_{so}) is the radiation that would hit a flat surface under cloudless conditions (Allen et al. 1998 [DIRS 157311], Equation 37, p. 51):

$$R_{so} = \left(0.75 + 2 \times 10^{-5} Z\right) R_a \quad \text{(Eq.D-29)}$$

where

Z = station elevation above sea level (m).

Example: Station elevation for meteorological Site 1 = 1,143 m and R_a for March 1, 1998 (day of year 60) = 25.4 MJ m^{-2} day^{-1} (Output DTN: MO0603SPAREFET.000).

$$R_{so} = \left(0.75 + 2 \times 10^{-5} \times 1143\right) 25.4 = 19.6 \text{ MJ m}^{-2} \text{ day}^{-1} \quad \text{(from Eq. D-29)}$$

Clear sky radiation is required to calculate net longwave radiation (R_{nl}), which is used directly in the calculation of R_n. Daily R_{so} values are in Output DTN: MO0603SPAREFET.000.

Net Solar (shortwave) Radiation (R_{ns})—Net solar radiation incorporates albedo (shortwave radiation reflected from the canopy of the grass reference crop) into incoming solar radiation and is used directly in the calculation of R_n (Allen et al. 1998 [DIRS 157311], Equation 38, p. 51):

$$R_{ns} = (1 - \alpha) R_s \quad \text{(Eq. D-30)}$$

Where α = albedo of grass reference crop = 0.23 (Allen et al. 1998 [DIRS 157311], p. 51).

Example: For March 1, 1998 R_s = 18.1 MJ m^{-2} day^{-1} (Output DTN: MO0602SPAWEATH.000).

$$R_{ns} = (1 - 0.23) 18.1 = 13.9 \text{ MJ m}^{-2} \text{ day}^{-1} \quad \text{(from Eq. D-30)}$$

Mean monthly R_{ns} values are in Output DTN: MO0603SPAREFET.000.

Net Longwave Radiation (R_{nl})—Net loss of radiant energy (R_{nl}) occurs primarily through thermal or longwave radiation. The Stefan-Boltzmann law predicts that black body radiation emission (radiation emitted by a perfect radiator) is proportional to surface temperature raised to the fourth power (Nobel 1983 [DIRS 159953], p. 347). Plants are virtually black body absorbers and emitters of longwave radiation. However, radiant energy is also absorbed and emitted by water vapor, carbon dioxide, ozone and clouds, which affects the outgoing energy flux. Because of this, the Stefan-Boltzmann law is corrected for humidity and cloudiness in the calculation of net outgoing longwave radiation (R_{nl} (Allen et al. 1998 [DIRS 157311], Equation 39, p. 52)):

$$R_{nl} = \sigma \left[\frac{T_{\max,K}^4 + T_{\min,K}^4}{2} \right] \left(0.34 - 0.14\sqrt{e_a}\right) \left[1.35\frac{R_s}{R_{so}} - 0.35\right] \qquad \text{(Eq. D-31)}$$

where

σ	=	Stefan-Boltzmann constant (4.903 10^{-9} MJ K^{-4} m^{-2} day^{-1}),
T_{max}, K	=	maximum absolute temperature during the 24-hour period (K = °C + 273.16),
T_{min}, K	=	minimum absolute temperature during the 24-hour period (K = °C + 273.16),
e_a	=	actual vapor pressure (kPa),
R_s/R_{so}	=	relative shortwave radiation (limited to ≤ 1.0),
R_s	=	measured (Present-Day climate) or calculated (future climate) solar radiation (MJ m^{-2} day^{-1}),
R_{so}	=	calculated clear-sky radiation (MJ m^{-2} day^{-1}).

Example: For March 1, 1988, T_{max} = 13.9°C and T_{min} = 2.3°C (Output DTN: MO0602SPAWEATH.000); e_a = 0.580 (Output DTN: MO0603SPAREFET.000); R_s = 18.1 MJ m^{-2} day^{-1} (Output DTN: MO0602SPAWEATH.000); R_{so} = 19.8 MJ m^{-2} day^{-1} (Output DTN: MO0603SPAREFET.000); and σT_{max}, K^4 = 33.3, σT_{min}, K^4 = 28.2 (Output DTN: MO0603SPAREFET.000).

$$R_{nl} = \left[\frac{33.3 + 28.2}{2}\right]\left(0.34 - 0.14\sqrt{0.580}\right)\left[1.35\left(\frac{18.1}{19.8}\right) - 0.35\right] \qquad \text{(from Eq. D-31)}$$

$$= 30.75 \times 0.233 \times 0.884 = 6.3 \text{ MJ m}^{-2} \text{ day}^{-1}$$

Daily R_{nl} values are in Output DTN: MO0603SPAREFET.000.

Net Radiation (R_n)—Net Radiation is the balance between net shortwave radiation (both incoming and reflected) and net loss of longwave radiation (Allen et al. 1998 [DIRS 157311], Equation 40, p. 53):

$$R_n = R_{ns} - R_{nl} \qquad \text{(Eq. D-32)}$$

Example: For March 1, 1998, R_{ns} = 13.9 and R_{nl} = 6.3 (Output DTN: MO0603SPAREFET.000).

$$R_n = 13.9 - 6.3 = 7.6 \text{ MJ m}^{-2} \text{ day}^{-1} \qquad \text{(from Eq. D-32)}$$

Daily R_n values are in Output DTN: MO0603SPAREFET.000.

Soil Heat Flux—According to Allen et al. (1998 [DIRS 157311], Equation 42, p. 54) daily soil heat flux (G_{day}) beneath the grass reference surface is small enough that it can be ignored:

$$G_{day} \approx 0 \qquad \text{(Eq. D-33)}$$

Wind Speed (u_2)—See Section D3.2 for description and correction of wind speed data. Daily wind speed values for the 1998, 2001, and 2002 water years are in Output DTN: MO0603SPAREFET.000.

D6.3 REFERENCE EVAPOTRANSPIRATION AND POTENTIAL TRANSPIRATION

Using the humidity, radiation, and wind speed values generated in this appendix for March 1, 1998, mean daily ET_0 can be calculated using Equation D-19.

Example: For March 1, 1998:

$\Delta = 0.072$

$Rn = 7.5$

$G = 0$

$\gamma = 0.059$

$T = 7.8$

$u_2 = 1.7$

$(e_s - e_a) = 0.574$

$$ET_o = \frac{0.408 * 0.072(7.5 - 0.0) + 0.059 \dfrac{900}{7.8 + 273} 1.7(0.574)}{0.072 + 0.059(1 + 0.34 * 1.7)} = 2.5 \text{ mm/day} \qquad \text{(from Eq. D-19)}$$

Daily ET_0 for the 1998, 2001, and 2002 water years are in Output DTN: MO0603SPAREFET.000. Reference evapotranspiration profiles were generated for each water year (Figure D-10).

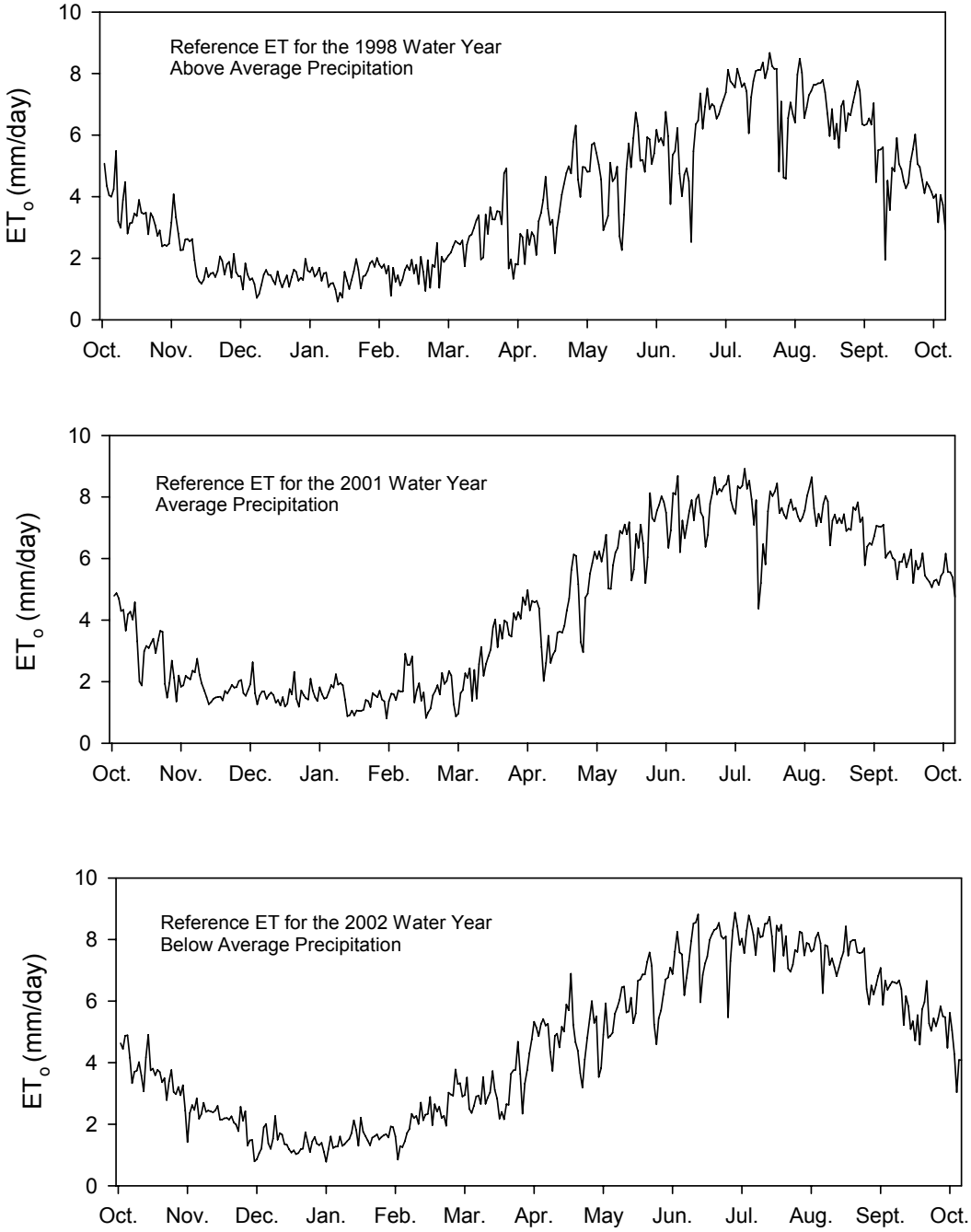

Source: Output DTN: MO0603SPAREFET.000.

Figure D-10. Reference Evapotranspiration (ET_0) for the 1998, 2001, and 2002 Water Years

Potential Transpiration Profiles—PT profiles (Figure D-11) for the three vegetation associations, water years, and *Bromus* monoculture (profile not shown) were generated using Equation D-1 (Figure 6.5.3.6-5).

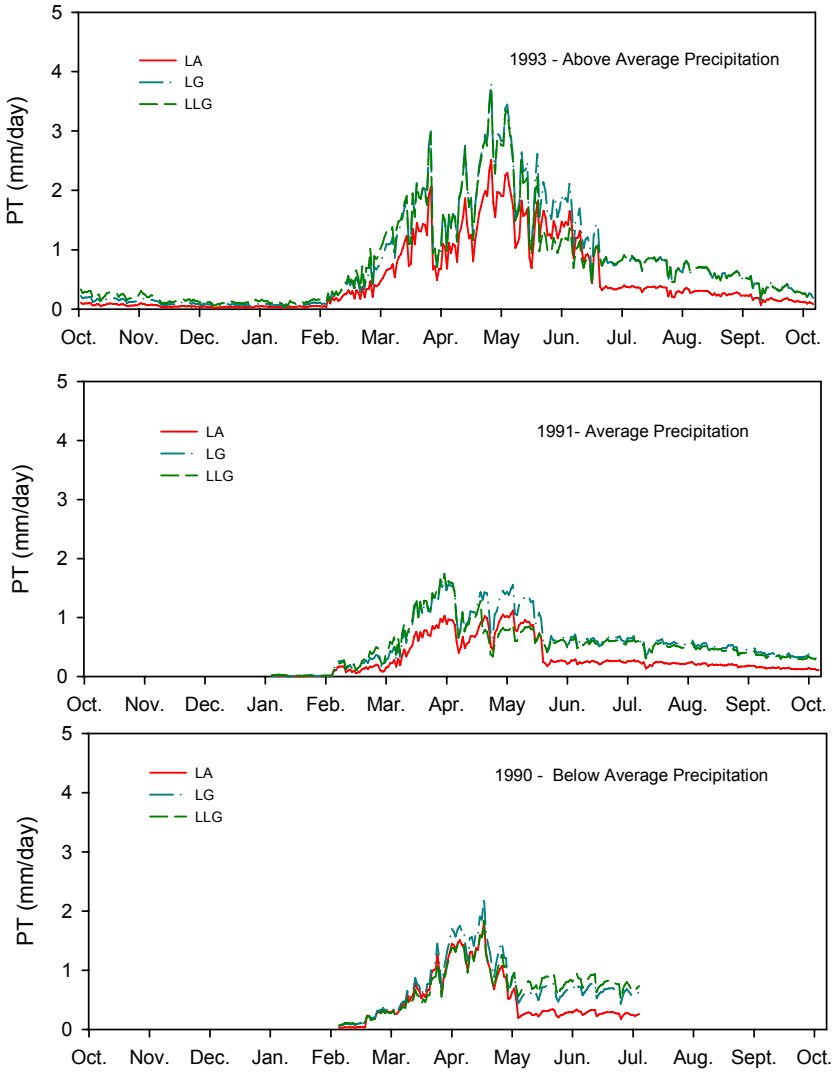

Source: Output DTN: MO0606SPABASAL.001.

Figure D-11. Potential Transpiration (PT) for the 1993, 1991, and 1990 Water Years for Three Vegetation Associations (LA = *Larrea−Ambrosia*, LG = *Lycium−Grayia*, LLG = *Larrea−Lycium−Grayia*)

Total *PT* for growing seasons was determined by summing the daily values in Figure D-11. There was little difference in total growing season *PT* between the LG and LLG associations across water years (Table D-37). Potential transpiration for the LA association ranged from about 54% to 68% of *PT* for the LG association. Even though the K_{cb} profiles for the 1990 water year appeared to converge, the greater cover of evergreen vegetation in the LG and LLG associations compared to the LA association resulted in about 36 mm more water use over the May through July time period (Table D-37).

Table D-37. Growing Season Potential Transpiration for Three Vegetation Associations

Vegetation Association	Potential Transpiration[a] for Growing Season
Wet Year (240 mm)[b]	
Larrea−Ambrosia	180 mm
Lycium−Grayia	286 mm
Larrea−Lycium−Grayia	276 mm
Average Year (150 mm)[b]	
Larrea−Ambrosia	87 mm
Lycium−Grayia	162 mm
Larrea−Lycium−Grayia	144 mm
Dry Year (60 mm)[b]	
Larrea−Ambrosia	78 mm
Lycium−Grayia	113 mm
Larrea−Lycium−Grayia	108 mm
Glacial Transition Climate (440 mm)[c]	
Bromus tectorum monoculture	276 mm

[a] Output DTN: MO0606SPABASAL.001.

[b] Approximate average annual precipitation for LA, LG, and LLG vegetation associations. Source: CRWMS M&O 1996 [DIRS 102235], p. 21, Figure 4-3.

[c] Average total yearly precipitation for Spokane, Washington. DTN: MO0605SPASPOKA.000 [DIRS 177135].

Potential transpiration for the *Bromus* monoculture was 276 mm, equal to that of the LLG association for the wet year. However, this amount was less than the mean annual precipitation estimates for the Glacial Transition climate state (about 440 mm) that the K_{cb}s were calculated for. This could indicate that cover for the *Bromus* monoculture at Yucca Mountain was underestimated by the methods used in Appendix D. It could also indicate that a *Bromus* monoculture would not use all the water available under Glacial Transition climate conditions. Under the right set of circumstances, this could result in available water for deeper rooted species to take hold in the system, perhaps preventing a monoculture from establishing. However, germination conditions for most Great Basin species do not occur until later in the spring when soil temperatures warm. *Bromus* is able to photosynthesize and use water at low temperatures, which could result in dry soils before germination of native species could occur.

Appropriateness of K_{cb}s for Desert Vegetation—To evaluate whether the magnitude of calculated K_{cb}s was reasonable for desert vegetation, *PT* was compared to average precipitation recorded on ESPs during WY1990, WY1991, and WY1993. Precipitation recorded on ESPs for those years were approximately 240 mm (1993), 150 mm (1991), and 60 mm (1990) (CRWMS M&O 1996 [DIRS 102235], p. 21, Figure 4-3). Potential transpiration exceeded precipitation by about 4 to 50 mm on the LG and LLG plots depending on the year (Table D-37). These amounts are minimal compared to variation in precipitation among sites that can occur at Yucca Mountain. It is important to note that the K_{cb} represents the potential water use for a given LAI or vegetation cover (i.e., water is not limiting for the green vegetation that is present on a site). Therefore, *PT* will generally be greater than actual transpiration. Actual transpiration is controlled in the infiltration model by soil water balance and K_s (Section 6.4.4).

PT for the less productive LA sites was less than water year precipitation during the average and above average precipitation years. The LA sites support fewer annual species, which account for much of the increased cover on LLG and LG sites during average and above average precipitation years. Because precipitation is not directly used in K_{cb} or ET_0 calculations, the correspondence between *PT* and precipitation provides an independent check suggesting that the K_{cb} values are appropriate for a desert system.

A second check on whether the magnitude of K_{cb}s was reasonable for a desert system was performed by comparing actual *ET* measured in the Mojave Desert to the *PT* values calculated for the three water years. In a study of plant water use by drought deciduous (*Ambrosia dumosa* and *Lycium pallidum*) and evergreen species (*Larrea tridentata* and *Ephedra nevadensis*), Yoder and Nowak (1999 [DIRS 177167], pp. 83 and 84) used soil moisture measurements (neutron probe) and soil water balance methods to estimate total annual *ET*. The study was conducted over a three-year time period (1995 to 1997) in the Mojave Desert vegetation zone on the Nevada Test Site. The elevation of field sites ranged from 950 to 1,150 m. Annual precipitation at the study sites ranged from 199 mm to 290 mm in 1995, 29 mm to 54 mm in 1996, and 79 to 125 mm in 1997, corresponding to above, below, and average precipitation years, respectively (Yoder and Nowak 1999 [DIRS 177167], pp. 84 and 85, Figure 1). Annual *ET* averaged for the study sites was about 225 mm in 1995, 50 mm in 1996, and 100 mm in 1997 (Yoder and Nowak 1999 [DIRS 177167], p. 88, Figure 3). These values were higher than *PT* estimated for the LA association for above average and average precipitation years by 47 mm and 13 mm, respectively, and lower than estimated *PT* for the remaining associations by 27 to 63 mm, depending on association and year. These differences are relatively small considering differences in water years, locations, and vegetation cover, and they provide additional evidence to suggest that the magnitude of K_{cb} values is reasonable for the Yucca Mountain area.

A third check on the appropriateness of the K_{cb} values was performed in Appendix E. In Section E7, actual *ET* for the LG association was simulated for the 1998 water year using ET_0 and daily fitted values for NDVI' that were scaled by precipitation (Figure E-25). Comparison of this estimated actual *ET* to the *PT* profile for LG (Figure E-26) showed remarkably good correspondence, suggesting that the K_{cb}s are appropriate for the Yucca Mountain system. See Appendix E for complete analysis.

Criticisms on the Use of Transpiration Coefficients in Desert Environments—Mata-Gonzalez et al. (2005 [DIRS 178523]) published a review paper criticizing the use of FAO-56 methods for calculating transpiration coefficients and the subsequent use of those coefficients to estimate *ET* for arid ecosystems. Their main criticisms were:

- K_c estimated for nonstressed plants produces high values not representative of field conditions in arid environments. Use of the dual crop coefficient ($K_c = K_{cb} + K_e$) does not adequately adjust for sparse vegetation because estimated K_{cb} values were not provided in FAO-56 for native desert vegetation. The water stress coefficient (K_s) that adjusts for soil water availability causes *ET* to be underestimated.

- Leaf area is the only variable in FAO-56 methods that determines water use of a plant.

- Plants are assumed to have maximum foliage coverage throughout the growing season.

- The core methods do not consider stomatal regulation, and the correction provided for stomatal regulation for arid land species is too complicated. Estimation of K_e for the dual crop coefficient is too complicated.

The authors do not recognize that methods are provided in FAO-56 for calculating K_{cb} from LAI or effective ground cover. These methods are described in Chapter 9 of FAO-56, and Equations 98, 100, 101, and 102 (Allen et al. 1998 [DIRS 157311], pp. 183 to 194) and were used in this analysis to calculate K_{cb}s (Appendix D). The use of effective ground cover measured on reference area plots at Yucca Mountain directly accounted for the sparse vegetation typical of the Yucca Mountain area. The authors stated that "…transpiration rates of a species are constant for a given day of the year, since they are a function of the species inherent potential water use (K_c) in relation to the maximum water use of a plant under ideal conditions (ET_0)…are inappropriate…." However, the assumption that ratios of *ET* by a specific vegetation to the climatic reference ET_0 is relatively constant for a given amount of vegetation cover is a proven and long-standing tenent of crop coefficient practice.

Variables in addition to leaf area in FAO-56 methods that are used to calculate K_{cb}, and that were used in this analysis, included wind speed, minimum relative humidity, plant height, and stomatal resistance. Thus, while leaf area and effective ground cover are important variables used in FAO-56 methods to estimate plant water use, additional variables are also accounted for that influence transpiration.

The K_s is used to adjust for soil water availability in the infiltration model. The basis for the criticism that use of K_s underestimates *ET* is derived from the assumption that K_s goes to zero at a wilting point of −1.5 MPa (−15 bar) (Mata-Gonzalez et al. 2005 [DIRS 178523], p. 291). A wilting point of −1.5 MPa is typical of many crop species. The authors point out that certain desert shrubs have been shown to maintain photosynthesis, extract soil moisture, and survive at much lower water potentials (−7.0 to −12 MPa [−70 to −120 bar], Mata-Gonzalez et. al. 2005 [DIRS 178523], p. 291). That transpiration can occur in desert shrub species at lower water potentials than −1.5 MPa is a valid point. FAO-56 never associates wilting point with a specific soil water potential, as this can vary with species. FAO-56 instead suggests that "Wilting point is the water content at which plants will permanently wilt" (Allen et al. 1998 [DIRS 157311, p. 162), which is considered to be a true statement. However, the water potentials listed by the authors are extreme values, and it is not likely that transpiration occurs at any appreciable rate when soils are this dry. For the infiltration model, a wilting point of −6.0 MPa (−60 bars) was selected for desert vegetation (BSC 2006 [DIRS 176335]). This value was based on ranges of water potentials at which conductance and/or photosynthesis was determined to be zero for several Mojave Desert species. Thus, it is not likely that transpiration is underestimated by use of a wilting point that is realistic for desert plants.

Satellite based vegetation indices and observed fractions of ground cover have been applied during estimation of K_c. These indices and thus K_c vary over time to account for seasonal changes in ground cover and leaf area. Additionally, in the calculation of K_{cb}s, ground cover was reduced for the initial growth stage from the maximum observations used during the midseason

growth stage (Section D3.2.2). Thus, it was not assumed that plants have maximum foliage coverage throughout the growing season.

The basis for the last of these criticisms (methods being too complex) was that the objective of using FAO-56 methods to estimate *ET* in arid environments was to provide a widely accepted and simple approach for estimating water use by vegetation (Mata-Gonzales et al. 2005 [DIRS 178523], pp. 291 and 292). The authors recognized that partitioning evaporation and transpiration for arid systems and applying corrections for stomatal control are appropriate measures but suggest that the increase in level of complexity is such that these steps are rarely taken. Both were accounted for in the infiltration model.

D7. NOMENCLATURE FOR EQUATIONS USED IN APPENDIX D

Symbol	Description	Units	Where Used*
K_{cb}	basal K_{cb} when plant density and/or leaf areas are lower than for full cover conditions	dimensionless	Eq. D-1 (D-9)
$K_{c\ min}$	minimum K_c for bare soil in the presence of vegetation ($K_{c\ min} \approx 0$)	dimensionless	Eq. D-1
$K_{cb\ full}$	estimated basal K_{cb} during the midseason at peak plant size or height and full ground cover	dimensionless	Eq. D-1 (D-7)
f_c	observed fraction of soil surface that is covered by vegetation type (0.01–1)	dimensionless	Eq. D-1 (D-2)
$f_{c\ eff}$	effective fraction of soil surface covered or shaded by vegetation type (0.01–1)	dimensionless	Eq. D-1 (D-2)
h	plant height	m	Eq. D-1
$\sin(\eta)$	sine of the mean angle of the sun, η, above the horizon during midday hours when maximum evapotranspiration is likely to occur	Sin(radians)	Eq. D-2 (D-3)
ψ	latitude	radians	Eq. D-3
δ	solar declination	radians	Eq. D-3 (D-4, D-24, D-27)
J	day of year	dimensionless	Eq. D-4 (D-26, D-27)
i	day number within the growing season (1…length of the growing season)	dimensionless	Eq. D-5
$K_{cb,\ i}$	transpiration coefficient on day *i*	dimensionless	Eq. D-5
$K_{cb\ prev}$	K_{cb} at the end of the previous stage	dimensionless	Eq. D-5
$K_{cb\ next}$	K_{cb} at the beginning of the next stage	dimensionless	Eq. D-5
L_{stage}	length of the stage under consideration	days	Eq. D-5
ΣL_{prev}	sum of the length of all previous stages	days	Eq. D-5
$K_{cb,h}$	adjustment for the influence of vegetation height for K_{cb} for full cover condition under standard climate	dimensionless	Eq. D-6
$K_{cb,\ h}$	K_{cb} for full cover vegetation under a standard climate	dimensionless	Eq. D-7
u_2	mean wind speed at 2−m height	m s^{-1}	Eq. D-7, Eq. D-19 (D-15)
RH_{min}	minimum daily relative humidity	%	Eq. D-7 (D-17)

Symbol	Description	Units	Where Used*
h	mean maximum plant height	m	Eq. D-7 (D-6)
F_r	stomatal resistance correction factor	dimensionless	Eq. D-8 (D-9)
Δ	slope of the saturation vapor pressure curve	kPa °C^{-1}	Eq. D-8, Eq. D-19 (D-16)
γ	psychrometric constant	kPa °C^{-1}	Eq. D-8, Eq. D-19
r_l	mean leaf resistance (stomatal) for the vegetation in question	s m^{-1}	Eq. D-8 (D-14)
CI	confidence interval	dimensionless	Eq. D-10
t	t−table value for single tailed test with α = 0.10 and n−1 degrees of freedom	dimensionless	Eq. D-10, Eq. D-11
s_c	standard deviation of cover data for ESPs	dimensionless	Eq. D-10 (D-11)
n	number of ESPs in mean calculation	dimensionless	Eq. D-10
n_c	the number of ESPs required to sample cover of an association to within 10% of the true population mean	dimensionless	Eq. D-11
d	precision that the true difference of the sample mean occurs from the population (= 0.10)	dimensionless	Eq. D-11
x_c	mean of cover data for ESPs	dimensionless	Eq. D-11
g_v	stomatal conductance in velocity units	m s^{-1}	Eq. D-12 (D-14)
g_m	stomatal conductance in molar units	mol m^{-2} s^{-1}	Eq. D-12
R	universal gas constant	8.314 Pa m^3 mol^{-1} K^{-1}	Eq. D-12
T_l	leaf temperature	K	Eq. D-12
P	atmospheric pressure	Pa	Eq. D-12
u_z	wind speed measured at z m aboveground surface	m s^{-1}	Eq. D-15
z	height of measurement aboveground surface	m	Eq. D-15
$\exp(x)$	2.7183 (base of natural logarithm) raised to the power (x)	dimensionless	Eq. D-16 (D-18)
$e°(T)$	saturation vapor pressure at temperature T	kPa	Eq. D-17, Eq. D-18, (D−−20, D-22)
T_{dew}	minimum daily air temperature minus 2 degrees	°C	Eq. D-17 (D-21, D-22)
T_{max}	maximum daily air temperature	°C	Eq. D-17, Eq. D-20
ET_0	reference evapotranspiration	mm/day	Eq. D-19
R_n	net radiation at the crop surface	MJ m^{-2} day^{-1}	Eq. D-19 (D-32)
G	soil heat flux density	MJ m^{-2} day^{-1}	Eq. D-19
T	mean daily air temperature at 2 m height	°C	Eq. D-19
e_s	saturation vapor pressure	kPa	Eq. D-19 (D-20)
e_a	actual vapor pressure	kPa	Eq. D-19 (D-22, D-31)
$e_s - e_a$	saturation vapor pressure deficit	kPa	Eq. D-19 (D-23)
T_{min}	minimum daily air temperature	°C	Eq. D-20 (D-21)
K_o	correction factor (= 2°C for arid climates)	°C	Eq. D-21

Symbol	Description	Units	Where Used*
R_a	extraterrestrial radiation	MJ m^{-2} day^{-1}	Eq. D-24 (D-29)
G_{sc}	solar constant = 0.0820	MJ m^{-2} min^{-1}	Eq. D-24
d_r	inverse relative distance Earth–Sun	L^{-1}	Eq. D-24 (D-26)
φ	latitude	rad	Eq. D-24 (D-25)
ω_s	sunset hour angle	rad	Eq. D-24
R_{so}	calculated clear sky radiation	MJ m^{-2} day^{-1}	Eq. D-29 (D-31)
Z	station elevation above sea level	m	Eq. D-29
R_{ns}	net solar (shortwave) radiation	MJ m^{-2} day^{-1}	Eq. D-30 (D-32)
α	albedo of grass reference crop (= 0.23)	dimensionless	Eq. D-30
R_{nl}	net outgoing longwave radiation	MJ m^{-2} day^{-1}	Eq. D-31 (D-32)
σ	Stefan−Boltzmann constant	MJ K^{-4} m^{-2} day^{-1})	Eq. D-31
T_{max}, K	maximum absolute temperature during the 24−hour period	K	Eq. D-31
T_{min}, K	minimum absolute temperature during the 24−hour period	K	Eq. D-31
R_s/R_{so}	relative shortwave radiation (limited to ≤ 1.0)	dimensionless	Eq. D-31
R_s	measured (present−day climate) or calculated (future climate) solar radiation	MJ m^{-2} day^{-1}	Eq. D-31 (D-30)
G_{day}	daily soil heat flux	MJ m^{-2} D^{-1}	Eq. D-33

* Defined in these equations. Equation numbers in parentheses show other equations where these terms are used but not redefined.

APPENDIX E
QUANTIFYING AND SIMULATING YUCCA MOUNTAIN VEGETATION RESPONSE

SUMMARY

One of the key issues in determining the net-infiltration at the Yucca Mountain repository is the ability to predict the interaction between vegetation and precipitation. Vegetation uses the moisture supplied from the atmosphere, allowing only the residual from this consumption to infiltrate into the media beyond the root zone – thus plant and canopy development is a surrogate measure of the water used. The net-infiltration model must capture this plant usage. To do this, vegetative patterns at the site were analyzed using remote sensor images, parameters governing these patterns were determined, and these parameters were then combined to simulate a seasonal, site specific response to moisture.

The principle behind vegetative analysis is simple. With the exception of green vegetation, most natural surfaces are about equally as bright in the red and near-infrared part of the spectrum. In vegetation, red light is strongly absorbed by photosynthetic pigments (such as chlorophyll) found in green leaves, while near-infrared light either passes through or is reflected by live leaf tissues. Thus, areas of bare soil having little or no green plant material will appear similar in both the red (R) and near-infrared (NIR) wavelengths, while areas with green vegetation will be very bright in the near-infrared and very dark in the red part of the spectrum. Because the remotely sensed images are 8-bit digital, every pixel corresponds to a number from 0 to 255 (zero being pure black and 255 being pure white). Vegetation indices are calculated using the pixel values for the red and near-infrared wavelengths. They are the reduction of multispectral scanning measurement to a single value for predicting and assessing vegetative characteristics such as plant leaf area, total biomass and general plant stress and vigor. This analysis used a normalized difference vegetation index (NDVI) that is calculated using near infrared and red spectral data from satellite images. Further, since the green response of vegetation is proportional to seasonal precipitation that is directly related to seasonal *ET*, NDVI as a surrogate measure for canopy response was used as a variable to help predict *ET* for the Mass Accounting System for Soil Infiltration and Flow (MASSIF) Model.

While the principle behind this vegetation analysis is simple, in practice there are many complications. In order to directly compare images taken on different dates, data must be:

- Adjusted for the gains and biases of each sensor (Section E2.1)
- Adjusted to account for the effect of having different solar zenith angles and compensated for different values of the exoatmospheric solar irradiances arising from spectral band differences (Section E2.1)
- Corrected for differing atmospheric conditions (Section E2.2)
- Corrected for nonsystematic variations, such as atmospheric opacity, soil albedo, ground level water content, atmospheric water content, and illumination geometry (Section E2.4)
- Aligned to a common geospatial coordinate system (Section E2.3).

In addition to the typical corrections mentioned above, the Yucca Mountain Site posed a unique challenge to data processing. Comparison between observed site vegetation and image analysis results showed there was a nonvegetation source that produced a strong depression in the red wavelength mimicking a vegetation response. It was concluded that the natural rock weathering processes over time produced desert varnish that caused this response. Because the site is very arid, the measured vegetation responses tend to be very low, and it was found that the signal from the desert varnish was high in comparison. Section E2.6 discusses the correction used for desert varnish.

A total of 33 images from three representative years (a very dry, an average, and a very wet year) were analyzed. The choice of image dates was made with regard to the satellite data available and ancillary data that were measured on and near Yucca Mountain. The images represented snapshots of the site during the growing season, emphasizing those times when the vegetation response was greatest (March through June of each year). These images were assembled to represent responses during a water year (WY), from October 1 through September 30 of subsequent years. A water year more naturally captures the cycle of winter precipitation and annual plant growth that is generally senescent in this environment during late summer.

The combined corrections discussed above resulted in a set of processing parameters for each image. These parameters were developed for the general site flora. As discussed in Appendix D, there are three predominant vegetation associations at the site. Analyses were completed to assure that the general processing parameters were appropriate for each of the three vegetation associations (Section E2.5). Analyses show that the corrected vegetation index, NDVI', has an inherent uncertainty of 0.01 ± 6%.

Once images had been processed so that they were directly comparable, a seasonal response to precipitation was developed that contained an annual peak for vegetation (occurring in about mid April), as described in Section E3. General response curves were developed which captured the variability induced by slope and azimuth. Slope and azimuth combinations will result in different amounts of sunlight reaching the ground at different times of the year and thus, influence the magnitude and/or timing of the vegetation growth response at that location. These influences are irrespective of soil conditions at a specific point and were examined by comparing responses for various slope/azimuth combinations. The calculations used averages of pooled sample groups in order to determine overall trends. Comparison of a predicted vegetation response using the general response curves to image data from lowlands showed that the general response curves somewhat underestimate vegetation response. However, because the repository footprint is overlain by rocky uplands, the vegetation response curves were developed to be most accurate for these areas. The curves will conservatively estimate the proportion of precipitation that will be available from infiltration in the lowlands.

To account for spatially varying conditions at the site, such as amount of exposed rock, soil depth, and water holding capacity, a potential vegetation response (PVR) for each model grid cell was produced (Section E4). PVR is calculated per pixel (each 0.2 acres in size) using subtraction of the peak vegetation response from a critically dry year (2002) from that measured at the peak of a very wet year (1998). This measurement is thus an estimate of the capability for each pixel in the modeled region to support vegetation. The minimum NDVI values, measured during a critically dry year, represent the signal from desert varnish. PVR was normalized by

dividing each value by the average value for model grid cells for a subset area overlying the proposed repository. This area was chosen as a rectangle of 12,702 grid cells (11.43 km^2). Normalization provided scaling to permit a better understanding of PVR distribution: a PVR of 1.0 represents the approximate average vegetation response overlying the repository.

An algorithm was developed to simulate vegetation for each model grid cell using results from the analyses. The general response curves provided the shape of the vegetation response through the growing season. They were then scaled for the general conditions for each growing year by a ratio of the precipitation of the year of interest to the wettest year (1998) that was used to fit the response curve. PVR was used as a scalar to represent plant growth potential within each model grid cell.

The uncertainty associated with the vegetation algorithm was only evaluated for the mathematical processing necessary to isolate the vegetation signal within the satellite data. Additional uncertainty associated with the response curve or the algorithm will be analyzed in the uncertainty of the MASSIF.

E1. GENERAL METHODS AND OVERVIEW FOR THEIR APPLICATION

The present Yucca Mountain site climate is arid, with the vegetation cover being limited by meager precipitation. Vegetation responds to periods of precipitation by increasing the leaves within the canopy and consuming the available soil water through transpiration (Scanlon et al. 2005 [DIRS 175977]). Data obtained by satellite were used for characterizing this vegetation response.

This section outlines pertinent points of the analyses, starting with some general notes. Section E1 provides the guiding principles used in the analyses, Section E2 provides background information on vegetation signals and NDVI, Section E3 describes how the vegetation signal was isolated from the background signal, and Section E4 discusses which years were chosen for the analyses. Pertinent points in these analyses include:

1. As described in Appendix D, the vegetation at the site is a mix of species typical of the Mojave Desert and the Great Basin. Although there is a variety of species, they are simulated in this analysis as a lumped vegetation response. Each pixel of the satellite image represents an area many times larger than the individual plants making up the canopy.

2. Vegetation response was characterized according to its greenness, viewed at multiple points through each year. Chlorophyll, the molecule within plant leaves that moderates photosynthesis, is green, and the greenness captured within each pixel is determined by the overall chlorophyll content within the canopy viewed. This basic relationship permits using remote sensing for vegetation study (Asrar et al. 1992 [DIRS 176754]). As briefly described in Section D2, gas exchange for photosynthetic uptake of CO_2 is proportional to transpiration as mediated by the atmospheric demand, expressed as ET_0. Thus, as the numbers of leaves increase, the greenness and the rate at which water is used by the plants increase

proportionally. A measure of vegetation canopy expression, as greenness, is a surrogate measure of the transpiration rate.

3. Although several vegetation associations exist on Yucca Mountain, the mix of plant species was not evaluated separately using this remote-sensing approach. The parameterization that resulted was sensitive to the rise and fall of the annual growth cycle of the overall site flora. The relationships developed to characterize the site vegetation responses were calibrated for the rocky uplands that overlie the proposed repository to ensure the greatest level of accuracy for vegetation simulation there.

4. As described in Appendix D, there are three major vegetation associations on Yucca Mountain and the surrounding area that are characterized by the ecological study plots (ESPs). The principal vegetation covering the repository has been given the abbreviation LG for two dominant genera (*Lycium* and *Grayia*). The two other important regional assemblages are LA (*Larrea* and *Ambrosia*) and LLG (*Larrea*, *Lycium,* and *Grayia*). The equation developed for the lumped vegetation response was tested using data extracted from the ESPs to verify its appropriateness for these three vegetation associations.

5. The analyses and processing to develop the plant simulation are documented in a series of spreadsheets that are referenced in this appendix with appropriate data tracking numbers (DTNs).

6. The analyses contained in this appendix were made entirely with three software packages. Remote sensing analyses were performed using Environment for Visualizing Images software (ENVI + IDL, Version 4.2: STN: 11204-4.2-00). Spatial output from ENVI was analyzed and displayed in ArcGIS (ArcGIS Desktop Version 9.1: STN: 11205-9.1-00). ENVI and ArcGIS were both used for extraction of remote sensing data that were then analyzed and graphically displayed in Microsoft Excel™

Note that there are a series of citations contained in this document with associated DIRS (document input reference system) numbers. None of these citations were used for direct input. Further, uncertainty calculations are included as text boxes, shaded grey, in each section.

E1.1 ASSUMPTIONS

Appendix E contains three assumptions. The first assumption was necessary for development of the processing parameters for atmospheric correction: the air mass overlying the region of Yucca Mountain at the time of each overpass was exemplified by the region chosen for estimation of the correction parameter. As part of the development of this correction parameter, it was also assumed that the properties of this air mass were evenly distributed over Yucca Mountain.

The two other assumptions concerned the development of an algorithm to simulate vegetation growth. The timing of the seasonal growth response for this algorithm was assumed to be represented by the response observed in WY1998. The final assumption concerns the

application of this algorithm: the vegetation algorithm developed should be generally applicable to related but different climates, either Monsoon or Glacial Transition.

E1.2 GUIDING PRINCIPLES

There are several guiding principles that enable the analysis of *ET* using a vegetation canopy expression. These underscore the link for climate (i.e., long-term patterns of dryness and temperature from year to year) and weather, with shorter-term variations and the consequent vegetation response.

- The present Yucca Mountain climate is arid and the plants operate in deficit conditions for most of the year.

- Vegetation cover/expression on Yucca Mountain rises and falls with the magnitude of total annual precipitation.

- Seasonal total *ET* is also determined by precipitation, since, without precipitation there is virtually nothing to evapotranspire. Thus, an estimate of vegetation cover is a surrogate measure of relative *ET*.

- With the exception of small amounts of net infiltration that have escaped below the root zone, virtually all annual precipitation is expended as *ET* because precipitation is meager and the driving force for evaporation extremely high. In general, the amount of infiltrated water is very low or virtually nonexistent if the soil is deep.

- The timing of the seasonal growth response is assumed to be represented by the response observed in WY1998. This assumption is described in Section 5.

- Given the extent of our knowledge, the vegetation algorithm developed should be applicable to related but different climates, either Monsoon or Glacial Transition. This assumption is described in Section 5.

Vegetation response to precipitation is particularly evident for Yucca Mountain in the comparison of wet versus dry years on satellite data. Figure E-1 shows three views of Yucca Mountain taken by Landsat TM (thematic mapper) during the spring vegetation growth peak for the three years chosen for characterizing vegetation: a wet year (WY1998), an intermediate year (WY2001), and a dry year (WY2002).

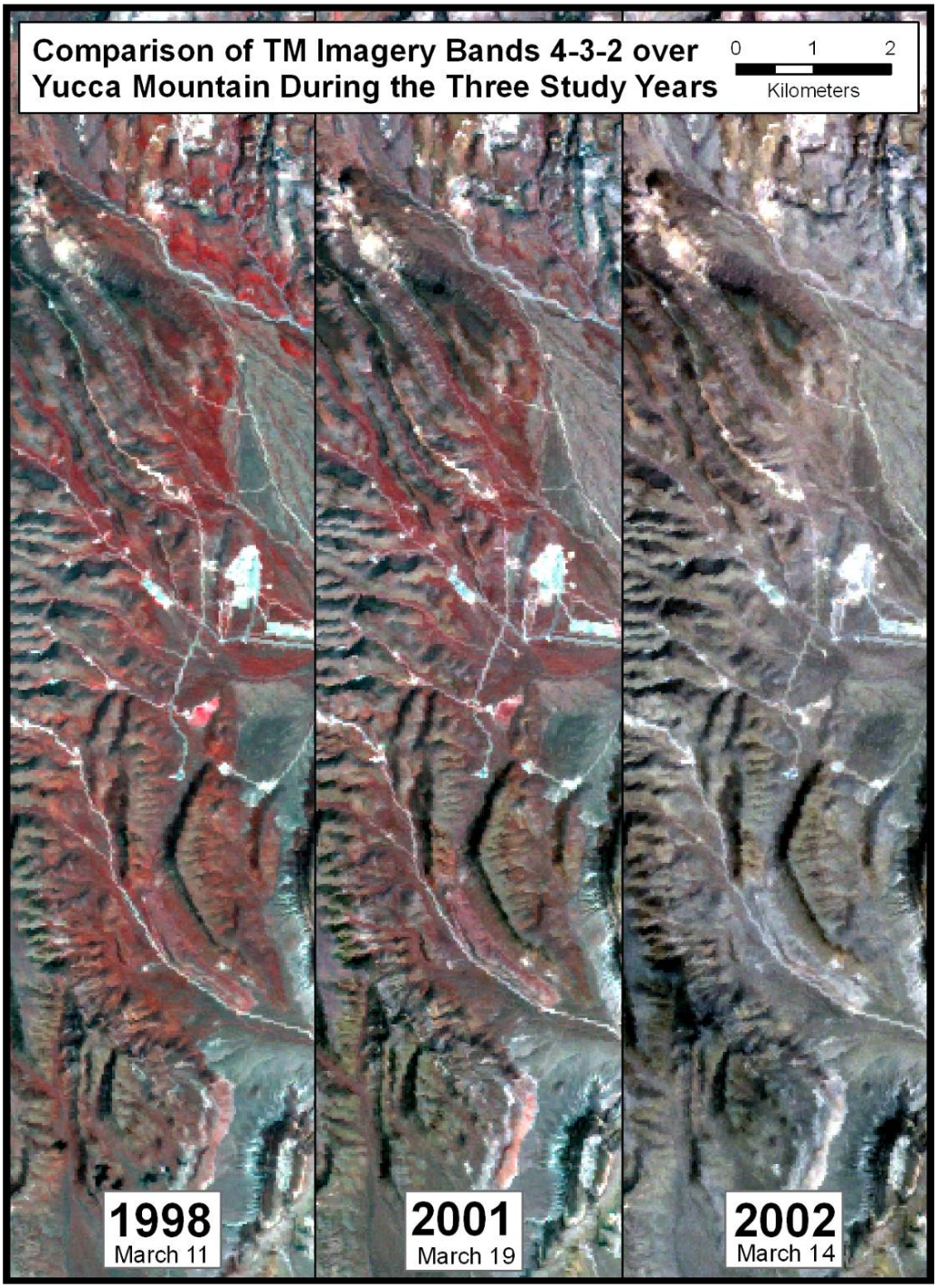

Source: Output DTN: SN0608NDVILSTM.001.

NOTES: TM Bands 4, 3, and 2 are shown in red, green, and blue, respectively. Vigorous vegetation appears red. These images were produced from the geocorrected TM data Output DTN: SN0608NDVILSTM.001 without further processing using ENVI Software.

Figure E-1. Views of a Portion of the Yucca Mountain area during Wet (1998), Approximately Average (2001), and Critically Dry (2002) Antecedent Weather Displayed in False Color (Verdant Vegetation Appears Red)

E1.3 BACKGROUND FOR NDVI AND VEGETATION SIGNAL

The regional scale of the infiltration model for Yucca Mountain (~50 square kilometers) is ideally suited for application of satellite data, particularly Landsat TM. Landsat TM has square pixels that are 28.5 m on a side; in area, each pixel is only about 1:140,000 of the area of the MASSIF model domain and constitutes an area of 0.2 acre. The wide spatial coverage (>100 km), digital form and high quality of TM data enable their use for the study of vegetation and its relationship to hydrology at the Yucca Mountain site.

Normalized difference vegetation index (NDVI) is an indicator of vegetation vigor often used for measurement of environmental response to landscape-scale hydrology, including global climate change (e.g., Running and Nemani 1991 [DIRS 176819]), rainfall (e.g., Wang et al. 2003 [DIRS 176761]), and evapotranspiration (*ET*) (e.g., Kustas et al. 1994 [DIRS 176757]; Seevers and Ottman 1994 [DIRS 176764]; Szilagyi et al. 1998 [DIRS 176839]; and Szilagyi 2002 [DIRS 176840]). For the TM sensor, Band 3 corresponds to the red wavelengths (R), while Band 4 corresponds to the near infrared wavelengths (NIR). NDVI utilizes the great difference between these two adjacent bands that occurs when viewing healthy green plants. Chlorophyll, responsible for the green color of plants, absorbs red light while leaf tissue reflects highly in near infrared (Buschmann and Nagel 1993 [DIRS 176736]). NDVI is calculated by subtracting the response in the red band from the reflectance in the near-infrared band and then dividing the sum of the reflectances for these two bands (Rouse et al. 1974 [DIRS 177246], Equation E-1).

$$NDVI = (NIR - R) / (NIR + R) \quad \text{(Eq. E-1)}$$

Chlorophyll is a physiologically expensive molecule for plants to produce, and the amount of chlorophyll relates directly to the rate of photosynthesis (Sellers et al. 1992 [DIRS 176824]). Photosynthesis requires leaf conductance for uptake of carbon dioxide, and during this process water is evaporated to the atmosphere in the process of transpiration. Because of these linkages, NDVI can be used as a competent surrogate for the estimation of *ET* (Kustas et al. 1994 [DIRS 176757]; Seevers and Ottman 1994 [DIRS 176764]; Szilagyi 2000 [DIRS 176839]; and Szilagyi 2002 [DIRS 176840]).

E1.4 NDVI CALCULATION TO ISOLATE LOW-COVER VEGETATION SIGNAL

The data set assembled for Yucca Mountain is multitemporal, with numerous time steps within each of the three years selected for analyses. Because the magnitude of NDVI in desert environments is very small, minute differences of NDVI are meaningful and must be discernible within the data. The challenge presented here was to employ processing methods to uncover the NDVI response from extremely low vegetation cover. These responses needed to be discernable from background signals. Desert varnish on ubiquitous rock surfaces also produces a positive NDVI signal, often in excess of the vegetation itself.

A common necessity for using multitemporal satellite data has been to minimize data set variability introduced by temporally changing conditions that affect individual data acquisitions. These include atmospheric opacity, soil albedo, ground-level and atmospheric water content, and illumination geometry (Huete and Liu 1994 [DIRS 176738]; Liu and Huete 1995 [DIRS 176739]; Carlson and Ripley 1997 [DIRS 176748]; and Song et al. 2001 [DIRS 176745]).

Soil background and atmospheric noise affecting NDVI may not be independent but interact in a complex manner since the atmosphere can also alter the soil background signal and vice versa (Liu and Huete 1995 [DIRS 176739]). Due to these complex interactions, when viewed temporally, raw NDVI tends to vary in a nonsystematic manner (Huete and Liu 1994 [DIRS 176738]; Liu and Huete 1995 [DIRS 176739]).

Nonsystematic scatter inherent in NDVI is nontrivial and, without correction, can mask vegetation response to changing hydrology, especially for vegetation of very low cover that consequentially produces a low NDVI signal. Fortunately, removing this scatter can be accomplished with a standard remote sensing technique. In the original correction described by Gillies et al. (1997 [DIRS 176763]), NDVI values were stretched to conform to a range from zero to one using Equation E-2:

$$NDVI^* = (NDVI - NDVI_0) / (NDVI_S - NDVI_0) \quad \text{(Eq. E-2)}$$

where: $NDVI_0$ = NDVI at zero vegetation cover,
$NDVI_S$ = NDVI at saturation.

Baugh and Groeneveld (2006 [DIRS 178678]) developed a modification to this correction called $NDVI_{offset}$ that simply subtracts the value $NDVI_0$ that is calculated by linear regression of the lowest linear portion of the cumulative distribution function. $NDVI_S$, representing peak vegetation expression, is often typified by cultivated fields. Although there are alfalfa fields in the Amargosa Valley adjacent to the YMP site, these do not reach a peak NDVI during winter months when they are cut, fallowed, or grazed. Calculation of NDVI* is thus difficult for this site. However, of 12 vegetation indices, including simple NDVI, NDVI*, and $NDVI_{offset}$, a comparison of the ability to predict a linear relationship with antecedent precipitation by Baugh and Groeneveld (2006 [DIRS 178678]), found that $NDVI_{offset}$ and NDVI* performed equally well and greatly outperformed all other indices, including simple NDVI. The formula for $NDVI_{offset}$ is given as Equation E-3:

$$NDVI_{offset} = NDVI - NDVI_0 \quad \text{(Eq. E-3)}$$

As explained later in this appendix, development of an algorithm to predict vegetation response for Yucca Mountain required one additional adaptation of NDVI, subtracting the lowest measured level of $NDVI_{offset}$ that occurred during late summer of a very dry year, WY2002. This new index, given the convention NDVI', removed the $NDVI_{offset}$ contributed by desert varnish and isolated the signal from the vegetation.

$NDVI_{offset}$ is calculated in Section E2.4 of this appendix.

E1.5 CHOICE OF DATA FOR ANALYSES: KEY YEARS – 1998, 2001, AND 2002

There are two important trends in annual weather for Yucca Mountain that determine the pattern of vegetation growth that occurs. These are hot, dry summers and cool winters that tend to receive the greatest portion of annual precipitation (Figure E-2, a and b). Because of these influences, wintertime native vegetation passes through a dormant period that then responds with a flush of spring growth funded by overwinter precipitation. The hot dry summers create a second period of annual dormancy after all available soil water has been exhausted. In terms of

the annual hydrologic cycle, the hot dry months of summer are essentially a break between cycles. For this reason, the characterization of vegetation growth will be tracked on a water year basis starting October 1 (of the previous calendar year) and ending 364 days later on September 30. In this appendix, water year is abbreviated WY and individual days within each water year are numbered sequentially, 1 to 365, and abbreviated WYDOY for water year day of year.

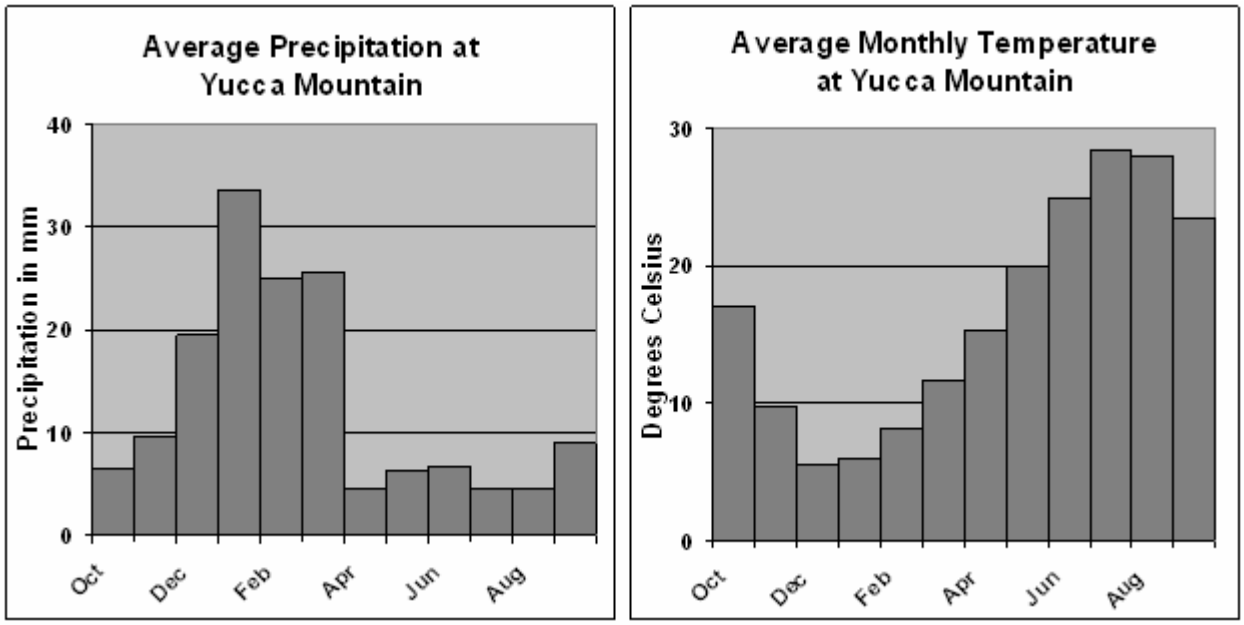

Source: DTN: MO9903CLIMATOL.001 [DIRS 116056]. Nine stations located at Yucca Mountain. Stations 1 to 5 from 1986 to 1997 and Stations 6 to 9 from 1993 to 1997.

NOTE: These data are presented only for illustration and were not used as direct inputs for the analyses.

Figure E-2. Yucca Mountain Average Monthly Precipitation (a) and Temperature (b) in Water Year Format as Background for Plant Growing Season and Precipitation Timing.

Three years were chosen for developing and testing the algorithm used to predict vegetation vigor using NDVI. These were an historic wet year (WY1998), an approximately average year (WY2001), and a very dry year (WY2002). Figure E-3 highlights these three years in the long term precipitation record for Station 4JA located 9 km from Yucca Mountain. During the wet year, WY1998, vegetation response was very high in comparison to the other two years. This is seen in the false color portrayals on Figure E-1. WY2002 was so dry that vegetation shows almost no response. This period of drought-induced quasi-zero vegetation cover is a baseline for minimal vegetation activity that was used in calculations to isolate the vegetation signal at Yucca Mountain. Vegetation expression during the record wet year (WY1998) was sufficiently robust for determining an ideal curve for annual vegetation response.

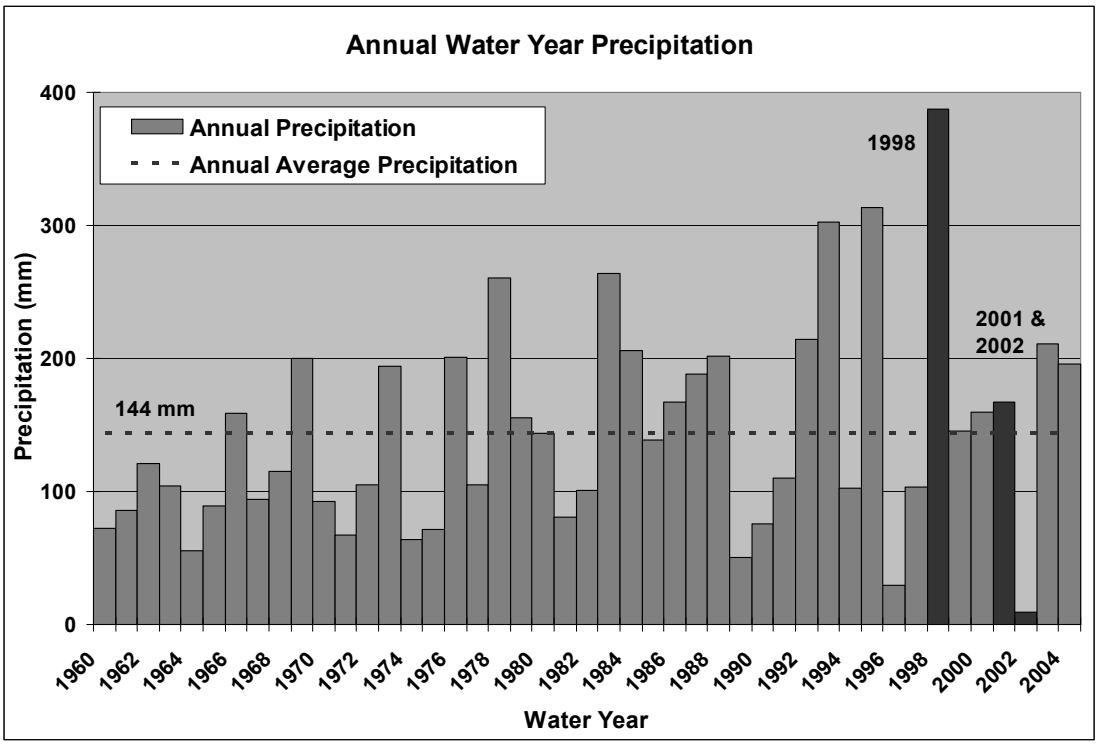

Source: 4JA east of Yucca Mountain 1959 to 2004: DTN: SN0601PRECPTMP.002 [DIRS 176122].

NOTE: These data were gathered sufficiently close to Yucca Mountain and have sufficient length of record to enable placing into context the three years that were chosen for analysis. All other data sets are either farther away from Yucca Mountain or have a comparatively short record. These data are presented only for illustration and were not used as direct inputs for the analyses.

Figure E-3. Water Year Total Precipitation Measured 12 km East of the Yucca Mountain Crest

Only three years were used for development and testing of the vegetation simulation and this small data set required characterization of seasonal growth response as a set response, hardwired for simplification, but scalable. Variations in plant growth according to intra-annual distribution of precipitation were, necessarily, not captured by the algorithm. Instead, as a simplification, vegetation growth will be fitted as proportional to antecedent precipitation occurring over the preceding winter. The peak precipitation, in March, also occurred in WY1998 (Figure E-4); however, for this year, precipitation was 2.6 times the annual average. Precipitation levels remained elevated through the summer of 1998.

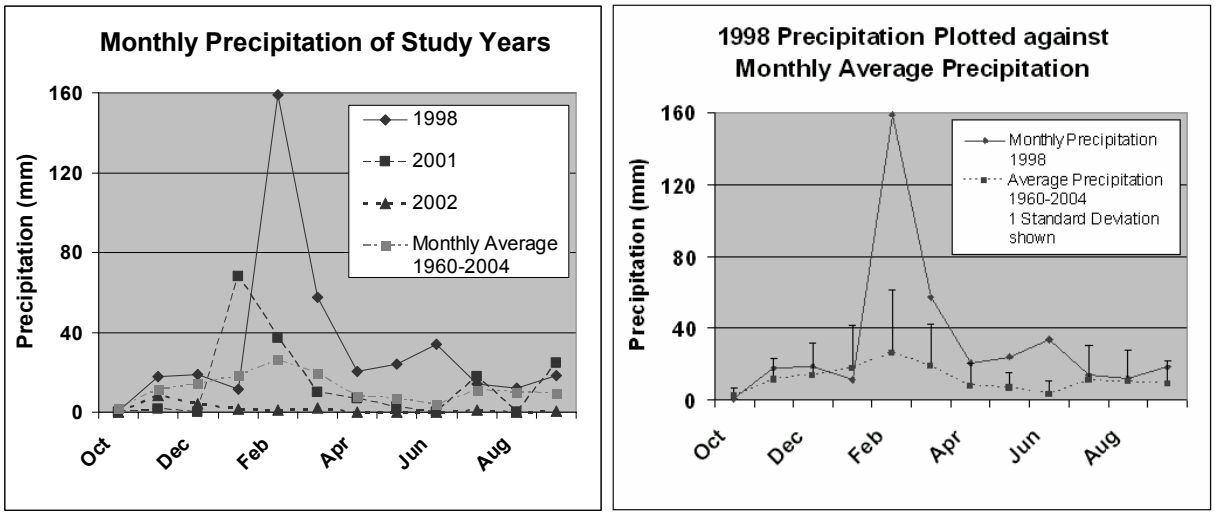

Source: Precipitation records from station 4JA east of Yucca Mountain 1959 to 2004: DTN: SN0601PRECPTMP.002 [DIRS 176122].

NOTE: These data are provided only for illustration and were not used as direct inputs.

Figure E-4. WY1998 Precipitation in Comparison to the Two Other Years (a) and the Statistics for Average Monthly Precipitation (b)

E2. DATA PROCESSING AND FUNCTIONAL RELATIONSHIPS

In order to calculate NDVI as a function of location and time across the Yucca Mountain region, it was necessary to process the acquired Landsat TM data. This processing included the following major steps: (1) conversion of all TM images to units of reflectance, (2) correction for differing atmospheric conditions, (3) selection of $NDVI_0$ to remove nonsystematic variation, and (4) geocorrection. A flow chart (Figure E-5) provides a visual map to follow the steps that are described in this section. The goal of the data processing was to isolate the vegetation signal by eliminating nonsystematic variation while selecting processing parameters in a nonarbitrary manner. A number of the data processing steps are standard, while others were developed specifically for the Yucca Mountain environment.

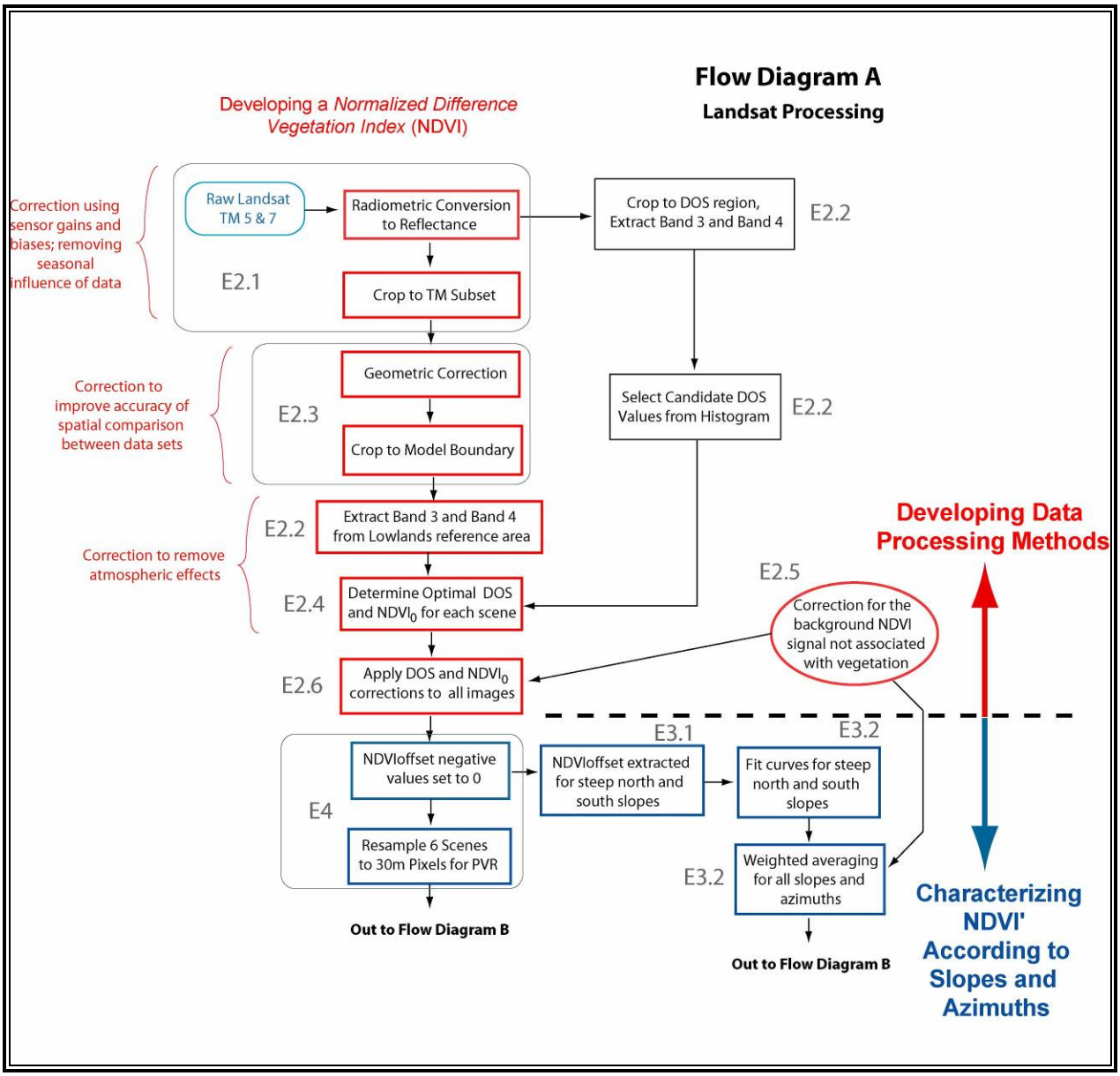

NOTE: Corroboration steps are given as ovals; processing and calculation as rectangles. Alpha-numeric designations are the sections in this appendix that describe these steps.

Figure E-5a. Flow Chart A for Processing and Analyzing Data Outputs that Feed to Flow Chart B

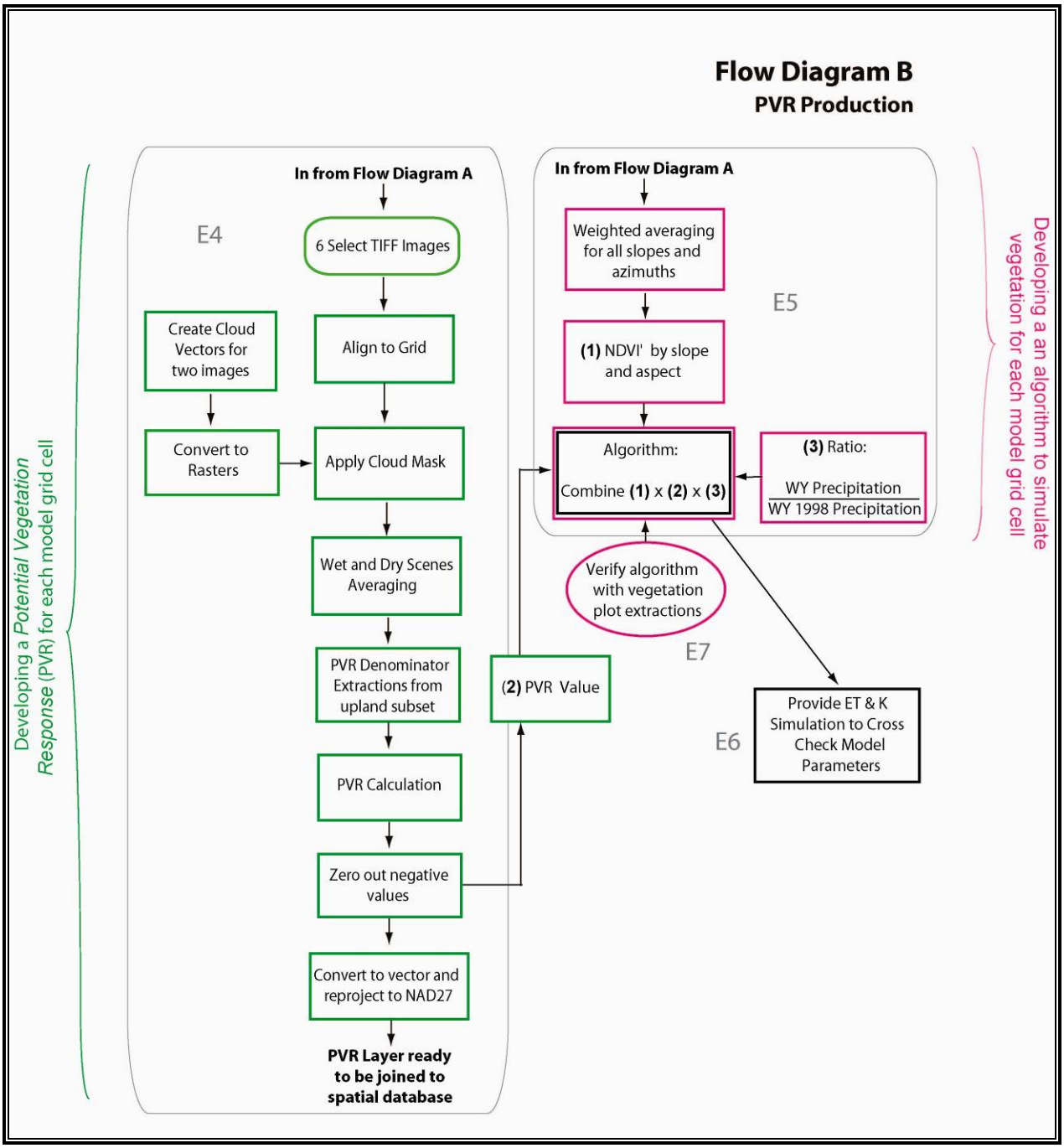

NOTE: Corroboration steps are given as ovals.

Figure E-5b. Flow Chart B for Processing and Analyzing Data Outputs from Flow Chart A

E2.1 INITIAL PROCESSING STEPS

Thirty three images were used for algorithm development (Table E-1). For the period chosen for development of the algorithm, there were two Landsat TM satellites, TM5 and TM7. TM7 was launched during 1999 and TM5 in 1982. These sensors pass directly over the Yucca Mountain region every 16 days. This time spacing is optimal for evaluating the growth and development of vegetation. However, cloud cover often occludes viewing the area of interest. The collection of satellite images was chosen as a minimal set for establishing vegetation responses through each growing season.

Table E-1. Landsat TM Data Used for Characterization of Yucca Mountain

WY1998		WY2001		WY2002	
Filename	**Sensor**	**Filename**	**Sensor**	**Filename**	**Sensor**
T519971102	TM5	T520001009	TM5	T520011012	TM5
T519980121	TM5	T520010129	TM5	T720011004	TM7
T519980310	TM5	T520010318	TM5	T720011207	TM7
T519980411	TM5	T520010419	TM5	T720020124	TM7
T519980427	TM5	T520010505	TM5	T720020225	TM7
T519981529	TM5	T520010606	TM5	T720020329	TM7
T519980630	TM5	T520010724	TM5	T720020414	TM7
T519980716	TM5	T720001220	TM7	T720020430	TM7
T519980817	TM5	T720010326	TM7	T720020516	TM7
		T720010630	TM7	T720020601	TM7
		T720010817	TM7	T720020617	TM7
				T720020719	TM7
				T720020804	TM7

Source: Output DTN: SN0601ALANDSAT.001.

NOTE: Filenames list satellite, year, month, and day.

Sensor memory effects in TM bands 3 and 4 when passing across highly contrasting targets (Helder and Ruggles 2004 [DIRS 176740], Section IV) prompted exclusion of data from the TM5 satellite during WY2002 (Figure E-6). Analyses of pixel patterning for NDVI along the high-contrast scarp face of the Yucca Mountain crest (edges in shadow and full sunlight) were used to study this phenomenon. This method confirmed that the TM5 data from WY2001 (including data from 10/12/01 of WY2002) were free from this effect and were included in the sample. There were five TM images that were eliminated from the analyses of WY2002 due to memory effects: May 8, May 24, June 9, June 25, and August 12.

Uncertainty Due to Integer Values for Digital Number

Details of the calculations are contained in Output DTN: SN0609LSTMPROC.001. In this appendix, details are provided for an example image. The example image was taken on 4/11/98, which is the peak of the growing season during a wet year. The statistics from this scene will be carried through the analyses to provide a measure of the greatest levels of uncertainty in the NDVI analyses.

Each image consists of raw digital numbers for each pixel and each band, supplemented by additional data, such as gain and bias corrections. Table E-Uncertainty−1 and Figure E-Uncertainty−1 indicate the range of values for the raw digital numbers for 4/11/1998. Truncation to an integer introduces a random uncertainty that is uniformly distributed over the range [−0.5, +0.5]. The standard uncertainty for that distribution is 0.3 (Appendix I). For each band, therefore, truncation produces a relative uncertainty that is random and is less than 1% of the mean measurement on 4/11/98 and less than 2% of the minimum measurement on that day.

Table E-Uncertainty−1. Landsat TM 5 04/11/1998 Pixel Value Statistics from within the Model Boundary

Band	Min	Max	Mean	Stdev
Band 3	20	196	61	12
Band 4	17	187	74	11

Source: Output DTN: SN0609LSTMPROC.001, *tm_processing_overview.xls*, worksheet *Process Steps*.

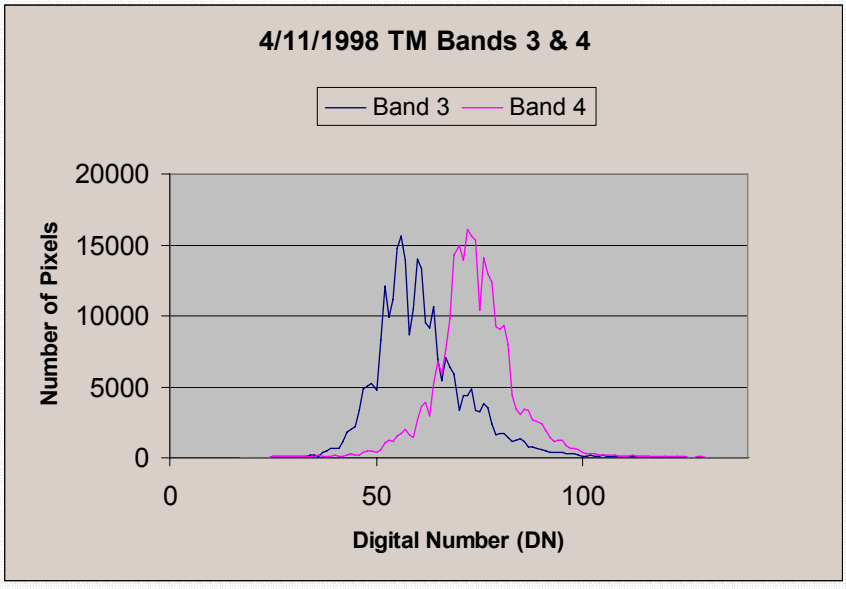

Source: Output DTN: SN0609LSTMPROC.001, *tm_processing_overview.xls*, worksheet *Process Steps*.

Figure E-Uncertainty−1. Histogram of Raw DN Numbers within the Model Boundary

Processing these TM data required an initial step to correct the data to radiance using the gains and biases of the sensors that accompany the satellite data. Radiance is the apparent light energy received at the satellite that is uncorrected for the strength of solar radiation incident to the target. The original signal from the satellite is output in digital numbers that are the readout from the sensors. The gains and offsets are, respectively, the slope and intercept of the linear relationship relating the radiance to the digital number. This correction removed the inherent differences between two sensors, Landsat TM5 and TM7, which were used in these analyses, and also corrected for sensor calibration drift (Markham and Barker 1987 [DIRS 177362]).

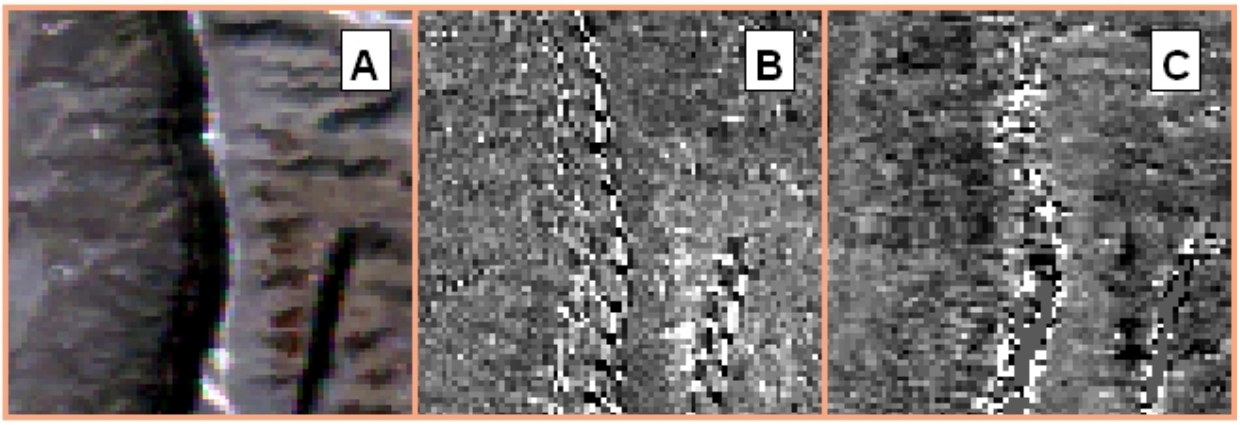

Source: Output DTN: SN0608NDVILSTM.001.

NOTES: A) A false color image from a TM 5 scene from May 8, 2002. B) The same showing NDVI. Note the systematic patterns along the crest and base of the shadowed slope due to the memory effect where high contrast existed between shaded and sunlit surfaces. C) The same location in a May 5, 2001, TM 5 scene exhibiting a normal NDVI response for comparison. The crest contains numerous high NDVI-response features.

Figure E-6. An Example of Observed Memory Effects in TM5 2002 Images

Development of a vegetation simulation for Yucca Mountain required evaluation of satellite images through the entire year. Thus, compensation for the differing solar radiation was necessary since the magnitude of solar radiation is much lower during the winter than the summer. Conversion to apparent (at satellite) reflectance is a step that effectively removes this seasonal influence by normalizing the measured data by the magnitude of solar radiation. This conversion process permits direct comparison of Landsat TM images taken throughout the year since, in essence, reflectance is radiance normalized by the strength of the solar irradiance. Each scene was converted to reflectance units using ENVI internal calibration utilities with the data for gains, offsets, and ephemeris from TM header files (Markham and Barker 1987 [DIRS 177362]). The formulae governing the calculation of radiance and reflectance are provided here in two steps (Equations E-4 and E-5), while the ENVI software provides this calculation in one step:

$$L_\lambda = Gain_\lambda \, DN_\lambda + Bias_\lambda \qquad \text{(Eq. E-4)}$$

where

L_λ = Exoatmospheric spectral reflectance
λ = Refers to either Band 3 or 4 value
$Gain_\lambda$ = Vvalue included with the satellite header
DN_λ = Digital number output from the sensor
$Bias_\lambda$ = Range of rescaled radiance in digital numbers.

$$\rho_\lambda = \frac{\pi L_\lambda d^2}{ESUN_\lambda \cos\theta_s} \quad \text{(Eq. E-5)}$$

where

ρ_λ = Exoatmospheric reflectance (i.e., measured at the sensor)
d = Earth–Sun distance
$ESUN_\lambda$ = Mean solar exoatmospheric irradiance
θ_s = Solar zenith angle in degrees.

Uncertainty for TM Band 3 and 4 Reflectance Calculation

The primary source of error influencing these calculations is in Equation E-4 because all of the inputs to Equation E-5 are matters of physics, are well known, and will tend to be small compared to the uncertainty involved in calibration. Table E-Uncertainty−2 lists the calibration coefficients for each of the images listed in Table E-1. These are colored to show that there are four groups with identical coefficients for all of the images that are in the same group. For the image on 4/11/98 (in the blue grouping), $Gain_3$ and $Gain_4$ are 1.04 and 0.87, while $Bias_3$ and $Bias_4$ are −1.17 and −1.51. Therefore, the value of L_λ is not much removed from the value of DN_λ.

Table E-Uncertainty−2. Calibration Coefficients for Images Used in this Appendix

	Band3		Band4	
TM Scene	Gain	Offset	Gain	Offset
t519971102	1.0398824	−1.1700000	0.8725882	−1.5100000
t519980121	1.0398824	−1.1700000	0.8725882	−1.5100000
t519980310	1.0398824	−1.1700000	0.8725882	−1.5100000
t519980411	1.0398824	−1.1700000	0.8725882	−1.5100000
t519980427	1.0398824	−1.1700000	0.8725882	−1.5100000
t519980529	1.0398824	−1.1700000	0.8725882	−1.5100000
t519980630	1.0398824	−1.1700000	0.8725882	−1.5100000
t519980716	1.0398824	−1.1700000	0.8725882	−1.5100000
t519980817	1.0398824	−1.1700000	0.8725882	−1.5100000
t520001009	1.0398824	−1.1700000	0.8725882	−1.5100000
t520010129	1.0398824	−1.1700000	0.8725882	−1.5100000
t520010318	1.0398824	−1.1700000	0.8725882	−1.5100000
t520010419	1.0398824	−1.1700000	0.8725882	−1.5100000
t520010505	1.0398824	−1.1700000	0.8725882	−1.5100000
t520010606	1.0398824	−1.1700000	0.8725882	−1.5100000
t520010724	1.0398824	−1.1700000	0.8725882	−1.5100000
t720001220	0.6216535	−5.6216431	0.6397638	−5.7397614
t720010326	0.9425197	−5.9425201	0.9692914	−6.0693054
t720010630	0.9425197	−5.9425201	0.9692914	−6.0693054
t720010328	0.9425197	−5.9425201	0.9692914	−6.0693054
t720010817	0.9425197	−5.9425201	0.9692914	−6.0693054
t520011012	1.0398824	−1.1700000	0.8725882	−1.5100000
t720011004	0.9425197	−5.9425201	0.9692914	−6.0693054
t720011207	0.9425197	−5.9425201	0.6397638	−5.7397614
t720020124	0.9425197	−5.9425201	0.6397638	−5.7397614
t720020225	0.9425197	−5.9425201	0.6397638	−5.7397614
t720020329	0.9425197	−5.9425201	0.9692914	−6.0693054
t720020414	0.9425197	−5.9425201	0.9692914	−6.0693054
t720020430	0.9425197	−5.9425201	0.9692914	−6.0693054
t720020516	0.9425197	−5.9425201	0.9692914	−6.0693054
t720020601	0.9425197	−5.9425201	0.9692914	−6.0693054
t720020617	0.9425197	−5.9425201	0.9692914	−6.0693054
t720020719	0.9425197	−5.9425201	0.9692914	−6.0693054
t720020804	0.9425197	−5.9425201	0.9692914	−6.0693054

Source: Output DTN: SN0609LSTMPROC.001; page “Gains_and_Offsets” *of tm_processing_overview.xls*.

Uncertainty for TM Band 3 and 4 Reflectance Calculation − Continued

An analysis by Chander et al. (2004 [DIRS 177572]) evaluated the uncertainty in the Gain coefficients for TM5 using cross−correlation with TM7 and a calibration uncertainty of 3% for TM7. Data from 1999 (close in time to the combined data set for WY1998 that feeds relationships to the MASSIF model) were compared to image pairs for spectrally stable features on the Railroad Valley Playa that showed a repeatability of approximately ± 2%, and for Bands 3 (R) and 4 (NIR) that are used to generate NDVI, a one sigma value for exoatmospheric radiance uncertainty of about ± 4 %. The Railroad Valley Playa is located about 70 km NNE of Yucca Mountain.

The exoatmospheric radiance uncertainty is a systematic uncertainty that applies to all of the values generated with the same values of Gain and Bias. The uncertainty from truncation is a random uncertainty.

Table E-Uncertainty−3 shows the range of values for radiance on 4/11/98, for individual pixels after processing through Equation E-5. Based on a relative uncertainty of 4%, the standard uncertainty of values near the mean is about 0.01, ranging from 0.002 at the minimum values to 0.02 at the maximum values.

Table E-Uncertainty−3. Reflectance Statistics of Pixel Values within the Model Boundary, Landsat TM5 4/11/1998

Band	Min	Max	Mean	Stdev
Band 3	0.05	0.52	0.16	0.03
Band 4	0.05	0.61	0.24	0.04

Source: DTN: SN0601ALANDSAT.001 [DIRS 177239]

Source: DTN: SN0609LSTMPROC.001, file *tm_processing_overview.xls,* worksheet “Process Steps.”

E2.2 ATMOSPHERIC CORRECTION

Up to this point, data processing produced values measured at the satellite sensor (exoatmospheric). Several steps were undertaken to remove the effects from the atmosphere through which light passed twice (incident and reflected). Atmospheric scatter due to the presence of airborne particles causes each of the TM bands to yield a higher reflectance than would be measured at the land surface in the absence of the entire atmospheric path. This scatter may especially confound ratiometric measurement such as NDVI because different concentrations of airborne particles such as smoke, water droplets, and dust may be present at the time of overpass that would affect R and NIR bands differently. In order to accurately evaluate low vegetation cover within multiple time steps, the effects of this scatter were removed.

A technique to remove atmospheric scatter, called dark object subtraction (DOS), assumes that there exists at least one or more pixels within the scene that will have zero reflectance. This lowest measured reflectance (the DOS value) represents the scatter at the assumed zero reflectance and is simply subtracted from all pixels in the region of interest (Chavez 1988 [DIRS 176788]). Areas where zero reflectance would be expected include still, open water, or deep shadows, two features that are unfortunately rare within the Yucca Mountain region. There are water bodies within the TM scenes, including Ash Meadows and Pahraganat Valley, (45 and 140 km distant, respectively). Sensitivity analyses indicated that the water bodies in these locations were not suitable due to desiccation during the critically dry year of 2002. At other times these water bodies gave very high reflectance values, possibly due to the entrainment of sediments or specular reflectance from winD-driven waves.

Because of the lack of specific DOS targets in all images, correction for atmospheric influences was approached using histogram functions for all TM images (Chavez 1988 [DIRS 176788]). First, candidate values for DOS (i.e., lowest values for reflectance) were chosen by examining histograms for extracted values within the region overlying a region larger than Yucca Mountain, as shown in Figure E-7. The region chosen for the analysis of Bands 3 and 4 extends beyond the Yucca Mountain infiltration model domain to include areas with deep shadows and dark basalt (located to the north, but within a sufficiently small area so that it is still representative of the air mass overlying Yucca Mountain). Because close-tolerance geocorrection was not important for this step, it was conducted on images as received from Eros Data center, with geocorrection generally within several hundred meters.

The DOS correction for atmospheric scatter makes the assumption that the air mass overlying the region of Yucca Mountain at the time of each overpass was exemplified by the region chosen for the DOS determination. Further, it was assumed that the properties of this air mass were evenly distributed over Yucca Mountain.

Sources: Output DTNs: SN0608NDVIANAL.001 and SN0608NDVIAUXD.001 The net infiltration modeling domain is outlined in green for reference. The figure was developed from a TM image developed for explanatory purposes in *B3_B4_DOS_ROI_2.xls*. The blue and green polygons are defined by *dos_region_.evf* and *nad27_boundary_.evf*.

Figure E-7. Map Showing Candidate DOS Region (Blue Polygon)

For extraction of candidate DOS values, each scene was cropped to the larger polygonal region portrayed in Figure E-7. All pixel reflectance values for Bands 3 and 4 were extracted from this area and placed into histograms (i.e., pixel counts within reflectance bins). Two possible candidate values for DOS for each band were chosen: DOS_{min} was taken as the lowest reflectance where a single pixel appeared. If this reflectance represented less than three pixels, an alternate value, DOS_{alt}, was also chosen. This was done to constrain potential error. TM data may include a small number of pixels with erroneous data (Vogelmann et al. 2001 [DIRS 176746]), and extracting the data for over six million pixels within the DOS region of interest introduces a likelihood for including an errant low value. The average of DOS_{min} and

DOS_{alt}, called DOS_{avg}, was used for the DOS value. The values for all TM images were developed in *B3_B4_DOS_ROI.xls* (Output DTN: SN0608NDVIANAL.001).

Uncertainty for Correction of Atmospheric Scatter (DOS)

For the image of 4/11/98, the lowest measured reflectance for Band 3 in the candidate DOS region was 0.034, which occurred in three pixels and became the value for DOS_3. For Band 4, the lowest value of 0.030 occurred in only one pixel and became DOS_{min}. The next higher value of 0.033 occurred in seven pixels and became DOS_{alt}. Therefore, DOS_4 was 0.032. These values for DOS are smaller than any measured reflectance within the model domain.

Based on this example, the standard uncertainty in DOS_λ from random effects is about 0.001, which is consistent with the truncation error, which should be about 3% of these values. On the other hand, all of the calculated values carry the systematic errors in the calibrations of Gain and Bias. However, subtraction of DOS from the reflectance will cancel the Bias term and, therefore, remove any effects from the uncertainty in Bias. This follows from the confidence interval of L_λ, defined as $CI(L_\lambda) = (Gain_\lambda \pm k\Delta G_\lambda)DN_\lambda + (Bias_\lambda \pm k\Delta B_\lambda)$ due to the uncertainty in gain and the uncertainty in bias.

We suppose that the function that transforms L_λ into ρ_λ does not bring any other uncertainty, so the confidence interval on ρ_λ is given by formulas described by Markham and Barker (1987 [DIRS 177362]):

$$CI(\rho_\lambda) = (Gain_\lambda \pm k_\theta \Delta G_\lambda)DN_\lambda \frac{\pi d^2}{ESUN_\lambda \cos\theta_\sigma} + (Bias_\lambda \pm k_\theta \Delta B_\lambda)\frac{\pi d^2}{ESUN_\lambda \cos\theta_\sigma}.$$

Thus, the error in bias does not stretch or compress the actual value of ρ_λ. It is an error in translation. When the DOS value is subtracted to ρ_λ, we move every value to a referential value and suppress the second term of the above equation (after the '+' sign). Therefore, this operation suppresses any error in bias term. The only uncertainty remaining is due to the uncertainty in gain (ΔG_λ).

E2.3 GEOCORRECTION

Landsat TM images are typically geocorrected by the Eros Data Center such that pixel locations may be correct to only several hundred meters, especially in mountainous terrain. In order to make comparisons among many images with fixed model grid cells of 30×30 m, it was necessary to improve the accuracy of that initial geocorrection. Due to the high degree of elevation variation within the Yucca Mountain infiltration model boundary, a comprehensive set of 100 ground control points (GCPs) were collected from a large variety of elevations (Output DTN: SN0608NDVIAUXD.001). The highest concentration of points was placed in the region lying above the proposed repository.

The set of 100 points was an aggregate from three data sources: borehole coordinates (DTN: MO9906GPS98410.000 [DIRS 109059]), field-acquired points (DTN: MO0512COV05112.000 [DIRS 177249]), and points derived from U.S. Geological Survey Digital Ortho-Quarterquads (DOQQs) for areas inaccessible to vehicles (DTN: SN0601DOQQYM98.001 [DIRS 177240]). The points in this set were chosen to be highly visible on the majority of the TM images (Figure E-8). The large number of points allowed for a 4th order polynomial warp of the imagery to fit the complex Yucca Mountain surface.

Using the set of GCPs, reference pixel locations were visually mapped to geographic coordinate locations using the standard ENVI Image to Map registration tools. Points were visually matched on the TM images to the surveyed coordinates or selected DOQQ feature coordinates chosen in remote locations. All 100 GCPs were used for each of the Landsat scenes to maintain the greatest continuity in scene geometry. For points where unequivocal surface features were not identifiable, the ENVI predict function was used to place the point—this function uses the geometry of the remaining points as a reference. Points were carefully positioned until the average root mean square error (RMS) was less than 0.30 and each individual pixel RMS was less than 0.5.

This geocorrection process also was used to resample the 28.5 m data from the original TM pixels into 30 m grid cells of the infiltration model domain using the ENVI cubic convolution algorithm. Cubic convolution is a spatially weighted average of portions of the original pixels that fall within the 30 m boundaries of each model cell. All of the geocorrected data were projected in UTM, NAD83 Zone 11N (a positioning coordinate system described in the glossary of Appendix B).

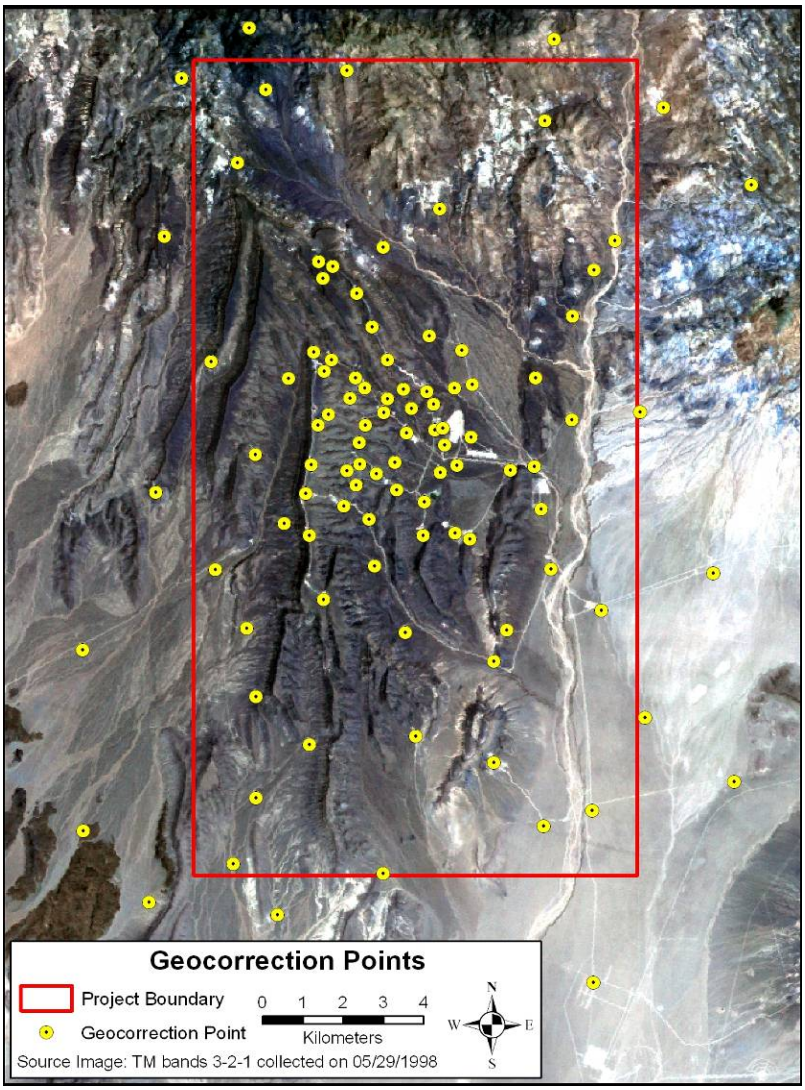

NOTE: This figure displays a set of geocorrection points from the points folder (Output DTN: SN0608NDVIAUXD.001).

Figure E-8. Ground Control Points for the Infiltration Model Domain Region

E2.4 TM BAND 3 AND 4 ATMOSPHERIC CORRECTION AND DETERMINING $NDVI_0$ TO CORRECT FOR NONSYSTEMATIC VARIATION

Following geocorrection, each TM scene was cropped to the Yucca Mountain infiltration model boundary, and the DOS_{avg} values that were calculated during the step described in Section E2.2 were applied to Bands 3 and 4. Data from Bands 3 and 4 were then extracted from specially chosen reference polygons for selection of the parameter $NDVI_0$ for calculation of $NDVI_{offset}$ (Eq. E-3).

Reference polygons were chosen from false-color satellite imagery and digital elevation model data to have relatively homogeneous vegetation cover on low relief terrain, avoiding any influence of differential seasonal shadowing or bidirection reflectance functions that can strongly

influence NDVI (Walthall et al. 1985 [DIRS 176737]; Walter-Shea et al. 1997 [DIRS 176752]). Such influences would likely be detrimental for understanding the sparse vegetation cover and its seasonal progression on Yucca Mountain. Reference polygons, called lowlands, were selected within the model boundary as shown in Figure E-9.

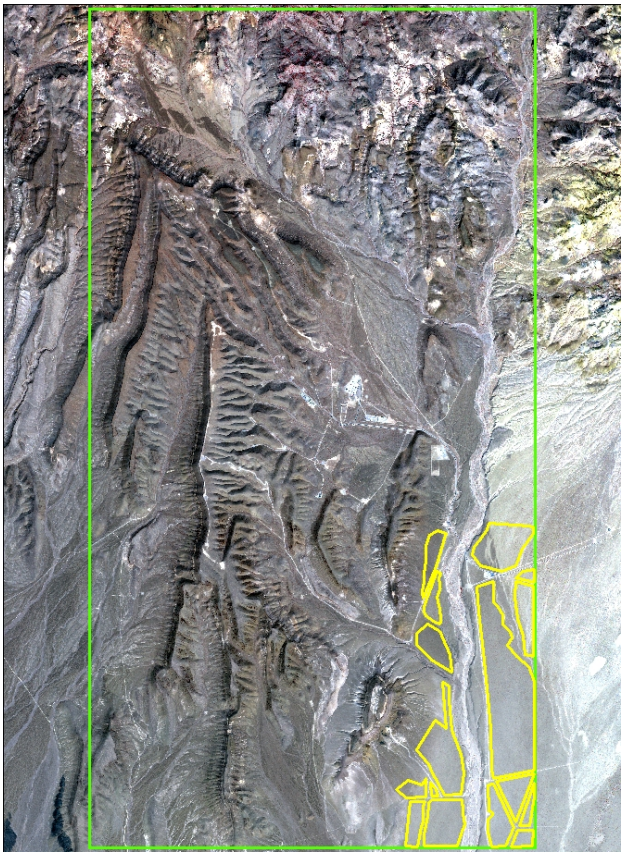

NOTE: Reflectance values for Bands 3 and 4 were selected from within these polygons for iterative evaluation and selection of DOS values. This figure was created using Lowlands_utm83.evf (Output DTN: SN0608NDVIAUXD.001), nad27_boundary_.evf (Output DTN: SN0608NDVIAUXD.001), and a TM scene (Output DTN: SN0608NDVILSTM.001).

Figure E-9. Yucca Mountain Infiltration Model Boundary (green) and a Series of Reference Polygons Representing Vegetation Cover on Low Relief Areas (Lowlands)

Uncertainty for Estimation of $NDVI_0$

In the example image of 4/11/98, there were 13,245 pixels that fell within one of the reference polygons representing lowlands. The NDVI values for those pixels were calculated in accordance with Equation E-1 after correcting NIR and R for the DOS values. Except for one pixel with NDVI of 0.11, the values ranged from 0.13 to 0.30, with a mean of 0.18.

Table E-Uncertainty−4 contains some example values and the resulting uncertainty. Because the subtraction of DOS eliminates any uncertainty in the Bias terms, only the uncertainty from truncation and the uncertainty in Gain are considered. The uncertainties in $Gain_3$ and $Gain_4$ are independent of each other and therefore combine (root−mean−square) when the bands are subtracted or added. As a result, the contribution of truncation uncertainty to NDVI uncertainty is negligible.

The uncertainty is dominated by the uncertainty in the numerator of Equation E-1. Everywhere within the lowland polygons, the uncertainty in NDVI is about 0.03. Choosing the lowest value of NDVI for $NDVI_0$ would introduce an uncertainty of 0.03.

Table E-Uncertainty−4. Example NDVI Calculations within Lowlands Polygons for 4/11/98

Pixel ID	ρ_4 [a]	ρ_3 [a]	$\rho_4 - DOS_4$ [b]	$\rho_3 - DOS_3$ [b]	NDVI Numerator[c]	NDVI Denominator [c]	NDVI
12,557	0.239 ±0.010	0.202 ±0.008	0.207 ±0.010	0.168 ±0.008	0.039 ±0.013	0.375 ±0.013	0.11 ±0.03
11,417	0.288 ±0.012	0.230 ±0.009	0.256 ±0.012	0.196 ±0.009	0.060 ±0.015	0.452 ±0.015	0.13 ±0.03
11,117	0.285 ±0.011	0.225 ±0.009	0.253 ±0.011	0.193 ±0.009	0.060 ±0.014	0.446 ±0.014	0.14 ±0.03
10,093	0.256 ±0.010	0.200 ±0.008	0.224 ±0.010	0.168 ±0.008	0.056 ±0.013	0.392 ±0.013	0.15 ±0.03
9,616	0.255 ±0.010	0.196 ±0.008	0.223 ±0.010	0.162 ±0.008	0.061 ±0.013	0.385 ±0.013	0.16 ±0.03
8,333	0.252 ±0.010	0.190 ±0.008	0.218 ±0.010	0.156 ±0.008	0.062 ±0.013	0.374 ±0.013	0.17 ±0.03
5	0.230 ±0.009	0.171 ±0.007	0.196 ±0.009	0.137 ±0.007	0.059 ±0.011	0.334 ±0.011	0.18 ±0.03
7,709	0.244 ±0.010	0.169 ±0.007	0.212 ±0.010	0.135 ±0.007	0.077 ±0.012	0.347 ±0.012	0.22 ±0.03
7,712	0.255 ±0.010	0.166 ±0.007	0.223 ±0.010	0.132 ±0.007	0.091 ±0.012	0.355 ±0.012	0.26 ±0.03
7,726	0.268 ±0.011	0.162 ±0.006	0.236 ±0.011	0.128 ±0.006	0.108 ±0.013	0.364 ±0.013	0.30 ±0.04

Source: The first three columns are from Output DTN: SN0609LSTMPROC.001, *tm_processing_overview.xls*, worksheet "4−11−1998 Intercept."

[a] Standard uncertainty estimated to be 4% of value.

[b] DOS_3 and DOS_4 are 0.034 and 0.032, respectively, with negligible uncertainty (Section E2.2).

[c] See Equation E-1. Standard uncertainty of sum or difference is root mean square of component uncertainties. Standard uncertainty of quotient is uncertainty in numerator divided by the value of denominator, which neglects uncertainty in denominator.

Further Explanation of Uncertainty in the Numerator of Equation E-1

That uncertainty in the calculation of NDVI is dominated by the uncertainty in the numerator of Equation E-1 can be further explained. Equation E-1 can be rewritten to include uncertainties:

$$\rho_4 - DOS_4 = M_4 \pm \sigma_4$$

$$\rho_3 - DOS_3 = M_3 \pm \sigma_3$$

With $0 < M_3 < M_4$

By considering $\rho_4 - DOS_4$ and $\rho_3 - DOS_3$ independent, the uncertainty on the numerator (N) and denominator (D) part of the estimate of NDVI can be estimated:

$$N = M_4 - M_3 \pm \sqrt{\sigma_4^2 + \sigma_3^2} \text{ and } D = M_4 + M_3 \pm \sqrt{\sigma_4^2 + \sigma_3^2}$$

$$\text{Thus, } NDVI = \frac{N}{D} = \frac{M_4 - M_3 \pm \sqrt{\sigma_4^2 + \sigma_3^2}}{M_4 + M_3 \pm \sqrt{\sigma_4^2 + \sigma_3^2}} \quad \text{(Eq. E1−bis)}$$

If $M_4 - M_3 << M_4 + M_3$ and $\sqrt{\sigma_4^2 + \sigma_3^2} << M_4 + M_3$, then Equation E1−bis can be approximated with

$$NDVI \approx \frac{M_4 - M_3}{M_4 + M_3} \pm \frac{\sqrt{\sigma_4^2 + \sigma_3^2}}{M_4 + M_3}.$$

In order to reduce the random uncertainty in $NDVI_0$, the extracted NDVI values (calculated after subtracting the atmospheric scatter, DOS_{avg}, were displayed as cumulative distribution functions (CDFs). These CDFs were analyzed by linear regression to determine the best fit for predicting an x-axis intercept ($NDVI_0$) from the linear portion of the CDF (Baugh and Groeneveld 2006 [DIRS 178678]). The effect of these calculations is shown at the end of this section.

The cumulative pixel count for the CDFs typically varied between 0 and 15,000, with the leading edge of the curve ending between 500 and 3,000 and the trailing edge of the curve starting between 10,400 and 13,300. Figure E-10 shows a CDF typical of the data. The linear portion of the CDF for each data set was determined automatically for a number of cumulative pixel count ranges. A linear fit was made to the data in each range, and the range resulting in the best fit (that having the highest squared regression coefficient, R^2) was used to define the linear portion of the CDF. As an example, Figure E-11 shows how the linear fit, and the resulting $NDVI_0$ value, varies based on the chosen linear portion of the CDF curve. In this example, the linear portion of the curve would be defined as those data between the cumulative pixel count values

of 2,500 and 12,000. The ranges for calculating the linear regression relationships were standardized for use on all data sets by observation and optimization for the general curve shapes and ranges.

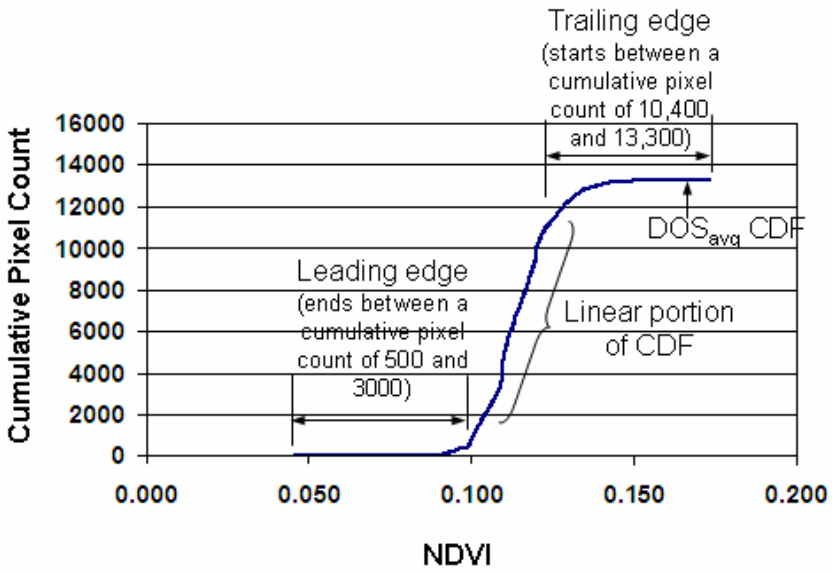

Source: Output DTN: SN0608NDVIANAL.001, *Atm_Cor.xls.*

NOTE: The CDF was extracted from within the lowland polygons shown in Figure 9.

Figure E-10. Cumulative Distribution Function for 11/2/1997 Data Set Showing Typical Ranges for the Ending Points of the Leading Edge and the Starting Point of the Trailing Edge for YMP Data

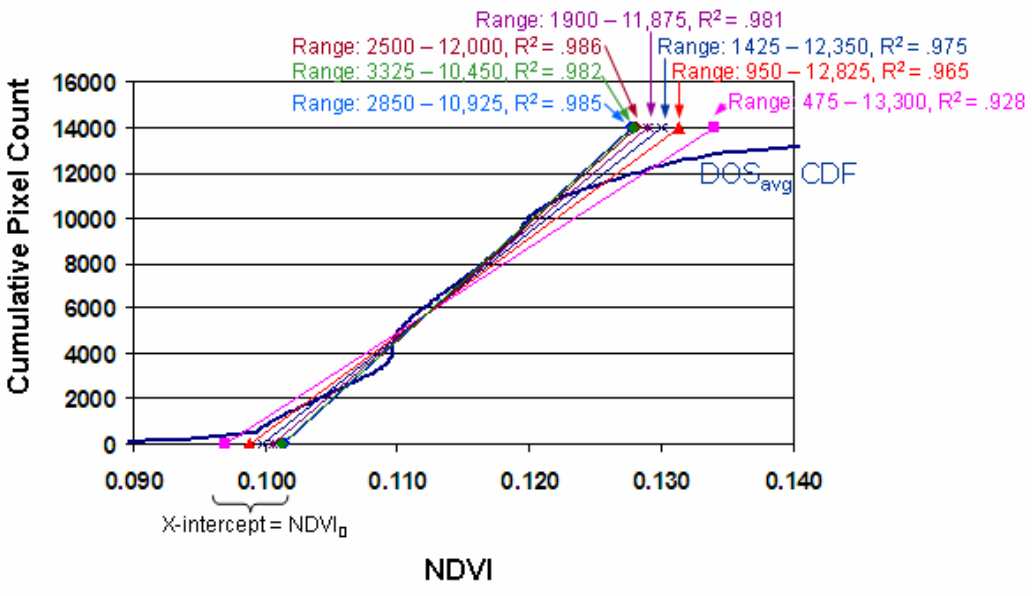

Source: Output DTN: SN0608NDVIANAL.001.

NOTE: The best fit for this example was produced by selection of the range 2,500 to 12,000.

Figure E-11. Example of Linear Fits to the CDF Curve (11/2/1997 Data Set) Showing the Range of $NDVI_0$ Values

The process for selecting the image processing parameters resulted in a table of final values for each water year in the study (Table E-2). These values were applied to the images for all subsequent steps. The workbook *Atm_Cor.xls* (Output DTN: SN0608NDVIANAL.001) contains the analysis sheet, copies of the data for each image, and a summary of the resulting values. Table E-2 also indicates the standard deviation from several possible fits to the linear portion, indicating that the random uncertainty in $NDVI_0$ is always less than 0.01.

Table E-2. DOS_{avg} Values in Reflectance Selected for TM5, Bands 3 and 4, and the Resulting $NDVI_0$ and $NDVI_{offset}$ for Each Image during all Three Water Years

	WY DOY	TM Date	TM Sensor	DOSavg Band 3	DOSavg Band 4	Average NDVI	$NDVI_o$ (Intercept)	$NDVI_{offset}$
WY 1998	33	11/2/1997	5	0.0180	0.0150	0.1145	0.1012	0.0133
	113	1/21/1998	5	0.0190	0.0150	0.1253	0.1041	0.0212
	161	3/10/1998	5	0.0240	0.0140	0.1493	0.1241	0.0252
	193	4/11/1998	5	0.0340	0.0315	0.1824	0.1504	0.0320
	209	4/27/1998	5	0.0405	0.0360	0.1998	0.1755	0.0242
	241	5/29/1998	5	0.0380	0.0315	0.1800	0.1626	0.0173
	273	6/30/1998	5	0.0360	0.0310	0.1521	0.1347	0.0173
	289	7/16/1998	5	0.0240	0.0280	0.1171	0.1025	0.0146
	321	8/17/1998	5	0.0280	0.0230	0.1312	0.1137	0.0174
WY 2001	9	10/9/2000	5	0.0050	0.0200	0.0591	0.0339	0.0252
	81	12/20/2000	7	0.0190	0.0145	0.1264	0.1017	0.0247
	121	1/29/2001	5	0.0370	0.0245	0.1492	0.1236	0.0256
	169	3/18/2001	5	0.0260	0.0135	0.1432	0.1179	0.0253
	177	3/26/2001	7	0.0275	0.0270	0.1493	0.1232	0.0261
	201	4/19/2001	5	0.0490	0.0370	0.1884	0.1628	0.0255
	217	5/5/2001	5	0.0375	0.0340	0.1488	0.1339	0.0148
	249	6/6/2001	5	0.0400	0.0285	0.1358	0.1204	0.0153
	273	6/30/2001	7	0.0445	0.0570	0.0865	0.0717	0.0147
	297	7/24/2001	5	0.0325	0.0250	0.1242	0.1088	0.0154
	321	8/17/2001	7	0.0405	0.0425	0.1039	0.0892	0.0147
WY 2002	4	10/4/2001	7	0.0220	0.0230	0.0986	0.0853	0.0133
	12	10/12/2001	5	0.0210	0.0145	0.1161	0.0995	0.0166
	68	12/7/2001	7	0.0060	0.0160	0.0869	0.0720	0.0149
	116	1/24/2002	7	0.0180	0.0150	0.1214	0.1058	0.0156
	148	2/25/2002	7	0.0190	0.0185	0.1238	0.1097	0.0141
	180	3/29/2002	7	0.0225	0.0250	0.0978	0.0848	0.0130
	196	4/14/2002	7	0.0310	0.0375	0.0823	0.0694	0.0130
	212	4/30/2002	7	0.0350	0.0330	0.1145	0.1023	0.0122
	228	5/16/2002	7	0.0490	0.0520	0.1051	0.0919	0.0132
	244	6/1/2002	7	0.0440	0.0395	0.1131	0.0999	0.0133
	260	6/17/2002	7	0.0475	0.0380	0.1321	0.1187	0.0133
	292	7/19/2002	7	0.0240	0.0260	0.0865	0.0748	0.0117
	308	8/4/2002	7	0.0510	0.0575	0.0970	0.0860	0.0110

Source: Output DTN: SN0608NDVIANAL.001, *atm_cor.xls*.

NOTE: The value for standard deviation was calculated from all of the potential linear fits as illustrated in Figure E-11 as a maximal representation of the potential error associated with the linear fit method.

The values in Table E-2 were then used to calculate $NDVI_{offset}$ according to Equation E-6.

$$NDVI_{offset} = [(B_4 - DOS_4) - (B_3 - DOS_3)] / [(B_4 - DOS_4) + (B_3 - DOS_3)] - NDVI_0 \quad \text{(Eq. E-6)}$$

where subscripts 3 and 4 refer to the two bands.

$NDVI_0$ is the fitted intercept value as illustrated in Figure E-11.

Figure E-12 illustrates how calculation of $NDVI_{offset}$ in Equation 6 corrects for nonsystematic variation in NDVI using five of the images from WY1998. By subtracting the intercept value, representing $NDVI_0$, this starts all of the curves at the same place and enables accurate comparison as was shown by Baugh and Groeneveld 2006 [DIRS 178678]

a.

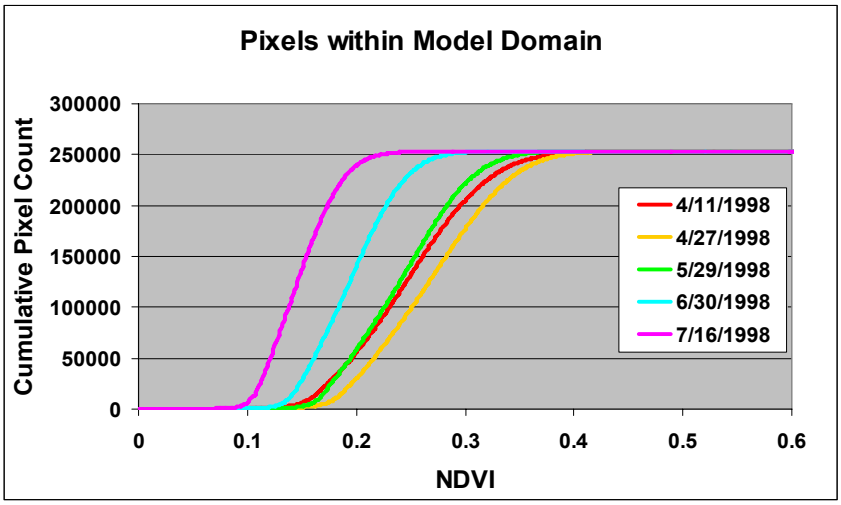

b.

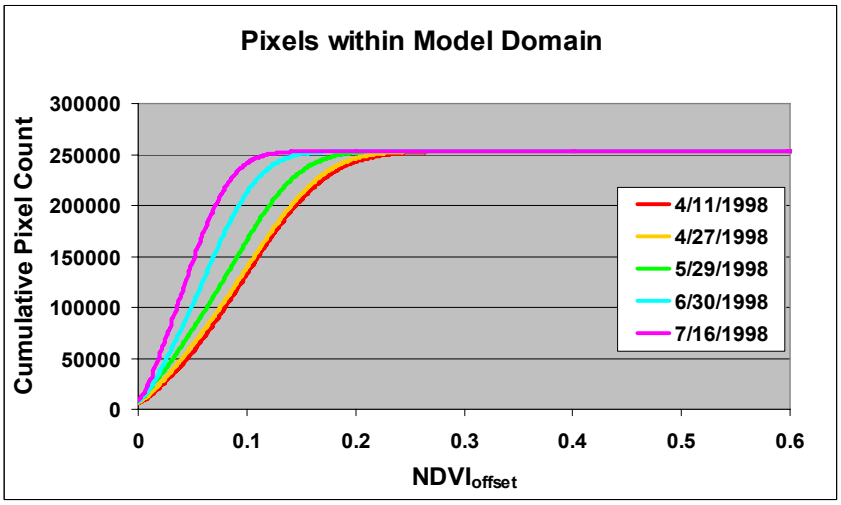

Source: Output DTN: SN0608NDVIANAL.001.

NOTE: The progression in plant phenology for this region had a peak in early April that declines through the growing season to midJuly. This progression is less apparent without removal of the nonsystematic scatter by subtraction of $NDVI_0$. $NDVI_{offset}$ was calculated using the $NDVI_0$ in Table E-2.

Figure E-12. CDFs for the Pixels of Five Images that Follow the Progression of the Growing Season within the Rectangular Area of the Model Domain Representing (a) as NDVI and (b) as $NDVI_{offset}$

There are a couple of important factors to note relative to Figure E-12. First, for the five images chosen, the progression of plant phenology declines from the overall average peak expression on the first image, April 11, 1998, to lowest $NDVI_{offset}$ expression during midsummer, July 16, 1998. Were the data not subjected to the calculation to derive $NDVI_{offset}$, the results would be not be in the correct order—a peak that declines to a minimum. In addition, these pixel data are extracted from the rectangular area of the model domain that contain large areas of lowlands where plant phenology is apparently accelerated over plant growth timing on the rocky uplands (hence, not equivalent to analyses for pixel extractions occurring later in this report).

A feature of $NDVI_{offset}$ is that its magnitude is far less than NDVI due to the subtraction of $NDVI_0$ and, thus, is not directly comparable to raw NDVI values. Though the range of $NDVI_{offset}$ is changed by this calculation and the values decreased, this does not pose a problem because $NDVI_{offset}$ is a dimensionless index that can be calibrated to other data, and this then enables spatial mapping.

Uncertainty for $NDVI_{offset}$

Table E-Uncertainty−5 shows sample calculations of $NDVI_{offset}$ for pixels measured on 4/11/98 within the model domain. For that day's image, $NDVI_0$ is 0.15 (Table E-2). The values of $NDVI_{offset}$ range from about −0.3 to about 0.4, though only about 2% of the pixels have negative values. These negative values correspond to graded roads, graded parking areas, and areas in deep shadow. For this image on 4/11/98, at about 10 a.m. local time, the sun is east and south of the zenith with an elevation of 52° (from the header file accompanying this image). The deep shadow is on steep northern and western slopes of the mountain. Negative values are set to zero before further processing. Table E-Uncertainty−5 also shows the propagation of estimated uncertainties. Through the calculation of NDVI, the uncertainty analysis is the same as that in Table E-Uncertainty−4. The dominant sources of uncertainty in both NDVI and $NDVI_0$ are the uncertainties in the two Bias values, with effects in the same direction. Therefore, the relative uncertainty in $NDVI_{offset}$ is approximately the relative uncertainty in NDVI but not less than the random uncertainty. The random uncertainty is dominated by the random uncertainty of 0.01 $NDVI_{offset}$. The standard uncertainties for positive values of $NDVI_{offset}$ range from 0.01 to 0.03, being approximately 0.01 + 6% $NDVI_{offset}$.

Table E-Uncertainty−5. Example $NDVI_{offset}$ Calculations within Model Domain on 4/11/98

Pixel ID	ρ_4 [a]	ρ_3 [b]	$\rho_4 - DOS_4$ [c]	$\rho_3 - DOS_3$ [c]	NDVI Numerator [d]	NDVI Denominator [d]	NDVI [e]	$NDVI_{offset}$ [f]
10,901	0.065 ±0.003	0.064 ±0.003	0.033 ±0.003	0.030 ±0.003	0.003 ±0.004	0.063 ±0.004	0.05 ±0.06	−0.10 ±0.12
253,574	0.259 ±0.011	0.201 ±0.008	0.227 ±0.011	0.167 ±0.008	0.060 ±0.014	0.394 ±0.014	0.15 ±0.04	0.00 ±0.01
116	0.202 ±0.008	0.152 ±0.006	0.170 ±0.008	0.118 ±0.006	0.052 ±0.010	0.288 ±0.010	0.18 ±0.03	0.03 ±0.01
136,394	0.225 ±0.009	0.161 ±0.006	0.193 ±0.009	0.127 ±0.006	0.066 ±0.015	0.320 ±0.015	0.21 ±0.05	0.06 ±0.01
212	0.207 ±0.008	0.144 ±0.006	0.175 ±0.008	0.110 ±0.006	0.065 ±0.010	0.285 ±0.010	0.23 ±0.04	0.08 ±0.01
253,447	0.263 ±0.011	0.171 ±0.007	0.231 ±0.011	0.137 ±0.007	0.094 ±0.013	0.368 ±0.013	0.26 ±0.04	0.11 ±0.02
234,601	0.226 ±0.009	0.150 ±0.006	0.194 ±0.009	0.116 ±0.006	0.078 ±0.011	0.310 ±0.011	0.25 ±0.04	0.10 ±0.02
147,056	0.199 ±0.008	0.124 ±0.005	0.167 ±0.008	0.090 ±0.005	0.077 ±0.009	0.257 ±0.009	0.30 ±0.04	0.15 ±0.02
147,067	0.234 ±0.009	0.131 ±0.005	0.202 ±0.009	0.097 ±0.005	0.105 ±0.010	0.299 ±0.010	0.35 ±0.03	0.20 ±0.02
136,365	0.299 ±0.012	0.147 ±0.006	0.267 ±0.012	0.113 ±0.006	0.154 ±0.013	0.380 ±0.013	0.41 ±0.03	0.26 ±0.02
42,795	0.204 ±0.008	0.098 ±0.004	0.172 ±0.008	0.064 ±0.004	0.108 ±0.009	0.236 ±0.009	0.46 ±0.04	0.31 ±0.03
24,753	0.196 ±0.008	0.082 ±0.003	0.164 ±0.008	0.048 ±0.003	0.116 ±0.009	0.212 ±0.009	0.55 ±0.04	0.40 ±0.03

[a] Source: Output DTN: SN0609LSTMPROC.001, *041198_band4.txt*). Standard uncertainty estimated to be 4%.
[b] Source: Output DTN: SN0609LSTMPROC.001, *041198_band3.txt*.. Standard uncertainty estimated to be 4%.
[c] DOS_3 and DOS_4 are 0.034 and 0.032, respectively, with negligible uncertainty (Section E2.2).
[d] See Equation E-1. Standard uncertainty of sum or difference is root mean square of component uncertainties.
[e] Standard uncertainty of quotient is uncertainty in the numerator divided by the value of denominator, which neglects uncertainty in the denominator.
[f] The relative uncertainty in $NDVI_{offset}$ estimated to be the same as relative uncertainty in NDVI, but not less than 0.01.

Uncertainty for $NDVI_{offset}$ (Continued)

The uncertainty associated with calculation of $NDVI_{offset}$ is considered to be the major source of uncertainty in the calculations and is equivalent to.01 + 6%. This estimate was made considering the sources of error within the calculations but does not acknowledge that uncertainty may be somewhat self correcting due the combinations of numbers that may be high combined with those that may be low, thus tending to force uncertainty to a more moderate value. This can be seen within the discussion of uncertainty contained in Section E7.4. The development of temporal (daily time step curves of expected NDVI' (developed from $NDVI_{offset}$ in Section E2.5 and E3) and spatial parameters PVR (potential vegetation response, Section E3) from $NDVI_{offset}$ are inputs for the MASSIF model and so, fall under modeling uncertainty. Uncertainty for these parameters is not estimated in this appendix.

E2.5 VERIFICATION OF PROCESSING PARAMETERS AND DEVELOPMENT OF NDVI'

The processing parameters for $NDVI_{offset}$ developed for the vegetation cover within the lowlands region shown on Figure E-9, were intended for application to all Yucca Mountain vegetation. Additional testing was performed to verify that the DOS parameters for NDVI measured over the "lowlands" region are appropriate for other vegetation cover closer to the repository footprint. This was accomplished using data from established ecological study plots.

There are 48 Ecological Study Plots (ESPs) for four vegetation associations established in and around Yucca Mountain where the vegetation growth was monitored during the late 1980s and early 1990s (CWRMS 1996 [DIRS 102235]). These plots, described at greater length in Appendix D, were established during 1988. Data for analyses using the vegetation plot data are listed within Output DTN: MO0606SPAVEGAS.001.

The three predominant Yucca Mountain vegetation associations were used for verification of the appropriateness of the processing parameters. Each of these vegetation associations contained 12 individual plots. These are shown on Figure E-13. For one of the associations, LA, 2½ plots lay outside of the infiltration model boundary and were excluded from consideration. As described in Appendix D, the names of the vegetation associations have changed since the plots were defined. The original naming convention will be used for these plots: LA for *Larrea–Ambrosia*, LLG for *Larrea–Lycium–Grayia*, and LG for *Lycium–Grayia*. The vegetation contained in the LG plots is most closely related to the vegetation of the rocky uplands that overly the repository and, thus, was of greater interest for verification and for later fitting of the simulation algorithm.

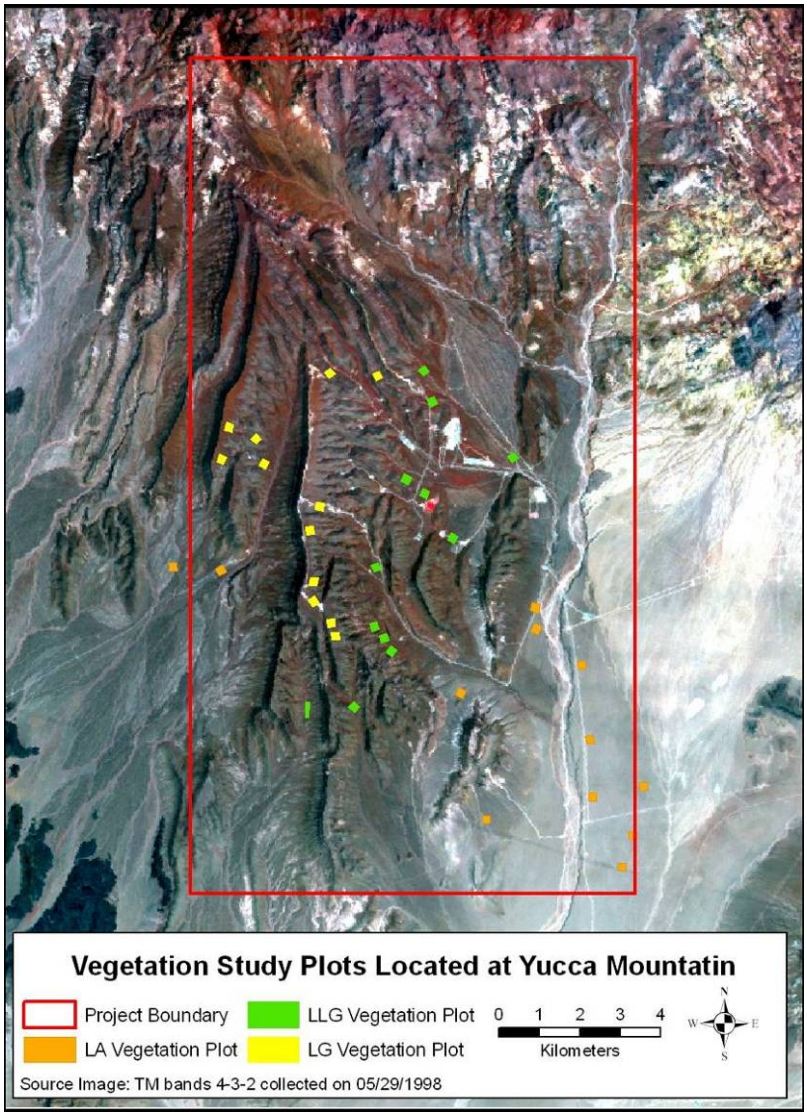

Source: Output DTN: SN0608NDVIANAL.001.

NOTE: The Yucca Mountain infiltration model boundary is shown in red (rectangle). Plots marked LG are most similar to the vegetation of the rocky uplands overlying the proposed repository. This figure was excerpted from *ESP_NDVI'_simET-K3.xls*.

Figure E-13. Location of Ecological Study Plots Used to Verify Atmospheric Correction and Simulations of Vegetation Response

$NDVI_{offset}$ values were calculated for the different vegetation associations using the $NDVI_0$ parameters in Table E-2. Model grid cell values of $NDVI_{offset}$ were extracted from each of the ESPs and then lumped by each vegetation association into single statistical populations. These data are contained in the workbook *ESP_NDVI'_simET-K.xls* (Output DTN: SN0608NDVIANAL.001). A description of the data extracted from the ESPs is contained in Table E-3.

Table E-3. Ecological Study Plots with Original Naming Convention and Measurements of the Total Pooled Area Evaluated for Verification

Original Name	Plots	30-m Grid Cells Extracted	Area in km^2	Avg. Area/Plot (m^2)
LA	9.5	445	0.401	42,200
LG	12	516	0.464	38,700
LLG	12	552	0.497	41,400

Source: Output DTN: SN0608NDVIANAL.001, *ESP_NDVI'_simET-K.xls*.

NOTE: If expressed as a square, on average, each ESP was approximately 200 m on a side.

Reasonable comparison of the curves formed by the calculated average $NDVI_{offset}$ values to the antecedent precipitation during each water year was taken to be confirmation that the processing parameters in Table E-2 were correct. The expected vegetation cycle, either remaining flat during the year with negligible precipitation (WY2002) or rising and falling through the growing season in the two years with average and significant precipitation (WY1998 and WY2001), were used to cross-check the $NDVI_{offset}$ curves. In all nine cases (3 vegetation associations * 3 years), the processing parameters yielded curves that were reasonable. The individual values of $NDVI_{offset}$, comprised of averages for the entire multiplot association, were well behaved and did not deviate greatly from the expected curve shapes, given the precipitation measured on Yucca Mountain. Because the same values of Gain were used for all pixels, averaging does not reduce the uncertainty.

Figure E-14 presents the results for the lumped LG plot data compared to the precipitation data for WY2002. Due to the intensity of the dryness and the lack of an effective precipitation event (events were less than 10 mm of rain, spaced widely apart in time), this year was expected to have near-zero vegetation response. For the $NDVI_{offset}$ calculated for these data, however, this is clearly not the case. Some other factor besides vegetation growth and canopy expression appears to be causing a background $NDVI_{offset}$ signal, and this signal significantly elevates the vegetation response curve well above the expected zero baseline. $NDVI_{offset}$ values above the baseline can be attributed to vegetation response to the precipitation (Figure E-15). This permanent nonvegetation factor causing upward zero-baseline displacement was identified as desert varnish that covers all undisturbed (in situ) exposed rock surfaces on Yucca Mountain. This effect, explained in Section E2.6, was known from the literature; however, the high magnitude of this response in comparison to the vegetation signal was unexpected.

To correct for the effect of the nonzero baseline, the lowest levels of expected vegetation cover measured on July 19 and August 4, 2002 (driest period during the driest year), were averaged and subtracted from all $NDVI_{offset}$ values through all years. This new NDVI parameter was given the designation NDVI'.

Values of NDVI' are also plotted on Figures E-14 and E-15 for WY2002 and WY1998. Since the promotional effect from desert varnish is not constant spatially, values of $NDVI_{offset}$ for a given area, for example the pooled ESP averages, must subtract the zero baseline developed for the same ground area (i.e., collections of pixels). Correcting for the permanent and highly variable concentration of desert varnish contained within each model grid cell (Section E2.6) is solved with the development of PVR (Section E4).

Uncertainty for NDVI'

The values of Gain for three WY2001 dates, March 26, June 30, and August 17, were the same as those for WY 2002. After averaging over the pixels associated with a vegetation plot, the uncertainty is if NDVI' is dominated by the uncertainty in Gain. As with the calculation of $NDVI_{offset}$ in Section E2.4, the effect is to make the standard uncertainty in NDVI' be approximately 6% of NDVI' for those three dates.

We consider here that the values for the lowest levels of expected vegetation are so low that the uncertainty is also relatively low. Its effect on NDVI' is negligible when compared to the effect of the uncertainty of $NDVI_{offset}$ for the selected period; thus, it can be ignored.

Because the values of Gain used for WY1998 and most of WY 2001 were different from the values used for WY 2002, the standard uncertainty in NDVI' for those dates is the root−mean−square of the two uncertainties. Because the values for WY 2002 are small, the standard uncertainty in NDVI' for those dates is approximately 0.01 + 6% NDVI'.

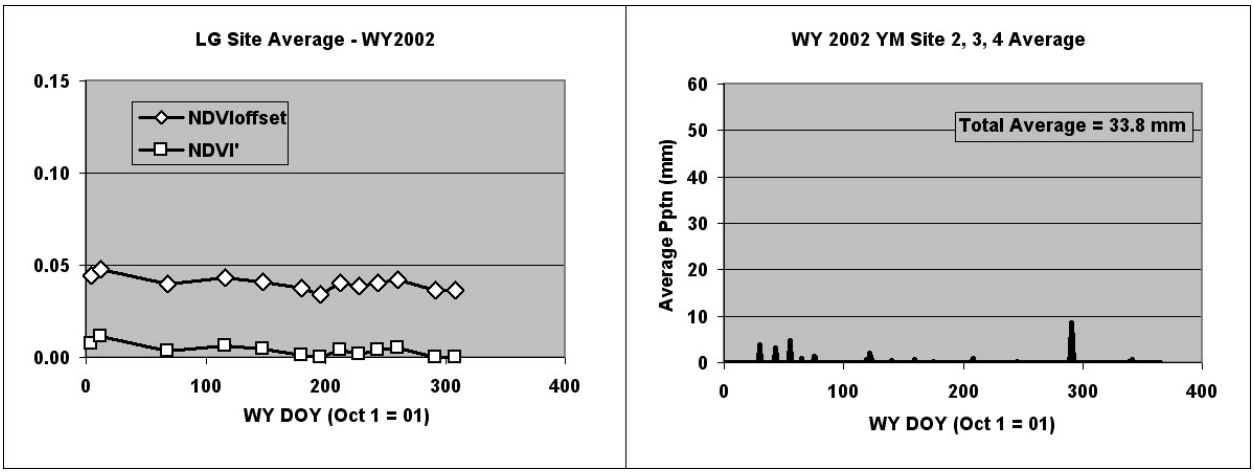

Source: Output DTN: SN0608NDVIANAL.001 (including average precipitation) *ESP_NDVI'_simET-K.xls*, worksheet "2. precip_table."

NOTE: From this very dry year, a zero NDVI vegetation response is expected during summer. Values of $NDVI_{offset}$ were apparently promoted by about 0.04 $NDVI_{offset}$ that is represented by the last two values of WY2002 (about WYDOY 300). This interval was subtracted to yield NDVI'.

Figure E-14. $NDVI_{offset}$ and NDVI' for Lumped Samples for WY2002 LG Plots

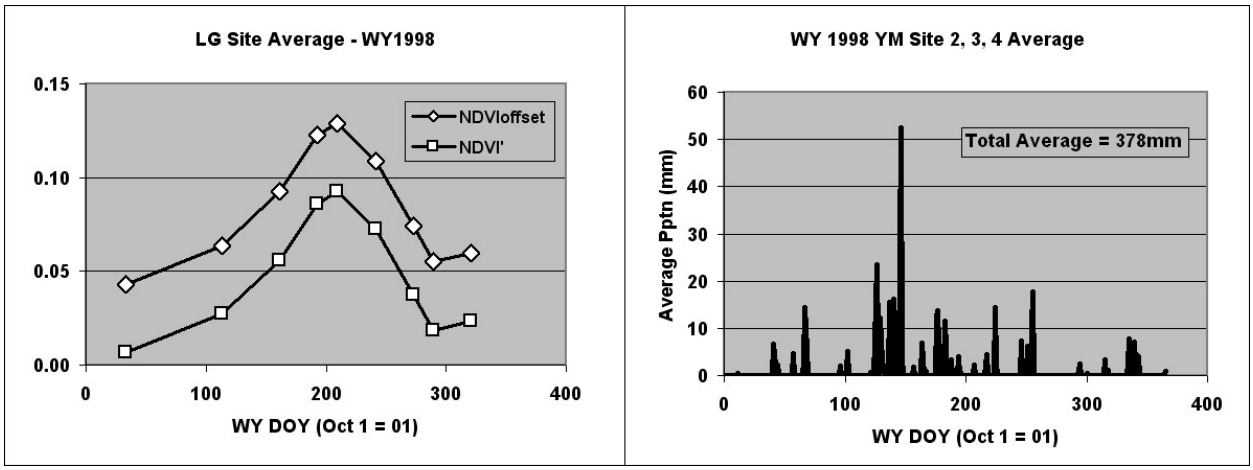

Source: Output DTN: SN0608NDVIANAL.001, *ESP_NDVI'_simET−K.xls*, worksheet "2. precip_table."

NOTE: $NDVI_{offset}$ is promoted by a nonvegetation related factor that was determined from the data in Figure E-14. The same zero baseline subtracted for Figure E-14 was subtracted from these data to yield NDVI'.

Figure E-15. Plot of $NDV_{loffset}$ and NDVI' for Lumped Samples from LG Plots for WY1998

Again, these analyses and their results, represented by Figures E-14 and E-15, were used as a guide to subsequent analyses because they developed an understanding of Yucca Mountain vegetation responses and verified that the processing parameters for DOS and for $NDVI_0$ produced reasonable results. These analyses were not used as input to the algorithm to simulate Yucca Mountain vegetation.

E2.6 NDVI SIGNAL FROM DESERT VARNISH

A Quickbird image (private sector satellite data collected by Digital Globe, Inc.) from August 30, 2002 (DTN: SN0601QBSAT802.001 [DIRS 177241]), was examined to confirm the source of the nonvegetation $NDVI_{offset}$ signal determined in Section E2.5. This multispectral image has high spatial resolution (2.4 m) pixels that were processed using ENVI Software to yield NDVI values. From observation of these data, it was concluded that the natural rock surfaces, devoid of vegetation and covered by desert varnish, produced the nonzero NDVI signal that was absent on nonvarnished rock surfaces such as the surfaces exposed for drill pads (Figure E-16). The NDVI signal from desert varnish has been identified by other researchers; however, the magnitude of the NDVI signal depends on the specific properties of the desert varnish and the rock (Spatz and Taranik 1989 [DIRS 176751]; Rivard et al. 1992 [DIRS 176758]; Rivard et al. 1993 [DIRS 176741]; and Kenea 2001 [DIRS 176760]). As can be seen in Figure E-16, the NDVI signal for Yucca Mountain desert varnish is of the same magnitude as the strength of the vegetation signal.

The desert varnish NDVI signal was removed in Section E2.5 by subtraction. For this calculation, the average $NDVI_{offset}$ extracted from the ESPs from the last two images in WY2002 (July 19 and August 4) were taken to represent only the NDVI from nonvegetation sources (desert varnish), since this was during a very dry year at a time when vegetation response would be expected to be near zero. This calculation was performed for the average $NDVI_{offset}$ values of each of the three vegetation associations for the verification step. This calculation used a mean

$NDVI_{offset}$ value calculated for the two approximated zero vegetation dates (July 19 and August 4, 2002) and was subtracted from all $NDVI_{offset}$ pixels of all images yielding a new adjusted index referred to as NDVI'. Because NDVI' has had all nonvegetation sources of NDVI removed, it represents only the NDVI response from vegetation expression.

a. False color view of a portion of the crest and eastern slopes of Yucca Mountain. Exposed rocks covered with desert varnish are visible on ridges to the right side of the view (dark brown). A roadway and drill pad, which were cut along the crest exposing fresh rock surfaces without desert varnish covering, are seen on the left side of the view (whitish).

b. The same scene displaying a colorized version of NDVI, where bright is high NDVI and black is zero response. The exposed rock areas with desert varnish (identified above) are the brightest portions of the image. In comparison, the freshly exposed rock along the crest has no NDVI response (black).

NOTE: The expected vegetation expression in this scene is near zero for all but scattered evergreen shrubs. These images were generated from data of Output DTN: SN0608NDVIQBIM.001.

Figure E-16. Quickbird Data from August 30, 2002, Following the Dry Summer during the Driest Year on Record for Yucca Mountain

The calculation of NDVI' does contain some bias because a small proportion of the canopy at the site is evergreen vegetation that would provide an NDVI signal even in a critically dry year. However, even the canopies of evergreen species can be expected to be at their lowest representation in late summer of a dry year, as is described in Section E4.

Identification of the NDVI signal in desert varnish and completion of the calculation methodology with NDVI' completed the first phase of the analyses—to determine how to process the data to isolate the vegetation signal. The next phase sought to develop an algorithm for simulating vegetation based upon its position on Yucca Mountain and its spatially discrete potential for growth response (measured as the difference between response to antecedent precipitation between wet, WY1998, and dry, WY2002, conditions.

E3. CHARACTERIZATION OF NDVI' ACCORDING TO SLOPE AND AZIMUTH

NDVI' was predicted by an algorithm for any specified location, day of year, and history of total annual precipitation. Location is thought to affect vegetation in several ways. Slope and azimuth combinations will result in different amounts of sunlight reaching the ground at different times of the year and thus influence the magnitude and/or timing of the vegetation signal at that location. For example, in the northern hemisphere, north-facing slopes will tend to receive less solar radiation than south-facing slopes, and the ratio of the energy for evaporating water that is received by these two azimuths will change as a function of the time of year. This is a set influence that will affect vegetation growth no matter what condition of soils exist at the location.

In addition to effect of slope and azimuth, different locations will have specific properties that influence vegetation growth at that location. Areas with little to no soil present will not be able to support plant growth while areas of deep, well drained soils can.

The naming convention for slopes used in these analyses is N and S for north and south, which are equivalent to N- and S-facing slopes.

Previous analyses were accomplished sequentially to (1) determine the processing parameters for the TM imagery, DOS values, and $NDVI_0$; (2) use the ESP data to verify the processing parameters and evaluate the generally curve shapes in response to seasonal timing and precipitation; and (3) to verify the effect of desert varnish on $NDVI_{offset}$ and develop a means to remove this effect (by calculating NDVI'). These three steps were accomplished with areas of homogeneous vegetation located on relatively low relief terrain, including the lowlands polygons (Figure E-9) and ESPs (Figure E-13).

In order to characterize the response of NDVI' on the complex topography overlying the proposed repository, data were extracted and processed on steep slopes to N and S azimuths. The results from this analysis were interpolated for the combinations of slope and azimuth that occur on Yucca Mountain.

E3.1 EFFECT OF SLOPE AND AZIMUTH

Creation of a simulation for vegetation growth represented by NDVI' (a surrogate for vegetation water use) required the vegetation response at Yucca Mountain be examined to determine its sensitivity to the orientation of the land surface. $NDVI_{offset}$ values were calculated for the model domain for extraction of data from grid cells on N versus S slopes (Output DTN: SN0608NSSLOPES.001). The suite of model grid cells that was sampled for this analysis is shown on Figure E-17. A total of 0.246 km^2 (273 model grid cells) were chosen from the model domain to represent north-facing slopes, and 0.364 km^2 (405 grid cells) were chosen

to represent south-facing slopes. The representative areas were chosen from the region of rocky uplands overlying the proposed repository in order to achieve the greatest accuracy in the most critical location.

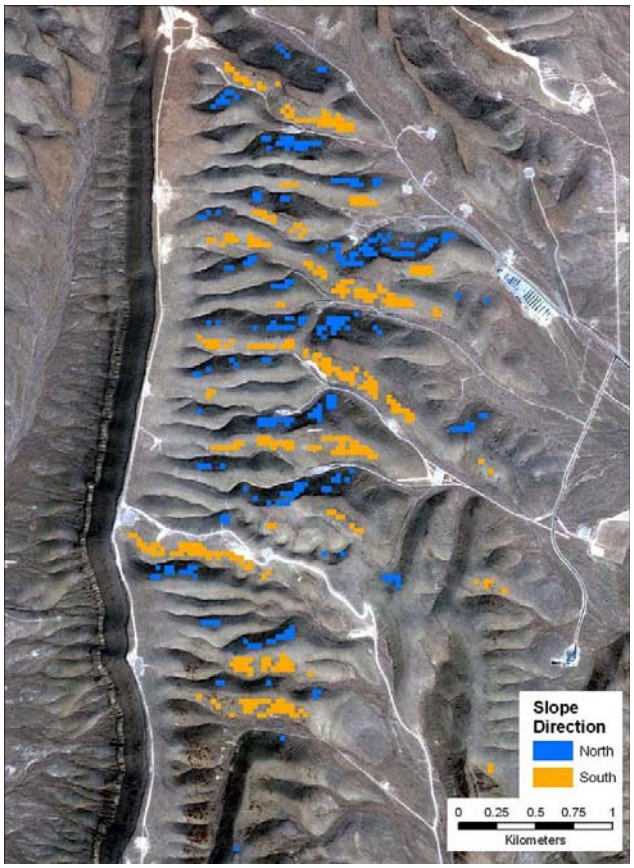

Source: Output DTN: SN0608NDVIANAL.001, *ALL_Years_N_S_18_24_slope_extractions3.xls*. The pixels indicating north- and south-facing slopes are identified in Output DTN: SN0608NSSLOPES.001.

Figure E-17. Model Grid Cells Sampled: S (orange); N (blue)

Figure E-18 represents the statistical distribution of model grid cells by slope for N and S slopes (30° arcs to either side) on the Yucca Mountain rocky uplands. N and S slopes of 18° to 24° were selected as a lumped sample for extraction of $NDVI_{offset}$ values to provide a population sufficient for characterizing the differences in temporal vegetation response. These slopes were selected because:

This slope range captured the peak of the cell distribution for the most limited sample of the two cardinal azimuths, N slopes.

Slopes of this steepness are at about the end of the distribution for normal vegetation growth, allowing any intermediate condition to be interpolated from these end members.

Slopes chosen to be any steeper than 24° would tend to have vegetation that is mostly constrained by rockiness

Note that further discussion concerning N and S slopes refers to the responses seen within the lumped sample for 18° to 24° grid cells that were extracted for analysis.

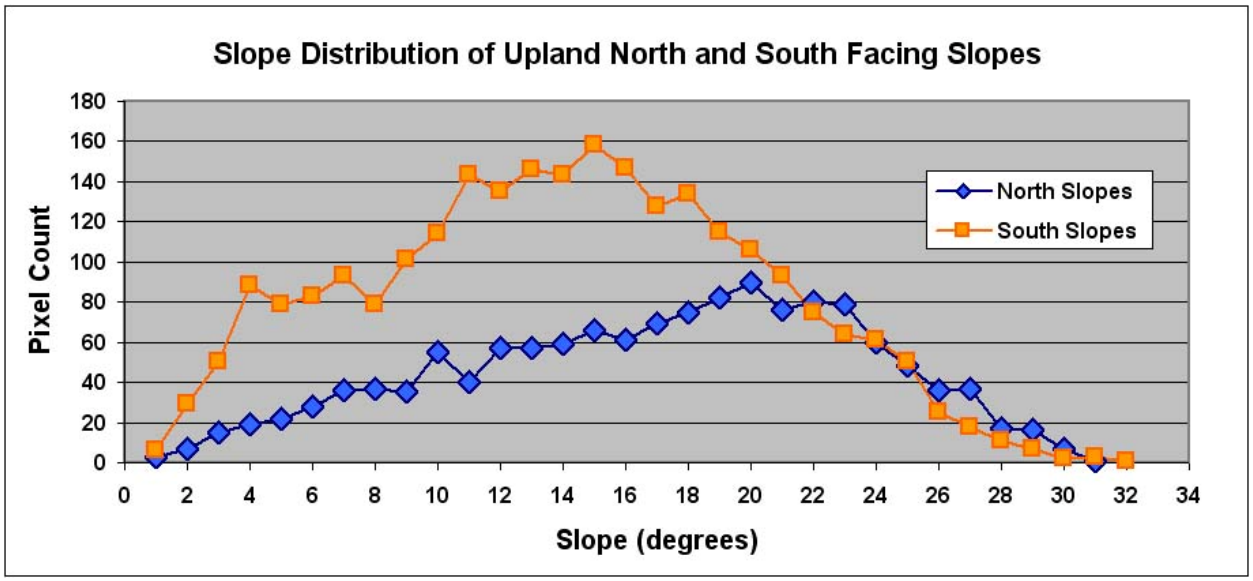

Source: Output DTN: SN0609AZSLPHST.001, north_south_slope_distibution.

Figure E-18. Statistical Distribution of Landsat TM Pixels on N and S Slopes within a Region Overlying the Proposed Repository

The first step for slope-azimuth characterization was to define the region of interest overlying the proposed repository and to identify the 30-m model grid cells that had N and S alignment to within an arc of 60° (30° either side of cardinal direction). This pool of candidate model grid cell $NDVI_{offset}$ was then displayed as a partial transparency over the August 30, 2002, Quickbird image that had been processed to reveal NDVI (Figure E-16b). Multiple contiguous pixels (2.4-m each) of high NDVI response were taken to be exposed rock surfaces covered by desert varnish (Yucca Mountain vegetation is not distributed in this manner) and were eliminated from consideration for slope-azimuth characterization.

Rather than each slope-azimuth class for Yucca Mountain being measured and fitted individually, the relationships for the N- and S-slope endmembers were first characterized. Then, the relationships for intermediate slopes and azimuths were interpolated from these endmembers. A more comprehensive sampling investigation for vegetation response of all combinations of slopes and azimuths was rejected because of four factors: (1) poor statistical representation of some combinations of slope and azimuth (Figure E-18), (2) potential confounding influences due to bidirectional reflectance functions, (3) time and budget considerations, and (4) robustness for fitting all relationships from the two N- and S-slope endmembers.

A simplified conceptual model of vegetation distribution was used for slope and azimuth. Given that all other factors remain consistent, such as soil depth and surface rock expression, the following logical principles were made for characterizing NDVI' response to slope and azimuth:

Logical Principle 1. Vegetation of arid Yucca Mountain is usually critically short of water; thus, small differences in water availability are reflected in proportional differences in vegetation cover.

Logical Principle 2. Factors that influence vegetation growth are related primarily to the temporal availability of water—and secondarily to season of year. Water availability is governed by precipitation, any redistribution due to runoff/run-on, and the rates of its loss through evapotranspiration.

Logical Principle 3. N slopes present less atmospheric driving force and are less conducive to evaporation than S slopes. Thus, N slopes have higher vegetation cover than S slopes because water is available longer for plant uptake and photosynthesis. This relationship was suggested by Stothoff et al. (1999 [DIRS 176705]) who measured higher vegetation cover and leaf area index on the N slopes of Yucca Mountain.

Logical Principle 4. Conditions affecting evaporation on east (E) and west (W) slopes represent an approximate average of the conditions that would exist on N and S slopes. Thus, vegetation on E and W slopes will be interpolated as a temporal average of N and S slopes.

Logical Principle 5. Vegetation response for flat and gentle slopes (<5°) are also averages between N and S slopes (and therefore, in this simple interpolation, equivalent to E and W slopes). Vegetation responses for all intermediate slopes and azimuths can be represented by weighted averaging between the endmember conditions for N and S slopes.

E3.2 CHARACTERIZING TEMPORAL VEGETATION RESPONSE

As mentioned above, the analyses completed prior to this step were made using data derived on low-relief lands away from the rocky highlands overlying the proposed repository. These lands include both the lowland region used for developing processing parameters (Figure E-9) and the ESP sites that were mostly located away from the repository footprint on nearly level ground (Figure E-13). In contrast, this step to characterize NDVI' seasonal responses used data from the rocky region overlying the proposed repository (Figure E-17). Results provided a set of general response curves that capture the variability induced by slope and azimuth for the vegetation directly overlying the proposed repository.

Extractions from the areas depicted in Figure E-17 yielded a suite of pixels for $NDVI_{offset}$ processed with the parameters developed in Section E2.4 for both N (n=273) and S (N=405) slopes. These values were placed into the workbook *ALL_Years_N_S_18_24_slope_extractions.xls* (Output DTN: SN0608NDVIANAL.001). All N and S grid values for the point in time represented by each image were collected together in the workbook *Daily_NDVI_Estimation.xls* for further analyses (Output DTN: SN0606T0502206.012). Correction of the average $NDVI_{offset}$ by subtracting the zero baseline (correcting for desert varnish) was completed as described in Section E2.4. The resulting values, 0.0298 for N slopes and 0.0316 for S slopes, were taken to represent average values for the zero baseline. When subtracted from all values of average $NDVI_{offset}$ at each time step, this yielded average NDVI' that were graphed against the day of year for each of the three water years (Figure E-19).

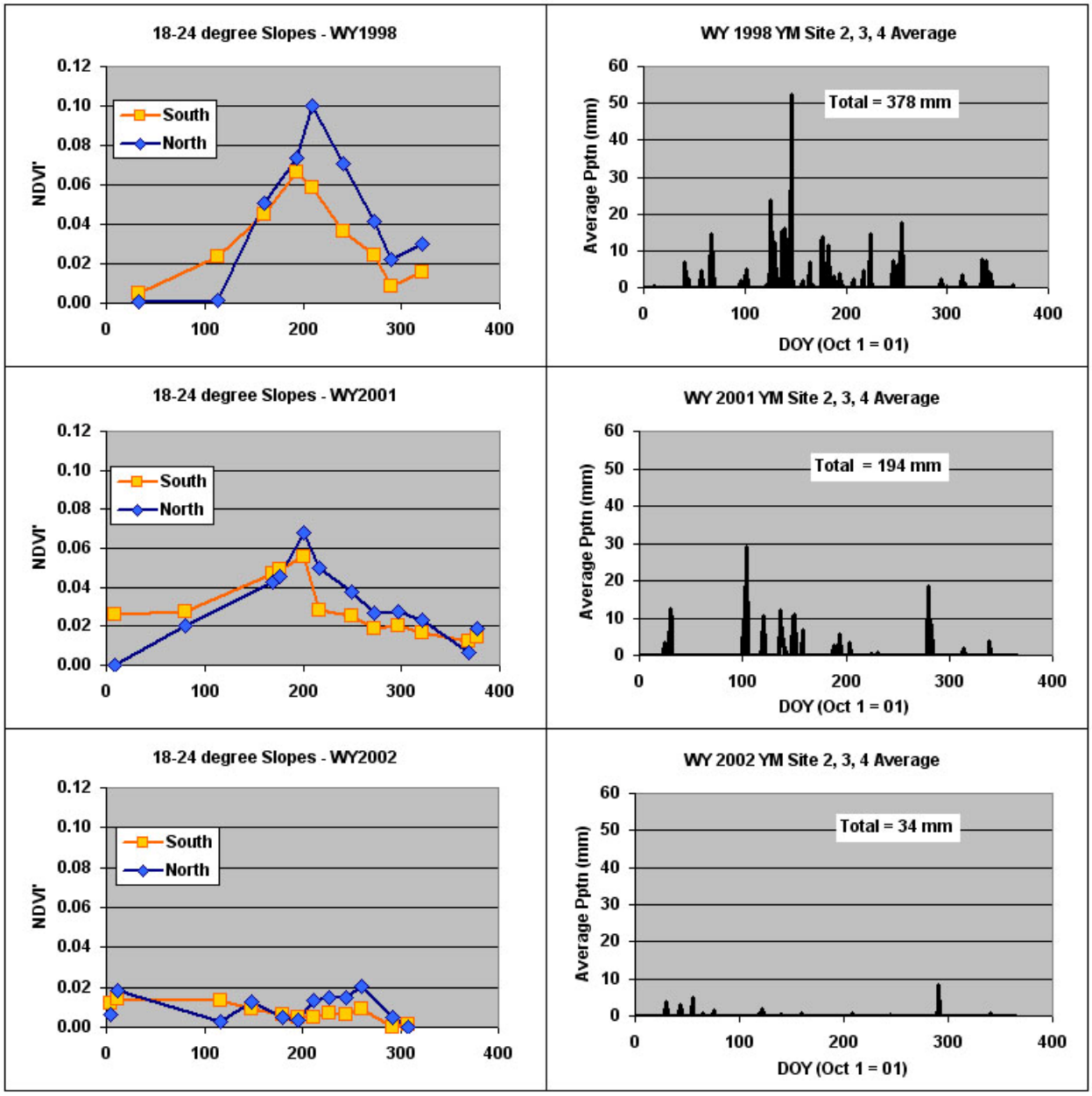

Source: Output DTN: SN0606T0502206.012, *Daily_NDVI_Estimation.xls*.

NOTE: Points from the beginning of WY2002 (October 4 and 12, 2001) are plotted as the two endpoints for the WY2001 plots.

Figure E-19. NDVI' Calculated for N- and S-Slope Extractions (18° to 24°) for the Three Yucca Mountain Study Water Years, Paired with Average Daily Precipitation from Sites 2, 3, and 4

As previously discussed, calculation of NDVI' is a necessary step to remove the response induced by the content of desert varnish on the rock surfaces. While the response remains stable through time, there is some error introduced in the results due to geospatial uncertainty (the amount of desert varnish associated with individual cells varies naturally). Averaging of the populations of N (n=273) and S (n=405) slope cells was employed to minimize the associated error.

There are five key points about Yucca Mountain vegetation response and its detection that are illustrated in Figure E-19:

N slopes were confirmed to have greater NDVI' response during all growing seasons.

Early season (winter) growth on N slopes lags behind S slopes.

For the two years with sufficient precipitation to fund strong vegetation growth responses (1998 and 2001), the NDVI' peaks occurred at about the same time (approximately WYDOY = 200; April 18). For these same years, a difference in the timing of peak annual expression (WYDOY – 200) was not discernible between N and S slopes.

NDVI' values for the dry year (WY2002) show a slight promotion for N slope over S slope. However, these values are close to their probable zero. When coupled with the lack of effective precipitation, this suggests that the small curve responses for the N slope NDVI' that are visible in Figure E-19 for late WY2002 may be noise from the combined sources of error affecting NDVI' in this environment.

Intermediate levels of precipitation (WY2001) produced an intermediate NDVI' response. Thus, the expected vegetation response to precipitation for the three years falls in the correct order from low to high.

E3.3 FITTING NDVI' RESPONSE CURVES TO REPRESENT SLOPE AND AZIMUTH

The NDVI' for WY1998 N and S slopes were selected for simulating vegetation annual response curves on Yucca Mountain. This year was chosen because it was extremely wet and vegetation canopy expression was at, or near, the potential maximum. This high vegetation response is desirable because it maximizes the signal to noise ratio for NDVI'.

Both N and S slope data for WY1998 (illustrated in the top-left graph of Figure 19) were spline-fitted to the ascending and descending limbs of NDVI'. The simplest mathematical function that provided a reasonable fit was chosen for each leg of the curve: 2nd Order polynomials. Expressed as curves they are:

18 to 24° North Slopes

Ascending Limb: $NDVI' = 0.000000931x^2 + 0.000681033x - 0.086604350$

Descending Limb: $NDVI' = 0.00000287x^2 - 0.00226123x + 0.44628979$

18° to 24° South Slopes

Ascending Limb: $NDVI' = 0.00000167x^2 + 0.00001369x + 0.00096664$

Descending Limb: $NDVI' = 0.00000198x2 - 0.00148230x + 0.27967664$

These relationships were used to estimate NDVI' for both N and S slopes in daily time steps for WY1998 (Figure E-20). Curves to represent all classes of slopes and azimuths were then interpolated between these fitted relationships. These calculations are found in *Daily_NDVI_Estimation.xls* (Output DTN: SN0606T0502206.012).

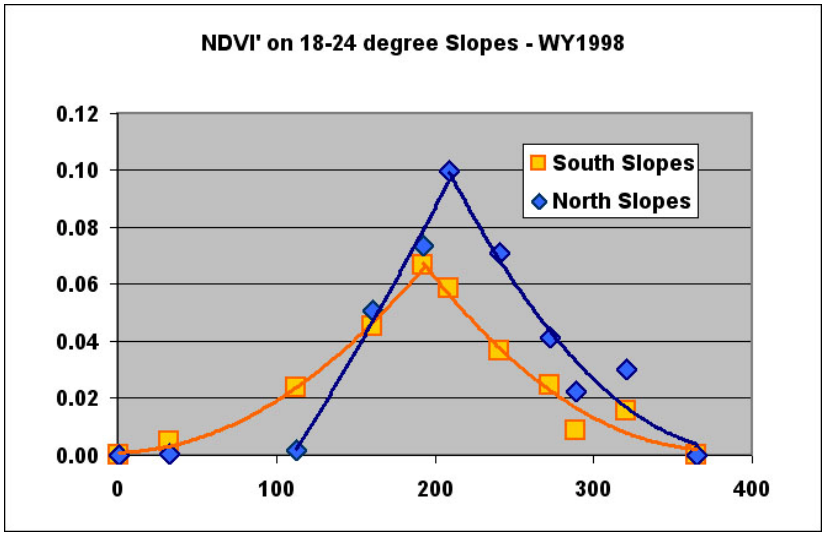

Source: Output DTN: SN0606T0502206.012, *Daily_NDVI_Estimation.xls*. The regression line was fitted to the N–S slope average.

Figure E-20. Plot of the Results for Calculation of NDVI' for the Pooled LG Vegetation Plots (x-axis) and for N and S Slopes and their Average

For characterization of vegetation for the class representing the combined flat-E−W slopes, the average per-time-step values of NDVI' for N and S slopes were combined as simple averages following Logical Principle 5, listed in Section E3.1. To test whether interpolating between N and S slopes was a reasonable approach for representation of quasi-level sites, these data were compared to the ESP data from LG sites. LG vegetation (dominated by genera *Lycium* and *Grayia*) predominates in the zone overlying the proposed repository.

Figure E-21 presents data paired by image time-step. The X-axis value is average NDVI' for the lumped pixels from LG ESPs (n=516). Paired with this are Y-axis values of average NDVI' for the steep N (n=273) and S (n=405) slopes and the N–S average (n=273+405). This results in three Y-values, WY1998, WY2001, and WY2002, for the n=31 unique X-axis values.

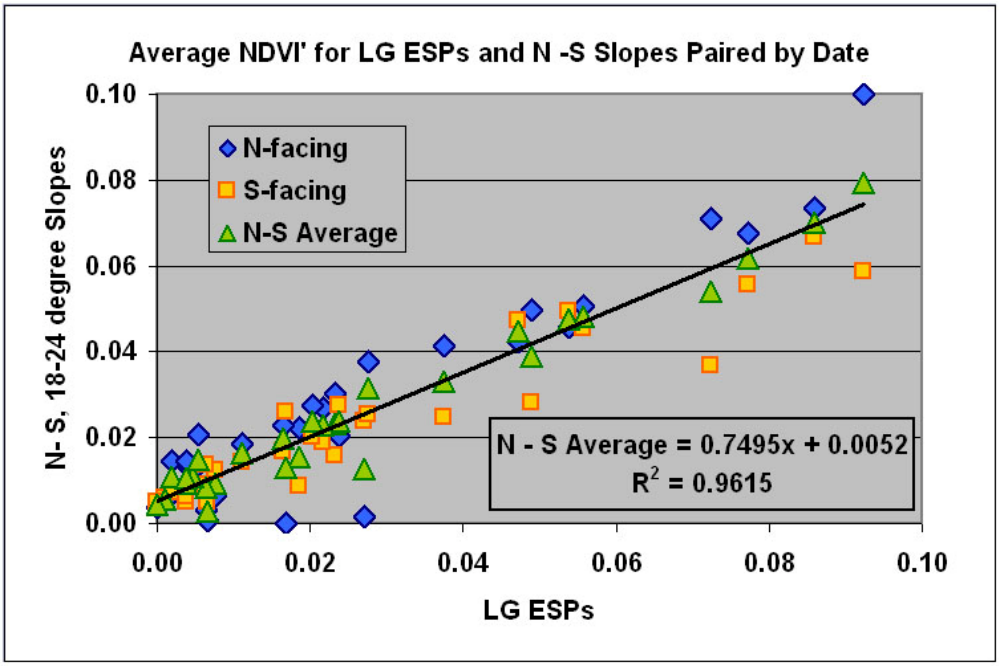

Source: Output DTN: SN0608NDVIANAL.001, *ESP_NDVI'_so, ET-K*; Output DTN: SN0606T0502206.012, *Daily _NDVI_Estimation*. The regression line was fitted to the N–S slope average. This average represents a tighter data cloud than, and is intermediate to, N or S slopes.

Figure E-21. Plot of NDVI' for N and S Slopes and their Average for all Images Years Versus Average NDVI' Extracted for LG Vegetation Plots (x-axis)

In Figure E-21, the N–S average is an intermediate condition between N and S endmembers. The slopes/azimuth for LG sites have low relief (i.e., nearly level) compared to the samples extracted for N and S slopes. As would be expected, there is a great deal more scatter for the N and S slope data than for their average. The S-slope data generally plots toward the lower side of the data cloud while N slopes plot above, again illustrating the predicted trend toward higher vegetation response on N slopes (Logical Principle 3, above).

A line fitted for the N–S average has a slope less than unity (about 0.76), indicating that the comparative strength of the upland vegetation response is lower than for the relatively flat sites that were chosen for LG ESPs. This reduction in vegetation for steep slopes of the rocky uplands may logically indicate that a proportion of precipitation is lost to runoff because soils are shallower and have limited water holding capacity compared to the gentle slopes of the LG ESPs. The shallow soils of the rocky uplands of Yucca Mountain limit the potential storage of incident precipitation (Stothoff et al. 1999 [DIRS 176705]).

Although the analysis in Figure E-21 shows that the LG sites and N–S slope average are not equivalent, they do have a strong linear relationship (Figure E-21). This confirms that the shape of the N–S average curve functions well as a predictor of the annual response for shallow slopes such as those presented by the LG vegetation plots (mostly <5°). However, and appropriately, the N–S slope NDVI' average is not equivalent (with a one-to-one relationship, nor would it be expected to be) to the NDVI' measured for the LG sites. The vegetation expression on Yucca Mountain is highly variable. Such spatial variability is addressed using a spatially correct scalar,

PVR, which was calculated for each model grid cell to adjust for the measured strength of the NDVI' response as the difference between wet and dry years (Section E4).

The daily time-step average of N- and S-slope curves that were used to represent environments that are nearly flat (<5°), and also for E and W slopes, are shown in Figure E-22. Table E-4 provides the calculation algorithms chosen for interpolating 13 unique slope-azimuth classes from the N–S slope results. E and W present roughly equivalent conditions. Thus, as an example, SW is equivalent to SE, NW to NE, and so forth. Figure E-23 presents the suite of curves to represent annual temporal NDVI' response for slope-azimuth combinations calculated with the algorithm in Table E-4 found in workbook *Daily_NDVI_Estimation.xls* (Output DTN: SN0606T0502206.012).

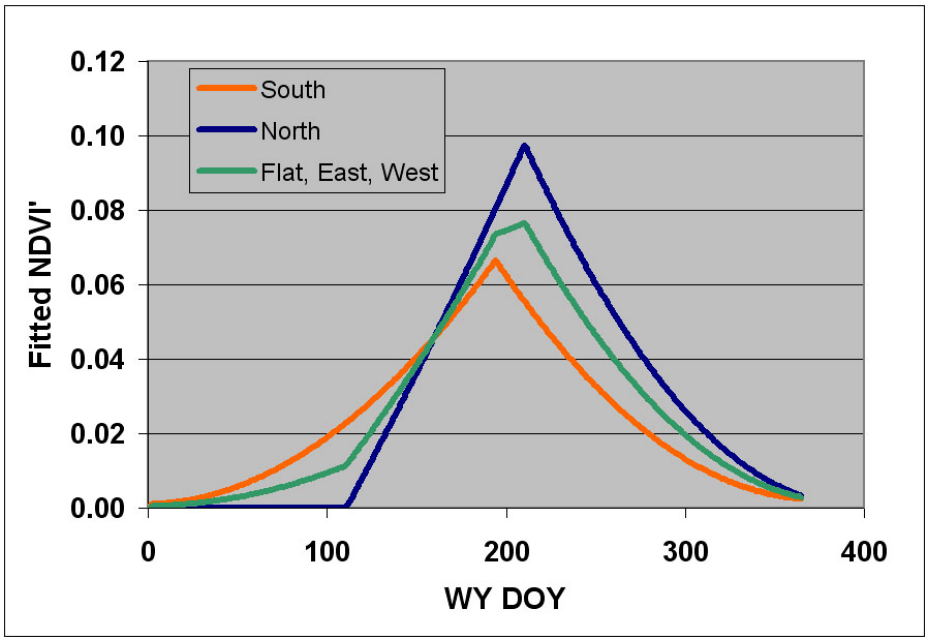

Source: Ouput DTN: SN0606T0502206.012, *Daily_NDVI_Estimation.xls*. By weighted averaging, these curves were adapted for various slope and azimuth combinations. The curve for flat, east, and west slopes is the temporal average of north and south and is calculated in file *Daily_NDVI_Estimation.xls*.

Figure E-22. Three Temporal Curves for NDVI' on Yucca Mountain

Table E-4. Algorithm for Calculating Slope- and Azimuth-weighted Temporal Average NDVI' Using Relationships Fitted for N- and S-facing Slopes (>18°) and Their Temporal Average (A)

Cardinal Direction	Azimuth Start	Azimuth End	Azimuth Center	>18 deg	11-18 deg	5 - 10 deg	<5 deg
N	337.5	22.5	360	**N**	(2N+A)/3 **B**	(N+2A)/3 **C**	**A**
NE	22.5	67.5	45	(N+A)/2	(A+B)/2	(A+C)/2	**A**
E	67.5	112.5	90	**A**	**A**	**A**	**A**
SE	112.5	157.5	135	(S+A)/2	(A+D)/2	(A+E)/2	**A**
S	157.5	202.5	180	**S**	(2S+A)/3 **D**	(S+2A)/3 **E**	**A**
SW	202.5	247.5	225	(S+A)/2	(A+D)/2	(A+E)/2	**A**
W	247.5	292.5	270	**A**	**A**	**A**	**A**
NW	292.5	337.5	315	(N+A)/2	(A+B)/2	(A+C)/2	**A**

Source: Output DTN: SN0606T0502206.012, *Daily_NDVI_Estimation.xls*.

NOTE: Formulae for weighted averaging are defined as units B to E and are abbreviated for application to other cells.

The scheme for interpolating daily time steps of NDVI' in Table E-4 uses combinations of three relationships. These are the relationships for N, S (for slopes >18°), and E−W-flat slopes (given the abbreviation A, in Table 5). The interpolation for all intermediate slopes and azimuths combines various portions of these three curves for each daily time step (365). As an example for averaging the effect of slope for N aspects, the two endmembers across, N and A, are interpolated by weighted averaging; (2N+A)/3 and (N+2A)/3. For brevity, these formulae were given the abbreviation B and C and thus formed endmembers for interpolation between N and NE and N and NW. In this simplified scheme, E and W were set to be equivalent (because they should receive about the same insolation) and so NW = NE and SW = SE.

As shown in Table E-4, the wide range of potential slopes and azimuths is characterized into four slope classes, >18°, 11° to 18°, 5° to 10°, and <5°, and by azimuths to the eight cardinal directions. The >18° class is represented by the curve shown in Figure E-20. The "flat" designation, <5°, was not classified as to azimuth. This system potentially gives rise to 25 separate classes; however, since the algorithm was simplified by choosing E = W, only 13 unique classes were created: [(4 azimuths × 3 slope classes) + 1 shallow-slope class at all azimuths].

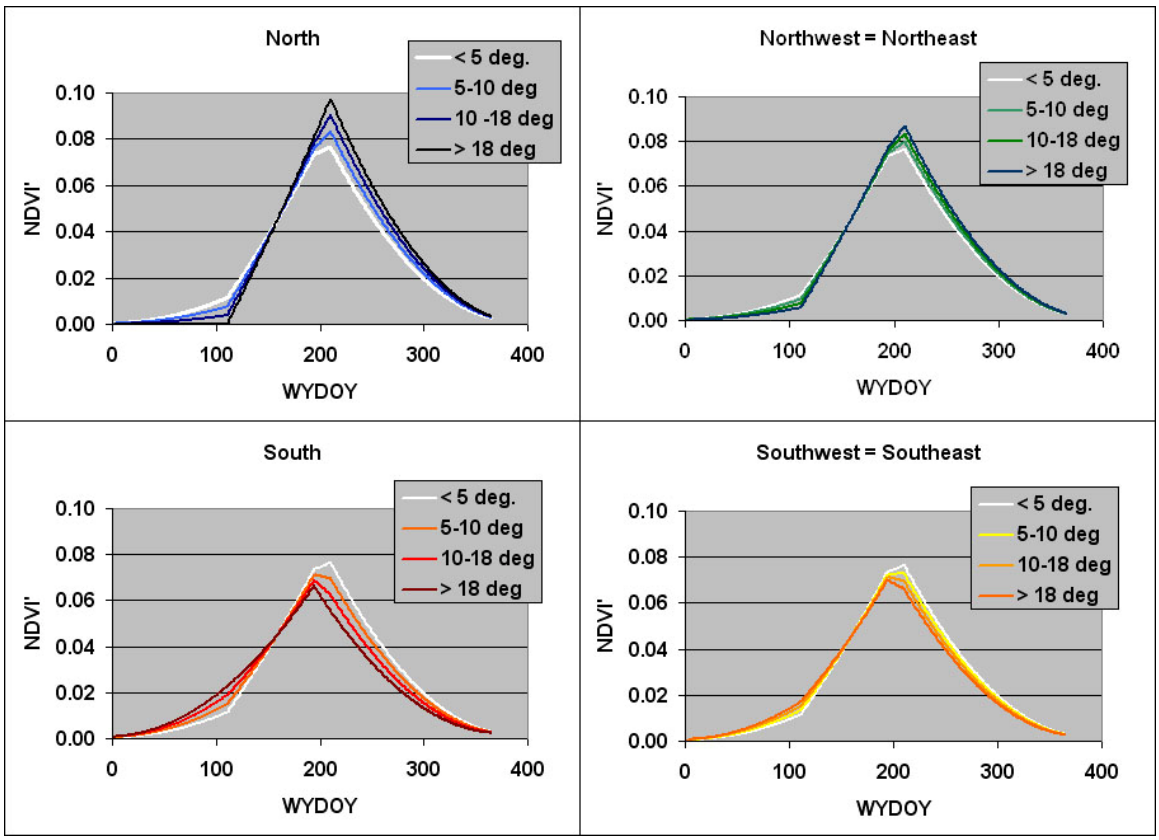

Source: Output DTN: SN0606T0502206.012, *Daily_NDVI_Estimation.xls*.

NOTE: There are 13 unique combinations of curves. The curve representing level ground (<5°) and E and W slopes is reproduced (as the white curve) in each graph.

Figure E-23. Temporal Curves Developed by the Weighting Functions in Table E-4

E4. POTENTIAL VEGETATION RESPONSE – SCALAR VALUES FOR EACH MODEL GRID CELL

Up to this point, all calculations were largely independent of location. Section E2 determined how to process the satellite data, and Section E3 derived the shape of the annual response of NDVI' for all slopes and azimuths. Rather than being tied to any single model grid cell, these calculations employed averages of pooled sampled groups in order to determine overall trends. This final step, calculation of potential vegetation response (PVR), provided values for each model grid cell that are scaled to the strength of the actual vegetation response within that cell. The calculation of the PVR values for each grid cell is done in Output DTN: SN0608PVRATYMT.001.

As described in Section E2.6, there are highly variable amounts of desert varnish-covered rock that can occur within each cell. This potentially confounding problem was solved in the parameter-verification step in Section E2.5 and in the NDVI' curve-fitting of Section E3 by subtracting out the background values enhanced by the effects of desert varnish. These background values were taken as the recorded values during a critically dry year (WY2000). PVR is calculated as shown in Equation E-7:

$$PVR_i = \frac{\left(NDVI'_i\right)_{\max} - \left(NDVI'_i\right)_{\min}}{\overline{NDVI'_{\max-\min}}} \qquad \text{(Eq. E-7)}$$

where $(NDVI'_i)_{\max}$ and $(NDVI'_i)_{\min}$ are the $NDVI'$ values for pixel i with the maximum and minimum expected vegetation responses, respectively. $\overline{NDVI'_{\max-\min}}$ is the average difference between $NDVI'$ values listed above for all pixels within the region of interest.

The denominator of PVR, the average value of grid cells within the area of interest, normalized the results for a subset area overlying the proposed repository. This area was chosen as a rectangle of 12,702 grid cells (11.43 km^2). Normalization provided scaling to permit better understanding PVR distribution: a PVR of 1.0 represents the approximate average vegetation response overlying the repository (i.e., the denominator in Equation 7). It is important to note that PVR was normalized specifically for the region overlying the repository to permit additional analyses where the vegetation responses are of greater interest. In general, however, large areas of deeper soil may push the actual average for these repository-normalized PVR to a higher level within the entire MASSIF model domain. Mathematically, this is inconsequential because those areas do have higher responses, they are mathematically ordinal, and because the crop coefficients developed in Appendix D will be calibrated to the simulated NDVI'.

As a consideration for accuracy in the calculation of PVR (Equation E-7), the farther apart the conditions represented by the max and min precipitation years (i.e., very dry and very wet), the better resolution they provide for estimation of the potential for vegetation growth. For Yucca Mountain vegetation, the two years chosen for the characterization, WY1998 and WY2002, represent extremely wet and dry conditions (Figure E-3). For the dry conditions of WY2002, the average precipitation received for Sites 2, 3, and 4 was about 34 mm. Most of this precipitation was likely lost through evaporation as only small amounts of water were deposited during each precipitation period. Conditions were profoundly dry, and the expected vegetation expression was at, or near, the lowest level that can be attained in this system.

Rather than using the late summer zero baseline as the previous analyses had done for calculation of NDVI', calculation of PVR used NDVI' from periods of expected peak annual growth for both wet and dry years. For WY1998, the dates selected were March 10, April 11, and April 27. For WY2002, the dates selected were March 29, April 14, and April 30. Equivalent time periods were chosen to avoid any possible influence from solar angle. Data for the three before and after dates were averaged for each 30-m model grid cell in the model domain. The method for calculation of $NDVI_{offset}$ (subtracting $NDVI_0$) can create slightly negative values for the lowermost, asymptotic portions of the NDVI curves. To avoid compounding errors in calculation, negative values were converted to zero (functionally correct, since vegetation cover and expression are never less than zero). Negative values occurred in

only 49 of the total grid cells (0.0039 of the rectangular sampled area). Within the rectangular subset area of 12,702 grid cells overlying the proposed repository, none of the values were negative.

The rectangular area overlying the repository was used for calculation of an appropriate average value for normalizing PVR. This normalized value was used to then investigate the statistical distribution of PVR values (*PVR-Max_Min_NDVI_subset_analysis.xls*, Output DTN: SN0608NDVIANAL.001). The average value of PVR for this subset, 0.071654, was divided into all pixels within the model domain: this was the denominator for normalizing PVR values (Equation E-7). Over the repository, the regionally normalized PVR ranged from zero to about three. Thus, for the repository region, normalized PVR had an average response of 1.0 and a peak response about 300% greater than average. In Figure E-24, a histogram of normalized PVR demonstrates the statistical distribution of PVR from within the subset area overlying the proposed repository.

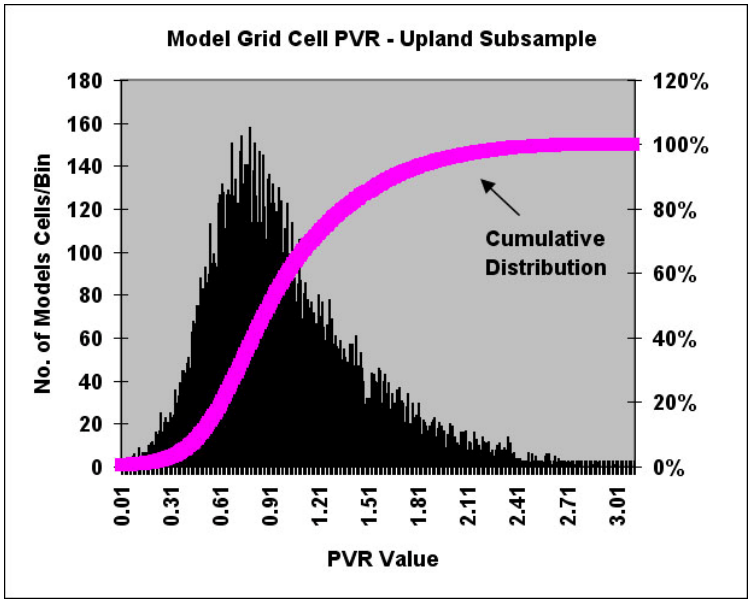

Source: Output DTN: SN0608NDVIANAL.001, *PVR-Max_Min_NDVI_subset_analysis.xls*.

NOTE: The maximum PVR range for the full infiltration modeling domain is about 4, which is higher than for this subregion.

Figure E-24. Histogram of Normalized PVR from the Subset Area Overlying the Proposed Repository

Figure E-25 presents a graphic view of PVR distribution for the region overlying and surrounding the proposed repository. Comparison of the distribution of the higher PVR values to the brighter red signatures on the false color images for WY1998 (Figure E-1) confirmed that PVR captured the distribution of heavy vegetation response. A comparison of data from the vegetation plots disclosed that high PVR values are associated with heavy infestation by *Bromus madritensis* spp. *rubens*, (common name, "red chess"), a weedy annual grass introduced from Eurasia. A close look at the PVR values displayed over the DOQQ or Quickbird images indicates that that PVR correctly identifies areas of low (or no) vegetation activity in rocky locations.

To codify vegetation response as PVR for each grid cell, the minimum (critically dry) year should have a functionally zero vegetation signal. This may actually not be the case for many model grid cells because of partial leaf retention by evergreen species such as *Larrea divaricata*, *Ehpedra* spp., and *Chrysothamnus* spp. that make up a portion of the vegetation on Yucca Mountain. The minimal canopies of these species would be present during the period chosen for the minimum expression and should be subtracted out. Fortunately, during extreme droughts these plants also lose leaves (Smith et al. 1995 [DIRS 103628]), reducing the potential error.

Though no data exist for recording the effect of uncounted evergreen species on the calculation of PVR, the potential bias due to evergreen species can be estimated. For the rocky uplands, only the *Ephedra* spp. and *Chrysothamnus* spp. are important since *Larrea* is excluded where soils are shallow. As an example, measurements by Stothoff et al. (1999 [DIRS 176705]) found one evergreen species (C*hrysothamnus teretifolius*) comprising about 10% of the perennial vegetation on the rocky uplands (0.03 of the 0.33 total cover). Thus, if the retained leaves during drought for this species were 10% of maximal canopy expression, the potential bias due to uncounted evergreen plants with leaves would be up to about 1% of the variation in the data (10% of 10%). This bias is insignificant in comparison to the uncertainty that exists in the data (discussed in Section E7). The bias associated with the LLG sites may be 2 or 3 times this amount due to a predominance of *Larrea*, though fortunately, is largely excluded from the target region for this simulation due to shallow soils in the rocky uplands overlying the proposed repository.

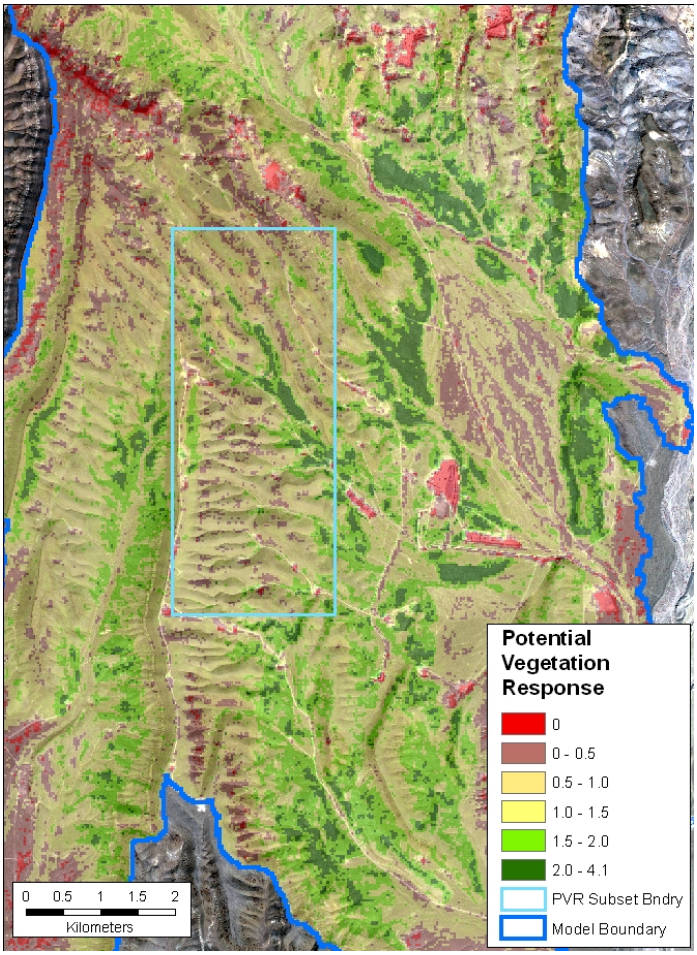

NOTE: Magnitude of PVR is reflected in the intensity of the green coloration. Pink areas are exposed rock or extremely low or near zero vegetation response. The irregular blue line is the boundary for watersheds included within the infiltration model. The light blue polygon is the region overlying the repository footprint selected for normalizing and evaluating the statistical distribution of PVR. The PVR values are calculated in Output DTN: SN0608PVRATYMT.001. The PVR Subset Boundary line is from *PVR_subset_.evf* and *nad27_boundary_evf* in Output DTN: SN0608NDVIAUXD.001. Grayscale background is from a Quickbird image from DTN: SN0601QBSAT802.001 [DIRS 177241].

Figure E-25. PVR Located over the Region of the Proposed Repository

E5. ALGORITHM TO SIMULATE VEGETATION FOR EACH MODEL GRID CELL

An algorithm to simulate annual vegetation response for each model grid cell was assembled from the resulting output from Sections E2, E3, and E4. In review, Section E2 established the proportionality for vegetation response to annual precipitation. In Section E3, a temporal curve for NDVI' was developed that was adjusted by weighted averaging to represent various classes of slope and azimuth. In Section E4, PVR was developed for each model grid cell to scale the magnitude of the vegetation response to antecedent precipitation, calibrating to the actual conditions that enhance or inhibit vegetation growth within that cell.

WY1998 was chosen for fitting all simulation parameters, including PVR, NDVI' slope/azimuth response curve, and a precipitation ratio for scaling the magnitude of the vegetation response. WY1998 is an ideal choice as the very high level of precipitation induced a maximal vegetation response. This maximal response corresponds to a strong signal in an environment that generally has a weak vegetation signal, hence maximizing the signal to noise ratio.

To simulate the strength of the vegetation response, the response curve is scaled using the total annual precipitation. This is accomplished by using the ratio of the annual precipitation of the year in question to the annual total WY1998 precipitation. Precipitation data were calculated as the average of three stations located on Yucca Mountain (Stations 2, 3, and 4). For WY1998, the yearly precipitation was 378 mm (in *ESP_NDVI'_simET-K.xls*, 2. precip_table (Output DTN: SN0608NDVIANAL.001). It is noted that the WY1998 yearly precipitation value can be varied within the infiltration model; for example, a projection for WY1998 precipitation based upon elevation could be used instead

The resulting outputs were combined to estimate NDVI' for any day in the water year for any location within the model domain (Equation E-8):

$$\text{sim NDVI}'_i = \text{NDVI}'_{j,\ i-curve} * \text{PVRi} * \text{WY precipitation (mm)} / 378\ \text{mm} \quad \text{(Eq. E-8)}$$

where: sim denotes simulated,

j is the j^{th} day of the water year,

i is the i^{th} model grid cell,

i−curve denotes the $NDVI'_j$ curve values appropriate for the slope and azimuth of the i^{th} cell.

This algorithm, along with the $NDVI'_j$ curve and PVR_i data, are used as input for the MASSIF model.

E6. *ET* AND K FACTOR SIMULATION FOR COMPARISON TO OTHER MASSIF MODEL PARAMETERS AND *ET* ESTIMATION

Although the data in this appendix were analyzed primarily to develop a simulation algorithm for vegetation response, they were also analyzed to enable comparison with the K_{cb} parameters developed and described in Appendix D. K_{cb}s are basal crop coefficients. These crop coefficients are multiplied by the reference *ET*, ET_0, to yield an estimate of actual *ET*. The calculations for this comparison are contained within spreadsheets in the workbook entitled *ESP_NDVI'_simET-K.xls* (Output DTN: SN0608NDVIANAL.001). This section provides scaled values of *ET* estimated using reference ET_0 for comparison to the K_{cb} developed in Appendix D.

For this analysis, daily time steps of ET_j were simulated (where j denotes the j^{th} day in the water year). In order to correlate the ET_j relationship from $NDVI'_j$, polynomial functions were fitted to the NDVI' time steps to provide predictors for $NDVI'_j$. As an example, the time-wise NDVI' data

shown on Figure E-19 for WY1998 were fitted with two polynomial relationships that enable estimation of daily time steps (Figure E-26).

$NDVI'_j$ values predicted by the polynomial curves were multiplied in daily time steps by the daily ET_0 estimated for Yucca Mountain using the FAO-56 Penman-Monteith method (Allen et al. 1998 [DIRS 157311]) in *Ref ET calcs_2002 water year_rev A2*, *Ref ET calcs_2001 water year_site 1 weatherdata_rev A2*, and *Ref ET calcs_2002 water year_rev A2* (Output DTN: MO0603SPAREFET.000). To scale each time step to provide estimates of ET_j, these individual ET_{0j} * $NDVI'_j$ products were summed for the water year and divided into the total annual precipitation (all units in mm). This scalar value was then multiplied by the value of ET_{0j} * $NDVI'_j$ to simulate ET_j for the average vegetation NDVI' measured (Figure E-27). Note that this calculation provides values intended simply for guidance for expected ET_j because it *ET* is computed to all pass through plants (this results from scaling the total of the ET_j and $NDVI'_j$ products by the total annual precipitation). This simplification does not account for the portion of water lost by evaporation at the soil surface or rock/canopy interception; however, these methods of water loss may be relatively small compared to the amount passing through the plants themselves. The ET_j relationship is given in Equation E-9.

$$\text{sim } ET_j = (ET_{0j} * NDVI'_j) * [\text{sum } (ET_{0j} * NDVI'_j) / \text{sum precipitation}_j] \qquad \text{(Eq. E-9)}$$

Simulation of ET_j enabled the estimation of a simulated vegetation water use coefficient, a K factor (Allen et al. 1998 [DIRS 157311]). Daily time steps were calculated by simply dividing ET_j by ET_{0j}. The shape of this curve, again at daily time steps, is the same as the NDVI' curve in Figure E-26, except scaled by precipitation to the correct dimensions for ET_j. These curves of K were intended for comparison to the K_{cb} values that are described in Appendix D.

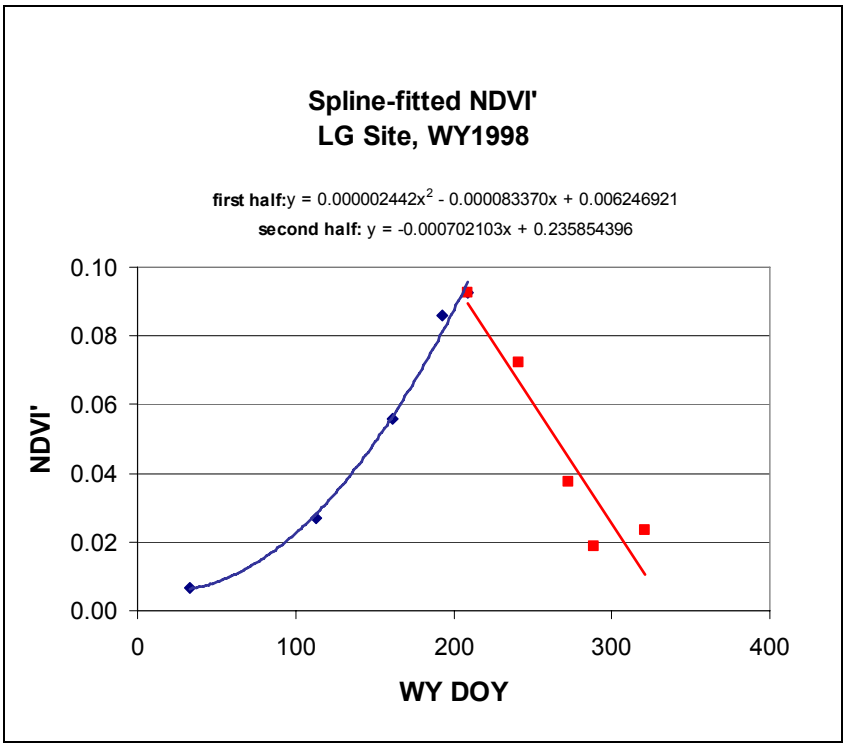

Source: Output DTN: SN0608NDVIANAL.001, *ESP_NDVI'_simET-K.xls*.

Figure E-26. Two Polynomial Curves, Ascending and Descending, Fitted to the NDVI' LG ESPs, WY1998, to Calculate Daily Time Steps through the Water Year

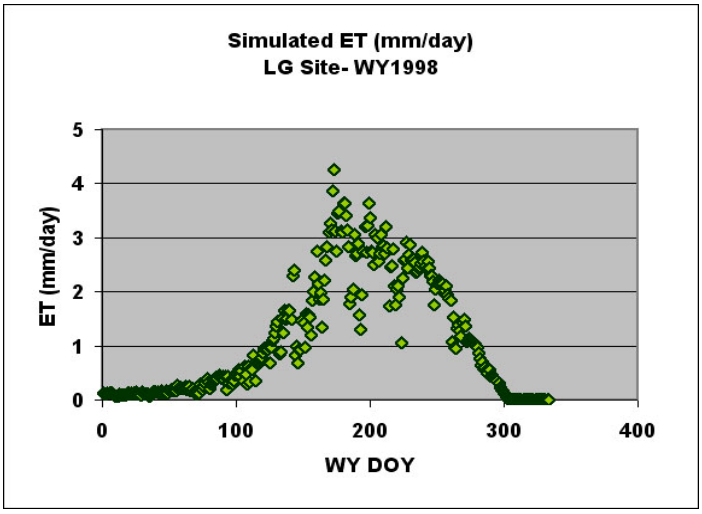

Source: Output DTN: SN0608NDVIANAL.001, *ESP_NDVI'_simET-K.xls*.

Figure E-27. ET_j Simulated for LG Sites in WY1998 Using ET_0, Daily Fitted Values for NDVI' and Scaled by the Water Available from Precipitation

E7. CORROBORATION OF THE NDVI' ALGORITHM AND OF THE POTENTIAL MAGNIDUDE OF UNCERTAINTY

The algorithm for simulating NDVI' was corroborated using three separate data sets. The data sets were extracted from the ESPs because these locations were used as input for estimation of *ET* and basal crop coefficient (K_{cb}) relationships (Appendix D), they are locations where vegetation properties were measured, and they are a potential source for other meta-data such as average slope and aspect.

Corroboration 1. For the ESPs, simulated NDVI' was compared to measured NDVI' for WY1998, WY2001, and WY2002. The simulated NDVI' values were calculated using PVR data measured for the ESPs in the developed algorithm (Equation E-7). A total of nine comparisons were completed (three different vegetation types for years of above average, average, and dry levels of precipitation).

Corroboration 2. NDVI' simulations for WY1990, 1991, and 1993 were compared with K_{cb} values calculated in Appendix D. As seen in Section E6, NDVI' is a value that is closely related to crop coefficients (K factors).

Corroboration 3. Vegetation cover was measured on the ESPs during 1990, 1991, and 1993. Annual water year precipitation totals that were measured at three Yucca Mountain stations (2, 3, and 4) were combined with the PVR data extracted from the ESPs to estimate a peak NDVI' for comparison to measured cover.

Each of these corroboration efforts is described in more detail below.

E7.1. CORROBORATION 1: APPROPRIATENESS OF THE ALGORITHM FOR WY1998, WY2001, AND WY2002.

NDVI' was simulated for daily time steps using Equation E-7 for the pooled samples of the three vegetation association-ESP sites (sampled locations on Figure E-13). For the simulation, the appropriate NDVI' curve was chosen to represent the average topographic slope and azimuth at each of the vegetation plots (typically <5 degrees). The daily time step curves were combined with average PVR values extracted for the model grid cells which fell within the vegetation plot boundaries. Sample sizes for PVR were robust: 445 cells for LA plots, 552 for LLG and 516 for LG. Data were averaged for the calculation of a single value to represent each of the three vegetation associations (Output DTN: SN0608NDVIANAL.001, workbook *Verify_NDVI'_Estimation.xls*). The resulting daily time-step curves were then compared with the average of NDVI' extracted and calculated for each image in Output DTN: SN0608NDVIANAL.001, workbook ESP_NDVI'_simET-K, as described in Section E2.5.

Figure E-28 provides a graphical comparison of simulated and measured NDVI' values. The comments here will be restricted to the LG vegetation that overlies the proposed repository. Of the two other vegetation types, LLG and LA, the simulation of LA appears to be qualitatively better than for the LLG type, while relative errors are greater in the early part of the season rather than in the latter portion for all three vegetation types.

Not surprisingly, the WY1998 simulation of LG vegetation is better than for WY2001. For example, the peak measured value for WY1998 NDVI' was 0.0924 while the simulated value for was 0.0852 (7.8% low). For peak point of the WY2001 growing season induced by moderate precipitation, the measured NDVI' was .0773, while the simulated value was 0.0422 resulting in an underprediction of about 45%. For the driest year, WY2002, the simulation correctly projected very low peak NDVI', 0.0073, that was less than 10% of either WY2001 or WY1998.

The simulation algorithm (Equation E-8) apparently induces a systematic underprediction during the first part of the WY relationships as can be seen in Figure E-28, where for LG plots, the estimation was about 1/2 of the measured values for WY2001. The declining leg of the simulated curve for WY2001 is closer, with the values at WYDOY 217 underpredicting the NDVI' by 25%.

Fortunately, the greatest potential for infiltration exists during the wet period where the simulation routine performs the best of the three cases.

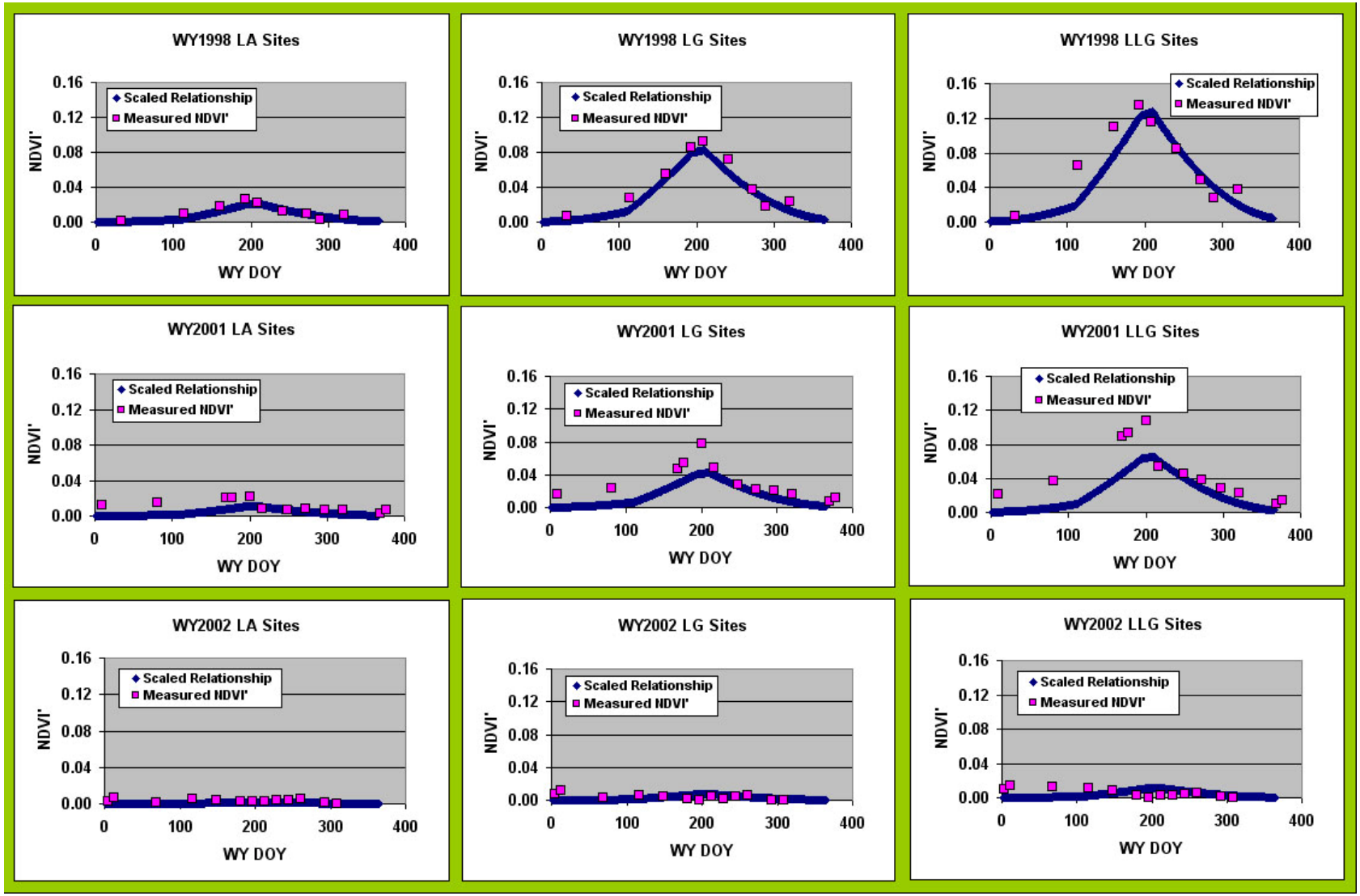

Source: Output DTN: SN0608NDVIANAL.001, *Verify_NDVI'_Estimation3.xls*.

Figure E-28. Simulated (Curves) Versus Measured Values of NDVI' on the Three Plots during the Three Years Chosen for Study

E7.2. CORROBORATION 2: COMPARE NDVI' SIMULATIONS FOR WY1990, WY1991, AND WY1993 WITH K_{cb} VALUES CALCULATED IN APPENDIX D

NDVI has been shown to be related linearly to K_{cb} in the literature (Hunsaker et al. 2003 [DIRS 176048], pp. 100 and 101, and Figure 6; Hunsaker et al. 2005 [DIRS 177302], pp. 10 and 11 and Figure 5). This step tested this linearity using the LG ESP data because it is most similar to the vegetation overlying the repository. The analysis used total water-year precipitation to scale the algorithm (total precipitation in desired year [mm]/total precipitation in wettest year [378 mm]). Three WYs were chosen (WY1990, WY1991 and WY1993). Results were applied to the lumped average PVR for each of the ESPs that were used for calculations in Section E7.1 from Output DTN: SN0608NDVIANAL.001, workbook *Verify_NDVI'_Estimation.xls*. Calculations are contained in Output DTN: SN0608NDVIANAL.001, workbook *ESP_90,91,93,NDVI'_simET-K.xls*. Figure E-29 shows the comparison for the LG plots of the K_{cb} values calculated for estimation of *ET* in Appendix D versus the simulated NDVI'.

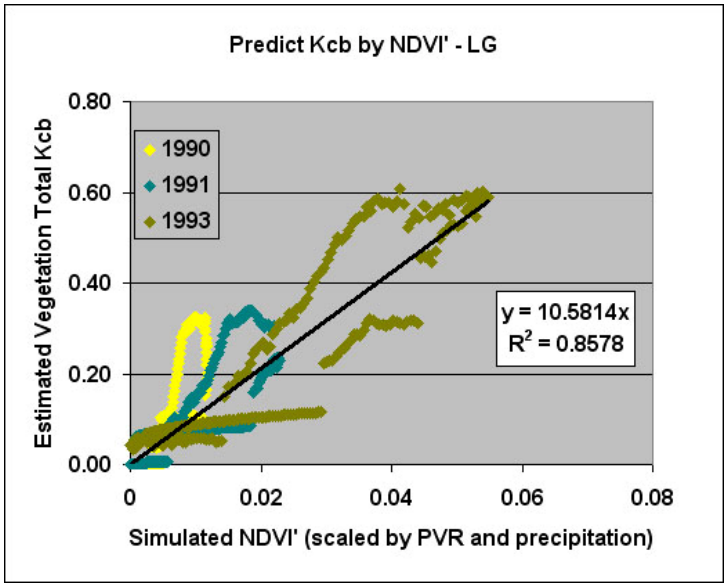

Source: Output DTN: SN0608NDVIANAL.001, *ESP_90,91,93,NDVI'_simET-K.xls*.

NOTE: The regression line was forced through the origin.

Figure E-29. Comparison of Simulated NDVI' to the K_{cb} Values, Paired by Daily Time Steps, for WY1990, WY1991, and WY1992 for the LG ESPs

Figure E-29 provides a linear relationship to relate the two data sets. K_{cb} is roughly a factor of ten higher than the simulated NDVI'. The systematic digressions from the NDVI' estimate occur as a hysteretic effect where the K_{cb} is higher during the early portion of the year when there is soil water available (plotting above the regression line), but much lower during the latter portions of the growing season when the plants are within a senescing cycle (below the regression line). All three years were lumped together to fit on this curve, and the driest year, WY1990, was distributed mostly above the predicted linear relationship.

E7.3 CORROBORATION 3: COMPARE VEGETATION COVER MEASURED ON THE ESPS DURING 1990, 1991, AND 1993 WITH PEAK NDVI' SIMULATED BY THE ALGORITHM

Vegetation cover was measured on the ESPs starting in 1988, and measurements were discontinued after 1993 (CRWMS 1996 [DIRS 102235]), so there is no way to compare the NDVI' used in this analysis (1998, 2001, and 2002) directly to measured ESP cover. Instead, measured data from the ESPs (Output DTN: MO0606SPAVEGAS.001) were compared to peak NDVI' values simulated using the PVR values extracted for the corroboration step described in Section E7.1. These analyses are contained in Output DTN: SN0608NDVIANAL.001, workbook *ESP_NDVI'sim_v_Cover.xls*.

As seen in all of the NDVI' response curves for Yucca Mountain vegetation (Figure E-19), the vegetation canopy expression is ephemeral. Therefore, the methods that were used to estimate vegetation counted each year's maximal canopy cover, whether green or senesced at the time of measurement (CRWMS 1996 [DIRS 102235]). Thus, measured cover at the ESPs represents peak vegetation standing crop. For this reason, ESP measured cover was compared to the peak NDVI' simulated with the algorithm. The NDVI' simulation employed PVR, precipitation scaling, and the peak NDVI' estimate provided by Equation E-8. For choosing the peak NDVI', the average slope and azimuth for each ESP was used to select the appropriate curve value from the suite of curves depicted in Figure E-23. Although the NDVI' values were calculated for each of the ESPs, only the lumped-average NDVI' is depicted for comparison to the lumped average cover measured for ESP vegetation associations (Figure E-30).

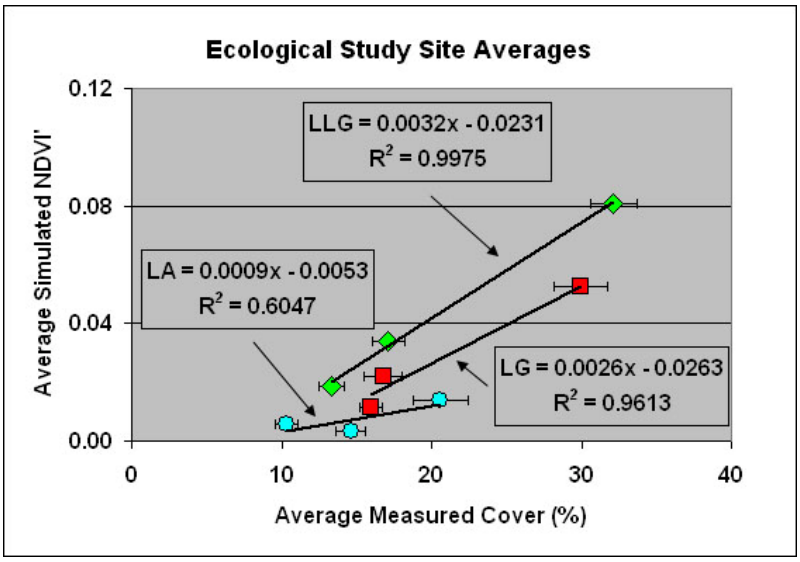

Source: This graph is excerpted from Output DTN: SN0608NDVIANAL.001, *ESP_NDVI'sim_v_Cover.xls*.

NOTE: Each point represents an annual value in order from lowest to highest: 1990, 1991, and 1992. The error bars associated with each point are the 90% confidence interval for cover (Output DTN: MO0606SPAVEGAS.001).

Figure E-30. Comparison of Lumped-Average Simulated NDVI' to Lumped-Average Cover Measured on the ESPs

The linear fits in Figure E-30 for the simulated NDVI' and the measured cover offer further corroboration that the magnitude of NDVI' predicted by the algorithm generally follows the response of vegetation cover on Yucca Mountain.

The comparison of ESPs to NDVI for the LA vegetation type violated this during one year as can be seen on Figure E-30. This occurred for WY1991 when the lowest cover of the three years was measured for the LA ESPs even though the precipitation recorded on Yucca Mountain Sites 2, 3, and 4 was almost twice that recorded in WY1990 (Output DTN: MO0607SEPTOTAL.003)[3] and may have arisen in the ground truth measurements.

E7.4 NUMERIC CORROBORATION OF RELATIVELY LOW UNCERTAINTY ASSOCIATED WITH SIMULATION OF NDVI'

Although the three preceding parts of Section E7 provide corroboration that the algorithm for NDVI' provides simulations that mimic vegetation responses in nature, they do not provide an independent assessment of the uncertainty involved with calculation of the basic data that were used for fitting the NDVI' algorithm. Although uncertainty was evaluated in parts of Section E2, they require independent corroboration, especially the degree of error tails off at low values of NDVI'. Because of the complexity of the calculations and the potential for some of the calculations to be self correcting through the series of required steps (i.e., an estimate that is high or low is pushed toward the central tendency by subsequent calculations), this corroboration was approached as a thought problem that referenced the N- and S-slope data that were used to develop the algorithm.

An estimate of uncertainty was derived by looking at WY2002 and the data extracted for the steep slopes of the rocky uplands overlying the repository that were used for developing the response curves in the algorithm of Equation E-8 (curves shown in Figure E-23). During WY2002, a stable, near-zero vegetation response is expected because insufficient precipitation fell to be effective for vegetation growth. This near-zero response was simulated as NDVI' using the algorithm in Equation E-8 that matched the actual NDVI' vegetation responses, as can be seen in Figure E-28.

Zero vegetation response was expected due to the intense drought conditions, so the unexpected curve transgressions for NDVI' during WY2002 (Figure E-19) form the basis for an estimate of uncertainty. These values are averages of the extracted NDVI' developed using the processing parameters, DOS_{avg}, and $NDVI_0$ developed in Section E2 and displayed in Table E-2.

Figure E-31 reproduces a rescaled version of the WY2002 data presented in Figure E-17. The N slope data have much higher fluctuations than S slope, possibly due to the influence of shading on the uncertainty of the estimates. Since the N slope has much larger fluctuations, this will be dealt with as a conservative worst case for estimating uncertainty. Fluctuations about a line for the average of nonzero N-slope values can be represented by the standard deviation. In this case,

[3] When the calculations were done, the source data was obtained from Output DTN: MO0605SEPTOTAL.001, which was later superseded by Output DTN: MO0605SEPTOTAL.002, that was subsequently superseded by Output DTN: MO0607SEPTOTAL.003. The source data used from the original DTN was not altered in the superseding DTNs as determined by a comparison check.

these digressions from the central tendency are 0.006 NDVI', thus showing that the degree of uncertainty tapers toward zero as the average NDVI' tapers toward zero.

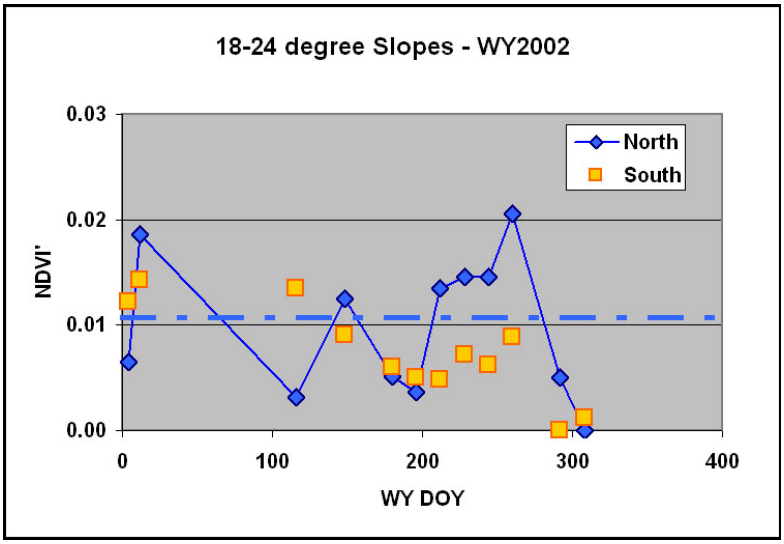

Source: Ouput DTN: SN0606T0502206.012, *Daily_NDVI_Estimation.xls*.

NOTE: The dashed blue line is the approximate average for the north slope values shown.

Figure E-31. WY2002 Average NDVI' from N and S Slopes that Approach Zero Vegetation Response

E8. CONCLUSIONS

These analyses developed a simple spatially and temporally appropriate algorithm to simulate vegetation response at the Yucca Mountain site during present climatic conditions. Precipitation is a potential source for infiltration at the proposed repository. Although vegetation cover is sparse at Yucca Mountain, most of the water supplied from the atmosphere is evaporated or transpired and only a small fraction is available for net infiltration. Thus, to be responsive to the actual physical conditions governing infiltration, the net-infiltration model must capture vegetation growth response as a function of both time and location. To do this, vegetation signatures were observed on satellite data and parameterized. These parameters were then combined to simulate responses to annual precipitation and seasonal factors, the two variables most influential to vegetation response.

In an arid environment such as Yucca Mountain, vegetation is dormant through much of the year. When water is present and growing temperatures are conducive, plants respond by growing leaves. Transpiration is a by-process to photosynthesis. In this context, plant and canopy development is an important factor in estimating the water used.

Vegetation water use is proportional to canopy leaf area. Green leaves can be detected using the Normalized Difference Vegetation Index (NDVI) and can be calculated using satellite data. Selected scenes from a 20-year archive of Landsat TM (thematic mapper) were chosen as the basis for characterizing Yucca Mountain vegetation.

This quantification and simulation of Yucca Mountain vegetation response first evaluated regional eco-hydrology, then characterized vegetation spatially on satellite data, and finally, assembled and corroborated an algorithm for simulating these responses. There were eight steps in this process:

- Characterizing the Yucca Mountain climate that drives the vegetation response. This was accomplished using precipitation and temperature data measured onsite.

- Choosing a set of years to capture vegetation response on which to base the simulation. This choice was made with regard to the satellite data available and ancillary data that were measured on and near Yucca Mountain. Three years were chosen: a wet year (WY1998), a critically dry year (WY2002), and a year with approximately average precipitation (WY2001). WY refers to water year, which corresponds to October 1 through September 30. The date is for the year most represented (i.e., WY1998 contains nine months in 1998 and only three months of 1997).

- Processing the satellite imagery for the chosen years to yield data in reflection units in their correct position on the landscape. Landsat TM imagery was used for the entire data suite. Images representing snapshots during the growing seasons of each year were selected to characterize vegetation canopy expression with an emphasis on the months when vegetation response was greatest (March through June of each year).

- Correcting the TM data to remove atmospheric effects (light scatter) and to remove nonsystematic variations inherent in the NDVI that was used to typify vegetation response. This resulted in a set of processing parameters that were unique to each image. These parameters were corroborated using data extracted from Ecological Study Plots (ESP) for three major vegetation associations typical of Yucca Mountain, and then applied to the entire data set.

- Fitting an annual relationship to characterize plant response, according to slope and azimuth, for the region overlying the proposed repository. This relationship used the wet year/high vegetation response: this maximal response was important because the vegetation signal is generally low due to Yucca Mountain's arid climate.

- Developing an index to capture the potential vegetation growth within each 30-m model grid cell. This index was given the name PVR (potential vegetation response) and was calculated for every model grid cell by subtraction of the minimal vegetation response during the dry year from the maximal vegetation expression during the wet year. These measures were normalized by the PVR values from a zone overlying the proposed repository.

- Developing an algorithm to simulate vegetation response that combines annual curves characterized by (1) slope and azimuth with scaling, (2) a precipitation adjustment to enable projection for any year, and (3) PVR to scale this generalized vegetation response specifically for each model grid cell and the water availability of the year in question.

The algorithm was corroborated by comparison to data developed for the ESPs (1) with actual data extracted for WY1998, WY2001, and WY2002; (2) with basal crop coefficients, K_{cb}, developed for Appendix D; and (3) for measured cover during WY1990, WY1991, and WY1993. A final corroboration of the uncertainty associated with these measurements was then made based upon reasonable interpretation of the inherent data scatter at a time when the vegetation was at its lowest response (during the driest time, late summer, of the driest year, WY2002).

In conclusion, the corroborated vegetation algorithm provides a set annual response that is scaled by precipitation and position on the landscape for incorporation into the infiltration model, MASSIF. Inputs include (1) a table of daily time steps for any azimuth or slope specified for each 30-m model grid cell, (2) PVR values to typify the spatially correct potential for vegetation growth within each model grid cell, and (3) a simple means to scale plant response relative to the precipitation for each year.

APPENDIX F
DEVELOPMENT OF STOCHASTIC PRECIPITATION AND OTHER CLIMATE INPUT FILES

This appendix supports Section 6.5.1, Weather Parameters for Anticipated Climate Episodes. Calculation of net infiltration requires an input file containing precipitation, temperature extremes, and mean wind speed on a daily basis. The MASSIF model varies precipitation and temperature with elevation and accepts input for an elevation of 1,524 m (5,000 ft), corresponding to the top of Yucca Mountain.

Section F1 is an explanation of the general methods for developing twelve precipitation parameters and twelve temperature parameters that together summarize the precipitation and temperature records at a meteorological station. Section F2 describes the application of these methods to the specific meteorological stations that are representative of each climate. Section F3 explains the development of twelve parameters for wind speed and the selection of 36 parameter uncertainty distributions to capture the range of uncertainty for each climate. Section F4 provides the general method for obtaining a weather input file from a particular set of parameter values.

In addition to the contents of the weather input file, this appendix provides the basis for the precipitation lapse rate. Section 6.5.1 provides the temperature lapse rate, two parameters of precipitation duration, and parameters of snowmelt and sublimation. Section 6.5.4 explains the selection of dew point parameters for each climate.

F1. PARAMETERIZATION OF PRECIPITATION AND TEMPERATURE RECORDS

Future Climate Analysis (BSC 2004 [DIRS 170002], Table 6-1) identified specific meteorological stations as being representative of anticipated climate episodes at Yucca Mountain. *Data Analysis for Infiltration Modeling: Extracted Weather Station Data Used to Represent Present-Day and Potential Future Climate Conditions within the Vicinity of Yucca Mountain* (BSC 2006 [DIRS 177081], Table 7.3-1) qualified data from those meteorological stations.

This section describes the methods for developing parameters that characterize the relevant characteristics of each climate. For precipitation and temperature, the first step is development of a set of parameters for each meteorological station. These station-specific parameters approximate the multiyear record of daily measurements at that station. Section F1.1 describes the methods for developing parameters for precipitation. Section F.1.2 addresses temperature parameterization.

F1.1 PARAMETERIZATION OF PRECIPITATION RECORDS

F1.1.1 Background

Precipitation may be characterized as a Markov process. This analysis models the sequence of wet and dry days as a first-order Markov process, which requires two parameters. The analysis models the amount of precipitation on a wet day as a random variable with a lognormal distribution, which requires two more parameters. The two parameters selected for the model of wet-day precipitation are the mean precipitation, λ, and the mean of the logarithm of precipitation, m. That is, the probability density for the amount of precipitation, P, is

$$p(P) = \frac{1}{Ps\sqrt{2\pi}} \exp\left[-\frac{1}{2s^2} \left(\ln P - m \right)^2 \right] \quad \text{(Eq. F-1)}$$

where

$$s^2 = 2\left(\ln \lambda - m \right) \quad \text{(Eq. F-2)}$$

Section 6.5.1 and this appendix describe twelve precipitation parameters that are arranged in four groups of three parameters. Each group of three parameters provides coefficients of a Fourier series for one of the following four functions of the day of the year, *d*, for *d* from 1 through 365 (March 1 through February 28):

- $p_{00}(d)$: the probability that day *d* is dry, given that day *D*-1 is dry,
- $p_{10}(d)$: the probability that day *d* is dry, given that day *D*-1 is wet,
- $\lambda(d)$: mean of the probability distribution for amount of precipitation on day *d*, given that it is a wet day,
- $m(d)$: mean of the probability distribution for the natural logarithm of the amount of precipitation on day *d*, given that it is a wet day.

The Fourier series representation of a continuous function $f(t)$ with domain (0,2π) is:

$$f(t) = a + \sum_{n=1}^{\infty} v_n \sin nt + \sum_{n=1}^{\infty} w_n \cos nt = a + \sum_{n=1}^{\infty} b_n \sin\left(\theta_n + nt \right) \quad \text{(Eq. F-3)}$$

where the first expression is the usual textbook form and the second is the polar form. The formulas for the coefficients are:

$$a = \frac{1}{2\pi} \int_0^{2\pi} f(t) dt \quad \text{(Eq. F-4)}$$

$$v_n = \frac{1}{\pi} \int_0^{2\pi} f(t) \sin(nt) dt \quad \text{(Eq. F-5)}$$

$$w_n = \frac{1}{\pi} \int_0^{2\pi} f(t) \cos(nt) dt \quad \text{(Eq. F-6)}$$

$$b_n = \sqrt{v_n^2 + w_n^2} \quad \text{(Eq. F-7)}$$

$$\theta_n = \arctan(w_n / v_n) \quad \text{(Eq. F-8)}$$

The sign of b_n must be consistent with the quadrant chosen for θ_n. The formulas derive their simplicity from the orthogonality of the trigonometric functions in Equation F-3; the integral of the product of two functions vanishes unless both functions are the same.

Fourier series can represent a finite set of observations, $f(t_i)$, $i = 1,2,...,I$, but the Fourier series becomes finite. Once the number of coefficients is equal to the number of observations, the series fits every point exactly and all higher terms are zero. The first few terms in a finite Fourier series reflect the general trend of the observations. In many cases, the next few terms are small. However, the last terms are larger as they create an exact fit to variations in the data; these last coefficients tend to be artifacts of the particular data set that is chosen. Consequently, Fourier representations of observations are usually truncated after a few terms.

However, when the formulas for the coefficients are based on a finite number of observations, the t_i must have a special distribution in (0,2π), such as a uniform distribution. A difficulty in representing a first-order Markov probability by a truncated Fourier series is that the observations are not uniformly distributed.

For a Markov-chain model of precipitation, each day's observation provides data for only one of the two probabilities, depending on whether the previous day was wet or dry. Some authors dealt with this problem by constructing, for each of the 365 days of a year, an average over several years, with special treatment of leap years. Barring bad luck, such as never having a wet day on January first, these averages provide a uniformly distributed set that can be used to evaluate up to 365 Fourier coefficients. However, this procedure gives the 365 averages equal weights, whereas they may be based on widely varying numbers of observations.

Woolhiser and Pegram (1979 [DIRS 176108], pp. 34 and 35) argued that least-squares estimates of Fourier coefficients are undesirable because the days of the year have unequal sample sizes. Instead, they used optimization software to maximize a likelihood function, either using software that solved for all parameters simultaneously or software that found only one parameter at a time and had to be iterated. Most of the subsequent literature is based on variations of this approach.

For the Yucca Mountain Project, it is desirable to have a procedure that is more transparent than optimization software. To develop the stochastic parameters, this model for Total System Performance Assessment for the License Application (TSPA-LA) uses a least-squares method that accounts for the unequal sample sizes. Instead of treating the average for each day, *d*, as the basic data for the Fourier analysis, this method takes the individual daily records, year by year, as the input to the Fourier analysis. This appendix develops the modified formulas for the Fourier coefficients.

F1.1.2 Least-Squares Formulas

For each of the four stochastic functions, a truncated Fourier series represents its variation with *d*, as follows:

$$p_{00}(d) = a_{00} + b_{00,1}\sin(\theta_{00,1} + d') + b_{00,2}\sin(\theta_{00,2} + 2d') \qquad \text{(Eq. F-9)}$$

$$p_{10}(d) = a_{10} + b_{10,1}\sin(\theta_{10,1} + d') + b_{10,2}\sin(\theta_{00,2} + 2d') \quad \text{(Eq. F-10)}$$

$$\lambda(d) = a_{\lambda} + b_{\lambda,1}\sin(\theta_{\lambda,1} + d') + b_{\lambda,2}\sin(\theta_{\lambda,2} + 2d') \quad \text{(Eq. F-11)}$$

$$m(d) = a_{m} + b_{m,1}\sin(\theta_{m,1} + d') + b_{m,2}\sin(\theta_{m,2} + 2d') \quad \text{(Eq. F-12)}$$

where

$$d' = 2\pi d / 365 \quad \text{(Eq. F-13)}$$

In each case, the last term is used only for estimating the uncertainty caused by truncating the series.

This appendix generalizes the three parameters in the form:

$$f(d) = a + b_1\sin(\theta_1 + d') + b_2\sin(\theta_2 + 2d') \quad \text{(Eq. F-14)}$$

The observations are available on a domain D_f; that is, D_f contains all pairs (d, y) for which there is an applicable observation. Here, d varies from 1 through 365, and y varies from 1 through the number of full years of observation.

In this least-squares approach, the coefficients for the polar form were evaluated one term at a time. First, a is chosen to minimize the sum of the squares of the deviations from a. That is, the derivative of the sum of squares with respect to a must be zero:

$$0 = \frac{\partial}{\partial a}\sum_{(d,y)\in D_f}\left[f(d,y) - a\right]^2 = -2\sum_{(d,y)\in D_f}\left[f(d,y) - a\right] \quad \text{(Eq. F-15)}$$

Therefore,

$$a = \underset{(d,y)\in D_f}{Mean}\left[f(d,y)\right] \quad \text{(Eq. F-16)}$$

Next, general formulas for b_n and θ_n were developed having chosen all preceding coefficients. That is, minimizing:

$$\sum_{(d,y)\in D_f}\left[\hat{f}_{n-1}(d,y) - b_n\sin(\theta_n + nd')\right]^2$$

where $\hat{f}_{n-1}(d,y)$ is $f(d,y)$ reduced by the preceding terms:

$$f_1'(d) = f(d) - a \quad \text{(Eq. F-17)}$$

$$\hat{f}_{n-1}(d) = f(d) - a - \sum_{m=1}^{n-1} b_m\sin(\theta_m + md'),\ n>2 \quad \text{(Eq. F-18)}$$

Minimizing with respect to b_n,

$$0 = \frac{\partial}{\partial b_n} \sum_{(d,y)\in D_f} \left[\hat{f}_{n-1}(d,y) - b_n \sin(\theta_n + nd')\right]^2 \quad \text{(Eq. F-19)}$$

$$0 = -2 \sum_{(d,y)\in D_f} \left[\hat{f}_{n-1}(d,y) - b_n \sin(\theta_n + nd')\right] \sin(\theta_n + nd') \quad \text{(Eq. F-20)}$$

$$b_n = \frac{\sum_{(d,y)\in D_f} \hat{f}_{n-1}(d,y) \sin(\theta_n + nd')}{\sum_{(d,y)\in D_f} \sin^2(\theta_n + nd')} \quad \text{(Eq. F-21)}$$

$$b_n = \frac{\sum_{(d,y)\in D_f} \hat{f}_{n-1}(d,y)\left(\sin\theta_n \cos nd' + \cos\theta_n \sin nd'\right)}{\sum_{(d,y)\in D_f} \left(\sin\theta_n \cos nd' + \cos\theta_n \sin nd'\right)^2} \quad \text{(Eq. F-22)}$$

$$b_n = \frac{\sin\theta_n \sum_{(d,y)\in D_f} \hat{f}_{n-1}(d,y) \cos nd' + \cos\theta_n \sum_{(d,y)\in D_f} \hat{f}_{n-1}(d,y) \sin nd'}{\sin^2\theta_n \sum_{(d,y)\in D_f} \cos^2 nd' + 2\sin\theta_n \cos\theta_n \sum_{(d,y)\in D_f} \sin nd' \cos nd' + \cos^2\theta_n \sum_{(d,y)\in D_f} \sin^2 nd'} \quad \text{(Eq. F-23)}$$

$$b_n \cos\theta_n = \frac{\tan\theta_n \sum_{(d,y)\in D_f} \hat{f}_{n-1}(d,y) \cos nd' + \sum_{(d,y)\in D_f} \hat{f}_{n-1}(d,y) \sin nd'}{\tan^2\theta_n \sum_{(d,y)\in D_f} \cos^2 nd' + 2\tan\theta_n \sum_{(d,y)\in D_f} \sin nd' \cos nd' + \sum_{(d,y)\in D_f} \sin^2 nd'} \quad \text{(Eq. F-24)}$$

Minimizing with respect to θ_n,

$$0 = \frac{\partial}{\partial \theta_n} \sum_{(d,y)\in D_f} \left[\hat{f}_{n-1}(d,y) - b_n \sin(\theta_n + nd')\right]^2 \quad \text{(Eq. F-25)}$$

$$0 = -2 \sum_{(d,y)\in D_f} \left[\hat{f}_{n-1}(d,y) - b_n \sin(\theta_n + nd')\right] b_n \cos(\theta_n + nd') \quad \text{(Eq. F-26)}$$

For $b_n \neq 0$,

$$b_n = \frac{\sum_{(d,y)\in D_f} \left[\hat{f}_{n-1}(d,y) \cos(\theta_n + nd') \right]}{\sum_{(d,y)\in D_f} \left[\sin(\theta_n + nd') \cos(\theta_n + nd') \right]} \qquad \text{(Eq. F-27)}$$

$$b_n = \frac{\sum_{(d,y)\in D_f} \hat{f}_{n-1}(d,y) \left[\cos\theta_n \cos nd' - \sin\theta_n \sin nd' \right]}{\sum_{(d,y)\in D_f} \left[\sin\theta_n \cos nd' + \cos\theta_n \sin nd' \right] \left[\cos\theta_n \cos nd' - \sin\theta_n \sin nd' \right]}$$

(Eq. F-28)

$$b_n = \frac{\cos\theta_n \sum_{(d,y)\in D_f} \hat{f}_{n-1}(d,y) \cos nd' - \sin\theta_n \sum_{(d,y)\in D_f} \hat{f}_{n-1}(d,y) \sin nd'}{\sum_{(d,y)\in D_f} \left[\cos\theta_n \sin\theta_n \cos^2 nd' - \sin^2\theta_n \cos nd' \sin nd' \right] + \sum_{(d,y)\in D_f} \left[\cos^2\theta_n \sin nd' \cos nd' - \sin\theta_n \cos\theta_n \sin^2 nd' \right]}$$

(Eq. F-29)

$$b_n \cos\theta_n = \frac{\sum_{(d,y)\in D_f} f'_{n-1}(d,y) \cos nd' - \tan\theta_n \sum_{(d,y)\in D_f} f'_{n-1}(d,y) \sin nd'}{\tan\theta_n \sum_{(d,y)\in D_f} \left(\cos^2 nd' - \sin^2 nd' \right) + \left(1 - \tan^2\theta_n \right) \sum_{(d,y)\in D_f} \sin nd' \cos nd'}$$

(Eq. F-30)

Equating the right-hand sides of Equations F-24 and F-30,

$$\frac{\tan\theta_n \sum_{(d,y)\in D_f} \hat{f}_{n-1}(d,y) \cos nd' + \sum_{(d,y)\in D_f} \hat{f}_{n-1}(d,y) \sin nd'}{\tan^2\theta_n \sum_{(d,y)\in D_f} \cos^2 nd' + 2\tan\theta_n \sum_{(d,y)\in D_f} \sin nd' \cos nd' + \sum_{(d,y)\in D_f} \sin^2 nd'}$$

$$= \frac{\sum_{(d,y)\in D_f} \hat{f}_{n-1}(d,y) \cos nd' - \tan\theta_n \sum_{(d,y)\in D_f} \hat{f}_{n-1}(d,y) \sin nd'}{\tan\theta_n \sum_{(d,y)\in D_f} \left[\cos^2 nd' - \sin^2 nd' \right] + \left[1 - \tan^2\theta_n \right] \sum_{(d,y)\in D_f} \sin nd' \cos nd'}$$

(Eq. F-31)

$$\left[\tan\theta_n \sum_{(d,y)\in D_f} \hat{f}_{n-1}(d,y)\cos nd' + \sum_{(d,y)\in D_f} \hat{f}_{n-1}(d,y)\sin nd'\right] \times \left[\tan\theta_n \sum_{(d,y)\in D_f}\left[\cos^2 nd' - \sin^2 nd'\right] + \left[1-\tan^2\theta_n\right] \sum_{(d,y)\in D_f} \sin nd'\cos nd'\right]$$

$$= \left\{\left[\sum_{(d,y)\in D_f} \hat{f}_{n-1}(d,y)\cos nd' - \tan\theta_n \sum_{(d,y)\in D_f} \hat{f}_{n-1}(d,y)\sin nd'\right] \times \left[\tan^2\theta_n \sum_{(d,y)\in D_f}\cos^2 nd' + 2\tan\theta_n \sum_{(d,y)\in D_f} \sin nd'\cos nd' + \sum_{(d,y)\in D_f}\sin^2 nd'\right]\right\}$$

(Eq. F-32)

$$\left\{\begin{aligned}
&\tan^3\theta_n\left(-\sum_{(d,y)\in D_f} \hat{f}_{n-1}(d,y)\cos nd' \sum_{(d,y)\in D_f}\sin nd'\cos nd'\right) \\
&+\tan^2\theta_n\left(\begin{aligned}&-\sum_{(d,y)\in D_f} \hat{f}_{n-1}(d,y)\sin nd' \sum_{(d,y)\in D_f}\sin nd'\cos nd' \\ &+\sum_{(d,y)\in D_f} \hat{f}_{n-1}(d,y)\cos nd' \sum_{(d,y)\in D_f}\left[\cos^2 nd' - \sin^2 nd'\right]\end{aligned}\right) \\
&+\tan\theta_n\left(\begin{aligned}&\sum_{(d,y)\in D_f} \hat{f}_{n-1}(d,y)\cos nd' \sum_{(d,y)\in D_f}\sin nd'\cos nd' \\ &+\sum_{(d,y)\in D_f} \hat{f}_{n-1}(d,y)\sin nd' \sum_{(d,y)\in D_f}\left[\cos^2 nd' - \sin^2 nd'\right]\end{aligned}\right) \\
&+\sum_{(d,y)\in D_f} \hat{f}_{n-1}(d,y)\sin nd' \sum_{(d,y)\in D_f}\sin nd'\cos nd'
\end{aligned}\right\}$$

$$= \left\{\begin{aligned}
&\tan^3\theta_n\left(-\sum_{(d,y)\in D_f} \hat{f}_{n-1}(d,y)\sin nd' \sum_{(d,y)\in D_f}\cos^2 nd'\right) \\
&+\tan^2\theta_n\left(\begin{aligned}&\sum_{(d,y)\in D_f} \hat{f}_{n-1}(d,y)\cos nd' \sum_{(d,y)\in D_f}\cos^2 nd' \\ &-2\sum_{(d,y)\in D_f} \hat{f}_{n-1}(d,y)\sin nd' \sum_{(d,y)\in D_f}\sin nd'\cos nd'\end{aligned}\right) \\
&+\tan\theta_n\left(2\sum_{(d,y)\in D_f} \hat{f}_{n-1}(d,y)\cos nd' \sum_{(d,y)\in D_f}\sin nd'\cos nd' - \sum_{(d,y)\in D_f} \hat{f}_{n-1}(d,y)\sin nd' \sum_{(d,y)\in D_f}\sin^2 nd'\right) \\
&\sum_{(d,y)\in D_f} \hat{f}_{n-1}(d,y)\cos nd' \sum_{(d,y)\in D_f}\sin^2 nd'
\end{aligned}\right\}$$

(Eq. F-33)

$$\left.\begin{aligned}
&\tan^3\theta_n\left(\begin{aligned}&\sum_{(d,y)\in D_f}\hat{f}_{n-1}(d,y)\sin nd'\sum_{(d,y)\in D_f}\cos^2 nd'\\&-\sum_{(d,y)\in D_f}\hat{f}_{n-1}(d,y)\cos nd'\sum_{(d,y)\in D_f}\sin nd'\cos nd'\end{aligned}\right)\\
&+\tan^2\theta_n\left(\begin{aligned}&\sum_{(d,y)\in D_f}\hat{f}_{n-1}(d,y)\sin nd'\sum_{(d,y)\in D_f}\sin nd'\cos nd'\\&-\sum_{(d,y)\in D_f}\hat{f}_{n-1}(d,y)\cos nd'\sum_{(d,y)\in D_f}\sin^2 nd'\end{aligned}\right)\\
&+\tan\theta_n\left(\begin{aligned}&\sum_{(d,y)\in D_f}\hat{f}_{n-1}(d,y)\sin nd'\sum_{(d,y)\in D_f}\cos^2 nd'\\&-\sum_{(d,y)\in D_f}\hat{f}_{n-1}(d,y)\cos nd'\sum_{(d,y)\in D_f}\sin nd'\cos nd'\end{aligned}\right)\\
&+\sum_{(d,y)\in D_f}\hat{f}_{n-1}(d,y)\sin nd'\sum_{(d,y)\in D_f}\sin nd'\cos nd'-\sum_{(d,y)\in D_f}\hat{f}_{n-1}(d,y)\cos nd'\sum_{(d,y)\in D_f}\sin^2 nd'
\end{aligned}\right\}=0$$

(Eq. F-34)

The left-hand side has a factor of $(1+\tan^2\theta_n)$ because that factor must be greater than zero.

$$\left.\begin{aligned}
&\tan\theta_n\left(\sum_{(d,y)\in D_f}\hat{f}_{n-1}(d,y)\sin nd'\sum_{(d,y)\in D_f}\cos^2 nd'-\sum_{(d,y)\in D_f}\hat{f}_{n-1}(d,y)\cos nd'\sum_{(d,y)\in D_f}\sin nd'\cos nd'\right)\\
&+\sum_{(d,y)\in D_f}\hat{f}_{n-1}(d,y)\sin nd'\sum_{(d,y)\in D_f}\sin nd'\cos nd'-\sum_{(d,y)\in D_f}\hat{f}_{n-1}(d,y)\cos nd'\sum_{(d,y)\in D_f}\sin^2 nd'
\end{aligned}\right\}=0$$

(Eq. F-35)

$$\theta_n=\arctan\left[\frac{\sum_{(d,y)\in D_f}\hat{f}_{n-1}(d,y)\cos nd'\sum_{(d,y)\in D_f}\sin^2 nd'-\sum_{(d,y)\in D_f}\hat{f}_{n-1}(d,y)\sin nd'\sum_{(d,y)\in D_f}\sin nd'\cos nd'}{\sum_{(d,y)\in D_f}\hat{f}_{n-1}(d,y)\sin nd'\sum_{(d,y)\in D_f}\cos^2 nd'-\sum_{(d,y)\in D_f}\hat{f}_{n-1}(d,y)\cos nd'\sum_{(d,y)\in D_f}\sin nd'\cos nd'}\right]$$

(Eq. F-36)

Notice that if the observations were uniformly distributed, Equation F-36 would have the form of Equation F-9.

F1.1.3 Implementation Notes

The treatment of leap year data follows the suggestion of Woolhiser and Pegram (1979 [DIRS 176108], p. 36). A year of observations begins on March 1 (d=1). The previous day (d=0) is the last day of February, whether the 28th or 29th. Thus, the estimation does not use observations on February 29th, except for defining the Markov probability to which the March 1

observation applies. A year qualifies for inclusion in the set of observations only if data are available from the last day of February through February 28.

Note that the arctan function can take either of two values over a range of 2π. In this case, the choice of θ_n determines the sign of b_n. That is,

$$b_n \sin(\theta_n + nd') = -b_n \sin(\theta_n \pm \pi + nd') \quad \text{(Eq. F-37)}$$

If the coefficients estimated from two similar sets of data seem to be quite different, it may be that one set be should be adjusted in accordance with Equation F-37.

F1.1.4 Precipitation Frequency and Mean Annual Precipitation

The probability that day *d* is dry is:

$$p_d(d) = p_{00}(d)p_d(d-1) + p_{10}(d)[1 - p_d(d-1)] \quad \text{(Eq. F-38)}$$

Because p_{00} and p_{10} change slowly from one day to the next, their values for one day are approximately the same as for the previous day. Therefore, $p_d(d-1)$ is approximately the same as $p_d(d)$, so:

$$p_d(d) \cong p_{00}(d)p_d(d) + p_{10}(d)[1 - p_d(d)] \quad \text{(Eq. F-39)}$$

(

$$p_d(d) \cong p_{10}(d)/[1 - p_{00}(d) + p_{10}(d)] \quad \text{(Eq. F-40)}$$

Making the further approximation of replacing each parameter with its mean value over the year, the fraction of days that are wet is approximately:

$$f_w \cong [1 - \frac{a_{10}}{1 - a_{00} + a_{10}}] = \frac{1 - a_{00}}{1 - a_{00} + a_{10}} \quad \text{(Eq. F-41)}$$

The expected mean annual precipitation (MAP) is:

$$MAP \cong 365 f_w a_\lambda \quad \text{(Eq. F-42)}$$

F1.2 PARAMATERIZATION OF TEMPERATURE RECORDS

Output DTN: SN0608T0502206.019 contains MathCAD files for the calculation of parameters to best-fit daily temperature data as a function of day of year, using a least-squares approach. There are four temperature models, one each for minimum temperature on wet days, minimum temperature on dry days, maximum temperature on wet days, and maximum temperature on dry days. Each temperature model is in the form of a sine function described by three parameters, α,

β, and γ, representing respectively the magnitude of the first-order term, the phase of the first-order term, and the zero-order term, as follows:

$$Twet_{\min} = \alpha wet_{\min} \sin\left(\frac{x - \beta wet_{\min}}{365/2\pi}\right) + \gamma wet_{\min} \quad \text{(Eq. F-43)}$$

$$Tdry_{\min} = \alpha dry_{\min} \sin\left(\frac{x - \beta dry_{\min}}{365/2\pi}\right) + \gamma dry_{\min} \quad \text{(Eq. F-44)}$$

$$Twet_{\max} = \alpha wet_{\max} \sin\left(\frac{x - \beta wet_{\max}}{365/2\pi}\right) + \gamma wet_{\max} \quad \text{(Eq. F-45)}$$

$$Tdry_{\max} = \alpha dry_{\max} \sin\left(\frac{x - \beta dry_{\max}}{365/2\pi}\right) + \gamma dry_{\max} \quad \text{(Eq. F-46)}$$

The parameters for this model have the following significance:

- x is the day of year from 1 to 365 (January 1 through December 31; February 29 on leap years is ignored).
- α represents half the annual difference in temperature (minimum or maximum) between summer and winter values, according to the model. It is the amplitude of the sine function and is in units of temperature.
- β represents the calendar day of the year (DOY) when the model temperature is rising and passes through its central value.
- γ is the mean value for the temperature, according to the model.

MathCAD routines were developed to organize the proxy climate site temperature data, including daily minima and maxima. Temperature records were organized by wet days and dry days for each of the proxy sites. For each meteorological station and each temperature model, the DTN includes derivation of values for α, β, and γ to best fit the minimum and maximum temperatures as a function of day of year using a least-squares approach. The three parameters are the result of applying the MathCAD function *minerr* to minimize the sum of the squares of the differences between the measured temperatures and the model temperatures.

As in the precipitation analysis, there are multiple equivalent solutions for the three parameters, with the values for the β parameter separated by half of a year and with the α parameter alternating between positive and negative. However, because all of the proxy sites are in the temperate region of the Northern hemisphere, the functions are very similar, and the initial values could be chosen such that the calculated values of the β parameter would all fall near DOY 115. The initial for α, β, and γ were 20°C, DOY 80, and 30°C, respectively.

Unlike the precipitation analysis, this procedure generates parameters that are not stochastic. In this temperature model, the temperature extremes depend only on the day of the year and whether or not there is precipitation on that day.

There is another aspect in which this analysis differs slightly from that of the precipitation analysis in Section F1.1. That analysis determined each zero-order term as the mean of its data, then the higher-order terms were developed without modifying the lower-order terms. This temperature analysis solves for the zero-order and first-order terms simultaneously. Therefore, although the zero-order term is the mean annual temperature (MAT) for the model, it may not be exactly the mean of the data. Nevertheless, the MathCAD application estimates the standard uncertainty for each zero-order term by making the same calculation that would be used for the standard error using the γ parameter in lieu of the mean of the data.

As an example of the results of this analysis, Figure F-1 shows the modeled and measured temperature extremes for wet days in the record for Beowawe, Nevada. Modeled versus measured temperatures for recorded dry days are shown in Figure F-2. The modeled temperatures do apply to all days of the year, not just those for which the record has applicable data. Similar figures for each of the proxy sites are contained in Output DTN: SN0608T0502206.019.

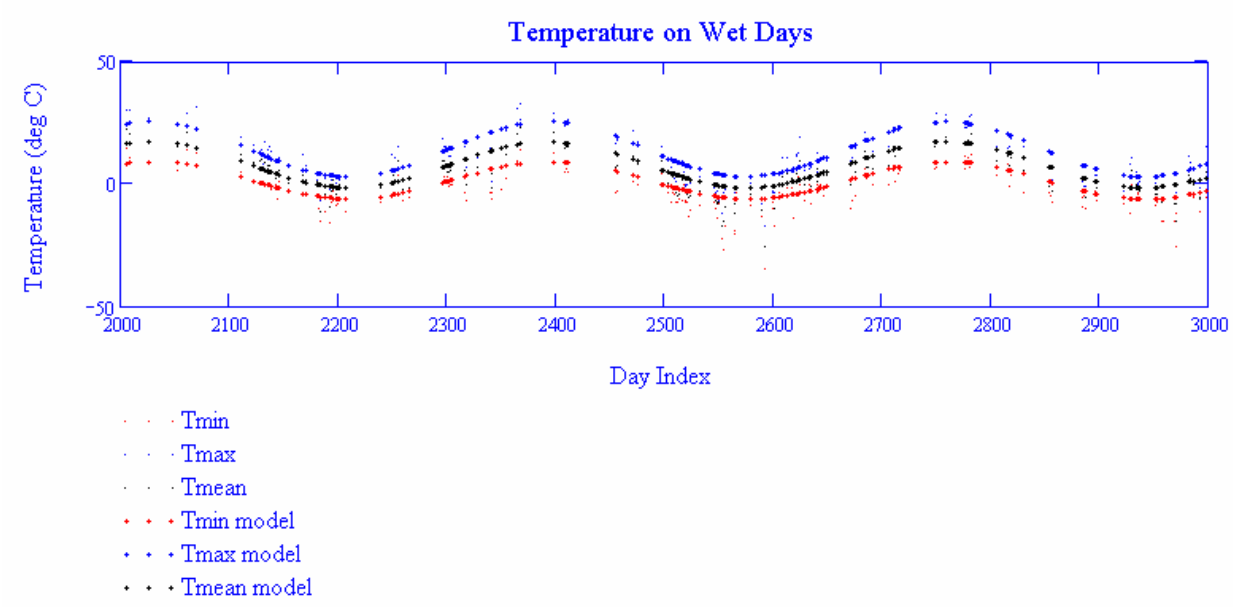

Source: Output DTN: SN0608T0502206.019.

Figure F-1. Model versus Measured Temperatures for Wet Days, Beowawe, Nevada

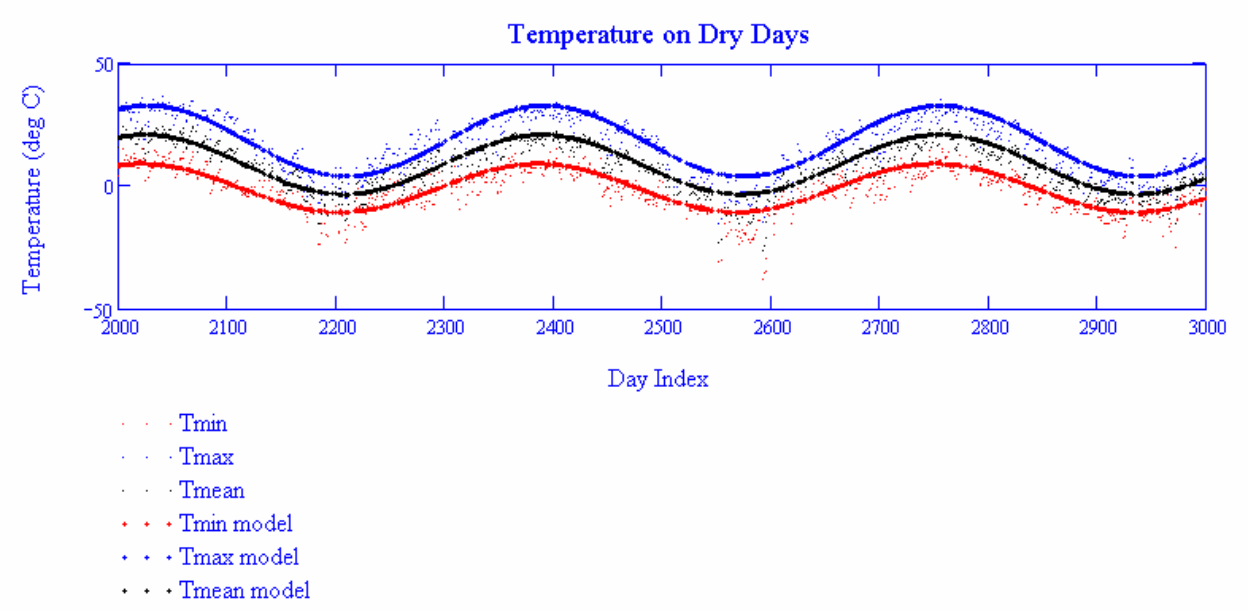

Source: Output DTN: SN0608T0502206.019.

Figure F-2. Model versus Measured Temperatures for Dry Days, Beowawe, Nevada

Applying the approximations of F1.1.4, the MAT is approximately

$$MAT = \frac{a_{10}}{1-a_{00}+a_{10}} \frac{\gamma dry_{\min} + \gamma dry_{\min}}{2} + \frac{1-a_{00}}{1-a_{00}+a_{10}} \frac{\gamma wet_{\min} + \gamma wet_{\min}}{2} \qquad \text{(Eq. F-47)}$$

F2. PARAMETERS FOR REPRESENTATIVE METEOROLOGICAL STATIONS

Data from ten site and regional meteorological stations, representing the range of weather anticipated during the remainder of the Present-Day climate, have been qualified in an analysis report (BSC 2006 [DIRS 177081]).

F2.1 STATIONS REPRESENTING THE PRESENT-DAY CLIMATE

DTNs: SN0601PRECPTMP.002 [DIRS 176122] and SN0608WEATHER1.005 [DIRS 177912] comprise the qualified precipitation records from the ten representative stations. Output DTN: SN0609T0502206.023 contains the Excel workbooks that performed the Fourier analyses of the ten precipitation records. Tables F-1 and F-2 report results of these analyses. The phase parameters are rounded to one hundredth of a radian (about half a day); the remaining parameters are rounded to a level of precision consistent with the standard error. Although the subsequent analysis omits second-order terms, these two tables provide their magnitudes ($b_{oo,2}$, $b_{1o,2}$, etc.).

Equations F-41 and F-42 provide a method for calculating the approximate MAP implied by the zero-order coefficients. For corroboration of the analyses, Table F-2a compares the MAP implied by the coefficients with the actual MAP at each station. In each case, the MAPs agree to within 10%.

Table F-1. Fourier Parameters for p_{00} and p_{10} at Stations Representing the Present-Day Climate

Station	Station Elevation (m)	a_{00}	a_{00} Standard Error	$b_{00,1}$	$\theta_{00,1}$ (Radians)	$b_{00,2}$	a_{10}	a_{10} Standard Error	$b_{10,1}$	$\theta_{10,1}$ (Radians)	$b_{10,2}$
4JA	1,043	0.939	0.002	0.024	−1.26	0.010	0.621	0.013	0.043	−1.24	0.067
40 MN	1,469	0.929	0.002	0.022	−1.43	0.012	0.514	0.011	0.046	−1.36	0.059
A12	2,283	0.911	0.003	0.025	−1.35	−0.015	0.504	0.011	0.026	−1.54	0.052
Amargosa Farms	747	0.955	0.002	0.023	−1.17	0.016	0.661	0.019	−0.039	+0.53	0.069
Cane Spring	1,219	0.934	0.002	0.028	−1.24	0.013	0.582	0.013	0.052	−1.34	0.072
YM Site 1	1,143	0.937	0.004	0.031	−1.20	−0.009	0.66	0.03	0.09	−1.48	0.09
YM Site 2	1,478	0.941	0.004	0.025	−1.30	0.015	0.60	0.03	0.10	−1.44	0.06
YM Site 3	1,279	0.937	0.004	0.029	−1.39	0.011	0.61	0.02	0.06	−1.42	0.05
YM Site 6	1,315	0.937	0.004	0.030	−1.34	0.017	0.63	0.02	0.06	−1.29	0.06
YM Site 9	838	0.947	0.004	0.031	−1.39	−0.006	0.67	0.03	−0.10	+1.47	−0.06

Source: Output DTN: SN0609T0502206.023.

Table F-2. Fourier Parameters for λ and m at Stations Representing the Present-Day Climate

Station	a_λ (mm)	a_λ Standard Error (mm)	$b_{\lambda,1}$ (mm)	$\theta_{\lambda,1}$ (Radians)	$b_{\lambda,2}$ (mm)	a_m (mm)	a_m Standard Error (ln mm)	$b_{m,1}$ (ln mm)	$\theta_{m,1}$ (Radians)	$b_{m,2}$ (ln mm)
4JA	4.42	0.17	−0.75	−0.38	−0.88	0.64	0.04	−0.22	−0.40	−0.16
40 MN	4.68	0.16	−0.54	+0.81	−0.99	0.68	0.03	−0.10	+0.04	−0.16
A12	5.75	0.17	−0.90	−0.64	−1.22	0.92	0.03	−0.19	−0.82	−0.15
Amargosa Farms	5.1	0.3	−0.3	−0.80	−1.1	0.90	0.05	−0.15	−0.84	−0.15
Cane Spring	5.3	0.2	−0.8	−0.36	−1.1	0.82	0.04	−0.17	−0.52	−0.20
YM Site 1	4.9	0.4	−0.8	−0.71	−1.3	0.71	0.08	−0.16	−1.04	−0.20
YM Site 2	5.4	0.4	0.6	+1.46	−1.03	0.85	0.07	−0.10	−1.31	0.20
YM Site 3	5.7	0.4	−0.8	−1.07	−1.49	0.90	0.07	−0.12	−0.91	−0.28
YM Site 6	5.9	0.4	−1.1	−1.27	−1.15	0.95	0.07	−0.10	−0.93	0.26
YM Site 9	3.7	0.3	−0.6	−0.49	−0.62	0.48	0.08	−0.20	−0.36	−0.13

Source: Output DTN: SN0609T0502206.023.

Table F-2a. Mean Annual Precipitation at Site and Regional Stations Compared with Values Implied by Fourier Coefficients

Meteorological Station	Station Elevation (m)	Measured MAP (mm)	MAP Implied by Coefficients (mm)	Years Used for Fourier Analysis (Mar. 1 to Feb. 28)
Amargosa Farms	747	1.1×10^2	1.2×10^2	26 years: 1968, 1969, 1979 to 2000, 2002, 2003
YM Site 9	838	1.1×10^2	1.0×10^2	11 years: 1993 to 2003
4JA	1,043	1.4×10^2	1.4×10^2	45 years: 1959 to 2003
YM Site 1	1,143	1.8×10^2	1.6×10^2	10 years: 1993 to 1998, 2000 to 2003
Cane Spring	1,219	2.0×10^2	2.0×10^2	39 years: 1965 to 2003
YM Site 3	1,279	2.1×10^2	1.9×10^2	11 years: 1993 to 2003

Table F-2a. Mean Annual Precipitation at Site and Regional Stations Compared with Values Implied by Fourier Coefficients (Continued)

YM Site 6	1,315	2.1×10^2	2.0×10^2	11 years: 1993 to 2003
40 MN	1,469	2.1×10^2	2.1×10^2	43 years: 1961 to 2003
YM Site 2	1,478	1.9×10^2	1.8×10^2	11 years: 1993 to 2003
A12	2,283	3.2×10^2	3.1×10^2	41 years: 1960 to 1994, 1998 to 2003

Source: BSC 2006 [DIRS 177081], Table 6.1.4; Section 6.2.5.1 (Measured MAPs); from Equations F-41 and F-42, using values from Tables F-1 and F-2 (Implied MAPs); Output DTN: SN0609T0502206.023 (Elevations and data years).

Adjustment to an elevation of 1524 m requires a lapse rate for each first-order precipitation parameter. For each station, Table F-3 shows its elevation and each first-order parameter, with parameter lapse rates and uncertainties calculated by the Excel function LINEST.

Generally, the frequency of dry days decreases with elevation and the average wet-day precipitation increases with elevation. However, the MASSIF model makes the approximation that all elevations have wet or dry days when the top of the mountain has a wet or dry day. Therefore, total annual precipitation is adjusted for elevation using an input lapse rate. Table F-3 includes the expected MAP for each station, calculated in accordance with Equation F-42, and a precipitation lapse rate and uncertainty calculated by the Excel function LINEST. The table also shows the MAP extrapolated to 1,524 m with the Excel function FORECAST and the precipitation lapse rate expressed as a percentage of the extrapolated value. Thus, the nominal precipitation lapse rate is equal to 134 mm/km divided by 213 mm, which gives 6.3%/100 m. The standard error on this lapse rate is calculated by dividing the standard error on the slope (14 mm/km) by 213 mm, which gives 0.7%/100 m.

Table F-3. Lapse Rates for Parameters of the Present-Day Climate

Station	Station Elevation (m)	a_{00}	a_{10}	a_λ (mm)	a_m (ln mm)	Elevation in 100s of Meters	Expected MAP (mm)
4JA	1,043	0.939	0.621	4.42	0.64	10.43	144
40 MN	1,469	0.929	0.514	4.68	0.68	14.69	207
A12	2,283	0.911	0.504	5.75	0.92	22.83	315
Amargosa Farms	747	0.955	0.661	5.1	0.90	7.47	119
Cane Spring	1,219	0.934	0.582	5.3	0.82	12.19	197
YM Site 1	1,143	0.937	0.66	4.9	0.71	11.43	156
YM Site 2	1,478	0.941	0.60	5.4	0.85	14.78	176

Table F-3. Lapse Rates for Parameters of the Present-Day Climate (Continued)

Station	Station Elevation (m)	a_{00}	a_{10}	a_λ (mm)	a_m (ln mm)	Elevation in 100s of Meters	Expected MAP (mm)
YM Site 3	1,279	0.937	0.61	5.7	0.90	12.79	195
YM Site 6	1,315	0.937	0.63	5.9	0.95	13.15	196
YM Site 9	838	0.947	0.67	3.7	0.03	8.38	99
Lapse Rate		−0.025 ±0.004 /km	−0.11 ±0.03 /km	0.9 ±0.5 mm/km	0.15 ±0.14 mm/km		134 ±14 mm/km
Extrapolated	1,524						213 mm
Percentage Lapse Rate							6.3 ±0.7 %/100m

NOTE: Data for stations is from Tables F-1 and F-2, except last column calculated using Equations F-41 and F-42. Lapse rates and their uncertainties are *m* and *se*1, calculated with the Excel function LINEST by setting the *known_y's* to the station values and the *known_x's* to station elevations. Extrapolated MAP calculated with the Excel function FORECAST by setting *x* to 1524 m, the *known_y's* to station values of MAP (mm) and the *known_x's* to station elevations. Percentage lapse rate for MAP calculated by dividing lapse rate and uncertainty by extrapolated MAP and dividing by ten to convert from km to 100 m (and multiplying by one hundred to get percentage).

In order to avoid exaggerating the range of uncertainty of each parameter, this section adjusts the values from the various stations to make them comparable. This is particularly necessary for the first-order terms, which have multiple equivalent forms, separated in phase by π. In Tables F-1 and F-2, some of the coefficients of the first-order terms (b_{00} and b_{10}) are negative. Tables F-4 and F-5 include adjustment of the first-order terms in accordance with Equation F-37, so that all of the coefficients are positive. In some cases, the phase has been adjusted by 2π to bring it closer to the adjusted phase values at other stations. The phases of the first-order terms correspond to relatively more winter than summer precipitation.

Tables F-4 and F-5 also include adjustment of the zero-order terms (a_{00} and a_{10}) to the reference elevation of 5,000 ft (1,524 m), using lapse rates from Table F-3. The following equation was used for adjusting values to the reference elevation:

$$\textit{adjusted value} = \textit{initial value} + (\textit{ref elev} - \textit{stn elev}) * \textit{lapse rate} \qquad \text{(Eq. F-48)}$$

where *rev elev* is the reference elevation of 5,000 ft (1,524 m), *stn elev* is the elevation for the station where the initial value was based, and *lapse rate* is the value from Table F-3.

Almost every summary value in Table F-4 or F-5 is used in Section F3.1 either directly in a parameter uncertainty distribution or indirectly in selecting a distribution. The parameters in the last line of each table are used in Section F3.2 to represent the lower bound of the Monsoon climate.

Table F-6 provides two additional properties for each station. One is the probability of a wet day, adjusted to the top of the mountain, calculated in accordance with Equation F-39, and rounded to the nearest 1%. The other is the adjusted value for MAP (Equation F-40). After adjustment to the top of the mountain, the range of MAP is about 170 to 250 mm, with only relatively short records falling below 190 mm.

Table F-4. Parameters for p00 and p10 at Stations Representing the Present-Day Climate Adjusted to an Elevation of 1,524 m

Station	Station Elevation (m)	a_{00} [a]	a_{00} Standard Error [b]	$b_{00,1}$ [b]	$\theta_{00,1}$ (Radians) [b]	a_{10} [a]	a_{10} Standard Error [b]	$b_{10,1}$ [b]	$\theta_{10,1}$ (Radians) [b]
4JA	1,043	0.927	0.002	0.024	−1.26	0.568	0.013	0.043	−1.24
40 MN	1,469	0.928	0.002	0.022	−1.43	0.508	0.011	0.046	−1.36
A12	2,283	0.930	0.003	0.025	−1.35	0.587	0.011	0.026	−1.54
Amargosa Farms	747	0.936	0.002	0.023	−1.17	0.576	0.019	0.039[c]	−2.61[c]
Cane Spring	1,219	0.926	0.002	0.028	−1.24	0.548	0.013	0.052	−1.34
YM Site 1	1,143	0.927	0.004	0.031	−1.20	0.62	0.03	0.09	−1.48
YM Site 2	1,478	0.940	0.004	0.025	−1.30	0.60	0.03	0.10	−1.44
YM Site 3	1,279	0.931	0.004	0.029	−1.39	0.58	0.02	0.06	−1.42
YM Site 6	1,315	0.932	0.004	0.030	−1.34	0.61	0.02	0.06	−1.29
YM Site 9	838	0.930	0.004	0.031	−1.39	0.59	0.03	0.10[c]	−1.67[c]
Mean		0.931		0.027	−1.31	0.58		0.06	−1.5
Standard Deviation		0.004		0.003	0.09	0.03		0.03	0.4
Minimum After Subtracting One Standard Error		0.924				0.50			
Maximum After Adding One Standard Error		0.944				0.65			
Maximum Plus One Standard Deviation				0.034				0.13	

[a] From Table F-1, adjusted in accordance with Equation F-48.
[b] From Table F-1, except as noted.
[c] Sign changed on b, and θ shifted by π.

Table F-5. Parameters for λ and m at Stations Representing the Present-Day Climate Adjusted to an Elevation of 1,524 m

Station	Station Elevation (m)	a_λ (mm) [a]	a_λ Standard Error (mm) [b]	$b_{\lambda,1}$ (mm) [b]	$\theta_{\lambda,1}$ (Radians) [b]	a_m (ln mm) [a]	a_m Standard Error (ln mm) [b]	$b_{m,}$ (ln mm) [b]	$\theta_{m,1}$ (Radians) [b]
4JA	1,043	4.85	0.17	0.75[c]	+2.76[c]	0.71	0.04	0.22[c]	+2.74[c]
40 MN	1,469	4.73	0.16	0.54[c]	+3.95[c]	0.69	0.03	0.10[c]	+3.18[c]
A12	2,283	5.07	0.17	0.90[c]	+2.50[c]	0.80	0.03	0.19[c]	+2.32[c]
Amargosa Farms	747	5.8	0.3	0.3[c]	+2.34[c]	1.02	0.05	0.15[c]	+2.30[c]
Cane Spring	1,219	5.6	0.2	0.8[c]	+2.78[c]	0.87	0.04	0.17[c]	+2.62[c]
YM Site 1	1,143	5.2	0.4	0.8[c]	+2.43[c]	0.77	0.08	0.16[c]	+2.10[c]
YM Site 2	1,478	5.4	0.4	0.6	+1.46	0.86	0.07	0.10[c]	+1.83[c]
YM Site 3	1,279	5.9	0.4	0.8[c]	+2.07[c]	0.94	0.07	0.12[c]	+2.23[c]

Table F-5. Parameters for λ and m at Stations Representing the Present-Day Climate Adjusted to an Elevation of 1,524 m (Continued)

Station	Station Elevation (m)	a_λ (mm) [a]	a_λ Standard Error (mm) [b]	$b_{\lambda,1}$ (mm) [b]	$\theta_{\lambda,1}$ (Radians) [b]	a_m (ln mm) [a]	a_m Standard Error (ln mm) [b]	$b_{m,}$ (ln mm) [b]	$\theta_{m,1}$ (Radians) [b]
YM Site 6	1,315	6.1	0.4	1.1[c]	+1.87[c]	0.98	0.07	0.10[c]	+2.21[c]
YM Site 9	838	4.3	0.3	0.6[c]	+2.65[c]	0.58	0.08	0.20[c]	+2.78[c]
Mean		5.3		0.7	+2.5	0.82		0.15	+2.4
Standard Deviation		0.6		0.2	0.7	0.14		0.04	0.4
Minimum After Subtracting One Standard Error		4.0				0.50			
Maximum After Adding One Standard Error		6.5				1.07			
Maximum Plus One Standard Deviation				1.3				0.26	

[a] From Table F-2, adjusted in accordance with Equation F-48.
[b] From Table F-2, except as noted.
[c] Sign changed on b, and θ shifted by π.

Table F-6. Wet Day Fraction and Mean Annual Precipitation Implied by Parameters Adjusted to an Elevation of 1,524 −m

Meteorological Station	Fraction of Days that are Wet, f_w (%)	Adjusted MAP (mm)	Years Used for Fourier Analysis (Mar. 1 to Feb. 28)
4JA	11	1.9×10^2	45 years: 1959 to 2003
40 MN	12	2.1×10^2	43 years: 1961 to 2003
A12	11	2.0×10^2	41 years: 1960 to 1994, 1998 to 2003
Amargosa Farms	10	2.1×10^2	26 years: 1968, 1969, 1979 to 2000, 2002, 2003
Cane Spring	12	2.5×10^2	39 years: 1965 to 2003
YM Site 1	11	2.1×10^2	10 years: 1993 to 1998, 2000 to 2003
YM Site 2	9	1.8×10^2	11 years: 1993 to 2003
YM Site 3	11	2.4×10^2	11 years: 1993 to 2003
YM Site 6	10	2.2×10^2	11 years: 1993 to 2003
YM Site 9	11	1.7×10^2	11 years: 1993 to 2003

NOTE: f_w and MAP from Equations F-41 and F-42, using values from Tables F-4 and F-5. Data years from Output DTN: SN0609T0502206.023.

DTN: SN0608WEATHER1.005 [DIRS 177912] contains the qualified temperature records from the Yucca Mountain meteorological stations. Excel files in Output DTN: SN0608T0502206.019 contain temperature records extracted for Yucca Mountain Sites 1, 2, 3, and 6. The output DTN also contains the MathCAD workbooks that analyzed the four temperature records. Tables F-7 and F-8 report the results of these analyses. The phase parameters are rounded to the nearest day; the remaining parameters are rounded to 0.1°C.

Section F3 uses the ranges of these coefficients as a guide to the uncertainty distributions for the Present-Day climate and for the Monsoon climate. For ease of reference, Tables F-7 and F-8 show the minimum and maximum values for each of the coefficients of the first-order terms.

Table F-7. Fourier Parameters for Wet Day Temperatures at Stations Representing the Present-Day Climate

Station	γwet_{min} (°C)	γwet_{min} Standard Error (°C)	αwet_{min} (°C)	βwet_{min} (DOY)	γwet_{max} (°C)	γwet_{max} Standard Error (°C)	αwet_{max} (°C)	βwet_{max} (DOY)
YM Site 1	9.2	0.4	9.0	123	18.3	0.5	12.0	118
YM Site 2	8.2	0.4	9.6	124	15.8	0.5	12.4	117
YM Site 3	9.0	0.4	9.0	122	16.9	0.5	12.1	117
YM Site 6	7.9	0.4	8.6	121	16.5	0.5	11.8	116
Minimum			8.6	121			11.8	116
Maximum			9.6	124			12.4	118

Source: Output DTN: SN0608T0502206.019; folder Present-Day-Temperature; files BSC1_parameters, BSC2_parameters, BSC3_parameters, and BSC6_parameters.

Table F-8. Fourier Parameters for Dry Day Temperatures at Stations Representing the Present-Day Climate

Station	γdry_{min} (°C)	γdry_{min} Standard Error (°C)	αdry_{min} (°C)	βdry_{min} (DOY)	γdry_{max} (°C)	γdry_{max} Standard Error (°C)	αdry_{max} (°C)	βdry_{max} (DOY)
YM Site 1	10.8	0.1	10.0	114	23.3	0.2	12.0	110
YM Site 2	12.2	0.1	10.0	116	21.0	0.2	12.4	109
YM Site 3	11.6	0.1	9.9	114	21.8	0.2	12.0	110
YM Site 6	9.1	0.1	9.4	114	21.6	0.1	11.9	110
Minimum			9.4	114			11.9	109
Maximum			10.0	116			12.4	110

Source: Output DTN: SN0608T0502206.019; folder Present-Day-Temperature; files BSC1_parameters, BSC2_parameters, BSC3_parameters, and BSC6_parameters.

Before comparing the zero-order coefficients, they are adjusted to an elevation of 1,524 m using a temperature lapse rate of −10°C/km (dry lapse rate from Maidment (1993 [DIRS 125317], p. 3.3)), as shown in Table F-9. That table also shows the minimum and maximum of these adjusted zero-order coefficients extended by one standard error in each direction.

Table F-9. Zero-Order Temperature Parameters for Stations Representing the Present-Day Adjusted to an Elevation of 1,524 m

Station	Station Elevation (m)	γwet_{min} (°C)	γwet_{max} (°C)	γdry_{min} (°C)	γdry_{max} (°C)
YM Site 1	1,143	5.4	14.5	7.0	19.5
YM Site 2	1,478	7.7	15.3	11.7	20.5
YM Site 3	1,279	6.6	14.5	9.2	19.4
YM Site 6	1,315	5.8	14.4	7.0	19.5
Minimum Less One Standard Error		5.0	13.9	6.9	19.2
Maximum Plus One Standard Error		8.1	15.8	11.8	20.7

NOTE: Values from Tables F-7 and F-8, adjusted in accordance with Equation F-48, using a lapse rate of −10°C/km.

F2.2 STATIONS REPRESENTING AN UPPER BOUND FOR THE MONSOON CLIMATE

*Future Climate Analysis s*elected meteorological stations to represent lower and upper bounds of precipitation during the Monsoon climate, including multiple stations for each extreme in order to minimize local effects on the climate parameters (BSC 2004 [DIRS 170002], p. 6-50). The site and regional stations presented in Section F2.1 represent the lower bound of Monsoon precipitation. For an upper bound, *Future Climate Analysis* selected meteorological stations at Hobbs, New Mexico, and Nogales, Arizona (DTN: GS000308315121.003 [DIRS 151139]).

DTN: SN0603DWEATHER.002 [DIRS 177917] contains the qualified precipitation records from the two stations. Output DTN: SN0609T0502206.023 contains the Excel workbooks that performed the Fourier analyses of the two precipitation records. Tables F-10 and F-11 report results of these analyses. The phase parameters are rounded to one hundredth of a radian (about half a day); the remaining parameters are rounded to a level of precision consistent with the standard error. For corroboration of the analyses, Table F-2a compares the MAP implied by the coefficients with the actual MAP at each of the two stations. In each case, the MAPs agree to within 3%.

Table F-10. Fourier Parameters for p_{00} and p_{10} at Stations Representing the Upper-Bound Monsoon Climate

Station	a_{00}	a_{00} Standard Error	$b_{00,1}$	$\theta_{00,1}$ (Radians)	$b_{00,2}$	a_{10}	a_{10} Standard Error	$b_{10,1}$	$\theta_{10,1}$ (Radians)	$b_{10,2}$
Hobbs	0.903	0.003	−0.042	−0.89	0.010	0.662	0.011	0.027	1.35	−0.020
Nogales	0.899	0.003	−0.059	−1.40	0.092	0.521	0.012	−0.069	−0.84	0.078

Source: Output DTN: SN0609T0502206.023.

Table F-11. Fourier Parameters for λ and m at Stations Representing the Upper-Bound Monsoon Climate

Station	a_λ (mm)	a_λ Standard Error (mm)	$b_{\lambda,1}$ (mm)	$\theta_{\lambda,1}$ (Radians)	$b_{\lambda,2}$ (mm)	a_m (ln mm)	a_m Standard Error (ln mm)	$b_{m,1}$ (ln mm)	$\theta_{m,1}$ (Radians)	$b_{m,2}$ (ln mm)
Hobbs	8.7	0.3	3.2	−1.09	1.2	1.28	0.03	0.36	−1.17	0.11
Nogales	7.1	0.2	−1.4	1.13	−0.3	1.24	0.03	−0.14	1.36	−0.11

Source: Output DTN: SN0609T0502206.023.

Table F-11a. Mean Annual Precipitation at Stations Representing the Upper-Bound Monsoon Climate Compared with Values Implied by Fourier Coefficients

Meteorological Station	Measured MAP (mm)	MAP Implied by Coefficients (mm)	Years Used for Fourier Analysis (Mar. 1 to Feb. 28)
Hobbs	4.0×10^2	4.1×10^2	37 years: 1952, 1954, 1955, 1957, 1959 to 1967, 1969 to 1980, 1982, 1983, 1985 to 1988, 1990, 1992 to 1994, 1996, 1998
Nogales	4.2×10^2	4.2×10^2	29 years: 1948, 1951, 1953 to 1958, 1960, 1962 to 1965, 1967 to 1982

Source: BSC 2006 [DIRS 177081], Section 6.3.5.1 (Measured MAPs); Equations F-41 and F-42 using values from Tables F-10 and F-11 (Implied MAPs); Output DTN: SN0609T0502206.023 (Data Years).

In Tables F-10 and F-11, some of the coefficients of the first-order terms (b_{00}, b_{10}, etc.) are negative. Tables F-12 and F-13 include adjustment of the first-order terms in accordance with Equation F-35 so that all of the coefficients are positive. Because these stations were chosen for their values of temperature and MAP without consideration of their elevation, they each represent conditions at the reference Yucca Mountain elevation of 5,000 ft (1,524 m) and need no adjustment for elevation.

Tables F-12 and F-13 also contain the average of each parameter for the upper-bound stations. For the zero-order parameters, the tables show the wetter value, reflecting the larger number of wet days at Nogales and the greater precipitation per wet day at Hobbs.

Table F-12. Adjusted Parameters for p_{00} and p_{10} at Stations Representing the Upper-Bound Monsoon Climate

Station	a_{00} [a]	a_{00} Standard Error [a]	$b_{00,1}$ [a]	$\theta_{00,1}$ (Radians) [a]	a_{10} [a]	a_{10} Standard Error [a]	$b_{10,1}$ [a]	$\theta_{10,1}$ (Radians) [a]
Hobbs	0.903	0.003	0.042[b]	2.25[b]	0.662	0.011	0.027	1.35
Nogales	0.899	0.003	0.059[b]	1.74[b]	0.521	0.012	0.069[b]	2.30[b]
Average Upper Bound	0.901	0.003	0.050	2.0	0.59	0.012	0.05	1.8
Standard Deviation	0.003		0.012	0.4	0.10		0.03	0.7
Wetter Value	0.899				0.521			
Minimum After Subtracting One Standard Error	0.896				0.509			
Maximum After Adding One Standard Error	0.906				0.673			

[a] From Table F-10, except as noted.
[b] Sign changed on b, and θ shifted by π.

Table F-13. Adjusted Parameters for λ and m at Stations Representing the Upper-Bound Monsoon Climate

Station	a_λ (mm) [a]	a_λ Standard Error (mm) [a]	$b_{\lambda,1}$ (mm) [a]	$\theta_{\lambda,1}$ (Radians) [a]	a_m (ln mm) [a]	a_m Standard Error (ln mm) [a]	$b_{m,1}$ (ln mm) [a]	$\theta_{m,1}$ (Radians) [a]
Hobbs	8.7	0.3	3.2	−1.09	1.28	0.03	0.36	−1.17
Nogales	7.1	0.2	1.4[b]	−2.01[b]	1.24	0.03	0.14[b]	−1.78[b]
Average Upper Bound	7.9	0.3	2.3	−1.55	1.26	0.03	0.25	−1.47
Standard Deviation	1.1		1.3	0.7	0.03		0.16	0.4
Wetter Value	8.7				1.28			
Minimum After Subtracting One Standard Error	6.9				1.21			
Maximum After Adding One Standard Error	9.0				1.31			

[a] From Table F-11, except as noted.
[b] Sign changed on b, and θ shifted by π.

DTN: SN0603DWEATHER.002 [DIRS 177917] contains qualified temperature records from the Hobbs and Nogales stations. Excel files in Output DTN: SN0605T0502206.019 contain temperature records extracted for these two stations. The output DTN also contains the MathCAD workbooks that analyzed the two temperature records. Tables F-14 and F-15 report the results of these analyses. The phase parameters are rounded to the nearest day; the remaining parameters are rounded to 0.1°C. Tables F-20 and F-21 also contain the minimum and maximum for each parameter. For the zero-order parameters, the extremes include extension by the maximum of the standard errors.

Table F-14. Fourier Parameters for Wet Day Temperatures at Stations Representing the Upper-Bound Monsoon Climate

Station	γwet_{min} (°C)	γwet_{min} Standard Error (°C)	αwet_{min} (°C)	βwet_{min} (DOY)	γwet_{max} (°C)	γwet_{max} Standard Error (°C)	αwet_{max} (°C)	βwet_{max} (DOY)
Hobbs	8.5	0.2	10.5	119	20.6	0.2	12.4	112
Nogales	9.5	0.2	8.2	122	22.2	0.2	10.5	116
Minimum	8.3[a]		8.2	119	20.4[a]		10.5	112
Maximum	9.7[a]		10.5	122	22.4[a]		12.4	116

Source: Output DTN: SN0608T0502206.019; folder Future_Climate_Temperature; *Hobbs_Parameters.xls* and *Nogales_Parameters.xls.*

[a] Minimum and maximum for γwet_{min} and γdry_{min} are extended by one standard error.

Table F-15. Fourier Parameters for Dry Day Temperatures at Stations Representing the Upper-Bound Monsoon Climate

Station	γdry_{min} (°C)	γdry_{min} Standard Error (°C)	αdry_{min} (°C)	βdry_{min} (DOY)	γdry_{max} (°C)	γdry_{max} Standard Error (°C)	αdry_{max} (°C)	βdry_{max} (DOY)
Hobbs	8.9	0.1	11.0	115	25.3	0.1	10.4	110
Nogales	4.9	0.1	9.7	120	26.8	0.1	8.4	117
Minimum	4.8[a]		9.7	115	25.2[a]		8.4	110
Maximum	9.0[a]		11.0	120	26.9[a]		10.4	117

Source: Output DTN: SN0608T0502206.019; folder Future_Climate_Temperature; *Hobbs_Parameters.xls* and *Nogales_Parameters.xls*.

[a] Minimum and maximum for γwet_{min} and γdry_{min} are extended by one standard error.

F2.3 STATIONS REPRESENTING THE GLACIAL TRANSITION CLIMATE

Five meteorological stations represent the range of precipitation anticipated during the Glacial Transition climate, three for the upper bound and two for the lower bound (DTN: GS000308315121.003 [DIRS 151139]). DTN: SN0603DWEATHER.002 [DIRS 177917] contains the qualified precipitation records from the five stations. Output DTN: SN0609T0502206.023 contains the Excel workbooks that performed the Fourier analyses of the five precipitation records. Tables F-16 and F-17 report the results of these analyses. The phase parameters are rounded to one hundredth of a radian (about half a day); the remaining parameters are rounded to a level of precision consistent with the standard error. For corroboration of the analyses, Table F-17a compares the MAP implied by the coefficients with the actual MAP at each of the five stations. In each case, the MAPs agree to within 3%.

Table F-16. Fourier Parameters for p_{00} and p_{10} at Stations Representing the Glacial Transition Climate

Station	a_{00}	a_{00} Standard Error	$b_{00,1}$	$\theta_{00,1}$ (Radians)	$b_{00,2}$	a_{10}	a_{10} Standard Error	$b_{10,1}$	$\theta_{10,1}$ (Radians)	$b_{10,2}$
Beowawe	0.884	0.006	0.074	−1.30	−0.012	0.56	0.02	0.02	−0.76	−0.02
Delta	0.870	0.004	0.028	−1.23	−0.016	0.608	0.011	−0.053	0.31	−0.044
Rosalia	0.794	0.005	0.090	−1.10	−0.044	0.477	0.009	0.063	−0.82	−0.029
Spokane	0.784	0.004	0.104	−1.04	0.048	0.489	0.007	0.112	−0.75	0.019
St. John	0.805	0.005	0.102	−1.05	0.051	0.534	0.011	0.108	−0.29	−0.021

Source: Output DTN: SN0609T0502206.023.

Table F-17. Fourier Parameters for λ and m at Stations Representing the Glacial Transition Climate

Station	a_λ (mm)	a_λ Standard Error (mm)	$b_{\lambda,1}$ (mm)	$\theta_{\lambda,1}$ (Radians)	$b_{\lambda,2}$ (mm)	a_m (ln mm)	a_m Standard Error (ln mm)	$b_{m,1}$ (ln mm)	$\theta_{m,1}$ (Radians)	$b_{m,2}$ (ln mm)
Beowawe	3.84	0.18	1.05	−0.52	0.73	0.80	0.04	0.16	−0.83	0.16
Delta	3.22	0.09	0.44	−0.95	0.50	0.51	0.03	0.09	−0.59	0.11
Rosalia	4.13	0.08	−0.36	0.22	−0.41	0.904	0.019	−0.161	−0.10	−0.077
Spokane	3.75	0.06	−0.26	0.74	−0.36	0.665	0.016	−0.089	−0.12	0.074
St. John	4.41	0.11	0.14	0.09	−0.45	0.86	0.03	0.08	1.54	−0.06

Source: Output DTN: SN0609T0502206.023.

Table F-17a. Mean Annual Precipitation at Stations Representing the Glacial Transition Climate Compared with Values Implied by Fourier Coefficients

Meteorological Station	Measured MAP (mm)	MAP Implied by Coefficients (mm)	Years Used for Fourier Analysis (Mar. 1 to Feb. 28)
Beowawe	2.4×10^2	2.4×10^2	10 years: 1983, 1986 to 1989, 1993 to 1995, 1999, 2001
Delta	2.1×10^2	2.1×10^2	29 years: 1972, 1973, 1975, 1976, 1978 to 1981, 1983 to 2003
Rosalia	4.6×10^2	4.5×10^2	28 years: 1953, 1956, 1958 to 1960, 1963 to 1971, 1973, 1975 to 1978, 1980 to 1983, 1985 to 1988, 1993
Spokane	4.2×10^2	4.2×10^2	52 years: 1948 to 1952, 1954 to 1994, 1998 to 2003
St. John	4.3×10^2	4.3×10^2	22 years: 1964 to 1969, 1972 to 1981, 1987, 1989 to 1991, 1994, 2001

Source: Measured MAPs from BSC 2006 [DIRS 177081], Section 6.3.5.1; implied MAPs from Equations F-41 and F-42 using values from Tables F-16 and F-17; data years from Output DTN: SN0609T0502206.023.

In Tables F-16 and F-17, some of the coefficients of the first-order terms (b_{00}, b_{10}, etc.) are negative. Tables F-18 and F-19 include adjustment of the first-order terms in accordance with Equation F-35 so that all of the coefficients are positive. In some cases, the phase has been adjusted by 2π to bring it closer to the adjusted values at other stations. Because these stations were chosen for their values of temperature and MAP without consideration of their elevation, they each represent conditions at the reference Yucca Mountain elevation of 5,000 ft (1,524 m) and need no adjustment for elevation.

Tables F-18 and F-19 also contain two averages for each parameter, one for the lower-bound stations and one for the upper-bound stations. For some first-order terms, these averages omit one of the stations. The lower-bound averages of $b_{1o,1}$ and $\theta_{1o,1}$ omit Beowawe because the magnitude of this first-order term is no larger than the standard error. The upper bound averages of $b_{\lambda,1}$, $\theta_{\lambda,1}$, $b_{m,1}$, and $\theta_{m,1}$ omit St. John because these first-order terms are out of phase with Rosalia and Spokane and because St. John has larger standard errors. For the zero-order parameters, the tables show the extent to which one standard error would extend the range of the parameter.

Because the magnitude of the first-order terms are larger for some of these stations than for stations previously considered, the choice of phase required further attention. The phase is more relevant when the amplitude is larger. Therefore, Tables F-18 and F-19 include weighted means of the phases and weighted standard deviations using the amplitudes as weighting factors.

Table F-18. Adjusted Parameters for p_{00} and p_{10} at Stations Representing the Glacial Transition Climate

Station	a_{00} [a]	a_{00} Standard Error [a]	$b_{00,1}$ [a]	$\theta_{00,1}$ (Radians)[a]	a_{10} [a]	a_{10} Standard Error [a]	$b_{10,1}$ [a]	$\theta_{10,1}$ (Radians) [a]
Beowawe	0.884	0.006	0.074	−1.30	0.56	0.02	0.02	−0.76
Delta	0.870	0.004	0.028	−1.23	0.608	0.011	0.053[b]	−2.83[b]
Rosalia	0.794	0.005	0.090	−1.10	0.477	0.009	0.063	−0.82
Spokane	0.784	0.004	0.104	−1.04	0.489	0.007	0.112	−0.75
St. John	0.805	0.005	0.102	−1.05	0.534	0.011	0.108	−0.29
Minimum	0.78[c]		0.028		0.468[c]		.02	
Maximum	0.89[c]		0.104		0.619[c]		.112	
Weighted Average[d]				−1.12				−0.93
Weighted Standard Deviation[d]				0.10				0.84

[a] From Table F-16, except as noted.
[b] Sign changed on *b,* and θ shifted by π.
[c] Minimum and maximum for a_{oo} and a_{1o} are extended by one standard error.
[d] Average and standard deviation values for θ are weighted by values of *b*.

Table F-19. Adjusted Parameters for λ and *m* at Stations Representing the Glacial Transition Climate

Station	a_λ (mm) [a]	a_λ Standard Error (mm) [a]	$b_{\lambda,1}$ (mm) [a]	$\theta_{\lambda,1}$ (Radians) [a]	a_m (ln mm) [a]	a_m Standard Error (ln mm) [a]	$b_{m,1}$ (ln mm) [a]	$\theta_{m,1}$ (Radians) [a]
Beowawe	3.84	0.18	1.05	−0.52	0.80	0.04	0.16	−0.83
Delta	3.22	0.09	0.44	−0.95	0.51	0.03	0.09	−0.59
Rosalia	4.13	0.08	0.36[b]	−2.92[b]	0.904	0.019	0.161[b]	−3.24[b]
Spokane	3.75	0.06	0.26[b]	−2.40[b]	0.665	0.016	0.089[b]	−3.26[b]
St. John	4.41	0.11	0.14	0.09	0.86	0.03	0.08	1.54
Minimum	3.13[c]		0.14		0.48[c]		0.08	
Maximum	4.52[c]		1.05		0.923[c]		0.161	
Weighted average[d]				−1.2				−1.5
Weighted standard deviation[d]				1.0				1.7

[a] From Table F-17, except as noted.
[b] Sign changed on *b,* and θ shifted by π.
[c] Minimum and maximum for a_λ and a_m are extended by one standard error.
[d] Average and standard deviation values for θ are weighted by values of *b*.

For the five stations that represent the Glacial Transition climate, DTN: SN0603DWEATHER.002 [DIRS 177917] contains qualified temperature data. Output DTN: SN0608T0502206.019 contains the MathCAD files that record the calculations of the temperature parameters for each station. Tables F-20 and F-21 report the results of these analyses. The phase parameters are rounded to the nearest day; the remaining parameters are rounded to 0.1°C.

Tables F-20 and F-21 also contain the minimum and maximum for each parameter. For the zero-order parameters, the extremes include extension by the maximum of the standard errors.

Table F-20. Parameters of Minimum Temperature at Stations Representing the Glacial Transition Climate

Station	αwet_{min} (°C)	βwet_{min} (DOY)	γwet_{min} (°C)	γwet_{min} Standard Uncertainty (°C)	αdry_{min} (°C)	βdry_{min} (DOY)	γdry_{min} (°C)	γdry_{min} Standard Uncertainty (°C)
Beowawe	7.6	114	1.4	0.2	9.9	106	−0.7	0.1
Delta	10.4	116	2.9	0.2	11.6	112	0.7	0.1
Rosalia	6.3	118	2.9	0.1	8.3	112	1.8	0.1
Spokane	7.9	116	3.5	0.1	10.0	116	2.5	0.1
St. John	6.4	114	3.8	0.1	7.5	111	1.6	0.1
Minimum	6.3	114	1.2[a]		7.5	106	−0.8[a]	
Maximum	10.4	118	3.9[a]		11.6	116	2. 6[a]	

Source: Output DTN: SN0608T0502206.019; folder Future_Climate_Temperature; files *Beowawe_Parameters.xls*, *Delta_Parameters.xls*, *Rosalia_Parameters.xls*, *Spokane_Parameters.xls*, and *StJohn_Parameters.xls.*

[a] Minimum and maximum for γwet_{min} and γdry_{min} are extended by one standard error using the maximum standard error.

Table F-21. Parameters of Maximum Temperature at Stations Representing the Glacial Transition Climate

Station	αwet_{max} (°C)	βwet_{max} (DOY)	γwet_{max} (°C)	γwet_{max} Standard Uncertainty (°C)	αdry_{max} (°C)	βdry_{max} (DOY)	γdry_{max} (°C)	γdry_{max} Standard Uncertainty (°C)
Beowawe	11.2	112	14.2	0.2	14.5	112	18.4	0.1
Delta	13.4	115	15.7	0.2	15.0	112	19.5	0.1
Rosalia	10.1	115	12.6	0.1	13.8	117	15.0	0.1
Spokane	10.8	113	11.8	0.1	14.8	115	14.7	0.1
St. John	10.4	111	14.3	0.1	13.8	114	16.6	0.1
Minimum	10.1	111	11.7[a]		13.8	112	14.6[a]	
Maximum	13.4	115	15.9[a]		15.0	117	19.6[a]	

Source: Output DTN: SN0608T0502206.019; folder Future_Climate_Temperature; *Beowawe_Parameters.xls*, *Delta_Parameters.xls*, *Rosalia_Parameters.xls*, *Spokane_Parameters.xls*, and *StJohn_Parameters.xls*.

[a] Minimum and maximum for γwet_{max} and γdry_{max} are extended by one standard error using the maximum standard error.

F3. SELECTION OF PARAMETER RANGES FOR EACH CLIMATE

For each meteorological station, Section F2 reports the station's parameters, adjusted as appropriate to be applicable to an elevation equivalent to the top of Yucca Mountain (5,000 ft or 1,524 m). The section you are now reading reports the development of a range of uncertainty for each climate parameter, first for the remainder of the Present-Day climate, then for the Monsoon climate, and finally for the Glacial Transition climate.

Each climate parameter represents an estimate of the value that would result if the analyses of Section F2 could be performed on the future record of a meteorological station located at the top of the mountain. Thus, the ranges of the parameters represent the full potential range of integrated weather over the future period, not the parameters for individual years. Standard uncertainties are calculated in accordance with formulas in Section I2.2. Values are rounded to accuracies consistent with the standard uncertainties.

Analyses with the MASSIF model require precipitation amounts and intensities, maximum and minimum temperatures, and wind speeds. Potential climates do not fit onto a linear scale. One climate may be hot, wet, and windy, with intense storms; another may be cold, wet, and windy, with long, slow snowfalls; and a third may be cold, dry, and still, with slow snowfalls. Where *Future Climate Analysis* refers to lower- and upper-bound representatives of a climate, those bounds refer to precipitation, not necessarily to any other parameter.

F3.1 PARAMETER RANGES FOR THE PRESENT-DAY CLIMATE

This section presents the nominal value and uncertainty for each weather parameter of the Present-Day climate. For precipitation and temperature parameters, the analyses of individual meteorological station records, which are reported in Section F2.1, provide the basis. However, for the analyses of wind speed and precipitation duration, meteorological stations are treated as a group, not separately.

Output DTN: SN0610T0502206.030 contains a MathCAD application that calculates monthly wind speeds averaged over four Yucca Mountain meteorological stations, Site 1, Site 2, Site 3, and Site 6. The calculation uses wind speed data from DTN: SN0608WEATHER1.005 [DIRS 177912].

This calculation converts these measurements to equivalent wind speed at 2 meters height, using the following equation (Allen et al. 1998 [DIRS 157311], Eq. 47):

$$u_2(u,z) = u\frac{4.87}{\ln(67.8z - 5.42)} \qquad \text{(Eq. F-49)}$$

where u is the wind speed measured at a height of z meters aboveground and u_2 is the equivalent wind speed at 2 m. The application calculates monthly averages, omitting days with no wind speed data, and determines the standard error in each average.

Table F-22 lists the nominal value and uncertainty for each parameter of the Present-Day climate. The approximate uncertainty distribution for each zero-order precipitation parameter

(a_{00} and a_{10}) is a uniform distribution. The extremes of the distribution are the minimum and the maximum values among those obtained by analysis of the ten stations, extended by one standard error. These values also appear in Tables F-4 and F-5. The nominal value is the midpoint between these extremes. For a uniform distribution that ranges from x to y, the standard uncertainty is $(y - x)/\sqrt{12}$. Section I2.2 provides the derivation of this formula.

Using Equations F-41 and F-42 and the nominal values of the zero-order parameters yields a value of 1.9×10^2 mm as a nominal MAP for the Present-Day climate. Section 7.1.1.3 discusses the uncertainty distribution for MAP during the remainder of the modern interglacial climate.

For each of the eight first-order precipitation parameters, the nominal value is the mean of the values for the ten meteorological stations. The approximate uncertainty distribution is usually a normal distribution, established by the mean and standard deviation for the 10 stations. The one exception is $b_{10,1}$, which is only two standard deviations above zero, so that a uniform distribution, defined by the extreme values from the 10 stations, is a more representative distribution of this nonnegative parameter. The values for the phase parameters are consistent with peak precipitation in the winter.

All of the temperature parameters have uncertainty distributions that are uniform, with a range determined by the minimum and maximum values for the four sites, as given in Tables F-8 through F-10. Each nominal value is at the center of its range.

The wind speed averages have normal distributions, based on the mean and standard error calculated in Output DTN: SN0610T0502206.030.

Table F-22. Nominal Values and Uncertainties for Parameters of the Weather Input File during the Present-Day Climate

Parameter Symbol	Nominal Value	Uncertainty Range	Uncertainty Distribution	Standard Uncertainty
a_{00}	0.934	0.924 to 0.944	uniform	0.006
$b_{00,1}$	0.027	0.027 ± 0.003	normal	0.003
$\theta_{00,1}$	−1.31 radians	−1.31 ± 0.09 radians	normal	0.09 radians
a_{10}	0.58	0.50 to 0.65	uniform	0.04
$b_{10,1}$	0.06	0.03 to 0.10	uniform	0.02
$\theta_{10,1}$	−1.5 radians	−1.5 ± 0.4 radians	normal	0.4 radians
a_{λ}	5.2 mm	4.0 to 6.5 mm	uniform	0.7
$b_{\lambda,1}$	0.7 mm	0.7 ± 0.2 mm	normal	0.2 mm
$\theta_{\lambda,1}$	+2.5 radians	+2.5 ± 0.7 radians	normal	0.7 radians
a_m	0.78 mm	0.50 to 1.07 ln mm	uniform	0.16 ln mm
$b_{m,1}$	0.15 mm	0.15 ± 0.04 ln mm	normal	0.04 ln mm
$\theta_{m,1}$	+2.4 radians	+2.4 ± 0.4 radians	normal	0.4 radians
αwet_{min}	9.1°C	8.6°C to 9.6°C	uniform	0.3°C

Table F-22. Nominal Values and Uncertainties for Parameters of the Weather Input File During the Present-Day Climate (Continued)

Parameter Symbol	Nominal Value	Uncertainty Range	Uncertainty Distribution	Standard Uncertainty
βwet_{min}	122 days	121 to 124 days	uniform	1 day
γwet_{min}	6.6°C	5.0°C to 8.1°C	uniform	0.9°C
αdry_{min}	9.7°C	9.4°C to 10.0°C	uniform	0.2°C
βdry_{min}	115 days	114 to 116 days	uniform	1 day
γdry_{min}	9.4C	6.9°C to 11.8°C	uniform	1.4°C
αwet_{max}	12.1°C	11.8°C to 12.4°C	uniform	0.2°C
βwet_{max}	117 days	116 to 118 days	uniform	1 day
γwet_{max}	14.8°C	13.9°C to 15.8°C	uniform	0.6°C
αdry_{max}	12.2°C	11.9°C to 12.4°C	uniform	0.1°C
βdry_{max}	110 days	109 to 110 days	uniform	0.3 days
γdry_{max}	20.0°C	19.2°C to 20.7°C	uniform	0.4°C
$u_2(1)$	2.36 m/s	2.36 ± 0.03 m/s	normal	0.03 m/s
$u_2(2)$	2.67 m/s	2.67 ± 0.04 m/s	normal	0.04 m/s
$u_2(3)$	2.84 m/s	2.84 ± 0.03 m/s	normal	0.03 m/s
$u_2(4)$	3.22 m/s	3.22 ± 0.04 m/s	normal	0.04 m/s
$u_2(5)$	2.97 m/s	2.97 ± 0.03 m/s	normal	0.03 m/s
$u_2(6)$	2.90 m/s	2.90 ± 0.02 m/s	normal	0.02 m/s
$u_2(7)$	2.75 m/s	2.75 ± 0.02 m/s	normal	0.02 m/s
$u_2(8)$	2.71 m/s	2.71 ± 0.02 m/s	normal	0.02 m/s
$u_2(9)$	2.64 m/s	2.64 ± 0.02 m/s	normal	0.02 m/s
$u_2(10)$	2.61 m/s	2.61 ± 0.03 m/s	normal	0.03 m/s
$u_2(11)$	2.47 m/s	2.47 ± 0.03 m/s	normal	0.03 m/s
$u_2(12)$	2.48 m/s	2.48 ± 0.03 m/s	normal	0.03 m/s

Source: Precipitation parameters from Tables F-4 and F-5; temperature values from Tables F-7 through F-9; wind speeds from Output DTN: SN0610T0502206.030.

F3.2 PARAMETER RANGES FOR THE MONSOON CLIMATE

According to *Future Climate Analysis,* the Monsoon climate is characterized in the Owens Lake record by species that imply a monsoon sufficient to generate diluting surface flow in the Owens River. As noted in Section F2.2, however, *Future Climate Analysis* selected the Present-Day sites and regional stations to represent one bound for the Monsoon climate. This bound has lower precipitation with more winter than summer precipitation (BSC 2004 [DIRS 170002], pp. 6-47 to 6-50).

An upper-bound value for the monsoon precipitation must have MAP higher than the range of values at the Haiwee station near Owens Lake (up to 270 mm) and MAT as high or higher than Owens Lake today. *Future Climate Analysis* selected the stations at Hobbs, New Mexico and Nogales, Arizona, reported to have MAP levels of 418 mm and 414 mm, respectively, but noted that the MAP at these sites may not be high enough to generate the appropriate lake in the Owens Basin. An expansion of the summer rain regime to the Owens Basin region also would have expanded well north of Yucca Mountain. Because Yucca Mountain would be more centrally

located within such a summer rain regime it may experience upper-bound levels of MAP that are higher than those identified from the anlogue meteorological stations (BSC 2004 [DIRS 170002], pp. 6-47 to 6-50).

For the Monsoon climate, one limit of precipitation behavior is wettest in the winter, whereas the other limit is wettest in the summer. For temperature, on the other hand, both limits are hottest in the summer. Therefore, the development of distributions for monsoon precipitation parameters differs from the procedure for monsoon temperature parameters. Furthermore, lacking qualified wind speed data from Hobbs or Nogales, the wind speed parameters are approximated by the parameters for the Present-Day climate.

For each parameter of the Monsoon climate, Table F-23 contains the nominal value and the uncertainty distribution for the Yucca Mountain analysis. Table F-23 also shows the standard uncertainty for each distribution. For a uniform distribution that ranges from x to y, the standard uncertainty is $(y-x)/\sqrt{12}$. Section I2.2 provides the derivation of this formula. Values in the table have been rounded to the level of accuracy indicated by the standard uncertainty.

For the zero-order precipitation terms, the uncertainty distribution is uniform. To ensure that the extremes capture the full range of uncertainty, the range is defined by the minimum and maximum of all values from the analyses of Present-Day (Tables F-4 and F-5) and upper bound Monsoonsites (Tables F-12 and F-13), extended by one standard error. The nominal value is the midpoint between these extremes.

For example, the zero-order parameter, a_{10}, in Table F-23 is defined by a uniform distribution between 0.50 to 0.67. The lower bound is the minimum value of this parameter after reduction by one standard error, considering all of the stations in Table F-4 and Table F-12. Station 40 MN has the minimum value after reduction by one standard error, 0.497 (0.508 minus 0.011, Table F-4). This result is rounded to the level of accuracy indicated by the standard uncertainty (see below). The upper bound is the maximum value of this parameter after addition of one standard error, 0.673 (Hobbs, 0.662 plus 0.11, Table F-12). The standard uncertainty is $(0.673 - 0.497)/\sqrt{12} = 0.05$, indicating a level of accuracy of two decimal places. Thus the range is 0.50 to 0.67.

Using Equations F-41 and F-42 and the nominal values of the zero-order parameters yields a value of 2.9×10^2 mm as a nominal MAP for the Monsoon climate. Section 7.1.1.4 discusses the uncertainty distribution for MAP during the Monsoon climate.

As forecast in *Future Climate Analysis,* the typical Monsoon climate is a climate where winter precipitation exists, but does not dominate MAP. However, by specifying that local and regional stations be used as a lower bound, *Future Climate Analysis* suggests that the climate during the monsoon period would vary from episodes of intense summer rain to Present-Day-like climates with relatively more winter and less summer precipitation (BSC 2004 [DIRS 170002], p. 6-50). Therefore, although the magnitude of the first-order precipitation term is uncertain, the phase of the first-order term must be that of the summer-precipitation upper-bound stations, not the winter-precipitation Yucca Mountain stations.

A Monsoon climate has strong seasonal variation in precipitation, which makes the first-order terms more important than for other climates. The amplitudes for the first-order terms differ greatly between the two upper-bound stations. Nogales has the greater seasonal variation in the probability that a day is wet. Hobbs has the greater variation in the average precipitation on wet days. Tables F-12 and F-13 show that the values for the two stations differ by more than a factor of two for $b_{10,1}$, $b_{\lambda,1}$, and $b_{m,1}$. Those tables also report standard deviations for $b_{00,1}$, $b_{\lambda,1}$, and $b_{m,1}$ that are larger than the standard deviations in the corresponding zero-order terms.

Because *Future Climate Analysis* describes these stations as "the best choices available" (BSC 2004 [DIRS 170002], p. 6-49), it is not clear that the two values for a first-order amplitude, as different as they are, actually capture the full range of uncertainty. An alternate interpretation is that these stations are just two samples of potential upper-bound stations. In this interpretation, the potential upper-bound stations have a distribution for each parameter that may be approximated as a normal distribution, with the average and standard deviation for the two stations providing estimates for the mean and variance of the distribution. A range from one standard deviation below the lower value to one standard deviation above the upper value captures about 90% of this hypothetical distribution for the climate upper bound. This observation guides the selection of a range for each first-order magnitude.

However, the magnitude of a first-order term is subject to constraints. The magnitude of a first-order term must be less than the magnitude of the zero-order term because neither a Markov probability nor an average precipitation can be less than zero. Also, the first-order term may not cause a Markov probability to exceed 1.0. Therefore, an approximate uncertainty distribution for the magnitude of a first-order term for the upper-bound Monsoon climate is a uniform distribution from one standard deviation below the lower value to one standard deviation above the upper value, subject to constraints.

Because the first-order terms for the lower-bound stations are completely out of phase with the first-order terms for the upper-bound stations, they may be represented by negative values of the *b*'s. In Table F-23 the complete range for the amplitude of a first-order term may range from the largest value for the Present-Day climate (Table F-3), plus one standard deviation, but taken as negative, to the larger of the values from the upper-bound stations, plus one standard deviation, taken as positive. For $b_{00,1}$, the range is from −0.03 to +0.07, with the larger value bringing p_{00} to greater than 1.0 when a_{00} takes on it largest value of 0.944. The constraint that p_{00} remain less than or equal to 1.0, must be observed in downstream use of these values. For $b_{10,1}$, the range is from −0.06 to +0.08, with no applicable constraints. For $b_{\lambda,1}$ the range is from −0.7 mm to +3.6 mm. For $b_{m,1}$ the range is from −0.15 ln mm to +0.30 ln mm.

The uncertainty distribution for the phase of each first-order precipitation term is a uniform distribution. The extreme values are the values for the two upper-bound stations.

For the temperature parameters, uncertainty distributions are uniform, with the limits determined by the extreme values from among all of the Present-Day and upper-bound monsoon stations. For wet-day temperature parameters, ranges of station values appear in Tables F-7 and F-14. The ranges for dry day parameters are in Tables F-8 and F-15. As before, the zero-order parameters are extended by one standard error; Table F-9 summarizes the effects of that extension for Present-Day stations. The parameter γdry_{min} provides an example. After extension

by one standard error, the values at the stations range from 4.8°C (Table F-15) to 11.8°C (Table F-9). Because the standard uncertainty for this uniform distribution is 2.0°C, Table F-23 shows the values rounded to 5°C and 12°C.

Table F-23. Nominal Values and Uncertainties for Parameters of the Monsoon Climate

Parameter Symbol	Nominal Value	Uncertainty Range	Uncertainty Distribution	Standard Uncertainty
a_{00}	0.920	0.896 to 0.944	uniform	0.014
$b_{00,1}$	0.02	−0.03 to +0.07	uniform	0.03
$\theta_{00,1}$	+2.00 radians	+1.74 to +2.25 radians	uniform	0.15 radians
a_{10}	0.58	0.50 to 0.67	uniform	0.05
$b_{10,1}$	−0.02	−0.13 to +0.10	uniform	0.07
$\theta_{10,1}$	+1.8 radians	+1.4 to +2.3 radians	uniform	0.3 radians
a_{λ}	6.5 mm	4.0 to 9.0 mm	uniform	1.4 mm
$b_{\lambda,1}$	1.6 mm	−1.3 to 4.5 mm	uniform	1.7 mm
$\theta_{\lambda,1}$	−1.6 radians	−2.0 to −1.1 radians	uniform	0.3
a_{m}	0.9 mm	0.5 to 1.3 ln mm	uniform	0.2 ln mm
$b_{m,1}$	0.1 mm	−0.3 to 0.5 ln mm	uniform	0.2 ln mm
$\theta_{m,1}$	−1.48 radians	−1.78 to −1.17 radians	uniform	0.18 radians
αwet_{min}	9.4°C	8.2°C to 10.5°C	uniform	0.7°C
βwet_{min}	122 days	119 to 124 days	uniform	1 day
γwet_{min}	7.4°C	5.0°C to 9.7°C	uniform	1.4°C
αdry_{min}	10.2°C	9.4°C to 11.0°C	uniform	0.5°C
βdry_{min}	117 days	114 to 120 days	uniform	2 days
γdry_{min}	8°C	5°C to 12°C	uniform	2°C
αwet_{max}	11.4°C	10.5°C to 12.4°C	uniform	0.5°C
βwet_{max}	115 days	112 to 118 days	uniform	2 days
γwet_{max}	18°C	14°C to 22°C	uniform	2°C
αdry_{max}	10.4	8.4°C to 12.4°C	uniform	1.2°C
βdry_{max}	113 days	109 to 117 days	uniform	2 days
γdry_{max}	23°C	19°C to 27°C	uniform	2°C
$u_2(1)$	2.36 m/s	2.36 ± 0.03 m/s	normal	0.03 m/s
$u_2(2)$	2.67 m/s	2.67 ± 0.04 m/s	normal	0.04 m/s
$u_2(3)$	2.84 m/s	2.84 ± 0.03 m/s	normal	0.03 m/s
$u_2(4)$	3.22 m/s	3.22 ± 0.04 m/s	normal	0.04 m/s
$u_2(5)$	2.97 m/s	2.97 ± 0.03 m/s	normal	0.03 m/s
$u_2(6)$	2.90 m/s	2.90 ± 0.02 m/s	normal	0.02 m/s
$u_2(7)$	2.75 m/s	2.75 ± 0.02 m/s	normal	0.02 m/s
$u_2(8)$	2.71 m/s	2.71 ± 0.02 m/s	normal	0.02 m/s
$u_2(9)$	2.64 m/s	2.64 ± 0.02 m/s	normal	0.02 m/s
$u_2(10)$	2.61 m/s	2.61 ± 0.03 m/s	normal	0.03 m/s
$u_2(11)$	2.47 m/s	2.47 ± 0.03 m/s	normal	0.03 m/s
$u_2(12)$	2.48 m/s	2.48 ± 0.03 m/s	normal	0.03 m/s

Source: Precipitation parameters from Tables F-4, F-5, F-12, and F-13; temperature values from Tables F-7 through F-9, F-14, and F-15; wind speeds from Output DTN: SN0610T0502206.030.

F3.3 PARAMETER RANGES FOR THE GLACIAL TRANSITION CLIMATE

Judged from the Owens Lake record, the change to the Glacial Transition climate was large and fast, shifting from a strong monsoon system dominated by summer precipitation to a winter regime with sufficient effective moisture to sustain a fresh and spilling Owens Lake. Therefore, the polar front must be resident in the region during much of the winter, lowering the MAT. The genesis of greater snowpack with a resident polar mass must also lower temperature and increase MAP at Yucca Mountain, but the cooler climate never becomes very cold with high effective moisture as was true of the last two full-glacial periods. The climate during the Glacial Transition period was typically a cool, usually wet winter season with warm (not hot) to cool summers that were usually dry relative to the Present-Day summers. The MAT should be no colder and preferably warmer than 8°C. The MAP should be higher than the 309 mm recorded near Owens Lake, because even the high historic discharge levels of that year would not be sufficient to fill and spill the lake as implied by the microfossil record. The three selected stations in eastern Washington, Rosalia, St. John, and Spokane, fit all of the criteria for the upper-bound Glacial Transition climate (BSC 2004 [DIRS 170002], pp. 6-50 to 6-52).

However, there are indications that there were also episodes during this climate period that were relatively warm and dry, thus demonstrating some degree of climate variability. The stations representing the lower bound should have a higher temperature, but lower than that for the Owens Lake Basin today. They may have MAP values that are similar to or even lower than Present-Day Owens Lake Basin, but dominated by winter precipitation. The set of meteorological data for Delta, Utah, fits all of these criteria. The site at Beowawe, Nevada, was added as a lower-bound station to avoid using a single site and because its data met most of the requirements (BSC 2004 [DIRS 170002], pp. 6-50 to 6-53).

Lacking qualified wind speed data from any of these five stations, the wind speed parameters are approximated by the parameters for the Present-Day climate.

For each parameter of the Glacial Transition climate, Table F-24 contains the nominal value and the uncertainty distribution for the Yucca Mountain analysis. Most of the uncertainty distributions for precipitation and temperature parameters are uniform, with the ranges determined in Section F2.3, extended by one standard error where applicable, and the nominal values are the means of the distributions. The exceptions are the phase coefficients for precipitation. The table assigns a normal distribution to the phase coefficients for the Markov probabilities, using the weighted average and standard deviation from Table F-18. In the case of the phase coefficients for the amount of precipitation of a wet day (Table F-19), however, the weighted standard deviations are so large that no nominal value seemed justified. These last two phase coefficients are considered as completely uncertain so that any value is possible.

Table F-24 also shows the standard uncertainty for each distribution. For a uniform distribution that ranges from x to y, the standard uncertainty is $(y-x)/\sqrt{12}$. Section I2.2 provides the derivation of this formula. Values in the table have been rounded to the level of accuracy indicated by the standard uncertainty or by a relevant standard error.

Table F-24. Nominal Values and Uncertainties for Parameters of the Glacial Transition Climate

Parameter Symbol	Nominal Value	Uncertainty Range	Uncertainty Distribution	Standard Uncertainty
a_{00}	0.84	0.78 to 0.89	uniform	0.03
$b_{00,1}$	0.066	0.028 to 0.104	uniform	0.02
$\theta_{00,1}$	−1.12 radians	−1.12 ± 0.10 radians	normal	0.010 radians
a_{10}	0.54	0.47 to 0.62	uniform	0.04
$b_{10,1}$	0.07	0.02 to 0.11	uniform	0.03
$\theta_{10,1}$	−0.93 radians	−0.93 ± 0.84 radians	normal	0.84 radians
a_{λ}	3.8 mm	3.1 to 4.5 mm	uniform	0.4 mm
$b_{\lambda,1}$	0.6 mm	0.1 to 1.0 mm	uniform	0.3 mm
$\theta_{\lambda,1}$	N/A	$-\pi$ to π radians	uniform	N/A
a_{m}	0.70 mm	0.48 to 0.92 ln mm	uniform	0.13 ln mm
$b_{m,1}$	0.12 mm	0.08 to 0.16 ln mm	uniform	0.02 ln mm
$\theta_{m,1}$	N/A	$-\pi$ to π radians	uniform	N/A
αwet_{min}	8.4°C	6.3°C to 10.4°C	uniform	1.2°C
βwet_{min}	DOY 116	DOY 114 to 118	uniform	1 day
γwet_{min}	2.6°C	1.2°C to 3.9°C	uniform	0.8°C
αdry_{min}	9.6°C	7.5°C to 11.6°C	uniform	1.2°C
βdry_{min}	DOY 111	DOY 106 to 116	uniform	3 days
γdry_{min}	0.9°C	−0.8°C to 2.6°C	uniform	1.0°C
αwet_{max}	11.8°C	10.1°C to 13.4°C	uniform	1.0°C
βwet_{max}	DOY 113	DOY 111 to 115	uniform	1 day
γwet_{max}	13.8°C	11.7°C to 15.9°C	uniform	1.2°C
αdry_{max}	14.4°C	13.8°C to 15.0°C	uniform	0.3°C
βdry_{max}	DOY 114	DOY 112 to 117	uniform	1 day
γdry_{max}	17.1°C	14.6°C to 19.6°C	uniform	1.4°C
$u_2(1)$	2.36 m/s	2.36 ± 0.03 m/s	normal	0.03 m/s
$u_2(2)$	2.67 m/s	2.67 ± 0.04 m/s	normal	0.04 m/s
$u_2(3)$	2.84 m/s	2.84 ± 0.03 m/s	normal	0.03 m/s
$u_2(4)$	3.22 m/s	3.22 ± 0.04 m/s	normal	0.04 m/s
$u_2(5)$	2.97 m/s	2.97 ± 0.03 m/s	normal	0.03 m/s
$u_2(6)$	2.90 m/s	2.90 ± 0.02 m/s	normal	0.02 m/s
$u_2(7)$	2.75 m/s	2.75 ± 0.02 m/s	normal	0.02 m/s
$u_2(8)$	2.71 m/s	2.71 ± 0.02 m/s	normal	0.02 m/s
$u_2(9)$	2.64 m/s	2.64 ± 0.02 m/s	normal	0.02 m/s
$u_2(10)$	2.61 m/s	2.61 ± 0.03 m/s	normal	0.03 m/s
$u_2(11)$	2.47 m/s	2.47 ± 0.03 m/s	normal	0.03 m/s
$u_2(12)$	2.48 m/s	2.48 ± 0.03 m/s	normal	0.03 m/s

Source: Precipitation parameters from Tables F-18 and F-19; temperature values from Tables F-20 and F-21; wind speeds from Output DTN: SN0610T0502206.030.

Using Equations F-41 and F-42 and the nominal values of the zero-order parameters yields a value of 3.2×10^2 mm as a nominal MAP for the Glacial Transition climate. Section 7.1.1.5 discusses the uncertainty distribution for MAP during the Glacial Transition climate.

F4. GENERATION OF A WEATHER INPUT FILE FROM A SET OF CLIMATE PARAMETERS

This section discusses the general method for developing a weather input file from a set of climate parameters. Appendix I presents the sample values used for calculations and the development of a specific weather input file for each set of sample values.

F4.1 GENERATION OF PRECIPITATION INPUT

F4.1.1 Stochastic Precipitation Model

The stochastic algorithm proceeds as follows to develop a 1,000-year sample of daily precipitation, $P(d,y)$, for d from 1 to 365 and y from 1 to 1,000.

For d from 1 to 365, evaluate the formulas in Equations F-9 through F-12 and Equation F-2.

Set $P(0,1)$ to 0.001 (starting with a wet day to avoid underestimating precipitation).

For each y from 1 to 1,000,

For each d from 1 to 365

If $P(d-1,y)$ is zero, select a random number, $0 < R < 1$.

If $R < p_{oo}(d)$, set $P(d,y)$ to zero.

Else, set $P(d,y)$ such that:

$$\int_0^{P(d,y)} \frac{e^{-[\ln x - m(d)]^2/2[s(d)]^2}}{xs(d)\sqrt{2\pi}} dx = R \qquad \text{(Eq. F-50)}$$

If using a built-in inverse lognormal function, verify the result.

Else, select a random number, $0<R<1$.

If $R < p_{1o}(d)$, set $P(d,y)$ to zero.

Else, set $P(d,y)$ such that:

$$\int_0^{P(d,y)} \frac{e^{-[\ln x - m(d)]^2/2[s(d)]^2}}{xs(d)\sqrt{2\pi}} dx = R \qquad \text{(Eq. F-51)}$$

If using a built-in inverse lognormal function, verify the result.

Set $T(y)$ to $\sum_{d=1}^{365} P(d,y)$.

Set $P(0,y+1)$ to $P(365,y)$.

(Sort y) Create $Y(i)$, i = 1 to 1,000, such that $T[Y(i)] \geq T[Y(i+1)]$, i = 1 to 1,000.

F4.1.2 Developing a Representative Subsample

This procedure groups the 1,000 sample years into bins. The first bin contains just the year with the greatest precipitation. The next bin contains the next two wettest years. Subsequent bins contain seven, twenty, and seventy years. The remaining 900 years are divided into five bins of 180 years each.

(Weights for sample years)

Set $W(1)$ to 0.001 (1,000-year event).

Set $W(2)$ to 0.002 (300-year event).

Set $W(3)$ to 0.007 (100-year event).

Set $W(4)$ to 0.02 (30-year event).

Set $W(5)$ to 0.07 (10-year event).

For i from 6 through 10, set $W(i)$ to 0.18.

(Select subsample years)

Set $S(1)$ to $Y(1)$.

Select a random number, 0<R<1, and set $S(2)$ to $Y(2+2R)$, truncating index.

Select a random number, 0<R<1, and set $S(3)$ to $Y(4+7R)$, truncating index.

Select a random number, 0<R<1, and set $S(4)$ to $Y(11+20R)$, truncating index.

Select a random number, 0<R<1, and set $S(5)$ to $Y(31+70R)$, truncating index.

For i from 6 through 10, select a random number, 0<R<1, and set $S(i)$ to $Y(101+180(i-6)+180R)$, truncating index.

F4.2 GENERATION OF TEMPERATURE INPUT

This section steps through how the daily minimum and maximum temperatures are determined for the 10 representative years generated in Section F4.1.

For x from 1 to 365, use the least squares approach to best fit each of the four temperature models defined by Equations F-43 through F-46 for each of the meteorological stations. Initial values for α, β, and γ are 20°C, DOY 80, and 30°C, respectively.

Determine the α, β, and γ values for each of the four temperature models for each of the three anticipated climate episodes. This is done by calculating the midpoint of the range for the α, β, and γ values calculated in Step I for the meteorological stations in each climate.

Using Equations F-43 through F-46 for x from 1 to 365, apply the α, β, and γ values to the 10 representative years generated in Section F4.1 for each of the three anticipated climates to obtain the daily minimum and maximum temperatures for dry or wet days as appropriate.

F4.3 GENERATION OF WIND SPEED INPUT

Wind speeds are calculated by averaging the monthly wind data collected at the four Yucca Mountain meteorological stations: Sites 1, 2, 3, and 6. These values are then converted to equivalent wind speed at 2 meters aboveground level using Equation F-49. Each monthly average is applied at the middle of the month and the wind speeds for other days are interpolated between two monthly averages. Output DTN: SN0610T0502206.030 contains details of the interpolation.

Since there is no qualified wind speed data for the Monsoon climate and Glacial Transition anlogue sites, those daily wind speed values are approximated by the Present-Day climate.

F5. NOMENCLATURE FOR EQUATIONS USED IN APPENDIX F

Symbol	Description	Units	Where Used*
P	Precipitation		Eq. F-1
p	Probability density		Eq. F-1
m	Mean of the logarithm of precipitation		Eq. F-1 (F-2)
s			Eq. F-1 (F-2)
λ	Mean precipitation		Eq. F-2
$f(t)$	Any continuous function of time	varies	Eq. F-3 (F-4; F-5; F-6)
a	Zero-order term in a Fourier series	varies	Eq. F-3 (F-4; F-14; F-15; F-16; F-17; F-18)
v_n	Coefficient of nth-order sine term in a Fourier series	varies	Eq. F-3 (F-5; F-7; F-8)
n	Index of term in a Fourier series	none	Eq. F-3 (F-5; F-6)

Symbol	Description	Units	Where Used*
w_n	Coefficient of nth-order cosine term in a Fourier series	varies	Eq. F-3 (F-6; F-7; F-8)
b_n	Coefficient of nth-order term in polar form of a Fourier series	varies	Eq. F-3
θ_n	Phase of nth-order term in polar form of a Fourier series	radians	Eq. F-3 (F-8)
$p_{00}(d)$	The probability that day *d* is dry, given that day *D*-1 is dry	none	Eq. F-9 (F-38; F-39; F-40)
$p_{10}(d)$	The probability that day *d* is dry, given that day *D*-1 is wet	none	Eq. F-10 (F-38; F-39; F-40)
$\lambda(d)$	Mean of the probability distribution for amount of precipitation on day *d*, given that it is a wet day	mm	Eq. F-11
$m(d)$	Mean of the probability distribution for the natural logarithm of the amount of precipitation on day *d*, given that it is a wet day	ln mm	Eq. F-12
a_{00}	Zero-order term in Fourier series for $p_{00}(d)$	none	Eq. F-9 (F-41; F-42; F-47)
a_{10}	Zero-order term in Fourier series for $p_{10}(d)$	none	Eq. F-10 (F-41; F-42; F-47)
$b_{00,1}$	Coefficient of first-order term in Fourier series for $p_{00}(d)$ (polar form)	none	Eq. F-9
$b_{00,2}$	Coefficient of second-order term in Fourier series for $p_{00}(d)$ (polar form)	none	Eq. F-9
$\theta_{00,1}$	Phase of first-order term in Fourier series for $p_{00}(d)$ (polar form)	radians	Eq. F-9
d'	$2\pi d / 365$	radians	Eq. F-9 (F-10; F-11; F-12; F-13; F-14; F-33)
$\theta_{00,2}$	Phase of second-order term in Fourier series for $p_{00}(d)$ (polar form)	radians	Eq. F-9 (F-10)
$b_{10,1}$	Coefficient of first-order term in Fourier series for $p_{10}(d)$ (polar form)	none	Eq. F-10
$\theta_{10,1}$	Phase of first-order term in Fourier series for $p_{10}(d)$ (polar form)	radians	Eq. F-10
$b_{10,2}$	Coefficient of second-order term in Fourier series for $p_{10}(d)$ (polar form)	none	Eq. F-10
$\theta_{10,2}$	Phase of second-order term in Fourier series for $p_{10}(d)$ (polar form)	radians	Eq. F-10
a_λ	Zero-order term in Fourier series for $\lambda(d)$	mm	Eq. F-11 (F-42)
$b_{\lambda,1}$	Coefficient of first-order term in Fourier series for $\lambda(d)$ (polar form)	mm	Eq. F-11
$\theta_{\lambda,1}$	Phase of first-order term in Fourier series for $\lambda(d)$	radians	Eq. F-11
$b_{\lambda,2}$	Coefficient of second-order term in Fourier series for $\lambda(d)$ (polar form)	mm	Eq. F-11
$\theta_{\lambda,2}$	Phase of second-order term in Fourier series for $\lambda(d)$	radians	Eq. F-11
a_m	Zero-order term in Fourier series for $m(d)$	ln mm	Eq. F-12

Symbol	Description	Units	Where Used*
$b_{m,1}$	Coefficient of first-order term in Fourier series for *m*(*d*) (polar form)	ln mm	Eq. F-12
$\theta_{m,1}$	Phase of first-order term in Fourier series for *m*(*d*)	radians	Eq. F-12
$b_{m,2}$	Coefficient of second-order term in Fourier series for *m*(*d*) (polar form)	ln mm	Eq. F-12
$\theta_{m,2}$	Phase of second-order term in Fourier series for *m*(*d*)	radians	Eq. F-12
$F(d)$	A precipitation parameter as a function of *d*	varies	Eq. F-14
d	Day of the year beginning with March 1	days	Eq. F-15 (F-16; F-17; F-18; F-20)
y	Year index	none	Eq. F-15 (F-16; F-20)
$f_1'(d)$	Residue of after subtracting zero-order term: $f(d)-a$	varies	Eq. F-17
$\hat{f}_{n-1}(d,y)$	Residue after subtracting terms through *n*−1: $f(d)-a-\sum_{m=1}^{n-1} b_m \sin(\theta_m + md')$	varies	Eq. F-18 (F-19; F-20; F-21; F-22; F-23; F-24; F-25; F-26; F-27; F-28; F-29; F-30; F-31; F-32; F-33; F-34; F-35; F-36)
$p_d(d)$	Probability that day *d* is dry	none	Eq. F-38 (F-39; F-40)
$Twet_{min}$	Minimum temperature on wet days	°C	Eq. F-43
αwet_{min}	Magnitude of sine term in sine function for $Twet_{min}$	°C	Eq. F-43
βwet_{min}	Spring day of zero sine term for $Twet_{min}$	days	Eq. F-43
x	Day of year from January 1, ignoring February 29	days	Eq. F-43 (F-44; F-45; F-46)
γwet_{min}	Zero-order term in sine function for $Twet_{min}$	°C	Eq. F-43 (F-47)
$Tdry_{min}$	Minimum temperature on dry days	°C	Eq. F-44
αdry_{min}	Magnitude of sine term in sine function for $Tdry_{min}$	°C	Eq. F-44
βdry_{min}	Spring day of zero sine term for $Tdry_{min}$	days	Eq. F-44
γdry_{min}	Zero-order term in sine function for $Tdry_{min}$	°C	Eq. F-42 (F-47)
$Twet_{max}$	Maximum temperature on wet days	°C	Eq. F-45
αwet_{max}	Magnitude of sine term in sine function for $Twet_{max}$	°C	Eq. F-45
βwet_{max}	Spring day of zero sine term for $Twet_{max}$	days	Eq. F-45
γwet_{max}	Zero-order term in sine function for $Twet_{max}$	°C	Eq. F-45
$Tdry_{max}$	Maximum temperature on dry days	°C	Eq. F-46
αdry_{max}	Magnitude of sine term in sine function for $Tdry_{max}$	°C	Eq. F-46
βdry_{max}	Spring day of zero sine term for $Tdry_{max}$	days	Eq. F-46
γdry_{max}	Zero-order term in sine function for $Tdry_{max}$	°C	Eq. F-46
u_2	Wind speed at 2 m aboveground	m/s	Eq. F-49

Symbol	Description	Units	Where Used*
u	Wind speed measured at a height of z meters aboveground	m/s	Eq. F-49
z	Height aboveground at which wind speed is measured	m	Eq. F-49
$P(d,y)$	Precipitation for day d (1 to 365) of year, y	mm	Eq. F-50 (F-51)
s	Parameter of lognormal distribution $s^2 = 2(\ln \lambda - m)$	ln mm	Eq. F-50 (F-51)
R	Random number between 0 and 1	none	Eq. F-50 (F-51)
f_w	Fraction of days that are wet	none	Eq. F-41

* Defined in these equations. Equation numbers in parentheses show other equations where these terms are used but not redefined.

INTENTIONALLY LEFT BLANK

APPENDIX G
DESCRIPTION OF THE MASSIF ROUTINES

PREFACE

The purpose of Appendix G is to document the MASSIF routines. It does not contain a listing or rationale for the property values, initial values, or options used for specific calculations. These are contained in the model and property descriptions of the report, or in the calculation results section.

Appendix G is a nearly exact reproduction of the electronic Mathcad file "Massif Documentation.xmcd", in which the MASSIF routines are documented step-by-step. The electronic file contains hypertext links to the actual MASSIF routines. The MASSIF routines contain reciprocal hypertext links to the documentation file as well as to tables of variable definitions, and to the primary FAO-56 references in electronic form. Appendix G **contains** pointers to sections of the model report that are **not** contained in the electronic version. The electronic version does not contain the pointers to the model report for two reasons:

1) Editing the report can result in changes in the sections numbers. Since it is desirable to "freeze" the electronic files before the report editing is complete, the electronic files do not contain most of the pointers.

2) Future revisions of the report may result in changes of the section numbers. Corresponding revisions of the electronic files should not be required unless there are accompanying changes in the model implementation.

Because the primary purpose of the electronic file is on-line documentation, the file and Appendix G have certain traits worth noting:

1) The variable names are identical to those in the Mathcad files but may be somewhat different than those used in other parts of the model report.

2) The documentation of the routines is organized according to phenomenological topic. Within each topic group, the primary routine is listed first. Secondary routines which are used by the primary routine follow within the group. One exception to this is the explanation of the water balance model. The balance model is explained first; the "group-balance" model that links the individual cells together is listed second.

G1. INTRODUCTION

MASSIF (**M**ass **A**ccounting **S**ystem for **S**oil **I**nfiltration and **F**low) is designed to provide an estimate of the net infiltration of water into the fractured rock which underlies the soil at Yucca Mountain. The core of MASSIF is a daily water balance for each cell in the watershed (Section 6.4). The daily water balance for the soil in each cell (30 m × 30 m) is:

$$R_{off} = P_{rain} + R_{on} + SM - \Delta\theta - ET - NI \qquad \text{(Eq. G-1a)}$$

where

R_{off}	=	runoff
P_{rain}	=	precipitation as rain
R_{on}	=	run-on
SM	=	snowmelt
$\Delta\Theta$	=	change in water storage in the soil
ET	=	evapotranspiration
NI	=	net infiltration.

The water balance is written as a calculation for the runoff from the cell. All the quantities to the right of the equals sign are computed from submodels. MASSIF deals only with self-contained watersheds that have no run-on from sources outside the watershed boundary.

The daily water balance on the snowpack for each cell is:

$$\Delta SP = P_{snow} - SUB - SM \qquad \text{(Eq. G-1b)}$$

where

ΔSP	=	change in the water storage of the snowpack
P_{snow}	=	precipitation as snow
SUB	=	sublimation
SM	=	snowmelt.

The model for the snowpack is simple (Appendix G3.5). Precipitation accumulates in the snow layer when the temperature is sufficiently low. While the temperature remains low, part of the snow sublimates. When the temperature increases, the snow melts and releases water into the soil.

The structure of MASSIF parallels that of FAO-56 (Allen et al. 1998 [DIRS 157311]), which is also the source of the submodel for evapotranspiration (ET). The water balance in FAO-56 utilizes the field capacity concept described in Section 6.2.2 of the modeling report. In the FAO-56 implementation of this concept, water in excess of the soil field capacity flows downward freely without rate restrictions. The daily water balance is performed in two steps. The first step (Appendix G3) handles the precipitation (or irrigation) event, and results in a calculation of net infiltration (NI) and the change in the water stored in the soil ($\Delta\Theta$). The duration of the precipitation event is included in this step, and the periods during and after the event are modeled separately (Appendix G3.2). The second step deals with the

evapotranspiration (ET) and results in another adjustment to the water stored in the soil ($\Delta\Theta$) (Appendix G4).

Water flow rate limits in the soil and rock can result in water runoff (R_{off}) when the rain intensity is sufficiently high. MASSIF uses saturated soil and rock conductivities to limit water flow between soil nodes (Figure G-1) and between the soil–rock interface. Runoff from a particular cell in the watershed appears as run-on in the cell immediately downstream. The calculation of runoff is part of the calculation step that deals with precipitation.

MASSIF is a collection of Mathcad "routines." The following sections describe each routine in detail. The highest-level routine, the "driver" is named *Massif* (note the italics). Examination of *Massif* reveals the architecture of the calculation. Details of the component parts "called" in *Massif* are contained in appropriate sections. This documentation is contained in both Appendix G and in the appropriate Mathcad files. Mathcad users are encouraged to begin with the Table of Contents file (*MASSIF Table of Contents.xmcd*). This file contains (double click) hyperlinks (indicated by underlined bold blue text) to all sections in all of files that are a direct part of the MASSIF calculation. Examination of the Mathcad files allows the user to understand the exact implementation of the constituent parts of the infiltration analysis. A table of MASSIF routines and the Mathcad files in which they are located is provided in Section G6.

The *Massif* driver is executed in Mathcad files called "front ends." These files feed the input stream into the *Massif* driver for the specific problem being examined. Results of the calculation are stored either in the front-end file in the form of embedded Excel worksheets, or as external ASCII files. Whenever the calculation in the front end is time-consuming, the call to the *Massif* driver is disabled; the disabled part of the front-end is colored pink. Documentation of these "front end" files and the associated postprocessing is included in *Massif Results Documentation.xmcd*.

Provisions have been made so that the user or reviewer can spot-check time-consuming calculations. Each of the front-ends used for the sensitivity analyses calculates the infiltration for ten (10) precipitation years in all eleven (11) watersheds in the domain for one realization in the Latin Hypercube Sampling (LHS) analysis. The CPU time for one of these files ranges from about 22 to 36 hours, depending upon the speed of the computer and the parameters of the LHS sample. Checking the entire calculation for a single realization would represent a considerable investment in time. In order to shorten and simplify the review process, the *Massif* driver is implemented for a single watershed and a single precipitation year specified by the user/reviewer. CPU time for this calculation can range from about 30 seconds for the smallest watershed to about 80 minutes for the largest watershed. Results of the spot check are displayed along with the results stored in the external ASCII file.

The structure of the MASSIF calculation is designed to realize three attributes of QUALITY consisting of TRANSPARENCY, TRACEABLILITY AND REPRODUCIBILITY. TRANSPARENCY is facilitated by including explanatory text adjacent to the Mathcad implementation of the modeled equations. Mathcad's graphical interface enables a quicker grasp of the specifics of implementation that is elusive in scripted languages such as FORTRAN or C. TRACABILITY is facilitated by the hyperlinked directory structure containing both the calculation files and the results of the calculation. REPRODUCIBILITY is possible because

specific portions of the front-ends can be reenabled and the results compared directly the archived results in the associated subdirectories.

G2. THE MASSIF DRIVER

The *Massif* driver consists of two sections. The first section includes the calculations that need be calculated only once. The second section includes the calculation of values that change daily. The following steps are executed in the *Massif* routine:

G2.1 SECTION 1: ONE-TIME EVALUATIONS

Step 1: Extract a subset of inputs from the input vectors/matrices.

Explanation: The input string to *Massif* consists of the name of the watershed (*Wshed*) and a series of vectors and matrices that contain the calculation inputs. The calculation inputs were condensed into vectors and matrices in order to keep the length of the variable string manageable. In many cases, the vectors and matrices are passed into called routines directly. However, some of the inputs must be extracted within the main driver (*Massif*).

Step 2: Read the watershed characteristics.

Explanation: *Wshed* is the name of the watershed file. The ID number, latitude, elevation, ID number of downstream cell, slope, azimuth, soil depth zone, soil type zone, rock zone (or type), and potential vegetative response is read for each cell in the watershed. The development of the Yucca Mountain watershed files are described in Section 6.5.2.1 and Appendix B.

Step 3: Calculate layer properties and assign initial conditions.

Explanation: The routine ***LayerProps*** calculates soil layer depths and extrinsic properties for each cell from the intrinsic soil properties and the soil depths. Additionally, the initial soil water levels are calculated for each node in each cell.

Step 4: Initialize the infiltration, total infiltration, snow level, monitored watershed output, and monitored cell output to zero at the start of the calculation.

Explanation: A vector of zeros and length equal to the number of cells is created by multiplying the vector *MaxInfil_rk* by zero. The initial daily infiltration (*Infil*), the cumulative infiltration (*Total*), and the snow level for each cell (*Slevel*) are then set to this zero vector. Next, the initial values of the monitored watershed values are set to zero. Finally, if no cell quantities are to be monitored ($icell_1 = -1$), then the first (and only) element of the cell monitor vector ($Monitor_{cell\_1}$) is set to zero.

Step 5: Calculate the psychrometric constant for each cell.

Explanation: The routine γ_{c_fcn} calculates the psychrometric constant as a function of elevation. The Mathcad vectorizing function (the arrow) is applied to

γ_{c_fcn} because the variable *elev* is a vector containing the elevation for each cell in the watershed.

Step 6: Calculate the column indices for the R_b constant for each cell.

Explanation: The R_b constant is used to calculate the partitioning between direct and diffuse radiation. An external look-up table contains the value of R_b for specific combinations of surface slope and aspect (columns of table) for each day of the calendar year (rows of the table). The routine *Index_Rb_fcn* calculates the four columns of the R_b look-up table that apply to a specific cell. The Mathcad vectorizing function (the arrow) is applied to *Index_Rb_fcn* so that the four columns in the R_b look-up table that apply to a specific cell are computed for each cell in the watershed.

Step 7: Calculate the interpolation constants for R_b for each cell.

Explanation: The value of R_b for a particular cell on a particular day is calculated by interpolating the four bounding values. The interpolation is conducted over the slope/azimuth space. Hence the interpolating coefficients calculated in the routine C_{Rb_fcn} are calculated once at the beginning of the infiltration calculation. The Mathcad vectorizing function (the arrow) is applied to C_{Rb_fcn} so that the interpolation coefficients that apply to a specific cell are computed for each cell in the watershed.

Step 8: Calculate the column indices for the NDVI table for each cell.

Explanation: An external look-up table contains the NDVI values for various ranges of surface slope and azimuth (columns of table) for each day in the calendar year. The routine *Index_NDVI_fcn* determines the index of the NDVI look-up table that applies for a particular slope/azimuth combination. The Mathcad vectorizing function (the arrow) is applied to *Index_NDVI* so that the index that applies to a specific cell is computed for each cell in the watershed.

Step 9: Find the upstream nodes that contribute to run-on.

Explanation: The geospatial file describing the watershed contains the ID of the single downstream cell to which runoff can move. However, run-on to a particular cell may come from multiple contributing cells. The routine *UpStream3* produces a list of cells that contribute run-on for each cell in the watershed.

Step 10: Calculate the annual precipitation used to scale the NDVI/K_{cb} correlation.

Explanation: The relationship between the vegetative coefficient (K_{cb}) and the NDVI measurement is adjusted for the cumulative amount of precipitation in the water year. The routine *precip_Kcb_fcn* sums up the precipitation for the water year(s) being modeled.

G2.2 SECTION 2: EVALUATIONS CONDUCTED FOR EACH DAY OF THE ANALYSIS

Step 11: Calculate the average, maximum, minimum, and dew temperatures for each cell in the watershed.

Explanation: The daily maximum and minimum temperatures specified in the weather file apply to a specific reference elevation (*elev_ref*). The routine T_{elev_cor} produces the average, maximum, minimum, and dew temperature for a given elevation. The Mathcad vectorizing function (the arrow) is applied to T_{elev_cor} so that the temperature vector that applies to a specific cell is computed for each cell in the watershed.

Step 12: Generate the temperatures for the average elevation of the watersheds.

Explanation: The air properties used to calculate the incident solar radiation are based upon temperatures computed at the average elevation (*elev_avg*) of the modeled region (Appendix C1.1).

Step 13: Generate the daily precipitations for each cell.

Explanation: The daily precipitations listed in the weather file apply to a specific reference elevation (*elev_ref*). The routine $Precip_{elev\_cor}$ produces the daily precipitation adjusted for the elevation of the cell of interest. The Mathcad vectorizing function (the arrow) is applied to $Precip_{elev\_cor}$ so that the temperature vector that applies to a specific cell is computed for each cell in the watershed.

Step 14: Calculate the "crop" coefficients and the vegetative canopy coefficients and adjust water levels of nodes in top layer due to varying canopy coefficient for each cell in the watershed.

Explanation: The top layer of soil is subdivided into two nodes. Node 1 models the bare soil. Node 2 models the soil under the vegetative canopy. The fraction of the soil covered by the vegetative canopy is described by the vegetative canopy coefficient (f_c). The input to the *Massif* driver permits two options for the canopy coefficient. If an invariant canopy coefficient is specified ($0 \leq f_{c\_switch} \leq 1$) the canopy coefficient is set equal to f_{c_switch}. If the correlation for vegetative canopy coefficient (f_c) is used ($f_{c\_switch} = -1$), the canopy coefficient changes from day to day (calculated for each cell in the watershed in routine K_{cb_fcn}). The change in the relative size of Nodes 1 and 2 necessitates a transfer of water from the shrinking node to the expanding node in order to conserve water. This transfer of water between Nodes 1 and 2 is performed in routine $Varying\_f_c$.

Step 15: Calculate the reference evapotranspiration for the day.

Explanation: The reference evapotranspiration (*ET0*) is calculated for each cell in the watershed in routine ET_0.

Step 16: Calculate the accumulation of snow and its influence on the water available to the soil.

Explanation: When the temperature is sufficiently low, precipitation will accumulate above the soil in the form of snow. When the temperature is sufficiently high, accumulated snow will melt and supply water to the soil. Routine *SnowB* calculates the snow level (*Slevel*), amount of precipitation that reaches the soil (*NetPrecip*), snow sublimation (*Sublimation*), and snowmelt (*SnowMelt*) for each cell in the watershed.

Step 17: Calculate changes in water levels, runoff, and run-on due to water redistribution for each cell in the watershed.

Explanation: The field-capacity model of water flow through soils permits water to instantaneously flow downward when the "water level" of a layer exceeds the field capacity. This soil flow model is implemented in the routine *Balance*. The routine *GroupBalance* implements the *Balance* routine on every cell in the watershed and keeps track of the amount of runoff and run-on for each cell.

Step 18: Calculate changes in water levels due to evaporation and transpiration for each cell in the watershed.

Explanation: The amount of transpiration and evaporation that occurs in the day is calculated and subtracted from the appropriate water levels in routine *ET*.

Step 19: Check global water conservation for the day and keep track of spatially integrated water values.

Explanation: The integrated amount of water leaving the watershed is subtracted from the integrated amount of water entering the watershed in routine *Masscheck_fcn*. The difference should be a small number that reflects the machine precision limitations of the algebraic operations. The individual components of the global balance equation are saved in an array (*addition1*) for output from the *Massif* routine.

The watershed output from *Massif* is contained in the matrix $Monitor_{WS}$. The information content of this matrix is decided by the user. If the user assigns a value of −1 to the input variable i_{WS}, then *Massif* returns cumulative values of the reported components for the modeled time period. If the user assigns a value of 1 to i_{WS}, *Massif* returns daily values of the reported components. A list of the reported quantities is contained with the routine *Masscheck_fcn*.

Step 20: Assemble calculated quantities for the monitored cells.

Explanation: If there is a list of monitored cells, append the monitored daily quantities assembled in $Monitor_{cell\_fcn}$ to the list of those quantities for previous days.

Routine Output: Return the output from the routine.

Explanation: *Massif* returns eight sets of calculated values:

1) Average annual net infiltration into the bedrock for each cell in the watershed
2) Average annual precipitation for each cell in the watershed
3) Average annual run-on for each cell in the watershed
4) Average annual runoff for each cell in the watershed
5) Global mass check for each day of the calculation
6) Monitored quantities for each monitored cell
7) Monitored watershed quantities
8) Clock time needed to complete the calculation.

G3. WATER FLOW

G3.1 THE CELL BALANCE MODEL

The cell "balance" model is a water conservation model in which water in excess of the field capacity flows into the underlying layer subject to the constraints of saturated conductivities. Fractured bedrock, characterized by rock saturated flow conductivity, underlies the bottom soil layer. The soil is divided into three layers. The thickness of the top layer is defined by the evaporation depth. The thickness of the second layer is defined by the difference between the rooting depth and the evaporation depth. The thickness of the third layer is defined by the difference between the soil depth and the rooting depth. When the soil depth is less than the rooting depth, the thickness of Layer 3 is zero. When the soil depth is less than the evaporation depth, the thickness of Layer 2 is zero. The thickness of Layer 1 is always finite, but it can be less than the evaporation depth. In such cases, the thickness of the top layer is equal to the soil depth.

The cell balance model in this analysis consists of four soil nodes (Figure G-1). The top layer is divided into two nodes. Node 1 is the evaporation region, which is not protected by the vegetation canopy. Node 2 lies under the vegetation canopy. Nodes 3 and 4 consist of the middle and bottom soil layers, respectively. Water from precipitation and runoff is added to the water levels of Nodes 1 and 2 before the balance model is "called." The balance model is called only when the water level in at least one of the nodes is greater than the layer field capacity.

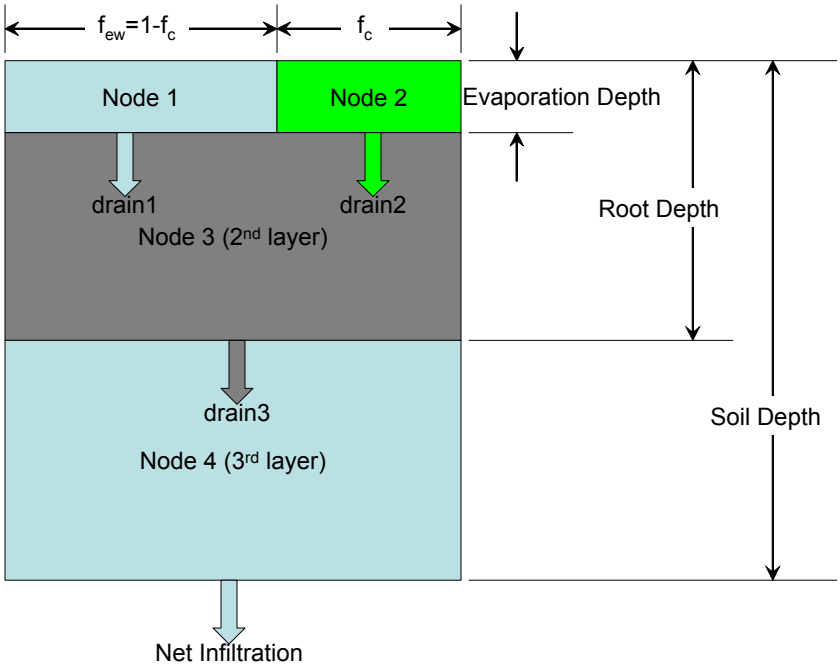

Source: Output DTN: SN0701T0502206.037.

Figure G-1. Water Infiltration in the Cell Balance Model

The balance model calculates, for a given water inventory in the nodes, the amount of water that flows into the underlying bedrock, and the amount that flows off the cell in the form of "runoff." It calculates these quantities in a two-stage calculation procedure. In the first stage, water is allowed to flow downward subject to saturated conductivity limits into the underlying node without regard to the capacity of the underlying node to hold the water. The net infiltration into the bedrock is calculated at the end of this stage. In the second stage, the capacity of the nodes to hold water is examined, and water that cannot fit within the node is passed upward into the overlying node. The runoff from the cell is calculated at the end of the second stage.

The two stage calculation procedure is merely an efficient numerical tool for the solution of the equations for water motion. The numerical artifices of overfilling a node with water and then pushing the excess water upward are not real physical processes. They are simply used as a method of applying volumetric constraints on a flow equation with split boundary conditions.

The use of two nodes in the top layer presents a complicating factor. It is possible that one of the top nodes might have an excess of water at the end of the second stage while the adjacent node is not fully filled. In this event, the excess water in one of the top nodes is first applied to fill the adjacent node. Only after the adjacent node is filled will excess water be applied to "runoff," which will migrate to the adjacent cell. This is justified because there will be several plants, each with its own evaporation zone and canopy zone, in a single 30-m × 30-m cell.

The following are the computational steps of the cell balance model (routine *Balance*). Note that the water available to the cell has already been added to the surface layer (Nodes 1 and 2) before the call to *Balance*.

Step 1: Calculate the amount of water that can drain from Node 1.

Explanation: The water level for Node 1 ($Wlevel_1$) is compared against the field capacity for that layer (FC_layer_1). The drainage from Node 1 (*drain1*) is then set to the difference between the water level and the field capacity. The drainage is then limited to the soil conductivity limit adjusted for the time period of the precipitation episode (*MaxInfil_sl_mod*). Finally, the drainage is subtracted from the water level.

Step 2: Calculate the amount of water that can drain from Node 2.

Explanation: The water level for Node 2 ($Wlevel_2$) is compared against the field capacity for that layer (FC_layer_2). The drainage from Node 2 (*drain2*) is then set to the difference between the water level and the field capacity. The drainage is then limited to the soil conductivity limit adjusted for the time period of the precipitation episode (*MaxInfil_sl_mod*). Finally, the drainage is subtracted from the water level.

Step 3: Transfer excess water from Node 1 to Node 2 if the drainage from Node 2 is less than the episodic soil conductivity limit.

Explanation: If there is excess water remaining in Node 1 and the drainage from Node 2 was not maximized, part or all of the excess water is transferred to Node 2. First, the drainage from Node 2 is restored to the node. The excess water in Node 1 (*ΔWlevel1_max*) is calculated. Then the change in the Node 2 water level needed to realize the flow limit (*ΔWlevel2_max*) is calculated. The actual change in the water level (*ΔWlevel2*) of Node 2 is the minimum of the *ΔWlevel1_max* corrected for the canopy fraction (f_C), and *ΔWlevel2_max*. The water level of Node 2 is increased by the amount *ΔWlevel2*. The drainage from Node 2 (*drain2*) is then calculated as the difference between the new Node 2 water level and the Node 2 field capacity (FC_layer_2). The drainage is subtracted from Node 2. Finally, the transferred water is subtracted from Node 1.

Step 4: Transfer excess water from Node 2 to Node 1 if the drainage from Node 1 is less than the episodic soil conductivity.

Explanation: If there is excess water remaining in Node 2 and the drainage from Node 1 was not maximized, part or all of the excess water is transferred to Node 1. First, the drainage from Node 1 is restored to the node. The excess water is Node 2 (*ΔWlevel2_max*) is calculated. Then the change in the Node 1 water level needed to realize the flow limit (*ΔWlevel1_max*) is calculated. The actual change in the water level (*ΔWlevel1*) of Node 1 is the minimum of the *ΔWlevel2_max* corrected for the canopy fraction (f_C), and *ΔWlevel1_max*. The water level of Node 1 is increased by the amount

$\Delta Wlevel1$. The drainage from Node 1 ($drain1$) is then calculated as the difference between the new Node 1 water level and the Node 1 field capacity (FC_layer_1). The drainage is subtracted from Node 1. Finally, the transferred water is subtracted from Node 2.

Step 5: Add the drainage from Nodes 1 and 2 to Node 3.

Explanation: The drainage from Nodes 1 and 2, weighted for the canopy fraction, is added to the water level of Node 3 ($Wlevel_3$).

Step 6: Excess water in Node 3 drains into Node 4.

Explanation: If the water level of Node 3 ($Wlevel_3$) exceeds the Node 3 field capacity (FC_layer_3), then let the excess water flow downward. First the drainage from Node 3 ($drain3$) is calculated as the difference between the water level and the node field capacity. Then the drainage is corrected for the soil saturated conductivity ($MaxInfil\_sl$). The drainage is subtracted from the Node 3 water level. Finally, the drainage is added to the Node 4 water level.

Step 7: Excess water in Node 4 drains into the bedrock.

Explanation: If the water level of Node 4 ($Wlevel_4$) exceeds the Node 4 field capacity (FC_layer_4), then let the excess water flow downward into the underlying fracture rock. First the drainage from Node 4 ($Infil$) is calculated as the difference between the water level and the node field capacity. Then the drainage is corrected for the soil saturated conductivity ($MaxInfil\_sl$). Next the drainage is corrected for the rock saturated conductivity ($MaxInfil\_rk$). The drainage is subtracted from the Node 4 water level.

Step 8: If the water content of Node 4 exceeds the pore volume, pass the excess water up into Node 3.

Explanation: If the water level of Node 4 ($Wlevel_4$) exceeds the pore volume of Node 4 ($Pore\_sl_4$), pass the excess water up into Node 3.

Step 9: If the water content of Node 3 exceeds the pore volume, pass the excess water up into Nodes 1 and 2.

Explanation: If the water level of Node 3 ($Wlevel_3$) exceeds the pore volume of Node 4 ($Pore\_sl_3$), pass the excess water ($\Delta Wlevel3$) up into Nodes 1 and 2. The excess water is prorated between Nodes 1 and 2 according to the amounts that originally drained into Node 3 during **Step 5**.

Step 10: Transfer excess water in Node 1 into Node 2 before computing runoff.

Explanation: If the water level in Node 1 ($Wlevel_1$) is greater than the pore volume of Node 1 ($Pore\_sl_1$) and the water level in Node 2 is less than the pore volume in Node 2 ($Pore\_sl_2$) and the canopy fraction (f_C) is greater than zero, transfer as much excess water to Node 2 before computing the runoff. First, compute the maximum amount of water that can be transferred from Node 1 ($DWlevel1\_max$). The actual change in the water level of Node 2 ($\Delta Wlevel2$) is the minimum of $\Delta Wlevel1\_max$ adjusted for the canopy fraction and the amount of water necessary to maximize the water content of Node 2 ($Pore\_sl_2 - Wlevel_2$). The actual change is added to the water level of Node 2. Finally, the actual change, adjusted for the canopy fraction, is subtracted from Node 1.

Step 11: Transfer excess water in Node 2 into Node 1 before computing runoff.

Explanation: If the water level in Node 2 ($Wlevel_2$) is greater than the pore volume of Node 2 ($Pore\_sl_2$) and the water level in Node 1 is less than the pore volume in Node 1 ($Pore\_sl_1$) and the canopy fraction (f_C) is greater than zero, transfer as much excess water to Node 1 before computing the runoff. First, compute the maximum amount of water that can be transferred from Node 2 ($\Delta Wlevel2\_max$). The actual change in the water level of Node 1 ($\Delta Wlevel1$) is the minimum of $\Delta Wlevel2\_max$ adjusted for the canopy fraction, and the amount of water necessary to maximize the water content of Node 1 ($Pore\_sl_1 - Wlevel_1$). The actual change is added to the water level of Node 1. Finally, the actual change, adjusted for the canopy fraction, is subtracted from Node 2.

Step 12: Transfer excess water in Node 1 to runoff.

Explanation: If the water level of Node 1 ($Wlevel_1$) is greater than the pore volume of Node 1 ($Pore\_sl_1$), transfer the excess water to runoff. The canopy fraction (f_C) is used to compute the weighted contribution of Node 1 to the runoff.

Step 13: Transfer excess water in Node 2 to runoff.

Explanation: If the water level of Node 2 ($Wlevel_2$) is greater than the pore volume of Node 1 ($Pore\_sl_2$), transfer the excess water to runoff. The canopy fraction (f_C) is used to compute the weighted contribution of Node 2 to the runoff.

Routine Output: The routine returns the water level for each node, the net infiltration into the bedrock, and the runoff from the cell.

G3.2 THE GROUP BALANCE MODEL

With the exception of the outlet cell in the watershed, runoff from one cell becomes run-on for another cell. Run-on is an additional source of water for infiltration into the soil. MASSIF keeps track of runoff and run-on for each cell. The cell indices of upstream contributors, computed by the *Upstream* routine, is contained in the vector Upstream. The water available for infiltration in an individual cell consists of the runoff from these upstream contributors, the cell precipitation, and the cell snowmelt.

The *GroupBalance* routine models the run-on/runoff connection between the individual cells in the watershed. The routine begins at the top of the watershed and computes the infiltration/runoff for this top-most cell using the cell balance model (*Balance*). It then proceeds to the next lower cell in the watershed and does the same for it. The routine proceeds through the entire watershed and ends at the lowest cell. Runoff from this last cell exits the watershed. Because the cells in the geospatial files describing the watersheds are ordered according to elevation, the progression from highest to lowest elevation cells occurs naturally.

The calculation of runoff and infiltration from individual cells when available water exists (i.e., when it rains or when there is snowmelt) is accomplished by two calls to the *Balance* routine. The first call accounts for infiltration and runoff during the precipitation event. In this call, both runoff and infiltration can take place. Soil saturated conductivity limits create the possibility of water contents greater than the field capacity at the end of a storm. Therefore, water can still drain from the soil after the storm has ended. The second call to *Balance* deals with this "drainage" stage. Although infiltration is possible during this second stage, addition runoff is not possible.

The steps in the group balance model (*GroupBalance*) are listed below. Only the processes within the loop that proceeds through the cells in the watershed are enumerated. The initialization and output that occurs before and after the loop are obvious. Note that a certain amount of logic has been added to avoid unnecessary calls to the *Balance* routine. This is done to minimize execution time.

Step 1: The runoff and run-on for the cell are each initialized to 0 mm.

Step 2: Calculate the run-on to the cell.

Explanation: *Upstream* is a vector of vectors. The vector component Upstream_n is, itself, a vector that contains the indices of the upstream contributors to cell n. The first contributor is listed as the second element of this vector; the second contributor is listed as the third element, and so on. There are no upstream contributors if this vector ($Upstream_n$) has only one element. If the length of $Upstream_n$ is greater than one, the run-on to cell n is set equal to the sum of the runoff of the upstream contributors.

Step 3: Compute the water available to the soil.

Explanation: The water available to the soil is the sum of the precipitation (when it does not appear as snow), the snowmelt, and the run-on. Note that the variable $NetPrecip_n$ is equal to zero when precipitation occurs as snow, and is equal to the cell precipitation when precipitation occurs as rain.

Step 4: Compute the fraction of the day during which precipitation takes place.

Explanation: This calculation is performed in anticipation of the calls to the *Balance* routine. It denotes the fraction of the day when the available water is exposed to the soil surface. Note that special provision is made for the case when precipitation is absent and snowmelt is present. For this specific case, the precipitation duration (normally set to zero in the absence of precipitation) is set to 12 hours. This allows a 12-hour exposure time for snowmelt to seep into the soil when precipitation does not occur.

Step 5: Add the available water to the nodes in Layer 1 (Nodes 1 and 2).

Explanation: The sum of the runon, snowmelt, and rainfall constitutes the water available for infiltration. This available water is added to Nodes 1 and 2. This is the initial condition at the start of the day. Note that the available water may exceed the holding capacity of the soil in this layer. This condition is examined in the following steps. Excess water is manifested as either infiltration or runoff in the subsequent portion of the calculation.

Step 6: If any water level of the current node exceeds the field capacity, implement the balance routine.

Explanation: There is no need to redistribute water using the *Balance* routine if the field capacity in at least one of the soil nodes is not exceeded.

Step 6a: If there is water available to the soil surface, separate the precipitation/ snowmelt event from the subsequent drainage phase.

Explanation: When water is available, the soil-filling phase is separated from the subsequent soil-draining phase. The first call to *Balance* computes net infiltration and runoff during the precipitation/snowmelt event. The second call to *Balance* computes net infiltration during the draining phase. No runoff can occur during the draining phase.

Step 6b: If there is no precipitation or snowmelt, the entire day is a drainage period.

Explanation: This condition can occur if draining and evapotranspiration that took place during the previous day was insufficient to lower the water levels in the soil to the field capacity. Only one call to *Balance* is needed under these circumstances.

Routine Output: The *GroupBalance* routine returns the water level for the four nodes, the net infiltration, run-on, and runoff for the day for every cell in the watershed.

G3.3 UPSTREAM CONTRIBUTORS TO RUN-ON

The run-on to a specific cell is equal to the runoff from the "upstream" cells that are above it. To calculate run-on, one needs a list of the contributing "upstream" cells for every cell in the watershed. However, the geospatial file describing the watershed lists the ID number of a single "downstream" cell for every cell in the watershed, to which the runoff flows. Only the last cell in the geospatial file, the exit cell, lacks a "downstream" cell. For this last cell, the "downstream" cell ID is listed as "−3."

The *Upstream* routine creates a vector of cell indices of the "upstream" cells that contribute to run-on for each cell in the watershed. It is easiest to describe this vector by an example. Suppose that the 50th cell in the watershed is the cell of interest and that the 25th, 35th, and 49th cells are the "upstream" cells that contribute to the run-on to the 50th cell. The upstream vector for the 50th cell would be:

$$\text{upstream}_{50} = \begin{pmatrix} 50 \\ 25 \\ 35 \\ 49 \end{pmatrix} \quad \text{(Eq. G-2)}$$

This vector contains four elements. The first element is the index of the cell for which the run-on is to be calculated. The remaining elements of the vector are the indices of the upstream contributing cells. The lengths of the actual vectors vary with the number of upstream contributors.

Some cells in the watershed have no "upstream" cells that contribute to run-on. The 1st cell in the watershed is such a cell because it has the highest elevation in the watershed. The upstream vector for the 1st cell in the watershed is always a vector with a single element:

$$\text{upstream}_1 = (1) \quad \text{(Eq. G-3)}$$

It is important to note that the cell ID number is not the cell index. The cell ID number has meaning only in the context of the software used to generate the geospatial file.

The steps in the *Upstream* routine are:

Step 1: Create the first element in the upstream vector of cell n for all cells.
Explanation: The first element of the upstream vector is the index of the cell.

Step 2: Find the downstream cell to which cell n contributes to run-on.
Explanation: Beginning with the 1st cell in the watershed, search for the ID number of the downstream cell. Because the cells are sorted by elevation, the downstream cell must have an index greater than the contributing cell (*m*>*n*). If the ID number of the downstream cell (*DnStn*) is the same as the cell ID number of the cell being checked (*locidm*), the index of the

contributing cell is added to the upstream vector of cell m (*upstreamm*). If the downstream cell ID has not been found after examining the last cell in the watershed (*Ncells*), an error message is generated that states that the geospatial file had not been sorted correctly at the time of its generation and the calculation is terminated.

Routine Output: The *Upstream* routine creates a vector for each cell that lists the indices of the contributors to run-on.

G3.4 WATER ADJUSTMENT FOR THE VARYING CANOPY COEFFICIENT (f_C)

The canopy coefficient can change from day to day when it is coupled to the crop coefficient (K_{cb}). In order to conserve water, the water level in the expanding node in the top soil layer must be adjusted to account for the water being transferred from the shrinking node in the top soil layer (Figure G-2).

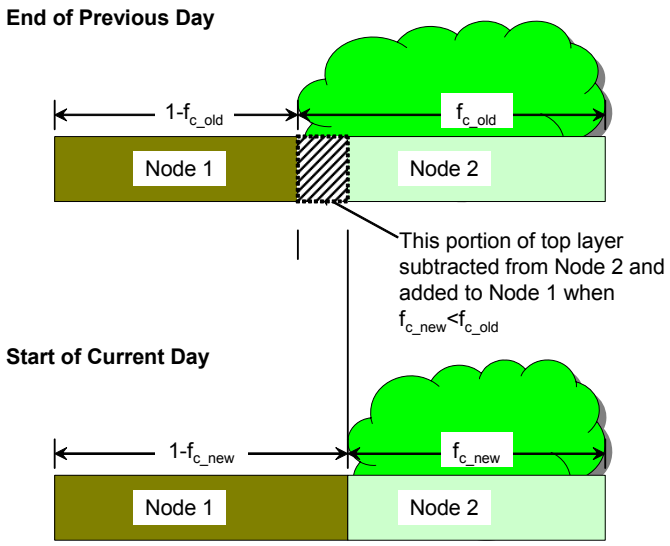

Source: Output DTN: SN0701T0502206.037.

Figure G-2. Daily Variation of Vegetative Canopy

Consider the case where the new canopy coefficient is less than the old canopy coefficient ($f_{c\_new}<f_{c\_old}$). The water level of Node 2 (the canopy region) remains the same. However, the water level of Node 1 (the evaporation region) must be adjusted. Before the change, the water is Node 1 is:

$$Water\_old_1 = A \cdot \left(1 - f_{c\_old}\right) \cdot Wlevel\_old_1 \qquad \text{(Eq. G-4)}$$

where A is the area of of the node. The water "transferred" from Node 2 to Node 1 is:

$$\Delta Water = A \cdot \left(f_{c\_old} - f_{c\_new} \right) \cdot Wlevel_2 \qquad \text{(Eq. G-5)}$$

The new water level in Node 1 is:

$$Wlevel\_new_1 = \frac{Water\_old_1 + \Delta Water}{A \cdot \left(1 - f_{c\_new} \right)}$$

$$Wlevel\_new_1 = \frac{\left[\left(1 - f_{c\_old} \right) \cdot Wlevel\_old_1 + \left(f_{c\_old} - f_{c\_new} \right) \cdot Wlevel_2 \right]}{\left(1 - f_{c\_new} \right)} \qquad \text{(Eq. G-6)}$$

Now consider the alternate case where the new canopy coefficient is greater than the old canopy coefficient ($f_{c\_new} > f_{c\_old}$). The water level of Node 1 (the evaporation region) remains the same. However, the water level of Node 2 (the canopy region) must be adjusted. Before the change, the water in Node 2 is:

$$Water\_old_2 = A \cdot f_{c\_old} \cdot Wlevel\_old_2 \qquad \text{(Eq. G-7)}$$

The water "transferred" from Node 1 to Node 2 is:

$$\Delta Water = A \cdot \left[\left(1 - f_{c\_old} \right) - \left(1 - f_{c\_new} \right) \right] \cdot Wlevel_1$$

$$\Delta Water = A \cdot \left(f_{c\_new} - f_{c\_old} \right) \cdot Wlevel_1 \qquad \text{(Eq. G-8)}$$

The new water level in Node 2 is:

$$Wlevel\_new_2 = \frac{Water\_old_2 + \Delta Water}{A \cdot f_{c\_new}}$$

$$Wlevel\_new_2 = \frac{f_{c\_old} \cdot Wlevel\_old_2 + \left(f_{c\_new} - f_{c\_old} \right) \cdot Wlevel_1}{f_{c\_new}} \qquad \text{(Eq. G-9)}$$

G3.5 THE SNOW MODEL

The snow model in MASSIF is simple. When the average temperature for the day is less than or equal to 0°C, precipitation occurs in the form of snow, and the "net precipitation" (i.e., the precipitation that can enter the soil) is equal to zero. When the average daily temperature is greater than 0°C, precipitation is manifested as rain, and the "net precipitation" is equal to the daily precipitation. Accumulated snow melts at a rate that is linearly proportional to the average

daily temperature (in °C). Snowmelt is tracked separately from net precipitation, even though both are available to the soil surface.

Sublimation is crudely modeled in MASSIF. The reference for sublimation of snow packs gives an estimate of the fraction of the snowpack that is lost over the entire snow season; no estimate of daily loss to sublimation is given. In the absence of a phenomenological model or a correlation, the sublimation fraction is applied at the time of precipitation (Section 6.4.2). As an example, suppose the seasonal sublimation fraction is 0.1. If the precipitation is 10 mm for a particular day, 9 mm of snow is added to the snow level. The remaining 1 mm of precipitation is credited to sublimation.

The routine *SnowB* computes the snow level for each cell in the watershed. The steps for each cell in *SnowB* are:

Step 1: Initialize the $SnowMelt_n$ and $Sublimation_n$ to zero. Initialize the $NetPrecip_n$ to the precipitation.

Step 2: If the average temperature of the day (T_{avg}) for the cell is less than or equal to zero, then

a) Set the sublimation for cell n ($Sublimation_n$) to the product of the precipitation for cell n ($precip_n$) and the sublimation coefficient ($C_{sublime}$).

b) Add the precipitation ($precip_n$) to the snow level ($Slevel_n$) and subtract the sublimation ($Sublimation_n$) to get the new snow level.

c) Set the net precipitation ($NetPrecip_n$, precipitation available for infiltration) to zero.

Step 3: If the average temperature of the day (T_{avg}) for the cell is greater than zero and the snow level for cell n ($SnowMelt_n$) is greater than zero, then

a) Set the snowmelt for cell n ($SnowMelt_n$) to the minimum of

(1) the product of the average temperature (T_{avg}) and the snowmelt coefficient ($C_{snowmelt}$), or

(2) the total amount of snow for cell n ($Slevel_n$).

Routine Output: *SnowB* returns the snow level, net precipitation, sublimation, and snowmelt for every cell in the watershed.

G4. EVAPOTRANSPIRATION

Evapotranspiration is the term applied for the transport of water to the atmosphere from the soil. It is so named because the mechanisms of evaporation from the soil and moisture transport through the plant structure and from the plant surfaces are difficult to completely separate. Hence the term implies an approach in which both phenomena are modeled within a single analytic framework.

The evapotranspiration paths, as contained in MASSIF, are shown below (Figure G-3). Nodes 1, 2, and 3 collectively describe the root zone. Node 4 extends from the bottom of the root zone to the bedrock. The top layer of the soil is divided into two nodes. Node 1 describes the near-surface bare soil region that lies outside of the vegetative canopy. Within Node 1, short term evaporative processes are modeled explicitly. Under the vegetative canopy (Node 2), the soil is shaded and evaporation rates are slower. The evaporative mechanisms in Nodes 2 and 3 are actually integrated into the correlations for transpiration. Transpiration is also attributed to the bare soil region (Node 1). This is because plant roots extend radially beyond the surface vegetative cover.

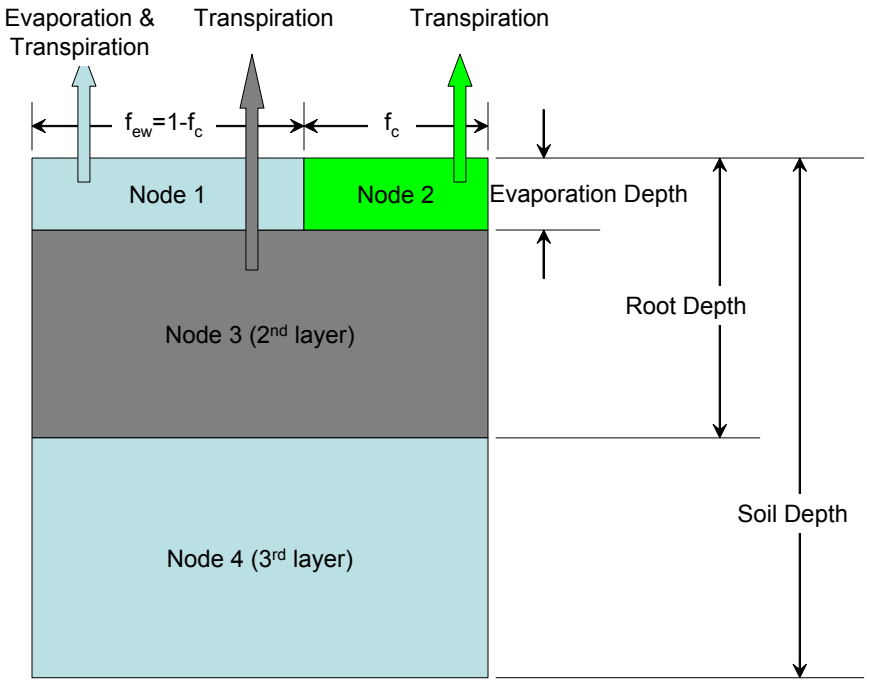

Source: Output DTN: SN0701T0502206.037.

Figure G-3. Evaporation and Transpiration in a Soil Cell

The foundation for the evapotranspiration model in MASSIF is the dual crop coefficient approach described in FAO-56 (Allen et al. 1998 [DIRS 157311], Chapter 7), and in a subsequent publication (Allen et al. 2005 [DIRS 176207]) that supports FAO-56. Within the FAO-56 procedure, water is presumed to drain without limitation to the field capacity whenever a surplus of water is introduced into the soil. The curve number approach can be used directly with the FAO-56 models when runoff is of interest. However, MASSIF utilizes saturated conductivity limits for the rock and soil to determine runoff. To accommodate this approach, the FAO-56 procedure has been adapted to the structure of MASSIF.

In FAO-56, the primary water balance is applied to the root zone, which is a combination of Nodes 1, 2, and 3 in the MASSIF calculation. MASSIF deals with evaporation in the bare soil region (Node 1) in the same way as FAO-56. The difference is that FAO-56 does not deal with the zone described by Node 2 explicitly. MASSIF must model Node 2 explicitly in order to deal

with the flow limits within the soil. This impacts the partitioning of transpiration within the root zone. Publications subsequent to FAO-56 (Allen et al. 2005 [DIRS 176207]) correlate the fraction of the transpiration that takes place in the evaporation zone (Node 1). A similar approach has been used to predict the fraction of transpiration that takes place in Node 2.

G4.1 REFERENCE EVAPOTRANSPIRATION

The reference evapotranspiration (ET_0) is the evapotranspiration that takes place for a reference vegetation (the reference grass) under the condition of adequate soil moisture content. It takes into account the amount of solar insolation and reference atmospheric conditions that affect the transport of water. Actual evapotranspiration (ET) is calculated by modifying the reference evapotranspiration (ET_0) for actual soil moisture contents and actual atmospheric conditions. The calculation of ET_0 is documented in Appendix C, which is used as the reference for the equations used in MASSIF. The steps enumerated in Appendix C have been parsed into several routines in MASSIF for reasons of calculation efficiency. The steps numbers that follow in this section correspond to the steps in the individual MASSIF routines and should not be confused with the step numbers in Appendix C.

G4.1.1 Calculation of Reference ET

The steps of the routine that actual produces ET_0 are examined first. The steps of individual supporting routines are enumerated after that.

The steps of the ET_0 routine are:

Step 1: Calculate the actual vapor pressure for the entire domain (Equation C-2).
Explanation: This quantity is used in the calculation of diffuse and direct components of the solar insolation. A single value is used to model the air mass through which the scattering takes place.

Step 2: Calculate the solar insolation on a horizontal surface.
Explanation: The solar insolation on a horizontal surface is calculated in routine R_{smhor_func}.

Step 3: Calculate the diffuse and direct components of solar insolation
Explanation: The diffuse and direct components of solar insolation are calculated in routine *DiffuseDirect*. Breaking solar insolation into diffuse and direct components is done in preparation for computing solar insolation on inclined surfaces.

The following steps take place for each cell in the watershed:

Step 4: Calculate the slope/aspect correction for direct beam radiation for cell n.
Explanation: The correction is calculated in routine *Rb_fcn*.

Step 5: Calculate the mean vapor pressure for cell n (Equation C-29a).

Explanation: The mean vapor pressure is used in the calculation of the estimated actual vapor pressure (Step 6).

Step 6: Calculate the estimated actual vapor pressure for cell n (Equation C-31).

Explanation: The estimated actual vapor pressure is used to calculate the reference ET.

Step 7: Calculate the net solar radiation on the inclined surface of cell n.

Explanation: The net solar radiation on the inclined surface is calculated in routine *SolarRad_inc*.

Step 8: Calculate the slope of the saturation vapor pressure curve for cell n (Equation C-32).

Explanation: Equation C-32 incorporates the equation for vapor pressure. The function for vapor pressure (*e0*) is used in the MASSIF implementation.

Step 9: Calculate the reference evapotranspiration (ET_0) using the Penman Monteith method for cell n (Equation C-37).

Routine Output: Routine *ET0* returns the reference ET for a 24-hour day in mm of water for every cell in the watershed for the day being analyzed.

G4.1.2 Calculation of Vapor Pressure from Temperature

The vapor pressure is used in the calculation of the Reference ET (Steps 1 and 5 of routine *ET0*). It is written as a simple function of temperature as specified by Equation C-2 in. In Equation C-2, the temperature of interest is a particular temperature: the general dew point temperature. Because the MASSIF implementation uses this vapor pressure in several capacities, the vapor pressure function has been written with a nonspecific temperature. The vapor pressure routine is named *e0*.

G4.1.3 Calculation of "Actual" Solar Insolation on a Horizontal Surface

In Step 2 of the *ET0* routine, the solar insolation on a horizontal surface is calculated from the clear sky solar flux in routine R_{smhor_func}. The steps in routine R_{smhor_func} are:

Step 1: Calculate the clear sky solar flux on a horizontal surface.

Explanation: The clear sky solar flux is calculated in routine R_{sohor_func}.

Step 2: Calculate the estimated "actual" solar flux on a horizontal surface (Equation C-13).

Explanation: This step corrects the clear sky radiation flux for weather conditions.

Step 3: Limit "actual" solar radiation to the value of the clear sky solar flux (sentence following Equation C-13).

Explanation: The clear sky solar radiation is an upper bound for the incident flux.

Routine Output: Routine R_{smhor_fcn} returns a vector containing 1) the extraterrestrial radiation on a horizontal surface, the clear sky radiation, and 2) the estimated "actual" radiation on a horizontal surface.

In **Step 1** of routine R_{smhor_func}, the clear sky solar insolation on a horizontal surface is calculated by a call to routine R_{sohor_func}. The steps in routine R_{sohor_func} are:

Step 1: Calculate the orbit eccentricity of the earth (Equation C-3).

Step 2: Calculate the solar declination (Equation C-4).

Step 3: Calculate the sunset hour angle (Equation C-5).

Step 4: Calculate the extraterrestrial radiation for daily periods (Equation C-6).

Explanation: The extraterrestrial solar radiation is calculated from the distance between the sun and the earth and the daylight period at a specific location on earth.

Step 5: Calculate the sine of the mean solar elevation weighted by extraterrestrial radiation (Equation C-7).

Step 6: Calculate the atmospheric pressure at the average elevation (station) (Equation C-8).

Explanation: This pressure is used to calculate the transmissivity of the air in the weather mass overlying the site on a given day. The average elevation of the domain is used to characterize the weather mass properties.

Step 7: Calculate the precipitable water for the weather mass (Equation C-9).

Step 8: Calculate the 24-hr transmissivity for beam radiation (Equation C-10).

Step 9: Calculate the 24-hr transmissivity for diffuse radiation (Equation C-11).

Step 10: Calculate the clear sky solar radiation over a 24 hour period (Equation C-12).

Routine Output: Routine R_{sohor_fcn} returns a vector containing 1) the extraterrestrial radiation on a horizontal surface and 2) the clear sky radiation.

G4.1.4 Partition the Total Incident Radiation into Diffuse and Direct Components

In Step 3 of the *ET0* routine, the solar insolation on a horizontal surface is partitioned into diffuse and direct components. The direct component can be partially or totally obscured from particular surface depending upon the slope and azimuth of the surface. The diffuse component reaches all surfaces independent of the surface orientation.

The routine *DiffuseDirect* performs the partitioning. The steps in *DiffuseDirect* are:

Step 1: Calculate the total short wave transmissivity (Equation C-14).

Step 2: Calculate the diffuse radiation transmissivity (Equation C-15).

Step 3: Calculate the direct beam transmissivity (Equation C-16).

Step 4: Calculate direct beam radiation on a horizontal surface (Equation C-17).

Step 5: Calculate diffuse radiation on a horizontal surface (Equation C-18).

Step 6: Calculate the anisotropic index (Equation C-21).

Step 7: Calculate the modulating function for horizontal brightness (Equation C-22).

Routine Output: Routine *DiffuseDirect* returns a matrix that contains the direct beam radiation, the diffuse radiation, the anisotropic index, and the modulating function.

G4.1.5 Calculation of the Slope/Azimuth Correction Factor for Direct Beam Radiation

In Step 4 of routine *ET0*, the correction factor for direct beam radiation for cell n (R_b) is calculated. The quantity R_b is the fraction of daily direct beam radiation for a horizontal surface that occurs on an inclined surface. The calculation of R_b, documented in Appendix C2, is performed in an Excel workbook (*Rb_ver1.2.03.xls*, Output DTN: SN0602T0502206.003), which is located in the Massif directory. The worksheet *Rb_LUT_ETo* contains a look-up table of R_b values. A portion of this worksheet is shown below (Table G-1) to make the description easier.

Table G-1. A Portion of the R_b Look-up Table

ID	1	2	3	4	5
Azimuth (deg)	0	0	0	0	0
Slope (deg)	0	2.5	7.5	15	25
DOY (J) \ K1	0	2.5	7.5	15.0	25.0
1	1.00	0.90	0.71	0.42	0.10
2	1.00	0.90	0.71	0.42	0.10
3	1.00	0.90	0.71	0.43	0.10
4	1.00	0.90	0.71	0.43	0.10
5	1.00	0.90	0.71	0.43	0.11
6	1.00	0.90	0.71	0.43	0.11

Source: Output DTN: SN0602T0502206.003, worksheet *Rb_LUT_ETo.*

Each row of the worksheet contains values of R_b for a particular day of the calendar year. Each column of the worksheet contains values of R_b for a specific slope/azimuth combination.

To use this worksheet, one first determines the four slope/azimuth columns listed in the table that bound the slope/azimuth of the cell of interest. Given the day of the year, one now has four

values of R_b for four slope/azimuth combinations. An interpolation routine is then used to determine the value of R_b for the cell of interest.

To maximize computational efficiency, the four columns appropriate to each cell are calculated in Step 6 of the *Massif* driver. The interpolation coefficients are calculated in Step 7 of the *Massif* driver. Both of these steps are executed before the daily calculations are executed, thereby eliminating redundant calculations. Only the final interpolation for R_b is conducted daily within the *ET0* routine.

The actual reading of the R_b look-up table takes place in *RefET.xmcd*. After the table is read into a variable called R_{b_lookup}, the table is cropped so that only the tabulated values of R_b remain; values of slope, aspect, and day of year are eliminated. These values are "hard wired" into the routine that finds the column indices. The Excel file that is read (*Rb_ver1.2.03.xls*) is identical to the one entered into Output DTN: SN0602T0502206.003.

Routine *Index_Rb_fcn* finds the four columns in the R_b look-up table that bound the slope/azimuth combination of a particular cell. This routine contains the following steps:

Step 1: Define Slope and Azimuth in terms of degrees.

Explanation: The default "unit" in Mathcad for angular displacement is radians. The angles in the look-up table are in degrees. The variables "azimuth" and "slope" are divided by the Mathcad unit "deg" so that their numerical value reflects an implied unit of degrees.

Step 2: Determine the slope indices that bound the input value of "slope."

Explanation: The look-up table contains values of R_b for slope values of 0, 2.5, 7.5, 15, 25, and 40 degrees. For a given value of "slope", the correct slope index pair is selected.

Step 3: Determine the azimuth indices that bound the input value of "azimuth."

Explanation: The look-up table contains values of R_b for azimuth values of 0, 30, 60, 90, 120, 150, 180, 210, 270, 300, 330, and 360 degrees. For a given value of "azimuth", the correct azimuth index pair is selected.

Routine Output: The four column indices that bound the input values of "slope" and "azimuth" are returned as a vector containing four elements.

The interpolation scheme (Figure G-4) used to obtain a value for R_b is a "nearest neighbor approach in which the weighted contribution of the four nearest neighbors is inversely proportional to the normalized distance to the "neighbor." The interpolation space is defined by the low and high slope and azimuth values (Az_{lo}, Az_{hi}, Sl_{lo}, Sl_{hi}) extracted from the R_b look-up table for a specific day of the year. The distances from the slope/azimuth combination of interest (Az, Sl) are $L1$, $L2$, $L3$, and $L4$ (see diagram below).

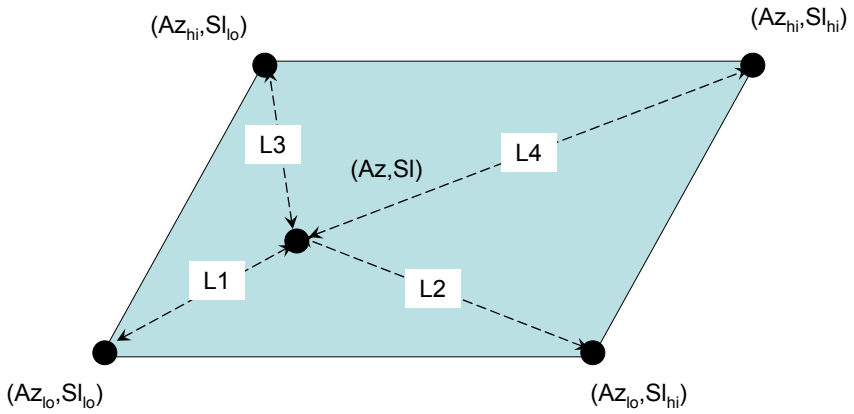

Source: Output DTN: SN0701T0502206.037.

Figure G-4. Interpolation Point Surrounded by Nearest Neighbors

The interpolated value in the Z direction (Z(Az,Sl)), using the nearest neighbor approach, is:

$$Z(Az,Sl) = \frac{\frac{Z(Az_{lo},Sl_{lo})}{L1} + \frac{Z(Az_{lo},Sl_{hi})}{L2} + \frac{Z(Az_{hi},Sl_{lo})}{L3} + \frac{Z(Az_{hi},Sl_{hi})}{L4}}{\frac{1}{L_1} + \frac{1}{L_2} + \frac{1}{L_3} + \frac{1}{L_4}} \quad \text{(Eq. G-10)}$$

where

$$\begin{pmatrix} L1 \\ L2 \\ L3 \\ L4 \end{pmatrix} = \begin{bmatrix} \sqrt{(Az - Az_{lo})^2 + (Sl - Sl_{lo})^2} \\ \sqrt{(Az - Az_{lo})^2 + (Sl - Sl_{hi})^2} \\ \sqrt{(Az - Az_{hi})^2 + (Sl - Sl_{lo})^2} \\ \sqrt{(Az - Az_{hi})^2 + (Sl - Sl_{hi})^2} \end{bmatrix}$$

This can be written as:

$$Z(Az,Sl) = C_{Rb} \cdot \begin{pmatrix} Z(Az_{lo},Sl_{lo}) \\ Z(Az_{lo},Sl_{hi}) \\ Z(Az_{hi},Sl_{lo}) \\ Z(Az_{hi},Sl_{hi}) \end{pmatrix} \quad \text{(Eq. G-11)}$$

where

$$C_{Rb} = \frac{1}{\left(\frac{1}{L1} + \frac{1}{L2} + \frac{1}{L3} + \frac{1}{L4}\right)} \cdot \begin{pmatrix} L1^{-1} \\ L2^{-1} \\ L3^{-1} \\ L4^{-1} \end{pmatrix}$$

The formulation shows that the interpolation coefficients (C_{Rb}) can be calculated separately from the actual interpolation. The interpolation coefficients are calculated in the routine C_{Rb_fcn}. The steps in this routine are as follows:

Step 1: Define Slope and Azimuth in terms of degrees.

Explanation: The default "unit" in Mathcad for angular displacement is radians. The angles in the look-up table are in degrees. The variables "azimuth" and "slope" are divided by the Mathcad unit "deg" so that their numerical value reflects an implied unit of degrees.

Step 2: Define the low and high ends of Azimuth.

Explanation: The R_b look-up table has R_b values for azimuths in 30-degree increments. The low bounding value of azimuth ($Azimuth_{lo}$) in the table is equal to the input value rounded down to the nearest integer multiple of 30. The high bounding value of azimuth ($Azimuth_{hi}$) is equal to $Azimuth_{lo}$ plus 30.

Step 3: Define the low and high ends of Slope.

Explanation: The look-up table contains values of R_b for slope values of 0, 2.5, 7.5, 15, 25, and 40 degrees. The values of $Slope_{lo}$ and $Slope_{hi}$ bound the input value of "slope".

Step 4: Calculate the interpolation distances ($L1$, $L2$, $L3$, and $L4$).

Explanation: These are the distances to the four nearest neighbors.

Routine Output: The routine returns a vector containing the four interpolation coefficients. When all of the interpolation distances are nonzero, the formula derive above is used. When one of the distances is zero, the standard formula contains a singularity. This situation occurs when one of the four bounding slope/azimuth combinations in the table is identical to the cell slope/azimuth pair. In this case, the interpolation coefficient vector must contain three zeros and one element of unity. This is performed in this routine by returning a vector of logical statements of the form "L*=0". When this logical statement is true, the statement returns a value of unity. When this logical statement is false, the statement returns a value of zero.

The actual calculation of R_b for cell n on a particular day of the year is performed in routine *Rb_fcn*. The calculation is performed in a single step. The interpolation coefficients (C_{Rb}), interpolation indices (*Index_Rb*), and day of the year (*DOY*) are passed into the routine. The routine returns the sum of the product of the interpolation coefficients and the appropriate values from the R_b look-table.

G4.1.6 Calculation of Solar Radiation on an Inclined Surface

The calculation of solar radiation on an inclined surface is performed in routine *SolarRad_inc*. The steps in this routine are as follows:

Step 1: Calculate the direct beam radiation on the inclined surface (Equation C-20).

Step 2: Calculate the diffuse radiation on the inclined surface (Equation C-23).

Step 3: Calculate the reflected radiation from lower lying terrain (Equation C-24).

Step 4: Calculate the total radiation received by the inclined surface (Equation C-25).

Step 5: Project the total radiation to a horizontal equivalent (Equation C-26).

Step 6: Calculate the horizontal equivalent for net short-wave radiation (Equation C-34).

Step 7: Calculate the net outgoing long-wave radiation (Equation C-35).

Step 8: Calculate the net radiation from the surface (Equation C-36).

Routine Output: This routine returns the net solar radiation on a single inclined surface.

G4.2 EVAPOTRANSPIRATION

Evapotranspiration from the soil is based upon the FAO-56 formulation. Short-term evaporation is extracted from a thin layer of soil lying outside the vegetative canopy cover (Node 1). Transpiration is extracted from the entire root zone (Nodes 1, 2, and 3). A paper by Allen et al. (2005 [DIRS 176207]) expands upon the FAO-56 procedure and presents a partition function that predicts the fraction of transpiration that comes from the evaporation layer (Node 1). This partitioning function has been extended in MASSIF to predict the fraction of transpiration that comes from the canopy zone (Node 2).

G4.2.1 Calculation of ET

The routine *ET* calculates evapotranspiration for all the cells in the watershed for a given day. All of the steps enumerated in this description apply to individual cells in the watershed. The steps in routine *ET* are:

Step 1: If the thickness of the 1st layer is zero, the evaporation and transpiration are each zero.

Explanation: When the soil depth for a particular cell is zero, the thicknesses of all the nodes in that cell are all set to zero in the *cdepth* routine. In the absence of soil, there is no storage of water in soil and, consequently, neither evaporation nor transpiration.

Step 2: Calculate the evaporation depletion depth.

Explanation: The evaporation depletion depth is calculated in routine D_{e_fcn}. The evaporation depletion depth is used in the calculation of evaporation from Node 1.

Step 3: Calculate the daily evaporation.

Explanation: For evaporation to occur in the evaporation layer (Node 1), the water level in that node must be greater than the half of the wilting point (Allen et al. 1998 [DIRS 157311], Figure 38 and discussion of soil evaporation reduction coefficient on pp. 144 to 146). Also, the snow level must equal zero because the presence of snow will strongly inhibit evaporation. When these conditions are met, the soil evaporation is calculated in three steps.

Step 3a: Calculate the evaporation reduction coefficient (Allen et al. 1998 [DIRS 157311], Equation 74 and Figure 38).

Explanation: The evaporation reduction coefficient is calculated in routine K_{r_fcn}.

Step 3b: Compute the evaporation coefficient (Allen et al. 1998 [DIRS 157311], Equation 71).

Explanation: The evaporation coefficient is calculated in routine K_{e_fcn}.

Step 3c: Calculate the daily evaporation (Allen et al. 1998 [DIRS 157311], Equation 69).

Explanation: The daily evaporation flux is equal to the product of the evaporation coefficient (K_e) and the reference evapotranspiration (ET_0). This is a flux that has been "smeared" over both Nodes 1 and 2. Evaporation can reduce the water level in Node 1 only to the wilting point. Therefore, the upper limit to the daily evaporation is the water content in Node 1 in excess of the wilting point multiplied by the complement of the vegetative canopy (f_c).

Step 4: Subtract the daily evaporation from the water level in the evaporation node.

Explanation: The daily evaporation flux is a quantity that has been "smeared" over both Nodes 1 and 2. However, the water comes only from Node 2. Hence, the flux must be divided by the complement of the vegetative canopy (f_C) before it is subtracted from the water level in Node 1.

Step 5: Compute the upper limits for transpiration from each node.

Explanation: Transpiration can reduce the water level in a node only to the wilting point. The **max** function with a lower limit of 0 mm is used in case the machine precision of the previous calculations has reduced the water level to something slightly below the wilting point.

Step 6: Compute the maximum value of total transpiration.

Explanation: The maximum possible transpiration in the cell is equal to the sum of the maximum possible transpirations in each node in that cell.

Step 7: Compute the total transpiration.

Explanation: When the maximum possible total transpiration is greater than zero, the total transpiration is computed in four steps.

Step 7a: Calculate the root zone depletion depth (Allen et al. 1998 [DIRS 157311], p. 167).

Explanation: The root zone depletion depth is calculated in routine D_{r_fcn}. It is based upon all the water in the entire root zone (Nodes 1, 2 and 3).

Step 7b: Calculate the unadjusted evapotranspiration (Allen et al. 1998 [DIRS 157311], Equation 69).

Explanation: "Unadjusted" means that the transpiration portion has not yet been adjusted for water stress.

Step 7c: Calculate the water stress coefficient (Allen et al. 1998 [DIRS 157311], Equation 84).

Explanation: The water stress coefficient is calculated in routine K_{S_fcn}.

Step 7d: Calculate the total daily transpiration (Allen et al. 1998 [DIRS 157311], Equation 80).

Explanation: The total daily transpiration is limited by the amount of water in the root zone in excess of the wilting point.

Step 8: Initialize the transpiration partition by placing all of the transpiration in the 2nd layer (Node 3).

Explanation: This is an initial guess that will be modified per the transpiration partitioning algorithms.

Step 9: Calculate the transpiration in the evaporation zone (Node 1) if the water level in the node is greater than the integrated wilting point.

Explanation: The fraction of the transpiration that comes from the evaporation layer (K_{tp}) is computed according to a paper by Allen et al. (2005 [DIRS 176009]) that expands the FAO-56 procedure. Equation 29 of that paper states that the partitioning coefficient (calculated in routine K_{tp_fcn}) is:

$$K_{tp} = \left(\frac{1 - \frac{D_{ep}}{TEW}}{1 - \frac{D_r}{TAW}} \right) \cdot \left(\frac{Z_e}{Z_r} \right)^{0.6} \qquad \text{(Eq. G-12)}$$

Because there is no irrigation in the MASSIF calculation, the evaporation depletion depth (D_e) used in this calculation is identical to the evaporation precipitation-depletion depth (D_{ep}) cited in the paper.

The transpiration in the evaporation layer (Node 1) is equal to the product of the partition coefficient (K_{tp}) and the total transpiration. The transpiration in the evaporation node (Node 1) is limited to the maximum possible transpiration computed in Step 6.

Step 10: Calculate the transpiration in the canopy zone (Node 2) if the water level in the node is greater than the integrated wilting point.

Explanation: As mentioned earlier, neither FAO-56 (Allen et al. 1998 [DIRS 157311]) nor subsequent expansions of the procedure deal explicitly with the zone described by Node 2. Therefore MASSIF treats this zone in a manner directly analogous to the evaporation zone. First a depletion depth is calculated for the canopy node (D_c) using the same formula used to compute D_e. Then a partitioning function is computed for the canopy zone (K_{tp_c}) using the same formula used for K_{tp} (above) with D_c substituted for D_e. The transpiration in the canopy node (Node 2) is limited to the maximum possible transpiration computed in Step 6.

Step 11: Recalculate the transpiration in the 2nd layer (Node 3).

Explanation: The transpiration in Node 3 is set equal to the total transpiration minus the sum of the transpiration in the evaporation and canopy nodes (Nodes 1 and 2). The upper bound on transpiration in the 2nd layer, computed in Step 6, is enforced.

Step 12: Recalculate the total transpiration.

Explanation: The total transpiration is set equal to the sum of the transpiration in Nodes 1, 2, and 3. This step is necessary because of the upper limit on transpiration enforced on Node 3 in Step 11.

Step 13: Subtract the transpiration from the water level in Node 1.

Step 14: Subtract the transpiration from the water level in Node 2.

Step 15: Subtract the transpiration from the water level in Node 3.

Routine Output: This routine returns the new water levels (*Wlevel*), amount of transpiration (*Transpiration*), and amount of evaporation (*Evaporation*) for each cell for the day examined.

G4.2.2 Evaporation

Evaporation (Section 6.4.4.2) from the evaporation layer (Node 1) is modeled in FAO-56 (Allen et al. 1998 [DIRS 157311], p. 142) as:

$$\text{Evaporation} = K_e \cdot ET_0 \qquad \text{(Eq. G-13)}$$

where K_e is the evaporation coefficient and ET_0 is the reference evapotranspiration (Section G4.1). It is important to note that, even though this component of evaporation comes only from the fraction of soil surface that is both exposed and wetted (f_{ew}), the flux computed by this equation applies to the entire soil surface (i.e., both the exposed and canopy regions). The actual flux from the exposed and wetted surface is:

$$\text{Evaporation}_{\text{exposed\_wetted}} = \frac{K_e \cdot ET_0}{f_{ew}} \qquad \text{(Eq. G-14)}$$

Also note that, because MASSIF does not include irrigation, the exposed and wetted fraction of the soil surface (f_{ew}) is equal to the complement of the canopy coefficient ($1-f_c$, Allen et al. 1998 [DIRS 157311], pp. 147 to 149 including Table 20).

The evaporation coefficient (K_e, calculated in routine *K_{e_fcn}*) is a function of the water in the evaporation layer (Node 1) and the vapor transport limitations at the soil surface. FAO-56 (Allen et al. 1998 [DIRS 157311], Equation 71) models this as:

$$K_e = \min\left[K_r \cdot \left(K_{c\_max} - K_{cb}\right), f_{ew} \cdot K_{c\_max}\right] \qquad \text{(Eq. G-15)}$$

where K_r is the evaporation reduction coefficient that is a function of the evaporation layer water content, K_{cb} is the basal crop coefficient, and K_{c_max} is the maximum value of the evapotranspiration coefficient ($K_c=K_e+K_{cb}$) following rain.

The evaporation reduction coefficient (K_r, calculated in routine *K_{r_fcn}*) accounts for water depletion in the evaporation layer (Node 1). It is discussed in FAO-56 (Allen et al. 1998 [DIRS 157311], pp. 144 to 146). It is modeled in FAO-56 (Allen et al. 1998 [DIRS 157311], Equation 74, Figure 38) as:

$$K_r = \max\left(0, \min\left(\frac{TEW - D_e}{TEW - REW}, 1\right)\right) \quad \text{(Eq. G-16)}$$

where D_e is the evaporation depletion depth, TEW is the total evaporable water, and REW is the readily evaporable water. REW, a property of the soil, is the amount of water that can be evaporated without water transport processes in the soil kicking in. TEW is the total amount of water available for evaporation in a well drained soil. The depletion depth (D_e) is the difference between the water content and the extrinsic field capacity in the evaporation layer. When the evaporation layer is filled to field capacity, the depletion depth is zero. When the evaporation is down to half of the wilting point, the depletion depth is equal to TEW (Allen et al. 1998 [DIRS 157311], Equations 73 and 78). The depletion depth is calculated in routine *D_{e_fcn}*.

G4.2.3 Transpiration

Transpiration, nominally, is water transport from the root zone (Nodes 1, 2, and 3 in MASSIF) to the atmosphere through the plant. In FAO-56 (Allen et al. 1998 [DIRS 157311], p. 135), the transpiration component of ET also includes "a residual diffusive evaporation component supplied by soil water below the dry surface and by soil water from beneath dense vegetation." The equation for transpiration is (Allen et al. 1998 [DIRS 157311], Equation 80):

$$\text{Transpiration} = K_S \cdot K_{cb} \cdot ET_0 \quad \text{(Eq. G-17)}$$

where ET_0 is the reference ET, K_{cb} is the basal "crop" coefficient, and K_S is the water stress coefficient.

G4.2.3.1 Water Stress Coefficient

The water stress coefficient (K_S) models the behavior of plant transpiration as the water content in the root zone drops below "optimum" levels (Allen et al. 1998 [DIRS 157311], Chapter 1). It is modeled in FAO-56 (Allen et al. 1998 [DIRS 157311], Equations 83 and 84) as:

$$K_S = \frac{TAW - D_r}{TAW - RAW} \quad \text{(Eq. G-18)}$$

where $RAW = p_{adj} \cdot TAW$

where TAW is the total available water in the root zone, RAW is the readily available water, p_{adj} is the fraction of TAW that a "crop" can extract from the root zone without suffering water

stress, and D_r is the root zone depletion depth. The "p" is adjusted according to the text at the bottom of page 162 of FAO-56 (Allen et al. 1998 [DIRS 157311]). Calculation of K_S is performed in routine *K_{S_fcn}*, which has the following steps:

Step 1: Calculate the adjusted *p*.

Explanation: The value of *p* is a function of the vegetation type (Section 6.4.4.2). However, *p* is also a function of the "evaporative power of the atmosphere." The text at the bottom of page 162 of FAO-56 (Allen et al. 1998 [DIRS 157311]) states: "A numerical approximation for adjusting *p* for ET_C rate is

$$p = p_{Table\_22} + 0.04 \cdot (5 - ET_C) \quad \text{(Eq. G-19)}$$

where the adjusted p is limited to $0.1 \leq p \leq 0.8$ and ET_C is in mm/day."

Setp 2: Calculate the readily available water (Allen et al. 1998 [DIRS 157311], Equation 83).

Step 3: Return a value of unity for the water stress coefficient if the root zone depletion depth is less than *RAW*.

Explanation: If there is sufficient water in the root zone, there is no water stress (K_S=1).

Step: 4 Return a value for the water stress coefficient according to Equation 84 of FAO-56 (Allen et al. 1998 [DIRS 157311]).

Explanation: The lower bound of 0 for K_S is not enforced here because the upper bound (TAW) for the root zone depletion depth (D_r) is enforced at its calculation.

The root zone depletion depth (routine *D_{r_fcn}*) is the water deficit for the entire root zone. The water levels for Nodes 1, 2 (weighted by the canopy coefficient f_C) and 3 are added, and that sum is subtracted from the integrated field capacity (product of soil field capacity and rooting depth) for the root zone. The difference is the root zone depletion depth.

G4.2.3.2 Calculation of "Crop" Coefficient (K_{cb}) and Canopy Coefficient (f_C)

MASSIF uses the results of satellite imagery coupled with studies of native vegetation to deduce the value of K_{cb} for every cell in the model domain (Section 6.4.4.1). The details of the satellite and plant studies are located in Section 6.5.3 and Appendices D and E. This discussion simply contains the basic implementation aspects.

The basal crop coefficient (K_{cb0}) is linearly related to a corrected satellite signature ($NDVI_{corrected}$):

$$K_{cb0} = C_1 + C_2 \cdot NDVI_{corrected} \quad \text{(Eq. G-20)}$$

$$NDVI_{corrected} = NDVI_{table} \cdot \frac{Annual\_Precip}{Annual\_Precip_{1998}} \cdot PVR$$

where

The quantity $NDVI_{table}$ is extracted from an "NDVI table" in which the satellite signature has been correlated by slope, aspect, and day of the 1998 water year (Output DTN: SN0606T0502206.012). The ratio of the water year precipitations (Annual_Precip/Annual_Precip1998) adjusts the quantity extracted from the NDVI table for precipitation. The quantity PVR (potential vegetative response) adjusts the NDVI signature for the specific cell in the watershed. The PVR constants are found in the geospatial files describing the watersheds. Tabulated quantities normally used in FAO-56 are corrected for actual wind speeds and relative humidities (RHs) (Allen et al. 1998 [DIRS 157311], Equation 70). Because satellite observations are direct, actual wind speeds and RHs are integral and implicit in the NDVI table and PVR adjustments.

The lower bound of K_{cb0} is zero. The upper limit is set to the general upper bound for tall vegetation adjusted for wind speed (u_2), relative humidity (RH_{min}), and plant height (h_{plant}) (Allen et al. 1998 [DIRS 157311], Equation 100 and text following Equation 101 on p. 189). That is:

$$K_{cb0} \leq 1.2 + adjust \qquad \text{(Eq. G-21)}$$

$$adjust = \left[0.04 \cdot \left(u_2 - 2\right) - 0.004 \cdot \left(RH_{min} - 45\right)\right] \cdot \left(\frac{h_{plant}}{3}\right)^{0.3}$$

where

The calculation of K_{cb0} for a single cell is performed in routine *K_{cb0_fcn}*.

The "crop" coefficient is calculated in every cell in the watershed in routine *K_{cb_fcn}*. In addition, this routine calculates the canopy coefficient for every cell from the cell "crop" coefficient using a correlation supplied by FAO-56. Finally, the routine calculates the maximum evapotranspiration coefficient. The steps in routine *K_{cb_fcn}* are:

Step 1: Calculate the ratio of annual precipitations.

Explanation: The satellite signatures are corrected for the cumulative precipitation of the water year of interest (*precip_Kcb*). The reference water year for the NDVI table is 1998. The cumulative precipitation for that water year is $PrecipRef_{NDVI}$.

Step 2: Calculate the day of the water year from the day of the calendar year.

Explanation: The precipitation file gives the day of the calendar year (*DOY*). The NDVI table is listed in terms of the day of the water year (*DOWY*). The routine *DOWY_fcn* calculates the day of the water year from the day of the calendar year based upon a 365 day calendar year.

The following steps apply to each cell in the watershed:

Step 3: Calculate the minimum relative humidity from the cell temperatures.

Explanation: The minimum relative humidity for the day is based on the ratio of the actual vapor pressure for the day and the saturation vapor pressure for the maximum temperature (T_{max}) for the day (Allen et al. 1998 [DIRS 157311], Equation 10). The actual vapor pressure is calculated from the dew temperature (T_{dew}) of the day (Allen et al. 1998 [DIRS 157311], Equation 14).

Step 4: Calculate the adjustment to the maximum basal crop coefficient (Allen et al. 1998 [DIRS 157311], Equation 100).

Step 5: Calculate K_{cb}, K_{c_max}, and f_c when PVR=0.

Explanation: When $PVR=0$, there is no vegetation on the cell. Intermediate calculations are not necessary. The "crop" coefficient (K_{cb}) is set to the minimum value (K_{c_min}), which accounts for diffusive evaporation from the soil. The canopy coefficient (f_c) is set to either 0.0001 ($f_{c\_switch}=-1$) or to the user-specified value. K_{c_max} is set to the adjusted value (Allen et al. 1998 [DIRS 157311], Equation 100). The loop proceeds to the next cell after these assignments are made.

Step 6: Calculate the basal "crop" coefficient from the NDVI data.

Explanation: Routine K_{cb0} (discussed above) is implemented to produce the basal crop coefficient from the NDVI data for the day of interest.

Step 7: K_{cb} is the maximum of K_{cb0} and K_{c_min}.

Explanation: The satellite signature detects the presence of active plants. When the plants are completely dormant or very sparse, the signature is null. Diffusive evaporation from the soil below the evaporation layer cannot be detected by the satellite measurement and is therefore not implicitly part of the correlation for K_{cb0}. Because this component is small for plants at peak transpiration, K_{c_min} is used as a lower bound for K_{cb}.

Step 8: Calculate the upper bound coefficient for ET (K_{c_max}, Allen et al. 1998 [DIRS 157311], Equation 72).

Step 9: Calculate the canopy coefficient, f_C (user specified or FAO-56, Equation 76).

Explanation: The user has the option of specifying a constant, uniform canopy coefficient or using the correlation specified by FAO-56 (Allen et al. 1998 [DIRS 157311], Equation 76) with the *Massif* input variable f_{C_switch}. If f_{C_switch} is equal to −1, the FAO-56 correlation is used. Otherwise, f_C is set equal to the value of f_{C_switch}. When the correlation is used, the canopy coefficient can be no less than 10^{-4}. This prevents singularity from occurring in another part of the calculation.

Routine Output: The routine returns K_{cb}, K_{c_max}, and f_C for every cell in the watershed.

G4.2.3.3 Calculation of Column Indicies for the NDVI Table

The NDVI table, which tabulates the correlation of satellite signature with the slope and azimuth of the terrain, consists of 365 rows and 25 columns. Cell slopes are grouped into 4 bins: 1) less than 5 degrees, 2) five to ten degrees, 3) ten to eighteen degrees, and 4) greater than eighteen degrees. The azimuths are grouped into eight bins: 1) North, 2) Northeast, 3) East, 4) Southeast, 5) South, 6) Southwest, 7) West, and 8) Northwest.

A small portion of the table is shown below (Table G-2). The column that precedes the table lists the days of the water year, which starts on October 1. The first column of the table consists of the correlated satellite signature for cells having a slope less than 5 degrees. Because the slope is small, the correlation with azimuth is negligible. Columns 2 thru 9 correspond to slopes between 5 and 10 degrees. Columns 10 thru 17 correspond to slopes between 10 and 18 degrees. Columns 18 thru 25 correspond to slopes greater than 18 degrees.

Table G-2. A Portion of the NDVI Table

	A'	C'	(A'+C')/2	A'	(A'+E')/2	E'	(A'+E')/2
Day	Flat (<5 deg)	North 5-10 deg	NorthEast 5-10 deg	East 5-10 deg	SouthEast 5-10 deg	South 5-10 deg	SouthWest 5-10 deg
1	0	0	0	0	0	0	0
2	0.0005	0.000334	0.000417	0.0005	0.000584	0.000667	0.000584
3	0.000511	0.000341	0.000426	0.000511	0.000597	0.000682	0.000597
4	0.000524	0.000349	0.000437	0.000524	0.000611	0.000699	0.000611
5	0.000538	0.000359	0.000449	0.000538	0.000628	0.000718	0.000628

Source: Output DTN: SN0701T0502206.037.

For a specific cell, only the row of the table, corresponding to the day of the water year, changes throughout the calculation; the index of the column remains constant. To save calculation time, the appropriate NDVI column index is determined at the beginning of the *Massif* routine; that index is carried into the ET calculation as a routine argument. The routine *Index_NDVI_fcn* determines the appropriate column for a given slope and azimuth.

G4.2.3.4 Transpiration Partition Coefficients

A paper by Allen et al. (2005 [DIRS 176009], Equation 29) presents an algorithm for the fraction of the transpiration (K_{tp}) that comes from the evaporation layer (Node 1):

$$K_{tp} = \left(\frac{1 - \frac{D_{ep}}{TEW}}{1 - \frac{D_r}{TAW}} \right) \cdot \left(\frac{Z_e}{Z_r} \right)^{0.6} \qquad \text{(Eq. G-22)}$$

where D_{ep} is the depletion depth in the portion of the evaporation zone that does not experience irrigation, D_r is the root zone depletion depth, TEW is the total evaporable water, TAW is the total available water, Z_e is the evaporation layer thickness, and Z_r is the root zone depth. The numerator and denominator of the first part of the expression are required to be greater than 0.001. The maximum value of K_{tp} is unity.

A number of slight modifications are required to implement this expression into MASSIF.

1) Because MASSIF is not concerned with irrigation, the evaporation depletion depth (D_e) is identical to D_{ep}.

2) In thin soil regions, the actual soil depth can be less than the rooting depth. Therefore, the thickness of Node 1 ($Thick_1$) is substituted for the evaporation layer thickness (Z_e), and the sum of the thicknesses of Nodes 1 and 3 ($Thick_1$+$Thick_3$) is substituted for the rooting depth (Z_r).

3) The description in the paper by Allen et al. (2005 [DIRS 176009]) requires that the minimum value of both the numerator and the denominator in the first part of the expression be greater than 0.001. The reason for limiting the denominator is obvious. When the depletion depth approaches TAW, the denominator becomes very small and the equation approaches a singularity (infinity). The problem is strictly mathematical, because the upper value of K_{tp} is unity.

The limitation on the numerator appears to be unnecessary and causes a problem with the conservation of water in MASSIF. When the evaporation depletion depth equals TEW, no further transpiration is allowed. If, however, the numerator is numerically kept above 0.001, a portion of the transpiration will be assigned to the evaporation node but will not actually be subtracted from the node; the water will be "lost." Because the limitation in the numerator serves no practical or physical purpose, it is not implemented in MASSIF.

These modifications are implemented in the routine *K_{tp_fcn}*. This routine implements the partitioning coefficient as:

$$K_{tp} = \min\left[\left(\frac{1-\frac{D_e}{TEW}}{\max\left(1-\frac{D_r}{TAW},0.001\right)}\right)\left(\frac{Thick_1}{Thick_1+Thick_3}\right)^{0.6},1\right] \quad \text{(Eq. G-23)}$$

As stated earlier, FAO-56 does not explicitly model the canopy region (Node 2). However, because of the way that MASSIF enforces soil saturated conductivity limits, the water balance for Node 2 must be explicit and complete. This requires that a transpiration partitioning coefficient be developed for Node 2.

The structure of the partitioning coefficient has two parts. The first part compares the water content of the evaporation node to the total water content of the root zone. If most of the water lies in the evaporation zone, then most of the transpiration should come from the evaporation zone; if the evaporation zone is relative dry, most of the transpiration should come from the balance of the root zone. The second part of the partitioning coefficient shows a dependency upon the relative thickness of the evaporation zone and the rooting depth. The exponent of 0.6 is related to a "root extraction pattern" that relates the location of transpiration with the depth of the root section.

Both of these elements are implemented in a partitioning coefficient for the canopy region (K_{tp_c}) by substituting a "canopy depletion depth" (D_c) for the evaporation depletion depth. Otherwise, the equation remains the same. The routine *$K_{tp\_c\_fcn}$* calculates the partitioning coefficient for the canopy region (Node 2) as:

$$K_{tp\_c} = \min\left[\left(\frac{1-\frac{D_c}{TEW}}{\max\left(1-\frac{D_r}{TAW},0.001\right)}\right)\left(\frac{Thick_1}{Thick_1+Thick_3}\right)^{0.6},1\right] \quad \text{(Eq. G-24)}$$

The canopy depletion depth (D_c) is calculated using the same formula as for D_e, with the Node 2 water level used instead of the Node 1 water level. The calculation of D_c is performed in routine *D_{c_fcn}*.

G4.2.3.5 Annual Cumulative Precipitation

The calculation of the "crop" coefficient from the NDVI table requires that the baseline value be adjusted for the cumulative precipitation over the water year (Section G4.2.3.2). Calculation of the cumulative precipitation is performed in routine *precip_Kcb_fcn*. The calculation requires

that the precipitation/weather file 1) begins on October 1, and 2) has at least 365 days. The steps in *precip_Kcb_fcn* are:

Step 1: Calculate the number of full water years in the weather file.

Explanation: The precipitation may include more than one water year. When actual weather data is used, one of the years may have 366 days rather than 365. Additionally, the weather file may include part of a water year in addition to one or more complete water years. The year count (*Nyears*) calculated in this step it the number of complete water years in the weather file.

Step 2: Assign a cumulative annual precipitation to each day in the water file.

Explanation: This process takes place within a loop that counts the years in the weather file. The counter is *nyr*.

Step 2a: Calculate the number of days in the weather file that precedes the year.

Explanation: When starting with the 1st year, the number of preceding days is zero. Otherwise, the number of preceding days is the sum of the days in each of the preceding years.

Step 2b: Calculate the number of days in year *nyr*.

Explanation: There are either 365 or 366 days in the year. The last day of the water year is September 30. If the day of the month of the 365th day of year *nyr* is 30, then water year *nyr* has 365 days. Otherwise, it has 366 days.

Step 2c: Calculate the reference annual precipitation for year nyr.

Explanation: The daily reference precipitation is summed over the number of days in year *nyr*.

Step 2d: Assign the lapse-corrected annual precipitation to every day in year *nyr*.

Explanation: The reference annual precipitation is lapse-corrected to the elevation used in the NDVI formulation (elev_NDVI). The corrected value is assigned to every day in year *nyr*.

Step 2e: If the weather file ends with a partial water year, the annual precipitation from the previous year is applied to the days of the partial water year.

Explanation: The annual precipitation for a partial water year cannot be calculated. Therefore, the annual precipitation from the previous water year is applied to the partial water year. This provision is made so that data from the end of a calendar year can be appended to the end of the last water year.

Routine Output: This routine returns a vector of length equal to the length of the weather file. The vector contains the annual precipitation for each day in the weather file.

G5. ANCILLARY ROUTINES

G5.1 LAYER DEPTHS AND PROPERTIES

The routine *cdepth* calculates the soil layer depths for each node in an individual cell (Figure G-5). When the soil depth is greater than the maximum root depth, the two nodes in the first layer have a thickness equal to the evaporation layer thickness, the second layer has a thickness equal to the difference between the root depth and the evaporation layer thickness, and the third layer contains the balance of the soil thickness. When the soil depth of a cell is less that root depth of the evaporation layer thickness, then the layer thickness(es) are truncated accordingly. In the extreme case where the soil depth is zero, the three layer thicknesses are equal to zero.

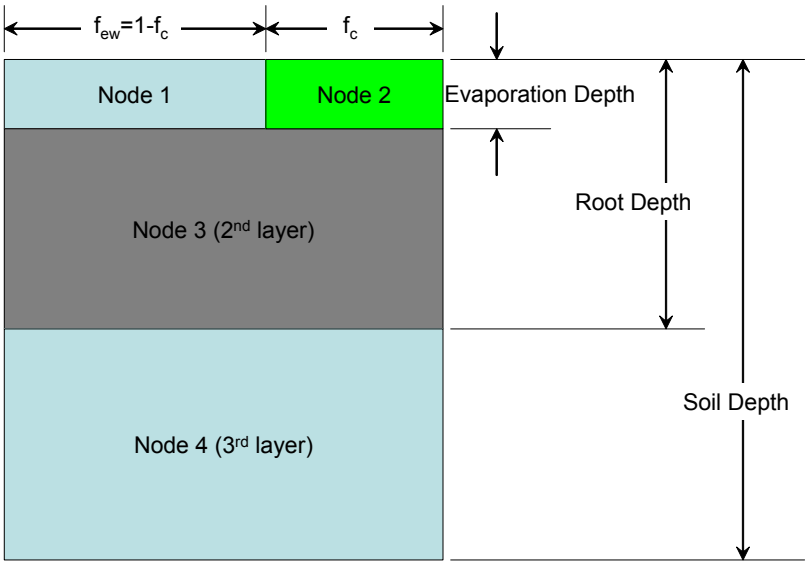

Source: Output DTN: SN0701T0502206.037.

Figure G-5. Soil Discretization in MASSIF

The routine *cdepth* contains the following steps:

Step 1: When the soil depth is less than the evaporation layer depth, the thickness of the two nodes in the first layer are set to the soil thickness. The thicknesses of 3rd and 4th nodes are set to zero.

Step 2: When the soil depth is less than the root depth and greater than the evaporation layer depth, the thickness of the two nodes in the first layer are set to the evaporation depth. The thickness of 3rd node is set equal to the difference between the soil depth and the evaporation layer thickness. The thickness of the 4th node is set to zero.

Step 3: When the soil depth is greater than the root depth, the thickness of the two nodes in the first layer are set to the evaporation depth. The thickness of 3rd node is set equal to the difference between the root depth and the evaporation layer thickness. The thickness of the 4th node is set to the difference between the soil depth and the root depth.

The routine *LayerProps* calculates extrinsic properties for each cell from the intrinsic soil properties and the soil depths. Additionally, the initial soil water levels are calculated for each node in each cell of the watershed. The following steps are contained in routine *LayerProps:*

Step 1: Determine the soil depth for cell n.

Explanation: The geospatial file for the watershed characterizes each cell with a depth zone number. The vector $depth_{soils}$ contains the soil depths for each of the depth zones.

Step 2: Calculate the node thicknesses for cell n.

Explanation: The thickness of each node in the cell is calculated from the cell soil depth, the evaporation layer thickness, and the root depth. The calculation is performed in routine *cdepth*. The vector element $thick_n$ is, itself, a vector containing four elements: the thicknesses of Nodes 1, 2, 3, and 4 of cell n.

Step 3: Calculate the layer water content associated with field capacity.

Explanation: The water content (level) associated with field capacity is the product of the node thickness and the field capacity for the cell. Each cell in the geospatial file is characterized by a soil zone number. The vector *fieldcap* contains the field capacities for each of the soil zones.

Step 4: Compute maximum daily infiltrations for cell n.

Explanation: The daily flow limit through a soil layer is the product of the soil conductivity (m/s) and the duration of a day (24 hrs). The daily flow limit into the bedrock is the product of the rock conductivity (m/s) and the duration of a day (24 hrs).

Step 5: Set the initial water content in each node of cell n.

Explanation: The user supplies values for a four-element vector, IC, which specifies the fractional distance between the wilting point and the field capacity for each node (4) in every cell of the watershed. Unless there is measured data to the contrary, the user should make the fourth element of the vector equal to 1 ($IC_4=1$). This is because there are no mechanisms in MASSIF that extract water from Node 4 below the field capacity. The first three elements of the vector (IC_1, IC_2, IC_3) can be any value between 0 and 1.

Step 6: Set the maximum possible water content for the nodes in cell n.

Explanation: The maximum water level in a node is the product of the thickness of that node and the saturated water content of the soil (*soilporo*). **Note:** Originally, the creator of these Mathcad files thought the cell porosity was being specified. This accounts for the variable name *soilporo*. In fact, the saturated water content is being specified, but the variable name remains unchanged.

Step 7: Calculate the water level associated with the wilting point for the four nodes of cell n.

Explanation: The water level associated with the wilting point (*Wilt_layer*) is the product of the layer thickness and the wilting point.

Step 8: Calculate the total evaporable water (*TEW*; Allen et al. 1998 [DIRS 157311], Equation 73) for cell n.

Explanation: The total evaporable water is the product of the thickness of the evaporation layer and the difference between the field capacity and half of the wilting point.

Step 9: Set the readily evaporable water of cell n (REW_n) to the user-specified value (*rew*).

Step 10: Calculate the total available water (*TAW*; Allen et al. 1998 [DIRS 157311], Equation 82) for cell n.

Explanation: FAO-56 defines the total available water as the product of the root depth and the difference between the field capacity and the wilting point. MASSIF allows soil depths that are less than the rooting depth. Hence the sum of the thicknesses of Layers 1 and 2 (i.e., Nodes 1 and 3) are used in place of the rooting depth to calculate TAW.

Routine output: This routine returns the node thicknesses, initial node water levels, maximum daily water flows through the soil and rock, TEW, REW, TAW, integrated node field capacities, integrated node wilting points, and maximum pore volumes for every cell in the watershed.

G 5.2 WEATHER ROUTINES

G5.2.1 Estimate of the Daily Dew Temperature

The daily dew temperature (T_{dew}) is calculated as an offset from the minimum temperature for the day (T_{min}). The offset for winter (K_{winter}) is different than the offset for the rest of the year (K_{rest}). Winter starts on the calendar year day K_{winter_start} and ends on the calendar year day K_{winter_end}. The parameters K_{winter}, K_{rest}, K_{winter_start}, and K_{winter_end}, are inputs to *Massif* and are described under *Miscellaneous Parameters* in Section 6.5. The dew temperature is calculated in routine T_{dew_fcn}.

G5.2.2 Correction of Temperature for Elevation

The temperatures in the weather files ($TairRef_{max}$, $TairRef_{min}$) are for a specific elevation (*elev_ref*). The temperatures for a specific cell (elevation *elev*) are calculated from these reference temperatures using a lapse rate correction for elevation (C_{TCor}). Temperature corrections are performed in T_{elev_cor}. The steps in routine T_{elev_cor} are:

Step 1: Calculate the lapse rate correction.
Explanation: The lapse rate correction is linear in temperature.

Step 2: Calculate the corrected maximum temperature.
Explanation: The corrected maximum air temperature is the reference maximum air temperature minus the lapse rate correction.

Step 3: Calculate the corrected minimum temperature.
Explanation: The corrected minimum air temperature is the reference minimum air temperature minus the lapse rate correction.

Step 4: Compute the mean daily temperature.
Explanation: The mean daily temperature is the average of the maximum and minimum daily temperatures (Allen et al. 1998 [DIRS 157311], Equation 9).

Step 5: Compute the dew point temperature.
Explanation: The dew point temperature is computed using routine T_{dew_fcn}.

G5.2.3 Correction of Precipitation for Elevation

The daily precipitation in the weather files is for a specific elevation (*elev_ref*). The precipitation for a specific cell (elevation *elev*) is calculated from this reference precipitation using a lapse rate correction for elevation ($C_{Precipcor}$). Precipitation corrections are performed in routine $Precip_{elev\_cor}$.

G5.2.4 Estimate of the Duration of the Precipitation Event

The duration of a precipitation event is estimated from a linear correlation of measured daily durations as a function of measured daily precipitation amounts (Section 6.5.1). The daily duration is no less than zero and no greater than 24 hrs. The duration of the precipitation event is calculated in routine *Duration_fcn*.

G5.3 READING THE WEATHER/PRECIPITATION FILE

The routine *Weather* is used to read the stochastically generated weather files (Section 6.5) used to model the three climates (present day, monsoon, and glacial). These weather files are Excel workbooks. The information on the first spreadsheet in the workbook is used in the infiltration calculation. The steps in *Weather* are:

Step 1: Read the reference elevation for the weather.

Explanation: The reference elevation is contained in row 2 of column 1 in the spreadsheet.

Step 2: Read the number of weather years.

Explanation: The number of weather years is located in row 2 of column 2 in the spreadsheet.

Step 3: Read the weight of each weather year.

Explanation: The relative probability of a weather year is its "weight." The "weights" are in column 2 and begin in row 5.

Step 4: Read the time information.

Explanation: The time information includes month, day of month, sequential year number, and day of the calendar year. The data begins in row 2 and extend to the end of the file. The time data is included in columns 3 through 6.

Step 5: Read the weather information for each weighted precipitation year.

Explanation: The weather information consists of daily precipitation, maximum temperature, minimum temperature, and wind speed at 2 m. This set of four adjacent columns is repeated for all the weighted weather years.

Step 6: Create a weather set for each of the weighted precipitation years.

Explanation: The weather set includes the time data, read in **Step 4**, and the weather data, read in Step 5.

Routine Output: The routine returns a vector of weather sets; each weather set is a matrix. It also returns the "weights" (or probabilities) of each weighted weather year, and the reference elevation.

G5.4 MONITORED OUTPUT

G5.4.1 Watershed-scale Monitored Quantities

On the scale of the watershed, *Massif* returns the:

1) Change in the water stored in the soil of the watershed
2) Change in the snow level for the watershed
3) Sum of the precipitation over the watershed
4) Sum of the evapotranspiration over the watershed

5) Sum of the infiltration over the watershed
6) Sum of the snow sublimation over the watershed
7) Runoff from the watershed.

When the user specifies a value of −1 for the input flag i_{WS}, the reported changes and sums are cumulative for the entire water year(s) of the calculation. If the user specifies a value of 1 for the input flag i_{WS}, the reported changes and sums are reported for each day of the water year(s) of the calculation. In addition, *Massif* returns the difference between all of the sources and sinks of water for the watershed. The magnitude of this "error" should always be approximately equal to the number of cell times the machine precision. For small watersheds, this is about 10^{-14}. For large watersheds, this is about 10^{-7}.

The daily watershed-scale mass check and its component parts are in routine *Masscheck_fcn*. The steps in *Masscheck_fcn* are:

Step 1: Calculate the change in the stored water.

Explanation: The daily change in the water content of an individual cell is computed using the daily changes in water levels for each of the four nodes that comprise the cell:

$$\Delta Wlevel = \Delta Wlevel_{Node1} \cdot \left(1 - f_c\right) + \Delta Wlevel_{Node2} \cdot f_c \ldots + \Delta Wlevel_{Node3} + \Delta Wlevel_{Node4} \quad \text{(Eq. G-25)}$$

The change for the entire watershed is the sum of the cell changes for all the cells in the watershed.

Step 2: Calculate the change in snow levels, and cumulative values of precipitation, evapotranspiration, runoff, net infiltration, and sublimation.

Explanation: All of these quantities vary from cell to cell. The watershed totals are merely sums over all the cells in the watershed. As in the case of runoff, the only interest is in runoff from the watershed. Therefore, the cell runoff is summed only for cells that have no downstream cells ($DnSt_n$=−3 in the geospatial file describing the watershed).

Step 3: Compute the change in water inventory.

Explanation: The change in water inventory (*Masscheck*) is calculated as:

$$Masscheck = (-Precip\_sum - ET\_sum - Infil\_sum - Sublimation\_sum - Runoff\_sum) \ldots + \Delta Wlevel\_sum + \Delta Slevel\_sum \quad \text{(Eq. G-26)}$$

This quantity should deviate from zero only due to machine precision limitations. The actual magnitude of *Masscheck* will be proportional to the number of cells in the watershed.

Step 4: Assemble the component part of the mass check.

Explanation: The component parts of the mass check are placed in the output variable $Monitor_{ws}$.

Routine Output: This routine returns the values for the daily mass check and the component parts of that mass check.

G5.4.2 Cell-scale Monitored Quantities

The user can also specify specific cells to monitor. The list of cells to be monitored is specified by the user in the vector i_{cell}. If, for instance, the user wishes to monitor cell numbers 1, 100, and 1,000, the user specifies:

$$i_{cell} := \begin{pmatrix} 1 \\ 100 \\ 1000 \end{pmatrix} \quad \text{(Eq. G-27)}$$

The monitored quantities are returned in the vector Monitorcell (see the output of the *Massif* driver). Each element of the output vector contains a matrix of monitored quantities for each monitored cell. For the example specified above, $Monitor_{cell_1}$ is a matrix that contains the monitored quantities for cell 1, $Monitor_{cell_2}$ is a matrix that contains the monitored quantities for cell 100, and $Monitor_{cell_3}$ is a matrix that contains the monitored quantities for cell 1,000. The rows of each matrix correspond to the days listed in the precipitation file. A 1-year precipitation would have 365(6) rows; a 2-year precipitation file would have 730(1) rows. The columns in each matrix correspond to the cell-monitored quantities. These quantities are shown in Table G-3.

Table G-3. Quantities Returned by $Monitor_{cell\_fcn}$

Column	Variable Name	Quantity
1	$Wlevel_1$	Water level in Node 1
2	$Wlevel_2$	Water level in Node 2
3	$Wlevel_3$	Water level in Node 3
4	$Wlevel_4$	Water level in Node 4
5	Slevel	Snow level (equivalent water height)
6	Runon	Run-on from upstream cells
7	Runoff	Runoff to downstream cells
8	Infil	Infiltration into rock
9	precip	Precipitation (adjusted for elevation)
10	NetPrecip	Amount of precipitation/snowmelt that is available to the soil
11	SnowMelt	Snowmelt for the day
12	ET0	Reference ET
13	Evaporate	Evaporation from the evaporation layer
14	Transpire	Transpiration from the root zone

Table G-3. Quantities Returned by $Monitor_{cell\_fcn}$ (Continued)

Column	Variable Name	Quantity
15	Sublimation	Snow sublimation
16	FC_layer_1	Product of layer thicknesses and field capacity for Layer 1 (Nodes 1 and 2)
17	FC_layer_3	Product of layer thicknesses and field capacity for Layer 2 (Node 3)
18	$Wilt\_layer_1$	Product of layer thickness and wilting point for Layer 1 (Nodes 1 and 2)
19	$Wilt\_layer_3$	Product of layer thickness and wilting point for Layer 2 (Node 3)
20	Masscheck_cell	Check of water conservation for the cell
21	MaxInfil_sl	Maximum daily (24 hr) water flow in the soil
22	MaxInfil_rk	Maximum daily (24 hr) water flow in the underlying rock
23	$Pore\_sl_1$	Soil pore volume of Node 1
24	$f_{c\ new}$	Vegetative canopy coefficient
25	K_{cb}	Adjusted crop coefficient
26	PVR	Potential vegetative response
27	Tmax	Maximum temperature (adjusted for elevation)
28	Tmin	Minimum temperature (adjusted for elevation)
29	$Precip_{total}$	Daily precipitation (adjusted for elevation) for the entire repository)

Source: Output DTN: SN0701T0502206.037.

The mass check for the individual monitored cells and the compilation of monitored cell properties is performed in the routine *Monitorcell_fcn*. The formulation for the individual cell mass check is explained in the description of the routine *Masscheck_fcn* (above).

G5.5 INPUT FILES: CONSTANTS AND NOMINAL INPUT VALUES

Numerical constants and nominal values of input parameters are included in a total of four Mathcad files. Constants are located in *Constants.xmcd*. Nominal soil properties are located in *SoilProperties.xmcd*. Nominal rock properties are located in *Rock Properties.xmcd*. The balance of most nominal input parameters is located in *Inputs Values.xmcd*. These files contain tables of numerical values as well as the references for those values. These values should be compared to Section 4.

The constants file is "referenced" in the MASSIF files where needed. The rock and soil properties files are referenced in the input values files so that only *Input Values.xmcd* need be referenced. When the user constructs a "front end" for the *Massif* routine, the user typically "references" the input values file. The user will then selectively supersede any of the nominal values listed in these files with the specific values of interest to the particular analysis. Other input values, such as the weather files, site elevation, and site latitude, are provided in the "front end" and are not part of the input files listed here.

G6. FILES AND ROUTINES

Table G-4 shows a list of the MASSIF routines and their corresponding Mathcad file names.

Table G-4. List of MASSIF Routines and Corresponding Mathcad File Names

MASSIF ROUTINE	MATHCAD FILE NAME
Balance	*Balance Model.xmcd*
cdepth	*Layer Depths and Properties.xmcd*
C_{Rb_fcn}	*RefET.xmcd*
D_{c_fcn}	*ET.xmcd*
D_{e_fcn}	*ET.xmcd*
DiffuseDirect	*RefET.xmcd*
DOWY_fcn	*ET.xmcd*
D_{r_fcn}	*ET.xmcd*
Duration_fcn	*Weather Correction.xmcd*
e0	*ET.xmcd and RefET.xmcd*
ET	*ET.xmcd*
ET_0	*RefET.xmcd*
GroupBalance	*Balance Model.xmcd*
Index_NDVI_fcn	*ET.xmcd*
Index_Rb_fcn	*RefET.xmcd*
K_{cb_fcn}	*ET.xmcd*
K_{cb0_fcn}	*ET.xmcd*
K_{e_fcn}	*ET.xmcd*
K_{r_fcn}	*ET.xmcd*
K_{s_fcn}	*ET.xmcd*
$K_{tp\_c\_fcn}$	*ET.xmcd*
K_{tp_fcn}	*ET.xmcd*
LayerProps	*Layer Depths and Properties.xmcd*
Masscheck_fcn	*Monitored IO.xmcd*
Massif	*Massif extended.xmcd*
Monitorcell_fcn	*Monitored IO.xmcd*
precip_Kcb_fcn	*AnnualCumulativePrecip.xmcd*
$Precip_{elev\_cor}$	*Weather Correction.xmcd*
Rb_fcn	*RefET.xmcd*
R_{smhor_func}	*RefET.xmcd*
R_{sohor_func}	*RefET.xmcd*
SnowB	*Snow.xmcd*
SolarRad_inc	*RefET.xmcd*
T_{dew_fcn}	*Weather Correction.xmcd*
T_{elev_cor}	*Weather Correction.xmcd*
Upstream3	*Upstream Contributors.xmcd*
Varying_f_c	*Balance Model.xmcd*
Weather	*Read_Weather_Routines.xmcd*
γ_{c_fcn}	*RefET.xmcd*

Source: Output DTN: SN0701T0502206.037.

APPENDIX H
SENSITIVITY ANALYSIS OF MEAN ANNUAL INFILTRATION

H1. METHODOLOGY

H1.1 INTRODUCTION

The purpose of uncertainty and sensitivity analysis is primarily to increase our understanding of a complex system. Formally, any system can be presented as:

$$\mathbf{y} = f(\mathbf{x})$$

where

- $\mathbf{y} = (y_1, y_2, \cdots, y_k)$ represents a vector of output data of the model (the quantities to be estimated). In this case, the output data considered is the spatially averaged mean annual net infiltration over the infiltration modeling domain (Section 6.5.7).
- $\mathbf{x} = (x_1, x_2, \cdots, x_n)$ represents a vector of input data
- f represents a function or set of functions, which is generally complex.

Uncertainty analysis is defined as the study of the uncertainty of **y** due to the uncertainty in the set of inputs **x**. In other words, because of uncertainty of the input values, uncertainty is induced in the output value (response). It is desirable to quantify and represent this uncertainty in order to know what could be the possible range (and distribution) of each element of **y**.

Sensitivity analysis is complementary to uncertainty analysis and is defined as the study of how the uncertainty in **y** can be apportioned to the uncertainty in each element of **x**. It is important to know how each input uncertainty affects a given element of **y**.

Ultimately, the sensitivity analysis helps in verifying the model by checking whether the influential uncertain parameters are concordant with what was expected from the equations. It is also a very good tool for planning a new set of experiments by indicating what benefit could be obtained (i.e., which reduction of uncertainty can be expected in a given element of **y**) by reducing the uncertainty in an element of **x**.

Different methods have been developed for performing sensitivity analysis such as local sensitivity analysis (based on derivatives), screening methods, reliability methods (e.g., FORM/SORM). The one used in this appendix is a sampling based method (Monte Carlo analysis).

A Monte Carlo analysis consists in sampling the input space in order to determine the distribution of the output space. This provides the tools necessary for both uncertainty and sensitivity analysis. Different techniques can be used to sample the input space. The technique chosen is the Latin Hypercube Sampling (LHS), which provides good coverage of the distribution of each parameter, due to its stratification.

Due to the high cost (in computer time and memory) of the MASSIF (Mass Accounting System for Soil Infiltration and Flow) code, the sample size chosen is relatively low (n=20). However, two replicates have been created in order to study the stability of the results.

H1.2 LIST OF CONSIDERED INPUTS

Appendix I lists the range of each uncertain parameter and provides the screening of parameters that are considered as uncertain in this analysis. This list of considered uncertain parameters is displayed below. The format is the following:

Sdepth4*:* *Soil depth for depth class 4* U[0.1 ; 0.5]

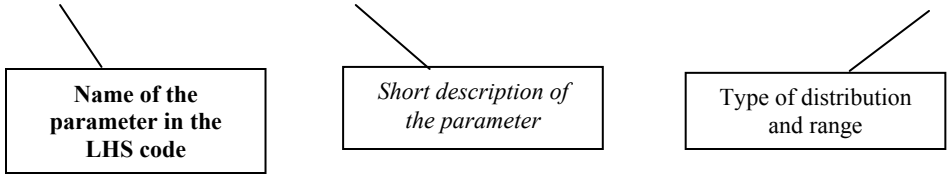

The acronyms for the type of distribution are:

U Uniform minimum and maximum values are given
LU Loguniform minimum and maximum values are given
N Normal 0.001 and 0.999 quantiles values are given
CDF Cumulative distribution function.

Certain precipitation parameters are represented as a first order Fourier series parameterized with three fitting parameters. The meaning of the precipitation parameters and the fitting parameters are defined below.

Precipitation parameters:

$p_{00}(d)$ Probability of a dry day given the previous day was dry (dimensionless)

$p_{00}(d)$ Probability of a dry day given the previous day was wet (dimensionless)

$\lambda(d)$ Mean of the probability distribution for the amount of precipitation on day, d, given that it is wet (mm)

$m(d)$ Mean of the probability distribution for the natural logarithm of the amount of precipitation on day, d, given that it is wet (ln(mm)).

Fitting parameters:

a Annual mean value
b Amplitude of the annual variation (equal to one half of the annual variation)
θ Phase shift for the seasonal variation.

Thus, to parameterize daily precipitation twelve stochastic parameters must be defined (a, b, and θ for each of the four precipitation parameters). An alternative way to analyze precipitation parameter sensitivity is to focus not on the individual stochastic parameters separately but rather to use the mean annual precipitation (MAP) resulting from the stochastic simulation. Both analysis methods are used in this appendix.

H1.2.1 Climate Independent Parameters

Sdepth4	Soil depth for depth class 4 (m)	U[0.1 ; 0.5]
Z_e	Evaporation depth (m)	U[0.1 ; 0.2]
KC_min	Minimum basal crop coefficient (dimensionless)	CDF
HC_579	Holding capacity for soil group 5/7/9 (m^3/m^3)	U[0.09 ; 0.17]
ln Rks_405	Natural log of rock conductivity for rock type 405 (Ln(m/s))	U[−16.39 ; −12.25]
ln Rks_406	Natural log of rock conductivity for rock type 406 (Ln(m/s))	U[−17.68 ; −11.77]
REW	Readily evaporable water (mm)	U[2.0 ; 10.0]
Ckcb2	Slope of the linear relationship between NDVi and K_{cb} (dimensionless)	N[3.2 ; 16.2].

H1.2.2 Modern Interglacial Climate Parameters

Z_r	Rooting depth (m)	U[0.6 ; 2.6]
h_plant	Plant height (m)	U[0.2 ; 0.6]
a_m	Annual average of *m(d)* (ln(mm))	U[0.5 ; 1.07].

Moreover, a_λ (average over the year of expected precipitation) is defined as a function of a_m. Thus **a_m** represent the influence of the couple (a_m,a_λ)

H1.2.3 Monsoon Climate Parameters

Z_r	Rooting depth (m)	U[0.6 ; 2.6]
h_plant	Plant height (m)	U[0.2 ; 0.6]
a_m	Annual average of *m(d)* (ln(mm))	U[0.5 ; 1.3]
a_{00}	Annual average $p_{00}(d)$ (dimensionless)	U[0.896 ; 0.944]
b_m	Amplitude of the annual variation in *m(d)* (ln(mm))	U[−0.3 ; 0.5]
gTmaxwet	Annual average of daily maximum temperature on days with precipitation (°C)	U[14 ; 22]
PDur_S	Slope of the linear relationship between precipitation duration and precipitation amount (mm/hr)	U[0.14 ; 0.43].

Moreover, a_λ, b_λ, b_m, b_{00}, and b_{10} are defined as a function of a_m. Thus a_m represent the influence of the group (a_m, a_λ), and b_m represents the influence of the group (b_λ, b_m, b_{00}, b_{10}).

The sampling of b_m and linear interpolation of other amplitude values conditional on b_m, may sometimes induce nonphysical results in the precipitation generation. The two possible nonphysical results are:

- The probability p_{00}(d) being greater than one
- $\lambda(d)$ being lower than $m(d)$.

The first item is unlikely to happen, but samples have been screened in order to be sure that such nonphysical results do not occur.

The second occurrence is more likely. In order to reduce its likelihood, a small positive correlation (=0.2) has been imposed between a_m and b_m.

H1.2.4 Glacial Transition Climate Parameters

Z_r	Rooting depth (m)	U[1.0 ; 4.0]
h_plant	Plant height (m)	U[0.6 ; 1.8]
$\mathbf{a_{00}}$	Annual average $p_{00}(d)$ (dimensionless)	U[0.78 ; 0.89]
$\mathbf{a_m}$	Annual average of $m(d)$ (ln(mm))	U[0.48 ; 0.92]
$\mathbf{\theta_m}$ **(Theta_m)**	Phase of annual variation in $m(d)$ (radians)	U[−3.14 ; 3.14]
PDur_S	Slope of the linear relationship between precipitation duration and precipitation amount (mm/hr)	U[0.32 ; 0.71].

Moreover, a_λ is defined as a function of a_m. Thus a_m represents the influence of the coupled parameters, a_m and a_λ. θ_λ is defined as a function of θ_m. Thus θ_m represents the influence of the coupled parameters, θ_λ and θ_m.

H1.3 DATA TRANSFORM

The methods used for sensitivity analysis quantify linear relationships that may exist between the input parameters and the output results of a calculation or model. It is possible to extend these methods to quantifying monotonic relationships by working with the rank of the data instead of the raw values. For each parameter (whether it is input or output), rank values are obtained by assigning the rank of 1 to the highest value, 2 to the next highest value, and so on. Identical values are assigned with the same rank number.

H1.4 STEPWISE REGRESSION APPROACH

The stepwise regression used on raw data quantifies the linear relationship between the inputs and the output.

The stepwise regression used on rank data quantifies the monotonic relationship between the inputs and the output.

The stepwise regression analysis works as follows:

- Step 1: Pick the most important variable and create a regression model
- Step 2: Pick the next most important variable and add it to the regression model
- Step 3: Pick the next most important variable and add it to the regression model
- Repeat until adding additional variables does not result in an improved regression model.

The degree of importance of the variables is defined by the coefficient of determination of the regression model once the variable is added. In other words, the most important variable is the variable that gives the "best" regression model using a single variable. The next most important variable is the variable that gives the "best" regression model using two variables including the first variable, and so forth.

The determination of influence is based on what is called an alpha cutoff. At each step, an alpha value is calculated. This value represents the probability that an input variable is considered as influential when in fact is it not. The alpha cutoff considered is equal to 0.10, which means that there is a 10% chance of having a noninfluential parameter considered as influential.

Moreover, a color coding has been used – if alpha is lower than 0.05 (i.e., less than a 5% chance of spurious correlation), then the number is in black. If alpha is between 0.05 and 0.10, then the number is shown in red. When alpha is above 0.10, the parameter is not included in the list because the regression model is not improved by including additional parameters.

The relevant parameters calculated are:

- R^2: Coefficient of determination of the regression model. It represents the fraction of uncertainty (percentage of variance) explained by the regression model. It indicates how good the regression model is and how well understood the input parameters influence is.
- SRC: Standardized Regression Coefficients of the regression model. They are standardized to suppress the "unit" effect (i.e., having the same results whether the input is in meters, millimeters or kilometers).
- SRRC: Standardized Rank Regression Coefficients. These are calculated as for the SRC, but are based on the rank of the data instead of raw data themselves.

The software used for this analysis is MVIEW 4.0 (STN: 10072-4.0-00) [DIRS 173438].

H1.5 SCATTERPLOT ANALYSIS

Scatterplot analysis is visual. Figures are created with plots whose abscissa corresponds to the input parameter value and whose ordinate corresponds to the mean net infiltration results, listed as the weighted mean annual net infiltration over the entire modeling domain. If net infiltration is sensitive to a given input parameter, a pattern should be seen in the scatterplot. Otherwise, the scatterplots will look like random distributions. Only input data explaining more than 10% of the infiltration variance are presented, as an influence of 10% and lower is generally not discernable.

H2. PRESENT-DAY CLIMATE

H2.1 STUDY OF REPLICATE 1 – ALEATORY UNCERTAINTY VARYING

Table H-1. Stepwise Regression (linear and rank) on Average Infiltration for Replicate 1: Present-Day Climate (aleatory uncertainty varying)

	Stepwise Regression (linear)				Stepwise Regression (rank)			
Step	**Variable**	**tot. R^2**	**inc. R^2**	**SRC**	**Variable**	**tot. R^2**	**inc. R^2**	**SRRC**
1	Sdepth4	0.33	0.33	−0.61	Sdepth4	0.37	0.37	−0.63
2	a_m	0.63	0.30	0.50	HC_579	0.66	0.28	−0.49
3	HC_579	0.82	0.19	−0.44	a_m	0.83	0.17	0.43
4	REW	0.86	0.04	0.19	REW	0.88	0.05	0.22

Source: Output DTN: SN0701T0502206.044, *Stepwise_Analysis_R1_MIC_VA.xls*.

H2.1.1 Linear Regression

The linear regression results for Replicate 1 of the Present-Day climate are shown in Table H-1. Soil Depth Class 4 explains 33% of the variance in net infiltration and has a strong negative effect (SRC = −0.61). The negative effect of soil depth is expected, since a deeper soil layer can store more water, which is later lost to evapotranspiration, resulting in less infiltration. a_m ranks second in importance with a positive effect (SRC=0.50). HC_579 ranks third with a small negative effect. Readily evaporable water (REW) ranks fourth with a very small positive influence (R^2 increment of 4%). However, the red text in Table H-1 indicates that this influence may be due to spurious correlation, with a probability higher than 5%.

Analysis performed while replacing the precipitation parameter with mean annual precipitation (MAP) values gives similar results and is therefore not presented here.

H2.1.2 Rank Regression

The rank regression results for Replicate 1 of the Present-Day climate are also shown in Table H-1. Soil Depth Class 4 is the top contributor, explaining 37% of the variance in average net infiltration. It has a strong negative effect (SRRC=−0.63). HC_579 and a_m also contribute, explaining an additional 28% and 17% of the net infiltration variance, respectively. Readily evaporable water (*REW*) explains 5% of the variance, with a small positive effect. However, the influence may be due to spurious correlation.

Analysis performed while replacing the precipitation parameter with MAP values gives similar results, and is therefore not presented here.

H2.1.3 Scatterplots

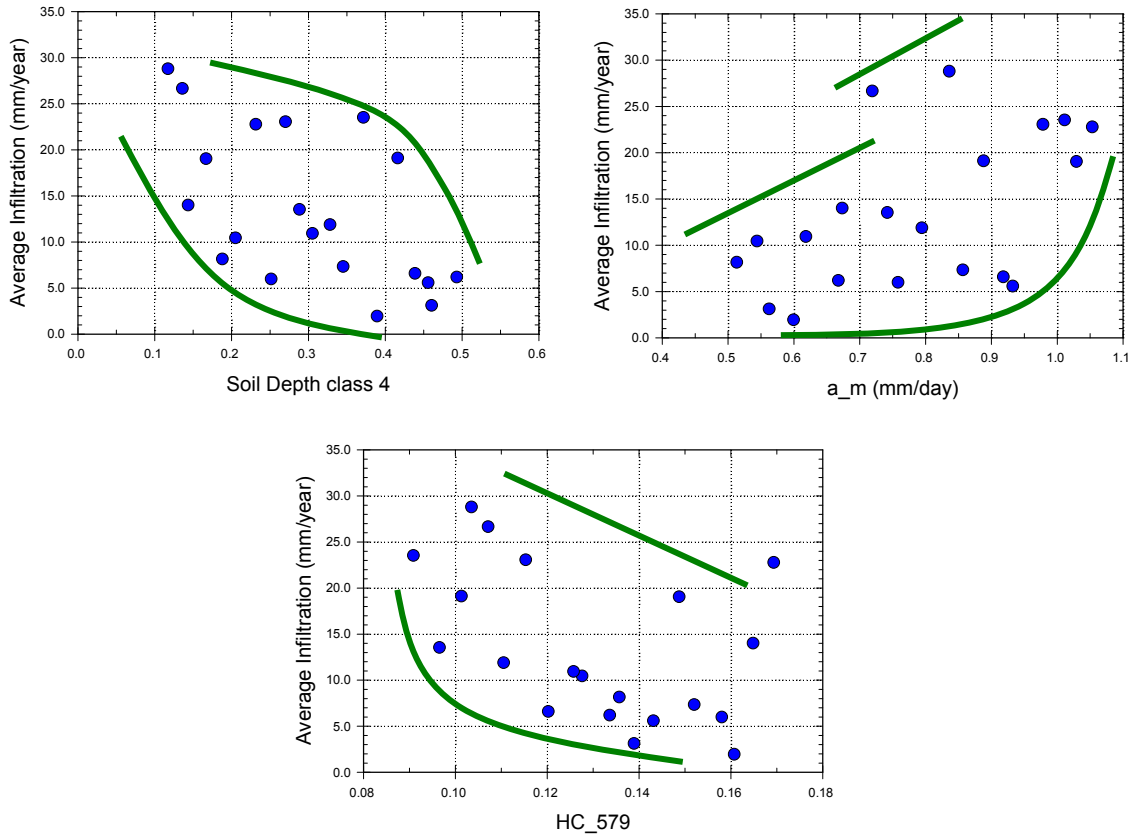

Source: Output DTN: SN0701T0502206.044, *scatterplots_R1_MIC-VA.JNB.*

Figure H-1. Scatterplots of Average Infiltration Versus Soil Depth Class 4 (upper left frame), a_m (upper right frame), and HC_579 (lower frame) - Replicate 1 - Present-Day Climate (aleatory uncertainty varying)

Scatterplot analysis (Figure H-1) shows clearly the influence of Soil Depth Class 4. The other parameters show less influence.

H2.2 STUDY OF REPLICATE 2 – ALEATORY UNCERTAINTY VARYING

Table H-2. Stepwise Regression (linear and rank) on Average Infiltration for Replicate 2: Present-Day Climate (aleatory uncertainty varying)

	Stepwise Regression (linear)				Stepwise Regression (rank)			
Step	**Variable**	**tot. R^2**	**Inc. R^2**	**SRC**	**Variable**	**tot. R^2**	**inc. R^2**	**SRRC**
1	Sdepth4	0.50	0.50	−0.74	Sdepth4	0.50	0.50	−0.74
2	a_m	0.85	0.35	0.58	a_m	0.83	0.33	0.57
3	HC_579	0.90	0.05	−0.21	HC_579	0.86	0.04	−0.19
4	REW	0.91	0.01	−0.12				

Source: Output DTN: SN0701T0502206.044, *Stepwise_Analysis_R2_MIC_VA.xls*.

H2.2.1 Linear Regression

The linear regression results for Replicate 2 of the Present-Day climate are shown in Table H-2. Soil Depth Class 4 explains 50% of the variance in net infiltration. It has a strong negative effect on infiltration (SRC = −0.74).

a_m has a positive effect on the average net infiltration (SRC=0.58), explaining an additional 35% of the variance. The positive influence of a_m is expected. By increasing the precipitation (and thus a_m), the water available at the surface and the resulting net infiltration are increased.

HC_579 has a negative effect, explaining an additional 5% in the variance of net infiltration. Readily Evaporable Water (*REW*) has a very small negative influence, explaining 1% of the variance of net infiltration, but it has more than a 5% chance of being due to spurious correlation.

H2.2.2 Rank Regression

The rank regression results for Replicate 2 of the Present-Day climate are also shown in Table H-2. The rank regression is identical to the linear regression, without the inclusion of *REW*. HC_579 (holding capacity for soil group 5/7/9) is highlighted in red, indicating that the influence is so small that it could be spurious.

H2.2.3 Scatterplots

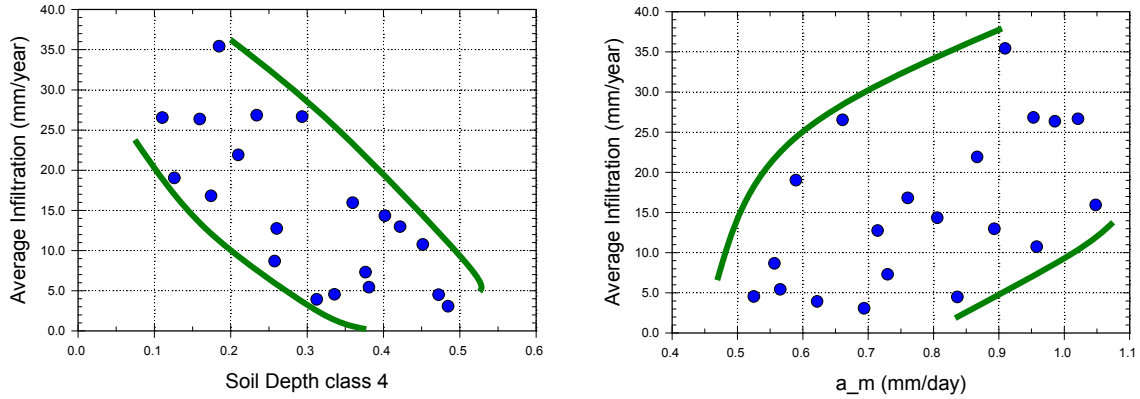

Source: Output DTN: SN0701T0502206.044, *scatterplots_R2_MIC-VA.JNB.*

Figure H-2. Scatterplots of Average Infiltration Versus Soil Depth Class 4 (left frame), a_m (right frame) Replicate 2 - Present-Day Climate (aleatory uncertainty varying)

Figure H-2 shows clearly the influence of Soil Depth Class 4 and a_m. The other parameters show less influence.

H2.3 CONCLUSION OF STUDY OF ORIGINAL DATA (ALEATORY UNCERTAINTY VARYING)

Sensitivity analyses on Replicates 1 and 2 of the Present-Day climate agree on the most influential parameters – Soil Depth Class 4 and a_m. They also agree on the relative importance of each parameter (R^2 increment of ~0.5 for Soil Depth Class 4 and ~0.2 for a_m). The third most important parameter is HC_579.

One of the problems of current analysis is that infiltration results are influenced by the precipitation years generated. Each set of 10 years is different for each LHS run. In other words, a different future is considered for each realization.

It is reasonable to consider a different future because the future is uncertain (random). However, it makes the sensitivity analysis of the physical parameters (system properties that can be physically measured) harder to interpret.

One possible solution is to eliminate the uncertainty in the future for the sensitivity analysis. In other words, the same set of 10 precipitation years is considered for any LHS run in MASSIF. In such a "Fixed Aleatory" scenario, only the physical parameters are varied. This scenario should provide a cleaner sensitivity analysis for the physical parameters but will ignore the influence of stochastic precipitation parameters.

Replicate 1 – Aleatory Uncertainty Fixed

Table H-3. Stepwise Regression (linear and rank) on Average Infiltration for Replicate 1: Present-Day Climate (aleatory uncertainty fixed)

	Stepwise Regression (linear)				Stepwise Regression (rank)			
Step	**Variable**	**tot. R^2**	**inc. R^2**	**SRC**	**Variable**	**tot. R^2**	**inc. R^2**	**SRRC**
1	Sdepth4	0.66	0.66	−0.85	Sdepth4	0.77	0.77	−0.90
2	HC_579	0.90	0.24	−0.46	HC_579	0.93	0.16	−0.40
3	CKcb2	0.93	0.03	−0.15				
4	h_plant	0.95	0.02	0.15				

Source: Output DTN: SN0701T0502206.044, *Stepwise_Analysis_R1_MIC_FA.xls*.

H2.3.1 Linear Regression

The linear regression results for Replicate 1, Fixed Aleatory, of the Present-Day climate are shown in Table H-3. Soil Depth Class 4 explains 66% of the variance. It has a strong negative effect on infiltration (SRC = −0.85). HC_579 has some negative effect, explaining 24% of the variance. CKcb2 and h_plant explain an additional 3% and 2% of the variance of infiltration, respectively.

H2.3.2 Rank Regression

The rank regression results for Replicate 1, Fixed Aleatory, of the Present-Day climate are also shown in Table H-3. Regression on the rank gives similar results to that of regression on raw

values for Soil Depth Class 4 (explaining 77% of the variance) and HC_579 (16% of the variance).

H2.3.3 Scatterplots

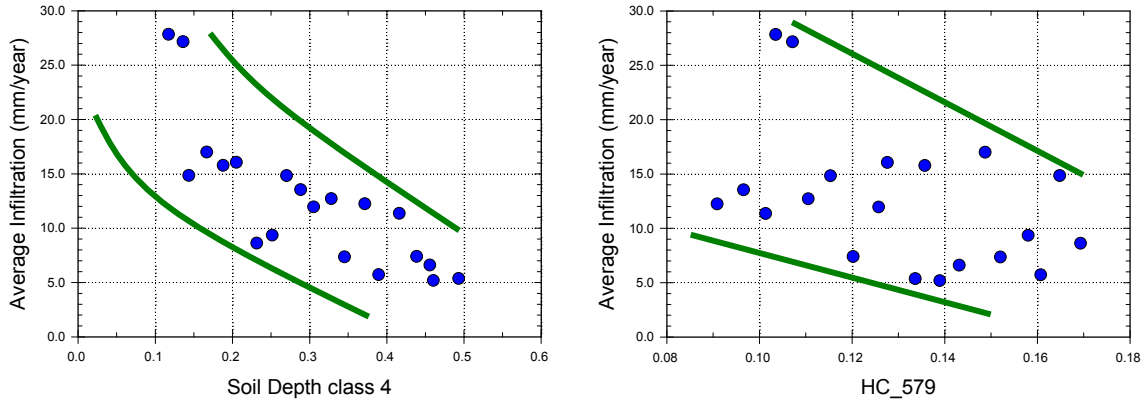

Source: Output DTN: SN0701T0502206.044, *scatterplots_R1_MIC_FA.JNB*.

Figure H-3. Scatterplots of Average Infiltration Versus Soil Depth Class 4 (left frame), and HC_579 (right frame) - Replicate 1 - Present-Day Climate (aleatory uncertainty fixed)

Scatterplot analysis (Figure H-3) clearly shows the influence of Soil Depth Class 4. The other parameters show less influence. This is mainly due to the strong influence of Soil Depth Class 4, which explains almost 80% of the variance of net infiltration.

H2.4 REPLICATE 2 – ALEATORY UNCERTAINTY FIXED

Table H-4. Stepwise Regression (linear and rank) on Average Infiltration for Replicate 2: Present-Day Climate (aleatory uncertainty fixed)

Stepwise Regression (linear)					Stepwise Regression (rank)			
Step	**Variable**	**tot. R^2**	**inc. R^2**	**SRC**	**Variable**	**tot. R^2**	**inc. R^2**	**SRRC**
1	Sdepth4	0.63	0.63	−0.80	Sdepth4	0.82	0.82	−0.91
2	HC_579	0.89	0.26	−0.49	HC_579	0.92	0.10	−0.32
3	lnRks_406	0.91	0.02	−0.16				

Source: Output DTN: SN0701T0502206.044, *Stepwise_Analysis_R2_MIC_FA.xls*.

H2.4.1 Linear Regression

The linear regression results for Replicate 2, Fixed Aleatory, of the Present-Day climate are shown in Table H-4. Soil Depth Class 4 explains 63% of the variance. It has a strong negative effect on infiltration (SRC = −0.80). HC_579 has some negative effect, explaining 26% of the variance on infiltration. lnRks_406 seems to have a small negative effect on infiltration. However, the influence is negligible (increment in R^2~ 2%).

H2.4.2 Rank Regression

The rank regression results for Replicate 1, Fixed Aleatory, of the Present-Day climate are also shown in Table H-4. Regression on the rank gives similar results to that of regression on raw values for the two most important parameters.

H2.4.3 Scatterplots

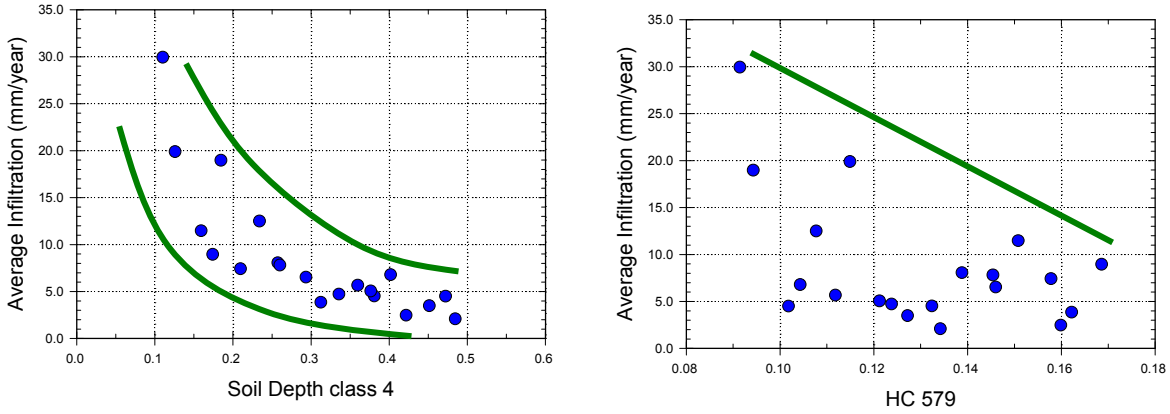

Source: Output DTN: SN0701T0502206.044, *scatterplots_R2_MIC_FA.JNB*.

Figure H-4. Scatterplots of Average Infiltration Versus Soil Depth Class 4 (left frame) and HC_579 (right frame) - Replicate 2 - Present-Day Climate (aleatory uncertainty fixed)

Scatterplot analysis (Figure H-4) clearly shows the influence of Soil Depth Class 4. The other parameters show less influence.

H2.5 CONCLUSIONS

When aleatory uncertainty is allowed to vary (different futures are considered) the results of the sensitivity analysis are more difficult to interpret because it is hard to distinguish between the influence of the variation in physical parameters (epistemic uncertainty) and the influence of randomness in future precipitation (aleatory uncertainty). These analyses shows the importance of Soil Depth Class 4 and precipitation amount (represented by the variation in a_m), but little can be discerned about the relative importance of the other physical parameters. When aleatory uncertainty is fixed, the importance of HC_579 is identified.

In conclusion, two physical parameters can be considered important and explain about 90% of the variance in infiltration when future weather is fixed: Soil Depth Class 4 and HC_579. In addition to these two parameters, the weather parameter a_m should be added since it controls the MAP and is an influential parameter in the varying aleatory uncertainty study.

H3. MONSOON CLIMATE (MC)

H3.1 REPLICATE 1 – ALEATORY UNCERTAINTY VARYING

Table H-5. Stepwise Regression (linear and rank) on Average Infiltration for Replicate 1: MC (aleatory uncertainty varying)

	Stepwise Regression (linear)				Stepwise Regression (rank)			
Step	**Variable**	**tot. R^2**	**inc. R^2**	**SRC**	**Variable**	**tot. R^2**	**inc. R^2**	**SRRC**
1	a_m	0.46	0.46	0.57	a_m	0.51	0.51	0.62
2	Sdepth4	0.79	0.33	−0.58	Sdepth4	0.81	0.30	−0.57
3	HC_579	0.87	0.08	−0.25	HC_579	0.91	0.11	−0.33
4	a_{00}	0.91	0.04	−0.19	a_{00}	0.94	0.03	−0.15
5	PDur_S	0.93	0.01	0.15	Ze	0.96	0.02	−0.15
6	Kc_min	0.94	0.01	−0.15	Kc_min	0.97	0.01	−0.12
7	Z_e	0.95	0.01	−0.13				
8	Z_r	0.96	0.01	−0.10				

Source: Output DTN: SN0701T0502206.044, *Stepwise_Analysis_R1_MC_VA.xls*.

Table H-6. Stepwise Regression (linear and rank) on Average Infiltration for Replicate 1, Where all Precipitation Parameters Have Been Replaced by Average Annual Precipitation: MC (aleatory uncertainty varying)

	Stepwise Regression (linear)				Stepwise Regression (rank)			
Step	**Variable**	**tot. R^2**	**inc. R^2**	**SRC**	**Variable**	**tot. R^2**	**inc. R^2**	**SRRC**
1	Sdepth4	0.46	0.46	−0.63	PPT_R1	0.44	0.44	0.57
2	PPT_R1	0.78	0.32	0.55	Sdepth4	0.75	0.31	−0.57
3	HC_579	0.86	0.08	−0.28	HC_579	0.86	0.11	−0.34

Source: Output DTN: SN0701T0502206.044, *Stepwise_Analysis_R1_Precipitation_MC_VA.xls*.

H3.1.1 Linear Regression

The linear regression results for Replicate 1 of the Monsoon climate are shown in Table H-5. a_m is the most important parameter, explaining 46% of the variance of infiltration. It has a positive effect, as expected. The next most important parameter is Soil Depth Class 4, with a negative effect on infiltration (SRC=−0.58). The third most importan parameter is HC_579, with a small negative effect (R^2 increment of 8%; SRC=−0.25). The other parameters in the table have negligible influence that may be due to spurious correlation.

MAP for the Monsoon climate is a function of the three independently sampled precipitation parameters (a_m, a_{00}, and b_m). A second stepwise regression analysis was performed to test the importance of this quantity (PPT_R1 in Table H-6). In this case, Soil Depth Class 4 is the most important parameter, explaining 46% of the variance. The next two most important parameters are MAP and HC_579.

H3.1.2 Rank Regression

The rank regression results for Replicate 1 of the Monsoon climate are also shown in Tables H-5 and H-6. The rank analysis results in the same top three parameters: a_m (or MAP) ranks first in importance, followed by Soil Depth Class 4 and HC_579.

H3.1.3 Scatterplots

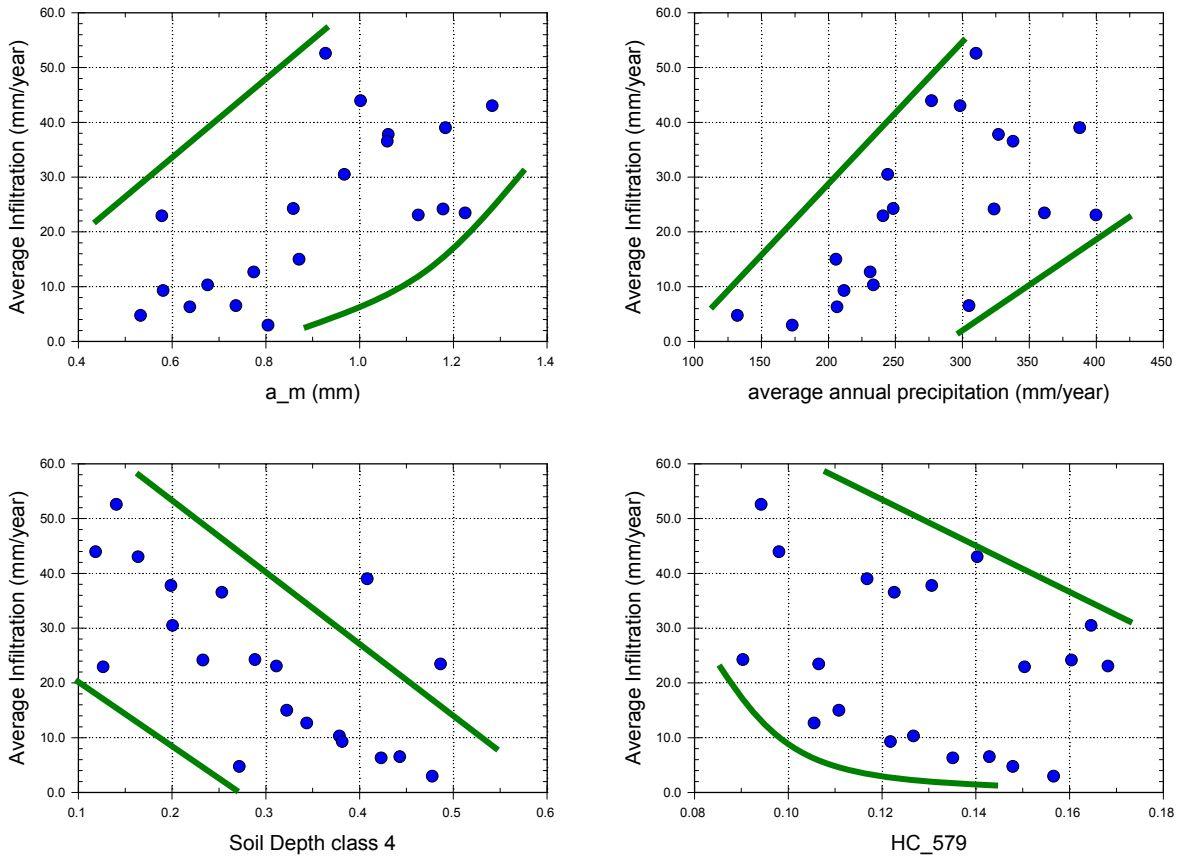

Source: Output DTN: SN0701T0502206.044, *scatterplots_R1_MC_VA.JNB*.

Figure H-5. Scatterplots of Average Infiltration versus a_m (upper left frame), MAP (upper right frame), Soil Depth Class 4 (lower left frame), and HC_579 (lower right frame) - Replicate 1 - MC (aleatory uncertainty varying)

Scatterplot analysis (Figure H-5) shows the influence of a_m and MAP on infiltration to be positive and significant. Soil Depth Class 4 has a visible negative effect on infiltration. The effect of HC_579 is discernable but very small.

H3.2 REPLICATE 2 – ALEATORY UNCERTAINTY VARYING

Table H-7. Stepwise Regression (linear and rank) on Average Infiltration for Replicate 2: MC (aleatory uncertainty varying)

	Stepwise Regression (linear)				Stepwise Regression (rank)			
Step	Variable	tot. R^2	inc. R^2	SRC	Variable	tot. R^2	inc. R^2	SRRC
1	a_m	0.44	0.44	0.60	a_m	0.58	0.58	0.76
2	Sdepth4	0.69	0.25	−0.41	Sdepth4	0.81	0.23	−0.39
3	a_{00}	0.74	0.05	−0.23	Z_e	0.88	0.07	−0.28
4	HC_579	0.79	0.05	−0.21	a_{00}	0.92	0.04	−0.21
5	b_m1	0.84	0.04	0.21	gTmaxwet	0.94	0.02	0.13
6	REW	0.87	0.04	−0.19				
7	lnRks_406	0.90	0.03	−0.20				
8	h_plant	0.93	0.02	−0.15				

Source: Output DTN: SN0701T0502206.044, *Stepwise_Analysis_R2_MC_VA.xls*.

Table H-8. Stepwise Regression (linear and rank) on Average Infiltration for Replicate 2, Where all Precipitation Parameters Have Been Replaced by Average Annual Precipitation: MC (aleatory uncertainty varying)

	Stepwise Regression (linear)				Stepwise Regression (rank)			
Step	Variable	tot. R^2	inc. R^2	SRC	Variable	tot. R^2	inc. R^2	SRRC
1	PPT_R2	0.57	0.57	0.76	PPT_R2	0.58	0.58	0.78
2	Sdepth4	0.84	0.27	−0.48	Sdepth4	0.83	0.25	−0.46
3	HC_579	0.89	0.05	−0.20	Z_e	0.86	0.03	−0.18
4	h_plant	0.91	0.02	−0.16	gTmaxwet	0.88	0.02	0.14
5	REW	0.93	0.01	−0.13	HC_579	0.90	0.02	−0.14
6	lnRks_406	0.94	0.01	−0.11				

Source: Output DTN: SN0701T0502206.044, *Stepwise_Analysis_R2_precipitation_MC_VA.xls*.

H3.2.1 Linear Regression

The linear regression results for Replicate 2 of the Monsoon climate are shown in Table H-7 (Section H3.2). a_m is the most important parameter, explaining 44% of the variance of infiltration. Soil Depth Class 4 comes next, explaining an additional 25% of the variance in infiltration, with a negative effect. The next parameter is a precipitation parameter, a_{00}, with a negative effect as expected. HC_579 comes next, explaining an additional 5% of the infiltration variance. The remaining parameters in Table H-7 have a very small influence on the variance of infiltration and may be due to spurious correlation.

When MAP (PPT_R2 in Table H-8)) is used as a replacement of the precipitation parameters, it becomes the most important parameter, explaining 57% of the variance in infiltration with a positive effect (as expected). The next most important parameter is Soil Depth Class 4, explaining 27% of the infiltration variance, with a negative effect (SRC=−0.52). HC_579 comes next, explaining an additional 5% of the infiltration variance. The next three parameters listed have a negligible influence.

H3.2.2 Rank Regression

The rank regression results for Replicate 2 of the Monsoon climate are also shown in Table H-7. The results of the rank regression are in agreement with linear regression for the two most important parameters, a_m and Soil Depth Class 4. The third most important parameter Z_e is different than for the linear regression but explains only 7% of the variance, which may be due to spurious correlation. The influence of the other parameters is negligible.

When precipitation parameters are replaced with the rank of MAP in the input set (PPT_R2 in Table H-8), it represents the most important parameter. Soil Depth Class 4 ranks next in importance. These top two parameters explain 80% of the variance in infiltration. The next three parameters explain 3%, 2%, and 2%, respectively.

H3.2.3 Scatterplots

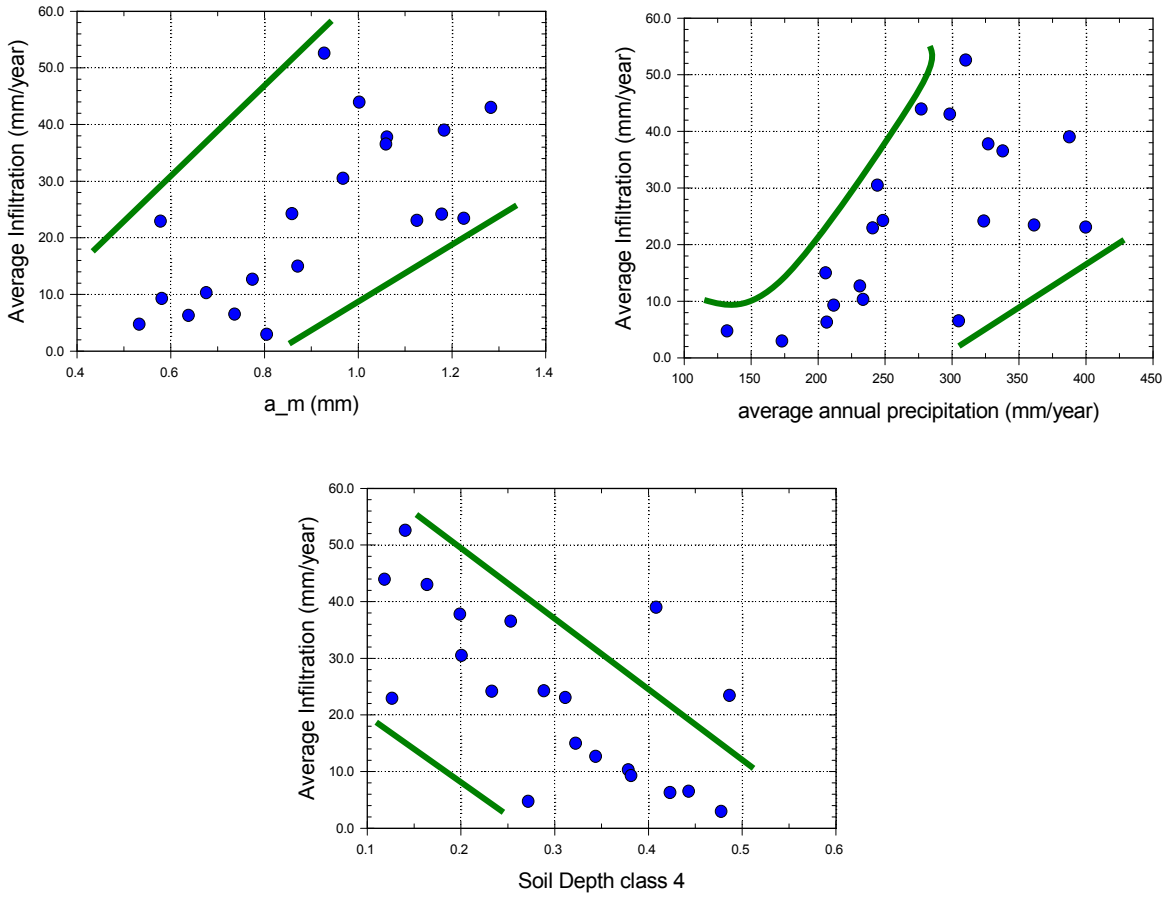

Source: Output DTN: SN0701T0502206.044, *scatterplots_R2_MC_VA.JNB*.

Figure H-6. Scatterplots of Average Infiltration versus a_m (upper left frame), MAP (upper right frame), and Soil Depth Class 4 (lower frame) - Replicate 2 - MC (aleatory uncertainty varying)

Scatterplot analysis (Figure H-6) shows a positive influence of a_m and MAP. The negative effect of Soil Depth Class 4 is also evident.

H3.3 CONCLUSION OF STUDY OF ORIGINAL DATA (ALEATORY UNCERTAINTY VARYING)

For Monsoon Climate, the two major contributors in the infiltration variance are the annual precipitation and the Soil Depth Class 4. The relative ranking of the top two parameters switches between replicates when MAP is substituted for the precipitation parameters. This result is not surprising given the small sample size used in the analysis and is not considered significant. Fixing the aleatory uncertainty helps to identify the importance of the other physical parameters and is discussed next for this climate.

H3.4 REPLICATE 1 – ALEATORY UNCERTAINTY FIXED

Table H-9. Stepwise Regression (linear and rank) on Average Infiltration for Replicate 1: MC (aleatory uncertainty fixed)

	Stepwise Regression (linear)				Stepwise Regression (rank)			
Step	Variable	tot. R^2	inc. R^2	SRC	Variable	tot. R^2	inc. R^2	SRRC
1	Sdepth4	0.63	0.63	−0.77	Sdepth4	0.65	0.65	−0.77
2	HC_579	0.89	0.26	−0.47	HC_579	0.86	0.21	−0.41
3	Z_r	0.92	0.03	−0.19	Kc_min	0.89	0.03	−0.20
4	Kc_min	0.94	0.02	−0.17	CKcb2	0.92	0.03	0.18
5	REW	0.95	0.01	−0.11	lnRks_406	0.93	0.02	−0.13
6					REW	0.95	0.01	−0.14
7					Z_r	0.96	0.02	−0.14
8					h_plant	0.97	0.01	−0.13
9					PDur_S	0.98	0.01	0.08
10					Z_e	0.99	0.01	0.07
11					gTmaxwet	0.99	0.00	0.07

Source: Output DTN: SN0701T0502206.044, *Stepwise_Analysis_R1_MC_FA.xls*.

H3.4.1 Linear Regression

The linear regression results for Replicate 1, Fixed Aleatory, of the Monsoon climate are shown in Table H-9. Soil Depth Class 4 is the most important parameter, explaining 63% of the infiltration variance, with a strong negative influence (SRC=−0.77). HC_579 ranks second in importance, with a negative influence, and explaining an additional 26% of the variance in infiltration. The influence of the other parameters displayed in the table is insignificant.

H3.4.2 Rank Regression

The rank regression results for Replicate 1, Fixed Aleatory, of the Monsoon climate are also shown in Table H-9. Results using rank transform are similar for the two most important parameters identified in the linear regression. Nine other parameters are displayed in Table H-9, but all of them have a small influence (3% or lower). Some of these parameters (in red) may be identified due to spurious correlations.

H3.4.3 Scatterplots

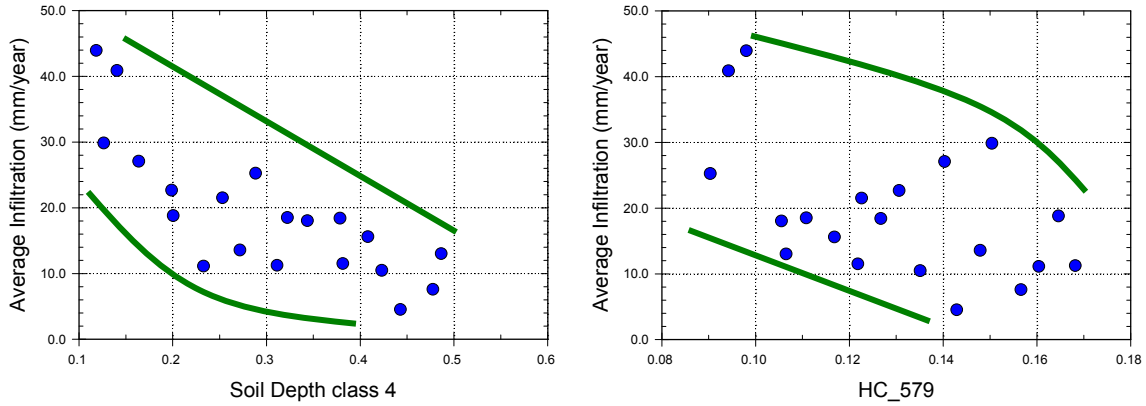

Source: Output DTN: SN0701T0502206.044, *scatterplots_R1_MC_FA.JNB*.

Figure H-7. Scatterplots of Average Infiltration Versus Soil Depth Class 4 (left frame), and HC_579 (right frame) - Replicate 1 - MC (aleatory uncertainty fixed)

Scatterplot analysis (Figure H-7) clearly shows the negative influence of Soil Depth Class 4. A less obvious negative influence of HC_579 is also illustrated.

H3.5 REPLICATE 2 – ALEATORY UNCERTAINTY FIXED

Table H-10. Stepwise Regression (linear and rank) on Average Infiltration for Replicate 2: MC (aleatory uncertainty fixed)

	Stepwise Regression (linear)				Stepwise Regression (rank)			
Step	**Variable**	**tot. R^2**	**inc. R^2**	**SRC**	**Variable**	**tot. R^2**	**inc. R^2**	**SRRC**
1	Sdepth4	0.58	0.58	−0.74	Sdepth4	0.57	0.57	−0.70
2	HC_579	0.84	0.26	−0.44	HC_579	0.81	0.23	−0.46
3	Z_r	0.88	0.04	−0.23	Z_r	0.89	0.08	−0.28
4	REW	0.91	0.03	−0.15	REW	0.92	0.03	−0.17
5	CKcb2	0.93	0.02	−0.13	PDur_S	0.94	0.02	0.16
6	PDur_S	0.95	0.02	0.13				
7	lnRks_405	0.96	0.01	0.13				
8	Kc_min	0.97	0.01	−0.13				
9	lnRks_406	0.98	0.01	0.10				

Source: Output DTN: SN0701T0502206.044, *Stepwise_Analysis_R2_MC_FA.xls*.

H3.5.1 Linear Regression

The linear regression results for Replicate 2, Fixed Aleatory, of the Monsoon climate are shown in Table H-10. Soil Depth Class 4 is the most important parameter, explaining 58% of the variance in infiltration, with a strong negative effect (SRC=−0.74). HC_579 ranks second in importance, explaining 26% of the remaining variance with a negative effect. The other

parameters found in Table H-10 have negligible influence (4% and lower), which indicates that this may be due to spurious correlations.

H3.5.2 Rank Regression

The rank regression results for Replicate 2, Fixed Aleatory, of the Monsoon climate are also shown in Table H-10. Results from rank regression are similar to the result of linear regression, with Soil Depth Class 4 and HC_579 identified as the first and second most important parameters. Rooting Depth (Z_r) has a small negative influence (R^2 increment of 8%). Other parameters have negligible influence.

H3.5.3 Scatterplots

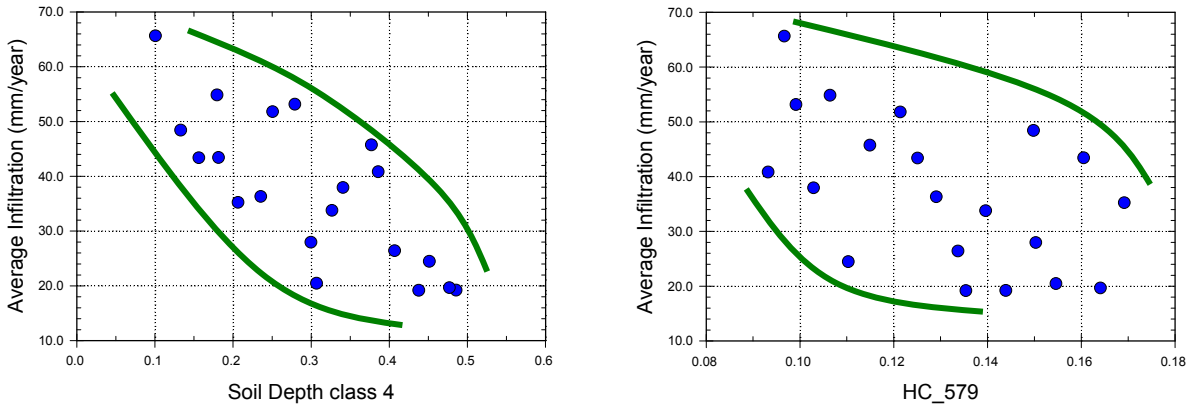

Source: Output DTN: SN0701T0502206.044, *scatterplots_R2_MC_FA.JNB*.

Figure H-8. Scatterplots of Average Infiltration Versus Soil Depth Class 4 (left frame), and HC_579 (right frame) - Replicate 2 - MC (aleatory uncertainty fixed)

Scatterplot analysis (Figure H-8) shows the influence of Soil Depth Class 4 and HC_579.

H3.6 CONCLUSIONS

The influence of the physical parameters on net infiltration for the Monsoon climate is similar to that observed for the Present-Day climate simulations, especially when aleatory uncertainty is fixed. This result increases confidence that the uncertainty in Soil Depth Class 4 and HC_579 are driving the uncertainty in infiltration, when future weather uncertainty is neglected (held constant). When future weather uncertainty is allowed to vary, a_{00} and a_m, which controls the MAP, are also important for estimating net infiltration.

H4. GLACIAL TRANSITION CLIMATE (GTC)

H4.1 REPLICATE 1 – ALEATORY UNCERTAINTY VARYING

Table H-11. Stepwise Regression (linear and rank) on Average Infiltration for Replicate 1: GTC (aleatory uncertainty varying)

	Stepwise Regression (linear)				Stepwise Regression (rank)			
Step	Variable	tot. R^2	inc. R^2	SRC	Variable	tot. R^2	inc. R^2	SRRC
1	Sdepth4	0.28	0.28	−0.51	Sdepth4	0.22	0.22	−0.42
2	a_{00}	0.53	0.25	−0.52	a_{00}	0.42	0.21	−0.46
3	Theta_m	0.67	0.14	0.41	a_m	0.59	0.17	0.40
4	a_m	0.80	0.13	0.36	Theta_m	0.71	0.12	0.35
5	CKcb2	0.90	0.10	−0.31	CKcb2	0.81	0.10	−0.31
6	Z_e	0.95	0.05	0.23	lnRks_406	0.86	0.05	0.23
7	lnRks_406	0.96	0.01	0.13				
8	PDurS	0.97	0.01	0.10				

Source: Output DTN: SN0701T0502206.044, *Stepwise_Analysis_R1_GTC_VA.xls*.

Table H-12. Stepwise Regression (linear and rank) on Average Infiltration for Replicate 1, Where All Precipitation Parameters Have Been Replaced by Average Annual Precipitation: GTC (aleatory uncertainty varying)

	Stepwise Regression (linear)				Stepwise Regression (rank)			
Step	Variable	tot. R^2	inc. R^2	SRC	Variable	tot. R^2	inc. R^2	SRRC
1	PPT_R1	0.43	0.43	0.67	PPT_R1	0.38	0.38	0.65
2	Sdepth4	0.73	0.30	−0.53	Sdepth4	0.65	0.27	−0.48
3	CKcb2	0.79	0.06	−0.26	CKcb2	0.73	0.08	−0.29
4	Z_e	0.83	0.03	0.18				

Source: Output DTN: SN0701T0502206.044, *Stepwise_Analysis_R1_Precipitation_GTC_VA.xls*.

H4.1.1 Linear Regression

The linear regression results for Replicate 1 of the Glacial Transition climate are shown in Table H-11. Soil Depth Class 4 is the most important parameter, explaining 28% of the variance with, as expected, a strong negative effect (SRC=−0.51) (see Table H-11). Next in importance are the three precipitation parameters. a_{00} ranks second in importance, explaining 25% of the variance in infiltration. It has a strong negative effect (SRC = −0.52). Higher values of a_{00} result in a lower frequency of precipitation, and consequently, it reduces average infiltration. Theta_m (θ_m) and a_m, explain 14% and 13% of the variance of infiltration, respectively. CKcb2 has a small negative influence, explaining an additional 10% of the variance. Other parameters have negligible influence.

MAP for the Glacial Transition Climate is a function of the three independently sampled precipitation parameters (a_m, a_{00}, and θ_m). A second stepwise regression analysis was performed to test the importance of MAP (PPT_R1 in Table H-12). In this analysis, MAP becomes the most important parameter, explaining 43% of the infiltration variance. Soil Depth Class 4 and CKcb2 rank second and third in importance, explaining 30% and 6% of the variance,

respectively. The last parameter listed, Z_e (evaporation depth) explains only 3% of the variance and has more than 5% chance of being due to spurious correlation.

H4.1.2 Rank Regression

The rank regression results for Replicate 1 of the Glacial Transition climate are also shown in Table H-11. Results of the rank regression are similar to results of the linear regression, with Soil Depth Class 4 explaining 22% of the variance. The next three parameters are all precipitation parameters, explaining together 50% of the remaining variance. CKcb2 ranks next in importance, explaining 10% of the variance in infiltration. lnRks_406 accounts for 5% of the variance.

When precipitation parameters are replaced with MAP (PPT_R1 in Table H-12), average annual precipitation becomes the most important parameter, explaining 38% of the variance. Soil Depth Class 4 and CKcb2 are ranked next in importance, explaining 27% and 8% of the variance of infiltration, respectively.

H4.1.3 Scatterplots

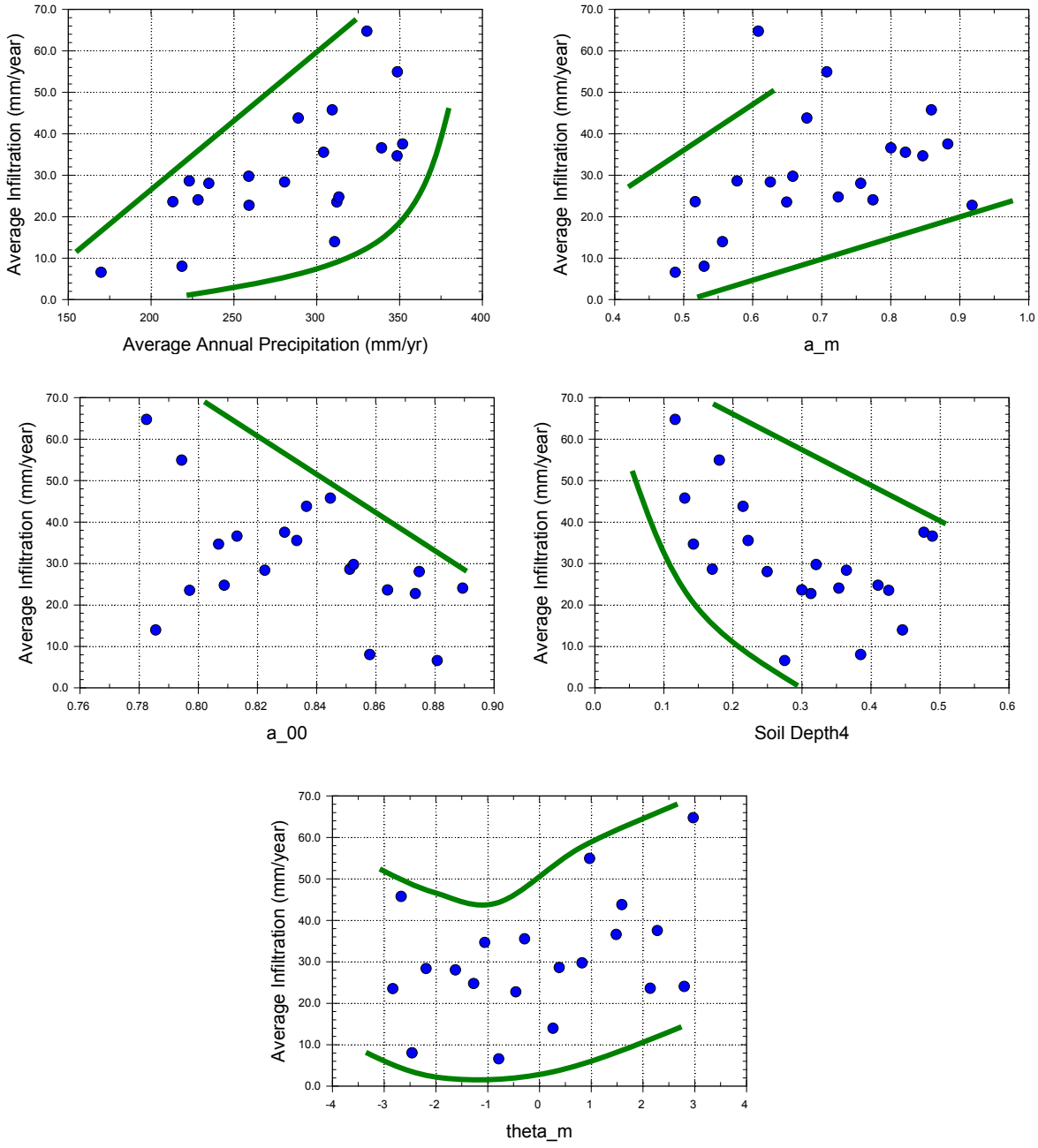

Source: Output DTN: SN0701T0502206.044, *scatterplots_R1_GTC_VA.JNB*.

Figure H-9. Scatterplots of Average Infiltration versus MAP (upper left frame), a_m (upper right frame), a_{00} (middle left frame), Soil Depth Class 4 (middle right frame) and θ_m (lower frame) - Replicate 1 - GTC (aleatory uncertainty varying)

Scatterplot analysis (Figure H-9) shows the influence of Soil Depth Class 4, a_{00}, a_m and, MAP. The importance of Theta_m (θ_m) is not clear in the figure.

H4.2 REPLICATE 2 – ALEATORY UNCERTAINTY VARYING

Table H-13. Stepwise Regression (linear and rank) on Average Infiltration for Replicate 2, Where All Precipitation Parameters Have Been Replaced by Average Annual Precipitation (MAP): GTC (aleatory uncertainty varying)

	Stepwise Regression (linear)				Stepwise Regression (rank)			
Step	**Variable**	**tot. R^2**	**inc. R^2**	**SRC**	**Variable**	**tot. R^2**	**inc. R^2**	**SRRC**
1	Sdepth4	0.43	0.43	−0.68	Sdepth4	0.41	0.41	−0.63
2	a_{00}	0.57	0.14	−0.37	a_m	0.61	0.20	0.51
3	a_m	0.70	0.13	0.41	a_{00}	0.75	0.13	−0.33
4	HC_579	0.79	0.09	−0.33	Kc_min	0.79	0.04	−0.21
5	Z_e	0.86	0.07	−0.24	CKcb2	0.83	0.04	−0.19
6	Kc_min	0.90	0.04	−0.16	PDurS	0.86	0.04	0.19
7	CKcb2	0.92	0.02	−0.16	HC_579	0.89	0.03	−0.17
8	PDurS	0.95	0.03	0.16				
9	Theta_m	0.96	0.01	0.12				

Source: Output DTN: SN0701T0502206.044, *Stepwise_Analysis_R2_GTC_VA.xls*.

Table H-14. Stepwise Regression (linear and rank) on Average Infiltration for Replicate 2, Where All Precipitation Parameters Have Been Replaced by Average Annual Precipitation: GTC (aleatory uncertainty varying)

	Stepwise Regression (linear)				Stepwise Regression (rank)			
Step	**Variable**	**tot. R^2**	**inc. R^2**	**SRC**	**Variable**	**tot. R^2**	**inc. R^2**	**SRRC**
1	Sdepth4	0.43	0.43	−0.68	Sdepth4	0.41	0.41	−0.64
2	PPT_R2	0.70	0.27	0.54	PPT_R2	0.73	0.32	0.58
3	HC_579	0.81	0.12	−0.37	HC_579	0.78	0.05	−0.22
4	Z_e	0.88	0.07	−0.25	CKcb2	0.82	0.04	−0.19
5	CKcb2	0.91	0.03	−0.17				
6	PDurS	0.93	0.02	0.13				
7	Kc_min	0.95	0.01	−0.12				

Source: Output DTN: SN0701T0502206.044, *Stepwise_Analysis_R2_Precipitation_GTC_VA.xls*.

H4.2.1 Linear Regression

The linear regression results for Replicate 2 of the Glacial Transition climate are shown in Table H-13. Soil Depth Class 4 is the most important parameter, explaining 43% of the variance. The parameters ranked second and third in importance are, a_{00} and a_m, explaining 14% and 13% of the variance, respectively. HC_579 is ranked next, explaining 9% of the variance, followed by Z_e, with 7% of the variance explained. The other parameters listed in Table H-13 have negligible influence.

If MAP (PPT_R2 in Table H-14) is used in place of the precipitation parameters, Soil Depth Class 4 is the most important parameter, with 43% of the variance of infiltration explained. It is followed in importance by MAP (incremental R^2 of 27%) and HC_579 (incremental R^2 of 12%). Z_e has a small negative influence and explains 7% of the variance. The other parameters have negligible influence.

H4.2.2 Rank Regression

The rank regression results for Replicate 2 of the Glacial Transition climate are also shown in Table H-13. Results of rank regression are similar to results of the linear regression. Soil Depth Class 4 and the precipitation parameters are the most important. No other parameters are found to be influential.

H4.2.3 Scatterplots

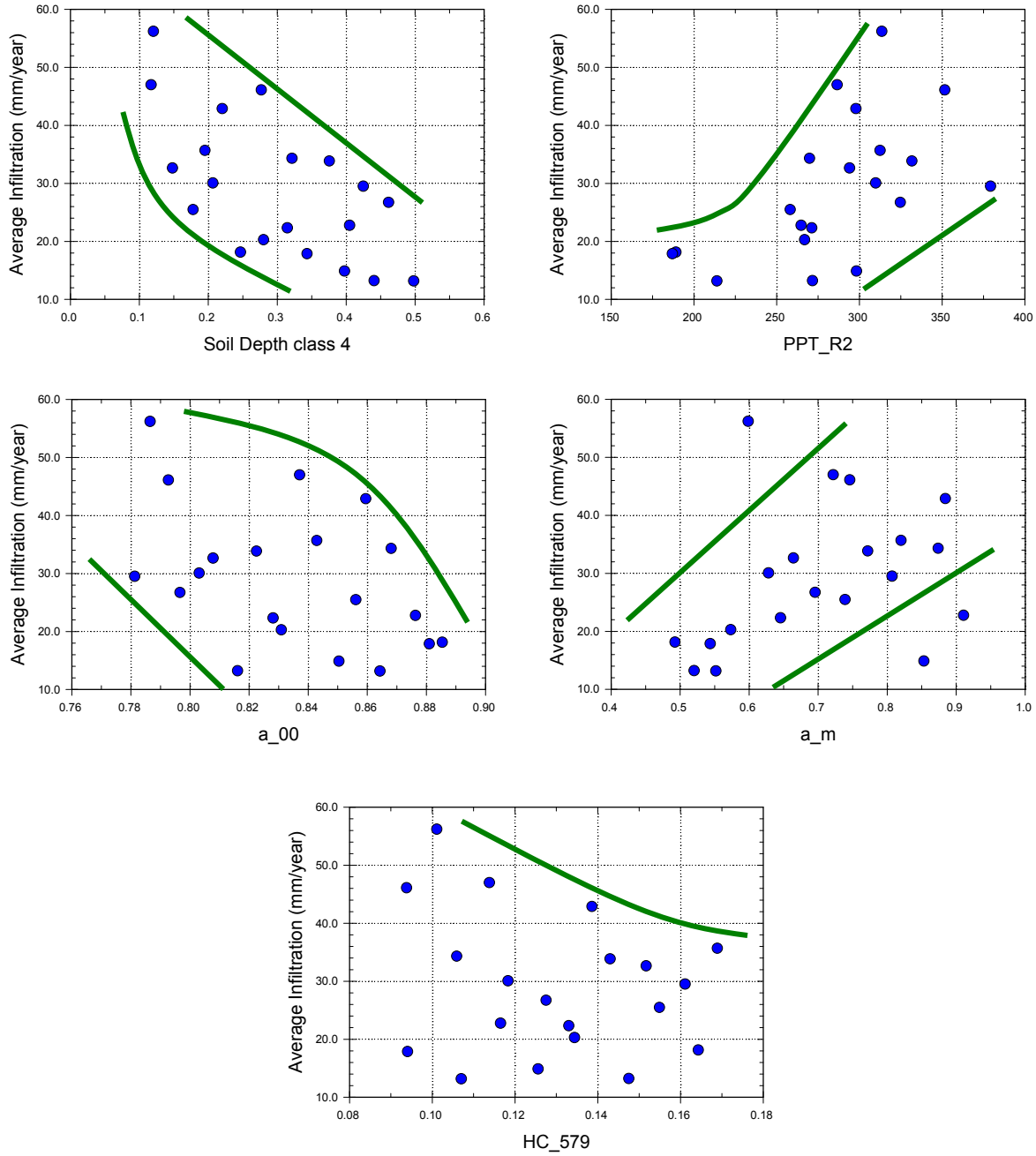

Source: Output DTN: SN0701T0502206.044, *scatterplots_R2_GTC_VA.JNB*.

Figure H-10. Scatterplots of Average Infiltration Versus Soil Depth Class 4 (upper left frame), MAP (upper right frame), a_{00} (middle left frame), a_m (middle right frame), and HC_579 (lower frame) - Replicate 2 - GTC (aleatory uncertainty varying)

Scatterplot analysis (Figure H-10) shows the influence of Soil Depth Class 4 and average annual precipitation. The influence of a_{00} and a_m is also evident. The influence of HC_579 is not that evident.

H4.3 CONCLUSION OF STUDY OF ORIGINAL DATA (ALEATORY UNCERTAINTY VARYING)

Sensitivity analyses done for Replicates 1 and 2 of the Glacial Transition climate result are generally consistent between replicates, in that the same top two parameters are identified for both replicates. Theta_m ranks third in importance for the linear regression results for Replicate 1, explaining 14% of the incremental variance. This may be a random result or it may reflect a genuine sensitivity. However, even with this question unresolved, it is clear that Soil Depth Class 4 and precipitation are the most important parameters for this climate.

The relative ranking of the top two parameters switches between replicates when MAP is substituted for the precipitation parameters. This result is not surprising given the small sample size used in the analysis and is not considered significant. Fixing the aleatory uncertainty helps to identify the importance of the other physical parameters and is discussed next for this climate.

H4.4 REPLICATE 1 – ALEATORY UNCERTAINTY FIXED

Table H-15. Stepwise Regression (linear and rank) on Average Infiltration for Replicate 1: GTC (aleatory uncertainty fixed)

	Stepwise Regression (linear)				Stepwise Regression (rank)			
Step	Variable	tot. R^2	inc. R^2	SRC	Variable	tot. R^2	inc. R^2	SRRC
1	Sdepth4	0.77	0.77	−0.87	Sdepth4	0.81	0.81	−0.88
2	HC_579	0.93	0.16	−0.41	HC_579	0.93	0.11	−0.36
3	CKcb2	0.95	0.02	−0.18	lnRks_406	0.94	0.01	0.11
4	Kc_min	0.97	0.01	−0.11	Z_e	0.95	0.01	−0.09
5	REW	0.98	0.01	−0.10	CKcb2	0.95	0.01	−0.09
6	Z_r	0.98	0.01	−0.08				

Source: Output DTN: SN0701T0502206.044, *Stepwise_Analysis_R1_GTC_FA.xls*.

H4.4.1 Linear Regression

The linear regression results for Replicate 1, Fixed Aleatory, of the Glacial Transition climate are shown in Table H-15. The most important parameter is Soil Depth Class 4. It has a strong negative effect and explains 77% of the variance of mean infiltration. The next most important parameter is HC_579 with a negative influence on infiltration, explaining 16% of the variance. All other parameters explain 2% or less of the variance of infiltration and may be due to spurious correlation.

H4.4.2 Rank Regression

The rank regression results for Replicate 1, Fixed Aleatory, of the Glacial Transition climate are also shown in Table H-15. Rank regression results are similar to the results of the linear regression. The top two parameters are Soil Depth Class 4 and HC_579, explaining 81% and 11% of the variance, respectively.

H4.4.3 Scatterplots

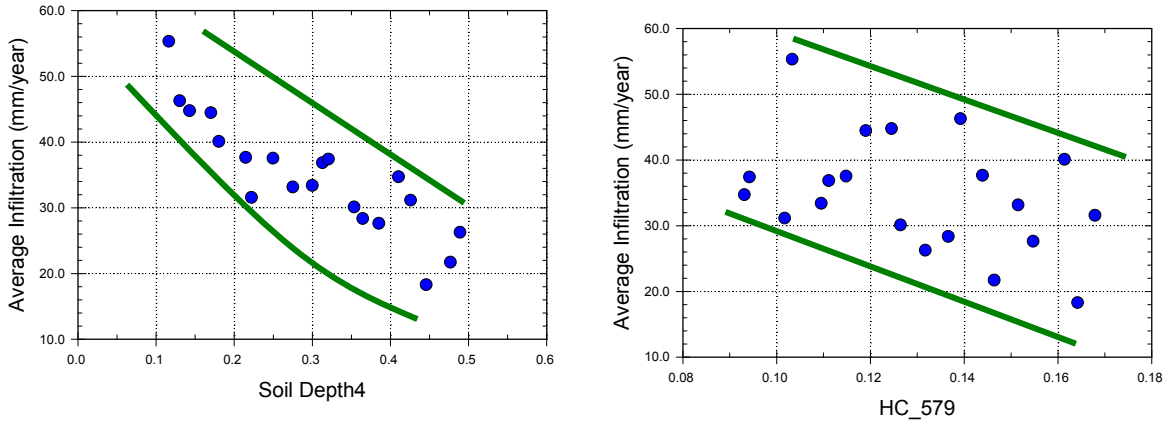

Source: Output DTN: SN0701T0502206.044, *scatterplots_R1_GTC_FA.JNB*.

Figure H-11. Scatterplots of Average Infiltration Versus Soil Depth Class 4 (left frame), and HC_579 (right frame) - Replicate 1 - GTC (aleatory uncertainty fixed)

Scatterplot analysis (Figure H-11) indicates a strong relationship between Soil Depth Class 4 and average infiltration. The influence of HC_579 is not as strong but is discernable.

H4.5 REPLICATE 2 – ALEATORY UNCERTAINTY FIXED

Table H-16. Stepwise Regression (linear and rank) on Average Infiltration for Replicate 2: GTC (aleatory uncertainty fixed)

	Stepwise Regression (linear)				Stepwise Regression (rank)			
Step	**Variable**	**tot. R^2**	**inc. R^2**	**SRC**	**Variable**	**tot. R^2**	**inc. R^2**	**SRRC**
1	Sdepth4	0.69	0.69	−0.89	Sdepth4	0.75	0.75	−0.90
2	HC_579	0.89	0.20	−0.46	HC_579	0.87	0.12	−0.32
3	CKcb2	0.95	0.06	−0.25	CKcb2	0.90	0.02	−0.18
4	Z_e	0.97	0.01	−0.10	Kc_min	0.93	0.03	−0.18
5	Kc_min	0.97	0.01	−0.08				
6	Z_r	0.98	0.01	−0.07				

Source: Output DTN: SN0701T0502206.044, *Stepwise_Analysis_R2_GTC_FA.xls*.

H4.5.1 Linear Regression

The linear regression results for Replicate 2, Fixed Aleatory, of the Glacial Transition climate are shown in Table H-16. Soil Depth Class 4 is the most important parameter, explaining 69% of the variance in net infiltration. HC_579 explains 20% of the variance. CKcb2 seems to have a small effect on infiltration, explaining 6% of the variance. The influence of the other parameters is negligible.

H4.5.2 Rank Regression

The rank regression results for Replicate 2, Fixed Aleatory, of the Glacial Transition climate are also shown in Table H-16. Results of the rank regression are very similar to the results of the linear regression, with Soil Depth Class 4 and HC_579 explaining 75% and 12% of the variance, respectively. CKcb2 and Kc_min rank third and fourth in importance but with very little influence.

H4.5.3 Scatterplots

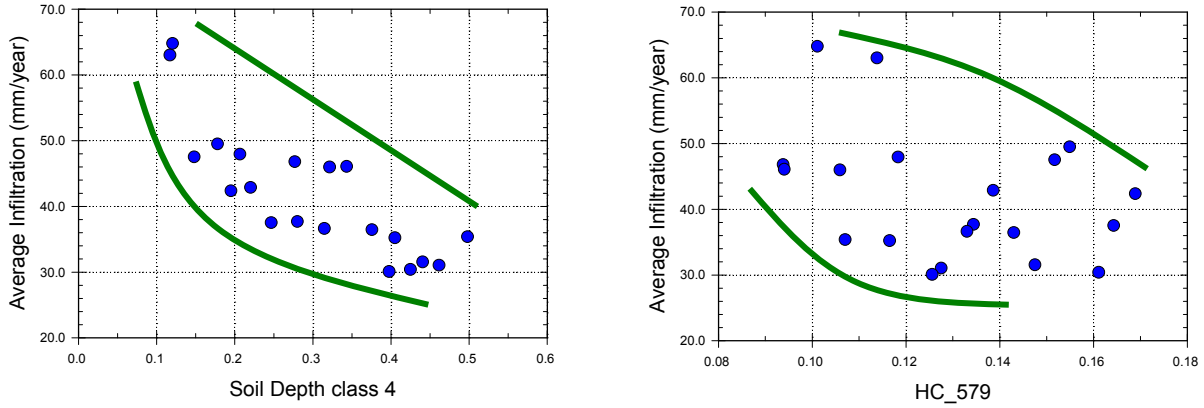

Source: Output DTN: SN0701T0502206.044, *scatterplots_R2_GTC_FA.JNB*.

Figure H-12. Scatterplots of Average Infiltration Versus Soil Depth Class 4 (left frame) and HC_579 (right frame) - Replicate 2 - GTC (aleatory uncertainty fixed)

Scatterplot analysis (Figure H-12) shows the influence of Soil Depth Class 4. The influence of HC_579 is not as pronounced but is discernable.

H4.6 CONCLUSIONS

The fixed aleatory analysis arrives at similar results to those obtained for the Present-Day and Monsoon climates. Soil Depth Class 4 and HC_579 together explain approximately 90% of the variance in net infiltration. When aleatory uncertainty is allowed to vary, and precipitation parameters (i.e. a_{00}, a_m, θ_m… etc.) are allowed to vary individually, the precipitation parameters are second in importance only to Soil Depth Class 4. If precipitation parameters are replaced by the MAP, the analysis suggests precipitation is as important as soil depth.

INTENTIONALLY LEFT BLANK

APPENDIX I
TREATMENT OF UNCERTAINTIES

This appendix addresses various details related to uncertainty analysis. Section I1 addresses the screening of parameters in order to select those included in the detailed analysis of parameter uncertainty. Section I2 presents background information on uncertainty, including definitions, commonly used uncertainty distributions, and key properties of those distributions.

I1. SCREENING OF PARAMETERS FOR UNCERTAINTY ANALYSIS

The first step in the uncertainty analysis was the elimination of parameters that do not have a large contribution to uncertainty in net infiltration. This step considered two properties associated with each parameter, its relative uncertainty and its influence on the average net infiltration.

In several places, the MASSIF model uses a formula that is an approximation for a function. Section I1.1, Parameters Included in Model Uncertainty, evaluates how the uncertainty in such approximations contributes to the uncertainty in calculated net infiltration. The concern in each case is the uncertainty of the approximate formula as a whole, not the uncertainty in the coefficients of the formula. Therefore, the sensitivity studies did not vary any coefficients of function approximations. The section identifies the coefficients that were not considered individually in the sensitivity studies but rather were included in model uncertainty.

Of the remaining parameters, some have different values for different climates. Others may have the same nominal values but different uncertainties. Parameters in either of these categories require a separate treatment for each climate.

First, however, Section I1.2 provides screening results for those parameters for which neither the nominal value nor its uncertainty varies appreciably for the three climates of interest. Sections I1.3, I1.4, and I1.5 summarize the screening for parameters specific to the Present-Day, Monsoon, and Glacial Transition climate, respectively.

Nominal values and limits have been rounded to be consistent with the standard uncertainty. The standard uncertainty is the uncertainty expressed as a standard deviation (ANSI/NCSL Z540-2-1997 [DIRS 157394], p. 3). Standard uncertainty has been rounded to one significant digit, except that a second significant digit may be included if the first digit is 1. Section I2.2 contains formulas for calculating standard uncertainty for various distributions.

A parameter is excluded from the sensitivity studies without further explanation if its standard uncertainty is less than 15% of a relevant value (relative uncertainty), often its nominal value, or if it is expected to have less than 15% influence on average net infiltration. A value of 15% was chosen arbitrarily for the sole reason that it resulted in a manageable number of parameters that were screened into the uncertainty analysis. Because of the time required to run the MASSIF calculation and the computer resources available, it was decided that approximately 40 realizations per climate could be accommodated. As described in Section 6.5.5, Latin Hypercube Sampling (LHS) was used to create a Monte Carlo analysis with which uncertainty in net infiltration could be estimated for each climate. LHS sampling works best when the number of realizations is less than 4/3 the number of sampled parameters. Therefore, a 15% cutoff, which resulted in between 11 and 15 sampled parameters, was chosen. Because there is no a priori basis upon which to choose a particular percent cutoff, it was deemed necessary to validate

the choice of the 15% value in a separate sensitivity study. This study, described in Section 7, applied a lower relative uncertainty cutoff which resulted in many more parameters being sampled by LHS. Two hundred realizations were generated and the MASSIF model was run on a single watershed (Drill Hole Wash), which covers the repository footprint. A global sensitivity study was performed on the results of this calculation and the parameters for which net infiltration is most sensitive were identified. The results of this study supported the use of the 15% cutoff for the uncertainty analysis for each climate, because the same parameters were identified as being most important in the larger LHS study as in uncertainty analyses using the 15% cutoff (see Section 7 for a detailed description of this validation study).

I1.1 PARAMETERS INCLUDED IN MODEL UNCERTAINTY

The formulas in this section contain over 50 coefficients. Each formula is a model approximation, the effects of which are considered as part of model uncertainty. Therefore, the parameter uncertainty analysis does not vary any of the coefficients in the following formulas or tables (see Section 6.4 and Appendix C):

- Formula for inverse relative distance Earth-Sun (Eq. C-3)
- Formula for solar declination (Eq. C-4)
- Formula for sine of mean solar elevation (Eq. C-7)
- Formula for total evaporable water (Eq. 6.4.4.2-2)
- Formula for atmospheric pressure (Eq. C-8)
- Formula for psychrometric constant (Eq. C-33b)
- Formula for saturation vapor pressure (Eq. C-2)
- Formula for precipitable water (Eq. C-9)
- Formula for 24-hour transmissivity for beam radiation (Eq. C-10)
- Table of slope-aspect corrections for direct beam radiation (Section C2)
- Formula for 24-hour transmissivity for diffuse radiation (Eq. C-11)
- Formula for diffuse radiation transmissivity for horizontal surface (Eq. C-15)
- Formula for diffuse radiation on inclined surface (Eq. C-23)
- Formula for net long wave radiation (Eq. C-35)
- Formula for reference evapotranspiration (Penman-Monteith equation) (Eqs. C-37 and 6.4.5-1)

- Formula for adjusting depletion factor for the evaporative power of the atmosphere (Eq. 6.4.4.2-6)

- Formula for vegetative cover fraction (canopy coefficient) (Eq. 6.4.4.1-3)

- Formula for upper limit on evaporation and transpiration (Eq. 6.4.4.1-1)

- Table of normalized differences between red and near-infrared bands as a function of DOY, slope, and azimuth, as measured at the Yucca Mountain site during reference year, $NDVI_{\_table}$

- Formula for fraction of transpiration that takes place in each node of the surface layer (Eqs. 6.4.4.2-8 and 6.4.4.2-9).

The following parameters are represented on a cell-by-cell basis within the MASSIF model. Being represented on a cell-by-cell basis means that each cell is assigned a unique value. Considering there are 139,092 cells in the infiltration modeling domain (Section 6.5.2.1), random uncertainty in these parameters will be small due to the large sample size used to obtain averages. Any systematic effects from the following parameters are contributors to model uncertainty, not parameter uncertainty.

- Precipitation during reference year for NDVI table, *PrecipRefNDVI*
- Potential Vegetative Response*, PVR*
- Slope, *slope*
- Azimuth**,** *azimuth*
- Elevation*, elev*
- Latitude*, lat*
- Longitude*, long*.

I1.2 SCREENING OF CLIMATE-INDEPENDENT PARAMETERS

This section lists the climate-independent parameters that are not coefficients of model approximations. For each such parameter that is excluded from the detailed uncertainty analysis, the current section provides information on its nominal value and either its uncertainty or its influence.

This section provides screening information for over 90 climate-independent parameters. Of these, the following eight meet the requirement for inclusion in the detailed uncertainty analysis:

- Soil depth of Depth Soil Class 4
- Saturated hydraulic conductivities of bedrock units 405 and 406 (K_{sat_rock})
- Soil water holding capacity for soil group 5/7/9 (θ_{HC})
- Readily evaporable water (*REW*) and the evaporation layer depth (Z_e)
- The minimum K_c for dry soil with no crop cover (K_{cmin})
- The slope of the relationship between NDVI' and K_{cb} (CK_{cb2}).

These parameters are compiled in tables of included parameters for each climate and can be found in Sections I1.3, I1.4, and I1.5.

Table I-1 lists the remaining climate-independent parameters, those that are excluded from the detailed analysis of parameter uncertainty. The holding capacity is not an input to the model; it is a surrogate for the field capacity, which is the sum of the wilting point and the holding capacity.

Table I-1. Climate Independent Parameters Excluded from the Uncertainty Analysis

Parameter Description	Parameter Symbol	Nominal Value	Low Range	High Range	Stand. Uncert.	Units	Relative Uncert.	Dist.	Reference	Reason for Exclusion
Terrain albedo	α_T	0.22	0.15	0.35	0.06	none	27%	Uniform	Table 6.5.4.1-4	Low influence; α_T has only a small impact on the solar radiation estimate and ET_0 (Section C1.3)
Intercept of linear fit of NDVI' and K_{cb}	C_{Kcb1}	−0.05	NA	NA	0.05	none	100%	Normal	Section 6.5.3.7	Low influence; at small values of NDVI', $K_{c\,min}$ overrides C_{kcb1}; at large values of NDVI', uncertainty in C_{kcb2} dominates (see Section 6.5.3.7.2)
Dew point offset from T_{min}, winter months	$K_{o\ winter}$	2	0	10	3	°C	140%	Uniform	Table 6.5.4.1-2	Low influence (extremes of uncertainty range cause less than 15% variation in standard evapotranspiration, ET_0; Section 6.5.4.1)
Dew point offset from T_{min}, rest of year	$K_{o\ rest}$	4.5	0	10	3	°C	60%	Uniform	Table 6.5.4.1-2	Low influence (extremes of uncertainty range cause less than 15% variation in standard evapotranspiration, ET_0; Section 6.5.4.1)
Precipitation lapse rate	$C_{Precipcor}$	6.3	NA	NA	0.7	%/100m	11%	Normal	Table F2.1-3	Low uncertainty
Maximum daily precipitation		983	NA	NA	NA	mm	NA	NA	Section 6.5.1 and Maidment 1993 [DIRS 125317], p. 3.36, Table 3.10.2	Low influence; this parameter was introduced to ensure that unrealistically high daily precipitation was not included in the analysis
Temperature lapse rate (dry adiabatic lapse rate)	*LR*	0.010	0.0095	0.0105	0.0003	°C/m	3%	Uniform	Maidment 1993 [DIRS 125317], p. 3.3	Low uncertainty
Fraction of snowfall that eventually sublimates	$C_{sublime}$	0.1	0	0.2	0.06	none	6%	Uniform	Table 6.5.1.7-1	Low uncertainty; uncertainty relative to total snowfall (1.0)

Table I-1. Climate Independent Parameters Excluded from the Uncertainty Analysis (Continued)

Parameter Description	Parameter Symbol	Nominal Value	Low Range	High Range	Stand. Uncert.	Units	Relative Uncert.	Dist.	Reference	Reason for Exclusion
Rate of increase of snowmelt with temperature	$C_{snowmelt}$	2	1	3	0.6	mm/day/ °C	30%	Uniform	Table 6.5.1.7-1	Low influence; difference in snowmelt rate affects days in which snowmelt is added to rainfall, does not affect total snowmelt
Adjustment coefficient in Hargreaves' radiation formula	K_{Rs}	0.19	0.15	0.22	0.02	$°C^{-0.5}$	11%	Uniform	Table 6.5.4.1-3	Low uncertainty
Average fraction of TAW that can be depleted from the root zone before reduction in ET	p	0.65	0.50	0.80	0.09	none	14%	Uniform	Table 6.5.4.2-3	Low uncertainty
Solar constant	G_{sc}	0.0820	0.0819	0.0821	0.0002	$MJ/m^2/min$	0.1%	Uniform	Table 6.5.4.1-5	Low uncertainty
Turbidity coefficient	K_{cln}	1.0	0.80	1.1	0.09	none	9%	Uniform	Table 6.5.4.1-6	Low uncertainty
Saturated hydraulic conductivity (cm/s)	$K_{sat\_soil}(1)$	8.0×10^{-5}	NR	NR	NR	cm/s	NR	NR	Table 6.5.2.3-1	Low influence; soil group less than 15% of UZ grid (Table 6.5.2.2-2)
	$K_{sat\_soil}(2/6)$	1.1×10^{-4}	NR	NR	NR	cm/s	NR	NR		
	K_{sat_soi} (3/4)	7.0×10^{-5}	NR	NR	NR	cm/s	NR	NR		
	$K_{sat\_soil}(5/7/9)$	6.8×10^{-5}	NA	NA	8%	cm/s	8%	Lognormal	Table 6.5.2.3-1	Low uncertainty
Saturated water content	$\theta_s(1)$	0.23	NR	NR	NR	m^3/m^3	NR	NR	Table 6.5.2.3-1	Low influence; soil group less than 15% of UZ grid (Table 6.5.2.2-2)
	$\theta_s(2/6)$	0.21	NR	NR	NR	m^3/m^3	NR	NR		
	$\theta_s(3/4)$	0.16	NR	NR	NR	m^3/m^3	NR	NR		
	$\theta_s(5/7/9)$	0.23	NA	NA	0.01	m^3/m^3	4%	Normal	Table 6.5.2.3-1	Low uncertainty
Soil wilting point	θ_{WP} (1)	0.040	NR	NR	NR	m^3/m^3	NR	NR	Table 6.5.2.3-1	Low influence; soil group less than 15% of UZ grid (Table 6.5.2.2-2)
	θ_{WP} (2/6)	0.037	NR	NR	NR	m^3/m^3	NR	NR		
	θ_{WP} (3/4)	0.024	NR	NR	NR	m^3/m^3	NR	NR		
	θ_{WP} (5/7/9)	0.039	NA	NA	0.002	m^3/m^3	5%	Normal	Table 6.5.2.3-1	Low uncertainty

Table I-1. Climate Independent Parameters Excluded from the Uncertainty Analysis (Continued)

Parameter Description	Parameter Symbol	Nominal Value	Low Range	High Range	Stand. Uncert.	Units	Relative Uncert.	Dist.	Reference	Reason for Exclusion
Soil water holding capacity	$\theta_{HC}(1)$	0.115	NR	NR	NR	m^3/m^3	NR	NR	Table 6.5.2.3-2	Low influence; soil group less than 15% of UZ grid (Table 6.5.2.2-2)
	$\theta_{HC}(2/6)$	0.114	NR	NR	NR	m^3/m^3	NR	NR		
	$\theta_{HC}(3/4)$	0.076	NR	NR	NR	m^3/m^3	NR	NR		
Depth of soil	$depth_{soil}(1)$	95	NR	NR	NR	m	NR	NR	Table 6.5.2.4-2	Low influence; soil depth class less than 15% of UZ grid (Table 6.5.2.4-1)
	$depth_{soil}(2)$	16.5	NA	NA	1.8	m	11%	Normal	Table 6.5.2.4-2	Low uncertainty
	$depth_{soil}(3)$	3.3	NR	NR	NR	m	NR	NR	Table 6.5.2.4-2	Low influence; soil depth class less than 15% of UZ grid (Table 6.5.2.4-1)
	$depth_{soil}(5)$	0	NR	NR	NR	m	NR	NR		
Bulk saturated hydraulic conductivity of bedrock	$K_{sat\_rock}(401)$	1.80×10^{-6}	NR	NR	NR	m/s	NR	NR	Table 6.5.2.6-1	Low influence; IHU less than 15% of the UZ grid (Table 6.5.2.5-1)
	$K_{sat\_rock}(402)$	1.20×10^{-6}	NR	NR	NR	m/s	NR	NR	Table 6.5.2.6-1	
	$K_{sat\_rock}(403)$	1.80×10^{-6}	NR	NR	NR	m/s	NR	NR	Table 6.5.2.6-1	
	$K_{sat\_rock}(404)$	7.70×10^{-7}	NR	NR	NR	m/s	NR	NR	Table 6.5.2.6-1	
	$K_{sat\_rock}(407)$	1.10×10^{-6}	NR	NR	NR	m/s	NR	NR	Table 6.5.2.6-1	
	$K_{sat\_rock}(408)$	1.70×10^{-6}	NR	NR	NR	m/s	NR	NR	Table 6.5.2.6-1	
	$K_{sat\_rock}(409)$	9.20×10^{-7}	NR	NR	NR	m/s	NR	NR	Table 6.5.2.6-1	
	$K_{sat\_rock}(410)$	2.70×10^{-6}	NR	NR	NR	m/s	NR	NR	Table 6.5.2.6-1	
	$K_{sat\_rock}(411)$	1.40×10^{-5}	NR	NR	NR	m/s	NR	NR	Table 6.5.2.6-1	
	$K_{sat\_rock}(412)$	4.90×10^{-6}	NR	NR	NR	m/s	NR	NR	Table 6.5.2.6-1	Low influence; IHU less than 15% of repository footprint (Table 6.5.2.5-1)
	$K_{sat\_rock}(413)$	3.90×10^{-6}	NR	NR	NR	m/s	NR	NR	Table 6.5.2.6-1	
	$K_{sat\_rock}(414)$	3.10×10^{-6}	NR	NR	NR	m/s	NR	NR	Table 6.5.2.6-1	
	$K_{sat\_rock}(415)$	9.40×10^{-6}	NR	NR	NR	m/s	NR	NR	Table 6.5.2.6-1	

Table I-1. Climate Independent Parameters Excluded from the Uncertainty Analysis (Continued)

Parameter Description	Parameter Symbol	Nominal Value	Low Range	High Range	Stand. Uncert.	Units	Relative Uncert.	Dist.	Reference	Reason for Exclusion
Bulk saturated hydraulic conductivity of bedrock (continued)	K_{sat_rock} *(416)*	1.70×10^{-5}	NR	NR	NR	m/s	NR	NR	Table 6.5.2.6-1	Low influence; IHU less than 15% of repository footprint (Table 6.5.2.5-1) (continued)
	K_{sat_rock} *(417)*	3.30×10^{-5}	NR	NR	NR	m/s	NR	NR	Table 6.5.2.6-1	
	K_{sat_rock} *(418)*	1.50×10^{-6}	NR	NR	NR	m/s	NR	NR	Table 6.5.2.6-1	
	K_{sat_rock} *(419)*	1.20×10^{-6}	NR	NR	NR	m/s	NR	NR	Table 6.5.2.6-1	Low influence; IHU less than 15% of the UZ grid (Table 6.5.2.5-1)
	K_{sat_rock} *(420)*	9.00×10^{-7}	NR	NR	NR	m/s	NR	NR	Table 6.5.2.6-1	
	K_{sat_rock} *(421)*	1.30×10^{-6}	NR	NR	NR	m/s	NR	NR	Table 6.5.2.5-1	
	K_{sat_rock} *(422)*	1.20×10^{-6}	NR	NR	NR	m/s	NR	NR	Table 6.5.2.6-1	
	K_{sat_rock} *(423)*	1.70×10^{-6}	NR	NR	NR	m/s	NR	NR	Table 6.5.2.6-1	
	K_{sat_rock} *(424)*	8.50×10^{-7}	NR	NR	NR	m/s	NR	NR	Table 6.5.2.6-1	
	K_{sat_rock} *(425)*	8.00×10^{-6}	NR	NR	NR	m/s	NR	NR	Table 6.5.2.6-1	
	K_{sat_rock} *(426)*	9.40×10^{-7}	NR	NR	NR	m/s	NR	NR	Table 6.5.2.6-1	
	K_{sat_rock} *(427)*	1.00×10^{-5}	NR	NR	NR	m/s	NR	NR	Table 6.5.2.6-1	
	K_{sat_rock} *(428)*	9.40×10^{-7}	NR	NR	NR	m/s	NR	NR	Table 6.5.2.6-1	
	K_{sat_rock} *(429)*	2.00×10^{-4}	NR	NR	NR	m/s	NR	NR	Table 6.5.2.6-1	
	K_{sat_rock} *(430)*	9.40×10^{-7}	NR	NR	NR	cm/s	NR	NR	Table 6.5.2.6-1	
	K_{sat_rock} *(432)*	9.40×10^{-7}	NR	NR	NR	cm/s	NR	NR	Table 6.5.2.6-1	
	K_{sat_rock} *(434)*	9.40×10^{-6}	NR	NR	NR	cm/s	NR	NR	Table 6.5.2.6-1	
	K_{sat_rock} *(435)*	1.50×10^{-6}	NR	NR	NR	cm/s	NR	NR	Table 6.5.2.6-1	
	K_{sat_rock} *(436)*	1.20×10^{-6}	NR	NR	NR	cm/s	NR	NR	Table 6.5.2.6-1	
	K_{sat_rock} *(437)*	6.40×10^{-7}	NR	NR	NR	cm/s	NR	NR	Table 6.5.2.6-1	
	K_{sat_rock} *(438)*	2.10×10^{-6}	NR	NR	NR	cm/s	NR	NR	Table 6.5.2.6-1	

NOTE: Uncertainty distribution not reported (NR) in this table for material properties that affect less than 15% of UZ grid.

I1.3 SCREENING OF PRESENT-DAY CLIMATE PARAMETERS

For the Present-Day climate, Table I-2 summarizes the eleven parameters varied independently in the uncertainty analysis (the eight climate-independent parameters plus three additional parameters). Two plant parameters were varied (the mean plant height and the maximum effective rooting depth).

One weather parameter, a_m, was also varied. Another weather parameter, a_λ, was not varied independently, but rather was correlated with a_m (Table I-3). Although the relative uncertainty in a_λ is somewhat less than the arbitrary 15% criterion, it was included in the uncertainty analysis so that its value would remain consistent with the value of a_m.

Approximately 30 other climate dependent parameters were screened. Table I-4 lists those parameters that are excluded from the detailed analysis of parameter uncertainty.

Table I-2. Parameters Varied Independently in Uncertainty Analysis for Present-Day Climate

Parameter Description	Parameter Symbol	Nominal Value	Low Range	High Range	Stand. Uncert.	Units	Relative Uncert.	Dist.	Reference	Comments
Constant term in Fourier series for m(d)	a_m	0.78	0.50	1.07	0.16	ln mm	20%	Uniform	Table F3.1-2	
Mean plant height	h_{plant}	0.40	0.20	0.60	0.12	m	30%	Uniform	Table 6.5.3.3-1	
Maximum effective rooting depth	Z_r	1.6	0.6	2.6	0.6	m	38%	Uniform	Table 6.5.3.2-1	
Depth of soil	$depth_{soil}(4)$	0.3	0.1	0.5	0.12	m	40%	Uniform	Section 6.5.2.4	Midpoint selected as nominal value; not used in calculations
Bulk saturated hydraulic conductivity of bedrock	$K_{sat\_rock}(405)$	1.1×10^{-6}	7.6×10^{-8}	4.8×10^{-6}	factor of 3	m/s	factor of 3	Loguniform	Table 6.5.2.6-1	
	K_{sat_rock} (406)	1.3×10^{-6}	2.1×10^{-8}	7.7×10^{-6}	factor of 5	m/s	factor of 5	Loguniform	Table 6.5.2.6-1	
Soil water holding capacity	$\theta_{HC}(5/7/9)$	0.13	0.09	0.17	0.02	m^3/m^3	15%	Uniform	Table 6.5.2.3-2	
Readily evaporable water	*REW*	6	2	10	2	mm	30%	Uniform	Table 6.5.4.2-5	
Minimum K_c for dry soil with no crop cover	K_{c_min}	0	0	0.2	0.06	none	30%	50% 0.0, 50% triangular	Table 6.5.4.2-2	Uncertainty relative to maximum
Evaporation layer depth	Z_e	0.15	0.1	0.2	0.03	m	19%	Uniform	Table 6.5.4.2-4	
Slope of relationship between K_{cb} to NDVI_cor	C_{Kcb2}	9.7	NA	NA	2.1	none	20%	Normal	Section 6.5.3.7	

Table I-3. Parameters Correlated with Other Parameters that Varied Independently in Uncertainty Analysis for Present-Day Climate

Parameter Description	Parameter Symbol	Nominal Value	Low Range	High Range	Stand. Uncert.	Units	Relative Uncert.	Dist.	Reference	Comments
Constant term in Fourier series for I(d)	a_λ	5.20	4.0	6.5	0.7	mm	13%	Uniform	Table F3.1-1	Included; correlated with a_m

Table I-4. Parameters Excluded from Uncertainty Analysis for Present-Day Climate

Parameter Description	Parameter Symbol	Nominal Value	Low Range	High Range	Stand. Uncert.	Units	Relative Uncert.	Dist.	Reference	Comments	Reason for Exclusion
Constant term in Fourier series for $p_{oo}(d)$	a_{00}	0.934	0.924	0.944	0.006	none	9%	Uniform	Table F3.1-1	Uncertainty relative to $1-a_{00}$	Low uncertainty
Magnitude of first order-term in Fourier series for $p_{oo}(d)$	$b_{00,1}$	0.027	NA	NA	0.003	none	5%	Normal	Table F3.1-1	Uncertainty relative to $1-a_{00}$	Low uncertainty
Phase of first-order term in Fourier series for $p_{oo}(d)$	$\theta_{00,1}$	−1.31	NA	NA	0.09	radians	3%	Normal	Table F3.1-1	Uncertainty relative to π	Low uncertainty
Constant term in Fourier series for $p_{10}(d)$	a_{10}	0.58	0.50	0.65	0.04	none	10%	Uniform	Table F3.1-1	Uncertainty relative to $1-a_{10}$	Low uncertainty
Magnitude of first-order term in Fourier series for $p_{10}(d)$	$b_{10,1}$	0.06	0.03	0.10	0.02	none	5%	Uniform	Table F3.1-1	Uncertainty relative to $1-a_{10}$	Low uncertainty
Phase of first-order term in Fourier series for $p_{10}(d)$	$\theta_{10,1}$	−1.5	NA	NA	0.4	radians	13%	Normal	Table F3.1-1	Uncertainty relative to π	Low uncertainty

Table I-4. Parameters Excluded from Uncertainty Analysis for Present-Day Climate (Continued)

Parameter Description	Parameter Symbol	Nominal Value	Low Range	High Range	Stand. Uncert.	Units	Relative Uncert.	Dist.	Reference	Comments	Reason for Exclusion
Magnitude of first-order term in Fourier series for I(d)	$b_{\lambda,1}$	0.7	NA	NA	0.2	mm	4%	Normal	Table F3.1-1	Uncertainty relative to a_{λ}	Low uncertainty
Phase of first-order term in Fourier series for I(d)	$\theta_{\lambda,1}$	2.5	NA	NA	0.7	radians	22%	Normal	Table F3.1-1	Uncertainty relative to π	Low influence; first order term less than 15% of magnitude of constant term
Magnitude of first-order term in Fourier series for m(d)	$b_{m,1}$	0.15	NA	NA	0.04	ln mm	5%	Normal	Table F3.1-1	Uncertainty relative to a_m	Low uncertainty
Phase of first-order term in Fourier series for m(d)	$\theta_{m,1}$	2.4	NA	NA	0.4	radians	13%	Normal	Table F3.1-1	Uncertainty relative to π	Low uncertainty
Starting DOY (calendar day) for winter dew point		335	274	335	18	days	10%	Uniform	Table 6.5.4.1-2	Uncertainty relative to 182 days	Low uncertainty
Ending DOY (calendar day) for winter dew point		90	90	151	18	days	10%	Uniform	Table 6.5.4.1-2	Uncertainty relative to 182 days	Low uncertainty
Magnitude of first-order term in Fourier series for $Twet_{min}(d)$	αwet_{min}	9.1	8.6	9.6	0.3	°C	4%	Uniform	Table F3.1-1	Uncertainty relative to $\gamma wet_{max} - \gamma wet_{min}$	Low uncertainty
Phase of first-order term in Fourier series for $Twet_{min}(d)$	βwet_{min}	122	121	124	1	days	0.5%	Uniform	Table F3.1-1	Uncertainty relative to 182 days	Low uncertainty

Table I-4. Parameters Excluded from Uncertainty Analysis for Present-Day Climate (Continued)

Parameter Description	Parameter Symbol	Nominal Value	Low Range	High Range	Stand. Uncert.	Units	Relative Uncert.	Dist.	Reference	Comments	Reason for Exclusion
Constant term in Fourier series for $Twet_{min}(d)$	γwet_{min}	6.6	5.0	8.1	0.9	°C	11%	Uniform	Table F3.1-1	Uncertainty relative to $\gamma wet_{max}-\gamma wet_{min}$	Low uncertainty
Magnitude of first-order term in Fourier series for $Tdry_{min}(d)$	αdry_{min}	9.7	9.4	10.0	0.2	°C	2%	Uniform	Table F3.1-1	Uncertainty relative to $\gamma dry_{max}-\gamma dry_{min}$	Low uncertainty
Phase of first-order term in Fourier series for $Tdry_{min}(d)$	βdry_{min}	115	114	116	1	days	0.5%	Uniform	Table F3.1-1	Uncertainty relative to 182 days	Low uncertainty
Constant term in Fourier series for $Tdry_{min}(d)$	γdry_{min}	9.4	6.9	11.8	1.4	°C	13%	Uniform	Table F3.1-1	Uncertainty relative to $\gamma dry_{max}-\gamma dry_{min}$	Low uncertainty
Magnitude of first-order term in Fourier series for $Twet_{max}(d)$	αwet_{max}	12.1	11.8	12.4	0.2	°C	2%	Uniform	Table F3.1-1	Uncertainty relative to $\gamma wet_{max}-\gamma wet_{min}$	Low uncertainty
Phase of first-order term in Fourier series for $Twet_{max}(d)$	βwet_{max}	117	116	118	1	days	0.5%	Uniform	Table F3.1-1	Uncertainty relative to 182 days	Low uncertainty
Constant term in Fourier series for $Twet_{max}(d)$	γwet_{max}	14.8	13.9	15.8	0.6	°C	7%	Uniform	Table F3.1-1	Uncertainty relative to $\gamma wet_{max}-\gamma wet_{min}$	Low uncertainty
Magnitude of first-order term in Fourier series for $Tdry_{max}(d)$	αdry_{max}	12.2	11.9	12.4	0.10	°C	1.3%	Uniform	Table F3.1-1	Uncertainty relative to $\gamma dry_{max}-\gamma dry_{min}$	Low uncertainty
Phase of first-order term in Fourier series for $Tdry_{max}(d)$	βdry_{max}	110	109	110	0.3	days	0.2%	Uniform	Table F3.1-1	Uncertainty relative to 182 days	Low uncertainty
Constant term in Fourier series for $Tdry_{max}(d)$	γdry_{max}	20.0	19.2	20.7	0.4	°C	4%	Uniform	Table F3.1-1	Uncertainty relative to $\gamma dry_{max}-\gamma dry_{min}$	Low uncertainty

Table I-4. Parameters Excluded from Uncertainty Analysis for Present-Day Climate (Continued)

Parameter Description	Parameter Symbol	Nominal Value	Low Range	High Range	Stand. Uncert.	Units	Relative Uncert.	Dist.	Reference	Comments	Reason for Exclusion
Wind speed at height of 2m during month m	$u_2(1)$	2.36	NA	NA	0.03	m/s	1.3%	Normal	Table F3.1-1	<9% of year	low uncertainty
	$u_2(2)$	2.67	NA	NA	0.04	m/s	1.5%	Normal	Table F3.1-1	<9% of year	low uncertainty
	$u_2(3)$	2.84	NA	NA	0.03	m/s	1.1%	Normal	Table F3.1-1	<9% of year	low uncertainty
	$u_2(4)$	3.22	NA	NA	0.04	m/s	1.2%	Normal	Table F3.1-1	<9% of year	low uncertainty
	$u_2(5)$	2.97	NA	NA	0.03	m/s	1.0%	Normal	Table F3.1-1	<9% of year	low uncertainty
	$u_2(6)$	2.90	NA	NA	0.02	m/s	0.7%	Normal	Table F3.1-1	<9% of year	low uncertainty
	$u_2(7)$	2.75	NA	NA	0.02	m/s	0.7%	Normal	Table F3.1-1	<9% of year	low uncertainty
	$u_2(8)$	2.71	NA	NA	0.02	m/s	0.7%	Normal	Table F3.1-1	<9% of year	low uncertainty
	$u_2(9)$	2.64	NA	NA	0.02	m/s	0.8%	Normal	Table F3.1-1	<9% of year	low uncertainty
	$u_2(10)$	2.61	NA	NA	0.03	m/s	1.1%	Normal	Table F3.1-1	<9% of year	low uncertainty
	$u_2(11)$	2.47	NA	NA	0.03	m/s	1.2%	Normal	Table F3.1-1	<9% of year	low uncertainty
	$u_2(12)$	2.48	NA	NA	0.03	m/s	1.2%	Normal	Table F3.1-1	<9% of year	low uncertainty
Minimum precipitation duration (intercept to 1)		1.07	NA	NA	NA	hr	NA	NA	Table 6.5.1.7-3		uncertainty captured in rate of duration increase with precipitation
Rate of duration increase with precipitation (slope)		0.38	NA	NA	0.05	hr/mm	13%	Normal	Table 6.5.1.7-3		low uncertainty

I1.4 SCREENING OF MONSOON CLIMATE PARAMETERS

Tables I-5 and I-6 summarize the 19 parameters varied in the uncertainty analysis for the monsoon climate, including the eight parameters that are climate-independent. Two plant parameters were varied (the mean plant height and the maximum effective rooting depth). The slope of precipitation duration versus amount of precipitation was varied for this climate.

Four weather parameters were varied directly. Four additional weather parameters were not varied independently but rather were correlated with a_m and b_{m1}. These seven weather parameters provided variation in the weather input files for model calculations.

The monsoon climate is described in *Future Climate Analysis* (BSC 2004 [DIRS 170002]) as being something between the current desert climate (with most of the rain in winter) and a classical monsoon climate (with most of the rain in summer). This uncertainty has been modeled by fixing the phase of the seasonal variation (all θ values) such that most of the rain falls in summer, and authorizing the amplitude (all b values) to vary between positive values (keeping most of the rain in summer) and negative values (switching the largest amount of rain to winter period).

One of the amplitude values, b_m, is varied independently. All the other amplitudes are estimated using simple linear regression. Even though there is no correlation between annual average (a values) and amplitude (b values), the resulting weather parameters have to be checked in order to suppress any physical impossibilities:

- First, $b_{00,1}$ cannot be higher than $1-a_{00}$ (as it will create a probability of having a dry day bigger than 1).
- Next, b_λ cannot be higher than a_λ, as it will create a negative value for some daily amounts of rain.

These configurations are unlikely to happen. Therefore, in the event that sampling results one vector that contains a physically impossible set of values, the entire set of sample vectors is discarded.

Table I-7 lists those parameters that are excluded from the detailed analysis of parameter uncertainty.

Table I-5. Parameters Varied Independently in Uncertainty Analysis for Monsoon Climate

Parameter Description	Parameter Symbol	Nominal Value	Low Range	High Range	Stand. Uncert.	Units	Relative Uncert.	Dist.	Reference	Comments
Constant term in Fourier series for $p_{oo}(d)$	a_{00}	0.920	0.896	0.944	0.014	none	18%	Uniform	Table F3.2-1	Uncertainty relative to $1-a_{00}$
Constant term in Fourier series for m(d)	a_m	0.9	0.5	1.3	0.2	ln mm	20%	Uniform	Table F3.2-1	
Magnitude of first-order term in Fourier series for m(d)	$b_{m,1}$	0.1	−0.3	0.5	0.2	ln mm	20%	Uniform	Table F3.2-1	Uncertainty relative to a_m
Constant term in Fourier series for $Twet_{max}(d)$	γwet_{max}	18	14	22	2	°C	18%	Uniform	Table F3.2-1	Uncertainty relative to $\gamma wet_{max}-\gamma wet_{min}$
Mean plant height	h_{plant}	0.4	0.2	0.6	0.12	m	30%	Uniform	Table 6.5.3.3-1	
Maximum effective rooting depth	Z_r	1.6	0.6	2.6	0.6	m	38%	Uniform	Table 6.5.3.2-1	
Rate of duration increase with precipitation (slope)		0.28	0.14	0.43	0.08	hr/mm	30%	Uniform	Table 6.5.1.7-4	Extremes extended by one standard error
Depth of soil	$depth_{soil}(4)$	0.3	0.1	0.5	0.12	m	40%	Uniform	Section 6.5.2.4	Midpoint selected as nominal value; not used in calculations
Bulk saturated hydraulic conductivity of bedrock	$K_{sat\_rock}(405)$	1.1×10^{-6}	7.6×10^{-8}	4.8×10^{-6}	factor of 3	m/s	factor of 3	Loguniform	Table 6.5.2.6-1	
	K_{sat_rock} (406)	1.3×10^{-6}	2.1×10^{-8}	7.7×10^{-6}	factor of 5	m/s	factor of 5	Loguniform	Table 6.5.2.6-1	
Soil water holding capacity	$\theta_{HC}(5/7/9)$	0.13	0.09	0.17	0.02	m^3/m^3	15%	Uniform	Table 6.5.2.3-2	

Table I-5. Parameters Varied Independently in Uncertainty Analysis for Monsoon Climate (Continued)

Parameter Description	Parameter Symbol	Nominal Value	Low Range	High Range	Stand. Uncert.	Units	Relative Uncert.	Dist.	Reference	Comments
Readily evaporable water	*REW*	6	2	10	2	mm	30%	Uniform	Table 6.5.4.2-5	
Minimum K_c for dry soil with no crop cover	K_{c_min}	0	0	0.2	0.06	none	30%	50% 0.0, 50% Triangular	Table 6.5.4.2-2	Uncertainty relative to maximum
Evaporation layer depth	Z_e	0.15	0.1	0.2	0.03	m	19%	Uniform	Table 6.5.4.2-4	
Slope of relationship between K_{cb} to NDVI_cor	C_{Kcb2}	9.7	NA	NA	2.1	none	20%	Normal	Section 6.5.3.7	

Table I-6. Parameters Correlated with Other Parameters that Varied Independently in Uncertainty Analysis for Monsoon Climate

Parameter Description	Parameter Symbol	Nominal Value	Low Range	High Range	Stand. Uncert.	Units	Relative Uncert.	Dist.	Reference	Comments
Constant term in Fourier series for I(d)	a_λ	6.50	4.0	9.0	1.4	mm	22%	Uniform	Table F3.2-1	Correlated with a_m
Magnitude of first-order term in Fourier series for I(d)	$b_{\lambda,1}$	1.6	−1.3	4.5	1.7	mm	26%	Uniform	Table F3.2-1	Uncertainty relative to a_λ; correlated with $b_{m,1}$
Magnitude of first order-term in Fourier series for p_{oo}(d)	$b_{00,1}$	0.02	−0.03	0.07	0.03	none	38%	Uniform	Table F3.2-1	Uncertainty relative to $1-a_{00}$; correlated with $b_{m,1}$
Magnitude of first-order term in Fourier series for p_{10}(d)	$b_{10,1}$	−0.02	−0.13	0.10	0.07	none	17%	Uniform	Table F3.2-1	Uncertainty relative to $1-a_{10}$; correlated with $b_{m,1}$

Table I-7. Parameters Excluded from Uncertainty Analysis for Monsoon Climate

Parameter Description	Parameter Symbol	Nominal Value	Low Range	High Range	Stand. Uncert.	Units	Relative Uncert.	Dist.	Reference	Comments	Reason for Exclusion
Phase of first-order term in Fourier series for $p_{oo}(d)$	$\theta_{00,1}$	2.00	1.74	2.25	0.15	radians	5%	Uniform	Table F3.2-1	Uncertainty relative to π	Low uncertainty
Constant term in Fourier series for $p_{10}(d)$	a_{10}	0.58	0.50	0.67	0.05	none	12%	Uniform	Table F3.2-1	Uncertainty relative to $1-a_{10}$	Low uncertainty
Phase of first-order term in Fourier series for $p_{10}(d)$	$\theta_{10,1}$	1.8	1.4	2.3	0.3	radians	10%	Uniform	Table F3.2-1	Uncertainty relative to π	Low uncertainty
Phase of first-order term in Fourier series for l(d)	$\theta_{\lambda,1}$	−1.6	−2.0	−1.1	0.3	radians	10%	Uniform	Table F3.2-1	Uncertainty relative to π	low uncertainty
Phase of first-order term in Fourier series for m(d)	$\theta_{m,1}$	−1.48	−1.78	−1.17	0.18	radians	6%	Uniform	Table F3.2-1	Uncertainty relative to π	Low uncertainty
Starting DOY (calendar day) for winter dew point		335	274	335	18	days	10%	Uniform	Table 6.5.4.1-2	Uncertainty relative to 182 days	Low uncertainty
Ending DOY (calendar day) for winter dew point		90	90	151	18	days	10%	Uniform	Table 6.5.4.1-2	Uncertainty relative to 182 days	Low uncertainty
Magnitude of first-order term in Fourier series for $Twet_{min}(d)$	αwet_{min}	9.4	8.2	10.5	0.7	°C	7%	Uniform	Table F3.2-1	Uncertainty relative to $\gamma wet_{max}-\gamma wet_{min}$	Low uncertainty
Phase of first-order term in Fourier series for $Twet_{min}(d)$	βwet_{min}	122	119	124	1	days	0.5%	Uniform	Table F3.2-1	Uncertainty relative to 182 days	Low uncertainty
Constant term in Fourier series for $Twet_{min}(d)$	γwet_{min}	7.4	5.0	9.7	1.4	°C	13%	Uniform	Table F3.2-1	Uncertainty relative to $\gamma wet_{max}-\gamma wet_{min}$	low uncertainty
Magnitude of first-order term in Fourier series for $Tdry_{min}(d)$	αdry_{min}	10.2	9.4	11.0	0.5	°C	3%	Uniform	Table F3.2-1	Uncertainty relative to $\gamma dry_{max}-\gamma dry_{min}$	Low uncertainty
Phase of first-order term in Fourier series for $Tdry_{min}(d)$	βdry_{min}	117	114	120	2	days	1.1%	Uniform	Table F3.2-1	Uncertainty relative to 182 days	Low uncertainty
Constant term in Fourier series for Tdrymin(d)	γdry_{min}	8	5	12	2	°C	13%	Uniform	Table F3.2-1	Uncertainty relative to $\gamma dry_{max}-\gamma dry_{min}$	Low uncertainty

Table I-7. Parameters Excluded from Uncertainty Analysis for Monsoon Climate (Continued)

Parameter Description	Parameter Symbol	Nominal Value	Low Range	High Range	Stand. Uncert.	Units	Relative Uncert.	Dist.	Reference	Comments	Reason for Exclusion
Magnitude of first-order term in Fourier series for Twetmax(d)	αwet_{max}	11.4	10.5	12.4	0.5	°C	5%	Uniform	Table F3.2-1	Uncertainty relative to $\gamma wet_{max}-\gamma wet_{min}$	Low uncertainty
Phase of first-order term in Fourier series for $Twet_{max}(d)$	βwet_{max}	115	112	118	2	days	1.1%	uniform	Table F3.2-1	Uncertainty relative to 182 days	Low uncertainty
Magnitude of first-order term in Fourier series for $Tdry_{max}(d)$	αdry_{max}	10.4	8.4	12.4	1.2	°C	8%	uniform	Table F3.2-1	Uncertainty relative to $\gamma dry_{max}-\gamma dry_{min}$	Low uncertainty
Phase of first-order term in Fourier series for $Tdry_{max}(d)$	βdry_{max}	113	109	117	2	days	1.1%	uniform	Table F3.2-1	Uncertainty relative to 182 days	Low uncertainty
Constant term in Fourier series for $Tdry_{max}(d)$	γdry_{max}	23	19	27	2	°C	13%	uniform	Table F3.2-1	Uncertainty relative to $\gamma dry_{max}-\gamma dry_{min}$	Low uncertainty
Wind speed at height of 2m during month m	$u_2(1)$	2.36	NA	NA	0.03	m/s	1.3%	normal	Table F3.2-1	<9% of year	Low uncertainty
	$u_2(2)$	2.67	NA	NA	0.04	m/s	1.5%	normal	Table F3.2-1	<9% of year	Low uncertainty
	$u_2(3)$	2.84	NA	NA	0.03	m/s	1.1%	normal	Table F3.2-1	<9% of year	Low uncertainty
	$u_2(4)$	3.22	NA	NA	0.04	m/s	1.2%	normal	Table F3.2-1	<9% of year	Low uncertainty
	$u_2(5)$	2.97	NA	NA	0.03	m/s	1.0%	normal	Table F3.2-1	<9% of year	Low uncertainty
	$u_2(6)$	2.90	NA	NA	0.02	m/s	0.7%	normal	Table F3.2-1	<9% of year	Low uncertainty
	$u_2(7)$	2.75	NA	NA	0.02	m/s	0.7%	normal	Table F3.2-1	<9% of year	Low uncertainty
	$u_2(8)$	2.71	NA	NA	0.02	m/s	0.7%	normal	Table F3.2-1	<9% of year	Low uncertainty
	$u_2(9)$	2.64	NA	NA	0.02	m/s	0.8%	normal	Table F3.2-1	<9% of year	Low uncertainty
	$u_2(10)$	2.61	NA	NA	0.03	m/s	1.1%	normal	Table F3.2-1	<9% of year	Low uncertainty

Table I-7. Parameters Excluded from Uncertainty Analysis for Monsoon Climate (Continued)

Parameter Description	Parameter Symbol	Nominal Value	Low Range	High Range	Stand. Uncert.	Units	Relative Uncert.	Dist.	Reference	Comments	Reason for Exclusion
Wind speed at height of 2m during month m (Continued)	$u_2(11)$	2.47	NA	NA	0.03	m/s	1.2%	normal	Table F3.2-1	<9% of year	Low uncertainty
	$u_2(12)$	2.48	NA	NA	0.03	m/s	1.2%	normal	Table F3.2-1	<9% of year	Low uncertainty
Minimum precipitation duration		0.91	0.76	1.07	0.09	hr	10%	uniform	Table 6.5.1.7-4		Low uncertainty

I1.5 SCREENING OF GLACIAL TRANSITION CLIMATE PARAMETERS

A total of 17 parameters were varied for the Glacial Transition climate, as listed in Tables I-8 and I-9. Eight of these were climate-independent. Two plant parameters were varied (the mean plant height and the maximum effective rooting depth). For this climate, the analyses varied both parameters of the precipitation duration model, but only one was varied independently, so that they could be correlated.

Three weather parameters were varied directly. Two additional weather parameters were not varied independently but rather were correlated (Table I-9). These five weather parameters provided variation in the weather input files for model calculations.

Table I-10 lists the parameters excluded from the detailed uncertainty analysis.

Table I-8. Parameters Varied Independently in Uncertainty Analysis for Glacial Transition Climate

Parameter Description	Parameter Symbol	Nominal Value	Low Range	High Range	Stand. Uncert.	Units	Relative Uncert.	Dist.	Reference	Comments
Constant term in Fourier series for $p_{oo}(d)$	a_{00}	0.84	0.78	0.89	0.03	none	19%	Uniform	Table F3.3-1	Uncertainty relative to $1-a_{00}$
Constant term in Fourier series for m(d)	a_m	0.70	0.48	0.92	0.13	ln mm	19%	Uniform	Table F3.3-1	
Phase of first-order term in Fourier series for I(d)	$\theta_{\lambda,1}$	NA	$-\pi$	$+\pi$	NA	radians	NA	Uniform	Table F3.3-1	
Rate of duration increase with precipitation		0.52	0.32	0.71	0.11	hr/mm	20%	Uniform	Table 6.5.1.7-4	
Mean plant height	h_{plant}	1.3	0.6	1.8	0.3	m	30%	Uniform	Table 6.5.3.3-2	
Maximum effective rooting depth	Z_r	2.5	1.0	4.0	0.9	m	40%	Uniform	Table 6.5.3.2-2	
Depth of soil	$depth_{soil}(4)$	0.3	0.1	0.5	0.12	m	40%	Uniform	Section 6.5.2.4	Midpoint selected as nominal value; not used in calculations
Bulk saturated hydraulic conductivity of bedrock	K_{sat_rock} *(405)*	1.1×10^{-6}	7.6×10^{-8}	4.8×10^{-6}	factor of 3	m/s	factor of 3	Loguniform	Table 6.5.2.6-1	
	$K_{sat\_rock}(406)$	1.3×10^{-6}	2.1×10^{-8}	7.7×10^{-6}	factor of 5	m/s	factor of 5	Loguniform	Table 6.5.2.6-1	
Soil water holding capacity	$\theta_{HC}(5/7/9)$	0.13	0.09	0.17	0.02	m^3/m^3	15%	Uniform	Table 6.5.2.3-2	
Readily evaporable water	*REW*	6	2	10	2	mm	30%	Uniform	Table 6.5.4.2-5	
Minimum K_c for dry soil with no crop cover	K_{c_min}	0	0	0.2	0.06	none	30%	50% 0.0, 50% Triangular	Table 6.5.4.2-2	Uncertainty relative to maximum
Evaporation layer depth	Z_e	0.15	0.1	0.2	0.03	m	19%	Uniform	Table 6.5.4.2-4	
Slope of relationship between K_{cb} to NDVI_cor	C_{Kcb2}	9.7	NA	NA	2.1	none	20%	Normal	Section 6.5.3.7	

Table I-9. Parameters Correlated with Other Parameters that Varied Independently in Uncertainty Analysis for Glacial Transition Climate

Parameter Description	Parameter Symbol	Nominal Value	Low Range	High Range	Stand. Uncert.	Units	Relative Uncert.	Dist.	Reference	Comments
Constant term in Fourier series for λ(d)	a_λ	3.8	3.1	4.5	0.4	mm	11%	Uniform	Table F3.3-1	Included; correlated with a_m
Phase of first-order term in Fourier series for m(d)	$\theta_{m,1}$	NA	$-\pi$	$+\pi$	NA	radians	NA	Uniform	Table F3.3-1	Included; correlated with $\theta_{\lambda,1}$
Minimum precipitation duration (Intercept – 1)		0.96	0.70	1.22	0.15	hr	16%	Uniform	Table 6.5.1.7-4	Uncertainty captured in rate of duration increase with precipitation

Table I-10. Parameters Excluded from Uncertainty Analysis for Glacial Transition Climate

Parameter Description	Parameter Symbol	Nom. Value	Low Range	High Range	Stand. Uncert.	Units	Relative Uncert.	Dist.	Reference	Comments	Reason for Exclusion
Magnitude of first-order term in Fourier series for λ(d)	$b_{\lambda,1}$	0.6	0.1	1.0	0.3	mm	8%	Uniform	Table F3.3-1	Uncertainty relative to a_λ	Low uncertainty
Magnitude of first order-term in Fourier series for $p_{oo}(d)$	$b_{00,1}$	0.066	0.028	0.104	0.02	none	13%	Uniform	Table F3.3-1	Uncertainty relative to $1-a_{00}$	Low uncertainty
Phase of first-order term in Fourier series for $p_{oo}(d)$	$\theta_{00,1}$	−1.12	NA	NA	0.010	radians	0.3%	Normal	Table F3.3-1	Uncertainty relative to π	Low uncertainty
Constant term in Fourier series for $p_{10}(d)$	a_{10}	0.54	0.47	0.62	0.04	none	9%	Uniform	Table F3.3-1	Uncertainty relative to $1-a_{10}$	low uncertainty
Magnitude of first-order term in Fourier series for $p_{10}(d)$	$b_{10,1}$	0.07	0.02	0.11	0.03	none	7%	Uniform	Table F3.3-1	Uncertainty relative to $1-a_{10}$	Low uncertainty
Phase of first-order term in Fourier series for $p_{10}(d)$	$\theta_{10,1}$	−0.93	NA	NA	0.84	radians	26%	Normal	Table F3.3-1	Uncertainty relative to π	Low influence; $b_{10,1}$ is barely 15% of $1-a_{10}$
Magnitude of first-order term in Fourier series for m(d)	$b_{m,1}$	0.12	0.08	0.16	0.02	ln mm	3%	Uniform	Table F3.3-1	Uncertainty relative to a_m	Low uncertainty
Starting DOY (calendar day) for winter dew point		274	244	274	9	days	5%	Uniform	Table 6.5.4.1-2	Uncertainty relative to 182 days	Low uncertainty

Table I-10. Parameters Excluded from Uncertainty Analysis for Glacial Transition Climate (Continued)

Parameter Description	Parameter Symbol	Nom. Value	Low Range	High Range	Stand. Uncert.	Units	Relative Uncert.	Dist.	Reference	Comments	Reason for Exclusion
Ending DOY (calendar day) for winter dew point		120	120	151	9	days	5%	Uniform	Table 6.5.4.1-2	Uncertainty relative to 182 days	Low uncertainty
Magnitude of first-order term in Fourier series for $Twet_{min}(d)$	αwet_{min}	8.4	6.3	10.4	1.2	°C	11%	Uniform	Table F3.3-1	Uncertainty relative to $\gamma wet_{max}-\gamma wet_{min}$	Low uncertainty
Phase of first-order term in Fourier series for $Twet_{min}(d)$	βwet_{min}	116	114	118	1	days	0.6%	Uniform	Table F3.3-1	Uncertainty relative to 182 days	Low uncertainty
Constant term in Fourier series for $Twet_{min}(d)$	γwet_{min}	2.6	1.2	3.9	0.8	°C	7%	Uniform	Table F3.3-1	Uncertainty relative to $\gamma wet_{max}-\gamma wet_{min}$	Low uncertainty
Magnitude of first-order term in Fourier series for $Tdry_{min}(d)$	αdry_{min}	9.6	7.5	11.6	1.2	°C	7%	Uniform	Table F3.3-1	Uncertainty relative to $\gamma dry_{max}-\gamma dry_{min}$	Low uncertainty
Phase of first-order term in Fourier series for $Tdry_{min}(d)$	βdry_{min}	111	106	116	3	days	2%	Uniform	Table F3.3-1	Uncertainty relative to 182 days	Low uncertainty
Constant term in Fourier series for $Tdry_{min}(d)$	γdry_{min}	0.9	−0.8	2.6	1.0	°C	6%	Uniform	Table F3.3-1	Uncertainty relative to $\gamma dry_{max}-\gamma dry_{min}$	Low uncertainty
Magnitude of first-order term in Fourier series for $Twet_{max}(d)$	αwet_{max}	11.8	10.1	13.4	1.0	°C	9%	Uniform	Table F3.3-1	Uncertainty relative to $\gamma wet_{max}-\gamma wet_{min}$	Low uncertainty
Phase of first-order term in Fourier series for $Twet_{max}(d)$	βwet_{max}	113	111	115	1	days	0.6%	Uniform	Table F3.3-1	Uncertainty relative to 182 days	Low uncertainty
Constant term in Fourier series for $Twet_{max}(d)$	γwet_{max}	13.8	11.7	15.9	1.2	°C	11%	Uniform	Table F3.3-1	Uncertainty relative to $\gamma wet_{max}-\gamma wet_{min}$	Low uncertainty
Magnitude of first-order term in Fourier series for $Tdry_{max}(d)$	αdry_{max}	14.4	13.8	15.0	0.3	°C	2%	Uniform	Table F3.3-1	Uncertainty relative to $\gamma dry_{max}-\gamma dry_{min}$	Low uncertainty
Phase of first-order term in Fourier series for $Tdry_{max}(d)$	βdry_{max}	114	112	117	1	days	0.6%	Uniform	Table F3.3-1	Uncertainty relative to 182 days	Low uncertainty
Constant term in Fourier series for $Tdry_{max}(d)$	γdry_{max}	17.1	14.6	19.6	1.4	°C	9%	Uniform	Table F3.3-1	Uncertainty relative to $\gamma dry_{max}-\gamma dry_{min}$	Low uncertainty

Table I-10. Parameters Excluded from Uncertainty Analysis for Glacial Transition Climate (Continued)

Parameter Description	Parameter Symbol	Nom. Value	Low Range	High Range	Stand. Uncert.	Units	Relative Uncert.	Dist.	Reference	Comments	Reason for Exclusion
Wind speed at height of 2m during month m	$u_2(1)$	2.36	NA	NA	0.03	m/s	1.3%	Normal	Table F3.3-1	< 9% of year	Low uncertainty
	$u_2(2)$	2.67	NA	NA	0.04	m/s	1.5%	Normal	Table F3.3-1	< 9% of year	Low uncertainty
	$u_2(3)$	2.84	NA	NA	0.03	m/s	1.1%	Normal	Table F3.3-1	< 9% of year	Low uncertainty
	$u_2(4)$	3.22	NA	NA	0.04	m/s	1.2%	Normal	Table F3.3-1	< 9% of year	Low uncertainty
	$u_2(5)$	2.97	NA	NA	0.03	m/s	1.0%	Normal	Table F3.3-1	< 9% of year	Low uncertainty
	$u_2(6)$	2.90	NA	NA	0.02	m/s	0.7%	Normal	Table F3.3-1	< 9% of year	Low uncertainty
	$u_2(7)$	2.75	NA	NA	0.02	m/s	0.7%	Normal	Table F3.3-1	< 9% of year	Low uncertainty
	$u_2(8)$	2.71	NA	NA	0.02	m/s	0.7%	Normal	Table F3.3-1	< 9% of year	Low uncertainty
	$u_2(9)$	2.64	NA	NA	0.02	m/s	0.8%	Normal	Table F3.3-1	< 9% of year	Low uncertainty
	$u_2(10)$	2.61	NA	NA	0.03	m/s	1.1%	Normal	Table F3.3-1	< 9% of year	Low uncertainty
	$u_2(11)$	2.47	NA	NA	0.03	m/s	1.2%	Normal	Table F3.3-1	< 9% of year	Low uncertainty
	$u_2(12)$	2.48	NA	NA	0.03	m/s	1.2%	Normal	Table F3.3-1	< 9% of year	Low uncertainty

I2. BACKGROUND ON UNCERTAINTY AND UNCERTAINTY DISTRIBUTIONS

I2.1 DEFINITIONS

There is no standard for the expression of uncertainty in predictions made with algorithms. However, algorithms are used to predict measurements. The treatment of uncertainty in this report is based on ANSI/NCSL Z540-2-1997, *American National Standard for Calibration —U.S. Guide to the Expression of Uncertainty in Measurement* [DIRS 157394]. The following are adapted from definitions that appear in the standard:

1. The **measurand** is the particular quantity subject to measurement and therefore to prediction. Its definition may require specification of the conditions under which the quantity is measured. The standard avoids the phrase "true value of the measurand" because the word "true" is viewed as redundant. The "true value of the measurand" is simply the value of the measurand (ANSI/NCSL Z540-2-1997 [DIRS 157394], p. 41).

2. The **measurement error** is the result of the measurement minus the value of the measurand (ANSI/NCSL Z540-2-1997 [DIRS 157394], p. 34). As used in this appendix, the **prediction error** is the result of the prediction minus the value of the measurand.

3. A **random component** of prediction error is an effect that, for multiple predictions with varying inputs, produces a mean error that is small relative to the standard deviation of the error from that effect. An example of a random component is the residual error after a formula has been adjusted to correlate with data.

4. A **systematic component** of prediction error is an effect that is not a random component.

5. If the systematic component of prediction error includes a systematic effect that is quantifiable, one may add a **correction** to the prediction to compensate for that effect. However, the necessary correction may not be practical in the intended application of the prediction.

6. The **uncertainty** of the result of a prediction is an estimate of the likelihood of nearness to the best value that is consistent with presently available knowledge (adapted from ANSI/NCSL Z540-2-1997 [DIRS 157394], p. 41). Components of uncertainty include estimates of random error, uncertainties in corrections, and estimates of uncorrected or unrecognized systematic effects.

7. **Standard uncertainty** $u(x)$, of a predicted value x is the uncertainty of the result of a prediction expressed as a standard deviation. It does not correspond to a high level of confidence.

8. A **Type A evaluation** of uncertainty is an evaluation by statistical analysis of a series of observations. A **Type B evaluation** of uncertainty is an evaluation by any other method. A Type B evaluation is founded on an a priori distribution of the possible values (ANSI/NCSL Z540-2-1997 [DIRS 157394], p. 3).

9. If the result of a prediction is a function of the values of a number of other quantities, the standard uncertainty in the prediction is the **combined standard uncertainty**.

10. For contributions to uncertainty that are independent, the **law of propagation of uncertainty** (ANSI/NCSL Z540-2-1997 [DIRS 157394], p. 19) determines the combined standard uncertainty. For $y = f(x_i \ldots, x_n)$, the combined standard uncertainty $u_c(y)$ is given by:

$$u_c^2(y) = \sum_{i=1}^{N} \left(\frac{\partial f}{\partial x_i} \right)^2 u^2(x_i) \qquad \text{(Eq. I-1)}$$

1. In some applications, it may be necessary to have a measure of uncertainty that encompasses a large fraction of the values that one could reasonably attribute to the measurand. If necessary, the user may multiply the standard uncertainty by a **coverage factor** to obtain an **expanded uncertainty**. In general, the coverage factor will be in the range 2 to 3 (ANSI/NCSL Z540-2-1997 [DIRS 157394], p. 24). This appendix uses a coverage factor of 2 to approximate a 95% confidence interval (ASME PTC 19.1-1998 [DIRS 153195], p. 95).

2. The **relative combined standard uncertainty** in a predicted positive value y is $u_c(y)/y$ (ANSI/NCSL Z540-2-1997 [DIRS 157394], p. 25, Sect. 7.2.1).

3. For nonzero values of the x_i, Equation I-1 may be rewritten for propagation of relative uncertainty:

$$\left[\frac{u_c(y)}{y} \right]^2 = \sum_{i=1}^{N} \left(\frac{x_i}{y} \frac{\partial f}{\partial x_i} \right)^2 \left[\frac{u(x_i)}{x_i} \right]^2 \qquad \text{(Eq. I-2)}$$

I2.2 UNCERTAINTY DISTRIBUTIONS

Most of the uncertainty distributions in this report are normal, uniform, or loguniform. The properties of normal distributions are available in any standard statistics text. The standard uncertainty is the square root of the variance of the distribution.

In general, the variance of a distribution that has a probability density $p_X(X)$ and a mean value μ_X is:

$$\sigma_X^2 = \int_{X_1}^{X_2} p_X(X)(X - \mu_X)^2 dX = \int_{X_1}^{X_2} p_X(X)(X^2 - 2\mu_X X + \mu_X^2) dX \qquad \text{(Eq. I-3)}$$

so that:

$$\sigma_X^2 \begin{cases} = \int_{X_1}^{X_2} p_X(X) X^2 dX - 2\mu_X \int_{X_1}^{X_2} p_X(X) X dX + \mu_X^2 \int_{X_1}^{X_2} p_X(X) dX \\ = \int_{X_1}^{X_2} p_X(X) X^2 dX - \mu_X^2 \end{cases} \quad \text{(Eq. I-4)}$$

which is a well-known relationship.

Uniform Distribution

This report assigns a uniform uncertainty distribution to many parameters. That is, the parameter is a random variable, X, which is equally likely to be anywhere within its range, from X_1 to X_2. Therefore, the cumulative probability distribution for X is:

$$P_X(X) = \frac{X - X_1}{X_2 - X_1}, \; X_1 \le X \le X_2 \quad \text{(Eq. I-5)}$$

The probability density function for X is:

$$p_X(X) = \frac{\partial P_X(X)}{\partial X} = \frac{1}{[X_2 - X_1]}, \; X_1 \le X \le X_2 \quad \text{(Eq. I-6)}$$

with the mean value of:

$$\mu_X = (X_1 + X_2)/2 \quad \text{(Eq. I-7)}$$

Therefore,

$$\int_{X_1}^{X_2} p_X(X) X^2 dX = \frac{1}{X_2 - X_1} \int_{X_1}^{X_2} X^2 dX = \frac{X_2^3 - X_1^3}{3[X_2 - X_1]} = \frac{X_2^2 + X_2 X_1 + X_1^2}{3} \quad \text{(Eq. I-8)}$$

Applying Equation I-4,

$$\sigma_X^2 = \frac{X_2^2 + X_2 X_1 + X_1^2}{3} - \frac{(X_1 + X_2)^2}{4} = \frac{(X_2 - X_1)^2}{12} \quad \text{(Eq. I-9)}$$

and the standard uncertainty is $(X_2 - X_1)/\sqrt{12}$.

Loguniform Distribution

Next the properties of a log uniform distribution are considered. Let a random variable, X, have a loguniform distribution from X_1 to X_2, which means that the logarithm of X has a uniform distribution. That is, defining a random variable Y that is equal to ln(X), Y has a uniform distribution from $Y_1 = \ln(X_1)$ to $Y_2 = \ln(X_2)$.

The median of the distribution for X is the geometric mean of the extremes, $\sqrt{X_1 X_2}$.

The standard uncertainty of the distribution for Y is $(Y_2 - Y_1)/\sqrt{12}$. In this report, the standard uncertainty in X is expressed as a factor of $\left(\frac{X_2}{X_1}\right)^{1/\sqrt{12}}$. Factors below 1.2 are expressed as a relative percent.

Special Triangular Distribution

The uncertainty distribution for the parameter K_{c_min} has the following cumulative probability distribution:

$$P(0) = 0.5 \qquad \text{(Eq. I-10)}$$

$$P(x) = 1 - \frac{(0.2 - x)^2}{2(0.2)^2} \qquad \text{(Eq. I-11)}$$

$$p(x) = \frac{dP(x)}{dx} = \frac{(0.2 - x)}{(0.2)^2} \qquad \text{(Eq. I-12)}$$

The root-mean-square deviation from the median value of zero is an estimate of the standard uncertainty, u. Therefore,

$$u^2 = \int_{x=0}^{0.2} x^2 \frac{(0.2 - x)}{(0.2)^2} dx = \int_{x=0}^{0.2} \frac{(0.2x^2 - x^3)}{(0.2)^2} dx \qquad \text{(Eq. I-13)}$$

$$u^2 = \frac{(0.2)^4}{3(0.2)^2} - \frac{(0.2)^4}{4(0.2)^2} = \frac{(0.2)^2}{12} = 0.0033 \qquad \text{(Eq. I-14)}$$

$$u = 0.06 \qquad \text{(Eq. I-15)}$$

INTENTIONALLY LEFT BLANK

APPENDIX J
SUPPORTING INFORMATION ON VALIDATION OF EVAPOTRANSPIRATION USING SOIL WATER STORAGE MEASUREMENTS IN WEIGHING LYSIMETERS

This appendix provides supporting information regarding the site-specific data, modeling setup, calculations, and modeling results for validation of the evapotranspiration study presented in Section 7.1.2.

Two lysimeter sites are considered in Section 7.1.2. The first lysimeter site is located in Area 5 Radioactive Waste Management Site (RWMS) of the Nevada Test Site (NTS) and represents an analogue to the present-day climate conditions at the Yucca Mountain. This site will be referred to further in this appendix as the NTS lysimeter site. The second site is located in Reynolds Creek Experimental Watershed (RCEW) in southwestern Idaho and represents a potential analogue to the future glacial transition climate conditions at Yucca Mountain. This site will be referred to further in this appendix as the RCEW lysimeter site. The sections within this appendix provide details for each of the two sites.

The data, modeling setup, calculations and results for the NTS lysimeter site is described in Section J1. Details of the NTS bare-soil and vegetated lysimeter simulations can be found in Sections J1.1 and J1.2, respectively. Section J1.3 describes an optimization process that was set up to estimate evapotranspiration and soil parameters by minimizing differences between the calculated and measured daily water storage values in both bare soil and vegetated lysimeters. Section J1.4 describes the details of the model simulations using HYDRUS-1D and MASSIF compared to the lysimeter storage data.

The data, modeling setup, calculations and results for the RCEW lysimeter site is described in Section J2. Details of the climate data are described in Section J2.1. Details of the geospatial data are described in Section J2.2. Other relevant data are discussed in Section J2.3. Section J2.4 describes the details of the model simulations using HYDRUS-1D and MASSIF compared to the lysimeter storage data.

Although direct comparisons between MASSIF and an alternative model, HYDRUS 1D, are documented in Sections 7.2.2 and in Appendix K, comparisons between MASSIF, HYDRUS-1D, and lysimeter field data are also presented in Section 7.1.2 and in Sections J1.4 and J2.4 in order to demonstrate that the comparisons between MASSIF and field data are similar to comparisons between HYDRUS-1D and field data. These comparisons show that a field capacity model such as MASSIF can closely simulate field data as well as a more physics-based flow model such as HYDRUS-1D.

J1. AREA 5 RADIOACTIVE WASTE MANAGEMENT SITE (RWMS) NEVADA TEST SITE (NTS)

The Area 5 RWMS is located in the northern Frenchman Flat on the NTS in southern Nevada. Frenchman Flat is a closed basin. The RWMS is at an elevation of 976 m on a bajada of the Massachusetts Mountains at the intersection of three alluvial fans on a slope of about l° (Levitt et al. 1999 [DIRS 177521]). The lysimeter site is located 400 m west of the Area 5 RWMS. The lysimeter site coordinates are: 36° 51' 9.13" (latitude) and 115° 56' 56.06" (longitude) (Scanlon et al. 2005 [DIRS 175977]).

The NTS lysimeter site is located approximately 40 km from the eastern boundary of the MASSIF model domain. The site elevation (976 m) is approximately the same as the lowest elevation of the MASSIF model domain (964 m). The predominant vegetation found at the lysimeter site is the same as found in the Larrea–Ambrosia vegetation association described in Appendix D. Given these similarities, the NTS lysimeter site is a good analogue to the low elevation areas of the Yucca Mountain model domain.

Two weighing lysimeters were installed at this site in 1994 to conduct water balance studies. Each lysimeter is a 2-m by 4-m by 2-m deep steel tank filled with native alluvium at a bulk density of about 1.5 kg/m^3 (Scanlon et al. 2005 [DIRS 175977]). The lysimeter schematics are shown in Figure 7.1.2-1 in Section 7.1.2. One lysimeter is vegetated with the creosote bush, four-wing salt bush, and annual grasses at the approximate density of the surrounding landscape (Desotell et al. 2006 [DIRS 176858]). This lysimeter will be referred as vegetated lysimeter. Another lysimeter is maintained under bare soil conditions and is referred to as bare soil lysimeter.

Eighteen core samples were collected throughout the lysimeter depth profile in 10-cm increments. The measured soil hydraulic properties are reported by Desotell et al. (2006 [DIRS 176858]) and include:

- Saturated hydraulic conductivity (geometric mean): 14 cm/hr
- Residual moisture content: 0.04 m^3/m^3
- Porosity: 0.357 m^3/m^3
- van Genuchten parameter alpha: 0.0328 cm^{-1}
- van Genuchten parameter n: 1.57.

Based on these parameters, the field capacity is 0.117 m^3/m^3 (calculated using pressure of −1/3 bar), and wilting point is 0.044 m^3/m^3 (calculated using pressure of −60 bars). Since a higher pressure may be more appropriate for the coarse-grained textured soils (up to −1/10 bars) than the pressure of −1/3 bars (medium textured soils), the bare soil lysimeter storage data were analyzed during periods with heavy precipitation over a few or more consecutive days. The largest storage value was 277.3 mm. This corresponds to the moisture content of 0.139 m^3/m^3 and a pressure of −2/10 bars. This is consistent with the pressure range of −1/3 bars to −1/10 bars at which field capacity is calculated.

The lysimeter storage observations are available for the period of time from 03/30/94 until 12/31/04. The storage data were copied from Di Sanza (2006 [DIRS 178797]) into the file ***NTSLysimeter.xls*** (***NTS*** folder in the Validation Output DTN: SN0607T0502206.016). The precipitation data are available for the lysimeter site. They were obtained from the file (Di Sanza 2006 [DIRS 178797]) and copied into the worksheet ***Original Climate Data*** in ***NTSLysimeter.xls*** (***NTS*** folder in the Validation Output DTN: SN0607T0502206.016).

The temperature data were not available for the lysimeter site. The daily minimum, maximum, and average temperatures collected at Well 5B located 1.5 km from the lysimeter site were used instead. These data were downloaded from DTN: MO0607SEPMED94.000 [DIRS 178079] into the worksheet ***Original Climate Data*** in ***NTSLysimeter.xls*** (***NTS*** folder in the Validation Output DTN: SN0607T0502206.016). The temperature data in this data set are not available for some

dates. The data gaps were filled with the temperatures that were calculated using linear interpolation between the closest points in which the data were available. The interpolated values are outlined in yellow in the ***Original Climate Data*** worksheet.

Since the MASSIF model can be run only for the whole number of the water years, the bare soil lysimeter simulations were for the period of time from 10/01/94 to 09/30/05. The climate data for the period of time from 01/01/05 to 09/30/05 were filled with the corresponding data from the previous year. This was done to satisfy MASSIF input requirements (whole water year). The results of the calculations for this period of time were not used. This does not affect in any way the results of the calculations for the period of time prior to 01/01/05. The climate data and the bare soil lysimeter storage data are in ***BS Input Data*** worksheet in ***NTSLysimeter.xls***. These data were copied into the built-in Excel files in the MASSIF interfaces ***Bare Soil Lysimeter*** and ***BS and Veget Optimization.*** The data are in the format required by MASSIF and corresponding MASSIF interfaces.

The vegetated lysimeter was irrigated for about a year to establish the vegetation cover, but the irrigation rates are not available, and it took about 1.5 years for the transplanted vegetation to equilibrate with moisture conditions in the lysimeter box. Consequently, the period of observations for the vegetated lysimeter was from 10/01/95 until 09/30/05. As in the case of the bare soil lysimeter, the climate data for the period of time from 01/01/05 to 09/30/05 were filled with the corresponding data from the previous year. The climate data and the vegetated lysimeter storage data are in ***Veg Input Data*** worksheet in ***NTSLysimeter.xls***. These data were copied into the built-in Excel files in the MASSIF interfaces ***Vegetated Lysimeter*** and ***BS and Veget Optimization.*** The data are in the format required by MASSIF and corresponding MASSIF interfaces.

Three MASSIF interfaces were designed to simulate NTS lysimeters. The input data used in these interfaces and the interface functions are described below.

J1.1 MASSIF INTERFACE *BARE SOIL LYSIMETER*

The interface is located in folder ***Validation Analyses*/*Lysimeter*** in the MASSIF package (Output DTN: SN0701T0502206.037). This interface was specifically designed to simulate soil water storage measured in the bare soil lysimeter. The interface reads the embedded Excel file with the climate and storage data. As discussed above, these data were copied into this file from ***BS Input Data*** worksheet in ***NTSLysimeter.xls*** (***NTS*** folder in Validation Output DTN: SN0607T0502206.016).

The interface reads an external Excel file with the geospatial data provided in the format required by MASSIF. The file name is ***NTS_location.csv***. It is located in the same directory ***Lysimeter***, in which the interface is located. The file consists of two lines; each line represents one watershed cell. The lysimeter site is represented by the first cell in this file (the first line). The second cell is not used in the analysis. The geospatial information includes the cell identification number (arbitrary number in this case), site latitude and longitude in degrees and UTM coordinates in meters, site elevation in meters, slope in degrees, aspect, soil type, soil depth class, bedrock type, *PVR* (potential vegetation response), and an identification number of the cell from which runoff is routed to this cell (it is set to −3 to exclude the run-on component using the

corresponding MASSIF option). The site longitude, latitude, and elevation are defined as described above. The slope at the site is 1° (as described above). Soil type is set equal to 5, soil depth class is set equal to 2, and bedrock type is set equal to 406. The *PVR* is set equal to 1. As described in Section 7.1.2, the parameter *PVR* can be set equal to an arbitrary value as long as the K_{cb} value is estimated by adjusting C_{kcb}. The *PVR* was set equal to 1 for convenience.

The other parameters required to run MASSIF are defined directly within the interface as follows:

- Reference elevation is set equal to site elevation (976 m) to avoid correction of temperature and precipitation with regard to the reference elevation.
- The albedo is set equal to 0.22 (see Sections 6.3.3 and 6.3.4)
- Weather parameters, such as first and last day of winter and precipitation duration coefficients were set equal to the values defined for the Present-Day climate (Sections 6.3.3 and 6.3.4).
- Dew point offset parameters were set equal to the default MASSIF values.
- Soil porosity and hydraulic conductivity of soil type 5 are set equal to the following values: porosity is 0.357 m^3/m^3 and hydraulic conductivity is 14 cm/hr. This redefines the values that MASSIF reads from the built-in look-up table with the soil properties for soil type 5.
- Bedrock hydraulic conductivity of bedrock type 406 is set equal to 10^{-10} m/s. This redefines the value that MASSIF reads from the built-in look-up table with the bedrock properties. This initial value was changed within a range from 0 to 4×10^{-5} m/s as a part of a sensitivity analysis. The high end of this range corresponds to the maximum hydraulic conductivity of the bedrock at the Yucca Mountain site. The low end of this range is consistent with a sealed bottom boundary of the lysimeter. The bedrock hydraulic conductivity did not affect the results of the calculations.
- The soil depth of the Soil Depth Class 2 is set equal to 2.00 m.
- The rooting depth was specified equal to 2.00 m.
- The vegetation cover is set equal to 0 (there is no vegetation).
- C_{kcb} coefficients (interception and slope of the NDVI'–K_{cb} linear regression line) are set equal to 0 (there is no vegetation).
- The plant height is set equal to 0.0 m (there is no vegetation).
- The water stress parameter *p* is set equal to 0.0.

- The evaporation depth Z_e is set equal to 100 mm (this parameter is not a part of the optimization scheme; however, it can be manually adjusted if needed).

- Readily evaporable water rew_1 is set equal to 6 mm (this parameter is not a part of the optimization scheme; however, it can be manually adjusted if needed).

- The diffusive evaporation parameter K_{c_min} is set equal to 0.0135 based on the results of optimization implemented in MASSIF interface ***BS and Veget Optimization***. This parameter can also be adjusted manually.

- Sublimation and snowmelt coefficient are set equal to default MASSIF values ($C_{sublime} = 0.1$ and $C_{snowmelt} = 2.0$).

- The initial moisture content in each layer is calculated as the lysimeter storage measured on 10/01/94 divided by the lysimeter depth. The resulting moisture content was 0.084 m^3/m^3.

- The field capacity (θ_1) and wilting point (θ_2) are calculated using (Simunek et al. 2005 [DIRS 178140], Equation 2.26):

$$\theta_i = \theta_r + s_i \times (\theta_s - \theta_r), \quad i=1,2 \qquad \text{(Eq. J-1)}$$

$$s_i = [(1+(h_i \times \alpha)^n]^{-m}$$

$$m = 1 - 1/n$$

$h_1 = -336.6$ cm (−1/3 bar) and $h_2 = -61{,}200$ cm (−60 bars)

- where θ_r is residual porosity, θ_s is saturated porosity, and α, n, and m are van Genuchten parameters defined by Simunek et al. (2005 [DIRS 178140]). The resulting field capacity and wilting point are 0.117 m^3/m^3 and 0.044 m^3/m^3, respectively.

- Field capacity and wilting point of soil type 5 are set equal to 0.117 m^3/m^3 and 0.044 m^3/m^3. This redefines the values that MASSIF reads from the built-in look-up table with the soil properties for soil type 5.

The interface performs the following functions. The interface displays the climate data. This includes the plots of the daily precipitation record and minimum, maximum, and average daily air temperatures. The percentage of time when mean daily temperature is below 0°C is calculated (1.3%). The examples are shown in the Figure J-1.

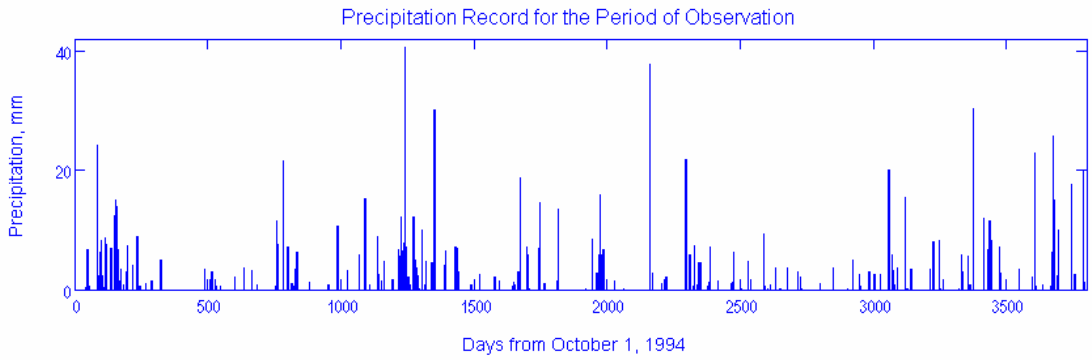

(a)

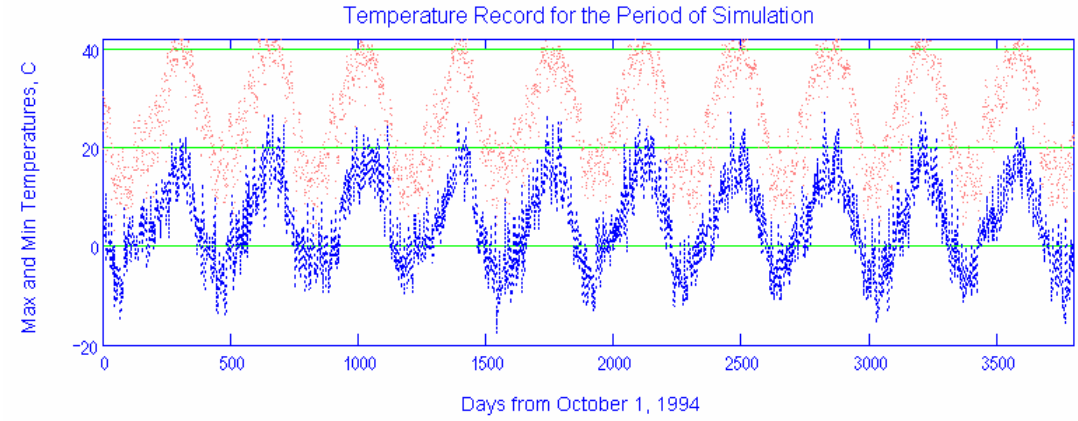

(b)

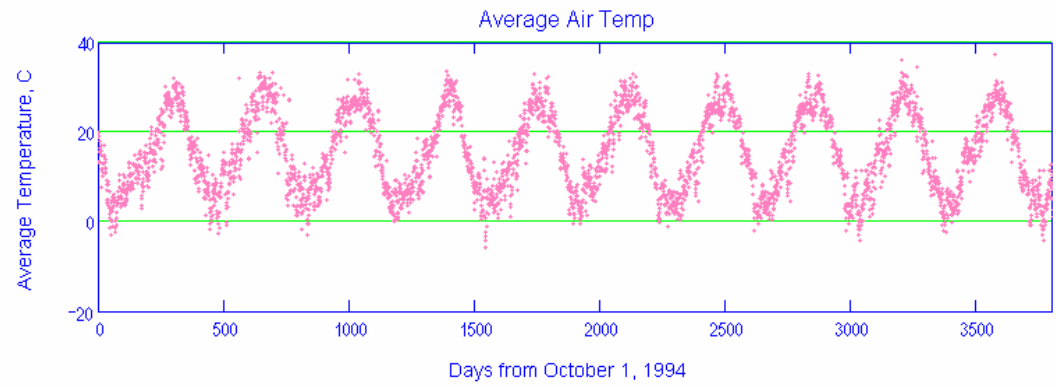

(c)

Source: Output DTN: SN0701T0502206.037, *\Welcome to Massif\Massif\Validation Analyses\Lysimeter\Bare Soil Lysimeter.xmcd*.

Figure J-1. Climate Data Plots for the MASSIF Simulation of Storage in the Bare Soil Lysimeter

The interface calculates the difference between the daily precipitation and the daily change in lysimeter storage. This difference should be either equal to 0 (if there is no evaporation) or be greater than 0 (if there is evaporation). The negative difference indicates that the precipitation was underestimated. The data points in which this difference is negative are shown in Figure J-2. Both the difference between the precipitation and storage and precipitation are shown.

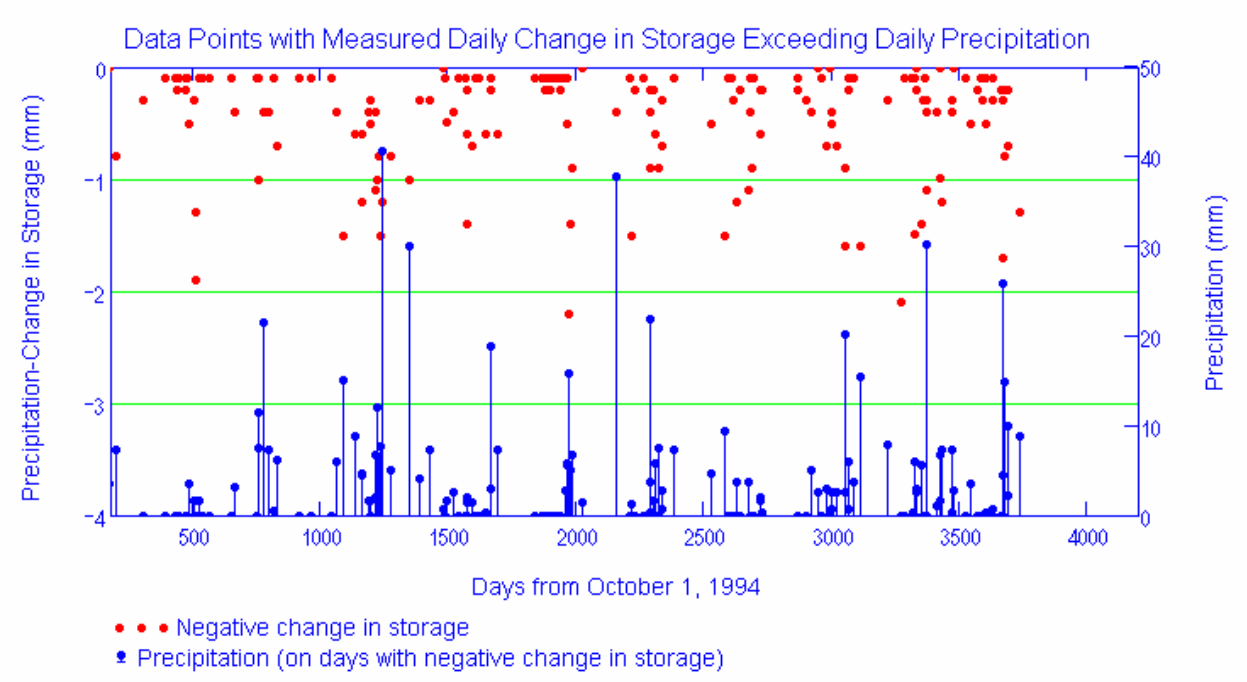

Source: Output DTN: SN0701T0502206.037, *\Welcome to Massif\Massif\Validation Analyses\Lysimeter\Bare Soil Lysimeter.xmcd.*

Figure J-2. Days with Negative Daily Difference between Precipitation and Change in Storage Calculated using MASSIF Bare Soil Lysimeter Interface

There are 196 points (5% of the data) in which precipitation was underestimated. This is consistent with the fact that rain gauges are subject to under-measurement caused by (1) splash out of drops, (2) blow-by of drops due to Venturi effects, and (3) evaporation of intercepted drops along the sides of the collector (Sevruk 1992 [DIRS 177480]). As can be seen from this figure, these points coincide in many cases with the large intensity precipitation events. The mean intensity of the precipitation events in these points is 6.9 mm, and the mean intensity of the precipitation events based on all precipitation data is 4.2 mm. The maximum negative difference was 3.4 mm. Since evaporation is calculated as the difference between precipitation and storage, the same error in precipitation measurement will result in the corresponding error in the evaporation estimate.

The interface runs MASSIF, stores the results of calculations, and calculates the lysimeter storage as a sum of the water depths within the four model layers. The interface displays the measured and calculated daily lysimeter storage. An example is shown in Figure J-3. The

parameters placed in the yellow box located just above the storage plot can be manually adjusted. Each adjustment results in a recalculation and a display of newly calculated storage values in the storage plot. This function was used in the sensitivity analysis. For the period of simulation, the interface calculates the water balance constituents such as total precipitation, total evaporation, total run-on, total runoff, and total infiltration. The total run-on is always zero since the lysimeter cell is not connected to any other cell in the geospatial file. The interface calculates the objective function value using Equation 7.1.2-2.

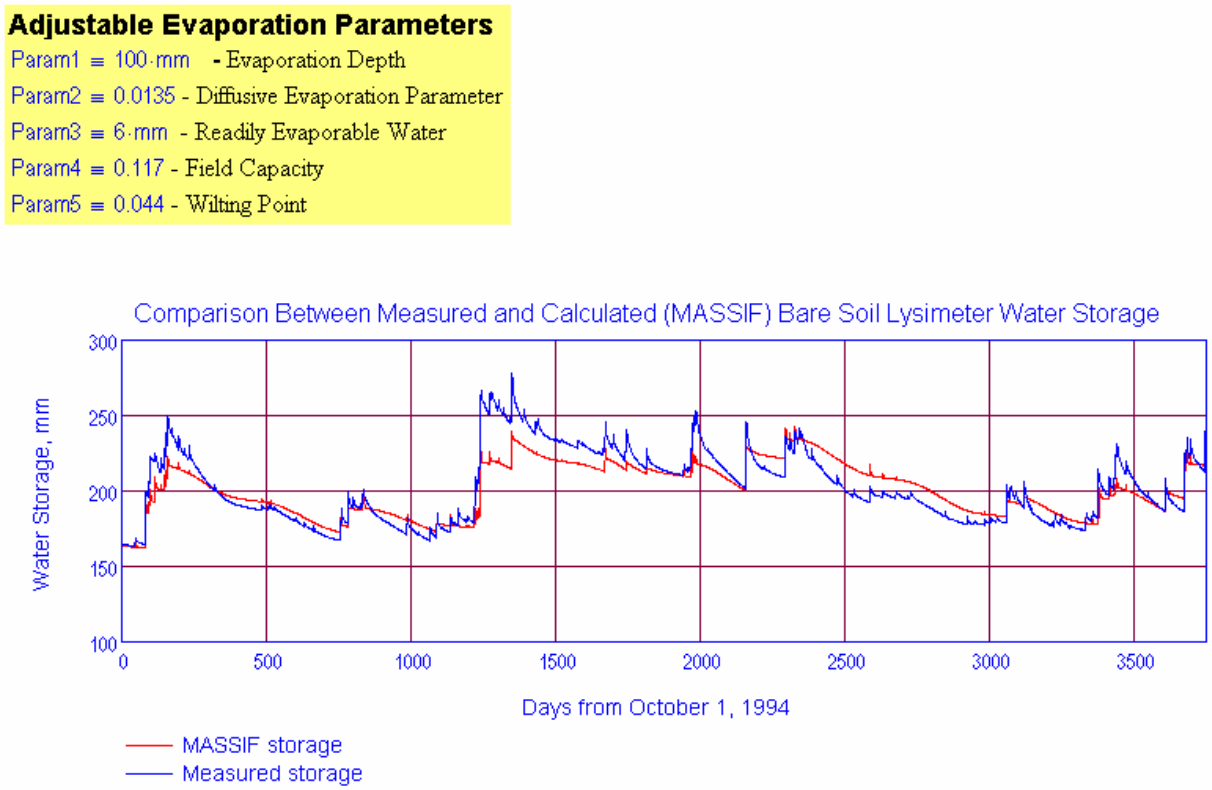

Source: Output DTN: SN0701T0502206.037, *\Welcome to Massif\Massif\Validation Analyses\Lysimeter\Bare Soil Lysimeter.xmcd.*

Figure J-3. Calculated versus Measured Lysimeter Storage using MASSIF Bare Soil Lysimeter Interface

The interface then checks the daily mass balance for the simulation and displays it as shown in Figure J-4.

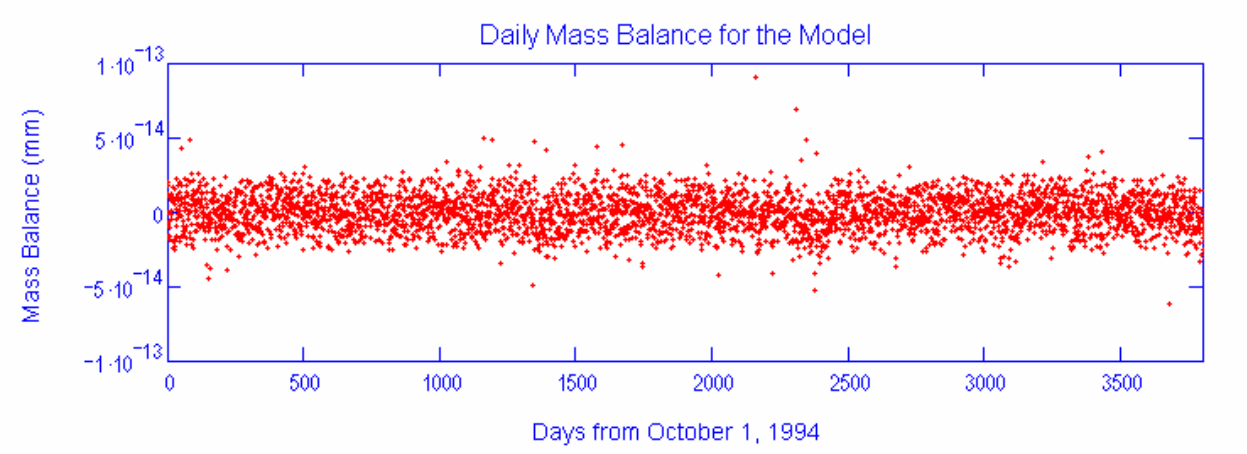

Source: Output DTN: SN0701T0502206.037, *\Welcome to Massif\Massif\Validation Analyses\Lysimeter\Bare Soil Lysimeter.xmcd*.

Figure J-4. Daily Mass Balance Displayed by MASSIF Bare Soil Lysimeter Interface

The interface reads an external Excel file ***Hydrus1D Data&Results.xls*** that contains HYDRUS-1D input data (including potential evapotranspiration) and modeling results (daily storage and infiltration). These data are in worksheet ***Bare Soil***. The description of the HYDRUS-1D modeling setup and details on how the potential evapotranspiration was calculated are provided below.

The interface displays the reference evapotranspiration calculated by MASSIF and potential evapotranspiration used as HYDRUS-1D boundary condition. An example is shown in Figure J-5.

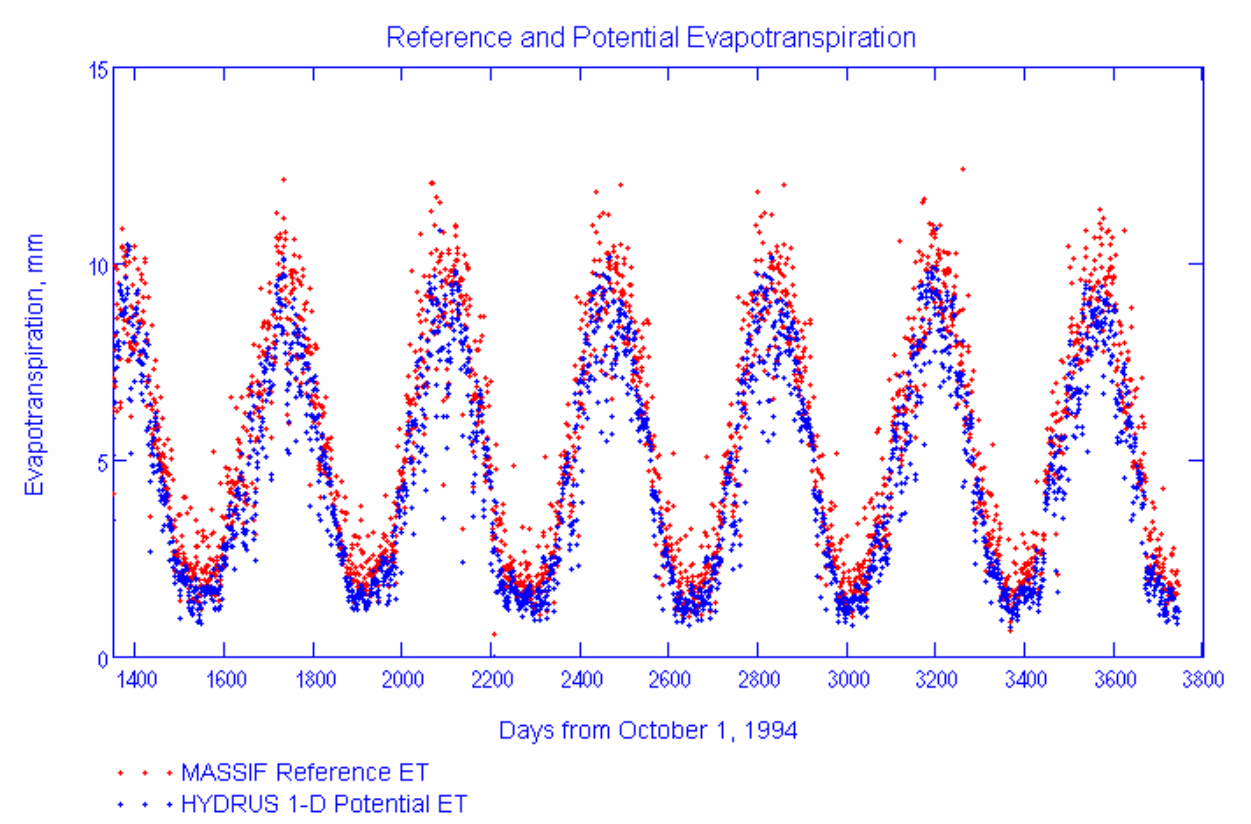

Source: Output DTN: SN0701T0502206.037, *\Welcome to Massif\Massif\Validation Analyses\Lysimeter\Bare Soil Lysimeter.xmcd*.

Figure J-5. Reference Evapotranspiration calculated with MASSIF and Potential Evapotranspiration Calculated using HYDRUS-1D.

The interface displays the observed lysimeter storage and lysimeter storage calculated with MASSIF and HYDRUS-1D as shown in Figure J-6.

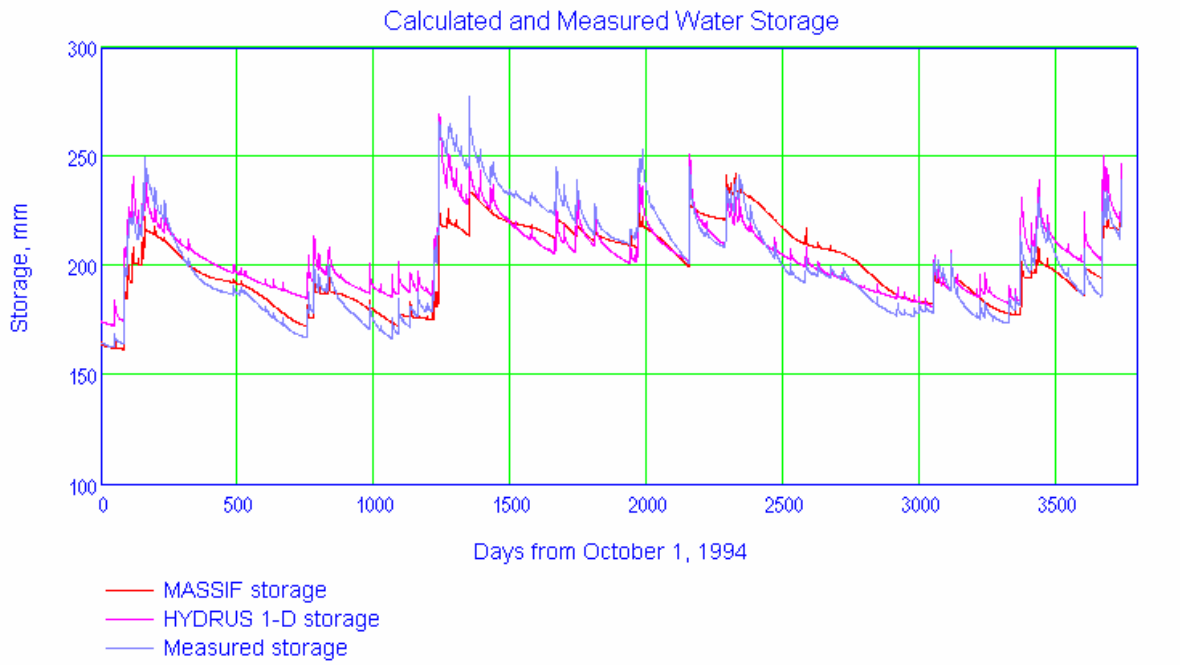

Source: Output DTN: SN0701T0502206.037, *\Welcome to Massif\Massif\Validation Analyses\Lysimeter\Bare Soil Lysimeter.xmcd*.

Figure J-6. Calculated (MASSIF and HYDRUS) and Measured Lysimeter Storage Displayed by MASSIF Bare Soil Lysimeter Interface

J1.2 MASSIF INTERFACE *VEGETATED LYSIMETER*

The interface is located in folder ***Validation Analyses/Lysimeter*** in the MASSIF package (Output DTN: SN0701T0502206.037). This interface was specifically designed to simulate the vegetated lysimeter. The interface reads the embedded Excel file with the climate and storage data. As discussed above, these data were copied into this file from the ***Veg Input Data*** worksheet in ***NTSLysimeter.xls*** (***NTS*** folder in the Validation Output DTN: SN0607T0502206.016). The interface reads an external Excel file ***NTS_location.csv*** with the geospatial data provided in a format required by MASSIF. The lysimeter site is represented by the second cell in this file (the second line). This is the same file used for bare soil lysimeter. The input data provided in the second line of this file are the same as described above under the interface ***Bare Soil Lysimeter***.

The other parameters required to run MASSIF are defined directly within the interface. These parameters are described below. Only the parameters that differ from the ones described under the bare soil lysimeter interface are provided below.

- The vegetation cover is set equal to 0.26 based on the results of optimization implemented in MASSIF interface ***BS and Veget Optimization***. This parameter can also be adjusted manually.

- The C_{kcb} coefficient for slope is set equal to 2.4 based on the results of optimization implemented in MASSIF interface ***BS and Veget Optimization***. This parameter can be manually adjusted if needed. The C_{kcb} coefficient for intercept is set equal to 0.

- The plant height is set equal to 0.3 m (this is a site-specific parameter).

- The water stress parameter p is set equal to the default value of 0.65 (see Sections 6.3.3 and 6.3.4).

- The initial moisture content in each layer is calculated as the lysimeter storage measured on 10/01/95 divided by the lysimeter depth. The resulting moisture content is 0.053 m^3/m^3.

The interface performs the following functions. The interface displays the climate data. This includes the plot of the daily precipitation record and minimum, maximum, and average daily air temperatures. The percentage of time when mean daily temperature is below 0°C is calculated (1.3%). The plots are the same as the ones shown above using the MASSIF interface ***Bare Soil Lysimeter***.

The interface calculates the difference between the daily precipitation and daily change in lysimeter storage. This difference should be either equal to 0 (if there is no evapotranspiration) or be greater than 0 (if there is evapotranspiration). The negative difference indicates that the precipitation was underestimated. The data points in which this difference is negative are shown in Figure J-7. Both the daily precipitation and the difference between the precipitation and change in storage are shown.

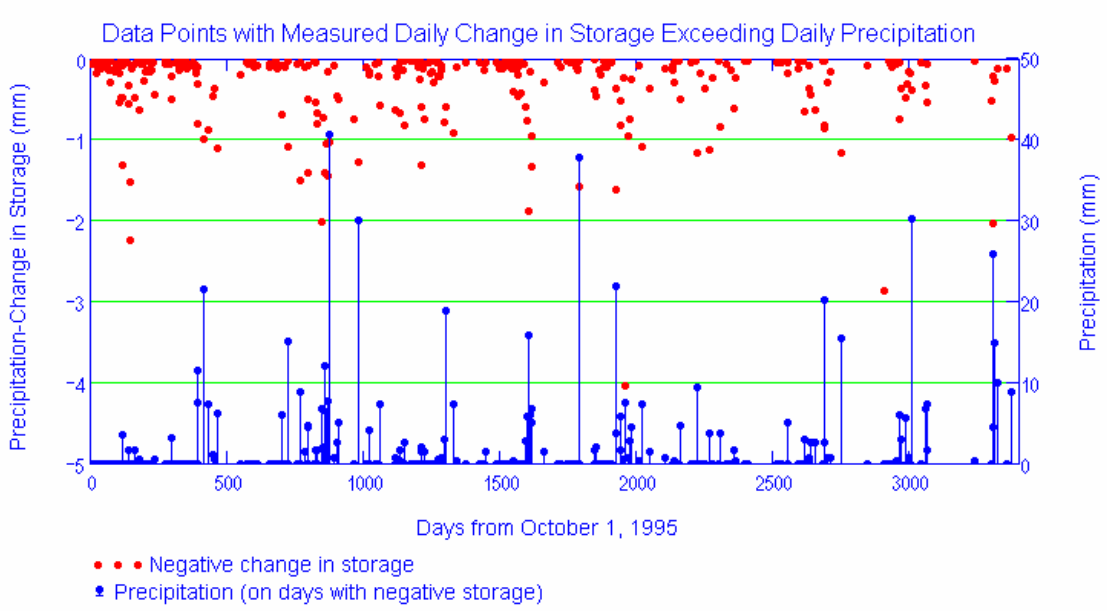

Source: Output DTN: SN0701T0502206.037, *\Welcome to Massif\Massif\Validation Analyses\Lysimeter\Vegetated Lysimeter.xmcd*.

Figure J-7. Data Points with Negative Daily Difference between Precipitation and Change in Storage Using the MASSIF Vegetated Lysimeter Interface

There are 341 points (10% of the data) in which precipitation was underestimated. As in the bare soil lysimeter case, these points coincide with large intensity precipitation events. The maximum negative difference is 4.1 mm. Since the ET is calculated as the difference between precipitation and storage, the same error in precipitation measurement will result in a corresponding error in the ET estimate.

The interface runs MASSIF, stores the results of calculations, and calculates the lysimeter storage as a sum of the water depths within the four model layers. The interface displays the measured and calculated daily lysimeter storage. An example is shown in Figure J-8. The parameters placed in the yellow box located just above the storage plot can be manually adjusted. Each adjustment results in a recalculation and a display of newly calculated storage values in the storage plot. This function is used in the sensitivity analysis.

For the period of simulation, the interface calculates the water balance constituents such as total precipitation, total evapotranspiration, total run-on, total runoff, and total infiltration. The total run-on is always zero since the lysimeter cell is not connected to any other cell in the geospatial file.

Adjustable Evaporation Parameters

Param1 ≡ 0.26 - Canopy fraction
Param2 ≡ 2.40 - NDVI-Kcb slope
Param3 ≡ .0135 - Diffusive evaporation parameter
Param8 ≡ 0.65 parameter p
Param5 ≡ 6 Readily evaporable water
Param6 ≡ 0.117 Field capacity
Param7 ≡ 0.044 Wilting point

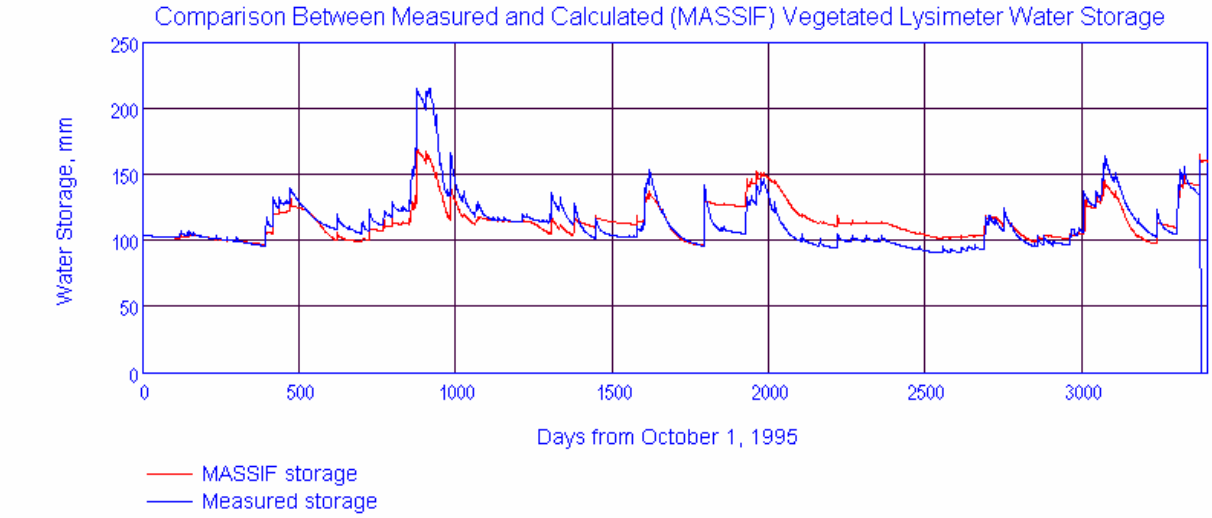

Source: Output DTN: SN0701T0502206.037, *\Welcome to Massif\Massif\Validation Analyses\Lysimeter\Vegetated Lysimeter.xmcd*.

Figure J-8. Calculated versus Measured Lysimeter Storage Plot Displayed by *Vegetated Lysimeter* Interface

The interface then checks the daily mass balance for the simulation and displays it as shown in Figure J-9.

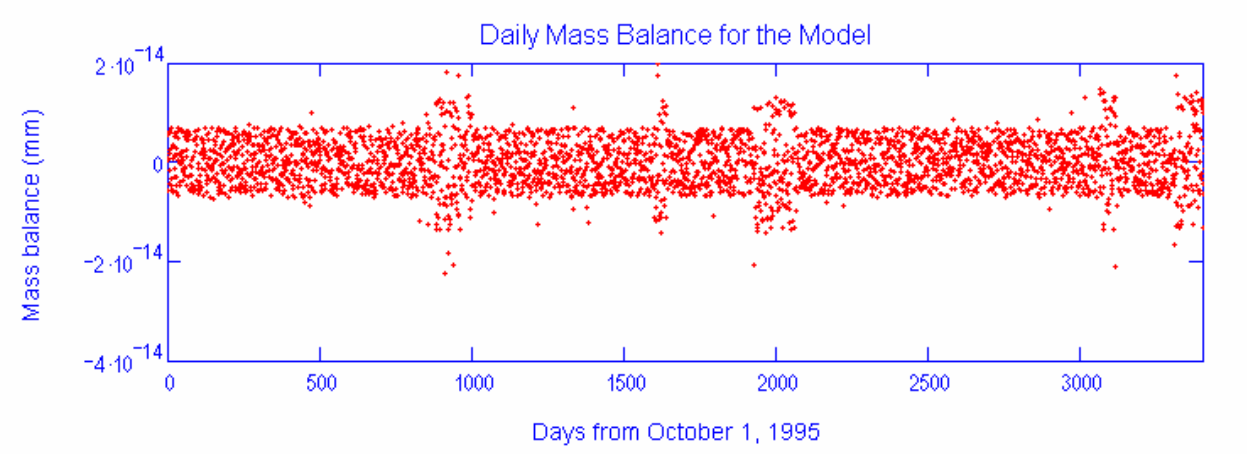

Source: Output DTN: SN0701T0502206.037, *\Welcome to Massif\Massif\Validation Analyses\Lysimeter\Vegetated Lysimeter.xmcd*.

Figure J-9. Daily Mass Balance Displayed by *Vegetated Lysimeter* Interface

The interface reads an external Excel file ***Hydrus1D Data&Results.xls*** that contains HYDRUS-1D input data (including potential evapotranspiration) and modeling results (daily storage and infiltration). These data are in worksheet ***Vegetated.*** The description of HYDRUS-1D modeling setup and details on how the potential evapotranspiration was calculated are provided below.

The interface displays the reference evapotranspiration calculated by MASSIF and the potential evapotranspiration used as HYDRUS-1D boundary condition. The plot is the same as the ones shown above under the MASSIF interface ***Bare Soil Lysimeter***.

The interface displays the observed lysimeter storage and the lysimeter storage calculated with MASSIF and HYDRUS-1D as shown in Figure J-10.

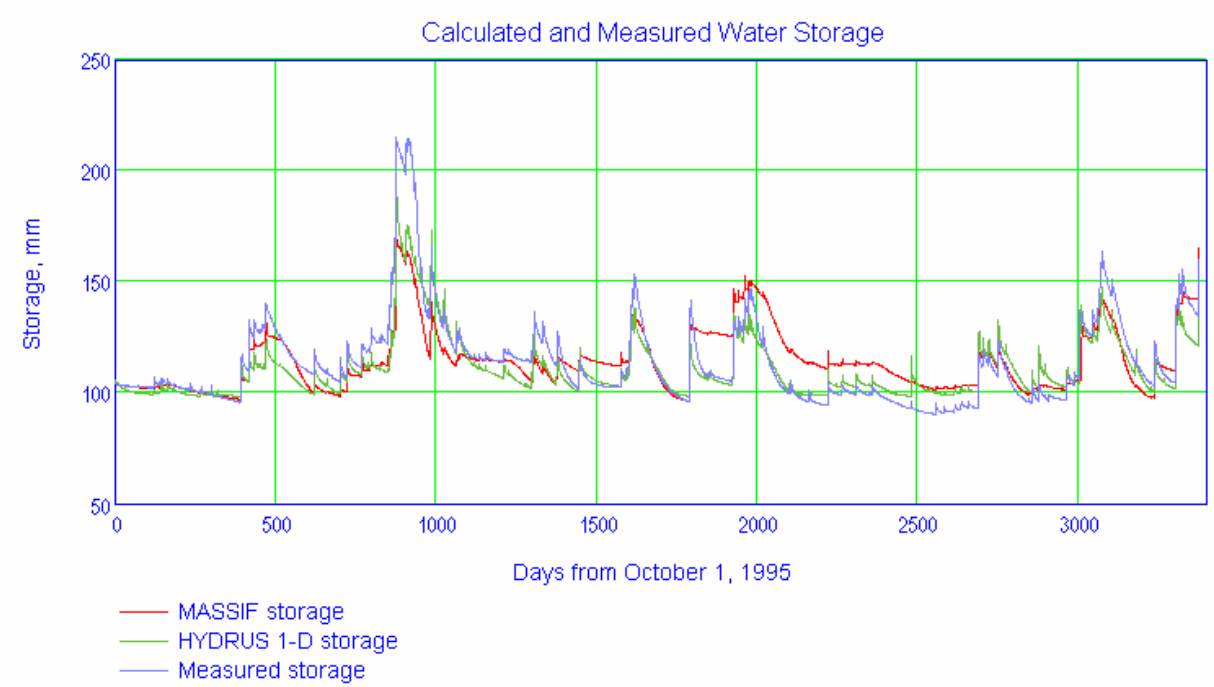

Source: Output DTN: SN0701T0502206.037, *\Welcome to Massif\Massif\Validation Analyses\Lysimeter\Vegetated Lysimeter.xmcd*.

Figure J-10. Calculated (MASSIF and HYDRUS-1D) and Measured Lysimeter Storage Displayed by Vegetated Lysimeter Interface

The interface calculates the mean root square error between the observed storage values and those calculated with MASSIF and HYDRUS-1D, and also between storage values calculated with MASSIF and those calculated with HYDRUS-1D. It displays the differences between the calculated and measured values in the form of histograms. The discussion of these results is provided in Section 7.1.2.

J1.3 MASSIF INTERFACE *BS AND VEGET OPTIMIZATION*

The interface is located in folder ***Validation Analyses*/*Lysimeter*** in the MASSIF package (Output DTN: SN0701T0502206.037). This interface was specifically designed to estimate evapotranspiration and soil parameters by minimizing differences between the calculated and measured daily water storage values in both bare soil and vegetated lysimeters. The interface reads the two embedded Excel files with the climate and storage data for the bare soil and vegetated lysimeters. The data for the bare soil lysimeter are from the *BS Input Data* worksheet in ***NTSLysimeter.xls*** and the data for the vegetated lysimeter are from the *Veg Input Data* worksheet in ***NTSLysimeter.xls*** (***NTS*** folder in Validation Output DTN: SN0607T0502206.016). These are the same data used in the simulation performed by interfaces ***Bare Soil Lysimeter*** and ***Vegetated Lysimeter***.

The interface reads an external Excel file ***NTS_location.csv*** with the geospatial data provided in a format required by MASSIF. The bare soil lysimeter site is represented by the first cell in this file and the vegetated lysimeter site by the second cell. As explained above, the input data in these two cells are the same. This is the same file used in ***Bare Soil Lysimeter*** and ***Vegetated Lysimeter*** interfaces. The input data read from this file are described above under the interface ***Bare Soil Lysimeter***.

The other parameters required to run MASSIF are defined directly within the interface as described above under the ***Bare Soil Lysimeter*** and ***Vegetated Lysimeter*** interfaces. The interface performs the following functions. The interface defines two optimization schemes in accordance with Equations 7.1.2-2 and 7.1.2-3. This includes the definition of the objective functions and initial values and ranges for the parameters to be estimated.

The optimization parameters for Scheme 1 are diffusive evaporation parameter K_{c_min}, vegetated lysimeter canopy fraction f_c, and vegetated lysimeter parameter C_{kcb}. The optimization parameters for Scheme 2 are diffusive evaporation parameter K_{c_min}, vegetated lysimeter canopy fraction f_c, vegetated lysimeter parameter C_{kcb}, and field capacity θ_f.

The interface runs the conjugate gradient minimization procedure, which is a built-in MathCAD function. The minimization procedure returns the values of the optimization scheme parameters that result in the minimum value of the corresponding objective functions. The interface lets the user define the optimization scheme parameters based on the result of the optimization. It then performs the final runs, one for the bare soil lysimeter and one for the vegetated soil lysimeter. The interface then calculates the mean root square error for the bare soil and the vegetated lysimeters.

The interface displays the observed bare soil and vegetated lysimeter storage values and the calculated bare soil and vegetated lysimeter storage values. An example is shown in Figure J-11.

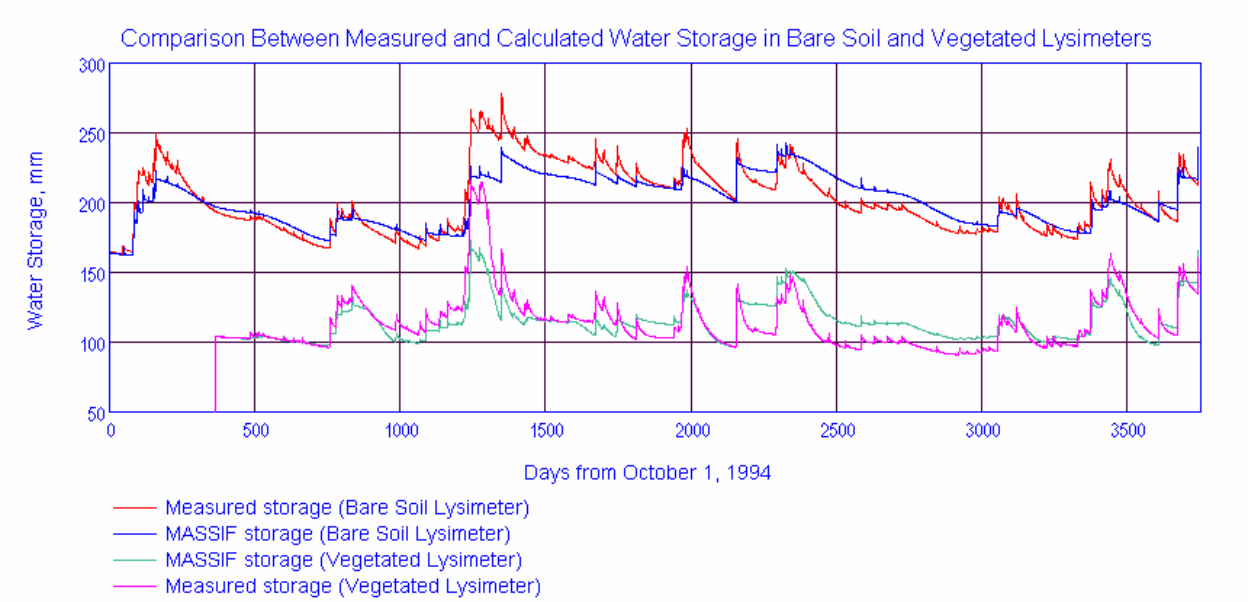

Source: Output DTN: SN0701T0502206.037, *\Welcome to Massif\Massif\Validation Analyses\Lysimeter\BS and Veget Optimization.xmcd*.

Figure J-11. Calculated and Measured Lysimeter Storage Displayed by BS and Veget Lysimeter Interface

The interface outputs the observed daily storage values and those calculated with MASSIF for bare soil and vegetated lysimeters into an embedded Excel file to assist in further data processing and display. These data were used to generate Figure 7.1.2.1-3 in Section 7.1.2. A discussion of these results is provided in Section 7.1.2.

J1.4 HYDRUS-1D MODELING SETUP

The MASSIF simulations were compared to the simulations performed using HYDRUS-1D code (Šimùnek et al. 2005 [DIRS 178140]). The HYDRUS-1D program numerically solves the Richards' equation for one-dimensional variably saturated water flow and heat and solute transport. The short description of HYDRUS-1D is provided in Section 6.2.4.1.

HYDRUS-1D was obtained from the Yucca Mountain Project Software Configuration Manager. The related communication and installation record are in ***HYDRUS_Gen*** directory (Validation Output DTN: SN0607T0502206.016). All the input and output HYDRUS-1D files for the bare soil lysimeter are in subdirectory ***NTSBar_P*** in the ***HYDRUS_Model*** directory in ***NTS*** folder in Validation Output DTN: SN0607T0502206.016. The input and output files in this subdirectory were created by running the HYDRUS-1D file ***NTSBar_P.h1d*** located in the ***HYDRUS_Model*** directory. All the input and output HYDRUS-1D files for the vegetated lysimeter are in subdirectory ***VL_90_10_Snow*** in the ***HYDRUS_Model*** directory in the ***NTS*** folder in Validation Output DTN: SN0607T0502206.016. The input and output files in this subdirectory were created by running HYDRUS-1D file ***VL_90_10_Snow.h1d*** located in the ***HYDRUS_Model*** directory.

The HYDRUS-1D modeling setup is described as follows. The simulated processes are water flow (including snow hydrology) and heat transport. The root uptake is simulated as the vegetated lysimeter. The depth of the soil profile is 200 cm. It is represented with 101 nodes. The first node is at the land surface (z = 0 cm) and the last node is at the lysimeter bottom (200 cm). The nodes are 2 cm apart. The soil profile is homogeneous. The initial moisture content is 0.08765 calculated as the lysimeter storage on 03/30/94 divided by the lysimeter depth. The initial temperature is 20°C. The van Genuchten model in HYDRUS-1D is used to represent relationships between the saturation and pressure head and between the saturation and hydraulic conductivity. The soil parameters are:

- saturated hydraulic conductivity is 336 cm/d
- saturated porosity is 0.357
- residual moisture content is 0.04
- van Genuchten parameter *alpha* is 0.0328 1/cm
- van Genuchten parameter *n* is 1.57
- pore connectivity parameter *l* is 0.5. Šimùnek et al. (2005 [DIRS 178140]) suggest leaving this parameter at its default value of 0.5.

The upper boundary is an atmospheric boundary with specified daily potential evaporation, potential transpiration (for the vegetated lysimeter only), precipitation, and temperature. The daily values of these parameters are defined for the entire period of simulation, which are 3,930 days for the bare soil lysimeter (03/30/94 to 12/31/04) and 3,380 days for the vegetated lysimeter (10/01/95 to 12/31/04).

The potential evapotranspiration ET_p was calculated using the Hargreaves formula (Jensen et al. 1997 [DIRS 177103]). This method was selected because the only site data required are daily average, maximum, and minimum air temperatures.

$$ET_p = 0.0023 R_a \left(T_m + 17.8\right)\sqrt{TR} \qquad \text{(Eq. J-2)}$$

where R_a is the extraterrestrial radiation in the same units as ET_p (e.g., mm d^{-1} or J $m^{-2}s^{-1}$), T_m is the daily mean air temperature, (°C), and TR is the temperature range between mean daily maximum and minimum air temperatures (°C). The extraterrestrial radiation, R_a (J $m^{-2}s^{-1}$), can be calculated as follows:

$$R_a = \frac{G_{sc}}{\pi}\, d_r(\omega_s \sin\varphi \sin\delta + \cos\varphi \cos\delta \sin\omega_s) \qquad \text{(Eq. J-3)}$$

where G_{sc} is the solar constant (J $m^{-2}s^{-1}$; 1,360 W m^{-2}), φ is the site latitude (rad), ω_s is the sunset hour angle (rad), d_r is the relative distance between Earth and Sun (−), and δ is the solar declination (rad). The last three variables are calculated as follows:

$$\omega_s = \arccos(-\tan\varphi \tan\delta) \quad \text{(Eq. J-4)}$$

$$d_r = 1 + 0.033 \cos\left(\frac{2\pi}{365} J\right) \quad \text{(Eq. J-5)}$$

$$\delta = 0.409 \sin\left(\frac{2\pi}{365} J - 1.39\right) \quad \text{(Eq. J-6)}$$

where J is the number of the day in the year (−).

The solar constant G_{sc} can be converted from J $m^{-2}s^{-1}$ to m s^{-1} as follows:

$$\begin{aligned} G_{sc} &= \lambda ET_0 = \lambda \rho_w G_{sc}^* \\ \lambda &= 2.501*10^6 - 2369.2\,T \\ G_{sc}^* &= \frac{G_{sc}}{\lambda \rho_w} = \frac{G_{sc}}{\rho_w \left(2.501*10^6 - 2369.2\,T\right)} = \\ &= \frac{1360}{10^3 * 2.454*10^6} = 5.54*10^{-7} \text{ m/s} = 4.789 \text{ cm/d} \end{aligned} \quad \text{(Eq. J -7)}$$

where λET_0 is the latent heat flux of evaporation (J $m^{-2}s^{-1}$), λ is the latent heat of vaporization of water (Jkg^{-1}, $ML^2T^{-2}M^{-1}$, L^2T^{-2}), T is temperature (°C), and ρ_w is the density of liquid water (ML^{-3}).

The input data used in these calculations and the resulting potential evapotranspiration values are in worksheet ***PET*** of ***NTSLysimeter.xls (NTS*** folder in Validation Output DTN: SN0607T0502206.016). The potential transpiration was assumed to be equal to 0.1 of the potential evapotranspiration. This corresponds to a vegetation fraction of 10 percent. The vegetation fractions of the LA association are 0.11, 0.15, and 0.21 for dry, average, and wet years, respectively (Appendix D). The NTS lysimeter site is drier than most of the Yucca Mountain model domain (based on elevation), so the use of a vegetation fraction of 10% is reasonable. In addition, a value of 20% was used and there was little change in soil water storage.

The potential evaporation is equal to potential evapotranspiration in the case of the bare soil lysimeter. The potential evapotranspiration values were copied into the built-in HYDRUS-1D time-dependent boundary condition spreadsheet for the bare soil lysimeter. The potential evaporation and transpiration values were copied into the built-in HYDRUS-1D time-dependent boundary condition spreadsheet for the vegetated lysimeter. The daily precipitation, mean daily temperature, and daily temperature amplitude values were copied from the ***PET*** worksheet as well.

The lower boundary is defined as a seepage boundary for flow and as a zero gradient boundary for the heat transport. The seepage boundary condition assumes that a zero-flux boundary condition applies as long as the local pressure head at the bottom of the soil profile is negative. However, a zero pressure head will be used as soon as the bottom of the profile becomes saturated. This type of boundary condition often applies to finite lysimeters that are allowed to drain under the gravity.

Heat transport was turned on in NTS and RCEW lysimeter simulations. The heat transport module must be turned on to simulate snow hydrology with HYDRUS-1D even when the heat transport is not of interest. The average daily temperature specified in this module was used in HYDRUS-1D to calculate whether the precipitation should be treated as snow and to maintain snow cover during the freezing periods. The snow hydrology has no impact on the NTS as temperatures rarely fall below freezing. However, this was a significant factor for the RCEW lysimeter where the snow cover may exist for 3 to 4 months during the winter.

The root water uptake is considered for the vegetated lysimeter only throughout 200 cm of the soil profile. The roots are uniformly distributed within this depth. The Feddes model in HYDRUS-1D is used for the stress response function (see Figure J-12). Water uptake is assumed to be zero when close to saturation (pressure head P_0). Root water uptake is also zero for pressure head P_3 which is less than the wilting point. Water uptake is considered optimal between pressure heads $P_1$and P_2, whereas for the pressure heads between P_2 and P_3, water uptake decreases linearly with pressure head. The parameters describing this function were taken from HYDRUS-1D database. The most common values were used. The sensitivity analysis showed that the Feddes model parameters have little impact on the calculations. The parameter values are provided below.

- Value of the pressure head below which roots start to extract water from the soil (P_0) is −10 cm
- Value of the pressure head below which roots extract water at the maximum possible rate (P_1) is −25 cm.
- Value of the limiting pressure head below which roots can no longer extract water at the maximum rate assuming a potential transpiration rate of 0.5 cm/d (P_{2h}) is −200 cm (this value is not used in calculations since the maximum potential transpiration during the period of simulation was 0.11 cm/day).
- Value of the limiting pressure head below which roots cannot longer extract water at the maximum rate assuming a potential transpiration rate of 0.1 (P_{2l}) is −800 cm.
- Value of the pressure head below which root water uptake ceases (P_3) is -15,000 cm. The maximum negative pressure under which the plants can extract water did not impact the calculations because the moisture in the soil profile was always higher than the limiting moisture.

The resulting water stress function is shown in Figure J-12. The water stress function plays the role similar to K_{cb}—it decreases the potential transpiration. The major difference is that the

Feddes water stress function reduces potential transpiration based on the pressure head in the soil profile (saturation), and the K_{cb} function reduces the potential transpiration based on the season of the year. Although saturation is low during the dry part of the year and high during the wet part, there is no direct translation from one function to the other.

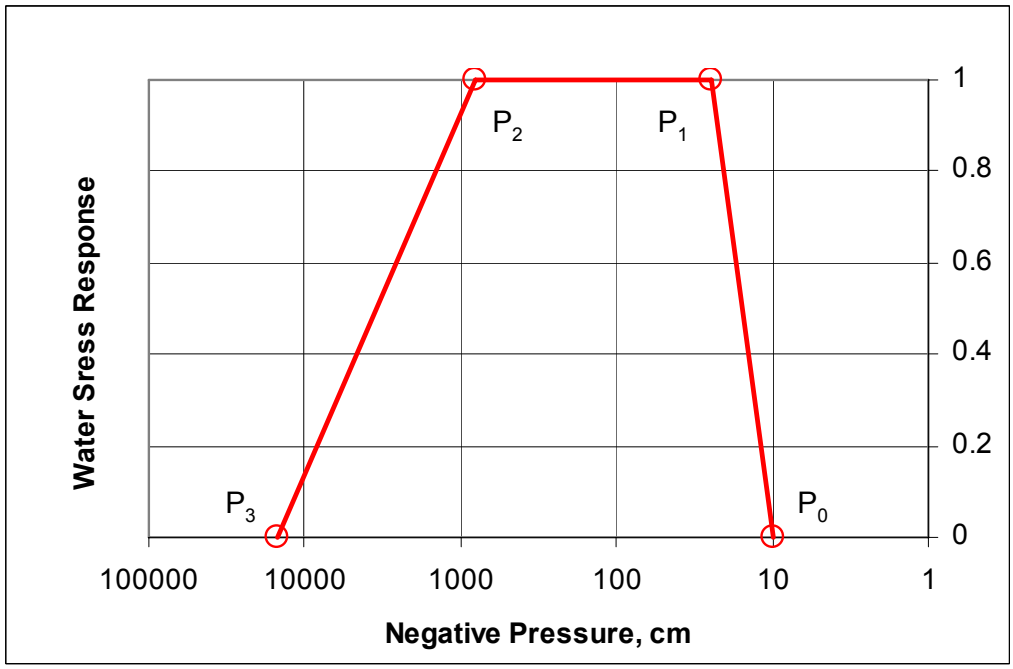

Source: Šimùnek et al. 2005 [DIRS 178140], Figure 2.1a, p. 15.

Figure J-12. Feddes Model Water Stress Function Used in HYDRUS-1D Modeling

HYDRUS-1D input and output files (all these files are text files) for the final runs are located in the subdirectories ***NTSBar_P*** (bare soil lysimeter) and ***VL_90_10_Snow*** (vegetated lysimeter) in the ***HYDRUS_Model*** directory in the ***NTS*** folder in Validation Output DTN: SN0607T0502206.016.

The input files have the extension *in* or *dat*. The output files have the extension *out*. The results presented in Section 7.1.2 are from the output files ***T_LEVEL.OUT***. These files provide the daily values of all the water balance components, including storage (column *"volume"*) and infiltration (column *"vBot"*) in centimeters. The storage values were copied from this file into ***HYDRUS1D Data&Results.xls*** that is an external file read by the interfaces ***Bare Soil Lysimeter*** and ***Vegetated Lysimeter***, as explained above. Comparison of the HYDRUS-1D results and MASSIF results is performed within the interface.

The HYDRUS-1D results for the vegetated lysimeter run (from ***NOD_INF.OUT*** in ***VL_90_10_Snow*** subdirectory in the ***HYDRUS_Model*** directory in the ***NTS*** folder in Validation Output DTN: SN0607T0502206.016) were used to plot the moisture profiles shown in Figure 7.1.2.1-3. A discussion of the HYDRUS-1D results is provided in Section 7.1.2.

J2. REYNOLDS CREEK EXPERIMENTAL WATERSHED LYSIMETER SITE

The Reynolds Creek Experimental Watershed (RCEW) data were collected by the U.S. Department of Agriculture (USDA) Northwest Watershed Research Center (NWRC), Boise, Idaho. The data are available from *ftp.nwrc.ars.usda.gov*. The data used in this analysis were obtained directly from USDA NWRC. The information included in a CD provided by the USDA NWRC is submitted as DTN: SN0608T0502206.020 [DIRS 179875].

The RCEW occupies 239 km^2 in the Owyhee Mountain region located in the southwestern Idaho, 80 km southwest of Boise (Hanson et al. 2001 [DIRS 177509]). Two pairs of soil lysimeters were installed in the RCEW in 1967, one pair at the Lower Sheep Creek climate station (designated the "east" and "west" lysimeters) and the other one at the Reynolds Mountain climate station (designated "north" and "south"). The long-term lysimeter database is described by Seyfried et al (2001 [DIRS 177515]). The database includes the lysimeter description, calibration, data collection, and data availability. The RCEW lysimeters are hydraulic weighing lysimeters in which an inner cylindrical tank containing soil is set within a slightly larger outer cylinder. The inner cylinder rests on a coil of 0.05-m-diameter butyl tubing filled with liquid (different low freezing point liquids were used). The inner cylinder was 1.22-m deep and 1.47 m in diameter.

The Lower Sheep Creek (LSC) lysimeter site (elevation 1,656 m) was selected for this analysis because the climatic conditions at this site are closer to the glacial transition climate conditions predicted for Yucca Mountain. The Reynolds Mountain lysimeter site is located at a much higher elevation (2,098 m) and is under significantly colder and wetter conditions than the glacial transition climate.

The mean precipitation at the LSC lysimeter site is 349 mm (Wight et al. 1986 [DIRS 177104]) and the mean annual temperature is 7.4°C (Wight and Hanson 1990 [DIRS 177113]). About 21% of precipitation comes from snow. The lysimeter latitude is 43° 08' 24.088", longitude is 116° 43' 57.732", and elevation is 1,656 m (DTN: SN0608T0502206.020 [DIRS 179875]).

The LSC lysimeter site is located next to the climate station 127x07 (see Figure J-13). The minimum and maximum temperatures and precipitation data are available for this climate station. The daily temperature data were taken from ***daily127x07climate.txt*** located in the directory ***climate*** (DTN: SN0608T0502206.020 [DIRS 179875]). The precipitation data were collected hourly. These data were taken from ***hourly127x07precipitation.txt*** located in the directory ***precipitation*** (DTN: SN0608T0502206.020 [DIRS 179875]). The daily precipitation was calculated from hourly precipitation data. Based on the availability of the lysimeter data, the considered period of observation was from 01/10/77 through 09/30/84. October 1, 1977 was selected as the beginning of the observation period to satisfy MASSIF input requirements (the data set must start at the beginning of the water year). The temperature and precipitation data were converted to a format required by MASSIF. The formatted data are in ***RCEWLysimeter.xls (worksheet "Climate Data")*** (DTN: SN0608T0502206.020 [DIRS 179875]). This file contains month number, day of the month number, day of the year number, year number, daily precipitation in mm, daily maximum temperature in degrees C, daily minimum temperature in degrees C, and daily average wind speed in m/s. The daily average wind speed was set to 2 m/s for the entire period of observation since no wind speed data were available.

The LSC site has two lysimeters LSCW (west lysimeter) and LSCE (east lysimeter) and six neutron probes. Three neutron probes (117079, 117186, and 117287) are installed at the LSCE lysimeter site, and three neutron probes are installed at the LSCW lysimeter site (127707, 127807, and 127907). The comparison between the lysimeter data and the neutron probe data is provided in Seyfried et al. (2001 [DIRS 177515]; 2001 [DIRS 177506]). It was shown that the LSCW lysimeter data are in good agreement with the neutron probe data. The LSCE lysimeter data differ from the LSCW lysimeter data (even though it is located only 3.6 m away) and are not in a good agreement with the neutron probe data. Based on this conclusion, the LSCW lysimeter was selected for the analysis.

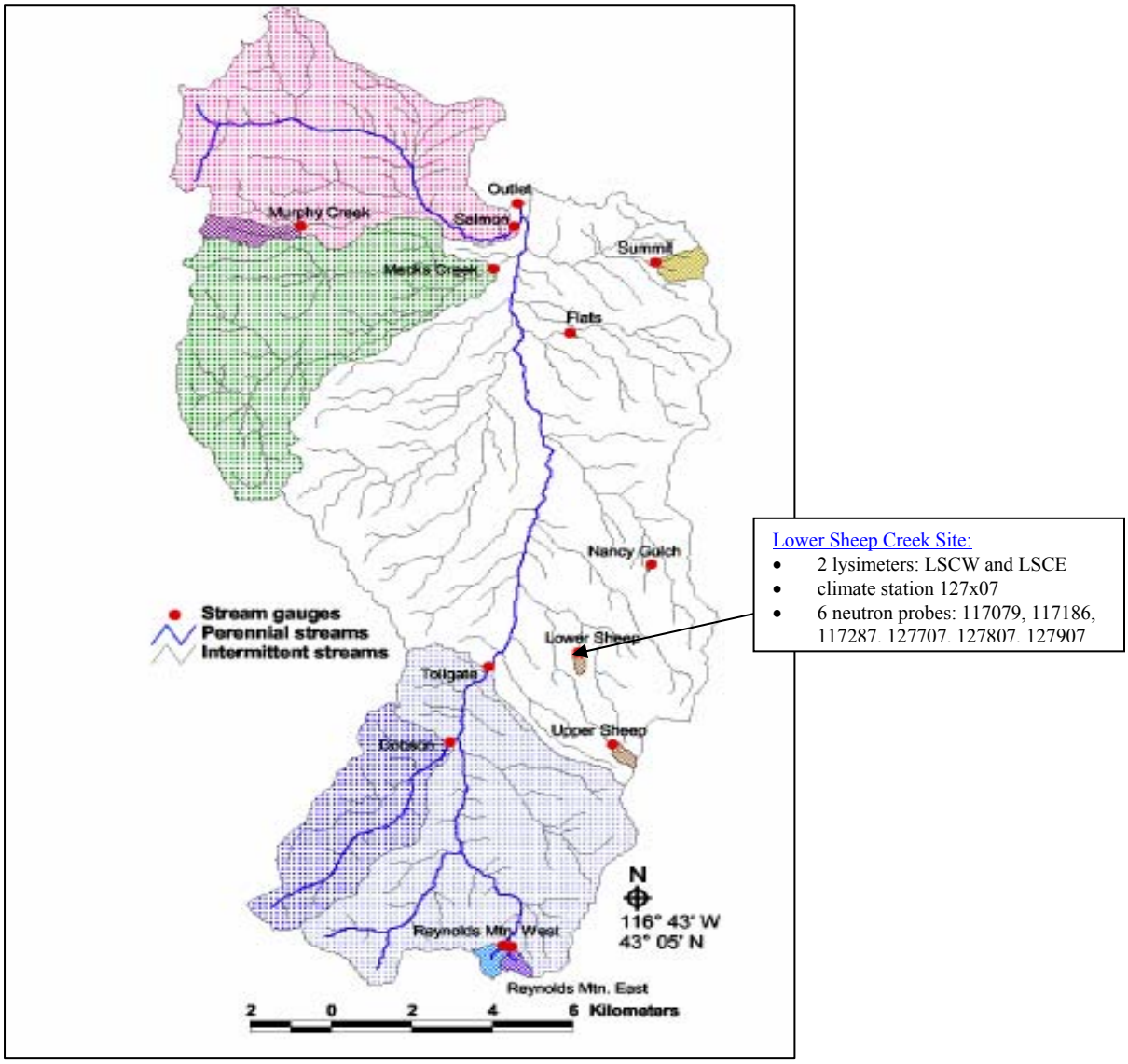

Source: Seyfried et al. 2001 [DIRS 177501], Figure 3.

Figure J-13. Locations of the 13 Weirs in the RCEW with Long-term Data

The LSCW lysimeter data were taken from ***daily127x07lysimeter.txt*** located in the directory ***soilmoisture*** (DTN: SN0608T0502206.020 [DIRS 179875]). These data represents the changes in lysimeter soil water storage in mm with regard to the storage measured on 04/13/1976. The data were taken irregularly during the no snow part of the year and were not taken during the snow season.

To convert the changes in lysimeter storage into the actual daily storage values, the initial storage must be known. The initial storage was calculated using the neutron probe data. These data were taken from ***neutronprobesoilwater127707.txt*** located in the directory ***soilmoisture*** (DTN: SN0608T0502206.020 [DIRS 179875]). This file contains data for the neutron probe 127707, which is 0.91 m deep. This probe was selected based on the analysis in Seyfried et al. (2001 [DIRS 177515], Figure 1) since probe 127707 data are in very good agreement with the LSCW lysimeter data. The moisture content in this file is provided for the following four readings: 15, 31, 61, and 91 cm. As suggested by Seyfried et al. (2001 [DIRS 177506]), the 15 cm reading represents soil water from 0 to 23 cm, the 31 cm reading represents soil water from 23 to 46 cm, the 61 cm reading represents soil water from 46 to 75 cm, and the 91 cm reading represents soil water from 75 to 106 cm. The lysimeter is 122-cm deep. It was assumed that the moisture within the last 16 cm of the lysimeter is the same as that within the 75- to 106-cm interval. The moisture contents measured in neutron probe 127707 were converted to the lysimeter storages (s) using the following formula:

$$s = \theta 1 \times \Delta z1 + \theta 2 \times \Delta z2 + \theta 3 \times \Delta z3 + \theta 4 \times \Delta z4 \qquad \text{(Eq. J-8)}$$

where Δz_1, Δz_2, Δz_3, and Δz_4 are the depth interval thicknesses (23 cm, 23 cm, 29 cm, and 46 cm from the top interval down) and θ_1, θ_2, θ_3, and θ_4 are the corresponding measured moisture contents. The data and the calculations are in worksheet ***"NP127707"*** of ***RCEWLysimeter.xls (RCEW*** folder in Validation Output DTN: SN0607T0502206.016). Plotted in Figure J-14 are the lysimeter storages from LSCW data and from neutron probe 127707 data. The lysimeter data are in good agreement with the neutron probe data except in the summers of 1978 and 1981.

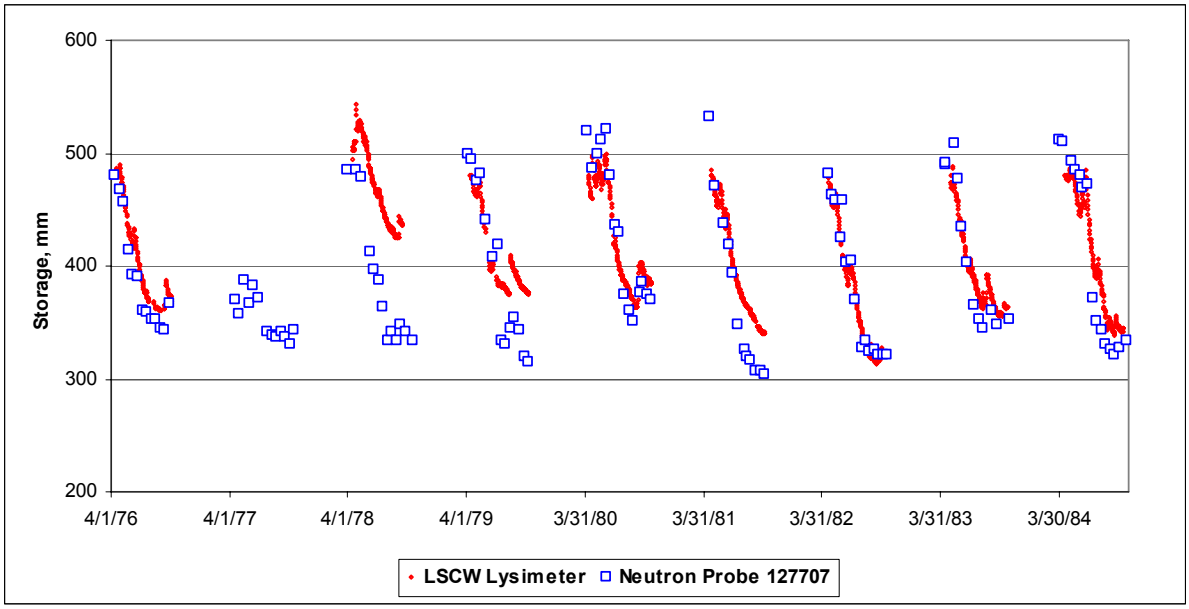

Source: Validation Output DTN: SN0607T0502206.016.

Figure J-14. Soil Moisture Storage in RCEW Lysimeter LSCW

The lysimeter storage data and precipitation are shown in Figure J-15. The storage data were added to the MASSIF input file because these data are required by the MASSIF interface ***"Reynolds Creek"*** that performs the analysis of the RCEW lysimeter data. These data are in worksheet ***"Climate Data"*** of ***RCEWLysimeter.xls (RCEW*** folder in Validation Output DTN: SN0607T0502206.016). The lysimeter calibration is described in Seyfried et al. (2001 [DIRS 177515]). As is concluded in this publication, the lysimeter observations have the precision of $\pm$8 mm ($\pm$ 2.2 % of the mean annual precipitation).

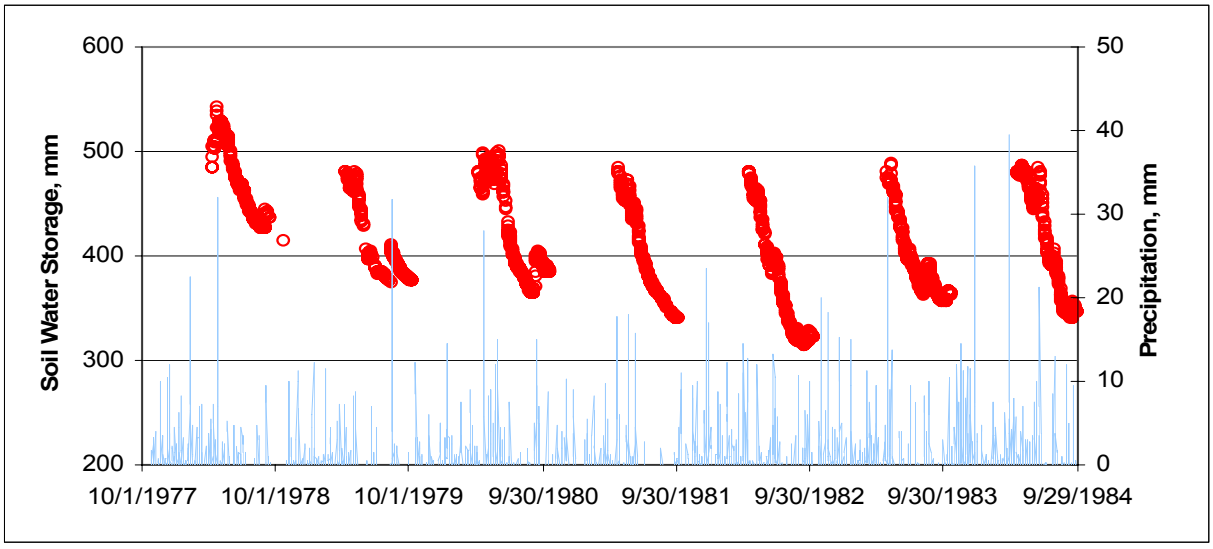

Source: Validation Output DTN: SN0607T0502206.016.

Figure J-15. RCEW LSCW Lysimeter Soil Water Storage and Precipitation Data Used in the Analysis

The maximum lysimeter storage during this period of observation is 542.7 mm. This corresponds to the moisture content of 0.445. The minimum lysimeter storage is 313.9 mm. This corresponds to the moisture content of 0.257.

The climate data in worksheet ***Climate Data*** of ***RCEWLysimeter.xls (RCEW*** folder in the Validation Output DTN: SN0607T0502206.016) are used to calculate potential evapotranspiration, which constitutes the upper boundary condition in the HYDRUS-1D model. The calculations of the potential evapotranspiration are implemented the same way as described above for the NTS lysimeter site. The Hargreaves formula (Jensen et al. 1997 [DIRS 177103]) is used in these calculations. The input data to these calculations are minimum, maximum, and average daily temperatures, and the site latitude. The average temperature is calculated from minimum and maximum temperatures. The transpiration is assumed to be 50% of evapotranspiration based on the estimate of the mean vegetation cover including live plants and litter at the site over the 11 years of observations provided in Wight et al. (1986 [DIRS 177104]). The input data and the calculations are in worksheet ***Potential ET*** of ***RCEWLysimeter.xls (RCEW*** folder in Validation Output DTN: SN0607T0502206.016). The average temperature and calculated potential evapotranspiration are shown in Figure J-16.

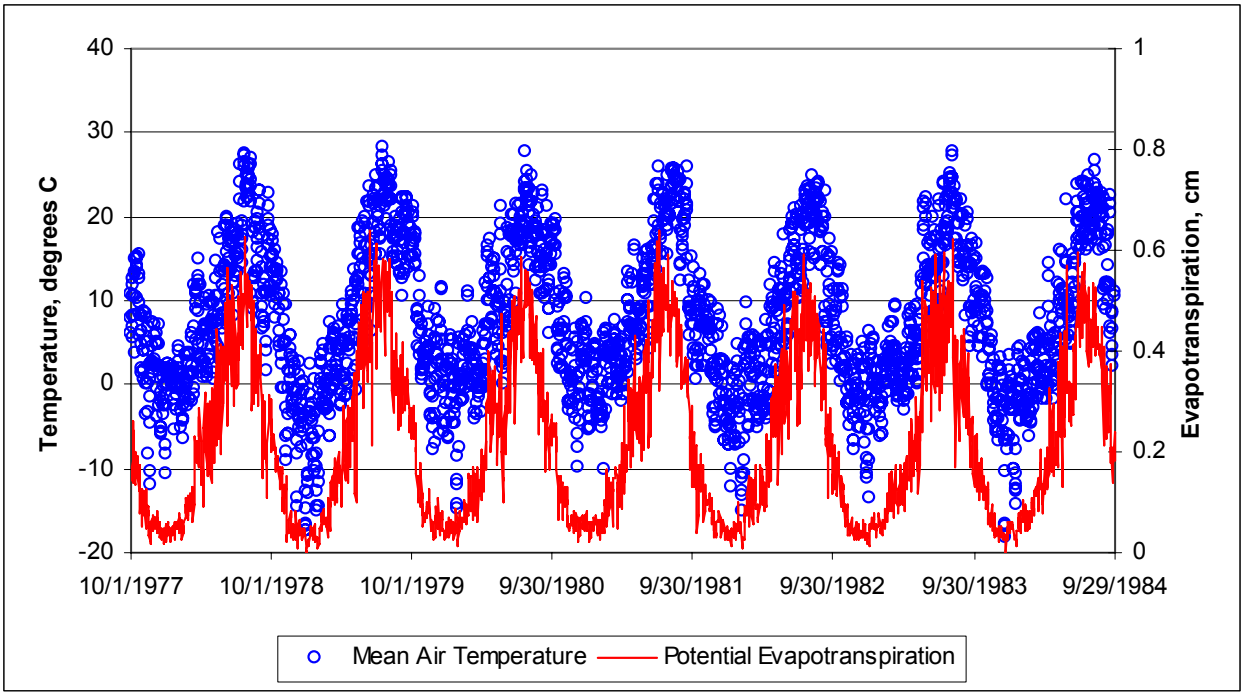

Source: Validation Output DTN: SN0607T0502206.016.

Figure J-16. Average Air Temperature and Calculated Potential Evapotranspiration at the RCEW LSCW Lysimeter Site

The remaining input parameters are initial moisture content, soil and bedrock properties and the vegetation parameters.

The initial conditions apply to 10/01/77, which is the beginning of the simulation. No storage data are available for this date. The storage measured on 09/15/78 was 435.5. This corresponds to an integrated water content within the profile of 0.36 m^3/m^3. The initial water content on 10/01/77 was likely to be higher, because the water year of 1977 was the highest in storage. Consequently, the initial moisture was set equal to 0.39 m^3/m^3. The initial moisture should not have a great effect on the calculations.

The soil properties were taken from ***neutronprobesoils.dbf*** located in the directory ***soilmoisture*** (DTN: SN0608T0502206.020 [DIRS 179875]). The soil properties were obtained from the neutron tube 127907, which is 183-cm deep. Nine soil horizons were described at this location. The soil data include the depth and thickness of each horizon; percent sand, clay, and silt; bulk density; field capacity (at −1/3 bars); wilting point (at −15 bars); parent material; texture; average slope; and other properties. Based on these data, the first 10.2 cm of the lysimeter site consists of loam/silty loam, the next 48.3 cm is clay/clay loam, and the remaining soil is loam/sandy loam. The bedrock at the site is basalt (which is the parent material for the lysimeter soils). The average slope is 4 degrees.

No information is available on the horizon saturated hydraulic conductivity, residual moisture content, porosity, van Genuchten parameters *alpha* and *n*, and bedrock saturated hydraulic conductivity. These parameters were obtained from the HYDRUS-1D module that allows for

estimating these soil properties using Rosetta Lite 1.1, June 2003. The horizon saturated hydraulic conductivity, residual moisture content, porosity, van Genuchten parameters *alpha* and *n* were estimated from percent sand, silt, and clay and bulk density, field capacity, and wilting point, except for horizons 2 and 4. The information on bulk density and field capacity was not available for these horizons, and only the available data on percent sand, silt, and clay were used. The original soil properties and estimated soil properties are in worksheet ***Soils*** of ***RCEWLysimeter.xls (RCEW*** folder in the Validation Output DTN: SN0607T0502206.016).

Since MASSIF is not designed to simulate heterogeneous soils, the soil properties were averaged over the 122 cm of the lysimeter depth. The geometric weighted mean (Fetter 2001 [DIRS 156668], p. 88) and inverse value mean were used for the hydraulic conductivities (Fetter 2001 [DIRS 156668]). These calculations are in worksheet ***Soils*** of ***RCEWLysimeter.xls (RCEW*** folder in the Validation Output DTN: SN0607T0502206.016). The averaged soil properties are summarized in Table J-1. The only situation in which soil saturated hydraulic conductivity can affect the MASSIF results is when there is runoff at the site. No noticeable runoff occurred at this site because it was designed to prevent both runoff and run-on. The residual moisture content and van Genuchten parameters *alpha* and *n* are not inputs to MASSIF. They are required for HYDRUS-1D simulations only. The saturated hydraulic conductivity of the bedrock is not available. The range considered was from 10^{-9} cm/s to 10^{-7} cm/s. This range is suggested for dense and vesicular basalt hydraulic conductivity by Freeze and Cherry (1979 [DIRS 101173], p. 162, Table 4.1). The bedrock hydraulic conductivity is a MASSIF parameter and is not a HYDRUS-1D parameter. In the HYDRUS-1D simulation the lower boundary is set at the bottom of the lysimeter, and a seepage boundary condition is defined in the same way as described above for the NTS lysimeter site.

The vegetation parameters are rooting depth, vegetation cover, plant height, water stress parameter p, the potential vegetation response parameter PVR, and transpiration parameter C_{kcb}. Note that the last four parameters are MASSIF inputs only. As described above, C_{kcb} is the slope of the linear regression line representing the $NDVI'–K_{cb}$ relationship (see Appendix E for details). Parameter PVR can be defined arbitrarily (it was set equal to 1), as explained in Section 7.1.2, because the optimization scheme estimates the product of K_{cb} and PVR.

As described by Seyfried et al. (2001 [DIRS 177515]), the vegetation at the lysimeter site is dominated by low sagebrush that grows to a height of about 0.3 m and is accompanied by perennial bunchgrasses and forbs. The lysimeter site contains a mature shrub along with the naturally associated plants with a slightly higher vegetation density than the surrounding landscape. The rooting depth is specified equal to 122 cm, which is the lysimeter depth. The vegetation cover used in HYDRUS-1D is set equal to 0.5. The vegetation cover in MASSIF is a parameter in the optimization scheme. There is no data to define C_{kcb}, which is the MASSIF input. It is a parameter in the optimization scheme as well. The plant height is set equal to 0.3 m and water stress is set to 0.8 in MASSIF calculations.

The default MASSIF values are used for the evaporation depth Z_e (100 mm), readily evaporable water rew_1 (6 mm), and sublimation and snowmelt coefficient. The terrain albedo was set equal to 0.15 based on the information from a journal article by Wight et al. (1986 [DIRS 177104]).

Table J-1. Averaged Soil Properties Used in MASSIF and HYDRUS-1D Calculations

Soil Property	Units	Input Category	Weighted Mean	Min	Max
Soil Porosity	m^3/m^3	H, M	0.467	0.422	0.506
Soil Field Capacity	m^3/m^3	M	0.332	0.273	0.415
Soil Wilting Point	m^3/m^3	M	0.187	0.118	0.267
Soil Saturated Hydraulic Conductivity (average of the inverse values)	cm/d	H, M	17.678	3.930	74.470
Soil Saturated Hydraulic Conductivity (geometric average)	cm/d	H, M	4.128	3.930	74.470
Soil van Genuchten alpha	1/cm	H	0.014	0.0059	0.0218
Soil van Genuchten n	–	H	1.335	1.24	1.59
Soil Residual Moisture	m^3/m^3	H	0.064	0.05	0.081
Bedrock Saturated Hydraulic Conductivity	cm/s	M	–	1.0×10^{-9}*	1.0×10^{-7}*

Source: Validation Output DTN: SN0607T0502206.016.

*Values from Freeze and Cherry 1979 [DIRS 101173], p. 162, Table 4.1).

H stands for HYDRUS-1D; M stands for MASSIF.

The site coordinates and elevation, climate data, soil and bedrock properties, and vegetation parameters described above are incorporated in the MASSIF interface (MathCAD file ***Reynolds Creek***). The geospatial data are in a separate text file. The climate data are embedded within the interface Excel file. The other data are directly defined within the interface. This is explained below.

J2.1 CLIMATE DATA

The interface reads the embedded Excel file with the climate data provided in the format required by MASSIF. The climate data are copied to this file from the worksheet ***Climate Data*** in ***RCEWLysimeter.xls*** (***RCEW*** folder in the Validation Output DTN: SN0607T0502206.016). In addition to the climate data required to run MASSIF (first 8 columns in the file), this file contains the lysimeter storage in mm required by the interface (10th column).

J2.2 GEOSPATIAL DATA

The interface reads an external Excel file with the geospatial data provided in a format required by MASSIF. The file name is ***RCEW_location.csv***. It is located in the same directory (***Lysimeter***) in which the interface is located. The file consists of two lines; each line represents one watershed cell. The lysimeter site is represented by the first cell in this file (the first line). The second cell is not used in the analysis. The geospatial information includes the cell identification number (arbitrary number in this case), site latitude and longitude in degrees and UTM coordinates in meters, site elevation in meters, slope in degrees, aspect, soil type, soil depth class, bedrock type, *PVR*, and an identification number of the cell from which the runoff is routed to this cell (it is set to −3 to exclude the run-on component using the corresponding MASSIF option). The site longitude, latitude, and elevation are defined as described above. The slope at the site is 4° (as described above). Soil type is set equal to 5, soil depth class is set equal to 2, and bedrock type is set equal to 406. The *PVR* is set equal to 1. As described above the

PVR can be set equal to an arbitrary value as long as the K_{cb} value is estimated by adjusting C_{kcb}. The *PVR* is set equal to 1 for the sake of convenience.

J2.3 OTHER PARAMETERS

The other parameters required to run MASSIF and discussed above are defined directly within the interface as follows:

- Reference elevation is set equal to site elevation to avoid correction of temperature and precipitation with regard to the reference elevation.
- The albedo is set equal to 0.15.
- Weather parameters, such as first and last day of winter and precipitation duration coefficients, were set equal to the values defined for the glacial transition climate (Sections 6.3.3 and 6.3.4).
- Dew point offset parameters were set equal to the default MASSIF values.
- Soil properties such as porosity, hydraulic conductivity, and wilting point of the soil type 5 are set equal to the weighted mean values defined in Table J-1 (inverse value mean is used for hydraulic conductivity). This redefines the values that MASSIF reads from the built-in look-up table with the corresponding soil properties for the soil type 5.
- Bedrock hydraulic conductivity of the bedrock type 406 is set equal to 10^{-9}cm/s (the lower bound defined above). This redefines the value that MASSIF reads from the built-in look-up table with the bedrock properties. This initial value was changed within the range considered above as part of the sensitivity analysis.
- The soil depth of the Soil Depth Class 2 is set equal to 183 cm.
- The rooting depth was specified equal to 122 cm.
- The vegetation cover is set equal to 0.5. The vegetation cover is a parameter in the optimization scheme and can also be adjusted manually.
- C_{kcb} coefficient representing the regression line slope is a parameter in the optimization scheme and can also be adjusted manually. C_{kcb} coefficient representing the regression line intercept is set equal to 0.
- The plant height is set equal to 0.3 m.
- The water stress parameter p is set equal to 0.65 (this parameter is not a part of the optimization scheme; however, it can be manually adjusted if needed).
- The evaporation depth Z_e is set equal to 100 mm (this parameter is not a part of the optimization scheme, however, it can be manually adjusted if needed).

- Readily evaporable water rew_1 is set equal to 6 mm (this parameter is not a part of the optimization scheme; however, it can be manually adjusted if needed).

- The diffusive evaporation parameter K_{c_min} is set equal to 0.0. This parameter is a parameter in the optimization scheme and can also be adjusted manually.

- Sublimation and snowmelt coefficients are set equal to the default MASSIF values.

- The initial moisture content in each layer is set equal to 0.39 m^3/m^3.

The functions performed by the interface are described as follows. The interface displays the climate data read for the period of simulation. This includes the plot of the daily precipitation record and minimum, maximum, and average daily air temperatures. The percentage of time when mean daily temperature is below 0°C is calculated (20.6 %). The examples are shown in the Figure J-17.

The interface runs MASSIF, stores the results of calculations, and calculates the lysimeter storage as a sum of the water depths within the three upper layers (top 122 cm of soil profile where the lysimeter is located).

The interface displays the measured and calculated daily lysimeter storage. An example is shown in Figure J-18. The parameters placed in the yellow box located just above the storage plot can be manually adjusted. Each adjustment results in recalculation and display of new calculated storage values in the storage plot. This function was used in the sensitivity analysis and in further adjustment of the parameters obtained via optimization scheme. The interface calculates the objective function value using Equation 7.1.2-4.

For the period of simulation, the interface calculates the water balance constituents such as total precipitation, total evaporation, total transpiration, total run-on, total runoff, and total infiltration. Note that the total run-on is always zero since the lysimeter cell is not connected to any other cell in the geospatial file. The interface checks the daily mass balance for the simulation and displays it as shown in Figure J-19.

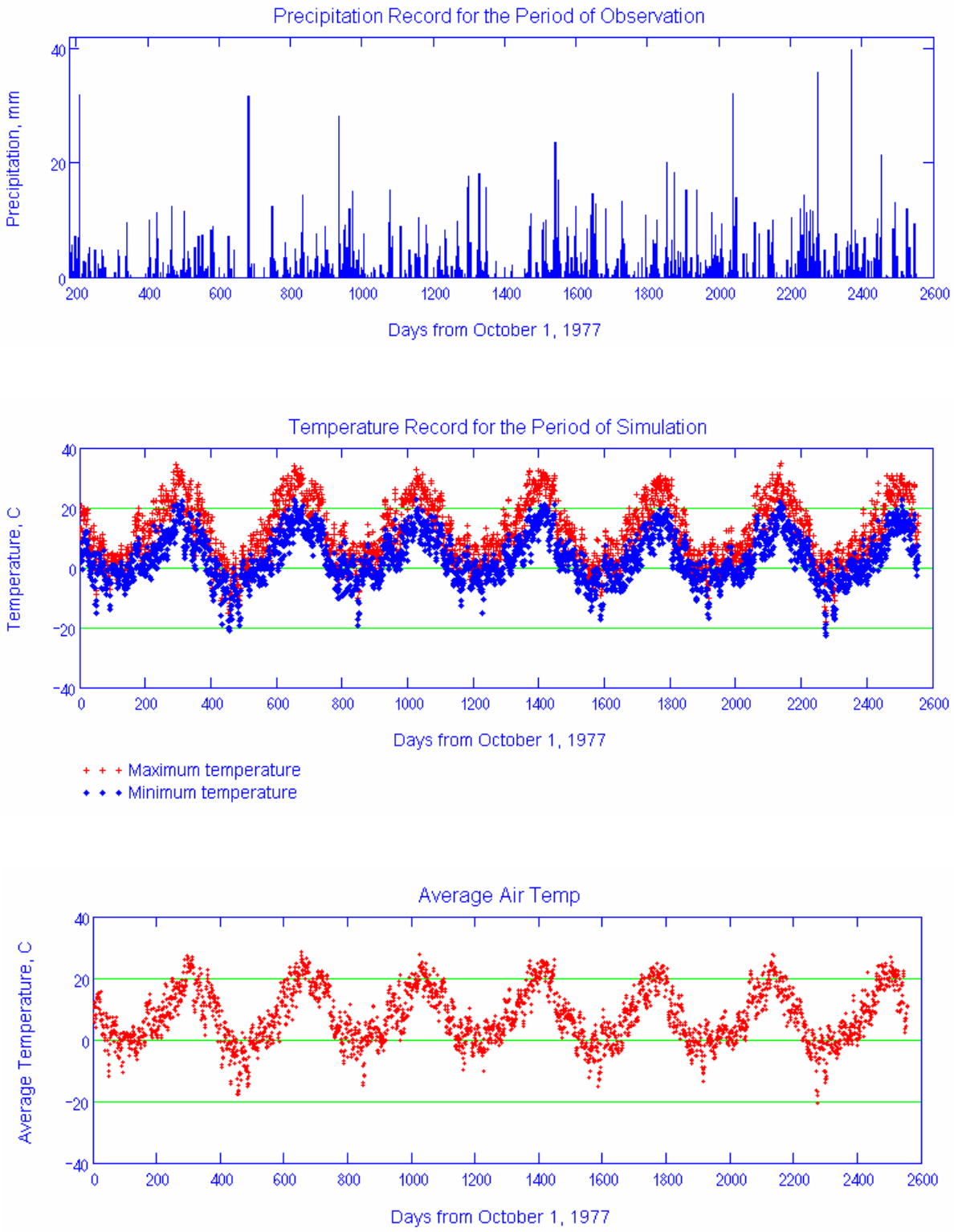

Source: Output DTN: SN0701T0502206.037, *\Welcome to Massif\Massif\Validation Analyses\Lysimeter\Reynolds Creek.xmcd*.

Figure J-17. Climate Data Plots for the RCEW Lysimeter Site Displayed by Reynolds Creek Interface

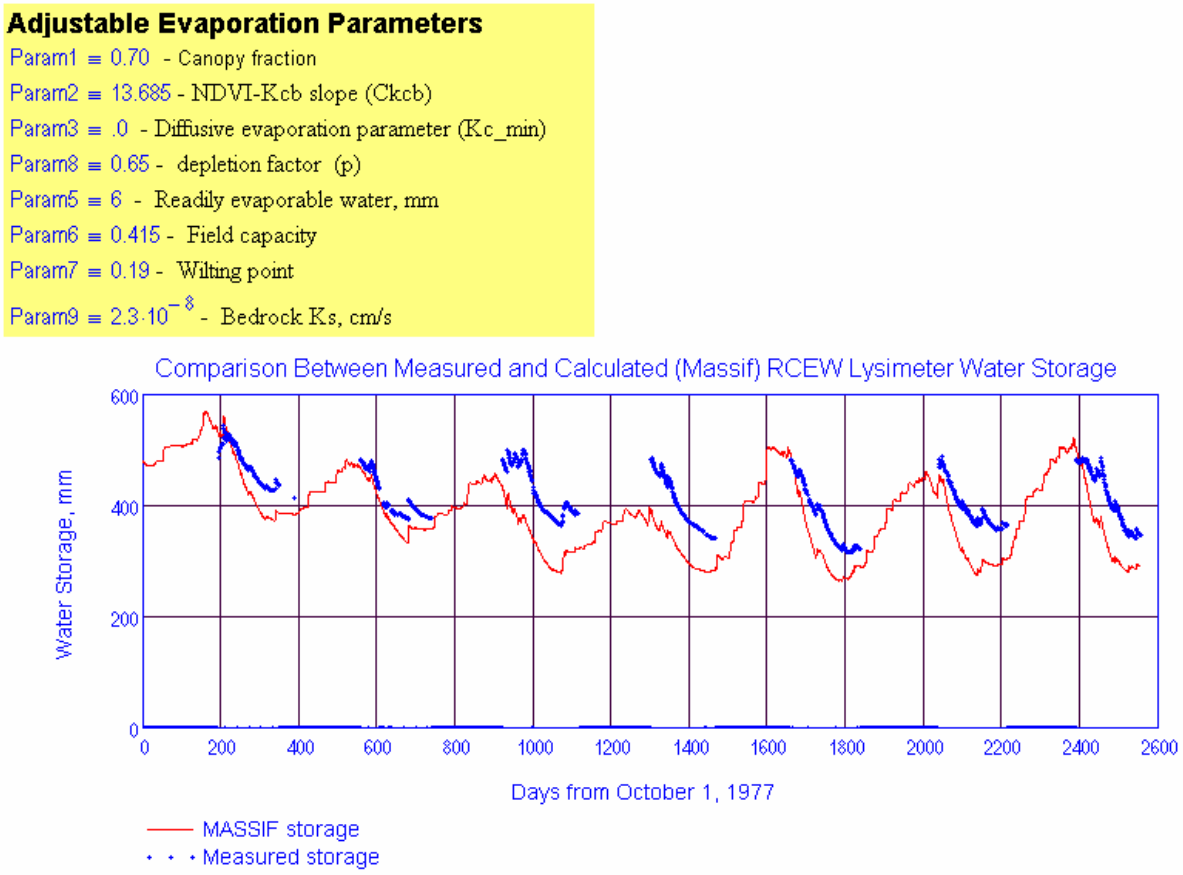

Source: Output DTN: SN0701T0502206.037, *\Welcome to Massif\Massif\Validation Analyses\Lysimeter\Reynolds Creek.xmcd*.

Figure J-18. Calculated versus Measured Lysimeter Storage Plot Displayed by Reynolds Creek Interface

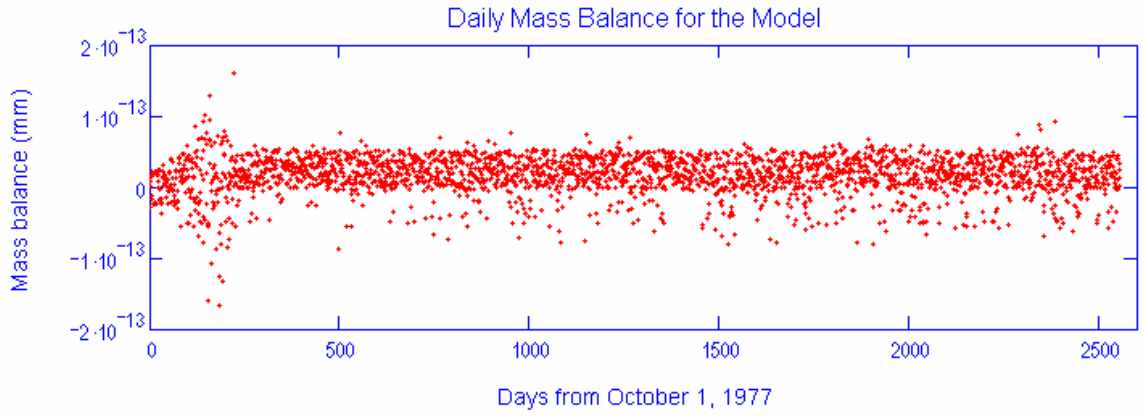

Source: Output DTN: SN0701T0502206.037, *\Welcome to Massif\Massif\Validation Analyses\Lysimeter\Reynolds Creek.xmcd*.

Figure J-19. Daily Mass Balance Displayed by Reynolds Creek Interface

The interface defines the optimization scheme in accordance with Equation 7.1.2-4. This includes the definition of the objective function and initial values and ranges for the parameters to be estimated. The optimization parameters are (see Section 7.1.2): diffusive evaporation parameter K_{c_min}, canopy fraction f_c, vegetation parameter C_{kcb}, and field capacity θ_f.

The interface runs the conjugate gradient minimization procedure, which is a built-in MathCAD function. The minimization procedure returns the values of the optimization scheme parameters that result in the minimum value of the objective function.

The interface reads an external Excel file ***Hydrus1D Data&Results*** that contains the HYDRUS-1D input data (including potential evapotranspiration) and modeling results (daily storage and infiltration). These data are in worksheet ***RCEW***.

The interface displays the reference evapotranspiration calculated by MASSIF and the potential evapotranspiration that is HYDRUS-1D input (boundary condition). An example is shown in Figure J-20.

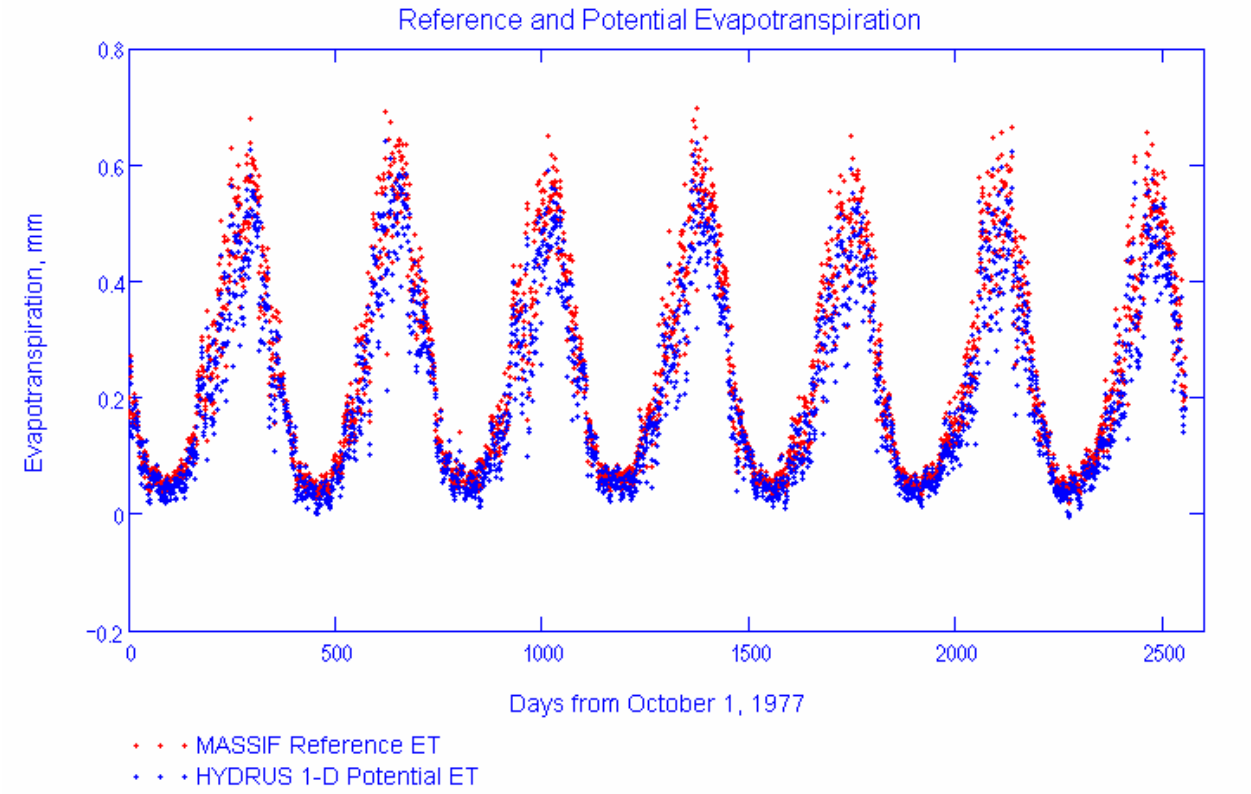

Source: Output DTN: SN0701T0502206.037, *\Welcome to Massif\Massif\Validation Analyses\Lysimeter\Reynolds Creek.xmcd*.

Figure J-20. Reference Evapotranspiration and Potential Evapotranspiration Displayed by Reynolds Creek Interface

The interface displays the observed lysimeter storage and lysimeter storage calculated with MASSIF and HYDRUS-1D as shown in Figure J-21.

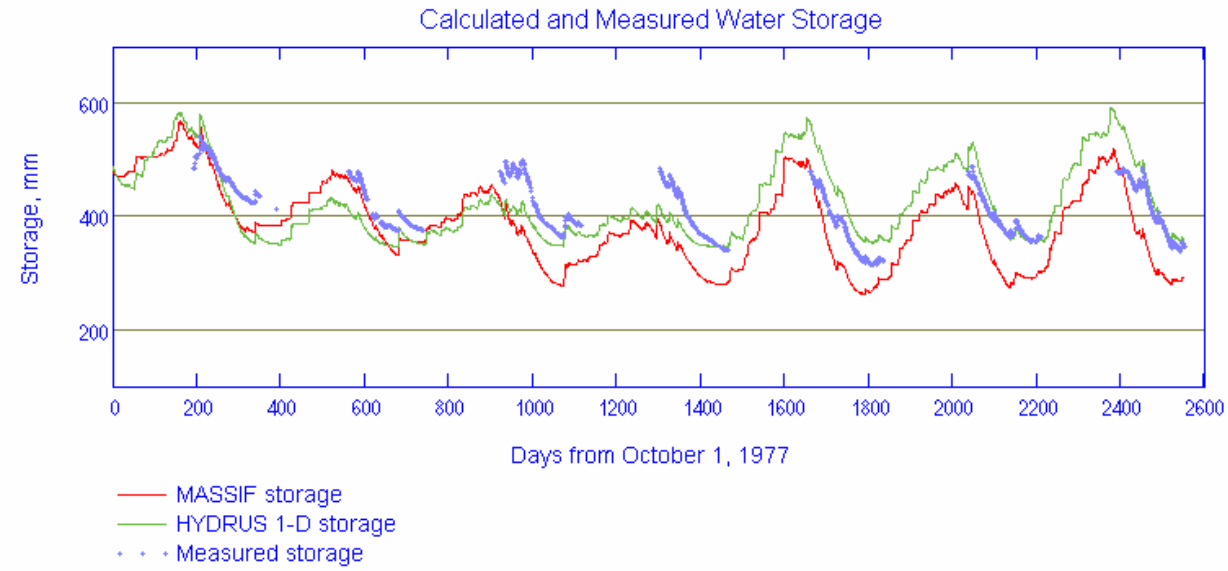

Source: Output DTN: SN0701T0502206.037, *\Welcome to Massif\Massif\Validation Analyses\Lysimeter\Reynolds Creek.xmcd*.

Figure J-21. Calculated and Measured Lysimeter Storage Displayed by Reynolds Creek Interface

The interface outputs the MASSIF daily storage and infiltration and the HYDRUS-1D daily storage and infiltration into an embedded Excel file to assist in further data processing and display. This file is used to generate Figure 7.1.2.2-2. The lysimeter storage measured in neutron probe 127707 is copied in this file from ***NP127707*** of ***RCEWLysimeter.xls (RCEW*** folder in Validation Output DTN: SN0607T0502206.016) to allow for comparison between the different measurements (lysimeter versus neutron probe).

The interface outputs the MASSIF daily actual evapotranspiration values into a built-in Excel file. These data are used within this file to calculate the average monthly rates of actual evapotranspiration for years 1978 and 1979 and to generate Figures 7.1.2.2-3 and 7.1.2.2-4 presented in Section 7.1.2. The file also contains the actual evapotranspiration data taken from Wight and Hanson (1990 [DIRS 177113]) needed to generate these figures. The spreadsheet ***RCEW Kcb*** in this built-in file contains calculations of daily K_{cb} values for the year 1978 through 1984, average annual K_{cb} values for the growing season (day 120 through 240), and average growing season K_{cb} value over the seven years of observations. The average growing season K_{cb} is compared to the data by Wight and Hanson (1990 [DIRS 177113]) in Section 7.1.2. These calculations use C_{kcb} value specified within the interface.

J2.4 HYDRUS-1D MODELING SETUP

All the input and output HYDRUS-1D files are in subdirectory ***RCEW_Homo*** in the ***HYDRUS_Model*** directory in ***RCEW*** folder in Validation Output DTN: SN0607T0502206.016. The input and output files in this subdirectory were created by running HYDRUS-1D file ***RCEW_homo.h1d*** located in the ***HYDRUS_Model*** directory. The HYDRUS-1D modeling setup is described below.

The simulated processes are water flow (including snow hydrology), heat transport, and root uptake. The depth of the soil profile is 122 cm. It is represented with 62 nodes. The first node is at the land surface (z=0 cm) and the last node is at the lysimeter bottom (122 cm). The nodes are 2 cm apart. The soil profile is homogeneous. The initial moisture content is 0.4 (see discussion above). The initial temperature is 6.1°C. The van Genuchten model in HYDRUS-1D is used to represent relationships between the saturation and pressure head and between the saturation and hydraulic conductivity. The soil parameters are (see Table J-1):

- saturated hydraulic conductivity is 18 cm/d
- van Genuchten parameter *alpha* is 0.014 1/cm
- pore connectivity parameter *l* is 0.5 Šimùnek et al. (2005 [DIRS 178140]) suggest leaving this parameter at its default value of 0.5.

The van Genuchten parameter *n*, saturated porosity, and residual porosity are adjusted during the simulations. These three parameters are found to have greatest impacts on the calculations. Note that the actual soil profile is heterogeneous, and the effective soil properties of the equivalent homogeneous profile are not known. Also, the saturated porosity, residual moisture content, and van Genuchten parameters *alpha* and *n* are not measured; they were estimated using HYDRYS-1D soil property database (see the discussion above). Consequently, the appropriate parameter values may be different from the corresponding weighted average values. Some small deviation from the parameter ranges defined in Table J-1 may be expected as well.

The upper boundary is an atmospheric boundary with specified potential evaporation, potential transpiration, precipitation, and temperature. The daily values of these parameters are defined for all the period of simulation (2557 days), which is from 10/01/77 to 09/30/84. The calculation of potential evapotranspiration is discussed above. The input data used in these calculations and the resulting potential evapotranspiration values are in worksheet ***Potential ET*** of ***RCEWLysimeter.xls (RCEW*** folder in Validation Output DTN: SN0607T0502206.016). The potential transpiration is assumed to be equal to 0.5 of the potential evapotranspiration, based on the vegetation cover of 0.5. The potential evaporation and transpiration values are copied into the built-in HYDRUS-1D time-dependent boundary condition spreadsheet. The daily precipitation, mean daily temperature, and daily temperature amplitude values were copied from ***Climate Data*** worksheet of ***RCEW_Lysimeter.xls (RCEW*** folder in Validation Output DTN: SN0607T0502206.016).

The lower boundary is defined as a seepage boundary for flow and as a zero gradient boundary for the heat transport. See the modeling setup for the NTS lysimeter for details concerning this boundary.

The root water uptake is considered throughout 122 cm of the soil profile. The roots are uniformly distributed within this depth. The Feddes model in HYDRUS-1D is used for the stress response function. The details concerning this function are provided above (see HYDRUS-1D modeling setup for the NTS lysimeters).

The parameters describing this function are taken from HYDRUS-1D database. The values for grass in this database are used. Grass is the closest equivalent to the vegetation at the lysimeter site found in HYDRUS-1D database. Also, the sensitivity analysis showed that the Feddes model parameters have little impact on the calculations. The parameter values are provided below.

- P_0 is −10 cm
- P_1 is −25 cm
- P_{2h} (under potential transpiration of 0.5 cm/day) is −300 cm (this value is not used in calculations since the maximum potential transpiration during the period of simulation was 0.32 cm/d)
- P_{2l} is −1,000 cm (under potential transpiration of 0.2 cm/day)
- P_3 is −15,000 cm.

The resulting water stress function is similar to one shown in Figure J-12.

A number of HYDRUS-1D simulations are performed to investigate the model sensitivity and to adjust three modeling parameters. The best fit (42.3 mm) was obtained using the saturated porosity of 0.5 m^3/m^3, residual moisture of 0.11 m^3/m^3, and van Genuchten n=1.15. These values are close to the corresponding values describing clay and clay loam layers (with saturated porosity 0.506 m^3/m^3, residual moisture content 0.081 m^3/m^3, and van Genuchten n=1.24). This means that the amount of water that can be stored in the clay and clay loam layers controls the lysimeter storage. The results of this simulation are presented in Section 7.1.2.

HYDRUS-1D input and output files (all these files are text files) for the final run are located in the subdirectory ***RCEW_Homo*** in the ***HYDRUS_Model*** directory in the ***RCEW*** folder in Validation Output DTN: SN0607T0502206.016. The input files have the extension *in* or *dat*. The output files have the extension *out*. The results presented in Section 7.1.2 are from the output file ***T_LEVEL.OUT***. This file provides the daily values of all the water balance components, including storage (column *"volume"*) and infiltration (column *"vBot"*) in cm. The storage and infiltration values are copied from this file into the ***HYDRUS1D Data&Results*** Excel file that is an external file read by the interface as explained above. The comparison of the HYDRUS-1D results and MASSIF results is performed within the interface.

APPENDIX K
SUPPORTING INFORMATION ON CORROBORATION OF INFILTRATION USING AN ALTERNATIVE MODEL APPROACH

Four net infiltration scenarios were implemented with both MASSIF and HYDRUS-1D models as a part of model corroboration of the MASSIF model. The intent of this corroboration exercise is to compare net infiltration predicted by MASSIF against that predicted by the alternative model, HYDRUS-1D using a representative set of input parameter values. The summary of this study is provided in Section 7.2.2. The details on the modeling setup and supporting calculations are described below.

The four scenarios (Models) represent one-dimensional homogeneous soil columns each with a different soil depth: 50 cm for Model 1, 100 cm for Model 2, 150 cm for Model 3, and 200 cm for Model 4. The soil parameters and the boundary and initial conditions considered are identical among the models. The plant rooting depth was assumed to be equal to the soil depth in each scenario. The simulations were performed for one water year (365 days).

K1. MASSIF INTERFACE *ALTERNATIVE* MODEL

An interface to MASSIF ***Alternative Model*** was designed specifically to implement the four conceptual models in consideration and to compare MASSIF and HYDRUS-1D results. The interface is supplied with the MASSIF package (Output DTN: SN0701T0502206.037). The interface performs the following functions described below.

The interface defines the following parameters:

- Site latitude is set equal to 36.8
- Site elevation is set equal to 1,000 m
- Soil saturated hydraulic conductivity is set equal to 6.82×10^{-5} cm/s
- Soil residual moisture content is set equal to 0.022 m^3/m^3
- Soil saturated porosity is set equal to 0.19 m^3/m^3
- Soil van Genuchten parameter *alpha* is set equal to 0.002 cm^{-1}
- Soil van Genuchten parameter *n* is set equal to 1.21.

The alternative model latitude is arbitrarily selected. The only condition considered is that it should be within the latitude range of the Yucca Mountain site. The elevation for each of the scenarios is set equal to reference elevation (1,000 m) to avoid needing to correct temperature and precipitation.

The residual moisture content and van Genuchten parameters *alpha* and *n* are not directly used in MASSIF calculations. They are used in the interface to calculate water contents at −1/3, −1/10, and −60 bars. These water contents are then used to define the field capacity and the wilting point as described below.

The interface calculates water content at −1/3, −1/10, and −60 bars using Equation J-1. The calculated field capacity at −1/3 bars is 0.173 m^3/m^3, at −1/10 bars is 0.184 m^3/m^3, and the wilting point at −60 bars is 0.083 m^3/m^3.

The interface reads the climate data from the built-in Excel file. The climate data includes precipitation, temperature, and wind speed. These data were copied from ***Weather Summary v2.1 for nominal of PD parameters.xls*** located in ***Present-Day Precipitation*** directory within

Validation Output DTN: SN0606T0502206.014. The climate data are for Set 4 (representative year 952) with the probability of occurrence equal to 0.02. Only one water year (365 days) is considered. Note that the actual source of this particular weather data is not important as long as the same weather data are used by both MASSIF and HYDRUS. Any one-year, representative set of weather data could have been used for this corroboration activity.

The interface displays the climate data for the period of observation as shown in Figure K-1.

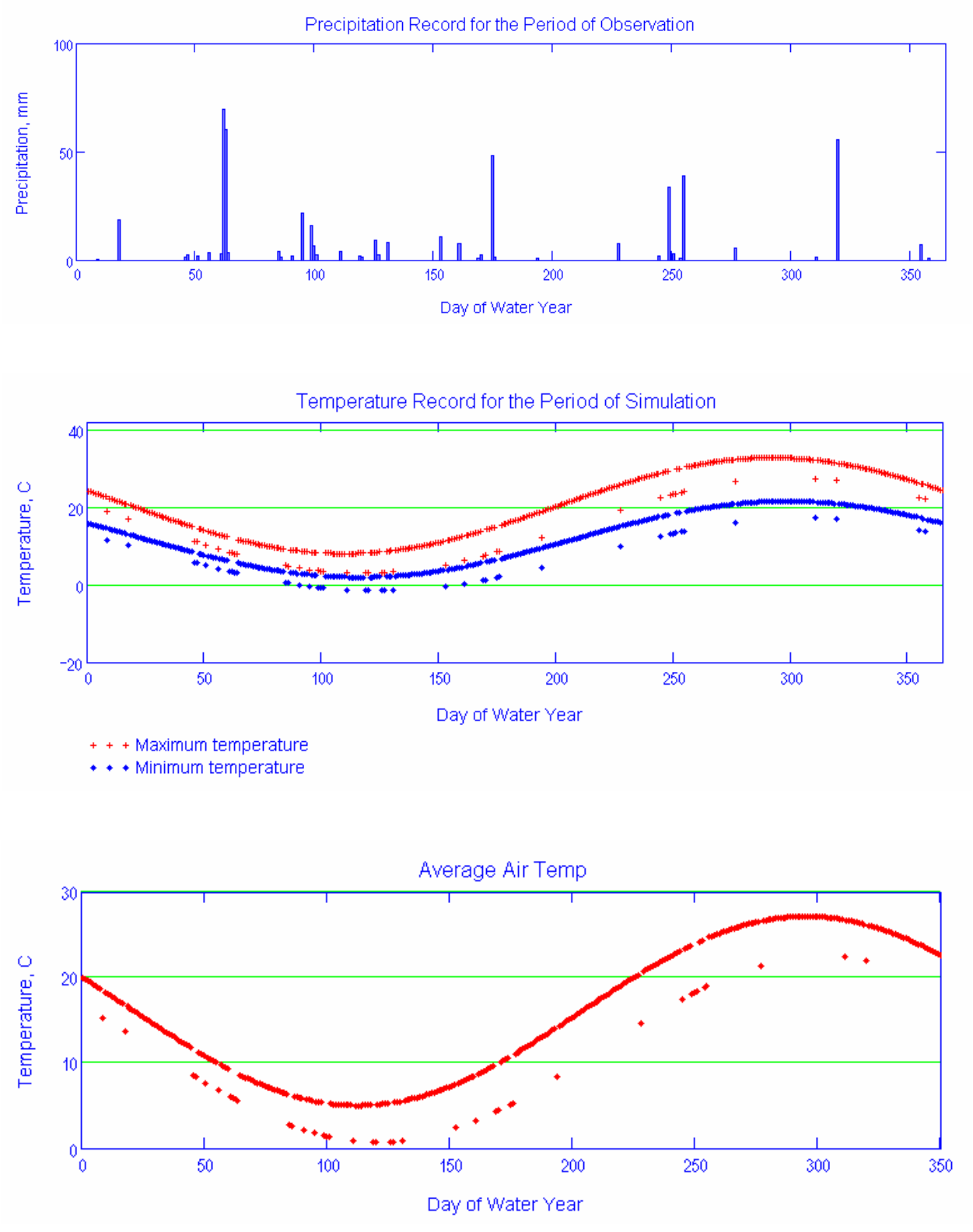

Source: Output DTN: SN0701T0502206.037, *\Welcome to Massif\Massif\Validation Analyses\Alternative Model\Alternative_Model.xmcd*.

Figure K-1. Climate Data Plots for the Alternative Model Site Displayed by Alternative Model Interface

The interface calculates the number of days with mean daily temperatures below freezing during this period of simulation. The number of these days is zero.

The interface reads the geospatial parameters from the external Excel file ***AM_location.csv***. The drainage basin defined for this simulation in this file consists of four cells. Cell 1 represents Model 1, Cell 2 represents Model 2, Cell 3 represents Model 3, and Cell 4 represents Model 4. All the parameters for these cells are the same, except for the soil depth class. The Soil Depth Class is set to Class 1 for cell 1, Class 2 for cell 2, Class 3 for cell 3, and Class 4 for cell 4. The soil type is set to Type 5, and the bedrock ID is set to 406. The corresponding properties are defined below in accordance with the properties of the alternative models. The slope angle is set to 0. The reference elevation is specified to be equal to the alternative model site elevation to avoid the correction of precipitation and temperatures by MASSIF. The downstream cell ID is set to −3 to exclude run-on to these cells. The potential vegetation response (PVR) is set equal to 1.

The following parameters are MASSIF default parameters for the Present-Day climate and are not redefined by the interface:

- Site albedo (0.22)
- Dew point and storm duration parameters
- Evaporation depth Z_e = 0.15 m
- Diffusive evaporation parameter K_{c_min} = 0
- Readily evaporable water parameter rew_1 = 6 mm
- Depletion factor parameter p = 0.65
- Plant height h_{plant} = 0.4 m
- K_{cb1} = −0.05 and K_{cb2} = 9.7.

The vegetation canopy fraction is set equal to 0.25.

The interface sets the initial moisture content in all layers equal to 0.08 m^3/m^3. This is an arbitrary value. The only condition used was that the moisture content at the beginning of the water year should be relatively low.

Soil porosity and hydraulic conductivity for Soil Type 5 are set equal to the values defined above. This redefines the values that MASSIF reads from the built-in look-up table with the soil properties for Soil Type 5, although the exact values for these parameters are not really important as long as the values used are identical to those used by HYDRUS-1D.

Hydraulic conductivity of bedrock was set equal to 1.13×10^{-6} m/s. This value is slightly different from the default value read by MASSIF (1.3×10^{-6} m/s); however it was set to be equal to what was used in the HYDRUS-1D runs.

Field capacity is set to the value defined at −1/10 bar above. Wilting point of Soil Type 5 is set equal to the value defined above. This redefines the values that MASSIF reads from the built-in look-up table with the soil properties for Soil Type 5, although the exact values for these parameters are not really important as long as the values used are identical to those used by HYDRUS-1D.

The interface reads the HYDRUS-1D results (daily storage and cumulative infiltration values in mm) for the four models. These results were copied to the built-in Excel file from ***Alternative_Model_Outputs.xls*** in Validation Output DTN: SN0609T0502206.022.

The interface defines the soil depth for each conceptual model and specifies the maximum rooting depth of 200 cm. Soil Depth Class 1 is redefined to be 50 cm, Soil Depth Class 2 is redefined to be 100 cm, Soil Depth Class 3 is redefined to be 150 cm, and the Soil Depth Class 4 is redefined to be 200 cm.

The interface runs MASSIF and stores the results of calculations for four alternative model cells. The interface calculates daily storage and daily cumulative infiltration values for each conceptual model, total annual values of the actual evapotranspiration, infiltration, and runoff, and change in storage over the one-year period. The interface calculates the mean root squared error between the daily storage calculated by MASSIF and HYDRUS-1D. The interface displays the results (daily storage and cumulative infiltration) as shown in Figures K-2 to K-5.

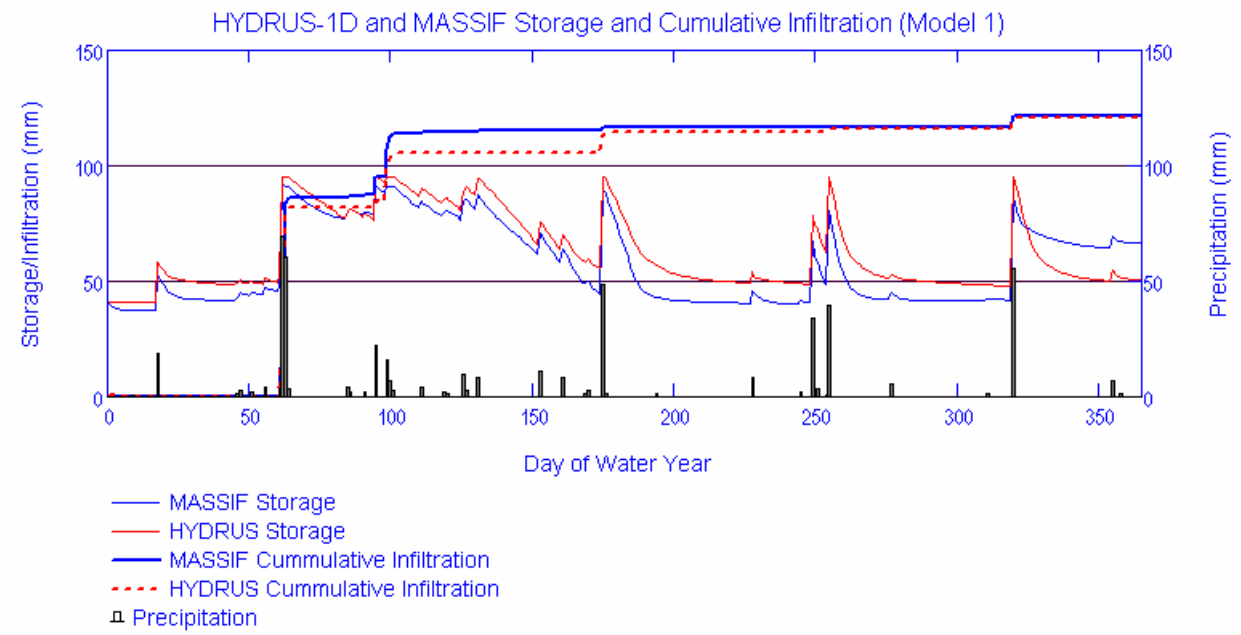

Source: Output DTN: SN0701T0502206.037, *\Welcome to Massif\Massif\Validation Analyses\Alternative Model\Alternative_Model.xmcd*.

Figure K-2. Results for Model 1 Displayed by the Alternative Model Interface

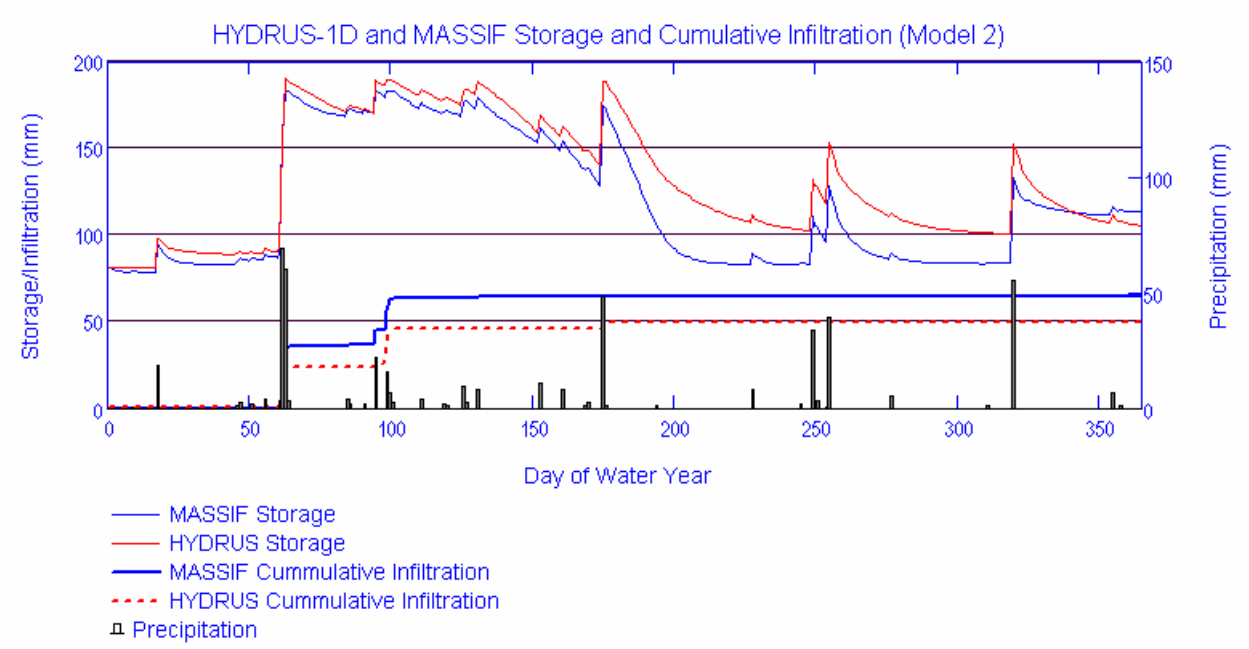

Source: Output DTN: SN0701T0502206.037, *\Welcome to Massif\Massif\Validation Analyses\Alternative Model\Alternative_Model.xmcd*.

Figure K-3. Results for Model 2 Displayed by the Interface *Alternative Model*

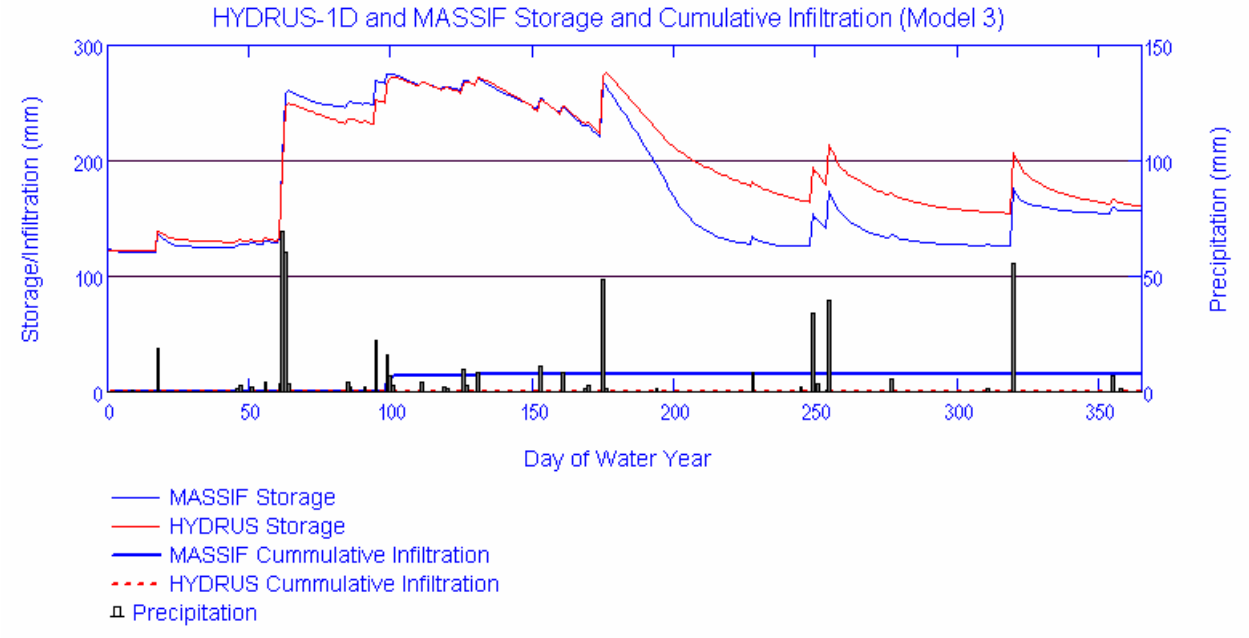

Source: Output DTN: SN0701T0502206.037, *\Welcome to Massif\Massif\Validation Analyses\Alternative Model\Alternative_Model.xmcd*.

Figure K-4. Results for Model 3 Displayed by the Alternative Model Interface

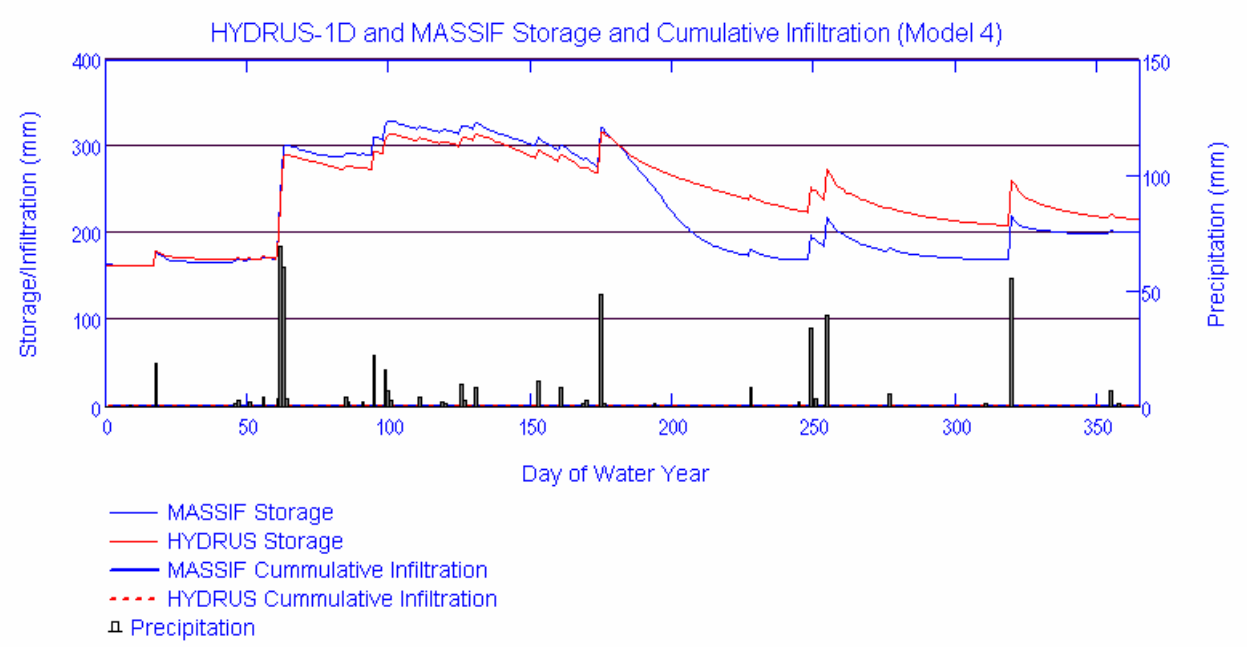

Source: Output DTN: SN0701T0502206.037, *\Welcome to Massif\Massif\Validation Analyses\Alternative Model\Alternative_Model.xmcd*.

Figure K-5. Results for Model 4 Displayed by the Alternative Model Interface

The interface outputs the daily storage and daily cumulative infiltration values for each conceptual model into the built-in Excel file. The interface outputs the total annual values of the actual evapotranspiration (MASSIF), infiltration (MASSIF and HYDRUS-1D), runoff (MASSIF), change in storage over the one-year period (MASSIF), and mean root square errors into the built-in Excel file. The interface displays the reference evapotranspiration calculated by MASSIF and potential evapotranspiration specified in HYDRUS-1D (see the HYDRUS-1D modeling setup below) as shown in Figure K-6.

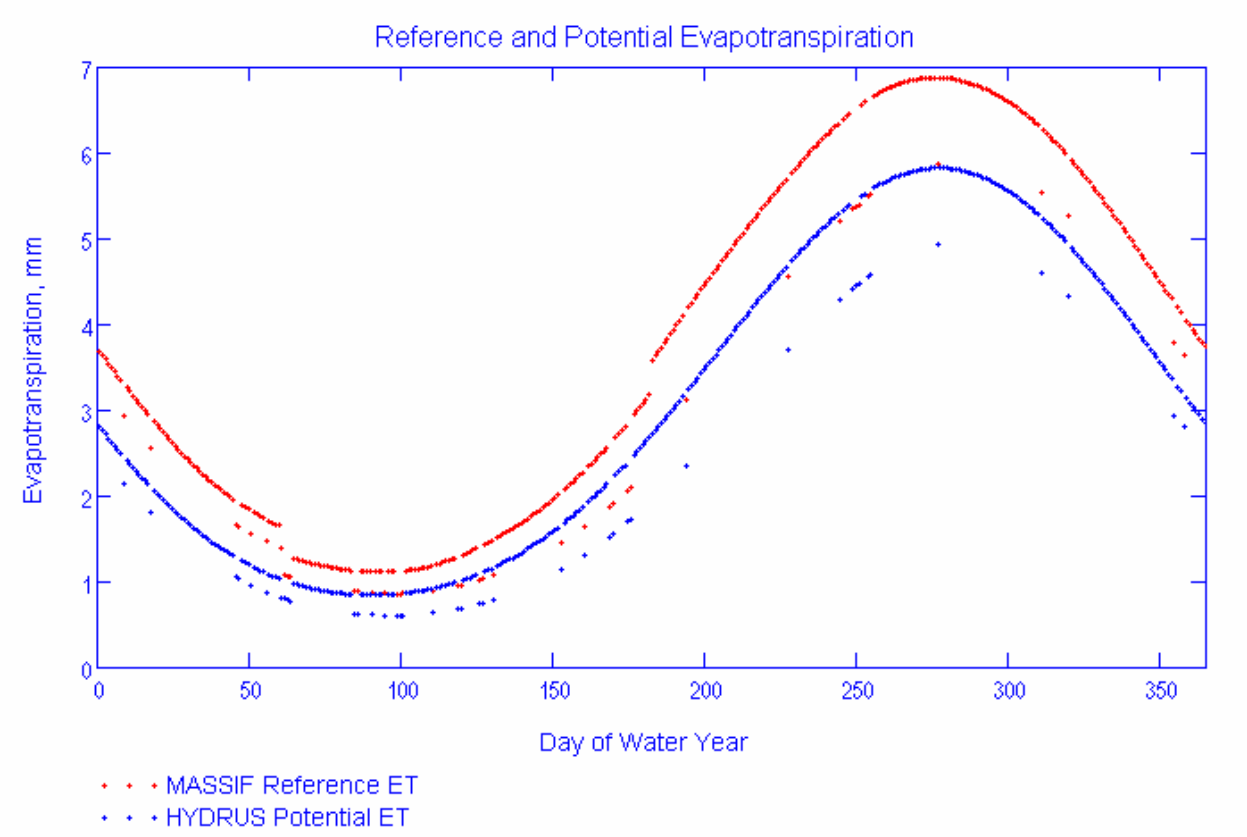

Source: Output DTN: SN0701T0502206.037, *Welcome to Massif\Massif\Validation Analyses\Alternative Model\Alternative_Model.xmcd*.

Figure K-6. Limiting Evapotranspiration Displayed by the Alternative Model Interface

K2. HYDRUS-1D MODELING SETUP

The MASSIF simulations were compared to the simulations performed using HYDRUS-1D code (Simunek et al. 2005 [DIRS 178140]). The HYDRUS-1D program numerically solves the Richards' equation for one-dimensional variably saturated water flow and heat and solute transport. A short description of HYDRUS-1D is provided in Section 6.2.4.1.

HYDRUS-1D was obtained from the Yucca Mountain Project Software Configuration Manager. The related communication and installation record are in the directory: /Alternative_Model_Inputs/HYDRUS_Gen (Validation Output DTN: SN0609T0502206.021).

All the input HYDRUS-1D files are provided in Validation Output DTN: SN0609T0502206.021. There are four subdirectories in this DTN in the main directory: "Alternative_Model_Inputs". Directory ***Alt_Model1*** contains all the input files for Model 1. These input files were created by running the HYDRUS-1D file ***Alt_Model1.h1d*** located in the main directory. Directory ***Alt_Model2*** contains all the input files for Model 2. These input files were created by running the HYDRUS-1D file ***Alt_Model2.h1d*** located in the main directory. Directory ***Alt_Model3*** contains all the input files for Model 3. These input files were created by running the HYDRUS-1D file ***Alt_Model3.h1d*** located in the main directory. Directory

Alt_Model4 contains all the input files for Model 4. These input files were created by running the HYDRUS-1D file ***Alt_Model4.h1d*** located in the main directory.

All the output HYDRUS-1D files are provided in Validation Output DTN: SN0609T0502206.022. There are four subdirectories in this DTN under the main directory: "Alternative_Model_Outputs". Directory ***Alt_Model1*** contains all the output files for Model 1. These output files were created by running the HYDRUS-1D file ***Alt_Model1.h1d*** located in the main directory. Directory ***Alt_Model2*** contains all the output files for Model 2. These output files were created by running the HYDRUS-1D file ***Alt_Model2.h1d*** located in the main directory. Directory ***Alt_Model3*** contains all the output files for Model 3. These output files were created by running the HYDRUS-1D file ***Alt_Model3.h1d*** located in the main directory. Directory ***Alt_Model4*** contains all the output files for Model 4. These output files were created by running the HYDRUS-1D file ***Alt_Model4.h1d*** located in the main directory.

The HYDRUS-1D modeling setup is described as follows and is the same in all four model scenarios.

The simulated process is water flow. The heat transport is not included since the mean daily temperature is above freezing during all the periods of simulation. The root uptake is simulated through the whole model depth. The roots are uniformly distributed within this depth. The Feddes model in HYDRUS-1D is used for the stress response function. The soil profile is homogeneous. The initial moisture content is 0.08 m^3/m^3. The van Genuchten model in HYDRUS-1D is used to represent relationships between the saturation and pressure head and between the saturation and hydraulic conductivity. The soil parameters are:

- Saturated hydraulic conductivity is 5.89 cm/d (6.82×10^{-5} cm/s)
- Saturated porosity is 0.19 m^3/m^3
- Residual moisture content is 0.022 m^3/m^3
- van Genuchten parameter *alpha* is 0.002 cm^{-1}
- van Genuchten parameter *n* is 1.21
- Pore connectivity parameter *l* is 0.5, Simunek et al. (2005 [DIRS 178140]) suggest leaving this parameter at its default value of 0.5.

The upper boundary is an atmospheric boundary with specified potential evaporation, potential transpiration, precipitation, and temperature. The daily values of these parameters are defined for all the period of simulation (365 days). The calculation of potential evapotranspiration is discussed in Appendix J. The input data used in these calculations and the resulting potential evapotranspiration values are in worksheet ***Potential ET*** of ***Alternative_Model_Inputs.xls*** in Validation Output DTN: SN0609T0502206.021. The potential transpiration is assumed to be equal to 0.25 of the potential evapotranspiration, based on the vegetation cover of 0.25. The potential evaporation and transpiration values are copied into the built-in HYDRUS-1D time-dependent boundary condition spreadsheet. The daily precipitation, mean daily

temperature, and daily temperature amplitude values were copied from ***Weather Summary v2.1 for nominal of PD parameters.xls*** located in directory ***Present-Day Precipitation***. The climate data are for Set 4 (representative year 952) with the probability of occurrence equal to 0.02. These are the same data that were used in MASSIF runs. The lower boundary is defined as a seepage boundary.

The depth of the soil profile in Model 1 is 50 cm. It is represented with 51 nodes. The first node is at the land surface (z = 0 cm) and the last node is at the bottom of the soil column (50 cm). The nodes are 1 cm apart. The depth of the soil profile in Model 2 is 100 cm. It is represented with 101 nodes. The first node is at the land surface (z = 0 cm) and the last node is at the bottom of the soil column (100 cm). The nodes are 1 cm apart. The depth of the soil profile in Model 3 is 150 cm. It is represented with 151 nodes. The first node is at the land surface (z = 0 cm) and the last node is at the bottom of the soil column (150 cm). The nodes are 1 cm apart. The depth of the soil profile in Model 4 is 200 cm. It is represented with 101 nodes. The first node is at the land surface (z = 0 cm) and the last node is at the bottom of the soil column (200 cm). The nodes are 2-cm apart.

HYDRUS-1D output files (all these files are text files) in Validation Output DTN: SN0609T0502206.022 have the extension *out*. The results presented in Section 7.2.2 are from the output file ***T_LEVEL.OUT***. Each of four directories has a file with this name. This file provides the daily values of all the water balance components, including storage (column *"volume"*) and infiltration (column *"vBot"*) in cm. The storage and infiltration values were copied from these files into ***Alternative_Model_Outputs.xls*** located in the main directory of Validation Output DTN: SN0609T0502206.022 and into the built-in Excel file in ***Alternative Model*** interface. The comparison of the HYDRUS-1D results and MASSIF results is performed within the interface.

APPENDIX L
PRELIMINARY RESULTS AND OUTPUTS

L.1 PRELIMINARY OUTPUT DATA TRACKING

This appendix documents a number of preliminary unqualified DTNs that contain preliminary model results. Several minor problems were identified with the inputs used to generate these results (documented in CR 9580); therefore, these results are not considered the qualified technical product output of this report. These preliminary results remain in TDMS because an effort is being made to qualify these results in a separate data qualification report per SCI-PRO-001. This report will include an impact assessment between the final technical output and the preliminary output. Initial evaluations have shown minimal impact to the downstream users of the preliminary infiltration results.

Table L-1. List of Preliminary Output DTNs Not Qualified by This Report

DTN Title	Preliminary DTN (NOT Qualified in this Report)	Qualified Output DTN (FINAL)
Calculated Weather Summary for Monsoon Climate	SN0609T0502206.025	SN0701T0502206.041
Calculated Weather Summary for Present-Day Climate	SN0609T0502206.026	SN0701T0502206.040
Calculated Weather Summary for Glacial Transition Climate	SN0609T0502206.027	SN0701T0502206.042
Latin Hypercube Sample (LHS) Input and Output Files for MASSIF Calculation of Net Infiltration at Yucca Mountain	SN0610T0502206.033	SN0701T0502206.043
Monsoon Net Infiltration Results	SN0609T0502206.024	SN0701T0502206.036
Present-Day Net Infiltration Results	SN0609T0502206.028	SN0701T0502206.034
Glacial Transition Net Infiltration Results	SN0609T0502206.029	SN0701T0502206.035
MASSIF Calculation of Net Infiltration at Yucca Mountain	SN0610T0502206.032	SN0701T0502206.037

INTENTIONALLY LEFT BLANK